Lecture Notes in Electrical Engineering 585

Yusheng Xue
Yuping Zheng
Saifur Rahman *Editors*

Proceedings of PURPLE MOUNTAIN FORUM 2019-International Forum on Smart Grid Protection and Control

Volume II

Springer

Lecture Notes in Electrical Engineering

Volume 585

Series Editors

The book series *Lecture Notes in Electrical Engineering* (LNEE) publishes the latest developments in Electrical Engineering - quickly, informally and in high quality. While original research reported in proceedings and monographs has traditionally formed the core of LNEE, we also encourage authors to submit books devoted to supporting student education and professional training in the various fields and applications areas of electrical engineering. The series cover classical and emerging topics concerning:

- Communication Engineering, Information Theory and Networks
- Electronics Engineering and Microelectronics
- Signal, Image and Speech Processing
- Wireless and Mobile Communication
- Circuits and Systems
- Energy Systems, Power Electronics and Electrical Machines
- Electro-optical Engineering
- Instrumentation Engineering
- Avionics Engineering
- Control Systems
- Internet-of-Things and Cybersecurity
- Biomedical Devices, MEMS and NEMS

For general information about this book series, comments or suggestions, please contact leontina.dicecco@springer.com.

To submit a proposal or request further information, please contact the Publishing Editor in your country:

China

Jasmine Dou, Associate Editor (jasmine.dou@springer.com)

India

Swati Meherishi, Executive Editor (swati.meherishi@springer.com)
Aninda Bose, Senior Editor (aninda.bose@springer.com)

Japan

Takeyuki Yonezawa, Editorial Director (takeyuki.yonezawa@springer.com)

South Korea

Smith (Ahram) Chae, Editor (smith.chae@springer.com)

Southeast Asia

Ramesh Nath Premnath, Editor (ramesh.premnath@springer.com)

USA, Canada:

Michael Luby, Senior Editor (michael.luby@springer.com)

All other Countries:

Leontina Di Cecco, Senior Editor (leontina.dicecco@springer.com)
Christoph Baumann, Executive Editor (christoph.baumann@springer.com)

**** Indexing: The books of this series are submitted to ISI Proceedings, EI-Compendex, SCOPUS, MetaPress, Web of Science and Springerlink ****

More information about this series at http://www.springer.com/series/7818

Yusheng Xue · Yuping Zheng ·
Saifur Rahman
Editors

Proceedings of PURPLE MOUNTAIN FORUM 2019-International Forum on Smart Grid Protection and Control

Volume II

Springer

Editors
Yusheng Xue
State Grid Electric Power Research Institute
Nanjing, Jiangsu, China

Yuping Zheng
NARI Group Corporation
Nanjing, Jiangsu, China

Saifur Rahman
Advanced Research Institute, Virginia Tech
Arlington, VA, USA

ISSN 1876-1100 ISSN 1876-1119 (electronic)
Lecture Notes in Electrical Engineering
ISBN 978-981-13-9782-0 ISBN 978-981-13-9783-7 (eBook)
https://doi.org/10.1007/978-981-13-9783-7

This Springer imprint is published by the registered company Springer Nature Singapore Pte Ltd.
The registered company address is: 152 Beach Road, #21-01/04 Gateway East, Singapore 189721, Singapore

Preface

Preface of International Seminar Paper Collection

Vigorous development of renewable energy has become a global consensus, which is also one of the symbolic features in the development of smart grid. The most essential characteristics of smart grid include: the two-way flow between power and information, and a highly automatic and widely distributed energy exchange network built based on that; the advantages of distributed computation and communication are introduced to the power grid to realize real-time information exchange and nearly instant supply–demand balance on the equipment level.

As renewable energy with high randomness, intermittence, and fluctuation is connected to the power system, with the fast increase in the permeability of power electronic devices, it has brought significant challenges to the dynamic balance of power, safety, and stability of grid. Many important challenges need to be addressed in order to realize positive interaction of multi-energy system and the comprehensive and efficiency utilization of various resources. These challenges involve many technological, system, and social issues. For example, the infrastructure requires extension, upgrade, and development; the security of computer network needs to be guaranteed; standard protocol for multi-system integration should be formulated; the load and power plan requires more accurate arrangement and scheduling; the potential of data sharing and information application needs to be further explored; the perception of the momentum of energy system should be further strengthened, so that the power market can be further opened; new regulations that can motivate investment in smart grid should be stipulated and issued soon; a permanent subject for future power development is to improve the reliability and flexibility of power grid, increase the energy utilization efficiency, and realize positive interaction with the user. In order to realize these goals, interdisciplinary cooperation is a necessary choice, while the legal framework and supervision, market design, and management reform are the basic guarantees for successful implementation of smart grid and to obtain necessary benefits.

With the publication of *The Third Industrial Revolution* written by the American scholar Jeremy Rifkin in 2011, the Energy Internet emerged with the arrival of the era of renewable energy. Based on the Internet thinking, the Energy Internet can be realized through the utilization of distributed energy, and the development of smart grid enters the 2.0 period. In order to realize the Energy Internet, in addition to the traditional power system control and dispatching technology, the development and utilization of energy transformation and comprehensive utilization technology, ICT technology, power electronics technology, data interface technology, energy storage technology, and Internet business mechanism are also indispensable. In 2019, the State Grid Corporation of China proposed the grand strategy to build "Three-Type and Two-Network." On the one hand, build and manage a strong smart grid with extra-high voltage as backbone network frame and coordinated development of power grid on various levels; on the other hand, fully utilize modern information technology and modern communication technology (such as the mobile Internet and artificial intelligence) to realize mutual connection between various links of power system and man–machine interaction, and build a universal power Internet of things (IoT) with comprehensive state perception, efficient information processing, and convenient and flexible application. After the goal of "three types and two networks" is realized, it will definitely bring subversive reform to the electrical energy industry.

"Purple Mountain Forum" is an international seminar co-sponsored by NARI Group Corporation and State Key Laboratory of Smart Grid Protection and Control under the major background of energy reform, which aims to promote the academic exchange and competition for technological development of power under the big energy background. This seminar is the fourth international seminar of "Purple Mountain Forum" academic forum, which will be held in Nanjing, China, from August 17 to August 18, 2019. More than 500 people attend the seminar, including the invited experts, copywriters, and common attendees. The attendees have in-depth discussion on related key technologies involved in the construction of smart grid, Energy Internet, and universal power IoT, including the AC/DC flexible power transmission and transformation technology, planning, operating and control technology for comprehensive energy system, application of new technologies (such as big data, cloud computing, IoT, mobile Internet, artificial intelligence) in smart grid, intelligent monitoring, related operation and maintenance technology, standard technical system for power grid, and related research direction.

Many papers are collected from the seminar, which is very inspiring. After strict editing and peer review, 169 papers are selected in the Seminar Paper Collection. Many innovative concepts, ideas, and methods have been proposed. We collect these results in a book to share with more colleagues in the industry.

The members of the editorial team appreciate all writers, review experts, organizing committee members, and seminar chairman who have contributed to this collection. Thank you for your selfless sharing and your concern with and attention to the quality of the publication.

Nanjing, China Yusheng Xue
Nanjing, China Yuping Zheng
Arlington, USA Saifur Rahman

Contents

Planning, Operation and Control of Integrated Energy Systems

Analysis and Suppression Strategy of Sub-synchronous Oscillation for Wind-Thermal-Bundled Power Transmitted by Series-Compensated System

Asaah Philip, Yushuo Zhang, Lili Hao, Yantong Zhou and Wei Li

Abstract Large-capacity wind farms may increase the risk of torsional vibration of turbine generator shafts in the wind-thermal-bundled power transmitted by series-compensated system, therefore the analysis and suppression strategy of sub-synchronous oscillation (SSO) in such system needs to be thoroughly studied. In this paper, the mechanism of electromechanical torsional interaction and the influence of wind farm integration on system oscillation are analyzed. In order to suppress the SSO, the mechanism of electromagnetic torque increment produced by additional damping control of static synchronous compensator (STATCOM) is studies, based on which, a SSO damping controller is designed. Based on the complex torque coefficient approach and time domain simulation approach simulation cases are built in DIgSILENT/PowerFactory. The results show the impact of wind farm integration and series compensation degree on system damping and verify the suppression effect of STATCOM on system SSO.

Keywords Wind-thermal-bundled system · Sub-synchronous oscillation (SSO) · Series compensation degree · Electromechanical torsional interaction · Additional damping control · Static synchronous compensator (STATCOM) · Complex torque coefficient approach

A. Philip · Y. Zhang · L. Hao (✉) · Y. Zhou
Nanjing Tech University, Nanjing 211816, China
e-mail: lili_hao@163.com

A. Philip
e-mail: asaahphilip@yahoo.com

Y. Zhang
e-mail: 1160752979@qq.com

Y. Zhou
e-mail: 171275008@qq.com

W. Li
NARI Group Corporation, State Key Laboratory of Smart Grid Protection and Control, Nanjing 211106, China
e-mail: 1808249046@qq.com

Y. Xue et al. (eds.), *Proceedings of PURPLE MOUNTAIN FORUM 2019-International Forum on Smart Grid Protection and Control*, Lecture Notes in Electrical Engineering 585, https://doi.org/10.1007/978-981-13-9783-7_1

1 Introduction

In order to improve the consumptive ability of wind power and make full use of the existing transmission channels, combining thermal generators and wind turbine generators is an effective transportation way [1–3]. In order to further improve the transmission capacity of the line and enhance the stability of the power grid, capacitor series compensation is often adopted for transmission lines. However, the excessive capacity of the series compensator may cause the SSO of the shaft system, which will cause rupture of the shaft in serious case, and then threaten the safety of the system [4]. Since the wind farm integration and series compensation degree of transmission lines will affect SSO, it is necessary to study the torsional vibration law of the shaft system, so as to effectively suppress the SSO and ensure the safe and stable operation of the power system.

The researches of wind-thermal-bundled system at home and abroad are mainly focused on transient stability, the operation characteristics and control strategies [5]. Some literatures have studied the influence of wind farm integration on SSO of the turbine generator. Literature [6] took the first IEEE SSO benchmark model with a doubly-fed induction generator (DFIG) as an example and established the mathematical model for small signal stability analysis, found that the damping ratio of the SSO mode decreases and the system damping decreases along with the increase of active output of wind farm. Literature [7, 8] built the transfer function between the output power of the wind farm and the rotational speed of the thermal power unit, and deduced the influence of active and reactive power of DFIG on system damping respectively, then proposed the conditions which can provide positive damping to the system. Because the additional damping control signal used is superimposed on the outer loop of the double-closed-loop control of the wind turbine, it is easy to create the oscillation of wind turbines. Based on the first IEEE SSO benchmark model connected with DFIG, literature [9] adopted eigenvalue method and time domain simulation method to analyze the wind farm influence on the thermal power units. Literature [10] established a typical model of wind-thermal-bundled system via DC system and analyzed the SSO mechanism, results showed that DFIG can alleviate the SSO caused by DC transmission. Current researches mostly focus on the impact of wind power access capacity on system oscillations and rarely consider the effect of line complement compensation. Most of the researches qualitatively discuss the suppression effect on sub-synchronous oscillations using time domain simulation, while few studies carry out the quantitative comparison of the system damping before and after the implement of suppression strategy, which may impede the display of suppression effect on the SSO of specific frequencies.

This paper analyzes the SSO mechanism of wind-thermal-bundled system via series compensation lines, introduces the basic principle of the complex torque coefficient approach, and studies the rules of electromagnetic torque increment produced by additional damping control of STATCOM and designs a SSO damping controller. The complex torque coefficient approach is used to analyze the influence of the series compensation on the electrical damping coefficient of the

system using the first IEEE SSO benchmark model combined with DFIG. Based on the DIgSILENT simulation platform, a typical system model of wind-thermal-bundled power transmitted by series-compensated lines is built, and the complex torque coefficient approach is used to analyze the influence of the series compensation on the electrical damping coefficient of the system, and the system short circuit test is used to verify it executed. Then the system electrical damping characteristic curve is compared before and after the STATCOM added, and the SSO suppression effect of the SSO is verified by the electromagnetic torque responses of thermal generator and wind turbine generators.

2 Mechanism Analysis of SSO for Wind-Thermal-Bundled Power Transmitted by Series-Compensated System

The serial access of a fixed capacitor in a line may lead to the interaction of electrical and mechanical systems, which may cause the instability of the generator shafting, and this phenomenon is called electromechanical torsional interaction [11, 12]. For electrical systems, the electrical system is stable if the total system damping is positive at the resonance frequency. For the shaft system of generators, the mechanical system is stable when the generator is not connected to power grid because of the existence of positive mechanical damping of the shafting, but when the generator is connected to the grid, if a tiny oscillation $\Delta\omega$ whose frequency is f_m appears on the rotor, the voltage and current components whose frequency are $f_0 - f_m$ and $f_0 + f_m$ respectively will be generated on the stator winding (f_0 is the power frequency). If f_m happens to be a shafting torsional vibration frequency, and it is complementary to the electrical resonance frequency f_e (that is, $f_0 = f_m + f_e$), the electrical and mechanical systems will interact with each other. The electromagnetic torque generated by the sub-synchronous current may be in phase with the rotor oscillation $\Delta\omega$, which may drive the amplitude of the oscillation $\Delta\omega$ increase. If the system damping is too small to prevent such torsional vibration interaction, the generator shaft system may be destroyed.

Researches show that neither the SSO modes nor their frequencies will be changed after the wind farm integration, but the system damping will be reduced. Because of the electromechanical torsional interaction in thermal power unit and the current disturbance in series compensation line, the SSO current component in the DFIG rotor winding is caused by magnetomotive equilibrium, and the current component will also induce the current component of the same resonance frequency in the stator winding because of the rotor magnetic field, which will further enhance the original disturbance and reduce the system damping.

3 Sub-synchronous Oscillation Suppression Using STATCOM

When the electrical distance between STATCOM and generator is small, the output voltage and current of the generator can be adjusted slightly by adjusting the reactive power output of STATCOM, so an electromagnetic torque increment can be produced in the steady-state electromagnetic torque of the generator shaft system. When the frequency and phase of the electromagnetic torque increment are suitable, the SSO can be suppressed. That is to say, the SSO can be suppressed by the fast continuous adjustment ability of STATCOM reactive power.

An important characteristic of shafting torsional vibration is the oscillation of generator shafting on the basis of synchronous speed. Intuitively, when the generator is accelerated, STATCOM increases its output of inductive reactive power, raises the output voltage and power of generator, also increases the electromagnetic torque, and for a constant mechanical torque input, the increment of electromagnetic torque makes the rotor decelerate; when the generator speed is slows down, STATCOM reduces its output of inductive reactive power, decreases the output voltage and power of the generator, then also reducing the electromagnetic torque, and for a constant mechanical torque input, the reduction of electromagnetic torque makes the rotor accelerate. If SSO occurs, STATCOM can response quickly to the torsional vibration of the turbine shaft system and suppress SSO.

The frequency complementary relationship between electrical quantity and electromagnetic torque increment in the damping control process is further analyzed. Assuming that the unit has a torsional vibration of ω_m in the shaft system, so the rotor speed of the unit is the sum of synchronous speed ω_0 and a torsional vibration ω_m. Only considering the reactive current component of the sub-synchronous frequency, the frequency components of the current between STATCOM and system are mainly sub-synchronous and hyper-synchronous components whose frequencies are $\omega_0 \pm \omega_m$

$$\begin{cases} \Delta i_a = A_m \sin(\omega_0 - \omega_m)t + A_m \sin(\omega_0 + \omega_m)t \\ \Delta i_b = A_m \sin\left[(\omega_0 - \omega_m)t - \frac{2}{3}\pi\right] + A_m \sin\left[(\omega_0 + \omega_m)t - \frac{2}{3}\pi\right] \\ \Delta i_c = A_m \sin\left[(\omega_0 - \omega_m)t + \frac{2}{3}\pi\right] + A_m \sin\left[(\omega_0 + \omega_m)t + \frac{2}{3}\pi\right] \end{cases} \quad (1)$$

After Park transformation

$$\begin{bmatrix} \Delta i_d \\ \Delta i_q \\ \Delta i_0 \end{bmatrix} = \frac{2}{3} \begin{bmatrix} \cos \omega t & \cos(\omega t - 2\pi/3) & \cos(\omega t + 2\pi/3) \\ -\sin \omega t & -\sin(\omega t - 2\pi/3) & -\sin(\omega t + 2\pi/3) \\ 0.5 & 0.5 & 0.5 \end{bmatrix} \begin{bmatrix} \Delta i_a \\ \Delta i_b \\ \Delta i_c \end{bmatrix} = \begin{bmatrix} 0 \\ -2A_m \cos \omega_m t \\ 0 \end{bmatrix} \tag{2}$$

When the torsional vibration occurs, the electromagnetic torque increment in the shaft system is mainly composed of two parts: one is caused by the interaction between the main flux of the generator and the current component of sub-synchronous frequency, and the other one is caused by the interaction of the magnetic field produced by the sub-synchronous frequency current component and the stator circuit current. Since the amplitude of the shafting torsional vibration speed is very small relatively to the synchronous speed, the magnetic field produced by the sub-synchronous current component is very weak relative to the main flux of the generator, the magnetic flux produced by the sub-synchronous current component can be ignored, and the main magnetic flux is still a stable magnetic field. The increment of electromagnetic torque generated by STATCOM additional damping control on the generator shafting is as follows

$$\Delta T_e = \psi_d \Delta i_q - \psi_q \Delta i_d = -2\psi_d A_m \cos \omega_m t \tag{3}$$

It can be seen that the additional damping control of STATCOM will produce an electromagnetic torque increment whose frequency is ω_m, which is the same as the frequency of the torsional vibration. When the phase of the torque increment is suitable, the shafting torsional vibration can be suppressed.

The reason for the generator torsional vibration is that the phase difference between the generator angular frequency deviation $\Delta\dot{\omega}$ and the electromagnetic torque variation $\Delta\dot{T}_e$ is more than 90°. In this paper, the generator angular frequency deviation $\Delta\omega$ is used as the input signal, after appropriate proportional amplification and phase shift, the output signal provides an additional electromagnetic torque $\Delta\dot{T}_e$ through the double-loop control loop, which makes the phase difference between the total electromagnetic torque variation $\Delta\dot{T}_e$ and the generator angular frequency deviation $\Delta\omega$ within 90°, and the system will eventually have a positive damping torque. Their phase relation is shown in Fig. 1.

Figure 2 is the structure diagram of the STATCOM damping controller. The generator angular frequency deviation $\Delta\omega$ is used as the input signal of additional damping control. Using the modal separation filter, each modal speed signal can be separated from the generator rotor speed deviation. The STATCOM reactive instruction ΔV_{aci} for restraining the torsional vibration of each mode can be obtained through the appropriate proportional amplification and phase compensation for each modal speed signal. The whole reactive instruction ΔV_{ac} for SSO

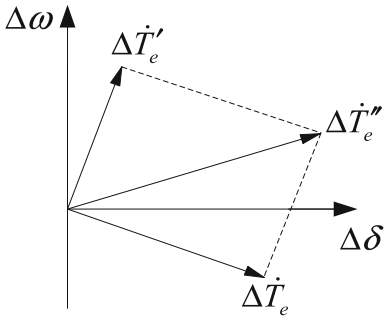

Fig. 1 The phase diagram of the additional electromagnetic torque and angular variation

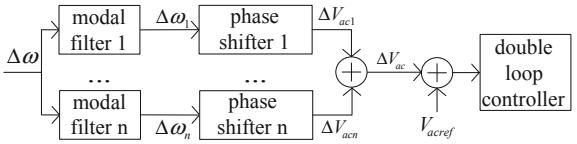

Fig. 2 The block diagram of STATCOM sub-synchronous damping controller

suppressing can be obtained by adding all the reactive instructions above. The final reactive power instruction is the sum of ΔV_{ac} and the reactive power instruction in steady state control mode, and the series switch signals of the STATCOM converter are generated by trigger control.

The phase compensation is the most critical step in STATCOM design, which directly affects the ability of STATCOM to suppress SSO. If the parameter selection is not appropriate, it may make STATCOM not only impossible to inhibit but also stimulate the SSO. The STATCOM uses the lead-lag stages for phase compensation such as $((1+sT_1)/(1+sT_2))^N$. N is the number of the lead-lag stages. The calculation method of its time constant T_1 and T_2 is as follows

$$\begin{cases} \alpha = \dfrac{T_2}{T_1} = \dfrac{1-\sin\varphi}{1+\sin\varphi} \\ \omega = 2\pi f \\ T_1 = \dfrac{1}{\omega\sqrt{\alpha}} \\ T_2 = \alpha T_1 \end{cases} \tag{4}$$

where f: the central frequency of the lead-lag stages, and φ: the compensation angle provided by the lead-lag stage at the center frequency. The central frequency can usually be selected according to the frequency of the oscillating mode to be compensated. If there are multiple oscillation modes in the system need to be compensated, the dominant mode with the weakest damping is generally chosen. According to the STATCOM controller structure, the phase to be compensated is the sum of the phase shift of modal filter and the link from STATCOM constant AC voltage controller to generator electromagnetic torque. Among them, the transfer

function of the link from STATCOM constant AC voltage controller to generator electromagnetic torque is difficult to be obtained by analytic method. In this paper, the lagging phase of this link will be obtained by the test signal method. The steps are as follows: a series of small AC voltage oscillation ΔV_{aci} (whose frequency range is from 5 to 55 Hz and frequency interval is 0.5 Hz) is applied to the external loop reference link of the constant AC voltage controller. When the system is simulated to steady state, the output response, the generator electromagnetic torque T_e is measured. And ΔT_e is obtained from the difference of the T_e before and after the small oscillating signals are applied to the generator. Then, ΔT_e and ΔV_{aci} are decomposed by Fourier transform and the phase difference between ΔT_e and ΔV_{aci} at different frequencies are calculated, that is the lagging phase required.

4 Case Studies

4.1 The System Model

The structure of the simplified wind-thermal-bundled power system is shown in Fig. 3. The G represents the thermal power unit and through the transformer T_1 access bus A; The C represents the doubly-fed wind farm and through the transformer T_2 access bus A. G and C will transmit power to the infinite power grid E by wind-thermal bundling via series compensation line. GSC and RSC represents the grid side converter and rotor side converter of doubly-fed generator respectively. $R_L + jX_L$ represents the impedance of transmission lines. X_c and X_{sys} represent capacitance reactance of series capacitor and connection reactance of infinite system respectively.

In Fig. 3, the thermal power unit, with the rated capacity of 892.4 MVA, the rated frequency of 60 Hz and the rated voltage of 500 kV, is modified from the first IEEE SSO benchmark model [13]. The unit shafting system is composed of six concentrated mass blocks: high pressure cylinder (HP), intermediate pressure cylinder (IP), low pressure cylinder A (LPA), low pressure cylinder B (LPB), generator (GEN) and exciter (EXC). The natural torsional frequencies of the

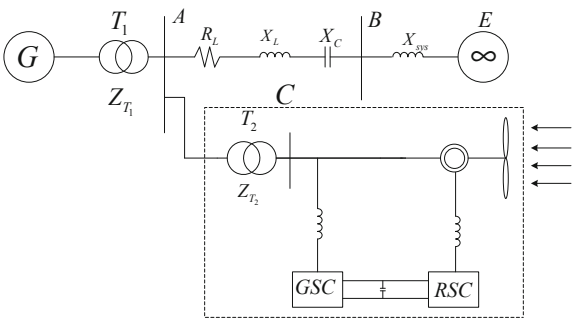

Fig. 3 The block diagram of STATCOM sub-synchronous damping controller

shafting are 15.71, 20.21, 25.55, 32.28 and 47.45 Hz. The ratio of mechanical torque applied to rotors of HP, IP, LPA and LPB are 0.3, 0.26, 0.22, and 0.22 respectively. The wind farm is equivalent to a DFIG model with the stator winding connected to the power grid directly and the rotor winding connected to the power grid through an AC-DC-AC converter. The DFIG model is mainly composed of wind turbine, generator, rotor-side converter, grid-side converter, DC bus, capacitor and the corresponding control module of each part. The converter adopts a double-loop control structure. The rotor-side converter realizes active and reactive decoupling control, and the grid-side converter realizes voltage control of DC bus between the two converters [14–16].

4.2 The Suppression of STATCOM on SSO

In the wind-thermal-bundled system as shown in Fig. 3, the wind farm integration capacity is supposed to be 100 MW, the corresponding thermal power unit is 703 MW, and the series compensation degree is 0.6. The SSO is suppressed by adding a STATCOM at bus A. The STATCOM DC capacitor voltage is set to be 1 kV, the converter output AC voltage is set to be 0.4 kV, and the converter capacity is 300 MVA. The frequency of minimum electrical damping coefficient is 20.5 Hz, which is the dominant oscillation mode, so 20.5 Hz is selected as the central frequency f need to be compensated. The lagging phase between the STATCOM constant AC voltage controller and generator electromagnetic torque is calculated to be about 55° at 20.5 Hz by test signal method, and the lagging phase of the modal filter is supposed to be about 5°. Therefore, four lead-lag stages are used to compensate for 60° of phase lag at 20.5 Hz, and each of which compensates for 15°. Calculated by formula (4), $T_1 = 0.101$ and $T_2 = 0.006$. The electrical damping characteristics curves, the electromagnetic torque response of the turbine generator and wind turbine before and after STATCOM is added are shown as below.

From Fig. 4, it can be seen that after the addition of STATCOM, at the original SSO frequency of 20.5 Hz, the electrical damping coefficient changes from negative to positive, which indicates that the addition of STATCOM increases the damping of the system and is beneficial to the suppression of SSO. From the time-domain simulation in Fig. 5, it can be seen that STATCOM has a significant suppression effect on the electromagnetic torque oscillation of thermal power units and wind turbines.

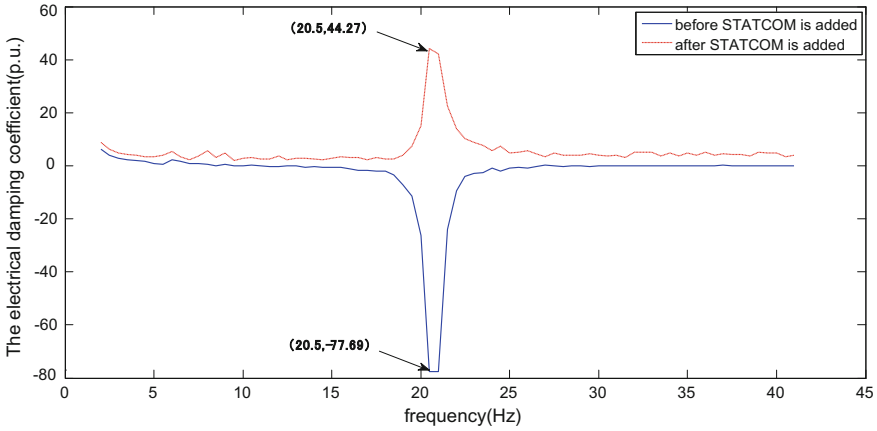

Fig. 4 The electrical damping characteristic curve with and without STATCOM

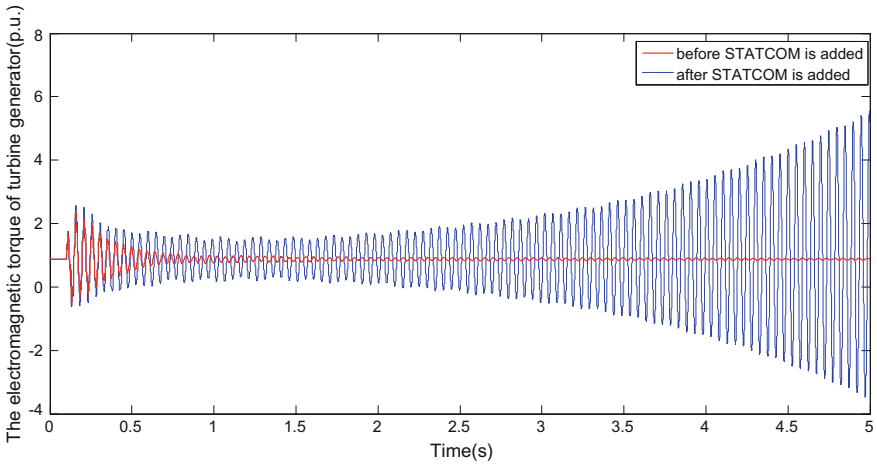

Fig. 5 The electromagnetic torque response of wind turbine with and without STATCOM

5 Conclusions

Through the mechanism analysis of STATCOM for SSO suppression, the STATCOM additional damping control will produce an electromagnetic torque increment with the same frequency as the torsional vibration of the shaft system. Reasonably controlling the frequency and phase of the electromagnetic torque increment can suppress the sub-synchronous oscillation. Through the time-domain analysis of wind-thermal-bundled power transmitted by series-compensation

system, the STATCOM really has a significant suppression effect on electromagnetic torque oscillation of thermal power units and wind turbines.

Acknowledgements The project was supported by State Key Laboratory of Smart Grid Protection and Control, and Six talent peaks project in Jiangsu Province (XNY-020).

References

1. Bai JH, Xing SX, Jia DX, Cheng L (2010) Study of major questions of wind power digestion and transmission in China. Power Syst Clean Energy 26(1):14–17
2. Zhang XG, Qiu WM, Fang R, Zhu L, Xu DG (2019) Impedance modeling and sub-synchronous resonance mitigation strategy of DFIG based wind turbine in static reference frame. Autom Electr Power Syst 43(6):41–48
3. Xie XR, Wang Y, Liu HK, He JB, Xu ZY (2016) Detection method for sub-synchronous and super-synchronous harmonic phasors in power system. Autom Electr Power Syst 40(21):189–194
4. Lu SR, Liu XP, Guo Q, Xia DZ (1999) Relationship between complex torque coefficients and eigenvalues in subsynchronous resonance analysis. Autom Electr Power Syst 94(3):16–18
5. Zhu YY, Dong P, Xie GP, Li GY (2013) Real-time simulation of UHVDC cooperative control Suitable to large-scale wind farms. Power Syst Technol 37(7):1814–1819
6. Li H, Cheng YJ, Li Y, Liu SQ, Yang D, Liang YY, Lan YS (2015) Impact of DFIG-based wind farms interconnected to power grid on subsynchronous oscillation of turbogenerator. Electr Mach Control 19(6):47–54
7. Li H, Cheng YJ, Zhao B, Yang C, Hu YG, Liu SQ, Yang D, Liang YY (2015) Analysis and control strategies for depressing system sub-synchronous oscillation of DFIG-based wind farms. Proc CSEE 35(7):1613–1620
8. Li H, Cheng YJ, Zhao B, Liu SQ, Yang D, Yang C, Hu YG, Liang YY (2014) Reactive power control of sub-synchronous oscillation damping system for DFIG-based wind farms. Electr Power Autom Equip 34(12):19–25
9. Li J, Zhang XP (2016) Impact of increased wind power generation on subsynchronous resonance of turbine-generator units. J Mod Power Syst Clean Energy 4(2):1–10
10. Zhao SQ, Zhang XW, Gao BF, Li R, Yang L (2017) Analysis and countermeasure of sub-synchronous oscillation in wind-thermal bundling system sent out via HVDC transmission. Adv Technol Electr Eng Energy 36(3):41–50
11. Widyan MS (2010) On the effect of AVR gain on bifurcations of subsynchronous resonance in power systems. Int J Model Simul 30(3):298–307
12. Zhang J, Xiao XN, Gao BF, Luo C, Chen TM (2013) Mechanism and characteristic study on sub-Synchronous control interaction of a DFIG-based wind-power generator. Trans China Electrotech Soc 28(12):142–149
13. IEEE Torsional Issues Working Group (1977) First benchmark model for computer simulation of subsynchronous resonance. IEEE Trans Power Appar Syst 96(5):1565–1572
14. Song R, Guo J, Li B, Zhou P, Du N, Yang D (2017) Mechanism and characteristics of subsynchronous oscillation in direct-drive wind power generation system based on input-admittance analysis. Proc CSEE 37(1):4662–4670
15. Wang L, Xie X, Jiang Q, Liu H (2014) Investigation of SSR in practical DFIG-based wind farms connected to a series-compensated power system. IEEE Trans Power Syst 30(5):1–8
16. Xu C, Lu JL, Zhang J, Zhou JL (2017) Control strategy for transient stability improvement of doubly-fed wind power generation system. Adv Technol Electr Eng Energy 34(6):45–51

Analysis on the Characteristics of 2016 Wind Damage Trips of Power Grid in China's Major Areas

Yuelun Di, Jun Guo, Xiaowei Huai and Yue Ye

Abstract Wind damage is one of the common disaster that has serious influence on China's power grid. The wind damage has a wide distribution and a low success rate of reclose, which makes the transmission line outage more likely. In this study, it is found that the 2016 wind damage of power grid in China's major areas mainly distributed in the southeastern coast, southwest region, north China and its surrounding areas. In temporal distributions, wind damage mainly occurs in summer and afternoon. In 2016, the first reclose success rate of wind damage trip is only about 10% during 330 kV and above voltage level transmission lines. 220 kV is a voltage level threshold of trip line: tripps number increases with voltage level decreases when above the threshold, otherwise trips number decreases with voltage level decreases. Transmission line wind damage trip trend has a large interannual variation from 2010 to 2016. This study analyzes the characteristics of wind damage trips in 2016, which provides guidance for wind damage prevention work in windbreak-prone areas and windbreak-prone periods.

Keywords Wind damage · Grid · Trip

1 Introduction

In recent years, with the development of economy and society, the demand for electricity keeps increasing, and China's transmission and distribution network is in a critical period of rapid development and extension. Especially the construction and operation of ±800 kV UHVDC, 1000 kV AC UHV and cross-region

Y. Di (✉) · J. Guo · X. Huai · Y. Ye
State Kay Laboratory of Disaster Prevention and Reduction for Power Grid Transmission and Distribution Equipment, 401205 Changsha, China
e-mail: diyuelun@163.com

Y. Di · J. Guo · X. Huai · Y. Ye
State Grid Hunan Electric Power Corporation Limited Disaster Prevention and Reduction Center, 401205 Changsha, China

Y. Xue et al. (eds.), *Proceedings of PURPLE MOUNTAIN FORUM 2019-International Forum on Smart Grid Protection and Control*, Lecture Notes in Electrical Engineering 585, https://doi.org/10.1007/978-981-13-9783-7_2

transmission lines have played a great role in the rational allocation of energy, industrial upgrading and environmental protection. However, many long-distance transmission lines exposed to outdoor environment will inevitably be attacked by various natural disasters, wind damage is one of the common disasters.

Wind damage on transmission lines mainly include typhoons, squall lines, tornadoes, local winds and other kinds. Typhoon is one of the main disasters affecting the power grid in the coastal areas [1]. According to statistics, more than 200 typhoon-level tropical cy-clones entered China from 1949 to 2010, which caused about 30% of the total line trips [2]. Research and application of typhoon early warning in power grid have been carried out: Wang Huimin et al. [3] started from the theory of disaster system, analyzed the existing problems of pre-assessment index system, and put forward an index system of typhoon disaster pre-assessment. Hitoshi et al. [4] proposed a loss assessment method for power grid typhoon disasters including linear regression model prediction and artificial neural network model correction. Huang et al. [5] proposed an early warning method for transmission line damage under typhoon disaster. Scholars [6] have studied the evaluation method of distribution network operation status under typhoon conditions. On the basis of the existing research on typhoon monitoring, forecasting and early warning, State Grid Corporation established the State Grid Typhoon Monitoring and Warning Center in 2017, which aims to carry out the guidance work of typhoon monitoring and early warning for power grid and enhance the ability of power grid typhoon prevention.

Equipment wind damage mainly include windage bias tripping, insulator and metal damage, grounding wire strand breakage and wire breakage, tower damage. It is called wind bias discharge that insulators incline toward towers, air gap between conductors and towers reduces, and the discharge phenomenon happens, under the action of strong wind [7]. Domestic and foreign studies have analyzed the mechanism of wind bias discharge by experiments and numerical simulation in different degrees and ways. An on-line monitoring system for wind bias of transmission lines is pro-posed, and a number of control measures for wind bias of transmission lines are given [8–11].

Compared with icing disasters, wind damage is more widely distributed, and occurs in southeastern coastal areas, north China, southwest and northwest China. Compared with lightning disasters, the success rate of wind damage trips is very lower [12], and has greater possibilities of transmission line outage. In 2016, wind damage tripping accidents of transmission lines with 66 kV and above voltage levels occurred frequently in major regions of China. The overall characteristics not only show the unique characteristics of the grid wind damage in that year, but also have the universality of the traditional grid wind damage. In this paper, the wind damage tripping of 66 kV and above voltage transmission lines in the main areas of China in 2016 is analyzed, which provides guidance for the work of wind-proof of power grid.

2 Wind Damage Trips of Transmission Lines in 2016

2.1 Spatial Distribution

Figure 1 shows the spatial distribution characteristics of the number of wind damage trips of transmission lines with 66 kV and above voltage levels in China's major areas in 2016. There are 208 wind damage trips of 66 kV and above transmission lines in the study area. Among them, 120 wind damage trips occurred in Fujian, accounting for 57.7% of the total wind damage trips, which exceeded the total of other provinces under the influence of typhoon landing. In 2016, the top seven provinces accounted for 90.9% of the total number of wind damage trips on 66 kV and above lines in that year. Wind trips in other provinces are less than 5 times (Table 1).

In 2016, the tripping of transmission lines caused by wind damage occurred in most parts of China. Among all kinds of wind damage, typhoon is the most important factor leading to transmission line tripping. Except for typhoons, other wind damages are mostly concentrated in the southwest, North China and its surrounding areas.

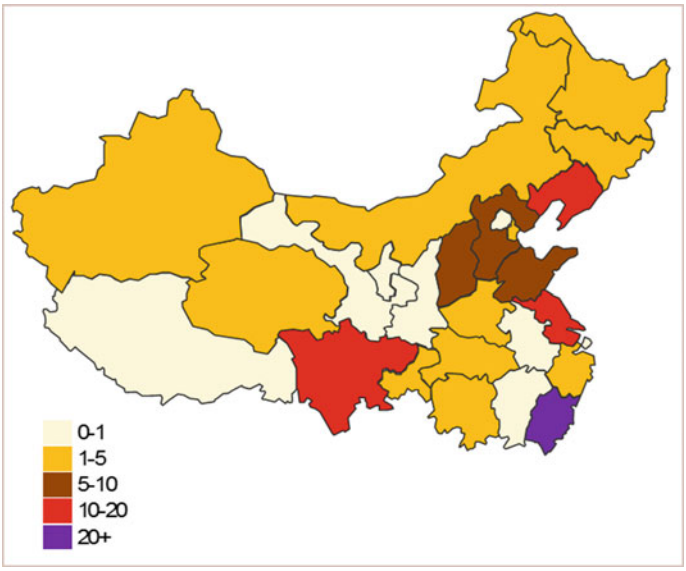

Fig. 1 Spatial distribution of 2016 wind damage trips for 66 kV and above voltage level in China's major areas

Table 1 Number of 2016 wind damage trips for 66 kV and above voltage level in China's major areas

Region	Number of trips	Ratio of trips (%)
Fujian	120	57.7
Sichuan	19	9.1
Liaoning	18	8.7
Jiangsu	16	7.7
Shandong	6	2.9
Shanxi	5	2.4
Hebei	5	2.4

2.2 *Temporal Distribution*

Figure 2 shows the monthly distribution characteristics of wind damage trips number on 330 kV and above voltage level transmission lines in 2016. There are 42 wind damage trips of 330 kV and above transmission lines, of which 37 occurred from late spring to early autumn (May to September), that is, in summer half year, accounting for 88% of the total wind damage trips of 330 kV and above transmission lines in 2016. September is the month with the largest number of wind damage trips on 330 kV and above transmission lines, totaling 11 trips, accounting for 26.2% of the total, and all of them are caused by typhoon. Therefore, spatial and temporal distribution shows that typhoon damage has a great impact on power grid in China's major areas in 2016. Except for typhoon, due to the frequent alternation of cold and warm air in late spring and early summer, the pressure gradient between regions is large, and strong gales often occur. In summer, the air level is unstable, and gusty gales and squall line winds are prone to occur. Therefore, summer monsoon damage occurs frequently.

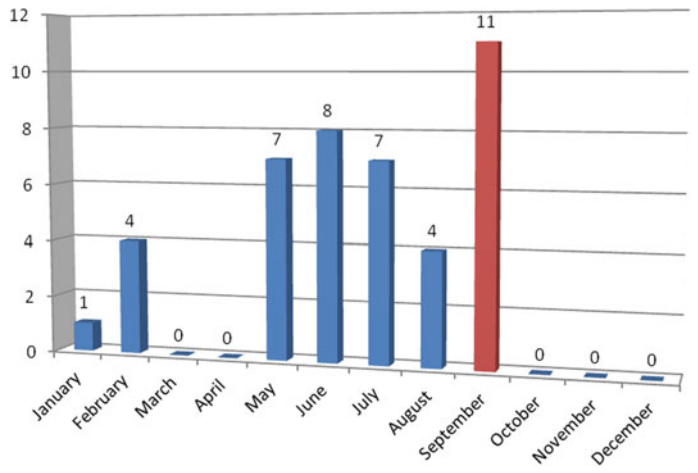

Fig. 2 Monthly distribution of the number of 2016 wind damage trips of 330 kV and above voltage level in China's major areas

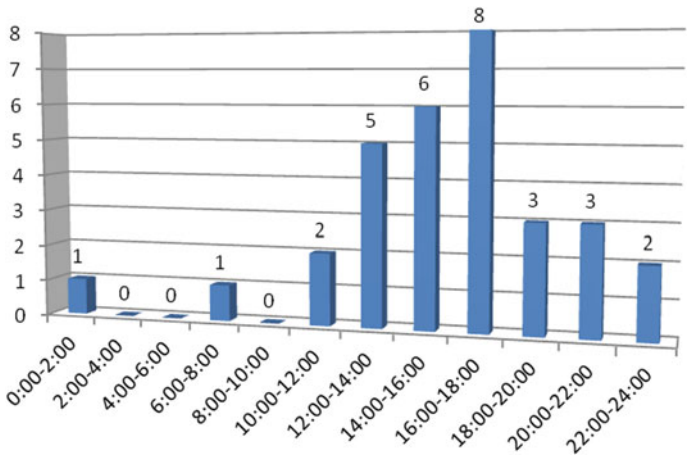

Fig. 3 Time interval distribution of 2016 wind damage trips in China's major areas

In the daily distribution of wind damage trips, because the typhoon trips are obviously related to the landing time of typhoon, the statistical significance is not obvious. Other wind trips on 330 kV and above lines (Fig. 3) mostly occurred in the afternoon: in 2016, 19 trips occurred between 12:00 and 18:00, accounting for 61.3% of all trips, of which 8 trips occurred between 16:00 and 18:00, which is the most vulnerable one in a day. Strong convective weather, such as squall line wind and tornado, which are easy to cause wind damage faults, usually requires unstable atmospheric stratification. This kind of environment is prone to occur in the summer afternoon after sunshine and warming, which may be an important reason for more wind damage tripping accidents during the 12:00–18:00 period.

2.3 Reclosure

After the disasters trips, the operation and maintenance unit will reclose the trip line according to the need. If the disaster damages the line greatly, it may lead to the failure of the first reclosure operation. At this time, it is necessary to reconsider the operation dispatch of the power grid and select the opportunity for the next reclosure operation. Therefore, the success of the first reclosure not only proves the impact of disasters on transmission lines, but also relates to the decision making of power grid operation and dispatch.

Table 2 shows the first reclosure of 2016 wind damage trip of 330 kV and above voltage level lines in major regions of China. It can be seen from the table that, the reclosure success rate of line trips caused by wind damage is only 12%. From the 42 wind damage trips lines, 37 lines failed to complete the first reclosure operation after tripping. In non-typhoon-induced wind damage trips accidents (Fig. 4), 90%

Table 2 The situation of first reclose of 2016 wind damage trips of 330 kV and above voltage level lines

Reclosure	Number	Ratio (%)
Success	5	12
Unsuccess	37	88

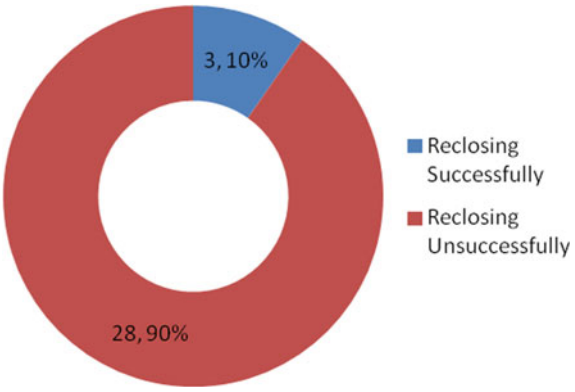

Fig. 4 The situation of first reclosing of non-typhoon 330 kV and above voltage level wind damage trips

of the lines will fail to reclose for the first time. It is generally believed that the main types of wind damage on transmission lines include wind bias trips, insulator and fittings damage, grounding wire strand breakage and tower damage. Wind bias tripping due to the insufficient electrical spacing caused by the windward yaw of conductors is the most common type of wind damage, and the success rate of reclosure is low. Typhoon and other strong winds can cause tower inversion accident, and also cause re-closure failure.

2.4 Voltage Level Distribution

It is generally believed that because of the large number and wider distribution of low voltage grade lines, they are more likely to be affected by disasters. However, from the distribution of voltage levels of 66 kV and above wind damage tripping lines in major regions of China in 2016 (Fig. 5), it can be seen that, 220 kV lines have the most trips, totaling 135 trips, reaching 65% of the total, which is 4.4 times the total number of low-voltage tripping lines (110 and 66 kV), exceeding the total number of other voltage-induced tripping lines. At the same time, when the voltage level decreases from 750 to 220 kV, the number of trips increases. When the voltage level continues to drop from 220 to 66 kV, the number of trips decrease as the voltage level drops.

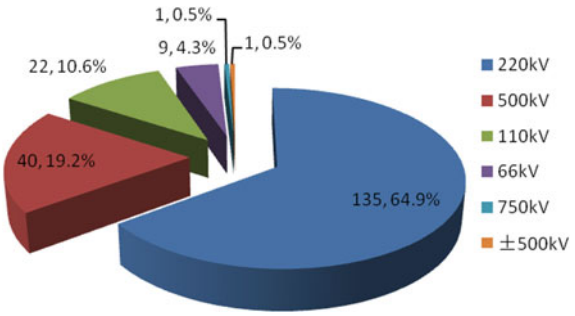

Fig. 5 Voltage distribution of 2016 wind damage trips for 66 kV and above voltage level in China's major areas

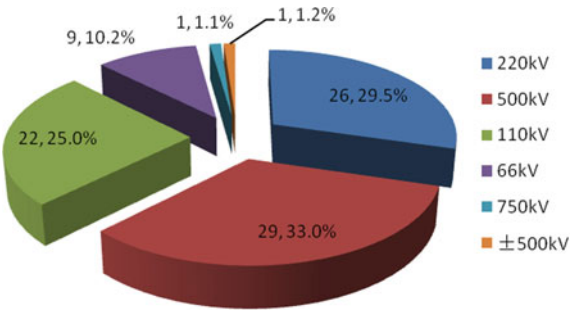

Fig. 6 Voltage distribution of 2016 non-typhoon wind damage trips for 66 kV and above voltage level in China's major areas

If the influence of typhoon is not taken into account (Fig. 6), 500 kV is the voltage level with the largest number of wind damage trips, totaling 29 trips, accounting for 33% of the total trips. The number of 220 kV wind damage tripping lines is close to that of 26 trips. The number of tripping lines of 110 kV and 66 kV decreases in turn. Therefore, in 2016, there were 11 trips on 500 kV lines and 109 trips on 220 kV lines caused by typhoon.

220 kV and above voltage level lines are the main grid structure of China's power grid. They are usually responsible for long-distance transmission across regions, while 110 kV and below power lines are mainly responsible for transmitting electricity to nearby towns. Therefore, the lines in the wildfield are mainly 220 kV and above, and the number of lines decreases with the increase of the voltage level, which causes the number of wind trips of 220 kV and above to decrease with the increase of voltage level. For towns and their surrounding areas with transmission lines of 110 kV and below, on one hand, local and seasonal gusts occur less, on the other hand, when typhoons are approaching, low-voltage lines are more likely to implement planned blackouts, for avoiding a trip accident caused by typhoon. The higher the voltage level, the more difficult it is to implement a planned power outage. Therefore, the number of wind trips on transmission lines of 110 kV and below decreases as the voltage level decreases.

3 Annual Variation Characteristics of Wind Damage Trip

From the annual variation of the number of wind damage trips of 330 kV and above trans-mission lines (Fig. 7), it can be seen that the trend of wind damage trips of 330 kV and above transmission lines is not obvious from 2010 to 2016, but the annual variation range of the number of trips is large, from 38 in 2010 to 17 in 2011, which rose rapidly to 52 in 2013, and then to 28 in 2014. Secondly, it maintained above 40 times in 2015 and 2016. Since 2010, the top three provinces in terms of wind damage trips have accounted for more than 40% of the total number of wind damage trips, and even more than 50% in 2010, 2011, 2014 and 2016. Therefore, windbreak tripping has the characteristics of wide-spread disaster distribution and serious disaster situation in some provinces.

Specifically, from the situation of wind damage suffered of each province from 2010 to 2016 (Fig. 8), there were 8 provinces with 330 kV and above grade lines with more severe wind damage trips (15 times or more). According to the number of wind damage trips, the order was Hebei, Shanxi, Henan, Zhejiang, Shandong, Sichuan, Shaanxi and Fujian. Except Zhejiang and Fujian, the other six provinces are located in the southwest, North China and its surrounding areas. Therefore, the spatial distribution characteristics of wind damage trips in 2016 basically continue this distribution trend.

It should be noted that in the seven years from 2010 to 2016, 15 trips of 330 kV and above occurred in Fujian, 10 of which were directly caused by the strong typhoon Moranti of 2016. Therefore, wind damage trips in coastal areas is closely related to landing typhoons, and the number and intensity of typhoons may directly affect the operation characteristics of landing provinces.

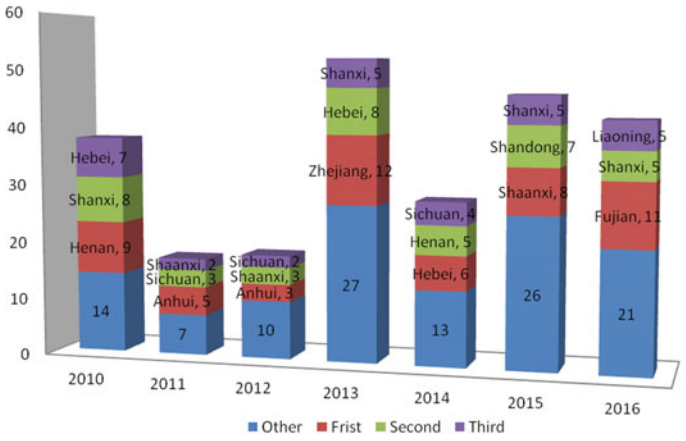

Fig. 7 Number change of 2010–2016 330 kV and above voltage level transmission line wind damage trips in China's major areas

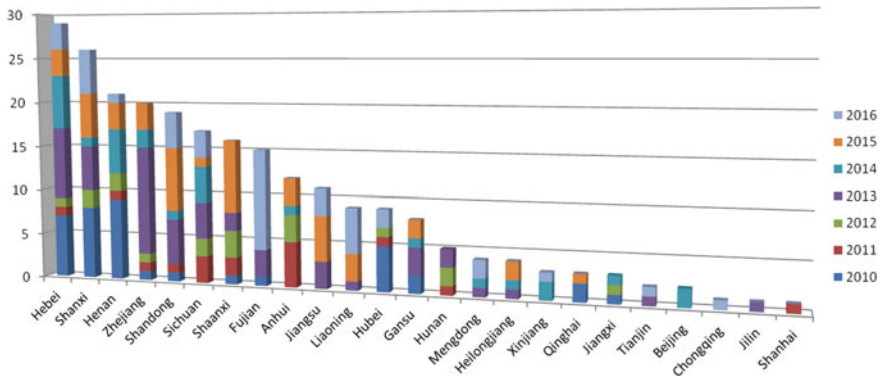

Fig. 8 Number of 330 kV and above the voltage level wind damage trips for mainly provinces from 2010 to 2016

4 Summary

Based on the analysis of 66 kV and above voltage level transmission line trips in China's major areas in 2016, it is found that temporal and spatial distributions of wind damage on large power grid have regularity and uniqueness. The main characteristics are as follows:

(1) Typhoon is the most important factor leading to transmission line trips. Except for the southeast coastal areas affected by typhoons, other wind damage are mostly concentrated in the southwest, North China and its surrounding areas.
(2) Summer half year of 2016 is a period of frequent wind damage, which is related to typhoon. Other wind damage trips mainly occur in afternoon, which is mainly related to the environmental characteristics of severe convective in summer afternoon.
(3) The success rate of the first reclosure after wind damage trips is usually relatively low. In 2016, it is just 12% during 330 kV and above voltage-level, while percentage of wind damage trips other than typhoons is only 10%.
(4) 220 kV is a threshold in 2016 wind trips lines: when voltage level is above 220 kV, number of trips increases with the decrease of voltage level; when voltage level is below 220 kV, number of trips decreases with the decrease of voltage level.
(5) In recent years, the interannual variation of the wind trips number of 330 kV and above lines is large, which may be affected by typhoon. Wind damage tripping has the characteristics of widely distribution with prominent emphasis.

The analysis of trip characteristics of wind damage in power grids can play an important decision basis for the key work deployment of wind damage prevention in areas where wind damage occur frequently and in periods when wind damage

occur frequently in power grids. In particular, it is necessary to distinguish the influence of local short-term strong winds on key line sections and the overall impact of typhoons on coastal power grids, especially through the classification of grid wind damage categories, and implement them based on different types of wind damage data. Research on grid typhoon impact characteristics, seasonal strong wind research and local strong wind research will provide support for targeted grid wind damage protection, avoid excessive and insufficient wind protection, and establish a comprehensive and effective grid wind damage prevention scheme to maintain grid security.

Acknowledgements The work is supported by Science and Technology Project of State Grid Corporation of China (Grant 5216A0180004).

References

1. Zeng H, Sun F, Li T et al (2017) Analysis of "9·28" blackout in South Australia and its enlightenment to China. Autom Electr Power Syst 41(13):1–6
2. Operation and maintenance department of State Grid Corporation. Transmission line "six prevention" working manual, Wind damage protection. China Power Press, Beijing (2015)
3. Wang H, Ye J, Lin Y et al (2013) On pre-evaluation indices of typhoon disaster: an early-warning perspective. J Subtrop Resour Environ 8(1):25–32
4. Takata H, Nakamura H, Hachino T (2004) On prediction of electric power damage by typhoons in each district in Kagoshima prefecture via LRM and NN. In: SICE 2004 annual conference, pp 781–786
5. Huang Y, Wei R, Zhou E et al (2018) Early warning method of transmission line damage under typhoon disaster. Autom Electr Power Syst 42(23):142–147
6. Chen B, Li C, Qin H et al (2018) Evaluation of typhoon resilience of distribution network considering grid reconstruction and disaster recovery. Autom Electr Power Syst 42(6):47–52
7. Xiao D (2009) Analysis and countermeasure on flashover between tower and conducting wires in domestic 500 kV transmission lines caused by windage yaw. Power Syst Technol 33 (5):99–102
8. St. Clair JG (1997) Clearance calculations of conductors to buildings. IEEE Trans Power Deliv 12(2):979–984
9. Yi H, Wang L, Liu K et al (2009) Research of effect of wind-blown rain on power frequency flashover characteristic of conductor-tower air gap. In: Asia-Pacific Power and Energy Engineering Conference (APPEEC), pp 1–6
10. Carrington, RJ, Brian WH (2002) High intensity winds. In: Proceedings of the conference: electrical transmission in a New Age, EIP02427150938
11. Li N, Lv Y, Ma F et al (2010) Research on overhead transmission line windage yaw online monitoring system and key technology. In: International Conference on Computer and Information Application (ICCIA 2010), pp 71–74
12. Long L, Hu Y, Li J et al (2006) Parameters for wind caused overhead transmission line swing and fault. In: 2006 IEEE Region 10 Conference (TENCON 2006), pp 1–4

Research on Correlation Between Wind Power and Load in Different Weather Conditions

Zixin Chen, Han Wang, Jie Yan, Yongqian Liu, Shuang Han and Li Li

Abstract The wind power and load are both affected by the meteorological factors. Studying on the correlation between wind power and load in different weather conditions is beneficial to reduce the double uncertainties on the sides of source and load, and significant to the planning, dispatching, safe and stable operation of the electric power system. First, the improved algorithm of traditional K-means clustering algorithm—X-means is adopted to divide the daily meteorological factors of wind speed and temperature, which mainly affect the wind power and load. Then, the Pearson, Kendall and Spearman correlation coefficients are used to analyze the correlation between wind power and load variables in different weather conditions. Finally, the optimal Copula function is selected from four commonly-used Copula functions to describe the joint distribution of wind power and load in each weather condition. Furthermore, the data in another place is used to verify the correlation between wind power and load with the weather condition. The conclusions are as follows: (1) the X-means algorithm can realize the effective classification of weather conditions. (2) The positive correlation between wind power and load is mainly concentrated in summer or near summer, the negative correlation between them is mainly concentrated in winter or near winter. (3) The correlation between wind power and load is quite varying in different weather conditions, but the joint distributions are basically consistent with the Archimedes Copula functions, and the tail correlation coefficients of their distribution are zero under most weather conditions. (4) There is a repeated rule between wind power and load with the weather condition.

Keywords Different weather conditions · Wind power · Load · Correlation · Copula function

Z. Chen
Chifeng Branch of China Datang Corporation, Inner Mongolia Autonomous Region, 024000 Chifeng, China

H. Wang · J. Yan (✉) · Y. Liu · S. Han · L. Li
School of Renewable Energy, North China Electric Power University, 102206 Beijing, China
e-mail: yanjie_freda@163.com

Y. Xue et al. (eds.), *Proceedings of PURPLE MOUNTAIN FORUM 2019-International Forum on Smart Grid Protection and Control*, Lecture Notes in Electrical Engineering 585, https://doi.org/10.1007/978-981-13-9783-7_3

1 Introduction

In the source side, with the high proportion of wind power integration, the volatility and intermittency of its output have a significant adverse impact on the reliability of power system and the power quality [1]. In the load side, as the proportion of activity load rises yearly, its uncertainty also increases greatly [2]. The double uncertainties of source and load sides pose huge challenges to the planning, scheduling, safe and stable operation of the electric power system [3, 4]. However, the wind power and load are both affected by the meteorological factors, studying on the correlation relationship between them under different weather conditions is beneficial to reduce the double uncertainties on the sides of source and load, improve the joint forecasting accuracy, and arrange the reserve capacity in advance, etc. [5].

Some scholars have already researched on the correlation between wind power and load at present. Li et al. [6] studied the correlation between wind power and load time series through the spatial transformation of probability distribution. The results show that the correlation relationship could impact the overload risk of the transmission line. Lin et al. [7] analyzed the linear correlation between the wind power time series and typical daily load, and proposed a new method to calculate the peak regulation capacity of wind power by considering the correlation between them. It is suggested from researches that the presented method shows great advantages when the wind power capacity of the regional power grid is more than 10% of the maximum load. Zhao et al. [8] researched on the correlation between wind power output and load change in a provincial power grid at the time scale of month and day, respectively. It can be seen that the monthly average output of wind power is negatively correlated with the load change of the power grid.

Some other scholars have considered the correlation between wind power and load in making investment decisions, calculating operation costs and assessing the adequacy of electric power system, etc. Baringo et al. [9] proposed two methodologies to generate the wind power and electric load time series which considered their uncertainty and the correlation between them. The results show that the scenario selection has a significant impact on the investment decision. Ak et al. [10] presented a multi-layer perceptron artificial neural network for interval forecasting of wind power and load, which accounting for the associated uncertainties of them simultaneously. Mazidi et al. [11] implemented a two-stage stochastic objective function which aiming at the minimization of the expected operation cost, and the reserve requirement in this function is provided by a combination of responsive load and renewable energy. Korkas et al. [12] presented a novel control algorithm for joint the demand response load, renewable energy and energy storage which considered the correlation between the source side and the load side. Liu et al. [13] proposed a two-stage robust security-constrained unit commitment method by considering the correlation of wind power and load, which could eliminate the undesirable scenarios and further limit the level of conservatism of the robust solution.

However, the above researches still have the following deficiencies. When the correlation between wind power and load is analyzed, the weather conditions are not taken into account and the correlation of them are not further studied in different scenarios. When the correlation between wind power and load is applied to the actual situation, the correlative differences between them in different scenarios are considered, but the correlation relationships are not stated. Therefore, the correlation between wind power and load is specific researched in different weather conditions in this paper. First, the improved algorithm of traditional K-means clustering algorithm—X-means is adopted to divide the daily meteorological factors of wind speed and temperature, which mainly affect the wind power and load. Then, the correlation between wind power and load variables in different weather conditions is studied based on the Pearson, Kendall and Spearman correlation coefficients, and the monthly distributions of different correlations are analyzed. Finally, based on the Euclidean distance, the optimal Copula function is selected from four commonly-used Copula functions, including t-student Copula function, Gumbel Copula function, Clayton Copula function and Frank Copula function to describe the joint distribution of wind power and load in each weather condition. The correlation between them is further studied on the basis of the optimal Copula function. Furthermore, the data in another place (Portland) is used to validate the correlation between wind power and load with the weather condition.

The remainder of this paper is organized as follows. In Sect. 2, the weather conditions are classified by using the X-means clustering algorithm according to the meteorological factors of wind speed and temperature. Section 3 studied the correlation between wind power and load in different weather conditions in Providence, and verified the obtained correlation in Portland. Section 4 concludes this paper.

2 Classification of Weather Conditions

The data used in this study is from two places, one is the Providence area of Rhode Island, USA, and the other is the Portland area of Maine, USA. The data in Providence is employed to analyze the correlation between wind power and load in different weather conditions, and the data in Portland is employed to validate the correlation with the weather condition. The wind power data, including the wind speed and output data, is derived from the grid integration data of National Renewable Energy Laboratory (NREL) [14]. The length and temporal resolution of the data is 6 years (from 2007 to 2012) and 5 min, respectively. The load and temperature data are the real time data of ISO New England electricity market, the dataset is publicly available on the official website of the ISO New England Incorporation [15]. The length and temporal resolution of the data is 8 years (from 2008 to 2015) and 1 h, respectively. Therefore, the data used in this study is from 2008 to 2012, and the temporal resolution is 1 h. Note, the data of Feb. 29 in 2008 and 2012, and Dec. 31 in these five years is missing.

First of all, the Pearson linear correlation coefficient, Kendall rank correlation coefficient and Spearman rank correlation coefficient are employed to analyze the correlation between wind power and load variables. The calculation method of each correlation coefficient is as follows.

(1) Pearson linear correlation coefficient (r)

Pearson linear correlation coefficient is the quotient of covariance and standard deviation between two variables and the calculation formula is shown in Eq. (1).

$$r = \frac{\mathrm{cov}(\bar{P}, \bar{L})}{\sigma(\bar{P})\sigma(\bar{L})} = \frac{E(\bar{P}\bar{L}) - E(\bar{P})E(\bar{L})}{\sigma(\bar{P})\sigma(\bar{L})} \tag{1}$$

Pearson correlation coefficient reflects the linear correlation relationship between the wind power time series $\bar{P}(t)$ and load time series $\bar{L}(t)$. The closer absolute value of r is to 1, the linear correlation between two variables is stronger.

(2) Kendall rank correlation coefficient (τ)

$$\tau = P((\bar{P}(i) - \bar{P}(j))(\bar{L}(i) - \bar{L}(j)) > 0) - P((\bar{P}(i) - \bar{P}(j))(\bar{L}(i) - \bar{L}(j)) < 0) \tag{2}$$

where, $P((\bar{P}(i) - \bar{P}(j))(\bar{L}(i) - \bar{L}(j)) > 0)$ and $P((\bar{P}(i) - \bar{P}(j))(\bar{L}(i) - \bar{L}(j)) < 0)$ represents the probability of harmony and disharmony, respectively, between the wind power and load at time of i and j. The difference of them is the Kendall rank correlation coefficient.

(3) Spearman rank correlation coefficient (ρ_s)

$$\rho_s = 3\{P((\bar{P}(i) - \bar{P}(j))(\bar{L}(i) - \bar{L}(k)) > 0) - P((\bar{P}(i) - \bar{P}(j))(\bar{L}(i) - \bar{L}(k)) < 0)\} \tag{3}$$

where, $P((\bar{P}(i) - \bar{P}(j))(\bar{L}(i) - \bar{L}(k)) > 0)$ and $P((\bar{P}(i) - \bar{P}(j))(\bar{L}(i) - \bar{L}(k)) < 0)$ represents the probability of harmony and disharmony, respectively, between $(\bar{P}(i), \bar{L}(i))$ and $(\bar{P}(j), \bar{L}(k))$.

The correlation coefficients between wind power and load time series from 2008 to 2012 can be calculated according to the above formulas, the results are as follows: $r = 0.012$, $\tau = 0.023$, $\rho_s = 0.035$. It can be seen that, the correlation relationship between wind power and load variables at the time scale of year, including the linear and nonlinear correlation, is extremely weak, i.e. the wind power and load are basically irrelevant if all data is used to analyze without filtering. Therefore, the correlation between wind power and load should be further studied in different scenarios.

The data used for analysis should be in the same magnitude, so the wind speed, temperature, wind power and load time series are normalized, respectively. The calculation formula is as follows.

$$\bar{X}(t) = \frac{X(t) - X_{\min}}{X_{\max} - X_{\min}} \tag{4}$$

The correlation between wind speed and wind power, temperature and load is analyzed, respectively, to illustrate the reasonableness of dividing the weather conditions based on meteorological factors of wind speed and temperature. As can be seen from Fig. 1, there is a cubic relationship between the wind speed and wind power when the wind speed is between the cut-in speed and the cut-off speed. The temperature and load is negatively correlated when the temperature is less than about 18 °C, and positively correlated when the temperature is larger than about 18 °C. Therefore, the wind speed and temperature variables are chosen as the main meteorological factors to classify the weather conditions in this study. The improved algorithm of traditional K-means clustering algorithm—X-means [16] is adopted to classify the weather conditions. Compared with the K-means algorithm, the X-means algorithm only need to give the range of clustering number (k) in advance, not the specific value of k. The clustering results will more scientific and effective with the X-means algorithm.

The daily normalized wind speed and temperature data are clustered by X-means algorithm and the weather condition in this area can be divided into 24 categories. In order to further verify the effective of X-means algorithm, the traditional K-means algorithm is adopted to cluster the daily normalized wind speed and temperature data, and the clustering number is set from 1 to 50. The clustering error of K-means is represented by the average Euclidean distance of each sample data to its cluster center. The clustering error of K-means algorithm under different clustering numbers is shown in Fig. 2. As can be seen that, with the increase of clustering number, the clustering error of K-means is decreased and the descent rate is gradually slow down. When the clustering number reaches 24, the descent rate is basically near to zero. The clustering error only reduced by 0.046 when the clustering number changes from 24 to 50. The results further illustrate the validity of X-means clustering algorithm.

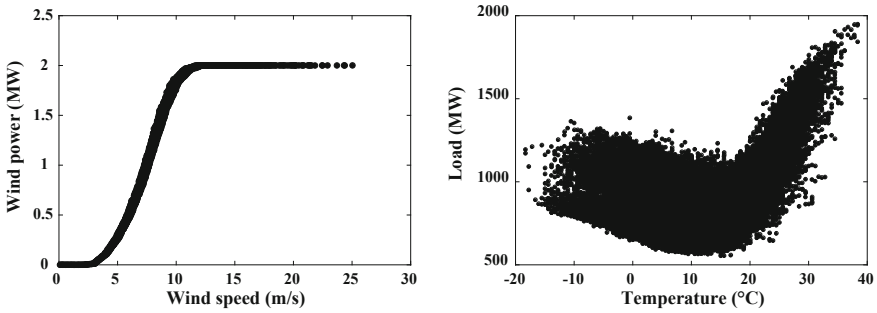

(a) Wind speed and wind power (b) Temperature and load

Fig. 1 Correlation between meteorological factors and wind power or load

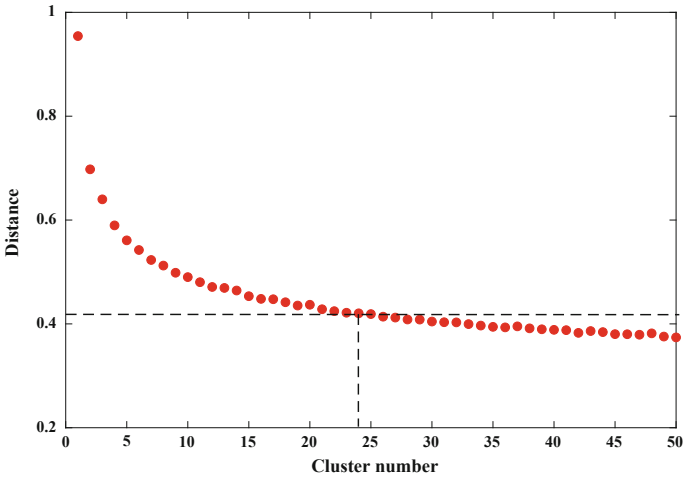

Fig. 2 Clustering error of K-means algorithm under different clustering numbers

3 Correlation Between Wind Power and Load in Different Weather Conditions

3.1 Linear and Rank Correlation Coefficients

In this section, Pearson linear correlation coefficient is used as an example to analyze the correlation between wind power and load variables in different weather conditions first. The Pearson correlation coefficients of wind power and load in the above 24 weather conditions (referred to as types in this paper) are calculated and listed in Table 1. It can be seen that, the correlation between wind power and load varies greatly in different weather conditions. The linear positive correlation coefficient can be up to 0.500 and the linear negative correlation coefficient can be low to 0.572.

Then, the monthly distribution of positive and negative linear correlation between wind power and load is calculated, respectively, according to the results of Pearson correlation coefficients in different weather conditions, as depicted in

Table 1 Pearson correlation coefficients in different weather conditions

Type	1	2	3	4	5	6	7	8
r	0.465	0.036	−0.082	0.333	0.128	0.402	−0.399	−0.227
Type	9	10	11	12	13	14	15	16
r	0.014	0.258	0.450	−0.084	0.355	0.442	−0.172	−0.092
Type	17	18	19	20	21	22	23	24
r	−0.572	0.250	−0.351	0.500	−0.491	0.473	0.243	−0.221

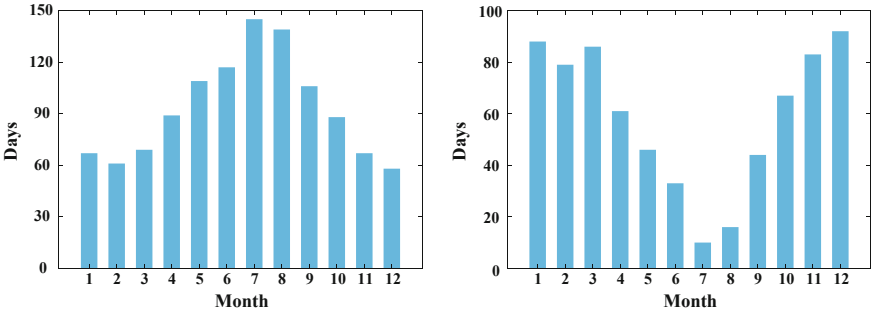

(a) Positive (1115days) (b) Negative (705 days)

Fig. 3 The monthly distributions of positive and negative linear correlations

Fig. 3. It can be seen that, (1) the frequency of positive correlation between wind power and load is higher than the negative correlation in these 5 years. The number of days with positive and negative correlation accounted for 61.3 and 38.7% of the total number of days, respectively. (2) The positive correlation between them is mainly concentrated in summer or near summer, and the negative correlation is mainly concentrated in winter or near winter.

In order to further analyze the linear correlation between wind power and load variables in different weather conditions, the monthly distributions of different degrees of linear correlation (moderate positive, weak positive, extremely weak positive, moderate negative, weak negative and extremely weak positive) are shown in Fig. 4. The discriminant basis is as follows, when $0.4 < |r| \leq 0.6$, the correlation is moderate; when $0.2 < |r| \leq 0.4$, the correlation is weak; when $|r| \leq 0.2$, the correlation is extremely weak. As can be seen from Fig. 4, (1) the weak correlation accounted for the largest proportion, followed by the moderate correlation, and the extremely weak correlation accounted for the smallest proportion among three degrees of the linear correlation. (2) The distributions of positive and negative correlation in different degrees are almost the same in each month. And the probability that a positive correlation occurs in summer or near summer, a negative correlation occurs in winter or near winter both increase with the correlation degree.

Then, the Kendall and Spearman correlation coefficients are used as the evaluation indexes to further study the nonlinear correlation between wind power and load variables in different weather conditions, as shown in Fig. 5. It can be seen that, the variation trend of the linear and rank correlation between wind power and load is basically the same in different weather conditions, the positive and negative correlations between random variables do not vary with the correlation coefficients. Therefore, the monthly distributions of nonlinear correlation are basically the same as Figs. 3 and 4.

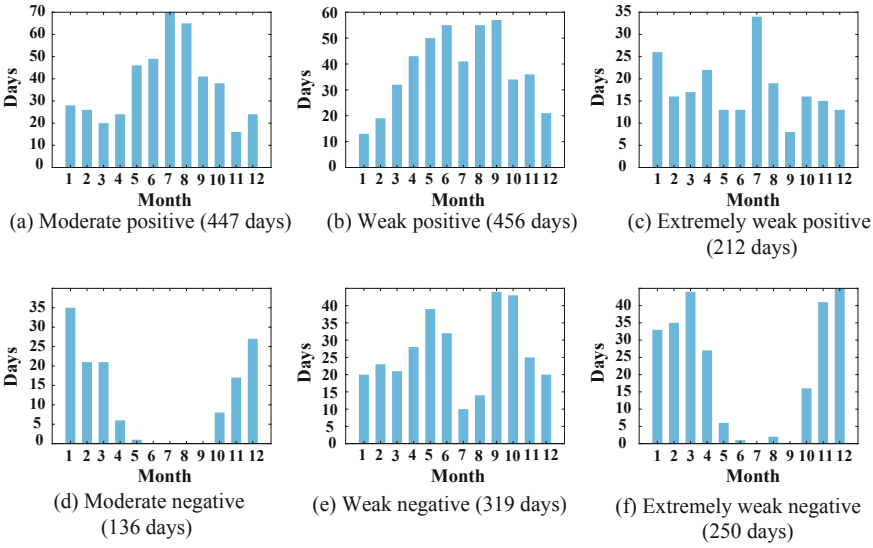

Fig. 4 The monthly distributions of different linear correlation degrees

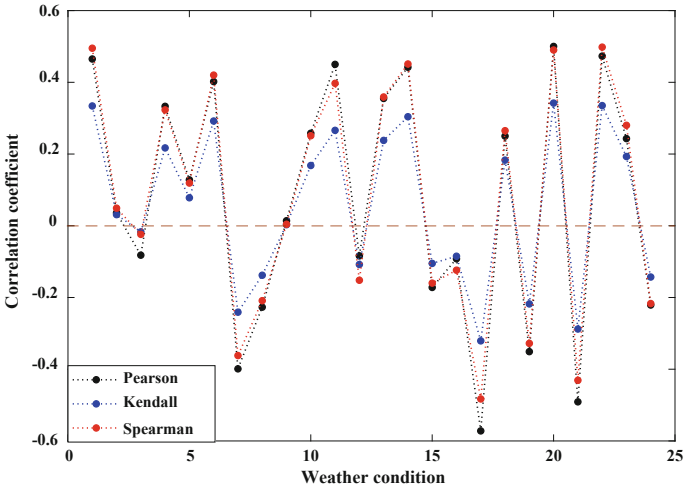

Fig. 5 Linear and rank correlation coefficients in different weather conditions

3.2 Joint Distributions Based on Optimal Copula Functions

Variables which with the same correlation coefficient may exhibit completely diverse characteristics due to the different correlation structures between them. For the research on the correlation between wind power and load, the real situation may

not be fully reflected if the relevant structure of them is ignored, which will lead to the inaccurate or even incorrect correlation analysis results. Therefore, the joint distributions of wind power and load are further analyzed in different weather conditions in this section.

Firstly, four commonly-used Copula functions [17, 18], including t-student Copula function, Gumbel Copula function, Clayton Copula function and Frank Copula function are employed to fitted the joint distribution of wind power and load in each weather condition. Among four Copula functions, Gumbel Copula function, Clayton Copula function and Frank Copula function are the commonly-used Copula functions of Archimedes. The four binary Copula distribution functions and their respective characteristics are as follows.

(1) Binary t-student Copula distribution function

$$C^t(u,v;\rho,k)=\int_{-\infty}^{t_k^{-1}(u)}\int_{-\infty}^{t_k^{-1}(v)}\frac{1}{2\pi\sqrt{1-\rho^2}}\left[1+\frac{s^2-2\rho st+t^2}{k(1-\rho^2)}\right]^{-\frac{k+2}{2}}dsdt \tag{5}$$

where, u, v is the marginal distribution function of wind power time series and load time series, respectively; ρ is the linear correlation coefficient between two variables; k is the degree of the freedom of binary t-student Copula.

(2) Binary Gumbel Copula distribution function

$$C(u,v;\alpha)=\exp\left(-[(-\ln u)^{\alpha}+(-\ln v)^{\alpha}]^{1/\alpha}\right) \tag{6}$$

where, $\alpha\in[1,\infty]$.

(3) Binary Clayton Copula distribution function

$$C(u,v;\alpha)=\max\left([u^{-\alpha}+v^{-\alpha}-1]^{-1/\alpha},0\right) \tag{7}$$

where, $\alpha\in[-1,\infty]\backslash\{0\}$.

(4) Binary Frank Copula distribution function

$$C(u,v;\alpha)=-\frac{1}{\alpha}\ln\left(1+\frac{(e^{-\alpha u}-1)(e^{-\alpha v}-1)}{e^{-\alpha}-1}\right) \tag{8}$$

where, $\alpha\in(-\infty,\infty)\backslash\{0\}$.

Binary t-student Copula function has a thick symmetrical tail and is sensitive to the tail-related changes between random variables, so it can capture the symmetrical tail correlation between variables. Binary Gumbel Copula function and binary

Clayton Copular function have an asymmetrical tail. The Gumbel Copula function can capture the upper tail correlation between variables, and the lower tail correlation coefficient of this Copula function is 0. The Clayton Copula function can capture the lower tail correlation between variables, and the upper tail correlation coefficient of this Copula function is 0. Binary Frank Copula function has an independent and symmetrical tail, and the tail correlation coefficients of this Copula function are both 0.

The more suitable Copula function which can describe the joint distribution of wind power and load is selected from the above four commonly-used Copula functions in each weather condition, according to the Euclidean distance among the four Copula distributions and the empirical Copula distribution, respectively, as depicted in Fig. 6 and listed in Table 2. The Kendall and Spearman rank correlation coefficients, upper and lower tail correlation coefficients are calculated based on the optimal Copula function, as listed in Table 2. The calculation formulas of the correlation coefficients based on the Copula function are shown from Eqs. (9) to (12).

$$\tau = 4 \int_0^1 \int_0^1 C(u, v) dC(u, v) - 1 \tag{9}$$

$$\rho_s = 12 \int_0^1 \int_0^1 C(u, v) du dv - 3 \tag{10}$$

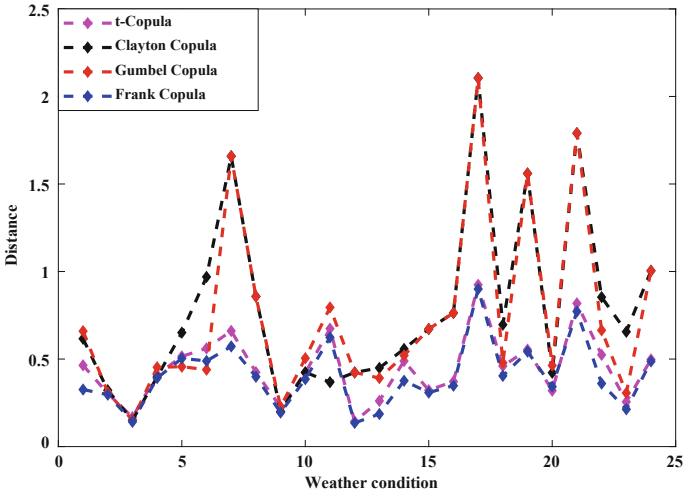

Fig. 6 Selection of Copula functions in different weather conditions

Table 2 Correlation of wind power and load in different weather conditions

Type	Optimal fitting					Type	Optimal fitting				
	Copula function	τ	ρ_s	λ_{up}	λ_{low}		Copula function	τ	ρ_s	λ_{up}	λ_{low}
1	Frank	0.349	0.506	0	0	13	Frank	0.242	0.357	0	0
2	Frank	0.032	0.048	0	0	14	Frank	0.321	0.467	0	0
3	Frank	−0.022	−0.034	0	0	15	Frank	−0.111	−0.165	0	0
4	Frank	0.224	0.331	0	0	16	Frank	−0.078	−0.117	0	0
5	Gumbel	0.080	0.119	0.107	0	17	Frank	−0.347	−0.502	0	0
6	Gumbel	0.276	0.400	0.348	0	18	Frank	0.186	0.276	0	0
7	Frank	−0.258	−0.380	0	0	19	Frank	−0.227	−0.336	0	0
8	Frank	−0.145	−0.217	0	0	20	t-student	0.375	0.536	0.001	0.001
9	Frank	0.004	0.006	0	0	21	Frank	−0.308	−0.450	0	0
10	Frank	0.175	0.260	0	0	22	Frank	0.352	0.510	0	0
11	Clayton	0.285	0.414	0	0.420	23	Frank	0.197	0.292	0	0
12	Frank	−0.109	−0.163	0	0	24	Frank	−0.151	−0.225	0	0

$$\lambda_{up} = \lim_{u \to 1^-} \frac{1 - 2u + C(u,u)}{1 - u} \tag{11}$$

$$\lambda_{low} = \lim_{u \to 0^+} \frac{C(u,u)}{u} \tag{12}$$

As can be seen from Fig. 6 and Table 2,

(1) when the wind power is positively correlated with load, the optimal Copula function which can describe the joint distribution between them is different with the weather condition. For example, Type 5 and Type 6 are more consistent with the Gumbel Copula function, Type 11 is more consistent with the Clayton Copula function, Type 20 is more consistent with the t-student Copula function, the remaining weather conditions are more consistent with the Frank Copula function. In addition, although the Euclidean distance between t-student Copula distribution function and the empirical Copula distribution function is smallest in Type 20, the upper and lower tail correlation coefficients are both only 0.001. It can be considered that the joint distribution of wind power and load is basically independent in the tail under this weather condition. When the wind power is negatively correlated with load, the optimal Copula function which can describe the joint distribution between them is more consistent with the Frank Copula function in each weather condition.

It can be concluded that the joint distributions of them are basically independent in the tail under most weather conditions, and only under a few weather conditions, the joint distributions of wind power and load show the upper tail correlation or the lower tail correlation.

(2) The correlation coefficients which calculated according to the wind power and load variables are basically the same as the correlation coefficients which calculated based on the optimal Copula function in different weather conditions, which further verifies the rationality of the selected optimal Copula functions.

Type 20, Type 6, Type 11, Type 17 and Type 22 are selected according to the results in Table 2 which is more consistent with the t-student Copula function, Gumbel Copula function, Clayton Copula function and Frank Copula function, respectively. The daily variation curves, actual frequency distributions and joint density distributions based on four Copula functions of wind power and load in these five typical weather conditions are depicted in Fig. 7, and the Euclidean distances among four Copula distributions and the empirical Copula distribution are also listed in Fig. 7. It can be intuitively seen from the figure that the selected optimal Copula function in each weather condition can better fit the frequency distribution between wind power and load, and can describe the tail correlation of the joint distribution between them accurately.

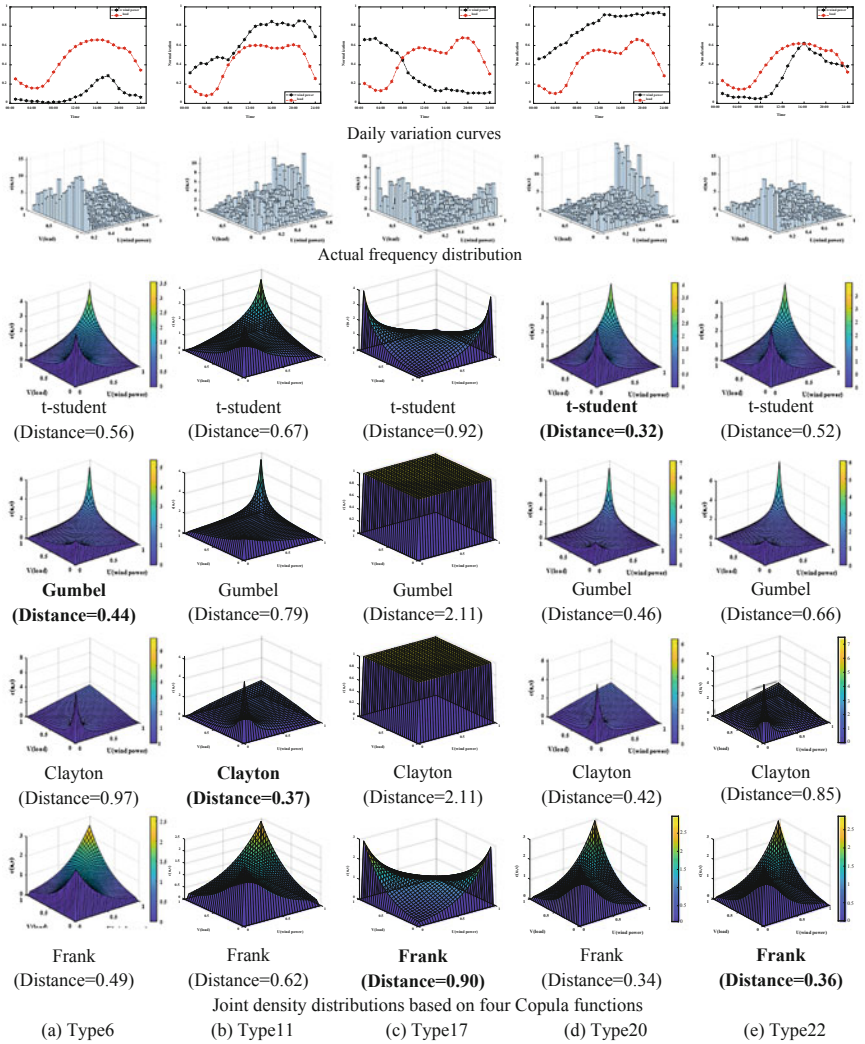

Fig. 7 Joint distributions of wind power and load in five typical weather conditions

3.3 Correlation Verification in Another Place

In this section, the data in Portland area of Maine, USA is used to validate the correlation between wind power and load in different weather conditions which is obtained above in Providence area of Rhode Island, USA. First, the daily normalized wind speed and temperature data in Portland is classified into 24 categories according to the cluster centers of wind speed and temperature in Providence based on the evaluation index of Euclidean distance. Then, the Pearson correlation coefficient is

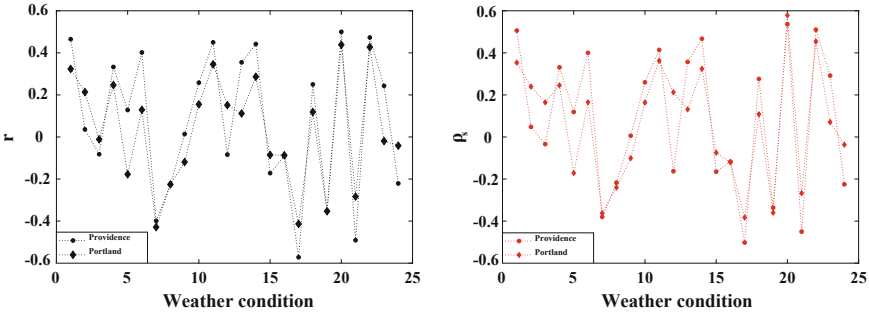

(a) Pearson correlation coefficients based on variables

(b) Spearman correlation coefficients based on the optimal Copula functions

Fig. 8 Correlation between wind power and load under different weather conditions in two places

employed to analyze the linear correlation between wind power and load variables in 24 weather conditions in Portland, and compared with the results in Providence, as shown in Fig. 8a. Finally, the joint distribution between wind power and load in each weather condition in Portland is also fitted based on four commonly-used Copula functions, including t-student Copula function, Gumbel Copula function, Clayton Copula function and Frank Copula function, and the optimal Copula function is selected according to the Euclidean distance among the four Copula distributions and the empirical Copula distribution. The Spearman rank correlation coefficients are calculated based on the optimal Copula functions in 24 weather conditions, and compared with the results in Providence, as shown in Fig. 8b.

As can be seen from Fig. 8, the variation trend of correlation between wind power and load in different weather conditions is basically the same in these two different places, i.e., there is a repeated rule between wind power and load with the weather condition. The results further illustrate the necessity and validity of studying the correlation between wind power and load in different weather conditions, rather than based on all the data directly.

4 Conclusion

The correlation between wind power and load in different weather conditions is systematically studied based on the correlation coefficients and Copula functions in this paper. The main work and corresponding conclusions are as follows.

(1) The improved algorithm of traditional K-means clustering algorithm—X-means is adopted to divide the daily meteorological factors of wind speed and temperature, and the weather condition is classified into 24 types. The rationality and effectiveness of X-means algorithm are verified according to the clustering error of K-means algorithm under different clustering numbers.

(2) The correlation between wind power and load variables in different weather conditions is analyzed based on the Pearson, Kendall and Spearman correlation coefficients. The results show that, the correlation between wind power and load is quite different with the weather condition. The positive correlation between them is mainly concentrated in summer or near summer, the negative correlation between them is mainly concentrated in winter or near winter, and the probability of occurrence is increase with the correlation degree. The positive and negative correlations between wind power and load variables do not vary with the correlation coefficients.
(3) Four commonly-used Copula functions, including t-student Copula function, Gumbel Copula function, Clayton Copula function and Frank Copula function are employed to describe the joint distribution of wind power and load in each weather condition. The results show that, the joint distributions of wind power and load are more consistent with Frank Copula function, and the tail correlation coefficients of their distribution are zero under most weather conditions. Only in a few weather conditions, the joint distributions of wind power and load are more consistent with Gumbel Copula function (Type 5 and Type 6) and Clayton Copula function (Type 11).
(4) The data in another place (Portland) is used to validate the correlation between wind power and load in different weather conditions. The results show that, there is a repeated rule between the wind power and load with the weather condition.

The research results of this paper can be applied for the planning and dispatching of the electric power system, which with the double uncertainties of source and load sides.

Acknowledgements This work was supported in part by the project of the National Natural Science Foundation of China funded project (51707063), and the project of China Datang Corporation Ltd.

References

1. Lu Z, Huang H, Shan B et al (2017) Morphological evolution model and power forecasting prospect of future electric power systems with high proportion of renewable energy. Autom Electr Power Syst 41(9):12–18
2. Sun Y, Wang Y, Wang B et al (2018) Multi-time scale decision method for source-load interaction considering demand response uncertainty. Autom Electr Power Syst 42(2):106–113 + 159
3. Rakipour D, Barati H (2019) Probabilistic optimization in operation of energy hub with participation of renewable energy resources and demand response. Energy 173:384–399
4. Deng T, Lou S, Tian X et al (2019) Optimal dispatch of power system integrated with wind power considering demand response and deep peak regulation of thermal power units. Autom Electr Power Syst 43
5. Jin H, Sun H, Niu T et al (2019) Coordinated dispatch method of energy-extensive load and wind power considering risk constraints. Autom Electr Power Syst 43

6. Li X, Zhang X, Wu L et al (2015) Transmission line overload risk assessment for power systems with wind and load-power generation correlation. IEEE Trans Smart Grid 6(3):1233–1242
7. Lin L, Zhou P, Wang S et al (2016) Analysis impact on regional wind power to peak regulation capacity by considering the correlation. Mod Electr Power 33(6):21–26
8. Zhao L, Xu D, Li P (2018) Study on wind power output characteristics and correlation between load of region power system. In: 2018 37th Chinese Control Conference (CCC). IEEE, Wuhan, China, pp 8982–8984
9. Baringo L, Conejo A (2013) Correlated wind-power production and electric load scenarios for investment decisions. Appl Energy 101(1):475–482
10. Ak R, Li Y, Vitelli V et al (2018) Adequacy assessment of a wind-integrated system using neural network-based interval predictions of wind power generation and load. Int J Electr Power Energy Syst 95:213–226
11. Mazidi M, Zakariazadeh A, Jadid S et al (2014) Integrated scheduling of renewable generation and demand response programs in a microgrid. Energy Convers Manag 86 (10):1118–1127
12. Korkas C, Baldi S, Michailidis I et al (2016) Occupancy-based demand response and thermal comfort optimization in microgrids with renewable energy sources and energy storage. Appl Energy 163:93–104
13. Liu X, Zhang Z, Wang W et al (2018) Two-stage robust optimal dispatch method considering wind power and load correlation. In: 2018 2nd IEEE Conference on Energy Internet and Energy System Integration (EI2). IEEE, Beijing, China, pp 1–6
14. Draxl C, Clifton A, Hodge B et al (2015) The Wind Integration National Dataset (WIND) Toolkit. Appl Energy 151:355–366
15. ISO New England Web Page of Pricing Reports, http://www.iso-ne.com/isoexpress/web/reports
16. Pelleg D, Moore A (2000) X-means: extending K-means with efficient estimation of the number of clusters. In: Intelligent Data Engineering and Automated Learning—IDEAL 2000, Data Mining, Financial Engineering, and Intelligent Agents. Morgan Kaufmann Publishers, Hong Kong, China, pp 308–313
17. Ji F, Cai X, Wang J (2014) Wind power correlation analysis based on hybrid copula. Autom Electr Power Syst 38(2):1–5 + 32
18. Han S, Qiao Y, Yan J et al (2019) Mid-to-long term wind and photovoltaic power generation prediction based on copula function and long short term memory network. Appl Energy 239:181–191

Research on Operational Optimization Technology of Regional Integrated Energy System Considering Operating Cost and Reliability

Xiaochen Zhang, Jinda Zhu, Dongmei Yang, Yonghua Chen and Wei Du

Abstract To solve the problem of operation optimization for regional integrated energy system, a kind of operation optimization method considering operating cost and reliability is proposed. Firstly, the difference between multi-objective integrated energy system and traditional dispatching is analyzed. A multi-objective operation optimization framework of integrated energy system is introduced. Secondly, the output characteristics of the main integrated energy system equipment are analyzed. Thirdly, the objective function with the lower operating cost and the higher reliability is established. Then, taking into account the system constraints of electricity, heating and cooling, the multi-objective running optimization model is solved by linear programming method. Finally, an integrated energy system scene with distributed generation and energy storage equipment is constructed. The Pareto solution set of the scene is searched. Meanwhile, the different operating modes of CCHP are compared. The results show that the proposed model can meet the requirements and provide a unified optimization solution for integrated energy system.

Keywords Operation optimization · Integrated energy system · Linear programming

1 Introduction

To be an important cornerstone of human survival and development, energy is the driving force and foundation for social economy. With the gradual depletion of traditional fossil energy and the widespread use of environmental pollution caused

X. Zhang (✉) · J. Zhu · D. Yang · Y. Chen · W. Du
NARI Group Corporation (State Grid Electric Power Research Institute), Nanjing 211106, China
e-mail: zhangxch2008@hotmail.com

X. Zhang · J. Zhu · D. Yang · Y. Chen · W. Du
NARI Technology Co., Ltd, Nanjing 211106, China

Y. Xue et al. (eds.), *Proceedings of PURPLE MOUNTAIN FORUM 2019-International Forum on Smart Grid Protection and Control*, Lecture Notes in Electrical Engineering 585, https://doi.org/10.1007/978-981-13-9783-7_4

by climate change, the application of distributed renewable energy on a large scale, changing the energy consumption structure, and establishing an efficient, safe and sustainable energy utilization model are one of the major challenges in the process of sustainable development [1–3]. As an important form of energy Internet, the integrated energy system has received extensive attention in recent years and is of great significance for its research.

Compared with traditional electricity dispatching, integrated energy system operation optimization technology faces greater challenges [4, 5]. First of all, the power supply and load types in the integrated energy system are more abundant, and there are strong uncertainties in the power and load demand of renewable energy. Secondly, the energy in the integrated energy system is coupled with each other, and the system constraints are more complicated. The optimization difficulty has been improved. Finally, under the incentive of the integrated energy trading market environment, the integrated energy system needs to continuously adjust the equipment output plan of the system according to the incentives of different energy markets. Therefore, it is necessary to conduct further research on the optimization technology of integrated energy system operation.

This paper analyzes the output characteristics and system operation optimization strategies of distributed energy sources in integrated energy system, fully considering the operational constraints of distributed energy equipment, the operational constraints of multi-energy network, and the coupling characteristics among multiple energy sources. Pursuing the lowest comprehensive cost and the highest reliability, a multi-objective optimization scheduling model for integrated energy systems is established. Aiming at the characteristics that constraint conditions are coupling in time, the linear programming method is adopted to solve the model. Finally, based on the typical integrated energy case, the optimal scheduling of the integrated energy system in different scenarios is simulated and analyzed, so the effectiveness of proposed model and solving method is verified.

2 Multi-objective Operation Optimization Framework

The integrated energy system is not a simple superposition of multiple independent energy supply subsystems. Through the coordinated control of multiple energy supply units, it can meet the system energy demand and achieve higher benefits than the independent operation of the energy subsystems [6, 7]. To improve the efficiency of energy utilization and realize the operation optimization of integrated energy system, this paper proposes a multi-objective operation optimization framework of integrated energy system. Figure 1 shows the operation optimization framework of integrated energy system.

The characteristics of the multi-objective operation optimization framework for integrated energy systems are as follows:

Multi-energy real-time optimization. Integrated energy system consists of multiple energy subsystems, each subsystem is satisfied by different types of energy

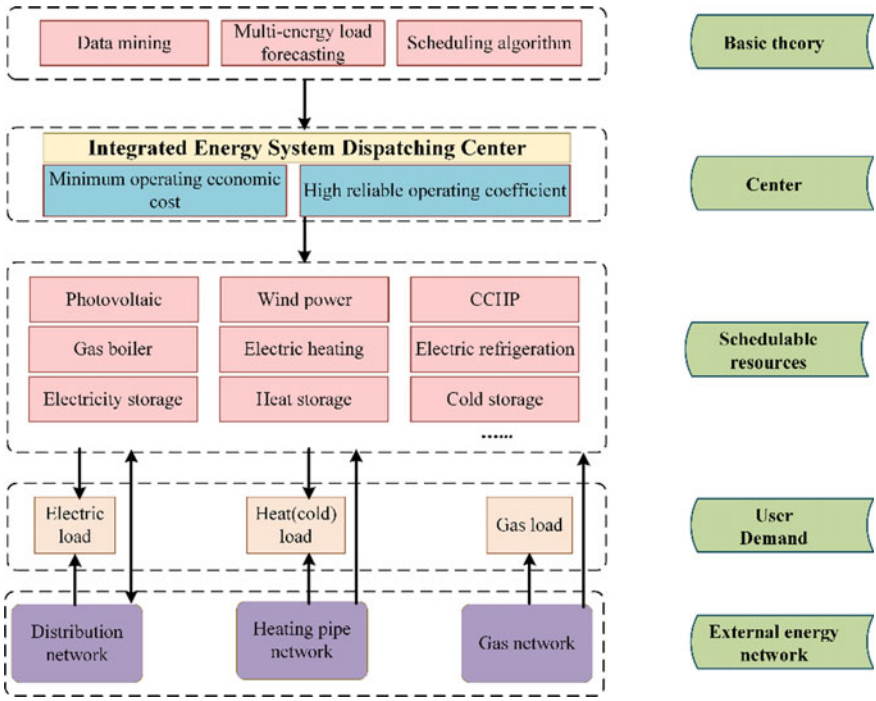

Fig. 1 The operation optimization framework of integrated energy system

supply units. There are complex coupling problems among multi-energy subsystems.

Multi-objective operation optimization. This system emphasizes not only the optimal operation cost, but also the optimal operation state of the system from the perspective of reliability.

3 Multi-objective Operation Optimization Model

3.1 Objective Function

In this paper, the integrated energy system contains two objectives: Firstly, the system has the lowest total operating cost within 24 h. The operating cost [8] mainly including the cost of purchasing electricity, purchasing gas, etc. The operating cost $C_{total,T}$ is expressed as follows:

$$C_{total,T} = C_{supply,T} + C_{net,T} \tag{1}$$

where $C_{supply,T}$ and $C_{net,T}$ are energy supply cost and power exchange cost, respectively. T is the scheduling cycle.

The energy supply cost consists of fuel consumption and equipment maintenance. The energy supply cost is as follows:

$$C_{supply,T} = \sum_{t=1}^{T} \sum_{u \in U} w_{u,t} c_u \tag{2}$$

where $w_{u,t}$ is the energy supply of uth equipment at time t. c_u is the unit energy supply cost of uth equipment. U is the device set in the integrated energy system.

The power exchange cost $C_{net,T}$ is the electricity exchange cost in the scheduling cycle T:

$$C_{net,T} = \sum_{t=1}^{T} \left(C_{pur,t} - D_{sale,t} \right) \tag{3}$$

where $C_{pur,t}$ and $D_{sale,t}$ are the electricity purchase cost and electricity sales revenue with the main network, respectively.

Secondly, the system reliability refers to the ratio of the system power supply to the total power demand in a certain period [9, 10]. Combined with the power type of the integrated energy system, the system reliable operation coefficient is as follows:

$$S_T = \frac{\eta_1 \sum_{t=1}^{T} W_{1,t} + \eta_2 \sum_{t=1}^{T} W_{2,t} + \cdots + \eta_n \sum_{t=1}^{T} W_{n,t}}{\sum_{t=1}^{T} W_{load,t}} \tag{4}$$

where $W_{n,t}$ is the power supply of the nth equipment. $W_{load,t}$ is the total power demand at time t. η_n is the reliable operation coefficient of the nth equipment.

The Pareto solution for solving the double-objective optimization with the lowest operating cost and the most reliable system is equivalent to: linearly weighted summation of two objective functions as a new objective function, and single-objective optimization for different weights. The objective F formula is as follows:

$$F = aC_{total,T} + bS_T \tag{5}$$

where a and b are the weights.

3.2 System Constraints

The integrated energy system mainly includes various distributed energy sources and energy storage equipment.

Photovoltaic power generation model. The photovoltaic upper output is directly affected by local solar radiation, solar panel area and solar conversion efficiency. Moreover, the photovoltaic output should be less than the rated power. The photovoltaic output P_{pv} is as follows:

$$\underline{P}_{pv} \le P_{pv} \le \bar{P}_{pv} \tag{6}$$

$$\bar{P}_{pv} = \min\left\{P_{capa}, \theta S_{pv}\eta_{pv}\right\} \tag{7}$$

where $\underline{P}_{pv}$ is the lower limit and $\bar{P}_{pv}$ is the upper limit. P_{capa} is the photovoltaic rated power. θ represents the local solar radiation. S_{pv} and η_{pv} are solar panel area and solar conversion efficiency, respectively.

Wind power generation model. The wind power generation is similar to the photovoltaic power generation. The upper limit of the wind power output $\bar{P}_{wind}$ is a piecewise function relationship with the meteorological conditions. The wind power generation P_{wind} calculation formula is:

$$\underline{P}_{wind} \le P_{wind} \le \bar{P}_{wind} \tag{8}$$

$$\bar{P}_{wind} = \begin{matrix} \frac{v - v_{in}}{v_{rate} - v_{in}} P_{rate} & v_{in} \le v \le v_{rate} \\ P_{rate} & v_{rate} < v \le v_{out} \end{matrix} \tag{9}$$

where P_{rate} represents the rated power. v_{rate} is the rated speed. v_{in} and v_{out} are cut-in wind speed and cut-out speed, respectively.

Gas turbine power generation model. The constraint of gas turbine power change rate ΔP_{gas} calculation formula is:

$$-D_{ngas}\Delta t \le \Delta P_{gas} \le U_{pgas}\Delta t \tag{10}$$

where D_{ngas} is the downward climbing rate constraint and U_{pgas} is the uphill climbing rate constraint.

Power storage model. If the storage equipment is in charging state, the storage equipment power is:

$$S_{t+1} = S_t(1 - \varepsilon) + P_c\eta_c \tag{11}$$

where S_t is the dump energy at time t. ε is the leakage rate. P_c is the charging power and η_c is the charging efficiency.

Homoplastically, if the storage equipment is in discharging state, the storage equipment power is as follows:

$$S_{t+1} = S_t(1-\varepsilon) - P_d\eta_d \tag{12}$$

Electric power equality constraint. In integrated energy system, the generation and consumption of the electricity should keep balance during the entire scheduling cycle.

$$\sum_{i=1}^{N} P_{DG} + P_{grid} + P_d - P_c = P_{load} \tag{13}$$

where P_{DG} is the power of the distributed generation. P_{grid} is the exchange power of main network. P_{load} is the electricity load.

Heating (cooling) power equality constraint. In integrated energy system, the generation and consumption of the heating (cooling) should keep balance during the entire scheduling cycle.

$$\sum_{i=1}^{M} H_i + H_e + H_{ss} = H_{load} \tag{14}$$

where H_i is the heating power of the ith gas turbine. H_e and H_{ss} are the heating power of electric heating equipment and heating storage equipment, respectively. H_{load} is the heating load. M is the number of gas turbines. The equation constraint of the colding load is similar to the equation constraint of the heating load.

4 Dispatching Model and Solution

Integrated energy operation optimization is a complex linear programming problem. The standard formula of the integrated energy system operation optimization is:

$$\begin{cases} \min F \\ s.t. \quad \mathbf{A}_1\mathbf{X} = \mathbf{B}_1 \\ \quad\quad \mathbf{A}_2\mathbf{X} \le \mathbf{B}_2 \\ x_{i,\min} \le x_i \le x_{i,\max} \end{cases} \tag{15}$$

where X are the variables. A1, B1, A2, B2 are the coefficient matrixes. For variable x_i, $x_{i,\min}$ is the lower limit and $x_{i,\max}$ is the upper limit.

In this paper, we transform the above model into a linear programming problem and solves it with CPLEX toolbox.

5 Case Study

5.1 Typical Case

Figure 2 shows a typical integrated energy system structure. This case include cooling load, heating load and electricity load. The facilities include photovoltaic equipment, wind turbine, Combined cooling heating and power (CCHP), power storage equipment and so on.

The system operation optimization period is 24 h, and the interval is 1 h. The load demand is shown in Fig. 3.

Table 1 shows the main device parameters. For the energy storage equipment, the state of charge (SOC) is 0.2–0.8. Next, let's discuss and analysis the running optimization results in this scenario.

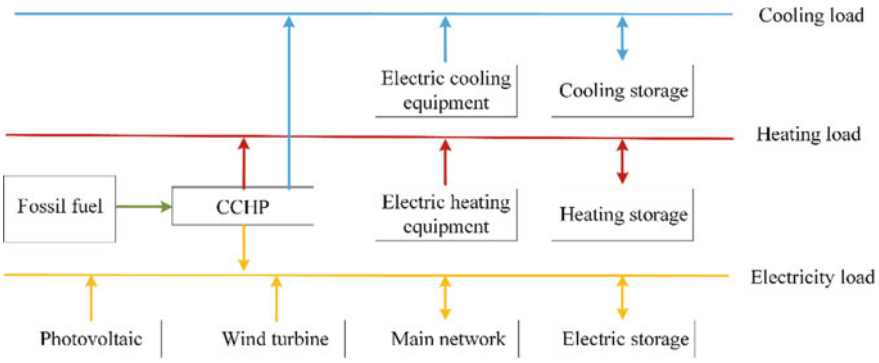

Fig. 2 Structure of a typical integrated energy system

Fig. 3 System load demand

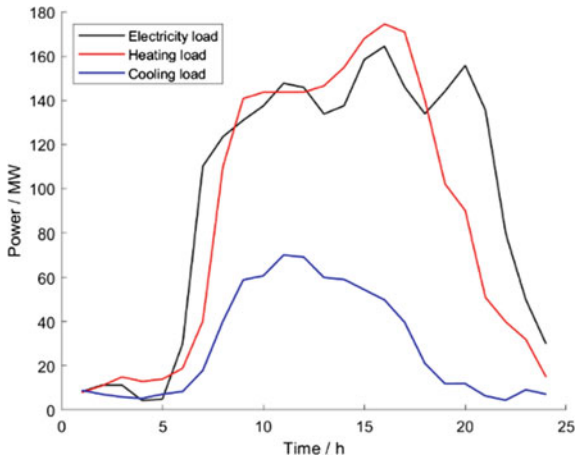

Table 1 Main device parameters

Device	Power lower limit (MW)	Power upper limit (MW)
Photovoltaic equipment	0	35
Wind turbine	0	30
CCHP (electricity)	60	100
Electric storage	−8	8
Heating storage	−8	8
Cooling storage	−8	8

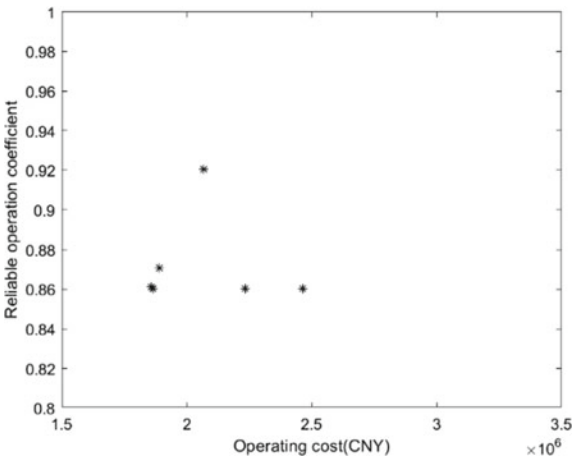

Fig. 4 Pareto optimal solution space

5.2 *Results and Discussion*

Based on the above scenario, with the operating cost and reliability as the optimization goals, the obtained Pareto solution set is shown in Fig. 4.

It can be seen from Fig. 4 that there is no optimal result that satisfies both low operating cost and high reliability. There is a contradiction between the operating cost and reliability, and it is difficult to obtain the most excellent solution.

The reasons are as follows: if the operating cost of the system needs to be reduced, the distributed energy sources such as photovoltaic and wind power should be used as far as possible. Although this strategy can minimize the purchase of electricity from the main network, it reduces the reliability of the system, so there is no high reliability solution in the low operating cost area. In order to improve the reliability of the system, we need to consider the purchase of electricity from the main network, so that we can not maximize the use of distributed energy. Therefore, there is no solution of low operating cost in high reliability areas. In practical planning, decision makers can choose schedulable solutions that are more

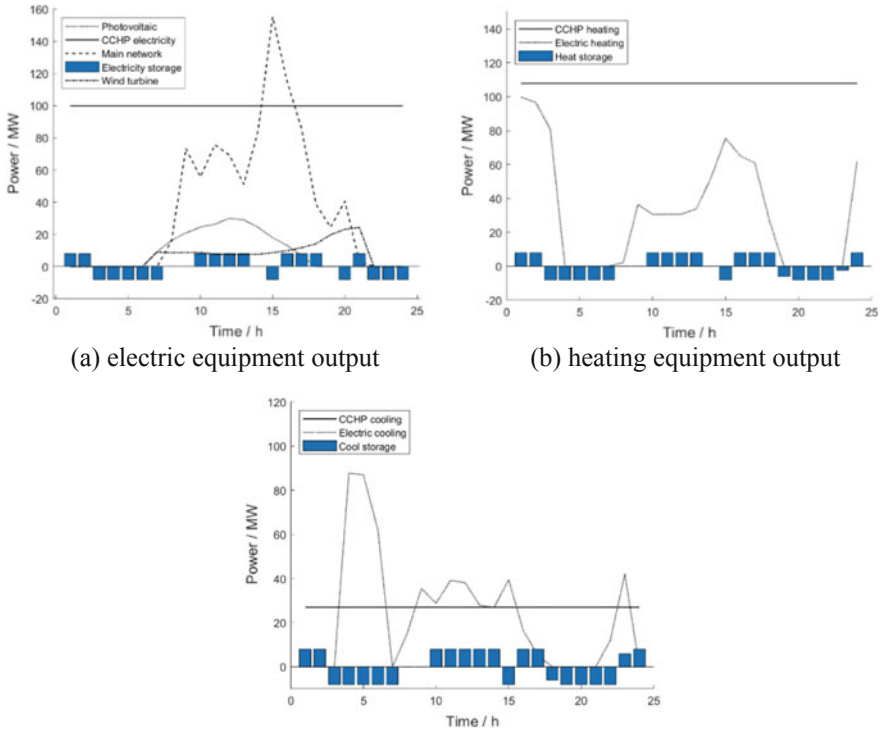

(a) electric equipment output

(b) heating equipment output

(c) cooling equipment output

Fig. 5 Equipment output power under CCHP full power mode

in line with the actual needs of the project, thus providing support for multi-objective optimization at the economic and technical levels.

For integrated energy system that include CCHP system, the CCHP's operating mode usually adopts full power mode. Next, we will use CCHP full power mode as the basic mode, optimize the CCHP's operation mode with the lowest operating cost as the optimization goal.

Figure 5 shows the equipment output power under CCHP full power mode. It is clear that the energy storage device is charged at 3–7 o'clock and discharged during the day. Figure 6 shows the equipment output power under CCHP optimal power mode. At night, the load demand is small, CCHP runs in low power mode from 23 to 7 o'clock, and the daytime load demand is large, CCHP full power mode.

Table 2 shows the operation cost under two modes. Obviously, under the optimal CCHP model, the total operating cost of the system is the lower, achieving the goal of minimum operating cost.

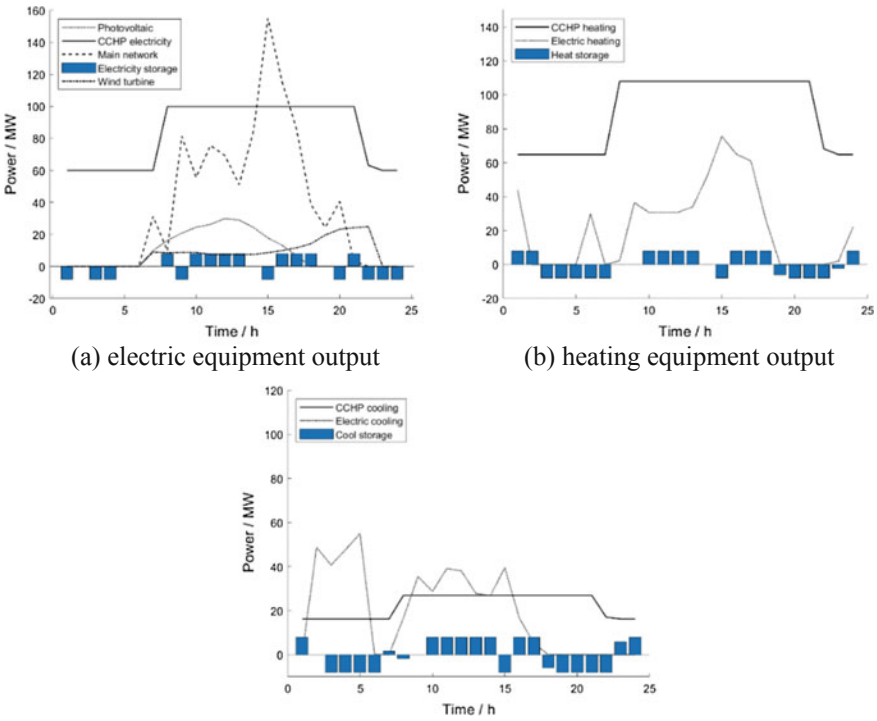

(a) electric equipment output

(b) heating equipment output

(c) cooling equipment output

Fig. 6 Equipment output power under CCHP optimal power mode

Table 2 Operation cost

CCHP operation mode	Total cost (RMB)	Electricity cost (RMB)	Gas cost (RMB)
Full power mode	2.58×10^6	0.85×10^6	1.73×10^6
Optimal power mode	2.31×10^6	0.87×10^6	1.45×10^6

6 Conclusion

This paper studies the multi-objective integrated energy system operation optimization technology, analyzes the output characteristics of the main integrated energy system equipment, and establishes the objective function with the lower operating cost and the higher reliability. Taking into account the system constraints of electricity, heating and cooling, the multi-objective running optimization model is solved by linear programming method. Finally, an integrated energy system case with typical equipment is constructed. The Pareto solution set of the case is solved.

Then the different operating modes of CCHP are compared. The results show that the proposed model can meet the requirements and provide a unified optimization solution for integrated energy system.

References

1. Zeng M, Yang Y, Li Y et al (2016) The preliminary research for key operation mode and technologies of electrical power system with renewable energy sources under energy internet. Proc CSEE 36(3):681–691
2. Sun H, Pan Z, Guo Q (2016) Energy management for multi-energy flow: challenges and prospects. Autom Electr Power Syst 40(15):1–8
3. Song C, Feng J, Yang D et al (2018) Collaborative optimization of integrated energy considering system coupling. Autom Electr Power Syst 42(10):38–45
4. Jia H, Wang D, Xu X (2015) Research on some key problems related to integrated energy systems. Autom Electr Power Syst 39(7):198–207
5. Cheng Y, Zhang N, Kang C et al (2017) Research framework and prospects of low-carbon multiple energy systems. Proc CSEE 37(14):4060–4069
6. Gu W, Lu S, Wang J et al (2017) Modeling of the heating network for multi-district integrated energy system and its operation optimization. Proc CSEE 37(5):1305–1315
7. Dong S, Wang C, Liang J et al Multi-objective optimal day-ahead dispatch of integrated energy system considering power-to-gas operation cost. Autom Electr Power Syst 42(11):8–15(2018)
8. Qin T, Liu H, Wang J et al (2018) Carbon trading based low-carbon economic dispatch for integrated electricity-heat-gas energy system. Autom Electr Power Syst 42(14):8–13
9. Zeng M, Han X, Li Y et al (2017) Multi-objective cooperative optimization based on Tent mapping chaos optimization NSGA-II algorithm for integrated energy system. Electr Power Autom Equip 37(6):220–228
10. Lyu J, Zhang S, Cheng H (2018) Reliability evaluation of integrated energy system considering thermal inertia and operation strategy. Autom Electr Power Syst 42(20):9–16

Voltage Optimization Strategy for Distribution Network Considering Distributed Photovoltaic Active Power Reduction

Wenbin Wang, Ning Wang, Qiao Zhang, Jinqing Yang and Wei Jin

Abstract A long-term scale voltage optimization control strategy for distributed photovoltaic actively participated with distribution network considering active reduction is proposed. The residual capacity of PV inverters outside the active power is used to participate in the reactive power optimization for voltage control. If the voltage still exceeds the threshold values, the active power curtailment strategy to PVs is applied to provide more capacity for reactive power optimization and maintain the voltage in range. Considering the uncertainties of photovoltaics and load outputs, the complex affine method is employed to establish the power output model in each time period. Combination of the Ybus power flow calculation and the linear decreasing weight particle swarm optimization is used to solve the proposed optimization model. Case studies on an IEEE 33-bus system are conducted to verify the effectiveness of the proposed optimization strategy.

Keywords Voltage and reactive power optimization · Distributed photovoltaics · Active power curtailment · Residual capacity of inverter

1 Introduction

With the increase permeability of photovoltaic, the randomness and uncertainty of distributed photovoltaic (DPV) output and the mismatch with load power, these problems make the voltage fluctuation of distribution network increase and lead to the problem of voltage exceeding the limit more prominent [1–3]. Traditional PV power supply usually works at the unity power factor and maximum power tracking

W. Wang · W. Jin
Xingtai Power Supply Company, State Grid Hebei Electric Power Co. Ltd, Xingtai, Hebei 054001, China

N. Wang · Q. Zhang · J. Yang (✉)
School of Electrical Engineering, Yanshan University, Qinhuangdao, Hebei 066004, China
e-mail: yangjinqing01@163.com

Y. Xue et al. (eds.), *Proceedings of PURPLE MOUNTAIN FORUM 2019-International Forum on Smart Grid Protection and Control*, Lecture Notes in Electrical Engineering 585, https://doi.org/10.1007/978-981-13-9783-7_5

control mode [4], which only plays the active power function of PV power supply. The revised scheme IEEE1547 and China's technical requirements for grid-connected distributed generation (DG) (GB/T 33593-2017) stipulate that DG should participate in the voltage regulation actively and adjust the output of active and reactive power according to the requirement of voltage and power supply. The new PV grid-connected inverters basically have the function of controlling power remotely [5]. DPV participating in voltage regulation has many advantages, such as fast response, bidirectional adjustable reactive power, no mechanical wear and tear, etc. It plays an important role in solving the voltage problem of high-density PV access to the power grid.

DG voltage control mainly adopts three strategies: decentralized autonomous control, distributed control and centralized control. The first strategy [6–8] controls DG and other reactive power devices autonomously based on local measurement information, which has the advantages of no information communication, flexible configuration and strong real-time performance. However, due to the lack of overall synergy, it has limited global voltage control capability. Jia et al. [7, 8] proposed several DG active-reactive power coordination modes based on whether the PCC voltage exceeded the limit or not. Tonkoski et al. [9, 10] proposed voltage regulation strategies to prevent voltage from exceeding the limit by reducing the active output of PV power, but only based on local information, the active power cannot be minimized from the perspective of the whole network. Distributed control strategy [11] uses local intelligent controllers as nodes to build communication links. Controllers are relatively autonomous and cooperative, forming a peer-to-peer networked control system. The centralized control strategy adopts master-slave structure and optimizes the voltage level of the whole network at the control center. It has the advantages of wide control range and good voltage regulation effect, and mature application. Zhang et al. [12] proposes a reactive power optimization strategy combining DG with capacitors and transformers. Lv et al. [13] considered the coupling between active and reactive power of PV, coordinate and optimize the controllable active and reactive power resources in distribution network to regulate voltage, and adopt a multi-time scale optimal control scheme which combines day-ahead optimization and on-line correction. Huang et al. [14] aims at the problem of voltage limit caused by DG access to distribution network, a long-time scale reactive power optimization model for distribution network is established to synthetically optimize the DG reactive power output and reactive power compensation equipment. Fu et al. [15] proposes with controllable DG, energy storage, sectional switches and reactive power compensation equipment as control strategy, and with the objective of minimizing the operation cost and risk of limit the distribution network, an advanced optimization model of active distribution network is established. Ren et al. [16] optimizes coordination of DG, flexible load, energy storage, compensation capacitors and power transformers. A multi-time scale active-reactive power coordination optimization model is established to minimize the operation cost of distribution network.

PV inverters have large residual capacity in most operating time, and the active power output may be close to full capacity only in less time with very good weather

conditions. Therefore, in the case of insufficient residual capacity, it is an economical and reasonable strategy to satisfy the voltage qualification by reducing active power. How to minimize active power reduction from the perspective of the whole network is a problem to be solved. In this paper, a voltage control method for distribution network considering DPV active power reduction strategy is proposed, and the optimization strategy is implemented according to whether voltage exceeds the limit.

The rest of the paper is organized as follows. Section 2 gives the complex affine model of the load and DPV. Sections 3 and 4 present the design plan of the coordination and optimization strategy for reactive-active power reduction with DPV. Section 5 shows how to set the model. And then the simulation results are shown in Sect. 6. Finally, Sect. 7 summarizes the conclusion.

2 Design of Complex Affine Model of DPV and Load

The active output of DPV fluctuates with weather conditions, and the load power consumption changes with time. Therefore, in the development of DPV grid-connected optimization strategy, it is necessary to consider the impact of the uncertainty of the two on the distribution network voltage. Among them, the most widely used is the probability-constrained planning method based on probability distribution [17], but it cannot change the PV output according to different weather conditions the next day. In this paper, the complex affine algorithm is used to establish the PV power supply and load uncertainty output model for each period. The affine mathematical method cannot only express this uncertainty, but also reduce the range of the solution in the calculation of power flow, while consider the completeness and accuracy of the solution.

2.1 Complex Affine Model of DPV

The DPV active output range is mainly related to the fluctuation of illumination intensity which has a great relationship with the change of clouds in the sky [18]. According to the weather information, the conditions of each time period can be obtained, and the affine expression of the cloud layer coefficient and the atmospheric layer illumination intensity is obtained by using the affine and interval conversion formula, which can be expressed as follows [18]:

$$\hat{J}_t = J_{0t} + h\varepsilon_{\mathrm{j}t} \tag{1}$$

$$\hat{G}_{\mathrm{a}t} = G_{0t} + k\varepsilon_{\mathrm{g}t} \tag{2}$$

where $\hat{J}_t$ and $\hat{G}_{at}$ are the complex affine value of cloud layer coefficient and atmospheric layer illumination intensity in t period, J_{0t} and G_{0t} are the central value of change of cloud layer coefficient and atmospheric layer illumination intensity in t period, h and k are the ratio of change of cloud layer coefficient, ε_{jt} and $\varepsilon_{\mathrm{gt}}$ are the noise element of cloud layer coefficient and atmospheric layer illumination intensity in t period, the range of $\varepsilon_{jt}, \varepsilon_{\mathrm{gt}}$, are $[-1,1]$.

2.2 Complex Affine Model of Load

The output of power load is characterized by uncertainty and time series variation. Therefore, the complex affine method is used to build the output of active and reactive power models for each period which can be expressed as follows:

$$\hat{P}_{\mathrm{L}it} = P_{\mathrm{L}it} + \delta_{\mathrm{L}t} P_{\mathrm{L}it} \varepsilon_{\mathrm{L}it} \tag{3}$$

$$\hat{Q}_{\mathrm{L}it} = Q_{\mathrm{L}it} + \delta_{\mathrm{L}t} Q_{\mathrm{L}it} \gamma_{\mathrm{L}it} \tag{4}$$

where $\hat{P}_{\mathrm{L}it}$ and $\hat{Q}_{\mathrm{L}it}$ are complex affine value of active power and reactive power of node i load in t period, $P_{\mathrm{L}it}$ and $Q_{\mathrm{L}it}$ are real values of active power and reactive power of node i load in t period, $\delta_{\mathrm{L}t}$ is uncertainty rate, reflecting the relative magnitude of uncertainty, which is related to time t. $\varepsilon_{\mathrm{L}it}$ and $\gamma_{\mathrm{L}it}$ are noise element of active power fluctuation and reactive power fluctuation of node i load in t period.

3 The Coordination and Optimization Strategy for Reactive-Active Power Reduction with DPV

DPV usually employs the MPPT controller to ensure the maximum active power of PV. However, when there is a risk of over-limit voltage in distribution network, the output of active power should be reduced and the reactive power should be increased.

In this paper, a voltage control strategy for distribution network is proposed, which coordinates DPV reactive and active power reduction, and a step-by-step voltage and reactive power optimization strategy and model are established to fully ensure that the whole network voltage is qualified and voltage deviation is minimum. The optimization of reactive and active power reduction coordination strategy with DPV is shown in Fig. 1.

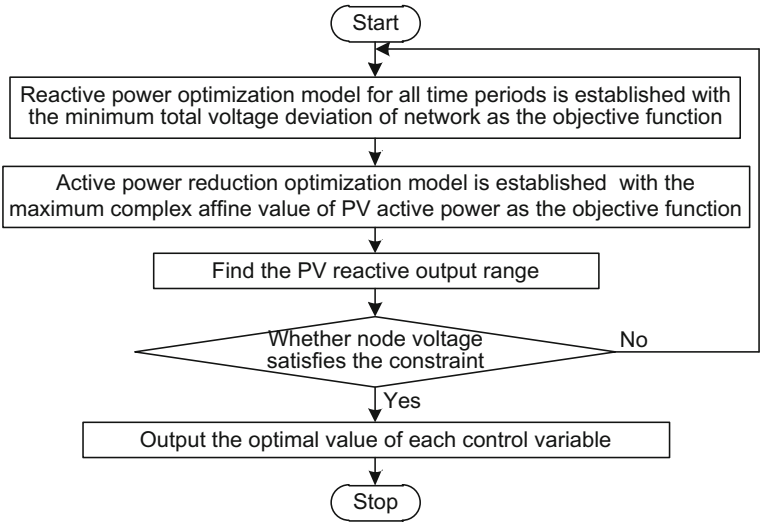

Fig. 1 Flow chart of reactive-active reduction coordination optimization strategy with DPV participation

4 The Coordination and Optimization Model for Reactive-Active Power Reduction with DPV

4.1 Objective Function

The objective function is to minimize the total voltage deviation in each period.

$$F_1 = \min\left(\sum_{i=1}^{n} |U_{it} - U_0|\right) \tag{5}$$

where U_{it} is median value of node i voltage interval in t period, U_0 is expected value of node voltage; m is number of divided periods; n is number of nodes.

The objective function is to maximize affine value of total active power of PV.

$$F_2 = \max\left(\sum_{f=1}^{N_{\mathrm{PV}}} \hat{P}_{\mathrm{PV}ft}\right) \tag{6}$$

where N_{PV} is number of PV power supply and $\hat{P}_{\mathrm{PV}ft}$ is complex affine value of PV active power output in t period.

4.2 Constraint Condition

Equality Constraints

PV output, load power and reactive power of compensation device should satisfy the following power flow equation:

$$\begin{cases} \hat{P}_{it} = \hat{U}_{it} \sum\limits_{j \in i} \hat{U}_{jt} \left(G_{ij} \cos \theta_{ij} + B_{ij} \sin \theta_{ij} \right) \\ \hat{Q}_{it} = \hat{U}_{it} \sum\limits_{j \in i} \hat{U}_{jt} \left(G_{ij} \cos \theta_{ij} - B_{ij} \sin \theta_{ij} \right) \end{cases} \tag{7}$$

$$\begin{cases} \hat{P}_{it} = \hat{P}_{\mathrm{PV}t} - \hat{P}_{\mathrm{L}it} \\ \hat{Q}_{it} = \hat{Q}_{\mathrm{PV}t} + Q_{\mathrm{c}it} - \hat{Q}_{\mathrm{L}it} \end{cases} \tag{8}$$

where $\hat{P}_{it}$ and $\hat{Q}_{it}$ are complex affine value of node i active power and node i reactive power in t period, $\hat{P}_{\mathrm{PV}t}$ and $\hat{Q}_{\mathrm{PV}t}$ are complex affine value of PV active power and PV reactive power in t period, $Q_{\mathrm{C}it}$ is output of node i reactive power compensation capacitor banks in t period, G_{ij} and B_{ij} are conductance and susceptance between node i and j, θ_{ij} is angular phase difference of voltage between node i and j.

Node Voltage Constraints

$$[U_{it}] \subseteq [U_{\min}, U_{\max}] \tag{9}$$

where $[U_{it}]$ is voltage amplitude interval of the node i in the period, $U_{\max}$ and $U_{\min}$ is upper and lower limits of voltage to satisfy operation requirements, respectively.

Inverter Operation Constraints

The reactive power generated by DPV is determined by the operation capacity of PV inverters and the active power output by PV, which can be expressed as follows:

$$0 \leq Q_{ft} \leq \sqrt{S^2 - P_{ft}^2} \tag{10}$$

where Q_{ft} is reactive power of PV in t period, S is installed capacity of PV inverters, P_{ft} is active power of PV inverters after reduction.

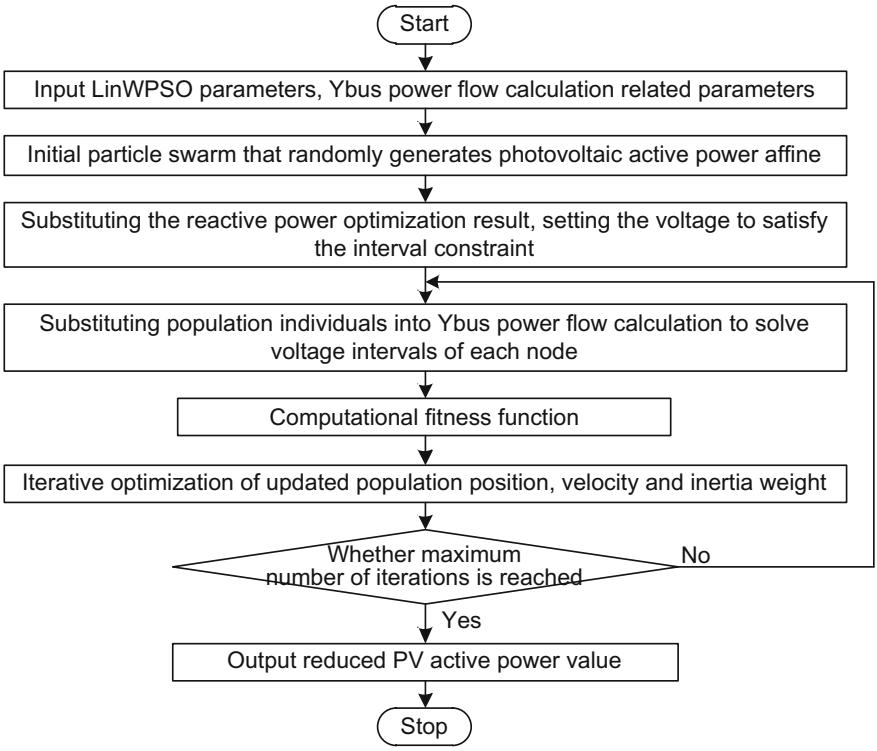

Fig. 2 Flow chart of active reduction optimization model solution

5 Model Solving Method

Ybus gauss iterative power flow calculation method has low requirement for initial value and does not need fast decoupling and its convergence will not be restricted by R/X [19]. LinWPSO algorithm overcomes the premature and oscillation phenomenon of the basic particle swarm optimization algorithm near the optimal solution, and has good convergence [13]. Therefore, this paper uses Ybus gauss iterative power flow calculation method and LinWPSO algorithm to solve the optimization model. The specific solution process is shown in Fig. 2.

6 Cases Analysis

The IEEE33-bus system is selected as a simulation example to verify the effectiveness of the optimization strategy proposed in this paper. The system topology is shown in Fig. 3. An on-load tap changer is connected between node 0 and 1, with a

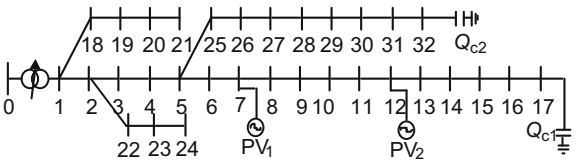

Fig. 3 IEEE33 node system structure diagram

variable ratio from 0.95 to 1.05, a total of 9 gears and a regulation step of 1.25%. DPVs are connected at nodes 7 and 12 respectively, with an installed capacity of 500 kW for each DPV, and a reactive compensation capacitor bank is connected to nodes 17 and 32, with a single capacity of 150 kvar, totaling 8 units. The parameters of algorithm are set as follows: population size of LinWPSO is 50, learning factor c_1 and c_2 are 2.0, dimension D is 5, inertial weight ω is 0.8, ω is between [0.4, 0.9] with an algebraic linear decline, and maximum number of iterations T is 60.

In this paper, one day's PV output and load are analyzed. The output power complex affine model of PV power supply and load is known from 2.1 to 2.2 sections. Cloud layer coefficient affine value under different weather conditions are obtained from actual meteorological information, as shown in Table 1.

According to Eq. (11), complex affine values of PV active power in each period can be obtained.

$$\hat{P}_{\mathrm{PV}t} = P_{STC}\frac{\hat{G}_{\mathrm{T}t}}{G_{STC}}\left[1 - 0.005\left(T_{\mathrm{a}} + C\hat{G}_{\mathrm{T}t} - 25\right)\right] \tag{11}$$

where P_{STC} is the maximum test power of PV system under standard test conditions taken as 408 kW; $\hat{G}_{\mathrm{T}t}$ is the complex affine value of illumination intensity in time period; G_{STC} is the illumination intensity under standard test conditions taken as 1000 W/m^2; T_{a} is the ambient temperature, in units of °C, C is 0.03.

Uncertainty of load data should be considered in power flow calculation. This paper assumes that uncertainty rates of load are basically the same in the same period, that means δ_t is the same. Then, the affine values of different node load in each period are calculated according to the Eqs. (3) and (4).

6.1 Analysis of Reactive Power Optimization Results

On the basis of known DPV and load complex affine output, reactive power optimization is carried out by coordinated control of PV inverters, On-load tap changer and reactive power compensation capacitors. The optimization results show that the reactive power optimization taking into account the PV reactive power regulation ability can improve voltage level. However, the problem of voltage over-limit condition occurs in some nodes during the 11–14 period, as

Table 1 Complex affine value of cloud layer coefficient

Weather condition	Complex affine value	Weather condition	Complex affine value
Sunny	$\hat{J} = 0.95 + 0.05\varepsilon_{it}$	Cloudy to overcast	$\hat{J} = 0.40 + 0.10\varepsilon_{it}$
Cloudy to sunny	$\hat{J} = 0.80 + 0.10\varepsilon_{it}$	Overcast	$\hat{J} = 0.25 + 0.05\varepsilon_{it}$
Cloudy	$\hat{J} = 0.60 + 0.10\varepsilon_{it}$	Sleet	$\hat{J} = 0.15 + 0.05\varepsilon_{it}$

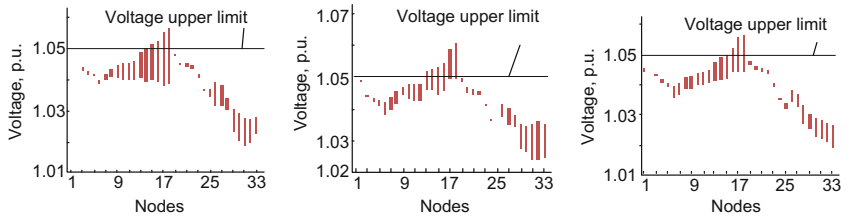

(a) Voltage Amplitude Interval of Nodes in 11-12 Period (b) Voltage Amplitude Interval of Nodes in 12-13 Period (c) Voltage Amplitude Interval of Nodes in 13-14 Period

Fig. 4 Voltage results of the 11–14 period after the reactive power optimization

shown in Fig. 4a–c is voltage amplitude range of each node in 11–12, 12–13 and 13–14 periods, respectively.

The reason of voltage over-limit is that the output of PV active power is larger, even more than 70% of the installed capacity, which reduces the effective utilization capacity of reactive power regulation. Even if all the remaining capacities of the inverters are used for reactive power regulation, the node voltage cannot be adjusted to the normal range.

6.2 *Analysis of DPV Active Power Reduction Optimization Results*

The aim of active power reduction optimization is to ensure the maximum absorption of PV power supply on the premise of qualified voltage. The reactive power optimization results of 11–14 periods which do not satisfy the requirements are selected. The reactive power reduction optimization of PV power supply is carried out based on DPV-participated reactive and active power reduction coordination optimization model. The results are shown in Table 2.

From Table 2, we can see that the output value of active power reduction optimization is reduced from 20 to 40 kW compared with the initial median value of PV power supply. The active power reduction value of PV 1 at node 7 is more

Table 2 Photovoltaic power active output value

Time interval	Initial value/kW	P_{PV1}/kW	PV_1 reduction/kW	P_{PV2}/kW	PV_2 reduction/kW
11–12	327	296	31	303	24
12–13	340	300	40	315	15
13–14	332	298	34	312	20

Table 3 Photovoltaic power reactive output value

Time interval	Q_{PV1max}/kvar	Q_{PV2max}/kvar	Q_{PV1}/kvar	Q_{PV2}/kvar
11–12	403	398	398.12	392.28
12–13	400	388	395.29	385.56
13–14	401	391	396.49	387.22

than that of PV 2 at node 12, which shows that the influence of PV 1 on voltage is greater than that of PV 2. Therefore, PV 1 can be operated preferentially when a successful reduction process is implemented.

6.3 *Analysis of Reactive Power Optimization Results After Increasing Reactive Power Adjustable Capacity*

The new range of PV reactive power output is obtained by solving the data substitution Eq. (10) in Table 3, and the reactive power optimization is carried out again. The reactive power value of PV supply in 11–14 period is obtained, as shown in Table 3. The optimized voltage results are shown in Fig. 5.

Table 3 shows that all the additional residual capacity of PV inverters is used for reactive power optimization and voltage regulation, and the minimum reactive capacity is used to achieve voltage lower than the upper limit.

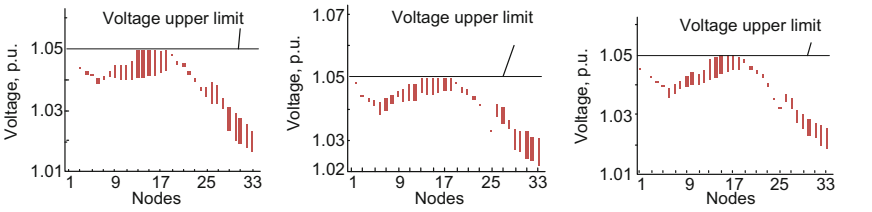

(a) Voltage Amplitude Interval of Nodes in 11-12 Period

(b) Voltage Amplitude Interval of Nodes in 12-13 Period

(c) Voltage Amplitude Interval of Nodes in 13-14 Period

Fig. 5 Voltage result of period 11–14 after active-reactive power coordination optimization

From Fig. 5, it can be seen that node voltages in Fig. 4 which do not satisfy the requirements fall into the [1.01, 1.05] range after PV active power reduction and reactive power optimization. Therefore, the coordinated optimal control strategy of reactive and active power reduction proposed in this paper can effectively solve the problem of over-voltage caused by inadequate reactive power capacity, and ensure the maximum output of PV.

7 Conclusion

A voltage coordination optimization method considering DPV active power reduction is proposed. DPV reactive power optimization model and active power reduction optimization model is established according to whether the voltage exceeds the limit or not, and the optimization strategy of DPV reactive and active power reduction coordination is established. The residual capacity of the inverters is used to optimize the voltage and reactive power. When the voltage requirement cannot be satisfied, minimizing DPV active output from a network-wide perspective, which ensures the voltage security and new energy absorption of the high permeability distribution network under complex and uncertain operation scenarios. The uncertain power output model of each period is established by complex affine method, and the adjustable range is given according to the weather conditions of the next day, so that the control strategy can better adapt to the uncertainties of the optimization scenario.

Acknowledgements This work is supported by the National Science Foundations of China under grant No. 51607153.

References

1. Deng N, Ding XQ, Deng CT et al (2018) Multi-objective coordinated optimization of active and reactive power for distribution network integrated with high proportion of photovoltaic generation. Autom Electr Power Syst 42(06):33–39+91
2. Xiao H, Pei W, Deng W et al (2016) Analysis of the impact of distributed generation on distribution network voltage and its optimal control strategy. Trans China Electrotechnical Soc 31(S1):203–213
3. Huang W, Liu SL, Yi YQ et al (2019) Multi-time-scale slack optimal in distribution network based on voltage optimization for point of common coupling of PV. Autom Electr Power Syst 43(03):92–107
4. Zhang HP, Lin SJ, Liu MB (2016) Robust optimal allocation of reactive power compensation in low voltage distribution networks considering uncertainty of photovoltaic generation. Power Syst Technol 40(12):3880–3887
5. Ma W, Wang W, Wu XZ et al (2019) Optimal dispatching strategy of hybrid energy storage system for smoothing power fluctuation of grid-connected photovoltaic. Autom Electr Power Syst 43(03):58–66

6. Calderaro V, Conio G, Caldi V et al (2014) Optimal decentralized voltage control for distribution systems with inverter-based distributed generators. IEEE Trans Power Syst 29 (01):230–241
7. Jia QQ, Qi XM, Ning SY et al (2015) Strategy research of voltage and reactive power operation involved with distributed PV system. Acta Energiae Solaris Sinica 36(12): 2954–2959
8. Wang N, Gao P, Jia QQ et al (2017) Research on active and reactive power coordination control strategy of PV grid-connected system for voltage regulation. Adv Technol Electr Eng Energy 36(08):23–29
9. Tonkoski R, Lopes LAC (2011) Impact of active power curtailment on overvoltage prevention and energy production of PV inverters connected to low voltage residential feeders. Renew Energy 36(12):566–3574
10. Tonkoski R, Lopes LAC, El-Fouly THM (2011) Coordinated active power curtailment of grid connected PV inverters for overvoltage prevention. IEEE Trans Sustain Energy 2(02): 139–147
11. Xing ZB, Wei G, He J et al (2017) A dual stage voltage control method in active distribution network based on graph theory. Trans China Electrotechnical Soc 32(01):40–47
12. Zhang L, Xu YQ, Wang ZP et al (2011) Reactive power optimization for distribution system with distributed generators. Trans China Electrotechnical Soc 26(03):168–174
13. Lv QJ, Wang S, Liu TL (2012) Active/reactive power integrated optimization in distribution networks with distributed generation. Power Syst Prot Control 40(10):71–76+83
14. Huang W, Liu SL, Wang W et al (2018) Optimal reactive power dispatch with long-time scale in distribution network considering uncertainty of photovoltaic. Autom Electr Power Syst 42 (05):154–162
15. Fu Y, Liao JB, Li ZK et al (2017) Day-ahead optimal scheduling and operating of active distribution network considering violation risk. Proc CSEE 37(21):6328–6338
16. Ren JY, Gu W, Wang Y et al (2018) Multi-time scale active and reactive power coordinated optimal dispatch in active distribution network based on model predictive control. Proc CSEE 38(05):1397–1407
17. Hu ZC, Wang XF, Gareth T (2010) Stochastic optimal reactive power dispatch: formulation and solution method. Int J Electr Power Energy Syst 32(6):615–621
18. Ding T, Cui HT, Gu W et al (2012) An uncertainty power flow algorithm based on interval and affine arithmetic. Autom Electr Power Syst 36(13):51–55
19. Huang L (2009) Research and application of parallel Y_bus load flow algorithm. North China Electric Power University, Beijing, pp 25–30

Two-Stage Optimal Allocation Model of User-Side Energy Storage Based on Generalized Benders Decomposition

Yuanxing Xia, Minglei Qin and Enlin Cheng

Abstract To cater for the commercial application of energy storage on the user side, a two-stage optimal configuration model of energy storage on the user side based on generalized Benders Decomposition algorithm is proposed. Firstly, according to the collected historical load data, the user can judge whether it is suitable to install the energy storage device. Then, aiming at maximizing the benefit of energy storage, a two-stage optimal energy storage allocation model with monthly scale and daily scale is established for users who are suitable for installing energy storage devices. Considering that the model is a nonlinear mixed integer optimization, the generalized Benders Decomposition algorithm is used to optimize the model. Finally, the load data of three typical large industrial users are collected, and the Benders Decomposition algorithm is compiled with MATLAB2017a to optimize the simulation, which verifies the economic effectiveness of the proposed model.

Keywords User-side energy storage · Two-stage optimization · Generalized benders decomposition · Life cycle · Demand management

1 Introduction

In recent years, in the context of the energy revolution, energy storage has gradually become an indispensable part of the energy Internet because of its flexible charging and discharging, convenient frequency modulation and good effect of peak shaving and valley filling. Compared with the large-scale centralized energy storage on the grid side, the distributed energy storage on the user side can further enhance the peak shaving capacity of the grid and store the excess energy of renewable energy [1].

At present, many scholars have researched into the optimal allocation and scheduling of energy storage. Since the development of energy storage is mainly restricted by the high cost of energy storage device, some scholars optimize energy

Y. Xia (✉) · M. Qin · E. Cheng
College of Energy and Electrical Engineering, Hohai University, Nanjing 210098, China
e-mail: Yuanxingxia_seu@qq.com

Y. Xue et al. (eds.), *Proceedings of PURPLE MOUNTAIN FORUM 2019-International Forum on Smart Grid Protection and Control*, Lecture Notes in Electrical Engineering 585, https://doi.org/10.1007/978-981-13-9783-7_6

storage configuration from the perspective of peak and valley arbitrage income of energy storage [2], government price subsidies [3], energy storage life cycle [4] and so on, in the hope to reduce the user's electricity cost. To solve the problem of large-scale distributed photovoltaic grid-connected, it is proposed in Ref. [5] to add energy storage devices to build grid-connected photovoltaic micro-grid to reduce the impact of photovoltaic grid-connected on the system and alleviate the light abandonment. At the same time, considering the demand side response, the impact on the economic benefits and energy storage configuration of the micro-grid is further analyzed. A set of economical and reasonable scheduling schemes for integrated energy storage system is designed in the Ref. [6], and then the optimization of allocation capacity of liquid metal battery energy storage system is proposed. The operation mode of integrated energy storage system can give full play to the advantages of the two energy storage modes and make full use of various energy sources such as light, hydrogen and electricity. Reference [7] has established a detailed cost and benefit economic value evaluation model for battery energy storage system participating in load side peak cutting and valley filling. The optimal capacity allocation of lithium ion battery energy storage system is obtained through practical examples, and the corresponding peak-shaving and valley-filling control strategy is formulated according to the capacity, which effectively realizes the peak-shaving and valley-filling. However, the above-mentioned literature focuses on the power supply side, and researches on distributed energy storage on the user side are relatively few, and the optimal allocation of energy storage in user-side scenarios is not considered.

In summary, there are few studies on user-side energy storage at home and abroad. This paper focuses on this aspect and establishes an optimal allocation model for energy storage with the goal of minimizing the user's electricity charge in the life cycle of energy storage. Because the allocation of energy storage capacity and the maximum monthly demand are based on the monthly time scale, and the optimal scheduling of energy storage and the daily arbitrage income of peak and valley peacetime are based on the daily time scale, this paper decomposes the optimization problem into two-stage optimization according to the time scale, uses the generalized Benders Decomposition Algorithm to solve the two-stage model successively and iteratively, and chooses the typical annual load of industrial users in Jiangsu and Zhejiang Province. The economic effectiveness of the proposed algorithm is validated through data.

2 User-Side Energy Storage Model

One of the main expenditures of industrial users is the cost of industrial power consumption. At present, the research on reducing the power consumption of large industrial users is mostly about the demand management [8]. This method controls the maximum demand on the load side of industrial users that exceeds the contract demand value in order to reduce the demand price of users, so as to reduce the total electricity price of users.

In the two-part tariff system, the basic tariff that the user needs to pay is the unit price multiplied by the maximum demand value of the detected load in the current month [9]. If the maximum demand value detected exceeds 5% of the contract demand value reported by the user before the month, certain penalties will be imposed according to the regulations, and the electricity price of the excess part will be doubled.

2.1 Energy Storage Assessment Model

The objective of the energy storage evaluation model is to minimize the monthly electricity tariff, and the optimal allocation model of energy storage is established. Because of the high cost of energy storage devices, the energy storage evaluation model proposed here is used to determine whether users are suitable to install energy storage devices, and to determine the optimal storage capacity and rated charging and discharging power of energy storage [10].

The user's monthly electricity consumption fee includes the electricity consumption fee, the basic electricity consumption fee and the cost of installing the energy storage device. Because the cost of energy storage devices is effective in the life cycle of energy storage, it is necessary to convert the cost of energy storage devices into the month of evaluation. The energy storage assessment model is as follows [11, 12]:

$$\min MEC = C_1 + C_2 + C_3 \tag{1}$$

Among them, MEC (monthly electricity charge) is the user's monthly electricity charge, C_1 is the user's electricity charge that month, C_2 is the user's basic electricity charge that month, and C_3 is the user's installed energy storage device cost converted to the monthly cost.

(1) **Electricity charges**

Because the energy storage system is installed on the user side, the load detected on the grid side is different from the actual load of the user. Taking 15 min as load sampling interval, the user side electricity charge is as follows:

$$C_1 = \sum_{i=1}^{N} \sum_{j=1}^{96} m\left(P_{L,i,j} + P_{C,i,j} - P_{D,i,j}\right)\Delta t \tag{2}$$

Among them, N is the number of days in the month, m is the price of each period in a day, $P_{L,i,j}$ is the load of the user in the jth period of the ith day, $P_{C,i,j}$ is the charge value of the storage energy in the jth period of the ith day, $P_{D,i,j}$ is the discharge value of the storage energy in the jth period of the ith day, and Δt is the sampling interval of the user load.

(2) **Basic electricity consumption**

Industrial users report to the grid company at the beginning of each month the maximum electricity demand value for this month. If the actual maximum demand value of this month is greater than the maximum demand value reported at the beginning of this month, the excess part of the electricity will be punished according to the charge standard of double demand price. The user-side basic electricity costs are as follows:

$$C_2 = \begin{cases} 40x, y \leq 1.05x \\ 40x + 80(y - 1.05x), y > 1.05x \end{cases} \tag{3}$$

Among them, x is the approved value of actual demand, and y is the maximum value reported before the month.

(3) **Energy storage installation cost**

The price of energy storage device is related to its capacity, so the cost model of initial energy storage construction is established as follows:

$$C_3 = \frac{cE}{12T} \tag{4}$$

Among them, c is the unit cost of energy storage, E is the allocation capacity of energy storage, T is the life cycle years of energy storage.

2.2 Optimizing Constraints

(1) **State of charge (SOC) constraints of energy storage on user side**

Overcharging or over-discharging of energy storage will damage the life of energy storage. Considering the time continuity of charging and discharging of energy storage, the overcharging and discharging of the former period will affect the normal scheduling of energy storage in the next period, so the constraints of charging state of energy storage are set:

$$SOC_{\min} \leq SOC_{i,j} \leq SOC_{\max} \tag{5}$$

Among them, $SOC_{i,j}$ is the state of charge in the jth period of the ith day of energy storage, and SOC_{min} and SOC_{max} are the lowest state of energy storage and the highest state of energy storage respectively.

(2) **Continuity constraints on charging state of energy storage**

$$SOC_{i,j+1} = SOC_{i,j} + \frac{P_{C,i,j}\eta_C}{E}\Delta t - \frac{P_{D,i,j}}{\eta_d E}\Delta t \tag{6}$$

Among them, $SOC_{i,j+1}$ is the state of charge in the j + 1 period of the first day of energy storage, $SOC_{i,j}$ is the state of charge in the j period of the ith day of energy storage, η_c is the charge efficiency of energy storage, η_d is the discharge efficiency of energy storage, and Δt is the charge and discharge period of energy storage, taking 15 min.

(3) **Energy storage charge and discharge state constraints**

It is impossible for energy storage to be in the state of charging and discharging at the same time. Therefore, binary variables should be introduced to restrict the state of charging and discharging of energy storage.

$$B_{D,i,j} + B_{C,i,j} \leq 1 \tag{7}$$

Among them, $B_{D,i,j}$ and $B_{C,i,j}$ are Boolean variables. $B_{D,i,j}$ takes 1 to indicate that the energy storage is discharging in this period, and $B_{C,i,j}$ takes 1 to indicate that the energy storage is charging in this period.

(4) **Energy storage charge and discharge power constraints**

Each type of energy storage has its own rated charging and discharging power parameters. When using this energy storage for charging and discharging, it should not exceed the rated power of energy storage. The corresponding models are as follows:

$$\begin{cases} 0 \leq P_{D,i,j} \leq B_{D,i,j} P_{D\max} \\ 0 \leq P_{C,i,j} \leq B_{C,i,j} P_{C\max} \end{cases} \tag{8}$$

Among them, P_{Dmax} is rated discharge power of energy storage and P_{Cmax} is rated charging power of energy storage.

(5) **Energy storage capacity constraints**

The capacity of general energy storage is proportional to its rated charging and discharging power, so the energy storage rate model is established as follows:

$$E = \beta P \tag{9}$$

Among them, P is the rated capacity of energy storage, and β is the energy ratio of batteries.

(6) **Peak and valley load constraints**

In order to avoid new load peaks caused by peak-valley tariff, the load on grid side is restrained by peak-valley tariff after energy storage. The restraint model is as follows:

$$L_{i,\min} \leq P_{L,i,j} + P_{C,i,j} - P_{D,i,j} \leq L_{i,\max} \tag{10}$$

Among them, $L_{i,min}$ is the minimum value on the ith day of load on the grid side, and $L_{i,max}$ is the maximum value on the ith day of load on the grid side.

2.3 Monthly Energy Storage Optimization Model

Large industrial users need to report the maximum demand value of this month before the month. This paper introduces the user side energy storage device to optimize the demand value of energy storage report before the month by reasonable scheduling. The electricity charges that users need to pay include electricity consumption and basic electricity charges. The model is as follows:

$$\min F_1 = C_1 + C_2 \tag{11}$$

Among them, F_1 is the current monthly electricity charge.

The constraints of optimization before month are the same as those in the model of optimal allocation of energy storage. They include the constraints of charging state, charging and discharging limit, continuity of charging state and charging and discharging state, i.e. formulas (5–8). At this time, the energy storage evaluation algorithm has been completed, so the optimal allocation capacity and optimal charging and discharging power of user side energy storage are known, and the optimization algorithm is calculated as parameter input months ago.

2.4 Optimal Dispatch of Daily Energy Storage

This paper establishes an optimization model to maximize the profit of peak-valley arbitrage within a day after adding energy storage.

$$\max F_2 = \sum_{i=1}^{96} m\left[P_{L,i} - \left(P_{L,i} + P_{C,i} - P_{D,i}\right)\right]\Delta t \tag{12}$$

Among them, F_2 is the peak-valley arbitrage profit of the optimal dispatch of energy storage in a day, $P_{L,i}$ is the load of the ith period of a day, $P_{C,i}$ is the charging power of energy storage in the ith period of a day, $P_{D,i}$ is the discharge power of energy storage in the ith period of a day.

The constraints of intra-day optimization are consistent with those of pre-month optimization. They are energy storage state constraints, charge-discharge limit constraints, energy storage state continuity constraints and charge-discharge state constraints. In addition, charging and discharging constraints are added to the day energy storage optimization model, to prevent excessive charging and discharging due to peak and valley arbitrage during the day optimal dispatching, which leads to penalties for exceeding the pre-month optimal demand load:

$$0 \leq P_{L,i} + P_{c,i} - P_{D,i} \leq 1.05x \tag{13}$$

3 Generalized Benders Decomposition Principle

Because the energy storage evaluation model involves Boolean binary variables and continuous variables, Benders Decomposition algorithm is applied to solve the problem. Because there are non-linear constraints in the constraints, the generalized benders algorithm (GBD) is used for decomposition and evaluation.

Because the process of pre-month optimization and intra-day optimization is consistent with that of energy storage evaluation algorithm, this paper only uses energy storage evaluation algorithm to illustrate the application of generalized benders algorithm in the proposed optimization algorithm.

The solving process is divided into solving the main problem and sub-problem. The main problem is a continuous variable with the maximum energy requirement and rated capacity reported as decision variables. The sub-problem is a decision variable with the daily charging and discharging power as decision variables with the variable types Boolean and continuous variables. The main problem initializes the maximum demand value and rated capacity substitution sub-problem. The sub-problem takes the lead in the feasibility test to determine whether the decision variables of the main problem satisfy all the constraints. If not, the decision variables of the main problem are returned to the infeasible cut to adjust until all the constraints are satisfied.

Step 1: Initialize the upper and lower bounds of the main problem $\mathrm{UB}_0 = +\infty, \mathrm{LB}_0 = -\infty$ and set the iteration number $\mathrm{k} = 1$. Initialize the energy storage and report the maximum requirement value C_2 and rated capacity C_3.

Step 2: Initialize the maximum requirement and rated capacity into the sub-problem to solve:

$$\min MEC\left(C_1, \widehat{C}\right) \tag{14}$$

$$s.t.g\left(C_1, \widehat{C}\right) \leq 0 \tag{15}$$

Among them, $\hat{\mathrm{C}}$ denotes $\mathrm{C}_2, \mathrm{C}_3$, $\mathrm{g}\left(\mathrm{C}_1, \hat{\mathrm{C}}\right) \leq 0$ determined after determining the maximum demand value and rated capacity, and all constraints related to decision variables $\mathrm{C}_1, \mathrm{C}_2, \mathrm{C}_3$.

Step 3: Construct Lagrange function if feasible solution exists.

$$L(C_1, C, u) = MEC(C_1, C) + u^T g(C_1, C) \tag{16}$$

The optimal solutions $\mathrm{C}_{1\mathrm{k}}$ and u_k are obtained and have $\mathrm{UB}_\mathrm{k} = \min\{\mathrm{UB}_{\mathrm{k}-1}, \mathrm{MEC}(\mathrm{C}_{1\mathrm{k}}, \mathrm{C}_\mathrm{k})\}$.

Constructing the main problem of feasible cut-back replenishment:

$$z \geq L(C_{1k}, C_k, u_k) + \nabla_C^T L(C_{1k}, C_k, u_k) \cdot (C - C_k) \tag{17}$$

If there is no feasible solution, a relaxation variable s is introduced to construct a new sub-problem.

$$\min s \tag{18}$$

$$s.t. g(C_1, C) - s \leq 0 \tag{19}$$

$$s \geq 0 \tag{20}$$

C_{1k} and u_k and $UB_k = UB_{k-1}$ are obtained.
The main problem of constructing infeasible cut-back replenishment is as follows:

$$0 \geq u_k^T \left[g(C_{1k}, C_k) + \nabla_C^T g(C_{1k}, C_k) \cdot (C - C_k) \right] \tag{21}$$

Step 4: To solve the main problem, the main problem is constrained by feasible cut and infeasible cut.

$$\min z \tag{22}$$

$$s.t. (17)(21) \tag{23}$$

z_k and C_k are obtained, and $LB_k = z_k$.
Step 5: If $LB_k \geq UB_k$, then the problem converges, otherwise return to **step 2**.

4 Optimal Configuration of Energy Storage on User Side

The user-side energy storage optimization algorithm proposed in this paper first uses the user-side energy storage evaluation model to optimize the installed energy storage capacity and charging and discharging power. Then, according to the three evaluation indicators, the user with installed energy storage value is optimized and dispatched monthly, and the optimal demand value reported monthly is calculated. Subsequently, the intra-day scheduling strategy is optimized according to the calculated optimal demand value. The overall flow of the algorithm is as follows:

Step 1: Read the user's historical load data and evaluate whether the user is suitable for installing user-side energy storage.
Step 2: If it is suitable for installation, Benders Decomposition algorithm is called to output the corresponding rated capacity and power of energy storage, and if it is not suitable for installation, the algorithm is withdrawn directly.
Step 3: On the basis of given storage capacity and power, Benders Decomposition algorithm is invoked to optimize the requirement value reported by users a month ago.

Step 4: Constrained by the maximum demand value, the Benders Decomposition algorithm is used to calculate the optimal charging and discharging strategy for energy storage in a day.
Step 5: Output the maximum monthly demand value of the user and the optimal scheduling strategy within the day.
Step 6: For the next month cycle optimization, refer to steps 2–5.

The flow chart of the corresponding algorithm is as follows (Fig. 1):

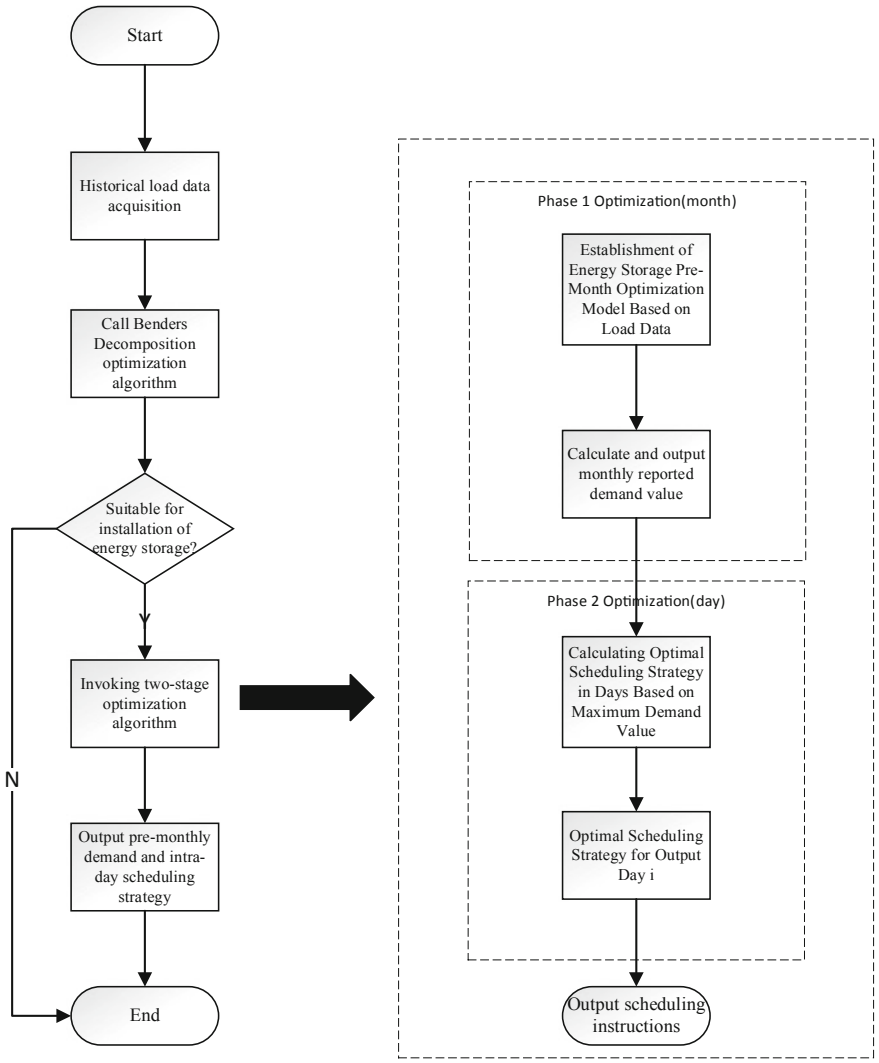

Fig. 1 Flow chart of two-stage optimization algorithm

5 Simulation

To verify the proposed two-stage optimization algorithm, the load data of three typical large industrial users in Jiangsu Suzhou Industrial Park in the whole year of 2017 are selected for simulation. The sampling interval of load data is 15 min, and a total of 96 data points are collected in a single day. The Benders Decomposition program is compiled under the development environment of MATLAB2017a to solve the problem. The characteristics of three typical loads are as follows:

(1) Load 1 is the electronic computer manufacturing industry. Because of the high degree of automation in the computer manufacturing industry, it is basically at the load peak all day, and the fluctuation of the load may occur during the staff handover.
(2) Load 2 is the textile and apparel manufacturing industry. There are night shifts in this industry. From 6 to 24 o'clock, it is in the peak period of load, and there are load fluctuations during the shift change.
(3) Load 3 is a typical 9-to-5 workload for paper mills, with higher workload during working hours and lower non-working loads.

In the simulation, the energy storage type is lithium battery, the energy ratio of the battery is 2.74, the charge-discharge efficiency is 82%, the life is 10 years, the unit electricity cost is 3 CNY/(kW h), the charge state limit of the energy storage is 0.2, the upper limit is 1, and the initial value of the charge state of the energy storage is 0.5. For large industrial users who install energy storage objects, Suzhou Power Supply Company adopts time-sharing tariff as follows (Table 1):

5.1 Energy Storage Assessment

In this section, the historical load data of the industrial user is used to optimize the configuration of the energy storage device installed by the user, and three types of typical users are evaluated by three kinds of evaluation indicators proposed in Sect. 2.3. The evaluation results are as follows:

According to Table 2, after installing energy storage devices, typical users 1 and 2 can recover costs in about 5–8 years, and the expected return on investment is

Table 1 Time-sharing electricity price for industrial users

Time interval	Time	Price/(CNY/kW·h)
Valley	0:00–8:00	0.3139
Flat	12:00–17:00, 21:00–24:00	0.6418
Peak	8:00–12:00, 17:00–21:00	1.0697

Table 2 Energy storage assessment results

Typical users	Optimum rated power of energy storage/kW	Optimal capacity of energy storage/kWh	Energy storage investment/$\times 10^4$ CNY	Life Cycle Projected Income/$\times 10^4$ CNY	Estimated recovery life/year	Return on investment/%
User 1	243.0	665.8	199.74	205.64	7.98	102.90
User 2	196.9	539.5	161.85	216.98	5.64	134.06
User 3	115.3	315.9	236.94	−2.07	10.60	−0.87

more than 100%. Analyzing the load of this kind of user, we can see that the load with large load and significant difference between peak and valley is more suitable for installing the energy storage device on the user side. The higher the peak value of load in the period with higher daytime hourly price, the greater the corresponding life-cycle income, and the shorter the life of cost recovery. Because the user 3 load is small and the load difference between peak and valley is not significant, it is difficult for the user 3 to compensate for the high installation cost of energy storage devices by the energy storage peak and valley arbitrage and peak cutting. Therefore, the cost cannot be successfully recovered in the life cycle of energy storage. Users with such load characteristics are not suitable for installing energy storage.

5.2 Energy Storage Optimization Before April and February

User 1 and user 2, which are suitable for installing energy storage in energy storage evaluation, are selected as examples for analysis. The results of user's pre-month optimization are as follows:

As can be seen in Table 3, the electricity cost of each user in the current month has dropped dramatically, and the electricity cost saved by User 2 is more, amounting to 94,400 CNY. This is because after energy storage is applied to demand management, daytime peak power consumption is effectively reduced to the maximum reported demand, thus saving basic electricity charges; in addition, due to the attraction of time-sharing price, energy storage "peak power Valley use", there are additional peak-valley arbitrage benefits.

Table 3 Pre-month optimized results of energy storage

Typical users	Maximum requirement value/kW	Peak valley arbitrage/($\times 10^4$ CNY/month)	Demand arbitrage/($\times 10^4$ CNY/month)	Total revenue/($\times 10^4$ CNY/month)	Life cycle benefits/$\times 10^4$ CNY
User 1	657.9	2.045	6.925	8.97	212.6
User 2	264.3	3.675	5.769	9.44	238.9

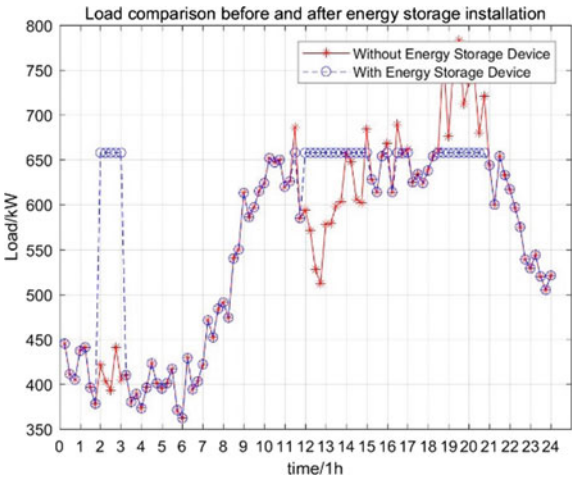

Fig. 2 Daily optimization results simulation (Take User 1 as an example)

5.3 Optimizing Daily Energy Storage

Although the peak-valley arbitrage profit of each user's energy storage increases slightly, between 2 and 4%, the profit of the whole life period is considerable due to the large power consumption of large users (10,000 CNY). In summary, energy storage can further save electricity charges and improve economic benefits through two-stage optimization.

User 1 is selected as an example in this paper. Because the user's daily curve is basically the same with the electricity consumption varied, this paper chooses one day's electricity consumption curve in this month. The load curves before and after installation of energy storage are shown in Fig. 2.

From Fig. 2, it can be seen that under the optimized charging and discharging strategy, the energy storage is attracted by the price difference between peak and valley, and the charging and discharging are selected in valley and normal periods. By reducing peak load, the final power consumption curve can be smoothed as much as possible while earning the benefits of peak and valley filling.

6 Conclusion

This paper presents a user-side energy storage evaluation and two-stage optimization model based on Benders Decomposition algorithm. The main content is as follows:

(1) Based on the collected historical load data of typical users, this paper establishes a user-side energy storage optimization model with the objective of minimizing the overall cost of users, calculates and evaluates whether the users

are suitable for installing energy storage and calculates the storage capacity and rated power suitable for installing. The example analysis shows that the users with large load peak-valley difference, higher load grade and peak load during the day are more suitable for installing energy storage devices on the user side.

(2) For users who are suitable for installing energy storage, a two-stage energy storage optimization model is established with the constraints of the capacity of energy storage and rated charging and discharging power calculated by the energy storage evaluation algorithm. In the optimization before the month, the minimum total electricity charge of users is taken as the objective function to determine the maximum demand reported. In the intra-day optimization, the maximum peak-valley arbitrage is taken as the objective function to optimize the charging and discharging power of energy storage and further improve the economic benefits of users.

(3) Because the model established in this paper is a non-linear mixed integer programming model, the Benders Decomposition algorithm is used to decompose the optimization model into the main problem and the sub-problem. The main problem is solved iteratively with the maximum energy requirement and rated capacity reported as decision variables, and the sub-problem is solved iteratively with the daily charging and discharging power as decision variables.

The energy storage is applied to the management of large industrial users' demand. The example proves that the user side energy storage has a shorter recovery period and a higher profit, which is conducive to the commercial promotion of energy storage battery.

References

1. Latif U, Javaid N, Zarin SS et al (2018) Cost optimization in home energy management system using genetic algorithm, bat algorithm and hybrid bat genetic algorithm. In: 2018 IEEE 32nd international conference on advanced information networking and applications (AINA), pp 667–677
2. Zakeri B, Syri S (2015) Electrical energy storage systems: a comparative life cycle cost analysis. Renew Sustain Energy Rev 42:569–596
3. Luo X, Wang J, Dooner M et al (2015) Overview of current development in electrical energy storage technologies and the application potential in power system operation. Appl Energy 137:511–536
4. Bonaccorso F, Colombo L, Yu G et al (2015) Graphene, related two-dimensional crystals, and hybrid systems for energy conversion and storage. Science 347(6217):1246501
5. Ma H, Wang B, Gao W, Zhu C, Zheng Z, Siyang, Yang Y (2019) Energy storage equipment in regional integrated energy system participates in the operation optimization of auxiliary services. Power Syst Autom 43(08):34–46+68
6. Liang Z, Song Z, Wang J et al (2018) Optimal configuration of liquid metal battery energy storage system in photohydrogen coupled microgrid. Power Syst Autom 42(4):64–69
7. Han X, Zhang Z, Xiu X et al (2016) Economic evaluation of fast charging station equipped with step battery energy storage system. Energy Storage Sci Technol 5(4):514–521

8. Chen L, Wu T, Liu H et al (2019) Two-stage large-user energy storage optimization model based on demand management. Power Syst Autom 43(01):262–271
9. Amrouche SO, Rekioua D, Rekioua T et al (2016) Overview of energy storage in renewable energy systems. Int J Hydrogen Energy 41(45):20914–20927
10. Ross M, Abbey C, Bouffard F et al (2018) Microgrid economic dispatch with energy storage systems. IEEE Trans Smart Grid 9(4):3039–3047
11. Hu W, Xu G, Shangze, Wang L, Wen F, Cheng H (2019) Joint planning of battery energy storage and demand response for peak shaving in Industrial Park [J/OL]. Power Syst Autom:1–8
12. Cheng L, Qining, Tian L (2019) Joint planning of generalized energy storage resources and distributed generation considering operation control strategies. Power Syst Autom 43 (10):27–40+43

Research on Power-Efficiency Synchronization of Wireless Power Transfer

Taiming Chen, Zhongyu Shen, Bo Yu, Xiaoqiang Zhu and Ke Wang

Abstract Aiming at the problem that the transmission efficiency and transmission power are difficult to achieve at the same time in the coupled resonant radio energy transmission process, based on the modeling and analysis of the equivalent structure of wireless power transmission S-S structure, this paper gives a method to synchronize transmission power and transmission efficiency under different loads and different distances, and further obtains that the optimal working frequency and the matching load resistance at a certain distance can make the power-efficiency synchronization reach the maximum value. By means of MATLAB simulation software, the experiment platform is set up to analyze the variation rule of system transmission efficiency and transmission power under different loads and different distances. The results demonstrate the correctness of the previous theory and provide a certain reference for improving the transmission efficiency and power of radio energy.

Keywords Coupled resonance · Power-efficiency synchronization · Optimal working frequency · Impedance matching

1 The Introduction

Traditional charging methods have safety hazards such as electric sparks and inconvenient operations. The emergence of wireless charging not only solves the above-mentioned troubles, but also makes great breakthroughs in some fields such as smart furniture, transportation, and medical care. It is a hot issue and research direction of research in recent years [1–4].

T. Chen (✉) · Z. Shen
School of Electrical & Automation Engineering, Nanjing Normal University, Nanjing Jiangsu 210023, China
e-mail: 807327512@qq.com

B. Yu · X. Zhu · K. Wang
State Grid Electric Power Research Institute Co., Ltd, Nanjing Jiangsu 211106, China

Y. Xue et al. (eds.), *Proceedings of PURPLE MOUNTAIN FORUM 2019-International Forum on Smart Grid Protection and Control*, Lecture Notes in Electrical Engineering 585, https://doi.org/10.1007/978-981-13-9783-7_7

The focus of current research is on transmission power and transmission efficiency. Literature [5] combined the characteristics of the system's output power, tracked its maximum power output point, and increased power, but did not consider efficiency. Literature [6] used the capacitance matrix method to achieve impedance matching, eliminating the problem of frequency offset, but it would make the structure complex and difficult to control. Literature [7, 12–14] proposed the concept of optimal frequency for transmission efficiency, and analyzed the relationship between maximum transmission efficiency and load or distance. Literature [8, 15, 16] analyzed the relationship between optimal operation frequency of transmission efficiency, optimal operation frequency of transmission power and impedance matching, and gave the idea of system power-efficiency synchronization factor. However, it did not further study the relationship between system power-efficiency synchronization under different distances, and the relationship between efficiency and load under specific distances.

In this paper, power-efficiency synchronization is realized under different loads and different distances, and the optimal working efficiency is obtained under certain distances, so as to realize power-efficiency synchronization.

2 System Modeling and Theoretical Analysis

This paper focuses on the function of S-S-type radio transmission. It consists of high frequency inverter output voltage V_{in}, internal resistance of power supply R_0, equivalent loss resistance R_1 and R_2 of transmit coil and receive coil, compensate capacitor C_1 and C_2 of transmit coil and receive coil, equivalent inductance L_1 and L_2 of transmit and receive coil, the mutual inductance M between transmitting coil and receiving coil and load impedance constitute R_L, The circuit is shown in Fig. 1:

The circuit shown in Fig. 1 can be derived from KVL:

$$\begin{cases} V_{in} = (Z_1 + R_0)I_1 + j\omega MI_2 \\ 0 = j\omega MI_1 + (Z_2 + R_L)I_2 \end{cases} \tag{1}$$

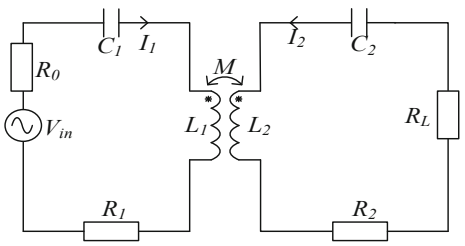

Fig. 1 S-S circuit topology

Among them:

$$\begin{cases} Z_1 = R_1 + j\omega L_1 + \dfrac{1}{j\omega C_1} \\ Z_2 = R_2 + j\omega L_2 + \dfrac{1}{j\omega C_2} \end{cases} \tag{2}$$

Because of the skin effect, the loss resistance R_i [9] and radiation resistance R_r [9] of the coil increase with increasing frequency, which can be approximated as:

$$R_i = \sqrt{\frac{\omega\mu_0}{2\sigma_i}} \cdot \frac{n_i r_i}{\alpha_i} = m_i\sqrt{\omega} \quad i = 1, 2 \tag{3}$$

$$R_r = \sqrt{\frac{\mu_0}{\varepsilon_0}}\left[\frac{\pi}{12}n^2\left(\frac{\omega r}{c}\right)^4 + \frac{2}{3\pi^2}\left(\frac{\omega h}{c}\right)^2\right] \tag{4}$$

In the above formula, μ_0 represents permittivity of vacuum; h is coil width; ε_0 represents the dielectric constant; c is the speed of light; $б_i$ indicates the conductivity of the receiving or transmitting coil; n_i indicates the number of turns of the receiving or transmitting coil; r_i represents the coil radius; α_i represents the wire diameter; m_i is a simplified expression. This paper studies the transmission of radio energy in the middle distance. At this time, the radiation resistance is much smaller than the loss resistance, so that the radiation resistance can be omitted in the following calculation.

From this it can be concluded that the input power and output power are:

$$P_{in} = I_1^2 \cdot Z_{in} = \frac{V_{in}^2\left[R_1R_2 + R_1R_L + (\omega M)^2\right](R_2 + R_L)}{\left[R_1R_2 + R_1R_L + R_2R_0 + R_LR_0 + (\omega M)^2\right]^2} \tag{5}$$

$$P_{out} = I_2^2 \cdot R_L = \frac{V_{in}^2(\omega M)^2}{\left[R_1R_2 + R_1R_L + R_2R_0 + R_LR_0 + (\omega M)^2\right]^2} \tag{6}$$

From the Eqs. (5) and (6), it can be concluded that the transmission efficiency of the system is:

$$\eta = \frac{P_{out}}{P_{in}} = \frac{(\omega M)^2 R_L}{(R_2 + R_L)\left[R_1R_2 + R_1R_L + (\omega M)^2\right]} \tag{7}$$

The main parameters of MATLAB simulation are shown in Table 1:

Table 1 Main parameters of simulation

Coil parameters	Transmit coil	Receive coil	Coil parameters	Parameter values
Radius r/mm	100	100	Voltage V_{in}/V	12
Wire diameter α_i/mm	2	2	Internal resistance R_0/Ω	50
Number of turns n_i	15	15	Conductivity δ_i/S/m	5.77×10^{-7}
Loss resistance R_i/Ω	0.3	0.1	Load resistance R_L/Ω	20
Mutual inductance M/mH	3.147		Resonant frequency f/kHz	51

We can see that the size of the load and the size of the mutual inductance affect the transmission efficiency and transmission power of the system. The efficiency and power of different loads and mutual inductances are also different.

It can be seen from Fig. 2 that with the change of the load resistance, the transmission power of the system reaches a maximum when the load resistance is 10–20 Ω, however the maximum transmission efficiency of the system is when the load value is about 25 Ω. From this we can see that the power and efficiency have reached the maximum under different load resistances, but there is no function to achieve power-efficiency synchronization.

It can be seen from Fig. 3 that as the distance between the two coils changes, the transmission power of the system reaches a maximum when the distance between the two coils is about 20 cm, but the transmission efficiency of the system reaches a maximum when the distance between the two coils is 10–15 cm. There is also no function to achieve power-efficiency synchronization. What is needed is to maximize the power and efficiency at the same time under the same load and the same distance to achieve the power-efficiency synchronization state, reduce system loss and improve the overall efficiency.

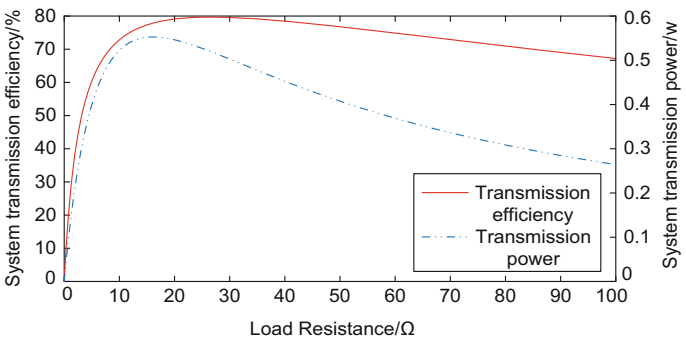

Fig. 2 Power-efficiency curve of load

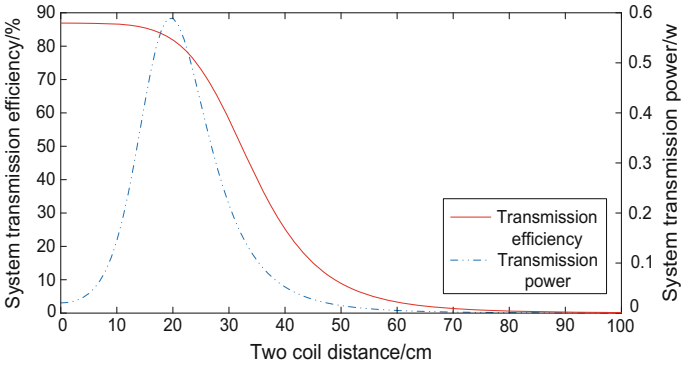

Fig. 3 Power-efficiency curve of distance

3 Power-Efficiency Synchronization Matching Parameters

3.1 Power-Efficacy Synchronization Analysis

Substituting the above formula (3) into (5), deriving the parameter ω can be obtained [9]:

$$2R_L R_0 + m(R_L + R_0)\sqrt{\omega} - 2(\omega M)^2 = 0 \quad (m_1 = m_2 = m) \tag{8}$$

Thereby, the optimal transmission power angular frequency and the optimal transmission efficiency angular frequency can be solved [11] as follows:

$$\omega_p = \frac{\sqrt{R_L R_0}}{M} \tag{9}$$

$$\omega_\eta = \frac{\sqrt{3}R_L}{M} \tag{10}$$

Under the same frequency condition, the optimal transmission power and the best transmission efficiency of the system can not be obtained at the same time. In order to get the best operating state, the power synchronization factor ξ [11] is defined to represent the ratio of the two optimal angular frequencies. Expressed as:

$$\xi = \frac{\omega_\eta}{\omega_p} = \sqrt{\frac{3R_L}{R_0}} \tag{11}$$

3.2 Impedance Matching Analysis

According to the maximum power transmission theorem, when the total system impedance is equal to the complex conjugate of the internal resistance of the power supply, the system power reaches the maximum. When impedance mismatch occurs, there must be energy loss to reduce transmission efficiency.

According to Fig. 1, the total impedance of the system is:

$$Z_{in} = R_1 + \frac{(\omega M)^2}{R_2 + R_L} \approx \frac{(\omega M)^2}{R_L} \tag{12}$$

When the system is in the state of power-efficiency synchronization, $(\omega M)^2/R_L = R_0$ can be obtained by substituting the system's best angular frequency ω and the power synchronization factor $\xi = 1$ into Eq. (12). Therefore, when the system works at the optimal operating frequency, not only the load power and transmission efficiency reach the maximum value at the same point, but also meet the condition of impedance matching. It can be seen that the impedance matching can realize the synchronization of the power of the wireless energy transmission system and realize the optimal utilization of energy.

In order to realize the function of power-efficiency synchronization, the above methods can be used to realize the optimal parameters of power and efficiency when selecting various parameters of the system, and simulation is performed in MATLAB.

4 Matlab Simulation Verification

When the system is operating at its optimal state, i.e.: $\omega_\eta = \omega_p = \omega_0$. Simulation of the above theory by MATLAB can be obtained:

It can be seen from the Fig. 4 that when the load is about 30 Ω, the transmission efficiency is 86%, the transmission power is 0.66 W, and the transmission efficiency and transmission power of the system reach the maximum at the same time, both the system realizes the power-efficiency synchronization. Compared with Figs. 3 and 5 can clearly see that the power and efficiency decrease as the distance increases, and the power-efficiency synchronization function is realized.

5 The Matching of Load and Distance

Different distances and different load corresponding synchronization of power and efficacy parameters are inconsistent. From the Eqs. (9) and (10), it can be concluded that [10]:

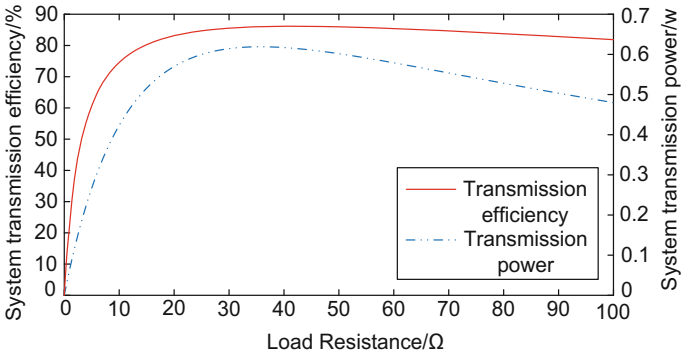

Fig. 4 Load synchronization curve

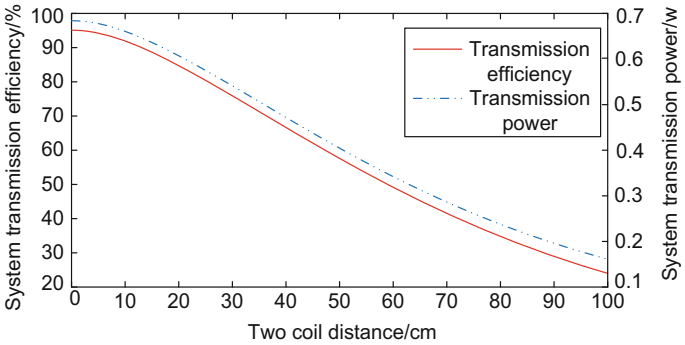

Fig. 5 Distance synchronization curve

$$f_p = \frac{\sqrt{R_L R_0}}{2\pi M} = \frac{\sqrt{R_L R_0}(D^2 + r_1^2)^{1.5}}{\pi^2 \mu_0 n_1 n_2 r_1^2 r_2^2} \tag{13}$$

$$f_\eta = \frac{\sqrt{3} R_L}{2\pi M} = \frac{\sqrt{3} R_L (D^2 + r_1^2)^{1.5}}{\pi^2 \mu_0 n_1 n_2 r_1^2 r_2^2} \tag{14}$$

In the above formula, D denotes the distance between the two coils; r_1 and r_2 denote the radius of the two coils; n_1 and n_2 represent the number of turns of the two coils. MATLAB simulation shows that:

From the Fig. 6, when the distance is 10 cm, the load is 17.3 Ω, and the frequency is 0.3037 MHz, the system can realize the power-efficiency synchronization.

When the power-efficiency synchronization factor is not equal to 1 ($\xi < 1$ or $\xi > 1$), that is to say, the situation of distance D = 10 cm, the optimum frequency is not equal to 0.3037 MHz as shown in Fig. 7 [12]:

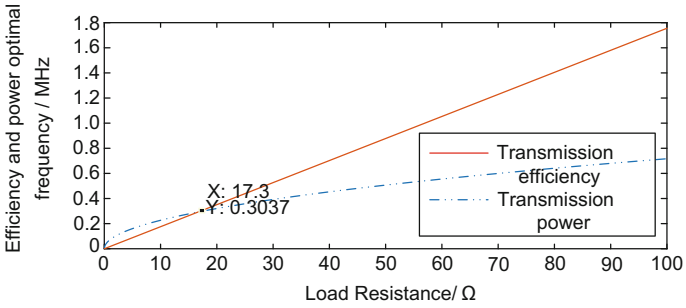

Fig. 6 Optimal working position

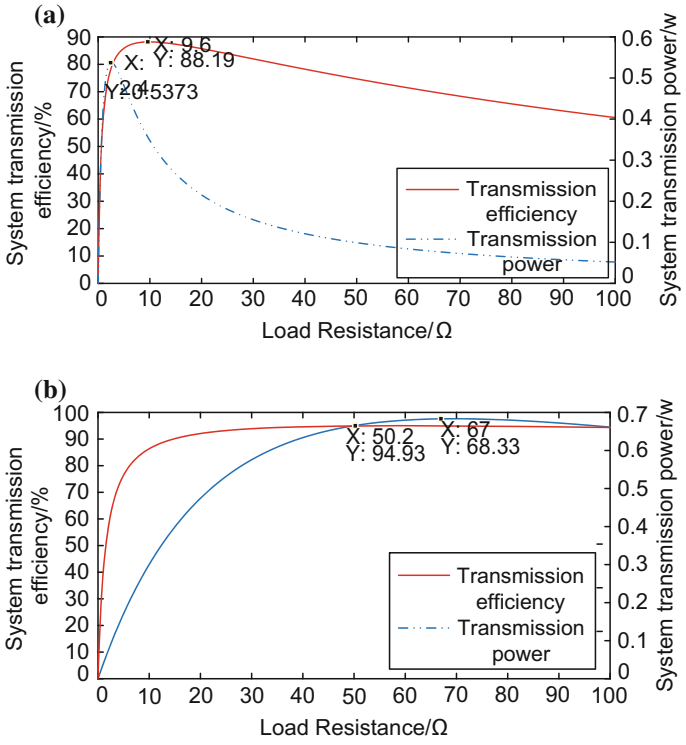

Fig. 7 D = 10 cm ($\xi \neq 1$)

From Fig. 7a, it can be seen that when D = 10 cm, the system operating frequency is less than the optimal operating frequency. The transmission power increases first and then decreases. When the load resistance reaches 2.4 Ω, the transmission power reaches the maximum value. The transmission efficiency also

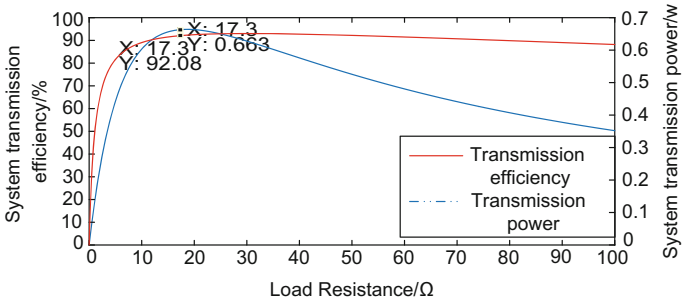

Fig. 8 D = 10 cm (ξ = 1)

increases first and then decreases. When the load resistance reaches 9.6 Ω, the transmission efficiency reaches the maximum. But they can't achieve power-efficiency synchronization. From Fig. 7b, it can be seen that when D = 10 cm, the system operating frequency is more than the optimal operating frequency. As with Fig. 7a, power-efficiency synchronization is not achieved.

When the system operating frequency is equal to the optimal operating frequency and the load satisfies the critical load conditions, the efficiency and power simulated by MATLAB are as follows [12].

It can be seen from Fig. 8 that when the distance D = 10 cm and the system operating frequency is equal to the optimum operating frequency, the transmission efficiency and power are maximized at different loads. When the load resistance reaches 17.3 Ω, the transmission power reaches a maximum of 92.08% and the transmission efficiency reaches a maximum of 0.663 W. In this case, the synchronization of power and efficiency can be achieved.

6 Conclusion

In order to synchronize transmission efficiency and transmission power in the coupled resonant wireless power transmission, we mainly study the transmission efficiency and transmission power of S-S structure pure resistive load. When the optimal frequency of the transmission efficiency is equal to the optimal frequency of the transmission power, the synchronization of power and efficacy can be realized. If not, the synchronization of power and efficacy can not be achieved. It can be achieved of synchronization of power and efficacy when the conditions of synchronization of power and efficacy are met under different loads and different distances. At the same time, the required frequencies are different at different distances. The farther the distance is, the higher of the required optimal operating frequency is. Through simulation, the correctness of the research results is obtained, and the optimal transmission of energy can be realized.

References

1. Zhao Z, Zhang Y, Chen K (2013) New progress of magnetically-coupled resonant wireless power transfer technology. Proc CSEE 33(3):1–13
2. Han KH, Lee BS (2008) The design evaluation of inductive power-transformer for personal rapid transit by measuring impedance. J Appl Phys 103(7):1–3
3. Wang W, Huang X, Tan L (2015) Effect analysis between resonator parameters and transmission performance of magnetic coupling resonant wireless power transmission system. Trans China Electrotechnical Soc 30(19):1–6
4. Huang X, Wang W, Tan L (2017) Research trends and application prospects of magnetically coupled resonant radio energy transmission technology. Autom Electr Power Syst 41(2):1–14
5. Li S, Fan S, Li F et al (2015) Power output characteristics analysis and maximum power point tracking of magnetically coupled resonant radio energy transmission system. Mod Electron Technol 38(12):146–149
6. Lim Y, Tang H, Lim S et al (2014) An adaptive impedance-matching network based on a novel capacitor matrix for wireless power transfer. IEEE Trans Power Electron 29(8): 4403–4413
7. Tang Z, Xu Y, Zhao M, Peng Y (2015) Optimal frequency of transmission efficiency for coupled resonant radio energy transmission. J Electr Mach Control 19(3):8–13
8. Tang Z, Yang F, Xu Y, Peng Y (2017) Study on the synchronization of magnetic coupling resonance radio energy transmission system. Trans China Electrotechnical Soc 32(21): 161–168
9. Liu Z, Liu R, Huang H (2015) Magnetically coupled resonant string-type radio energy transmission research. Mod Electron Technol 38(17):127–132
10. Narusue Y, Kawahara Y, Asani T Maximum efficiency point tracking by input control for a wireless power transfer system with a switching voltage regulator. In: IEEE wireless power transfer conference. Boulder, Australia, pp 1–4
11. Li C, Zhang H, Cao J et al (2015) Analysis and optimal design for power and efficiency transmission characteristics of magnetic resonance coupling power transmission systems. Autom Electr Power Syst 39(8):92–97
12. Qiang H, Huang X, Tan L et al (2012) Achieving maximum power transfer of inductively coupled wireless power transfer system based on dynamic tuning control. Autom Electr Power Syst 42(7):830–837
13. Zhang W, Wu X, Xia C et al (2019) Analysis of the effect about compensation parameters on the characteristics of Series/Series compensation radio power transmission system. Autom Electr Power Syst 43(07):166–177
14. Chen K, Zhao Z, Liu F et al (2019) Resonant topology analysis of electric vehicle two-way wireless charging system. Autom Electr Power Syst 43(07):166–177. 2017 41(02):66–72
15. Zhang W, Wu X, Xia C et al (2017) Modeling analysis of serial/string compensated radio energy transmission system. Autom Electr Power Syst 41(10):135–140
16. Li C, Zhang H et al (2015) Analysis and optimization of power and efficiency transmission characteristics of magnetic resonance coupled power transmission system. Autom Electr Power Syst 39(08):92–97

Day-Ahead Optimized Economic Dispatch of Integrated Electricity-Heating Systems Considering Wind Power Consumption

Zhiyu Gao, Li Han and Huitian Jin

Abstract Considering that air source heat pumps have the advantages of fast heat supply response, high heat supply efficiency and environmental protection, air source heat pumps can quickly follow the change of wind power when wind power changes rapidly, and timely eliminate wind power. Air source heat pumps are considered in the day-ahead dispatch model of integrated electricity-heating system in this paper. The model regards generation cost for traditional units and combined heating power (CHP) units, operation cost for air source heat pumps and electric boilers and curtailment cost of wind power as its optimization target. The response speed of air source heat pumps and electric boilers are first considered in the constraint conditions. The wind power can be converted into heat energy by air source heat pumps so that improve the consumption of wind power when the wind curtailment is serious. The heat generated is used to provide system heat. The excess of heat can be stored in the thermal storage energy devices, which released to provide system heat at low troughs. Finally, the comparison between the examples shows that air source heat pumps not only can quickly respond to the change of wind power, but also have low operation cost and reduce system power generation cost.

Keywords Integrated electricity-heating systems · Wind power consumption · Air source heat pump (ASHP) · Speed of response

1 Introduction

In recent years, with the rapid development of renewable energy represented by wind power, it not only has alleviated the energy crisis, but also reduced environmental pollution. However, the phenomenon of wind curtailment is serious [1] due to the randomness, the volatility and anti-peaking characteristics of wind power

Z. Gao · L. Han (✉) · H. Jin
China University of Mining and Technology, 221116 Xuzhou, China
e-mail: dannyli717@163.com

Y. Xue et al. (eds.), *Proceedings of PURPLE MOUNTAIN FORUM 2019-International Forum on Smart Grid Protection and Control*, Lecture Notes in Electrical Engineering 585, https://doi.org/10.1007/978-981-13-9783-7_8

output, which bringing huge losses to the economy. Determining-power-by-heat operation mode of the combined heating power (CHP) units gradually becomes a main reason for the curtailment of wind in "Three North" region of china [2], and limits the adjustment capacity of the CHP units, which does not provide enough space for wind power consumption. The coupling devices such as electric boilers, heat pumps and thermal storage energy devices can promote the direct conversion between electric energy and thermal energy [3] and decouple the CHP units from 'heat set' constraint, thus they can provide upside space for wind power consumption. The excess of wind power can be converted into heat energy by electric boilers and heat pumps so that improve the consumption of wind power. Therefore, it is of practical significance to study the optimized dispatch of the integrated electricity-heating system under wind power consumption.

Scholars have made some research on the integrated electricity-heating system under wind power consumption at present. In the literature [4], the use of thermal storage energy devices to improve the capacity of wind power consumption was studied. In Ref. [5], the authors quantified the regulation capacity of thermal storage energy devices to CHP units during heating period. The authors in Refs. [6, 7] introduced the scheme of eliminating the wind curtailment after the electric power plant was configured with electric boilers. Some scholars have jointly considered thermal storage energy devices and electric boilers, and proposed a combined arrangement of thermal storage energy devices and electric boilers [8, 9] and the application of regenerative electric boilers [10, 11] after analyzing the CHP units alone to configure thermal storage energy devices or electric boilers. In Ref. [8], the authors compared the economy considering thermal storage energy devices worked alone or did not work. In Ref. [9], the multi-agent of electricity-heat model based on electric boilers and thermal storage energy devices was introduced, which considered the scheduling difficulty of the thermal storage energy device and electric boilers. In Ref. [10], the authors proposed the wind power accommodation dispatch model based on the regenerative electric boilers and thermal storage energy devices and proved that they had less operation cost. In Ref. [11], the authors did research on the effect of power of electric boilers regulated by electromechanical components and proposed the model aiming at the minimum number of electrode adjustments of regenerative electric boilers and the maximum amount of wind power consumption. In Ref. [12], a comprehensive coordination model of thermal storage energy devices and heat release rate of ultimate wind power consumption and the electric power of electric boiler was established. In Ref. [13], a distributional robust coordinated dispatch model for integrated electricity-heating system considering uncertainty of wind power was proposed in this paper. In Ref. [14], the electric heating characteristics of heat pumps was gradually considered and they were applied to wind power consumption in electricity-heating integrated systems. In the electricity-heating system with wind power, the difference in wind power variation above was only considered, but they did not take into account the rate of wind power variation. Electric boilers, heat pumps and thermal storage energy devices may not be able to absorb wind power in time due to the limitation of their own regulation rate in actual dispatching. However, the clean heating devices

represented by air source heat pumps attract extensive attention due to their fast heat supply response, high heat supply efficiency and environmental protection [15–20], which had been applied in the field of clean heating [15–17] and intelligent building heat storage [19, 20] and achieve good results. But air source heat pumps are not considered in the rate of wind power change [21–23]. This paper will consider the influence of air source heat pumps to adjust the power speed, and pay attention to the influence of equipment characteristics of air source heat pumps on the amount of wind curtailment and system cost when wind power changes.

In this paper, air source heat pump are added to the coordinated optimization scheduling model of integrated electricity-heating system with traditional units, CHP units and thermal storage energy devices based on the existing paper. The effect of different response when wind power varies quickly on the total operating cost and the amount of wind curtailment in the electric boilers and air source heat pumps is compared. Finally, the comparison between the examples shows that air source heat pumps not only can quickly respond to wind power changes, reduce the amount of abandoned wind, but also have low operating costs and reduce system power generation costs.

2 Integrated Electricity-Heating System Structure with Air Source Heat Pump

2.1 Air Source Heat Pump

The working principle of air source heat pumps is shown in Fig. 1. An air source heat pump is mainly composed of a compressor, an evaporator, an expansion valve and a condenser. Based on the principle of reverse Carnot cycle, the air source heat pump obtains the external air low temperature heat source (QA) through the evaporator, vaporizes into low temperature and low pressure steam. Then it consumes a small amount of electric energy (QB) to drive the compressor, and the compressor converts the inhaled low temperature and low pressure steam into high temperature and high pressure steam. Therefore, the high pressure gaseous refrigerant enters. The condenser exchanges heat with the outside environment (QC). The condensate becomes a high-pressure liquid after the heat is released, and then the pressure of the throttle machine drops to a low-pressure and low-temperature liquid. Thereby liquid continues thermal cycle of evaporating, compressing, condensing, throttling, and re-evaporating in the evaporator. The conversion efficiency of the air source heat pump is generally between 3 and 5.

$$QC = QA + QB \tag{1}$$

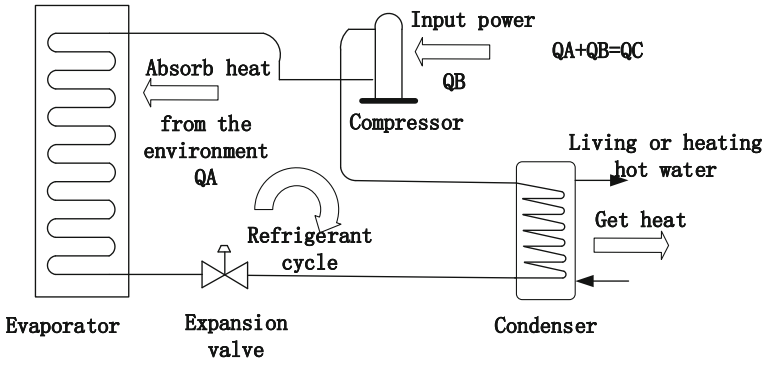

Fig. 1 Working principle of air source heat pumps

2.2 *Integrated Electricity-Heating System*

The structure of the integrated electricity-heating system in this paper is shown in Fig. 2. The system includes CHP units, traditional units, wind units, electric boilers (EB), air source heat pumps (ASHP), and thermal storage energy devices.

Air source heat pumps can configure with thermal storage energy devices in the electricity-heating system, which can promote the direct conversion between electric energy and thermal energy and decouple the CHP units from 'heat set' constraint, thus they can provide upside space for wind power consumption. The excess of wind power can be converted into heat energy by air source heat pumps so that improve the consumption of wind power when the wind curtailment is serious.

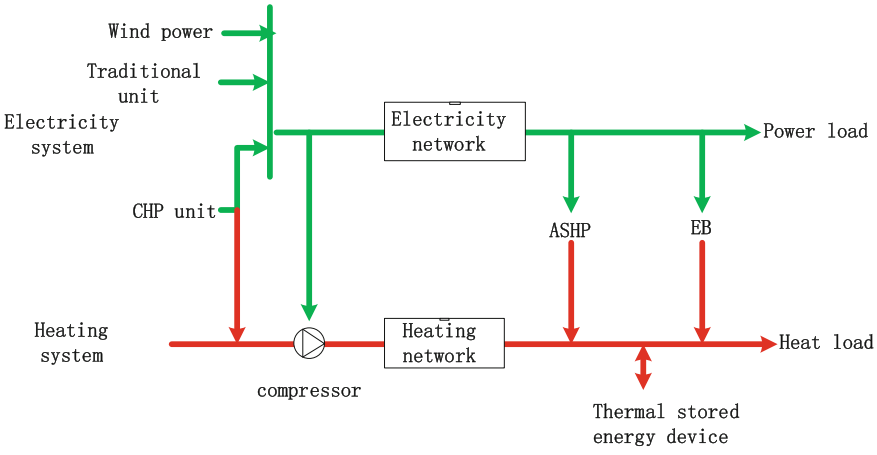

Fig. 2 Structure of the integrated electricity-heating systems

Considering that air source heat pumps have the advantages of fast heat supply response, high heat supply efficiency and environmental protection, air source heat pumps can quickly follow the change of wind power when wind power changes rapidly, and timely eliminate wind power. There is great prospect in the future efficient use of renewable energy and low carbon operation.

3 Model of the Integrated Electricity-Heating System

3.1 Objective Functions

The operating cost of CHP units, the power generation cost of traditional units, the operating cost of air source heat pumps, the operating cost of electric boilers and curtailment cost of wind power are the objective functions in this paper when the economical optimization of electricity-heating system with wind power is carried out. The formula can be given as follows:

$$\min(\mathrm{C}_{NC} + \mathrm{C}_{NG} + \mathrm{C}_{EB} + \mathrm{C}_{ASHP} + \mathrm{C}_{loss}) \tag{2}$$

where: C_{NC} is the operating cost function of combined heat and power (CHP) units; C_{NG} is the function of the generating power of traditional units; C_{EB} is the operating cost function of electric boilers; C_{ASHP} is the operating cost function of air source heat pumps; C_{loss} is the function of the curtailment cost of wind power.

(1) Operating costs of CHP units. The CHP units set up in this paper set to normally open state, and only their operating cost is considered, the formula can be given as follows:

$$\mathrm{C}_{NC} = \sum_{t\in T}\sum_{i\in NC}\left\{a_i^{chp}\left(P_{i,t}^{chp}\right)^2 + b_i^{chp}P_{i,t}^{chp} + c_i^{chp}\right\} \tag{3}$$

where: T is the scheduling period, NC is the number of CHP units, and $P_{i,t}^{chp}$ is the electric power of the ith CHP unit at time t, a_i^{chp}, b_i^{chp}, c_i^{chp} is expressed as the cost coefficient of the ith CHP unit.

(2) The cost of power generation for traditional units. The power generation cost of a traditional unit consists of the unit start-up cost and operating cost. The formula can be given as follows:

$$\mathrm{C}_{NG} = \mathrm{C}_{NG1} + \mathrm{C}_{NG2} \tag{4}$$

$$\mathrm{C}_{NG1} = \sum_{t\in T}\sum_{i\in NG} CS_{i,t}\left(1 - U_{i,t-1}\right)U_{i,t} \tag{5}$$

$$C_{NG2} = \sum_{t \in T} \sum_{i \in NG} \left\{ a_i P_{i,t}^2 + b_i P_{i,t} + U_{i,t} c_i \right\} \tag{6}$$

where: C_{NG1} is the start-up cost of the traditional units, C_{NG2} is the operating cost of the traditional units, NG is the number of traditional units, and $CS_{i,t}$ is the cost coefficient of the start-up of the ith traditional unit at time t. $U_{i,t}$ is expressed as the ith traditional unit start-stop state at time t, 0 is the unit shutdown state, 1 is the unit start-up state, and $P_{i,t}$ is expressed as the ith traditional unit at the time t, and a_i, b_i, and c_i are expressed as the power cost coefficient of the ith traditional unit.

(3) Operating costs of electric boilers. The cost of electric boilers is regarded as the electric cost of electricity consumed by electric boilers, and the cost of electric boilers is linearized in this paper. The formula can be given as follows:

$$C_{EB} = \sum_{t \in T} \sum_{i \in EB} a_{EB} P_{i,t}^{EB} \tag{7}$$

where: a_{EB} is expressed as the operating cost coefficient of electric boilers, and $P_{i,t}^{EB}$ is the electric power consumed by the ith electric boiler at time t.

(4) Operating costs of air source heat pumps. The cost of air source heat pumps is regarded as the electricity cost of air source heat pumps, and the cost of air source heat pumps is linearized in this paper. The formula can be given as follows:

$$C_{ASHP} = \sum_{t \in T} \sum_{i \in ASHP} a_{ASHP} P_{i,t}^{ASHP} \tag{8}$$

where: a_{ASHP} is expressed as the operating cost coefficient of air source heat pumps, and $P_{i,t}^{ASHP}$ is the electric power consumed by the ith air source heat pump at time t.

(5) Curtailment cost of wind power. In the integrated electricity-heating system, in order to improve wind power consumption, the cost of abandoning wind is added to the objective function. The formula can be given as follows:

$$C_{loss} = \sum_{t \in T} \sum_{i \in NW} \delta \left(P_{i,t}^{W0} - P_{i,t}^{W} \right) \tag{9}$$

where: NW is expressed as the number of wind farms, δ is expressed as the cost coefficient of discarding wind, $P_{i,t}^{W0}$ is expressed as the predicted output of the ith wind farm at time t, $P_{i,t}^{W}$ For the ith wind farm, the active output is actually dispatched at time t.

3.2 Constraints of the Model

(1) Electric power balance constraints

$$\sum_{i\in NC} P_{i,t}^{chp} + \sum_{i\in NG} P_{i,t} + \sum_{i\in NW} P_{i,t}^{w} = P_t^L + \sum_{i\in EB} P_{i,t}^{EB} + \sum_{i\in ASHP} P_{i,t}^{ASHP} \tag{10}$$

where: P_t^L represents the total electrical load power at time t.

(2) Thermal power balance constraints

$$\sum_{i\in NC} Q_{i,t}^{chp} + \sum_{i\in EB} Q_{i,t}^{EB} + \sum_{i\in ASHP} Q_{i,t}^{ASHP} + \sum_{i\in Ehs} Q_{i,t}^{Ehs} = Q_t^L \tag{11}$$

where: $Q_{i,t}^{chp}$ is the thermal power generated by the ith CHP unit in the t period, and $Q_{i,t}^{EB}$ is expressed as the thermal power generated by the ith electric boiler in the t period, $Q_{i,t}^{ASHP}$ indicates the thermal power generated by the ith air source heat pump in the t period. $Q_{i,t}^{Ehs}$ is expressed as the storage and release of thermal power of the ith thermal storage energy device in the t period, and $Q_{i,t}^{Ehs} > 0$ indicates heat storage, $Q_{i,t}^{Ehs} < 0$ indicates exotherm, and Q_t^L indicates total heat load power at time t,

(3) Electric boiler constraints

$$Q_{i,t}^{EB} = \eta_{EB} P_{i,t}^{EB} \tag{12}$$

$$P_{i,t}^{EB} - P_{i,t-1}^{EB} \le R_{U,i}^{EB} \tag{13}$$

$$P_{i,t-1}^{EB} - P_{i,t}^{EB} \le R_{D,i}^{EB} \tag{14}$$

where: η_{EB} represents the thermal efficiency of the electric boiler. $\eta_{EB} = 0.98$, $R_{U,i}^{EB}$ and $R_{D,i}^{EB}$ represent the upper limit of the electric power up and down slope of the ith electric boiler in this paper, respectively.

(4) Air source heat pump constraints

$$Q_{i,t}^{ASHP} = \eta_{ASHP} P_{i,t}^{ASHP} \tag{15}$$

$$P_{i,t}^{ASHP} - P_{i,t-1}^{ASHP} \le R_{U,i}^{ASHP} \tag{16}$$

$$P_{i,t-1}^{ASHP} - P_{i,t}^{ASHP} \le R_{D,i}^{ASHP} \tag{17}$$

where: η_{ASHP} represents the thermal efficiency of air source heat pumps. $\eta_{EB} = 3.25$, $R_{U,i}^{EB}$ 和 and $R_{D,i}^{EB}$ represent the upper limit of the up-down slope of the electric power of the ith air source heat pump in this paper, respectively.

Unit upper and lower limits and upper and lower ramping rate constraints, wind power output constraint, electricity-thermal coupling of CHP constraints and thermal storage energy device constraints are shown in Ref. [13].

4 Case Study

4.1 Composition of Case Study System

This case selects the modified IEEE-39 node system for verification. The air source heat pump is connected to node 8. The location of the remaining equipment nodes is shown in Ref. [13]. The case diagram is shown in Fig. 3. The predicted values of electric/heat load and wind power output in the integrated electricity-heating system of this example, the data of CHP units, traditional units and thermal storage energy devices are shown in Ref. [13]. The values of electric boilers and air source heat pumps parameters are shown in Table 1. The entire study was solved by using the commercial solver CPLEX on a computer with Intel Core 2.60 GHz and 4G RAM.

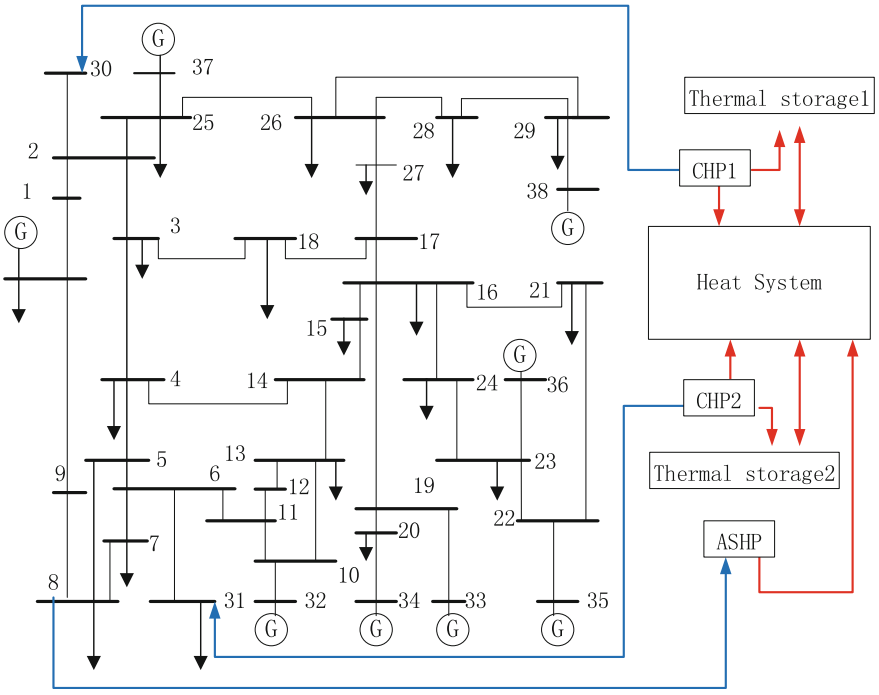

Fig. 3 Case diagram

Table 1 The parameters of electric boiler and air source heat pump

η_{EB}	$P_{i,\min}^{EB}$	$P_{i,\max}^{EB}$	$R_{U,i}^{EB}$	$R_{D,i}^{EB}$	a_{EB}
0.98	0	600	100	100	0.5
η_{ASHP}	$P_{i,\min}^{ASHP}$	$P_{i,\max}^{ASHP}$	$R_{U,i}^{ASHP}$	$R_{D,i}^{ASHP}$	a_{ASHP}
3.25	0	600	200	200	0.5

In Table 1, $R_{U,i}^{EB} = 100\,\text{MW/h}$ and $R_{D,i}^{EB} = 100\,\text{MW/h}$ means that the electric boiler can rise or fall 100 MW in one hour, $R_{U,i}^{ASHP} = 200\,\text{MW/h}$ and $R_{D,i}^{ASHP} = 200\,\text{MW/h}$ means that the air source heat pump can rise or fall 200 MW in one hour.

4.2 Analysis of Wind Curtailment Power and System Cost in the Electricity-Heating System

4.2.1 Case Analysis

In order to compare the effects of air source heat pumps configuration thermal storage energy devices, the normal operation of the system without them, the system configuration thermal storage energy devices, and electric boilers configuration thermal storage energy devices for the amount of wind curtailment power and cost of system operation, this paper sets 4 scenarios as following:

Scenario 1: The electricity-heating system is not configured with thermal storage energy devices, electric boilers and air source heat pumps. The system operates in the traditional mode.
Scenario 2: The electricity-heating system is configured with thermal storage energy devices, and electric boilers and air source heat pumps are not configured.
Scenario 3: The electricity-heating system is configured with thermal storage energy devices and electric boilers. Air source heat pumps are not configured.
Scenario 4: The electricity-heating system is configured with thermal storage energy devices and air source heat pumps, and no electric boiler is configured.

This paper firstly discusses the scenario 1 and scenario 2, compares the influence of the system configuration thermal storage energy devices on the amount of wind curtailment power, and then discusses scenario 3 and scenario 4, compares the response speed of air source heat pumps with the response speed of electric boilers to analyze the effect of response speed on the amount of wind curtailment power. Finally, the differences between the four scenarios and the amount of wind curtailment power are analyzed.

4.2.2 Scenario 1 and Scenario 2

With comparing scenario 1 and scenario 2, this paper does research on the influence of the system configuration thermal storage energy devices on the amount of wind curtailment power. The amount of wind curtailment power is shown in Fig. 4. The initial heat storage of the two thermal storage energy devices are 1500 and 1000 MW in scenario 2 of this paper, respectively. The heat storage and heat release of the thermal storage energy devices is shown in Fig. 4.

As shown in Fig. 4, the wind curtailment power is reduced from 12,511 to 11,714 MWh after thermal storage energy devices are added, and the wind power consumption is increased by 797 MWh. It can be seen from Fig. 3 that the serious phenomenon of wind curtailment mainly occurs in 1–8 h and 22–24 h. It can be seen from Fig. 4 that the thermal storage energy devices mainly release heat in the 1–9 h and 16–24 h to meet the demand of heat load, they reduce the output of the CHP units, and provide the rising space for the wind power consumption. It can be seen that the amount of wind curtailment power can be reduced to some extent by adding thermal storage energy devices to the system. It is possible to make the wind curtailment power completely consumed during the period when the amount of wind curtailment power is small.

4.2.3 Scenario 3 and Scenario 4

With comparing scenario 3 and scenario 4, this paper does research on the effects of electric boilers and air source heat pumps on the amount of wind curtailment power and system operating cost. The amount of wind curtailment power is shown in

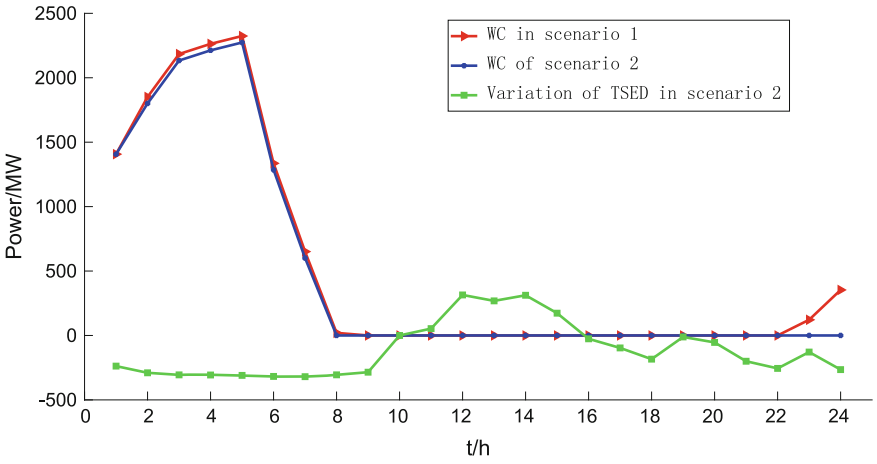

Fig. 4 Wind curtailment (WC) power in scenario 1 and scenario 2 and Variation of thermal stored energy devices (TSED) in scenario 2

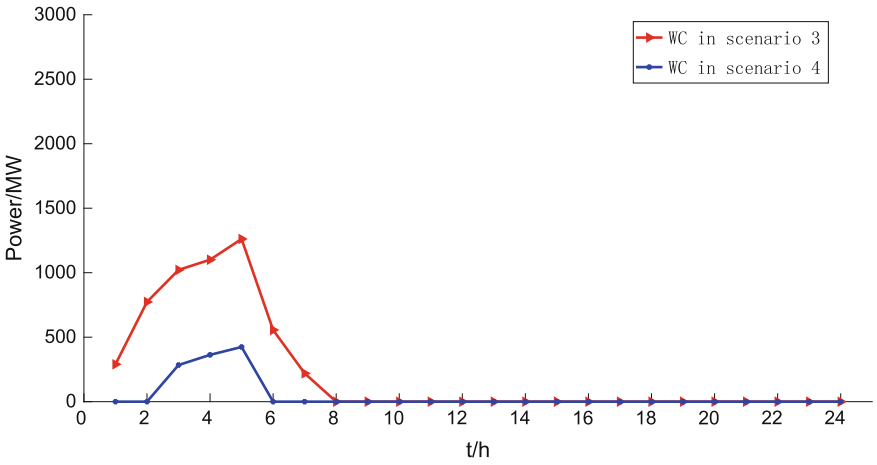

Fig. 5 WC power in Scenario 3 and Scenario 4

Fig. 5. The output of electric boilers, the air source heat pumps and CHP units is shown in Fig. 6. In scenario 3 and scenario 4 of this paper. The initial heat storage of the two thermal storage energy devices are 200 and 200 MW respectively, and the storage and release heat changes of the thermal storage energy devices in scenario 3 and 4 are as Fig. 7.

In scenario 3 and scenario 4, the wind curtailment power in Scenario 3 is 5222 MWh as shown in Fig. 5. The wind curtailment power is 1071 MWh in Scenario 4, and the amount of wind curtailment power is reduced by 4151 MWh, which is reduced by 76.5%. It can be seen from Fig. 6 that when the wind power changes,

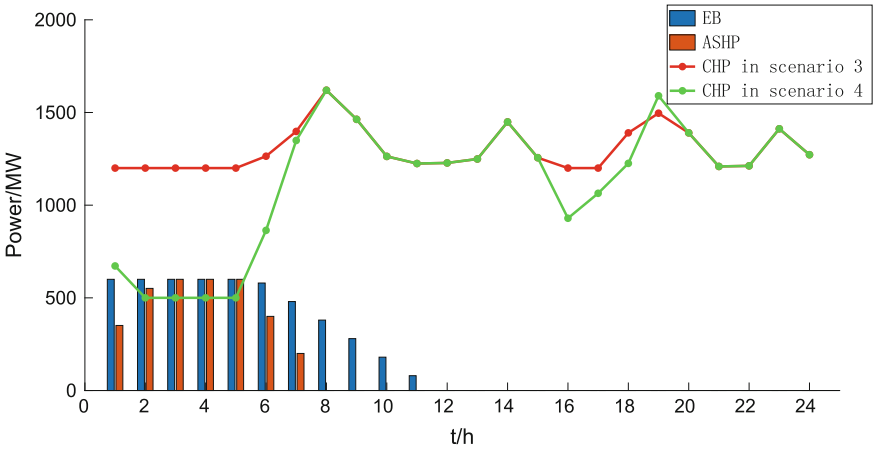

Fig. 6 Power outputs of EB, ASHP and CHP units in Scenario 3 and 4

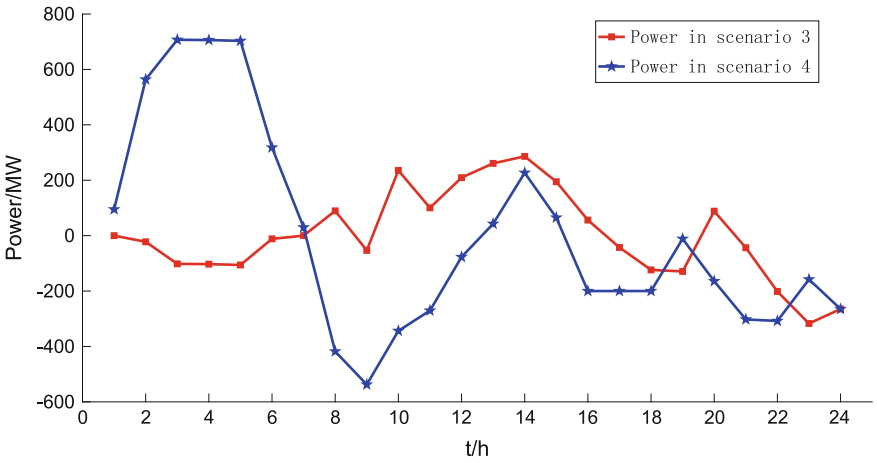

Fig. 7 Variation of thermal stored energy device in Scenario 3 and Scenario 4

air source heat pumps can absorb wind power more quickly and can adjust power more quickly. The adjustment time of electric boilers output is 6 h and the adjustment time of air source heat pumps output is 4.245 h in Fig. 6. The output of the CHP units can be reduced more quickly since air source heat pumps adjust the power faster and generate more heat in a short time. Therefore, the wind power can be completely absorbed in the 0–1 h period and the 6–8 h period in Fig. 5, and the electric boilers cannot absorb the same amount of wind curtailment power completely. At the same time, Fig. 6 show the different effects of electric boilers and air source heat pumps on the output of the CHP units. In Fig. 6, the output of the CHP units in Scenario 3 in the period of 1–9 h is around 1200 MWh. And, the output of the CHP units in Scenario 4 is about 500 MW during the period of 1–9 h of wind curtailment power, and the system with the air source heat pumps is compared with the CHP units in the system of electric boilers. The output of CHP units is significantly reduced, reduced by about 700 MWh, and reduced by about 58.3%.

The advantages of high heat supply efficiency of air source heat pumps through the variation of the thermal storage energy devices are shown in Fig. 7. During the 1–7 h period, the air source heat pumps store 3466 MW more heat than the electric boilers. During the 8–14 h period, the thermal storage energy devices in the system of air source heat pumps releases 2506 MW more than that in the system of electric boilers. The air source heat pump can produce more heat than heat produced by the electric boils during the serious period of wind curtailment and allow the thermal storage energy devices to release more heat during periods of low wind power.

Only the output of traditional units in scenario 4 is shown in Fig. 8. And the output of traditional units in other scenarios is not shown because of the space limitations.

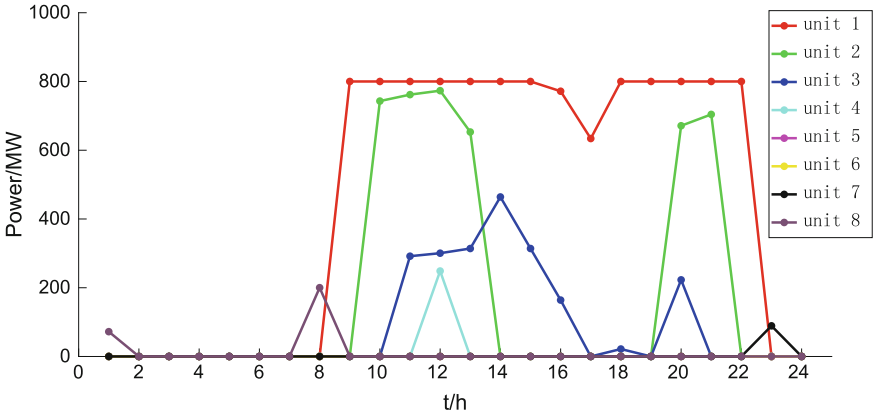

Fig. 8 Power outputs of traditional units in scenario 4

4.2.4 Scenarios 1–4

The air source heat pumps and the electric boilers are respectively arranged with thermal storage energy devices of 400 MW in the initial heat distribution of the thermal storage energy device compared with scenarios 1–4. The initial heat of the thermal storage energy devices is separately set to 2500 MW. The air source heat pumps and the electric boilers reduce the requirements for initial heat of the thermal storage energy devices significantly. If the initial heat is too low, the wind curtailment power will not be absorbed.

In order to visually see the difference between the operation of system in the traditional mode, the thermal storage energy devices, the electric boilers configuration thermal storage energy devices and the air source heat pumps configuration

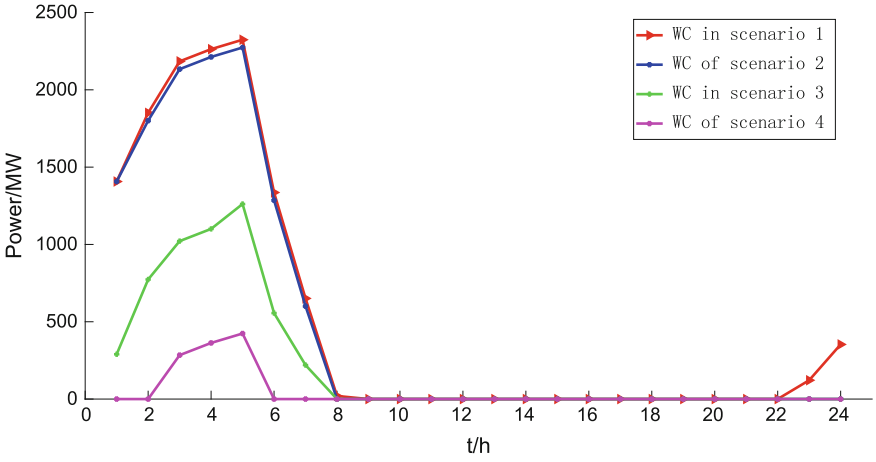

Fig. 9 Wind curtailment (WC) power in Scenarios 1–4

Table 2 Wind curtailment (WC) power in Scenarios 1–4

Scenario 1	Scenario 2	Scenario 3	Scenario 4
12,511	11,714	5222	1071

Table 3 The total cost of system operation in Scenarios 1–4

Scenario 1	Scenario 2	Scenario 3	Scenario 4
1,511,300	1,302,100	1,249,800	1,078,800

thermal storage energy devices, the wind curtailment power in the scenarios 1–4 is drawn in Fig. 9. Table 2 shows the amount of wind curtailment power in scenarios 1–4.

Compared with scenario 2, the amount of wind curtailment power in scenario 3 is reduced by 6492 MWh, which was reduced by 55.4%. In Scenario 4, the electric boilers of Scenario 3 are replaced with the air source heat pumps, and the amount of wind curtailment power is reduced to 1071 MWh, and the amount of wind curtailment power became less. Combined with scenarios 1–4, it can be seen that the coupling effect of the electricity-heating system can greatly reduce the output of the CHP units and eliminate the wind curtailment power.

The total operating cost of the system in scenarios 1–4 in order to compare the total cost of system operation is shown in Table 3.

It can be seen that the total costs of system operation decrease after thermal storage energy devices, electric boilers configuration thermal storage energy devices and air source heat pumps configuration thermal storage energy devices are added. The system's operating cost of the scenario 2 is reduced by 209,200 compared with the system's operating cost of the scenario 1, which is reduced by 13.8%. The system's operating cost of the scenario 3 is reduced by 261,500 compared with the system's operating cost of the scenario 1, which is reduced by 17.3%. The system's operating cost of the scenario 4 is reduced by 432,500 compared with the system's operating cost of the scenario 1, which is reduced by 28.6%.

In terms of the amount of wind curtailment power, air source heat pump configuration thermal storage energy devices can completely eliminate the wind in the period of 1–2 h and 6–8 h, and the other methods can not completely eliminate the wind in this period. In terms of the cost of system operation, air source heat pumps have the lowest cost of system operation. It can be seen that air source heat pumps configuration thermal storage energy devices not only can absorb more wind curtailment power, but also can reduce the total operating cost of the system.

5 Conclusion

A model of integrated electricity-heating system for wind power consumption is proposed in this paper in order to eliminate the wind curtailment in time. The coupling unit based on air source heat pumps can absorb wind power timely in the

electricity-heating system with wind power, and can also reduce the operating cost of the system. Through the analysis of the example, the following conclusions are obtained:

(1) Air source heat pumps configuration thermal storage energy devices can consume the excess of wind curtailment power more quickly and provide more heat. And reduce the output of the CHP units more quickly and the cost of system.
(2) The initial heat of the separated heat storage devices is reduced after the system is configured with electric boilers and air source heat pumps. It can reduce the cost of thermal storage energy devices.
(3) The thermal storage energy device, the electric boiler and the air source heat pump have a certain degree of promoting effect on the wind power consumption. Air source heat pumps configuration thermal storage energy devices can completely eliminate the wind curtailment power during certain periods of time.

Funding This research was funded by National Natural Science Foundation of China (61703404).

References

1. China's National Energy Administration (2019) Wind power grid operation in 2018 [EB/OL]. China's National Energy Administration, Beijing, 2019. http://www.nea.gov.cn/2019-01/28c_137780779.htm
2. Yang JI, Zhang N, Wang Y, Kang C (2018) Multi-energy system towards renewable energy accommodation: review and prospect. Autom Electr Power Syst 42(4):11–24
3. Wang W, Wang D, Jia H et al (2016) Review of steady-state analysis of typical regional integrated energy system under the background of energy internet. Proc CSEE 36(12):3292–3305
4. Xu F, Min Y, Chen L et al (2014) Combined electricity-heat operation system containing large-capacity thermal energy storage. Proc CSEE 34(29):5063–5072
5. Ge W, Wang S, Luo H, Ge Y, Zhou G, Cui D (2018) The leverage effect of large capacity centralized heat storage for wind power consumption. In: 2018 2nd IEEE conference on energy internet and energy system integration (EI2), Beijing, 2018, pp 1–6. https://doi.org/10.1109/ei2.2018.8582549
6. Guo F, Hu L, Zhou S (2018) Dispatching model of wind power accommodation based on heat storage electric boiler for peak-load regulation in secondary heat supply network. Autom Electr Power Syst 42(19):50–56
7. Li Y, Wang X, W. Zhang W (2018) Heat and power combined dispatching model with renewable energy, electrical heat pumps, and electrical boilers. In: 2018 IEEE power & energy society general meeting (PESGM), Portland, OR, 2018, pp 1–5. https://doi.org/10.1109/pesgm.2018.8586465
8. Yang C, Zhi C, Gangui Y et al (2016) Coordinated wind power accommodating dispatch model based on electric boiler and CHP with thermal energy storage. Proc CSEE 36(15):4072–4081

9. Yang L, Zhang X, Gao P (2018) Research on heat and electricity coordinated dispatch model for better integration of wind power based on electric boiler with thermal storage. In: IET generation, transmission & distribution, vol 12 no 15. 28 8 2018. pp 3736–3743. https://doi.org/10.1049/iet-gtd.2017.2032
10. Yang C, Zhuang Y, Chen Z et al (2019) Economic analysis of wind power accommodation schemes with the electric-thermal time shift characteristics of regenerative electric boiler. Thermal Power Gener 1–9
11. Li G, Zhuang G, Tian C et al (2018) Multi-objective optimization control of wind power consumption based on regenerative electric boiler system integrated with large-scale energy storage. Electr Power Autom Equipment 38(10):1006–6047. https://doi.org/10.16081/j.issn
12. Lu Z, Yang Y, Geng L et al (2018) Low-carbon economic dispatch of the integrated electrical and heating systems based on benders decomposition. Proc CSEE 38(7):1922–1934
13. Yue S, Liu J, Gao H et al (2018) A distributionally robust coordinated dispatch model for integrated electricity and heating systems considering uncertainty of wind power. Proc CSEE, 2018 38(24):7235–7247, 7450
14. Wang W, Yang L, Wang L, Zhang P, Huang J, Wang K (2018) Optimal dispatch of integrated electricity-heat energy system considering heat storage characteristics of heating network. Autom Electr Power Syst 42(21):45–52
15. Wu D, Hu B, WANG RZ et al (2017) Present situation, technology and policy of air source heat pump heating in China. Refrig Technol 37(5):1–7
16. Min J, Xu J et al (2019) Analysis on the principle and application of solar coupled air source heat pump technology. Shandong Chem Ind 48(02):115–118
17. Longfei MA et al (2017) Research on influence of large-scale air-source heat pump start-up characteristics to power grid. In: 2017 IEEE conference on energy internet and energy system integration (EI2), Beijing, 2017, pp 1–4. https://doi.org/10.1109/ei2.2017.8245377
18. Song D (2018) Study on compound energy supply system of gas-fired distributed combined heating and power cogeneration unit with air-sourced heat pump. Shanghai Energy Conserv (10):785–790
19. Chen X, Zhang X, Zhao X (2016) Air source heat pump energy storage heating system for smart building. In: 2016 Chinese control and decision conference (CCDC), Yinchuan, 2016, pp 3635–3639.https://doi.org/10.1109/ccdc.2016.753161
20. Craciun VS, Trifa V, Bojesen C, Andreasen SJ (2012) Air source heat pump a key role in the development of smart buildings in future energy systems: Low cost and flexible experimental setup for air source heat pumps. In: 2012 international conference and exposition on electrical and power engineering, Iasi, 2012, pp. 984–989.https://doi.org/10.1109/icepe.2012.6463805 (2012)
21. Zhou W, Z Jng, Sun H, Li G, Kong J, Zhang F (2018) An interval rolling estimation method for daily wind power forecast errors based on hidden Markov model. Autom Electr Power Syst 42(21):90–95
22. Zhu J, Liu Y, Xu L, Jiang Z, Ma C (2019) Robust day-ahead economic dispatch of microgrid with combined heat and power system considering wind power accommodation. Autom Electr Power Syst 43(4):40–48
23. Gan W, Guo J, Ai X, Yao W, Yang B, Yao L, Wen J (2019) Multi-scale multi-index sizing of energy storage applied to fluctuation mitigation of wind farm. Autom Electr Power Syst 43:01–07

Comprehensive Evaluation Model of Decommissioned Battery for Electric Vehicles Based on AHP-CRITIC

Na Yu, Feng Li, Xiaoyu Han, Jinlan Hu, Yajing Gao, Dongwei Li and Yuhan Liu

Abstract With the rapid development of new energy vehicles in China, the trend of decommissioning of power batteries has arrived, and the stagger utilization of decommissioned power batteries has become the focus of the industry. Once a power battery is decommissioned, the retired power battery needs to undergo relevant tests and evaluations before it can be carried out the cascade development and utilization. In this paper, we creatively propose the AHP-CRITIC method. Firstly, according to the health characteristics of the decommissioned power batteries, the improved K-means cluster analysis is used to analyze the curve characteristics of the decommissioned power batteries. Secondly, for the economic indicators of decommissioned batteries, we take advantage of the AHP-CRITIC method to evaluate the decommissioned power batteries. Then, a comprehensive evaluation model that synthetically considers the health characteristics and economics of decommissioned power batteries is established. Finally, an example is given to verify the effectiveness of the proposed evaluation model.

Keywords Electric vehicle · Decommissioned battery · Comprehensive evaluation · K-means clustering · AHP-CRITIC

N. Yu
Guangdong Power Grid Co., Ltd, 757 Dongfeng East Road, Yuexiu District, Guangzhou City, China

F. Li · J. Hu
Power Grid Planning Research Center, Guangdong Power Grid Co., Ltd., 6-8 Dongfeng East Road Shui Jungang, Yuexiu District, Guangzhou City, China

X. Han (✉) · Y. Gao · D. Li · Y. Liu
Technical and Economic Consulting Center for Electric Power Construction of China Electricity Council, No. 13 Baiguang Road, Xicheng District, Beijing City, China
e-mail: ncepuhxy@163.com

Y. Xue et al. (eds.), *Proceedings of PURPLE MOUNTAIN FORUM 2019-International Forum on Smart Grid Protection and Control*, Lecture Notes in Electrical Engineering 585, https://doi.org/10.1007/978-981-13-9783-7_9

1 Introduction

With the increasing pressure of environmental protection and the development of electric vehicles, electric vehicles have become the hot spot and trend of automotive industry research [1–3]. Along with the advent of the tide of China's power battery decommissioning, there are more and more researches on decommissioned power batteries [4, 5]. The cascade utilization technology of decommissioned batteries for electric vehicles is of great significance to improve the utilization value of their life cycle, reduce the cost of lithium batteries, and alleviate environmental pollution [6–9].

This paper presents a comprehensive evaluation model of decommissioned power batteries for electric vehicles based on AHP-CRITIC. Firstly, there are two different dimensions of curve characteristics and economic factors to evaluate the decommissioned power batteries. Secondly, an improved K-means clustering analysis model based on health factors of the batteries is established. Furthermore, the economic indicator of decommissioned batteries is evaluated in the economic dimension by AHP-CRITIC method. Finally, a comprehensive evaluation of decommissioned batteries is carried out by totally considering the health and economic factors.

2 Evaluation of Health Factors of Decommissioned Batteries Based on Improved Clustering Analysis

2.1 Extraction of Health Characteristics of Decommissioned Batteries

In the evaluation of decommissioned power batteries, in order to extract the health characteristics of decommissioned power batteries, a 2.5 C constant current discharge test is exploited to test the decommissioned lithium batteries from literature [10, 11]. The stopping time is 10 s, i.e. discharging for 10 s and then silencing for 10 s. Reciprocating tests are carried out on the full impulse decommissioned lithium batteries, and the internal resistance parameters of lithium batteries are recorded when the discharge current jumps. The internal resistance-SOC curve of decommissioned power batteries can be obtained through correlation processing. The health characteristics of decommissioned power batteries can be extracted by analyzing the obtained curves.

Through actual measurement and analysis, it can be seen that since the Ohmic internal resistance-SOC curve satisfies the characteristics of quadratic curve, the internal resistance-SOC quadratic curve can be defined as follows:

$$\begin{cases} R_o = a_{\mathrm{p}} S_{\mathrm{oc}}^2 + b_{\mathrm{p}} S_{\mathrm{oc}} + c_{\mathrm{p}} \\ R_{o,\min} = (4a_{\mathrm{p}} c_{\mathrm{p}} - b_{\mathrm{p}})/4a_{\mathrm{p}} \\ S_{o,\min} = -b_{\mathrm{p}}/2a_{\mathrm{p}} \end{cases} \tag{1}$$

where a_{p}, b_{p}, c_{p} are the coefficients of the quadratic curve; $R_{o,\min}$, $S_{o,\min}$ are the vertex and abscissa of the quadratic curve, respectively representing the minimum resistance value of the internal resistance-SOC curve and its SOC state.

Therefore, by calculating the first derivative and the second derivative of the curve, the health characteristics of curve slope can be extracted, namely:

$$\begin{cases} \dfrac{dR_o}{dS_{\mathrm{oc}}} = 2a_{\mathrm{p}} S_{\mathrm{oc}} + b_{\mathrm{p}} \\ a_{\mathrm{s}} = \dfrac{d^2 R_o}{dS_{\mathrm{oc}}^2} = 2a_{\mathrm{p}} \end{cases} \tag{2}$$

Based on the curve characteristics of decommissioned batteries in different health states, the health grade of decommissioned batteries is divided, so as to realize the evaluation of the characteristics of decommissioned batteries. The specific evaluation process is realized by means of clustering.

2.2 Clustering Evaluation Model of Health Factors of Decommissioned Batteries

Clustering Model of Power Battery Based on Gravitational Model.
Gravitation is a kind of interaction characteristic widely existed in nature. This paper introduces the gravitational model into the K-means clustering model. By evaluating the clustering effect, as a condition for the termination of the cluster iteration, it is determined that the given data should be attributed to a corresponding cluster.

Clustering Model of Universal Gravitation:

$$EI_{\mathrm{i}} = W \cdot \frac{P \cdot p_{\mathrm{i}}}{r_i^2} \tag{3}$$

where, *EI* (Evaluation Index) is the evaluation index of clustering effect; P and p_i are the values of two data points on the curve respectively; W denotes the evaluation adjustment coefficient, which is usually 0.03–0.08 after optimization calculation, and 0.05 in this paper; r_i denotes the distance between a specific data point and the cluster center.

Where r_i is expressed as

$$r_i = \left\| x_i - c_j \right\| \tag{4}$$

where x_i is the i-th data point; c_j is the cluster center of a certain class. x_i is attributed to the category of c_j by using Max (EI_i). After x_i is classified into a specific class, the cluster center needs to be updated, and the corresponding expression is:

$$c_j = \frac{1}{|c_j|} \sum_{j=1}^{|c_j|} x_i \tag{5}$$

Basic Flow of Improved K-means Clustering Based on Gravitational Model. The basic flow of the improved K-means clustering algorithm based on the universal gravitational model is: Step 1: randomly select K data sets as the original cluster centers; Step 2: Calculate the distance between the remaining data point objects and the K cluster centers; Step 3: According to the proposed gravitational model, determine the size of the evaluation index EI (in this process, the value of W needs to be determined by the method of data cut-off), and divide the corresponding clusters by calculating the size of the EI, update cluster centers according to Formula (5); Step 4: When the value of indicator EI reaches a certain value or the number of iterations reaches the specified number of times, stop the iteration, otherwise turn to Step 2.

Evaluation of Health Factors of Decommissioned Batteries. According to the test results of the existing decommissioned power batteries, the internal resistance-SOC curve of the obtained plurality of batteries are clustered and analyzed, and the curves of the decommissioned power batteries under different health conditions can be acquired.

3 Evaluation of Economic Indicators of Decommissioned Batteries Based on AHP-CRITIC

3.1 Classification of Economic Indicators

By comparing the decommissioned power batteries with the conventional energy storage batteries, the economic indicators of batteries are assessed from five aspects: the economic cost value of batteries, the economic time cost value of batteries (i.e. the economic characteristics of batteries in consideration of their life cycle), the national dividend subsidy for the development of batteries, the economic cost under the safety performance of batteries, and the economic cost of operation and maintenance.

3.2 Quantitative Processing of Indicator Characteristics

Economic Value Assessment of Decommissioned Power Batteries.
According to the actual investigation and analysis, it can be known that the evaluation rules for the economic indicators of decommissioned power batteries are shown in Table 1.

Time Cost Assessment of Decommissioned Power Batteries.
Depending on the use of the battery over its life cycle, generally the longer the battery can be used, the lower the cost of its corresponding time investment. To evaluate the battery time cost, the specific quantization rules are shown in Table 2.

Government Policy Dividend Subsidy.
In the process of battery application, it will be subsidized by government policies. It is necessary to quantify the support of policies for batteries [12]. The specific quantification rules are shown in Table 3.

Table 1 Quantitative rules for the economic value of decommissioned power batteries

Conventional energy storage battery capacity	>50	25–50	10–25	5–10	<5
Decommissioned power battery capacity 1	>100	60–100	40–60	20–40	<20
Decommissioned power battery capacity 2	>150	90–150	60–90	30–60	<30
Decommissioned power battery capacity 3	>250	150–250	100–150	50–100	<50
Quantitative value	5	4	3	2	1

Note The units are Ah. The capacity of decommissioned power batteries 1, 2 and 3 in the table represent the quantified value of the economic cost corresponding to the decommissioned health degree under the capacity of 0.9–1.0, 0.7–0.9 and <0.7 respectively

Table 2 Quantification rules for the time cost of decommissioned power batteries

Service life of conventional energy storage batteries	<1	2–3	3–4	4–5	>5
Service life of decommissioned power batteries	<0.5	0.5–1	1–1.5	1.5–2	>2
Quantitative value	5	4	3	2	1

Table 3 Quantification rules for policy subsidies of batteries

Subsidy of conventional energy storage batteries/(yuan/Wh)	1.0	1.0–1.5	1.5– 2.0	2.0–2.5	>2.5
Subsidy of decommissioned power batteries/(yuan/Wh)	1.2	1.2–2.3	2.3–2.5	2.5–3.0	>3.0
Quantitative value	5	4	3	2	1

Note In this paper, the battery subsidy standard is compiled according to the relevant policies

Table 4 Economic quantification of battery safety

Service life of conventional energy storage batteries	>5	4–5	3–4	2–3	<1
Service life of decommissioned power batteries	>2	1.5–2	1–1.5	0.5–1	<0.5
Quantitative value	5	4	3	2	1

Table 5 Cost quantification of the operation and maintenance of batteries

Type of battery	Quantitative value
Conventional energy storage batteries	2
Decommissioned power batteries	5

Safety Assessment of Decommissioned Power Batteries.
Generally speaking, the longer the service life of the battery, the more obvious the potential safety hazards and the higher the corresponding economic cost. The specific measurement criteria, evaluation and quantitative rules are shown in Table 4.

Cost Assessment of Operation and Maintenance.
During the actual operation of batteries in the installation site, it is inevitable to invest human, material and financial resources to maintain and repair the battery. Its basic cost assessment is based on investigation and practical application. The specific quantitative rules are shown in Table 5.

3.3 Evaluation of Comprehensive Economic Indicators

In the calculation of index weights, the two main ideas of subjective and objective weighting methods are combined. The subjective weights are calculated by the analytic hierarchy process (AHP) [13] in the subjective weighting methods. The objective weights are calculated by CRITIC (Criteria Importance Though Intercriteria Correlation) [14]. The concrete steps of calculating objective weights are as follows:

Step 1: Dimensionless data processing. Since all the indicators in this evaluation system have been converted into quantitative values, the process can be omitted.

Step 2: Calculate the information content contained in the indicators.

The conflicting quantitative indicator of the jth indicator and other indicators is as follows:

$$\theta_j = \sum_{t=1}^{n} \left(1 - r_{tj}\right) \tag{6}$$

where r_{tj} is the correlation coefficient between indicator t and indicator j.

The objective weight of each indicator is considered comprehensively by contrast intensity and contradiction. Assuming that C_j represents information content contained in the jth evaluation index, C_j can be denoted as:

$$C_j = \delta_j \sum_{t=1}^{n} (1 - r_{tj}) \tag{7}$$

where δ_j is the standard deviation of the jth evaluation index.

Step 3: Calculate the objective weight of each index

The larger the C_j value is, the more information the jth evaluation index covers, and the more important the index is. Therefore, the objective weight of the jth index can be characterized as:

$$\beta_j = C_j \Big/ \sum_{j=1}^{m} C_j \tag{8}$$

Combine the subjective weights calculated by AHP with the objective weights calculated by the CRITIC to calculate the comprehensive weight. The formula is as follows:

$$\omega_j = \frac{(\alpha_j \beta_j)^{1/2}}{\sum_{j=1}^{n} (\alpha_j \beta_j)^{1/2}} \tag{9}$$

The weighting coefficients of each economic index in the battery evaluation model can be obtained as shown in Table 6.

4 Optimal Evaluation Model of Decommissioned Power Batteries Based on Curve Characteristics and Economic Dimensions

4.1 Objective Function

For the evaluation model of decommissioned power batteries based on clustering analysis, the objective function of the optimal evaluation model is considered from

Table 6 Weighting coefficient of economic indicators

Indicators	Economic cost	Time cost	Policy subsidy	Safety cost	Operation and maintenance cost
Weights	0.3054	0.1333	0.3270	0.0701	0.1641

the following two aspects: (1) the characteristics of internal resistance-SOC curve of decommissioned power batteries; (2) the economic index of decommissioned power batteries in the whole life cycle.

Objective Function 1: Evaluation index of curve characteristics of the decommissioned power batteries

$$\min f_1 = e \cdot \frac{1}{p} \cdot \sum_{m=1}^{p} \frac{\left| x_{im} - x_{jm} \right|}{x_{im}} \tag{10}$$

where e means the parameter of curve index converted into economic index; p means the point number of curve characteristics; i and j represent the characteristic indexes of characteristic curve and characteristic curve to be evaluated under the datum value respectively.

Objective Function 2: Cost function of decommissioned power batteries under economic indicators

The cost of decommissioned power batteries for energy storage is mainly due to their purchase, transportation, testing, installation and maintenance. Therefore, the economic cost function for decommissioned power batteries is composed as follows: the cost of purchasing power batteries to be decommissioned, the cost of transportation, inspection and installation, and the cost of maintenance.

The weight of the index in item J of WJ is the quantified value of the index in item J of w_j.

$$f_2 = \sum w_j \cdot c_j \tag{11}$$

In the formula, w_j means the weight of the jth refinement indicator, and c_j represents the user's quantified value for this refinement indicator.

4.2 Constraints

- Upper and lower limit constraints on health factors of decommissioned power batteries

$$SOH_{low} < SOH < SOH_{high} \tag{12}$$

In the formula, SOH_{low} and SOH_{high} are the upper and lower limits of the decommissioned power batteries, respectively, which are taken as 0.7 and 1.0.

- Upper and lower limit constraints of characteristic curve parameters

$$x_{low} < x < x_{high} \tag{13}$$

In the formula, x_{low} and x_{high} are the upper and lower limits of the characteristics of the decommissioned power battery curve, respectively.

- Upper and lower limits constraints of batteries in charged state

$$c_{low} < c < c_{high} \tag{14}$$

In the formula, c_{low} and c_{high} are the upper and lower limits of the economic quantitative indicators of decommissioned power batteries, respectively.

4.3 Model Solution

In order to solve the above multi-objective optimization model, the particle swarm optimization algorithm is used to solve the problem.

5 Example Analysis

Based on the actual data of a city's electric bus charging station, some decommissioned batteries are used as experimental data for example analysis. The power battery used in the charging station is ternary lithium battery, with electric energy of 282 Ah, rated discharge current of 280 A, peak discharge current of 330 A, rated charging current of 140 A, single battery rated voltage of 3.68 V, and operating temperature range of 20–60 °C. The economic indicators of decommissioned power batteries and conventional energy storage batteries are mainly obtained through the investigation of some energy storage websites and batteries. The cost of conventional energy storage is 2000 yuan/kWh and that of cascaded power batteries is 800 yuan/kWh.

According to the results of clustering, we can see that the test curves of decommissioned batteries can be roughly divided into three different categories, which are embodied as the three different distribution zones in Fig. 1. The characteristic curves of decommissioned batteries are characterized by internal resistance-SOC characteristic curves. According to the evaluation in Ref. [13], the fitting degrees of the corresponding health status are 0.84, 0.75 and 066, and the available capacities of the batteries in this paper are 236.88, 211.5 and 186.12 Ah, the corresponding proportions are 50, 30 and 20%, respectively.

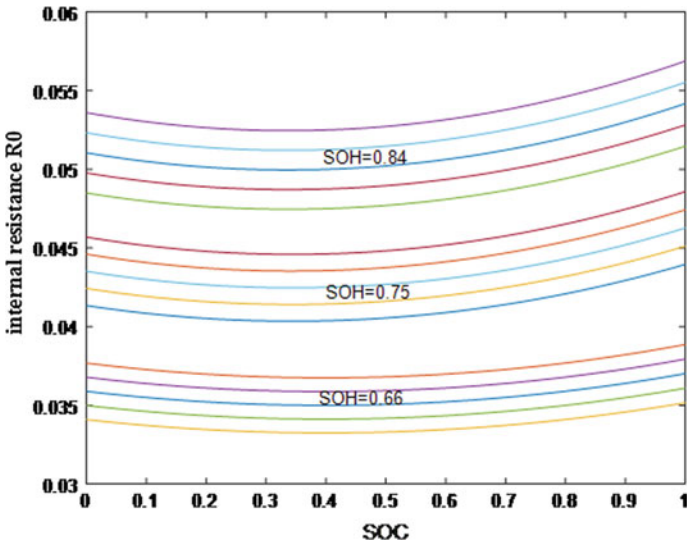

Fig. 1 Clustering results of multiple batteries

Using Formula (11) to calculate the quantified values of four indicators of each group of decommissioned power batteries in the economic dimension, a total of 30 sets of characteristic index vectors of decommissioned power batteries are obtained.

According to the economic analysis of decommissioned cascade energy storage and conventional energy storage in Ref. [15], the comparison of the total cost of conventional energy storage and cascade energy storage is expressed in Fig. 2 (taking the installation scale of 2000 Ah as an example). The specific evaluation results are as follows.

It can be seen from Fig. 2 that after cascade utilization of energy storage of decommissioned batteries, when the cost of cascade energy storage is less than 940 yuan/kWh, the cost of cascade energy storage is lower than that of conventional batteries. In practical applications, the cost of cascade energy storage is generally much lower than this value, which shows that retired batteries have great advantages over conventional energy storage.

Among the 30 groups of decommissioned battery packs, the 6 sets of batteries with the lowest comprehensive optimization scores are removed, and 24 sets of decommissioned power batteries with higher evaluation score were selected. In order to reflect the comprehensive indicators of decommissioned power batteries under different evaluation dimensions, these comprehensive indicators are shown in Fig. 3.

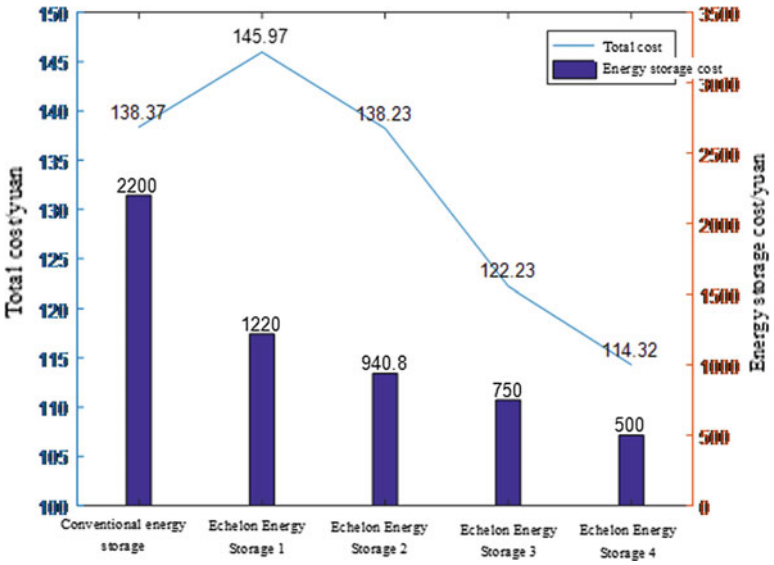

Fig. 2 Cost comparison between decommissioned battery energy storage and conventional energy storage

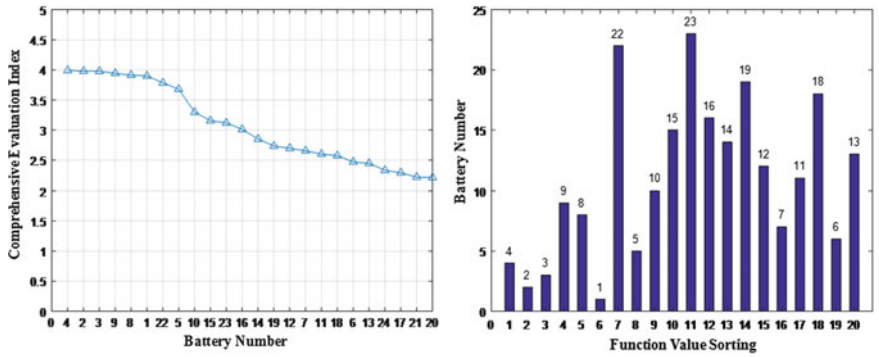

(a) Battery number sorting under comprehensive evaluation

(b) Battery optimization sorting

Fig. 3 Comprehensive evaluation index of decommissioned power batteries

Therefore, through the optimization sorting of the comprehensive indicators, the comprehensive indicators of the decommissioned power batteries can be distinguished. According to the optimization of the objective function value, the rating of the decommissioned power batteries to be graded can be evaluated, which has certain guiding significance for the application of decommissioned batteries in the future.

6 Conclusion

According to the health characteristics of decommissioned power batteries, the improved clustering method is used to cluster the curve characteristics of decommissioned power batteries. In addition, the AHP-CRITIC method is adopted to evaluate the economic indicators of decommissioned power batteries. Then, a comprehensive evaluation model considering the health characteristics and economic characteristics of decommissioned power batteries is established. Finally, an example is given to validate the proposed evaluation model. The results show that the proposed model and algorithm can provide guidance for the subsequent cascade utilization of decommissioned power batteries.

References

1. Li J et al (2015) Prospects for electric energy storage technology under the background of energy internet. Autom Electr Power Syst 39(23):15–25
2. Liu J (2017) Application potential and cost analysis of energy storage of retired batteries for electric vehicles. Energy Storage Science and Technology 6(2):243–249
3. He W, Zhao G, Wenlong Wu et al (2016) Performance analysis of retired batteries for pure electric bus under charging mode. Power Technol 40(7):1412–1415
4. Li X, Chen Q, Guan Y et al (2013) Characteristic analysis of lithium ion power battery with echelon utilization. Power Technol 37(11):1940–1943
5. Hu S et al (2019) Power system risk dispatch considering flexible load of decommissioned batteries. Autom Electr Power Syst, 1–9
6. Bai W, Li N, Fan M et al (2017) Research on engineering technology route of massive echelon utilization battery energy storage system. North China Electr Power Technol (3):39–45
7. Li N et al (2017) Research on the consistency maintenance method of step-by-step battery energy storage system. Chin Foreign Energy 22(4):89–96
8. Xu J (2014) Study on the variation of capacity and internal resistance of cascade utilization of lithium ion batteries. Beijing Jiaotong University
9. Zou Y (2014) Modeling and parameter estimating based on capacity, internal resistance and charge state of decommissioned lithium power batteries. Central South University
10. Sun D, Xu S (2018) Health status prediction of lithium batteries by cascade utilization. J Electr Technol 33(9):2021–2029
11. Zeyu M et al (2014) Balance strategy design for cascade utilization of lithium batteries in energy storage systems. Autom Electr Power Syst 38(03):106–111
12. Zhao M et al (2016) Emergency power supply strategy for electric vehicles based on fuzzy k-means algorithm. Autom Electr Power Syst 5:91–95
13. Zhao H, Li N (2016) Performance evaluation for sustainability of strong smart grid by using stochastic AHP and fuzzy TOPSIS methods. Sustainability 8(2):129
14. Diakoulaki D et al (1995) Determining objective weights in multiple criteria problems: The critic method. Comput Oper Res 22(7):763–770
15. Liu D et al (2017) Economic analysis of cascade battery energy storage based on photovoltaic power plant scenario. Electr Power Eng Technol 36(6):27–31

Improved Control Strategy of Virtual Synchronous Generator in Response to Power Grid Harmonics

Shuhuan Wang, Li Han and Kai Chen

Abstract By virtual synchronous generator (VSG) technology, the inverter can be controlled simulating the operation characteristics of synchronous generators and regarded as an access of renewable energy. The harmonics contained in the power grid brings the same order harmonics to the grid-connected current generated by VSG, result in an increasement of harmonic content in the power grid. In order to solve this problem, an improved VSG control strategy is proposed. Firstly, the equivalent model of VSG is established. Based on the analysis of the impact of harmonics on the grid-connected current generated by VSG, an improved algorithm for obtaining inductance current reference value based on double second-order generalized integral is proposed. Inertial integral link is used to replace differential operation in full feed-forward control for grid voltage, and the mechanism of current regulator is analyzed. The current tracking and harmonic suppression can be realized by choosing the corresponding current regulator. Finally, a simulation and experimental platform is built to verify the validity of the improved VSG control strategy.

Keywords Virtual synchronous generator · Grid harmonics · Grid voltage feed-forward · Current regulator

1 Introduction

With the increase of installed capacity of distributed inverters in power system, the proportion of installed capacity of traditional synchronous generators gradually decreases [1, 2]. Due to the lack of inertia and damping of traditional synchronous generators in distributed generation systems with power electronic converters, power systems are more vulnerable to power fluctuations and system faults [3, 4].

S. Wang · L. Han (✉) · K. Chen
School of Electrical and Power Engineering, China University of Mining and Technology, Xuzhou 221008, China
e-mail: dannyli717@163.com

Y. Xue et al. (eds.), *Proceedings of PURPLE MOUNTAIN FORUM 2019-International Forum on Smart Grid Protection and Control*, Lecture Notes in Electrical Engineering 585, https://doi.org/10.1007/978-981-13-9783-7_10

Virtual synchronous generator (VSG) enables the distributed generation based on grid-connected inverters to simulate or partially simulate the frequency and voltage control characteristics of synchronous generators from the external characteristics, which can provide certain inertia and damping for the grid, thereby improving the stability of the distributed system [5].

The concept of virtual synchronous generator was first proposed in Ref. [6]. The ontology model of VSG is established, and the design of the parameters for control loop is completed [7, 8]. On this basis, the flexibility of VSG is enhanced by improving the control without frequency difference [9–11]. The influence of inertia on the output characteristics of VSG is analyzed. By introducing frequency variation into inertia control to form adaptive control of inertia [12–15], the advantages of virtual inertia in improving frequency stability of microgrid system are demonstrated. The high-order small signal model of VSG is constructed [16]. The idea of virtual synchronous generator is applied to the field of wind power generation, which reflects its universality [17, 18].

Many literatures have studied the grid-connected control strategy of VSG. The influence of VSG parameter perturbation on grid-connected power tracking is quantitatively analyzed, and the influence of virtual inertia and damping parameters on the system and the tuning method [19]. The small signal stability of VSG under grid-connected and off-grid modes is analyzed. It is pointed out that the variation of inertia time constant, damping coefficient and reactive power sag coefficient has great influence on system stability [20]. Based on the "power-voltage-current" three-loop control strategy with pre-synchronization device, seamless switching between grid-connected and off-grid operation modes of VSG is realized [21].

The above researches on VSG are all based on the condition that the grid voltage does not contain harmonics. However, in actual operation, the grid voltage often contains harmonics, which will introduce the same frequency harmonics to the grid-connected current and directly affect the output current quality of VSG. In order to ensure the quality of grid-connected power, a series of standards and technical specifications have been formulated by relevant departments at home and abroad [22–26]. For the control of conventional inverters under grid voltage distortion, a double closed-loop control strategy based on inductance voltage differential and grid-connected current feedback is proposed [27]. A direct power control strategy based on resonant sliding mode is proposed [28]. The stability and convergence of the proposed control strategy are analyzed in depth. In order to improve the instantaneous current overshoot during the fault ride through of inverters, the phase advance compensation link of the feed-forward component of the grid voltage is introduced into the current loop [29]. A flexible harmonic control method for three-phase grid-connected inverters without harmonic detection is proposed [30]. For the control of VSG under grid voltage distortion, a method combining

virtual impedance with phasor current limiting is proposed for direct voltage system, which effectively limits the transient and steady components of fault current [31]. By controlling the reference values of positive and negative sequence currents separately, the output balanced current of VSG under unbalanced grid voltage is achieved [32–34]. A novel voltage feed-forward compensation strategy based on notch filter is proposed, which can suppress the harmonic with particular order of grid-connected current [35]. An improved algorithm of inductance current reference value based on double second-order generalized integral is proposed [36]. The influence of harmonics caused by grid voltage is eliminated by feedforward method, which improves the quality of output current in the whole frequency domain. However, the full feedforward control process of grid voltage needs differential operation, and it is easy to introduce additional harmonic components and slow the response time.

On the basis of the existing research, an improved VSG control strategy is proposed to deal with the harmonics of power grid. Firstly, an improved algorithm of inductance current reference value based on double second-order generalized integral is added. Secondly, the differential operation needed in the full feed-forward control process of grid voltage is replaced by inertial integral. Finally, the corresponding current regulator is selected to realize current tracking, so as to achieve the purpose of harmonic suppression. The simulation and experimental results prove the correctness and effectiveness of the proposed control strategy.

2 Basic Principles of VSG

VSG simulates the rotor equation of synchronous generator. In active-frequency control, virtual inertia and damping are introduced. In reactive-voltage control, excitation regulation of synchronous generator is simulated. The governing equation is:

$$\frac{P_{\text{ref}} - P_{\text{e}}}{\omega} = J\frac{d\omega}{dt} + D\Delta\omega \tag{1}$$

$$\Delta\omega = \omega - \omega_0 \tag{2}$$

$$V = V_0 + D_{\text{q}}(Q_{\text{ref}} - Q) \tag{3}$$

where P_{ref} and P_{e} are the given active power and electromagnetic power of VSG; ω and ω_0 are the angular frequency of VSG and the angular frequency of power grid; J and D are the inertia and damping coefficient of VSG; Q_{ref} and Q are the given and actual value of reactive power; V_0 and V are the rated and measured voltage values; D_{q} is the reactive power-voltage sag coefficient.

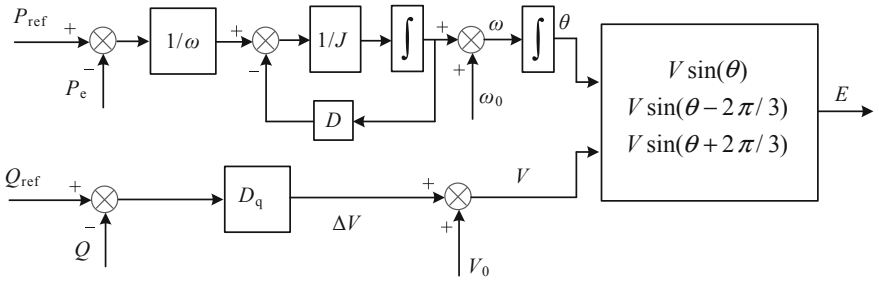

Fig. 1 Control block diagram of VSG

The control block diagram of VSG is shown in Fig. 1. The amplitude and phase angle of reference voltage are obtained through VSG control algorithm by P_{ref} and Q_{ref}, and the voltage reference instruction is output.

3 Improved VSG Control Strategy for Harmonics in Power Grid

3.1 Equivalent Model Analysis of VSG

The control block diagram is shown in Fig. 2 when the feedback control scheme of grid voltage and inverter side current is adopted.

In Fig. 2, u_{gc} and i_{Lc} are respectively measured values of grid voltage and inverter side current. According to the control block diagram shown in Fig. 2, the closed-loop transfer function of the system is obtained:

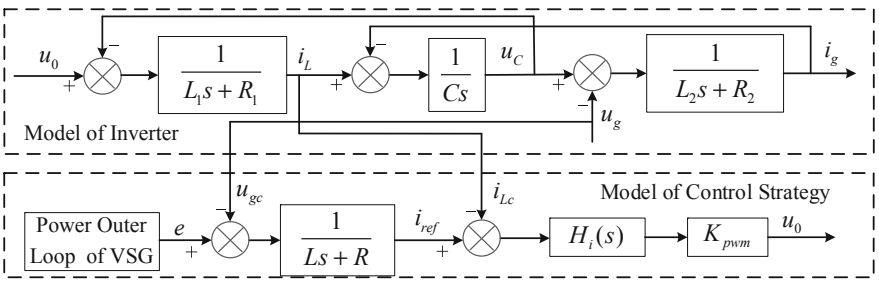

Fig. 2 Equivalent model of grid voltage and inverter side current feedback control scheme

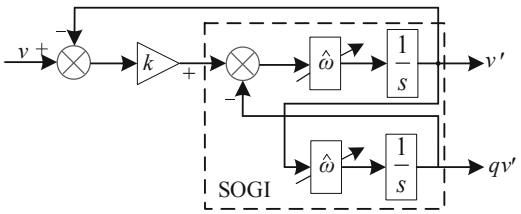

Fig. 3 An adaptive filter based on SOGI-QSG

$$i_g = G_i(s)i_{ref} + G_g(s)u_g \tag{4}$$

Where

$$\begin{cases} i_{ref} = \frac{1}{Ls+R}\left(e - u_{gc}\right) \\ G_i(s) = \frac{H_i(s)K_{pwm}}{D(s)} \\ G_g(s) = \frac{H_i(s)K_{pwm}Cs + L_1Cs^2 + R_1Cs + 1}{D(s)} \\ D(s) = (L_2Cs^2 + R_2Cs + 1)H_i(s)K_{pwm} + L_1L_2Cs^3 \\ \quad + (R_1L_2 + R_2L_1)Cs^2 + (R_1R_2C + L_2 + L_1)s + R_1 + R_2 \end{cases}$$

It can be seen that the grid-connected current of LCL grid-connected inverters with current feedback on the inverter side is affected by the reference value of inductance current on the one hand, and the grid voltage on the other. In actual operation, when the grid voltage contains certain harmonics, the grid voltage can be decomposed into fundamental component and harmonic component. Correspondingly, the reference value of inductance current is affected by grid voltage, which contains fundamental component and harmonic component. At the same time, the disturbance component of grid voltage to grid current also contains harmonic component, which directly makes grid-connected point current contain a large number of harmonics. If the control parameters or filter parameters are not properly designed, the quality of grid current may be lower than some standard provisions, which is disadvantageous in the stable operation of the system.

Therefore, it is necessary to improve the control strategy from two aspects: improving the reference value of inductance current and eliminating the influence of grid voltage. Because of the low bandwidth of power loop, the reference value of output voltage generated by VSG power outer loop contains only the positive sequence component of fundamental wave. From the expression of i_{ref}, it can be seen that the reference value of inductance current is directly related to the measured value of grid voltage. Therefore, for the improvement of the reference value of inductance current, it is necessary to extract the fundamental component of the

measured value with grid voltage to calculate the reference value of inductance current without harmonic effect. For the improvement of grid voltage, it is necessary to add a specific feedback link in the control loop to eliminate the influence of u_g on the output current.

3.2 Extraction of Inductance Current Reference Value Based on Improved Double Second-Order Generalized Integral

The equivalent model of VSG shows that the grid voltage with harmonics can be decomposed into fundamental component and harmonic component. If a suitable method is used to extract the fundamental positive sequence component of the grid voltage measurement for calculating the reference value of inductance current, the reference value will only contains the fundamental component, and the harmonic component of the grid current will be greatly suppressed.

Among the commonly used methods for extracting positive sequence components of fundamental wave, the method based on double second-order generalized integral (DSOGI) has small delay and good dynamic performance. Adding this module will not bring obvious influence to the whole control link. Therefore, the improved DSOGI will be selected to extract the positive sequence component of fundamental voltage and calculate the reference value of inductance current. Figure 3 is the principle block diagram of quadrature signal generator based on second-order generalized integrator (SOGI-QSG), where v is the input, and v' and qv' are the two outputs of signal generator. The fundamental positive sequence components of v' and v are equal in amplitude and phase, and the amplitudes of qv' and v are equal, but their phase lag is 90°.

Judgment of the value of k in quadrature signal generator: From Fig. 3, it can be seen that the transfer function of SOGI-QSG system is as follows:

$$D(s) = \frac{v'(s)}{v(s)} = \frac{k\omega s}{s^2 + k\omega s + \omega^2} \tag{5}$$

From the bode diagram of Fig. 4, it can be seen that the smaller the value of k, the better the filtering effect, but the slower the response speed. Therefore, according to the actual compromise, considering the filtering effect and response time, $k = \sqrt{2}$ is selected.

The principle block diagram of fundamental positive sequence component extraction is shown in Fig. 5. Where v_α and v_β are the components of α and β axes of grid voltage in two-phase stationary coordinates, and v_α+ and v_β+ are the positive sequence components of fundamental wave of extracted grid voltage in α and β axes, respectively. ω_0 is the fundamental wave angle frequency. The improved principle block diagram of fundamental positive sequence component extraction is

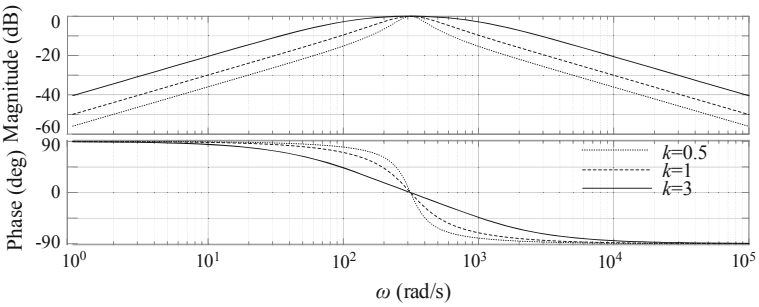

Fig. 4 Bode diagram of the relationship between D(s) and k

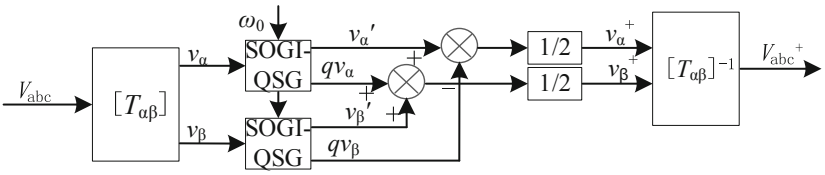

Fig. 5 Fundamental positive sequence component separation based on DSOGI-QSG

shown in Fig. 6. Because the positive sequence separation method based on DSOGI-QSG will be affected by harmonics when the grid voltage contains multiple harmonics, a harmonic elimination module is added in Fig. 6 to eliminate the influence of each harmonic on the extraction of fundamental components. Where, the value of n is the highest number of harmonics.

Formula (6) is obtained from the harmonic elimination module in Fig. 6.

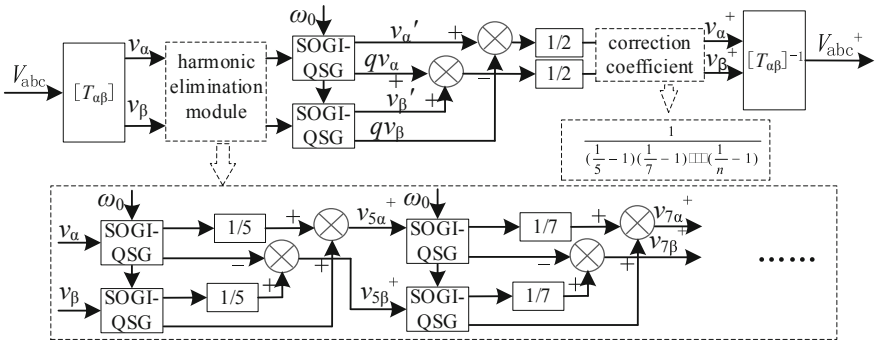

Fig. 6 An improved block diagram for extracting positive sequence components of fundamental wave based on DSOGI-QSG

$$\begin{cases} v_{5\alpha\beta}^{+} = \left(\dfrac{1}{5} - 1\right) v_{\alpha\beta} \\ v_{7\alpha\beta}^{+} = \left(\dfrac{1}{7} - 1\right) v_{5\alpha\beta}^{+} \\ \vdots \\ v_{n\alpha\beta}^{+} = \left(\dfrac{1}{n} - 1\right) v_{(n-1)\alpha\beta}^{+} \end{cases} \tag{6}$$

Therefore, $v_{n\alpha\beta}^{+} = (1/5-1)(1/7-1)\cdots(1/n-1)v_{\alpha\beta}$, The correction coefficient in Fig. 6 can be obtained as follows:

$$\frac{1}{(1/5-1)(1/7-1)\cdots(1/n-1)}$$

Comparison for simulation results of voltage fundamental wave positive sequence component extraction before and after improvement. The simulation conditions are as follows: the grid voltage contains 5% 5th and 7th harmonics, 2% 11th and 23rd harmonics. Figures 7 and 8 are the simulation results of i_{ref} before and after improvement.

By comparing the simulation results of Figs. 7 and 8, it can be seen that by extracting the fundamental positive sequence component of the grid voltage measurement, the inductance current reference value is greatly improved, and the harmonic distortion rate of inductance current reference is lower.

From the above analysis, it can be known that the harmonic content of the reference value of inductance current which needs to be tracked decreases after adding the improved double second-order generalized integral algorithm, so that the harmonic component of grid-connected current can be better suppressed.

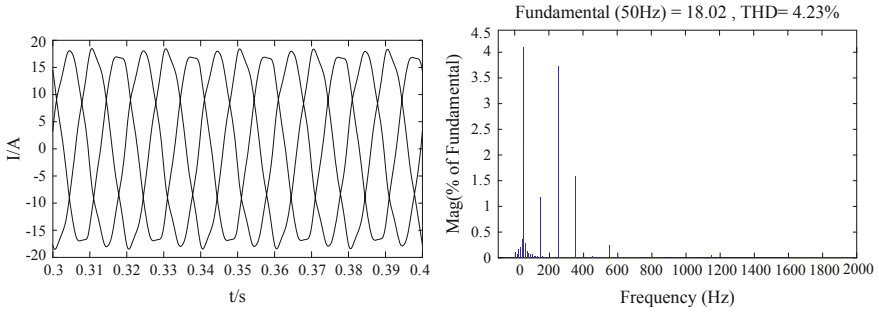

Fig. 7 Simulation results of i_{ref} before improvement

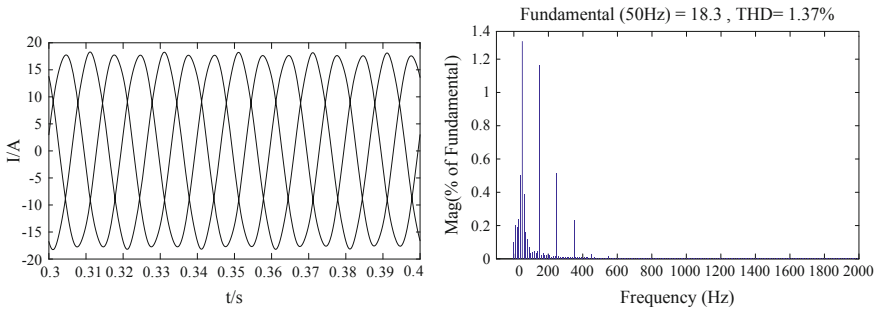

Fig. 8 Simulation results of i_{ref} after improvement

3.3 Full Feed-Forward Control of Grid Voltage Based on Inertial Integral Link

It can be known from Eq. (1) that the LCL grid-connected inverter adopts the improved inductor current reference value strategy, which can only partially eliminate the influence of the grid voltage on the grid-connected point current. Therefore, it is necessary to find out the grid voltage feed-forward strategy suitable of the current on the inverter side feedback for LCL grid-connected inverter, so as to eliminate the influences of grid voltage on the grid-connected point current. It can be seen from Fig. 2 that the position suitable for feeding the grid voltage signal into the actual control system can only be before and after the current regulator, as shown in Fig. 9, where A and B are the transfer functions to be determined.

Figure 9 shows that:

$$i_g = G_i(s)i_{ref} + G_{gf}(s)u_g \tag{7}$$

where

$$G_{gf}(s) = \frac{(A - Cs)H_i(s)K_{pwm} + BK_{pwm} - (L_1Cs^2 + R_1Cs + 1)}{D(s)}$$

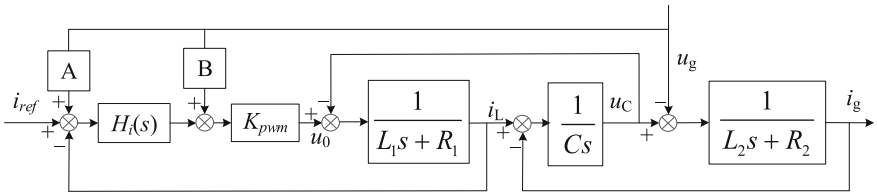

Fig. 9 Feedforward control of grid voltage

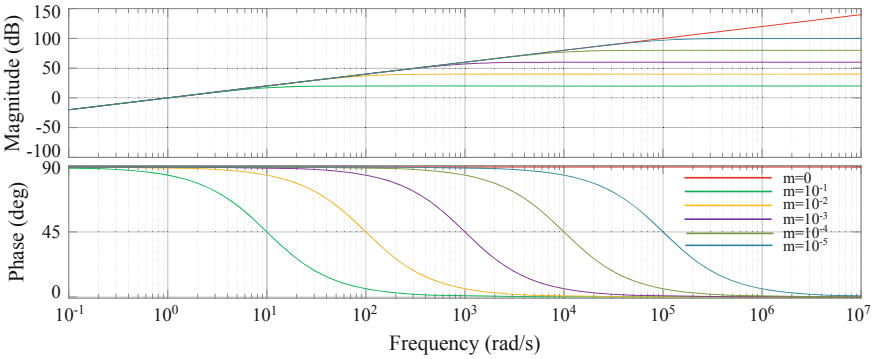

Fig. 10 Bode diagram of F(s) with different values of m

To completely eliminate the impact of grid voltage on grid current, it must meet:

$$\begin{cases} A = Cs \\ B = \frac{L_1 Cs^2 + R_1 Cs + 1}{K_{pwm}} \end{cases} \tag{8}$$

As can be seen from Eq. (8), the transfer functions A and B contain differential operations, which is easy to introduce additional harmonic components. Therefore, this paper considers the differential link to be replaced by the inertial integral link to make the same effect. The inertia integral link transfer function is expressed by Eq. (9), where m is an approximation coefficient.

$$F(s) = \frac{s}{ms + 1} \tag{9}$$

Figure 10 shows the bode diagram of F(s) when m takes different values. As the coefficient decreases, the frequency domain characteristics of F(s) coincide with the differential link more and more. Considering the harmonic number and the harmonic content in the actual system, the better effect can be achieved when m = 10^{-4}, which reduces the additional harmonic components brought by differential operation to the system.

After adding the feed-forward term of the grid voltage, the transfer function of the grid current is as follows:

$$i_g = G_i(s) i_{ref} \tag{10}$$

Although the feedback control of the current on the inverter side is adopted, the grid current is closely tracked by the grid voltage feed-forward control strategy, and is not disturbed by the grid voltage. Formula (10) also shows that the characteristic equation of the system remains unchanged after adding the feedforward strategy of grid voltage, so its stability is consistent with that without feedforward strategy of

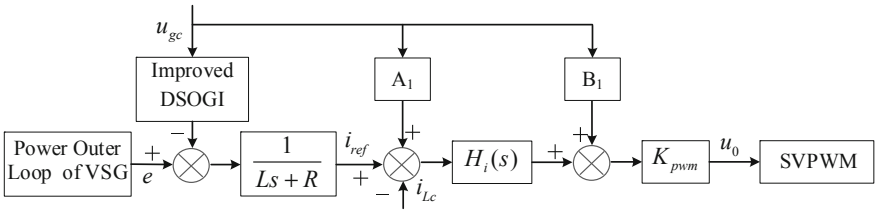

Fig. 11 Overall improved control strategy

grid voltage. The overall improved control strategy of the system is shown in Fig. 11, where A1 and B1 are the transfer functions A and B which replace the differential terms.

After improving the reference value of inductance current for harmonic suppression, it is necessary to further suppress the harmonic through the feed-forward control of grid voltage. In the further control, the additional harmonic components caused by differential operation and response time are reduced by adding a specific transfer function after substitution, and the influence of grid voltage on the harmonic content of grid-connected current is eliminated.

Current regulator plays an important role in tracking current reference value and voltage feedback value. It has a certain influence on response time and complexity of control system. Therefore, current regulator is analyzed and selected in the next section.

3.4 Analysis and Selection of Current Regulator

For the vector control method based on grid voltage orientation, when the grid voltage contains harmonics and other disturbances, it will directly affect the detection of fundamental voltage vector phase angle, thus affecting the accuracy and control performance of the vector orientation method. In order to restrain the influence of grid voltage on vector orientation and control performance, the traditional improved method can adopt vector control based on virtual flux orientation.

The structure of vector control based on virtual flux orientation is shown in Fig. 12. Because of the flux vector orientation, the formula for calculating the position angle of the flux vector is as follows:

$$\begin{cases} \sin\gamma = \dfrac{\psi_\beta}{\sqrt{\psi_\alpha^2 + \psi_\beta^2}} \\ \cos\gamma = \dfrac{\psi_\alpha}{\sqrt{\psi_\alpha^2 + \psi_\beta^2}} \end{cases} \tag{11}$$

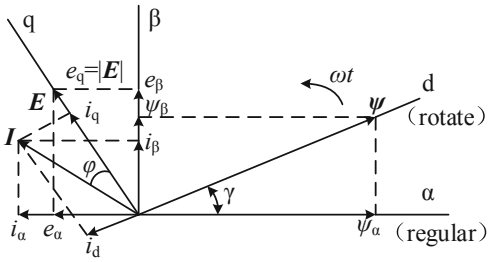

Fig. 12 Vector diagram of vector control based on virtual flux orientation

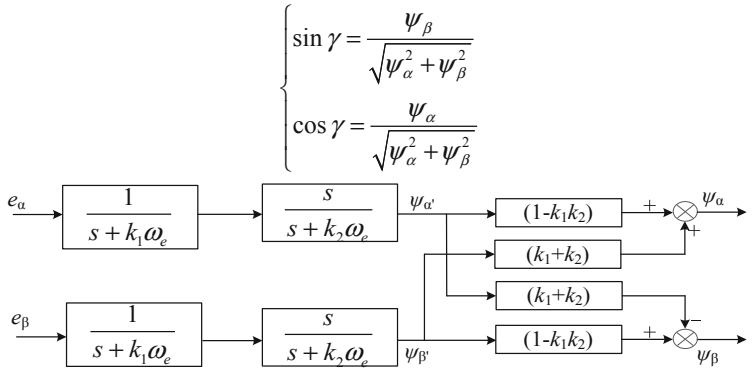

Fig. 13 Block diagram of the algorithm for virtual flux

The algorithm block diagram of virtual flux is shown in Fig. 13. In Fig. 13, ω_e is the fundamental frequency of the power grid. Generally, according to the optimal range of cut-off frequency, k_1 can be set to 0.2–0.3, while k_2 is usually set to $k_1/2$, where $k_1 = 0.2$ and $k_2 = 0.1$.

As the VSG control strategy has the following characteristics, in the active-frequency link, the rotor motion characteristics and primary frequency modulation characteristics of synchronous generator are simulated. The reference phase is generated by the active-frequency equation and virtual inertia using the mechanical and electromagnetic power of VSG. Therefore, the reference phase generated here is considered to replace the phase obtained by vector control with virtual flux orientation. Under the same simulation conditions as Sect. 3.2, the comparison results of vector control based on virtual flux orientation and reference phase generated by VSG are shown in Fig. 14.

As can be seen from Fig. 14, the reference phase generated by VSG basically coincides with the phase obtained by vector control based on virtual flux orientation. However, the reference phase generated by VSG is a necessary link in the simulation of synchronous generators. This reference phase can be used not only to generate reference voltage, but also in coordinate transformation. As a result, the

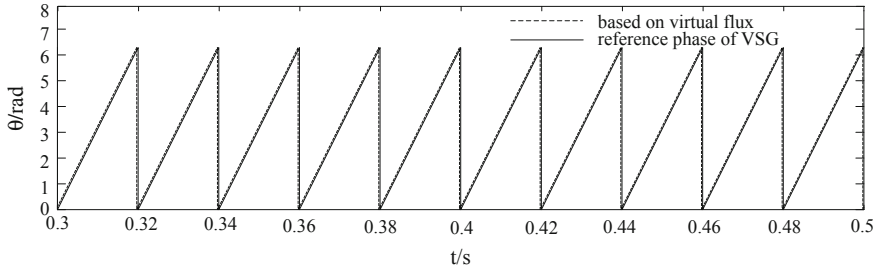

Fig. 14 Generates a reference phase contrast based on virtual flux orientation and VSG

above-mentioned vector control based on virtual flux orientation is omitted, which makes the control system simpler. Therefore, in this paper, a typical PI regulator combined with the reference phase generated by VSG is used to realize the zero steady-state error control of AC signal.

4 Simulation and Experimental Results

4.1 Simulation Results

The improved control strategy proposed in this paper is simulated and tested under the environment of Matlab/Simulink software. Its main parameters are shown in Table 1.

Simulation condition 1: The grid voltage contains 5% of the 5th and 7th harmonics, 2% of the 11th harmonic and 23th harmonic. It is consistent with the voltage harmonic content of the grid in literature [36]. At this time, The waveform of the grid voltage is shown in Fig. 15a, and the harmonic analysis is shown in Fig. 15b. The total harmonic distortion of the grid voltage is 7.61%.

Table 1 System simulation parameters

Name of parameter	Value and unit
U_{dc}	600 V
E	220 V
L_1, R_1	4.8 mH, 0.5 Ω
L_2, R_2	1.2 mH, 0.1 Ω
J	0.05 kg·m^2
D	10
D_q	0.001
f_s	5 kHz
K_{pwm}	$\sqrt{2}$

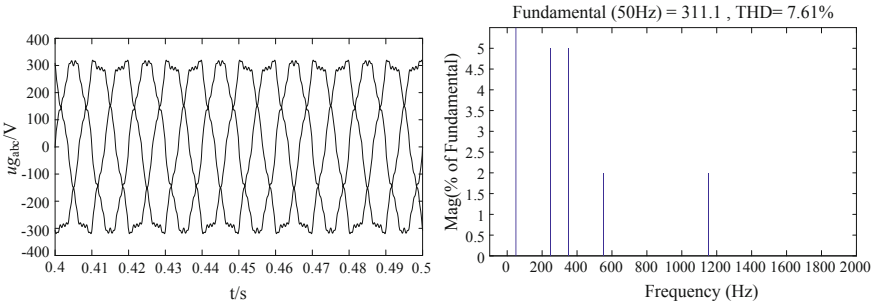

(a) Waveform of grid voltage (b) Analysis of harmonics

Fig. 15 Simulation 1: Voltage waveform and harmonic analysis of grid

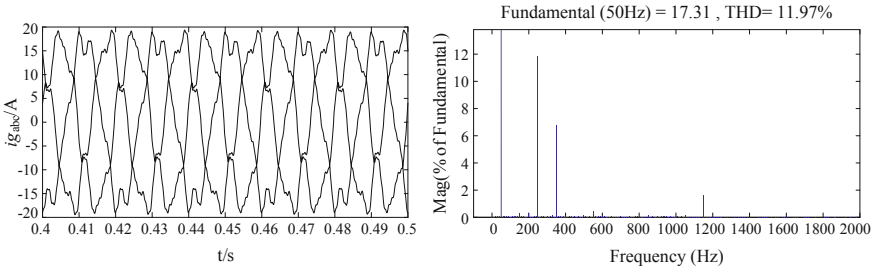

(a) Waveform of grid-connected current (b) Analysis of harmonics

Fig. 16 Simulation 1: Simulation results without improved control strategy

Under the condition of simulation 1, when the improved control strategy is not adopted, the grid-connected current waveform and the A-phase current harmonic analysis are shown in Fig. 16. The grid-connected current THD is as high as 11.97%, which is greater than the national grid-connected standard.

Under the condition of simulation 1, after using the improved strategy proposed in this paper, the grid-connected current waveform and phase-A current harmonic analysis are shown in Fig. 17. The total THD of the grid-connected current dropped to 1.81%, which is in line with the grid-connected standard, and at the same time, the harmonic content was lower than the harmonic content of the simulation results in literature [36].

In order to verify that the improved control strategy proposed in this paper is not only effective for specific order harmonics [35], but has the suppression effect on all harmonics in the full frequency domain, setting up simulation condition 2: the grid voltage contains 5% of the 5th harmonic and 7th harmonic, 3% of the 11th harmonic and 13th harmonic, 2% of the 23th harmonic and 25th harmonic. At this time, the waveform of the grid voltage is shown in Fig. 18a, and the harmonic analysis is shown in Fig. 18b. The total harmonic distortion rate of the grid voltage is 8.80%.

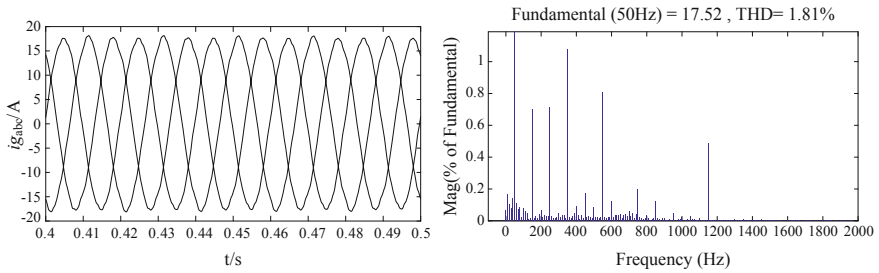

(a) Waveform of grid-connected current (b) Analysis of harmonics

Fig. 17 Simulation 1: Simulation results with improved control strategy

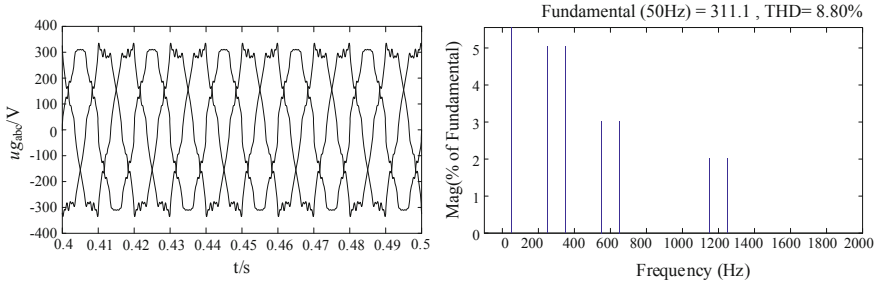

(a) Waveform of grid voltage (b) Analysis of harmonics

Fig. 18 Simulation 2: Voltage waveform and harmonic analysis of grid

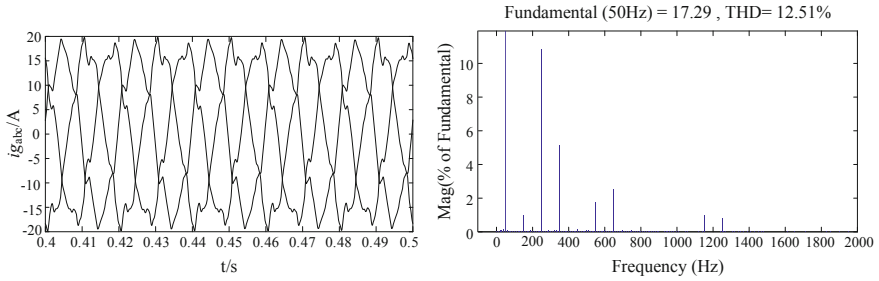

(a) Waveform of grid-connected current (b) Analysis of harmonics

Fig. 19 Simulation 2: Simulation results without improved control strategy

Under the condition of simulation 2, when the improved control strategy is not adopted, the grid-connected current waveform and the A-phase current harmonic analysis are shown in Fig. 19. The grid-connected current THD is as high as 12.51%, which is much larger than the national grid-connected standard.

Under the condition of simulation 2, after the improved strategy proposed in this paper, the grid-connected current waveform and phase-A current harmonic analysis are shown in Fig. 20. The total THD of the grid-connected current dropped to 2.56%, which is in line with the grid-connected standard.

In order to verify the dynamic response performance of the improved control strategy, the active power command value is abruptly changed from 5 to 8 kW at 0.3 s, and the reactive power command value is abrupt from 0 to 1 kvar. At this time, the power simulation result and the grid-connected current waveform are shown in Fig. 21.

It can be seen from Fig. 21a, b that when the active power and the reactive power are abrupt, the grid-connected current has a faster response speed, and the harmonics of the grid-connected current can still be well suppressed in the dynamic change process of the power mutation.

Combined with the above simulation results, it can be seen that under the condition that the grid voltage contains harmonics and the power variation, the

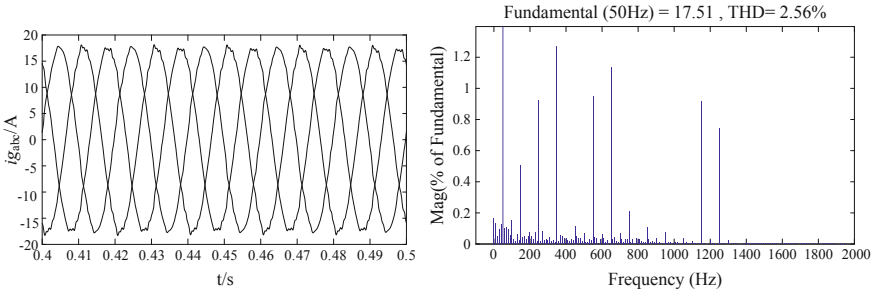

(a) Waveform of grid-connected current (b) Analysis of harmonics

Fig. 20 Simulation 2: Simulation results with improved control strategy

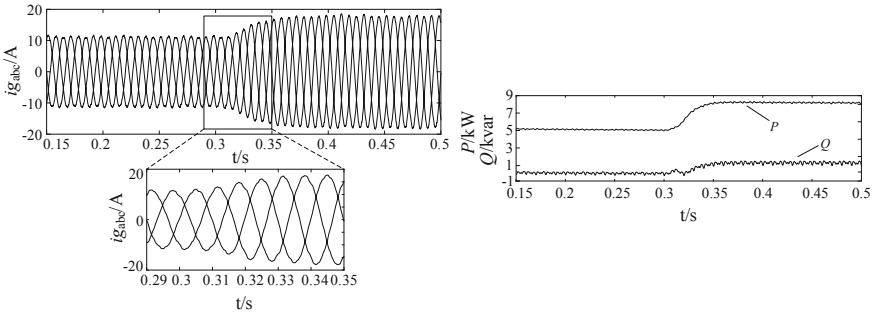

(a) Waveform of grid-connected current (b) Waveform of power

Fig. 21 Simulation results of improved control strategy under power variation

improved method in the VSG control strategy can suppress the grid-connected current harmonics to a large extent, which proves the correctness and effectiveness of the work done in this paper from the perspective of simulation.

4.2 Experimental Results

In order to further verify the correctness and effectiveness of the proposed control method, an experimental platform based on DSP control board is built. The core controller adopts TMS320F28335 of TI company, and the IGBT adopts BSM50GB120DLC of infineon. The condition of experimental 1 is the same as the simulation 1, and the condition of experimental 2 is the same as the simulation two. Under the condition of experiment 2.

Figures 22 and 23 respectively show the experimental results obtained before and after the improvement under the grid voltage of the condition of experimental one. Comparing Figs. 22a and 23a, it can be seen that under the condition of harmonic distortion of the power grid, the grid current waveform distortion is very serious if the improved control method is not adopted, while the grid-connected current waveform is obviously improved when the improved control method is adopted. It can be seen from Figs. 22b and 23b that the grid-connected current harmonic distortion rate is reduced from 12.233 to 2.229% with the improved control strategy.

Figures 24 and 25 respectively show the experimental results obtained before and after the improvement under the grid voltage of the condition of experimental 2. Comparing Figs. 24a and 25a, it can be seen that under the condition of harmonic distortion of the power grid, the grid current waveform distortion is very serious if the improved control method is not adopted, while the grid-connected current waveform is obviously improved when the improved control method is adopted. It can be seen from Figs. 24b and 25b that the grid-connected current harmonic distortion rate is reduced from 13.369 to 3.189% with the improved control strategy.

When the active power and reactive power are abrupt, the experimental results of the output power and the three-phase grid-connected current are shown in Fig. 26.

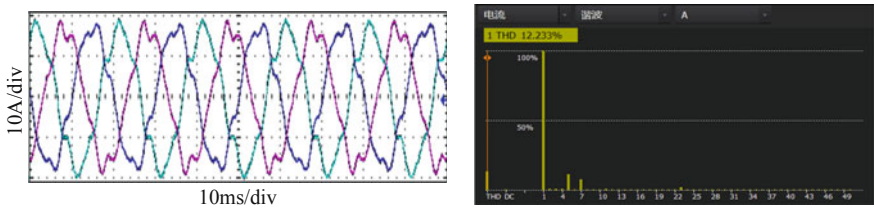

(a) Waveform of grid-connected current (b) Analysis of harmonics

Fig. 22 Experiments 1: Experimental results without the improved control strategy

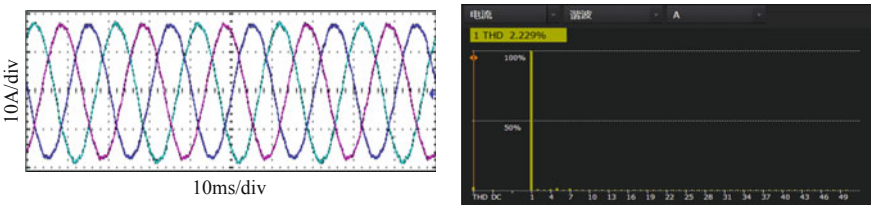

(a) Waveform of grid-connected current (b) Analysis of harmonics

Fig. 23 Experiments 1: Experimental results with the improved control strategy

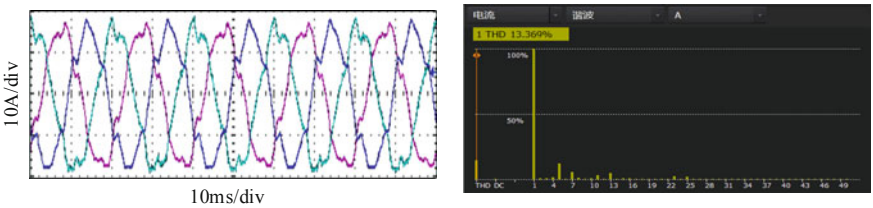

(a) Waveform of grid-connected current (b) Analysis of harmonics

Fig. 24 Experiments 2: Experimental results without the improved control strategy

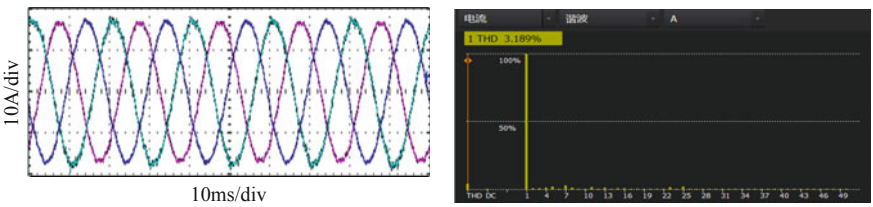

(a) Waveform of grid-connected current (b) Analysis of harmonics

Fig. 25 Experiments 2: Experimental results with the improved control strategy

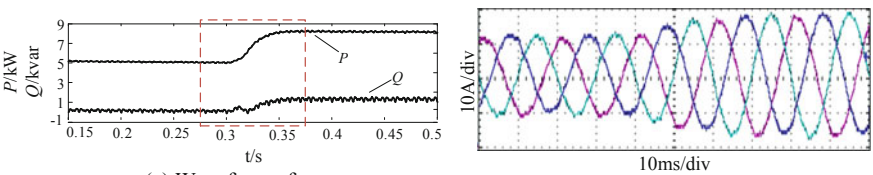

(a) Waveform of power (b) Grid-connected current in power change

Fig. 26 Experimental results of improved control strategy under power variation

As can be seen from Fig. 26, during the dynamic power change process, the grid-connected current tends to be stable in one cycle, and the current harmonics can be well suppressed. The experimental results show that the improved VSG control strategy for grid harmonics can effectively suppress the harmonic components of grid-connected current and improve the grid-connected power quality.

5 Conclusion

In order to deal with the working conditions of harmonics in the power grid, the VSG control strategy is improved in this paper. The improved method based on double second-order generalized integral is used to extract the fundamental positive sequence component of the grid voltage measurement value, which is used to improve the inductance current reference value. On this basis, replaces the differential operation required for the full feed-forward control process of the grid voltage with the inertial integral link and selects the corresponding current regulator to achieve current tracking, thus eliminating the influence of grid voltage harmonics on the grid-connected current. The feasibility of the proposed control strategy is verified by simulation and experimental results, and the following conclusions are obtained.

(1) The improved method based on double second-order generalized integral is used to extract the fundamental positive sequence component of the grid voltage measurement value, which greatly reduces the harmonic component of the inductance current reference value.
(2) The differential operation needed in the full feedforward control process of grid voltage is replaced by the inertial integral link, which eliminates the additional harmonic components that may be introduced in the differential link and does not affect the response time of the system.

References

1. Azmy AM, Erlich I (2005) Impact of distributed generation on the stability of electrical power systems. In: IEEE Power Engineering Society General Meeting, vol 2, 16 June, pp 1056–1063
2. Tan WS, Hassan MY, Majid MS et al (2013) Optimal distributed renewable generation planning: a review of different approaches. Renew Sustain Energy Rev 18:626–645
3. Zhong Q (2017) Virtual synchronous machines and autonomous power systems. Proc CSEE 37(2):336–348
4. van Wesenbeeck MPN, de Haan SWH, Varela P et al (2009) Grid tied converter with virtual kinetic storage. In: 2009 IEEE PowerTech. Bucharest, pp 1–7
5. Zheng T, Chen L, Chen T et al (2015) Review and prospect of virtual synchronous generator technologies. Autom Electr Power Syst 39(21):165–175
6. Beck HP, Hesse R (2007) Virtual synchronous machine. In: 2007 9th international conference on Electrical Power Quality and Utilisation, Barcelona, Spain, pp 1–6

7. Wu H, Ruan X, Yang D et al (2015) Modeling of the power loop and parameter design of virtual synchronous generators. Proc CSEE 35(24):6508–6518
8. Ding M, Yang X, Su J (2009) Control strategies of inverters based on virtual synchronous generator in a microgrid. Autom Electr Power Syst 33(8):89–93
9. Zhao Y, Chai J, Sun X (2016) Flexible virtual governor model based on virtual synchronous generator. Autom Electr Power Syst 40(10):8–15
10. Yang J, Liu Y, Pan H et al (2016) Method of frequent deviation-free control of microgrid inverter based on virtual synchronous generator control. Power Syst Technol 40(7):2001–2008
11. Lv Z, Sheng W, Liu H et al (2017) Application and challenge of virtual synchronous machine technology in power system. Proc CSEE 37(2):349–359
12. Song Q, Zhang H, Sun K et al (2017) Improved adaptive control of inertia for virtual synchronous generators in islanding micro-grid with multiple distributed generation units. Proc CSEE 37(2):412–423
13. Miguel A, Torres L, Luiz A et al (2014) Self-tuning virtual synchronous machines: a control strategy for energy storage systems to support dynamic frequency control. IEEE Trans Energy Convers 29(4):833–840
14. Alipoor J, Miura Y, Ise T (2014) Power system stabilization using virtual synchronous generator with adoptive moment of inertia. IEEE J Emerg Sel Top Power Electron 3(2): 451–458
15. Cheng C, Yang H, Zen Z et al (2015) Rotor inertia adaptive control method of VSG. Autom Electr Power Syst 39(19):82–89
16. D'Arco S, Suul JA, Fosso OB (2015) A virtual synchronous machine implementation for distributed control of power converters in smartgrids. Electr Power Syst Res 122(6):180–197
17. Wang S, Hu J, Yuan X (2015) Virtual synchronous control for grid-connected DFIG-based wind turbines. IEEE J Emerg Sel Top Power Electron 3(4):932–944
18. Zhao Y, Chai J, Sun X (2015) Virtual synchronous control of grid-connected DFIG-based wind turbines. In: 2015 IEEE Applied Power Electronics Conference and Exposition (APEC), Charlotte, NC, USA, pp 2980–2983
19. Lü Z, Sheng W, Zhong Q (2014) Virtual synchronous generator and its applications in micro-grid. Proc CSEE 34(16):2591–2603
20. Meng J, Wang Y, Shi X et al (2014) Control strategy and parameter analysis of distributed inverters based on VSG. Trans China Electrotechnical Soc 29(22):1–10
21. Shi R, Zhang X, Xu H et al (2017) The active and reactive power control of virtual synchronous generator based on adaptive mode switching. Trans China Electrotechnical Soc 32(12):127–137
22. IEEE Recommended Practice for Utility Interface of Photovoltaic (PV) Systems. IEEE Standard 929, 2000
23. IEEE Standard for Interconnecting Distributed Resources with Electric Power Systems. IEEE Standard 1547, 2003
24. Generating Plants Connected the Medium-Voltage Network. BDEW technical guideline, 2008
25. Technical rule for distributed resources connected to power grid. State Grid Corporation Enterprise Standard Q/GDW480 2010
26. Technical rule for connecting photovoltaic power station to power grid. State Grid Corporation Enterprise Standard Q/GDW617 2011
27. Wang X, Ruan X, Liu S (2011) Control strategy for grid-connected inverter to suppress current distortion effected by background harmonics in grid voltage. Proc CSEE 31(6):7–14
28. Quan Y, Nian H (2014) Resonance-based sliding mode control of grid connected inverters under unbalanced and harmonic grid voltages. Proc CSEE 34(9):1345–1352
29. Wei Z, Wang J, Ru X et al (2016) Zero voltage ride-through control strategy of photovoltaic grid-connected inverter based on compensation for phase of feed-forward grid voltage. Autom Electr Power Syst 40(4):78–84

30. Huang Y, Luo A, Wang Y (2016) A flexible harmonic control method for three-phase grid-connected inverter without harmonic detection. Trans China Electrotechnical Soc 31 (24):213–222
31. Shang L, Hu J, Yuan X et al (2017) Modeling and improved control of virtual synchronous generators under symmetrical faults of grid. Proc CSEE 37(2):403–411
32. Chen T, Chen L, Wang Y et al (2016) Balanced current control of virtual synchronous generator considering unbalanced grid voltage. Power Syst Technol 40(3):904–909
33. Wan X, Hu H, Nie X et al (2017) An improved control strategy for virtual synchronous generator under unbalanced grid voltage. Power Syst Technol 41(11):3573–3581
34. Tianwen Z, Laijun C, Yan G et al (2017) Comprehensive control strategy of virtual synchronous generator under unbalanced voltage conditions. IET Gener Transm Distrib:1621–1629
35. Geng Y, Tian F, Sun S et al (2018) A method of current harmonics suppression based on VSG. Trans China Electrotechnical Soc 33(5):1040–1050
36. Chen J, Shen P, Wei T et al (2018) Control scheme for synchronverters under non-ideal grid condition. Autom Electr Power Syst 9(42):127–133

Study and Application of the Integrated Energy Management and Service System

Zheng Tao, Dai Zemei, Cao Jing, Chi Yawei and Xu Wei

Abstract The expansion of business management and outward service of new market participants, for example integrated energy service corporations, results in the increasing demand for developing the integrated energy management and service system. By analyzing the business feature of integrated energy, a comprehensive system architecture, which features distributed self-control, centralized coordination, hierarchical operation and bidirectional interaction, is proposed to match the characteristics of multi-type, multi-operator, multi-customer and multi-service requirement of IES. Core techniques including comprehensive steady energy-flow model, IES comprehensive decision-making based on hierarchical analysis were studied. The effectiveness, applicability and functional completeness of the proposed system architecture are demonstrated by its successful application in practical projects such as Tongli Project.

Keywords Integrated energy system (IES) · Smart grid · Energy internet · System architecture · NIES5000 platform

1 Introduction

Energy is an important and decisive factor in economic and social development. There exists various types of energy systems in industry production and human life, such as electricity, natural gas, heat and cold. Different kinds of energy have their own advantages, meanwhile they can be replaced by or transformed into each other.

Z. Tao · D. Zemei · C. Jing · C. Yawei (✉) · X. Wei
NARI Group Corporation (State Grid Electric Power Research Institute), Nanjing 211106, China
e-mail: chiyawei@sgepri.sgcc.com.cn

Z. Tao · D. Zemei · C. Jing · C. Yawei · X. Wei
NARI Technology Co. Ltd, Nanjing 211106, China

Z. Tao · D. Zemei · C. Jing · C. Yawei · X. Wei
State Key Laboratory of Smart Grid Protection and Control, Nanjing 211106, China

Y. Xue et al. (eds.), *Proceedings of PURPLE MOUNTAIN FORUM 2019-International Forum on Smart Grid Protection and Control*, Lecture Notes in Electrical Engineering 585, https://doi.org/10.1007/978-981-13-9783-7_11

Therefore, people have recently proposed the Energy Internet (EI) [1–6] based on the smart grid. To catch up with the rapid advancement of China's power system reform, traditional energy companies, such as State Grid, China Southern Power Grid, and ENN Group, have expanded their business scope from single energy supply to integrated energy service. The appearance of new market entities such as electricity suppliers for incremental distribution network, and integrated energy service providers, brings changes to the energy supply methods and consumption patterns. New forms of integrated energy services are created to meet the increasing demand for energy management, optimal control and value-added services for integrated energy, which plays an important role in improving energy utilization efficiency, optimizing energy structure, and promoting the competition and cooperation. The power grid is the core to integrated energy system (IES), because electricity is much easier to be transported, converted and used, compared to other forms of energy. Before the establishment of the IES, the smart grid has been fully developed, which can provide a great demonstration and reference for the development of IESs.

The IES has received worldwide attention [7], with lots of studies carried out focusing on its overall structure. The American National Renewable Energy Laboratory (NERL) proposes the Electricity Distribution Bus (REDB) approach to connect the energy layer, device layer, simulating test layer, monitoring and data acquisition layers [8, 9]. Professor Pasquale Andriani et al. proposed a basic architecture for the Future Smart Energy Internet Project (FINSENY) consisting of the smart energy application layer, intelligent energy information communication technology (ICT) layer and user layer [10, 11]. Professor Hongbin Sun's group from Tsinghua University draws on the concept of smart grid EMS family [12], pointing out that the basic structure of energy Internet consists of two layers: "Internet-like energy system" and "Internet plus". To adapt to the requirements of multi-agent management, they proposed the multi-energy EMS family concept and distributed architecture. Energy management can be achieved through self-discipline and synergy among the family members [13]. Professor Tao Zhang of National University of Defense Technology proposed a hierarchical controlling architecture, which is suitable for the energy management systems (EMS) of energy Internet [14]. Based on the construction of Beijing Yanqing Smart Grid Innovation Demonstration, Renle Huang, from Beijing Electric Power Company, designed a fundamental structure for energy Internet, containing energy production and consumption layer, energy transmission layer, big data platform layer for integrated energy management, and application layer [15].

The architecture researches on integrated energy management systems mentioned above are mainly focused on the management and controlling optimization for integrated energy, with low correlation to smart grid and weak support for the development and interactivity for integrated energy services. Some investigations only proposed the ideas or concepts on architectural level, lacking of various projects verification for the practicality of the architectures.

In the present work, an overall architecture system, with smart grid as the core, is proposed for integrated energy management and service system (IEMSS), based on

the analysis of the characteristics of IES. We analyzes the key technologies of integrated modeling for steady energy-flow, joint dispatch and comprehensive decision making. Furthermore, the integrated energy management and service system NIES5000 was developed based on the proposed system and key technologies. Its feasibility, flexibility and integrity has been validated by the successful application practice in several domestic projects.

2 The Overall Architecture of IEMSS

The conventional micro-grid EMSs often employ the centralized structure of "information and decision-making concentration" [16], which is mature enough to meet the requirements of safe and economic operation. However, with the appearance of IESs, the conventional micro-grid EMSs can no longer meet the requirements of monitoring, coordinated optimization and scheduling of multiple energy sources. Therefore, based on the "architectural characteristics of hierarchy" [17], a new architecture of EMS is proposed in present work, considering the business characteristics of the IES. Characterized as "distribution self-discipline, centralized coordination, hierarchical partitioning, two-way interaction", this architectural is divided into five layers from bottom to top, as shown in Fig. 1, including distributed self-discipline user layer, energy internet layer, partition management area layer, collaborative management center layer, and supply and demand interactive service layer.

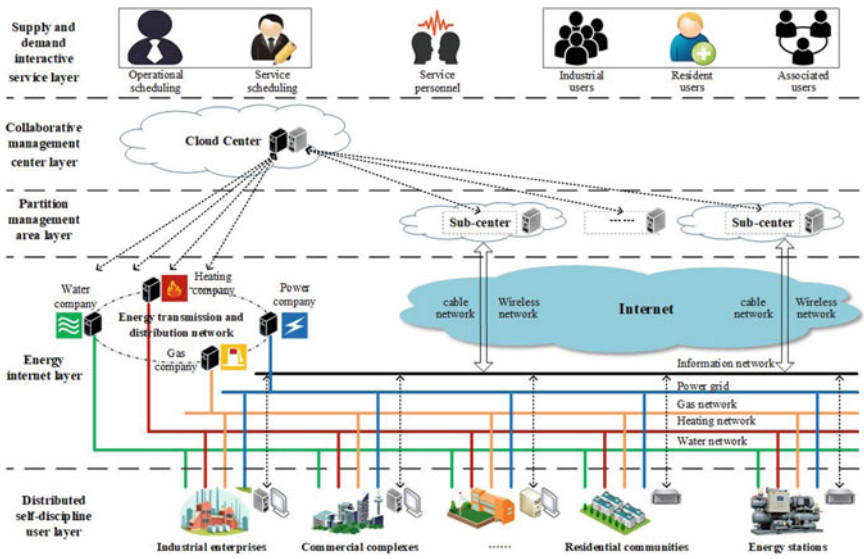

Fig. 1 The overall architecture of integrated energy management and service system

(1) **Distributed self-discipline user layer**. Industrial enterprises, commercial complexes, residential communities and other users as well as regional energy stations are usually energy sub-grids which contains heterogeneous energy sources such as electricity, water, gas, heat and cold. In order to achieve higher economic or environmental benefits, the subnet can be connected to the superior IEMSS of the upper level as an energy node, which is helpful to give full play to the adjusting ability of the controllable resources in the subnet.
(2) **Energy internet layer**. This layer consists of energy transmission and distribution network, information Internet, and externally accessible energy management system for electricity, water, gas, heat, etc. By means of the information Internet, the energy subnets physically distributed in each user station form a logical centralized energy information network, where each insider user can share the adjustable resources and exchange energy information. The energy transmission and distribution network is the carrier of energy flow. Therefore, the access of various energy management systems, which is the foundation of multi-user energy optimization, can realize the interaction and integration of various energy operation and measurement data.
(3) **Partition management area layer**. As a resource allocation center for rapid response to energy services in IEMSS, this layer usually has one or more sub-centers, depending on the requirements of fragment management for energy service. The regional sub-center can be merged with the cloud center if there is no requirement for fragmentation management.
(4) **Collaborative management center layer**. As a supervision and scheduling center for IEMSS, this layer exchanges data through standardized interfaces with third-party systems. It is in charge of the centralized control and service allocation for regional sub-centers or user stations.
(5) **Supply and demand interactive service layer**. As the supporting layer for the information release and service interaction of the IEMSS, this layer allows operators to dispatch regulatory services of the energy information network, such as monitoring, optimization, measurement, billing and transaction, to schedule service personnel as well as competitive service including analysis, evaluation and emergency maintenance. Industrial users, resident users, government and other associated users could enjoy online services through web pages and APPs.

Compared with the energy management system of conventional micro-grid, the IEMSS proposed in this paper has the following characteristics:

(1) **Integrated Platform**. The IEMSS provides an integrated support platform to achieve integrated modeling for multi-energy & multi-service, integrated acquisition and processing of multi-data, integrated management of multi-user, multi-service integration and integration display for multi-application.
(2) **Flexible deployment**. The IEMSS provides different choices from small scale to large scale, which can be deployed separately or in a cloud environment and adapt to different security level requirements. This IEMSS could satisfy the

increasing demand from the user group in different stages of the business development, and could also take into account the needs of all participants to build the system.

(3) **Interaction of supply and demand**. The IEMSS provides an interface for the interaction between service provider and demander. The two parties can share information, energy and value through the system, which improves user participation and system stickiness.

3 Functional Design of Energy Management System for Integrated Energy

The conventional micro-grid EMS system usually targets at the safe and economic operation of the grid. It only needs to optimize the electricity dispatching with simple target and few constraints. While the IEMSS needs to ensure the safety and stability of the multi-energy system, under the constraints of operation, node balance, coupling, etc. It also needs to consider the overall efficiency, the absorption rate of green energy, and the pollutant. Therefore, compared with conventional micro-grid EMS system, IEMSS needs to integrate more complex functions.

Similar to the typical cloud computing architecture, the IEMSS contains three layers: infrastructure services (IaaS), platform service (PaaS), and software service (SaaS), as shown in Fig. 2.

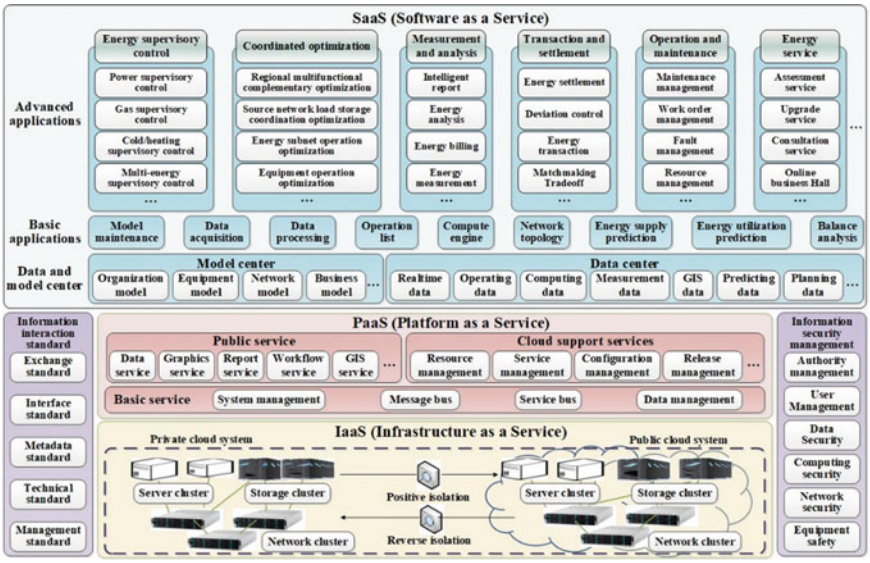

Fig. 2 Software architecture of IES

The IaaS layer provides virtualized computing, storage, and networking resources. The PaaS layer provides an online operating environment that supports the application's operation. The SaaS layer is the core of the IEMSS, providing users with a variety of application services, including the following categories:

(1) **Energy monitoring application**. The SaaS layer collects the information of various energy to maintain the balance between supply and the demand of integrated energy, guarantee the normal operation of pipe network and equipment, interact with other applications like maintenance and repairing.
(2) **Coordinated optimization application**. Various adjustable and controllable resources, such as the triple supply of cold, heat and electricity, distributed power, energy storage, charging piles, can be optimized and scheduled in three aspects: equipment operation, energy subnet operation, and complementation of regional multi-energy, resulting in scientific allocation and orderly use of energy, and improvement on energy efficiency.
(3) **Measurement analysis application**. Through the centralized collection and processing of measurements of integrated energy supply, the customer's overall and subordinate units are analyzed in terms of energy consumption, efficiency and cost, to provide data support for comparative analysis of optimization effects of energy optimized applications, statistical data release for energy service applications, analysis of energy saving potential, and consultation on energy conservation retrofits.
(4) **Transaction clearing application**. For the users trading outsourced energy or requiring self-management management, the SaaS layer allows them to purchase or sell energy in one-stop manner. It supports various energy trading modes such as protocol price and open bidding, guaranteeing a safe, open, fair, and efficient energy trading market.
(5) **Maintenance and repair application**. It provides GIS-based visual operation and APP-based mobile maintenance for cold heat and electricity systems. The whole process of various operation and maintenance services is managed in a standard and closed-loop way, ensuring the safe, reliable and efficient operation of the system. It also provides a fast, accurate and efficient cooperation mechanism for the user-side energy maintenance business.
(6) **Energy service application**. The industry and regional energy statistics are released through the online hall, which can provide users with comprehensive, one-stop, and diversified services, including consulting, query, withholding, payment, rapid repairing, maintenance, custody, energy-saving diagnosis, equipment transformation, and energy efficiency assessment.

4 Key Technology

4.1 Steady-State Energy-Flow Modeling Technology for Integrated Energy

In order to accurately describe the operation mechanism of IES for multi-energy type, a comprehensive energy integrative model is established in present work by combining different energy subsystem models and interface conversion equations, providing a base model for multi-energy complementary and schedule optimization.

(1) **Energy subsystem model**. The electricity, gas and heat subs-models of integrated energy characterize the distribution of steady energy-flow of different energy systems in the subsystem, including the electromagnetic model with the tide equation reflecting the voltage and power distribution in power system, as well as the thermodynamic and hydrodynamic models reflecting distributions of temperature, pressure, flow rate, and other physical quantity in the heat, gas, or other fluid systems. As shown in Fig. 3, the steady-state distribution of the subsystem in each group of models can be represented by algebraic equations. In Fig. 3, S_e, P_e, Q_e, U_e, I_e, Y represent separately the apparent power, active power, reactive power, voltage, current and admittance matrix in power system; P_h is thermal energy, C_p is heat coefficient, A_h is association matrix of heat network, v_{hm} is mass flow rate of heat network, T_{in}, T_{out} are the supply/return temperature of water or vapor in heat network, P_g is the gas horsepower, V_{gin} is inlet flow of power consumption equipment, α is the index for gas flow, η_g is energy conversion efficiency, P_{in}, P_{out} are inlet/outlet pressure of power consumption equipment, E_{in}, E_{out} are inlet/outlet energy of energy conversion equipment, H is conversion efficiency, $\circ$ represents Hadamard.

(2) **Conversion interface model**. The conversion interface model describes the conversion of steady energy flows between different energy systems,

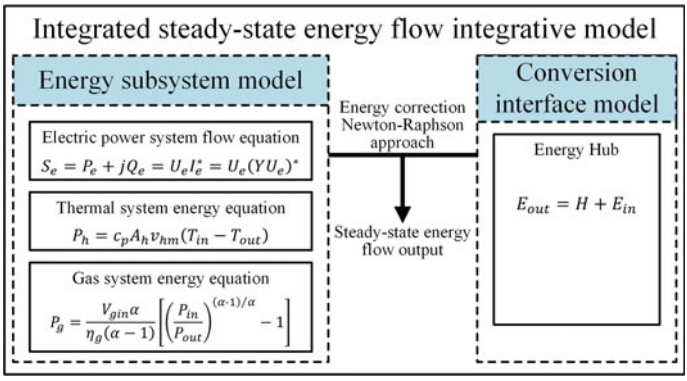

Fig. 3 Integrative model of steady-state energy flow in IES

correlating and coupling different energy systems. The conversion relationship between heterogeneous energy can be represented by an energy hub. In the energy hub model, a conversion efficiency matrix that characterizes the overall energy input to output relationship can be obtained by establishing the conversion coefficients between inputs and outputs for each energy.

(3) **Integrated model**. The integrated model can solve the steady energy flow of different energy subsystems under coupled conditions, providing the optimization base model for multi-energy joint scheduling. Firstly, the energy subsystem are integrated with the conversion interface model, and then the input and output energy at the interface are corrected by using conversion interface model and substituted into the corresponding energy subsystem. Finally, the steady-state energy-flow will be solved by using the nonlinear equation solving algorithm (such as the method of Newton-Raphson [18]. As shown in Fig. 3, the steady-state energy-flow integrative model for the integrated energy can exactly reflect the energy balance of the multiple energy-flow subsystem, and help to analyze the interaction between the steady-state energy-flows of the multi-energy system under equilibrium conditions.

4.2 Comprehensive Decision Technology for Integrated Energy Based on Hierarchical Analysis

In order to evaluate the service quality provided by IES to the multi-service objects and assess the overall operation quality of multi-service demand system, it is necessary to evaluate the effect of optimization scheduling on integrated energy through online evaluation and subsequent statistics. Therefore, this paper establishes the evaluation indicators that reflect different management and service performance, and then establishes the priority order of different evaluation indicators by using the method of Analytic Hierarchy Process (AHP). This set of indicators can provide comprehensive decision-making information for the dispatcher and other management personnel to determine the scheduling effect.

(1) **Evaluation indicators for integrated energy**. Based on previous research [19, 20], an evaluation index system for the IEMSS, as shown in Table 1, is established by referring to development experience of NIES5000 system. They are indispensable for the subsequent evaluation of the operational effects of the IES.

(2) **Comprehensive decision based on hierarchical analysis**. For the evaluation system including multiple indicators as shown in Table 1, it is necessary to establish the priority of different indicators in the decision-making process to facilitate the decision-making of dispatchers. Firstly, the decision weights of different second-class indicators are established by using the AHP method [32]. Then, after normalizing each index value and the corresponding decision

Table 1 Evaluation system of IES

First class	Safety	Economy	High quality	Environmentally friendliness
Second class	Load rate of pipeline/ network	Unit cost for energy supply	Qualified rate of energy supply	Amount of energy saving and emission reduction
	Failure rate of key equipment	Average cost for equipment maintenance	Energy complementarity	Substitution rate for electricity
	N−1 pass rate of equipment	Energy efficiency for integrated energy	Coefficient of valley to peak	Electrification rate of renewable energy
	Average time for incident recovery	Energy self-sufficiency	The complaint rate of users in recent 7 days	Local absorption rate of new energy

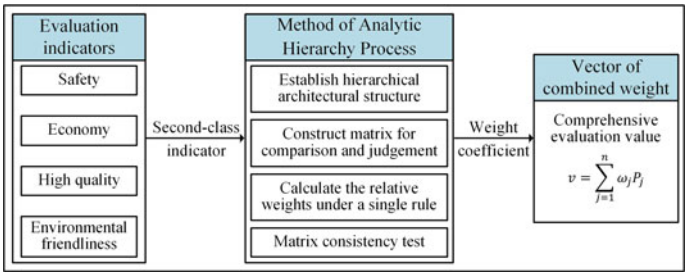

Fig. 4 Diagram of AHP-based comprehensive decision

weights, the weighted sum of the system comprehensive indicators is obtained to measure the overall optimization scheduling effect of the system. As shown in Fig. 4, ω_j and P_j represent the weight coefficient and the evaluation value of the jth index, v is the comprehensive evaluation value.

5 Applications

According to the architecture system and key technologies proposed in present work, the author's team developed NIES5000, the management and service system for integrated energy system, which has been initially applied in several projects such as Tongli project. Based on the application of these projects, the following conclusions can be drawn:

(1) For different types of projects (park users, integrated energy suppliers, incremental placement companies), the architecture proposed in present paper can satisfy the requirements.
(2) The architecture proposed here can provide flexible architecture for the different characteristics of various projects and specific individual demands. For example, small- and medium-sized projects at the industrial park can be deployed as first level. Large and medium-sized projects such as distribution power companies and integrated energy service providers can be deployed at multiple levels. Private deployment and Internet deployment can be flexibly selected based on service range and mode. Security zone and Internet zone can be combined flexibly according to the asset property and security requirements.
(3) The architecture proposed in this paper can provide a complete range of services. The service covers both regulated and competitive services, and can consider the local application of the user layer and the global application of the regional layer and the central layer.

6 Conclusion

This paper expands the concept of "horizontal integration, vertical penetration, and safety division" of the smart grid control system D5000, proposing an architecture system of "distribution self-discipline, centralized coordination, hierarchical partitioning, two-way interaction". Several key technologies for integrated energy management and service system are put forward including steady-state energy-flow integrated modeling and comprehensive decision-making based on hierarchical analysis. As a results, the comprehensive energy management and service system NIES5000 was developed, whose application in Project Tongli and others verified the flexibility, integrity and feasibility of the proposed key architecture and the ability to meet the overall needs of the service.

In addition, as a new technical direction, the integrated energy management and service system just start to develop. Therefore, there is still a lot of research and construction needs to be carried out, such as the online planning, online simulation for integrated energy, which has not been discussed within this paper.

Acknowledgements This work was supported by the National Key Research and Development Program of China (2018YFB0905000) and the project of "Study and application of multi-energy micro-grid source-network-load-storage coordinated control system" of NARI Group Corporation (State Grid Electric Power Research Institute).

References

1. Dong Z, Zhao J, Wen F et al (2014) From smart grid to energy internet: basic concept and research framework. Autom Electr Power Syst 38(15):1–11. https://doi.org/10.7500/aeps20140613007
2. Li C, Li X, Tian S et al (2017) Challenges and prospects of risk transmission in deep fusion of electric power and information for energy internet. Autom Electr Power Syst 41(11):17–25. https://doi.org/10.7500/aeps20160927014
3. Han DD, Yu YX (2014) Future smart grid is energy internet. China Strateg Emerg Ind 22:44–45
4. Sun H, Guo Q, Pan Z (2015) Energy internet: concept, architecture and frontier outlook. Autom Electr Power Syst 39(19):1–8. https://doi.org/10.7500/aeps20150701007
5. Sun HB, Guo QL, Pan ZG et al (2015) Energy internet: driving force, review and outlook. Power Syst Technol 11:3005–3013
6. Yao J, Gao Z, Yang S (2015) Understanding and prospects of energy internet. Autom Electr Power Syst 39(23):9–14. https://doi.org/10.7500/aeps20151101004
7. Wu J (2016) Drivers and state-of-the-art of integrated energy systems in Europe. Autom Electr Power Syst 40(5):1–7. https://doi.org/10.7500/aeps20150512001
8. O'Malley M, Kroposki B (2017) Unlocking flexibility energy system integration. IEEE Power Energ Mag 1:10–13
9. National Renewable Energy Laboratory, https://www.nrel.gov/continuum/utility_scale/esif.html. Last access 13 May 2011
10. Finseny white paper, http://www.fi-ppp-finseny.eu/finsenywhite-paper. Last access 06 Oct 2012
11. Block C, Briegel F, Fey B et al (2010) Internet of energy: ICT for energy markets of the future. Breite Straße, Berlin
12. Sun HB, Zhang BM, Wu WC et al (2014) Autonomous-synergetic energy management system family for smart grids: concept, architecture and cases. Autom Electr Power Syst 9:1–5
13. Sun H, Pan Z, Guo Q (2016) Energy management for multi-energy flow: challenges and prospects. Autom Electr Power Syst 40(15):1–8. https://doi.org/10.7500/aeps20160522006
14. Zhang T, Zhang FX, Zhang Y (2016) Study on energy management system of Energy Internet. Power Syst Technol (1):146–155
15. Huang R, Pu T, Liu K et al (2015) Design of hierarchy and functions of regional energy internet and its demonstration applications. Autom Electr Power Syst 39(9):26–33. https://doi.org/10.7500/aeps20141229010
16. Sun M, Gao Y, Yan Y et al (2015) Clustering technology for smart grid dispatching and control systems. Autom Electr Power Syst 39(1):31–35. https://doi.org/10.7500/aeps20141009017
17. Bi Y, Jiang L, Wang X et al (2015) Design and investigation on service-oriented architecture-based smart grid dispatching and control system. Autom Electr Power Syst 39 (2):92–99. https://doi.org/10.7500/aeps20140919013
18. Liu X, Mancarella P (2016) Modelling, assessment and Sankey diagrams of integrated electricity-heat-gas networks in multi-vector district energy systems. Appl Energy 67:3 36–352
19. Chen B, Liao Q, Liu D et al (2018) Comprehensive evaluation indices and methods for regional integrated energy system. Autom Electr Power Syst 42(4):174–182. https://doi.org/10.7500/aeps20170605005
20. Zeng M, Liu YX, Zhou PC et al (2018) Review and prospects of integrated energy system modeling and benefit evaluation. Power Syst Technol (6):1697–1708

Energy Storage System Investment Decision Based on Internal Rate of Return

Jincheng Wu, Shufeng Dong, Chengsi Xu, Ronglei Liu, Wenbo Wang and Yuanyun Dong

Abstract The continuous integration of new energy sources has aggravated the fluctuation of power load in power systems. In recent years, the rapid development of energy storage technology has matched the demand for the balance of supply and demand of power load. At the same time, the peak and valley electricity price policy of power system makes it possible for the investor to make a profit with the investment of building energy storage systems. So it is necessary to plan the construction of the energy storage system from the perspective of investor. Based on the internal rate of return of investment, considering the various financial details such as annual income, backup electricity income, loan cost, income tax, etc., this paper establishes a net cash flow model for energy storage system investment, and uses particle swarm optimization algorithm based on hybridization and Gaussian mutation to get the energy storage capacity that maximizes the internal rate of return of the investment. And this internal rate of return is compared with the set internal rate of return of the investment to determine whether the energy storage system is worth building. The paper illustrates the effectiveness of the investment planning model through the planning process of two users.

Keywords Energy storage · Internal rate of return · Investment decision · Hybridization and Gaussian mutation

1 Introduction

Large-scale grid connection of new energy sources increases the volatility and randomness of the power system, which aggravates the load imbalance between the power supply and demand, and affects the stability of the power system [1]. In order

J. Wu · S. Dong (✉) · C. Xu
College of Electrical Engineering, Zhejiang University, Hangzhou 310027, China
e-mail: dongshufeng@zju.edu.cn

R. Liu · W. Wang · Y. Dong
Zhejiang Wanke New Energy Technology Co., Ltd., Hangzhou 310051, China

Y. Xue et al. (eds.), *Proceedings of PURPLE MOUNTAIN FORUM 2019-International Forum on Smart Grid Protection and Control*, Lecture Notes in Electrical Engineering 585, https://doi.org/10.1007/978-981-13-9783-7_12

to alleviate this problem through market means, the grid has proposed the peak-to-valley electricity price policy and the power plant assessment and compensation rules. However, due to the uncertainty of the user side power consumption and the limitation of the power generation side output regulation technology, this problem has not been properly solved.

In recent years, the vigorous development of energy storage technology has brought a glimmer of life to the solution of this problem. The energy storage system has a fast power regulation speed and can respond quickly to the command. It can be used to assist the power plant to perform frequency modulation on the power generation side, as well as cut peaks and fill the valley on the user side. However, due to the current high cost and limited operating life of energy storage devices, it is difficult to be widely promoted. Therefore, the application of energy storage systems in power systems requires feasibility studies. The Ref. [2] investigates and analyzes the application status of megawatt-scale energy storage FM projects at home and abroad, and makes recommendations about how to promote the commercialization of China's energy storage FM from three perspectives: policy makers, market participants and dispatching agencies. In Ref. [3], a real-time modified optimization control strategy of battery based on dynamic programming is proposed. In Ref. [4] a linear programming model is applied under the target, and a modeling method for optimally configuring the capacity of different AGC power supplies is proposed. In Ref. [5], an initial power command allocation method considering the unit's climbing rate limit is designed, and its effectiveness is proved by simulation experiments. In Ref. [6], the method of analyzing the high frequency and low-frequency modulation requirements by discrete Fourier transform is used to quantitatively analyze the proportion of high-frequency components in the whole system. Most of the research done in the above references require major changes to the unit's output plan of the existing power plant and less combined with the existing frequency modulation policy and the benefits of building an energy storage system from the perspective of the power plant.

Reference [7] studies the charging and discharging strategy and the optimal capacity allocation calculation method of the hybrid energy storage device combined with the traditional unit participating in the automatic power generation control (AGC). Based on the interpretation of the "two rules" of East China Power Grid, Ref. [8] proposes multiple energy storage and discharge strategies for the assessment indicators of the power grid, considering the impact of frequent actions on life and establishing an objective function related to energy storage economy. Reference [9] proposes a response characteristic model that includes actual energy storage, translatable load, transferable load, and load reduction. The double-layer optimization architecture is used to solve the joint planning problem of energy storage resources and distributed power sources. Reference [10] proposes an effective increase of the regulation resources of the distribution network system through the controllable load, significantly reducing the fixed energy storage configuration capacity and reducing the operating cost of the system. Reference [11] proposed a microgrid energy storage capacity optimization model that takes into account both the economic operation of the system and battery life. The method

proposed in the above references combined with the grid policy to carry out technical and economic planning from the perspective of the power generation side has certain practical guiding significance, but does not consider the financial details in the investment process of the energy storage system. These financial expenses include output tax, value-added tax, income tax, loan interest, etc., which account for a large part of the annual cash flow and need to be taken into account in the planning of energy storage systems.

From the perspective of investors, this paper takes the peak-valley spread as the main source of income, considers a series of financial details and constraints of energy storage equipment, electricity price policy and financial cost, and makes investment decisions with the objective of maximizing the internal rate of return of investors. Under the condition, the capacity planning model of the energy storage system is constructed, and the optimal solution of the plan is obtained by the particle swarm optimization algorithm based on hybridization and Gaussian mutation.

2 Energy Storage System Net Cash Flow Model

2.1 Energy Storage System Cash Inflow Model

The cash inflow sources of the user-side energy storage system include the backup electricity income, the peak-to-valley electricity price difference, and the saving capacity fee, etc. The most important source is the peak-to-valley electricity price difference, which means the storage system is discharged during the peak electricity consumption period and is used during the electricity low period.

The annual income of peak-to-valley electricity price difference in a certain year is calculated as follows:

$$D_m = S \times d_m \tag{1}$$

$$F_{Dm} = D_m \times (T_{Dm1} \times P_1 + T_{Dm2} \times P_2 + T_{Dm3} \times P_3 + T_{Dm4} \times P_4)/T_{Dmtotal} \tag{2}$$

$$C_m = D_m/\left[\eta_b \times \eta_{ups} \times (1 - \delta)\right] \tag{3}$$

$$F_{Cm} = C_m \times (T_{Cm1} \times P_1 + T_{Cm2} \times P_2 + T_{Cm3} \times P_3 + T_{Cm4} \times P_4)/T_{Cmtotal} \tag{4}$$

$$F_Y = \sum F_{Dm} - \sum F_{Cm} \tag{5}$$

D_m means discharged electricity for the m-th cycle of the year, S means system design capacity, d_m means depth of discharge for the m-th cycle, F_{Dm} means electricity charge for the m-th cycle discharge, T_{Dm1} means the m-th cycle low valley discharge duration, T_{Dm2} means the m-th cycle flat section discharge duration, T_{Dm3} means the height discharge time of the m-th cycle, T_{Dm4} means the m-th

cycle peak discharge duration, $T_{Dmtotal}$ means total length of the m-th cycle discharge, P_1 means low valley electricity price, P_2 means flat price, P_3 means height electricity price, P_4 means peak electricity price. F_{Cm} means the m-th cycle charging electricity fee, T_{Cm1} means the m-th cycle low valley charging time, T_{Cm2} means the charging time of the m-th cycle flat section, T_{Cm3} means the height charging time of the m-th cycle, T_{Cm4} means the peak charging time of the m-th cycle, $T_{Cmtotal}$ the total duration of charging for the m-th cycle, η_b means battery charge and discharge efficiency, η_{ups} means UPS efficiency, δ means line loss rate, F_Y means annual income of electricity.

The i-year cash inflow model of the energy storage system is shown in (6):

$$C_{in\_i} = F_{Yi} + F_{Si} + F_{Ci} + F_{Oi}(+F_{asset}) \tag{6}$$

C_{in_i} means the cash inflow of i-th year, F_{Yi} means the income of i-th year, F_{Si} means electricity backup income. It comes from the compensation for improving the reliability of power supply. F_{Ci} means the fee from saving capacity of i-th year, F_{Oi} means the i-year operating fee income, F_{asset} means residual value of energy storage system assets after the life cycle, and it is only taken into account when calculating the cash inflow for the last year.

2.2 Energy Storage System Cash Outflow Model

The cash outflow during the investment and operation of the user side energy storage system includes pre-investment expenses, site rental fees, labor costs, spare parts costs, maintenance materials, insurance, travel expenses, daily business expenses, general sales and management expenses, and value-added Taxes, etc.

The cash outflow of the energy storage system for the 0th year can be calculated according to formula (7):

$$C_{out\_0} = F_d + F_{c0} + F_b + F_t + F_{con} \tag{7}$$

C_{out_0} is the cash outflow of the 0-th year; F_d is the equipment and engineering investment cost, including battery system cost, supporting system cost, system integration cost, engineering investment cost; F_{c0} is the total amount of upfront expense; F_b is the business cost; F_t is service fee for winning the bid; F_{con} is the construction period fee.

The i-year cash outflow of the energy storage system can be calculated according to formula (8):

$$\begin{aligned} C_{out\_i} = & F_{rent\_i} + F_{labor\_i} + F_{spare\_i} + F_{m\_i} + F_{ins\_i} + F_{tra\_i} \\ & + F_{db\_i} + F_{sm\_i} + F_{vat\_i} + F_{sur\_i} + F_{tax\_i} + F_{other\_i} \end{aligned} \tag{8}$$

C_{out_i} is the i-year cash outflow, F_{rent_i} is the i-year venue rental fee, F_{labor_i} is the i-year labor cost, F_{spare_i} is the i-year spare parts fee, F_{m_i} is the i-year maintenance material fee, and F_{ins_i} is the i-year insurance premium F_{tra_i} is the travel fee for the i-year, F_{db_i} is the daily business fee for the i-year, F_{sm_i} is the general sales and management fee for the i-year, F_{vat_i} is the value-added tax for the i-year, F_{sur_i} is the value-added tax for the i-year, F_{tax_i} is the first i-year loan income with fees, F_{other_i} is other expenses for the i-year.

Therefore, the calculation formula for the net cash inflow of the energy storage system in the i-year is:

$$C_i = C_{in\_i} - C_{out\_i} \tag{9}$$

2.3 Internal Rate of Return

Internal rate of return (IRR) [12] refers to the rate of return that project investment is expected to achieve. Essentially, it is the discount rate that enables the project's net present value to be equal to zero. That is, in the case of considering the time value, the present value of the cash flow generated by an investment in the future is exactly equal to the return rate of the investment cost.

The internal rate of return is a basic indicator of the economic performance of the project. Refers to the discount rate of the current value of the net cash flow of each year during the construction and production service period. This analysis method considers the time value of money and can measure the profitability of each scheme, so it is one of the important methods of investment forecast analysis.

It is the rate of return that an investment is eager to achieve, and the bigger the indicator, the better. In general, the project is feasible when the internal rate of return is greater than or equal to the benchmark rate of return. The sum of the discounted value of the cash flow of each year of the investment project is the net present value of the project, and the discount rate when the net present value is zero is the internal rate of return of the project.

The advantage of the internal rate of return method is that it can link the income of the project life to its total investment, point out the profit rate of the project, and compare it with the benchmark investment return rate of the industry to determine whether the project is worth building.

The internal rate of return is the present value of the cash flow generated by an investment in the future, considering the time value of the investment. It is just equal to the discount rate of the investment cost. Generally speaking, the higher the internal rate of return, the more you invest. The cost is relatively small, but the benefits are relatively large.

Internal rate of return (IRR) can be calculated according to Eq. (10):

$$-C_{out\_0} + \left[C_1/(1+IRR) + C_2/(1+IRR)^2 + C_3/(1+IRR)^3 + \cdots C_N/(1+IRR)^N\right] = 0 \tag{10}$$

N is the engineering life cycle, C_i is the net cash inflow of the energy storage system in the i-year.

2.4 Planning Path

Figure 1 is a flow chart for the calculation of internal investment yield. The input part of the figure includes financial information such as charge and discharge demand, electricity price at each time period, loan ratio, loan interest rate, battery life, battery purchase cost, etc. The process ① indicates that the cash inflow per year is calculated according to formulas (1)–(6). The process ② indicates that the cash outflow for each year is calculated according to the formulas (7) and (8), and the process ③ represents the calculation of the net cash inflow for each year according to the formula (9). The process ④ represents the internal investment yield in the case where the energy storage design capacity is calculated according to the formula (10).

In the whole planning process, only the energy storage capacity is a variable, and finally a capacity value that maximizes the internal rate of return is obtained, and the internal rate of return is compared with the internal rate of return threshold. If it is higher than this threshold, it means the investment is feasible and constructed using the obtained capacity value. If it is lower than this threshold, this investment plan is not feasible and needs to be planned separately.

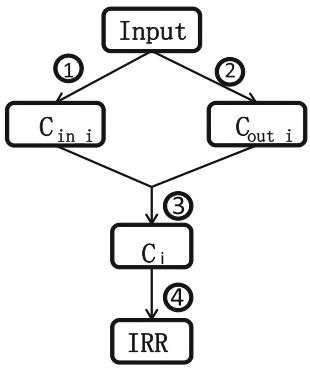

Fig. 1 Internal rate of return calculation flow chart

3 Particle Swarm Optimization Algorithm Based on Hybridization and Gaussian Mutation

The particle swarm optimization algorithm [13, 14] is essentially a random search algorithm, which is suitable for optimization in dynamic and multi-objective optimization environments. Compared with traditional optimization algorithms, it has faster calculation speed and better global search ability.

In a D-dimensional target search space, there are N particles forming a group, where the i-th particle is represented as a D-dimensional vector:

$$X_i = (x_{i1}, x_{i2}, x_{i3}, \ldots x_{i\mathrm{D}}),\ i = 1, 2 \ldots \mathrm{N} \tag{11}$$

The velocity of the i-th particle is also a D-dimensional vector, which is written as:

$$V_i = (v_{i1}, v_{i2}, v_{i3}, \ldots v_{i\mathrm{D}}),\ i = 1, 2 \ldots \mathrm{N} \tag{12}$$

The optimal position that the i-th particle has searched so far is called the individual extremum, which is written as:

$$p_{\mathrm{best}} = (p_{i1}, p_{i2}, p_{i3}, \ldots p_{i\mathrm{D}}),\ i = 1, 2 \ldots \mathrm{N} \tag{13}$$

The optimal position searched by the entire particle swarm so far is the global extremum, which is written as:

$$g_{\mathrm{best}} = (g_1, g_2, g_3, \ldots g_{\mathrm{D}}) \tag{14}$$

After finding the two optimal values, the particles update their speed and position according to Eqs. (15) and (16).

$$v_{ij}(t+1) = v_{ij}(t) + c_1 r_1(t) \cdot \left[p_{ij}(t) - x_{ij}(t)\right] + c_2 r_2(t) \cdot \left[p_{gj}(t) - x_{ij}(t)\right] \tag{15}$$

$$x_{ij}(t+1) = x_{ij}(t) + v_{ij}(t+1) \tag{16}$$

c_1 and c_2 are learning factors; r_1 and r_2 are uniform random numbers in the range [0,1]; $v_{ij} \in [-v_{max}, v_{max}]$, and v_{max} is the speed of the limiting particles. r_1 and r_2 are random numbers between 0 and 1, reflecting the randomness of particle changes. The right side of the Eq. (21) consists of three parts: the first part represents the tendency of the particle to maintain its previous speed; the second part represents the tendency of the particle to approach its best historical position; the third part represents the approach of the particle to the best position of the group history.

The particle swarm optimization algorithm searches for spatial optimal solutions by cooperating and competing with each other.

In order to better develop the detection capability of the particle swarm algorithm, the Ref. [15] introduces inertia weights.

$$\omega = \omega_{\max} - \frac{k(\omega_{max} - \omega_{min})}{iter_{\max}} \tag{17}$$

ω_{max} is the initial weight, ω_{min} is the final weight, $iter_{\max}$ is the maximum number of iterations, k is the current number of iterations.

So Eq. (15) is updated to:

$$v_{ij}(t+1) = \omega v_{ij}(t) + c_1 r_1(t) \cdot \left[p_{ij}(t) - x_{ij}(t)\right] + c_2 r_2(t) \cdot \left[p_{gj}(t) - x_{ij}(t)\right] \tag{18}$$

When ω is large, the chance that V_{ij} is close to the global best and historical advantage is small, and V_{ij} will deviate from the current best, so that it is possible to explore the best advantage. Therefore, the best method now used is ω, which is a method of decreasing iterations, that is, selecting a large ω value at an early stage and a smaller ω value at the end. This is in line with the early exploration of the ability of particles, and the need to maintain its convergence in the late stage, which is currently the universally accepted standard particle swarm algorithm.

However, as the number of iterations increases, the optimal particle control will gradually increase, resulting in a decline in the diversity of the whole particle population, and the population is more likely to fall into local optimum. Therefore, in order to increase the diversity of the population, a certain proportion of the particles in the population are randomly hybridized to generate new particles, thereby changing the direction and speed of the optimal particles, allowing them to enter other regions for searching and discovering new individual extremum. The hybridization process is defined as follows:

$$x_{child1} = p_i \times x_{parent1} + (1 - p_i) \times x_{parent2} \tag{19}$$

$$x_{child2} = p_i \times x_{parent2} + (1 - p_i) \times x_{parent1} \tag{20}$$

$$v_{child1} = \frac{v_{parent1} + v_{parent2}}{\left|v_{parent1} + v_{parent2}\right|} \left|v_{parent1}\right| \tag{21}$$

$$v_{child2} = \frac{v_{parent1} + v_{parent2}}{\left|v_{parent1} + v_{parent2}\right|} \left|v_{parent2}\right| \tag{22}$$

p_i is a random variable between [0, 1].

Finally, the Ref. [16] proposes a Gaussian mutation method, and its validity is illustrated by an example. The calculation formula is as follows:

$$mut(x) = x \times (1 + gaussian(\sigma)) \tag{23}$$

σ is set to be 0.1 times the length of the search space in one dimension, it's good exactly from experience obtained in some experiments.

In summary, this paper adopts a particle swarm optimization algorithm based on hybridization and Gaussian mutation to solve the net cash flow model of the energy storage system. The process steps are as follows:

1. Randomly initialize the velocity and position of each particle in the population, and set the historical optimality of the individual as the current position, and the optimal individual in the group as the current global optimal;
2. Updating the inertia weight according to Eq. (17);
3. Updating the speed and position of each particle according to Eqs. (16) and (18), respectively;
4. In each evolution of the generation, calculate the fitness function value of each particle;
5. If the current fitness function value of the particle is better than its historical optimal value, replace the historical optimal position of the individual with the current position;
6. If the historical optimality of the particle is better than the global optimal, then the global optimal will be replaced by the historical optimality of the particle;
7. Generating new particles and performing hybridization variation according to formulas (19, 20, 21, 22 and 23);
8. It is judged whether the termination condition is satisfied, and if it is not satisfied, the process proceeds to step 2, otherwise, the output result is ended.

4 Case Analysis

Due to the different regions of different users, the user's load, regional electricity price policy, and construction cost are also different, so it is impossible to invest in the same way in different regions. Suppose now that we are considering building energy storage systems for electricity customers in two different regions. The investment internal rate of return threshold is set to 6%. If the final internal rate of return of the investment is greater than 6%, the investment is feasible, and if not, the investment is not feasible. The basic situation of the two users is shown in Tables 1 and 2.

Table 1 Basic situation of user 1

User 1			
Load	4 MWh	Peak price	1.5611
Loan ratio	50%	Height price	1.0245
Lending rates	8%	Flat price	0.667
Annual backup electricity return income	50,000	Low valley price	0.3706
Charge and discharge depth	80%	Charge and discharge efficiency	90%

Table 2 Basic situation of user 2

User 2			
Load	12 MWh	Peak price	1.0612
Loan ratio	77%	Height price	0.9724
Lending rates	8%	Flat price	0.667
Annual backup electricity return income	100,000	Low valley price	0.3706
Charge and discharge depth	90%	Charge and discharge efficiency	90%

The unit of electricity price in the above table is yuan/kWh, and the unit of the income is yuan.

The steps of the entire energy storage system investment decision process are as follows:

1. Establish a net cash inflow model for the energy storage system as described in the second section above.
2. Randomly initialize the velocity and position of each particle in the particle swarm, and set the optimal position of the individual history and the optimal position of the group history.
3. Each particle fitness calculation process for each generation is shown in Fig. 1. Calculate the annual net cash inflow based on the basic information entered and the design capacity, and then calculate the internal rate of return, which is the fitness value of the particle.
4. Using the particle swarm optimization algorithm based on hybridization and Gaussian mutation described above to obtain the capacity value of the energy storage system that maximizes the internal rate of return.
5. Compare the calculated internal rate of return of the investment with the threshold of the internal rate of return of the investment. If it is greater than the threshold, the investment is feasible. Less than the threshold indicates that the investment needs to be further planned.

Through the above process, the result parameters of user 1 and user 2 are shown in Tables 3 and 4.

Table 3 Energy storage planning result of user 1

User 1			
Storage capacity	12 MWh	IRR	9.91%
Energy storage battery system investment	1520	Post-tax fixed assets formed after investment	1451.18
Revenue sharing	118	Fixed asset input tax	225.73
Customer division	188	Annual depreciation of fixed assets	108.84
Electricity sharing	70.1	Upfront cost investment	79.37

Table 4 Energy storage planning result of user 2

User 2			
Storage capacity	24 MWh	IRR	5.57%
Energy storage battery system investment	2280	Post-tax fixed assets formed after investment	2090.1
Revenue sharing	97.8	Fixed asset input tax	334.36
Customer division	168	Annual depreciation of fixed assets	156.76
Electricity sharing	70.1	Upfront cost investment	121.22

The unit of the cost is yuan

As can be seen from the above table, the optimal investment capacity of User 1 is 12 MWh, the internal rate of return is 9.91%, and the optimal investment capacity of User 2 is 24 MWh and the internal investment return rate is 5.57%. Investment is feasible based on User 1, and investment based on User 2 is not feasible.

5 Conclusion

This paper proposes an investment decision-making method based on the investment internal rate of return to calculate annual cash inflow and cash outflow, which takes into account various financial details, including various taxes, loan interest rates, labor costs, operation and maintenance costs, site rental fees, etc. And using particle swarm optimization algorithm based on hybridization and Gaussian mutation to calculate the energy storage capacity value of the project's life cycle to maximize the internal rate of return of the investment. And comparing the internal rate of return with the IRR of the same industry investment to guide investment construction. The planning method is more closely related to the actual project, closely related to the interests of the investors, and has a strong practical guiding significance.

Acknowledgements This work was supported by science and technology project "Key Technology of Energy Management Research and Intelligent Operation Platform Development of Integrated Energy System (K18-510102-031)" of Zhejiang Wanke New Energy Technology Co., Ltd.

References

1. Han Z (2013) Power system analysis, 5th edn. Zhejiang University Press
2. Sun B, Yang S, Liu Z et al (2017) Analysis on present application of megawatt-scale energy storage in frequency regulation and its enlightenment. Autom Electr Power Syst (AEPS), 41 (11): 8–16, 38

3. Bao G, Lu C, Yuan Z et al (2012) Real-time optimization of peak-filling and valley filling of battery energy storage system based on dynamic programming. Autom Electr Power Syst (AEPS) 36(12):11–16
4. Chen D, Zhang Z, Ma L (2014) A new method for clearing and optimizing modeling of AGC markets with energy storage participation. Autom Electr Power Syst 38(13):79–84
5. Tang J, Li X, Huang J, Xu P, He C Capacity allocation method of secondary frequency modulation for energy storage battery with maximum net benefit. J Electr Technol:1–10
6. Hu Z, Xie X, Zhang F et al (2014) Research on automatic generation control strategy incorporating energy storage resources. Proc CSEE 34(29):5080–5087
7. Niu Y, Zhang F, Zhang H et al (2016) Hybrid energy storage optimization control and capacity planning for improving AGC performance of thermal power units. Autom Electr Power Syst (AEPS) (10)
8. Chen L, Jiang Y, Wang C (2017) Strategy and capacity of energy storage for improving AGC performance of power plant. Electr Power Autom Equip 37(8):52–59
9. Cheng L, Qi N, Tian L, Yang W () Joint planning of generalized energy storage resources and distributed power supply considering operation control strategy. Autom Electr Power Syst (AEPS):1–10 [2019-04-30].http://kns.cnki.net/kcms/detail/32.1180.TP.20190403.1547.018.html
10. Mao M, Liu Y, Zhang L et al (2019) Optimal configuration of generalized energy storage in distribution network with high-penetration renewable energy. Autom Electr Power Syst 43 (8):77–85. https://doi.org/10.7500/aeps20180615002
11. Xiao H, Pei W, Yang Y et al (2015) Energy storage capacity optimization for microgrid considering battery life and economic operation. High Voltage Eng 41(10):3256–3265
12. Internal Rate of Return (IRR). https://baike.baidu.com/item/%E5%86%85%E9%83%A8%E6%94%B6%E7%9B%8A%E7%8E%87/2016027?fr=aladdin. Last accessed 11 Apr 2019
13. Tang J, Wang D, Jia H et al (2018) Optimal economic operation of active distribution networks based on hybrid algorithm of surrogate model and particle swarm optimization. Autom Electr Power Syst 42(4):95–103. https://doi.org/10.7500/aeps20170630006
14. Bao Z, Yu J (2016) Intelligent optimization algorithm and its MATLAB example. Electronic Industry Press
15. Shi YH, Eberhart RC (1998) A modified particle swarm optimizer. In: The 1998 IEEE international conference on evolutionary computation proceedings, IEEE world congress on computational intelligence
16. Higashi N, Iba H (2003) Particle swarm optimization with Gaussian mutation. IEEE swarm intelligence symposium, 2003, Indianapolis, Indiana, USA, pp 72–79

Coordination Control Method and Realization of Micro Grid Synchronized Connection

Kuo Tan, Hai Wu, Guo Hu and Peng Jin

Abstract In recent years, with the large number of renewable energy connected, the problems about intermittence and volatility of renewable energy grid-connected have gradually emerged. Micro grid has flexible and controllable characteristics, that's the foundation for solving the grid-connected problem of distributed generation, also that's the inevitable choice to solve the problem that the high proportion of renewable energy connected to the grid. Compared with substations, the requirement for synchronized connection of micro grids has changed greatly. This paper introduces coordination control method of synchronized connection for micro grids and application. It fully considers the characteristics of multi-operation modes and load power fluctuation of micro grids, based on GOOSE (Generic Object Oriented Substation Event) transmission mechanism, it realizes real-time adjustment of voltage and mode switching through controlling energy storage devices. it meets the application requirements of micro grid grid-connected, it also realizes smooth connection of micro grid. The control device based on this method has been successfully applied in the demonstration a national 863 project of Luxi Island Micro grid.

Keywords Micro grid · Smooth connection · Synchronized voltage adjustment · Coordinated control device · GOOSE

K. Tan (✉) · H. Wu · G. Hu · P. Jin
NARI Technology Co., Ltd, 211000 Nanjing, China
e-mail: tankuo@sgepri.sgcc.com.cn

NARI Group Corporation (State Grid Electric Power Research Institute), 211000 Nanjing, China

State Key Laboratory of Smart Grid Protection and Control, 211000 Nanjing, China

Y. Xue et al. (eds.), *Proceedings of PURPLE MOUNTAIN FORUM 2019-International Forum on Smart Grid Protection and Control*, Lecture Notes in Electrical Engineering 585, https://doi.org/10.1007/978-981-13-9783-7_13

1 Introduction

In recent years, with the increasing tension of conventional energy supply, environmental and energy issues have attracted great attention. Therefore, distributed generation technology with low investment and low energy consumption has been widely used in the world. In order to maximize the advantages of distributed generation technology in economy, energy and environment, many countries have incorporated construction of micro grid into the future power grid development agenda [1–6]. In order to achieve smooth grid connection of micro grid and reduce the impact of grid connection, how to realizing the coordinated control technology of synchronization grid-connected has become a new problem in micro grid. At present, the synchronization connection of micro grid is usually achieved by the power electronic equipment adjusting and controlling the amplitude, frequency and phase angle directly [7–9]. In time sequence, it is generally used to adjust the frequency into the allowable range, and then to adjust the phase angle [10, 11]. However, this kind of method is complex and involves many links, and the different frequency difference also has impact on the phase adjustment, it causes the poor effect of synchronization grid-connected of coordinated control through power electronic equipment directly [12]. In addition, the unbalanced load of micro grid leads to three-phase unbalance and other power quality problems. Therefore, simply judging the voltage synchronization on both sides of the grid-connected switch without considering the power quality will result in excessive shock and other problems, which can not meet the grid-connected requirement of micro grid [13, 14].

This paper introduces a synchronized grid-connected method of coordinated control for micro grid. Through pattern recognition and matching technology, it solves the problems of grid-connected coordinated control caused by the diversification of operation status of micro grid; through on-line monitoring and prediction technology of power quality, it solves the problem of excessive grid-connected shock impact caused by unbalanced characteristics of micro grid through coordinated control device. The coordinated control of the energy storage device realizes the real-time voltage adjustment on the side of the micro grid. The device can predict the closing point, it solves the problems of complex control caused by frequency and phase adjustment through power electronic equipment directly.

In the process of grid-connected coordinated control in micro grid, it requires the real-time communication between coordinated control device and energy storage device. With the popularization and application of IEC 61850 standard in the field of distribution automation, it will be an inevitable trend for micro grid communication to output synchronized adjustment information through the general object-oriented substation event (GOOSE) data model [15–18]. Based on GOOSE communication mechanism, the synchronized grid-connected coordinated control method of micro grid takes the coordinated control device as auxiliary regulating device, monitors and judges the voltage and power quality on both sides of the

grid-connected point, and controls the energy storage device in real time through GOOSE communication. Finally, it achieves the ideal grid-connected effect and realizes smooth grid-connected.

2 Micro Grid System Structure

Micro grid is generally composed of micro-power (photovoltaic generator, windmill generator, etc.), energy storage system (battery, super capacitor, etc.), load and coordinated control device [19]. In this paper, The synchronized grid-connected function of the micro grid is completed by the coordinated control device in the micro grid. The typical Micro grid system structure is shown in Fig. 1.

The voltage on both sides of the grid-connected switch is connected and collected to the coordinated control device through PT. The device processes and calculates the sampling values to power quality prediction and logical judgment when grid-connected synchronization, and collects the positions of the grid-connected switches for operation pattern recognition and matching. When the device receives the grid-connected command and the mode matching is successful, it enters the judgment of grid-connected. If the grid-connected condition is satisfied synchronization, the grid-connected operation can be completed by outputting the closing pulse through the relay. When the condition of synchronization is not satisfied, the synchronization order or GOOSE adjustment signal should be blocked to the energy storage device for synchronization real-time adjustment according to different conditions and wait for re-judgement. If the synchronization is not successful within a limited time, the synchronization decision will be withdrawn after timeout.

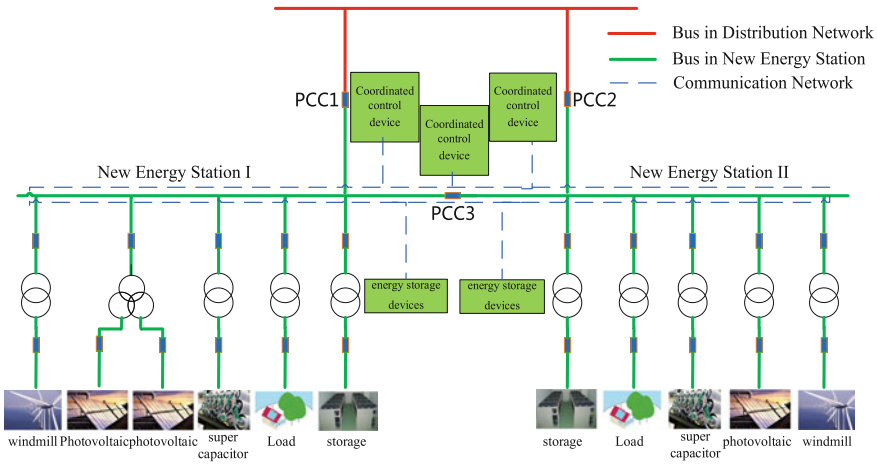

Fig. 1 The structure of micro grid

3 Realization of Synchronized Grid-Connected Coordinated Control Function in Micro Grid

Micro grid is different from substation. It has many characteristics, such as many power and electronic equipments, large harmonic pollution, unbalanced three-phase load, inconsistent transformers on both sides of grid-connected switch, long closing time of switch and diversified operation status, and so on. The requirement for synchronization becomes different too.

3.1 Implementation Scheme

This paper improves the existing synchronization grid-connected technology, realizes automatic amplitude, phase angle compensation, on-line monitoring and prediction of power quality, real-time voltage adjustment and synchronization closing point prediction. Through the above technologies, the micro grid is smoothly connected to the grid at the optimum angle, which minimizes the shock impact, prolongs the service life of the power equipment, and improves the power quality and stability of the grid. The synchronization process is shown in Fig. 2.

3.2 Identification and Matching of Operation Mode of Micro Grid

The micro grid can be divided into several operation states. Take Fig. 1 for instance, coordinated control device connects the status information of the current grid-connected switch and determine whether its operation state can be synchronized connection. Various operation modes of micro grid are shown in Table 1.

In order to ensure the reliability of mode matching, besides judging the current operation status of micro grid, adding have voltage and no current information as auxiliary criteria to ensure the safety and reliability of grid-connected process, the mode matching process is shown in Fig. 3.

3.3 Synchronized Measurement Value Calculation and Power Quality Judgment

After collecting the instantaneous values of three-phase voltage on both sides of the grid-connected switch, the fundamental and harmonic components of the voltage on both sides are calculated by fast Fourier transform (FFT). The fundamental component is used to calculate the amplitude, frequency and phase angle, and then to

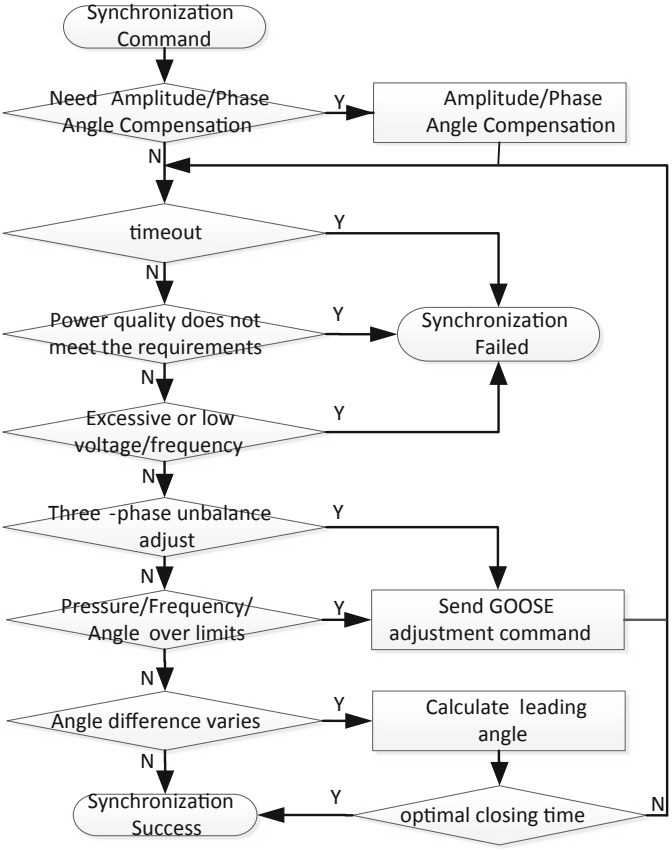

Fig. 2 Logical judgment process of synchronization

Table 1 Various operation modes of micro grid

Operation mode	PCC1	PCC2	PCC3	Matching results
Unconnected operation	Open	Open	Open	PCC1/PCC2 Matching success
Unconnected operation	Open	Open	Close	PCC1/PCC2 Matching success
Micro grid I connected operation	Open	Close	Open	PCC1 Matching success
Micro grid II connected operation	Close	Open	Open	PCC2 Matching success
Connected operation	Open	Close	Close	Matching failure
Connected operation	Close	Open	Close	Matching failure
Connected operation	Close	Close	Open	Matching failure

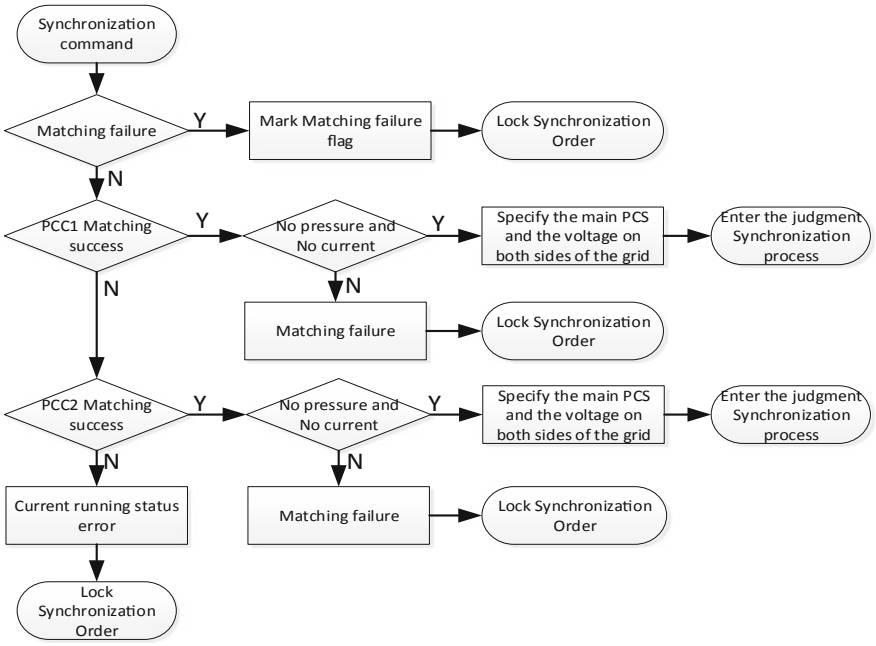

Fig. 3 Pattern recognition process

calculate the voltage difference, frequency difference, angle difference and frequency difference acceleration on both sides of the switch. The extracted harmonic component is used to judge the harmonic distortion rate at the grid-connected point, and the three-phase voltage is used to calculate power quality data, power quality data include the three-phase unbalance, voltage fluctuation and flicker. If the harmonic distortion rate or the three-phase unbalance is too high, or the power quality such as voltage fluctuation and flicker does not meet the requirements, the logic judgment process will not be entered. Real-time monitoring and prediction of power quality, it lays a foundation for subsequent logical judgement synchronization. It avoids the impact of three-phase unbalance and other power quality problems on grid-connected power system synchronization.

3.4 Prediction of Synchronized Closing

Compared with the large power grid, the voltage level of micro grid is lower and the closing time of switches at grid-connected points is longer. Therefore, when grid-connected synchronization, it is necessary to send a closing order before the

voltage angle difference between the two sides of the switch is 0° to ensure that the angle difference is 0° when the switch contacts, so that the shock current is the smallest at closing time.

The time from sending the closing signal to closing the main contact of the switch is the leading time T_L of the switch. The leading time mainly includes the action time of the outlet relay and the closing time of the switch. The leading angle can be calculated according to the leading time of closing and the frequency difference and acceleration of the voltage on both sides of the closing point.

$$\delta = \triangle\omega T_L + \frac{1}{2}\frac{\triangle\omega}{\triangle t}T_L^2$$

T_L is the leading time before closing.
$\triangle\omega$ is the angular velocity of frequency difference
$\frac{\triangle\omega}{\triangle t}$ is the angular acceleration of frequency difference

Considering the characteristics of micro grid, this paper adopts a multi-point smoothing method to calculate the frequency difference angular velocity and frequency difference angular acceleration.

The coordinated control device calculates N frequency differences angular velocity $\triangle\omega_i$ in 1 s, forming N point sequence $\triangle\omega = \left\{\triangle\omega_1, \triangle\omega_{2,}\ldots, \triangle\omega_M \ldots \triangle\omega_N\right\}$ smoothes M $\triangle\omega_i$ of them, M can be dynamically selected according to the daily load fluctuation rate of the project site. The formula for calculating the recommended value is as follows:

$$M = N * \text{Daily load volatility}$$

When the daily load fluctuation rate is high, M should choose a larger value to stabilize the fluctuation, on the contrary, when the daily load fluctuation rate is small, it does not need to be smooth.

calculates $\frac{\triangle\omega}{\triangle t}$ by Difference algorithm:

$$\frac{\triangle\omega}{\triangle t} = (\triangle\omega_N - \triangle\omega_M) * N/(N - M + 1)$$

Through the prediction of synchronized closing point, the problems of many intermediate links, complex control and mutual influence caused by direct frequency and phase control of power electronic equipment are solved, and the optimal angle closing and grid connection are realized.

3.5 Real-Time Regulation and Seamless Switching Technology of Synchronous Grid Connection Based on GOOSE Communication

In the process of synchronized grid-connection, when the voltage on both sides of the grid-connected switch does not meet the conditions of synchronized grid-connection, it is not necessary to block the grid-connected command directly, on the contrary, it should control the energy storage device to adjust the voltage in real time, and then judge the synchronization until the synchronized adjustment succeeds, fails or exceeds the time limitation.

In order to realize seamless switching of grid-connected in micro grid, the timeliness of communication between coordinated control device and energy storage device is particularly important. GOOSE (Generic Object Oriented Substation Event) is a mechanism used in IEC 61850 standard to meet the fast message requirement of power automation system. It has the advantages of fast, efficient, economical and reliable to realize information transmission based on GOOSE network transmission instead of traditional hard wiring. It is an effective means to meet the real-time adjustment of fast message requirement and realize seamless switching of grid connection. Verified by network analyzer, a GOOSE signal from sending to receiving via switch has a delay of less than 1 ms.

When the coordinated control device receives the grid-connected command and matches successfully, it enters the judgment process of synchronization judgement. When the synchronization conditions are not satisfied, the coordinated control device sends GOOSE signals such as power, unbalanced voltage, voltage regulation and frequency modulation to the energy storage device in real time. The energy storage device adjusts the real-time voltage according to the current situation on the side of the micro grid until the synchronization conditions are satisfied. The coordinated control device immediately outputs the closing pulse. It ensures voltage synchronization both sides of the system and reduces the impact of grid connection. At the same time, in order to avoid the "conflict" caused by the simultaneous supply of two voltage sources in the same system, the grid-connected coordinated control sends the P/Q prefabricated command to the energy storage device while issuing the closing pulse, and the energy storage device enters the ready state of mode switching. When the position of grid-connected switch is changed from sub-position to in- position, and then P/Q switching command is sent to the energy storage device. After receiving the command, the energy storage device can switch from U/F mode to P/Q mode in less than 1 ms. So far, the real-time voltage regulation during the same period has been completed, and the seamless switching of micro grid in the same period has been realized.

3.6 Establishment of GOOSE Model

The unbalanced voltage and other signals on the side of the micro grid are calculated by the coordinated control device and sent to the energy storage device through GOOSE transmission mechanism. Therefore, the corresponding information nodes need to be added to the IEC61850 model of the coordinated control device. In IEC 61850-7-4, the logical nodes of measurement (MMXU) and phase sequence unbalance node (MSQI) are defined. PhV and PV nodes under MMXU are used for data objects of phase voltage and line voltage respectively. ImbV and ImbPPV nodes under MSQI are used for data objects of unbalanced phase voltage and unbalanced line voltage respectively. The synchronization adjustment signal transmitted by GOOSE-based synchronization grid-connected adjustment technology described in this paper can be transmitted using the above-mentioned logical nodes.

3.7 Off-Grid Control Technology of Microgrid

The off-grid control technology of microgrid can be divided into active off-grid and passive off-grid. In active off-grid process, an off-grid command issued by the dispatching center or the micro grid control system, it separates the micro grid from the main grid and achieves island operation.The coordination control device sends the disconnection pulse command to the grid-connected switch after receiving the disconnection command, and sends GOOSE prefabricated command of U/F mode to energy storage devices at the same time. When it recognizes that the grid-connected switch has been successfully separated, it immediately sends the U/F mode switching command to realize active disconnection. In passive off-grid process, a fault occurs (bus, line, etc.) in micro grid. in order to protect the main grid from being affected, the micro grid needs to be disconnected from the main grid and remove the fault to achieve island operation. The coordination control device receives a fault isolation GOOSE signal and sends the disconnection pulse command to the grid-connected switch and sends GOOSE prefabricated command of U/F mode to energy storage devices at the same time. When it recognizes that the grid-connected switch has been successfully disconnected, it immediately sends the U/F mode switching command to realize passive disconnection.

It is worth noting that if the energy storage devices capacity is not enough to support the full load operation of the microgrid, the load power of the microgrid should be calculated or collected in real time. The load should classified different levels and the lower priority load should be cut off to realize uninterrupted power supply for important loads.

4 Application

The synchronized grid-connected method of coordinated control introduced in this paper, the coordinated control device has been successfully applied to the Luxi Island Micro grid Project in Zhejiang Province. The demonstration project of Luxi Island Micro grid belongs to National 863 Plan, the key technology research and development project of smart grid. This paper takes the test data of the project as the analysis data. The correctness of the scheme is verified by the gas parameter curve through the synchronized power generation during the grid-connected process. The system schematic diagram of Luxi Micro grid is shown in Fig. 4.

Before grid-connected, the micro grid is in off-grid operation, PCC1 and PCC2 switches are in open position, PCC3 switches are close position, and energy storage devices operates in U/F mode.

The coordinated control device identifies the current operation status of the micro grid, and calculates the corresponding synchronized electric value in real time, which are used for pattern recognition and synchronized logical judgment of the synchronized grid-connected station respectively. After receiving the grid-connected command, the device judges the power quality and synchronization logic, and sends the command to the energy storage device to complete the real-time voltage adjustment and mode switching, finally realizes the smooth grid-connected of the micro grid.

The voltage adjustment curve during the synchronization is shown in Fig. 5.

It can be seen from Figs. 5 and 6 that after 12 ms of GOOSE signal is sent out, the energy storage device will start voltage adjustment. The whole voltage adjustment process is 48 MS and the whole grid-connected process time is 81 ms, which meets the real-time requirements of the grid-connected process synchronization.

The change curve of phase difference between two sides of the switch and the prediction of the closing point of the switch are shown in Fig. 7. The variation curve of current during the grid-connected period is shown in Fig. 8.

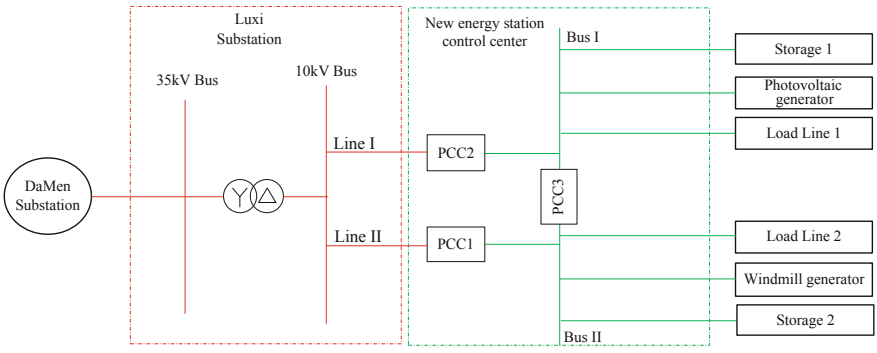

Fig. 4 Luxi island' micro grid system

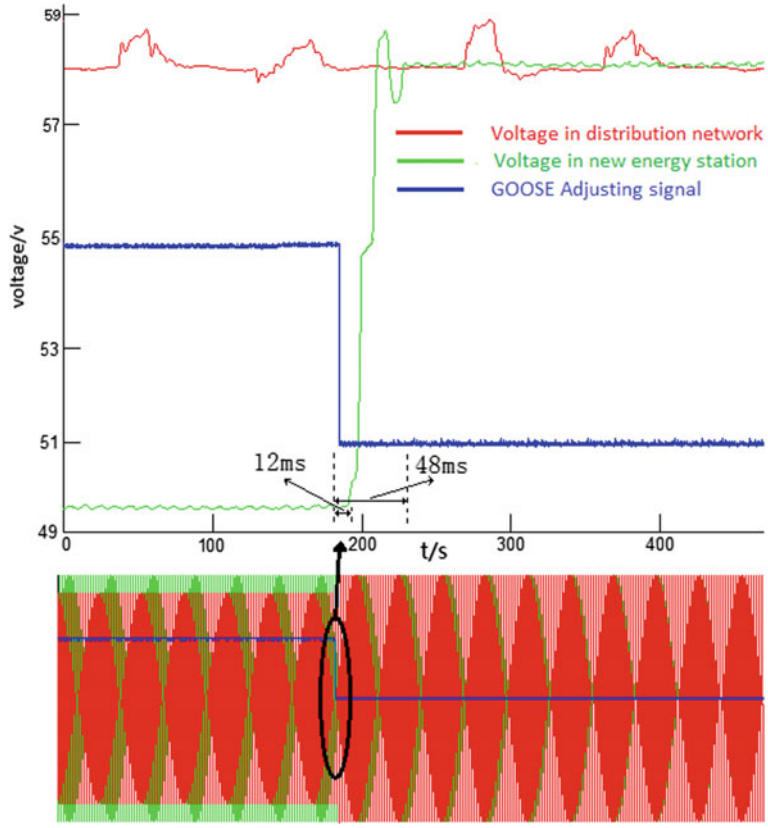

Fig. 5 Change curve of voltage adjustment

From the grid-connected curve, it can be seen that the whole process of grid-connected is smooth. As shown in Fig. 7, the coordinated control device sends out the closing pulse before the voltage angle difference between the two sides of the switch is 0°, it ensures that the phase difference between the contacts of the switch is 0°, it achieves accurate synchronization prediction and ensures the optimal angle closing. As shown in Fig. 8, the grid-connected switch has no impulse current during the process of grid-connected, which achieves the effect of smooth grid-connected of micro grid.

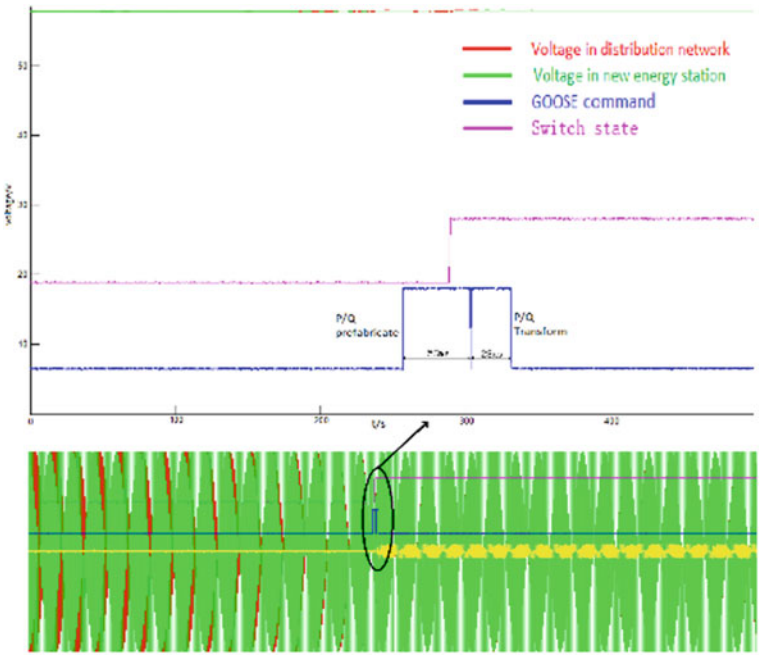

Fig. 6 Process curve of mode switching

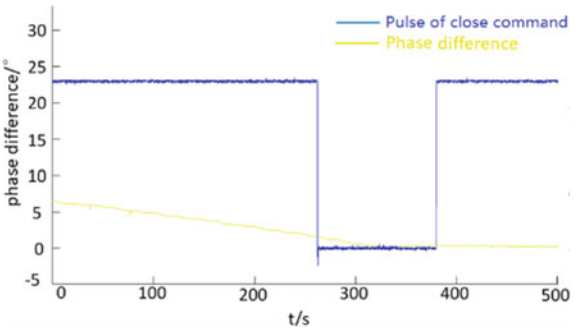

Fig. 7 Change curve of phase difference

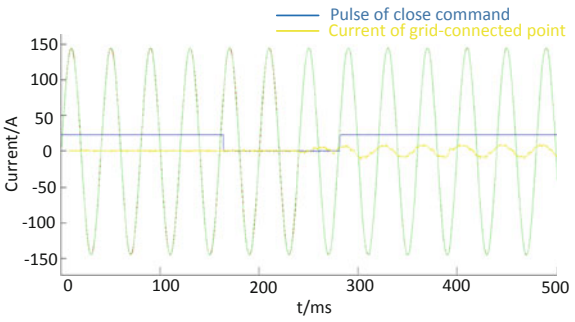

Fig. 8 Change curve of grid-connected current

5 Epilogue

This paper introduces a coordinated control method for synchronized grid connection in micro grid. This method fully considers the various operation states of micro grid, the power quality problems such as more operation state and electronic equipment characteristic, three-phase unbalance, and the long closing time of grid-connected switches. The calculation of synchronized amplitude, frequency and phase angle is realized by fast Fourier transform. Through real-time monitoring operation state self-identification, self-matching, and monitoring power quality, such as three-phase unbalance, based on GOOSE communication, predicting of closing synchronization points, This method solves the complex problems of grid-connected coordination and control and realizes smooth grid-connected in micro grids. This method has been implemented in the coordinated control device and applied in many domestic micro grid projects. After field operation verification, The grid-connected function fully meets the grid-connected requirements of micro grid synchronization.

References

1. Zhang J, Shi J, Zheng D et al (2018) Development and analysis of microgrid operation and control standards of international electrotechnical commission. Autom Electr Power Syst 42 (24):1–10
2. Mao M, Ding Y, Wang Y et al (2017) Microgrid-an "organic cell" for future energy interconnection system. Autom Electr Power Syst 41(19):1–11
3. National Development and Reform Commission, National Energy Administration. Proposed regulation for promoting the development of grid connected microgrid[EB/OL].[2017-07-24]
4. Tao W, Li J, Ding M et al (2016) Development and comparison on standard for interconnecting distributed resources with electric power systems. J Electri Eng 11(4):1–8
5. Li P, Lian P, Chen A et al (2018) Decentralized coordinated control method of multiple bidirectional converters in AC/DC hybrid microgrid. Autom Electr Power Syst 42(22): 151–158
6. Zhang L, Hou M, Zhu G et al (2019) Seamless transfer strategy of operation mode for microgrid based on collaborative control of voltage and current. Autom Electr Power Syst 43 (5):129–135
7. Gao Y, Ai Q (2018) Distributed hierarchical coordinated control of active distribution network with multiple microgrids based on sparse communication optimization. Autom Electr Power Syst 42(4):135–141
8. Bian X, Jiang Y, Zhao Y et al (2018) Coordinated frequency regulation strategy of wind, diesel and load for microgrid with high-penetration renewable energy. Autom Electric Power Syst 42(15):102–109
9. Wang D, Zhang X, Liu Q et al (2018) Ensemble learning for generation-consumption coordinated frequency control in an islanded microgrid. Autom Electr Power Syst 42(10): 46–52
10. Hou L, Xu Lin, Wei Y et al (2018) Passive network optimization design for seamless switching of controllable switches in microgrid. Autom Electr Power Syst 42(7):171–177

11. Yu M, Tang F, Wu X et al (2018) Coordinated power control of virtual combined three-phase converter in single-phase/three-phase hybrid microgrid. Autom Electr Power Syst 42(7): 192–198
12. Liu Y, Chen J, Hou X et al (2018) Dynamic frequency stability control strategy of microgrid based on adaptive virtual inertia. Autom Electr Power Syst 42(9):75–82
13. CHEN Anwei (2018) Coordination control and mode switching strategy for hybrid AC/DC microgrid with multi-bus structure. Autom Electr Power Syst 42(17):175–183
14. Jia K, Lin Y, Chen Y et al (2018) Energy management method for microgrid based on real-time corrected double-loop control of energy storage. Autom Electr Power Syst 42 (14):131–138
15. Fan K, Xu B, Chen Y et al (2016) GOOSE over UDP transmission mode for real-time data of distributed control applications in distribution networks. Autom Electr Power Syst 40(4): 115–120
16. Zhang S, Zhu Y, Tang C et al (2015) Fault location and isolation of microgrid based on GOOSE communication. Autom Electr Power Syst 39(12):179–183
17. Wang Z, Wang G, Tong J et al (2017) Efficient integrity authentication method for GOOSE packet. Autom Electr Power Syst 41(2):173–177
18. Yao C, Huang G, Zhong Y, Chen L (2012) A realization scheme of substation area control system based on GOOSE message in station level. Autom Electr Power Syst 36(18):159–160
19. Chen Y, Yang P, Zeng Z et al (2019) Planning of distributed energy resources for distribution network considering dispatchable region of microgrids. Autom Electr Power Syst 43(3): 83–91

The Optimal Configuration of AC/DC Hybrid Microgrid with Mobile Energy Storage Considering Seasonal DC Load

Mufan Wang, Ruoxuan Sun, Yuchao Luo, Jianlong Sun, Liang Cheng and Zaijun Wu

Abstract In order to solve the problem that the seasonal DC load causing the energy's idle in other seasons and the inability of the power exchanging from DC to AC side during the abnormal operation of AC/DC Hybrid microgrid (MG), this paper first proposes a mobile energy storage (MES)'s transfer strategy and then establishes a two-layer optimal configuration model of AC/DC hybrid MG considering seasonal DC load and the MES's transfer strategy, which takes the minimum cost of MG's life cycle as the outer level objective function and the minimum average daily rental amount of MES as the inner level objective. The results of configuration of WT, ES, inverter and MES are compared, and the charge and discharge power characteristics of ES and MES during normal or abnormal operation are analysed in case study, which verifies that both the MES and MES's transfer strategy improve the economy of MG considering seasonal DC load.

Keywords AC/DC hybrid microgrid · Seasonal DC load · Mobile energy storage · Transfer strategy · Bi-level configuration optimization

State Grid corporation Science and Technology Project "Modular Design and Empirical Re-search on Distribution Network of High Reliability Power Supply Area" (5210K017000B).

M. Wang (✉) · R. Sun · Z. Wu
Southeast University, Nanjing, China
e-mail: jennifer1995624@vip.qq.com

Y. Luo · J. Sun
Research Institute of Economics and Technology of State Grid Jiangsu Power Company, Nanjing, China

L. Cheng
State Grid Jiangsu Electric Power Co. Ltd, Nanjing, China

Y. Xue et al. (eds.), *Proceedings of PURPLE MOUNTAIN FORUM 2019-International Forum on Smart Grid Protection and Control*, Lecture Notes in Electrical Engineering 585, https://doi.org/10.1007/978-981-13-9783-7_14

1 Introduction

MG is a small power system that integrates distributed sources, energy storage (ES), inverters, control and protection devices [1]. Local power balance and energy optimization can be realized in MG, and there are two modes of operation: grid-connected and islanded operation [2]. In the energy Internet environment, the demand for ES is increasing [3]. In reference [4], the rigid capacity of ES was configured for ensuring reliable power supply of important load for 30 min in the absence of solar radiation. Literature [5] established a model based on the continuous power supply time of important load under MG islanded operations with electric vehicles (EV). However, the existing research is simply based on AC-MG's planning when switching to off-grid operation. AC and DC busbars exist in the AC/DC hybrid MG, which directly reduces the cost of AC/DC converters [6, 7]. With the research on the topology, control mode and scheduling of AC/DC hybrid MG [8–11] whose planning has gradually become a new direction for future research, which should consider the abnormal operation of AC/DC side to side disconnection.

Reference [12] clearly compared the characteristics of different types of MGs, but cannot propose a specific AC/DC hybrid MG planning model. In reference [13], a multi-objective optimal configuration model of grid-connected AC/DC hybrid MG considering economic cost, converter loss and self-equilibrium ratio was established. Literature [14] used Monte Carlo method to simulate the running state of the MG equipment to further improve the optimal configuration model of AC/DC hybrid MG. In literature [15], it concluded that the orderly charging strategy of EV can reduce the expansion cost from AC-MG to AC/DC hybrid MG. However, the existing research doesn't consider seasonal DC load like charging pile load for EVs which can be removed after the winter games, causing the energy's idle in other seasons.

In order to improve the situation, this paper chooses MES, which is completely controlled by the purchaser company with the characteristics of strong environmental adaptability, easy installation and high scalability [16], to rent on DC side for seasonal DC load's power supply instead of ES and distributed sources, and then proposes a MES's transfer strategy in abnormal operation of MG to realize the energy exchanging from AC to DC side to establish a two-layer optimal configuration model of AC/DC hybrid MG with MES considering seasonal DC load. The results of configuration of WT, ES, inverter and MES are compared, and charge and discharge characteristics of ES and MES during normal/abnormal operation are analysed in the case study, which verifies that the MES and MES's transfer strategy improve the economy of MG considering seasonal DC load.

2 The Transfer Strategy of MES Based on the Structure of AC/DC Hybrid MG

2.1 The Structure of AC/DC Hybrid MG in Normal Operation

Aiming to achieve the autonomy of MG proposed by the National Energy Administration of China, this paper proposed two abnormal operation cases of AC/DC hybrid MG to ensure reliable power supply for no less than 2 h.

Case 1: The faulty of the PCC point causes the MG's operating mode switching from the grid-connected to the off-grid state.
Case 2: The faulty of the flexible substation causes AC/DC side to side disconnection, resulting in the DC and AC sub-grid both in the off-grid state.

Obviously, when the Case 2 have the ability to realize the 2 h' power supply for important load, Case 1 can also satisfy the autonomy of the MG.

Based on the topology and control mode of AC/DC Hybrid MG proposed in literature [17–20], a topology structure with flexible substation taking Case 2 as abnormal operation is proposed in Fig. 1. WT are configurated on AC side while ES and MES are on DC side considering the inverters' cost. In the abnormal operation, the unimportant load is cut off and MES units are transferred between DC and AC side.

2.2 The Transfer Strategy of MES in Abnormal Operation

Under normal operating conditions, all MES units are connected on DC side for seasonal DC load supply. In the condition of abnormal operation, the 2 h after the

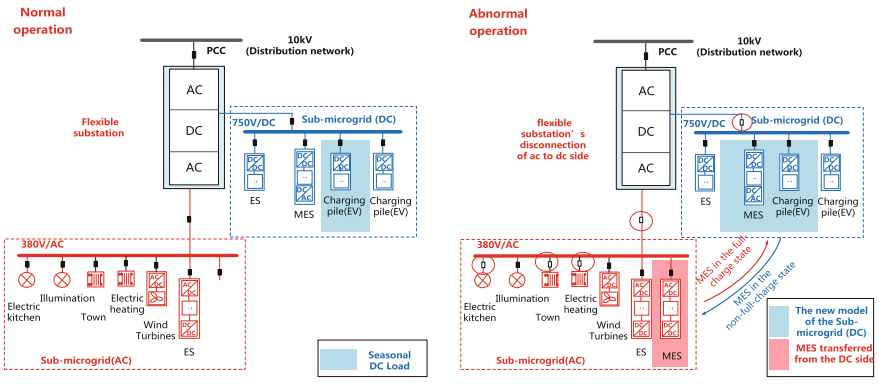

Fig. 1 The AC/DC hybrid MG structure in normal/abnormal operation

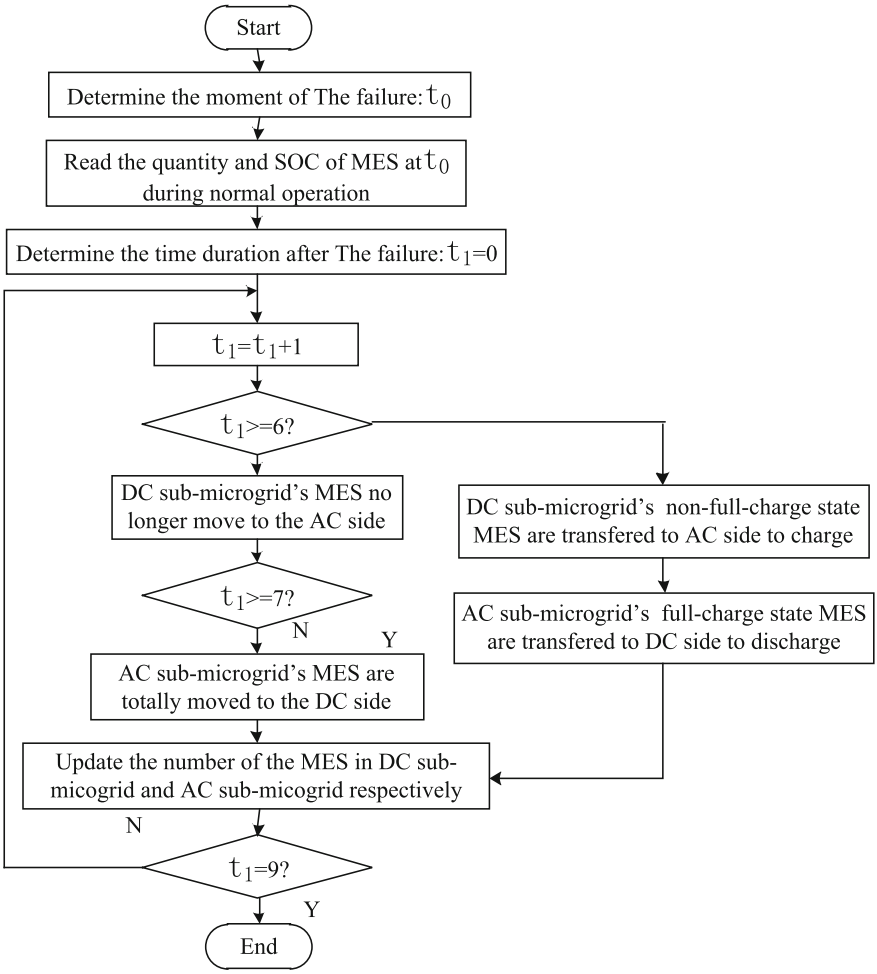

Fig. 2 The flow chart of the MES's transfer strategy

fault occurrence time (t_0) is divided into 8 time segments (t_1), and the duration of each time segment T is 0.25 h. Due to the close construction distance between the AC and DC sub-MG, the transfer time of the MES is less than 0.25 h. During each time period, the MES in the non-full-charge state on DC side is transferred to the AC side to charge, while the MES in the full-charge state on the AC side is transferred to the DC side to discharge. The MES of the AC sub-MG is totally transferred back to the DC sub-MG after the 6th time segment, while the MES on DC side is no longer transfer to AC side after the 7th time segment. The flow chart of the MES's transfer strategy is shown in Fig. 2.

3 The Two-Layer Optimal Configuration Model of AC/DC Hybrid MG with MES Considering Seasonal DC Load

3.1 The Outer Optimization Configuration Model

The overall configuration model could be expressed as:

$$\begin{cases} obj: \min F = \min(C_{aic} + C_{aom} + C_{MES\_rent}) \\ s.t.: \text{Normal operation constraints} \\ \text{Abnormal operation constraints} \end{cases} \quad m = \{m_1, m_2, m_3, m_4\} = \{1, 2, 3, 4\} \tag{1}$$

where C_{aic} and C_{aom} are the initial investment and the operation and maintenance costs for ES, WT, and ES's converters respectively. C_{MES_rent} is the rental cost for MES. m represents the typical days of a year, and m_1, m_2, m_3, and m_4 represent four typical days of spring, summer, autumn, and winter, respectively.

The objective of the outer optimization configuration model. Due to the short planning period, the system's full life cycle cost only needs to consider the initial investment cost, operation and maintenance cost and the rental cost of MES, which are composed of the following parts.

$$C_{aic} = c_{WT\_p} P_{WT}^{\max} + c_{IV\_p} P_{IV}^{\max} + c_{BS\_e} \sum_{p=1}^{2} E_{BS}^{\max}(p) + c_{BS\_p} \sum_{p=1}^{2} P_{BS}^{\max}(p) \tag{2}$$

$$C_{aom} = \sum_{t=1}^{Y} \left(c_{WT\_op} P_{WT}^{\max} + c_{IV\_op} P_{IV}^{\max} + \sum_{p=1}^{2} c_{ES\_op} P_{ES}^{\max}(p) \right) \left(\frac{1+i_r}{1+d_r} \right)^t \tag{3}$$

where $P_{WT}^{\max}, P_{IV}^{\max}$ indicate the rated capacity of the WT and the ES's converter, respectively. $E_{ES}^{\max} P_{ES}^{\max}$ indicate the rated capacity and rated charge/discharge power of the ES, respectively. p represents the type of ES configurated on DC (p_1) or the AC (p_2) side respectively. c_{WT_p}, c_{IV_p}, c_{ES_e}, c_{ES_p} and c_{ES_op}, c_{WT_op}, c_{IV_op} indicate the investment and the annual operation cost of WT's, converter's and ES's unit charge/discharge power and the cost of ES's unit capacity power, respectively. Y is the year of the project's life. i_r is the inflation rate and d_r is the discount rate.

$$C_{MES\_rent} = YDC_{MES}N_{MES} \tag{4}$$

where D, C_{Mes} and N_{MES} are the MES's rental days per year, daily rental cost and the daily rental quantity, respectively.

The Constraints of the Outer Optimization Configuration Model. The normal operation constraint can be expressed as:

(1) *The System Side's Constraints*

The DC sub-MG's power balance constraint can be expressed as:

$$\begin{aligned} P_{Load\_S\_DC}(m,t)+P_{Load\_US\_DC}(m,t)+P_{DCtransAC}(m,t)+P_{BS\_C}(m,t,p_1) \\ +P_{MBS\_C\_DC}(m,t)=\eta_{ACtransDC}P_{ACtransDC}(m,t) \\ +P_{BS\_D}(m,t,p_1)+P_{MBS\_D\_DC}(m,t) \end{aligned} \tag{5}$$

where $P_{load\_S\_DC}$ and $P_{load\_US\_DC}$ are the seasonal and unseasonal DC load respectively. P_{ES_C}, P_{ES_D} and $P_{MES\_C\_DC}$, $P_{MES\_D\_DC}$ are the charge/discharge power for ES and MES in normal operation, respectively. $\eta_{ACtransDC}$ and $P_{ACtransDC}$ are the efficiency and power transmitted from the DC to AC side, respectively. $P_{DCtransAC}$ is the power transmitted from the AC to DC side.

The AC sub-MG's power balance constraint can be expressed as:

$$\begin{aligned} P_{Load\_AC}(m,t)+P_{ACtransDC}(m,t)+P_{BS\_C}(m,t,p_2)+P_{ACtogrid}(m,t) \\ =P_{WT}(m,t)+\eta_{DCtransAC}P_{DCtransAC}(m,t) \\ +P_{BS\_D}(m,t,p_2)+P_{gridtoAC}(m,t) \end{aligned} \tag{6}$$

where P_{load_AC} is the AC load. P_{WT} is the power output of WT. $\eta_{DCtransAC}$ is the efficiency for transmission from the AC to DC side. $P_{ACtogrid}$ and $P_{gridtoAC}$ are the incoming and outgoing power between the distribution network and MG.

The On-grid constraint can be expressed as:

$$0\le\eta_{ACtransAC}P_{GridtoAC}(m,t),\eta_{ACtransAC}P_{ACtoGrid}(m,t)\le P_{trans}^{\max} \tag{7}$$

where $\eta_{ACtransAC}$ is the transmission efficiency from the AC to AC side. $P_{trans}^{\max}$ is the maximum transfer power for the grid-connected converter.

The MG's self-balancing rate constraint can be expressed as:

$$1-\frac{\sum P_{GridtoAC}(m,t)}{\sum P_{Load\_AC}(m,t)+\sum P_{Load\_DC}(m,t)+\sum P_{Load\_DC\_add}(m,t)}\ge R_{self\_set} \tag{8}$$

where R_{self_set} is the setting value of the system's self-balancing rate.

(2) *The Renewable Energy Side's Constraint*

$$0\le P_{WT}(m,t)\le P_{WT}^{\max} \tag{9}$$

where $P_{WT}^{\max}$ is the rated output power of the WT.

(3) *The ES and MES Side's Constraint*

The charge and discharge power constraints of ES and MES can be expressed as:

$$\begin{cases} 0 \le P_{ES\_C}(m,t,p), P_{ES\_D}(m,t,p) \le p_{ES}^{\max}(p) \\ 0 \le P_{MES\_C\_DC}(m,t), P_{MES\_D\_DC}(m,t) \le N_{MES} p_{MBS\_DC}^{\max} \end{cases} \tag{10}$$

where $P_{ES}^{\max}$ is the rated charge and discharge power of ES, $P_{MES\_DC}^{\max}$ is rated charge and discharge power of a single MES unit.

The state of charge constraint of ES and MES in the normal operation can be expressed as:

$$\begin{cases} SOC_{ES}^{\min} E_{ES}^{\max}(p) \le W_{ES}(m,t,p) \le SOC_{ES}^{\max} E_{ES}^{\max}(p) \\ W_{ES}(m,t+T,p) = W_{ES}(m,t,p) + T\eta_{inv} P_{ES\_C}(m,t,p) - T\frac{P_{ES\_D}(m,t,p)}{\eta_{inv}} \\ SOC_{MES}^{\min} N_{MES} E_{MES} \le W_{MES\_DC}(m,t) \le SOC_{MES}^{\max} N_{MES} E_{MES} \\ W_{MES\_DC}(m,t+T) = W_{MES\_DC}(m,t) + T\eta_{inv} P_{MES\_C\_DC}(m,t) - T\frac{P_{MES\_D\_DC}(m,t)}{\eta_{inv}} \end{cases} \tag{11}$$

where $SOC_{ES}^{\min}$, $SOC_{MES}^{\min}$, $SOC_{ES}^{\max}$ and $SOC_{MES}^{\max}$ are the minimum and maximum state of charge of the ES and MES. W_{ES} and W_{MES_DC} is the ES's and MES's stored energy. ηinv is the charge and discharge efficiency of the ES and MES. E_{MES} is the rated capacity of a single MES unit.

In order to ensure the sustainability of ES and MES's charging and discharging during the whole life cycle, the ES and MES's energy conservation constraint is established as follows,

$$\begin{cases} W_{ES}(m,0,p) = W_{ES}(m,96,p) \\ W_{MES\_DC}(m,0) = W_{MES\_DC}(m,96) \end{cases} \tag{12}$$

Using the total discharging energy method from reference [18], the ES's lifetime loss constraint is established as follows,

$$\frac{365Y}{4} \sum_{m=1}^{4} \sum_{t=T}^{96T} (\eta_{inv} T P_{ES\_C}(m,t,p) + \frac{T P_{ES\_D}(m,t,p)}{\eta_{inv}} \le 2N(SOC_{ES}^{\max} - SOC_{ES}^{\min}) E_{ES}^{\max}(p) \tag{13}$$

where N is the number of cycles of ES and 2 N is the total number of charging and discharging of ES. The left side of the equation is the actual discharging energy of ES during the whole life cycle, while the right side of the equation is the maximum discharging energy of the ES during the whole life cycle.

(4) *The Converter Side's Constraint*

The flexible substation's converting power constraint is:

$$0 \le P_{DCtransAC}(m,t), P_{ACtransDC}(m,t) \le P_{trans}^{\max} \tag{14}$$

The ES's converting power constraint is:

$$0 \le P_{ES\_C}(m,t,p_2), P_{ES\_D}(m,t,p_2) \le P_{IV}^{\max} \tag{15}$$

In order to ensure the important load in islanded AC and DC sub-MG can be reliably powered for 2 h. The abnormal operation constraint can be expressed as:

(1) *The DC sub-MG's islanded reliable operation constraint*

$$\begin{aligned} P_{Load\_DC\_main}(m_4,t_0) \le{}& P_{ES\_D\_abn}(m,t_0,t_1,p_1) \\ &- P_{ES\_C\_abn}(m,t_0,t_1,p_1) + P_{MES\_D\_abn}(m,t_0,t_1,p_1) \end{aligned} \tag{16}$$

where $P_{Load\_DC\_main}$ is the main load in the DC sub-MG. $P_{BS\_C\_abn}$, $P_{ES\_D\_abn}$ and $P_{MES\_C\_abn}$, $P_{MES\_D\_abn}$ are the ES and MES's charge and discharge power in the MG's abnormal operation. t_0 is the fault occurrence time and t_1 are the 8 time period of the 2 h after t_0.

(2) *The AC sub-MG's islanded reliable operation constraint*

$$\begin{aligned} P_{Load\_AC\_main}(m_4,t_0) \le{}& P_{WT}(m,t_0) + P_{ES\_D\_abn}(m,t_0,t_1,p_2) \\ &- P_{ES\_C\_abn}(m,t_0,t_1,p_2) - P_{MES\_C\_abn}(m,t_0,t_1,p_2) \end{aligned} \tag{17}$$

where $P_{Load\_AC\_main}$ is the main load of AC sub-MG.

(3) *The state of charge constraint of ES and MES in the abnormal operation*

$$\begin{cases} SOC_{ES}^{\min} E_{ES}^{\max}(p) \le W_{ES\_abn}(m,t_0,Tt_1,1) \le SOC_{ES}^{\max} E_{ES}^{\max}(p) \\ W_{ES\_abn}(m,t_0,Tt_1,p) = W_{ES\_abn}(m,t_0,Tt_1-T,p) + T\eta_{inv} P_{ES\_C\_abn}(m,t_0,t_1,p) - T\frac{P_{ES\_D\_abn}(m,t_0,t_1,p)}{\eta_{inv}} \\ SOC_{MES}^{\min} N_{MES\_abn}(m,t_0,t_1,p) E_{MES} \le W_{MES\_abn}(m,t_0,Tt_1,p) \le SOC_{MES}^{\max} N_{MES\_abn}(m,t_0,t_1,p) E_{MES} \\ W_{MES\_abn}(m,t_0,Tt_1,p_1) = W_{MES\_re}(m,t_0,Tt_1-T,p_1) - T\frac{P_{MES\_D\_abn}(m,t_0,t_1,p_1)}{\eta_{inv}} \\ W_{MES\_abn}(m,t_0,Tt_1,p_2) = W_{MES\_re}(m,t_0,Tt_1-T,p_2) + T\eta_{inv} P_{MES\_C\_abn}(m,t_0,t_1,p_2) \\ W_{MES\_abn}(m,t_0,0,p_1) = W_{MES\_DC}(m,t_0), \quad W_{MES\_abn}(m,t_0,0,p_2) = 0 \end{cases} \tag{18}$$

where $(Tt_1 - T) \cup Tt_1 = [0,7T] \cup [T,8T] = [0,8T]$ is the discrete time within 2 h after the fault. W_{ES_abn} and W_{MES_abn} is the ES's and MES's stored energy in abnormal operation. The initial stored energy of MES in abnormal operation is equal to the stored energy of MES in the time of t_0 in normal operation. The initial value is 0 for the reason that there is no MES on AC side in normal operation. W_{MES_re} is the residual energy of MES and N_{MES_abn} is the quantity of MES on DC/AC sides, which can be expressed as follows.

$$W_{MES\_re}(m,t_0,Tt_1-T,p_2)=\begin{cases}0 & t_1=1,7,8\\ W_{MES\_abn}(m,t_0,Tt_1-T,p_2) & \\ -N_{MES\_ACtoDC}(m,t_0,t_1)E_{MES}SOC_{MES}^{\max} & \\ +W_{MES\_DCtoAC}(m,t_0,t_1-1) & 3\le t_1\le 6\end{cases} \tag{19}$$

$$W_{MES\_re}(m,t_0,Tt_1-T,p_1)=\begin{cases}N_{MES\_abn}(m,t_0,t_1,p_1)E_{MES}SOC_{MES}^{\max} & t_1=1\\ N_{MES\_abn}(m,t_0,t_1,p_1)E_{MES}SOC_{MES}^{\max} & \\ +\eta_{MEStrans}N_{MES\_ACtoDC}(m,t_0,t_1-1))E_{MES}SOC_{MES}^{\max} & 2\le t_1\le 6\\ W_{MES\_abn}(m,t_0,Tt_1-T,p_1) & \\ +\eta_{MEStrans}N_{MES\_ACtoDC}(m,t_0,t_1-1))E_{MES}SOC_{MES}^{\max} & 7\le t_1\le 8\end{cases} \tag{20}$$

$$N_{MES\_abn}(m,t_0,t_1,p_1)=\begin{cases}N_{MES\_SOC_{\max}}(m,t_0,Tt_1-T,p_1) & t_1=1\\ N_{MES\_SOC_{\max}}(m,t_0,Tt_1-T,p_1) & \\ +N_{MES\_ACtoDC}(m,t_0,t_1-1) & 2\le t_1\le 6\\ N_{MES\_DC}(m,t_0,t_1-1)+N_{MES\_ACtoDC}(m,t_0,t_1-1) & 7\le t_1\le 8\end{cases} \tag{21}$$

$$N_{MES\_abn}(m,t_0,t_1,p_2)=\begin{cases}0 & t_1=1,7,8\\ N_{MES\_abn}(m,t_0,t_1-1,p_2) & \\ -N_{MES\_ACtoDC}(m,t_0,t_1) & \\ +N_{MES\_DCtoAC}(m,t_0,t_1) & 2\le t_1\le 6\end{cases} \tag{22}$$

where W_{MES_DCtoAC} and N_{MES_DCtoAC} is the MES's energy and quantity transferred from ac to dc side. $N_{MES\_SOC_{\max}}$ is the amount of MES in the fully charged state of the DC or AC side.N_{MES_ACtoDC} is the quantity of MES transferred from the AC to DC side, which can be expressed as follows.

$$W_{MES\_DCtoAC}(m,t_0,t_1)=\eta_{MEStrans}(W_{MES\_abn}(m,t_0,Tt_1-T,p_1)-N_{MES\_abn}(m,t_0,t_1,p_1)E_{MES}SOC_{MES}^{\max}) \tag{23}$$

$$N_{MES\_SOC_{\max}}(m,t_0,Tt_1-T,p)=floor(W_{MES\_abn}(m,t_0,Tt_1-T,p)/(E_{MES}SOC_{MES}^{\max}) \quad 1\le t_1\le 8 \tag{24}$$

$$N_{MES\_ACtoDC}(m,t_0,t_1)=\begin{cases}0 & 1\le t_1\le 2,t_1=8\\ N_{MES\_SOC_{\max}}(m,t_0,t_1,p_2) & 3\le t_1\le 6\\ N_{MES}(m,t_0,t_1,p_2) & t_1=7\end{cases} \tag{25}$$

$$N_{MES\_DCtoAC}(m,t_0,t_1)=\begin{cases}0 & t_1=7,8\\ N_{MES}-N_{MES\_SOC_{\max}}(m,t_0,0,p_1) & t_1=1\\ N_{MES\_abn}(m,t_0,t_1-1,p_1) & \\ -N_{MES\_SOC_{\max}}(m,t_0,Tt_1-T,p_1) & 2\le t_1\le 6\end{cases} \tag{26}$$

Based on the MES's transfer strategy proposed in Sect. 2.2. In Formula (19) and Formula (22), the MES's residual energy/quantity on AC side is the sum of its current energy/quantity and the non-full charge state MES's energy/quantity transferred from DC sides in the previous time, minus the full charge state MES's energy/quantity transferred to DC sides. In Formula (20) and Formula (21),the MES's residual energy/quantity on DC side is the sum of current full charge state MES's energy/quantity on DC side and the full charge state MES's energy/quantity transferred from AC sides in the previous time. In Formula (19) and Formula (22), the MES's energy/quantity on AC side are both 0 after the 6th time segment. In Formula (20) and Formula (21), the MES's energy/quantity on DC side are no longer transfer to AC side after the 7th time segment.

3.2 The Inner Optimization Configuration Model

The objective function of the inner model is the minimum average daily rental quantity of the MES. The constraints include normal and abnormal operation constraints. The normal operating constraints include system side, ES and MES's side, and converter side constraints, while the abnormal operation constraints include the AC and DC sub-MG's islanded reliable operation constraint and ES and MES's side constraint. The overall configuration model can be expressed as:

$$\begin{cases} obj: \min f = \min(N_{MES}) \\ s.t.: \text{Normal operation constraints} \quad m = m_4 = 4 \\ \text{Fault operation constraints} \end{cases} \tag{27}$$

Other constraints are the same as the upper optimization configuration model expect for the ES's lifetime loss constraint which is established as follows.

$$365Y \sum_{t=T}^{96T} \left(\eta_{inv} TP_{ES\_C}(m,t,p) + \frac{TP_{ES\_D}(m,t,p)}{\eta_{inv}}\right) \leq 2N\left(SOC_{ES}^{\max} - SOC_{ES}^{\min}\right) E_{ES}^{\max}(p) \tag{28}$$

3.3 The Solving Process and Advantages of Bi-level Configuration Model

The solution process of this paper can be expressed as follows.

1) Read the basic data contains wind speed, unseasonal load curve, WT, ES, MES's technical parameters and seasonal DC load curve.

2) Initial the value of N_{MES} and seasonal DC load to 0.
3) Solve the outer optimization model and transfer the result to the inner layer.
4) Solve the inner optimization model and transfer the value of seasonal DC load and configuration result to the outer layer.
5) Repeat steps (3) through (4) until finding a solution with the lowest life cycle cost and the minimum daily average rental number of MES.

The Bi-level configuration model is more versatile for speeding up the solution of some expansion planning models in AC/DC hybrid MG whose ES and WT has been put into use for some time in further research. The solution process is that the ES and WT's value of configuration are substituted into the lower layer model to solve the rental number of MES in the case of not accurately considering the loss of energy storage life.

4 Case Study

4.1 Comparative Analysis of Three Optimized Configuration Methods

An actual project is planning to construct an AC/DC hybrid MG with WT, ES and MES. The length of the project is 10 years. $i_r = 0.02$, $d_r = 0.1$, $R_{self\_set} = 0.7$. The initial state of charge of ES and MES are both 0.5. The transfer energy loss is 10%. The basic input data of load, WT, ES and MES are shown in Appendix.

The configuration results of the two-layer optimization model adopted in this paper are shown in Table 1 and the total discharging energy results of ES can be seen in Table 2. Method 1 is an optimal configuration method for AC/DC hybrid MG with WT and ES without MES considering seasonal DC load. Method 2 and Method 3 are both the optimal configuration methods for AC/DC hybrid MG with WT, ES and MES considering seasonal DC load. The difference is that method 3 considers the transfer strategy of MES in the abnormal operation.

Comparing the Method 2 and 1, using MES to supply power for seasonal DC load resulting in decrease of cost and the increase of lifetime utilization of ES neglecting the slightly changes on the self-balancing. Comparing the Method 2 and 3, using the MES's transfer strategy in abnormal operation to achieve energy exchange from AC to DC side further reduce the cost neglecting the slightly changes on the self-balancing and the lifetime utilization of ES.

Table 1 The configuration results of the two-layer optimization model

Method	ES (AC)		ES (DC)		MES	WT	Inverter	Self-balancing rate	Cost (yuan)
	Rated capacity (kWh)	Rated power (kW)	Rated capacity (kWh)	Rated power (kW)	N_{MES}	Rated capacity (kW)	Rated capacity (kW)		
1	0	0	1467.1	700	0	2041.8	0	0.7384	2.6338×10^7
2	0	0	733.56	350	15	2078.8	0	0.7316	2.5371×10^7
3	0	0	733.56	350	11	2078.8	0	0.7332	2.4792×10^7

Table 2 The total discharging energy results of ES

Item	Method 1	Method 2	Method 3
The total discharging energy of ES (kWh)	6.9808×10^6	3.5211×10^6	3.2496×10^6
The maximum of total discharging energy of ES (kWh)	7.0421×10^6	3.5211×10^6	3.5211×10^6
The lifetime utilization of ES	99.1%	100%	92.3%

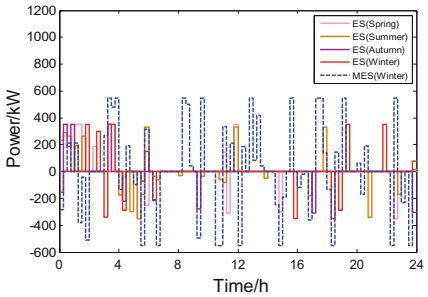

(1) The optimal charge/discharge power of ES and MES in normal operation

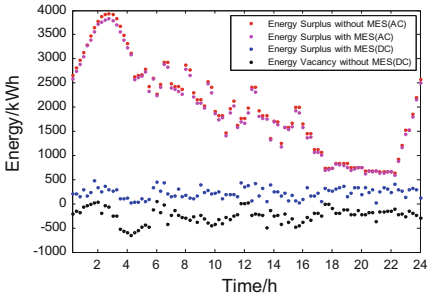

(2) Energy condition of DC and AC sub-MG at t_0 in normal operation

Fig. 3 The optimal charging/discharging power curve and energy in normal operation

4.2 *The Analysis of Charge and Discharge Characteristics of ES and MES During Normal Operation*

As can be seen from Fig. 3, in normal operation, the discharging energy of MES is larger than that of ES for not considering the life loss of MES, and there is an energy deficiency at time of t_0 in the DC sub-MG for the reason that the AC sub-MG has less important load and more excess wind energy.

4.3 *The Analysis of Charge and Discharge Characteristics of ES and MES During Abnormal Operation*

As can be seen from Fig. 3, MES's transfer strategy decreases the energy surplus on AC side and energy vacancy on DC side and the amount of MES during transmission in abnormal operation can be seen Fig. 4. The influence of MES's transfer strategy on charging/discharging power of ES are compared when $t_0 = 12$ h. As shown in Fig. 5, Comparing Method 2 and Method 3, the maximum charging/discharging power of MES is reduced, which affects the rated power of MES, thus reducing the cost of MES's supplier.

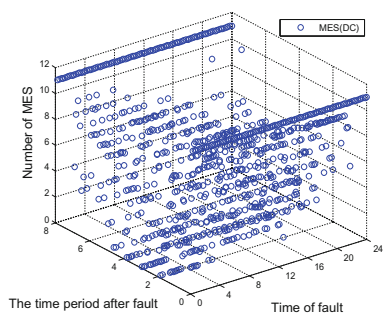

(1) The amount of MES on DC side

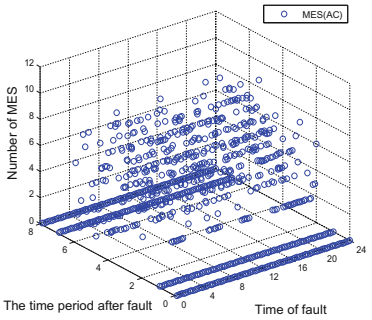

(2) The amount of MES in the AC side

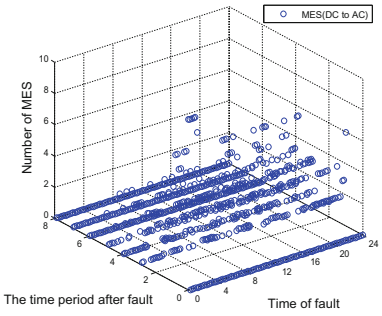

(3) The amount of MES in DC to AC process

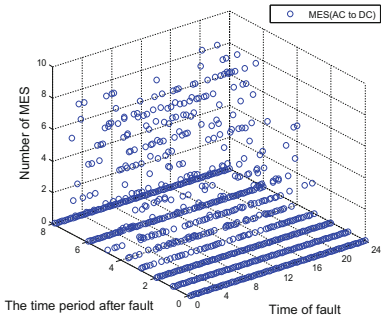

(4) The amount of MES in AC to DC process

Fig. 4 The amount of MES during transmission in abnormal operation

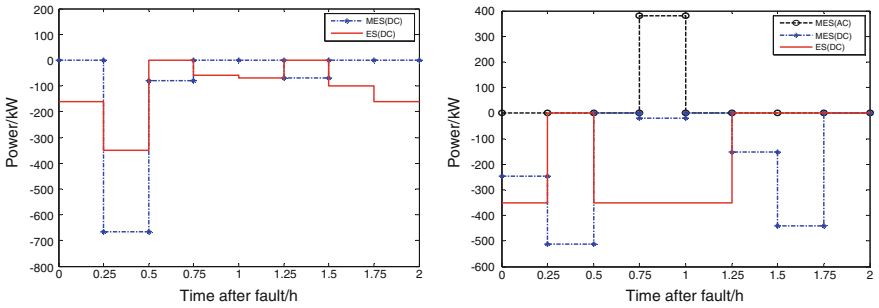

Fig. 5 Method 2 and 3's charging/discharging power curve of ES and MES

5 Conclusion

In this paper, a two-layer optimal configuration model of AC/DC hybrid MG considering seasonal DC load and MES's transfer strategy is established. The following conclusions are drawn from the analysis of the results of configuration.

(1) The MES supply the power for seasonal DC load to decrease the configuration results of WT and ESs and finally decrease the cost of microgrid.
(2) The transfer strategy of MES realizes the energy exchange from AC to DC side, further reducing the cost neglecting the slightly changes on the self-balancing and the lifetime utilization of ES.
(3) The transfer strategy of MES improves the ES and MES's charging/discharging power, thus reducing the cost of MES's supplier. Further research is needed to weigh the interests of MG operators and MES's suppliers to form a long-term cooperation price advantage.

Appendix

See Figure 6 and Tables 3, 4, 5.

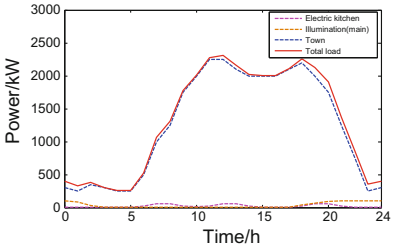

(a) AC load curve (typical day of spring)

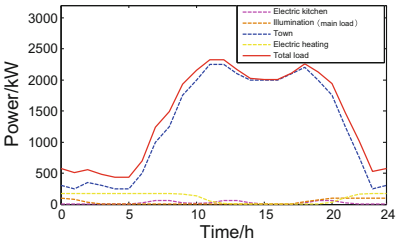

(b) AC load curve (typical day of summer)

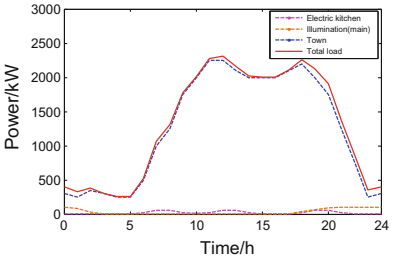

(c) AC load curve (typical day of autumn)

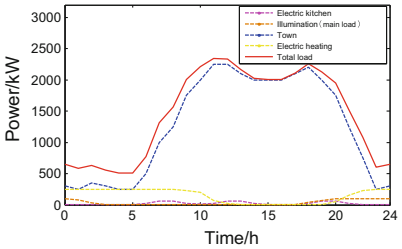

(d) AC load curve (typical day of winter)

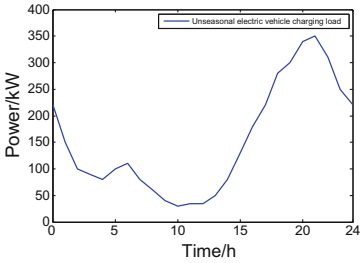

(e) Unseasonal DC load curve (Typical day of a year)

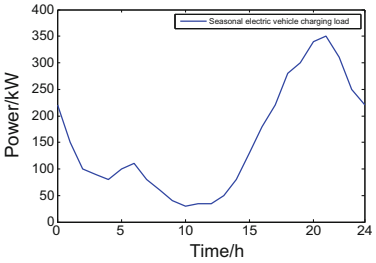

(f) Seasonal DC load curve (Typical day of winter)

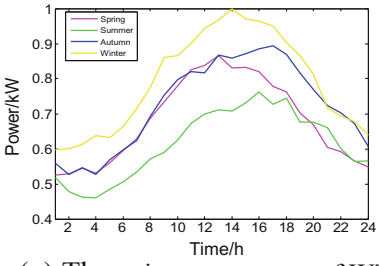

(g) The unit output power of WT

Fig. 6 The basic input data of load and WT

Table 3 The cost of the WT and ES's converter on AC side

Item	Installation cost (yuan/(kW))	Operation and maintenance cost (yuan/(kWÿa))
WT	10,000	100
ES's inverter on AC side	2000	2

Table 4 The cost and technical parameters of ES

Item	c_{ES_p} (yuan/(kW)	c_{ES_e} (yuan/(kWh))	$c_{ES\_o\ p}$ (yuan/(kWÿa))	η_{inv}	N	$SOC_{BS}^{\min}$	$SOC_{BS}^{\max}$
ES	1170	2230	95	0.9	3000	0.1	0.9

Table 5 The cost and technical parameters of MES

Item	C_{Mes} (yuan/day)	E_{Mes} (kWh)	η_{inv}	N	$SOC_{MBS}^{\min}$	$SOC_{MBS}^{\min}$
ES	100	50	0.9	3000	0.1	0.9

References

1. Rezkallah M, Chandra A, Singh B et al (2017) Microgrid: configurations, control and applications. IEEE Trans Smart Grid 1–1
2. Yang X, Su J, Lu PZ et al (2014) Overview on micro-grid technology. Proc CSEE 34(1):57–70 (in Chinese)
3. Ding M, Shi SL, Liu XY et al (2018) Study of optimal configuration of a hybrid AC/DC microgrid. Power Syst Prot Control 46(14):17–25 (in Chinese)
4. Ding M, Shi SL, Liu XY et al (2018) Solution and its key issue analysis for load transfer without power interruption of distribution lines with 30 phase angle difference. Autom Electr Power Syst 42(1):32–38 (in Chinese)
5. Ding YX, Xu QS, LÜ Y et al (2019) Optimal configuration of user-side energy storage considering power demand management. Power Syst Technol 43(4):1179–1186 (in Chinese)
6. Wang P, Goel L, Liu X et al (2013) Harmonizing AC and DC: a hybrid AC/DC future grid solution. IEEE Power Energ Mag 11(3):76–83
7. Lotfi H, Khodaei A (2017) Hybrid AC/DC microgrid planning. Energy 118:37–46
8. Majumder R (2014) A hybrid microgrid with DC connection at back to back converters. IEEE Trans Smart Grid 5(1):251–259
9. Loh PC, Li D, Blaabjerg F (2011) Autonomous control of interlinking converter with energy storage in Hybrid AC-DC microgrid. IEEE Trans Ind Appl 49(3):1374–1382
10. Chen A (2018) Coordination control and mode switching strategy for hybrid AC/DC microgrid with multi-bus structure. Autom Electr Power Syst 42(17):175–186
11. Zhang Z, Wu J, Luo Z et al (2018) Optimal scheduling for independent AC/DC hybrid microgrid considering operation characteristics of energy storage. Autom Electr Power Syst 42(19):118–127
12. Lotfi H, Khodaei A (2015) AC versus DC microgrid planning. IEEE Trans Smart Grid 1–1
13. Wang XJ, Zhao B, Wu HB et al (2016) Optimal sizing analysis of grid-connected hybrid AC-DC microgrid. Autom Electr Power Syst 40(13):55–62 (in Chinese)

14. Zhou L, Fang W, Liu L et al (2016) Battery storage multi-objective optimization for capacity configuration of PV-based microgrid considering demand response. Power Syst Technol 40 (6):1709–1716 (in Chinese)
15. Zhang MR, Xie QQ, Ou YL (2016) Battery storage multi-objective optimization for capacity configuration of PV-based microgrid considering demand response. Electr Power Autom Equip 36(9):25–32 (in Chinese)
16. Abdeltawab HH, Mohamed ARI (2017) Mobile energy storage scheduling and operation in active distribution systems. IEEE Trans Ind Electron 99:1
17. Xia Y, Wei W, Yu M et al (2017) Power management for a hybrid AC/DC microgrid with multiple subgrades. IEEE Trans Power Electron 1–1
18. Pan H, Ding M, Chen A, Bi R, Sun L, Shi S (2018) Research on distributed power capacity and site optimization planning of AC/DC hybrid micrograms considering line factors. Energies 11:1930
19. Zhou J, Zhang R, Chen Y et al (2019) Key control strategy for DC/AC converter in flexible substation in Zhangbei Data Center. Autom Electr Power Syst 1–7
20. Zhao B, Wang XJ, Zhang XS et al (2018) Two-layer method of microgrid optimal sizing considering demand-side response and uncertainties. Trans China Electrotechnical Soc 33 (14):3284–3295 (in Chinese)

A Method for Consistency Determination of Battery Energy Storage System Based on Fuzzy Comprehensive Evaluation

Yu Cai, Shufeng Dong and Jiaxiang Wang

Abstract A method to evaluate the consistency of battery packs was proposed in this article. With such evaluation, the administrator of the energy storage system could understand the deterioration of the battery packs and remove the abnormal state to avoid the potential failures and extend the battery life. First of all, selecting the indicators of the evaluation which can effectively reflect the consistency. And then calculating the fuzzy relation matrix by applying the fuzzy functions to the operating data from the battery management system (BMS); employing the anti-entropy weight method to obtain the weights of each indicator. Finally, acquiring the consistency grade with the weights and relation matrix. The method is applied to a storage system to verify that the evaluation result is aligned with the real-time observation.

Keywords Energy storage · Consistency · Fuzzy function

1 Introduction

In recent years, as China's economy keeps booming, the demand for electricity continues to soar. The complexity, stability, and vulnerability of large-scale centralized power generation systems are becoming a prominent challenge for the electricity entity. Even a tiny disturbance may have a large impact on the entire power grid. The smart grid or the distributed energy, which enjoys the benefits from its flexibility and decentralization was proposed to solved the problem. It can reduce

Y. Cai · S. Dong (✉)
Zhejiang University, 310027 Hangzhou, China
e-mail: dongshufeng@zju.edu.cn

Y. Cai
e-mail: 21710206@zju.edu.cn

J. Wang
Wanke Energy Technology Co., Ltd, 310051 Hangzhou, China
e-mail: wangjiaxiang@wankeauto.com

Y. Xue et al. (eds.), *Proceedings of PURPLE MOUNTAIN FORUM 2019-International Forum on Smart Grid Protection and Control*, Lecture Notes in Electrical Engineering 585, https://doi.org/10.1007/978-981-13-9783-7_15

the dependence of the external network and ensure the stability of the power supply. The distributed power supply is generally composed of renewable energy such as solar system or wind power, with which the intermittent problems are always accompanying. To this concern, the energy storage system (ESS) is an effective regulation mean to ensure the energy quality and secure the operation [1]. A failure of the energy storage system may lead to a disastrous collapse of the whole system. Since the energy storage system is quite critical, it's of great significance to develop a health diagnosis and monitoring strategy to protect the system.

There are a lot of options to build an energy storage system, like hydroelectricity, pumped-storage, compressed air and thermal storage etc. Among them, the advantage of deploying the lithium battery is significant, which has a long life, high energy density and it's environmental friendly. As the price of the lithium battery declines, more battery packs will be used in the energy storage system. However, a method on health diagnosis of the large-scale battery is quite challenging. As the system could consist of hundreds of battery packs and the battery pack is composed by hundreds of cells in series. The battery cells impact with each other, in another word, a malign cell could not only lower the system performance but also harm other cells in the pack because of overheat or overload [2]. Here comes to the conclusion that the consistency is a significant part of the health diagnosis of the energy storage system [3].

Although some articles [4–7] do have analysis on battery packs in the electric vehicle, since the operation strategy in power system is totally different from that in electric vehicle, whether those conclusions could be applied to the power system remains unknown. The article [8] proposes an evaluation method, but its conclusion is decided over a period of time. As the consistency of the battery varies during the charging and discharging period, the consistency at an exact moment is quite necessary.

An evaluation method of consistency by analyzing the system's operational data is proposed in this article. The evaluation result will be presented on the user interface of the monitoring system so that the administrators will understand the state of the storage system more clearly. A better understanding of the consistency among battery cells could help them identify and remove the abnormal batteries in advance to avoid further failures. The process of the evaluation method is shown in Fig. 1.

Fig. 1 Consistency evaluation process

2 Evaluation Indicators

The consistency problem of the battery is generally caused by two factors. On one hand, the manufacture technology is far from enough to make sure that every battery cell is perfectly similar. On the other hand, due to the control strategy and environment variation, the aging speeds among the battery cells are different so that their performances diverge from the initial value differently in the pack, in another word and the consistency of the pack deteriorates. To quantify the difference among the cells, some electrical features which could reflect the consistency effective are selected as indicators of the consistency.

Generally, the voltage and the state of health are the indicators for battery consistency. Latest researches find out that, as the battery is a complicated electrochemical entity, its performance is also affected by other factors like the internal resistance, operating current and temperature [9] etc. Chen et al. [10] also conclude that the charging-discharging efficiency is a major indicator for consistency. The consistency indicators of energy storage are listed on Fig. 2.

2.1 State of Charge (SOC) and Internal Resistance

Some researches emphasizes the importance of SOC [10, 11], but SOC is not an electrical quantity that can be directly measured. As the algorithms to estimate the SOC embedded inside the Battery Management System (BMS) may be different, the SOC estimation result could be different. And the accuracy of this estimation is not guaranteed. Before making sure that the SOC estimation is reliable, the evaluation of the consistency should exclude the SOC indicator.

As the battery cell ages, the internal resistance will constantly changes [12]. This is a useful feature to assert its health state or the life circles. Cells with different internal resistance perform differently in the pack and it obviously damage the consistency of the system. In fact, if the cells are in series, then the same circuit go through those cells, and the cell that has larger resistance would release more heat. Therefore, the temperature indicator is highly related to the resistance indicator, to simplify the calculation, the method proposed in this paper excludes the resistance indicator.

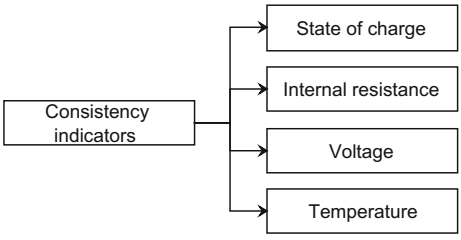

Fig. 2 Indicators of the consistency

2.2 Voltage

The voltage is a key and intuitive parameter that reflects battery performance, the difference of voltage among the cells cause an internal circulation which releases a large amount of heat constantly, leads to capacity attenuation and accelerates the battery aging. Hence, voltage consistency must be considered. The battery voltage range is the largest gap values among battery cells in the same battery pack, defined as followed:

$$U_{\max-\min} = U_{\max} - U_{\min} \tag{1}$$

The battery voltage standard deviation reflects the degree of variation of all battery voltages in one pack, and is also a very intuitive consistency indicator. The calculation formula is as listed below:

$$U_{std} = \sqrt{\frac{\sum_{i=1}^{n} (U_i - U)^2}{n}} \tag{2}$$

where U is the average voltage and n is the number of the battery cells.

In the left of Fig. 3, it presents the cell voltages of one battery pack in a period of time. It implies that when the battery voltage is high (at this stage, it is fully charged) the voltage of every cells are almost the same, that is, the consistency of the battery pack is excellent. And when the battery voltage is low (at this stage, it is almost discharged) the voltage consistency is terrible. Therefore, when the cells are almost empty after discharging, the voltage consistency is alarming. Keeping the packs at low voltage is not recommended.

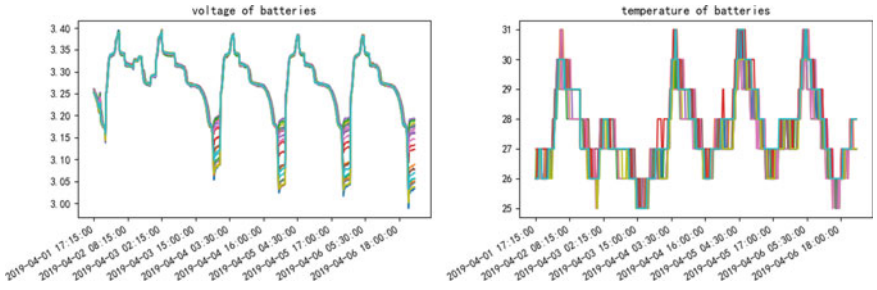

Fig. 3 The voltage and temperature of batteries

2.3 Temperature

Temperature also profoundly affects the performance of the battery as it impacts the activity of the battery electrolyte and the chemical reaction process. High temperature may cause fire or even explosion. Low temperature numbs the cells, lowers their capacity and reduces the working efficiency. Therefore, the operating temperature of the battery is a key factor that reflects the internal characteristics of the battery cells.

The temperature range and the temperature standard deviation can be calculated similar to the formulas mentioned above to calculate the voltage indicators.

3 Fuzzy Comprehensive Evaluation Method

There is no mathematical model could accurately describe the impact of various battery indicators of consistency. The influence of factors on the final result has certain ambiguity as those factors twisted and coupled together to reflect the consistency. Therefore, the fuzzy comprehensive evaluation model is practical enough to evaluate the consistency of the energy storage system. In electrical section, fuzzy comprehensive evaluation method has proved its reliability and applicability to the state evaluation of protective relays [13], transformer and wind power system etc. In this article, the indicators of the consistency are the judgement parameters evaluated by the fuzzy numbers.

3.1 Determination of Evaluation Grades

According to the Guide for condition evaluation of combined wind turbine photovoltaic and battery energy storage power generation system, which is released by the state grid corporation of China, the consistency of the energy storage system is set to the following four grades {'A', 'B', 'C', 'D'}, respectively corresponding to four levels including 'excellent', 'average', 'attention', and 'alarming'.

3.2 Normalization of Indicator Data

The smaller the difference among the cells in the pack the better the consistency of the system. Therefore, the range of voltage, the standard deviation of voltage, the range of temperature and the standard deviation of temperature can be regarded as a cost indicator and must be standardized as the formula below:

$$\tilde{x} = \frac{x_{\max} - x}{x_{\max} - x_{\min}} \tag{3}$$

where $x_{\max}$ is maximum possibility of the related data and $x_{\min}$ is the minimum possibility.

3.3 Establishment of Relation Matrix by Fuzzy Membership Function

Using triangular function as a fuzzy membership function is simple and reliable, which has little difference with other complex functions such as ridge function. The threshold values are set based on the manual of the battery released by the manufacturer. The following formulas are the fuzzy membership function of the range of voltage:

$$Range\ of\ Voltage_A = \begin{cases} 1, & x \geq 1 \\ 3x - 2, & 0.66 \leq x < 1 \\ 0, & x < 0.66 \end{cases} \tag{4}$$

$$Range\ of\ Voltage_B = \begin{cases} 1, & x \geq 1 \\ 3x - 2, & 0.66 \leq x < 1 \\ 0, & x < 0.66 \end{cases} \tag{5}$$

$$Range\ of\ Voltage_C = \begin{cases} 1, & x \geq 1 \\ 3x - 2, & 0.66 \leq x < 1 \\ 0, & x < 0.66 \end{cases} \tag{6}$$

$$Range\ of\ Voltage_D = \begin{cases} 1, & x \geq 1 \\ 3x - 2, & 0.66 \leq x < 1 \\ 0, & x < 0.66 \end{cases} \tag{7}$$

Similarly, the fuzzy membership function of other indicators can be obtained. After that, the relation matrix could be established:

$$\mathrm{R} = \begin{bmatrix} r_{11} & \cdots & r_{1m} \\ \vdots & \ddots & \vdots \\ r_{n1} & \cdots & r_{nm} \end{bmatrix} \tag{8}$$

where m is the numbers of grades, in this case, m is 4, and n is the number of indicators, in this case, n is 4.

3.4 Determination the Weights by Anti-entropy Weights Method

Some articles generally use the analytic hierarchy process (AHP) method [14] when determining the weights of each indicator. However, it is necessary to invite the experts to point out the relative importance between the indicators. By far, there is no convincing argument to clarify the significance between different indicators of consistency. The method based on AHP is hard to be employed from one system to another if the systems are not similar in every aspect. This article employ a more objective method based on the entropy theory.

Entropy is a measurement of the degree of disorder of the system. According to the basic principle of information theory, the smaller the entropy of indicator, the less information it could provide. Therefore, the information entropy tool is generally used to calculate the weights of indicators in the comprehensive evaluation [15]. The battery management system generally has a self-protection mechanism, which directly alarms the shutdown for serious consistency problems. The entropy weight method is very sensitive upon this mechanism. Because of such sensitivity, some certain weights may be extremely minor during the weights allocation. Anti-entropy weight method [16] is a better way to eliminate the effects of sensitivity. The calculation formulas are listed as follows:

$$p_{ij} = \frac{r_{ij}}{\sum_{k=1}^{m} r_{kj}} \tag{9}$$

$$A_j = -\sum_{i=1}^{m} p_{ij} \ln\left(1 - p_{ij}\right) \quad (j = 1, 2, \ldots, n) \tag{10}$$

$$W_j = \frac{1 - A_j}{n - \sum_{i=1}^{n} A_i} \, (j = 1, 2, \ldots, n) \tag{11}$$

The Fig. 4 points out the difference between the entropy weight method and the anti-entropy weight method. The weights assigned by the entropy weight method have greater differences than that by the anti-entropy weight method. In another word, the anti-entropy weight method smooths the sensitivity of the indicator information.

4 Case Analysis

4.1 Case 1

Citing a real energy storage system as example, processing the battery data from 2019-04-08 00:00:00 to 2019-04-08 04:00:00, and calculating the consistency at

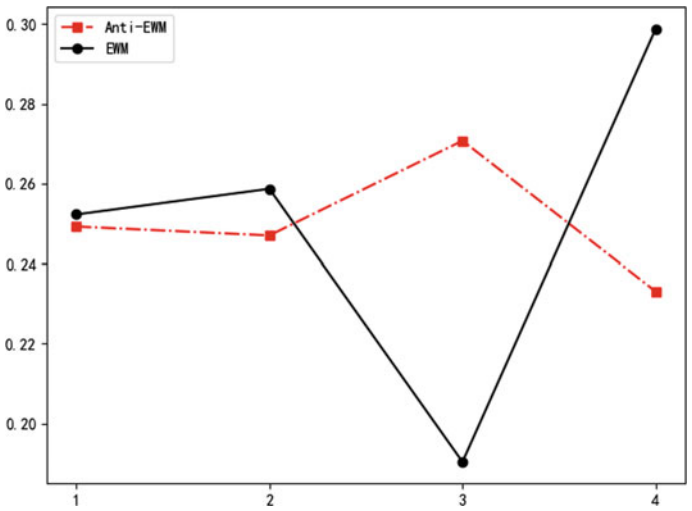

Fig. 4 Comparison of the anti-entropy weights method and entropy weights method

each moment during this period. Figure 7 lists the consistency grades obtained by the method in this article. The method proposed by JIA et al. [8] employs the priori probability as the relation matrix, which gives out only one result over a period of time and the consistency of this system is 'A'. As most of the results calculated with the method proposed in this article are 'A', which are listed in Fig. 5. The results of these two methods are not much different. However, calculating the consistency at each moment would be much more practical, as it could rise an alert when consistency is really alarming under certain situations. For example, as mentioned above in Sect. 2.3, during the discharging the consistency may be very alarming, the administrator has to stop the discharging if the consistency reaches its limit.

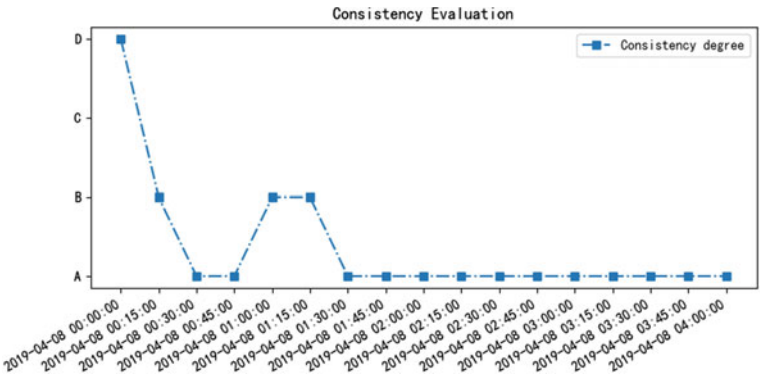

Fig. 5 Consistency evaluation result

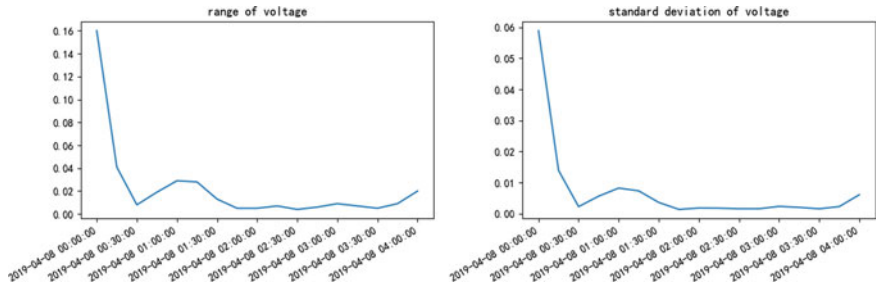

Fig. 6 Consistency of voltage

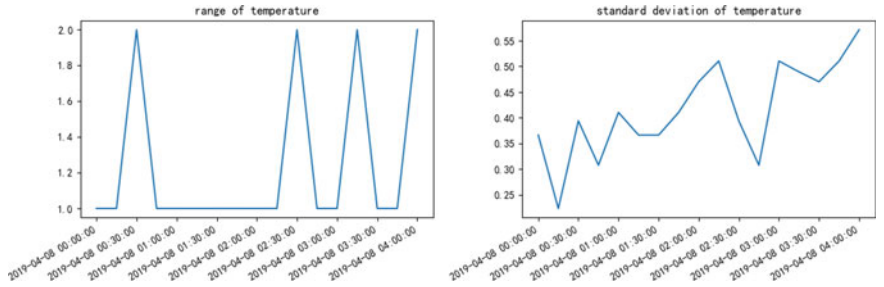

Fig. 7 Consistency of temperature

The Fig. 6 points out that voltage range and voltage standard deviation sharply decrease from the beginning, and the Fig. 7 shows that the temperature indicators don't vary sharply during this period of time. Therefore, in this period of time, it is the voltage consistency that impacts the final result.

Comparing the graphics in the Figs. 5, 6 and 7, all the line charts share a same trend, it means that the final consistency aligned with the voltage consistency. That is, the final result reflects the consistency correctly.

4.2 Case 2

In this case, the data of a whole day, from 2019,04,05 00:00 to 23:45, is observed. The Fig. 8 figures out that the voltage of the cells is almost similar except the moment at 5:00 or the moments after 20:00. And the temperature of each cells is different from each other, which means that the temperature consistency is poor. Figure 9 could better reveal that the voltage consistency is poor at the beginning, at 05:00 and at the end of the day. The Fig. 19 indicates that temperature consistency is poor from 03:00 to 15:00 (Fig. 10).

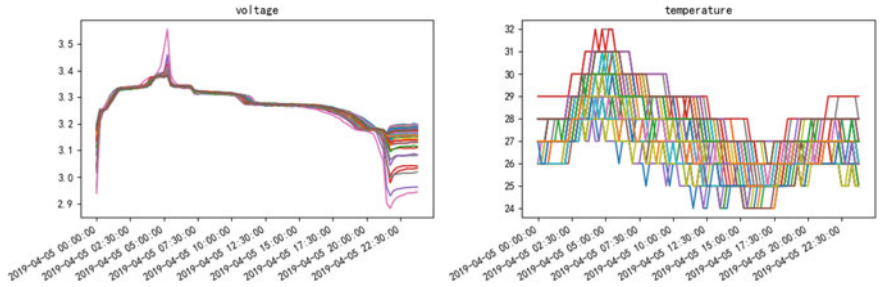

Fig. 8 The voltage and temperature of the battery cells

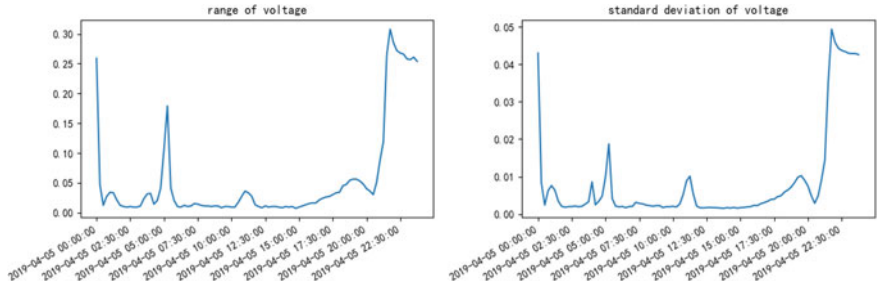

Fig. 9 The voltage range and the voltage standard deviation

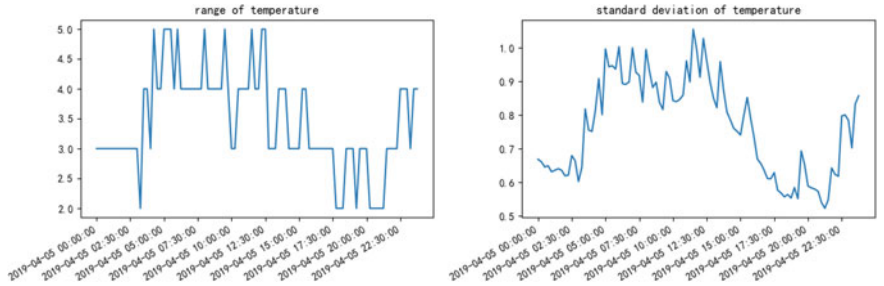

Fig. 10 The temperature range and the temperature standard deviation

Combined with the observation of the voltage and temperature, a preliminary conclusion could be asserted that the at the beginning of the day, from 05:00 to 15:00 and the end of the day are the moments that the consistency is not promising. The Fig. 11 lists the final evaluation based on the method proposed in this article. The results are consistent with the preliminary observation, which means that this method is reliable and practical.

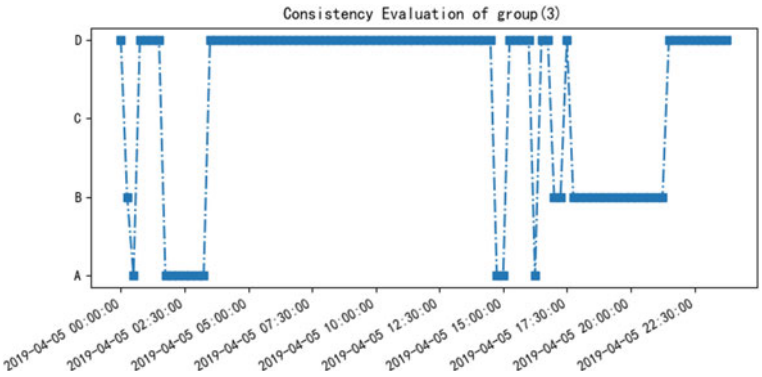

Fig. 11 The evaluation results of the consistency

5 Summary

This paper analyzes the operation data of a battery energy storage system, and considers the influence of voltage and temperature on the consistency. The voltage range, voltage standard deviation, temperature range, and temperature standard deviation are selected as indicators. Finally calculating the consistency with anti-entropy weight method and fuzzy evaluation method. The evaluation results could provide the administrators with more intuitive guidance in an energy storage system. This storage system is still in the beginning stage of operation, and has not experienced some sudden failures so that the method does not consider the consistency deterioration under such circumstances. All in all, the method needs to be revised and improved continuously during the operation of the system.

References

1. Huaiqing L, Dong L, Yuhui H (2010) A study on compatibility of smart grid based on large—scale energy storage system. Autom Electr Power Syst 34(2):15–19
2. Ma Z, Jiang J, Wen F et a1 (2013) Design of equilibrium strategy of echelon use li—ion battery pack for battery energy storage system. Autom Electr Power Syst 38(3):106–111, 117
3. Fan L, Wang K, Zhang B, Li Gs (2016) Modeling and simulation of battery energy storage system considering intrinsic inconsistency. Autom Electr Power Syst 38(3):110–115
4. Feng W, Cheng L, Jiuchun, J, Zhanguo W A new evaluation method to the consistency of lithium-ion batteries in electric vehicles. Power Energy Eng Conf IEEE
5. You XU, Zhijian Z, Qun G, Xiaonan L A consistency evaluation and maintenance method of electric vehicle lithium-ionbattery. Acta Scientiarum Naturalium Universitatis Sunyatseni
6. Jin YD, Song Q, Liu WH (2011) Large scaled cascaded battery energy storage system with charge/ discharge balancing. Electr Power Autom Equip 31(13):6–11 in Chinese
7. Xiang-Zhe LI, Hong-Bin P (2005) Study on the uniformity of storage batteries. Chinese Battery Industry

8. Jia X, Li X, Wang H, Zhang Y, Hui D (2017) Research on consistency assessment method for energy storage battery based on operating data fusion. Distrib Utilization v. 34 197(04):29–35
9. Plett, G. L., & Klein, M. J. (2009, May).: Simulating battery packs comprising parallel cell modules and series cell modules. In Proc. of EVS (pp. 1–17)
10. Chen H, Diao J, Bai K et al (2016) Research on evaluation indicators for a comprehensive assessment of operating status of lithium battery energy storage. Electr Power 49(5):149–156
11. Huet F (1998) A review of impedance measurements for determination of the state-of-charge or state-of-health of secondary batteries. J Power Sources 70(1):59–69
12. Sato S, Kawamura A (2002) A new estimation method of state of charge using terminal voltage and internal resistance for lead acid battery. IEEE Pcc Osaka 2(22):565–570
13. Wu J, Cai Z, Hu C et al (2012) Status evaluation of protective relays based on the membership function in fuzzy normal distribution. Power Syst Prot Control 40(5):48–52
14. Saaty TL Euro J Oper Res Slowinski R, Artalejo J, Billaut JC, Dyson R et al How to make a decision: the analytic hierarchy process. Euro J Oper Research
15. Liu P, Zhang X (2011) Research on the supplier selection of a supply chain based on entropy weight and improved electre-iii method. Int J Prod Res 49(3):637–646
16. Zhang H, Han D, Liu Y et al (2012) Smart grid evaluation based on anti-entropy weight method. Power Syst Prot Control 40(11):24–29 in Chinese

Mesh Method for Distribution Network Planning Model Based on Bi-level Planning

Junxiao Zhang, Ziyao Wang, Junxi Tang, Chong Gao, Huazhen Cao and Tao Yu

Abstract Traditional distribution network planning model is established with 0–1 variables, and its efficiency will be greatly reduced in the face of large-scale distribution network planning. Based on the basic ideas of path planning and mesh method, a mesh method for distribution network planning model is proposed in this paper. Firstly, the distribution network planning area is abstracted, divided and merged according to mesh method to form the distribution network planning topology. The upper-level planning model is established with the reliability and economy as the objective function, and the connection relationship of the grid nodes in the planning area is optimized with the elite ant colony algorithm. After connection is determined, the connection switch and spare line are determined based on the shortest path method as the lower level planning model. Considering distribution network connection mode, economy and reliability, a bilevel planning model is established. In order to verify the effectiveness of the model and algorithm proposed in this paper, the model and algorithm are applied to calculate in an unbuilt business district in Guangzhou. The calculation results show that the method proposed in this paper can obtain the planning scheme and various economic and reliability indexes under different connection modes at a fast speed, which provides a reference for planners.

Keywords Mesh method · Reliability · Elite ant colony algorithm · Connection mode · Bi-level planning model

J. Zhang · J. Tang · C. Gao · H. Cao
Grid Planning & Research Center, Guangdong Power Grid Co., Ltd., CSG, Guangzhou 510030, China

Z. Wang · T. Yu (✉)
South China University of Technology, Guangzhou 510640, China
e-mail: taoyu1@scut.edu.cn

Y. Xue et al. (eds.), *Proceedings of PURPLE MOUNTAIN FORUM 2019-International Forum on Smart Grid Protection and Control*, Lecture Notes in Electrical Engineering 585, https://doi.org/10.1007/978-981-13-9783-7_16

1 Introduction

With the development of economy, people's requirement of power supply reliability is increasing. Traditional distribution network planning methods are difficult to meet the requirement of modern smart distribution network construction.

In order to provide better distribution network planning schemes, mesh method is proposed, (power grid planning method is to break the fragmented layout and plan the unbuilt area with the modular approach) which is widely used in the distribution network planning projects [1]. However, there are few distribution network planning models based on mesh method in previous papers involving mesh method.

Most distribution network planning studies only consider radial topological constraints, and do not take into account the important influencing factors of connection mode [2, 3].

Distribution Network planning model is always a mixed integer programming problem (MIP), which can be solved by various mathematical optimization theories such as dynamic programming [4], approximate algorithm [5], heuristic algorithm [6]. However, the distribution network planning model is usually a NP hard problem and large-scale node system, which is difficult to be solved by using classical mathematical optimization theory. Therefore, heuristic algorithms are often used to solve problems, such as genetic algorithm (GA), simulated annealing algorithm (SA), swarm intelligence optimization. Inspired by the Traveling Salesman Problem (TSP) and Vehicle Routing Problem (VRP), the improved ant colony algorithm [7] is used to solve the planning model in this paper, which achieves better results.

There are few distribution network planning models for mesh method. The significance of the mesh method is to classify the load of the power supply grid, so as to calculate the outage loss of different loads, which is the key to realize the refined planning. This paper establishes a distribution network planning model considering connection mode, reliability of target network frame and mesh method. By applying the elite ant colony algorithm proposed in this paper, the planning schemes of an unbuilt business district (94 nodes) under different connection modes as well as the reliability and economic index of each scheme can be obtained in a relatively short time.

2 Distribution Network Abstraction

2.1 Actual Grid Abstraction

In order to facilitate planning and theoretical analysis, we must abstract the distribution network into grid nodes and grid branches. Firstly, the geographic information data of the unbuilt area can be obtained in GIS. In GIS, information

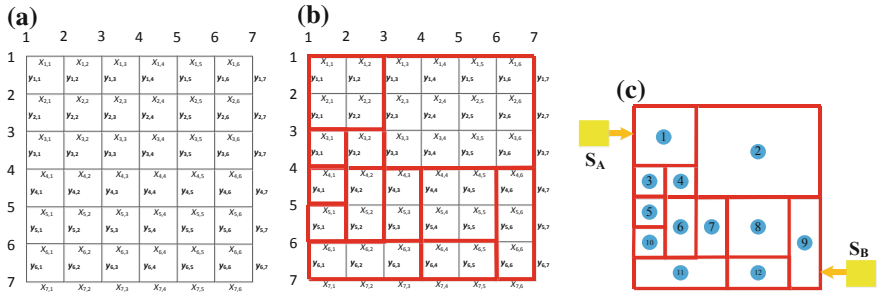

Fig. 1 Divide, merge and abstract distribution network

such as the geo-graphical environment of the planning area can be obtained, which formed a network topology relationship. Then, the planning area is divided into several natural blocks and stored the grid data in grid length matrix. For example, 7×7 grid is shown in Fig. 1a.

Most area to be planned is often irregular graphics. In order to facilitate the data storage and modeling analysis, this paper covers the entire planning area with a regular large grid and divide it into several small grids.

Number the network with the numbers of the horizontal and vertical axes, and define X and Y as the horizontal and vertical axes respectively. The length can be obtained in GIS and stored in the form of X-axis length and Y-axis length.

In Fig. 1a, X_m and Y_n are respectively the total length vector of the m-th horizontal axis and the total length vector of the n-th vertical axis. $X_{m,n-1}$ is the length between the intersection point of the n-th grid on the m-th horizontal axis and the intersection point of the $(n-1)$ grid, and $Y_{m-1,n}$ is the length between the intersection point of the $(m-1)$ grid on the n-th vertical axis and the intersection point of the m-th grid.

For modeling analysis, the same type of grid needs to be merged. The load value of each grid is determined according to the load density and the grid area. It can be seen from Fig. 1b that the actual grid node area size is different. In order to simplify the analysis, the grid is converted into nodes. The simplified diagram shown in Fig. 1c is adopted for analysis and modeling.

2.2 *Distribution Network Connection Pattern Topology Abstraction*

For the distribution network, the choice of connection mode is an essential aspect. This paper mainly introduces three connection modes commonly used in urban 10 kV distribution networks, including radial network (RN), single ring network (RN), two-supply and one-backup (TSOB). In order to consider the connection mode, it is necessary to study and abstract the basic unit of each connection mode,

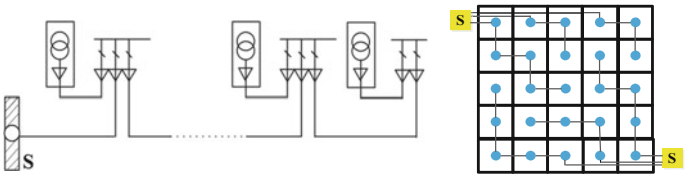

Fig. 2 Radial network abstraction

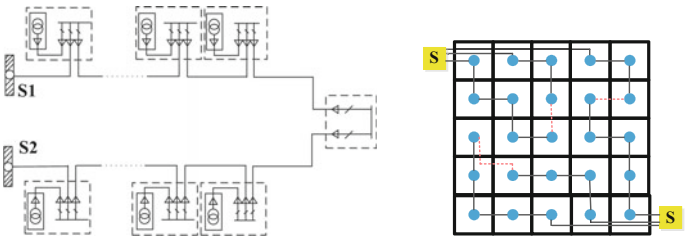

Fig. 3 Single ring network power supply abstraction

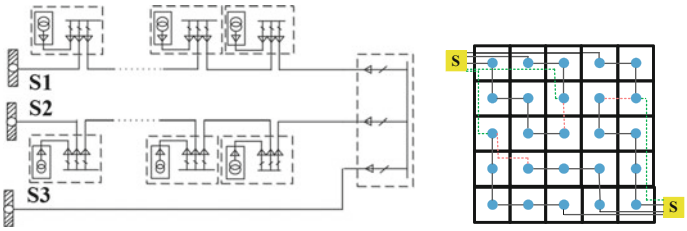

Fig. 4 Two supplies and one backup abstraction

and then apply the connection unit to the topology of the entire distribution network planning. Taking a 25-node system as an example, its topological graph is shown in Figs. 2, 3 and 4.

The radial network starts from the substation node and connects several load points. Each load point contains switch cabinet, transformer and user load. Therefore, the topology of the radial network connection mode can be abstracted as a radial connection from the substation node to the load node (the node includes the transformer and the load, and the branch includes the switch box).

Single ring mode is based on the radial network, with a tie switch between load nodes. Based on the shortest path method, two groups of the nearest feeders are contacted in this paper.

The two supplies and one backup connection mode is based on the single-ring network, with a backup line and backup switch between the power supply and the load node.

3 Mesh Method for Distribution Network Planning Model

After abstracting the grid, distribution network planning is transformed into power supply from substation nodes to each grid load node. The objective function of the planning model is the minimum investment cost and the highest power supply reliability. It is apparent that economic and reliability index are two different dimensions, which cannot be added directly. For this reason, this paper transforms the reliability objective function into the power outage risk and then optimizes it.

3.1 Upper Level Planning

Objective Function

$$\min F = F_I + F_R \tag{1}$$

where, F_I is the cost of investment. F_R is the power outage loss. The power outage loss function F_R is obtained according to the reliability index *ENS* and grid load type.

- *Cost of investment*

$$F_I = \frac{r(1+r)^{\tau}}{(1+r)^{\tau}-1}\left(C_{branch} + C_{equipment}\right) \tag{2}$$

$$C_{branch} = \sum_{i,j \in S} N_{branch} L_{ij}[K_D P_{cable} + (1 - K_D)P_{line}]] \tag{3}$$

$$C_{equipment} = N_{equipment}[(1 - K_D)P_{switch} + K_D P_{box}] \tag{4}$$

where, τ is the planning time, which is 5 years in this paper. r is the discount rate, which is 10% in this paper. i, j represent the node in the network. S represents the set of all nodes in the planning area. N_{branch} is the number of new lines planned for distribution network planning. K_D is the cable rate. $1 - K_D$ is overhead line rate. L_{ij} is the length of the grid line. P_{cable} is the investment cost per unit length of cable line. P_{line} is the investment cost per unit length of overhead line. $N_{equipment}$ indicates the number of new switches. P_{switch} is the unit price of the column switch. P_{box} is the unit price of the switch box.

- *Power outage loss*

Distribution network reliability indicators are closely related to the distribution network topology connection relationship [8], so the reliability index is also one of

the optimization objectives in the planning model. In order to consider reliability, we combine *ENS* with the importance of grid load to get the following expression.

$$F_R = \sum_{i=1}^{n} (k\alpha_i ENS_i + \beta_i ENS_i + \gamma_i ENS_i) \tag{5}$$

where, ENS_i indicates the expected power shortage of the i-th load point, n is the number of grids in planning area. α_i, β_i, γ_i are the weights of the i-th load safety, economy, and particularity, respectively. Load importance is one of {1, 2, 3, 4, 5}. The most important load indexes for several types of loads are shown in Appendix A.

Constraints

In the distribution network planning, it is necessary to ensure that the constructed grid can operate stably under normal conditions. This paper mainly considers operation constraint and topology constraint. The part of power flow calculation in this paper is solved by Matpower 7.0b1 toolbox.

- *Distribution network operation constraint*

– *Grid node voltage constraint*

$$U_{\min,i} \le U_i \le U_{\max,i}, \quad \forall i \in S \tag{6}$$

where, U_i is the voltage of node i, $U_{\min,i}$ and $U_{\max,i}$ are the lowest voltage and the highest voltage allowed by node i, respectively.

– *Feeder power constraint*

$$P_l^2 + Q_l^2 \le S_{\max,l}^2 \quad \forall l \in FEEDER \tag{7}$$

where, P_l and Q_l is the active power and reactive power of feeder group l. $S_{\max,l}$ is the maximum capacity of the feeder group l. *FEEDER* represents the set of feeder groups.

- *Topology constraint*

– *Radial network constraint*

It is assumed that all load nodes are supplied by substation nodes. Distribution network connectivity and radial constraints on topology need to meet the following requirements:

(1) All nodes are connected by branches (each grid load node is connected to a station node)

(2) The number of nodes n and branches m satisfies the formula:

$$k = m - n \tag{8}$$

where k is the number of substation nodes in a feeder group.

– *Actual construction constraints*

Considering the great difficulty in the construction of a certain section of the line or the branch of the line that cannot be connected in the actual project, set its length as infinite, then node i and j cannot be connected.

$$L_{ij}=\infty, \quad i,j \in S \tag{9}$$

where L_{ij} represents the grid distance between nodes i, j, and S represents the set of grid nodes.

3.2 Lower Level Planning

In the lower level planning, Dijkstra algorithm is used to optimize the position of tie line, tie switch, backup line and backup switch. The part of the shortest path method in this paper is solved by MATLAB graph toolbox.

The main steps are as follows:

- The result of the connection of the radial connection is obtained in the upper planning model, then search the terminal nodes of each feeder groups to form a set of terminal nodes of the feeder group. At the same time, the adjacency matrix D_{ij} is formed according to the road network constraints.
- If the connection mode is single ring network connection mode, two nodes with the shortest path are found in the terminal nodes of the feeder group, and a tie line and a tie switch are set between the two nodes.
- If the connection mode is two supplied and one backup, not only the shortest paths between the two nodes should be found at the terminal nodes of the feeder group, but also the nearest node to the substation should be found between the two nodes to form backup lines and backup switches between the substation node and the load node.

4 Planning Model Solving Method

Considering the grid planning model of connection mode, the upper level planning is a complex non-linear multi-constrained optimization problem, and the lower level planning is a shortest path optimization problem. In this paper, a combination

of elite ant colony algorithm and Dijkstra algorithm is used to solve the grid planning model of large-scale distribution network.

Step 1: Abstract the substation and grid load into nodes after meshing and merging.
Step 2: Input the coordinates of the substation and grid load, initialize the ant colony algorithm parameters.
Step 3: The shortest path between the nodes of the grid is generated based on the shortest path method Floyd, and stored in the adjacency matrix D_{ij}.
Step 4: Place m ants of each generation randomly at N power supply points. Each ant selects the next node s according to the pheromone matrix τ, and stores the path length of the ant [9, 10].
Step 5: After visiting the grid node, the visited node is recorded in the tabu search table to prevent repeated visits to the same node. At the same time, the load on the visited node is added to the $Load_i$. If it exceeds the maximum load, then return to the nearest power point and set *Load* to zero. (Indicating that a new feeder is pulled out from the substation for grid network planning).
Step 6: The radial network planning scheme can be obtained from the upper level planning after each ant completes the tour. Then, the lower level planning is solved by using the shortest circuit method, and the positions of the tie switches and other components are obtained to form the complete distribution network topology.
Step 7: After all the ants have completed the calculation, select the best ant (the ant with minimum F) in each generation as elite ant, which is updated based on the 2-opt rule. Besides, the pheromone matrix τ is updated according to the pheromone update formula.
Step 8: Repeat the steps 4, 5, 6, 7 until the condition is met.
Step 9: Obtain the optimal solution and its economic index and reliability index.

5 Test Result

5.1 Description of Planning Area

This paper takes a business district as an example for analysis. There are 10 horizontal roads and 14 vertical roads. This paper divides the whole area into 12 $\times$ 16 networks. After grid meshing and merging, the planning area is divided into 92 load nodes and 2 substations nodes. The node distribution is shown in Fig. 5a and the best cable trench planning strategy is shown in Fig. 5b.

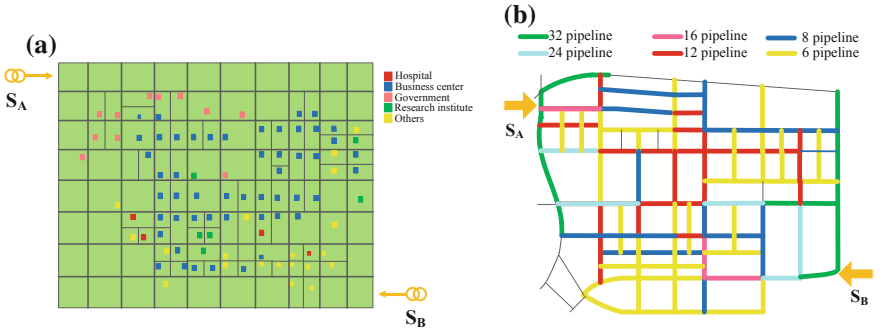

Fig. 5 Grid node distribution and cable trench plannnig strategy

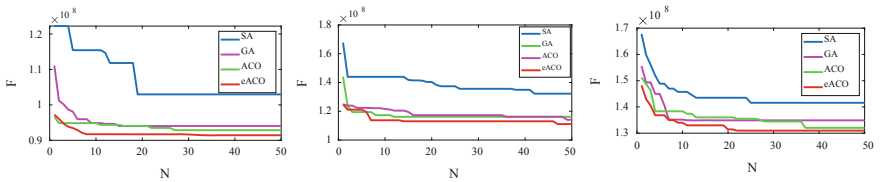

Fig. 6 Schematic diagram of convergence of ant colony algorithm calculation results under different connection mode

5.2 *Optimization Solution*

MatlabR2018a was used to solve the model, and the computer CPU was i7-4710, as shown in Fig. 6. The connection relationship of the output connected feeder groups is shown in Appendix C. The economic indicators and reliability indicators of various connection modes are shown in the Table 1.

Table 1 Index calculation results in three connection modes

Connection mode	Total cost (million)	Power outage cost (million)	SAIDI (hours per user)	SAIFI (times per user)	CAIDI (hours per user)	ASAI (%)
RN	91.77	23.59	1.0614	3.0500	2.8750	99.9652
SRN	112.20	17.43	0.9224	2.6248	2.8844	99.9700
TSOB	133.60	10.69	1.0194	2.8702	2.8185	99.9672

5.3 Result Analysis

- **Comparison of solving efficiency**

It can be seen from the Fig. 6, the convergence rate and convergence result of SA and GA are both worse than ACO. SA has a strong dependence on the initial solution and small optimization space. As the temperature drops, it is easy to fall into local optimization. GA is prone to precocity because it is difficult to find suitable mutation mechanism. Ant colony algorithm is more suitable for solving discrete path planning problems. It can be seen that the convergence speed and result of eACO proposed in this paper are better than ACO. The traditional ant colony algorithm will result in the loss of information of the most suitable individuals which cannot be transmitted to the next generation. After the application of the elite strategy, the most suitable individuals in each generation can be retained.

In the three connection mode calculation times, the more complicated the connection mode, the longer the calculation time. The solution time of the three connection modes solved by elite ant colony is 195.72. 298.77, 335.98 s. Because SRN and TSOB considers the factors such as the tie line, the tie switch, the backup line and the backup switch, which increases the computational complexity.

- **Comparison of Economic Index**

Compared with the SRN, the RN has increased the investment cost by 22.26% due to the investment in the contact switch and the tie line. Compared with the SRN, TSOB increases the investment cost by 10.91%.

It can be clearly seen that the power outage loss of the TSOB is significantly less than that of the SRN (38.67%). This is because the tie lines are often connected to nodes near important loads, which can greatly reduce the power outage time of important loads, thus reducing the losses caused by power outages. The SRN power outage loss is also significantly less than the radial (26.11%), because the SRN uses a tie line to ensure that power can be restored when the power is off.

- **Comparison of Reliability Index**

Among the three connection modes, the highest reliability index calculation result is SRN. This is because after applying the SRN, a certain fault of the line can be restored by the contact switch, thereby reducing the power outage time of the user and improving the reliability index of the system as a whole. Since the reliability calculation does not take into account the re-power supply capacity limitation of each tie switch, the reliability of the TSOB is lower than that of the SRN, and the tie switch itself has a certain failure rate, so the reliability index is lower than SRN. Because the limit of switching power supply capacity of each tie switch is not considered in the reliability calculation, and the tie switch itself has a certain failure rate, the reliability index of TSOB is lower than that of the SRN.

6 Conclusion

In this paper, a grid planning model is established, which provides a new idea for the design of traditional planning methods. After gridding the planning area, it is easy to classify the grid load, which shows the advantage of mesh method. By abstracting RN, SRN and TSOB connection modes, the constraint of connection mode on distribution topology is obtained. The optimization model is solved by using the elite ant colony algorithm, and the planning scheme and its corresponding reliability and economic index can be obtained under a variety of connection modes in an actual multi-node planning area at a fast speed, which can provide reference and basis for planners.

The follow-up work of this paper mainly includes the following aspects:

- In the reliability calculation of this paper, the limit of the transfer capacity of power supply has not been considered, and the subsequent research will further consider the transfer capacity to improve the reliability calculation model.
- Transforming the above model into a multi-objective optimization model (economy and reliability) which can obtain the Pareto frontier, provides more choice for planners.

Acknowledgements Foundation item: Supported by the Technical Projects of China Southern Power Grid (No. GDKJXM20172942).

References

1. Xu M, Wang Z, Wang J et al (2018) Medium—voltage distribution network planning based on mesh optimization generation. Autom Electr Power Syst 42(22):159–164 + 186 + 165–169
2. Xu H, Dong S, Zhu J et al (2018) Path description based planning method for power corridor of distribution network. Autom Electr Power Syst 42(16):80–86 + 226–227
3. Moreirajc ME, Vilacha C et al (2011) Large-scale network layout optimization for radial distribution networks by parallel computing. IEEE Trans Power Deliv 26(3):1946–1952
4. Li J (2018) Research on the plan economy of the distribution network of Shijiazhuang. North China Electric Power University
5. Lotero RC, Contreras J (2011) Distribution system planning with reliability. IEEE Trans Power Deliv 26(4):2552–2562
6. Bai X, Guo W (2018) Review and prospect of distribution network planning. Electr Power Autom Equip 12:200–211
7. Yin L, Liu T, Wang J et al (2018) Adjustment for power grid configuration to limit short-circuit current based on improved ant colony optimization. Autom Electr Power Syst 42 (16):80–86 + 226–227

8. Peng J, He Y, Zhou Z et al (2010) Distribution system reliability evaluation based on up-stream delivering and down-stream merging of reliability indices. Proc CSEE 01:40–46
9. Bell JE, McMullen PR (2004) Ant colony optimization techniques for the vehicle routing problem. Adv Eng Inform 18(1):41–48
10. Dorigo M (1999) Ant colony optimization: a new meta-heuristic. In: Proceedings of the 1999 Congress on Evolutionary Computation-CEC99

An Online Equivalent Method of Large-Scale Wind Power Based on Multi-source Data Fusion

Minghui Yan, Zhen Yuan, Haifeng Zhou and Wei Xu

Abstract With the rapid increase of wind power centralized grid-connection scale, the security and stability of power grid are greatly affected. In order to simulate the dynamic characteristics of wind farm accurately, a large-scale wind power online equivalent method based on multi-source data fusion is proposed. The operating state of the state estimation modeling network is identified by the fusion of multi-source real-time data such as SCADA, PMU and security and stability control system. When the error of branch power flow or node voltage at the boundary is large, the active power regulation range of wind power generators is determined by comprehensively considering the actual measurement collected by the wind farm centralized control system and the prediction information of the wind power prediction system. The active power of each wind farm is determined by quadratic programming model. The wind power generators are grouped according to the topology in the wind farm, then each group is subdivided according to static characteristic and operating state in turn. The dynamic models and static parameters of equivalent wind power generators and equivalent transformers are calculated. The proposed method is proved to be fast and effective through the analysis of a practical power grid example.

Keywords Large-scale wind power · Multi-source data fusion · Quadratic programming · Equivalent wind power generators

1 Introduction

With the further enhancement of power supply and transmission capacity, the network source structure was further optimized, and the installed scale of new energy increased significantly. In 2017, the installed capacity of new energy

M. Yan (✉) · Z. Yuan · H. Zhou · W. Xu
NARI Group Corporation, State Grid Electric Power Research Institute, Nanjing 210003, China
e-mail: yanminghui@sgepri.sgcc.com.cn

Y. Xue et al. (eds.), *Proceedings of PURPLE MOUNTAIN FORUM 2019-International Forum on Smart Grid Protection and Control*, Lecture Notes in Electrical Engineering 585, https://doi.org/10.1007/978-981-13-9783-7_17

generation nationwide accounted for 53.7% of the total power generation, exceeding 50% for the first time. Northwest China accounted for 32.8% of the new energy units added [1]. The incremental contribution of new energy generation has also grown significantly. In 2017, new energy power generation increased by 36.6% year-on-year, 30.1% higher than the growth rate of total power generation. Nine provinces, including Qinghai and Gansu, account for more than 10% of the province's electricity generation [1].

At present, some farms and networks in the new energy cluster control system are not modeled in the Energy Management System. As a result, it cannot take into account the impact of unmodeled plants and network during the online security and stability analysis and scheduling operation auxiliary decision-making, new energy accommodation capacity calculation and emergency control. The corresponding fault, monitoring elements, sections and adjustment measures cannot be set. The accuracy of online security stability analysis results is affected [2–4].

The operating characteristics of wind farm determine its influence on power system. Power flow calculation and electromechanical transient simulation are important measures to study the influence of wind farm on power system [5–7]. On the one hand, the SCADA system only covers the low-voltage side busbar of the wind farm transformer currently, so it cannot provide a detailed model of the wind farm. On the other hand, the wind farm is composed of multiple wind turbines with small capacity. If detailed models are used in power flow calculation and electromechanical transient simulation, the models are not only complex and huge in scale, but also take a long time to calculate, which is not suitable for engineering applications [2–9].

In the part of state estimation modeling network, aiming at the serious problems such as bus voltage over-limit and equipment overload caused by the fault of new energy farms, the safety and stability control emergency control devices (the third security defense line) are usually used to implement automatic control of the power grid, such as load cutting and system splitting. Due to the asynchrony and accuracy difference between the state estimation data and the measured data of security and stability control system, the reliability and rapidity of the real-time control are affected. This paper identifies the real-time operation state of power grid by integrating multi-source real-time data including SCADA, PMU and security and stability control system. Based on power flow calculation and analysis of power grid, it can provide high-quality basic data for rapid, reliable and accurate control of overloading of power grid bus voltage and equipment.

By using the measured data of the new energy real-time monitoring system, the boundary of the state estimation modeling network is identified automatically through network topology analysis. The new energy power station model is added to the state estimation model. Therefore, new energy operation characteristics and control strategies can be fully considered to improve the accuracy of online security and stability analysis and decision-making. The active power regulation range of

the new energy unit is determined by comprehensively considering the actual measurement collected by the wind farm centralized control system and the prediction information of the wind power prediction system. The quadratic programming model is adopted to determine the active power of each wind farm and to reduce the error of new energy fluctuation to the measurement to keep the power flow of boundary node and tie lines unchanged. By using the online equivalent technology of wind power generators, and combining the real-time wind power data, stability parameters, protection configuration and other model information, the units in the wind farm and their corresponding transformers are grouped into equivalent groups to meet the requirements of online calculation.

2 Multi-source Data Fusion

Multi-source real-time data of SCADA, PMU and security and stability control system are integrating to identified the real-time operation state of power grid by considering the different characteristics of real-time data reliability, precision and sampling period.

2.1 Multi-source Data Acquisition and Self-checking

According to measuring time of security and stability control system data, the minimum time deviation of the measured data from PMU is extracted. According to the feasible areas of active power, reactive power and bus voltage measured data of the equipment, the real-time data of PMU, security and stability control system and latest RTU are respectively checked for error data. Then the error data can be removed.

2.2 Multi-source Remote Measurement Data Fusion

For the same station with multiple sets of safety control devices, the average value of the real-time data of each device is taken as the real-time data of the station in the security and stability control system. For the remote measurement x of RTU data, if the remote measurement x has corresponding real-time data x_1 of security and stability control system and measured data x_2 of PMU, formula (1) is used to calculate the remote measurement x. The weighted coefficient is λ.

$$x = \lambda x_1 + (1 - \lambda)x_2 \tag{1}$$

2.3 Multi-source Remote Sign Data Fusion

According to the principle that the reliability of the remote measurement data is greater than the remote sign data, the remote sign data of the real-time data of security and stability control system and the measured data of PMU are checked and corrected respectively. For the remote sign data of the real-time data of the security and stability control system, the remote measurement data of the real-time data of the security and stability control system should be used to check and correct the remote sign data of circuit breakers and disconnectors in the real-time data of the security control system. Similarly, for the remote sign data of PMU measured data, according to the measured data of PMU in the same station, the remote measurement data of PMU measured data should be taken as the standard to check and correct the remote sign data of circuit breakers and disconnectors in the measured data of PMU.

The values of the remote sign data of circuit breakers and disconnectors in the real-time data of the security and stability control system were used to update the corresponding values in the RTU data. Then, the values of the remote sign data of circuit breakers and disconnectors in the PMU measured data were used to update the values of other corresponding in the RTU data. If the real-time data doesn't exist corresponding measurement data security and stability control system data or PMU, according to the RTU data in the same station, check and correct the remote sign data of circuit breakers and disconnectors in RTU data according to the remote measurement in RTU data. Now, the remote sign data of circuit breakers and disconnectors in the whole network fused with multi-source data can be generated.

2.4 Network Topology Update and Node Power Balance Check

According to the checked and modified RTU data, the grid topology analysis can obtain the information of the computing nodes and the topology islands of the grid. The power balance of the calculated nodes is checked. For the calculated nodes whose power unbalance is greater than the set threshold value, the power unbalance can be reduced and eliminated by equipment turnover in the station and modifying the injection power of equivalent branches.

3 Wind Farm Flow Adjustment

New energy power station is excluded in state estimation generally. In order to accurately simulate the dynamic characteristics of wind farm, the new energy power station model by artificial modeling mode is automatically integrated. The measured value acquired by the centralized control system of wind farm is taken as the initial active value of new energy generator.

Because data source of the unmolded network (hereinafter referred to as low voltage network) is inconsistent with the state estimation model part (hereinafter referred to as main network), and the actual measurement collection cycle is inconsistent, boundary power flow may have errors. When boundary branch flow or node voltage has a larger deviation, it is necessary to regulate the wind farm flow to ensure the flow rationality of all network.

Wind farm generator and load of the low voltage network are selected as the adjustable node. The active adjustment range of new energy generator is confirmed by the forecast information of wind power forecast system in order to adjust the active power of tie line in low voltage network. According to the active power sensitivity of adjustable nodes to tie lines and the target value of the AC line active power transmission (measured value), the minimum sum of weighted adjustment active quantity is taken as the target, and the active adjustment quantity of adjustable node is worked out by quadratic programming algorithm. The constraints will be relaxed when the quadratic programming algorithm has no solution. When the solution is given out, the AC line and deviation value not accorded with the constraints are given out at the same time.

The above problem model can be described as formula (2):

$$\begin{aligned} \min f &= \sum_{i=1}^{N} \alpha_i \Delta P_i^2 \\ s.t. &\sum_{i=1}^{N} K_{ji} \cdot \Delta P_i = \Delta P_{lj} \quad j = 1,\ldots,M \end{aligned} \tag{2}$$

The active (reactive) adjustment quantity of adjustable node i is ΔP_i. ΔP_{lj} is the differential value of target AC line j between the low voltage network and main network. α_i is the weighted value of adjustable node i. K_{ji} is the active (reactive) sensitivity of the adjustable node i to the target AC line j. N is the scale of adjustable nodes. M is the scale of target AC lines.

This problem has the solution under the condition of the partial derivative of equation $L = \sum_{i=1}^{N} \alpha_i \cdot \Delta P_i^2 + \sum_{j=1}^{M} \lambda_j \cdot (\sum_{i=1}^{N} K_{ji} \cdot \Delta P_i - \Delta P_{li})$ are zero on ΔP_i and λ_j, namely:

$$\begin{cases} \frac{\partial L}{\partial \Delta P_i} = 2\alpha_i \Delta P_i + \sum_{j=1}^{M} \lambda_j \cdot K_{ji} = 0 \quad i = 1, \ldots, N \\ \frac{\partial L}{\partial \lambda} = \sum_{i}^{N} K_{ji} \cdot \Delta P_i - \Delta P_{ij} = 0 \qquad j = 1, \ldots, M \end{cases} \tag{3}$$

For the node voltage, first to select the adjustable node according to the sensitivity relationships between the voltage of main network node and the reactive of low voltage network node. Then, according to the length of the steps, the reactive load of low voltage network load node is adjusted by quadratic programming algorithm. Finally, the active flow is verified after successfully matched the voltage.

4 Wind Farm Equivalent

According to the measured data of wind farm, static model parameters, protective parameters of wind power generator, terminal transformer parameters and other relevant data information are used to group wind turbines. Then, wind turbines will be grouped according to on-off state, type of wind power generator, rated active, dynamic model parameters, protective setting value, active power and pitch angle. All wind power generators and their corresponding terminal transformers will be divided into several teams. Each team contains several groups, and every group contains several wind power generators. The rated active, upper limit and lower limit of active power, active power, reactive power and other parameters of equivalent wind power generator and equivalent transformer are calculated to meet the requirements of online security and stability analysis.

4.1 Wind Farm Parameters

The real-time information of wind power generator in all wind farms, static model parameters, protective parameters, terminal transformer parameters and other information are obtained by external system.

According to the reasonable range of the equipment parameters, the rationality check for the obtained data is carried out combined with the Expert System judgement based on the above information. The error existed in the data and the suspicious data are corrected.

4.2 Wind Power Generator Grouping

According to the topological connection relationships between wind power generator and feeder, the wind power generators and terminal transformers in wind farm are divided into several teams. The wind power generators in each team are grouped according to on-off state, type of wind power generator, rated active, stable parameters, protective setting value, active power and pitch angle in turn. The achievement steps are shown as below:

1. The wind power generators in wind farm are grouped by the topological connection relationships between wind power generator and feeder. The wind power generators connected to the same feeder are divided into the same team.
2. The terminal transformers in wind farm are grouped by the topological connection relationships with the feeder. The terminal transformers connected to the same feeder are divided into the same team.
3. The wind power generators in all teams are grouped by the on-off situation, the power-on wind power generators are divided to the same group. The power-off wind power generators are divided to another group.
4. The wind power generators in all groups are grouped by the types of wind power generators (including constant speed, double feeder and direct drive). The same type wind power generators are divided to the same group.
5. According to the rated active of all wind power generators, the wind power generators with the same or similar rated active (rated active is within $\pm$ 5% is regarded as similar) are furtherly divided to the same group.
6. According to the stable parameters of wind power generators, the ones with the same stable parameters are furtherly divided into the same group.
7. According to the protective setting value of wind power generator. The ones with the same protective setting values are furtherly divided into the same group.
8. For the groups with double feeder or direct drive type, according to the active power of wind power generator, the wind power generators in groups are furtherly divided into 3 groups within three ranges (active power is between 0 and P_{set}, active power is between P_{set} and 1.0 pu, active power is equal 1.0 pu). P_{set}(using per unit) is the presetting active power threshold, which is set by the engineering's practical requirements.
9. Aim at the groups with double feeder or direct drive type, and active power is 1 pu, the wind power generators in groups are furtherly divided into 3 groups within three ranges (pitch angle is lower than the rated minimum $\beta_{\min}$, pitch angle is larger than the rated maximum $\beta_{\max}$, pitch angle is between rated minimum $\beta_{\min}$ and rated maximum $\beta_{\max}$).

In 5–9 grouping process, if the number of groups is larger than $N_{\max}$ after grouping, grouping will be stopped in this step. $N_{\max}$ is the presetting maximum grouping number, which is set by the engineering's practical requirements.

4.3 Wind Power Generator Equivalent

According to the grouping result, the wind power generator in each group is equivalent to an equivalent wind farm generator. Then the parameters of all equivalent generators and equivalent terminal transformers are worked out.

The rated active, active maximum, active power, reactive power, wind generator number of equivalent generators, as well as the rated capacity of equivalent transformer all can be obtained by Formula (4) polymeric single generator or transformer. The rated capacity of a single wind power generator is solved by formula (5). $P_{eq,nom}$, N_{eq} are respectively the rated active of equivalent generator and the quantity of wind power generator. The active lower limit, reactive upper and lower limit of equivalent generator are all solved by formula (6). $k_{p\min}, k_{q\max}, k_{q\min}$ are respectively the active lower limit coefficient, reactive upper limit coefficient, reactive lower limit coefficient. The resistance, reactance of equivalent transformer are equal to the parallel resistance, reactance of the operating transformers in the team. The conductance, susceptance of equivalent transformer are equal to the parallel conductance, susceptance of the operating transformers in the team.

$$x_{eq} = \sum x_i \tag{4}$$

$$P_{nom} = P_{eq,nom}/N_{eq} \tag{5}$$

$$\begin{cases} P_{\min} = k_{p\min} \cdot P_{eq,nom} \\ Q_{\max} = k_{q\max} \cdot P_{eq,nom} \\ Q_{\min} = k_{q\min} \cdot P_{eq,nom} \end{cases} \tag{6}$$

After finished the above equivalent processes, the measured result of the original output wind farm is replaced by the equivalent wind farm model parameters, which are used for online security and stability.

5 Case Verification

A certain wind farm in the state estimation data is equivalent to a 35 kV load, the power is 1.1383 + j0 MVA. With 12 wind farm generators in total in wind farm, the topological relationship is shown in Fig. 1.

Parameters (known value) of every transformer are $R = 0.23$, $X = 4.6$. No. 1–7 wind power generators are stopped, and the measured value of others are shown in Table 1.

According to the wind farm equivalent methods as stated in Sect. 4 of this paper, all the wind power generators in this wind farm can be divided into 3 groups. The generators within the dotted circle in Fig. 1 are the same group. The equivalent topological diagram is shown in Fig. 2, and the power of all equivalent machines

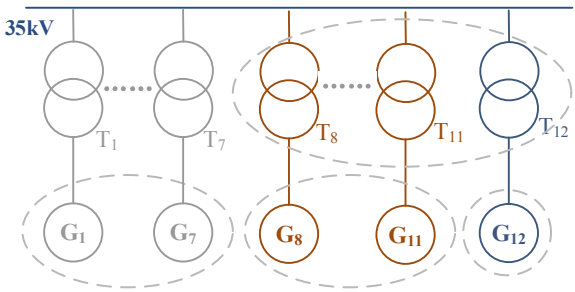

Fig. 1 Grouping for the generators in a certain wind farm

Table 1 Measured value of all wind power generators

Generator number	Measured value (MVA)
8	0.16 + j0.03
9	0.33 + j0.07
10	0.248 + j0.05
11	0.315 + j0.06
12	1.478 + j0.3

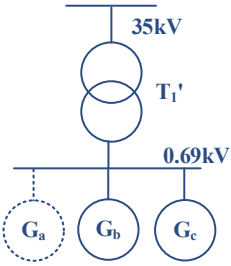

Fig. 2 Equivalent topological diagram

are shown in Table 2. The parameters (known value) of equivalent transformer are $R = 0.046$, $X = 0.92$.

At last, according to the methods stated in Sect. 3 of this paper, adjust the boundary branch flow and node voltage to the target values. The adjusted result is shown in Table 2. Therefore, the online equivalent of this wind farm is achieved.

Based on the practical power grid, the large-scale wind power online equivalent method is verified by the following cases:

Case 1: Disregard wind farm model, wind farm is equivalent in high voltage side bus;
Case 2: Regard wind farm model, large-scale wind farm is equivalent online according to the methods as stated in this paper.

When the area near a certain wind farm has the fault, the comparative curve of 330 kV bus voltage is shown in Fig. 3, and the active and reactive power curves of outgoing AC line are shown in Fig. 4 and in Fig. 5 respectively.

Table 2 Power flow of equivalent generator

Generator number	After equivalent (MVA)	After adjustment (MVA)
A	0 + j0	0 + j0
B	1.054 + j0.214	0.508 − j0.168
C	1.478 + j0.3	0.631 + j0.168

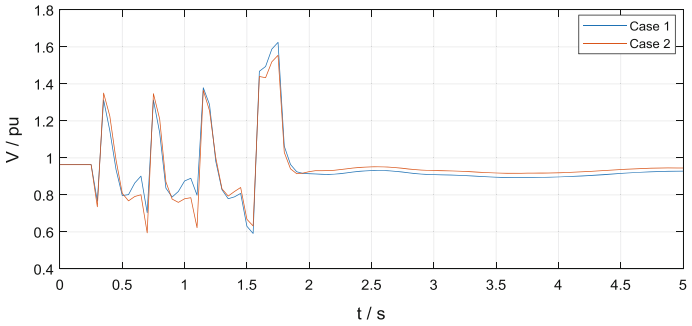

Fig. 3 Bus voltage curve after the fault

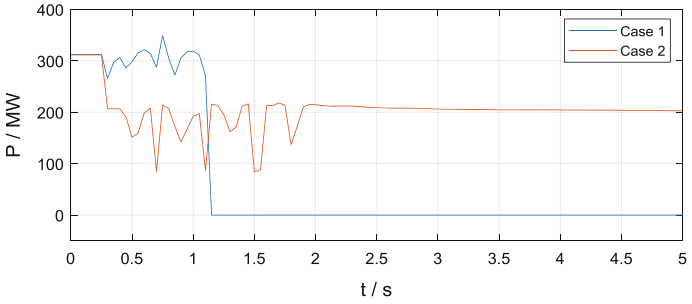

Fig. 4 AC line active curve after the fault

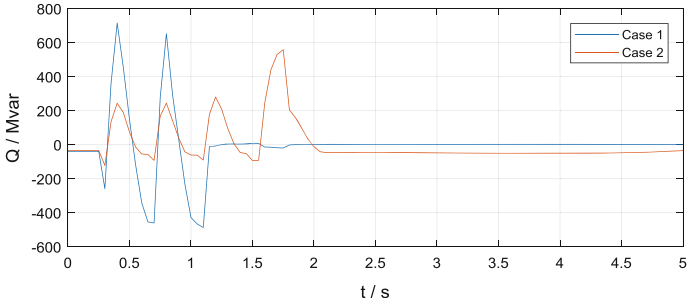

Fig. 5 AC line reactive curve after the fault

In case 2, after the area near the wind farm has the serious fault, the related new energy generators are offline due to the control measures. Due to case 1 hasn't the detailed wind farm model, the capacity is more different from the practical result when it simulated the new energy generator to be offline. The simulation comparison result shows that the equivalent model after online considered the large-scale wind farm can reflect the operation state of the practical power grid more accurately.

6 Conclusion

This paper put forward an online equivalent method of large-scale wind power based on multi-source data fusion. For the state estimation modeling network, multisource data from security and stability control system, PMU, SCADA are integrated to improve the accuracy of the data. According to the real measurement acquired by the centralized control system of wind farm and the forecast information of wind power forecast system, the active power of all wind farms is adjusted by quadratic programming model. The network scale is greatly reduced for simulation calculation by the wind farm equivalent to meet the requirements of online security and stability. The operation result of the practical power grid verified the accuracy and feasibility of this method.

Acknowledgements The work described in this paper was supported by "Key Technologies Research and Application of Global Analysis and Control Adapt to Active Dispatching Demand of Power Grid" program.

References

1. Annual Report on the Development of China's Power Sector. China Electricity Council, 2018/06/14
2. Liu Q, Fang J, Zhao J et al (2019) Layered wind power dispatching control strategy based on DSA power prediction model. Electr Power Constr 40(2):63–70
3. Chen N, He W, Qian M et al (2011) Design and application of reactive power control system for wind farm. Autom Eletr Power Syst 35(23):32–36
4. Zhao J, Zhang G, Huang Y (2014) Status and prospect of state estimation for power system containing renewable energy. Electr Power Autom Equip 34(5):7–20, 34
5. Yang B, Shu H, Qiu D et al (2019) Nonlinear robust state estimation feedback control of doubly-fed induction generator under variable wind speeds. Autom Electr Power Syst 43(4):60–69
6. Zhang X, Qiu W, Fang R et al (2019) Impedance modeling and sub-synchronous resonance mitigation strategy of doubly-fed induction generator based wind turbine in static reference frame. Autom Electr Power Syst 43(6):41–48
7. Liang H, Cheng Z, Sun H et al (2019) Optimization of power network reconstruction with wind farm considering uncertainty of wind power prediction error. Autom Electr Power Syst 43(7):151–158

8. Zhang G, Li F, Zhou S et al (2019) Wind power real-time active dispatch considering friendliness of wind farm integration. Power Syst Technol 43(2):664–669
9. Li X, Xing Z, Chen Z et al (2010) Design of large clusters of wind power active intelligent control system. Autom Electr Power Syst 34(17):59–63

Multi-objective Optimal Allocation of Distributed Generation Considering Environmental Target and Uncertainty of EV

Huazhen Cao, Yaxiong Wu, Chong Gao, Junxi Tang and Lvpeng Chen

Abstract Based on the typical timing characteristics of Distributed Generation (DG) and user power load, considering the uncertainty of large-scale electric vehicles and the environmental benefits of different distributed power sources, the operating cost, network loss and environmental benefit of the distribution network are used as the objective function. In this paper, a Monte Carlo simulation method is used to simulate the charging characteristic of the electric vehicle, and the model is solved by the binary bat algorithm. By comparing with a single-purpose distributed power optimization configuration model, the simulation results verify the rationality and validity of the proposed model and method.

Keywords Distributed generation · Electric vehicle · Time-sequence characteristics of load · Multi-objective bat optimization algorithm

1 Introduction

In order to solve the energy shortage and environmental problems, distributed generation technology and electric vehicle industry are developing rapidly [1–3]. Because the output characteristics of Distributed Generation (DG) are random and

Foundation item: Supported by the Technical Projects of China Southern Power Grid (No. GDKJXM20172939).

H. Cao · Y. Wu · C. Gao · J. Tang
Grid Planning & Research Center, Guangdong Power Grid Co., Ltd., CSG, Guangzhou 510030, China

H. Cao · Y. Wu · C. Gao · J. Tang
Guangdong Power Grid Development Research Institute Co., Ltd., Guangzhou 510030, China

L. Chen (✉)
Suzhou Huatian Power Technology Co., Ltd., Suzhou 215000, China
e-mail: chenlvpeng123@163.com

Y. Xue et al. (eds.), *Proceedings of PURPLE MOUNTAIN FORUM 2019-International Forum on Smart Grid Protection and Control*, Lecture Notes in Electrical Engineering 585, https://doi.org/10.1007/978-981-13-9783-7_18

intermittent, when a large number of DGs connected to the distribution network, it will have a huge impact on the operation of the distribution network.

The charging characteristics of the electric vehicle (EV) have great space-time uncertainty. With the increasing of the permeability of the EV, the existing distribution network will likely have a problem of operation [4]. Therefore, the planner should consider the uncertain characteristics of the DG and the EV in the planning of the DG optimization configuration, so as to be of great significance to the development of the distribution network.

At present, many scholars have done a lot of research on the problem of DG optimal allocation, and have achieved relevant results [5]. The model established in reference [6] takes into account the cost of purchasing electricity, the cost of lack of power, the cost of loss and the cost of delaying network renewal. The random characteristics of DG and PEV under different permeability are considered in reference [7], but the genetic algorithm has the disadvantage that it is easy to fall into precocity.

In this paper, the charging characteristics of EV are modeled, and the timing characteristics of DG and conventional load are analyzed and extracted. The multi-objective DG optimal configuration model is established based on the distribution network loss, the operation cost of DG construction, and the environmental benefit as the objective function. The binary bat algorithm is used to solve the model. The numerical results show that the proposed optimization model and method are effective and flexible.

2 Probabilistic Modeling and Simulation of EV Charging Characteristics

2.1 Behavior Characteristics of EV

According to the results of the American household traffic survey data (NHTS) [8], it is found that the time T of the car owner's last end trip obeys the normal distribution. Its probability density can be expressed as (1):

$$f(T) = \begin{cases} \dfrac{1}{\sqrt{2\pi}\sigma_T} \exp\left[-\dfrac{(T-\mu_T)^2}{2\sigma_T^2}\right], (\mu_T - 12) < T \le 24 \\ \dfrac{1}{\sqrt{2\pi}\sigma_T} \exp\left[-\dfrac{(T+24-\mu_T)^2}{2\sigma_T^2}\right], 0 < T \le (\mu_T - 12) \end{cases} \tag{1}$$

where μ_T= 17.6; σ_T= 3.4.

2.2 Characteristics and Charging Mode of EV's Battery

It is assumed that the battery characteristic parameters adopted in this paper are as follows: the capacity of EV battery is 30 kWh, the initial SOC meets normal distribution **N**(0.5, 0.01) at the beginning of charging. The charging efficiency is 95% and the charging power factor is 0.95. The charging power is assumed to be constant and the charging power is 3.5 kW. The car owner will adopt the disordered charging mode. Suppose the owner's charging time is at the end of the last trip. According to (1) and battery characteristics of electric private car, Monte Carlo simulation method can be used to simulate the charging load characteristics of EV.

3 Time-Sequence Characteristics of DG and Load

3.1 Time-Sequence Characteristics of DG

The output characteristics of Wind turbine generator (WT) and photovoltaic generator (PV) both have volatility and randomness. However, there is a certain regularity within a certain time scale (for example, daily). The typical daily output curves of WT and PV are shown in Fig. 1. The output data of WT and PV are selected from a distributed power plant under heavy load period in Maoming City, Guangdong Province.

It can be seen from the typical output curves that there is a certain complementarity between the output rule of WT and PV. The complementary characteristics between WT and PV naturally smooth the peak-valley difference of distribution system to a certain extent.

Micro-turbine generator (MT)is a widely used distributed generator. Different from WT and PV affected by geographical location and natural conditions, their

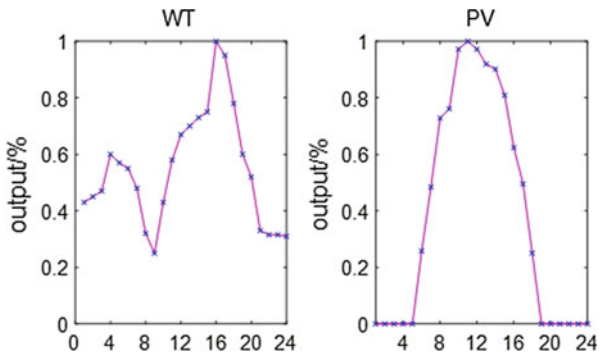

Fig. 1 Typical output curves of WT and PV on July 23, 2018

time series output characteristics are precisely controllable. Therefore, the time series output characteristic is regarded as constant in this paper.

3.2 Extraction Method of Time-Sequence Characteristics of Load

With the continuous development of social economy, especially the emergence of new load, the characteristic difference of electric load time series curve is gradually increasing. DG optimal configuration planning also needs to extract the timing characteristics of the load. In this paper, Fuzzy C-Means (FCM) is selected as the extraction method of load timing characteristics [9].

4 Multi-objective DG Optimal Configuration Model

4.1 Objective Function

Distribution Network Loss Target.

$$C_{\mathrm{L}} = 365 \times price_{\mathrm{loss}} \sum_{N_{\mathrm{T}}}^{N_{\mathrm{T}}} \sum_{l=1}^{N_{\mathrm{L}}} I_{tl}^2 R_l \Delta t \tag{2}$$

where C_{L} is the annual cumulative loss cost after DG is configured, $price_{\mathrm{loss}}$ is the loss price, N_T is the segment number of the time series characteristic curve, this paper takes 24 N_L as the total branch number of the optimized regional distribution network. The I_{tl} is the current on the branch l after the DG is connected to the distribution network, the R_l is the branch resistance of the branch l, and Δt is the time interval.

DG Construction Operation Cost Target. The DG construction operating cost target consists of the DG construction cost $\mathrm{C_{CON}}$ and the operational maintenance cost $\mathrm{C_{OM}}$, as shown in (3):

$$C_{\mathrm{DG}} = \sum_{k=1}^{N_{\mathrm{DG}}} S_k \left[\left(\frac{\eta(1+\eta)^{n_{\mathrm{DG},k}}}{(1+\eta)^{n_{\mathrm{DG},k}} - 1} \right) C_{\mathrm{CON},k} + 8760 C_{\mathrm{OM},k} \right] \tag{3}$$

where N_{DG} is the number of DG in distribution network, η is fixed annual interest rate, unit is %, $n_{\mathrm{DG},k}$ is the repayment period of construction funds, which is equal

to the economic operating life of DG, S_k is the planning capacity of the kth DG. $C_{\mathrm{CON},k}$ and $C_{\mathrm{OM},k}$ are the unit capacity construction cost and operation maintenance cost of the kth DG, respectively.

Environmental Benefit Target [10]:

$$C_{\mathrm{E}} = \sum_{k=1}^{N_{\mathrm{DG}}} Q_k \sum_{i=1}^{N_{\mathrm{P}}} (C_{\mathrm{F}i} - C_{\mathrm{DG}ki}) \tag{4}$$

$$Q_k = 365 \times \sum_{t=1}^{N_T} P_{kt} \Delta t \tag{5}$$

where C_E is the annual environmental benefit after DG is configured, N_{DG} is the number of DG configured in distribution network, Q_k is the annual power generation of the kth DG, N_P is the number of pollutants, and N_{DG} is the number of DG in distribution network. C_{Fi} and C_{DGki} are the environmental value costs of thermal power generation and the ith pollutant emitted by the kth DG distributed power source, respectively. P_{kt} is the active contribution of the kth DG in the t-period of the daily load series.

4.2 Constraint Condition

Power Flow Constraints

$$\begin{cases} P_{is} = U_i \sum_{j \in i} U_j (G_{ij} \cos\theta_{ij} + B_{ij} \sin\theta_{ij}) \\ Q_{is} = U_i \sum_{j \in i} U_j (G_{ij} \sin\theta_{ij} - B_{ij} \cos\theta_{ij}) \end{cases} \tag{6}$$

where P_{is} and Q_{is} are the active power injection power and reactive power injection power of node i, respectively, U_i and U_j denote the voltage amplitude of node i and node j, and $j \in i$ denote all nodes directly connected to node i, respectively, and U_i and U_j denote the voltage amplitude of node i and node j, respectively. G_{ij} and B_{ij} represent conductance and admittance between node i and node j respectively, θ_{ij} is the phase angle difference between node i and node j.

Node Voltage Constraint

$$U_i^{\min} \le U_i \le U_i^{\max} \tag{7}$$

where U_i^{min} and U_i^{max} represents the upper and lower limits of the voltage of node i.

Transmission Line Capacity Constraints

$$P_{ij} < P_{ij,\max} \tag{8}$$

where P_{ij} represents the transmitted power from node i to node j.

Total DG Access Capacity Constraint

$$S^{\min} \le \sum_{k=1}^{N_{\mathrm{DG}}} S_k \le S^{\max} \tag{9}$$

where $S_{\min}$ and $S_{\max}$ represents the upper and lower limits of the capacity in a distribution network that allows access to a distributed source.

4.3 Synthetic Objective Function

To sum up, the above three optimization objectives conflict with each other, so the coordination optimization is difficult. Therefore, the weighted variable ω_m is introduced to express the decision preference of different objectives. The synthetic objective function is shown in (10).

$$\min C = \omega_1 C_{\mathrm{L}} + \omega_2 C_{\mathrm{DG}} - \omega_3 C_{\mathrm{E}} \tag{10}$$

where ω_1, ω_2 and ω_3 are the weight coefficients of each objective, and $\omega_1+ \omega_2+ {}_3 = 1$. Each weight can be selected according to experience. The more close to 1 the weight coefficient is, the more important it is to consider its corresponding index. This paper mainly considers transmission loss, environmental benefit and DG construction cost as the influencing factors of weight selection.

5 Solution of the Model

5.1 Particle Position Coding Scheme Setting

Particle position information includes the type of access to the DG and the DG access capacity. The encoding method is binary coded, as shown in (11)

$$X = \{K_1, S_1, K_2, S_2, \ldots, K_{N_{\text{bus}}}, S_{N_{\text{bus}}}\} \tag{11}$$

where X is the location information of bats, K_i is the type of DG at distribution node i, and S_i is the capacity of DG at distribution node i.

5.2 Binary Bat Algorithm

Bat Algorithm (BA) is a new intelligent optimization algorithm, which is suitable for solving the continuous optimization problem of decision variables. The DG optimization problem is an integer optimization problem, so the standard BA cannot be adopted directly. By modifying the process of updating the speed and position of the BA, the standard BA is transformed into the Binary Bat Algorithm (BBA) to solve the DG optimal configuration problem [11].

The specific process is described as follows:

Step (1): Initializes the BBA algorithm parameters. Set the sound level A, the pulse frequency r, and the number of populations n. Initial the ith bat position X_i^0 randomly by binary coding method, and initial the bat speed V_i^0 randomly.
Step (2): Calculate the initial fitness $f(X_i^0)$ of each bat, and find the bat position of the initial optimal fitness function, recorded as X_{best}^0.
Step (3): Update the pulse frequency vector F_i^k of the bat individual and the velocity vector V_i^k

$$F_i^k = F_{\min} + (F_{\max} - F_{\min})\beta \tag{12}$$

$$V_i^k = V_i^{k-1} + \left(X_i^k - X_{\text{best}}^{k-1}\right)F_i^k \tag{13}$$

where F_i^k is the pulse frequency of the ith bat at the kth iteration; $F_{\min}$ is minimum frequency; $F_{\max}$ is the maximum frequency; different pulse frequencies will increase the diversity of bats; $\beta \in [0,1]$ is to satisfy the uniform distribution The random number; F_i^k and X_i^k are the velocity and position of the ith bat at the kth iteration, respectively; X_{best}^k is the optimal position at the kth iteration.
Step (4): Calculate the speed conversion vector T_i^k for each bat;

$$T_i^k = \left|\frac{2}{\pi}\arctan\left(\frac{\pi}{2}V_i^k\right)\right| \tag{14}$$

Step (5): Update bat position.

$$X_{i,m}^{k-1} = \begin{cases} (X_{i,m}^{k-1})^{-1}, rand_1 < T_{i,m}^{k} \\ X_{i,m}^{k-1}, other \end{cases} \tag{15}$$

$$X_{i,m}^{k-1} = \begin{cases} X_{i,m}^{k-1}, r < rand_2 \\ X_{i,m}^{k-1}, other \end{cases} \tag{16}$$

where, $X_{i,m}^{k}$ is the value of the mth coded bit of the ith bat l at the kth iteration; $T_{i,m}^{k}$ is the velocity conversion of the mth coded bit of the ith bat at the kth iteration; $(.)^{-1}$ is inverse function; $rand_1$ and $rand_2$ are random numbers of [0, 1]; r is pulse frequency.

Step (6): Calculate the fitness value of all bats. If $rand_3$ < A and $f(X_i^k) < f(X_{best}^k)$, accept the value, otherwise retain the fitness value obtained from the last iteration calculation.

Step (7): The fitness values of the individual bat individuals are sorted to find the individual position X_{best}^{k} and the fitness value $f(X_{\text{best}}^{k})$ of the optimal fitness function at the current iteration.

Step (8): If the algorithm iteration does not reach the maximum number of iterations, return to Step (3), otherwise, output the optimal solution.

5.3 Stochastic Power Flow Calculation Method

In this paper, the uncertainty of EV and the timing characteristics of DG and conventional load are considered. In this paper, the stochastic power flow method based on Monte Carlo simulation (MCS) is used to solve the distribution network power flow with uncertain factors. According to the random sampling of the EV state at different times in the system, the corresponding state of the system is obtained by extracting the DG at different time and the output of the conventional load. Then the power distribution of each branch of the system is obtained by using the deterministic power flow calculation method to calculate the power loss target and so on [12].

6 Simulation Analysis

6.1 Simulation System Configuration

The method proposed in this paper is used to optimize the DG planning and configuration of the IEEE33 node distribution system. Installation cost of WT, PV, MT are 1400$/kW, 1800$/kW and 700$/kW, respectively; power loss price is 0.07 $/kWh; load and distributed power factor is 0.9; upper limit of total access capacity

for DG is 380 kW. Suppose a total of 400 EVs in one day are connected to the area. All nodes in the distribution network have access to the DG conditions.

The population size of the algorithm is 25; the maximum number of iterations is 300, the penalty factor is $K = 100$; the sampling times of Monte Carlo is $N_{\text{mcs}} = 100$.

6.2 Clustering Processing Results of Load Time-Sequence Data

In this paper, the daily load curve data of a certain area in Guangdong Province, China are selected as clustering samples. The typical load sequence curve obtained by normalized clustering is shown in Fig. 2.

According to the analysis results, it can be seen that there are three typical load characteristics in this area. The load type of each node in the IEEE33 node system is set as follow: Type1: 4,10,11,13; Type2: 2,3,5,6,8,12,16,17,18,19,20,22, 23,29,30,32,33; Type 3: 7,9,14,15,21,24,25,26,27,28,31.

6.3 Simulation Results and Analysis

Comparison of Single-Objective and Multi-Objective Optimization Effects. The single-objective optimization of each objective and multi-objective optimization are carried out. The results are shown in Table 1. The distribution network loss target weight, each target weights are all taken as 1/3, that is, $\omega_1 = \omega_2 = \omega_3 = 1/3$.

It can be seen from the table that distribution network loss optimization results with the goal of minimum construction operation cost (i.e. no DG access) are higher than other optimization scenarios, which shows that the access of DG can effectively reduce the distribution network loss. In addition, compared with the single-objective optimization results for distribution network losses, the

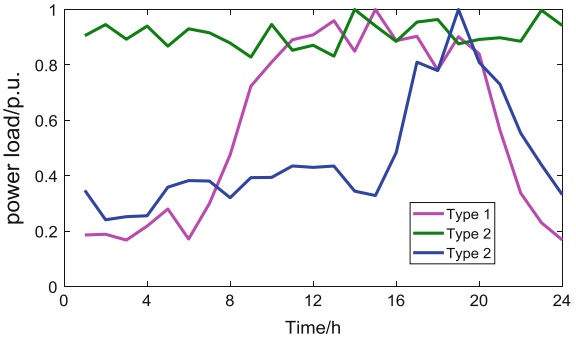

Fig. 2 Clustering results of load time series characteristics

Table 1 Results of single and multiple objectives optimizations

Target	Distribution network loss target/10^4\$	DG construction operation cost target/10^4\$	Environmental benefit target/ 10^4\$
Minimum network loss	5.74	17.39	6.27
Minimum construction operation cost (without DG access)	7.46	0	0
Maximum environmental benefit	6.03	27.11	9.64
Multiple target	6.21	19.02	8.77

optimization results of the multi-objective algorithm in this paper balance the objectives of all aspects, sacrificing a small amount of distribution network losses and DG construction operation costs. The goal of environmental benefit has been greatly raised. It is of great significance to improve the environmental quality and improve the living standard of the people in the planned area.

Analysis of Optimization Effect Under Different Target Weight Setting.

Case 1: the optimization target focuses on the social environmental protection benefits, and the weight setting of each goal is $\omega_1 = 0.4$; $\omega_2 = 0.1$; $\omega_3 = 0.5$;

Case2: the optimization goal focuses on the investment operation cost of the power supply enterprise, and its target weights are $\omega 1 = 0.4$; $\omega 2 = 0.5$; $\omega 3 = 0.1$.

The optimization results are shown in Tables 2, 3 and 4.

Comparison and analysis of overall optimization results. From the optimization results of Table 2, we can see that the network loss costs of the two optimization modes are 12.46 and 10.17% lower than those without DG access, respectively. This shows that reasonable DG access can effectively reduce the cost of network loss. In addition, two cases are compared and analyzed. Case 1 focuses on social environmental protection, and the environmental benefit is the highest in the optimization results, which is more than that of Case 2, but the construction and operation cost of DG is increased. Case 2 focuses on the investment operation cost of the power supply enterprise, and the construction operation cost of the optimization result is less than that of the case 1, but it is replaced by reducing the

Table 2 Optimization results comparison of different case

Case	Cost of network loss/10^4\$	Construction operation cost/10^4\$	Environmental benefits/10^4\$
Without DG access	7.46	0	0
1	6.53	11.60	4.27
2	6.70	9.38	3.37

Table 3 Configuration results of distributed generator optimization

Case1			Case2		
Node number	DG access Type	Access capacity /kW	Node number	DG access Type	Access capacity/kW
3	WT	50	12	PV	70
10	PV	30	13	WT	30
11	PV	50	15	PV	30
16	MT	40	17	PV	20
21	PV	30	21	MT	20
23	MT	20	26	PV	30
25	PV	30	30	WT	30
27	PV	40	31	PV	30
29	WT	60	33	MT	40
32	PV	30	–	–	–

Table 4 Access quantity and access proportion of distributed generation

Case1			Case2		
DG type	Access/ kW	Access ratio (%)	DG type	Access/ kW	Access ratio (%)
WT	110	28.95	WT	60	17.64
PV	210	55.26	PV	180	52.94
MT	60	15.79	MT	100	29.41
Total access	380	100	Total access	340	100

environmental benefit. This is because DG power generation has the characteristics of clean and environmental protection, DG access to the distribution network to replace the traditional coal-fired units to generate electricity, will improve the social and environmental benefits. However, the larger the DG access capacity, the higher the construction operation cost.

Comparison and analysis of the results of distributed generator configuration. It can be seen from the optimization results that the total access capacity of DG in the two schemes is 380 kW and 340 kW, respectively. In the optimization scheme, WG and PV access are the main ones, which is because the environmental benefit target is considered in the optimization goal, and the contribution of these two types of non-polluting DG to the environmental benefit is greater. In addition, in the two schemes, PV access is relatively stable. In case 2, compared with case 1, the proportion of WG access decreased from 28.95 to 17.64%, and the proportion of MT access increased from 15.79 to 29.41%. This is due to the fact that the cost of WG is higher than that of MT when it comes down When the objective weight of

environmental benefit and the operation cost of DG are raised, the algorithm will adjust the configuration of distributed generator, reduce the access capacity of WG and PV, which contribute greatly to the environmental benefit, and increase the access ratio of MT.

7 Conclusion

The main work of this paper is summarized as follows:

(1) considering the uncertainty of EV access distribution network, the probability model of EV charging characteristics is established. In addition, the clustering method is used to extract the typical timing characteristics of distributed power supply and conventional load, which makes the planning model more close to the actual scene.
(2) A multi-objective DG optimal configuration model is established, which integrates the operation cost of DG construction, distribution network loss and environmental benefit cost. Planners can flexibly change the weights of different objectives according to the requirements of planning tasks, and obtain different optimal allocation results.
(3) using the binary bat algorithm to solve the programming model, the rationality and effectiveness of the proposed model and method are verified.

References

1. Cheng H, Hu X, Wang L et al (2019) Review on research of regional integrated energy system planning. Autom Electr Power Syst 43(7):2–13
2. Pan Z, Zhang X, Yu T et al (2017) Hierarchical real-time optimized dispatching for large-scale clusters of electric vehicles. Autom Electr Power Syst 41(16):96–104
3. Pan J, Wu H, Xu D et al (2019) Capacity optimization of rooftop photovoltaic based on photovoltaic/electric vehicle/load game. Autom Electr Power Syst 43(1):186–193
4. Hu Z, Luo H (2018) Research status and prospect of automatic generation control with integration of large-scale renewable energy. Autom Electr Power Syst 42(8):2–15
5. Zhu J, Wei G, Lou G et al (2017) Learning automata-based methodology for optimal allocation of renewable distributed generation considering network reconfiguration. IEEE Access 5(99):14275–14288
6. Dugan RC, Mcdermott TE, Ball GJ (2001) Planning for distributed generation. IEEE Ind Appl Mag 7(2):80–88
7. Huang X (2018) Capacity optimization of distributed generation for stand-alone microgrid considering controllable load. Proc CSEE 38(07):1962–1970
8. U.S. Department of transportation, federal highway administration [DB/OL]. National household travel survey, 2009. http://nhts.ornl.gov

9. Yang Z, Lin X, Jiang W et al (2017) An electricity data cluster analysis method based on SAGA-FCM algorithm. In: IEEE International Conference on Networking. IEEE
10. Qian K (2008) Environmental benefits analysis of distributed generation. Proc CSEE 28 (29):11–15
11. Mirjalili S, Mirjalili SM, Yang XS (2014) Binary bat algorithm. Neural Comput Appl 25(3–4):663–681
12. Peng X, Lin L, Liu Y et al (2015) Optimal distributed generator allocation method based on correlation latin hypercube sampling monte carlo simulation embedded crisscross optimization algorithm. Proc CSEE 35(16):4077–4085

Research on Optimal Configuration of Energy Hub Considering System Flexibility

Xu Zhu, Ming Zhou, Zimo Xiang, Lijun Zhang, Yikai Sun and Gengyin Li

Abstract The energy hub with renewable energy integrated with cold, heat, electricity and gas can improve energy efficiency, demand side flexibility and environmental benefits. To deal with the fluctuation of net load and promote the accommodation of renewable energy, an optimal configuration scheme of energy hub considering system flexibility is presented. In this paper, the mathematical model of the energy hub structure considering the integrated demand response is firstly established. Then, the flexibility demand of the energy hub is obtained according to wind power output, photovoltaic output and load characteristic curves of typical days in different seasons. Meanwhile, two sets of flexibility indexes, system upward/downward flexibility supply and upward/downward system flexibility potential, are proposed. Furthermore, an optimal capacity configuration model of energy hub aimed at annual total cost consisting of economic cost, inadequate system flexibility penalty cost and environmental protection cost is established. In this model, the system flexibility adequacy constraints are introduced and integrated demand response is taken into account. Finally, different energy supply modes and demand response strategies under flexibility adequacy constraints are simulated and analyzed. The results show that the integrated demand response can significantly improve the economy of the configuration scenarios, and the proposed model can effectively improve the flexibility of the integrated energy system.

Keywords Energy hub · Optimal configuration · Power system flexibility · Integrated demand response

X. Zhu (✉) · M. Zhou · Z. Xiang · G. Li
State Key Laboratory of Alternate Electrical Power System with Renewable Energy Sources, North China Electric Power University, Changping District 102206, Beijing, China
e-mail: joyvix@yeah.net

L. Zhang · Y. Sun
State Grid Zhejiang Electric Power Economy and Technology Research Institute, Hangzhou 310008 Zhejiang Province, China

Y. Xue et al. (eds.), *Proceedings of PURPLE MOUNTAIN FORUM 2019-International Forum on Smart Grid Protection and Control*, Lecture Notes in Electrical Engineering 585, https://doi.org/10.1007/978-981-13-9783-7_19

1 Introduction

In recent years, energy shortage and environmental pollution have promoted the extensive development of renewable power generation. However, the uncertainty and volatility of net load lead to the increasing contradiction between the stable operation of power system and the absorption of renewable energy [1]. Therefore, the power system should have enough adjusting and responding ability, system flexibility, to deal with power fluctuation, otherwise it will cause problems such as load shedding, wind and light abandonment [1, 2]. In this context, system flexibility should be considered in planning to match the scale of renewable energy. At present, the research of incorporating flexibility into power system planning model is in its infancy. By quantifying the risk cost of insufficient flexibility, the energy storage capacity of active distribution network with flexibility, security and economy is optimized in [3].

Integrated energy system (IES) with multiple energy coupling and interconnection, such as electricity, natural gas, heat, cold and renewable energy, can enhance the flexibility, economic and environmental benefits of the system by exploiting the complementary potential of energy sources [4, 5]. The concept of energy hub (EH) is currently widely used in IES modeling, which can describe the conversion, allocation and storage processes among multiple energy sources in IES optimization planning and operation [5]. There are some achievements in EH optimal configuration research at current stage. Reference [6] takes reliability into account in EH optimal configuration to choose type and capacity of hub components, aiming at the lowest cost in planning period. Reference [7] divides the IES of electricity, gas, heat and cold into two layers, optimizes the lower structure of EH and solves the expansion scheme of the upper network.

Integrated demand response (IDR) extends the traditional demand response (DR) based on electricity price and incentive utilizing the multi-energy complementarity of IES [8]. Electricity load can be transferred in peak period by changing energy use mode, which can fully reduce the cost of EH operation and configuration. Reference [8] proposes an optimal operation model for commercial parks considering IDR of central air conditioning (AC) load, which reduces peak-valley difference of equivalent load, electricity purchase cost and total operation cost. Reference [9] extends the concepts of translatable load and transferable load to cooling/heating load, which 9 significantly improves the economy of EH configuration. Reference [10] establishes the architecture of IDR to build the EH model considering IDR, and summarizes the existing research of IDR in EH optimal operation and planning.

IDR mechanism in IES provides a new way to improve the flexibility of power system. However, the above research on IDR mainly focuses on the energy efficiency and economy improvement, which ignores the contribution of substitutable characteristics among loads to flexible regulation ability. In addition, the current study of EH optimal configuration only considers the economic and environmental costs, but overlooks insufficient flexibility problem caused by the fluctuation of net load.

To solve the above problems, typical structure of EH is firstly built in Sect. 2. Taken as a flexible resource, IDR is modeled to participate in system regulation and the indexes of system flexibility are put forward. Then aiming at improving system economy, flexibility and environmental protection, Sect. 3 establishes an EH optimal configuration model to minimum annual total cost, under the premise that system flexibility meets expectation. In Sect. 4, simulation examples are given and analysed to verify the effectiveness of the presented EH optimization model considering system flexibility. Finally, conclusions are drawn in Sect. 5.

2 EH, IDR and System Flexibility Modeling

2.1 EH Structure and Modeling

The typical EH structure considered is shown in Fig. 1. Its inputs include gas consumption, electricity purchasing from the grid, photovoltaic (PV) and wind power; there are three kinds of loads at the output side: electricity, heat and cooling load; the energy conversion equipment include combined cooling heating and power (CCHP) composed of combined heat and power (CHP) system and absorption refrigerator (AR), gas boiler (GB), heat pump (HP) and electric chiller (EC); the energy storage equipment consist of electricity storage (ES) and heat storage (HS).

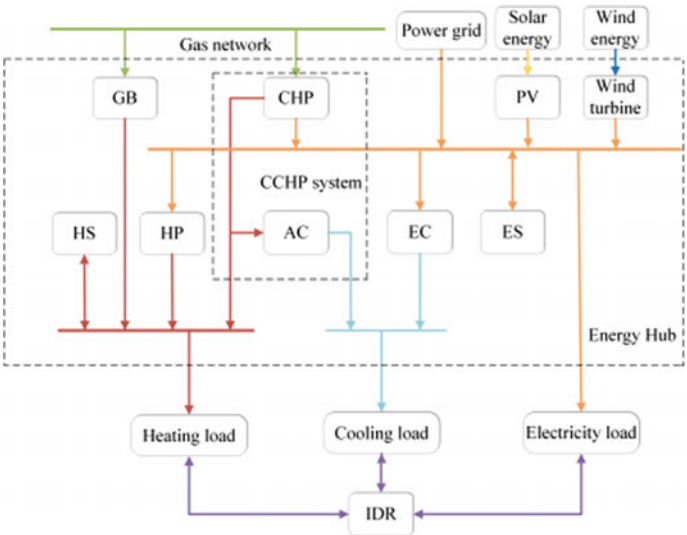

Fig. 1 Typical structure of an energy hub

Taking into account IDR, the power-form mathematical model of EH shown in Fig. 1 is established as follows:

$$\boldsymbol{L}_t = \boldsymbol{C}\boldsymbol{P}_t + \boldsymbol{M}_t \tag{1}$$

$$\begin{cases} \boldsymbol{L}_t = \left[L_{\mathrm{e},t} - C_t^{\mathrm{L}} - \Delta L_{\mathrm{e},t}^{\mathrm{IL}} - \Delta L_{\mathrm{e},t}^{\mathrm{AC}} - \Delta L_{\mathrm{e},t}^{\mathrm{WH}} L_{\mathrm{h},t} + \Delta L_{\mathrm{e},t}^{\mathrm{WH}} \eta_{\mathrm{WH}} L_{\mathrm{c},t} + \Delta L_{\mathrm{e},t}^{\mathrm{AC}} \eta_{\mathrm{AC}} \right]^{\mathrm{T}} \\ \boldsymbol{C} = \begin{bmatrix} (1 - v_{\mathrm{HP}} - v_{\mathrm{EC}})\eta_{\mathrm{T}} & v_{\mathrm{CHP}}\eta_{\mathrm{e}}^{\mathrm{CHP}} \\ v_{\mathrm{HP}}\eta_{\mathrm{T}}\eta_{\mathrm{HP}} & (1 - v_{\mathrm{CHP}})\eta_{\mathrm{GB}} + v_{\mathrm{CHP}}\eta_{\mathrm{h}}^{\mathrm{CHP}}(1 - v_{\mathrm{AR}}) \\ v_{\mathrm{EC}}\eta_{\mathrm{T}}\eta_{\mathrm{EC}} & v_{\mathrm{CHP}}\eta_{\mathrm{h}}^{\mathrm{CHP}} v_{\mathrm{AR}}\eta_{\mathrm{AR}} \end{bmatrix} \\ \boldsymbol{P}_t = \left[P_{\mathrm{e},t}^{\mathrm{buy}} + P_t^{\mathrm{PV}} - C_t^{\mathrm{PV}} + P_t^{\mathrm{wind}} - C_t^{\mathrm{wind}} P_{\mathrm{g},t} \right]^{\mathrm{T}} \\ \boldsymbol{M}_t = \left[P_{\mathrm{d},t}^{ES} - P_{\mathrm{c},t}^{ES} \; P_{\mathrm{d},t}^{HS} - P_{\mathrm{c},t}^{HS} 0 \right]^{\mathrm{T}} \end{cases} \tag{2}$$

where $\boldsymbol{L}_t$, $\boldsymbol{P}_t$ and $\boldsymbol{M}_t$ are the vector of equivalent load, input power and energy storage correction at time t. $\boldsymbol{C}$ is the coupling matrix. C_t^{L}, C_t^{PV} and C_t^{wind} are load, wind power and PV power curtailment. $\Delta L_{\mathrm{e},t}^{\mathrm{IL}}$, $\Delta L_{\mathrm{e},t}^{\mathrm{AC}}$ and $\Delta L_{\mathrm{e},t}^{\mathrm{WH}}$ are flexibility supply of interruptible load (IL), electricity-cooling load substitution (ECLS) and electricity-heating load substitution (EHLS). η_{AC} and η_{WH} are the energy efficiency ratio of AC and water heater. $P_{\mathrm{e},t}^{\mathrm{buy}}$, P_t^{PV}, P_t^{wind} and $P_{\mathrm{g},t}$ show the purchasing electric power, gas consumption rate, PV and wind power output. v_{HP}, v_{EC}, v_{CHP} and v_{AR} are the energy distribution coefficient of HP, EC, CHP and AR. η_{T}, η_{GB}, η_{HP}, η_{AR}, η_{EC}, $\eta_{\mathrm{e}}^{\mathrm{CHP}}$ and $\eta_{\mathrm{h}}^{\mathrm{CHP}}$ show the energy conversion efficiency of transformer, GB, HP, AR, EC, CHP electrical and thermal output. $P_{\mathrm{c},t}^{\mathrm{ES}}$ and $P_{\mathrm{d},t}^{\mathrm{ES}}$ are the charging and discharging power of ES. $P_{\mathrm{c},t}^{\mathrm{HS}}$ and $P_{\mathrm{d},t}^{\mathrm{HS}}$ represent the heat storing and releasing power of HS.

2.2 System Flexibility Demand and Indexes

System flexibility demand. The net load $P_{\mathrm{nl},t}$ is the difference between renewable power generation and electricity load of EH. System flexibility demand comes from the fluctuation of net load, which is expressed by the differential sequence $\Delta P_{\mathrm{nl,t}} = P_{\mathrm{nl},t+1} - P_{\mathrm{nl},t}$. The direction of net load change has two directions, which correspond to upward flexibility demand $I_{\mathrm{D},t}^{\mathrm{up}} = \max\{\Delta P_{\mathrm{nl},t}, 0\}$ and downward flexibility demand $I_{\mathrm{D},t}^{\mathrm{down}} = -\min\{\Delta P_{\mathrm{nl},t}, 0\}$, respectively. Using the flexibility demand in typical days, the flexibility demand threshold for the whole year is inferred as follows:

$$I_{\mathrm{D,lim}}^{d}=\left\{\max I_{\mathrm{D},t}^{d}\middle|\Pr\left(I_{\mathrm{D},\varepsilon}^{d}\le I_{\mathrm{D},t}^{d}\right)\le\frac{1+q}{2},t\in T_n\right\} \tag{3}$$

where $I_{\mathrm{D,lim}}^{d}$ is the corresponding flexibility demand threshold in the direction d of the quantile at a given confidence level q; $I_{D,\varepsilon}^{d}$ is the system flexibility demand in the direction d at any time ε; T_n is the total time series length of n typical days.

System flexibility supply. System flexibility supply reflects the actual flexibility supply of the system at time t within time scale Δt. The lack of upward flexibility leads to electricity load shedding, while insufficient downward flexibility causes light and wind abandonment. Therefore, system upward and downward flexibility supply $I_{\mathrm{S},t}^{\mathrm{up}}$ and $I_{\mathrm{S},t}^{\mathrm{down}}$ can be expressed as follows:

$$I_{\mathrm{S},t}^{\mathrm{up}}=I_{\mathrm{D},t}^{\mathrm{up}}-C_t^{\mathrm{L}},\ I_{\mathrm{S},t}^{\mathrm{down}}=I_{\mathrm{D},t}^{\mathrm{down}}-\left(C_t^{\mathrm{PV}}+C_t^{\mathrm{wind}}\right) \tag{4}$$

System flexibility potential. System flexibility potential is the sum of the maximum flexibility that can be provided by flexible resources at time t within time scale Δt. System flexibility potential mainly comes from "source-network-load-storage" four aspects of flexible resources, in particular to CHP, power grid, IDR and ES of EH, and it is also directional, which can be divided into system upward and downward flexibility potential $I_{\mathrm{P},t}^{\mathrm{up}}$ and $I_{\mathrm{P},t}^{\mathrm{down}}$. The upward and downward flexibility potential provided by CHP is as follows:

$$I_{\mathrm{PCHP},t}^{\mathrm{up}}=\min\left(r_{\max}^{\mathrm{CHP}}\Delta t,\mu_t^m C_{\mathrm{CHP}}\beta_{\mathrm{CHP}}^{\max}-P_{\mathrm{e},t}^{\mathrm{CHP}}\right),I_{\mathrm{PCHP},t}^{\mathrm{down}}=\min\left(r_{\max}^{\mathrm{CHP}}\Delta t,P_{\mathrm{e},t}^{\mathrm{CHP}}-\mu_t^m C_{\mathrm{CHP}}\beta_{\mathrm{CHP}}^{\min}\right) \tag{5}$$

where μ_t^m is 0–1 state variable, which indicates whether equipment m is put into operation. C_{CHP} is the installation capacity of CHP. $\beta_{\mathrm{CHP}}^{\min}$ and $\beta_{\mathrm{CHP}}^{\max}$ are the minimum and maximum load rate of CHP. $P_{\mathrm{e},t}^{\mathrm{CHP}}$ is the electric power output of CHP.

EH can obtain flexibility from power grid through tie-line, and its flexibility potential is limited by the transmission capacity and security fluctuation of tie lines. The upward and downward flexibility potential of power grid are shown as:

$$I_{\mathrm{PG},t}^{\mathrm{up}}=\min\left\{\Delta P_{\mathrm{e,max}}^{\mathrm{buy}},P_{\mathrm{e,max}}^{\mathrm{buy}}-P_{\mathrm{e},t}^{\mathrm{buy}}\right\},I_{\mathrm{PG},t}^{\mathrm{down}}=\min\left\{\Delta P_{\mathrm{e,max}}^{\mathrm{buy}},P_{\mathrm{e},t}^{\mathrm{buy}}\right\} \tag{6}$$

where $\Delta P_{\mathrm{e,max}}^{\mathrm{buy}}$ and $P_{\mathrm{e,max}}^{\mathrm{buy}}$ are the maximum fluctuation of tie-line power and the upper limit of purchasing power.

The first-order equivalent thermal parameter method is used to model the AC load $P_{\mathrm{e},t}^{\mathrm{AC}}$ with direct load control strategy [11] and hot water load $P_{\mathrm{e},t}^{\mathrm{WH}}$ is calculated by the model established in [12]. According to the flexible adjustment range of IDR, their flexibility potential can be obtained separately as follows.

$$I_{\mathrm{PAC},t}^{\mathrm{up}}=P_{e,t}^{\mathrm{AC}}-\Delta L_{\mathrm{e},t}^{\mathrm{AC}},\ I_{\mathrm{PAC},t}^{\mathrm{down}}=\Delta L_{\mathrm{e},t}^{\mathrm{AC}},\ I_{\mathrm{PWH},t}^{\mathrm{up}}=P_{\mathrm{e},t}^{\mathrm{WH}}-\Delta L_{\mathrm{e},t}^{\mathrm{WH}},\ I_{\mathrm{PWH},t}^{\mathrm{down}}=\Delta L_{\mathrm{e},t}^{\mathrm{WH}} \tag{7}$$

where $I_{\mathrm{PIL},t}^{\mathrm{up}}$, $I_{\mathrm{PAC},t}^{\mathrm{up}}$ and $I_{\mathrm{PWH},t}^{\mathrm{up}}$ are the upward flexibility potential of IL, ECLS and EHLS. $I_{\mathrm{PIL},t}^{\mathrm{down}}$, $I_{\mathrm{PAC},t}^{\mathrm{down}}$ and $I_{\mathrm{PWH},t}^{\mathrm{down}}$ are the downward flexibility potential of IL, ECLS and EHLS. $\Delta L_{\mathrm{e,max}}^{\mathrm{IL}}$ is the maximum interrupt capacity. k_{IL} is the proportion of the IL to the electricity load.

Due to the limit value and current power state of ES, upward and downward flexibility potential of ES $I_{\mathrm{PES},t}^{\mathrm{up}}$ and $I_{\mathrm{PES},t}^{\mathrm{down}}$ are expressed as follows:

$$I_{\mathrm{PES},t}^{\mathrm{up}}=\min\left(C_{\mathrm{ES}}\theta_{\mathrm{d}}^{\mathrm{ES}}-P_{\mathrm{d},t}^{\mathrm{ES}}+P_{\mathrm{c},t}^{\mathrm{ES}},\frac{(E_t^{\mathrm{ES}}-C_{\mathrm{ES}}\delta_{\mathrm{min}}^{\mathrm{ES}})\eta_{\mathrm{d}}^{\mathrm{ES}}}{\Delta t}-P_{\mathrm{d},t}^{\mathrm{ES}}+P_{\mathrm{c},t}^{\mathrm{ES}}\right) \tag{8}$$

$$I_{\mathrm{PES},t}^{\mathrm{down}}=\min\left(C_{\mathrm{ES}}\theta_{\mathrm{c}}^{\mathrm{ES}}-P_{\mathrm{c},t}^{\mathrm{ES}}+P_{\mathrm{d},t}^{\mathrm{ES}},\frac{C_{\mathrm{ES}}\delta_{\mathrm{max}}^{\mathrm{ES}}-E_t^{\mathrm{ES}}}{\eta_{\mathrm{c}}^{\mathrm{ES}}\Delta t}-P_{\mathrm{c},t}^{\mathrm{ES}}+P_{\mathrm{d},t}^{\mathrm{ES}}\right) \tag{9}$$

where C_{ES} and E_t^{ES} are the installation and storage capacity of ES. $P_{\mathrm{c},t}^{\mathrm{ES}}$, $\theta_{\mathrm{c}}^{\mathrm{ES}}$ and $\eta_{\mathrm{c}}^{\mathrm{ES}}$ are the charging power, rate and efficiency of ES. $P_{\mathrm{d},t}^{\mathrm{ES}}$, $\theta_{\mathrm{d}}^{\mathrm{ES}}$ and $\eta_{\mathrm{d}}^{\mathrm{ES}}$ are the discharging power, rate and efficiency of ES. $\delta_{\mathrm{min}}^{\mathrm{ES}}$ and $\delta_{\mathrm{max}}^{\mathrm{ES}}$ are the minimum and maximum storage rate of ES.

3 Optimal Configuration Model of EH Considering Flexibility

3.1 Objective Function

The optimal configuration model of EH aims to improve the system economy, flexibility and environmental protection. The objective function is to minimize the annual total cost consisting of economic cost F_{EC}, insufficient system flexibility penalty cost F_{ISF} and environmental protection cost F_{EP}.

Economy. The economic cost of system configuration is modeled by equivalent annual cost, including initial installation cost, energy use cost, equipment operation regulation cost and IDR regulation cost [9].

$$\begin{aligned}F_{\mathrm{EC}}=&\sum_m\omega_m C_m\alpha_m\frac{k(1+k)^{l_m}}{(1+k)^{l_m}-1}+\sum_n d_n\sum_t\left(\frac{1}{Q_{\mathrm{G}}}P_{\mathrm{g},t}\lambda_t^{\mathrm{G}}+P_{\mathrm{e},t}^{\mathrm{buy}}\lambda_t^{\mathrm{E}}\right)\Delta t\\&+\sum_n d_n\sum_t\sum_m P_t^m\xi_m+\sum_n d_n\sum_t\left(\lambda^{\mathrm{IL}}\Delta L_{\mathrm{e},t}^{\mathrm{IL}}+\lambda^{\mathrm{IDR}}\left(\Delta L_{\mathrm{e},t}^{\mathrm{AC}}+\Delta L_{\mathrm{e},t}^{\mathrm{WH}}\right)\right)\end{aligned} \tag{10}$$

where ω_m and C_m are the installation cost per unit capacity and installation capacity of equipment m. α_m and l_m are the conversion coefficient of annual equivalent investment and average life of equipment m. k is the discount rate. d_n is the number of typical day n. P_t^m and ξ_m are the output power and per unit output power cost of equipment m. λ^{IL} and λ^{IDR} are the load interruption and substitution cost per unit capacity. Q_{G} is the calorific value of natural gas. λ_t^{E} and λ_t^{G} are the price of natural gas and electricity.

Flexibility. According to the definition of system flexibility supply, its maximum is equivalent to the minimum of load shedding and renewable power generation limitation. In order to reflect system flexibility, F_{ISF} is shown as:

$$F_{\mathrm{ISF}}=\sum_n d_n \sum_t \left(\rho_{\mathrm{ISF,load}}^{\mathrm{up}} C_t^{\mathrm{L}}+\rho_{\mathrm{ISF,PV}}^{\mathrm{down}} C_t^{\mathrm{PV}}+\rho_{\mathrm{ISF,wind}}^{\mathrm{down}} C_t^{\mathrm{wind}}\right)\Delta t \tag{11}$$

where $\rho_{\mathrm{ISF,load}}^{\mathrm{up}}$, $\rho_{\mathrm{ISF,PV}}^{\mathrm{down}}$ and $\rho_{\mathrm{ISF,wind}}^{\mathrm{down}}$ are the penalty cost of load, wind power and PV per unit power curtailment, respectively.

Environmental protection. The pollution penalty brought by energy output is taken as the target of environmental protection, and the pollution caused by burning natural gas and coal-fired electricity from power grid are mainly considered.

$$F_{\mathrm{EP}}=\sum_n d_n \sum_t \left(P_{\mathrm{e},t}^{\mathrm{buy}}\varphi_{\mathrm{e}}+P_{\mathrm{e},t}^{\mathrm{CHP}}\varphi_{\mathrm{CHP}}+P_{\mathrm{h},t}^{\mathrm{GB}}\varphi_{\mathrm{GB}}\right)\Delta t,\quad \varphi_s=\sum_r D_r V_r \tag{12}$$

where $P_{\mathrm{h},t}^{\mathrm{GB}}$ is the thermal power output of GB. φ_{e}, φ_{CHP} and φ_{GB} are the pollution penalty of per unit energy purchasing from power grid, generated by CHP and GB. The main pollutants discharged from energy production are CO_2, NO, CO and SO_2 [13]. φ_s is the type s pollution penalty. D_r is the pollutant r emission of per unit energy output and V_r is the environmental value of pollutant r.

3.2 Constraints

Power balance constraints. The electrical, thermal and cold power balance in EH is the input-output power relationship shown as (1)–(2) above.

Equipment investment constraint.

$$\gamma_m C_m^{\min}\le C_m\le \gamma_m C_m^{\max} \tag{13}$$

where γ_m is 0–1 state variable, which indicates whether equipment m is installed. $C_m^{\min}$ and $C_m^{\max}$ are the lower and upper limits of installation capacity.

Equipment operation constraints.
Energy conversion equipment operation constrain.

$$\mu_t^m C_m \beta_{\min}^m \le P_t^m \le \mu_t^m C_m \beta_{\max}^m,\ \left|P_{t+1}^m - P_t^m\right| \le r_{\max}^m \Delta t \tag{14}$$

where $\beta_{\min}^m$ and $\beta_{\max}^m$ are the minimum and maximum load rate of equipment m.$r_{\max}^m$ is the maximum climbing rate of equipment m.

Energy storage equipment operation constraints. The power and capacity constraints combined with the relationship between energy and power of energy storage equipment are shown as:

$$\begin{cases} 0 \le P_{c,t}^m \le \psi_{c,t}^m, C_m \theta_c^m 0 \le P_{d,t}^m \le \psi_{d,t}^m C_m \theta_d^m, 0 \le \psi_{c,t}^m + \psi_{d,t}^m \le 1 \\ E_{t+1}^m = (1-\tau_m) E_t^m + \left(P_{c,t+1}^m \eta_c^m - \frac{P_{d,t+1}^m}{\eta_d^m}\right)\Delta t \\ C_m \delta_{\min}^m \le E_t^m \le C_m \delta_{\max}^m,\ E_0^m = E_T^m \end{cases} \tag{15}$$

where $P_{c,t}^m$ and $P_{d,t}^m$ are storing and releasing power of energy storage equipment m. $\psi_{c,t}^m$ and $\psi_{d,t}^m$ are 0–1 state variables, which indicate whether equipment m is storing. θ_c^m and θ_d^m are storing and releasing rate of equipment m. E_t^m and τ_m are the storage capacity and self-loss rate of equipment m. η_c^m and η_d^m are the storing and releasing efficiency of equipment m. $\delta_m^{\min}$ and $\delta_m^{\max}$ are the minimum and maximum storage rate of equipment m. E_0^m and E_T^m are the initial and terminal energy of the cycle.

IDR constraints.

$$0 \le \Delta L_{e,t}^{IL} \le \min\left\{\Delta L_{e,\max}^{IL}, k_{IL} L_{e,t}\right\} \tag{16}$$

$$0 \le \Delta L_{e,t}^{AC} \le P_{e,t}^{AC},\ T_{\max}^{in} \le T_t^{in} \le T_{\min}^{in},\ 0 \le \Delta L_{e,t}^{WH} \le P_{e,t}^{WH},\ T_{\max}^{w} \le T_t^{w} \le T_{\min}^{w} \tag{17}$$

where T_t^{in} is the indoor temperature and $\left[T_{\min}^{in}, T_{\max}^{in}\right]$ is its interval range. T_t^{w} is the temperature of hot water and it is controlled in the interval range $\left[T_{\min}^{w}, T_{\max}^{w}\right]$.

System flexibility adequacy constraints. To achieve a certain degree of system flexibility adequacy, system flexibility potential should be no less than system flexibility demand at the confidence level q at any time t.

$$I_{P,t}^{up} \ge I_{N,\lim}^{up},\ I_{P,t}^{down} \ge I_{N,\lim}^{down} \tag{18}$$

Energy distribution coefficient constraints.

$$0 \le v_c \le 1, \sum_c v_c = 1 \tag{19}$$

where v_c is the energy distribution coefficient of energy conversion equipment c.
Tie lines constraints.

$$0 \le P_{g,t} \le P_{g,\max}, 0 \le P_{e,t}^{buy} \le P_{e,\max}^{buy}, \left| P_{e,t+1}^{buy} - P_{e,t}^{buy} \right| \le \Delta P_{e,\max}^{buy} \tag{20}$$

where $P_{g,\max}$ is the upper limit of gas consumption rate.

3.3 Model Solution

The model established in this paper is a two-level programming problem. The outer level decides the configuration capacity of equipments, and the inner level is the optimal operation of typical days. To improve the solution efficiency of the mixed integer nonlinear optimization model, the constraints containing the product of binary variables and continuous variables are linearized according to the method in [9]. Finally, the proposed model is solved by CPLEX Optimizer based on YALMIP platform in MATLAB environment.

4 Case Study and Discussion

4.1 Basic Data

Taking a demonstration park in Jiangsu Province as an example, the system structure is shown in Fig. 1. The technical parameters of energy conversion and storage equipment of EH are listed in Tables 1 and 2. The storing and releasing rate of energy storage equipment are both 0.25. The minimum and maximum storage rate of them are 0.2 and 0.8. The value standard of pollutants and its emission from energy output are cited from [13]. Based on the local climatic characteristics, the whole year can be divided into winter (December-March), summer (June-September) and transition season (April-May, September-October). The electricity, heating and cooling loads of three typical days are shown in Fig. 2a. The PV and wind power output in the park are shown in Fig. 2b, c respectively. The time interval is 15 min, and the day is divided into 96 periods. Time-of-use tariff is taken from [8]. The price of natural gas is 2.75 yuan/m^3, and the low calorific value of natural gas is 9.7 kWh/m^3. The penalty costs of load shedding, PV and wind power

Table 1 The parameters of energy conversion equipment

Equipment	Efficiency	Installation cost	Operation regulation cost	Load rate	Life
CHP	0.35/0.5 (Elec./Th.)	4800 (yuan/kW)	0.015 (yuan/kW)	0.2–1	25 (a)
HP	3.5	2500 (yuan/kW)	0.004 (yuan/kW)	0.1–1	20 (a)
EC	3.2	1000 (yuan/kW)	0.001 (yuan/kW)	0.1–1	15 (a)
GB	0.85	800 (yuan/kW)	0.001 (yuan/kW)	0.26–1	20 (a)
AR	0.8	1200 (yuan/kW)	0.002 (yuan/kW)	0.05–1	30 (a)

Table 2 The parameters of energy storage equipment

Equipment	Efficiency	Installation cost	Operation regulation cost	Self-loss rate	Life
ES	0.95	900 (yuan/kWh)	0.003 (yuan/kW)	0.002	8 (a)
HS	0.9	720 (yuan/kWh)	0.002 (yuan/kW)	0.005	10 (a)

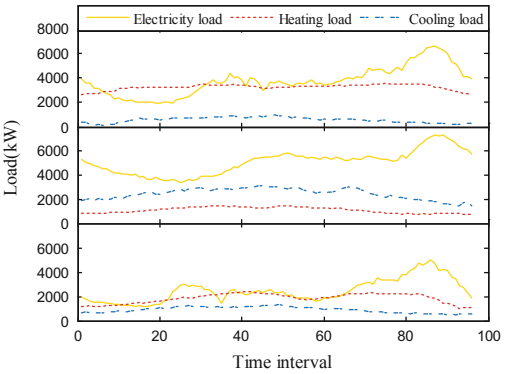

(a) Loads of typical days

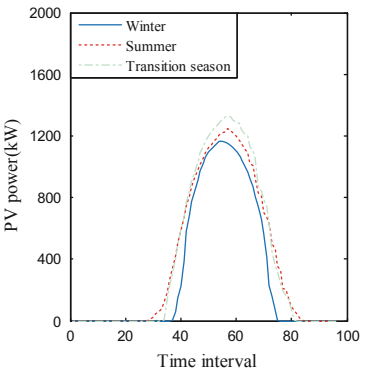

(b) PV power of typical days

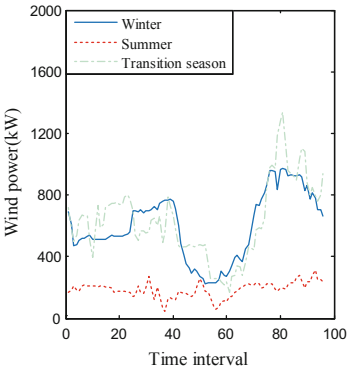

(c) Wind power of typical days

Fig. 2 Loads, PV and wind power of typical days

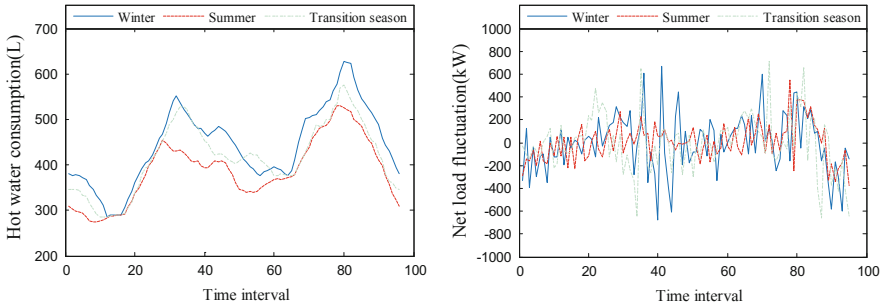

(a) Hot water consumption of typical days (b) Net load fluctuation of EH

Fig. 3 Hot water consumption and net load fluctuation of typical days

curtailment are 50 yuan/kWh, 20 yuan/kWh and 12 yuan/kWh. The maximum proportion of load shedding, PV and wind power curtailment are 7, 20 and 20%, respectively.

The unit capacity compensation cost of load interruption and substitution are 0.4 yuan and 0.5 yuan. The maximum proportion of IL is 3%, and its upper limit is 100 kW. The rated power, energy efficiency ratio and temperature control interval of AC are 0.82 kW, 3 and [24,28]°C, respectively. The control cycle of AC is 7 periods, and 280 ACs divided into 7 groups participate IDR in the period [29,92] of summer.

The hot water consumption of typical days is shown in Fig. 3a. The temperature control interval of hot water is [45,55]°C, and cold water temperature is 10 °C. The efficiency of water heater is 0.95, and the specific heat capacity of water is 4.187 kJ/kg °C. According to the net load fluctuation of EH shown in Fig. 3b, system flexibility demand can be obtained. Under the confidence level, the upward and downward flexibility demand thresholds are 445.7242 and 422.4026 kW, respectively.

4.2 Optimal Configuration Results Analysis

To verify the validity of the proposed model, four Cases are set up: Case 1 is the traditional energy supply system with the electricity from power grid, heating by GB, cooling by EC, and without flexibility constraints. Case 2, Case 3 and Case 4 are CCHP systems under the confidence level q = 95%. Case 2 is the basic example without considering IDR. Only IL is taken into account in Case 3, while IL, ECLS and EHLS are considered in Case 4. Optimal configuration capacity and costs of EH are listed in Tables 3 and 4, and the final confidence level of system flexibility in Case 1 is 74.16%.

As can be seen from the results, compared with Case 2, the initial investment and operation adjustment costs are lower in Case 1, but the energy use cost in Case 1 is

Table 3 Optimal configuration capacity of EH

Equipment	Case 1	Case 2	Case 3	Case 4
CHP (kW)	0	3906.89	3772.11	3653.19
HP (kW)	0	2094.89	2088.89	1857.52
EC (kW)	3139.20	1178.62	1026.32	985.36
GB (kW)	3535.47	337.07	329.35	315.74
AR (kW)	0	3069.31	3057.60	2837.32
ES (kWh)	0	1178.24	802.74	652.81
HS (kWh)	0	9891.52	9840.92	8102.07

Table 4 Costs of configuration schemes

Cost	Case 1	Case 2	Case 3	Case 4
Initial installation cost (¥ Million)	0.8062	3.6427	3.5371	3.2192
Operation regulation cost (¥ Million)	0.0424	2.2325	2.2199	2.2085
Energy use cost (¥ Million)	28.2843	19.5824	19.4532	19.2064
Insufficient flexibility penalty cost (¥ Million)	7.7918	1.5203	1.3646	0.2432
Environmental cost (¥ Million)	3.3435	0.8975	0.8941	0.8903
Annual total cost (¥ Million)	40.2682	27.8754	27.4689	25.7676

much higher. Although the confidence level of flexibility is reduced by 20.84%, the insufficient flexibility penalty cost and environmental cost are still higher. It proves that the complementarity of multi-energy in EH can improve the energy efficiency, system flexibility and environmental protection.

On the basis of Case 2, Case 3 and Case 4 take into account the regulation effect of IDR, which reduces the configuration capacity and energy use cost. This is because the electricity load decreases during peak period by IDR. Under the same confidence level of flexibility, insufficient flexibility penalty cost is decreases obviously in Case 4, which illustrates IDR can provide flexibility for the system. In addition, due to the decline of energy use, the environmental benefits is improved in both Case 3 and Case 4. Introducing ECLS and EHLS, the initial installation cost in Case 4 is 8.99% lower than that in Case 3, and insufficient flexibility penalty cost is reduced by 82.18%.

4.3 System Flexibility of Typical Days Analysis

Taking Case 3 as an example, according to the operation optimization results in the inner level of the model, system flexibility of typical days is analyzed. The load shedding and new energy power limitation of typical days can be obtained as shown in Fig. 5a, b. The centralized periods of insufficient system flexibility are 8:30–11:30, 17:30–21:00 and 22:00–24:00, which are consistent with the time of rapid

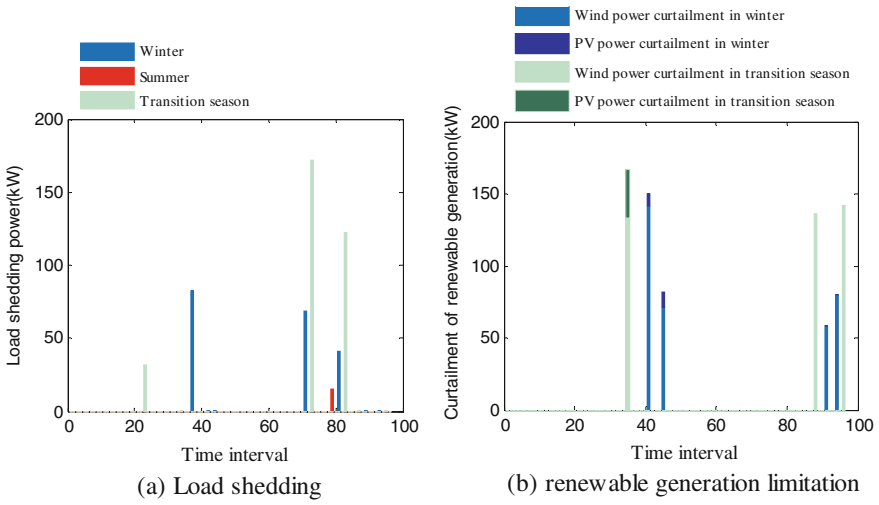

Fig. 5 Load shedding and renewable generation limitation

changing net load. The highest insufficient system flexibility can be 172.11 kW in the transition season, and it occurs most frequently in winter, reaching 2.43%.

The presented flexibility indexes in two directions of typical days are shown in Figs. 6 and 7, respectively. In Fig. 6, the optimization objective of flexibility is to punish load and renewable power curtailment, so the system will try to provide more flexibility, but not exceed the flexibility demand of the current system. In Fig. 7, the system flexibility potential is the maximum flexibility provided by the system of current state. Due to the limitation of regulation scope, the increase of upward flexibility potential will generally lead to the decrease of the downward flexibility potential and vice versa. Because of the system flexibility constraints, their minimum values are flexibility demand thresholds. The maximum system upward and downward flexibility potential are 667.6 and 654.3 kW, respectively.

Fig. 6 System flexibility supply of EH

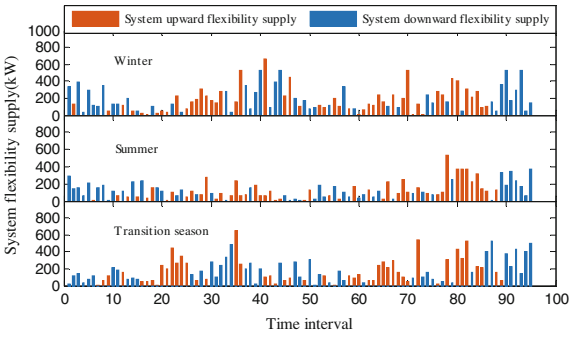

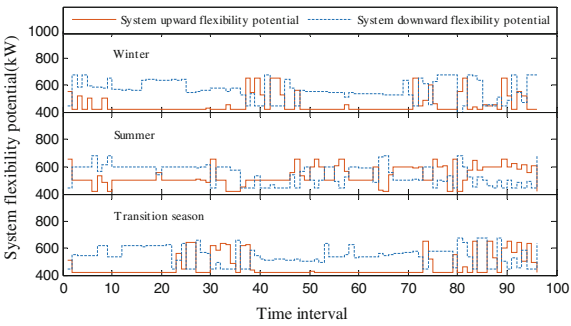

Fig. 7 System flexibility potential of EH

5 Conclusion

In this paper, an optimal configuration model of EH is proposed, which takes into account IDR and system flexibility. The following conclusions are drawn from the simulation analysis of cases:

Compared with the traditional independent energy supply mode, the CCHP system improves the economy, flexibility and environmental benefits of configuration.

By introducing IDR composed of IL, ECLS and EHLS, system flexibility can be improved. In addition, IDR has an effect on reducing the configuration costs of EH, and enhances the environmental protection by reducing energy use.

The two sets of indexes, system flexibility supply and system flexibility potential can effectively reflect the flexibility of the current system. In the process of optimal configuration of EH, considering system flexibility constraints can help decision makers achieve the optimal comprehensive benefits while meeting the expected flexibility level of the system. More flexible resources can be introduced and the presented indexes can be applied to power network planning in the following research.

References

1. Wang Q, Hodge B (2017) Enhancing power system operational flexibility with flexible ramping products: a review. IEEE Trans Industr Inf 13(4):1652–1664
2. Lu Z, Li H, Qiao Y (2016) Power system flexibility planning and challenges considering high proportion of renewable energy. Autom Electr Power Syst 40(13):147–158
3. Wen F, Li H, Wen H, Liu W (2019) Planning for energy storage system considering risk of inadequate flexibility in active distribution network. Power System Technology. https://doi.org/10.13335/j.1000-3673.pst.2018.2528, last accessed 2019/04/10
4. Dong S, Wang C, Xu S, Zhang L, Cha H, Liang J (2018) Day-ahead optimal scheduling of electric-gas-thermal integrated energy system considering network dynamic characteristics. Autom Electr Power Syst 42(13):12–19

5. Liu F, Mou L, Zhang T, Zhu T (2018) Modeling and optimization of multi-energy coupling hub in micro-energy network. Autom Electr Power Syst 42(14):91–98
6. Dolatabadi A, Mohammadi-ivatloo B, Abapour M, Tohidi S (2017) Optimal stochastic design of wind integrated energy hub. IEEE Trans Industr Inf 13(5):2379–2388
7. Huang W, Zhang N, Dong R, Liu Y, Kang C (2018) Coordinated planning of multiple energy networks and energy hubs. Proc CSEE 38(18):5425–5437
8. Guo Z, Li G, Zhou M, Li Z (2018) Optimal operation of energy hub in business park considering integrated demand response. Power Syst Technol 42(08):2439–2448
9. Cui P, Shi J, Wen F et al (2017) Optimal energy hub configuration considering integrated demand response. Electr Power Autom Equip 37(6):101–109
10. Xu Z, Sun H, Guo Q (2018) Review and prospect of integrated demand response. Proc CSEE 38(24):7194–7205
11. Song M, Gao C, Su W (2016) Modeling and controlling of air-conditioning load for demand response applications. Autom Electr Power Syst 40(14):158–167
12. Song Y, Wang Y, Yi J (2018) Microgrid energy source optimization planning considering demand side response and thermo-electrical coupling. Power Syst Technol 42(11):3469–3476
13. Zhou C (2018) Optimal planning and operation of district integrated energy system. South China University of Technology

Design and Evaluation of Primary Frequency Modulation Control Strategy for Wind-Storage Combined System

Junhui Li, Yunbao Ma, Gang Mu, Jun Qi, Zheshen Zhang, Dacheng Hu and Jiajun Zou

Abstract Due to its own volatility and intermittentness, wind power has increased the burden on the power system after the grid connection, which has a serious impact on its safe operation. Considering the parallel and serial control strategy adopted by traditional-wind storage system, and taking into account the economy and the effect of primary frequency modulation, this paper puts forward an optimal control strategy for comprehensive utilization of energy storage system (ESS). Finally, a comprehensive evaluation method for the energy storage system to participate in the primary frequency modulation of the power grid is proposed. And in the current domestic frequency modulation market, the evaluation method is used to verify that the optimal control strategy has the best frequency modulation performance.

Keywords Wind power · Energy storage system (ESS) · Optimization control strategy · Comprehensive evaluation

J. Li (✉) · G. Mu · Z. Zhang · D. Hu
Key Laboratory of Modern Power System Simulation and Control & Renewable Energy Technology, Ministry of Education (Northeast Electric Power University), Jilin 132012, China
e-mail: lijunhui@neepu.edu.cn

Y. Ma
State Grid Shandong Electric Power Company, Zaozhuang Power Supply Company, Shandong, Zaozhuang 277100, China

J. Qi
Hohhot Power Supply Bureau, State Grid Inner Mongolia Electric Power Company Limited, Hohhot 010020, China

J. Zou
Jilin Province Electric Power Company of National Grid, Changchun 130000, China

Y. Xue et al. (eds.), *Proceedings of PURPLE MOUNTAIN FORUM 2019-International Forum on Smart Grid Protection and Control*, Lecture Notes in Electrical Engineering 585, https://doi.org/10.1007/978-981-13-9783-7_20

1 Introduction

By the end of 2018, China's wind power installed capacity has reached 221 million kilowatts [1–3], and China has become a major wind energy utilization country. Because of its own volatility, intermittent and other characteristics [3–6], wind power will increase the burden of frequency modulation after it is connected to the grid. And overburdened frequency modulation may lead to power system collapse [7, 8]. In order to meet the current demand of power system frequency modulation, some researchers had carried out research on the frequency modulation control of wind and energy storage systems.

At the research level of increasing the frequency modulation capability of wind turbines: In [9, 10], based on the zero inertia characteristics of wind turbines, the load reduction control strategy of wind turbines was proposed. By reducing the load capacity of wind turbines, the reserve capacity of frequency modulation system was increased. In [11, 12], they proposed a sub-optimal power curve tracking method for wind turbines based on the problem of insufficient frequency backup capability of wind turbines.

The energy storage system has the characteristics of high power density and fast response [13, 14], which provides a new solution for primary frequency modulation of power systems.

At the level of energy storage system and wind power coordinated control participating in grid frequency modulation, in [15, 16], considering the high cost of energy storage system, they proposed that energy storage system and wind turbine adopt hierarchical coordinated control to take part in frequency modulation. In [17], considering the response speed of energy storage system, the frequency division control method is proposed for energy storage system and wind turbine. In [18, 19], considering the energy storage system and the wind turbine's frequency modulation capability, they proposed the control strategy of the energy storage system to compensate the wind power inertia.

The above literatures don't consider how the energy-wind power are distributed after the frequency modulation command was issued. Therefore, a combination of serial and parallel optimization control strategies is proposed. And the effectiveness of the control strategy is verified by simulation. Then, a comprehensive evaluation method for the wind-energy system to participate in the primary frequency modulation is proposed. In the current domestic frequency modulation market, it is verified that the proposed optimal control strategy has the best score.

2 Mathematical Model Construction

The primary frequency modulation resources of power system are modeled separately. The primary frequency modulation model of hydropower and thermal power participating in power system adopts the classical model [20, 21], which is commonly used now. The model of wind turbine and energy storage system are as follows.

2.1 Wind Turbine Model

The transfer function of virtual inertial control is as follows

$$G(s) = \frac{\Delta P_{wind1}}{\Delta f} = -\frac{k_{vd}s}{1 + T_{wind1}s} \tag{1}$$

k_{vd} is the virtual inertial response coefficient and usually takes the value of 8; T_{wind1} is an inertial response time constant and usually takes the value of 0.1 s.

The transfer function of pitch control is as follows

$$G(s) = \frac{\Delta P_{wind2}}{\Delta f} = -\frac{k_{change}}{1 + T_{wind2}s} \tag{2}$$

K_{change} is a primary frequency modulation coefficient, usually with a value of 20; T_{wind2} is the pitch time constant, 3 s.

The wind turbine virtual frequency response transfer function is as follows:

$$G_w(s) = -\frac{(k_{vd}T_{wind2})s^2 + (k_{change}T_{wind1} + k_{vd})s + k_{change}}{1 + (T_{wind2} + T_{wind1})s + T_{wind2}T_{wind1}s^2} \tag{3}$$

2.2 Energy Storage System Model

The transfer function model of energy storage system is established.

$$G_w(s) = \frac{\Delta P_{Energy}(s)}{\Delta f(s)} = -\frac{k_{vd}s + k_{change}}{T_{Energy}s + 1} \tag{4}$$

T_{Energy} is the response time of energy storage system, 0.3 s.

3 Control Strategy Design

According to the principle of "who pollutes, who governs" in the power grid. The specific allocation is as follows

$$\Delta P_{tra} = (1 - p) * P_{all} \tag{5}$$

$$\Delta P_{w+e} = p * P_{all} \tag{6}$$

ΔP_{w+e} is the frequency modulation instruction that the wind-storage system should respond to; p is the proportion of wind power installed, 0.2; P_{all} is the general regulation instruction for the power system.

3.1 Control Strategy of Wind-Storage System

(1) Target Function Construction

Combining with the traditional serial and parallel control strategies, this paper proposes an optimal control method. The objective function of the optimal control mode is as follow

$$\min[C_1 \times (\Delta f_{dev} + \Delta f_{sta}) + C_3 \times S] \tag{7}$$

C_1 is the penalty factor of primary frequency modulation technical index, 0.5; C_3 is penalty factor for energy storage cost, 0.5; Δf_{dev} is the maximum frequency deviation of the power system, Hz; is the steady-state frequency deviation of the power system, Hz; Δf_{sta} $S$is the cost coefficient under different control strategies of the energy storage system.

K is the frequency allocation proportion of the energy storage system using serial control strategy in the optimization strategy; t_0 is the time when the control mode changes the proportion.

The schematic diagram of optimal control strategy is shown in Fig. 1.

When the optimal control strategy is adopted in the wind storage system, the total output of the combined system is as follows.

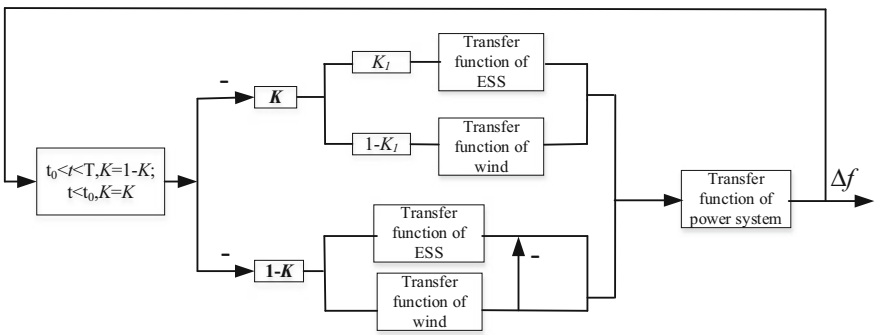

Fig. 1 Schematic diagram of optimal control strategy for wind storage system

$$t \le t_0 \begin{cases} \Delta P_{t<t_0} = \Delta P_{chu1} + \Delta P_{bin1} \\ \Delta P_{chu1} = \Delta P_{echu1} + \Delta P_{wchu1} \\ \Delta P_{bin1} = \Delta P_{ebin1} + \Delta P_{wbin1} \\ \Delta P_{echu1} = \Delta P_{w+e}(1-K) - \Delta P_{wchu1} \\ \Delta P_{wbin1} = \Delta P_{w+e} \times K \times (1-K_1) \\ \Delta P_{ebin1} = \Delta P_{w+e} \times K \times K_1 \\ \Delta P_{wchu1} = \Delta P_{vir-ine1} + \Delta P_{change-\beta 1} \end{cases} \tag{8}$$

In the period of $0 < t < t_0$, ΔP_{chu1} is the serial output status of the combined wind storage system under the optimal control strategy, MW; ΔP_{bin1} is the parallel output of the combined wind storage system under the optimal control strategy, MW; ΔP_{wchu1} is the serial output of wind turbines under the optimal control strategy, MW. When $t > t_0$, K and $1 - K$ exchange positions.

(2) Setting Control Parameters

The control variable method is used to calculate K and t_0. The flow chart of K value calculation is shown in Fig. 2.

According to the calculation process, K and t_0 are calculated. The results show that when $K = 0.5$ and $t_0 = 4.5$, the frequency deviation and cost are the smallest.

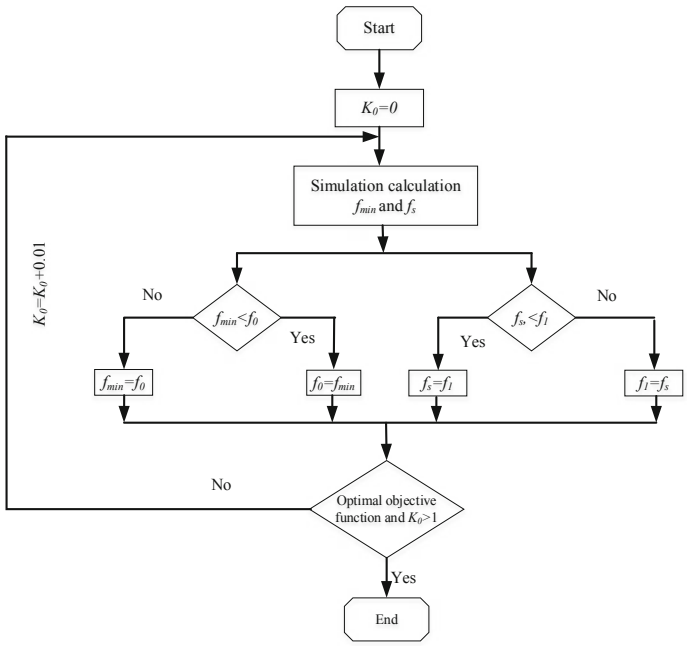

Fig. 2 Flow chart for optimizing control strategy parameters

3.2 Capacity Requirement Analysis of ESS

3.2.1 Energy Storage System Configuration Constraints

At any time t, the *SOC* calculation formula of energy storage system is as follows.

$$SOC_t = SOC_{t-T} + \frac{\int_{t_1}^{t} P_e dt}{E} \tag{9)}$$

$$SOC_{\min} \leq SOC \leq SOC_{\max} \tag{10}$$

t_1 is the starting time of energy storage, s; E is the rated capacity of energy storage system, MWh. $SOC_{\min}$ is the lower limit of energy storage system operation, 0.05; $SOC_{\max}$ is the upper limit of energy storage system operation, 0.95.

Considering the constraints of P_{wind} in the actual operation of the energy storage system, the specific constraints are as follows.

$$P_{wind1} \leq P_e \leq P_{wind2} \tag{11}$$

P_{wind1} is the lower limit of adjustable output of wind power, MW; $P_{\max}$ is the upper limit of adjustable output of wind power, MW.

3.2.2 Energy Storage System Configuration Process and Results

The configuration process of rated power and capacity of energy storage system is shown in Fig. 3.

The final configuration results of the energy storage system under different control strategies are shown in Table 1.

4 Evaluation of Primary Frequency Modulation Effect

4.1 Evaluation System

The specific evaluation method is as follows.

$$G = \left(\sum_{i=1}^{n} g_i * D_i\right) \Big/ n \tag{13}$$

G is the overall frequency modulation effect score; N is the number of factors influencing the score of frequency modulation effect; D_i is the weight coefficient of

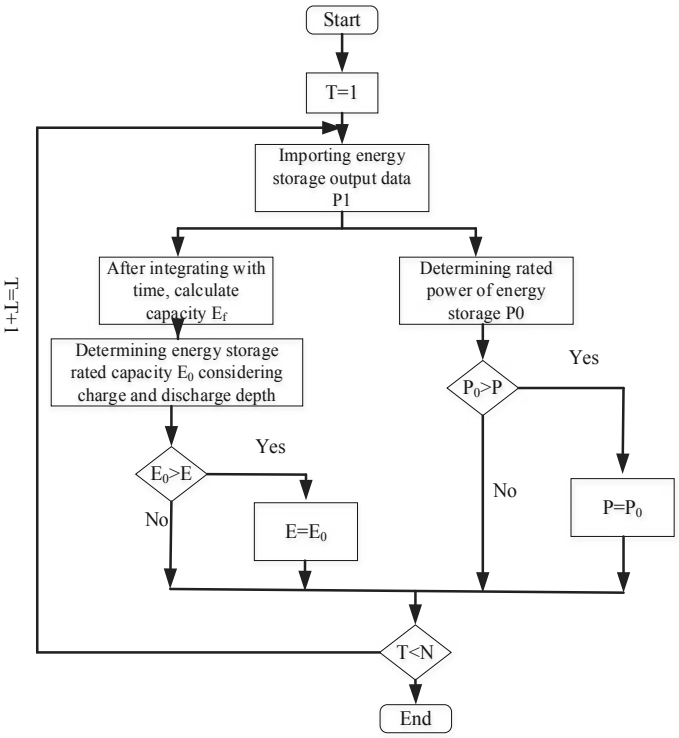

Fig. 3 Flow chart of capacity allocation for ESS

Table 1 Energy storage capacity allocation results under different control strategies

Control strategy	Rated power (MW)	Rated capacity (MWh)
Serial control	4.84	0.524
Parallel control	6.54	1.062
Optimize control	5.84	0.636

the *i*th influencing factor; g_i is the score of single frequency modulation influencing factor.

The maximum frequency deviation score G_{dev} of power system is shown as follows.

$$G_{dev} = \frac{\Delta f_{dev} - f_{dev-xia}}{f_{dev-sha} - f_{dev-xia}} * (G_{dev-sha} - G_{dev-xia}) + G_{dev-xia} \tag{14}$$

$f_{dev-xia}$ is the lower limit of frequency in the interval of Δf_{dev}; $f_{dev-sha}$ is the upper limit of frequency in the interval of Δf_{dev}; $G_{dev-sha}$ is the upper limit of scoring in the interval of Δf_{dev}; $G_{dev-xia}$ is the lower limit of scoring in the interval of Δf_{dev}.

The steady-state frequency deviation score G_{sta} of power system is shown as follows.

$$G_{sta} = \frac{\Delta f_{sta} - f_{sta-xia}}{f_{sta-sha} - f_{sta-xia}} * (G_{sta-sha} - G_{sta-xia}) + G_{sta-xia} \tag{15}$$

Frequency modulation economy score G under different control strategies is shown as follows.

$$G_{eco} = \frac{P_{fre-cb}}{P_{fre-sy}} * (G_{eco-sha} - G_{eco-xia}) + G_{eco-xia} \tag{16}$$

P_{fre-cb} is the cost of energy storage participating in primary frequency modulation; P_{fre-sy} is the benefit of energy storage participating in primary frequency modulation.

5 Simulation Analysis

Based on the above description, a power system primary frequency modulation simulation model is established in MATLAB/Simulink (R2014b). Specific parameters are as follows: the load is 1000 MW, the rated power of wind farm is 200 MW, and the load disturbance is 100 MW (0.1 p.u).

5.1 Simulation Results Under Different Control Strategies

Firstly, the frequency drop of power system with and without wind storage system is analyzed. The simulation results are as Fig. 4.

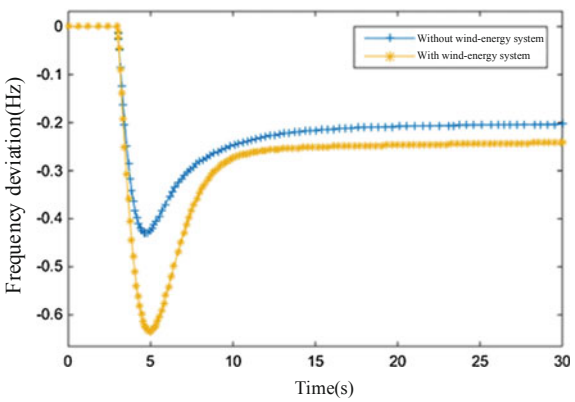

Fig. 4 Frequency regulation results with/without wind power and ESS

Table 2 Frequency deviation with/without wind power and ESS

Data type	Maximum deviation (Hz)	Steady deviation (Hz)
Wih wind-storage system	−0.425	−0.205
Wihout wind-storage system	−0.647	−0.249

The simulation results are shown in Table 2.

The output of frequency modulation resources under different control strategies is simulated and analyzed.

(A) Energy Storage System Output

The simulation results are shown in Fig. 5.

After the start-up of traditional frequency modulation resources, Under parallel control, the output of energy storage system is stable at 0.019 p.u. under serial control, the output of energy storage system is basically zero. Under optimal control, the output of energy storage system is stable at 0.0037 p.u.

(B) Wind Farm Output

The simulation results of wind power under different control strategies are shown in Fig. 6.

In serial control, wind power is the main reserve resource of wind storage system, and the maximum output of wind power is 0.02 p.u. In parallel control, the output of wind power and energy storage system is 0.015 p.u. Under the optimal control strategy, the output of wind turbine is 0.0197 p.u.

The frequency simulation results are shown in Fig. 7.

Under different control strategies, the lowest frequency and steady-state frequency deviation of primary frequency modulation in power system are shown in Table 3.

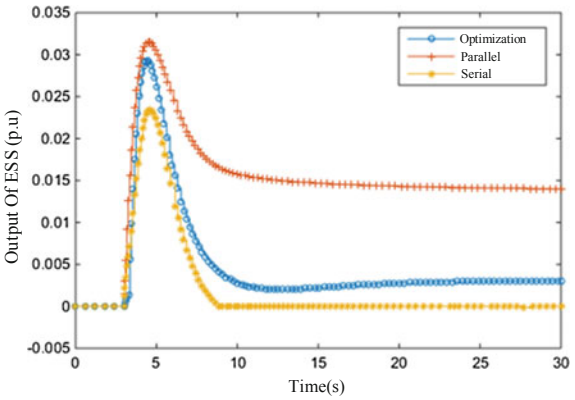

Fig. 5 Comparison of energy storage capacity under different control strategies

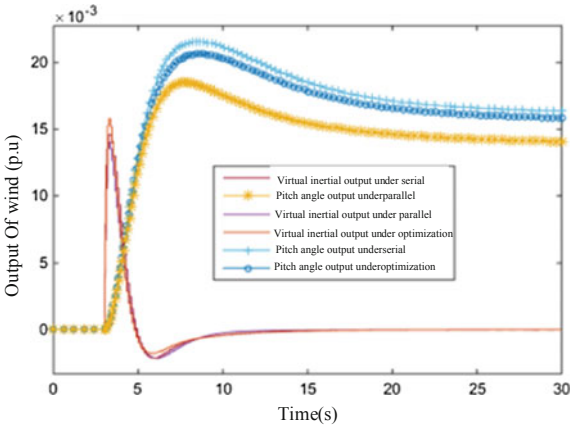

Fig. 6 Comparison of wind power under different control strategies

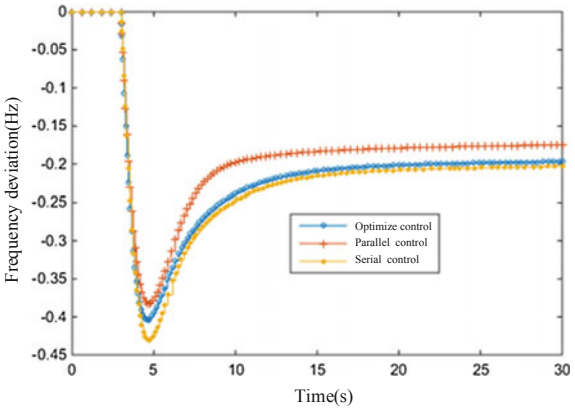

Fig. 7 Comparison of frequency regulation effect under different control strategies

Table 3 Frequency deviation under different control strategies

Control strategy	Maximum deviation (Hz)	Steady deviation (Hz)
Serial control	−0.442	−0.241
Parallel control	−0.387	−0.187
Optimize control	−0.401	−0.205

Current sources of revenue from battery energy storage can be divided into two parts. At first, the benefits of recycling and reusing non-ferrous metals in lithium batteries after the use of lithium batteries [22, 23]. The above simulation results are evaluated comprehensively according to the evaluation method in Sect. 3. The evaluation results are shown in Table 4.

Table 4 Scoring table for different control strategies

Control strategy	Lowest frequency score	Frequency steady score	Cost score	Total score
Parallel control	7.2	10	4.255	6.427
Optimize control	7.05	9.75	5.92	7.122
Serial control	5.95	9.35	5.59	6.72

6 Conclusion

The main work of this paper is as follows.

The frequency modulation effect of different control strategies under the same disturbance is simulated by the Simulink. The results show that the maximum frequency deviation is reduced by 0.044 Hz and the steady-state frequency deviation is reduced by 0.041 Hz compared with the serial control strategy. Compared with parallel control strategy, the power demand of energy storage system is reduced by 0.7 MW and the capacity demand is reduced by 0.462 MWh.

Through the proposed evaluation method, the frequency modulation effect under different control strategies is analyzed. The results show that the comprehensive score of optimal control strategy for wind storage system is 7.122. Its score is higher than 6.72 points of serial control and 6.427 points of parallel control. The scoring results show that the optimal control strategy of wind storage system participating in primary frequency modulation of power grid can give good consideration to the primary frequency modulation effect and the economy of frequency modulation.

Acknowledgements Supported by the National Natural Science Foundation of China (U1766204) special fund for industrial innovation of Jilin Province Development and Reform Commission (2017C017-2).

References

1. Jin H, Sun H, Niu T et al Robust unit combination considering uncertainty of wind power and high-load load dispatching. Autom Electr Power Syst 1–8
2. Yan G, Zhao W, Zhang L (2018) Research on integrated control of deloading frequency regulation for variable speed and variable pitch angle wind turbines. J Northeast Electr Power Univ 38(05):1–8
3. Shen G, Li C, Xu B et al (2018) Economic allocation for energy storage system considering wind power. J Northeast Electr Power Univ 38(04):27–34
4. Yu N, Li T (2017) Optimal scheduling of virtual power plant considering wind power uncertainty. J Northeast Electr Power Univ 37(05):14–18

5. Li S, Tang H, Deng C et al (2019) Wind power penetration limit calculation considering frequency constraints and frequency modulation of wind turbines. Autom Electr Power Syst 43(04):33–43
6. Xu Z, Chen Y, Yue S et al (2018) Retrospect and prospect of research on frequency regulation technology of power system by wind power. Power Syst Technol 42(06):1793–1803
7. Li J, Feng X, Yan G et al (2018) Survey on frequency regulation technology in high wind penetration power system. Power Syst Prot Control 2:163–170
8. Li X, Huang J, Chen Y et al (2016) Review on large-scale involvement of energy storage in power grid fast frequency regulation. Power Syst Prot Control 44(7):145–153
9. Xing P, Shi Q, Wang G et al (2018) Response characteristics and mechanism analysis about virtual inertia control of wind generators. High Voltage Eng 44(04):1302–1310
10. Sun Y, Li Z, Liu D et al (2018) An optimization control strategy for intelligent UFLS using dynamically aggregated controllable loads. Proc CSEE 38(7)
11. Bian X, Jiang Y, Zhao Y et al (2018) Coordination frequency modulation strategy of windwood and load in high permeability renewable energy microgrid. Autom Electr Power Syst 42(15):102–109 + 209–214
12. Tan Y, Meegahapola L, Muttaqi KM (2016) A suboptimal power-point-tracking-based primary frequency response strategy for DFIGs in hybrid remote area power supply systems. IEEE Trans Energy Convers 31(1):93–105
13. Wu J, Lu Z, Qiao Y et al (2018) Optimal operation of wind farm with hybrid storage devices considering efficiency characteristics of dynamic charging and discharging. Autom Electr Power Syst (11):41–47 + 101
14. Li J, Ma H, Yuan X et al (2017) Overview on key applied technologies of large-scale distributed energy storage. Power Syst Technol 41(10):3365–3375
15. Cehn Z, Jing Z, Chen D (2018) Analysis of pricing mechanism of FM ancillary service market in the United States. Autom Electr Power Syst 42(12):1–10
16. Sun B, Tang Y, Ye L et al Integrated frequency control strategy for wind power cluster with multiple temporal-spatial scale coordination based on H-DMPC. Proc CSEE 1–13
17. Hu Z, Xie X, Zhang F et al (2014) Research on automatic generation control strategy incorporating energy storage resources. Proc CSEE 34(29):5080–5087
18. Yan G, Wang Y, Zhong C et al (2016) Frequency control strategy for wind storage combined system. Electr Power Constr 37(12):55–60
19. Zheng Z, Yang Z, Li W (2017) Analysis and comparison of primary frequency control technology for wind power and thermal power unit. Electr Power Autom Equip 37(12): 92–101
20. Yu N, Li Z (2017) Optimal dispatching of virtual power plants considering wind power uncertainty. J Northeast Electr Power Univ 37(05):14–18
21. Kundur P (2001) Power system stability and control. China Electric Power Press
22. Chen D, Zhang L, Wang L (2016) Control strategy of energy system for frequency regulation and evaluation of investment income. Mod Electr Power 33(1):80–86 (in Chinese)
23. Li J, Xu Z, Ji Z et al An overview on the current technologies of recycling spent lithium-ion batteries. Chin J Rare Metals 1–11

Optimization of Multi-energy Storage Configurations for Regional Integrated Energy Systems

Xuan Xia, Ran Tao and Dongmei Zhao

Abstract The configurations of multi-energy storage devices in the regional integrated energy system (RIES) can greatly improve the economic benefits of the system and it is an important research direction of RIES planning. However, at present the research on the optimization of electric/thermal/gas multi-energy storage configuration in RIES is insufficient. Under this background, the method to deploy the rated capacity and power of multi-energy storage systems for RIES containing power to gas (P2G) device was proposed in this paper. Bi-level optimization model was established in the purpose of considering the interaction between the configuration and operation of the multi-energy storage systems at the same time. The upper level was optimized for configuration, and the lower level was optimized for operation. By the Kuhn–Tucker approach, the bi-level problem was transformed into a single level optimization problem that can be solved with Gurobi optimizer. Finally, the correctness of the proposed model was verified by an example.

Keywords Regional integrated energy system · Multi-energy storage systems · Bi-level optimization model · Configurations

1 Introduction

1.1 Background and Aim

With the development of the Energy Internet and increased connection of energy sources such as electricity, gas and heat, the clean and efficient use of energy has gradually become the focus of attention, and the integrated energy system (IES) has emerged as the times require [1, 2]. The RIES is a typical Energy Internet based on multi-energy complementary structure and multi-energy network coordination as the core of scheduling [3]. The electricity sectors and heat sectors are interconnected by

X. Xia (✉) · R. Tao · D. Zhao
North China Electric Power University, Changping District 102206, Beijing, China
e-mail: ncepu_xiaxuan@163.com

Y. Xue et al. (eds.), *Proceedings of PURPLE MOUNTAIN FORUM 2019-International Forum on Smart Grid Protection and Control*, Lecture Notes in Electrical Engineering 585, https://doi.org/10.1007/978-981-13-9783-7_21

technologies such as combined heat and power (CHP), electric heat pump (HP), and electric boiler (EB), and it has been recently recognized as a prominent example for creating add-on values for both sectors [4, 5]. In recent years, the mature P2G technology has enhanced the integration between power-gas networks, providing new ideas for the consumption of new energy in RIES. The "Implementation Opinions on Promoting the Construction of Multi-energy Complementary Integration Optimization Demonstration Project" issued by the National Energy Administration [6] also pointed out that "energy complementarity and coordinated supply should be realized through electric heating triple supply and distributed renewable energy".

Therefore, the research on RIES has important practical significance, while the overall optimization of equipment capacity and operation strategy in IES is the basis for efficient, economical and reliable operation of the system.

1.2 Literature Review and Contributions

The research of RIES planning is mainly divided into two categories [7]: (1) The structure of RIES is known to optimize the capacity or model of the system equipment; (2) optimizing the system structure and capacity or model of the RIES Simultaneously. Energy storage systems has played an important role in improving the operation efficiency and reducing the costs of RIES, but in the first type of planning, research on configuration of the energy storage system is currently relatively rare [8, 9]. Most of the research on energy storage is based on battery models, while less research involves thermal storage and gas storage systems [10]. Reference [11–13] use electric/thermal energy storage systems to increase the wind power consumption rate of the system.P2G and gas energy storage are adopted in multi-source microgrid to improve its economics in [14, 15]. Reference [16] optimizes the configuration of energy storage equipment in the IES by a bi-level planning approach, but does not involve the gas storage system. None of the researches above proposed configuration model of electric-gas-thermal energy systems. Mutual influence between electric/thermal/gas energy storages is studied in [17], and the conclusion that multi-energy systems have the optimal economics is obtained, however, the capacity of the energy storage equipment has a certain impact on the above conclusion, which is lack of further discusses.

In general, there are many studies on IES planning with electric and thermal loads as terminal loads. However, the load demand in RIES is diversified, and the gas load is gradually becoming an indispensable energy demand, but the research on IES planning with electric/thermal/gas loads as terminal loads is insufficient. In this paper, the method to deploy the rated capacity and power of multi-energy storage systems for RIES in off-grid/grid-connected mode with electric/thermal/gas loads as terminal loads is proposed. For this purpose, a bi-level planning approach is considered to model the interaction between the configuration and operation of

the multi-energy storage systems at the same time. The model is transformed to a single level problem by the Kuhn–Tucker approach.

1.3 Paper Organization

The remaining sections of this paper are as follow:

In Sect. 2 the short description of the RIES structure is presented. The bi-level optimization model for RIES is introduced in Sect. 3. Case studies and result analyses are illustrated in Sect. 4. At last, summary and conclusions are denoted in Sect. 5.

2 The RIES Structure

Typical RIES generally contain multiple forms of energy, such as electricity, gas, heat, etc. The RIES structure studied in this paper is shown in Fig. 1, consisting of photovoltaic (PV), wind turbine (WT), CHP, EB, P2G, gas boiler (GB), bromine cooler (BC), electrical energy storage (EES), thermal energy storage (TES), gas energy storage (GES), electrical loads, heat loads, gas loads and others.

The mathematical models of the main equipment involved in the RIES studied in this paper (such as CHP, P2G, EB, etc.) are referred to references [11, 14, 17]. It will not be repeated in this paper due to space limitations.

According to the energy balance relationship of each device in the RIES in Fig. 1, the energy flow model of the RIES can be described in the following matrix form:

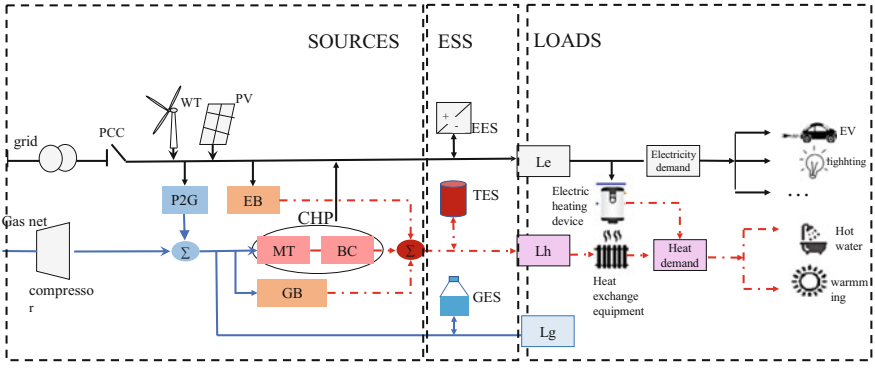

Fig. 1 The RIES structure

$$\begin{bmatrix} L_{\mathrm{e}}(t) \\ L_{\mathrm{h}}(t) \\ L_{\mathrm{g}}(t) \end{bmatrix} = \begin{bmatrix} \beta_{\mathrm{PV}}(t) & \beta_{\mathrm{WT}}(t) & 1 & -1 & -1 & 0 \\ 0 & 0 & \frac{\eta_r(1-\eta_{\mathrm{MT}}-\eta_{\mathrm{L}})C_0}{\eta_{\mathrm{MT}}} & \eta_{\mathrm{EB}} & 0 & \eta_{\mathrm{GB}} \\ 0 & 0 & 1/\eta_{\mathrm{MT}} & 0 & \eta_{\mathrm{P2G}} & 1/\eta_{\mathrm{GB}} \end{bmatrix} \begin{bmatrix} P_{\mathrm{PV}}(t) \\ P_{\mathrm{WT}}(t) \\ P_{\mathrm{MT}}(t) \\ P_{\mathrm{EB}}(t) \\ P_{\mathrm{P2G}}(t) \\ P_{\mathrm{GB}}(t) \end{bmatrix} + \begin{bmatrix} uP_{\mathrm{e}}(t) \\ 0 \\ P_{\mathrm{g}}(t) \end{bmatrix} + \begin{bmatrix} P_{\mathrm{e,dis}}(t) \\ P_{\mathrm{h,dis}}(t) \\ P_{\mathrm{g,dis}}(t) \end{bmatrix} - \begin{bmatrix} P_{\mathrm{e,ch}}(t) \\ P_{\mathrm{h,ch}}(t) \\ P_{\mathrm{g,ch}}(t) \end{bmatrix} \tag{1}$$

where $L_e(t)$, $L_h(t)$, $L_g(t)$ is the electrical loads, heat loads, gas loads at time t; $P_{\mathrm{WT}}(t)$, $P_{\mathrm{PV}}(t)$, $P_{\mathrm{MT}}(t)$, $P_{\mathrm{EB}}(t)$, $P_{\mathrm{P2G}}(t)$, $P_{\mathrm{GB}}(t)$ is the power of WT, PV, MT, EB, P2G, GB at time t; $P_{\mathrm{e}}(t)$, $P_{\mathrm{g}}(t)$ is interaction power with the grid, Natural gas network at time t; u is the 0–1 variable,1 represent the grid-connected mode, 0 represent the off-grid mode; $P_{\mathrm{e,ch}}(t)$, $P_{\mathrm{h,ch}}(t)$, $P_{\mathrm{g,ch}}(t)$ is the charge power of electrical, thermal, gas energy storage at time t; $P_{\mathrm{e,dis}}(t)$, $P_{\mathrm{h,dis}}(t)$, $P_{\mathrm{g,dis}}(t)$ is discharge power of electrical, thermal, gas energy storage at time t; $\beta_{\mathrm{PV}}(t)$, $\beta_{\mathrm{WT}}(t)$ is the PV, WT utilization rate at time t; η_{MT}, η_{L} is the efficiency and heat loss rate of MT; C_{O}, η_{r} is the heating coefficient and smoke recovery rate; η_{P2G}, η_{EB}, η_{GB}, is the efficiency of P2G, EB, GB.

3 Multi-energy Storage Configuration Model

3.1 Bi-level Planning Approach

In this paper, bi-level optimization model is established in the purpose of considering the interaction between the configuration and operation of the multi-energy storage systems at the same time. The upper level is optimized for configuration, and the lower level is optimized for operation. The two levels have their own objectives and constraints. Correspondingly, there are also two classes of decision vectors, namely, leader's (upper level) decision vectors and follower's (lower level) decision vectors. The bi-level optimization mathematical model is referred to [16].

3.2 Upper Level Optimization Model

According to the RIES structure shown in Fig. 1, the decision vectors of the upper level optimization model are electrical/thermal/gas energy storage capacity and power, and the objective function is the lowest total cost. The upper level optimization mathematical model is:

$$\begin{cases} C_{\text{total}} = C_{\text{investment}} + C_{\text{operation}} \\ \quad C_{\text{investment}} = C_{\text{investment}} = \sum_i \left(C_{E,i}E_i + C_{P,i}P_i\right) \frac{r_0(1+r_0)^{Y_i}}{365((1+r_0)^{Y_i}-1)} \\ \text{s.}t. \\ \quad E_{i,\min} \le E_i \le E_{i,\max} \\ \quad P_{i,\min} \le P_i \le P_{i,\max} \end{cases} \tag{3}$$

where C_{total} is the total cost, consisting of the daily average investment cost of the energy storage system $C_{\text{investment}}$ and the daily operation and maintenance cost $C_{\text{operation}}$, which reflects the impact of system operation on the energy storage configuration. $C_{\text{operation}}$ is the lower level optimization objective function, which is transmitted from the lower level optimization. It is the key variable connecting the upper and lower levels, while it is related to the energy storage configuration and the system operation at the same time. Subscript i denote the types of energy storage (electric, heat, gas); $C_{E,i}$, $C_{P,i}$ is the unit capacity and unit power installation cost of energy storage; Y_i is the life of energy storage; r_0 is the annual depreciation rate. Constraints are energy storage capacity and power installation limits. E_{i}, P_{i} is the decision vectors; $E_{i,\max}$, $E_{i,\min}$, $P_{i,\max}$, $P_{i,\min}$ is upper and lower limits of energy storage capacity and power installation.

3.3 Lower Level Optimization Model

On the basis of the upper level optimization, the lower level optimizes the system operation problem. The power of electric/thermal/gas energy storage system, CHP, EB, and P2G are the lower level optimization decision variables, and the objective function is the total operating cost of the RIES, including gas cost, unit start-stop cost, maintenance cost, and penalty cost, so the lower level optimization problem is essentially a system power allocation optimization problem. The lower level optimization mathematical model is:

$$
\begin{cases}
\min\ C_{\text{operation}} = \sum_{t=1}^{T} \left(C_{\text{buy}}(t) + C_{\text{st}}(t) + C_{\text{mt}}(t) + C_{\text{cut}}(t)\right)\Delta t \\
C_{\text{buy}}(t) = uC_{\text{e}}P_e(t) + C_{\text{g}}P_g(t) \ + \ \varepsilon C_{\text{CO}_2}P_{\text{P2G}}(t)\eta_{\text{P2G}} \\
C_{\text{st}}(t) = \max\{0, U_{\text{EB}}(t) - U_{\text{EB}}(t-1)\}C_{\text{st,EB}} + \ \max\{0, U_{\text{MT}}(t) - U_{\text{MT}}(t-1)\}C_{\text{st,MT}} \\
\qquad + \ \max\{0, U_{\text{GB}}(t) - U_{\text{GB}}(t-1)\}C_{\text{st,GB}} \\
C_{\text{mt}}(t) = C_{\text{PV}}P_{\text{PV}}(t) + C_{\text{WT}}P_{\text{WT}}(t) + C_{\text{MT}}P_{\text{MT}}(t) + \ C_{GB}P_{GB}(t) + C_{\text{EB}}P_{\text{EB}}(t) \\
\qquad + C_{\text{P2G}}P_{\text{P2G}}(t) + \ \sum_i C_{s,i}\left|P_{i,\text{ch}}(t) - P_{i,\text{dis}}(t)\right| \\
C_{\text{cut}}(t) = C_{\text{cut}}P_{\text{WT}}(t)(1 - \beta_{\text{WT}}(t)) + P_{PV}(t)(1 - \beta_{\text{PV}}(t)) \\
s.t. \\
\quad \text{equation (1)} \\
P_{\text{emin}} \le P_{\text{e}}(t) \le P_{\text{emax}} \\
P_{\text{emin}} \le P_{\text{g}}(t) \le P_{\text{emax}} \\
a = \begin{cases} P_{\text{MT min}} \le P_{\text{MT}}(t) \le P_{\text{MT max}} \\ P_{\text{GB min}} \le P_{\text{GB}}(t) \le P_{\text{GB max}} \\ P_{\text{EB min}} \le P_{\text{EB}}(t) \le P_{\text{EB max}} \\ P_{\text{P2G min}} \le P_{\text{P2G}}(t) \le P_{\text{P2G max}} \end{cases} \quad , b = \begin{cases} \Delta P_{\text{MT,down}} \le \Delta P_{\text{MT}}(t) \le \Delta P_{\text{MT,up}} \\ \Delta P_{\text{GB,down}} \le \Delta P_{\text{GB}}(t) \le \Delta P_{\text{GB,up}} \\ \Delta P_{\text{EB,down}} \le P_{\text{EB}}(t) \le \Delta P_{\text{EB,up}} \end{cases} \\
c = \begin{cases} \xi_{\text{e min}}E_{\text{e}} \le E_{\text{EES}}(t) \le \xi_{\text{e max}}E_{\text{e}} \\ \xi_{\text{e min}}E_{\text{h}} \le H_{\text{TES}}(t) \le \xi_{\text{h max}}E_{\text{h}} \\ \xi_{g\,\text{min}}E_{\text{g}} \le G_{\text{GES}}(t) \le \xi_{g\,\text{max}}E_g \end{cases} \quad , d = \begin{cases} u_{\text{i,ch}}(t)P_{i\,\text{min}} \le P_{i,\text{ch}}(t) \le u_{i,\text{ch}}(t)P_i \\ u_{i,dis}(t)P_{i\ \text{min}} \le P_{i,\text{dis}}(t) \le u_{i,dis}(t)P_{\text{i}} \\ u_{i,\text{ch}}(t) + u_{i,dis}(t) \le 1 \end{cases} \\
\sum_{t=1}^{T} (2 - \beta_{\text{WT}}(t) - \beta_{\text{PV}}(t)) \le \beta_{\text{n}}
\end{cases}
\tag{4}
$$

where $C_{\text{buy}}(t)$, $C_{\text{st}}(t)$, $C_{\text{mt}}(t)$, $C_{\text{cut}}(t)$ is the interaction cost with grid and natural gas network, start-stop cost, maintenance cost and abandonment cost; T is the total number of daily scheduling periods, and Δt is the unit scheduling time; C_{e}, C_{g} is the electricity and natural gas prices; ε, C_{CO2} is the CO_2 coefficient required to generate unit natural gas, CO_2 price; $C_{\text{st,EB}}$, $C_{\text{st,MT}}$, $C_{\text{st,GB}}$ is the EB, MT, GB start-up costs. U_{EB}(t), U_{MT}(t), U_{GB}(t) is the EB, MT, GB start and stop status at time t; C_{MT}, C_{PV}, C_{WT}, C_{GB}, C_{EB}, C_{P2G}, $C_{\text{s},i}$ is the unit power maintenance cost of MT, PV, WT, GB, EB, P2G, energy storage systems; C_{cut} is the unit abandonment cost of PV and WT; P_{emax}, P_{emin} is the upper and lower limits of the interaction power between the RIES and the distribution network; P_{gmax}, P_{gmin} is the upper and lower limits of the interaction power between the RIES and the natural gas network; a-class constraint is the upper and lower limit of the power, P_{MTmax}, P_{MTmin}, P_{GBmax}, P_{GBmin}, P_{EBmax}, P_{EBmin}, P_{P2Gmax}, P_{P2Gmin} is the upper and lower limits of MT, GB, EB, P2G power; b-class constraint is a climbing constraint, $\Delta P_{\text{MT,down}}$, $\Delta P_{\text{MT,up}}$, $\Delta P_{\text{GB,down}}$, $\Delta P_{\text{GB,up}}$, $\Delta P_{\text{EB,down}}$, $\Delta P_{\text{EB,up}}$ is the up and down climbing rate of the MT, GB, EB. c-class constraint is the energy storage equipment capacity constraint, $E_{\text{EES}}(t)$, $H_{\text{TES}}(t)$, $G_{\text{GES}}(t)$ is the remaining energy of the electricity, heat, gas storage energy at time t; ξ_{emax}, ξ_{emin}, ξ_{hmax}, ξ_{hmin}, ξ_{gmax}, ξ_{gmin} is the upper and lower limits of the

electric, thermal, gas energy storage equipment remaining energy, for the purpose of extending the life of energy storage equipment; β_n is the constraint of abandonment rate.

3.4 Model Solving

The purpose of constructing the bi-level model is to combine the configuration and optimization of two different time scales, and to find the global optimal solution through the upper and lower level iterations. The classical algorithm for solving the bi-level optimization model is to convert the bi-level into a single-level standard optimization [18]. When the lower level problem is convex and sufficiently regular, it is possible to replace the lower level optimization problem with its Karush–Kuhn–Tucker (KKT) conditions. The KKT conditions appear as Lagrangian and complementarity constraints, and reduce the overall bi-level optimization problem to a single-level constrained optimization problem [19]. Analysis of the established bi-level model shows that the lower level optimization problem is convex continuous and differentiable, and can replace the lower level optimization problem with its KKT condition. The single-level model obtained after transformation is:

$$\max \quad -C_{\text{total}} = -(C_{\text{investment}} + C_{\text{operation}}) \tag{5}$$

$$\begin{aligned} &\text{s.}t. \\ &E_{i,\min} \le E_i \le E_{i,\max} \\ &P_{i,\min} \le P_i \le P_{i,\max} \end{aligned} \tag{6}$$

$$\begin{aligned} &\sum_{j=1}^{m} \lambda_j + \sum_{k}^{n} \mu_k \nabla_x h_k\left(P_g, P_s, P_l\right) = c_x, x = P_g, P_s, P_l \\ &g_j(P_g, P_s, P_l) = 0,\ j = 1, \ldots, m \\ &h_k(P_g, P_s, P_l) \le 0,\ k = 1, \ldots, n \\ &\mu_k \ge 0 \\ &\mu_k h_k(P_g, P_s, P_l) = 0,\ k = 1, \ldots, n \end{aligned} \tag{7}$$

where

$$P_g = \{P_{\text{PV}}, P_{\text{WT}}, P_{\text{MT}}, P_{\text{EB}}, P_{\text{P2G}}, P_{GB}\}, P_s = \left\{P_{i,ch}, P_{i,dis}\right\}, P_l = \left\{L_e, L_h, L_g\right\} \tag{8}$$

The single-level model obtained after transformation belongs to the mixed integer programming linear programming problem. In the Matlab software, the Yalmip toolbox is used to model the model, and the Gurobi [20] solver is called to solve the model. The test platform solved by this model is: Intel Core i7-4710HQ 2.5 GHz CPU; 16 GB memory; software version: Matlab R2016b; Yalmip R20180926; Gurobi 8.1.

4 Case Study

This paper makes some changes based on the examples shown in reference [14, 17], the typical winter day is selected for analysis to verify the correctness of the configuration method. The operating parameters of the equipment in the RIES are shown in Table 1. The decision vector parameters of the energy storage systems are shown in Table 2. The electricity, heat, gas loads and wind, photovoltaic power forecast are shown in Fig. 2. Other parameters, such as C_{MT}, C_{PV}, C_{WT}, etc. are referred to references [14, 17].

In order to compare and analyze the impact of energy storage system and P2G on the RIES, four cases are set in this paper. case1: there is no P2G in the RIES on the off-grid mode; case2: there is P2G in the RIES on the off-grid mode; case 3: there are no energy storage systems in the RIES on the grid-connected mode; there are energy storage systems in the RIES on the grid-connected mode. The result is as follows: the energy storage system configuration scheme is shown in Table 3; the output of each device in case 2 is shown in Fig. 3a; the output of the energy storage equipment in case 4 is shown in Fig. 3b.

As shown in the Table 3, the battery configuration capacity and the total cost in case 2 is dropped significantly compared with case 1, where there is no P2G equipment in the RIES, and the total cost is reduced from 3071.28 to 2448 yuan, down 20.28%, while the abandoned wind rate is 0 compared with 8.47% in case 1. The reason is that there is P2G equipment in case 2, which can convert abandoned wind into natural gas, reducing the cost of abandoned wind and selling natural gas to bring benefits to the system at the same time. It can be seen from Fig. 3a, where P2G works in the period when the wind power is high, electric load is low conversely.

As shown in the Table 3, the battery configuration capacity and the total cost in case 4 is dropped significantly compared with case 3, where there is no energy storage equipment in the RIES, and the total cost is reduced from 3943.97 to 1905.63 yuan, down 51.43%, while the abandoned wind rate is 0 compared with 11.25% in case 3. Obviously, the configurations of multi-energy storage devices in the RIES can greatly improve the economic benefits of the system, improving its

Table 1 Operating parameters of the equipment in the RIES

Type	Power lower limit/kW	Power upper limit/kW	Lower climbing rate/(kW h)	Upper climbing rate/(kW h)	Unit maintenance cost (yuan/kW)
MT	40	180	5	15	0.025
EB	0	100	12	12	0.016
GB	0	100	11	11	0.012
P2G	0	100			0.021
WT	0	400			0.0196
PV	0	250			0.0235

Table 2 The decision vector parameters

Type	Efficiency	Self-release rate	Unit capacity cost (yuan/kW h)	Unit power cost (yuan/kW)	Unit maintenance cost (yuan/kW)	Life/year
EES	0.9	0.001	1000	200	0.0018	10
TES	0.88	0.01	150	30	0.0017	10
GES	0.9	0.1	130	300	0.0015	20

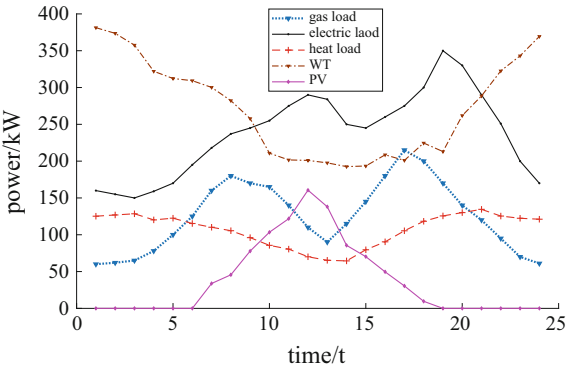

Fig. 2 The electricity, heat, gas loads and wind, photovoltaic power forecast

Table 3 The energy storage system configuration scheme

	EES configuration scheme		TES configuration scheme		GES configuration scheme		Total cost/yuan	Abandoned wind rate/%
	Capacity/kW h	Power/kW	Capacity/kW h	Power/kW	Capacity/kW h	Power/kW		
Case1	889.31	114.48	304.25	80.41	333.91	97.37	3071.28	8.47
Case2	445.12	188.58	145.94	34.70	377.71	71.19	2448.91	0
Case3	1014.20	254.43	407.22	43.46	301.98	41.98	3943.97	11.25
Case4	436.91	141.92	178.22	36.19	218.93	86.70	1905.63	0

ability to accept wind power Simultaneously. As shown in the Fig. 3b, electric/thermal/gas storage systems work in the peak stage of the corresponding load, indicating that under the premise that the overall demand is meted by the various energy storage devices, the storage capacity is mainly optimized according to the changes of the corresponding load. In multi-energy storage mode, the amount of electricity stored in the storage device can be sold to the main network during the peak price period for greater profit. At the same time, the heat storage equipment and the gas storage equipment make the system more capable of coping with the

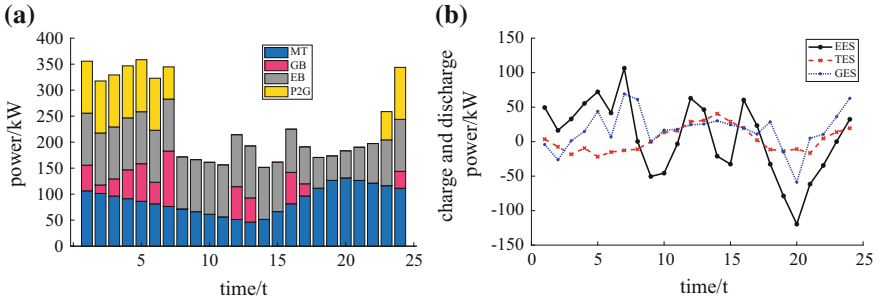

Fig. 3 **a** The output of each device in case 2; **b** The output of the energy storage equipment in case 4

peak value of gas and heat load, and the number of starts of the EB is also reduced, resulting in a reduction in starting cost. It can be seen that in the multi-energy storage mode, the energy storage equipment works together to optimize the storage output and optimize the system cost under the premise of meeting the system load requirements.

5 Conclusion

In this paper, the method to deploy the rated capacity and power of multi-energy storage systems for RIES in off-grid/grid-connected mode with electric/thermal/gas loads as terminal loads is proposed. A bi-level planning approach is considered to model the interaction between the configuration and operation of the multi-energy storage systems, the upper level is optimized for configuration, and the lower level is optimized for operation. By the KKT condition, the bi-level model is converted into a single-level mixed integer programming linear programming problem, which is solved by Gurobi optimizer. The example compares the total system configuration cost and the abandonment rate in different cases, and draws the following conclusions:

(1) P2G can reduce the configuration capacity and power of the energy storage system in the RIES, improving the ability of the RIES to accept wind power, and greatly improving the economics of the system at the same time.
(2) In the multi-energy storage systems mode, the economic benefits of the RIES can be greatly improved, while the ability to accept wind power of the system is improved Simultaneously.

References

1. Cheng H (2019) Review on research of regional integrated energy system planning. Autom Electr Power Syst 43(7):2–13. https://doi.org/10.7500/aeps20180416006
2. Wu J (2016) Drivers and state-of-the-art of integrated energy systems in Europe. Autom Electr Power Syst 40(5):1–7. https://doi.org/10.7500/aeps20150512001
3. Chen Q (2017) Integral transport model for energy of electric-thermal integrated energy system. Autom Electr Power Syst 41(13):7–13. https://doi.org/10.7500/aeps20161209002
4. Yilmaz HU, Keles D, Chiodi A, Hartel R, Mikulić M (2018) Analysis of the power-to-heat potential in the European energy system. Energy Strategy Rev 20:6–19
5. Lund H (2014) 4th generation district heating (4GDH): integrating smart thermal grids into future sustainable energy systems. Energy 68:1–11
6. National Energy Administration (2016) Implementation Opinions on Promoting the Construction of Multi-energy Complementary Integration Optimization Demonstration Project; National Energy Administration: Beijing, China
7. Huang W (2018) Multi-energy network and energy hub joint planning method. Proc CSEE 38 (18):5425–5437
8. Qiu J (2015) Multi-stage flexible expansion co-planning under uncertainties in a combined electricity and gas market. IEEE Trans Power Syst 30(4):2119–2129
9. Bie Z (2017) Summary and prospect of energy internet planning research. Proc CSEE 37 (22):6445–6462
10. Shao C (2016) Preliminary study on multi-energy system analysis planning. Proc CSEE 36 (14):3817–3829
11. Yu Y (2017) Operation strategy for heat storage tank to improve wind power accommodation. Autom Electr Power Syst 41(7):37–43. https://doi.org/10.7500/aeps20160510006
12. Guo F (2018) Dispatching model of wind power accommodation based on heat storage electric boiler for peak-load regulation in secondary heat supply network. Autom Electr Power Syst 42(19):50–56. https://doi.org/10.7500/aeps20180130009
13. Cui Y (2016) Coordination scheduling model for abandoned wind consumption based on heat storage cogeneration unit and electric boiler. Proc CSEE 36(15):4072–4081
14. Guandalini G (2015) Power-to-gas plants and gas turbines for improved wind energy dispatchability: energy and economic assessment. Appl Energy 147:117–130
15. Liu W (2018) Multi-objective planning of micro energy network considering P2G-based storage system and renewable energy integration. Autom Electr Power Syst 42(16):11–20. https://doi.org/10.7500/aeps20180228003
16. Guo L (2017) A two-stage optimal planning and design method for combined cooling, heat and power microgrid system. Energy Convers Manag 74(10):433–445
17. Men X (2018) Construction and energy storage mode analysis of energy interconnected microgrid multi-energy complementary system. Proc CSEE 38(19):5727–5737 + 5929
18. Angelo JS (2013) Differential evolution for bilevel programming. Evol Comput. IEEE
19. Dutta J (2013) Approximate KKT points and a proximity measure for termination. J Global Optim 56(4):1463–1499
20. Gurobi Optimization, LLC. (2018) Gurobi optimizer reference manual. https://www.gurobi.com

Study on Reliability Improvement of Distribution Network Based on Self-healing System

Gangjin Ye, Junhai Wang, Tianyu Zhao, Xuan Yang, Weibin He, Yongcheng Hu, Huafeng Jin and Lei Tian

Abstract In order to meet the increasing reliability requirements of urban distribution network, based on the typical wiring of urban cable ring network, combined with three typical automated protection modes, this paper uses the analytical method to study the data about power outage caused by faults occurred on outlet circuit breakers, line segments, subsection switches, load switches and distribution transformers (DTs) respectively. Then the corresponding reliability improvements are put forward. The analysis results show that to assure the reliability of class A region, the centralized distribution automation and load switches should be adopted instead of decentralized system and subsection switches. To assure the reliability of class A+ region, the scheme of differential protection plus self-healing should be used, with subsection switches and tie switches replaced by circuit breakers and each circuit breaker in the ring main units (RMUs) enclosed in either Vacuum or SF6 box separately.

Keywords Distribution network · Reliability evaluation · Distribution automation (DA) · Distribution transformer (DT) · Differential protection

G. Ye · J. Wang · T. Zhao · X. Yang · W. He
Hangzhou Power Supply Company, Hangzhou 310000, China

Y. Hu (✉) · H. Jin
Hangzhou Yuanwei Electric Power Design Consulting Corp., Ltd., Hangzhou 310000, China
e-mail: huyongcheng03@163.com

L. Tian
China Telecom Zhejiang Branch, Hangzhou 310000, China

Y. Xue et al. (eds.), *Proceedings of PURPLE MOUNTAIN FORUM 2019-International Forum on Smart Grid Protection and Control*, Lecture Notes in Electrical Engineering 585, https://doi.org/10.1007/978-981-13-9783-7_22

1 Introduction

In China, the distribution network has been divided into six categories as A+, A, B, C, D, E in reference [1]. Their corresponding load density, reliability on service in total (RS-1), system average interruption duration index (SAIDI) and voltage qualified rate are given in Table 1.

RS-1 is defined as the uninterrupted durations of customers divided by the whole durations in reference [2].

$$\text{RS-1} = \left(1 - \frac{\text{SAIDI}}{whole\ durations}\right) \times 100\% \tag{1}$$

$$\text{where SAIDI} = \frac{\sum customer\ interruption\ duration}{\sum customer\ serverd}$$

The interruption durations in RS-1 include both forced and scheduled outage time. In 2018, the average customer hours of scheduled outages in Hangzhou per month is 28,223.69, while that of forced outages is 20,809.08. The customer severed is 89,773. Then RS-1 is 99.927%, which cannot meet the requirements in Table 1.

The researches on the distribution system reliability focused on the evaluation techniques, which can be divided into three basic categories—analytical methods [3], simulation methods [4, 5] and hybrid methods [6, 7].

Analytical methods build the reliability models based on the functional relationship between system components, synthesize and analyze all the fault states to obtain the relevant reliability indices. These methods are easy to apply, and the results are accurate. However, for complex systems, there are too many fault states enumerated and the implementation is difficult.

Simulation methods mainly refer to the Monte Carlo (MC) method. The principle of MC is to calculate the required reliability indices based on probability statistics. Compared with analytical methods, MC method can be applied to more complex systems, while the disadvantages are of slow convergence and big errors.

Table 1 Reliability indices of different distribution network

Distribution network	A+	A	B	C	D	E
Power supply area	Downtown	City	City	Town	Village	–
Load density σ (MW/km^2)	$\sigma \geq 30$	$30 > \sigma \geq 15$	$15 > \sigma \geq 6$	$6 > \sigma \geq 1$	$1 > \sigma \geq 0.1$	–
RS-1	≥ 99.999%	≥ 99.990%	≥ 99.965%	≥ 99.863%	≥ 99.726%	–
SAIDI	≥ 5 min	≥ 52 min	≥ 3 h	≥ 12 h	≥ 24 h	–
Voltage qualified rate	≥ 99.99%	≥ 99.97%	≥ 99.95%	≥ 98.79%	≥ 97.00%	–

Hybrid methods take advantage of the two methods above. They first use analytical methods to obtain part of the running states of the power system, then sample the states with simulation methods. So, the amount of processing required in analytical methods are reduced and the convergence in MC method is getting fast.

However, neither the current distribution network planning work nor the researches on distribution network reliability has elaborated on how to configure automation and self-healing schemes of distribution network protection to improve the power supply reliability. This paper then focuses on the protection schemes to improve the reliability of the distribution network using an analytical method.

2 Introduction of Distribution Network Protection

2.1 Distribution Network Structure

Typical wiring of urban cable ring network is shown in Fig. 1. The outgoing lines and branch lines of the substation are equipped with circuit breakers. The line subsections are equipped with load switches or circuit breakers.

A 10 kV line is disconnected in the middle by a tie switch, and the two ends of the line are connected to two 10 kV busbars from different substations. Generally, the load on both ends of the tie switch is evenly distributed, and the line capacity ratio is 2:1. When there is a fault on one end of the line, the load can be transferred by closing the tie switch, and the power can be supplied by the substation on the opposite side.

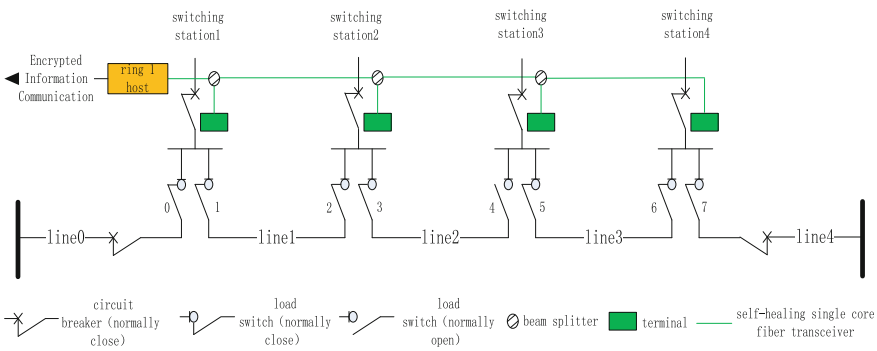

Fig. 1 Typical wiring of urban cable ring network

2.2 Typical Configuration of Distribution Network Protection

The circuit breakers in Fig. 1 are configured with three-stage over-current protection [8] and overload alarm. Fuses are placed at the incoming lines of the distribution stations.

In the load concentrated city, the action current for transient rapid-break over-current protection (stage I) is set as 3000–5000 A. The action current for time-bound rapid-break over-current protection (stage II) is set as 1.5 times rated current, and the action time is set to 0.5 s. The action current for definite time over-current protection (stage III) is set more than the inrush current of the DT. The RMUs are usually equipped with Data Transfer units (DTUs) for each busbar to communicate with the master station to fulfil telesignal, telemetry and telecontrol.

2.3 Longitudinal Protection and Self-healing System

Compared to over-current protection, longitudinal protection has good selectivity [9], which includes longitudinal direction protection, longitudinal distance protection and fiber differential protection. While the first two need define many relay setting values and collect data of phase currents and phase voltages, differential protection does not. It depends on relatively high standard of fiber communication to achieve high sensitivity and selectivity. For urban fiber optic distribution network in Shanghai and Zhejiang, differential protection is generally adopted. Fiber differential protection is configured according to line segments. It can be distributed or centralized.

For a distribution network line segment with two ends, each end is equipped with a set of fiber differential protection devices, which communicates with the opposite end by a receiving and a sending dedicated fiber optic cable. For a T topology line segment with three ends, each end is equipped with a set of fiber differential protection devices, which communicates with the other two ends by two receiving and two sending dedicated fiber optic cables. The self-healing system is separately configured. The distributed differential protection has been used successfully in Shanghai urban area. All subsection or branch line switches are required to be circuit breakers and too many fiber optics occupied. So, this protection is of high cost and hard to maintain. It is not suitable for lines with more than three ends.

To overcome the shortcomings, Shenzhen power supply company has integrated self-healing system into differential protection. Each bus in switching stations is equipped with a set of protective self-healing devices, which collects data about bus phase voltages, incoming and outgoing voltages of main lines, phase currents of all branch lines. The system also has telesignal, telemetry and telecontrol capabilities. Four groups of one receiving and one sending fiber are configured to connect with

maximum two sets of line differential protection for incoming and outgoing separately. The number of devices and the maintenance cost are reduced to one third of the original one while the differential protection ability is almost the same as above.

The centralized differential protection has one host and several terminals. Each terminal is configured at one busbar and communicates with the host through a fiber communication interface integrating transceiver and transmitter to form an independent passive fiber network by passive splitter cascading [10, 11]. All terminals synchronize by internal clock benchmark of the host through an independent synchronization protocol to realize synchronous sampling among them. The SV, GOOSE and MMS mentioned in IEC-61850-9-2 [12, 13] can be merged in one. Each terminal uploads the current signals of each phase and switch states obtained by synchronous sampling to the host through fiber network, and the host automatically generates differential protection scheme corresponding to segments according to the primary network structure and determines where faults occur by real-time calculating. In case of system failure, the faults can be isolated instant by switches and non-fault load can be recovered quickly.

Compared with the distributed scheme, the centralized one has a host where all protection and self-healing algorithms are completed. The terminals only collect local data and realize the protection automation that does not depend on channels. So, the centralized scheme is of high reliability, small operation and maintenance workload, and allows for "plug and play" easily. Though the function of the host is complex, due to the real-time status information perceived about the entire ring, it can reduce the requirements for the primary system. For example, there is no need to replace all the subsection switches by circuit breakers, only the first switch connected with the substation needed to be upgraded to a circuit breaker. When faults occur, the host orders related circuit breakers to cut off the fault current, then isolate the faults by load switches. For the full circuit breaker system, the rapidity is not affected. Because of the adoption of fiber optical network with integrated transceiver, transmitter and passive splitter connection, lots of fiber resources are saved. With high reliability and good scalability, the system has been piloted in parts of Shanghai, Zhejiang and Yunnan.

3 Analysis of Outage Duration Under Protection Schemes

Approximate evaluation algorithm for reliability indices is adopted in this research. Let $T_{(x,k)}$ is the outage time caused by equipment failures. Here, x represents an equipment; k represents the node number. When system faults caused by equipment x, the yearly outage duration of a DT on node k can be obtained as follow.

$$T_{(x,k)} = \lambda_x \left(A_{x,k} t_1 + B_{x,k} r_x + C_{x,k} t_2 \right) \tag{2}$$

where,

λ_x: Failure rate of equipment x. For line segments, it is obtained by multiplying the failure rate of unit length by the length of the segment line
t_1: Time between power loss and successful reclosing after equipment x fails
t_2: Time between power loss and successful transferred re-power after x fails
r_x: Time of fault recovery of x
$A_{x,k}$: Number of customers affected during t_1
$C_{x,k}$: Number of customers affected during t_2
$B_{x,k}$: Number of customers out of power caused by faulted x, only after repair or replacement of x, the customers can be re-powered.

$T_{(x,k)}$ can be affected by different equipment failures and protection automation configurations of the distribution network. In this paper, we calculate $T_{(x,k)}$ in a distribution system that has evenly distributed four nodes, each of the node with four DTs, and fully transferred lines of which segment length is 0.5 km. The protection automation configurations in the distribution system are as following three modes.

1. Only circuit breakers on the outlet of transformers and overcurrent protection devices on branch lines are configured. Fault location, reclosing breakers and load transfer are operated manually. Usually, it is acceptable that $t_1 = 2.5$ h and $t_2 = 3$ h.
2. Circuit breakers on the outlet of transformers and overcurrent protection devices on branch lines are configured. Fault location, reclosing breakers and load transfer are operated by centralized distribution network automation. So t_1 and t_2 can be shortened as 0.15 and 0.2 h.
3. Differential protection and fast self-healing system are configured. Fault location, reclosing breakers and load transfer are instantaneous. So t_1 and t_2 can be set as 0.05 and 0.05 h.

Under the above assumption, we will discuss how faults of an equipment (such as an outlet circuit breaker, a line segment, a subsection switch, a load switch, a DT or branch line) affect the reliability index $T_{(x,k)}$.

3.1 Outlet Circuit Breaker Failures

In Table 2, the failure rate of this equipment is 0.008. Regardless of the automation method used, such failures will certainly cause all loads to Off position, but power can be transferred through contact switches. Therefore, $A_{x,k} = 0$, $B_{x,k} = 0$,

Table 2 Outage duration caused by outlet circuit breaker failures

Protection mode	λ_x	t_2(h)	$C_{x,k}$	$T_{(x,k)}$(h)
Mode 1	0.008	3	16	0.3840
Mode 2	0.008	0.2	16	0.0256
Mode 3	0.008	0.05	16	0.0064

$C_{x,k} = 16$. According to formula 2, for outlet circuit breaker failures, the outage duration $T_{(x,k)}$ under three automation protection modes is about more than one order of magnitude. They are 0.3840, 0.0256 and 0.0064 h separately.

3.2 Line Segment Failures

Each line segment is 0.5 km long, and λ_x is 0.0125. Load before the fault segment can be resupplied by reclosing, and that after the fault segment be transferred through connection switches. According to formula 2, about line segment failures, the total outage durations under three automation protection modes are 2.75, 0.175 and 0.05 h (Table 3).

3.3 Subsection Switch Failures

Assuming λ_x of each subsection switch configured at the node and both sides of the line segments has the same value of 0.005, then $\lambda_x = 0.01$. A subsection switch fails, the number of customers affected are equal. So, $B_{x,k} = 4$ and $r_x = 6.5$. When faults occur, all the other switches on the same bus should be turned off to repair or replace the faulty one. So, the total power outage time caused by the subsection switch faults is obviously greater than that of lines. The total outage durations under the three automation protection modes are 2.36, 1.124 and 1.064 h (Table 4).

Table 3 Outage duration caused by line segment failures

Protection mode	Line no.	t_1(h)	t_2(h)	$A_{x,k}$	$C_{x,k}$	$T_{(x,k)}$ (h)	Total (h)
Mode 1	0	2.5	3	0	16	0.6000	2.75
	1	2.5	3	4	12	0.5750	
	2	2.5	3	8	8	0.5500	
	3	2.5	3	12	4	0.5250	
	4	2.5	3	16	0	0.5000	
Mode 2	0	0.15	0.2	0	16	0.0400	0.175
	1	0.15	0.2	4	12	0.0375	
	2	0.15	0.2	8	8	0.0350	
	3	0.15	0.2	12	4	0.0325	
	4	0.15	0.2	16	0	0.0300	
Mode 3	0	0.05	0.05	0	16	0.0100	0.05
	1	0.05	0.05	4	12	0.0100	
	2	0.05	0.05	8	8	0.0100	
	3	0.05	0.05	12	4	0.0100	
	4	0.05	0.05	16	0	0.0100	

Table 4 Outage duration caused by subsection switch failures

Protection mode	Switch no.	t_1 (h)	t_2 (h)	$A_{x,k}$	$C_{x,k}$	$T_{(x,k)}$ (h)	Total (h)
Mode 1	0.1	2.5	3	0	12	0.6200	2.36
	2.3	2.5	3	4	8	0.6000	
	4.5	2.5	3	8	4	0.5800	
	6.7	2.5	3	12	0	0.5600	
Mode 2	0.1	0.15	0.2	0	12	0.2840	1.124
	2.3	0.15	0.2	4	8	0.2820	
	4.5	0.15	0.2	8	4	0.2800	
	6.7	0.15	0.2	12	0	0.2780	
Mode 3	0.1	0.05	0.05	0	12	0.2660	1.064
	2.3	0.05	0.05	4	8	0.2660	
	4.5	0.05	0.05	8	4	0.2660	
	6.7	0.05	0.05	12	0	0.2660	

3.4 Load Switch Failures

Assuming that λ_x of four load switches configured on the node has the same value of 0.005, then $\lambda_x = 0.02$. Any load switches fail, the number of customers affected are equal. So, $B_{x,k} = 4$ and $r_x = 6.5$. Similar as subsection switch failures, the power outage time caused by the load switch faults is obviously greater than that of lines. The total outage durations under the three automation protection modes are 4.72, 2.248 and 2.128 h (Table 5).

Table 5 Outage duration caused by load switch failures

Protection mode	Switch no.	t_1 (h)	t_2 (h)	$A_{x,k}$	$C_{x,k}$	$T_{(x,k)}$ (h)	Total (h)
Mode 1	0–3	2.5	3	0	12	1.2400	4.72
	4–7	2.5	3	4	8	1.2000	
	8–11	2.5	3	8	4	1.1600	
	12–15	2.5	3	12	0	1.1200	
Mode 2	0–3	0.15	0.2	0	12	0.5680	2.248
	4–7	0.15	0.2	4	8	0.5640	
	8–11	0.15	0.2	8	4	0.5600	
	12–15	0.15	0.2	12	0	0.5560	
Mode 3	0–3	0.05	0.05	0	12	0.5320	2.128
	4–7	0.05	0.05	4	8	0.5320	
	8–11	0.05	0.05	8	4	0.5320	
	12–15	0.05	0.05	12	0	0.5320	

3.5 DT or Branch Line Failures

When a DT fails, usually the branch line protection devices are trigged. If the breakers or switches refuse to act, the outage range expands because of overstep tripping. The time of outage caused by a DT consists of up to four parts, as shown in formula 3.

$$T_{(t,k)} = \lambda_t\left(A_{t,k}t_1 + r_t + C_{t,k}t_2 + B_{t,k}t_3\right) \tag{3}$$

where,

$\lambda_t r_t$: Outage time of customers connected to the faulted DT
$\lambda_t B_{t,k} t_3$: Outage time of other DTs at the same node of the faulted DT
$\lambda_t A_{t,k} t_1$: Outage time of customers on the potentially affected nodes between the faulted node and the power
$\lambda_t C_{t,k} t_2$: Outage time of customers on the potentially affected nodes between the faulted node and transfer switches (Table 6).

When a DT corresponding to 4 nodes and 16 switches fails, it is set that $\lambda_t = 0.037$, $r_t = 5.5$ h, the probability of a overstep tripping is 20%. When a load switch fails to operate and causes the overstep tripping, in modes 1 and 2, all the faults are cut off by the outlet circuit breakers, and then isolated manually to restore the power supply to the customers in non-fault sections. In mode 3, the subsection switches of the node are trigged by the busbar differential protection and failure protection devices, so the customers before the fault point will not be affected and the ones behind the point can be automatically transferred by the system to re-power reply. The total outage durations under the three automation protection modes are 2.0128, 1.0982 and 1.0449 h.

Table 6 Outage duration caused by DT or branch failures

Protection mode	DT no.	t_1 (h)	t_2 (h)	t_3 (h)	$A_{x,k}$	$B_{x,k}$	$C_{x,k}$	$T_{(x,k)}$ (h)	Total (h)
Mode 1	0–3	2.5	3	2.5	0	0.6	2.4	0.5254	2.0128
	4–7	2.5	3	2.5	0.8	0.6	1.6	0.5106	
	8–11	2.5	3	2.5	1.6	0.6	0.8	0.4958	
	12–15	2.5	3	2.5	2.4	0.6	0	0.4810	
Mode 2	0–3	0.15	0.2	2.5	0	0.6	2.4	0.2768	1.0982
	4–7	0.15	0.2	2.5	0.8	0.6	1.6	0.2753	
	8–11	0.15	0.2	2.5	1.6	0.6	0.8	0.2738	
	12–15	0.15	0.2	2.5	2.4	0.6	0	0.2723	
Mode 3	0–3	0.05	0.05	2.5	0	0.6	2.4	0.2634	1.0499
	4–7	0.05	0.05	2.5	0	0.6	1.6	0.2620	
	8–11	0.05	0.05	2.5	0	0.6	0.8	0.2605	
	12–15	0.05	0.05	2.5	0	0.6	0	0.2590	

4 Reliability Improvement

According to the analysis in part 3, in three different protection modes, the average customer interruption duration caused by all faults is 0.7642, 0.2919, 0.2683 h respectively. Thus,mode 1 cannot satisfy the reliability requirements of class A and A+ regions, while mode 2 and 3 can meet those of class A region but fail at the A+ region. To improve distribution network reliability standard, there are two ways to implement, one is to decouple, the other is to speed up.

Decoupling is to limit the fault area as fast as possible. In extreme emergency services, closing the loop is necessary, so the customer's power supply cannot be affected. To realize decoupling, the electivity, rapidity, sensitivity and reliability of protection should be improved, so the probability of overstep tripping can be lowered from 20 to 1% or even below. To provide a single rather than shared cabinet for each equipment in RMUs, decoupling can just isolate the faulted one without affecting others.

Speeding up is to accelerate the rate of repair, replacement, isolation or recovery of faulted equipment manually or systematically. It is usually not more than 100 ms for a circuit breaker to execute a command. While for a load switch, it may be 3–5 s. In mode 3, if the subsection switches are replaced by circuit breakers, the time to isolate the faults gets shortened, and the fault area is narrowed. The decoupling is then realized by speeding up.

For outlet circuit breaker failures, without closing the loop, all the loads on the lines will certainly be affected. However, if the tie switches can be configured as circuit breakers and equipped with self-healing functions such as no pressure tripping plus automatic busbar transfer, the blackout time can be within 3 s, and the total outage duration is less than 0.000107 h.

For line failures, mode 2 cannot accomplish decoupling. It is difficulty to improve the speed of manual operation. In Mode 3, if all the subsection and tie switches are all converted into circuit breakers, t_2 can be shortened to 3 s, and $A_{x,k}$ equals to 0. The outage duration can be reduced to 0.025 h.

For subsection switch faults, the rapid replacement is an effective way to shorten the outage time of load at the same node. In mode 3, the use of circuit breakers instead of switches can also shorten the outage time. If the replacement time is reduced to 1 h, the outage duration can be 0.1602 h.

For the load switches, if the fault point on the busbar side, it equals to busbar failure, and all load nodes on the same busbar will be out of power. In mode 3, if the circuit breakers replace switches, the load near the power supply side will not be affected, and the outage time can be shortened to 0.3204 h.

For DT failures, the changing interval of switches or the DT can be shortened to 1 h for isolated cabinets in RMUs. With the improved characteristics of branch protection, the correlation coefficient of the influence on other DTs is reduced to 1%. So, the power outage time caused by DT faults is reduced to 0.1524 h.

To summarize, in mode 3, adopting self-healing protection configuration, replacing subsection switches and tie switches with circuit breakers, improving the

reliability of branch protection, using isolated cabinets in RMUs, the outage duration can be shortened to 2.468 m per customer every year and can meet the reliability requirements of class A+ regions.

5 Conclusions

This paper uses an approximate estimation algorithm to analyze the power outage duration of typical wiring of urban cable ring network under three different protection and automation modes. The analysis results show that mode 2 and 3 can satisfy the reliability requirements of class A region, while to meet those of A+ region, mode 3 is recommended and followed by several steps. Firstly, all the subsection switches and tie switches of lines shall be replaced by circuit breakers. Secondly, each circuit breaker in the ring main units (RMUs) is enclosed in either Vacuum or SF6 box separately, and the replacement or maintenance time of the faulted switches should be shortened to 1 h. At last, when transformers or branch lines fail, the probability of protection operation rejection should be reduced to less than 1%. It still remains to be further studied about how to shorten the replacement or maintenance time of faulted switches and reduce the probability of branch line protection operation rejection.

References

1. DL/T 5729-2016 (2016) The guide for planning and design of distribution network. National energy administration, China
2. DL/T 836-2012 (2012) Reliability evaluation code for customer service in power supply system. National energy administration, China
3. Li G, Bie Z et al (2016) Researches on the reliability evaluation of active distribution systems. Distrib Util 8(2)
4. Du J (2015) The study of algorithms for power system reliability evaluation based on monte carlo simulation. Master Dissertation of Zhejiang University
5. Chen P, Tao S, Xiao X, Li L (2016) Source-load model improvement and parallel computing for reliability evaluation of active distributed networks. Autom Electr Power Syst 40(18)
6. Wan G, Ren Z et al (2004) Hybrid Method for the Reliability Evaluation of the Complex Distribution System. Proceedings of CSEE 24(9):92–98
7. Zhao S, Singh C (2018) A hybrid method for reliability evaluation of line switching operations. Electr Power Syst Res 163:365–374
8. Yang Y, Zhu L, Li F, Wu Z, Cai C (2016) Research on the power line three-stage over-current protection simulation. In: 6th international conference on advanced design and manufacturing engineering (ICADME 2016)
9. Zhu S (2014) Principle and technology of relay protection for high voltage network. China Electric Power Press
10. Yan D (2007) EPON-, a new generation of broadband optical access technology and application. Mechanical Industry Press

11. Liu P (2012) Application of IEEE 1588 technology in passive optical network. Mob Commun 36(18):74–78
12. IEC 61850-9-1 Ed.1.0 en (2003) Communication networks and systems in substations—Part 9-1: specific communication service mapping (SCSM)—sampled values over serial unidirectional multidrop point to point link. ANSI
13. IEC 61850-9-2, Ed.1.0 en (2004) Communication networks and systems in substations—Part 9-2: specific communication service mapping (SCSM)—sampled values over ISO/IEC 8802-3. ANSI

Power Frequency Coordination Control Method for High Penetration Renewable Energy Resources

Junyu Wang and Haibing Zhang

Abstract The disturbance of integrated power will increase while the rotational inertia that can restrain the change of system frequency will decrease when large-scale renewable energy is integrated to the power grid. This produces new problems and challenges for AGC Control. Based on the model of sub operating area, this paper proposed the fundamental principle of AGC control when large-scale renewable energy, thermal and hydro units are participating in the process of frequency regulation. These three types of resources can undertake the total ARR (Area Regulation Requirement) of the whole operating area by equal proportional regulation capacity ratio strategy or priority coordinated control strategy. Besides, this paper also described how to track inner stable tie-lines and how to coordinate with upper level load dispatch center to jointly regulate system frequency. These research results are helpful for practical applications of AGC regulation.

Keywords Large-scale renewable energy · AGC control model · Multi-target coordinated control · Priority control

1 Introduction

With the increasing attention of energy crisis and environmental issues, the development of renewable energy has become a focus of attention. However, its grid-connection problem has brought challenges to the safe and stable operation of power system due to its stochastic and random characteristics. And the problem of renewable energy consumption has become increasingly prominent. When China is continuously optimizing its power supply structure, the grid-connected generation capacity of renewable energy is rapidly growing as well. It plays an important role

J. Wang (✉) · H. Zhang
NARI Group Corporation (State Grid Electric Power Research Institute), Nanjing 211106, Jiangsu, China
e-mail: wangjunyu@sgepri.sgcc.com.cn

Y. Xue et al. (eds.), *Proceedings of PURPLE MOUNTAIN FORUM 2019-International Forum on Smart Grid Protection and Control*, Lecture Notes in Electrical Engineering 585, https://doi.org/10.1007/978-981-13-9783-7_23

in relieving energy crisis and reducing environmental pollution in China. Meanwhile, power utility operators are facing more challenges to meet AGC requirements which aim to maintain system frequency and tie-line interchange to get close to scheduled values. This brings new problems and challenges to Automatic Generation Control [1, 2]. Power system's frequency resources and dispatching capabilities would be placed under great pressure especially when impact load disturbances occurred in the power grid, which becomes one of the main constraints of absorbing large-scale renewable energy [3].

For the purpose of breaking the bottleneck of renewable energy integration, it would be effective to find out an appropriate approach to integrate renewable energy resources into the power grid to improve the quality of frequency regulation and to promote the adjusting efficiency [4].

In order to totally bring the regulating potential of renewable energy resources and traditional AGC units into full play, this paper first introduced the modeling method of enclosing operating area to realize the local balance of active power. Then it improves the existed AGC coordination strategy which utilize the unique confirmed participation factor and local priority strategy to undertake area regulation requirement. In this new approach, AGC control groups are set up based on main operating area and all the AGC units come under different control groups according to their adjusting characteristics, regulating reserve or geographic attributes. Area regulation requirement is allocated to every control group and then to the units in each group. There are two kinds of allocating strategies between groups and units, manual participation factor and priority strategy. When the latter is adopted, the actual participation factor is determined by the specified allocating strategy. Both of these two strategies are suitable for task allocation between control groups and within any group. In order to make sure all the AGC commands are secure enough for generating units, vibrating zone strategies and security verification task will be carried out just during and after the process of active power allocation.

2 Model of Sub-control Operating Area

2.1 Sub-control Operating Area

Different from the hierarchical division style of Chinese power dispatching regions, the sub-control operating area here refers to the division method of internal electrical islands in a provincial dispatch center. According to the traditional dispatch pattern, many of the provincial power grids in China adopt single area model to complete AGC control. Their control objects are relatively clear and explicit. With the expansion of power system's scale, the electrical connections become more complicated than before. It is necessary for dispatching administrative regions to divide the operating area into proper parts and respectively control these parts

simultaneously, no matter from the prospective of power grid's distribution characteristics, actual dispatching management requirements, or from the aspect of energy-saving dispatching. This is an effective way for the original operating area to satisfy the multi-object control requirements. Besides, the establishment of sub control area can provide basic conditions for power grid to face with splitting emergencies.

Modeling schematic diagram of sub-control areas is shown in Fig. 1. Area S_1 to S_n are the minimum control areas of the whole operating area. Any control areas inside the whole area A_1 can be composed by these minimum areas. Though these recombination areas can be derived from the minimum sub-control areas from the point of physical interconnection, they have to be assembled independently when modeling.

The main control operating area (A_1) carries out the regulation task before the sub areas are produced. It was established by traditional modeling style and the calculation method depends on actual control mode. Renewable energy resources are considered as equivalent generating units according to their geographic attributes and participate in the process of ARR allocation together with traditional thermal and hydro units.

When TBC (Tie-line Bias Control) method is adopted by AGC, as is shown in Fig. 1, the model of the main operating area A_1 simultaneously contains frequency component and tie-line interchange component. The ACE calculation method of the main operating area can be expressed as:

$$ACE = 10B(f - f_0) + (I - I_0) \tag{1}$$

where, f represents the real-time telemetered system frequency of the main control area, f_o stands for scheduled value of frequency, B indicates the frequency bias coefficient of the whole operating area, I is the tie-line interchange power between the main control area and its adjacent external operating area, I_0 represents the scheduled value of tie-line interchange.

Those generating units, tie-lines and other objects, which need to be monitored inside the operating area, can form their sub-control areas according to the actual dispatching administrative regions and results of sensitivity calculations. In Fig. 1,

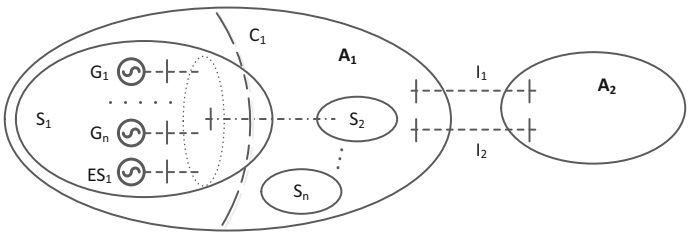

Fig. 1 Schematic diagram of sub-control area modeling method considering energy storage resources

C_1 is the sub internal tie-line needed to be monitored. Generating units from G_1 to G_n and the related renewable energy resource ES can form the sub-control area S_1. The frequency regulation resources of this sub-control area constitute an independent cut-set for the control object (the single transmission or the tie-line). I_1, I_2 represent tie-line interconnections of adjacent operating area A_2.

When regulation objects of the main operating area and the sub-control area are the same, the sub-control area can be seemed as a subordinate area of the main control area and can't be operated independently. Therefore, the modeling process of sub-control area will only describe its generating units, tie-line interface and other objects that need to be monitored.

If the main operating area and the sub-control area track different control objects, their data sources of ACE may be from different ways. So every sub-control area needs to add an ACE component data source and operating parameters in the actual control process.

In the established sub-control area models, the newly formed electrical island can be controlled independently if the sub-control area is disconnected from the adjacent operating area when specific dispatching management meaning is assigned to the sub-control area. This sub-control area modeling method is a necessary precondition of multi-object control and splitting emergencies. The judgment of network splitting can be the combination of important telemetries and status values. Besides, the result of State Estimation can also be considered as a criterion of power grid splitting.

2.2 Control Group

Control group is the intermediate layer between operating area and AGC units. It's the container of AGC resources but responsible for undertaking the regulation requirement of operating area and reallocating it to each unit.

Generally speaking, the control group model should be set up on the basis of regulating area. Each area can have several control groups and each control group can own at least one AGC unit. To meet the requirements of each different aspect, control group and AGC unit can adopt different strategies when distributing regulation power. AGC units can be categorized into different control groups according to the following characteristics [3, 4]:

(1) Basic attribute of unit, such as hydro unit or thermal unit;
(2) The regulating capacity of unit, such as small hydro power station and high-capacity hydro plant;
(3) The regulating speed of each unit;
(4) The relationship between unit and important tie-lines;
(5) The upstream and downstream relationship between different hydro units;
(6) Geographic characteristics of different units.

3 Multi-object Coordinated Control Strategies

3.1 Coordinated Control Strategies Between Renewable Energy Resources and Traditional Units

When the frequency regulation resources in an operating area involve renewable energy resources and traditional hydro and thermal units at the same time, the coordination strategy among diverse frequency regulation resources needs to be taken into account. Renewable energy resources are the best frequency regulation resource among them. They can reach their maximum capacity within several milliseconds and can maintain the stable output at the set point. The regulation performance of hydro units is better than thermal ones. In addition, the regulation resources inside the operating area have different performances at different time periods because of several constraints. When all of these three resources are put into AGC control, it is necessary to establish discriminate strategies to control them [5–7].

According to the operating style of control area, the proportional regulation capacity ratio of different resources and the whole adjusting object of the whole area, the following control strategies are suitable for coordinating all of these three resources, which can mainly satisfy the real-time control requirements of CPS evaluation criteria.

3.1.1 Renewable Energy Resources and Hydro Units Are Responsible for ARR Regulation, Thermal Units Track Ahead the Changing Tendency of System Load

This type of control strategy is suitable for those areas that have adequate renewable energy resources and hydro regulation capacities. Both of these two resources have a fast regulation speed and a short response time, which can face with the fluctuation of ACE when the reserve capacity is abundant.

In order to better utilize thermal units, they can be controlled to keep pace with change of system load and adjust their output in advance with the results of very-short-term load forecast. This is helpful for hydro units and renewable energy resources to release their adjusting capacities and relieve their regulation burdens.

3.1.2 Hydro, Thermal and Renewable Energy Resources Undertake ARR According to Proportional Regulation Capacity Ratio [8–10]

The AGC reserve capacity of renewable energy resources is relatively small when compared to the regulation capacities of traditional thermal and hydro units. The operating area can't fully rely on renewable energy resources to fulfill frequency

regulation requirements before their grid-connected capacity is large enough. However, the regulation capacity of hydro units may be limited by season and weather conditions. So it's necessary to exploit the potential of thermal units to better participate in the AGC regulation process.

This strategy needs to categorize renewable energy resources, hydro and thermal units into different groups. The total participation ratio and the regulation direction of thermal and hydro units also need to be classified. Participation factor of each equivalent AGC unit can be obtained after the regulation requirement of the whole operating area is calculated. It is dynamically adjusted according to the up/down-regulating capacity and is limited to responsive regulating capacity. Take thermal unit's up-regulating direction for example:

$$\alpha_T = \frac{\sum_{i=1}^{k} R_{Ti}^{up}}{\left(\sum_{i=1}^{k} R_{Ti}^{up} + \sum_{i=k+1}^{\mathrm{m}} R_{Hi}^{up} + \sum_{i=m+1}^{n} R_{\mathrm{ES}i}^{up}\right)} \tag{2}$$

where, α_T is the total participation factor of thermal units' regulating capacity, R_{Ti}^{up}, R_{Hi}^{up}, $R_{\mathrm{ES}i}^{up}$ respectively stand for the up-regulation capacity of thermal, hydro and renewable energy resources.

If the adjusting capacity of AGC units is adequate enough, the regulating priority of each type of resources can be confirmed by regulating capacities. When the total regulating capacity of certain resource is not enough, it can be chosen to undertake regulation power before other resources. The part of ARR requirement that is not distributed to this type of resource can be undertaken by other two types of units [11].

After the participation factor has been confirmed, increasing and decreasing sequences can be formed as well. When units are required to increase their generation, AGC main program will first choose those control groups that have smaller participation factors, and when decreasing is required, the main algorithm will choose bigger participation factors first.

When proportion method is utilized in group allocation, total participation factors of control groups are first used to calculate the regulation power undertaken by groups. Then redundant regulation power will be disposed by maximum regulating reserve of the group. If there still has more regulation power, those groups that have high abundance will undertake the surplus regulation power.

3.1.3 Control Strategy in Terms of Space Coordination

In addition to coordinate renewable energy resources and thermal and hydro units in the time axis, they can be decoupled to track different control objects from the point of different space attributes. In this case, renewable energy resources and hydro units still undertake the regulation task of tie-line interchange between provincial

operating areas. Thermal units can be set to monitor those important internal tie-line sets in the context of security constraints.

In fact, it's an important task for dispatch center to maintain the transmission tie-line sets into stable limits when regulating AGC equivalent units. If the regulation objects of preventive control and corrective control can be allocated to AGC's traditional regulation task, it can well reduce system operators' work load [12].

- Track specified tie-line set inside the operating area and transmit active power as much as possible without exceeding specified tie-line set limit. This type of control mode can realize hierarchical and zone control inside the operating area.

By matching the critical tie-line set and sub-control area that are already established inside the whole area, every sub-control area can get a corresponding tie-line set. Those AGC units of the sub-control area that are specified to adjust the internal tie-line active power will not participate in the regulation of system frequency and tie-line interchange between adjacent whole operating areas. The SCE (Sub-area Control Area) can be calculated through the following formula:

$$SCE = P_T - P_{TMAX} \tag{3}$$

where, P_T is the current transmitting active power, P_{TMAX} indicates the transmitting limits.

Similar to the concept of ACE in traditional AGC control, dead band, normally regulation region and emergency region can be set according to the value of SCE. AGC regulating resources will not adjust their output until SCE enters the region of normally regulating zone and emergency zone. The adjustment can be intensified properly by setting different gain coefficient of their control areas.

- The preventive control and corrective control of stable tie-line sets can be realized by combining AGC and SCD (Security Constrained Dispatch) into a closed-loop control system. Preventive control is to limit the regulation direction of AGC units according to their sensitivity coefficients to the tie-line set if it is in a heavy load situation. Corrective control is to complete the limit relieving adjustment if the tie-line set has exceeded its stable limit.

The method of combining AGC and SCD can take several tie-line sets into account at the same time. But it will impact the regulating direction and regulation range of AGC units to some extent, which is suitable for those systems that contain adequate AGC units [13].

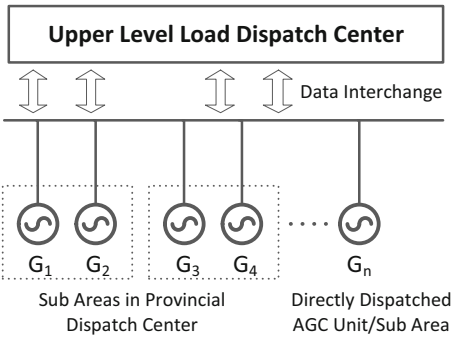

Fig. 2 Centralized control mode of regional power dispatch center

3.2 Hierarchical and Centralized Control Strategy

Each sub-control area can specify their own regulating target and ACE calculation method according to their actual requirements. Different from sub-area control, hierarchical control reflects more about the coordination aspect between the control targets of sub-areas and the whole operating area [13, 14].

(1) The control target of sub-area is to guarantee the regulating target inside the sub-control area can be achieved by adjusting the output of AGC units inside this sub-area.
(2) From the view of upper dispatching area, all the hydro/thermal units and renewable energy resources can be considered as equivalent units of the upper operating area.
(3) Tie-line set constraints can be converted to the regulating range of AGC units. The coordination of different control targets can be achieved by adjusting the constraints of regulating ranges (Fig. 2).

4 Simulation Experiment

The coordinated control strategies proposed in this paper have been simulated based on the data of a provincial power system in China. This province used to rely on hydro units to undertake AGC regulation power, and the regulating reserve of thermal units is not adequately developed. The operation data before and after the coordinated control strategy was utilized were chosen for the simulation and energy storage resources were considered as equivalent AGC units.

The operation days when traditional strategy and the coordinated control strategy were respectively used are from 20th April 2017 to 1st May 2017. Figure 3 has shown the comparison conditions.

As can be seen from Figs. 3 and 4, when the coordinated control strategy proposed in this paper was adopted, the regulating times decreased in a large extent,

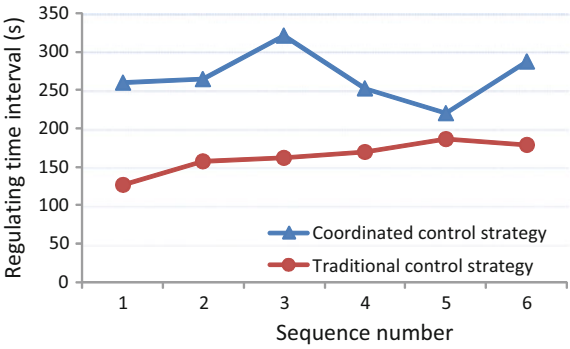

Fig. 3 Centralized average regulating time intervals of AGC commands

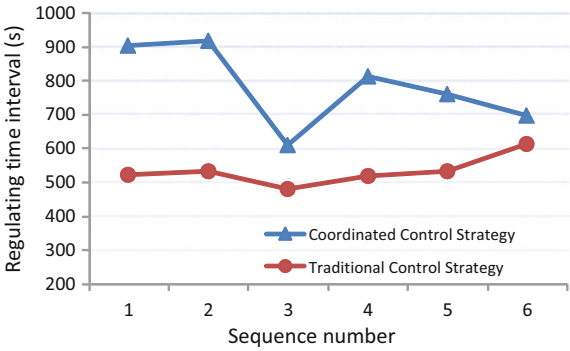

Fig. 4 Average time intervals of AGC round-trip regulation

especially the round trip regulations which were not quite good for the normal operation of thermal units. After the coordinated control strategy was adopted, the regulating amplitude of thermal units was obviously getting smaller, and the unit abrade became much less.

As can be seen from Figs. 5 and 6, the regulating times of hydro PLCs also obviously decreased when the new coordinated control strategy was utilized in the main station AGC system. But the CPS1 index did not change much clearly.

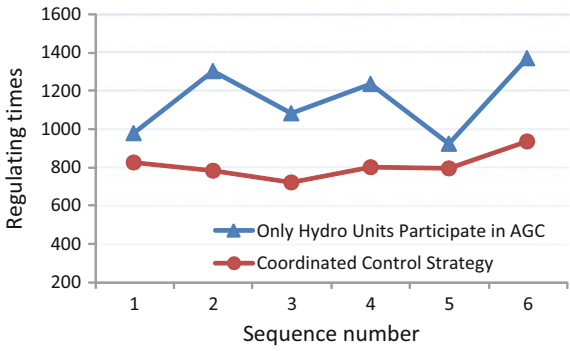

Fig. 5 Hydro regulating times before and after the new approach

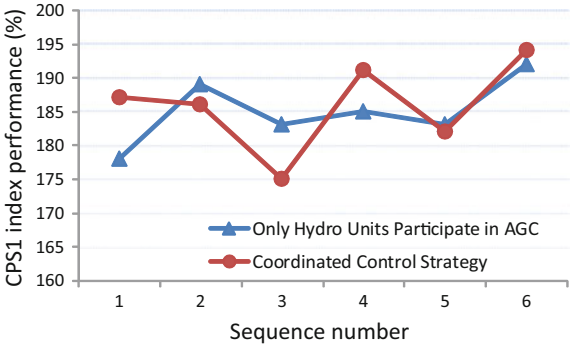

Fig. 6 CPS1 index before and after the new approach was utilized

This would not do any harm to the index evaluation system for the provincial electric power network. The regulating times and regulating amplitudes of hydro units obviously decreased when this new approach was adopted in AGC system, and thermal units were more active in AGC regulating process. The shortcomings of thermal units that their ramp rates were comparatively slow could effectively be avoided. ACE and CPS1 indexes of the operating area were not deteriorated and the effects of system frequency regulating and tie-line deviation correcting did not decline.

5 Conclusion

The fast development of technologies in recent years has brought huge influences to the integration of large-scale renewable energies. Meanwhile, traditional frequency regulation units can't respond to the fluctuation of renewable generation in time because of their slow ramp rates. With rapid response to regulation requirement and accurate control of their output power, chemical renewable energy resources can better cover the shortage of traditional units, which provides a new measure for system frequency regulation.

This paper proposed a sub-control area modeling method to satisfy the multi-object coordination control requirements and multi-island control after splitting emergency occurs. Based on this, equal proportional regulation capacity ratio strategy and priority coordinated control strategy were proposed to allocate ARR among hydro/thermal units and renewable energy resources. All of these three equivalent units can be coordinated both in the aspect of time and space axis. Tie-line set control strategy and centralized coordination between current and upper level dispatching centers provide other optimal allocation method to a larger extent. Control strategies discussed in this paper are suitable for large-scale renewable energy resources to participate in AGC regulation process.

References

1. Hu Z, Luo H (2018) Research status and prospect of automatic generation control with integration of large-scale renewable energy. Autom Electr Syst 42(8):2–15
2. Li X, Huang J et al (2016) Review on large-scale involvement of energy storage in power grid fast frequency regulation. Power Syst Prot Control 44(7):145–153
3. Liu H, Shi H, Teng X (2009) Hydro-thermal AGC generators coordinated optimization control strategy in Yunnan power grid. Autom Electr Power Syst 33(20):96–99
4. Zhou W, Qiao Z, Si F (2010) Multi-objective load optimal dispatch and decision-making guidance of power plant. Proc CSEE 30(2):29–34
5. Ding M, Wang W et al (2014) A review on the effect of large-scale PV generation on power systems. Proc CSEE 34(1):1–14
6. Sun H, Liu X, Ben C et al (2018) Multi-objective risk scheduling model of power system containing power station with integrated wind power and energy storage. Autom Electr Power Syst 42(5):94–101
7. Zhu D, Liu W, Cai W et al (2018) Load-source coordinated dispatch method for program wind power accommodation based on rolling optimization of energy and power. Autom Electr Power Syst 42(5):80–85
8. Chen D, Zhang L et al (2016) Control strategy of energy storage for frequency regulation and evaluation of investment income. Mod Electr Power 33(1):80–86
9. Hu Z, Xu X, Zhang F et al (2014) Research on automatic generation control strategy incorporating energy storage resources. Proc CSEE 34(29):5080–5087
10. Xu J, Tang X, Xu Q et al (2018) Frequency control considering deep and fast load changing capability of thermal power units. Autom Electr Power Syst 42(8):74–82
11. Niu Y, Zhang Y, Zhang H et al (2016) Optimal control strategy and capacity planning of hybrid energy storage system for improving AGC performance of thermal power units. Autom Electr Power Syst 40(10):38–45
12. Yin G, Li X, Guo L et al (2015) Application of hybrid energy storage system on wind/solar hybrid microgrid. Proc CSU-EPSA 27(1):49–53
13. Teng X, Gao Z et al (2015) Requirements analysis and key technologies for automatic generation control for smart grid dispatching and control systems. Autom Electr Power Syst 39(1):81–87
14. Zhao B, Xiao C et al (2017) Penetration based accommodation capacity analysis on distributed photovoltaic connection in regional distribution network. Autom Electr Power Syst 41(21):105–111

Optimal Configuration Method of Distributed Hybrid Energy Storage Systems in Distribution Network with Large Scale of Wind Power Generation

Tianmeng Yang, Zhentao Han and Jing Gao

Abstract To promote the coordinated development between distributed wind generation and distribution network, and to improve the absorptive capacity of wind generation, a hybrid energy storage system allocated in the distribution network is put forward, which is composed by battery and small-scale compressed air energy storage system. And the optimal configuration method is discussed. The battery is used to mitigate the wind power output fluctuation thanks to its quick response capacity, and the small-scale compressed air energy storage system is used for peak regulation thanks to its flexible allocation and large energy density. The operational principle of the hybrid energy storage system is discussed, and the peak load regulation method of the small-scale compressed air energy storage system is presented. Based on the research of the allocation of hybrid energy storage system, the capacity optimization and the optimal operation, the optimal configuration method of the hybrid energy storage system is discussed. The proposed model and the method are verified on the modified distribution network, and the results prove the effectiveness and flexibility of the model.

Keywords Distributed wind generation · Distribution network · Hybrid energy storage system · Battery storage · Compressed air energy storage system · Optimal sizing

1 Introduction

With the increasing troubles of the centralized power supply, and based on the quick development of the distributed wind generation and the increasing integration scale, the inherent nature of random fluctuation and intermittent bring adverse

T. Yang (✉) · Z. Han · J. Gao
Economic Technical Research Institute of Liaoning Electric Co. Ltd., Shenyang, China
e-mail: 18240369315@163.com

Y. Xue et al. (eds.), *Proceedings of PURPLE MOUNTAIN FORUM 2019-International Forum on Smart Grid Protection and Control*, Lecture Notes in Electrical Engineering 585, https://doi.org/10.1007/978-981-13-9783-7_24

effects on the stable operation of the power system [1]. Thanks to the quick response nature, the energy storage systems become an effective way to relief the uncertainty of the renewable energy resources to the power system operation.

Currently, the researches about the configuration of the distributed energy storage system to increase the utilization rate of renewable energy resources have already get some conclusions [2–9]. In [2], the configuration method of battery energy storage system is proposed, which aims to receive the maximum profits in the distribution network. In [3–5], an optimal sizing method of the energy storage system is proposed, but the sizing and locating method are not included. In [6, 7], the optimal configuration method of the distributed energy storage system is proposed, which aims to mitigate the output fluctuation of the renewable resources. In [8, 9], the distributed energy storage systems configured in the active distribution network are discussed in two aspects, which are operation strategy and the planning decision. Among these researches above, the researches of the energy storage are concentrated on single type of energy storage system, till now there isn't any research about the hybrid energy storage system to allocate in the distribution network.

The remainder of this paper is organized as follow. The operational principle of the hybrid energy storage system and the peak load regulation method of the small-scale compressed air energy storage system are discussed in Sect. 2. The optimal sizing model of the hybrid energy storage system and the optimal method are proposed in Sect. 3. Section 4 carries on a case study. Finally, the final discussion and conclusions are provided in Sect. 5.

2 The Operational Principle of Hybrid Energy Storage System in Distribution Network with Distributed Wind Generation

2.1 The Operational Principle of Hybrid Energy Storage System

By comparing the economic indicators, the BESS is used for power fluctuation mitigation and the CAES is used for peak shaving are the most economical combination.

The operational principle of the hybrid energy storage system (HESS) composed by battery and the small-scale compressed air energy storage system is shown in Fig. 1. The battery energy storage system (BESS) is installed in some nodes of the distribution network, and it is used to mitigate the wind power output fluctuation and improve the power quality thanks to its quick response capacity. The small-scale compressed air energy storage system (CAES) takes the high pressure air holer as the containers, since they have the flexible configuration and without the geographical limitation. Thus, the small-scale CAES is installed in the distribution

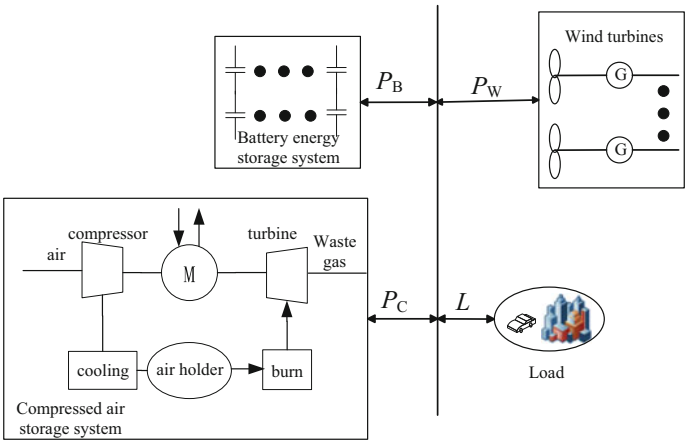

Fig. 1 Flow chart of constructing semantic framework

network for peak load regulation thanks to its large energy density and flexible configuration. And it can reduce the load difference between peak and valley, which can help improve the operational efficiency of the system and reduce the abandoned wind energy. The fluctuation mitigation strategy is shown in [10].

2.2 The Peak Load Regulation Method of the Small-Scale Compressed Air Energy Storage System

Based on the analysis of the operational principle of the CAES, the installation of the small-scale CAES is used for peak load regulation, which can reduce the peak load regulation pressure and improve the load characteristics. The small-scale CAES absorb the extra electricity to drive the motor at the valley load period, and it compress air into the gas storage tank. And at peak load period, it promotes the expander to work to generate electricity. Therefore, the small-scale CAES power output is flexible enough to be arranged to meet the load demand.

Therefore, through the forecast load data of the system and the capacity of the CAES, we can analyze the peak shaving depth by analyzing the power output of the CAES, and to confirm the optimal capacity of the CAES. Where, the power output of the CAES is determined by the difference between the system load and the mean value and the peak load shaving coefficient, as is shown in Formula (1),

$$P_{\mathrm{CA},t} = \sigma \cdot (L_t - L_{\mathrm{avg}}) \tag{1}$$

where, $P_{CA,t}$ represents the power output of the CAES, $P_{CA,t} > 0$ represents the CAES charging to storage electricity and $P_{CA,t} < 0$ represents the CAES discharging; σ represents the peak load shaving coefficient; L_t represents the load value at tth period; L_{avg} represents the average value of load data.

Based on the consideration of the system economy, it mainly consider about the effects of the CAES's costs, which is determined by the capacity of CAES. Therefore, by introducing peak load shaving coefficient σ to measure the effect of peak load regulation, as is shown in Formula (2). Considering about the economy of the power system, the capacity of CAES is smaller than the ideal peak load shaving energy, that is to say σ is smaller than 1.

$$\sigma = \frac{E_{CA}^{N}}{E_{peak}} \tag{2}$$

where, E_{CA}^{N} is the rated capacity of the CAES; E_{peak} is the ideal peak load shaving energy, and it is the summation of the load difference at each period, as is shown in Formula (3).

$$E_{peak} = \sum \left(L_t - L_{avg}\right) \cdot \Delta T_L T_{peak} = \left\{t | L_t \geq L_{avg}\right\} \tag{3}$$

where, L_{avg} is the average load in a day; L_t is the load value at tth period; T_{peak} is the set of the period that the load value is larger than the mean value; ΔT_L is the time interval of the peak load curve.

From above, if the capacity of the CAES is large enough, the regulation effect of peak load shaving is better, and it can reduce the peak load regulation pressure. However, considering about the economic factor, it is enough if the capacity of CAES can meet the requirement to reduce the load difference.

3 The Optimal Configuration Model of the Battery and Small-Scale Compressed Air Energy Storage System

3.1 Objective Function

The objective function of the hybrid energy storage system are the system costs, which contains the network loss costs, the investment costs of the hybrid energy storage system, the costs of injection reactive power into the distribution network, the electricity transaction costs and the opportunity compensation costs caused by the wind power output fluctuation rate limit, as is shown in Formula (4). Where,

considering about the operating periods, the costs are converted into annual value of investment.

$$\min F = F_{\mathrm{INV}} + F_{\mathrm{LOSS}} + F_{\mathrm{HV}} + F_{\mathrm{DG}} + F_{\mathrm{TR}} + F_{\mathrm{PUN}} \tag{4}$$

where, F represents the system total costs; F_{INV} represents the investment costs of the hybrid energy storage system; F_{LOSS} represents the costs of network loss; F_{HV} represents the reactive power absorbing costs from the high voltage network; F_{DG} represents the reactive power costs caused by the distributed wind power generation; F_{TR} represents the electricity transaction costs; F_{PUN} represents the compensation costs caused by the wind power output fluctuation rate limit.

(1) **The investment costs of the energy storage system**

The investment costs of the battery and the small-scale CAES are determined by their power and energy capacity.

$$F_{\mathrm{INV}} = F_{\mathrm{B}} + F_{\mathrm{CA}} \tag{5}$$

$$F_{\mathrm{B}} = n_{\mathrm{B}} \cdot \left(\pi_B^P \cdot P_B^N + \pi_B^E \cdot E_B^N\right) \cdot CRF(r, Y_{\mathrm{B}}) \tag{6}$$

$$F_{\mathrm{CA}} = n_{\mathrm{CA}} \cdot \left(\pi_{\mathrm{CA}}^P \cdot P_{\mathrm{CA}}^{\mathrm{N}} + \pi_{\mathrm{CA}}^E \cdot E_{\mathrm{CA}}^{\mathrm{N}}\right) \cdot CRF(r, Y_{\mathrm{CA}}) \tag{7}$$

where, F_{B} is the investment costs of BESS; F_{CA} is the investment costs of small-scale CAES; n_{B} is the quantity of BESS; $\pi_{\mathrm{B}}^{\mathrm{P}}$, $\pi_{\mathrm{B}}^{\mathrm{E}}$ is the unit costs of power and energy of BESS; $P_{\mathrm{B}}^{\mathrm{N}}$, $E_{\mathrm{B}}^{\mathrm{N}}$ is the rated power and energy capacity of BESS; n_{CA} is the quantity of small-scale CAES; $\pi_{\mathrm{CA}}^{\mathrm{P}}$, $\pi_{\mathrm{CA}}^{\mathrm{E}}$ is the unit costs of power and energy of small-scale CAES; $P_{\mathrm{CA}}^{\mathrm{N}}$, $E_{\mathrm{CA}}^{\mathrm{N}}$ is the rated power and energy capacity of CAES; CRF (r,Y) is the uniform annual value of the investment costs; r is the discount rate; Y_{B} and Y_{CA} is the lifetime of BESS and CAES.

(2) **The loss costs of the distribution network**

The loss costs is the summation of the costs caused by power loss of each line at all periods in all typical days, as is shown in Formula (8),

$$F_{\mathrm{LOSS}} = \sum_{m=1}^{N_{\mathrm{d}}} \left(N_{\mathrm{days},m} \cdot \sum_{l=1}^{N_l} \sum_{t=1}^{T} \left(\pi_{\mathrm{LOSS},t} \cdot P_{\mathrm{LOSS},lt} \cdot \Delta T_{\mathrm{P}}\right) \right) \tag{8}$$

where, N_{d} is the types of typical days in a year; $N_{\mathrm{days},m}$ is the number of each typical day; $\pi_{\mathrm{LOSS},t}$ is the unit loss costs at tth period; $P_{\mathrm{LOSS},lt}$ is the power loss at tth period of the lth line; ΔT_{P} is the time interval of each period; N_l is the quantity of all lines in the distribution network.

(3) **The costs of absorbing reactive power from high voltage side**

This costs is the summation of absorbing reactive power from high voltage side at each period in all typical days, as is shown in Formula (9),

$$F_{\mathrm{HV}} = \sum_{m=1}^{N_{\mathrm{d}}} \left(N_{\mathrm{days},m} \cdot \sum_{t=1}^{T} \left(\pi_{\mathrm{HV},t} \cdot Q_{\mathrm{HV},t} \cdot \Delta T_{\mathrm{P}} \right) \right) \tag{9}$$

(4) **The costs of the reactive power provided by the distributed wind power supply**

The wind generators will increase power loss while providing reactive power and it will decrease the active power transaction to meet the reactive power need. Thus, it is essential to calculate the costs of the reactive power provided by the wind generators of each node in the distribution network, as is shown in Formula (10),

$$F_{\mathrm{DG}} = \sum_{m=1}^{N_{\mathrm{d}}} \left(N_{\mathrm{days},m} \cdot \sum_{k=1}^{N_{\mathrm{W}}} \sum_{t=1}^{T} \left(\pi_{\mathrm{DG},t} \cdot Q_{\mathrm{DG},kt} \cdot \Delta T_{\mathrm{P}} \right) \right) \tag{10}$$

where, N_{W} is the quantity of distributed wind power generation; is the unit cost of the distribution power source at tth period; $Q_{\mathrm{DG},kt}$ is the reactive power output of the kth wind power generation at tth period.

(5) **The electricity transaction costs**

The electricity of the distribution network is mainly provided by the distributed wind power generation, and the other is obtained from the high voltage side. Since the wind power generators are installed in the distribution network, the transaction costs can only calculate the costs to purchase electricity, as is shown in Formula (11),

$$F_{\mathrm{TR}} = \sum_{m=1}^{N_{\mathrm{d}}} \left(N_{\mathrm{days},m} \cdot \sum_{t=1}^{T} \left(\pi_{\mathrm{En},t} \cdot P_{\mathrm{En},t} \cdot \Delta T_{\mathrm{P}} \right) \right) \tag{11}$$

where, $\pi_{\mathrm{En},t}$ is the unit cost to purchase electricity from the high voltage side; $P_{\mathrm{En},t}$ is the active power provided from the high voltage side.

(6) **The opportunity compensation costs**

Since the wind power output fluctuation have serious influence on the stable operation of the power system, many countries including China have put forward the limitation of wind power fluctuation rate to reduce the effects. If the energy storage systems (ESS) are installed in the distribution network to mitigate the wind power output fluctuation, and considering about the costs of ESS, the capacity of ESS can't be totally determined by the wind power output limitation. Therefore, there will exist the high frequency wind power output component, which will

produce serious influence on the power system. Thus, the system should be kept stable by those flexible power sources, which will increase the system operating costs. Therefore, the opportunity compensation costs are proposed to measure this part of risks, as is shown in Formula (12),

$$F_{\mathrm{PUN}} = \sum_{m=1}^{N_{\mathrm{d}}} \left(N_{\mathrm{days},m} \cdot \sum_{n=1}^{N_{\mathrm{S}}} \pi_{\mathrm{PUN}} \cdot \mathrm{d}P_{\mathrm{W}} \cdot \Delta T_{\mathrm{S}} \right) \tag{12}$$

where, π_{PUN} is the coefficient of opportunity compensation costs; $\mathrm{d}P_{\mathrm{W}}$ is the power difference that the wind power exceed the limitation of the wind power output fluctuation rate; ΔT_{S} is the sampling period of wind power output.

3.2 Constraints

(1) **The power flow constraints of all nodes in the system**

$$\begin{aligned} P_{it} &= U_{it} \sum_{j=1}^{N} U_{jt} \left[G_{ij} \cos\left(\delta_{it} - \delta_{jt}\right) + B_{ij} \sin\left(\delta_{it} - \delta_{jt}\right) \right] \\ Qit &= U_{it} \sum_{j=1}^{N} U_{jt} \left[G_{ij} \sin\left(\delta_{it} - \delta_{jt}\right) - B_{ij} \cos\left(\delta_{it} - \delta_{jt}\right) \right] \end{aligned} \tag{13}$$

where, P_{it}, Q_{it} is the active and reactive power output of ith node at tth period; U_{it}, U_{jt} is the voltage of ith and jth node at tth period; δ_{it}, δ_{jt} is the phase angle of node i, j at tth period; G_{ij}, B_{ij} is the real part and imaginary part of the element at ith row and jth column in the node admittance matrix.

(2) **The power output constraints of the distributed wind power generation**

$$P_k^{\min} \leq P_{\mathrm{W},kt} \leq \mathrm{P}_k^{\max} \tag{14}$$

where, $\mathrm{P}_{\mathrm{W},kt}$ is the wind power output of kth node at tth period; $P_k^{\min}$, $P_k^{\max}$ is the minimum and maximum power output of the kth wind power generation.

(3) **The voltage value constraints of each node**

$$U_i^{\min} \leq U_{it} \leq U_i^{\max} \tag{15}$$

where, $U_i^{\min}$, $U_i^{\max}$ is the minimum and maximum voltage value of ith node.

(4) **The power output constraints of each line**

$$-P_l^{\max} \le P_{lt} \le P_l^{\max} \tag{16}$$

where, P_{lt} is the power output at tth period of the lth branch; $P_l^{\max}$ is the maximum active power output of the lth branch.

(5) **The capacity balancing and power output constraints of BESS**

$$\max\left(-P_{\mathrm{B}}^{\mathrm{N}}, \frac{E_{\mathrm{B},n} - E_{\mathrm{B}}^{\mathrm{N}}}{T_{\mathrm{S}}} \cdot \eta_{\mathrm{B,d}}\right) \le P_{\mathrm{B},n}^{\mathrm{act}} \le \min\left(P_{\mathrm{B}}^{\mathrm{N}}, \frac{E_{\mathrm{B},n} - E_{\mathrm{B}}^{\min}}{T_{\mathrm{S}} \cdot \eta_{\mathrm{B,c}}}\right) \tag{17}$$

$$E_{\mathrm{B},n} = E_{\mathrm{B},n-1} + T_{\mathrm{S}}\left(P_{\mathrm{B},n}^{\mathrm{act}} \cdot \eta_{\mathrm{B},c} + \frac{P_{\mathrm{B},n}^{\mathrm{act}}}{\eta_{\mathrm{B,d}}}\right) \tag{18}$$

$$E_{\mathrm{B}}^{\min} \le E_{\mathrm{B},n} \le E_{\mathrm{B}}^{\mathrm{N}} \tag{19}$$

where, $P_{\mathrm{B},n}^{\mathrm{act}}$ is power output of the BESS at tth period; $P_{\mathrm{B},n}^{\mathrm{act}} > 0$ represents the BESS charging, $P_{\mathrm{B},n}^{\mathrm{act}} < 0$ represents the BESS discharging; $E_{\mathrm{B},n-1}$ and $\mathrm{E}_{\mathrm{B},n}$ is the electricity capacity of CAES at $n-1$th and nth period; $\eta_{\mathrm{B,c}}$, $\eta_{\mathrm{B,d}}$ is the charging and discharging efficiency of CAES; $P_{\mathrm{B}}^{\mathrm{N}}$ is the rated power output of BESS; $E_{\mathrm{B}}^{\min}$ is the minimum electricity capacity of BESS.

(6) **The capacity balancing and power output constraints of CAES**

$$\max\left(-P_{\mathrm{CA}}^{\mathrm{N}}, \frac{E_{\mathrm{CA},t} - E_{\mathrm{CA}}^{\mathrm{N}}}{\Delta T} \cdot \eta_{\mathrm{CA,d}}\right) \le P_{\mathrm{CA},t} \le \min\left(P_{\mathrm{CA}}^{\mathrm{N}}, \frac{E_{\mathrm{CA},t} - E_{\mathrm{CA}}^{\min}}{\Delta T \cdot \eta_{\mathrm{CA,c}}}\right) \tag{20}$$

$$E_{\mathrm{CA},t} = E_{\mathrm{CA},t-1} + \Delta T\left(P_{\mathrm{CA},t} \cdot \eta_{\mathrm{CA,c}} + \frac{P_{\mathrm{CA},t}}{\eta_{\mathrm{CA,d}}}\right) \tag{21}$$

$$E_{\mathrm{B}}^{\min} \le E_{\mathrm{B},n} \le E_{\mathrm{B}}^{\mathrm{N}} \tag{22}$$

where, $P_{\mathrm{CA},t}$ is the power output of CAES at tth period, $P_{\mathrm{CA,t}} > 0$ represents the CAES charging, $\mathrm{P}_{\mathrm{CA},t} < 0$ represents the CAES discharging; $E_{\mathrm{CA,t}}$ and $E_{\mathrm{CA,t}-1}$ is the electricity capacity of CAES at tth and $t-1$th period; $\eta_{\mathrm{CA,c}}$, $\eta_{\mathrm{CA,d}}$ is the charging and discharging efficiency of CAES; $P_{\mathrm{CA}}^{\mathrm{N}}$ is the rated power of CAES; $E_{\mathrm{CA,min}}$ is the minimum electricity capacity of CAES; $E_{\mathrm{CA},t}$ is the electricity capacity at tth period.

(7) **The number constraints of the BESS and CAES**

$$n_{\mathrm{B}} \leq n_{\mathrm{B}}^{\max} \tag{23}$$

$$n_{\mathrm{CA}} \leq n_{\mathrm{CA}}^{\max} \tag{24}$$

where, n_{B}, n_{CA} is the quantity of BESS and CAES; $n_{\mathrm{B}}^{\max}$, $n_{\mathrm{CA}}^{\max}$ is the maximum value of BESS; $n_{\mathrm{B}}^{\max}$, $n_{\mathrm{CA}}^{\max}$ is the maximum value of BESS and CAES to install in the system.

(8) **The voltage fluctuation rate limit constraints of all nodes in the system**

$$\Delta U_i < \Delta U^{\max} \tag{25}$$

$$\Delta U_i = \frac{\max(U_i) - \min(U_i)}{U_{\mathrm{N}}} \times 100\% \tag{26}$$

where, ΔU_i is the voltage fluctuation rate of ith node; $\Delta U\max$ is the maximum voltage fluctuation rate limit; U_{N} is the rated voltage of the power system.

3.3 The Optimal Method of the Hybrid Energy Storage System

The optimal configuration of the hybrid energy storage system includes 3 parts, which are the location optimization, the capacity optimization of the hybrid energy storage system and the coordinated operation of the power system. The optimization flow chart is as in Fig. 2.

3.4 The Solving Method of the Configuration Model

Based on the configuration model above, the IBM optimizer engine CPLEX is called in matlab to solve this model.

4 Case Study

In the case, take a distribution network of 17 nodes as an example, and it is modified considering about the actual facts, as is shown in Fig. 3. And in Fig. 3, node 1 is the high voltage node.

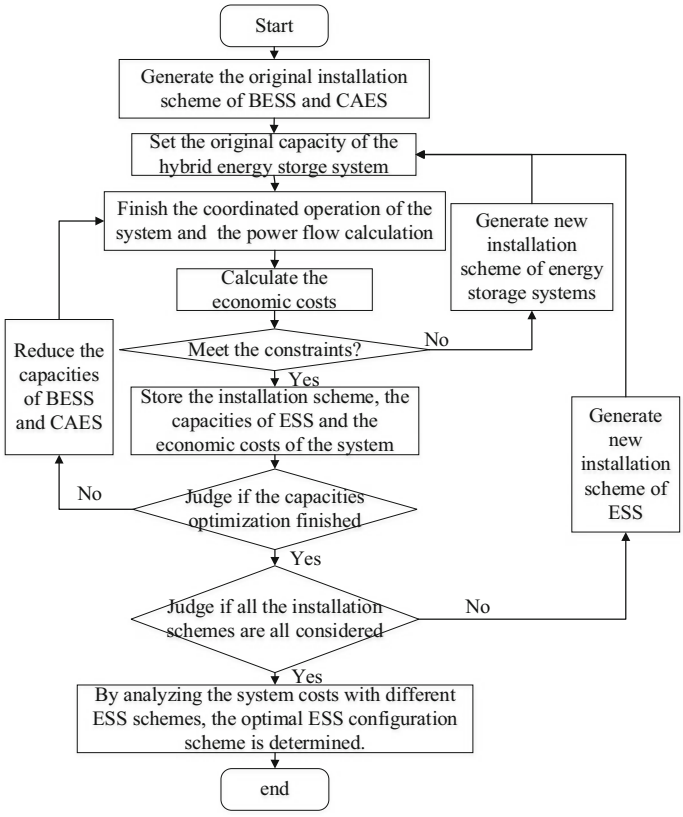

Fig. 2 Flow chart of constructing semantic framework

The load data and the line data of the distribution network are shown in [11, 12]. In this system, the reserve rate of system load is 0.2. Based on this distribution network integrated with high penetration of wind power, the optimization method of hybrid energy storage system is discussed. The distributed wind power generations are installed in the node 6, 8, 9,11,13,17, and the power factor of one single wind power generation is 0.5, and the rated capacity is 0.5 MW.

The unit network loss cost, the unit reactive power absorbing cost and the unit cost that the HESS provide reactive power is all related with the electricity cost of the power system. And in this case, time of use price is applied. π_{LOSS} represents the electricity of the same period; π_{HV} is 6% of π_{HV}, and π_{DG} is 3% of π_{LOSS}.

Since the vanadium redox flow battery has large energy density and great application prospect, it is used as the battery energy storage system in our case. And the unit power and capacity cost is 426 $/kW and 100 $/kWh [13, 14], the lifetime of the battery is 5 years. The discount rate is 10%. The unit opportunity compensation cost π_{PUN} is 100 $/MW, the unit punish cost of discarding wind power is 1000 $/MWh. The unit power and capacity of CAES is 580 $/kW and 28 $/kWh

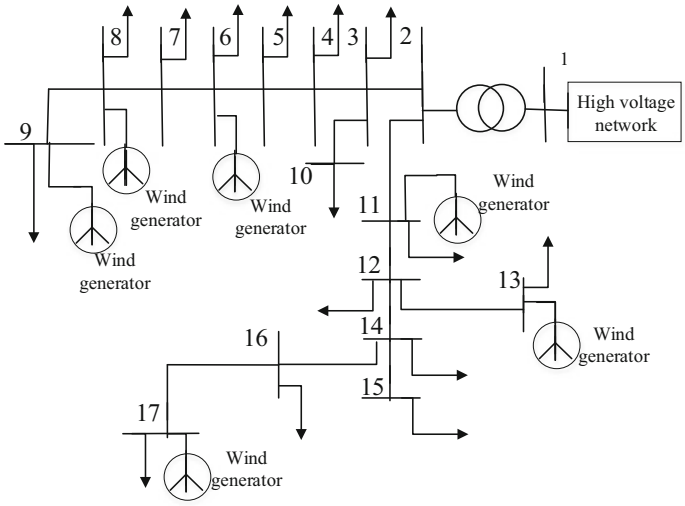

Fig. 3 Flow chart of constructing semantic framework

[15]. The charging and discharging efficiency of BESS is 0.9, and the limitation of SOC is 0.2 and 0.9. The charging and discharging efficiency is 0.6, and the limitation of SOC is 0.2 and 0.9.

4.1 The Power Output Determination Method of the Battery and CAES

The history data of wind power output is used, and pick the wind curves with large fluctuation amplitude and high fluctuation frequency as the typical wind curves. And based on the analysing of the wind power output and the load data, the optimal output curves of BESS and CAES are shown in Figs. 4 and 5.

4.2 The Optimal Configuration of the Hybrid Energy Storage System

Based on the optimal output curve of BESS and CAES above, the optimal capacity of BESS and CAES are calculated. And the optimal capacity of BESS and CAES are shown in Table 1, the concrete data of the system costs are shown in Table 2. From the results above, we can reach some conclusions as follow,

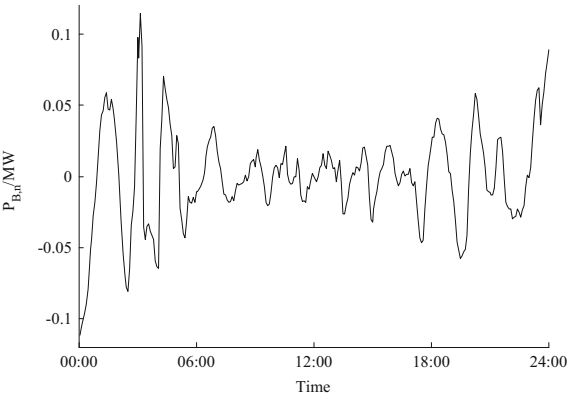

Fig. 4 The daily output curve of the battery energy storage system flow chart of constructing semantic framework

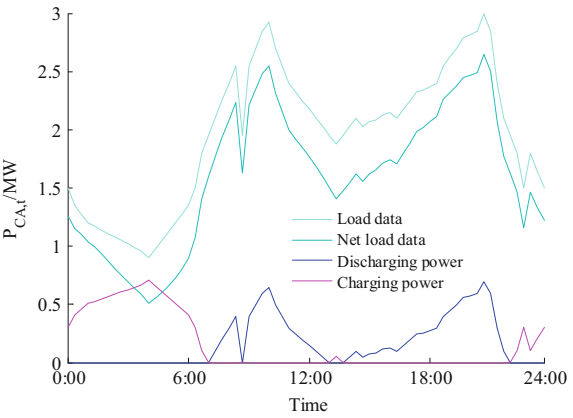

Fig. 5 The daily output curve of the compressed air energy storage system

Table 1 Optimal configuration results of the hybrid energy storage systems

Installation way	Installation schemes			Parameters		System costs ($\times 10^4$ \$)
	Node	P_B^N/E_B^N MW/(MW h)	P_{CA}^N/E_{CA}^N MW/(MW h)	ΔU %	ΔP %	
Without ESS	/	/	/	3.12	27.8	1321.8
With ESS	6	0.127/0.13	1.16/7.3	1.67	4.2	1319.4
	8	0.127/0.13	/			
	9	0.127/0.13	/			
	11	0.127/0.13	/			
	13	0.127/0.13	/			
	17	0.127/0.13	/			

Table 2 Calculation results of the system costs

Costs	Without ESS	With ESS
F_{LOSS} ($)	82,178	80,339
$F_{Q.HV}$ ($)	241,126	241,398
$F_{Q.DG}$ ($)	256,800	256,800
F_{ESS} ($)	/	155,225
F_{PA} ($)	12,518,445	12,460,538
F_{pun} ($)	119,489	0
F ($)	13,218,040	13,194,301

(1) In the distribution network with wind power generation integrated, the quality of voltage becomes poor without any energy storage system installed in the system. The maximum voltage fluctuation rate reached 3.12%, which exceed the limitation of the voltage fluctuation rate. And with the BESS installed in the system, the qualities of voltage of all nodes have improved, the fluctuation rate decreased to 1.67%, which proved the effectiveness of BESS.
(2) Since the random fluctuation of wind power output, it has great influence on the stable operation of the power system. And the power output fluctuation rate is reduced thanks to the energy storage system.
(3) From the optimization results of ESS we can get, the CAES can be installed in one optimal node for peak load regulation, and the electricity transaction costs have decreased and the investments of CAES are smaller than the reduced costs, which prove the effectiveness of the CAES installed in the system.

5 Conclusions

In order to improve the utilization rate of wind power, the hybrid energy storage system composed of BESS and small-scaled CAES is proposed, and the capacity optimization model and the calculation method are discussed. And by analyzing the case of the distribution network, the model and the method are verified and the conclusions are as follow,

(1) By introducing peak load shaving coefficient σ to measure the effects of peal load regulation, the peak load regulation method is discussed, and the power output of CAES is optimized.
(2) By analyzing the operational principle of the hybrid energy storage system in the distribution network, the BESS is used for wind power fluctuation mitigation and CAES is used for peak load regulation, which can improve the economic efficiency of the system.
(3) The optimization model is discussed from 3 parts, which are the location optimization, the capacity optimization of the hybrid energy storage system and the coordinated operation of the power system. By analyzing the economic

efficiency of the system, the optimal configuration scheme is determined. And the proposed model and operation method are verified on the modified distribution network, the results are presented to prove the feasibility and effectiveness of the proposed model and method.

Acknowledgements This work was supported in part by the Youth Promotion Fund "The design of checking and statistical analysis system for power grid Equipment based on data mining technology".

References

1. Zhang Y, Bai J, Xin S (2010) Study on the key issues concerning development and consumption of wind power in China. Energy Technol Econ 22:1–6
2. Wu W (2012) The optimal placement of different types of distributed generation in distribution network. Mod Electr Power 29:6–11
3. Atwa YM, El-Saadany EF (2010) Optimal allocation of ESS in distribution systems with a high penetration of wind energy. IEEE Trans Power Syst 25:1815–1822
4. Xiang Y, Wei Z, Sun G (2015) Life cycle cost based optimal configuration of battery energy storage system in distribution network. Power Syst Technol 39:264–270
5. Hu R, Ren R, Yand F (2014) Optimal allocation of energy storage system in distribution network. East China Electr Power 42:345–349
6. Tang W, Liang W, Cui R (2015) Optimal allocation method of distribution energy storage system in distribution network. Electr Power Constr 36:38–45
7. Tao Q, Sang B, Ye J et al (2016) Optimal configuration method of distribution network with high penetration of photovoltaic. High Voltage Eng 42:2158–2165
8. You Y, Liu D, Zhong Q (2014) Multi-objective optimal placement of energy storage systems in an active distribution network. Autom Electr Power Syst 38:46–52
9. Shen X, Zhu S, Zheng J (2015) Active distribution network planning-operation co-optimization considering the coordination of ESS and DG. Power Syst Technol 39:1913–1920
10. Lou S, Yang T, Wu Y et al (2016) Coordinated optimal operation of hybrid energy storage in power system accommodated high penetration of wind power. Autom Electr Power Syst 40:30–35
11. Technical rule for connecting wind farm to the power system, GB/T 19963–2011. China Standard Press, Beijing, 2011
12. Carpinelli G, Celli G, Mocci S et al (2013) Optimal integration of distributed energy storage devices in smart grids. IEEE Trans Smart Grid 4:985–995
13. Chacra FS, Bastard F, Fleury G et al (2005) Impact of energy storage costs on economical performance in a distribution substation. IEEE Trans Power Syst 20:1–5
14. Jiang K, Li H, Li W (2013) On several battery technologies for power grids. Autom Electr Power Syst 37:47–53
15. Tian C, Zhang C, Li K (2015) Composite energy storage technology with compressed air energy storage in microgrid and its cost analysis. Autom Electr Power Syst 39:36–41

Analyses on Back to Back Test of Grid-Side Battery Storage Stations Based on Semi-isolated Bidirectional Converter

Hao Xu, Xinjue Xia, Weijun Zhu, Yabin Yan, Bin Yu, Siyuan Guo, Fan Ouyang and Gang Li

Abstract Although battery energy storage technology has been born for a long time, it is mainly built with new energy power generation. This paper focuses on the back to back test of battery energy storage stations, which is seldom carried out in the field of new energy. On the basis of structure anatomy and principle analysis, combined with the engineering debugging example of Changsha Langli energy storage station, the back to back test method, process and mechanism of battery energy storage stations based on semi-isolated bidirectional converter are deeply analyzed, and PDP protection action and group control of the back to back test are studied and solved. Functional verification and other key issues are expected to provide useful reference for relevant practitioners and engineering applications.

Keywords Semi-isolated · Voltage source converter · Grid-side · Battery storage stations · Back to back test

1 Introduction

The space-time migration ability of energy storage system to power and energy is an effective measure to solve the inherent problems of intermittent new energy such as power output fluctuation, intermittent and so on. With the widespread application of new energy technologies such as wind power generation and photovoltaic power generation, energy storage system has developed rapidly. Grid-side battery energy storage stations (BESS) have the functions of participating in peak-load and valley-filling, frequency regulation, reactive power support and emergency control.

H. Xu (✉) · W. Zhu · Y. Yan · B. Yu · S. Guo · F. Ouyang · G. Li
State Grid Hunan Electric Power Co., Ltd., Research Institute, Changsha 410007, China
e-mail: 702110505@qq.com

X. Xia
Powerchina Hebei Electric Power Design & Research Institute Co., Ltd., Shijiazhuang 050031, China

Y. Xue et al. (eds.), *Proceedings of PURPLE MOUNTAIN FORUM 2019-International Forum on Smart Grid Protection and Control*, Lecture Notes in Electrical Engineering 585, https://doi.org/10.1007/978-981-13-9783-7_25

Large-scale construction of BESS can effectively enhance the flexibility, stability, economy and cleanliness of the system operation [1–4]. In recent years, under the guidance of relevant policies, they have developed rapidly. Local governments and power grid enterprises in Jiangsu, Hunan, Henan, Qinghai and other places are positively position and promote the construction of BESS on the grid side.

Battery energy storage technology has been born for a long time, but it is seldom used in power grid except as low-voltage DC power supply for power plants and stations. In essence, the low-voltage DC power supply system can be classified as miniature BESS, but the technical innovation and strict requirements of battery material, scale, dynamic performance and operation flexibility of BESS make the technology of power grid-side BESS become a hot research topic nowadays. Relevant scholars and practitioners have made in-depth research on BESS modeling and operation strategy optimization, but few literature related to the specification and optimization of on-site adjustment technology [5–9]. In fact, a series of regulations, such as power grid construction, operation and maintenance and safety management, are different from new energy power plants. The experience accumulated by battery energy storage technology in the field of new energy is not fully applicable to the power grid. During the on-site adjustment of Changsha Langli BESS, the authors found that the power conversion system (PCS) back to back test should be carried out to verify the safety and correctness of communication and functional interaction among the three systems of energy management system (EMS), PCS and battery management system (BMS) before the BESS is connected to the grid. In the field of new energy, there is no requirement, so the relevant manufacturers do not have relevant test experience, which once led to slow progress and frequent errors and omissions during the on-site adjustment. In view of this, this paper will comb the operation principle and back to back test method of the BESS on the grid side in accordance with the on-site adjustment practice of the first phase demonstration project of Hunan Changsha BESS. Based on the primary system structure of the BESS, the optimization scheme of back to back test and the group control test scheme under the off-grid mode will be put forward, including the PDP protection action. In order to provide useful reference for relevant practitioners and engineering debugging and maintenance, this paper makes an in-depth discussion on the subject.

2 Operation Principle of BESS

2.1 System Structure of the Isolated PCS

The single PCS system includes voltage source converter (VSC), isolation transformer, switching and cable connection equipment, as shown in Fig. 1. After the AC side of the grid-connected contactor and the DC side of the capacitor charging circuit are charged, the VSC can start normally. Then the capacitor charging circuit

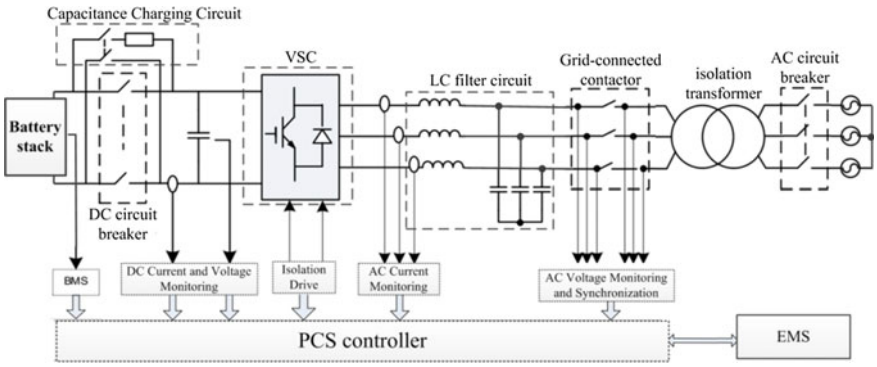

Fig. 1 Main circuit block diagram of isolated converter

is first connected to charge the capacitor of the DC side of the VSC. After filling up, the capacitor charging circuit is automatically disconnected, the DC circuit breaker and the grid-connected contactor are closed, and the trigger pulse is adjusted to realize power transmission and conversion.

PCS can be divided into two types: isolation and non-isolation. Isolated converter refers to PCS and system isolated by AC circuit breaker, and non-isolated converter refers to PCS dry converter connected directly to the system. Figure 1 shows that if the BESS or system fails, fault isolation can be achieved by blocking VSC trigger pulse and disconnecting DC circuit breakers, AC contactors and AC circuit breakers on the unsigned low-voltage side of the isolation transformer, and AC circuit breakers on the high-voltage side of the isolation transformer can be avoided. Unless the maintenance of isolation transformer, 10 kV bus and other related equipment is involved, the AC circuit breaker in Fig. 1 is on closed state after the BESS is put into operation. Because the AC circuit breaker on the isolated transformer side operates fewer times, the switch at present can't be remotely controlled in most PCS manufacturers' supply, so the switch must be manually switched on or off locally. For safety reasons, manual separation of AC side circuit breakers is forbidden in the start-up, operation and shutdown stages of BESSs, so the physical coupling of PCS in the station is actually formed, which is not conducive to the separate control of PCS and accurate isolation of faults. At the same time, due to the physical coupling of isolation transformer, when the BESS is electrified, it is often that multiple isolation transformers are electrified at the same time. The coupling and superposition of inrush current will raise the relative fixed value of upper protection equipment, and then reduce the sensitivity of protection, which is not conducive to the safe and stable operation of the system. In this paper, PCS that isolated transformer and grid is connected by AC circuit breaker which cannot be remotely controlled is called semi-isolated bi-directional converter, and its structure is still the same as that in Fig. 1.

2.2 Control Principle

The basic system structure of PCS can be simplified to Fig. 2. In the figure, U_{pa}, U_{pb} and U_{pc} are the output three-phase AC voltage for PCS respectively; U_{sa}, U_{sb} and U_{sc} are the three-phase AC voltage for system respectively; L_a, L_b and L_c are equivalent reactance between PCS and system respectively; I_a, I_b and I_c are three-phase currents on the connection line of PCS and system respectively; C is parallel capacitor of DC side of PCS. PWM technology is based on the principle of pulse equivalence. The DC bus voltage is divided into equal-amplitude and unequal- width SPWM waves by fast on-off coordination of full-controlled transistor IGBT bridge, and then three-phase AC voltage is output after LC filtering. By changing the modulation ratio and IGBT trigger pulse time, PCS can flexibly adjust the amplitude and phase of output three-phase AC voltage.

Assuming that the impedance between PCS and the system is pure inductive, the active and reactive power exchanged between PCS and the system can be expressed as [10]:

$$\begin{cases} P = \left(V_s V_p \sin\delta\right)/(\omega L) = (mV_s V_{dc} \sin\delta)/(\omega L) \\ Q = V_s\left(V_s - V_p \cos\delta\right)/(\omega L) = V_s(V_s - mV_{dc} \cos\delta)/(\omega L) \end{cases} \tag{1}$$

where V_s and V_p are three-phase AC voltages from the system and PCS respectively; δ is phase difference between V_s and V_p; L is the impedance between PCS and the system; ω is system angular frequency; m is the modulation ratio; V_{dc} is the DC side voltage of PCS. Given the active and reactive power command values, m and δ can be calculated according to Formula (1), and the amplitude and phase of signal wave can be obtained according to m and δ, and then the orderly control of IGBT bridge can be realized. Because the system voltage is relatively stable, the connection current between PCS and the system is controlled by Formula (1). The widely used control strategy of PCS in engineering practice is direct current control, i.e. the closed-loop control of the connection current between PCS and the system is realized by controlling the output three-phase AC voltage of PCS. Formula (1) shows that active power and reactive power are coupled. In order to realize the

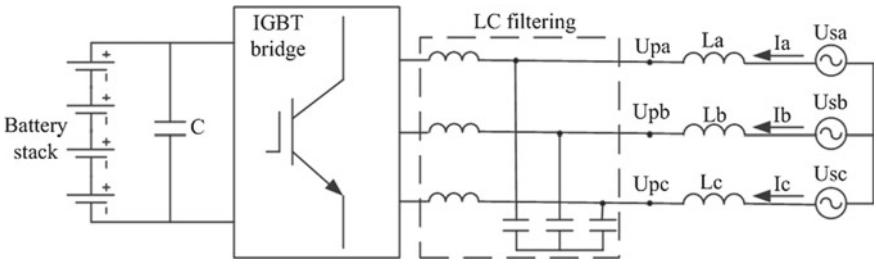

Fig. 2 PCS simplified system structure diagram

single regulation of active and reactive power, the alternating current and voltage are further converted by DQ transformation and supplemented by feed-forward compensation in engineering to realize the decoupling control of active and reactive power and the suppression of steady-state error.

From the point of view of coordination function positioning, there are two main operation modes of grid-side battery energy storage station: constant power control and voltage frequency control. Under the constant power control mode, EMS can distribute power orderly according to the charge/discharge capacity of each PCS, while under the voltage-frequency control mode, PCS can automatically adjust power output according to the closed-loop control of AC voltage and frequency. Battery energy storage station normally operates in constant power control mode and adjusts the power level of the whole station according to AGC, AVC instructions and automatic power curve.

3 Back to Back Test and Analysis of Its Key Problems

Back to back test is actually a joint test of two or more PCS in the BESS under the condition of isolated network. It is an effective means to test the communication and functional interaction performance of EMS, PCS and BMS. The analysis in this section will be based on the engineering example of Langli BESS, which has a rated capacity of 24 MW/48 MWh and contains 48 PCS. There are differences in the details of some switch control modes, circuits and control strategies between different stations, but the overall test mode is still applicable.

There must be only one PCS in the voltage and frequency control mode for back to back test, that is, as a balance contact, and the other PCS involved in back to back test are in the constant power control mode. The background of EMS sends power instructions to PCS in power control mode separately, while the latter responds to power regulation instructions, the balance contacts follow the response by voltage and frequency control, thus realizing the power charge-discharge balance. Before the back to back test is completed, the BESS does not have the grid connection conditions to avoid the energy storage system failure affecting the safe and stable operation of the power grid. The two PCS of the same isolation transformer of the Langli BESS can not operate simultaneously in the voltage-frequency control mode and the constant power control mode respectively. Therefore, the back to back test includes at least two sets of PCS belonging to different isolated transformers, as shown in Fig. 3. Figure 3 contains two PCS, 1-1 and 2-1, respectively. Some manufacturers can operate two PCS under the same isolation transformers in voltage frequency control mode and constant power control mode respectively for back to back test, but this method is still applicable.

In back to back test, a PCS must be started first through the voltage and frequency control mode. In this mode, the AC voltage can be set up without load after the DC side voltage is established. The example of starting PCS 1-1 first is illustrated. Before starting 1-1, all switches in battery stack 1-1 must be closed to

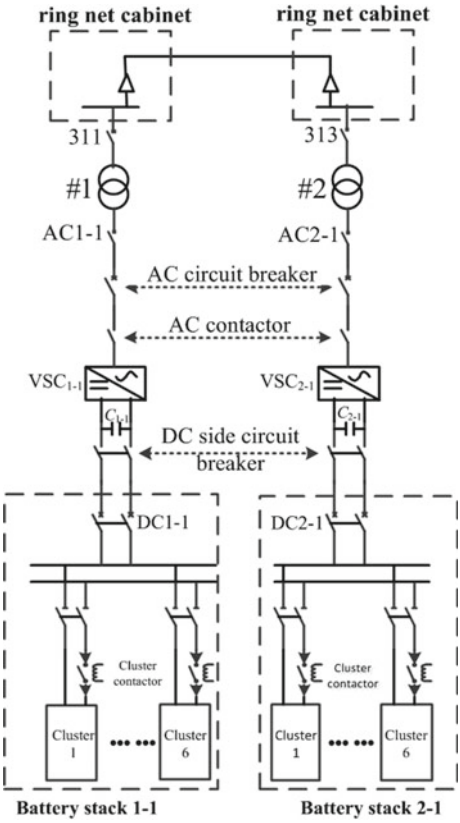

Fig. 3 Basic structure diagram of back to back test

establish the DC side voltage of PCS1-1. Then set VSC1-1 as voltage-frequency control mode and start VSC1-1. After VSC1-1 is started, the capacitor charging circuit is connected to charge the capacitor of the DC side of VSC. After the capacitor is charged, the capacitor charging circuit is automatically disconnected, the VSC DC side circuit breaker and AC contactor are closed, so that the AC side of PCS is voltage-built. At this time, the voltage and temperature of each cluster of the battery stack, the voltage and temperature of the single cell of the battery stack, and PCS can be checked. DC side voltage and AC side voltage and other parameters.

In constant power mode, the situation is slightly on the contrary. Before starting, both AC side and DC side of PCS must have voltage. PCS1-1 is in the voltage-frequency control mode, and PCS2-1 should be set on the constant power control mode accordingly. Before starting PCS2-1, the opposite operation flow can be adopted, that is, after 1-1 sets up AC voltage in voltage-frequency mode and manually closes AC2-1 to provide AC voltage for PCS2-1. Then PCS2-1 is set locally as constant power control mode, and PCS2-1 is started after the DC side voltage of PCS2-1 is established. PCS 1-1 and PCS 2-1 form an isolated network after PCS 2-1 is started up, and PCS 1-1 and PCS 2-1 charge and discharge each

other by sending power instructions to PCS 2-1 through EMS. In this process, the cluster current, total current, cell temperature, PCS AC current, power and charge/discharge capacity of the stack can be checked.

The above is the back to back test flow of two PCS. During the back to back test process, each PCS should be charged and discharged at least once to verify the function and power direction of the three systems. If conditions permit, multiple PCS can participate the back to back test at the same time, but from the point of view of communication channel and signal check, the back to back test of multiple PCS should also send power instructions to each PCS one by one. Due to the long start time of PCS in voltage-frequency mode, the back to back test of multiple PCS can avoid multiple no-load start-up of PCS at the same time, thus significantly improving the test efficiency.

3.1 Analysis of Key Problems in Back to Back Test

PDP Protection Action Problem. The back to back test of multiple PCS can improve the test efficiency, but there may be PDP protection action problems. PDP protection will operate when there is a fault signal in the driver board, or if there is an overcurrent in the hardware (including AC and DC overcurrent), or if there is a direct connection in the PWM. However, from the field debugging, the main reason for PDP action is the hardware overcurrent (including AC and DC overcurrent). There are two kinds of over-current phenomena in back to back test: one is No-load isolated transformer starting, the other is multiple no-load isolated transformers starting simultaneously. No-load isolated transformer starting, that is, when one PCS is started by voltage-frequency control and starting another PCS connected on the AC side may produce a larger inrush current, resulting in hardware overcurrent. Because the no-load transformer starting will produce larger inrush current, the isolated transformer participating in back to back test should start at the same time with the PCS in the voltage-frequency control mode, and reduce the inrush current through the smooth control of AC voltage during the start-up process of PCS. However, when multiple isolated transformers start at the same time, the parallel effect of the equivalent capacity of the device may produce larger capacitive currents, resulting in hardware overcurrent. Therefore, the realization of multi-PCS back to back test depends on the parameter configuration of PCS and its external circuit; when conditions are not allowed, only the back to back test of two PCS which takes a long time can be adopted.

Group Control Function Verification. Group control refers to the manual setting or receiving the whole station power instructions of AGC, AVC master station and automatic power curve in the background, after EMS distributes the total power instructions to each available PCS according to certain principles, each PCS adjusts trigger pulses independently according to the received power instructions, which is the most important function of EMS. The main principle of power allocation in EMS is the possible charging and discharging active power and

absorbable reactive power of each PCS. That is to say, PCS limited by the operation state of BMS will operate at a low power level appropriately. Before the whole station performance test, the EMS group control function can not be verified on site. Therefore, during the back to back test, the group control function of EMS can be validated according to the site conditions, and problems can be found and dealt with in time, so as to gain valuable time for the project to be put into operation as soon as possible. It should be noted that during the back to back test, AGC and AVC do not have the ability of remote control, but they can use external access equipment to simulate the main station to send instructions. During the back to back test, it is not necessary to take all PCS for group control. At least three PCS are needed, and one of them is voltage and frequency control mode. It should be noted that the PCS in the voltage control mode participates in the power allocation of EMS group control, but does not execute the group control power regulation instructions. Therefore, the total power of all participated PCS in the constant power control mode will be lower than the power instructions issued by EMS.

4 Conclusions

The reduction of construction cost of BESS lays a realistic foundation for large-scale storage of electric power. However, at present, the construction of grid-side BESS is still in the experimental demonstration stage, and the relevant debugging methods, technologies and specifications are scarce. This paper focuses on the field debugging technology of BESS. On the basis of a comprehensive analysis of the system structure and operation principle of BESS on the grid side, combined with the engineering debugging example of Changsha Langli BESS, it deeply analyses the back to back test method, process, mechanism and key issues of BESS based on semi-isolated bidirectional converter, hoping to provide reference for engineering practice and scientific research.

References

1. Sun B, Yang S, Li Z et al (2017) Analysis on present application of megawatt-scale energy storage in frequency regulation and its enlightenment. Autom Electr Power Syst 41(11):8–16
2. Ren L, Bai Z, Yu C et al (2014) Research on active power control strategy for wind/photovoltaic/energy storage hybrid power system and its engineering application. Autom Electr Power Syst 38(7):105–111
3. Che Q, Wu Y, Zhu Z et al (2019) Carbon trading based optimal scheduling of hybrid energy storage system in power systems with large-scale photovoltaic power generation. Autom Electr Power Syst 43(03):76–83
4. Chen L, Wu T, Liu H et al (2019) Demand management based two-stage optimal storage model for large users. Autom Electr Power Syst 43(01):194–203
5. Zhu Z, Zhao J, Wei W et al (2016) Optimal charging and discharging scheme of battery energy storage system in active distribution network. Autom Electr Power Syst 40(20):47–53

6. Li R, Li L, Tan X et al (2018) Integrated control strategy considering energy storage battery participating in secondary frequency regulation. Autom Electr Power Syst 42(8):74–82
7. Hu Z, Xie X, Zhang F et al (2014) Research on automatic generation control strategy incorporating energy storage resources. Proc CSEE 34(29):5080–5087
8. Ma W, Wang W, Wu X et al (2019) Optimal dispatching strategy of hybrid Energy storage system for smoothing power fluctuation caused by grid-connected photovoltaic. Autom Electr Power Syst 43(3):58–66
9. Yang Y, Niu L, Tian L et al (2015) Configuration of energy storage devices in regional distribution network considering optimal load control. Power Syst Technol 39(4):1019–1025
10. Peng S, Cao Y, Cai X (2011) Control of large scale battery energy storage system interface to microgrid. Autom Electr Power Syst 35(16):38–43

Cooperative Control Strategy of Hybrid Energy Storage System under Isolated Operation of Micro-grid

Houcheng Chu, Xiaohong Wang, Xiaochun Mou, Ming Gao and Haifei Liu

Abstract Wind and photovoltaic(PV) power generation have strong randomness, fluctuation and intermittence, so it is necessary to configure energy storage devices in micro-grid to suppress its output fluctuation. Aiming at the characteristics of islanded operation mode of micro-grid, a coordinated control strategy of hybrid energy storage system with lithium batteries (Li-b) and super capacitors (SC) is designed. The two-stage filter structure of the first-order low-pass filter and the second-order high-pass filter is adopted to distribute the load power gap. On this basis, considering the state of charge (SOC) of Li-b and the voltage of SC, a cooperative control strategy of hybrid energy storage system is designed. Then, according to the coordinated control strategy, the control structure of the two-stage energy storage converter (including DC/DC converter and DC/AC converter) is designed. Finally, a simulation model is built in MATLAB/Simulink to verify the effectiveness of the control strategy of the hybrid energy storage system designed in this paper.

Keywords Micro-grid · Hybrid energy storage system · Energy storage converter · Collaborative control strategy

1 Introduction

The micro-grid has two typical operating modes: grid-connected and isolated islands [1, 2]. The fluctuation, intermittence and randomness of new energy sources such as wind and PV will have a great impact on the power balance and quality of

H. Chu (✉) · X. Wang · X. Mou · M. Gao · H. Liu
NARI Group Corporation/State Grid Electric Power Research Institute, Nanjing 210000, China
e-mail: 1450095931@qq.com

X. Wang · X. Mou
NARI Technology Development CO., Ltd., Nanjing 210000, China

Y. Xue et al. (eds.), *Proceedings of PURPLE MOUNTAIN FORUM 2019-International Forum on Smart Grid Protection and Control*, Lecture Notes in Electrical Engineering 585, https://doi.org/10.1007/978-981-13-9783-7_26

the system when the micro-grid operates in isolated islands. It is very important to configure energy storage system to suppress the power fluctuation [3, 4].

At present, the technology of using single energy storage medium in micro-grid has been mature, but the energy storage system based on single energy storage medium has inherent limitations in performance, which cannot meet the multi-scale and multi-index requirements of capacity and response speed of micro-grid for energy storage system. Li-b, as the representative of energy storage media, are widely used in energy storage because of their high energy density. However, their low power density and slow dynamic response make it difficult to provide large instantaneous output current [5, 6]. The power-type energy storage medium represented by SC has low energy density, but high power density, can withstand short-term high rate charge-discharge current [7]. The hybrid energy storage system combines energy storage and power storage in a certain way, so that it has both high energy density and high power density characteristics [8]. Therefore, the hybrid energy storage system based on the complementary characteristics of Li-b and SC has gradually become a research hotspot. The collaborative control of Li-b and SC is particularly important for hybrid energy storage systems to respond effectively to micro-grid and load requirements.

Reference [9] proposes a dynamic power allocation control strategy, which uses the idea of sectional control to provide different input references for SC current closed-loop according to the battery output current to reduce the peak output power of battery. Reference [10] proposes to decompose the original power instructions into power signals of different frequency bands by using multi-scale wavelet packet decomposition theory. However, the decomposed signal components will change because of the different choice of fundamental wave, and bring errors in the reconstruction process. References [11, 12] uses first-order Butterworth filter to decompose the original power instructions to compensate for different frequency components, but the response speed of the energy storage system will be affected because of the integral link in the filtering process. Reference [13] proposes a power self-balancing control strategy, in which the hybrid energy storage system distributes the gap power between the battery and the SC reasonably, optimizes the working process of the battery and prolongs its service life.

In this paper, a Li-b-SC hybrid energy storage system under islanded operation mode of micro-grid is proposed, aiming at the disturbance of wind and solar power fluctation to micro-grid. Firstly, a power allocation strategy for two-stage hybrid energy storage system based on first-order low-pass filter and second-order high-pass filter is proposed for the “source-load” power difference under isolated islands. Based on the above power allocation results, the coordination control of Li-b and SC is carried out on the basis of considering SOC_b of Li-b and U_{sc} of SC voltage. Finally, a Li-b-SC hybrid energy storage system simulation model is built in MATLAB/Simulink, and the simulation results verify the effectiveness of the proposed method.

2 Cooperative Control of Hybrid Energy Storage System

2.1 Power Distribution Strategy

Traditional power allocation methods are usually based on single-stage first-order low-pass filters, while the cut-off characteristics of first-order low-pass filters at cut-off frequencies are poor. Therefore, the decomposed high-frequency power instructions contain low-frequency components near the cut-off frequency, which causes the charge-discharge power instructions to be larger than the actual power gap to be compensated, and the phenomenon of overcharge and over-discharge occurs. In addition, the integration of the first-order low-pass filter will reduce the response speed of energy storage. Therefore, a two-stage power allocation strategy based on the first-order low-pass filter and the second-order high-pass filter is proposed. The steps of the active power allocation strategy are as follows.

(1) The actual output power signal P_{load} of micro-grid load is different from the output power P_{NE} of wind and PV power generation system, and the difference of power required by load ΔP is obtained.

$$\Delta P = P_{\text{load}} - P_{\text{NE}} \tag{1}$$

(2) The output power reference value P_{HESS} of the hybrid energy storage system is obtained by decomposing ΔP with the first-order low-pass filter and making a difference with P_{low} after decomposition.

$$\Delta P_{\text{low}} = \frac{1}{1 + T_1 \text{s}} \Delta P \tag{2}$$

$$P_{\text{HESS}} = \Delta P - \Delta P_{\text{low}} = \frac{T_1 \text{s}}{1 + T_1 \text{s}} \Delta P \tag{3}$$

(3) The P_{HESS} is decomposed by a second-order high-pass filter to obtain the high-frequency compensation power component $P_{\text{sc\_high}}$ of SC, and then the reference value $P_{\text{b\_ref}}$ of low-frequency compensation power component of Li-b is obtained by subtracting $P_{\text{sc\_high}}$ from P_{HESS}.

$$P_{\text{sc\_ref}} = \left(\frac{T_2 \text{s}}{1 + T_2 \text{s}} \right)^2 P_{\text{HESS}} \tag{4}$$

$$P_{\text{b\_ref}} = P_{\text{HESS}} - P_{\text{sc}} = \frac{1 + 2T_2 \text{s}}{(1 + T_2 \text{s})^2} P_{\text{HESS}} \tag{5}$$

Similarly, reactive power is decomposed into $Q_{\text{sc\_high}}$ and $Q_{\text{b\_ref}}$. (Fig. 1).

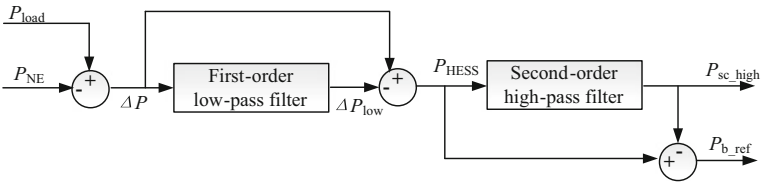

Fig. 1 Power instruction allocation

2.2 *Cooperative Control Strategy for Lithium Batteries and Super Capacitors*

Overcharge and over-discharge of Li-b and SC will greatly reduce their life, so it is necessary to consider avoiding overcharge and over-discharge in the design of control strategies. In this paper, SOC_b and U_{sc} are introduced to characterize the charging and discharging depths of batteries and SCs. The state of charge SOC_b and U_{sc} were divided into the following categories: $0.3 = SOC_{b\_min} < SOC_b < SOC_{b\_max} = 0.8$, $0.2 = U_{sc\_min} < U_{sc} < U_{sc\_max} = 0.9$.

Then, based on the power allocation strategy of the previous section, the collaborative control between Li-b and SC is realized.

(1) If $\Delta P < 0$, the output power of wind and PV is larger than the load power. It is necessary for energy storage devices to absorb excess power. It is necessary to further determine the SOC of energy storage devices.

① When $SOC_b < SOC_{b\_max}$ and $U_{sc} < U_{sc\_max}$, the power superposition value of the SC in the energy storage control system is set to P_{sc}, where, $P_{sc} = P_{sc\_high} < 0$. The high-frequency fluctuation of wind and PV can be tracked quickly by using the fast charging and discharging characteristics of SC. The remaining low-frequency fluctuation can be compensated automatically by Li-b in order to maintain the voltage, frequency stability and power balance of micro-grid.

② When the charging and discharging status of Li-b and SC does not meet the above conditions, the fan and PV components need to be removed step by step or put into load step by step to ensure that the micro-grid continues to supply power to important loads.

(2) If $\Delta P > 0$, the output power of fan and PV is less than the load power. It is necessary to determine the SOC of the energy storage device by discharging compensation power gap.

① When $SOC_b > SOC_{b\_min}$ and $U_{sc} > U_{sc\_min}$, the power superposition value of SC in energy storage control system is set to P_{sc}, where $P_{sc} = P_{sc\_high} > 0$.

② When the charging and discharging status of Li-b and SC does not meet the above conditions, it is necessary to put fan and PV components into

the grid step by step or cut off the load step by step to ensure that the micro-grid continues to supply power to the important load.

(3) If $\Delta P = 0$, the output power of fan and PV equals the load power, and there is no power exchange between the energy storage system and the micro-grid, but at this time energy storage devices can exchange energy.

① When $U_{sc} > U_{sc\_max}$ and $SOC_b < SOC_{b\_max}$, SCs are charged to Li-bs in order to adjust the charging state of SCs within the normal range because of the high power of SCs. The power superposition value of SC is P_{sc}, where $P_{sc} = P_{disc} = P_{sc\_high} > 0$, and P_{disc} is the discharge power of SC.

② When $U_{sc} < U_{sc\_min}$ and $SOC_b > SOC_{b\_min}$, Li-bs are charged to the SCs in order to adjust the voltage the SC to return to the normal range. The power superposition value of SC in energy storage control system is P_{sc}, that is $P_{sc} = P_c = P_{sc\_high} < 0$, where P_c is the charging power of SC.

③ If the charging state of the energy storage device does not satisfy the above conditions, the energy storage device will neither charge nor discharge.

3 Control Design of Energy Storage Converter

The structure of the micro-grid system with hybrid energy storage devices is shown in Fig. 2. The hybrid energy storage device adopts two-element and two-stage structure, that is, the energy storage medium is Li-b and SC, and the energy storage converter is composed of DC/DC converter and DC/AC inverter. By adding the intermediate DC/DC converter link, the end voltage of the energy storage medium is reduced, and the circulation between the energy storage medium is avoided. Besides, the charge and discharge control among the energy storage medium units is realized independently.

The DC/DC converter used in this paper is a Buck/Boost bidirectional converter. The controller adopts a double loop structure of voltage outer loop and current inner loop. The DC/AC inverter used is a three-phase half-bridge structure, and the controller adopts a power outer loop and a current double closed loop structure. The difference is that the SC energy storage module controller introduces charge and discharge power limit values P_{sc} and Q_{sc_high} in the power outer loop, which takes into account the source-to-charge power difference and the super capacitor SOC state. The above two-stage DC/DC converter and DC/AC inverter can realize independent control of energy and power between different energy storage media and different energy storage modules. Figure 3 shows the structure of the SC energy storage module controller.

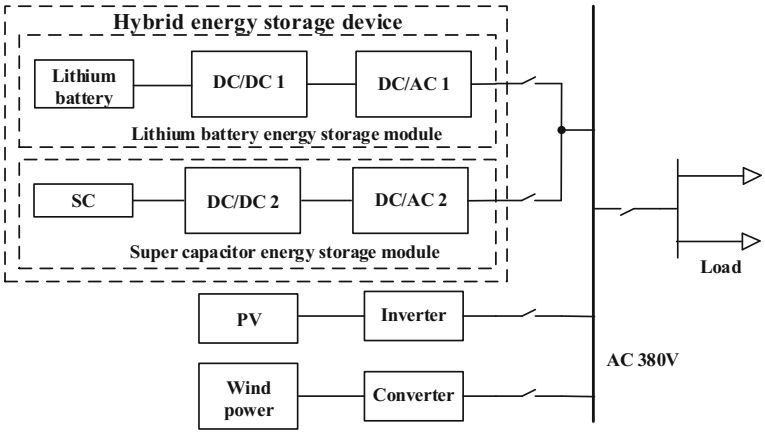

Fig. 2 Structural of micro-grid with hybrid energy storage system

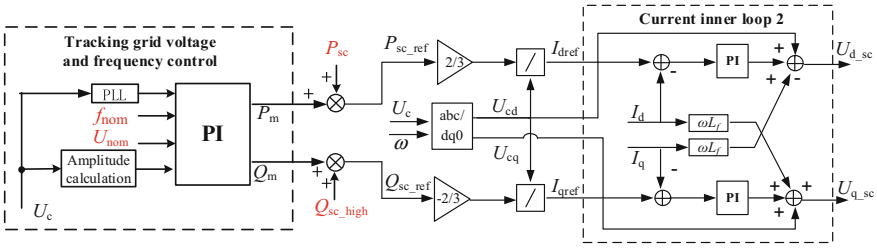

Fig. 3 Control principle diagram of DC/AC converter for SC module

3.1 Tracking the Control of Grid Voltage and Frequency

The amplitude of voltage and frequency of bidirectional DC/AC converter 2 is detected by phase-locked loop, which is then inferior to the voltage U_{nom} and frequency f_{nom} of the power grid. After PI controller, the power reference values P_m and Q_m of SC energy storage module before calibration are obtained.

3.2 Current Inner Loop 2 Control

P_{sc_ref} is obtained by adding P_{sc} and Pm generated by power allocation strategy; similarly, Q_{sc_high} and Q_m are added to get Q_{sc_ref}. The active power P_{sc_ref} and reactive power Q_{sc_ref} are decoupled, and the reference values I_{dsc_ref} and I_{qsc_ref} of current inner loop 2 are obtained. Compared with the actual measured inductance current I_{dsc} and I_{qsc}, the error signal obtained passes through the PI controller

of instantaneous current loop as the modulation voltage signal of bidirectional DC/AC converter 2. Figure 6 shows the control principle of bidirectional DC/AC converter 2.

4 Simulation Verification

According to the structure diagram of micro-grid with hybrid energy storage device shown in Fig. 2, a simulation model is built under the environment of MATLAB/Simulink. The basic components of the micro-grid model include: wind power generation system, photovoltaic power generation system, hybrid energy storage device (Li-b energy storage module and SC energy storage module) and micro-grid load. Due to the limitation of simulation time, the wind speed and illumination transformation set in this paper is expressed as a certain period of a day. The fan output fluctuates up and down in the basic wind speed, and the PV output fluctuates up and down in the basic illumination. In the simulation, the daily actual output changes of fan and PV are represented by the 35 s simulated fan and PV output curve. The installed capacity of wind power is 30 MW and that of PV is 20 MW.

By analyzing the typical wind output fluctuations over a period of time, the fluctuation extremes and fluctuation times of high frequency power and low frequency power are calculated according to the two-stage filtering proposed in this paper. At the same time, consider the sudden change in load at the ultra-short-term time scale (several seconds). On this basis, considering the constraints of minimum system power fluctuation, minimum energy demand, and minimum ratio of Li-b to SC capacity, the power and energy quotas of different energy storage media in hybrid energy storage system are calculated according to the multi-objective optimization method [14]. The energy ratio of Li-b energy storage and SC energy storage obtained in this paper is 10:1, and the Li-b power capacity configuration meeting the performance requirement and lower cost is 160 kW, and the energy configuration is 60 MW h. The SC power configuration is 0.6 Mw and the energy configuration is 6 MW h (Table 1).

Figure 4 shows the wind-solar complementary output power curve, which has both ultra-short-term high-frequency fluctuation components and low-frequency large-value power fluctuation components, which is consistent with the typical wind and light output models. Figure 5 is the load fluctuation curve. The load is increased by 30 MW at 15 s and removed at 20 s. At 25 s, 20 MW load is reduced,

Table 1 Parameters of hybrid energy storage device

Parameter	SC	Li-B
Rated capacity/MWh	0.6	60
SOC limit/%	2–90	30–80
Initial state of charge/%	50	50
Charging and discharging efficiency/%	95	80

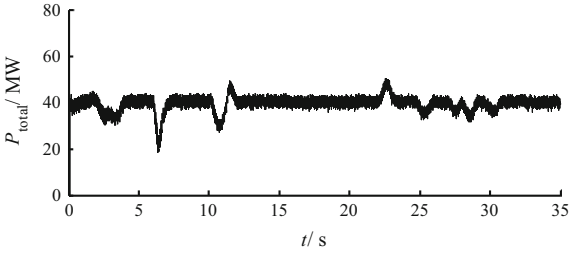

Fig. 4 Wind-solar complementary output power

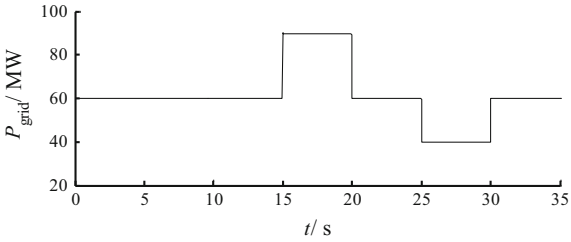

Fig. 5 Load power

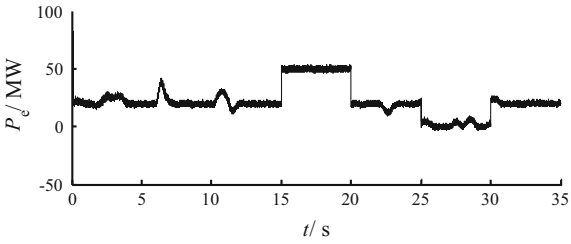

Fig. 6 Hybrid energy storage power

and at 30 s, the removed load is re-supplied. A set of curves is used to simulate the load forecasting curve.

Figure 6 shows the total output power of the hybrid energy storage. It can be seen from the figure that the power required by the load is supplied by the hybrid energy storage device, except the wind-solar complementary output power.

The output power of the SC module and the li-b energy storage module is obtained after two-stage first-order low-pass filter and second-order high-pass filter. The output power values of the SC module and the lithium battery energy storage module are shown in Figs. 7 and 8, respectively.

In Fig. 7, the Li-b energy storage can compensate for the low-frequency large-value power fluctuation, and mainly responds after the wind power output and the load mutation for several seconds. In Fig. 8, the SC energy storage can compensate for high frequency and small amplitude power fluctuations, and mainly responds quickly when the wind output and load are sudden, to meet the ultra-short-term demand of the system. Long time scale and high power amplitude

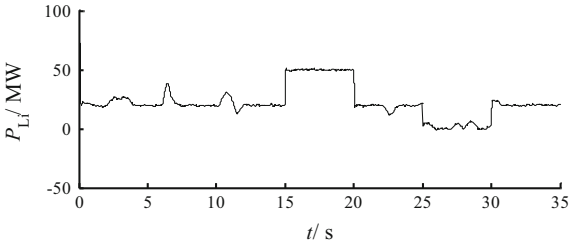

Fig. 7 Output power of Li-b

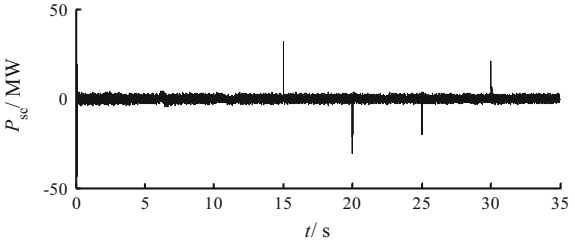

Fig. 8 Output power of SC

of low frequency power fluctuations are compensated by lithium batteries, while short time scale and low power amplitude of high frequency power fluctuations are compensated by SC, and ultimately the power balance in micro-grid is achieved. It has been proved that in peak load period, hybrid energy storage devices supply power to AC buses of micro-grid to offset peak load, and when load decreases, wind-solar complementary superfluous power is injected into hybrid energy storage devices through AC buses.

5 Conclusion

This paper analyses the fluctuation, intermittence and randomness of wind and solar output under islanded operation of micro-grid, and the inherent limitations of the performance of a single energy storage medium. Aiming at the characteristics of power and energy storage elements, a coordinated control strategy of hybrid energy storage system in islanded micro-grid mode is proposed: two-stage first-order low-pass filter and second-order high-pass filter are used to distribute the power of hybrid energy storage system. Then, according to the power gap of the load, and under the premise of introducing the charging state of lithium battery and the voltage of SC terminal, the coordinated control strategy of lithium battery energy storage module and SC energy storage module is designed.

According to the coordinated control strategy of the hybrid energy storage system, the control structure of two-stage energy storage converter (including DC/DC converter and DC/AC converter) is designed, in which the DC/AC converter of

lithium battery energy storage module and SC energy storage module are designed with different structures. Finally, a simulation model is built in MATLAB/Simulink to verify the effectiveness of the control strategy of the hybrid energy storage system designed in this paper. Finally, the stability of the micro-grid and the safe and continuous power supply to the load are realized, and the interference of the fluctuation of new energy power to the micro-grid is avoided. Finally, the power quality and power supply reliability of the important loads in the micro-grid are realized, and the safe and stable operation of the micro-grid is realized.

References

1. Zheng J, Li X, Wang Y et al (2012) Small signal stability analysis of a microgrid switching to islanded mode. Autom Electr Power Syst 36(15):25–32
2. Qiu L, Xu L, Zheng Z et al (2014) Control method of microgrid seamless switching. Trans China Electrotechnial Soc 29(2):171–176
3. Li J, Tian L, Lai X (2015) Outlook of electrical energy storage technologies under energy internet background. Autom Electr Power Syst 39(23):15–25
4. Zhou H, Bhattacharya T, Tran D et al (2011) Hybrid energy storage system involving battery and ultracapacitor with dynamic energy management in microgrid application. IEEE Trans Power Electron 26(3):923–930
5. Yao L, Yang B, Cui H et al (2016) Challenges and progresses of energy storage technology and its application in power systems. J Modern Power Syst Clean Energy 4(4):519–528
6. Liu W, Niu S, Xu H (2017) Optimal planning of battery energy storage considering reliability benefit and operation strategy in active distribution system. J Modern Power Syst Clean Energy 5(2):177–186
7. Liu M, Guo L, Wang C et al (2012) A coordinated operating control strategy for hybrid isolated microgrid including wind power, photovoltaic system, diesel generator, and battery storage. Autom Electr Power Syst 36(15):19–24
8. Ding M, Lin G, Chen Z et al (2012) A control strategy for hybrid energy storage systems. Proc CSEE 32(7):1–6
9. Dougal RA, Liu S, Ralph EW (2002) Power and life extension of battery-ultracapacitor hybrids. IEEE Trans Compon Packaging Technol 25(1):120–131
10. Han X, Chen Y, Zhang H et al (2013) Application of hybrid energy storage technology based on wavelet packet decomposition in smoothing the fluctuations of wind power. Proc CSEE 33 (19):8–13
11. Zhang K, Mao C, Xie J et al (2012) Optimal design of hybrid energy storage system capacity for wind farms. Proc CSEE 32(25):79–87
12. Yang J, Zhang J, Gui X (2013) Grid-Connected wind and PV power generation system. Power Syst Technol 27(5):1209–1216
13. Cheng Z, Li Y, Xie Y et al (2015) Control strategy for hybrid energy storage of photovoltaic generation microgrid system with super capacitor. Power Syst Technol 39(10):2739–2745
14. Yang S, Li J, Hui D, et al (2014) Optimal capacity configuration of battery energy storage system to track planned output of wind farm. Power Syst Technol 38(6):1485–1491

Multi-objective Optimization Configuration of Multi-energy Complementary Park Integrated Energy Supply Center Considering Electric Gas Conversion Planning

Ming Chen, Huixiang Chen, Yajing Gao, Shun Ma, Chao Han, Xiuna Wang and Mingrui Zhao

Abstract This paper comprehensively considers the economic, environmental and reliability impacts of energy supply systems and establishes a two-level multi-objective optimization configuration model for multi-energy complementary park integrated energy systems with multiple energy supply equipment. The upper layer has the minimum annual cost as the objective function; the lower layer has the lowest annual operating cost, the highest annual energy supply reliability and the best DG output characteristics as the objective function. The improved immune genetic algorithm based on fuzzy membership and variance weighting is used to solve the model nested. The conclusion shows that the correctness and validity of the model and algorithm.

Keywords Multi-energy complementary park distributed energy · Electricity-to-gas two-level optimization improved immune genetic algorithm

1 Introduction

With the expansion of the global industrial scale, problems such as environmental degradation, global warming, and excessive energy consumption have become increasingly prominent [1, 2]. Many countries have mentioned energy conservation

M. Chen · H. Chen · S. Ma
Guangdong Power Grid Co., Ltd. Power Grid Planning Research Center, 6–8, Shuijungang, Dongfeng East Road, Yuexiu District, Guangzhou, China

Y. Gao · C. Han · X. Wang · M. Zhao (✉)
China Electricity Council Technical and Economic Consulting Centre of Electric Power Consturction, No. 13, Baiguang Road, Xicheng District, Beijing, China
e-mail: 15810833709@163.com

Y. Xue et al. (eds.), *Proceedings of PURPLE MOUNTAIN FORUM 2019-International Forum on Smart Grid Protection and Control*, Lecture Notes in Electrical Engineering 585, https://doi.org/10.1007/978-981-13-9783-7_27

and energy efficiency as their primary strategic position. The massive access of distributed generation (DG), multi-energy interconnection and energy marketization are effective ways to promote energy efficient and clean utilization [3, 4]. The diversity of load and energy types makes energy interconnection an inevitable trend, and multi-energy complementary parks become one of the typical forms of comprehensive energy utilization. Park is a gathering place for urban energy consumption. It is composed of multiple individuals with similar energy characteristics, and has the characteristics of energy concentration, large energy demand, and collection of electric/heat/cold loads [5–10].

In this paper, a multi-energy complementary park integrated energy supply center optimization considering P2G planning is proposed, the electric/heat/cold energy flow difference and the energy conversion, space-time translation characteristics of power to gas (P2G) equipment in multi-energy complementary parks are combined. Based on the annual planning cycle, the economic, environmental and reliability impacts of the integrated multi-energy complementary park energy supply system are based on the minimum objective function, with the lowest annual operating cost, the highest annual energy supply reliability and the most DG output characteristics. Excellent for the lower objective function, a two-layer multi-objective optimization configuration model including multiple energy supply devices is established.

2 Construction of Two-Level Multi-objective Optimization Configuration Model for Multi-energy Complementary Park Integrated Energy Supply Center

As a complex energy system, the multi-energy complementary park involves the production, transfer, storage and utilization of electric/heat/cold multiple energy sources, with complex load characteristics, large load demand and high energy supply reliability requirements. In the park, the energy production unit usually includes wind turbine (WT), photovoltaic (PV), micro-turbines (MT), gas-fired boiler (GB), etc. The energy conversion unit includes heat pump. (heat pump, HP), air conditioner (AIR), heat-exchanger (HE), electric chiller (EC), absorption chiller (AC), and electric ventilating Power to gas (P2G), etc. The energy storage unit includes electric energy storage device (ES), thermal energy storage device (HS), cold energy storage device (CS) And the gas energy storage device (GS); The energy utilization unit includes electric load (Eload), heat load (Hload), and cold load (Cload).

2.1 Objective Function

(1) Upper objective function: The upper layer has the minimum annual cost as the objective function, including equipment installation fee, fuel cost, operation and maintenance fee, interaction with the grid cost and environmental cost.

$$\mathrm{Min}C_{year} = \mathrm{Min}\left(C_{inves} + C_{fuel} + C_{grid} + C_{opera} + C_{envir}\right) \tag{1}$$

$$C_{inves} = \sum_{i=1}^{N_I} \beta_i^{equ}\left(C_i^{inves} w_i^{equ}\right)\gamma_i^{equ} \tag{2}$$

$$C_{fuel} = N_J \sum_{t=1}^{N_T}\left(\frac{P_t^{Gas}\Delta t}{\eta_{Gas} v_{LHV}} C_{gas} + \xi_{P2G} C_{P2G} P_t^{P2G\_out}\Delta t\right) \tag{3}$$

$$C_{grid} = N_J \sum_{t=1}^{N_T}\left[\left(\frac{C_{t,sale} + C_{t,buy}}{2}\right)P_t^{grid}\Delta t + \left(\frac{C_{t,buy} - C_{t,sale}}{2}\right)\left|P_t^{grid}\right|\Delta t\right] \tag{4}$$

$$C_{opera} = N_J \sum_{t=1}^{N_T}\sum_{i=1}^{N_I} C_i^{main} P_{t,i}^{equ}\Delta t \tag{5}$$

$$\begin{aligned} C_{envir} = N_J \sum_{t=1}^{N_T}\sum_{u=1}^{N_U}\Bigg[R_u\Bigg(k_u^{MT}\frac{P_t^{MT}}{\eta_t^{MT}} + k_u^{GB}\frac{Q_t^{GB}}{\eta^{GB}} \\ + k_u^{grid}\frac{P_t^{grid}}{\eta_{grid}}\psi_t^{grid}\Bigg)\Delta t - R_{\mathrm{CO_2}} k_{\mathrm{CO_2}} P_t^{P2G\_out}\Delta t\Bigg] \end{aligned} \tag{6}$$

where: C_{year}, C_{inves}, C_{fuel}, C_{grid}, C_{opera}, C_{envir} are the multi-energy complementary park annual cost, equipment investment cost, fuel cost, and grid Interaction cost, operation and maintenance cost, and environmental cost; N_i is the type of investment equipment; C_i^{inves}, w_i^{equ}, γ_i^{equ} are the unit cost investment cost, installation capacity and installation factor of equipment i, respectively. If the device is installed, $\gamma_i^{equ} = 1$, otherwise 0; β_i^{equ} is the present value coefficient of device i, as in Eq. (7):

$$\beta_i^{equ} = \frac{r_i^{equ}\left(1 + r_i^{equ}\right)^{Lf_i^{equ}}}{\left(1 + r_i^{equ}\right)^{Lf_i^{equ}} - 1} \tag{7}$$

where: r_i^{equ}, Lf_i^{equ} are the discount rate of equipment i (generally taken as 7%) and the whole life cycle; N_j is the total number of days in the planning period; N_t is the total number of periods of a typical day; P_t^{Gas}, $P_t^{P2G\_out}$, P_t^{grid}, P_t^{equ}, i, P_t^{MT}, Q_t^{GB}, η_t^{MT}, η^{GB}, Ψ_t^{grid} are the power of the daily interaction with the natural

gas network, the natural gas power value of the P2G output, and the interaction with the grid. Electric power, output power of device *i*, electric/thermal power value of MT, GB and its efficiency and interaction power factor with the grid, if $P_t^{grid} > 0$, then $\Psi_t^{grid} = 1$, and vice versa 0; Δt is the time interval, taken here as 1 h; η^{Gas} is the power transmission efficiency of the natural gas network; C_{gas}, v_{LHV} is the natural gas purchase price and the low calorific value of natural gas combustion; ξ_{P2G}, C_{P2G} are the CO_2 coefficient and CO_2 price required for the production of unit natural gas in the P2G process, respectively; $C_{t,sale}$, $C_{t,buy}$ are the time-division power distribution and time respectively. Purchase electricity price; C_i^{main} is the unit capacity operation and maintenance cost of equipment i; N_u is the number of pollutant types, including CO_2, SO_2, NO_x, etc.; R_u is the environmental value of pollutant u; η_{grid}, k_u^{MT}, k_u^{GB}, k_u^{grid} respectively the emission intensity of pollutants u for MT, GB and interaction with the grid; η_{grid} is the transmission efficiency of the grid; R_{CO_2} is the environmental value of the pollutant CO_2; k_{P2GCO_2} is the CO_2 during the process of P2G consumption intensity.

(2) Lower objective function: The lower layer has the lowest annual operating cost, the highest annual energy supply reliability, and the optimal DG output characteristic as the objective function.

$$\mathrm{Min}C_{year\_opera} = \mathrm{Min}\left(C_{fuel} + C_{grid} + C_{opera} + C_{envir}\right) \tag{8}$$

$$\mathrm{Max}f_{REL} = \mathrm{Max}\left\{ \frac{\sum_{t=1}^{N_T} \left[\begin{array}{l} \left(P_t^{WT} + P_t^{PV} + P_t^{MT} + P_t^{grid} + P_t^{ES} - P_t^{EC\_in} - P_t^{HP\_H} \right. \\ \left. - P_t^{HP\_C} - P_t^{AIR\_H} - P_t^{AIR\_C} - P_t^{P2G\_in}\right)\Delta t \\ + \left(Q_t^{MT\_HE} + Q_t^{GB} + H_t^{HS} + Q_t^{HP\_H} + Q_t^{AIR\_H} - Q_t^{AC\_in}\right)\Delta t \\ + \left(Q_t^{EC\_out} + Q_t^{AC\_out} + C_t^{CS} + Q_t^{HP\_C} + Q_t^{AIR\_C}\right)\Delta t \end{array} \right]}{\sum_{t=1}^{N_T} \left(P_t^{load} + H_t^{load} + C_t^{load}\right)} \right\} \tag{9}$$

$$\mathrm{Max}f_{DG\_uti} = \mathrm{Max}\left[\sum_{t=1}^{N_T} \left(P_t^{WT} + P_t^{PV}\right) / \sum_{t=1}^{N_T} \left(P_t^{WT} + P_t^{PV}\right) \right] \tag{10}$$

where: C_{year_opera}, f_{REL}, f_{DG_uti} are the annual operating costs, annual energy supply reliability and wind output characteristics of the multi-energy complementary park, respectively. If the energy supply value is greater than the load value at a certain time, the power supply reliability at this time is taken as 1; P P_t^{WT}, P_t^{PV}, $P_t^{EC\_in}$, $P_t^{HP\_H}$, $P_t^{HP\_C}$, $P_t^{AIR\_H}$, $P_t^{AIR\_C}$, $P_t^{P2G\_in}$ are the output power of WT and PV for typical intraday time t, the input electric power value

of EC refrigeration, HP, AIR heating and cooling, and P2G equipment, respectively. The electric power value consumed; $Q_t^{MT\_HE}$, $Q_t^{AC\_in}$, $Q_t^{HP\_H}$, $Q_t^{AIR\_H}$ are the MT output thermal power of the MT at a typical intraday time t, respectively. AC input thermal power and HP and AIR heating output thermal power values; $Q_t^{EC\_out}$, $Q_t^{AC\_out}$, $Q_t^{HP\_C}$, $Q_t^{AIR\_C}$ are Output cold power values for EC, AC, HP, and AIR cooling at typical intraday time t; P_t^{ES}, H_t^{HS}, C_t^{CS} are the net energy value, as follows:

$$\begin{cases} P_t^{ES} = \left(p_t^{dis}/\eta_{pdis}\right) z_t^{p,dis} - p_t^{ch}\eta_{pch} z_t^{p,ch} \\ H_t^{HS} = \left(h_t^{dis}/\eta_{hdis}\right) z_t^{h,dis} - h_t^{ch}\eta_{hch} z_t^{h,ch} \\ C_t^{CS} = \left(c_t^{dis}/\eta_{cdis}\right) z_t^{c,dis} - c_t^{ch}\eta_{cch} z_t^{c,ch} \end{cases} \tag{11}$$

where: p_t^{dis}, h_t^{dis}, c_t^{dis} and p_t^{ch}, h_t^{ch}, c_t^{ch}. The charge and discharge rate values of ES, HS, and CS for a typical intraday time t; $z^{p,dist}$, $z^{h,dist}$, $z^{c,dis}$t and $z^{p,cht}$, $z^{h,cht}$, $z^{c,cht}$ respectively For the typical day-to-day time t, the charge and discharge energy flag of ES, HS, CS, if put, $z^{p,dist}$, $z^{h,dist}$, $z^{c,dist}$ is 1, and vice versa, if charged, $z^{p,cht}$, $z^{h,cht}$, $z^{c,cht}$ is 1, and vice versa 0; η_{pch}, η_{hch}, η_{cch}, η_{pdis}, η_{hdis}, η_{cdis} are respectively ES, HS, CS charge and discharge efficiency; P^{WT_pret}, P^{PV_pret} are the typical intraday time t WT and PV predicted output value.

2.2 Constraints

$$\begin{cases} P_t^{load} = P_t^{WT} + P_t^{PV} + P_t^{MT} + P_t^{grid} + P_t^{ES} - P_t^{EC\_in} \\ \qquad - P_t^{HP\_H} - P_t^{HP\_C} - P_t^{AIR\_H} - P_t^{AIR\_C} - P_t^{P2G\_in} \\ H_t^{load} = Q_t^{MT\_HE} + Q_t^{GB} + H_t^{HS} + Q_t^{HP\_H} + Q_t^{AIR\_H} - Q_t^{AC\_in} \\ C_t^{load} = Q_t^{EC\_out} + Q_t^{AC\_out} + C_t^{CS} + Q_t^{HP\_C} + Q_t^{AIR\_C} \\ \left(G_t^{MT}\eta_t^{MT} + G_t^{GB}\eta^{GB}\right) v_{LHV} = P_t^{P2G\_out} + P_t^{Gas} + \left(g_t^{dis}/\eta_{gdis}\right) z_t^{g,dis} - g_t^{ch}\eta_{gch} z_t^{g,ch} \end{cases} \tag{12}$$

$$\gamma_i^{equ} w_{i,\min}^{equ} \le w_i^{equ} \le \gamma_i^{equ} w_{i,\max}^{equ} \tag{13}$$

$$\mu_t^i S_t^{i,\min} \le S_t^i \le \mu_t^i S_t^{i,\max} \tag{14}$$

$$\begin{cases} P_t^{MT} - P_{t-1}^{MT} \le R_{up}^{MT} \\ P_{t+1}^{MT} - P_t^{MT} \le R_{down}^{MT} \end{cases} \tag{15}$$

$$P_{\min}^{grid} \le \left|P_t^{grid}\right| \le P_{\max}^{grid} \tag{16}$$

$$P_{\min}^{P2G} \le P_t^{P2G\_out} \le P_{\max}^{P2G} \tag{17}$$

$$P_{\min}^{Gas} \le P_t^{Gas} \le P_{\max}^{Gas} \tag{18}$$

$$-en_t^{dis,\max} \le En_t \le en_t^{ch,\max} \tag{19}$$

$$SOC_{\min}^{En} C_{En} \le E_t^{En} \le SOC_{\max}^{En} C_{En} \tag{20}$$

$$z_t^{En,dis} + z_t^{En,ch} \le 1 \tag{21}$$

where: Eq. (12) is the electrical/heat/cold/gas power balance constraint at each time; Eq. (13) is the equipment capacity configuration constraint; Eq. (14) is the energy unit's output constraint; Eq. (15) is the MT climb Slope rate constraint; Eq. (16) is the grid interaction power constraint; Eqs. (17) and (18) are the P2G equipment output at each time and the gas source point supply flow upper and lower limits respectively; Eqs. (19) and (20) are respectively stored It can set the maximum storage energy rate and energy storage capacity constraint; formula (21) is (0,1) variable constraint, ensuring that the energy storage device can not store energy (gas) and energy (gas) at the same time. Among them, P_t^{load}, H_t^{load}, C_t^{load} are the electric/thermal/cold load values in the multi-energy complementary park in the typical intraday time t; g_t^{dis}, g_t^{ch}, $z_t^{g,dis}$, $z_t^{g,ch}$ are the GS charge and discharge rate value and the charge and discharge gas mark at a typical intraday time t. If deflated, $z_t^{g,dis} = 1$, otherwise it is 0. If inflated, $z_t^{g,ch} = 1$, otherwise 0; G_t^{MT}, G_t^{GB} are the natural gas consumption of MT and GB for a typical intraday time t; $w_{i,\min}^{equ}$, $w_{i,\max}^{equ}$ are the upper and lower limits of the installation capacity of equipment i, respectively; S_t^i, μ_t^i is the output value and scheduling factor of the energy unit i in the typical intraday time t, respectively, if the energy unit is scheduled, the value is 1 and vice versa 0; P_{t+1}^{MT}, P_t^{MT}, P_{t-1}^{MT} is the MT output value of typical intraday time t + 1, t, t − 1; $S_t^{i,\min}$, $S_t^{i,\max}$, R_{up}^{MT}, R_{down}^{MT}, $P_{\min}^{grid}$, $P_{\max}^{grid}$, $P_{\min}^{P2G}$, $P_{\max}^{P2G}$, $P_{\min}^{Gas}$, $P_{\max}^{Gas}$ are the output of each energy unit, MT climbing rate, grid transmission power, P2G generation natural gas power and upper and lower limits of interaction power with natural gas network at each moment; En is the type of energy storage and gas storage device, including ES, HS, CS and GS; En_t, E_t^{En}, $en_t^{dis,\max}$, $en_t^{ch,\max}$, $SOC_{\min}^{En}$, $SOC_{\max}^{En}$, C_{En}, z_t^{xEn}, $z_t^{En,ch}$ are the energy storage device change rate, the energy storage device capacity, the maximum charge and discharge energy (gas) rate, the charge energy upper and lower limits, and the energy storage (gas) capacity values of a typical intraday time t, respectively. And the storage and release energy (gas) flag; ηgch, ηgdis are the charge and discharge efficiency of GS, respectively.

2.3 Model Solution

For the multi-objective two-layer optimal configuration model of the multi-energy complementary park integrated energy supply center established in this paper, the improved immune genetic algorithm [9] based on fuzzy membership and variance weighting is used for nesting solution.

3 Case Analysis

3.1 Overview of the Case

The planned area of the park is about 230,000 m^2, which is composed of industrial, commercial, municipal, and residential areas. Electrical/heat/cold load demand requirements in all areas, the park has a large demand for electric/heat load, and the demand for cold load is relatively small. Moreover, due to the integrated pipe gallery inside the park, the electric/heat/cold load is mostly concentrated. The maximum installed capacity of wind power and photovoltaic in the park are 780 and 600 MW respectively, and the maximum electric/heat/cold annual loads are 1260, 1140 and 680 MW respectively. The maximum power for interaction with the grid and natural gas network is 400 and 120 MW respectively. The energy time-sharing price is shown in Table 1. The relevant parameters of pollutants in each equipment are shown in Table 2. The upper and lower limits of the climbing rate of the micro gas turbine are taken as 30 MW/h, the heat loss coefficient is taken as 0.15, the minimum load rate is taken as 0.3, the minimum load rate of other equipment is taken as 0, and the maximum load rate is taken as 1; The CO_2

Table 1 Energy time-sharing price

Time/h	$C_{t,buy}$/[$/MW h]	$C_{t,sale}$/[$/MW h]	C_{gas}/[$/$m^3$]
(10:00, 15:00], (18:00, 21:00]	1.217	0.608	3.45
(7:00, 10:00], (15:00, 18:00], (21:00, 23:00]	0.875	0.437	
(0:00, 7:00], (23:00, 24:00]	0.524	0.267	

Table 2 Related parameters of pollutants in each equipment operation

Types of device	NO_x		CO_2	
	K_{NO_x}/(kg/MW h)	R_{NO_x}/($/kg)	K_{CO_2}/(kg/MW h)	R_{CO_2}/($/kg)
Micro gas turbine	$0.20e^{-3}$	8	0.2019	0.044
Gas boiler	$0.2556e^{-3}$		0.7426	
Power grid	0.015		0.9970	

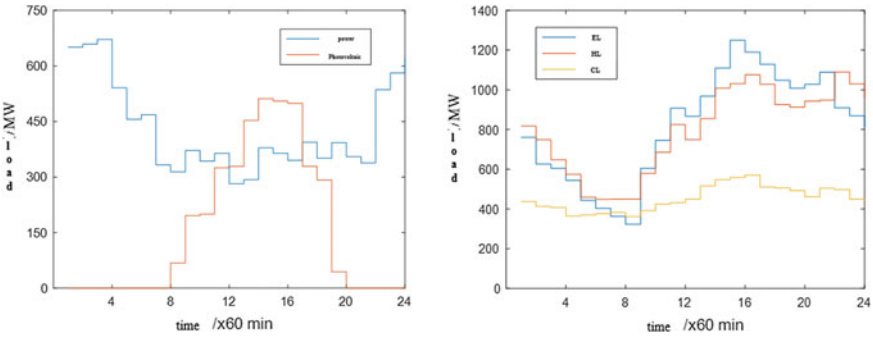

(a) Wind power / PV output curve (b) Electric / hot / cold load output curve

Fig. 1 Typical daily wind power/photovoltaic and electric/hot/cold load output

coefficient and CO_2 price required to produce a unit of natural gas are taken as 0.2 and 0.36$/MW h respectively. A typical daily wind/photovoltaic output curve and electricity/heat/cold load curve in the park as shown in Fig. 1:

3.2 Optimized Configuration Results and Analysis of Multi-energy Complementary Park Integrated Energy Supply Center

(1) Comparison of optimized configuration results under different energy supply strategies

Based on a typical daily wind power/photovoltaic output and electric/heat/cold load curve, the proposed two models and the algorithm are used to optimize the following two multi-energy complementary park energy supply strategies.

Energy supply strategy 1: traditional energy supply mode, i.e. distribution network supply power, GB supply heating, EC supply cooling; Energy supply strategy 2: Combined Cooling Heating and Power (CCHP), consider the addition of DG and P2G equipment; The optimal configuration results and objective function pairs under two different energy supply strategies are shown in Tables 3 and 4.

Comparing the two energy supply strategies, it can be seen that the addition of the cold joint supply system can realize the coordinated and complementary utilization of the electric/heat/cold multi-energy flow in the multi-energy complementary park, reduce the system energy supply cost, and improve the

Table 3 Optimized configuration results under different energy supply strategies

Energy supply strategy	Energy supply strategy 1	Energy supply strategy 2	Energy supply strategy	Energy supply strategy 1	Energy supply strategy 2
WT	–	700	EC	700	80
PV	–	540	AC	–	280
MT	–	600	P2G	–	320
GB	1200	520	ES	–	390
HE	–	680	HS	–	680
HP	–	160	CS	–	300
AIR	–	120	GS	–	560

Table 4 Comparison of objective functions under different energy supply strategies

Energy supply strategy	Energy supply strategy 1	Energy supply strategy 4	Energy supply strategy	Energy supply strategy 1	Energy supply strategy 4
Equipment investment fee/e^4\$	11.12	281.08	Environmental cost/e^4\$	241.74	28.17
Fuel cost/e^4\$	273.69	21.56	Total energy cost/e^4\$	1213.37	416.31
Grid interaction fee/e^4\$	678.80	45.11	Annual energy supply reliability	–	0.8800
Operation and maintenance fee/e^4\$	8.02	40.39	DG output characteristics	–	0.9574

system power supply reliability; The DG satisfies part of the system's electrical load demand, and the energy supply cost is further reduced. However, considering the DG output has a certain degree of confidence, its energy supply reliability is slightly reduced. In addition, the coordinated use of P2G equipment and MT has played the role of "shaving peaks and filling valleys". To some extent, it has suppressed the uncertainty of DG output, and the characteristics of various objective functions have been improved to varying degrees.

(2) Typical day optimization scheduling results analysis

Based on the typical daily optimization configuration results of the multi-energy complementary park, the optimal scheduling of electric/heat/cold/gas power at each time is shown in Fig. 2:

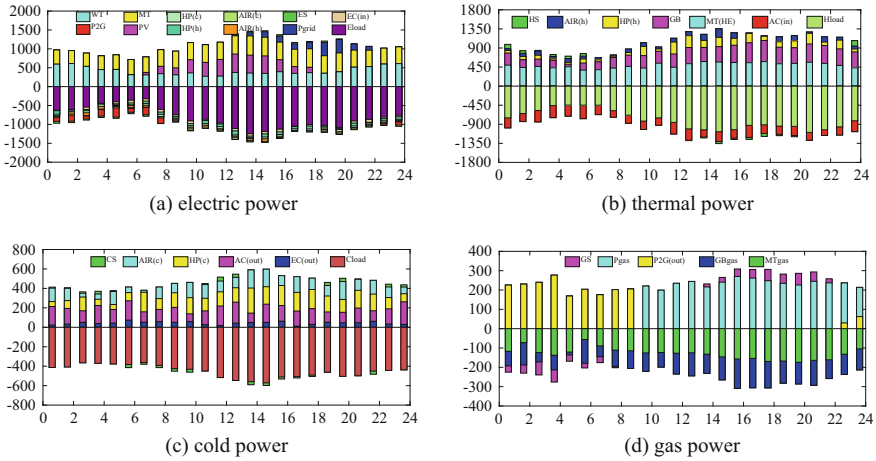

Fig. 2 Typical daily electric/thermal/cold/gas power balance diagram

4 Conclusion

For the optimal configuration of multi-energy complementary park integrated energy supply center, this paper combines the electric/heat/cold multi-energy flow difference and the energy conversion and spatio-temporal shift characteristics of P2G equipment, proposes a two-layer multi-objective optimization configuration model with multiple energy-providing devices affected by system economy, environmental protection and reliability. Combined with the relevant examples, the correctness and feasibility of the proposed optimal configuration model are verified.

References

1. Malinowski M, Leon JI, Abu-Rub H (2017) Solar photovoltaic and thermal energy systems: current technology and future trends. Proc IEEE (99):1–15
2. Deng L, Sun H, Chen R et al (2016) Study on node energy price of cogeneration system for energy internet. Power Syst Technol 40(11):3375–3382
3. Dall'Anese E, Mancarella P, Monti A (2017) Unlocking flexibility: integrated optimization and control of multi energy systems. IEEE Power Energ Mag 15(1):43–52
4. Correa-Posada CM, Sánchez-Martín P (2015) Integrated power and natural gas model for energy adequacy in short-term operation. IEEE Trans Power Syst 30(6):3347–3355
5. Galbusera L, Theodoridis G, Giannopoulos G (2015) Intelligent energy systems: introducing power-ICT interdependency in modeling and control design. IEEE Trans Industr Electron 62 (4):2468–2477
6. Lin C, Jing Z, Renle H et al (2017) Case analysis of multi-scenario planning for integrated energy systems based on multi-energy complementation. Electr Power Autom Equip 37 (6):282–287

7. Wu C, Tang W, Bai M et al (2017) User-side energy Internet planning based on two-tier planning. Trans China Electrotech Soc 32(21):53–62
8. Huang W, Ge L, Hua L, Chen Y (2019) A recent comprehensive optimization of regional integrated energy systems participating in the dual market. Autom Electr Power Syst: 1–8 [2019-05-10]
9. Fang Z, Song S, Lin Y, Lin X, Cheng G (2019) State estimation of active power distribution system with photovoltaic power station and battery energy storage system. Autom Electr Power Syst: 1–9[2019-05-10]
10. Sun H, Guo Q, Wu W, Wang B, Xia, Zhang B (2019) Multi-energy integrated energy management system for energy Internet: design and application. Autom Electr Power Syst 1–8 [2019-05-10]

Adverse Control Effects on Steady-State Voltage Stability in Wind Power Systems Based on Sensitivities of B and L Indices

Shenghu Li, Jing Xue, Bijun Li, Yunsong Yan and Ning Sun

Abstract The proximity of B and L indices to 1 indicates the level of voltage instability of power system and load points, which varies with changing system conditions. To quantify the effect of control measures, the sensitivities of B and L indices to the control measures are newly proposed, based on which the adverse control effects with different sites of load shedding, the non-optimality of local load shedding, the opposite effects of tap adjustment, and the inconsistency of L and B indices with the same control measures, are quantified. The numerical results validate the accuracy of the sensitivity model by comparing with the continual calculation.

Keywords Voltage stability · L index · B index · Sensitivity · Control effect · Load shedding · Tap setting · Wind power system

1 Introduction

Voltage instability is caused by load increase, loss of generators or transmission lines, violation to the excitation limiters, violation to the limit of shunt/series compensators [1, 2]. It may occur independently, or simultaneously with the rotor angle swing, followed by loss of load, undesirable tripping [3], or cascading events [4].

The increasing wind power may cause imbalance of active and reactive powers, and fluctuation or depression of bus voltage [5]. Although the wind turbine generators (WTGs) are required to have low-voltage ride-through capability against short faults, their reactive power capability is limited by the capacity constraints of the relative converters [6]. Even the capacities of the converters are large enough,

S. Li (✉) · J. Xue
Hefei University of Technology, Hefei 230009, China
e-mail: shenghuli@hfut.edu.cn

B. Li · Y. Yan · N. Sun
State Grid Electric Power Research Institute, Nanjing 211106, China

Y. Xue et al. (eds.), *Proceedings of PURPLE MOUNTAIN FORUM 2019-International Forum on Smart Grid Protection and Control*, Lecture Notes in Electrical Engineering 585, https://doi.org/10.1007/978-981-13-9783-7_28

dispatch to the reactive power of the WTGs is difficult due to the number of the WTGs.

The voltage instability may be defined by short or long-term [7]. The former is solved by the step-by-step simulation [8]. Steady-state voltage instability is caused by deficiency or imbalance of reactive power, and solved with power flow equations.

There are several models to quantify the steady-state voltage stability. The optimal power flow quantifies load shedding to maintain the performance index [9, 10]. The continual power flow yields PV or QV curve and decide the load margin [11, 12]. Cao and Hill show that zero eigenvalue yields singularity of the Jacobian matrix [13–15]. Li decomposes outputs of rotating machines to the steady-state and dynamic components to avoid the optimistic or pessimistic judgment to stability margin [16].

Divergence of power flow equations, or singularity of the Jacobian matrix, overestimates voltage stability, since the generators or lines may trip earlier than the divergence. The control measures are critical to describe voltage depression. The L index is defined by Kessel, Löf, et al. [17, 18] for the load buses. By ignoring the real part of the admittance matrix, L is reduced to B index by Tuan to save the calculation effort [19]. However, the increment of L index defined by Tuan is wrongly.

The control measures, e.g. the on-load tap changers, improve L index of some load buses but decrease that of others; some measures deteriorate instead of improve stability under certain scenarios. The undesirable, adverse, or dangerous effects may be found if we can quantify the control effects and define the adverse effects.

To reduce the risk of voltage instability in power systems with time-varying and complex conditions and multiple choices of the countermeasures, the adverse effects of the control measures on the steady-state voltage stability are studied with the sensitivity models. At first, the sensitivity models for B and L indices are derived. Then, the sensitivity models to load shedding and tap setting are proposed. Finally, the adverse cases are defined by the signs of the sensitivities.

2 Sensitivities of B and L Indices

2.1 Sensitivity of B Index

The system buses are classified by sets D and G. The former have constant outputs. The latter are generators with voltage control capability. The bus currents are,

$$\begin{bmatrix} \bar{\boldsymbol{I}}_D \\ \bar{\boldsymbol{I}}_G \end{bmatrix} = \begin{bmatrix} \boldsymbol{Y}_{DD} & \boldsymbol{Y}_{DG} \\ \boldsymbol{Y}_{GD} & \boldsymbol{Y}_{GG} \end{bmatrix} \begin{bmatrix} \bar{\boldsymbol{V}}_D \\ \bar{\boldsymbol{V}}_G \end{bmatrix} \tag{1}$$

The real part of $\boldsymbol{Y}$ is ignored to yield the B index,

$$\bar{B}_i = 1 + \left[\frac{\text{Imag}(\boldsymbol{Y}_{DD})^{-1}\text{Imag}(\boldsymbol{Y}_{DG})\bar{\boldsymbol{V}}_G}{\bar{\boldsymbol{V}}_D}\right]_i = B_{Ri} + jB_{Ii} \tag{2}$$

The erroneous definition to incremental B index (3) in [19] is newly defined as (4),

$$\Delta B_i = \sqrt{\Delta B_{Ri}^2 + \Delta B_{Ii}^2} \tag{3}$$

$$\Delta B_i = \sqrt{(B_{Ri} + \Delta B_{Ri})^2 + (B_{Ii} + \Delta B_{Ii})^2} - \sqrt{B_{Ri}^2 + B_{Ii}^2} \tag{4}$$

With the help of the Jacobian matrix of load flow equations, the sensitivity of the B index to the bus power is derived,

$$\begin{bmatrix}\Delta \boldsymbol{B}_R \\ \Delta \boldsymbol{B}_I\end{bmatrix} = -\begin{bmatrix}\frac{\partial \boldsymbol{B}_R}{\partial \boldsymbol{\theta}} & \frac{\partial \boldsymbol{B}_R}{\partial \boldsymbol{V}} \\ \frac{\partial \boldsymbol{B}_I}{\partial \boldsymbol{\theta}} & \frac{\partial \boldsymbol{B}_I}{\partial \boldsymbol{V}}\end{bmatrix}\boldsymbol{J}^{-1}\begin{bmatrix}\Delta \boldsymbol{P} \\ \Delta \boldsymbol{Q}\end{bmatrix} = \begin{bmatrix}\frac{\partial \boldsymbol{B}_R}{\partial \boldsymbol{P}} & \frac{\partial \boldsymbol{B}_R}{\partial \boldsymbol{Q}} \\ \frac{\partial \boldsymbol{B}_I}{\partial \boldsymbol{P}} & \frac{\partial \boldsymbol{B}_I}{\partial \boldsymbol{Q}}\end{bmatrix}\begin{bmatrix}\Delta \boldsymbol{P} \\ \Delta \boldsymbol{Q}\end{bmatrix} \tag{5}$$

2.2 Sensitivity of L Index

The L index is defined by (6), decided by the local voltage, and the voltages of all the buses in set G. Low load voltage yields large L_i, thus close to the instability.

$$\bar{L}_i = 1 + \frac{\left(\boldsymbol{Y}_{DD}^{-1}\boldsymbol{Y}_{DG}\bar{\boldsymbol{V}}_G\right)_i}{\bar{V}_i} = L_{Ri} + jL_{Ii}, \quad i \in D \tag{6}$$

The linear model of $\boldsymbol{L}_R$ and $\boldsymbol{L}_I$ to bus powers is similar to (5). The sensitivities of L to bus powers are newly defined by the partial derivatives,

$$\begin{cases} s_{L_iP_j} = \dfrac{\partial L_i}{\partial P_j} = \dfrac{L_{Ri}}{L_i}\dfrac{\partial L_{Ri}}{\partial P_j} + \dfrac{L_{Ii}}{L_i}\dfrac{\partial L_{Ii}}{\partial P_j} \\ s_{L_iQ_j} = \dfrac{\partial L_i}{\partial Q_j} = \dfrac{L_{Ri}}{L_i}\dfrac{\partial L_{Ri}}{\partial Q_j} + \dfrac{L_{Ii}}{L_i}\dfrac{\partial L_{Ii}}{\partial Q_j} \end{cases} \tag{7}$$

When the power angle of WTGs is fixed, the sensitivity to the active power with simultaneous changes of reactive power is defined as,

$$s_{L_iPQ_j} = \frac{\partial L_i}{\partial \boldsymbol{P}_j} + \frac{\partial L_i}{\partial Q_j}\tan\varphi_j \tag{8}$$

The on-load tap-changers are used to redistribute reactive power and maintain the bus voltages. For them, the linear power flow model is extended with the tap k,

$$\begin{bmatrix} \Delta \boldsymbol{P} \\ \Delta \boldsymbol{Q} \end{bmatrix} + \begin{bmatrix} \boldsymbol{J}_{P\theta} & \boldsymbol{J}_{PV} & \boldsymbol{J}_{Pk} \\ \boldsymbol{J}_{Q\theta} & \boldsymbol{J}_{QV} & \boldsymbol{J}_{Qk} \end{bmatrix} \begin{bmatrix} \Delta \boldsymbol{\theta} \\ \Delta \boldsymbol{V} \\ \Delta \boldsymbol{k} \end{bmatrix} = \begin{bmatrix} \boldsymbol{0} \\ \boldsymbol{0} \end{bmatrix} \tag{9}$$

Since L is defined by $\boldsymbol{Y}$ matrix, which is related to the tap changers, the partial derivative of $\boldsymbol{Y}$ matrix to k, the linear expression of $\boldsymbol{L}_R$ *and* $\boldsymbol{L}_I$ is extended to include the tap changer, the derivative of $\bar{L}_i$ to the tap changer is given by,

$$\frac{\partial \boldsymbol{L}}{\partial \boldsymbol{k}} = \frac{\partial \left(\boldsymbol{Y}_{DD}^{-1} \boldsymbol{Y}_{DG} \dot{\boldsymbol{V}}_G \right)}{\partial \boldsymbol{k}} = \left(\frac{\partial \boldsymbol{Y}_{DD}^{-1}}{\partial \boldsymbol{k}} \boldsymbol{Y}_{DG} + \boldsymbol{Y}_{DD}^{-1} \frac{\partial \boldsymbol{Y}_{DG}}{\partial \boldsymbol{k}} \right) \dot{\boldsymbol{V}}_G \tag{10}$$

Then the sensitivities of $\boldsymbol{L}_R$ and $\boldsymbol{L}_I$ to the tap changer are quantified by,

$$\begin{bmatrix} \Delta \boldsymbol{L}_R \\ \Delta \boldsymbol{L}_I \end{bmatrix} = \begin{bmatrix} \frac{\partial \boldsymbol{L}_R}{\partial \boldsymbol{\theta}} \frac{\partial \boldsymbol{\theta}}{\partial \boldsymbol{k}} + \frac{\partial \boldsymbol{L}_R}{\partial \boldsymbol{V}} \frac{\partial \boldsymbol{V}}{\partial \boldsymbol{k}} + \frac{\partial \boldsymbol{L}_R}{\partial \boldsymbol{k}} \\ \frac{\partial \boldsymbol{L}_I}{\partial \boldsymbol{\theta}} \frac{\partial \boldsymbol{\theta}}{\partial \boldsymbol{k}} + \frac{\partial \boldsymbol{L}_I}{\partial \boldsymbol{V}} \frac{\partial \boldsymbol{V}}{\partial \boldsymbol{k}} + \frac{\partial \boldsymbol{L}_I}{\partial \boldsymbol{k}} \end{bmatrix} \Delta \boldsymbol{k} = \begin{bmatrix} s_{L_R k} \\ s_{L_I k} \end{bmatrix} \Delta \boldsymbol{k} \tag{11}$$

Finally, sensitivity of L_i to the tap changer k is defined as,

$$\frac{\partial L_i}{\partial k} = \frac{\partial \sqrt{L_{Ri}^2 + L_{Ii}^2}}{\partial k} = \frac{L_{Ri} s_{L_{Ri} k} + L_{Ii} s_{L_{Ii} k}}{L_i} \tag{12}$$

3 Adverse Effects of Control Measures

3.1 Adverse Effects of Load Shedding

Case (a). As shown in Fig. 1a, if sensitivities of L to active and reactive powers have different signs,

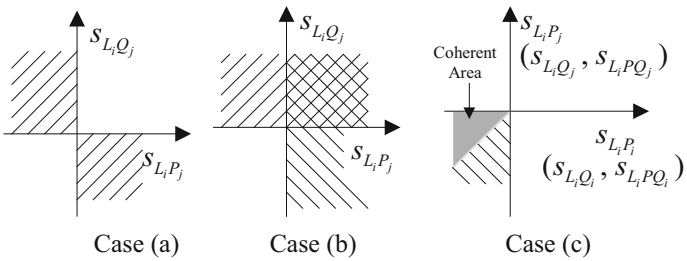

Fig. 1 Adverse cases (**a**)–(**c**) illustrated in complex plane

$$s_{L_iP_j} s_{L_iQ_j} < 0 \tag{13}$$

i.e. shedding of active and reactive loads yields opposite effects on voltage stability, which is possible to wind farms with the positive/negative active/reactive outputs [20].

Case (b). With the load shedding, L_i is expected to decrease, thus a positive sensitivity to bus power means adverse effect,

$$s_{L_iP_j} > 0, \text{ or } s_{L_iQ_j} > 0 \tag{14}$$

As shown in Fig. 1b, the cases (a) and (b) overlap, with the non-adverse zone of the 3rd quadrant, i.e. $s_{L_iP_j} < 0$, and $s_{L_iQ_j} < 0$.

Case (c). The local load shedding is usually assumed most effective to improve the voltage stability. Thus the exception is seen as adverse effect, as shown in Fig. 1c.

$$s_{L_iP_i} > s_{L_iP_j}, \; s_{L_iQ_i} > s_{L_iQ_j}, \text{ or } s_{L_iPQ_i} > s_{L_iPQ_j} \tag{15}$$

The cases (a) to (c) contribute to the desirable non-adverse area within the 3rd quadrant, with the angle between π and 5π/4.

Case (d). If L_{Ri} and $s_{LRi,PQj}$ have the same signs, i.e. $L_{Ri} > 0$ and $s_{LRi,PQj} > 0$, or $L_{Ri} < 0$ and $s_{LRi,PQj} < 0$, simultaneous shedding to the active and reactive loads increases the magnitude of L_{Ri}, which is not necessarily adverse, but possibly doubtful. Similar concern exists if L_{Ii} and $s_{LIi,PQj}$ have the same signs.

3.2 Adverse Effects of Tap Setting

Case (e). If the sensitivity of L_i to tap setting k is positive, i.e. $s_{L_ik} > 0$, while L_j to k is negative, i.e. $s_{L_jk} < 0$, the tap changer k yields the opposite effects on L_i and L_j.

3.3 Inconsistency of L and B

Due to ignorance of the conductance matrix, B is different from L. Their sensitivities are also different. For Case (f), signs of the sensitivities of B and L are different,

$$s_{B_i*} s_{L_i*} < 0 \tag{16}$$

where the subscript $*$ denotes load shedding or the tap setting.

Cases (b) and (a) are unexpected and should be avoided. Case (c) is undesirable due to the non-optimal load shedding. Case (d) not necessarily affects voltage stability. Case (e) is inevitable, since the tap changer is not reactive source. Case (f) is caused by the solution methods; if it exists, B index may be wrong.

4 Numerical Analysis

The IEEE 14-bus system is applied. With the loads and generators connected via the transformers, 16 additional buses are introduced. Buses 16, 18, 22, and 24 are seen as the constant PV type. Buses 15, 16, 18, 22, and 24 are classified to the set G, while others buses classified to the set D.

4.1 L and B Indices

The L/B indices are drawn in Fig. 2a. The difference is obvious, especially for buses with large L/B indices. With the branch resistance r doubled, the indices increase. The relative error of B index compared with L index is shown in Fig. 2b. For most buses (except for bus 8), the error is positive, i.e. B is larger than L, yielding pessimistic judgment to voltage stability. With r doubled, the error is more prominent.

The buses vulnerable to voltage instability are shown in Table 1. With r doubled, there are more vulnerable buses, and B yields the false sequence of buses 14 and 25.

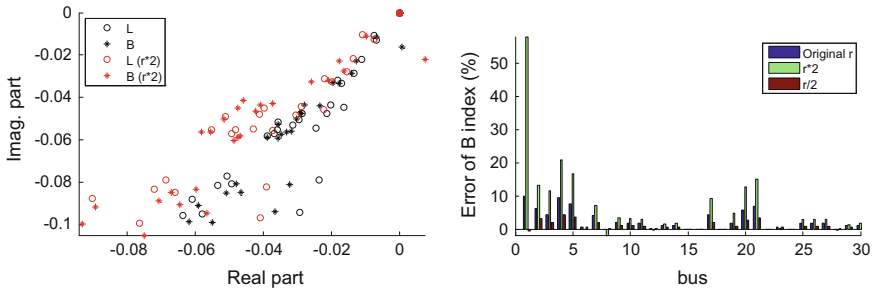

(a) L/B indices in complex plane

(b) Error of B index compared with L index

Fig. 2 Comparison of L and B indices under different system stress

Table 1 Load buses with large L/B indices

Original parameters			$r * 2$		
Bus	L	B	Bus	L	B
30	0.1149	0.1162	30	0.1340	0.1365
25	0.1113	0.1133	14	0.1257	0.1280
14	0.1071	0.1084	25	0.1252	0.1291
19	0.0989	0.1008	26	0.1102	0.1136
			9	0.1074	0.1112
			19	0.1052	0.1102
			10	0.1046	0.1080
			20	0.0910	0.1026

4.2 Sensitivities of L and B

For bus 30 with the largest L/B, the sensitivities to bus powers are shown in Fig. 3. The sensitivities of B have smaller magnitude compared with those of L; B underestimates the impact of load shedding on voltage stability. Table 2 gives some relative errors between $|s_{L30,PQj}|$ and $|s_{B30,PQj}|$, which is more notable with larger resistance.

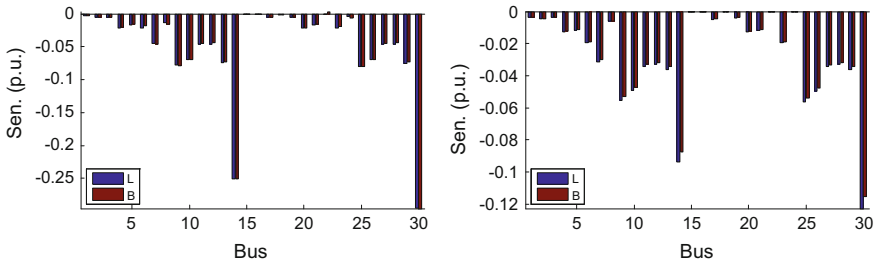

(a) Sensitivity to active power (b) Sensitivity to reactive power

Fig. 3 Sensitivities of L/B indices at bus 30 to bus powers

Table 2 Relative error of sensitivity of B index using Tuan's model

Original r		$r * 2$	
Bus j	Error of sen. (%)	Bus j	Error of sen. (%)
20	7.22	23	10.29
28	4.82	28	7.06
21	3.09	20	3.64
23	1.91	21	2.21
		27	1.07
		19	1.01

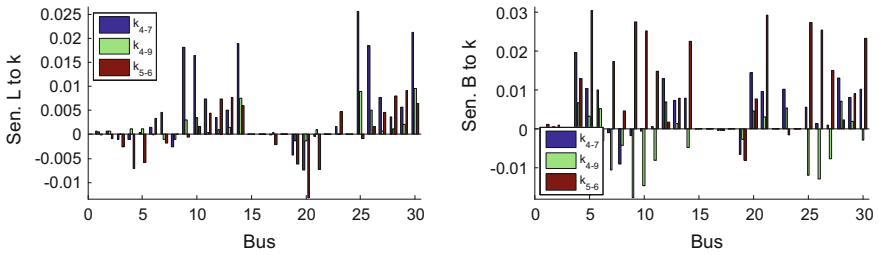

(a) Sensitivity of L index to tap changer (b) Sensitivity of B index to tap changer

Fig. 4 Sensitivities of L/B indices to tap changers

The sensitivities of L/B to the tap changers are shown in Fig. 4, which show different control effects of the tap changers on different load buses. Notable difference exists between the sensitivities of L/B to the tap changers.

4.3 Validation to Sensitivity of L Index

The sensitivities of L index to load change or tap changer are validated by comparing with continuous calculation, as shown in Fig. 5. The former is consistent with the exact results, thus can quantify the risk of the voltage instability and decide the control measures to maintain voltage stability.

4.4 Adverse Effect Analysis Based on L Index

No **case (a)** exists in the system. But as shown in Table 3, with r doubled, $s_{L20,P8} = -0.014124$, while $s_{L20,Q8} = 0.000454$, thus the active and reactive load

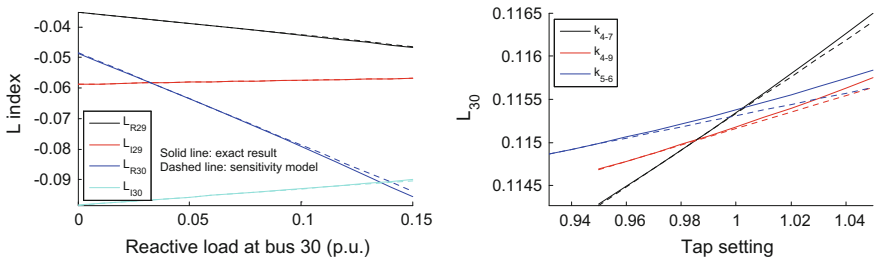

(a) With reactive bus power (b) With tap setting

Fig. 5 Error of sensitivity model of L index

Table 3 Adverse effect with positive sensitivity to bus powers

Bus i	*Bus j*	s_{LiPj}	s_{LiQj}	Case
20	8	−0.014124	0.000454	a, b
9	22	0.000276	0	b
10	22	0.000357	0	b
13	22	0.000031	0	b
14	22	0.000564	0	b
25	22	0.000466	0	b
26	22	0.000414	0	b
30	22	0.000531	0	b

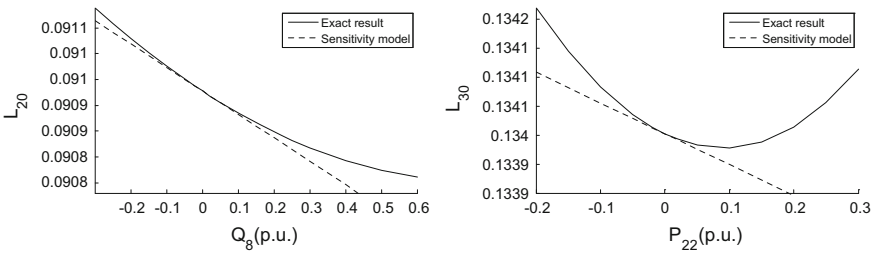

(a) Case (a) (b) Case (b)

Fig. 6 Validation to adverse effects

shedding at bus 8 yields opposite effects on L_{20}. To validate the adverse effect, the reactive load at bus 8 is changed, as shown in Fig. 6a, showing that case (a) exists.

No **case (b)** exists in the original system. However, with r doubled, adverse effect appears at several buses. With active load at bus 22 changed the sensitivity model is validated in Fig. 6b. The tangent line is consistent with $s_{L30,P22}$.

Under system stress, the cases (a) and (b) are sensitive to the bus powers. With r doubled, if Q_{D8} decreases from 0 to −0.1 p.u., cases (a) and (b) increase to 3 and 10 respectively. If decreased to −0.2 p.u., the numbers are 18 and 28. If decreased to −0.3 p.u., the numbers increase to 33 and 43.

Based on the sensitivity of L, **cases (c)** are shown in Table 4. The step-down transformers are the contributing factor to case (c). As shown in Fig. 3, to reduce L_i, load shedding at bus j reduces the branch loss, better than that at bus i. There are more adverse effects with the reactive powers than those with the active powers.

Case (d) is shown in Fig. 7a, where the real/imaginary parts of L are shown in the vertical axis, active/reactive bus powers are shown in the horizontal axis, and * shows adverse effects. The upper right has most cases of adverse effects, followed by the bottom left, then the bottom right. Identification of case (d) helps to exactly relocate the real and the imaginary parts of the L index.

Case (e). The negative sensitivities between L and the tap changers are given in Table 5. For buses 3, 19, and 20, L decreases with increase of either tap changer.

Table 4 Adverse effect of case (c)

Sen. to active power				Sen. to reactive power			
i	s_{LPii}	j	s_{LPij}	i	s_{LQii}	j	s_{LQij}
2	−0.0244	17	−0.0247	2	−0.0090	17	−0.0092
3	−0.0376	19	−0.0390	3	−0.0108	19	−0.0112
4	−0.0556	20	−0.0566	5	−0.0169	21	−0.0169
5	−0.0554	21	−0.0556	6	−0.0138	13	−0.0138
6	−0.0350	23	−0.0352			23	−0.0139
9	−0.1140	25	−0.1160			29	−0.0139
10	−0.1536	26	−0.1544	9	−0.0641	25	−0.0654
11	−0.1565	27	−0.1567	10	−0.0718	26	−0.0723
12	−0.1934	28	−0.1937	11	−0.0497	27	−0.0498
13	−0.1261	29	−0.1267	12	−0.0248	13	−0.0338
14	−0.2474	30	−0.2491			14	−0.0256
						28	−0.0249
						29	−0.0340
						30	−0.0257
				13	−0.0383	12	−0.0391
						28	−0.0392
						29	−0.0386
				14	−0.0925	30	−0.0931

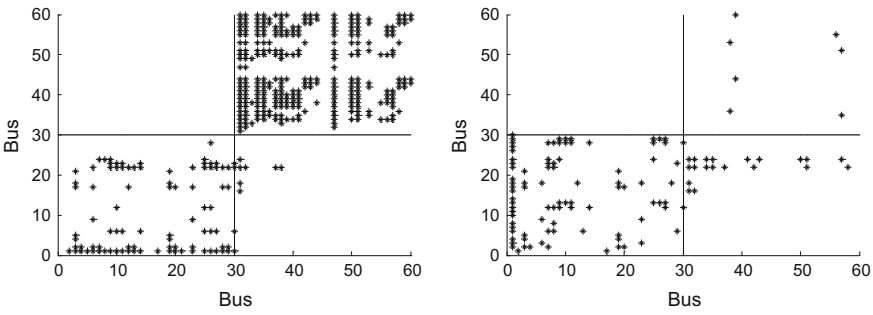

(a) Case (d) (b) Case (f)

Fig. 7 Adverse effect of cases (**d**) and (**f**)

For other buses, three tap settings have the opposite effect on L. The buses not listed have positive sensitivities, i.e. L decreases with lower setting of any tap changer.

Case (f). $s_{Li,PQj}$ and $s_{Bi,PQj}$ with different signs are shown in Fig. 7b. The bottom left has the most adverse cases, followed by the bottom right, then the upper-right. With different signs, sensitivities of B index to bus powers yields the expected control effect opposite to that of L index, thus is not trustworthy.

Table 5 Adverse control effect of case (e)

Bus	$k_{4\text{-}7}$	$k_{4\text{-}9}$	$k_{5\text{-}6}$
1	0.000711	0.000536	−0.000103
2	0.000637	0.000638	−0.000935
3	−0.000952	−0.000010	−0.002534
4	-0.001059	0.001200	−0.007092
5	0.000356	0.001218	−0.005770
6	0.001520	−0.000093	0.003345
7	0.004637	−0.000989	−0.001820
8	−0.002557	−0.001007	0.000003
9	0.018073	0.002965	−0.000534
17	−0.000145	0.000340	−0.002181
19	−0.004331	−0.001316	−0.006223
20	−0.007468	−0.001318	−0.013193
21	−0.000339	0.000961	−0.007298
25	0.025599	0.009009	−0.000935

5 Conclusions

This paper proposes the sensitivity models of B and L indices for steady-state voltage stability, and defines the cases of the adverse effects of the control measures, which are valuable for wind power system with time-varying and complex system conditions and multiple choices of the countermeasures. Some conclusions are found,

(i) The adverse cases are related to the system stress, and sensitive to the bus powers, which are differentiated by the sensitivities with little calculation effort.
(ii) Some adverse cases show increase of L, similar to that for the reliability analysis. Some show different effects, similar to that for the transient stability analysis.
(iii) Among the adverse cases, the adverse control effect of load shedding is rare, but the most undesirable to the voltage stability of the load buses.

Acknowledgements This work is supported by the Natural Science Foundation of China (51877061).

References

1. Kundur P, Paserba J, Ajjarapu V et al (2004) Definition and classification of power system stability. IEEE Trans Power Syst 19(2):1387–1401

2. Ye X, Le J, Liu Y et al (2018) A coordinated consistency voltage stability control method of active distribution grid. J Mod Power Syst Clean Energy 6(01):85–94
3. Li S, Ding M, Du S (2009) Transmission loadability with field current control under voltage depression. IEEE Trans Power Del 24(4):2142–2149
4. U.S.-Canada Power System Outage Task Force, Final report on the August 14, 2003 blackout in the United States and Canada: causes and recommendations, Apr 2004. [Online]. Available: https://reports.energy.gov
5. Lu Y, Lin S, Liu M et al (2018) Computation of static voltage stability margin for power system considering fluctuation interval of wind farm output. Autom Electr Power Syst 42 (08):92–100
6. Li S (2014) Operation region of doubly-fed induction generators based on rotor slip under MPPT control and power dispatch. Electr Power Compon Syst 42(8):808–817
7. Wang Z, Guo C, Liu W et al (2017) Multi-time scale voltage control and coordinated correction for distribution networks considering load characteristics. Autom Electr Power Syst 41(15):51–57
8. Potamianakis EG, Vournas CD (2006) Short-term voltage instability effects on synchronous and induction machines. IEEE Trans Power Syst 21(2):791–798
9. Chen P, Xiao X, Wang X (2019) Interval optimal power flow applied to distribution networks under uncertainty of loads and renewable resources. J Mod Power Syst Clean Energy 7 (01):139–150
10. Bian Q, Qiu Y, Wu W et al (2018) Generation dispatch method based on maximum entropy principle for power systems with high penetration of wind power. J Mod Power Syst Clean Energy 6(06):1213–1222
11. Ajjarapu V, Christy C (1992) The continuation power flow: a tool for steady state voltage stability analysis. IEEE Trans Power Syst 7(1):416–423
12. Chowdhury BH, Taylor CW (2000) Voltage stability analysis V–Q power flow simulation versus dynamic simulation. IEEE Trans Power Syst 15(4):1354–1359
13. Cao GY, Hill DJ (2010) Power system voltage small-disturbance stability studies based on the power flow equation. IET Gener Transm Distrib 4(7):873–882
14. Tamimi AA, Pahwa A, Starrett S (2012) Effective wind farm sizing method for weak power systems using critical modes of voltage instability. IEEE Trans Power Syst 27(3):1610–1617
15. Aryaa LD, Pandeb VS, Kothari DP (2005) A technique for load-shedding based on voltage stability consideration. Int J Electr Power Energy Syst 27(7):506–517
16. Li S (2013) Configuration of Jacobian matrix in steady-state voltage stability analysis based on rotor flux dynamics of rotating machines. Int J Emerging Electr Power Syst 14(3):239–244
17. Kessel P, Glavitsch H (1986) Estimating the voltage stability of a power system. IEEE Trans Power Del 1(3):346–354
18. Löf PA, Andersson G, Hill DJ (1993) Voltage stability indices for stressed power systems. IEEE Trans Power Syst 8(1):326–332
19. Tuan TQ, Fandino J, Hadjsaid N et al (1994) Emergency load shedding to avoid risks of voltage instability using indicators. IEEE Trans Power Syst 9(1):341–347
20. Li S (2016) Sensitivity model of L index for steady-state voltage stability of wind power systems with DFIGs. Electr Power Compon Syst 44(18):2017–2024

Application of New Energy Microgrid System in Industrial Park

Nan Cui and Jun Mu

Abstract The continuous growth of electrical load, a high cost of electricity, environmental protection, renewable energy utilization, and power quality problems have become severe challenges facing the power industry. As an important part of the future energy internet, the development of micro-grid has been widely concerned by all sectors of society. Based on specific engineering projects, this paper discusses the feasibility of the application of integrated micro grid system in industrial parks from the perspectives of load characteristics, solutions, control methods and investment returns.

Keywords Industrial park · New microgrid system · Energy management · Benefit

1 Introduction

Global energy crisis and environmental pollution promote the development of microgrid technology and electric vehicle industry [1]. The construction of the new energy microgrid fully responds to the policy guidance of the "Internet + intelligent energy" and the energy Internet, which is conducive to promoting the realization of the energy supply side reform and promoting the establishment of the regional energy management ecosystem [2–7].

In the traditional micro grid, most of the electricity generated by photovoltaic, wind turbine and battery energy storage unit which are dc or non-power frequency alternating current, and the power battery of electric vehicle is also dc energy. At present, the large power grid is dominated by ac transmission and distribution.

N. Cui (✉)
Sichuan University, South Section of the First Ring Road 24, 610065 Chengdu, China
e-mail: 2016141452114@stu.scu.edu.cn

J. Mu
Qingdao TGOOD Electric Co., Ltd, Songling Road,
Laoshan District, 336, 266100 Qingdao, China

Y. Xue et al. (eds.), *Proceedings of PURPLE MOUNTAIN FORUM 2019-International Forum on Smart Grid Protection and Control*, Lecture Notes in Electrical Engineering 585, https://doi.org/10.1007/978-981-13-9783-7_29

Therefore, the study of micro grid in the early stage is more about ac micro grid. Although ac micro grid is the main form of micro grid, its shortcomings gradually become prominent, such as multiple power conversion links, large network loss, and complex power grid operation control, which are inconsistent with the economic, efficient, reliable and high-quality power supply service we expect [8–11].

In this paper studies the new form of micro grid in the industrial park. To realize the economic power in user side, increase locally cost of distributed clean energy, smooth the difference between peak and valley in power requirement, improve energy efficiency in grid side and demand side response of the power grid dispatch system, AC/DC hybrid micro grid was used as technical options to integrate all kinds of subsystems that include power transform, power distribution, photovoltaic, energy storage, charging & discharging equipment and so on. In this way, we can give full play to the role of power electronics technology in power conversion, to achieve efficient conversion, precise control, flexible regulation, improve energy efficiency and power supply quality. The practice of intelligent operation and management of micro grid, combined with energy management system to achieve steady state economic operation and dynamic stability control, provide the basic conditions of business operation for the consumption and utilization of distributed new energy, large-scale electric vehicles orderly charge and discharge management.

2 Overview of the New Microgrid System

Traditional micro-grid is a micro-power system that can supply power to a region independently. It has the functions of power generation, transmission, substation, distribution and power consumption. It consists of a distributed power supply, energy storage device, energy conversion device, electric vehicle, load, monitoring, and protection device, etc. It can operate independently as well as in grid connection [12]. This paper introduces the application of a new micro-grid (hereinafter referred to as the new micro-grid). The biggest difference between the traditional micro-grid and the new micro-grid is that the electric vehicle elements are integrated into the micro-grid, and the orderly charging and discharging function of the electric vehicle are realized. The V2G technology of the electric vehicle into the grid participates in the frequency regulation of the micro-grid, which brings certain economic benefits to the electric vehicle users and the micro-grid and promotes the absorption of renewable. It improves the frequency stability of microgrid and reduces the cost of construction and operation of controllable power supply in the microgrid [1].

The necessity of photovoltaic introduction

The installation of photovoltaic is flexible which can make full use of idle roof, building surface in the industrial park. The construction of distributed photovoltaic power generation systems can realize nearby directly incorporated into the user side

power supply load, avoid the loss of power transmitted over a long distance, improve the user's profits, lowering the operating costs for the park [13].

In order to realize the efficient utilization of photovoltaic power generation, this scheme chooses to directly connect the photovoltaic power generation to the dc bus to reduce the energy loss caused by multi-level transformation. To ensure 100% PV absorption index, the proportion of PV system installed capacity should be determined by comprehensive analysis of factors such as installation area, load size of the park, power consumption period of load, hours of photovoltaic power generation, etc.

The necessity of energy storage introduction

Through energy storage equipment (including mobile energy storage of electric vehicles), the electricity of photovoltaic residual power and off-peak electricity price can be stored and used in peak or high electricity price period, so as to select the energy consumption strategy with the lowest cost for users. At the same time, it can also participate in the collaborative dispatching of the power grid, provide a demand-side response, and provide peak load regulation service for the power grid. Moreover, it can also increase the capacity of the temporary load. When the power supply condition is insufficient, energy storage battery and electric vehicle are used to provide the load demand for a temporary capacity increase [14, 15].

The necessity of management on charging and discharging of electric vehicles

The charging of electric vehicles can be regarded as an energy load. In the process of charging demand, there are various uncertainties in charging time, charging area, charging demand load, etc., which mainly manifests in disordered charging. The load of disordered charging will be superimposed on the peak of power consumption in the park, resulting in a higher peak value, which will inevitably cause serious impact on the power grid. For the unit of power consumption, a large amount of disorder or peak power will increase the power consumption. Since there is no intelligent power distribution system, distributed power cannot be fully absorbed, and resources are wasted and increase investment risks [16].

New micro-grid system can be clean energy such as electric vehicle charging and optical storage in the park, the integration of the given distributed energy, reduce the impact on power network, the use of electric discharge function at the same time, as a storage object, achieve peak power cut and cooperate in intelligent management of large power unit, further reduce the energy cost.

3 Application Case Analysis

In this case, a high-tech industrial park in Qingdao is taken as an example. The park is a large industrial electricity property, and the Peak-Valley Price Strategy is implemented. It is hoped to introduce clean energy and reduce energy costs.

3.1 Power Environment and Load Characteristics

The power environment and load characteristics have the following characteristics.

(1) The photovoltaic roof installations such as roofs, glass facades and outdoor carports in the industrial park are abundant and can be used to develop building photovoltaics. This time, the roof of the workshop is used as a photovoltaic carrier, with an installation area of nearly 15,000 m^2 and a 1 m high parapet wall and fan on the roof.
(2) The scale of electric vehicles is gathered: the park has nearly 100 electric car charging spaces. The charging demand is large, and the electric vehicle can be charged and discharged in an orderly manner.
(3) Typical peak-to-valley difference energy: large industrial electricity characteristics, large peak-to-valley difference, high electricity cost, electricity price and segment as shown as below (see Fig. 1), according to the monthly electricity bill of the park and the large industrial electricity price in Qingdao area.
(4) There are a large number of DC loads: EV DC fast chargers, LED displays, etc., DC power demand is high, the LED screen power demand which provided by the owners shows that is 225 kW.
(5) The owner provides a distribution load of 800 kW, of which the important load need to be guaranteed are the exhibition hall and office building. The conditions for uninterrupted power supply are required, and the load is considered at 160 kW.

3.2 System Scale Approval

After combining the above park load characteristics and energy demand requirements, and conducting site surveys, the project is more suitable for AC/DC hybrid networking. The planning of each component is as follows:

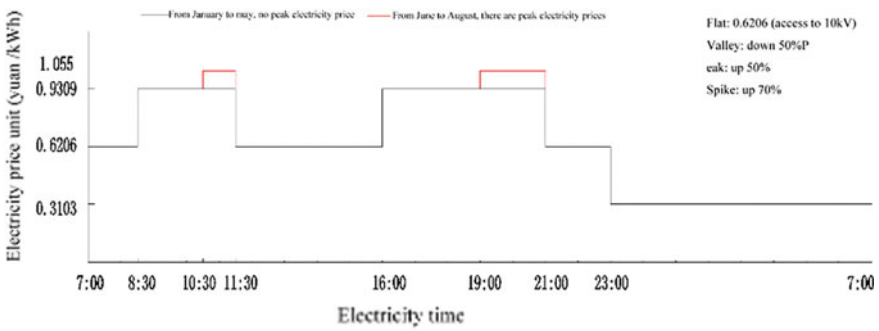

Fig. 1 Typical peak-to-valley energy gap curve

Power distribution system. According to the distribution load provided by the owner, consider using 10 kV voltage level access. The power supply is taken from a 10 kV switching station of the park. The distribution transformer uses a 1.25 MVA double-split dry-type transformer.

Photovoltaic system. The project is roofing photovoltaic, the roof installation area is 15,000 m^2, and the planned installed capacity is 1 MWp, all of which are fixed installation.

Energy storage system. According to the power supply demand of 320 kW important load, the time is considered in 1 h (combined with historical power outage time), 320 kWh energy storage battery is configured, and PCS power is configured according to 320 kW; in order to ensure the economic efficiency of energy storage, the peak load shifting strategy is picked. When the valley strategy is running, the power supply company has a line maintenance plan, and then consider switching to an operational strategy that guarantees important loads.

Electric vehicle charging and discharging system. The electric vehicle in the park serves the charging of employee's EVs and commute buses. Through the division of the area and the parking space, 32 passenger cars and 2 buses can be connected to the system. The charging and discharging power of the passenger car is 10 kW. The bus has a charging power of 40 kW. The total charging load is 400 kW.

Finally, The following Table 1 gives a total system scale of the AC/DC microgrid as follows:

3.3 System Networking Scheme

In view of the above analysis, a four-quadrant power converter and a bidirectional DC/DC converter are taken as the core components, and the subsystems of the industrial park are highly integrated, transformed, lighted, stored, charged, and

Table 1 The scale of the distribution system in the park is optimized

Microgrid element	Numerical value	Microgrid element	Numerical value
Access voltage grade	10 kV	Distribution load	800 kW
Photovoltaic system	1 MWp	Important load	320 kW
Energy storage system	320 kWh	DC load	225 kW
EV charging power	400 kW	Off-grid switching	No perception
Electric vehicle 10 kW	32 vehicles	Double split transformer capacity	1250 kVA
Electric bus 40 kW	2 vehicles	Structure and type	High protection
Energy management system	Matching	Local management system	Matching

placed in an outdoor box. In the power equipment, monitoring and control are realized through automated devices.

The AC/DC dual bus system effectively combines different source and load of the park, the high voltage side is connected to the 10 kV AC distribution network, and the low voltage side is divided into two sets of fully symmetrical low voltage busbars through the double split transformer. 400 V AC busbar is connected to the traditional AC load, and make distinction between important load and normal load; distributed photovoltaic (2 * 500 kWp), battery energy storage (2 * 160 kWh) and electric vehicle charge and discharge (200 kW) are connected to two sections of 765 V respectively. DC bus system, AC and DC bus are coupled by four-quadrant converter, the whole system constitutes AC-DC hybrid micro-grid system, the system composition is shown as follows (see Fig. 2).

In the system, the AC bus can also be connected to other AC power sources, such as wind turbines, which can complement the advantages of photovoltaic resources; can be connected to diesel generators, gas generators, etc., as a secondary backup when the system is running alone. power supply.

The four-quadrant inverter in the system integrates the functions of photovoltaic inverter and energy storage converter and has integrated functions such as rectification, inverter, reactive power compensation and harmonic control. The charging and discharging module of an electric vehicle is simplified from the traditional AC/DC design to DC/DC.

In the system, the electric vehicle is taken as a controllable element, which can directly absorb the fluctuating photovoltaic power generation and enhance the stability of the micro-grid system. Meanwhile, electric vehicle discharge and fixed energy storage are coordinated to ensure reliable power consumption of important loads and realize orderly charging and discharging management of electric vehicles.

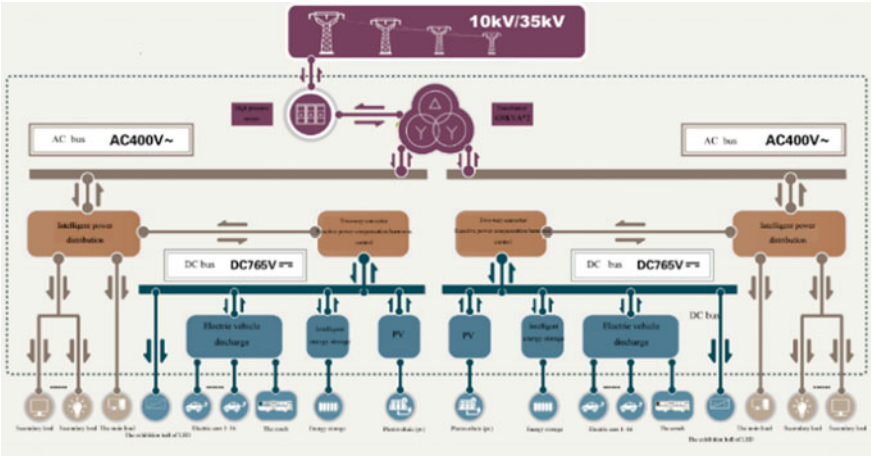

Fig. 2 Network diagram of the new microgrid system

3.4 System Technology Advantage

Combine with Substation-Distribution-PV-Energy storage to realize comprehensive investment cost reduction by 20–30%

Compared with the traditional micro-grid networking mode, the new micro-network innovative structure and product form, cleverly carried out the system 4 in 1 to improve the system integration and energy conversion efficiency, reduce the equipment footprint and achieve factory pre-installation (see Fig. 3).

The value brought to the customer is to achieve a comprehensive investment decline of up to 20–30%, the specific analysis results are shown in Table 2.

Energy costs cut down by 25–30% due to AC/DC hybrid network

The system connects the photovoltaic power generation, energy storage battery, electric vehicle and other DC loads to the DC bus through the AC/DC dual bus system. The DC source and the load are directly supplied to each other through the DC bus, eliminating the redundant conversion of the inverter-rectification power. Through the scheduling strategy of the energy management platform, it is possible to realize peak-peak power consumption, energy storage system peak-filling and valley filling, electric vehicle economical charging, and realizing the release of surplus power during the peak power consumption period, thereby achieving the goal of reducing the energy cost.

The following model is the energy efficiency model of the actual operation of the park on a certain day. The original electricity cost of pure load + charging load is ¥13,998. After the introduction of photovoltaic power generation in the park, the cost of electricity is reduced to ¥8730, and the value of the microgrid is continuing. After photovoltaic, through the various energy management and control strategies such as electric vehicle economic charging, intelligent discharge and energy storage

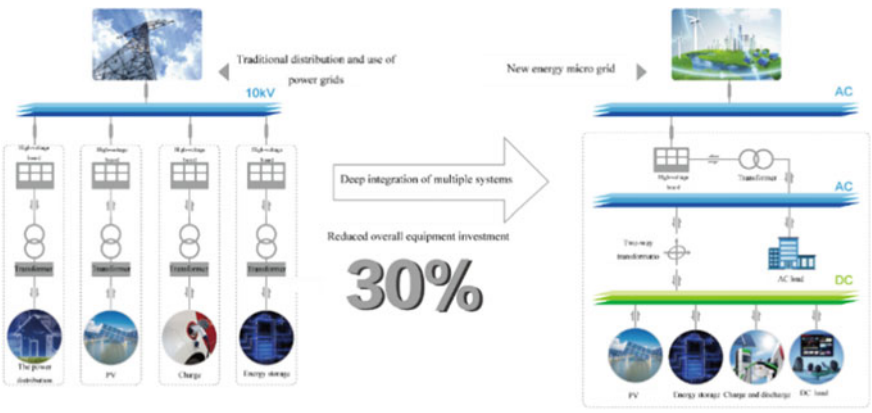

Fig. 3 Comparison of traditional microgrid and new microgrid

Table 2 Comparison of initial investment between the new micro-grid system and traditional micro-grid system

Name	System structure	Equipment investment of traditional micro-grid	Equipment investment of new micro-grid	Investment savings
Micro-grid system (without PV and charging device)	Distribution system	5.85 million	4.38 million	1.47 million
	PV system			
	Energy storage system			
	Charge-discharge system			
	Energy management system			

Fig. 4 Typical energy efficiency model of weekday

discharge, the energy cost can be reduced from ¥8730 to ¥6200 yuan, which can be further realized on the base of photovoltaic power saving cost. The cost of energy can be reduced by 25–30% (see Fig. 4).

Electric vehicles are charged and discharged in an orderly manner to achieve new energy consumption and peak shifting

With the organic combination of the distribution network, photovoltaic power generation, fixed energy storage, there are many ways to develop advantages of electric vehicles, strengthen cooperation with periodic PV generation to improve accommodation of solar power in the daytime, achieve flexible power supply to the conventional load. Energy is absorbed in the trough of electricity consumption, and released in the peak of electricity consumption, showing the tidal characteristics of orderly and controllable electric energy. This mode forms friendly interaction and deep integration of vehicles, loads and power grid.

The adjustable characteristics of electric vehicles are fully utilized in the system. As a load, electric vehicles can optimize the intermittent power generation of renewable energy, consume new energy power generation locally, and reduce the occurrence of solar power abandon. As a power source, EV is a zero-cost distributed and mobile energy storage, which can help the grid to cut peak load and fill valley to improve the economic efficiency of the Park.

No sense of safety self-healing, realize the important load uninterrupted power supply

According to the control of operation strategy, the new energy micro-grid system can realize quick perception of on-grid or off-grid, automatic rapid switch, and flexible adjustment. When the power is cut off, the system will automatically change to the isolated island operation state from the normal state of connecting with the grid and use new energy power generation, energy storage, and electric vehicles discharge to ensure the continuous power supply of important loads within a certain period. When the main power grid is restored, the system will automatically switch back to the grid-connected operation state to ensure quick response in millisecond-level time, realize the entire off-grid switching process without sense perception, which can provide high quality and reliable power supply for the sensitive load in the park.

3.5 The Profits of the Project

Economic benefit analysis

After implementation of this system, the revenue can be divided into following parts: revenue of new energy power generation system, revenue of smart energy storage system, revenue of charging and discharging system of electric vehicles. Among them, the benefits of the new energy power generation system are reflected in the use of clean energy power generation to reduce purchase cost from power grid and the subsidiary fee from project construction site for clean energy power generation; The benefits of the smart energy storage system are reflected in the fact that under the condition of constant electricity consumption, the power consumption between peak electricity price can be reasonably reduced, and the power consumption between valley electricity price can be correspondingly increased, which can effectively reduce the payment of electricity purchase fee and basic electricity charges from the grid. This system is applicable to regions with a large difference between peak and valley electricity prices. The benefits of an EV charging system are reflected in the charging service fee income from self-operating charging terminals and the subsidiary fee from the project construction site for the construction and operation of charging piles. The income of electric vehicle discharge is the same as the fixed energy storage system income. Shows in Table 3.

Table 3 Project income of new energy micro-grid system

Name	Components of income	Annual revenue	Total system investment	Payback period	Note
New energy micro-grid system	PV generation for self-use and surplus electricity selling income	1.48 million	11.38 million	7.6 years	The total investment includes PV and charging peripherals
	Energy storage and EV for peak-shaving and valley-filling revenue				
	Income of EV charging service fee				

Social benefit analysis

The investment of this project entirely conforms to the requirements of relevant national industrial policies. It will contribute to the realization of the 13th five-year plan on energy conservation and emission reduction and increase social benefits. Considering the installed capacity of PV on the rooftop of the workshop in the park, the average annual power generation of PV system can reach 1.23 million kW/h, saves 369 tons of coal and realize 9.4787 million tons of carbon dioxide emission reduction.

Considering 7L (92#) of fuel consumption for a gasoline car for every 100 km and each car travels 20,000 km a year, 30,000 gasoline vehicles can consume gasoline annually: 30,000 * 1400 L * 0.75 kg/L = 31,500 tons; Discount standard coal: 31,500 * 14,714 = 46,300 tons. Replacing gasoline vehicles with the same number of electric vehicles will reduce carbon dioxide emissions by 115,400 tons, sulfur dioxide emissions by 3400 tons and nitrogen oxide emissions by 1600 tons per year.

4 Conclusion

The system scheme can solve several pain points of industrial park fundamentally by AC/DC hybrid networking, applying electric vehicle group control ordered charging and discharging technology, bidirectional power conversion technology, electric vehicle discharge monitoring technology, and off-grid switching technology. The customer's multiple pain points, including the problem of multi-energy integration of wind and light storage, the problem of low energy efficiency utilization, the problem of high energy cost, DC load access problem, electric vehicle V2G participation in peak shaving, etc. The extensive type can be converted to finer energy, and the project is highly reproducible. In addition to the application in the

industrial park, the micro-network system introduced in this paper has seen applications in islands, characteristic towns, schools, hospitals, household villas, data centers, highways, ports, etc. In the next 5–10 years, the market size, regional distribution and application site distribution of micro-grid will change significantly and the future is bright.

References

1. Qihui L, Shengjia L (2018) Charge and discharge control strategy of electric vehicle virtual synchronous machine participating in micro-grid frequency modulation. Autom Electr Power Syst 42(9):171–179
2. Huang AQ, Crow ML et al (2011) The future renewable electric energy delivery and management (FREEDM) system: the energy internet. Proc IEEE 99(1):133–48
3. Khajenasir I, Estebsari A, Verhelst M et al (2017) A review on Internet of Things solutions for intelligent energy control in buildings for smart city applications. Energy Procedia 111: 770–779
4. Tsoukalas L, Gao R (2008) From smart grids to an energy internet: assumptions, architectures and requirements. In: Proceedings of the 2008 third international conference on electric utility deregulation and restructuring and power technologies. IEEE, pp 94–98
5. Chuyuan W, Yongzhen L (2011) Design of energy consumption monitoring and energy-saving management system of intelligent building based on the Internet of things. In: Proceedings of the 2011 international conference on electronics, communications and control (ICECC). IEEE, pp 3650–3652
6. Yi X, Jianhua Z, Wenye W et al (2011) Energy router: architectures and functionalities toward energy internet. In: Proceedings of the 2011 IEEE international conference on smart grid communications (SmartGridComm). IEEE, pp 31–36
7. Guyuan D (2018) "Dream" of the distribution network. State Grid 4:16–19
8. Hosseinzadeh M, Salmasi FR (2018) Fault-tolerant supervisory controller for a hybrid AC/DC micro-grid. IEEE Trans Smart Grid 9(4):2809–2823
9. Senapati MK, Pradhan C, Samantaray SR et al (2018) Improved power management control strategy for renewable energy-based DC micro-grid with energy storage integration. IET Gener, Transm Distrib
10. Heyderi R, Peyghami S, Yang Y et al (2018) DC micro-grids for photovoltaic powered systems. Iet. 389–414
11. Saraswathy K, Paul FM, Mathew A (2018) Four quadrant operation of BLDC motor suitable for DC micro grid for elevator application. In: 2018 international conference on power, signals, control and computation (EPSCICON). IEEE. pp 1–5
12. Zhongzhou L (2012) Research on steady-state fault analysis of microgrid with inverter power supply. Tianjin University
13. Zhengming Z, Yi L, Fanbo H et al (2011) Summary of technology for large-capacity grid-connected photovoltaic power plants. Autom Electr Power Syst 35(12):101–107
14. Guoju Z, Xisheng T, Zhiping Q (2010) Application of supercapacitor and battery hybrid energy storage system in microgrid. Autom Electr Power Syst 34(12):85–89
15. Mingyong C, Chutong W, Yucui W et al (2018) Optimized configuration of microgrid multi-energy storage system in independent mode. Autom Electr Power Syst 42(4):30–38
16. Ming D, Shengliang S, Hao P et al (2018) AC/DC hybrid microgrid planning with electric vehicle charging load. Autom Electr Power Syst 42(1):32–38

A Local Quadratic Wavelet Neural Network Method for Predicting Dispersed Wind Power Generation

Yiqing Lian, Changcheng Zhou, Zhiyong Yuan, Jinyong Lei and Si-yu Tao

Abstract In this paper, a new local quadratic wavelet neural network (LQWNN) method is proposed for short-term wind power generation prediction in power system. Due to the nonlinear structure of its local quadratic model (LQM), this method can effectively simulate the nonlinear behavior of wind power generation. In the time domain and frequency domain, wavelet function sets the effective region of LQMs in LQWNN, thus improving the learning efficiency and structural transparency of the overall model. The proposed LQWNN method employs a simple and effective particle swarm optimization (PSO) algorithm and optimizes its parameters. Through two real cases studies, namely the wind power forecast of the Irish power grid and the Jiuquan wind power plant in Gansu province, the performance of the proposed wind power forecasting method is evaluated and compared with other methods. The results show that the LQWNN method proposed in this paper is very effective in predicting wind power generation and has a good application prospect.

Keywords Neural networks · Local quadratic wavelets · Particle swarm optimization · Power systems · Wind power forecasting

1 Introduction

With the large-scale development and utilization of fossil energy worldwide, environmental pollution, climate change and other issues have become increasingly prominent. The development and utilization of clean energy has become a common

Y. Lian · C. Zhou (✉) · Z. Yuan · J. Lei
Electric Power Research Institute of China Southern Power Grid, Guangzhou 510663, China
e-mail: zhoucc@csg.cn

Y. Lian
e-mail: lianyq@csg.cn

S. Tao
Southeast University, Nanjing, China

Y. Xue et al. (eds.), *Proceedings of PURPLE MOUNTAIN FORUM 2019-International Forum on Smart Grid Protection and Control*, Lecture Notes in Electrical Engineering 585, https://doi.org/10.1007/978-981-13-9783-7_30

choice to cope with climate change worldwide. Therefore, dispersed wind power generation is developing rapidly in the world, and the installed capacity of wind turbines is increasing rapidly. By the end of 2008, the nameplate capacity of wind turbines around the world has reached 1.212 million kilowatts, accounting for about 1.5% of the global electricity consumption [1]. According to the current outlook, more than 12% of the world's energy consumption by 2020 will be generated by wind power [2]. Due to the intermittent nature of dispersed wind power generation, its integration with traditional power system brings many operational and economic challenges to the system operators, which hinders the integration between wind power generation and power system operators [3]. Wind power generation in wind farms is influenced by many meteorological factors, so accurately predicting wind energy, even in the short term, is a challenging task. For example, in August 2010, the series of wind power generation generated by wind farms in Ireland is shown in Fig. 1, and its nonlinear behavior and high frequency variation are obvious.

In the past decade, scholars have proposed various methods for short—and long-term dispersed wind power generation prediction. Generally speaking, these methods can be divided into two categories, namely, physical methods and time series methods [4]. Physical methods use physical and meteorological information, including descriptions of topography, roughness, obstacles, pressure and temperature, to simulate wind power generation and predict its future value. These methods have a satisfactory effect on the long-term prediction of wind power generation [5]. On the other hand, the time series method requires less data and information than the physical method. It requires some key meteorological variables, such as wind speed and direction, to establish wind prediction model with time series method. Sometimes, only historical wind energy data are used by time series models to predict dispersed wind power generation [6]. For wind speed and power prediction, researchers put forward traditional statistical models such as automatic regression (AR) model and automatic regression integrated moving average (ARIMA) model [7].

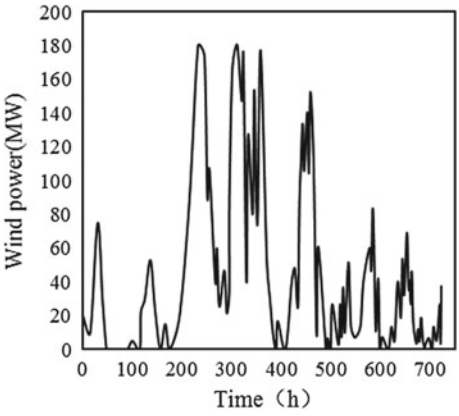

Fig. 1 Irish grid wind power in August 2010

Computational intelligence (CI) methods are also used to predict wind power generation. Computational intelligence (CI) methods are also used to predict wind power generation. It has been reported that a CI based approach can outperform both physical and conventional time series models in short-term wind prediction. For example, Amjady et al. proposed a hybrid neural network model for short-term wind power generation prediction. In another study, Amjady et al. developed a spinal wave neural network to predict the wind speed in the day ahead [8]. The ANFIS model has also been used by many scholars to predict future wind power generation projects.

This paper presents a local quadratic wavelet neural network (LQWNN) method for short-term wind prediction. In neural network, the connection weight between hidden layer nodes and output nodes is replaced by local quadratic model. In addition, an efficient particle swarm optimization (PSO) algorithm is used to train LQWNN network. In this paper, two real cases of wind power generation prediction are presented, and the performance of the proposed prediction method is evaluated and compared with other methods. The results show that the LQWNN method is very effective for dispersed wind power generation prediction.

2 Local Quadratic Wavelet Neural Network

The standard form of wavelet neural network (WNN) is:

$$f(x) = \sum_{i=1}^{M} \omega_i \psi_i(x) = \sum_{i=1}^{M} \omega_i |a_i|^{-\frac{1}{2}} \psi_i\left(\frac{x - b_i}{a_i}\right) \tag{1}$$

where, ψ_i is the wavelet activation function of the i-th node of the hidden layer, $x = [x_1, x_2, \ldots x_n]$ is the n-dimensional input vector, ω_i is the connection weight between the i-th node of the hidden layer and the output layer, and M is the number of nodes in the hidden layer. The parameters a_i and b_i are scale and translation parameters respectively. In fact, these parameters determine that the wavelet function is located in the i-th node of the hidden layer.

In wavelet theory, the function ψ_i called a generating function is local in both time and frequency domains. The position of the wavelet function leads to a characteristic of WNN network, and the wavelet function sets the effective region of its relative connection weight as a local constant model. This local feature brings learning efficiency and structural transparency to the WNN network.

Despite the advantages of WNN networks, many hidden nodes are required for high dimensional problems. This is due to the fixed structure of the constant local model, which lacks the flexibility of different input values. In this paper, we consider a local quadratic model (LQM) rather than a constant local model to avoid a large number of hidden nodes. In fact, for a process that requires many constant models, a quadratic model is sufficient.

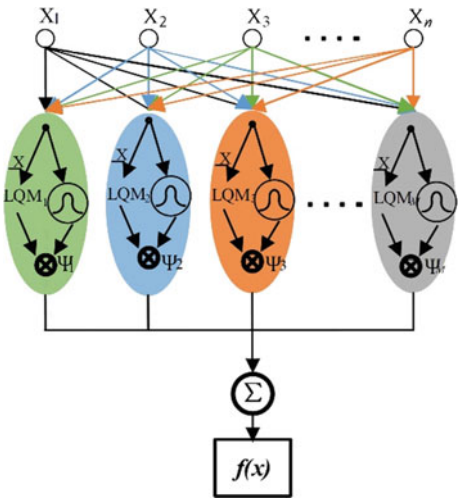

Fig. 2 LQWNN structure with n inputs and M hidden nodes

The structure of local quadratic wavelet neural network is:

$$\begin{aligned} f(x) &= \sum_{i=1}^{M} \left(\begin{array}{l} \omega_{i0} + \omega_{i0} x_1 + \cdots \omega_{in} x_n + \omega_{i(n+1)} x_1^2 \\ \quad + \omega_{i(n+2)} x_1 x_2 + \cdots + \omega_{in_t} x_n^2 \end{array} \right) \psi_i(x) \\ &= \sum_{i=1}^{M} \left(\begin{array}{l} \omega_{i0} + \omega_{i0} x_1 + \cdots \omega_{in} x_n + \omega_{i(n+1)} x_1^2 \\ \quad + \omega_{i(n+2)} x_1 x_2 + \cdots + \omega_{in_t} x_n^2 \end{array} \right) \times |a_i|^{-\frac{1}{2}} \psi_i \left(\frac{x - b_i}{a_i} \right) \end{aligned} \tag{2}$$

where, $\omega_i = [\omega_{i0}, \ldots, \omega_{in_t}]$ is the weight of the i-th LQM, and n_t is the total weighted parameter of each LQM. Note that since the quadratic terms are combined in Eq. (2), the nonlinear behavior of the process can be easily and accurately modeled. Figure 2 is the structure of the proposed LQWNN model.

The model given in formula (2) has two sets of parameters, namely the weighted parameters of the local quadratic model and the parameters of the wavelet function. These two sets of parameters are determined by a simple but effective particle swarm optimization (PSO) algorithm in the training process. The algorithm is described in the next section.

3 PSO Algorithm Training of LQWNN Model

As mentioned at the end of the previous section, PSO algorithm is used to train LQWNN model. On this basis, the global optimal (g_{best}) particle swarm optimization (PSO) algorithm is adopted to optimize the weighted parameters of LQM and the proportion and shift parameters of the wavelet function.

PSO algorithm is fast and computationally efficient, and it is an easy-to-code search technology based on the cooperation of particle architecture. Particles flow in a multi-dimensional search space, and each particle's position is adjusted according to its own experience and that of other particles. In the g_{best} algorithm, the new position of particle i on time $t + 1$ can be found by adding velocity separation to the previous position.

$$x_i(t+1) = x_i(t) + v_i(t+1) \tag{3}$$

$$v_{ij}(t+1) = v_{ij}(t) + c_1 r_{1j}(t)\left[p_{ij}(t) - x_{ij}(t)\right] + c_2 r_{2j}(t)\left[\hat{p}(t) - x_{ij}(t)\right] \tag{4}$$

where $x_{ij}(t)$ is the position of particle i in j dimension space and time t. $V_{ij}(t)$ is the velocity of particle i in j dimension space and time t, c_1 and c_2 are acceleration constants, r_1 and r_2 are constants uniformly distributed in [0,1]. In most applications, the constants c_1 and c_2 are set to 2, and $c_1 = c_2 = 2$ is also chosen for this article.

In the training process of LQWNN algorithm, all LQM and wavelet function parameters are updated synchronously in each iteration. The process is shown in Fig. 3. In the training process of PSO, if there are M hidden nodes and n input variables, $M \times [2n + n(n - 1)/2 + 1]$ parameters must be optimized by PSO algorithm. In the training process, the number of hidden nodes M is first set, and the

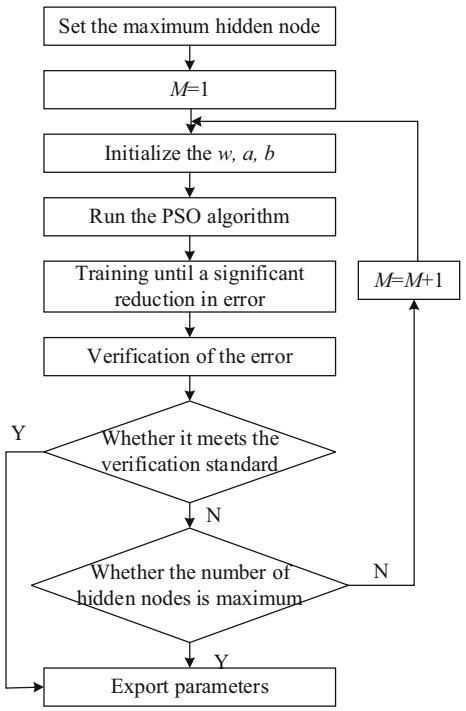

Fig. 3 PSO algorithm for LQWNN training process

parameters of the model are optimized from the LQWNN of a hidden node ($M = 1$), and then the number of hidden nodes is increased one by one. This process continues until either the stop criterion is met or the maximum number of hidden nodes (M_{max}) is reached.

4 Dispersed Wind Prediction of LQWNN

In this section, the proposed LQWNN model is used for wind prediction of two different wind fields in Ireland (case 1) and Jiuquan (case 2) in Gansu province. In the two case studies, available wind power generation data for the first 48 days were used as training data to predict hourly wind power generation during the test week. Table 1 lists the training data of these two case cycles. Note that 24-h predictions are made during each test week. In other words, during the 24 h of the test week, the prediction window will move 24 h in advance, and then the model parameters will be updated through the training algorithm, and the future wind power generation will be predicted. This process continued until it was possible to predict the amount of wind power generated per hour for seven days of the test week.

In addition, univariate time series prediction was conducted for both cases. Where, only the previous wind power generation is used to predict its current value, and appropriate input lag is selected for the LQWNN model through autocorrelation analysis. In this analysis, the autocorrelation coefficient (ACF) of the dispersed wind generation time series is calculated, and different hysteresis is calculated. The highest ACF hysteresis is considered as the possible input of the prediction model.

As mentioned in the previous section, the training process of PSO algorithm needs a stopping criterion. For wind prediction, we use the validation data set as a stop criterion. Therefore, the number of hidden nodes in LQWNN will continue to increase until the verification data error decreases. In this article, the verification data for each day of the test week is the previous day's wind power generation.

For wind power generation prediction, Mexican hat wavelet function is applied in the structure of LQWNN and WNN models:

$$\psi\left(\frac{x-b_i}{a_i}\right) = \left[1-\left(\frac{x-b_i}{a_i}\right)\right] e^{-\frac{1}{2}\left(\frac{x-b_i}{a_i}\right)^2} \tag{5}$$

Table 1 Data cycles for both cases

Case	Training data cycle	Test data cycle
1	August 5–September 23, 2010	September 24–September 30, 2010
2	November 5–December 22, 2015	November 23–November 29, 2015

In order to evaluate the accuracy of wind power generation prediction, this paper adopts two error measurement methods, namely root mean square error (RMSE) and mean absolute percentage error (MAPE). They are:

$$\mathrm{RMSE} = \sqrt{\frac{1}{N}\sum_{t=1}^{N}(P_t - \hat{P}_t)^2} \tag{6}$$

$$\mathrm{MAPE} = \frac{1}{N}\sum_{t=1}^{N}\frac{|P_t - \hat{P}_t|}{\bar{P}_t} \times 100 \tag{7}$$

$$\bar{P}_t = \frac{1}{N}\sum_{t=1}^{N} P_t \tag{8}$$

where, at time t, P_t and $\hat{P}_t$ are the actual and predicted wind power respectively, while N is the predicted quantity.

In formula (7) of calculating MAPE, the average P_t value is used in the denominator instead of the hourly value of the actual wind force. This is because the force of the wind might be close to zero in an hour, and if you use the actual force of the wind in the denominator in an hour, MAPE might be close to infinity. In addition, the wavelet neural network of Eq. (1) will also be trained by the PSO algorithm, and its predicted value will be compared with the proposed LQWNN model.

(1) **Dispersed wind power generation prediction of wind farms in Ireland**

As case 1, this paper will forecast the dispersed wind power generation in the Irish power grid in the last week of September 2010. Ireland's electricity grid and wind farms are run by EirGrid. Since 2006 EirGrid has operated high-voltage power grids and directed the flow of electricity in Ireland and Northern Ireland, where the local electricity supply authority (ESB) maintains and repairs them. Under the renewable energy plan, Ireland and Northern Ireland have pledged to increase their consumption of renewable energy to 40% by 2020.

In this paper, the training and test data set of the total wind power generation of the Irish power grid was collected from the website of EirGrid. EirGrid also published its 24-h wind power generation forecast, and these data will be used for comparison with the model in this paper.

First, in order to train LQWNN and WNN models, 100 particles were used in the PSO algorithm. Figure 4 shows the relationship between RMSE data and the number of hidden nodes. Obviously, LQWNN and WNN have the smallest error when the number of hidden nodes is 4 and 9. It should be noted that the minimum RMSE of LQWNN is lower than that of WNN, and each model is constructed with four inputs selected from the previous time series of dispersed wind power

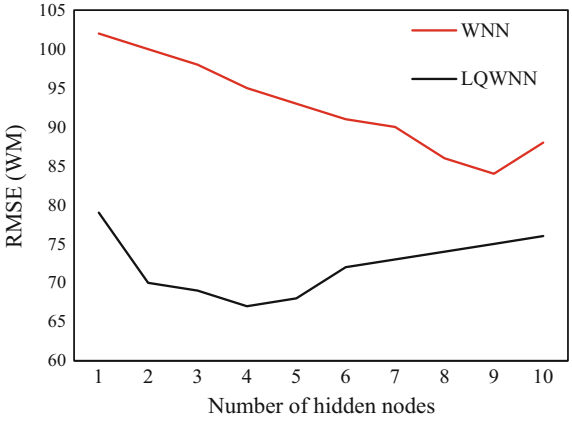

Fig. 4 RMSE for different number of hidden nodes in WNN and LQWNN (case 1)

Table 2 WNN and LQWNN model parameters in case 1

Model	Number of hidden nodes	The number of arguments	Mean square error training	Verification of mean square error
1	9	85	77.89	82.50
2	4	58	45.25	66.46

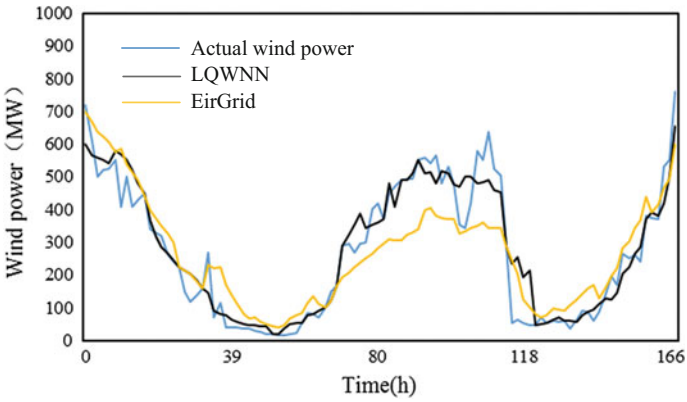

Fig. 5 Actual and predicted wind power generation (case 1)

generation. Table 2 shows the number of hidden nodes, number of parameters and training errors of each model, among which the number of parameters of LQWNN is much smaller than that of WNN.

Figure 5 compares predictions for the last week of September 2010 with actual wind and EirGrid forecasts. It is clear that LQWNN models have been successful in

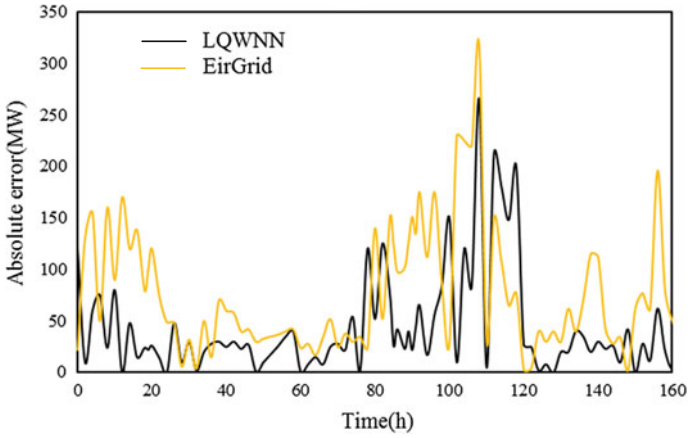

Fig. 6 Comparison of absolute error between LQWNN model and EirGrid hourly prediction (case 1)

Table 3 Comparison of RMSE and MAPE in case 1

Case	RMSE	MAPE (%)
WNN	132.66	51.22
EirGrid	89.68	30.65
LQWNN	62.26	18.45

tracking changes in wind power, whereas EirGrid's predictions have not been fully tracked. Figure 6 shows the absolute prediction error of LQWNN model and EirGrid Company. The predicted value of LQWNN is in good agreement with the actual wind force, which shows the superior performance of the model.

Table 3 shows RMSE and MAPE of test weeks obtained by WNN model, EirGrid company and LQWNN model in this paper. As can be seen from the table, the results of the method in this paper are better than those of the other two methods.

(2) **Wind power generation prediction of Jiuquan wind farm in Gansu province**

Case 2 is the wind farm in Jiuquan, Gansu province. Jiuquan is China's first 10 million kilowatt wind power base, but also the world's largest wind power base. Jiuquan wind power plant is another landmark project of the western development after the west-to-east gas transmission, west-to-east oil transmission, west-to-east power transmission and Qinghai-Tibet railway. By the end of 2015, the planned total installed capacity of Gansu Jiuquan ten million kilowatt wind power base reached 12,710 MW, accounting for 71.6% of the total installed capacity of wind power in the province and 6.2% of the total installed capacity of the whole country.

Table 4 WNN and LQWNN model parameters in case 2

Model	Number of hidden nodes	The number of arguments	Mean square error training	Verification of mean square error
WNN	10	105	21.65	30.36
LQWNN	3	60	17.60	22.51

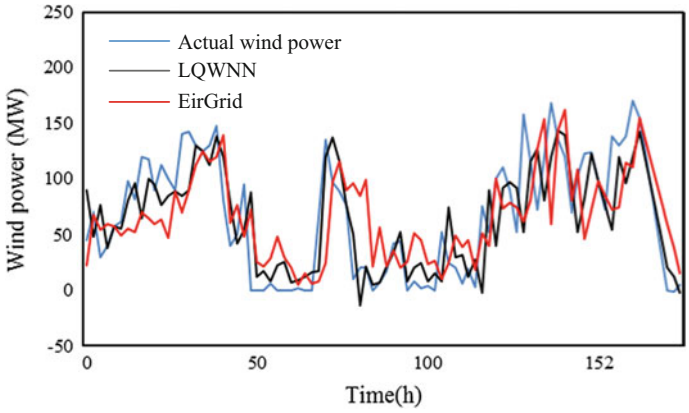

Fig. 7 Actual and predicted wind power generation (case 2)

Similar to the Irish case, all models are first trained, and the optimal number of hidden nodes is selected by validation data set error. The results show that WNN and LQWNN models have 3 and 10 hidden nodes respectively. In addition, each model selected five inputs from the previous wind power series. LQWNN has approximately half as many parameters as WNN. This makes the LQWNN model simpler and easier to train. Table 4 shows the number of hidden nodes, number of parameters and training errors of each model in the case study. Figure 7 shows the comparison between the predicted and actual wind energy values of the two models. Compared with WNN model, LQWNN model with fewer hidden nodes has better prediction performance.

LQWNN models can accurately track even sudden changes in wind power. Figure 8 compares the hourly absolute prediction error of WNN and LQWNN models. Table 5 shows RMSE and MAPE values of this case. It can be seen that the LQWNN model proposed in this paper has better performance.

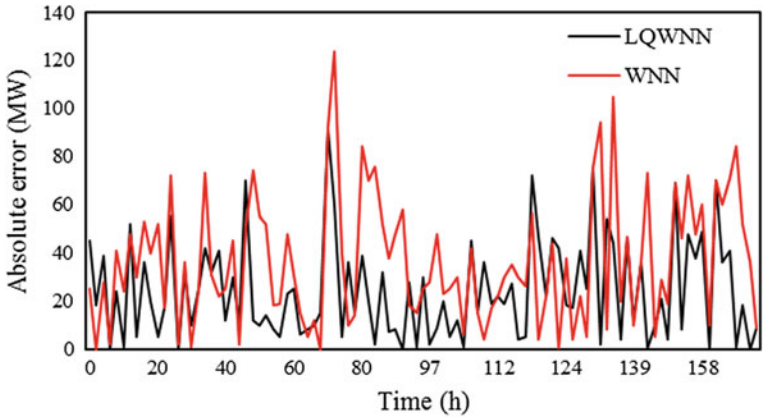

Fig. 8 Comparison of absolute error between LQWNN model and EirGrid hourly prediction (case 2)

Table 5 Comparison of RMSE and MAPE in case 2

Case	RMSE	MAPE (%)
WNN	46.47	22.34
LQWNN	20.24	13.80

5 Conclusion

Wind energy has significant intermittency and volatility, so accurately and reliably predicting its future value is the key to integrate wind farm with traditional power grid. In this paper, a local quadratic wavelet neural network model is proposed, and a highly efficient particle swarm optimization algorithm is used to predict short-term wind power generation. The model constructs nonlinear local quadratic sub-model and localizes the corresponding wavelet function, which has the ability to simulate wind power generation accurately. The study on two wind farms in Ireland and Jiuquan in Gansu province proves the effectiveness of this method. Compared with the predicted values provided by WNN model and power system of Ireland, this model has better prediction accuracy and engineering application prospect.

Acknowledgements Work in this paper is supported by "Science and Technology Project of China Southern Power Grid (ZBKJXM20180015)".

References

1. Methaprayoon K, Yingvivatanapong C, Lee WJ, Liao JR (2007) An integration of ANN wind power estimation into unit commitment considering the forecasting uncertainty. IEEE Trans Ind Appl 43(6):1441–1448
2. Kusiak A, Zheng H, Song Z (2009) Models for monitoring wind farm power. IEEE Trans Renew Energy 34:583–590
3. Kavasseri RG, Seetharaman K (2009) Day-ahead wind speed forecasting using f-ARIMA models. IEEE Trans Renew Energy 34(5):1388–1393
4. Catalao J, Pousinho H, Mendes V (2011) Hybrid intelligent approach for short-term wind power forecasting in Portugal. IET Renew Power Gener 5(3):251–257
5. Amjady N, Keynia F, Zareipour H (2011) Wind power prediction by a new forecast engine composed of modified hybrid neural network and enhanced particle swarm optimization. IEEE Trans Sustain Energy 2(3):265–276
6. Flores P, Tapia A, Tapia G (2005) Application of a control algorithm for wind speed prediction and active power generation. IEEE Trans Renew Energy 30:523–536
7. Amjady N, Keynia F, Zareipour H (2005) Short-term wind power forecasting using ridgelet neural network. IEEE Trans Electr Power Syst Res 81:2099–2107
8. Chen YH et al (2000) Evolving wavelet neural networks for system identification. Proc Int Conf Electr Eng 279–282

Multi-point Access Decentralized Wind Power Time Series Model Based on MCMC Algorithm and Hierarchical Clustering Algorithm

Zhiyong Yuan, Changcheng Zhou, Yiqing Lian, Qingshan Xu and Siyu Tao

Abstract In this paper, a medium and long term output analysis model of multi-point access decentralized wind power based on Markov chain Monte Carlo method is proposed. The model considers the correlation among multi-point access decentralized wind farms and the multivariate first order Markov process is obtained by analogy with univariate higher order Markov process. Based on this, the state transition matrix of multi-point access decentralized wind power output is established, and the output distribution of four decentralized wind farms in Shantou is simulated according to the model. The statistical parameters such as mean, standard deviation, probability density function (PDF) and autocorrelation coefficient (ACF) of the generated wind power time series and historical series are compared. The results show that the statistical parameters of the simulated series are very close to those of the historical series. The model presented in this paper is very effective. Then this paper proposes a method for selecting typical daily output of decentralized wind power based on hierarchical clustering algorithm, and simulates the typical daily output of summer and winter of four decentralized wind farms in Shantou based on the model.

Keywords Decentralized wind power · Output analysis · Markov chain monte carlo · Hierarchical clustering · Typical daily output

Z. Yuan · C. Zhou (✉) · Y. Lian
Electric Power Research Institute of China Southern Power Grid, Guangzhou 510663, China
e-mail: zhoucc@csg.cn

Z. Yuan
e-mail: yuanzy1@csg.cn

Q. Xu · S. Tao
Southeast University, Nanjing, China

Y. Xue et al. (eds.), *Proceedings of PURPLE MOUNTAIN FORUM 2019-International Forum on Smart Grid Protection and Control*, Lecture Notes in Electrical Engineering 585, https://doi.org/10.1007/978-981-13-9783-7_31

1 Introduction

Decentralized wind power output has obvious volatility characteristics, and its grid connection will affect the system's voltage distribution, power flow, relay protection, short-circuit current and power quality. Especially for decentralized wind power projects connected to the distribution network, due to the relatively small number of wind turbines, the smoothing effect between the wind turbines is small, which will have a greater impact on the voltage regulation of the distribution network.

Studying the output characteristics of decentralized wind power and using simulation technology to simulate time series with similar characteristics has the following advantages: (1) It can generate time series of arbitrary length and has similar random fluctuation characteristics with historical sequences, which can solve the problem that the current wind power prediction cannot predict the long-term time series. (2) The simulation method can make up for defects such as historical data loss or recording errors. (3) It can provide basic data for reliability calculation [1–3], peaking margin estimation [4], stochastic production simulation [5], wind power confidence capacity calculation [6], power balance analysis and probabilistic load calculation [7] for power systems with wind farms.

The current time series modeling methods of wind power output are mainly divided into two categories: indirect method (that is, wind speed-based modeling method) and direct method (that is, power-based modeling method) [8]. This paper only discusses the power-based modeling methods.

In order to accurately grasp the fluctuation law of wind farm output, domestic and foreign research scholars have done a lot of research on the fluctuation characteristics of wind farm output, and have also achieved fruitful results. In [9], combined with actual wind power data, the fluctuation and smoothing effect of wind power output under different weather types are analyzed, and the intrinsic relationship between weather type and overall output characteristics is revealed. In [10], the historical output sequence of the wind farm is divided into multiple fluctuation processes, and the wind power fluctuation category and the fluctuation statistical parameters are sampled monthly to simulate the wind farm output sequence. When several adjacent wind farms are connected to the power system at the same time, there is spatial correlation between the output of each wind farm [11]. In [12], in order to simulate the spatio-temporal series of multi-wind farm output, the measured power data of wind farm are analyzed from the perspective of spatio-temporal series. In [13], the joint distribution of output power among multi-wind farms is constructed by introducing Copula theory.

Although a lot of research has been done on the model of wind power output characteristics at home and abroad, the current research is limited to large-scale centralized wind power, and there is very little research on the decentralized wind power output characteristic model. In this paper, based on the Markov chain-Monte Carlo method, a multi-point access decentralized wind power medium- and long-term output time series model is established, and the statistical parameters of

the simulated sequence and the historical sequence are compared. The results show that the model proposed in this paper is very effective. Then, based on the hierarchical clustering algorithm, a daily output time series model of decentralized wind power is established.

2 Medium and Long Term Output Analysis Model

2.1 Markov Process for Multipoint Access

State Transition Matrix. The Markov chain corresponds to a series of discretized states, and each of the power generation values of the intermittent power source will belong to a specific state. Assuming that the output range of a decentralized wind farm is (P_{min}, P_{max}) in a certain period of time and the number of discrete states is N, the power interval covered by each state is ($P_{max} - P_{min}$)/N.

According to the definition of wind power state, the concept of state transition matrix is introduced here. The state transition matrix $\boldsymbol{P_r}$ is an $N \times N$ matrix, where N is the number of states divided by the wind power output range. The value of p_{ij} for each element in $\boldsymbol{P_r}$ represents the probability that the wind power at the current moment is state i and will be transferred to state j at the next moment. As shown in the following formula:

$$p_{ij} = P_r(X_t = j | X_{t-1} = i) = n_{ij} / \sum_{k=1}^{N} n_{ik} \tag{1}$$

where X_t and X_{t-1} represent the states of time t and $t-1$, respectively. p_{ij} represents the probability of transition from state i to state j. n_{ij} is the number of transitions of successive processes $i \rightarrow j$; P_r represents the probability function.

Affected by geographical regions, illumination, climate and other factors, multiple wind farms often show a certain correlation. Assuming that the output of k decentralized wind farms is correlated, and the discrete state is expressed by the k-dimensional variable $\boldsymbol{X}$, where $\boldsymbol{X} = (X_1, \ldots, X_i, \ldots, X_k)$ and $X_i \in (1, \ldots, N)$. By analogy with the high order Markov process of a single variable, the state transition probability is defined as:

$$\begin{aligned} p_{i_k \cdots i_{i+1} i_{i-1} \cdots i_1 i_i j} &= P_r(X_i^{(n)} = j | X_i^{(n-1)} = i_i, X_1^{(n-1)} = i_1, \ldots, X_{i-1}^{(n-1)} = i_{i-1}, X_{i+1}^{(n-1)} \\ &= i_{i+1}, \ldots, X_k^{(n-1)} = i_k) \end{aligned} \tag{2}$$

Formula (2) constitutes the state transition matrix $\boldsymbol{P_{ri}}$ of X_i, whose dimension is $N^k \times N$. Taking $k = 2$, $N = 3$ as an example, the matrix $\boldsymbol{P_{r1}}$ corresponding to X_1 can be expressed as:

$$\mathbf{P}_{r1} = \begin{array}{cc} x_1^{(n-1)} & x_2^{(n-1)} \\ 1 & 1 \\ 1 & 2 \\ 1 & 3 \\ 2 & 1 \\ 2 & 2 \\ 2 & 3 \\ 3 & 1 \\ 3 & 2 \\ 3 & 3 \end{array} \begin{array}{c} x_1^{(n)} \\ \begin{array}{ccc} 1 & 2 & 3 \end{array} \\ \begin{bmatrix} p_{111} & p_{112} & p_{113} \\ p_{121} & p_{122} & p_{123} \\ p_{131} & p_{132} & p_{133} \\ p_{211} & p_{212} & p_{213} \\ p_{221} & p_{222} & p_{223} \\ p_{231} & p_{232} & p_{233} \\ p_{311} & p_{312} & p_{313} \\ p_{321} & p_{322} & p_{323} \\ p_{331} & p_{332} & p_{333} \end{bmatrix} \end{array} \tag{3}$$

Cumulative Probability Transfer Matrix. On the basis of the state transition matrix, the generating method of the cumulative probability transition matrix $\boldsymbol{P_{cum}}$ is shown in formula (4):

$$p_{cum,mn} = \begin{cases} 0 & n = 1 \\ \sum_{j<n} p_{mj} & 1 < n \leq N+1 \end{cases} \tag{4}$$

If the dimension of $\boldsymbol{P_r}$ is $N \times N$, then the dimension of $\boldsymbol{P_{cum}}$ is $N \times (N + 1)$.

MCMC Method Modeling Steps. Using MCMC method to generate multi-access decentralized wind power time series includes the following steps:

(1) Define the state of random variables and convert the original wind power data into discrete state points.
(2) Generate a state transition matrix $\boldsymbol{P_r}$ based on original wind power data.
(3) Generate cumulative probability transfer matrix $\boldsymbol{P_{cum}}$.
(4) Generate a random number u with uniform distribution [0,1] and the current wind power is in state m. Compare u with the m-line element of $\boldsymbol{P_{cum}}$. If the relationship $p_{cum,mn} < u < p_{cum,m(n+1)}$ is satisfied, then the next state is taken as n.
(5) If the generated time series of wind power has met the length requirement, it stops. Otherwise, the current state becomes n and return to step (4) to continue.
(6) Convert the series of discrete state numbers generated above to wind power using a method of superimposing noise on discrete state points.

Cross-correlation analysis. In order to analyze the temporal-spatial coupling correlation of wind power time series more intuitively, the cross-correlation function of multi-dimensional series is used for analysis. The cross-correlation function of time series is:

$$R_{xy}(k) = \frac{E((x(t) - \bar{x}(t))(y(t+k) - \bar{y}(t)))}{\sigma_{x(t)}\sigma_{y(t)}} \tag{5}$$

where $x(t)$ and $y(t)$ are two sets of time series; $\bar{x}(t)$ and $\bar{y}(t)$ are the average values of $x(t)$ and $y(t)$, respectively; $\sigma_{x(t)}$ and $\sigma_{y(t)}$ are the variances of $x(t)$ and $y(t)$, respectively; E is the expectation of the sequence; k is the number of time delays.

3 Time Series Model of Typical Daily Output

3.1 Clustering Process of Hierarchical Clustering Algorithm

In this section, a hierarchical clustering algorithm is used to select typical daily output scenarios for decentralized wind power generation.

Taking the number of objects to be clustered as 5 and the ordinal numbers of data objects as a, b, c, d and e respectively as examples.

The distance relationship between five data objects can be expressed by the distance matrix $D_{n\times n} = [d(i,j)]$. $L(k)$ denotes the hierarchy of category k, and the category composed of object m is denoted as (m). The distance between category (r) and category (s) is denoted as $d[(r), (s)]$.

Assuming that after the first and second clustering operations, the clustering results are category (a, b), category (c, d) and category (e). For convenience of remembering, they are named category (x), category (y) and category (z). The distance matrix formed in the third clustering operation is a third order matrix [14]:

$$D_{3\times 3} = \begin{bmatrix} 0 & d[(x),(y)] & d[(x),(z)] \\ d[(x),(y)] & 0 & d[(y),(z)] \\ d[(x),(z)] & d[(y),(z)] & 0 \end{bmatrix} \tag{6}$$

Since category (x) = category (a, b), category (y) = category (c, d), according to the definition of selecting the shortest distance between categories as the distance between categories in the Single-Linkage method, there are the following relations:

$$d[(x),(y)] = \min\{d[(a,b),(c,d)]\} = \min\{d(a,c), d(a,d), d(b,c), d(b,d)\} \tag{7}$$

$$d[(x),(z)] = \min\{d[(a,b),(e)]\} = \min\{d(a,e), d(b,e)\} \tag{8}$$

Then in the third clustering operation, find out $\min\{d(x,y),d(x,z),d(y,z)\}$ according to the third-order distance matrix $D_{3\times 3}$ and divide the two categories of the shortest distance into the same category.

Each iteration of clustering operation cycle can divide two categories into the same category. By analogy, all data objects can be divided into one big class by constantly finding the shortest distance between the initial M categories.

3.2 Method of Generating Typical Daily Output

The data of L distributed wind power output collected for n consecutive days and m equal intervals every day can be expressed as:

$$X_W = [x_{a,b}] = \begin{bmatrix} x_{1,1} & x_{1,2} & \cdots & x_{1,mL} \\ x_{2,1} & x_{2,2} & \cdots & x_{2,mL} \\ \vdots & \vdots & \vdots & \vdots \\ x_{n,1} & x_{n,2} & \cdots & x_{n,mL} \end{bmatrix} \tag{9}$$

Wherein, the sampling days $a = 1, 2,\ldots, n$ and sampling time $b = 1, 2,\ldots, m$. The wind power data of L decentralized wind power on day i are as follows:

$$\begin{bmatrix} x_{i,1} & x_{i,2} & \cdots & x_{i,m} \end{bmatrix}, \cdots, \begin{bmatrix} x_{i,m(L-1)+1} & x_{i,2} & \cdots & x_{i,mL} \end{bmatrix} \tag{10}$$

Based on hierarchical clustering algorithm, the typical daily output generation steps of decentralized wind power with multi-access are as follows:

(1) n data objects of decentralized wind power output data are divided into n categories, that is, each category consists of one object.
(2) Calculate the initial distance matrix $D_{n\times n}$ and draw an initial tree diagram. Set the sequence number $m = 0$, $L(m) = 0$.
(3) Find the minimum distance $d[(r), (s)] = \min\{d[(i), (j)]\}$ in distance matrix D. Merge the two categories (r) and (s) that obtain the minimum distance into a new category (r, s). Let $m = m_1$, $L(m) = d[(r), (s)]$ and update the tree diagram.
(4) Update distance matrix D. Delete corresponding rows and columns representing the category (r) and category (s) in the distance matrix, and adding rows and columns corresponding to the new category (r, s) in the matrix D. The distance between the new category (r, s) and the old category (k) is defined as $d[(k), (r,s)] = \min\{d[(k), (r)],d[(k), (s)]\}$.
(5) Repeat steps (3) and (4) until all objects are finally merged into a large category.
(6) According to the final tree diagram, continuously adjust the Height value from large to small and intercept the tree diagram. The number of clusters and the corresponding clustering results are selected according to the actual engineering needs and objective conditions.
(7) The data of all objects in each category at each time are averaged separately, and all the averages obtained are linked into a line and recorded as the clustering center of the current category.
(8) The cluster center corresponding to the clusters with the largest number of data objects in the clustering results is selected as the typical daily output of decentralized wind power with multi-point access.

4 Evaluation of the Model

In order to evaluate the validity of the modeling method in this paper, the following error evaluation indexes are given:

$$e = \frac{|S_p - \bar{S}_p|}{S_p} \times 100\% \tag{11}$$

where S_p is the statistical parameter of historical sequence and $\bar{S}_p$ is the statistical parameter of simulation sequence.

5 Case Studies

5.1 MCMC Algorithm Simulation

In order to verify the effectiveness of the multivariable MCMC method, the wind power time series of four decentralized wind farms in Shantou in 2014 is taken as an example. The simulation length is set to one year and the number of discrete states is 50. After verifying that the number of convergences required to calculate the limit transition matrix is 500, the number of iterations required is 35,540. The statistical parameters such as the mean, standard deviation, probability density function (PDF) and autocorrelation coefficient (ACF) of the simulated wind power power time series and the original wind power data are compared. Figure 1 is the

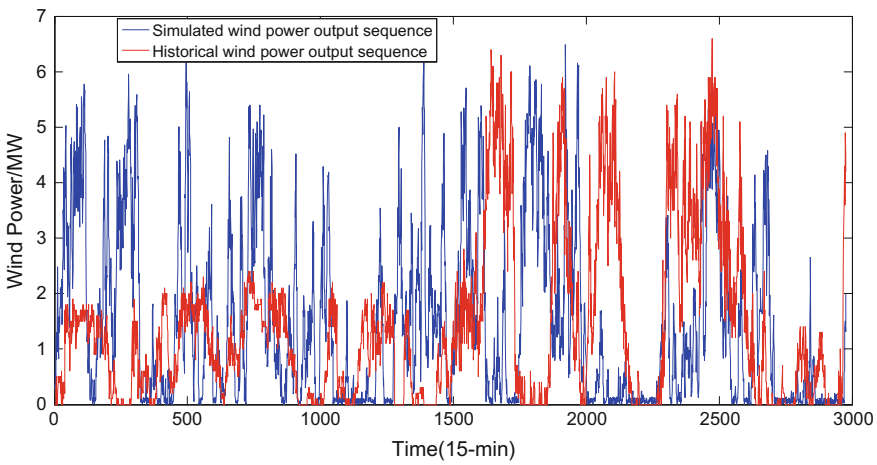

Fig. 1 Comparison of historical sequence and simulation sequence of Southern wind energy wind farm in December

Table 1 Comparison of general statistical parameters

		Southern wind energy	Dan Nan wind power	Fuao wind power	Niutouling wind energy
Mean value	Historical sequence	0.5897	5.2446	0.5497	3.0542
	Simulation sequence	0.6188	5.2197	0.5172	3.3038
		0.5879	5.3271	0.5891	3.0347
		0.5886	5.0564	0.5449	2.7526
Standard deviation	Historical sequence	0.8532	5.7882	0.8189	3.1148
	Simulation sequence	0.8458	5.7399	0.7824	3.1757
		0.8028	5.8175	0.8190	3.0995
		0.8678	5.5646	0.8070	3.0315

comparison of historical sequence and simulation sequence of Southern Wind Energy wind farm in December. Table 1 compares the general statistical parameters of the historical sequence and simulation sequence of four decentralized wind farms.

As can be seen from Table 1, the mean and standard deviation of each simulation sequence are not identical, but they are all around the corresponding statistical parameters of the historical sequence. The maximum error of the mean values of the four wind farm simulation sequences is 9.87%, and the maximum error of standard deviation of four wind farm simulation sequences is 5.91%.

Figure 2 is the probability density comparison of historical sequence and simulation sequence of Southern Wind Energy wind farm. Here the statistical probability density is approximated by the frequency distribution.

As can be seen from Fig. 2, when the number of states is 50, the probability density of the simulated wind power time series is very close to that of the historical

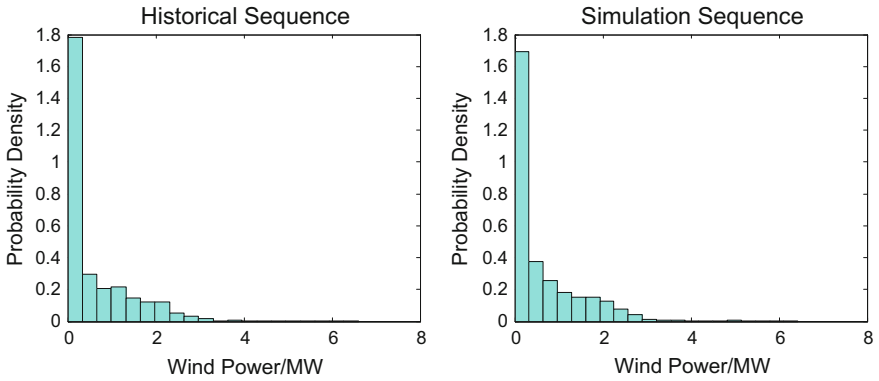

Fig. 2 Probability density comparison of historical sequence and simulation sequence of Southern wind energy wind farm

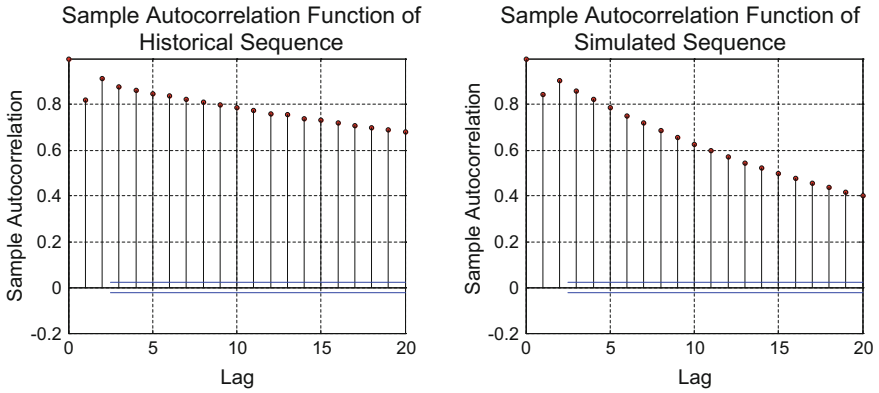

Fig. 3 Autocorrelation coefficient comparison of historical sequence and simulation sequence of Southern wind energy wind farm

wind power time series, which shows the validity of the multi-variable MCMC method in fitting the probability density of the multi-point access decentralized wind farms.

Figure 3 is the autocorrelation coefficient comparison of historical sequence and simulation sequence of Southern Wind Energy wind farm. ACF describes the degree of correlation between the values of power generated by a single intermittent power source at different times, that is, the time-varying characteristics of the variable itself. As can be seen from Fig. 3, when the number of states is 50, the autocorrelation coefficient of the simulated wind power time series is very close to that of the historical wind power time series.

In summary, using the multivariate MCMC method proposed in this paper to simulate the time series of multi-point access decentralized wind farm power can maintain the statistical characteristics of historical sequences. At the same time, this method has the randomness of Markov process and is suitable for the simulation analysis and calculation of power system.

5.2 Selection of Typical Daily Output

According to the wind power output data of four decentralized wind farms in Shantou in winter, the tree diagram of the clustering results is shown in Fig. 4.

Adjust the Height value from large to small and intercept the tree diagram. It can be seen that when the Height value is 60, the number of categories is 4. At this point, the large category is divided into two larger subcategories and two separate categories. And the height value of the four subcategories is about 60–65. The large value of Height indicates that the relationship between the four sub-categories is alienated, so the classification result is considered to be unsatisfactory.

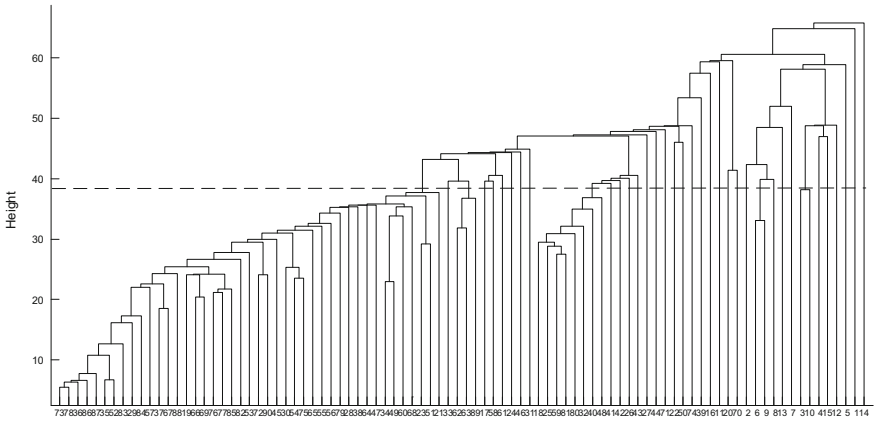

Fig. 4 The clustering results of four decentralized wind farms in Shantou in winter

When the Height value is reduced to 39, the classification number of the results intercepted on the tree is 37. The Height value is low and the relationship between branches in the tree is distant, so it is considered that there are obvious differences among different categories. At this time, the clustering results are reasonable.

The cluster with the largest number of data objects contains the ordinal number: 19, 23, 28, 29, 30, 34, 35, 36, 37, 38, 45, 47, 49, 51, 52, 53, 54, 55, 56, 57, 60, 64, 65, 66, 67, 68, 69, 72, 73, 75, 76, 77, 78, 79, 82, 83, 84, 85, 86, 87, 88, 90.

The data of all objects in this category are averaged at each time, and all the averages obtained are linked into a line and recorded as the cluster center of this category. The cluster center is the typical daily output of four decentralized wind farms in Shantou. The typical daily output is shown in Fig. 5.

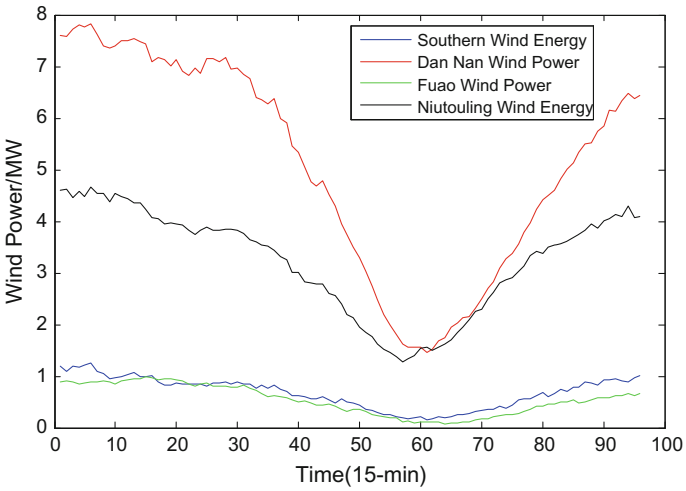

Fig. 5 The typical daily output of four decentralized wind farms in Shantou

6 Conclusion

In this paper, the medium and long-term output analysis model and typical daily output analysis model of multi-access decentralized wind power are established respectively. Firstly, a medium and long term output analysis model of multi-access decentralized wind power based on Markov-Monte Carlo method is proposed. The model takes into account the correlation of output among several decentralized wind farms, and establishes the state transition matrix of multi-point access decentralized wind power output. The results show that the statistical parameters of the simulated sequence are very close to those of the historical sequence, which proves that the model presented in this paper is very effective. This paper also proposes a method of selecting typical daily output of decentralized wind power based on hierarchical clustering algorithm, and simulates the typical daily output of four decentralized wind farms in Shantou in winter according to the model. In the future work, the combination of wind power generation time series model and optimization dispatch can be considered.

Acknowledgements Work in this paper is supported by "Science and Technology Project of China Southern Power Grid (ZBKJXM20180015)".

References

1. Dobakhshari AS, Fotuhi-Firuzabad M (2009) A reliability model of large wind farms for power system adequacy studies. IEEE Trans Energy Convers 24(3):792–801
2. Wang M, Zong X, Yuan Y (2013) Reliability analysis of power generation system containing photovoltaic power station. Proc CSEE 33(34):42–49
3. Fang X, Guo Q, Zhang D (2012) Confidence capacity assessment of photovoltaic power station considering weather uncertainty. Autom Electr Power Syst 36(10):27–32
4. Zhang N, Zhou T, Duan C (2010) Impact of large-scale wind farm access on peak shaving of power system. Power Syst Technol 34(1):152–158
5. Zou B, Li D (2012) Stochastic production simulation of power system containing wind farm based on effective capacity distribution. Proc CSEE 32(7):23–31
6. Zhang N, Kang C, Chen Z (2011) Wind power trusted capacity calculation method based on sequence operation. Proc CSEE 31(25):1–9
7. Fan R, Chen J, Duan X (2011) Analysis of the influence of wind speed correlation on probabilistic power flow calculation. Autom Electr Power Syst 35(4):18–22
8. Luo G, Shi D, Chen J (2014) MCMC method for wind power generation power time series simulation. Power Syst Technol 38(02):321–327
9. Li P, Guan X, Wu J (2015) Analysis of overall output characteristics of wind farms based on weather classification. Power Syst Technol 39(7):1866–1872
10. Li C, Liu C, Huang Y (2015) Research on time series modeling method of wind power output based on wave characteristics. Power Syst Technol 39(1):208–214
11. Xue Y, Chen N, Wang S (2017) Review on wind speed prediction based on spatial correlation. Autom Electr Power Syst 41(10):161–169
12. Zou J, Zhu J, Lai X (2019) Simulation of wind power output series based on space-time auto-regressive moving average mode. Autom Electr Power Syst 43(3):101–108

13. Xie M, Xiong J, Ji X (2017) Two-stage compensation algorithm for dynamic economic dispatch of power grid considering correlation of multiple wind farms. Autom Electr Power Syst 41(7):44–53
14. Lin L, Fei H, Liu R (2018) Typical scene selection method for regional wind power output based on hierarchical clustering algorithm. Power Syst Protect Control 46(07):1–6

New Technologies for Substation Automation

Fault Diagnosis Method of Intelligent Substation Based on Improved Association Rule Mining Algorithms

Li Chen, Liangyi Wang, Qian He and Hui Liu

Abstract With the digitalization and intellectualization of substations, the amount of state data collected by intelligent components is becoming larger and larger. Traditional data mining technology cannot meet the requirements of real-time data processing and application speed. For a typical smart substation, a fault diagnosis method based on improved association rule mining algorithm is proposed for transformer near-zone fault analysis. Firstly, an improved association rule data mining algorithm based on rough set is designed to extract information from massive data and diagnose faults. Then genetic algorithm is applied to improve association rule data mining algorithm to speed up data processing. Finally, simulation analysis is carried out to demonstrate the effectiveness and rapidity of the proposed method. The results show that the intelligent substation fault diagnosis method based on improved association rule mining algorithm has fast and powerful reduction ability in data processing. It can extract useful data from intelligent substation components to accurately judge fault information, reduce data scale and improve fault processing speed.

Keywords Intelligent substation · Improved association rules · Rough set · Genetic algorithms · Intelligent electronic device

1 Introduction

For a typical large-scale power system, with the wide application of data acquisition and monitoring system, geographic information system, management information system and real-time information system of power grid operation, all kinds of real-time data are explosively growing. Traditional statistical methods have gradually been difficult to meet the processing requirements, which is the premise of ensuring the reliability, economy and security of the system operation. Next, we

L. Chen (✉) · L. Wang · Q. He · H. Liu
State Grid Chongqing Electric Power Company, Chongqing 400015, China
e-mail: uts_ipr@126.com

Y. Xue et al. (eds.), *Proceedings of PURPLE MOUNTAIN FORUM 2019-International Forum on Smart Grid Protection and Control*, Lecture Notes in Electrical Engineering 585, https://doi.org/10.1007/978-981-13-9783-7_32

need to find new methods to dig deeper rules in order to provide faster and more effective decision support [1]. The emergence and development of data mining technology has attracted extensive attention of power workers.

Nowadays, the technology of data mining has been successfully applied in many fields of power system, showing broad application prospects [2]. Intelligent Electronic Device (IED) of intelligent substation stores two kinds of information: real-time operation data; state and control data. The continuous information is transmitted from the process layer of the intelligent substation to the condition monitoring system of the station control layer. With the accumulation of a large number of data in transformer operation and maintenance, problems such as excessive information, difficult to digest, difficult to unify the form of information, too large information noise and difficult to identify have arisen [3].

With the development of computer technology, there are many ways to study how to deal with the state data of intelligent substation quickly. For example, expert system, fuzzy theory, neural network, etc. [4] However, there are some problems in expert system, such as monotony of reasoning, fragility of knowledge and bottleneck of knowledge acquisition, shortcomings in fuzzy theory that need to rely on experience or expert theory to determine the fuzzy membership function and obtain fuzzy rules [5], and problems in neural network, such as easy to fall into local extremum, slow convergence speed, poor judgment ability to singular samples, etc.

Based on the improved association rule data analysis method of rough set, this paper designs an IED data information reduction algorithm for intelligent substation. The whole algorithm makes full use of genetic algorithm to search adaptively in complex and huge search space and find the optimal or quasi-optimal solution. The powerful reduction ability of rough set makes the whole reduction result more accurate and diagnosis faster.

2 Improved Association Rule Data Mining Algorithms Based on Rough Sets

Rough set can pre-process data in data mining, and the improved association rule data mining algorithm based on rough set proposed in this paper can process data more efficiently, so that to discover the relationship between data and carry out fault diagnosis.

As shown in Fig. 1, the algorithm of association rule mining based on Rough Set includes 4 steps, which start with data initial and end up with rule extraction. In step 2, the data preprocessing includes 4 tasks, which are data cleaning, data integration, data conversion and data subtraction. Data cleaning will eliminate bad data, but the system will record the number of bad data for system evaluation.

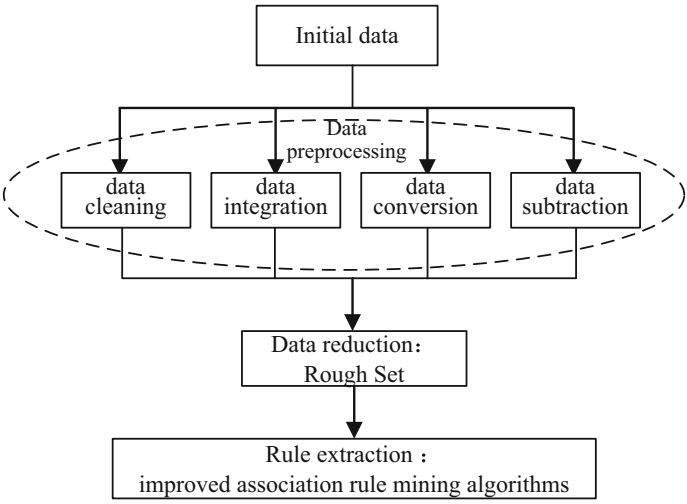

Fig. 1 The algorithm of association rule mining based on rough set

2.1 Rough Set Technology

Rough set is a data mining method. A significant advantage of rough set is that it can perform both information reduction and rule generation. It can not only reduce redundancy and provide decision support for irrelevant data, but also analyze data in substation historical database [6].

When various IEDs are used in smart substations, the amount of information collected from the power system is huge. Rough set theory can find the smallest valuable information theory from massive data. With this representation system, we call these attribute sets "simplicity". The common point of all reductions is that they have "core" attributes. The process of discovering the most important data from IED data is the process of discovering its simplicity and core attributes from information/decision system.

(1) Basic concepts: A knowledge system is expressed by $S = (U, A, V, f)$. U, which called universe, is a non-empty finite set of objects; $A = C \cup D$, $C \cap D = \emptyset$, C is a conditional attribute set, D is a decision attribute set; $V = \underset{a \in A}{Y} V_a$, V_a is the value range; f represents an information function.

(2) Support degree of conditional attributes to decision attributes [7]: If $U/C = \{X_1, X_2, \ldots, X_n\}$, $U/D = \{Y_1, Y_2, \ldots, Y_m\}$, then the support of desicion attribute D to conditional attribute C as follows:

$$K_C(D) = \frac{1}{|U|}\sum_{i=1}^{m}|\underline{C}Y_i| = \frac{1}{|U|}\sum_{i=1}^{m}|pos_c(Y_i)|, Y_i \in U/D \quad (1)$$

where $pos_c(Y_i)$ is the lower approximation set of C for Y_i; $|\cdot|$ is the number of elements contained in the set; $K_C(D)$ represents the support degree of conditional attribute C for overall decision U/D, usually $0 \leq K_C(D) \leq 1$.

2.2 Association Rules

$I = \{I_1, I_2, I_3, \ldots, I_n\}$ is called the set of items, abbreviated as the itemset, and $n = k$ is the set of K items, such as $\{I_1, I_2, I_3, \ldots, I_k\}$. Transaction database $T = \{t_1, t_2, t_3, \ldots, t_n\}$, where each t_i in the transaction database contains one or more items in item set I.

(1) Support degree: There exists a support degree for itemset X, which is expressed by $\sup(X)$ and its formula is:

$$\sup(X) = \frac{Count(X)}{\|T\|} * 100\% \quad (2)$$

where, $Count(X)$ is the number of transactions in the X itemset; $\|T\|$ represents the total transactions number in the transaction database.

(2) Confidence level: If events X and Y occur simultaneously as C, the confidence of association rule $X \rightarrow Y$ is the value of support for event C divided by the value of support for event X and expressed in *conf* [8]. Then:

$$conf(X \rightarrow Y) = \frac{\sup(C)}{\sup(X)} = \frac{\sup(X \cup Y)}{\sup(X)} \quad (3)$$

Strong association rules: If support threshold min supp and confidence threshold min *conf* are set in advance, then in transaction database T, if $\sup(X \rightarrow Y) \geq \min \text{supp}$ and $conf(X \rightarrow Y) \geq \min conf$, $X \rightarrow Y$ is a strong association rule.

2.3 An Improved Association Rule Mining Algorithm Based on Rough Set

Data reduction rules use fuzzy sets for data processing. For an information system, there are at most $C_n^{n/2}$ reductions in attribute reduction.

Suppose $R = \{a, b, c, d\}$, $C = \{a, b\}$ and $D = \{c, d\}$, that is, the information system is composed of four attributes a, b, C and D. Using this property, in the first step of mining association rules, we only need to scan the transaction database once and calculate the frequent 1-itemsets first.

3 Application of Genetic Algorithms in Improving Association Rule Based Data Mining

The proposed data mining algorithm includes two steps. Firstly, the frequent sets should be obtained according to transaction records of the database, in which the support threshold should be satisfied. The second step is to construct association rules according to frequent sets, which need to satisfy the confidence threshold. The core of the algorithm is the first step, which requires global optimization to find the item set that meets the minimum support, while genetic algorithm has strong global optimization ability.

3.1 Implementation of Genetic Algorithms

Coding method: In order to solve the problem of reduction, the first step is to solve the problem of data encoding. Because of the practical characteristics of knowledge reduction, we adopt binary one-dimensional coding based on {0,1} symbol set. Using the following encoding method [9]: Let the set of conditional attributes be $C = \{c_1, c_2, \ldots, c_n\}$, conditional attribute set Ω_C can be easily mapped to chromosomes of Genetic Algorithm. Chromosomes are binary bit sets of length n, and each element corresponds to a conditional attribute [10].

Fitness function selection: Fitness function is the only deterministic index to evaluate the adaptability of individual elements, so the selection of fitness function directly determines the evolutionary direction of population. According to the requirements of practical problems, an improved fitness function is proposed to optimize the algorithm [11].

$$fitness(R) = \left(\frac{Count(R)}{m} * \frac{1}{\min \text{supp}}\right) * P(R) - 1 \tag{4}$$

where, m is the size of the population; $Count(R)$ represents the total number occurrences of the rule in the population; the value of $\frac{Count(R)}{m} * \frac{1}{\min \text{supp}}$ is greater than or equal to 1, which means that the rule can be retained to the next generation, otherwise it should be eliminated; $P(R) = \frac{\beta}{1 + e^{\alpha(k_0 - k(R))}} (\alpha \geq 0)$ is the penalty function,

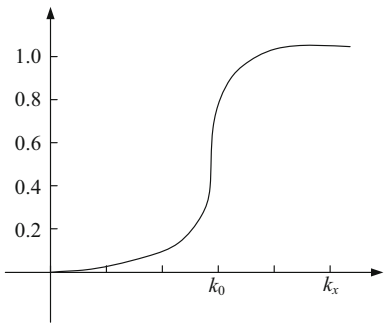

Fig. 2 The curve of penalty function

α is the penalty factor, where $k(R)$ is the support degree of the conditional attribute C contained in R to the decision attribute D. The penalty function image is shown in Fig. 2.

Operational process of Genetic Algorithm: To change the default, adjust the template as follows.

- Choice: The selection operation is to replicate individuals with high fitness to the next generation, thus ensuring that individuals are gradually optimized. Individuals with fitness greater than or equal to 0 can enter the next generation, while those with fitness less than 0 will be eliminated. In order to keep the individual m unchanged, some individuals with fitness values should be copied to the next generation [12, 13].
- Crossover operation: In order to ensure that the corresponding loci of the attributes in the nucleus do not change, we adopt the uniform crossover operation, that is, each bit in the chromosome bit string crosses randomly and evenly according to the same probability. Assuming new individuals $s_1 = a'_{11}, a'_{12}, \ldots, a'_{1n}$ and $s_2 = a'_{21}, a'_{22}, \ldots, a'_{2n}$ generated by uniform crossover operators, the operation is described as follows:

$$O(P_c, x) : a'_{1i} = \begin{cases} a_{1i}, x > 1/2 \\ a_{2i}, x \leq 1/2 \end{cases}, a'_{2i} = \begin{cases} a_{2i}, x > 1/2 \\ a_{1i}, x \leq 1/2 \end{cases} \quad (5)$$

  where, x is a random variable with uniform distribution on [0,1], and P_c is a crossover probability.
- Variation: In this paper, the uniform mutation strategy is used, that is, under the control of mutation probability, random selection of a position for mutation operation [14], and the number on the mutation bit is replaced by uniform random number.

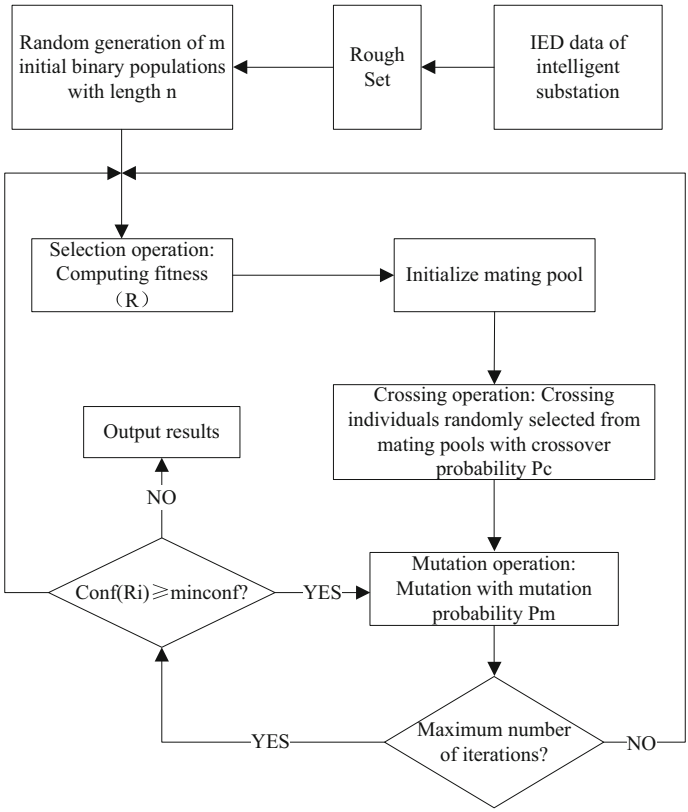

Fig. 3 Algorithm flow chart

3.2 Algorithm Design

This algorithm needs genetic algorithm to mine frequent item sets, and then generates association rules by setting minimum confidence and minimum support, so that to judge the operation status of intelligent substation [15, 16]. The specific steps of the algorithm are shown in Fig. 3.

4 Simulation Analysis

An intelligent substation secondary system state perception method based on innate convolutional neural network is proposed. The experimental results show that it effectively solves the problem of the lack of state detection and evaluation methods of ancillary equipment in intelligent substation. The future direction of the research

is that how to comprehensive consider secondary equipment status evaluation results, the whole life cycle cost and risk of equipment operation, the relationship between the three to develop reasonable maintenance strategy, thus improve the intelligent substation secondary system operation maintenance of safety and economy, is a work of great research significance.

The typical 110 kV intelligent substation is simulated, as shown in Fig. 4. In this intelligent substation, 110/35 kV intelligent substation powered by the same power supply consists of two transformers, each transformer operates at 50–60% power.

When the simulation time t = 1 s, there will be a fault between A and B positions of transformer T2. IED5 and IED7 will act to trip circuit breaker 5 and 7. When transformer T2 exits, the branch power of transformer T1 will be loaded to 100–110%. Because of the quick interruption of the protection action, the simulation ends at t = 3 s.

In this paper, four states of IED are defined, and the meanings of each state are shown in Table 1.

The unprocessed data in IEDs are shown in Table 2. Where, the value of L is lower than that of normal, the value of H is higher than that of normal, the unit of voltage V is kV, and the unit of current I is A.

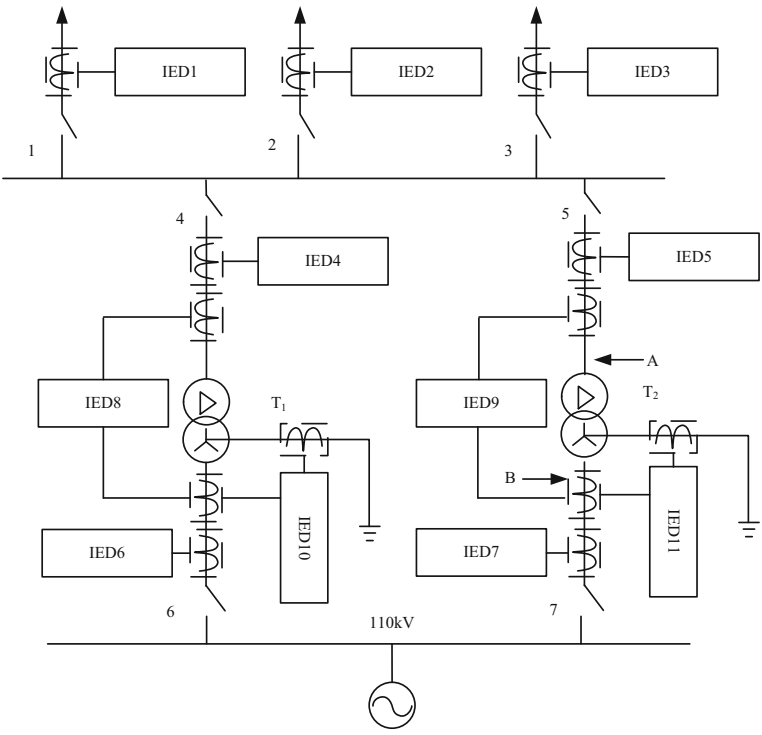

Fig. 4 IED distribution of 110 kV substation protection

Table 1 Status description

Status description	
Status	Description
N	Parameter and load stability
A	One or more of the voltages are raised but the current is normal or one or more of the current increases but the voltage is normal
E	Abnormal current and voltage of two or more items
S	As the circuit breaker moves, the voltage and current are normal

Table 2 List of the IED data which combine the operation data

Time/s	IED5 action		IED7 action		IED5				IED7			
	Relay action	Directional overcurrent protection	Relay action	Quick break protection	I_c	I_a	I_b	I_c	I_a	I_b	I_c	I_a
0.98	1	1	1	1	N	N	N	N	N	N	N	N
1	0	1	0	0	–	–	–	–	–	–	–	–
1.06271	0	0	1	0	L	L	L	–	–	H	H	H
1.14478	0	1	1	1	–	–	–	L	–	–	–	–
1.16655	0	0	0	0	–	H	H	–	L	–	–	–
1.17478	1	1	1	1	–	–	–	–	–	H	H	H

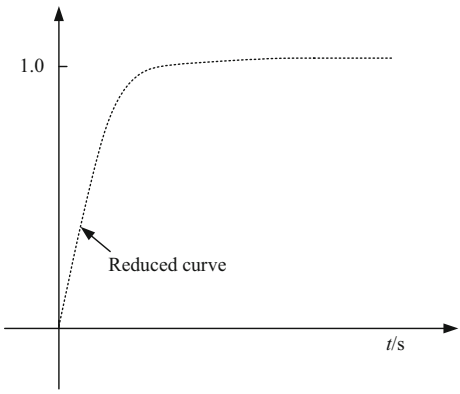

Fig. 5 Genetic algorithm reduction procedure

The algorithm is implemented in Table 2. The parameters in the simulation are: population size m = 11, cross probability Pc = 0.8, penalty factor $\alpha = 15$. The reduction process is shown in Fig. 5. Redundant information is removed in a short time, and the minimum relative reduction is IED5 and IED7.

The simplified results of genetic algorithm are listed in Table 2. In the simulation, IED5 and IED7 are the important objects of fault analysis, as fault areas. Because IED5 has the function of directional relay, it helps to determine the fault

location. What we are most concerned about is the amount of change when the fault occurs, but the unchanged quantity and attributes are not needed. In Table 2, we use "–" instead.

Because IED5 and IED7 are minimal, they contain information about the operation of circuit breakers and relays. The redundancy analysis of operation information and voltage and current in IED5 and IED7 is carried out to remove redundancy information and reduce the amount of information. The simplified results are shown in Table 2. Among them, 0 represents no action and 1 represents action. Table 2 contains the necessary information for fault analysis in simulation. From Table 2, it can be seen that the data size has been significantly reduced.

5 Conclusion

The method proposed in this paper is applied to the reduction of fault diagnosis decision tables in intelligent substations. It can quickly get the best combination of reduction, integrate the reduction results, establish an analysis decision table reflecting the true state of the fault, and apply it to the fault diagnosis. It is helpful for the attendants to analyze the fault situation timely and accurately, judge the fault location, weaken the impact of the fault on the system, and improve the reason of the operators. Barrier handling speed ensures the safe operation of the system. But the proposed method does not analysis the influence of the CT saturation and inrush current, which is what needs to be improved in the later stage of work.

Acknowledgements This work was supported by Science and Technology Project of State Grid Chongqing Electric Power Company in 2018. The project name is "Integrated Operational Support Technology of Intelligent Substations Based on Total Service Data" (No. 2018#35).

References

1. Liu F, Bie Z, Liu S et al (2018) Framework design transaction mechanism and key issues of energy internet market. Autom Electr Power Syst 42(13):108–117
2. Glowacz A, Glowacz W, Glowacz Z et al (2018) Early fault diagnosis of bearing and stator faults of the single-phase induction motor using acoustic signals. Measurement 113(7):1–9
3. Gao C, Cao X, Yan H et al (2017) Energy management of data center and prospect for participation in demand side resource scheduling. Autom Electr Power Syst 41(23):1–7
4. Ming Z, Jiang Z, Feng K (2017) Research on variational mode decomposition in rolling bearings fault diagnosis of the multistage centrifugal pump. Mech Syst Signal Process 93(460):460–493
5. Peng H, Wang J, Ming J et al (2018) Fault diagnosis of power systems using intuitionistic fuzzy spiking neural P systems. IEEE Trans Smart Grid 9(5):4777–4784
6. Shi W, Zhu Y, Tian H et al (2017) An integrated data preprocessing framework based on apache spark for fault diagnosis of power grid equipment. J Sig Process Syst 86(2–3): 221–236

7. Torabi AJ, Meng JE, Xiang L et al (2017) Application of clustering methods for online tool condition monitoring and fault diagnosis in high-speed milling processes. IEEE Syst J 10(2): 721–732
8. Tyagi S, Panigrahi SK (2017) A hybrid genetic algorithm and back-propagation classifier for gearbox fault diagnosis. Appl Artif Intell 4:1–20
9. Huang Z, Wang Z, Zhang H (2018) Multiple open-circuit fault diagnosis based on multistate data processing and subsection fluctuation analysis for photovoltaic inverter. IEEE Trans Instrum Meas 67(3):516–526
10. Liu R, Yang B, Zio E et al (2018) Artificial intelligence for fault diagnosis of rotating machinery: a review. Mech Syst Sig Process 108:33–47
11. Ghoneim SSM (2018) Intelligent prediction of transformer faults and severities based on dissolved gas analysis integrated with thermodynamics theory. IET Sci Meas Technol 12(3): 388–394
12. Jiang S, Wang F, Shen L et al (2018) Local detrended fluctuation analysis for spectral red-edge parameters extraction. Nonlinear Dyn 93(3):995–1008
13. Wu Y, Xiao Y, Hohn F et al (2018) Bad data detection using linear WLS and sampled values in digital substations. IEEE Trans Power Delivery 33(1):150–157
14. Hong J, Liu CC (2019) Intelligent electronic devices with collaborative intrusion detection systems. IEEE Trans Smart Grid 10(1):271–281
15. Chattopadhyay A, Ukil A, Jap D et al (2018) Toward threat of implementation attacks on substation security: Case study on fault detection and isolation. IEEE Trans Industr Inf 14(6): 2442–2451
16. Jiang Z, Li Z, Wu N et al (2018) A Petri net approach to fault diagnosis and restoration for power transmission systems to avoid the output interruption of substations. IEEE Syst J 12(3): 2566–2576

Protection Scheme for Kilometer-Level High Temperature Superconducting Line

Chen Liang, Hong Yu, Tonghua Wu, Yuping Zheng, Yanxin Li and Wei Xie

Abstract This paper introduces the system structure of the kilometer-level superconducting cable demonstration project of Shanghai and presents an overall scheme of relay protection configuration for superconducting lines. The scheme takes differential protection and quench protection as the primary protection for quick isolation of the internal faults, and takes over-current protection as the back-up protection for timely removal of superconducting cables when there are line faults or external faults after the differential protection is out of service, ensuring the safety of the superconducting cable equipment. Also, the feasibility of application of reclosure and inverse time over-current is discussed. Aiming at the wiring method of the kilometer-level superconducting cable demonstration project of Shanghai, this paper introduces the tripping and closing logic and matching mode of breakers on both sides of the superconducting line, so as to realize a consistent supply of electricity when the superconducting cable is in fault. Non-electric quantity information such as temperature, pressure, flow rate, etc. is an important monitoring indicator for the state of the superconducting cable. The application of non-electric quantity status information on both ends of the kilometer-level superconducting cable line in relay protection device is introduced.

Keywords High temperature superconducting · Differential protection · Current compensation · Failure protection · Tripping failure

C. Liang (✉) · H. Yu · T. Wu · Y. Zheng · Y. Li
NARI Group Corporation, Nanjing 211106, China
e-mail: liangchen@sgepri.sgcc.com.cn

T. Wu · Y. Zheng
State Key Laboratory of Smart Grid Protection and Control, Nanjing 211106, China

T. Wu · Y. Zheng
College of Energy and Electrical Engineering Hohai University, Nanjing 210098, China

W. Xie
State Grid Shanghai Municiple Electric Power Company, Shanghai 200122, China

Y. Xue et al. (eds.), *Proceedings of PURPLE MOUNTAIN FORUM 2019-International Forum on Smart Grid Protection and Control*, Lecture Notes in Electrical Engineering 585, https://doi.org/10.1007/978-981-13-9783-7_33

1 Introduction

HTS (High temperature superconducting) cable has the characteristics of high power transmission, low line loss, less environmental pollution, compact structure, etc. Under transmission of the same electric energy, HTS cable can reduce the voltage level by 1–2, which is suitable for use in rapidly developing big cities and high-density urban areas [1]. The world's first set of grid-connected high temperature superconducting cables are 30 m/three-phase/30 kV/1250A high-temperature superconducting cables developed by Southwire Company of U.S.A., which were connected to the grid at the end of 1999 [2]; on July 10, 2004, the first set of high temperature superconducting cable system of China was put into operation in Phuket Substation in Kunming of Yunnan Province. The length of the superconducting cable body is 33.5 m, and the protection is equipped with a three-layer over-current protection scheme based on different current levels [3]. With the development of the manufacturing technology of high temperature superconducting cables in China, now the construction of kilometer-level high temperature superconducting cable demonstration project has been started. In the future, the long distance transmission of electricity may be realized through superconducting cables. Therefore, it is necessary to study the relay protection configuration scheme for long distance superconducting lines.

In electrical characteristics, the superconducting cables differ greatly from the conventional cable lines. The resistance of the superconducting cable is related to the current density. When the current density is less than the critical current density, the resistance of the superconducting cable is almost zero. When the current density is larger than the critical current density, the resistance of the superconducting cable will increase. Meanwhile, the resistance of the superconducting cable is also related to temperature. If the temperature is lower than the critical temperature, it is in the superconducting state; if the temperature is greater than the critical temperature, it is in the quench state. In addition, as the distributed capacitance of the superconducting cable is larger, there are some challenges along the way of application of the existing low-voltage line protection principle in the superconducting line.

For differential protection, as the distributed capacitance of the superconducting cable is larger than that of the conventional cable, it is necessary to consider whether the distributed capacitance of the kilometer-level superconducting cable will affect the differential protection functions.

For distance protection, as the transmission capacity increases, the short-circuit impedance becomes smaller and smaller. In case of short circuits, the short circuit fault current will be generally larger than the critical current transmitted by the superconducting cable, and the resistance of the superconducting cable will increases rapidly with the increase of the fault current. Moreover, the impedance of the kilometer-level superconducting cable is smaller, so the distance protection is no longer applicable.

For conventional cables and superconducting cables, the setting idea of over-current backup protection is not completely consistent. The cooperation between upper and lower levels is considered in over-current protection setting of conventional cables, without failure to operation or incorrect operation. While for superconducting cables, in case of over current, the faults are removed before the temperature reaches the upper temperature limit allowed by the superconducting cable, so as to ensure there will be no irreparable damage to the performance of the superconducting cable. There are some troubles in the setting.

For quench protection, it is mainly to install a sensor on the superconducting cable body to monitor the non-electric quantity information of the conductor such as temperature and pressure, etc. For the kilometer-level superconducting line, only the terminals on both sides are convenient for installation and information collection, which has some limitations on the fast reflection of quench of the superconducting cable on the whole.

In view of the characteristics of the superconducting line, this paper puts forward a practical protection configuration scheme, and combined with the actual situation of the kilometer-level superconducting line of Shanghai, presents a scheme for tripping and closing of the superconducting line.

2 Analysis of Characteristics of the Superconducting Cable

The electrical parameters of HTS cables depend on the materials and geometric sizes used in the superconducting cable. Figure 1 shows the typical structure drawing of the three-phase belted-type superconducting cable, respectively copper support, HTS conductor layer, insulation layer, superconducting shielding layer, copper shielding layer, liquid nitrogen layer and armor layer from inside to outside. Compared with conventional power cables of the same voltage level, the electrical parameters of HTS cables have the following characteristics: the resistance of HTS cables is basically zero when it is in the superconducting state, and the reactance of HTS cables is larger than that of the conventional cables. This is because the inductive impedance approximation is proportional to the logarithm of the distance between three phases. However, the phase-to-phase spacing of high-temperature cables is larger than that of the conventional cables, and the capacitance of HTS cables is larger than that of the conventional cables. This is because the thicknesses of insulation layers of both are basically the same, and the cooling channel in the superconducting cable leads to the increase of the equivalent radius of the conductor wire core, so the capacitance increases.

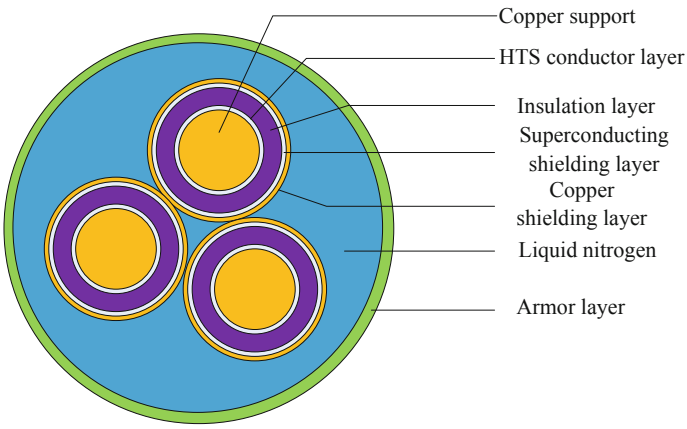

Fig. 1 Typical structure diagram of three-phase superconducting cable

3 Introduction of the Kilometer-Level Superconducting Cable Demonstration Project

3.1 Brief Introduction of the Demonstration Project

The line from Changchun Station to Caoxi Station is selected as the demonstration application scene for the kilometer-level superconducting line in Shanghai. The primary system chart is shown in Fig. 2. Based on the advantages of small size, light weight, low loss and large transmission capacity of the superconducting cable, this paper attempts to substitute the superconducting cable for transmission of power distribution network lines. One circuit of 35 kV superconducting cables is newly built from 220 kV Changchun Station to 220 kV Caoxi Station. 30 chambers are stored in 35 kV bus section IV in Changchun Station for use by Caoxi Station. 30 chambers are reserved in 35 kV bus section V and 37 chambers are reserved in 35 kV bus section VI. The original two circuits of Changchun-Caoxi 833 Line A and Changchun-Caoxi 833 Line B from Changchun Station to Caoxi Station are changed to backup lines. This method is similar to the current grid structure in Shanghai without major changes. Meanwhile, on the premise of ensuring the reliability of power supply, it is convenient for long-term operation, maintenance and dispatching.

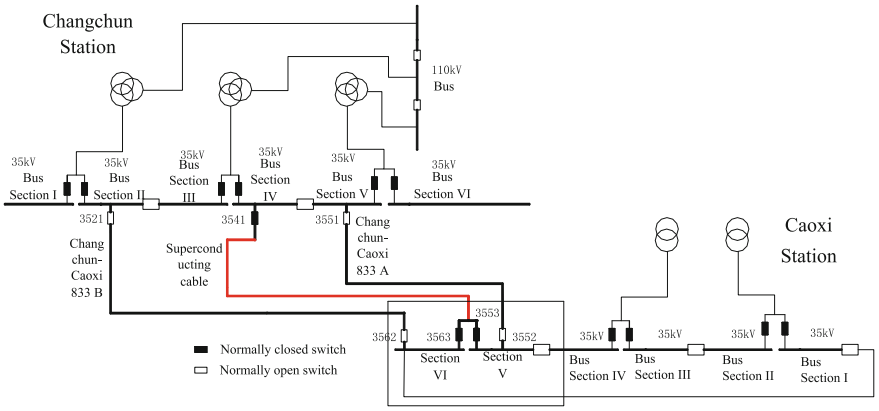

Fig. 2 Wiring diagram of kilometer-level superconducting cable demonstration project

3.2 System Structure of the Superconducting Cable in the Demonstration Project

The kilometer-level superconducting cable system mainly consists of the superconducting cable body, intermediate joint, terminal and cooling system, with the structure shown in Fig. 3.

The superconducting cable adopts the three-phase belted-type cold insulation method. With compact structure, small transmission loss and low stray magnetic field, its superconducting current-carrying layer, high-voltage insulation layer and superconducting shielding layer are all in the liquid nitrogen temperature region. The superconducting wires are wound in layers around the supporting framework. The distribution of conductors and the winding pitch will directly affect the current

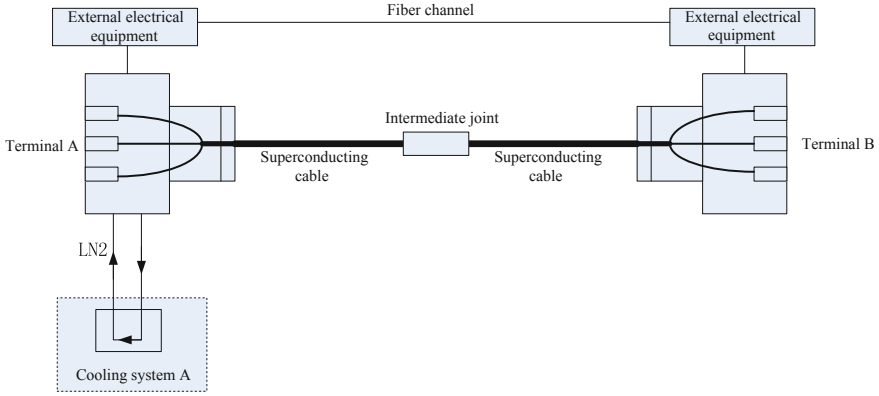

Fig. 3 Diagram of system structure of kilometer-level superconducting cable

division between layers and the size of AC (alternating current) loss; the coaxial double-layer bellows forms a forced flow cooling channel, and the inside of the bellows should keep high vacuum and be embedded with the multiple-layer radiation protection screen, so as to enable the cable core to be thermally insulated from the external environment and ensure a low temperature environment required for cable operation.

As the head end of the cable, the cable terminal is the connection channel between the superconducting cable and the external electrical equipment as well as between the cooling medium and the refrigeration equipment. It is responsible for the transition between temperature and potential. In order to ensure the connection between cable core and conventional conductor at low resistance, maintain good electrical insulation between phases and ground, and bear the temperature gradient of the system and the surrounding environment to achieve vacuum isolation, in addition to the electrical connection and insulation performance, the inhibition of heat leakage should be considered in the design and manufacturing of terminals.

The intermediate joints are used to connect cables of the kilometer-level superconducting line so as to achieve long-distance power transmission. As the connecting channel between the superconducting cable cooling medium and the refrigeration equipment, the joint is also responsible for the transition between temperature and potential. It is required to not only ensure the connection between cable cores at low resistance and maintain good electrical insulation between phases and ground, but also bear the temperature gradient of the system and the surrounding environment so as to achieve vacuum isolation.

The cooling system is consisted of the refrigerator, liquid nitrogen pump, super-cooled box, storage tank, circulation circuit, standby set, etc. The basic cooling principle of the cable is to use the sensible heat of the super-cooled liquid nitrogen to bring the thermal load produced in the operation process to the cooling device, and then send the super-cooled liquid nitrogen to the cooling channel of the cable after being cooled by the refrigerator, forming a closed circuit, so as to keep the superconducting transmission line an appropriate operation temperature, liquid nitrogen coolant pressure and flow rate.

4 Protection Scheme for Kilometer-Level Superconducting Lines

The HTS cable usually has a high power transmission. In the event of power system faults, late removal of the fault will cause serious damage to the superconducting cable body and may endanger the stability of the entire power system. Therefore, the kilometer-level superconducting line is necessary to be equipped with the whole-line quick-action protection of differential protection and quench protection as the main protection. The over-current protection should be equipped as the backup protection.

For the cable transmission line, the fault is usually permanent, and there are backup lines for the superconducting cables in this demonstration project. Section 5 describes the auto-switching logic of backup lines in case that the superconducting line malfunctions. The continuity and reliability of power supply can be ensured, so the reclosure is not necessary. The breaker failure protection can be equipped to ensure the reliable isolation of faults in case that the superconducting cable malfunctions and the breaker fails.

4.1 Differential Protection

The differential protection has natural selectivity towards internal and external faults and can remove the internal faults quickly, the advantage of the differential protection as the main protection of the superconducting cable is obvious. The factors affecting the performance of the differential protection action mainly include the following 5 aspects [4]. The first is the error and unbalanced current of the current transformer; the second is the capacitance current of the transmission line; the third is the saturation of the current transformer; the fourth is the disconnection of the secondary circuit of the current transformer; the fifth is the reliability of the fiber channel. Except for the second one, there is no difference for other factors between the superconducting line and the conventional cable line. And all can be solved by the differential protection through fixed value setting and algorithm. Therefore, it is only necessary to consider whether the kilometer-level superconducting line is affected by the capacitance current.

The neutral ungrounded operation mode is mostly adopted in China's medium-voltage distribution network. With the expansion of the urban power grid and the increase of cable lines, the grounding current of the distribution network increases day by day. The regulations stipulate that when the 10 and 35 kV grid capacitive current is greater than 20 and 10 A respectively, the arcing coil should be installed to compensate the capacitive current [5]. The ability to accurately measure the capacitance current of distribution network determines whether arc suppression coil is needed and the ability to accurately compensate arc suppression coil. It is an important subject to study the measurement method of capacitive current in distribution network for small current grounding system [6–8]. When a superconducting line is used in a low-current grounding system, if the capacitance current is large, it will be compensated by the arc suppression coil. After compensation, the grounding arc should be automatically extinguished. When superconducting cables are used in grounding systems, The method of capacitance current compensation should be studied.

The capacitance current compensation method based on time domain can compensate the capacitance current at various frequencies and has good compensation effect for both steady and transient capacitance current.

For the capacitance current compensation method based on time domain, the relation between capacitance current and voltage is:

$$i_c = C\frac{du}{dt} \tag{1}$$

Figure 4 is a three-phase cable line $\prod$-type equivalent circuit.

The current of phase A on both sides of the cable can be obtained according to Eq. (1):

$$\begin{cases} ic_m^a = \frac{C_{pg}}{2}\cdot\frac{du_m^a}{dt} + \frac{C_{pp}}{2}\cdot\frac{du_m^{ab}}{dt} + \frac{C_{pg}}{2}\cdot\frac{du_m^{ac}}{dt} \\ ic_n^a = \frac{C_{pg}}{2}\cdot\frac{du_n^a}{dt} + \frac{C_{pp}}{2}\cdot\frac{du_n^{ab}}{dt} + \frac{C_{pg}}{2}\cdot\frac{du_n^{ac}}{dt} \end{cases} \tag{2}$$

where, Cpg is the phase to ground capacitance of the superconducting cable, Cpp is the phase to phase capacitance, which is related to the positive sequence and zero sequence capacitance of the line as follows:

$$\begin{cases} C_{pg} = C_0 \\ C_{pp} = \dfrac{C_1 - C_0}{3} \end{cases} \tag{3}$$

The phase voltage is collected by the protection device, the equation can be known by the approximate derivation of discrete sampling points:

$$\frac{du(t)}{dt} = \frac{u(t+\Delta t) - u(t-\Delta t)}{2\Delta t} \tag{4}$$

Using formula (4), $ic_m^a(\mathrm{t})$, $ic_n^a(t)$ can be obtained by formula (2), and then phase A compensation currents of both sides are:

$$\begin{cases} i_m^a(t) = i(t) - ic_m^a(t) \\ i_n^a(t) = i(t) - ic_n^a(t) \end{cases} \tag{5}$$

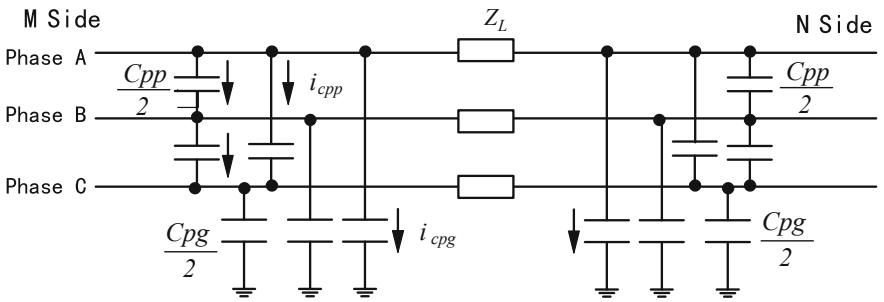

Fig. 4 Superconducting cable line $\prod$-type equivalent circuit

Table 1 Comparison of the parameters between superconducting cable and conventional cable

35 kV	Resistance (Ω/km)	Reactance (Ω/km)	Capacitance (μF/km)
Conventional cable	0.0626	0.14	0.141
Superconducting cable	0.000053	0.033	0.27

Based on the calculation of parameters of the cold insulation three-phase belted-type superconducting cable in this demonstration project, the comparison with the parameters of the conventional cable is shown in the Table 1.

The superconducting cable line model was established to verify the compensation effect of capacitance current only, and the temperature rise caused by the increase of superconducting cable current was not considered in the modeling.

Because of the space limitation, only the switching on simulation results are listed.

In the Fig. 5, the blue waveform is the differential current before compensation and the green one is after compensation. It can be seen from the figure that the capacitance current compensation method based on time domain has a certain compensation effect on the capacitance current of the superconducting cable.

Therefore, if the voltage level of the superconducting cable is high and the cable length is long, the capacitance current should still be considered. The capacitance current compensation mechanism should be adopted for differential protection to improve the sensitivity of differential protection.

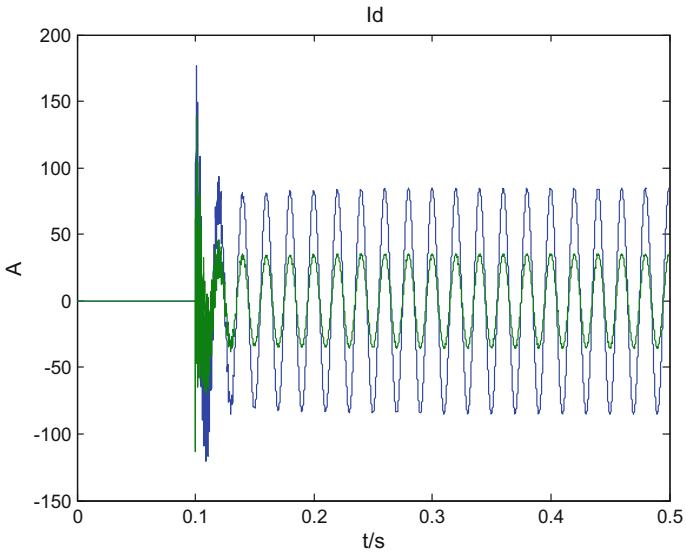

Fig. 5 The waveforms of before and after compensation when switching on

For the demonstration project of km-class superconducting cable, although the capacitance per kilometer of the superconducting cable is higher than that of the conventional cable, due to low voltage level and short line, the calculated capacitance current is still low The primary value of the steady-state capacitive current is about 1.7 A, the CT variable-ratio is 1250/5, and the secondary value is about 0.0068 A. Although the transient capacitive current of the line generated by out-of-area faults and empty charging of the line may reach several times of the steady-state current [9], the value is still very small. The line differential protection used in this demonstration project does not need to consider capacitor current compensation. The differential threshold value is set according to the unbalance current (CT measuring error, capacitance current) of the dodging system, and the sensitivity is ≥ 2.

4.2 Quench Protection

When the superconductor runs into the superconducting state, there are three critical values: critical temperature Tc, critical field Hc and critical current Ic. The research shows that when any of the above three basic parameters of the superconductor exceeds its critical value in the process of operation, the superconductivity of the superconductor will disappear and part of it will enter the "normal state". At present, the quench detection of the superconductor at home and abroad is all based on these three basic parameters. The main factors affecting these three parameters are faults of the cooling system, internal faults of the superconducting cable, short circuit faults, etc. As the temperature, liquid nitrogen pressure and liquid nitrogen flow of the superconducting cable can directly reflect the state of the superconducting cable, the conventional quench protection generally consists of the monitoring and judgment of the above non-electric quantity. An independent fault identification unit is set up to receive the non-electric quantity information collected by the sensor of the superconducting cable in real time, analyze the dynamic characteristics in real time, identify the fault and send the fault signal to the relay system through the preset program. The fault identification unit can be thought of as an independent IED, plugged into a process-layer GOOSE network, and implemented as an information interaction with line protection via GOOSE, or passed directly to the protection via cable wiring. The quench protection system diagram is shown in Fig. 6.

The general quench detection methods include temperature rise detection, pressure measurement, flow rate detection, ultrasonic detection, voltage detection, etc. [10]. Considering the sensor installation technology and the requirements on heat leakage of cable system, the sensor is actually suitable to be installed only at the port of the superconducting line to monitor the temperature, pressure and flow rate, etc. at the port. When the port data such as temperature, pressure, flow rate, etc. is found to be abnormal, the quench alarm will be raised by fault identification unit, if serious, the quench tripping signal may be sent for tripping both this side and the other side by the protective device (Fig. 7).

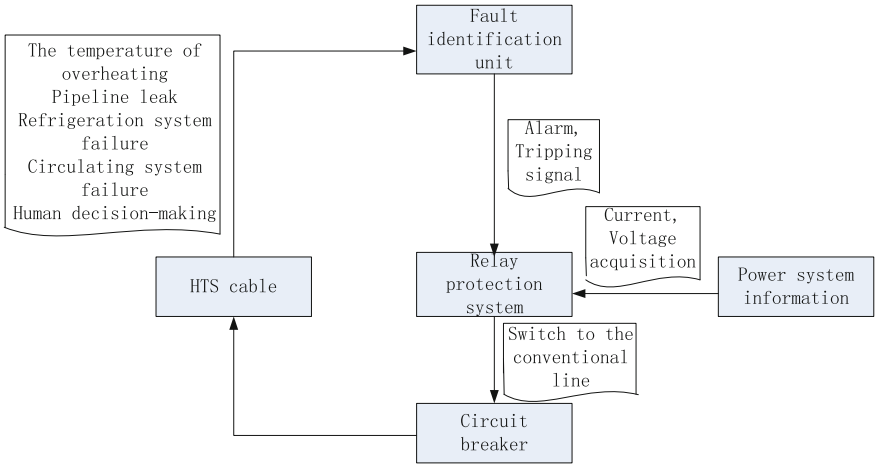

Fig. 6 Quench protection system diagram

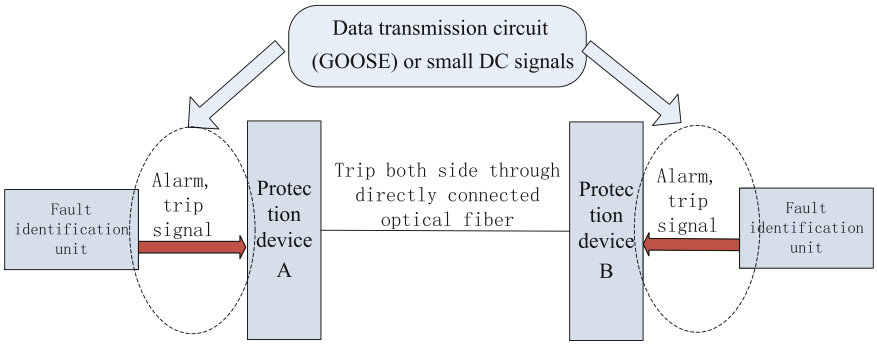

Fig. 7 Diagram of transmission circuit of non-electric quantity signals

5 Discussion on New-Type Protection Function

5.1 Information Collection Method Based on Wireless Communication Technology

Based on the current manufacturing technology of the superconducting cable, the installation environment on the site as well as the installation technology, the long-distance superconducting cable can be constructed in sections (the length of each section should not be too long) by the method of tap connection. This method provides a condition for tapped installation of the sensor. All the sensors on the superconducting cable serve as collection terminals to monitor the temperature, pressure, liquid nitrogen flow rate, etc. of the superconducting cable in real time and

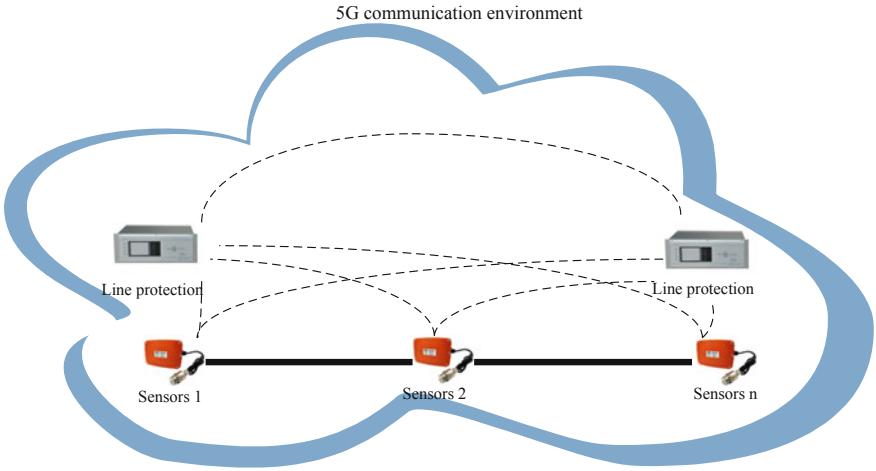

Fig. 8 Diagram of information collection of wireless communication technology

upload the information to the protection device or monitoring system so as to realize the overall information collection of the superconducting cable, condition monitoring and protection of feedback control system. In the traditional method, the sensor needs to send the data to the monitoring device, which uploads the data by means of communication. This kind of method can be easily realized in the substation, but is difficult to be implemented at the tapping point. The development of 5G wireless communication technology provides a technical basis for the construction of ubiquitous Internet of things, enabling the power equipment and information collection platform to be connected to all terminals to collect information in an all-around, multi-dimensional and faster manner [11], and achieving a more perfect protection and control scheme. As the super-high frequency band is applied in 5G technology, the data transmission speed can reach 1 Gbp per second, the transmission distance can also reach 2 km, and the data transmission delay can reach below 1 ms [12]. These key indicators make the application of 5G technology in short line protection possible. As important power equipment for power transmission and distribution network of the power system, the superconducting cable may, based on 5G wireless communication technology, realize the data interaction between the line protection devices on both sides as well as the information interaction between the device and the sensor. Within the kilometer-level scope, it can be exempted from the limitation of tap installation locations. The protection device will build a new-type quench protection based on all data collected from the sensors of the whole line (Fig. 8).

6 Tripping and Closing Logic of the Superconducting Cable

There are two backup lines (old lines) for the superconducting cables in this demonstration project. The backup lines are put into service before the superconducting cable is out of service due to internal fault, cooling system fault, cable body fault, etc. to ensure uninterrupted power supply. This section discusses the auto-switching function of incoming line and the tripping logic in case of breaker failure.

6.1 Configuration of Protection Device

As shown in Fig. 2, the 35 kV bus section IV of Changchun Station passes through the superconducting cable zone to be connected with two buses of Caoxi Station, respectively 35 kV bus section V and VI. As the power restoration time for faults of the superconducting cable is longer than that of the conventional cable, Changchun-Caoxi Line A and Changchun-Caoxi Line B are set for the purpose of ensuring the reliability of power supply. In the event of a failure of the superconducting cable, the power can be supplied from these two conventional cable lines to ensure the continuity of power supply. Changchun-Caoxi Line A, Changchun-Caoxi Line B and the superconducting cable are respectively equipped with a set of optical fiber longitudinal differential protection, with the configuration shown in Fig. 9. The line protection of the three lines forms an overall protection through the GOOSE networks and direct-connected channels on both stations. Logically, the cooperation between each other can be easily realized.

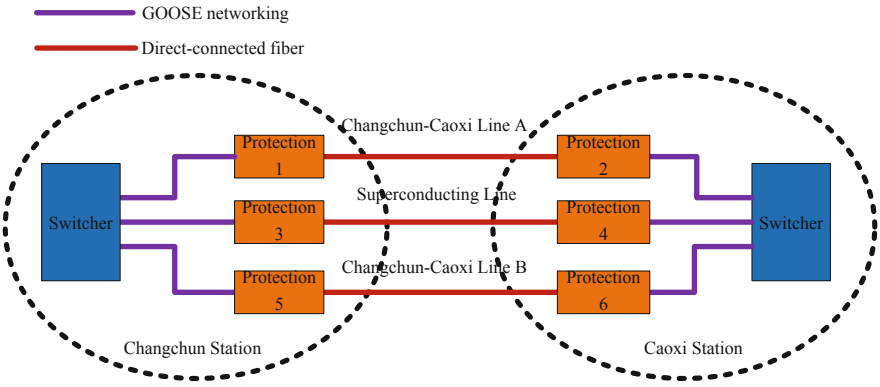

Fig. 9 Diagram of protection configuration for superconducting and backup lines

6.2 *Tripping and Closing and Failure Logics of the Superconducting Cable*

Under normal conditions, the bus section V and bus section VI of Caoxi Station are powered by the superconducting line, Switch 3551 and Switch 3521 are in the closed position, and Changchun-Caoxi 833 Line A and Changchun-Caoxi 833 Line B are in the hot-standby state. In general, there are two types of faults in the superconductor: one is internal fault, which is removed by differential protection action trip; the other is quench of superconductor, which is removed by quench protection trip. The tripping logic of the line protection for the superconducting cable is: switches 3562 and 3552 are closed and switches 3541, 3553 and 3563 are tripped; the specific process is that after fault trip inside the superconducting line area or receipt of the quench signal, the protection 4 sends the GOOSE closing signal, and protection 2 and 6 subscribe to the GOOSE closing signal of protection 4; the switches are closed respectively after each has judged that there is voltage on the line, thus the input of the backup line of the superconducting cable can be completed. Protection 4 subscribes to the position signals of protection 2 and protection 6. After the two lines are confirmed to have been put in, tripping of the breakers and remote tripping of protection 3 are started to complete the tripping logic. The tripping logic of the superconducting line is shown in Fig. 10. If protection 2 or protection 6 judges that there is voltage on the line, but it is not satisfied, or protection 4 fails to receive the closing position signals from the two lines after the closing commander has been sent, it means that the closing is not successful and the closing failure should be reported after short-time delay. The failure of the closing will not affect the tripping logics of protection 3 and protection 4.

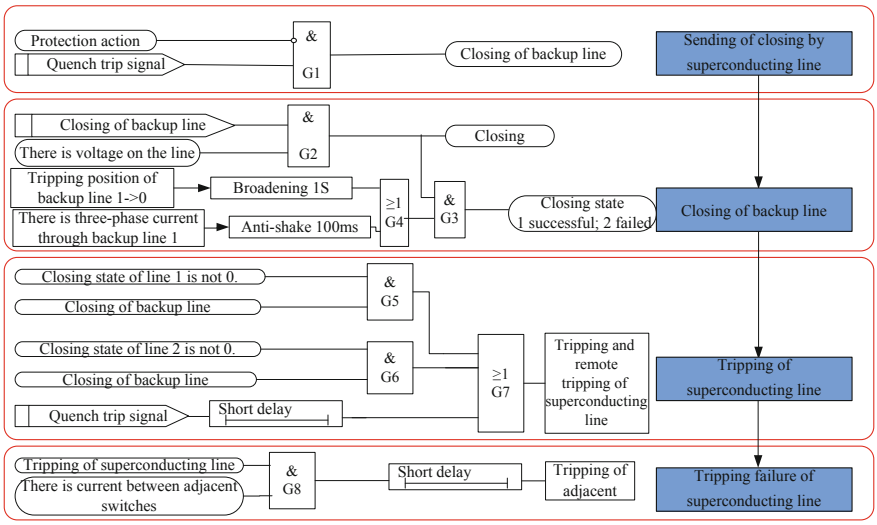

Fig. 10 Tripping logic of superconducting cable

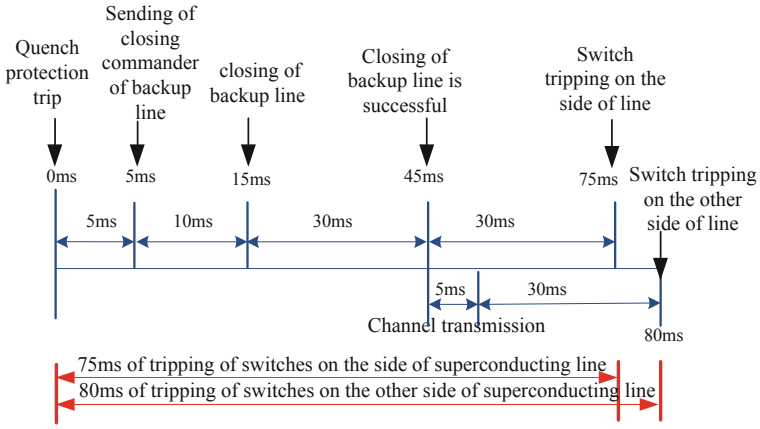

Fig. 11 Tripping time of superconducting cable

If there are faults inside the superconducting line area, the late removal of the faults may cause the superconductor to be damaged, resulting in larger loss and failing to be reactivated within a short time. Therefore, the breaker failure protection of the superconducting line should be considered. The interval protection between adjacent breakers (line protection or bus section protection) should subscribe to the tripping signal of the superconducting line, judge the breaker failure based on its own current and trip off the adjacent superconducting breakers through short time delay, so as to realize the failure isolation.

The closing logic of the superconducting cable is: switches 3541, 3553 and 3563 are closed and switches 3521, 3562, 3551 and 3552 are tripped.

The tripping and closing exit of the superconducting line is realized by the line protection through the GOOSE network of the process level in the station and the remote tripping of differential protection at the opposite side. The tripping and closing time of GOOSE is less than 10 ms. The pilot channel delay is less than 5 ms, the opening time of 35 kV breaker takes 30 ms, and as shown in Fig. 11, the overall tripping time of the superconducting line is less than 80 ms.

7 Conclusion

This paper introduces the wiring forms of the kilometer-level superconducting cable demonstration project, puts forward a whole set of protection configuration scheme taking differential and quench protection as the main protection, presents an auto-switching scheme for introduction of the superconducting line which is not based on the backup auto-switching, and considers the breaker failure of the superconducting line. It provides useful reference value for the protection device

configuration of the kilometer-level superconducting cable demonstration project. The practicability of it remains to be further verified in actual projects. As for the superconducting cable, the primary equipment of power system which requires high protection reliability, this paper puts forwards an information collection method based on 5G communication, which needs to be improved and studied in the future.

Acknowledgements Scientific Research Project of the State Grid Corporation of China "Key Technology and Demonstration Application Research of Domestic Kilometer-level High Temperature Superconducting Cable System" (SGSHDK00SPJS1800272).

References

1. Qiu M (2017) Applications of superconducting power transmission in power grid. Adv Technol Electr Eng Energy 36(10):55–62. https://doi.org/10.12067/ateee1707030
2. Wei D, Zong X et al Xu C (2015) Demonstration project of 35 kV 2000 a cold dielectric high temperature superconductive power cable system. Electr Wire & Cable 2(1):1–5
3. Yang J, Zhang Z, Tang Y et al (2005) Development of HTS cable's monitoring and protection device. Autom Electr Power Syst 29(7):101–104
4. Jiali HE (2006) Power system relay protection principle and practical technology[M]. China Electric Power Press, Beijing
5. Zeng X, Yi W, Liu Z et al (2008) A novel technique of capactive current resonance measurement with signal injected for distribution networks. Autom Electr Power Syst 32 (4):77–80
6. Zhou Q, Zhang X, Zhang K et al (2017) Formula erratum for non-power frequency method in power industry standard and new measuring method of capacitive current. Autom Electr Power Syst 41(1):161–167. https://doi.org/10.7500/aeps20160307013
7. Chen R, Zhou F, Weng H et al (2017) Active arc-suppression method based on double closed —loop control under single-phase grounding faults in distribution networks. Autom Electr Power Syst 41(5):128–133. https://doi.org/10.7500/AEPS20160418003
8. He L, Ge L, Sun J (2018) Capacitive current measuring method for distribution networks based on resonant frequency prediction model. Autom Electr Power Syst 42(2):143–147. https://doi.org/10.7500/aeps20170802010
9. National Electric Power Dispatching and Communication Center (2009) State grid relay protection training materials[M]. China Electric Power Press, Beijing
10. Yu X, Li J, Tang Y (2003) The basic study for Q uench detection in superconducting electric equipments. Eng Sci 5(10):73–77
11. Yang X (2019) The construction of the ubiquitous power Internet of things can meet more individual needs. State grid report (1)
12. Sun Z (2019) Internet of things technology supported by 5G mobile communication. Electron Technol Softw Eng 5:26

State Perception Method of Intelligent Substation Secondary System Based on FCE and DCNN

Hongbing Li, Junyong Zhu and Ling Luo

Abstract Aiming at second equipment lacks comprehensive and effective state detection and simple and reliable evaluation method, a state perception method of intelligent substation secondary system based on fuzzy comprehensive evaluation (FCE) and deep convolutional neural network (DCNN) is proposed. Firstly, combining with the factors of auxiliary equipment state evaluation, the FCE method is adopted to evaluate the influence degree of each secondary equipment. Secondly, DCNN was used to learn the regional and edge features respectively, and the significance and non-significance confidence of the detected region was obtained. Finally, combined with the influence degree of each secondary equipment and the significant and non-significant confidence level, the state of the secondary equipment in intelligent substation is evaluated. The experiment results indicate that the proposed method can effectively solve the deficiency of the corresponding equipment status detection and evaluation method of intelligent substation.

Keywords Deep convolutional neural network · Intelligent substation · Secondary system · Method of state perception · State detection · Fuzzy comprehensive evaluation

1 Introduction

Smart substation is one of the key technology of the smart grid which plays an irreplaceable role in the operation of the power grid [1]. Compared with traditional substation, intelligent substation secondary equipment has greatly improved in performance, but its cannot working stably without so many links in the whole grid system which is related with the effective connection [2]. The intelligent substation secondary system is different from the traditional application of substation, which is much more complicated. The equipment in the operation of the secondary system

H. Li (✉) · J. Zhu · L. Luo
State Grid Chongqing Electric Power Company, Chongqing 400015, China
e-mail: spr_stic@126.com

Y. Xue et al. (eds.), *Proceedings of PURPLE MOUNTAIN FORUM 2019-International Forum on Smart Grid Protection and Control*, Lecture Notes in Electrical Engineering 585, https://doi.org/10.1007/978-981-13-9783-7_34

function often appear problem, but it difficult to detect the specific failure accurately, which affects the stable operation of the entire system [3]. Therefore, it is significant and practical value to study the state perception method of the secondary system of intelligent substation [4].

Many experts and scholars have conducted in-depth research on the state perception method of intelligent substation secondary system. Literature [5] proposed a hidden fault diagnosis method based on the static characteristics monitoring of the relay protection device by making use of the difference between the measurement and calculation results of the wide area measurement system and the relay protection device. Literature [6] proposes carrying out hidden fault diagnosis of relay protection measurement circuit based on relay protection information management system. Literature [7] carries out hidden fault diagnosis of protection measurement circuit by comparing the same electrical quantity of different devices. Literature [8] expands the starting node of the existing fault recording device and realizes online fault detection of transmission line protection device based on the recorded dynamic information. Literature [9] constructed the current observer model of the line and transformer, compared the output of the observer and the electronic transformer, and the residual fault information formed is used to diagnose the transformer's gradual fault. The performance of state detection and evaluation methods for secondary equipment in the above methods still need to be improved better.

A state perception method for the secondary system of an intelligent substation based on deep convolutional neural network is proposed. Its main innovations are:

(1) In most existing methods, due to the defects of the secondary system itself and the lack of state detection of the ancillary equipment, there is the possibility of failure and instability in the smart grid. The goal of the proposed method is making a correct evaluation of the state of secondary equipment through the equipment status monitoring technology and self-diagnosis technology. Combine with the off-line inspection data and online operation information of secondary equipment, and the maintenance time and maintenance items are scientifically arranged according to the state evaluation results.
(2) In most existing methods, the subordinate system of intelligent substation lacks scientific and effective evaluation methods, so that the probability of the secondary system's hidden fault outbreak increases greatly. The proposed method establishes a systematic and reasonable state evaluation method, integrates the deep convolutional neural network to learn the region and edge features respectively, and obtains the significance and non-significance confidence of the detection region.
(3) Most existing methods lack practical operational experience, and the operational state of secondary equipment is uncertain and fuzzy. The proposed method compares the important characteristics of the conventional evaluation methods, which proves that the fuzzy comprehensive evaluation (FCE) method is more accurate for the state evaluation of intelligent substation secondary equipment.

Experimental results indicate that the proposed method can effectively solve the problem of the lack of state detection and evaluation methods of consequential equipment in smart grid.

2 The Proposed Method

In the proposed method, deep convolutional neural network (DCNN) was used to learn about the region and edge features respectively, and the significance and non-significance confidence of the detection region was obtained. The FCE method is implement for the state evaluation of intelligent substation secondary equipment. The flow chart of the proposed method is shown in Fig. 1.

2.1 The Secondary Equipment

In the intelligent substation, all the secondary equipment is based on the IEC61850 protocol standard. Comprehensive understanding of the overall situation of the

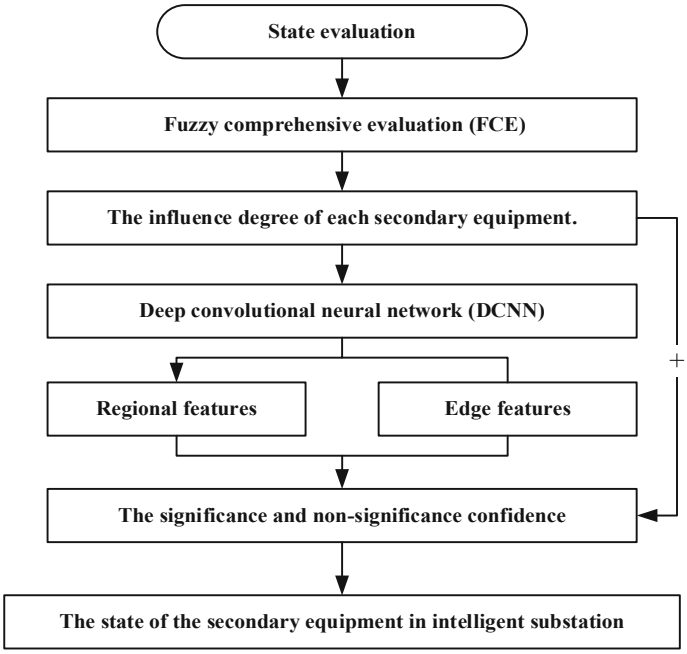

Fig. 1 Flow chart of the state perception method for intelligent substation secondary system based on FCE and DCNN

secondary equipment are obtained after comprehensively analyze the status monitoring and corresponding information of the equipment. And a scientific and economical maintenance mechanism and cycle is planned. Adjust the time limit according to the specific situation, reduce the maintenance cost, reduce the occurrence of maintenance accidents, shorten the duration of equipment outage and improve the power supply efficiency, which is the main purpose of the condition-based maintenance of secondary equipment. The secondary circuit and the secondary equipment are the main objects of the state monitoring of the secondary system. The latter includes the relay protection device, the intelligent terminal and the merging unit, the safety automatic device. The monitoring objects of secondary equipment statue in substation include AC, DC measurement, logic evaluation, communication and shielding grounding. The integrity of the secondary circuit of the current and voltage transformer, the normal insulation of the circuit and the integrity of the measuring elements are all included in the AC measurement system.

2.2 Evaluation Method Analyses

Intelligent substation secondary equipment is complex and powerful. In the process of operation, the equipment state is restricted and affected by numerous factors. Accurate evaluation method is very complex, but necessary to analyze the various current evaluation methods. Therefore, it's important to choose the optimal evaluation method of intelligent substation secondary equipment state.

Now commonly used evaluation methods include analytic hierarchy process, comprehensive scoring method and FCE method, which are implemented in many different fields. Comprehensive scoring method is based on a certain standard for the impact of various factors on the state of the equipment scoring, and by adding up weighted finally get the actual total score. The advantage of this method is that the calculation is straightforward, but the disadvantage is that there are many subjective factors in the evaluation process, and the risk of error is large.

The principle of FCE method is to adopt the method of comprehensive evaluation for functional problems with the help of fuzzy mathematics theory. Compared with the traditional evaluation method, the clear consequences and strong systematicness is the advantages, which is suitable for the evaluation of complex problems involving a large number of factors. Therefore, it can deal the unclear boundary and unidentifiable situation of intelligent substation secondary equipment operation better than the traditional methods, and the problem can be solved more reasonably. Therefore, the state of the secondary equipment of the intelligent substation is evaluated through the proposed method.

2.3 State Characteristic Quantity of Intelligent Substation Secondary Equipment

The characteristic quantity of the inferior equipment of the intelligent substation is the characteristic parameter which can represent the health condition of the equipment. Mainly including time, steady state, electrical and maintenance performance. Time performance characteristics include absolute delay, action time, message sending time and response message delay. Steady-state performance characteristics include sampling amplitude error, sampling phase error, message consistency and familial defects. Characteristic parameters of electrical performance include insulation resistance, dielectric strength and impulse voltage; The maintenance performance characteristic quantity includes the periodic maintenance and the functional inspection two items.

2.4 Models Based on FCE

Establishment of FCE model. The steps of establishing the evaluation model through fuzzy comprehensive evaluation method are as follows:

Find out the factor set, U represents the set of all factors that affect the evaluation object.

$$U = (\mu_1, \mu_2, \mu_3 \ldots, \mu_{\mathrm{m}}) \tag{1}$$

Establish comment set, V represents the set of status of each evaluation index in factor set U.

$$V = (\upsilon_1, \upsilon_2, \upsilon_3 \ldots, \upsilon_{\mathrm{m}}) \tag{2}$$

Determine the evaluation matrix, R is the fuzzy relation from U to V.

$$R = \begin{bmatrix} r_{11} & r_{12} & \cdots & r_{1n} \\ r_{21} & r_{22} & \cdots & r_{2n} \\ \vdots & \vdots & \ddots & \vdots \\ r_{m1} & r_{m2} & \cdots & r_{mn} \end{bmatrix} \tag{3}$$

where r_{ij} is the membership degree of U_I in U to vi in V.

Calculate the weight vector W according to the follow formulation:

$$W = (\mathrm{w}_1, \mathrm{w}_2, \mathrm{w}_3 \ldots, \mathrm{w}_{\mathrm{m}}) \tag{4}$$

The methods to calculate the weighted value include analytic hierarchy process (ahem), factor analysis, Delphi method, expert scoring method and method of marital value. Each weight value calculation method has its own characteristics to meet diverse evaluation objects, so that the weight value distribution can get better results [10].

In the theory of fuzzy assessment, fuzzy synthesis operator is used to calculate generally includes: the main factors to highlight type M $(\cdot,\vee)$, main factors determine type M $(\wedge,\vee)$, the weighted average model M $(\cdot\ \cdot,\oplus)$ and uneven average model M $(\wedge,\oplus)$.

The weighted average operator is generally accepted as the most reasonable, which can comprehensively consider as the indicators and make better use of the data information of these indicators. Therefore, the weighted average operator is used according to the final calculation.

Mathematical model:

$$B = W.R = (\mathrm{b}_1, \mathrm{b}_2, \ldots, \mathrm{b}_\mathrm{m}) \tag{5}$$

where, "." is the symbol of generalized fuzzy calculation; the results of FCE represent the degree of subjection of evaluation objects to each comment.

The evaluation index is divided according to the level, the mathematical model of FCE is extended, and the multilevel FCE model is obtained [11]. The calculation formula of the corresponding second-level mathematical model is as follows:

$$B = W.R = W.\begin{bmatrix} B_1 \\ B_2 \\ \vdots \\ B_n \end{bmatrix} \tag{6}$$

where, B_1, B_2, …, B_n are the results of second-level FCE.

Calculate the evaluation results. The results obtained are of comprehensive results are divide into Ordinary, good and best three grades.

2.5 Selection of Membership Functions

The selection of membership function is very important, and the fuzzy relation matrix R can be calculated after the membership function is determined. The fuzzy relation matrix *R* can be calculated more scientific and reasonable only by selecting a membership function that conforms to the actual situation. When selecting the membership function, we should try to overcome the subjective factors and ensure the objectivity of the membership function.

The selection of membership function includes exemplification, fuzzy statistics and assignment. The example method calculates the membership function based on the obtained data. The fuzzy statistical method deduces the whole part according to the statistical law and then obtains the membership function according to the objectivity of membership degree. The assignment method is more subjective and empirical. Normal distribution function as a fuzzy distribution, when the expected value 3 range covers 99.73% area, so it can cover more obvious advantages of information, so this paper uses the normal distribution model membership function to calculate the membership degree. The specific formula is as follows:

$$\begin{cases} r_1(u) = \begin{cases} 1, \ u \le & \mu_{\min} \\ \mathrm{e}\dfrac{(u-\mu_{\min})^2}{2\delta^2}, \mu_{\min} < u \le \mu_0, \ \delta_1 = \dfrac{\mu_0 - \mu_{\min}}{3} \end{cases} \\ r_2(u) = \begin{cases} \mathrm{e}\dfrac{(u-\mu_0)^2}{2\delta_{21}^2}, \mu_{\min} < u \le \mu_0, & \delta_{21} = \dfrac{\mu_0 - \mu_{\min}}{3} \\ \mathrm{e}\dfrac{(u-\mu_0)^2}{2\delta_{22}^2}, \mu_0 < u \le \mu_{\max}, & \delta_{22} = \dfrac{\mu_{\max} - \mu_0}{3} \end{cases} \\ r_3(u) = \begin{cases} \mathrm{e}\dfrac{(u_{\max}-\mu)^2}{2\delta^2}, \mu_{\min} < u \le \mu_{\max}, \delta_3 = \dfrac{\mu_{\max} - \mu_0}{3} \\ 1, & u \ge \mu_{\max} \end{cases} \end{cases} \tag{7}$$

The formula includes three levels: ordinary, better, and excellent. If the smaller the better state indicator, $\mu_{\min}$, μ_0, μ_{Max} are the expected value when the indicator is "excellent", "better", "ordinary"; On the contrary, $\mu_{\min}$, μ_0 and μ_{Max} are the expected values when the indicators are "normal", "better" and "excellent" respectively. The relevant standards and regulations on the status of secondary equipment of smart substation are applied in this paper.

2.6 *Deep Convolutional Neural Network*

Firstly, the algorithm performances of the proposed method and the traditional Monte Carlo-based method in the case with the same iterations are studied. To evaluate the algorithm performance, the error between the assessment results and the practical value is adopted as the index [12].

DCNN is a kind of deep neural network structure with recognition. Feature mapping layer, also known as sample, which belongs to calculate layer. DCNN is also a multilayer structure. The wiring way of neural network, a mapping layer mapped to a plane, which sharing network weights by constraining neurons. The image translation, scaling, rotation and deformation makes the network structure has a high degree of invariance, which is approved by AMO [13]. Firstly, the

learning structure of training multi-layer neural network model is implemented. Then, the multi-level convolution layer and the down-sampling layer are connected to one or more connection layers, and the output of the connection layer is finally output.

Figure 2 is the general structure diagram of the DCNN. Convolutional neural network consists of several convolution layers and lower sampling layers, and its operation has certain particularity. The former focuses on feature extraction, while the latter focuses on feature computation. Subjective understanding is the detection of areas of interest to the human eye, which is closely related to the human visual system [14]. Objectively speaking, there is a sub-region with the most obvious features in the image. Therefore, the key to saliency detection lies in feature learning and extraction [15]. Aiming at the power function of deep learning in this respect, this method solves the saliency detection problem of deep convolution neural network items. The specific model is shown in Fig. 3

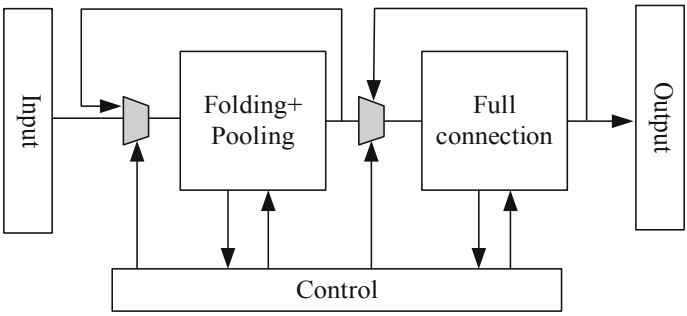

Fig. 2 General structure diagram of DCNN

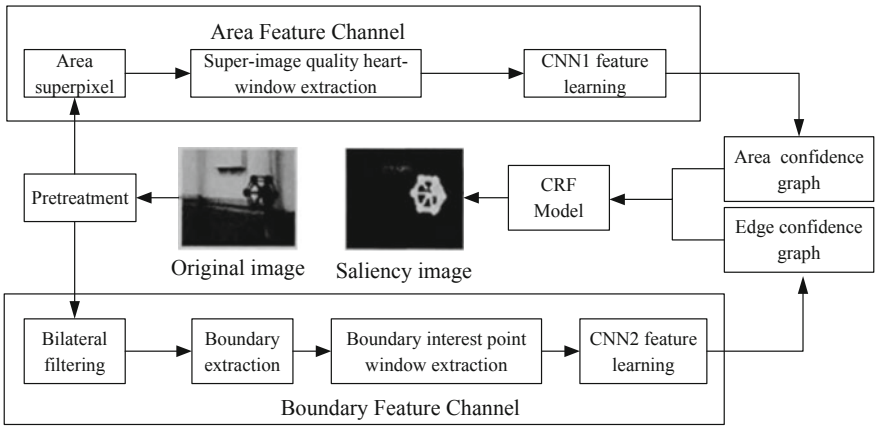

Fig. 3 Specific model of DCNN

3 Experimental Results and Analysis

Taking an intelligent terminal of a common specification as an example, the proposed method is used to evaluate its state to verify the practicability of the method. The detailed steps are as follows:

(1) Establish factor set W

Factor set W is determined by referring to the peculiar state of the intelligent terminal. Six performance factors, such as time performance, are set as first-level evaluation indexes. Then, the first-level evaluation indexes are divided in detail to generate the corresponding second-level indexes. The evaluation factor set U is as follows:

$$U = (u_1, u_2, u_3, u_4, u_5, u_6)\boldsymbol{c} \tag{8}$$

(2) Establish comment set V

Ordinary, good, excellent 3 grades, comments set as follows:

$$V = (\upsilon_1, \upsilon_2, \upsilon_3) \tag{9}$$

(3) Establish fuzzy relation matrix

The precise parameters of the membership function used for calculation and the measured values given are shown in Table 1. The data in the table are used to calculate the fuzzy relation matrix.

Table 1 Membership function parameters and measured values of intelligent terminal

Evaluation indicators	$\mu_{\min}$	μ_0	$\mu_{\max}$	μ_i
Equipment aging failure μ_{31}	0 year	4 year	8 year	0.5 year
Power aging μ_{32}	0 year	3 year	3 year	0.6 year
Family defects μ_{33}	2	3	5	0
Insulation resistance μ_{41}	58	63	99	75
Dielectric strength μ_{42}	58	63	99	7
Impulse voltage μ_{43}	58	63	99	85
High temperature influence μ_{51}	55	60	95	75
Low temperature impact μ_{52}	55	60	95	75
The temperature influence μ_{53}	55	60	95	75
Harmonic effects μ_{61}	65	70	100	75
Switch action μ_{62}	65	70	100	80
Lightning strikes μ_{63}	65	70	100	80
Its influence μ_{64}	65	70	100	80

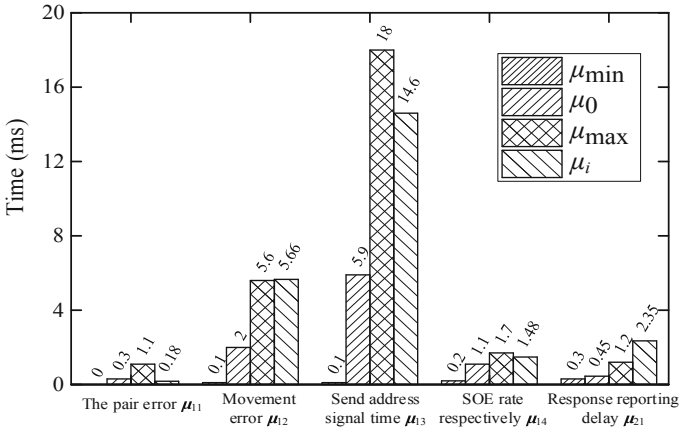

Fig. 4 Membership function of time parameters and measured values

Table 2 Results of comprehensive evaluation

Best	Good	Ordinary
42%	19%	46%

The above data obtain the membership degree of each performance index with the help of the membership function (7), and further obtain the fuzzy relation matrix.

The evaluation indicators of time consumption are shown in Fig. 4.

As shown in Fig. 4, the proposed method is more comprehensive for the evaluation of secondary equipment in intelligent substations.

(4) Determine the evaluation results

The final comprehensive evaluation of cerebral terminal equipment is shown in Table 2.

Combined with Table 2 and the judgment basis of referring to the maximum membership degree, the final result of the intelligent terminal state assessment in the example is mutual. The evaluation results are consistent with those obtained by the analytic hierarchy process and the comprehensive scoring method, which are more accurate.

4 Conclusion

An intelligent substation secondary system state perception method based on innate convolutional neural network is proposed. The experimental results show that it could solves the problem of the lack of state detection and evaluation methods for

secondary equipment in intelligent substation effectively. The future direction of the research is how to comprehensive consider secondary equipment status evaluation results with the whole life cycle cost and risk of equipment operation. The relationship between the three factors are complex and reasonable maintenance strategy needed to be developed to improve the intelligent substation secondary system operation. The intelligent substation works safely and economically is a work of great research significance.

Acknowledgements This work is supported by Science and Technology Project of State Grid Chongqing Electric Power Company in 2018. The project name is "Integrated Operational Support Technology of Intelligent Substations Based on Total Service Data" (No. 2018#35).

References

1. Wen B, Hong M, Wu D et al (2018) Research on SCD management and control technology in smart substation. In: IOP conference series: earth and environmental science, vol 170(4). IOP Publishing, p 042130
2. Jiang HT, Chen C, Bu J (2014) Design of performance analysis system of secondary circuit in intelligent substation based on NI platform. Adv Mater Res 986–987:1934–1937
3. Ciwei G, Xiaojun C, Huaguang Y, Weihua S (2017) Energy management of data center and prospect for participation in demand side resource scheduling. Autom Electr Power Syst 41 (23):1–7
4. Haijun X, Haozhong C, Jingfei Y et al (2016) Distribution network expansion planning considering multiple active management strategies. Autom Electr Power Syst 40(23):70–76,167
5. Wang H, Zhou B, Zhang X (2018) Research on the remote maintenance system architecture for the rapid development of smart substation in China. IEEE Trans Power Delivery 33 (4):1845–1852
6. Zhang S, Cheng P, Wang B et al (2019) Research on coordinated attack protection method based on global time synchronization system of intelligent substation. J Netw Comput Appl 4:14–20
7. Zheng Z, Yan Z, Yu T (2018) Design of conformance verification system for intelligent substation configuration file. In: 2018 Chinese control and decision conference (CCDC). IEEE. pp 4307–4310
8. Yang N, Pouget J, Letrouvé T et al (2019) Techno-economic design methodology of hybrid energy systems connected to electrical grid: An application of hybrid railway power substation. Math Comput Simul 158:107–119
9. Wu T, Liu S, Ni M et al (2018) Model design and structure research for integration system of energy, information and transportation networks based on ANP-fuzzy comprehensive evaluation. Global Energy Interconnection 1(2):137–144
10. Wang Q, Han R, Huang Q et al (2018) Research on energy conservation and emissions reduction based on AHP-fuzzy synthetic evaluation model: a case study of tobacco enterprises. J Clean Prod 201:88–97
11. Zhao H, Guo S, Zhao H (2019) Comprehensive assessment for battery energy storage systems based on fuzzy-MCDM considering risk preferences. Energy 168:450–461
12. Feng L, Cui C, Ma R et al (2018) Deep learning algorithm for preliminary siting of substations considering various features in distribution network planning. In: IOP conference series: earth and environmental science, vol 192 (1). IOP Publishing, p 012032

13. Fu CZ, Si W R, Huang H et al (2018) Research on a detection and recognition algorithm for high-voltage switch cabinet based on deep learning with an improved YOLOv2 Network. In: 2018 11th international conference on intelligent computation technology and automation (ICICTA). IEEE, pp 346–350
14. Li Q, Han B, Yu M et al (2018) Modeling of multiple heating substations based on long short-term memory networks. In: International conference on smart city and intelligent building. Springer, Singapore, pp 515–524
15. Zhinong W, Yu C, Wenjin H et al (2018) Optimal allocation model for multi-energy capacity of virtual power plant considering conditional value-at-risk. Autom Electr Power Syst 42 (4):39–46

Risk Assessment Method for Smart Substation Secondary System Based on Deep Neural Network

Zhian Zeng, Shuyou Yao and Tingbai Zhang

Abstract In the risk assessment for the smart substations, the traditional Monte Carlo-based methods rely on prior distribution knowledge and cannot cover all the potential failure scenarios. In this paper, a risk assessment method based on the deep neural network for the smart substation secondary system is proposed. Firstly, a deep neural network established by the deep auto-encoders is proposed to quantitatively evaluate the operational risk of the smart substation. Secondly, the key indicators that affect the substation operations are hierarchically combed and refined, and are used as the inputs of the deep neural network. Finally, numerical simulation results from an actual smart substation show that compared with the traditional Monte Carlo-based assessment methods, the accuracy of the proposed method for assessing the operation states of the smart substation can be improved by 48.03% under the same iterations. In addition, the running time of the proposed method is less by 12.3% than the time of traditional method in the case with the same iterations. Hence, effectiveness and feasibility of the proposed method can be verified.

Keywords Smart substations · Secondary systems · Risk assessment · Deep neural network · Deep auto-encoders

1 Introduction

The secondary system in a smart substation provides services such as protection, control, monitoring and so on for the primary system. It plays a vital role in the safe and reliable operation of the smart substations [1]. However, the secondary system also brings the primary system a lot of uncertainties. In recent years, the accidents in power systems caused by the secondary system failures have been frequently reported [2]. Therefore, ensuring the safe operation of the secondary system in the

Z. Zeng (✉) · S. Yao · T. Zhang
State Grid Chongqing Electric Power Company, Chongqing 400015, China
e-mail: really2001@163.com

Y. Xue et al. (eds.), *Proceedings of PURPLE MOUNTAIN FORUM 2019-International Forum on Smart Grid Protection and Control*, Lecture Notes in Electrical Engineering 585, https://doi.org/10.1007/978-981-13-9783-7_35

smart substation has attracted considerable attention from both the academic and the industry [3, 4]. Hence, developing the risk assessment method for the secondary system in the smart substations can improve operation safety effectively.

Recently, a lot of the risk assessment methods have been developed for the smart substation secondary system. For example, a risk assessment method for evaluating the cyber security of power systems with the protection systems is presented in literature [5]. A method of power system network security assessment considering the protection system is proposed. The expected load curtailment index and the Monte Carlo method are used to quantify the potential system losses. In literature [6], vulnerability models for a single component and the whole power system are established firstly. Then a probabilistic multi-time and multi-region elasticity assessment method based on optimal power flow and sequential Monte Carlo simulation have been introduced. However, the drawback of Monte method is that the prior knowledge of failure distributions must be required. In addition, a representative probability is used to calculate the influences of the substation automation system failures on the distribution network branch net failure rate in literature [7]. However, this method relies on the precise knowledge of the secondary system framework and hence is unsuitable for evaluating the operational risk in the substation with more coupling secondary equipment.

Given the characteristics such as a large amount of secondary equipment, complex coupling relationships and so on in the smart substations, in this paper, the risk assessment method based on the deep neural network modeled by the deep auto-encoders for evaluating the secondary system safe operation is proposed. The main indexes of the secondary system which affect the smart substation safety and reliability are adopted as the input data of the proposed deep neural network while the corresponding output is the quantitative risk assessment results. Compared with the traditional Monte Carlo-based risk assessment methods, our proposed method does not require the relevant prior knowledge of the failure distribution and the accurate framework of the smart substation secondary system.

2 Risk Assessment Model Based on Deep Neural Network

2.1 Secondary System in a Smart Substation

A modern smart substation includes the intelligent primary devices (e.g., electronic transformers and intelligent switches) and the networked secondary system. The secondary system can be further divided into three layers called the process layer, bay layer, and substation layer. All the state variables and the instructions are communicated following the IEC 61850 standard. Hence, the information sharing and inter-operating among the intelligent electrical devices in the substation can be realized. Figure 1 illustrates a typical framework of the secondary system in a smart substation. The monitoring equipment for the primary devices (e.g., the

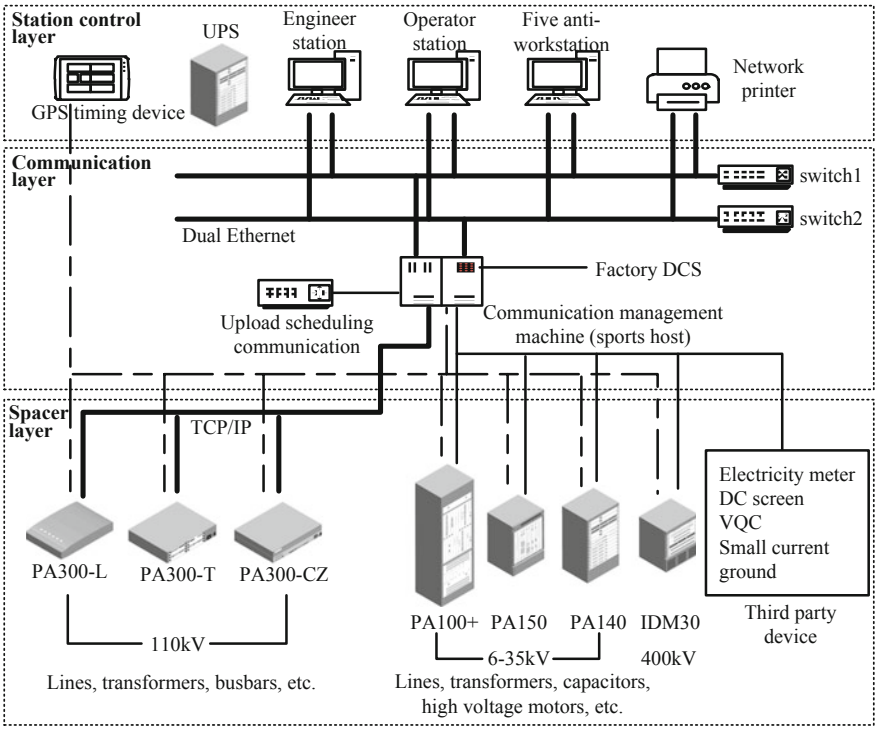

Fig. 1 Intelligent electrical devices in the substation

transformers, capacitors and circuit breakers) locate in the process layer. The sensing data sampled and collected by the sensors are transmitted to the substation layer over the communication network in the bay layer. Then the operation risk assessment is evaluated in the substation layer.

2.2 Deep Neural Network Risk Assessment Model

The tradition back propagation (BP) neural network is easy to trap in the local optimum with the number of hidden layers increasing. The reason is that the increasing hidden layer enhances the gradient disappearance, affects the back propagation process and reduces the training performance. Deep neural networks (DNN), also known as the neural network-based deep learning algorithm, is one of those modified methods to overcome the gradient descent in traditional BP network algorithm. It has stronger feature discriminating and learning ability and is more suitable for the complex pattern recognition problems [8].

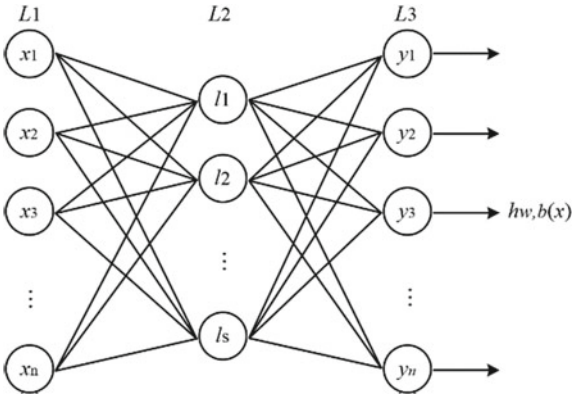

Fig. 2 The structure of DAE-DNN

(1) **Basic Principles of Deep Neural Networks**

Similar to the traditional BP network, the DNN alogrithm conatins the following three processes: pre-training, weighting coefficient initializing and updating. Moreover, the DNN can be established by adapting the deep auto-encoders method (DAE) [9]. Figure 2 illsutrates the stcutre of the DAE based DNN where the number of the neurons in the input layer is equal to the number of the devices of the seconary system. In Fig. 2, $\{x_1, x_2, \ldots, x_n\}$ represents the neurons in input layer; $\{l_1, l_2, \ldots, l_s\}$ represents the neurons in hidden layer; $\{y_1, y_2, \ldots, y_n\}$ represents the neurons in output layer.

In this paper, the sigmoid function is used as the activation function. Generally, if the output of a neurons is equal to 1, this neuron is viewed as to be "active". Conversely, if the output of a neurons is unequal to 1, this neuron is viewed as to be "inactive". The goal of the DAE-DNN is to let the neurons be inactive most of the time. Hence, let $a_j(x)$ denote the jth neuron in the hidden layer. Then the active neuron in hidden layer can be expressed as

$$a = \text{sigmoid}(WX + b) \tag{1}$$

where $X = [x_1, x_2, \ldots, x_n]$ is the input data vector, W is the weighting matrix connecting the input layer and hidden layer, b is the deviation matrix between the two layers. Hence, the average of the active function of the jth neuron in hidden layer can be calculated by

$$\rho_j = \frac{1}{n}\sum_{i=1}^{n}\left[a_j(x(i))\right] \tag{2}$$

In the DAE-DNN, most of the neurons are required to be inactive, i.e., the average of the active function is required to close to a constant ρ which is approximate to zero. Hence, a punishment term is introduced to make ρ_j stay around the constant ρ. In this paper, the Kullback-Leibler (KL) divergence is used to meet the above requirement.

$$PN = \sum_{j=1}^{S_2} KL(\rho||\rho_j) \tag{3}$$

where S_2 is the number of the neurons in hidden layer, $\mathrm{KL}(\rho\|\rho_j)$ is the KL divergence as follow

$$KL(\rho||\rho_j) = \rho \ln \frac{\rho}{\rho_j} + (1-\rho) \ln \frac{1-\rho}{1-\rho_j} \tag{4}$$

Moreover, the cost function can be given by

$$\begin{aligned} C(W,b) = &\left[\frac{1}{n}\sum_{i=1}^{n}\frac{1}{2}\left\|h_{w,b}(x(i)-y(i))\right\|^2\right] + \frac{\gamma}{2}\sum_{l=1}^{m_l}\sum_{i=1}^{S_l}\sum_{j=1}^{S_l}(W_{ij}(l)) \\ &+ \beta\sum_{j=1}^{S_2} KL(\rho||\rho_j) \end{aligned} \tag{5}$$

The goal of DAE-DNN is to obtain the optimal matrixes W and b. The optimization process can be relized by using the back propagation algorithm. The update equations are given by

$$W_{ij}(l) = W_{ij}(l) - \varepsilon \frac{\partial}{\partial W_{ij}(l)} C(W,b) \tag{6}$$

$$b_i(l) = b_i(l) - \varepsilon \frac{\partial}{\partial b_i(l)} C(W,b) \tag{7}$$

where ε is the learning rate

(2) **Indicator Selection**

Given the complex coupling in the secondary system in the smart substation, the indicator system for risk assessment is proposed as shown in Table 1.

Table 1 Indicator system for risk assessment

Primary indicator	Secondary indicators
Subject level risk indicator	Basic subject risk
	System body level risk
Equipment level risk indicator	Protection equipment risk
	Measurement and control equipment risk
	Switch equipment risk
System level risk indicator	Network level risk
	Station level risk
	Interval risk

In the power system, the secondary device has a functional subject. The smallest unit of the functional subject is the basic subject set, and one basic subject set corresponds to the unique primary device. Therefore, the risk index of the secondary system is divided into the subject-level, device-level and system-level, subject level failure affects its own secondary device and the primary device corresponding to it. The device level failure affects the functional subject set containing the failed basic subject and the corresponding content contained in the subject set. System-level failure refers to the impact of secondary failure on the overall system.

(a) *Subject-level risk indicators*

The main cause of the risk at the base subject level is that the failures of one or more subjects within the subject will directly affect their corresponding one or more primary devices. Hence, R_{I} is used to indicate the risk of the basic subject set. R_{I} contains two items: basic subject risk (denoted as R_{I1}) and system body level risk (denoted as R_{I2}). The following relationship exists:

$$R_{\mathrm{I}} = R_{\mathrm{I1}} + R_{\mathrm{I2}} \tag{8}$$

$$R_{\mathrm{I1}} = P_{\mathrm{I}} C_{\mathrm{I1}} \tag{9}$$

$$R_{\mathrm{I2}} = \sum_{i=1}^{n} P_M C_{Mi} \tag{10}$$

where P_{I} is the probability that the primary device D cannot work normally due to the failure, C_{I1} the corresponding loss cost caused by the primary device failure, n is the number of subjects, P_{Mi} is the failure probability, and C_{Mi} is the self-loss after the failure.

(b) *Equipment-level risk indicators*

Equipment-level risk mainly considers the secondary equipment functional risk and the primary equipment risk corresponding to the related subject set. R_{II} is used to indicate the risk of the secondary devices which contains two parts: the risk corresponding to the primary device (denoted as R_{II1}) and the risk caused by the secondary system (denoted as R_{II2}). The following relationship exists:

$$R_{II} = R_{\mathrm{II1}} + R_{\mathrm{II2}} \tag{11}$$

$$R_{\mathrm{II2}} = \sum_{p=1}^{N_a} P_{M_{ap}} C_{M_{ap}} \tag{12}$$

where N_a is the node degree of the secondary device a, $P_{M_{ap}}$ is the failure probability of device a, $C_{M_{ap}}$ is the corresponding loss cost.

(c) *System-level risk indicators*

System-level indicators are used to assess the risk of the whole system, and the risks of all subject sets in the system are integrated according to the probability and statistics. It can usually be obtained from equipment-level risk and subject-set risk indicators.

Analogously, R_{III} is used to indicate the risk of the system main set also containing two parts: the risk in the presence of primary system (denoted as R_{III1}) and risk in the presence of secondary system (denoted as R_{III2}). The following relationship exists:

$$R_{\mathrm{III}} = R_{\mathrm{III1}} + R_{\mathrm{III2}} \tag{13}$$

$$R_{\mathrm{III1}} = \sum_{g=1}^{l} \max(R_{I1}^{D_g}, R_{I2}^{D_g}, \ldots, R_{Ik_g}^{D_g}) \tag{14}$$

$$R_{\mathrm{III2}} = \sum_{k=1}^{m} R_{Ik} - \sum_{k=1}^{m} \sum_{i=1}^{n} [(N_{ki} - 1) P_{Mki} g C_{Mki}] \tag{15}$$

where g is the number of primary devices served by the subject set, k_g is the number of base subjects servicing the gth primary device, P_{Mki} and C_{Mki} are the failure probability and corresponding loss cost, respectively, R_{Ik} is the risk of the kth basic subject set, N_{ki} is the degree of the ith subject in the kth basic subject set.

3 Numerical Results and Discussions

3.1 Test Bed

To verify the effeteness and feasibility of the proposed method, the traditional Monte Carlo-based method [10] is adopted in this paper as the comparison. Let us take a given 220 kV substation in Chongqing Province as an example. The corresponding primary and secondary systems are demonstrated in Figs. 3 and 4, respectively.

The relevant data set containing 10,000 samples is first established. The data sources come from the maintenance log and substation automation management system database in the past five years. According to the samples, the failure probabilities of the secondary devices in the substation can be calculated, as shown in Table 2.

The proposed deep auto encoders-based deep neural network is implemented in the Tensorflow environment. Concrete configurations are as follows: Windows 10 Ultimate, Intel i5-3230M CPU and 10 GB RAM. The training set containing 7000

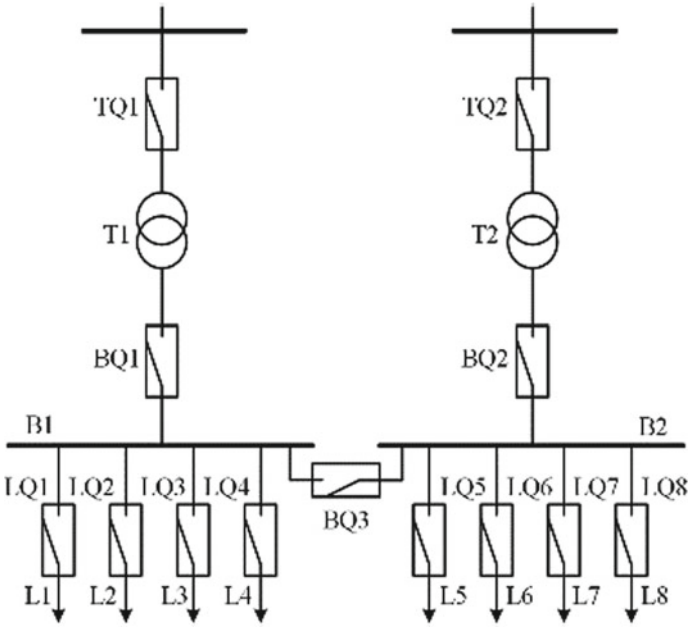

Fig. 3 Substation wiring diagram of primary devices

samples are stochastically generated from the above-mentioned data set while the rest 3000 samples are used as the test set.

For the secondary system in Fig. 4, each secondary device is viewed as a node. More precisely, nodes *a–f* represent the devices in the process layer; node *h* represents the network analyzer; nodes *i–n* represent the devices in the bay layer, nodes *g* and *o* represent the networks of process layer and substation layer, respectively; node *p* represents the local monitor, and the telecontrol workstation not considered here within the scope of risk assessment.

3.2 Numerical Studies

Firstly, the algorithm performances of the proposed method and the traditional Monte Carlo-based method in the case with the same iterations are studied. To evaluate the algorithm performance, the error between the assessment results and the practical value is adopted as the index.

Let both of the two algorithms be executed 1000 times independently. Table 3 and Fig. 5 illustrate the assessment results of all the secondary devices and the absolute value of relative errors, respectively. For all the nodes, the error between the assessment results calculated by the proposed method and the practical results

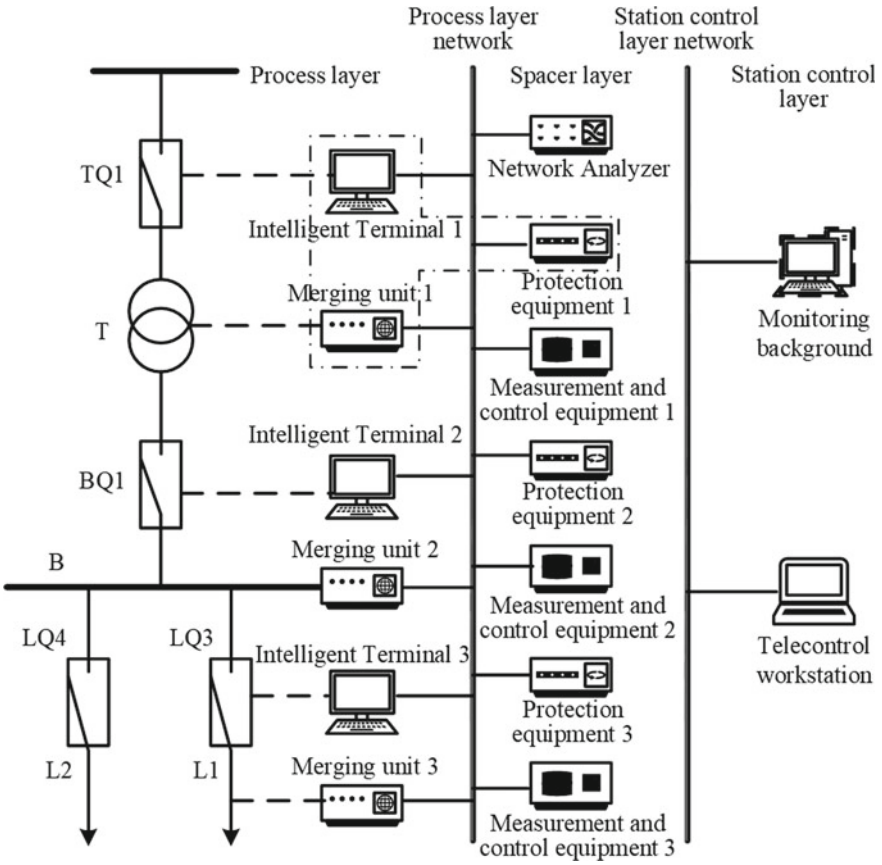

Fig. 4 Wiring diagram of primary and secondary system of substation

Table 2 The failure probabilities of the secondary devices

Device	Failure rate	Device	Failure rate
Merging terminal 1	0.0018	Protection 1	0.0014
Intelligent terminal 1	0.0025	Measurement and control 1	0.0012
Merging terminal 2	0.0017	Protection 2	0.0024
Intelligent terminal 2	0.0015	Measurement and control 2	0.0013
Merging terminal 3	0.0024	Protection 3	0.0017
Intelligent terminal 3	0.0013	Measurement and control 3	0.0015
Network analyzer	0.0031	Monitoring background	0.0024
Process layer network	0.0024	Intelligent remote motive	0.0014
Station control layer network	0.0016	Scheduling master station	0.0003

Table 3 Monte Carlo and DNN algorithm performance

Node	Monte Carlo	DNN	Real value
a	150.66	158.95	165.42
b	149.37	166.13	159.81
c	142.27	126.26	131.90
d	141.05	148.59	153.68
e	36.82	35.95	34.52
f	35.69	31.97	33.34
g	243.14	255.08	267.45
h	38.16	37.55	39.73
i	98.53	111.69	107.50
j	47.48	48.90	51.75
k	92.17	86.71	90.63
l	42.96	45.36	47.69
m	21.36	24.36	23.26
n	14.07	14.70	15.48
o	147.26	130.55	135.53
p	36.79	41.30	40.16

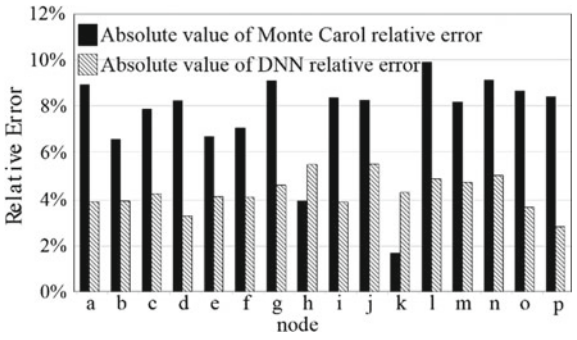

Fig. 5 Relative error of DNN/Monte Carlo for different nodes

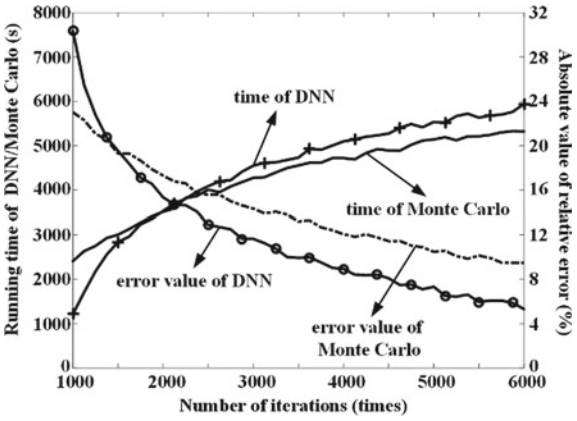

Fig. 6 Running time and relative error of DNN/Monte Carlo

are −5.5, −4.73% while the error between the assessment results calculated by the traditional Monte Carlo-based method with the practical results are −9.92, −8.65%. The average error between the real value and the assessment results with the Monte Carlo method and our proposed method are −3.56 and −1.85%, respectively. Hence, the assessment accuracy of our proposed method can be improved by 48.03% compared with the Monte Carlo-based method. Moreover, it can be seen that the risk assessment results of most the nodes are closer to the practical values compared with the traditional Monte Carlo-based method, i.e., the proposed method can reflect the real operation state of the secondary system in smart substation better. This is because that the weighting coefficients of all the layers in the deep neural network are continuously optimized by the back propagation mechanism. Hence, the final accuracy of the risk assessment can be improved.

Moreover, the running time when the above two methods reach the same assessment accuracy is discussed. Let the iteration of the algorithms be terminated when the error converges to less than 5%. Figure 6 illustrates the running times of the above two algorithms. It can be seen that the running time of the traditional Monte Carlo-based method are 12.3% longer than the proposed method.

4 Conclusions

In this paper, a risk assessment method based on the deep neural network for evaluating the safe operation of the secondary system in the smart substation is proposed. Key indexes which may affect the safety and reality of the secondary system are firstly determined and then used as the input data of the deep neural network.

Hence, the operation state of the smart substation secondary system can be quantitatively assessed by utilizing the advantage of nonlinear fitting of the deep neural network. Numerical results show that the proposed method has a better performance of the running time and the assessment accuracy. In the future, we will focus on improving the assessment accuracy of the deep neural network.

Acknowledgements This work was supported by Science and Technology Project of State Grid Chongqing Electric Power Company in 2018. The project name is “Integrated Operational Support Technology of Intelligent Substations Based on Total Service Data” (No. 2018#35).

References

1. Yang T, Rui Z, Zhang W et al (2017) On the modeling and analysis of communication traffic in intelligent electric power substations. IEEE Trans Power Delivery 32(3):1329–1338
2. Wu HT, Jiao CQ, Cui X et al (2017) Transient electromagnetic disturbance induced on the ports of intelligent component of electronic instrument transformer due to switching operations in 500 kV GIS substations. IEEE Access 5(99):5104–5112

3. Hengtian WU, Jiao C, Cui X et al (2017) Analysis and simulated experiment for port disturbance voltage due to switching operation in GIS substation. High Voltage Eng 43 (10):3387–3395
4. Ghoneim SSM (2018) Intelligent prediction of transformer faults and severities based on dissolved gas analysis integrated with thermodynamics theory. IET Sci Meas Technol 12 (3):388–394
5. Lubbers N, Smith JS, Barros K (2018) Hierarchical modeling of molecular energies using a deep neural network. J Chem Phys 148(24):241715
6. West MD, Labat I, Sternberg H et al (2018) Use of deep neural network ensembles to identify embryonic-fetal transition markers: repression of COX7A1 in embryonic and cancer cells. Oncotarget 9(8):7796–7811
7. Chen B, Li C, Qin H et al (2018) Evaluation of typhoon resilience of distribution network considering grid reconstruction and disaster recovery. Autom Electr Power Syst 42(6):47–52
8. Bains M, Warriner D, Behrendt K (2018) Primary and secondary care integration in delivery of value-based health-care systems. Br J Hosp Med 79(6):312–315
9. Yin Q, Duan B, Shen M et al (2019) Intelligent diagnosis method for open-circuit fault of sub-modules in modular five-level inverter. Autom Electr Power Syst 43(01):162–170
10. Śniegocki M, Nowacka A, Smuczyński W et al (2018) Intramedullary spinal cord metastasis from malignant melanoma: a case report of a central nervous system secondary lesion occurred 15 years after the primary skin lesion resection. Postepy Dermatol Alergol 35(3):325

Research of Scheme for Mapping Between Virtual and Real Link and Fault Diagnosis in Smart Substation Based on SPCD

Geng Li, Dan Rao, Jia Li and Rui Fan

Abstract Aiming at the problem that description of physical link information in SCD file is blank and physical link cannot be quickly located by alarm information of virtual link failure in operation and maintenance of substation, this paper proposes to extract physical link information from SPCD file, extend physical link model in SCD model, and construct mapping between virtual-real link in smart substation. This paper provides technical support for the visualization of physical circuit of substation and a feasible scheme for fast fault location.

Keywords Smart substation · SCD · SPCD · Physical link · Mapping between virtual and real link

1 Introduction

Smart substation, based on IEC61850, is able to transmit signal between secondary devices using optical cable and can replace electric cable [1]. This transmission changes from a single signal transmitted by electric cable to a multi-channel signal transmitted by optical cable [2]. Smart substation uses SCD to describe virtual secondary circuit [3],currently many tools can provide visual capabilities for virtual secondary circuit by using SCD. Engineers can view virtual secondary circuit intuitively [4, 5]. But the mapping between real circuit and virtual circuit cannot be achieved from SCD, and SCD configure tool lacks the data source which can show the mapping between virtual and real link. So, engineers cannot achieve virtual link information from an optical cable, and the physical links one virtual link passes, which is not favorable to check the errors during maintenance of substation [6–9].

G. Li (✉) · D. Rao · J. Li · R. Fan
NARI Technology Co. Ltd., Nanjing 211106, China
e-mail: 540343693@qq.com

G. Li · D. Rao · J. Li · R. Fan
State Key Laboratory, Smart Grid Protection and Control, Nanjing 211106, China

Y. Xue et al. (eds.), *Proceedings of PURPLE MOUNTAIN FORUM 2019-International Forum on Smart Grid Protection and Control*, Lecture Notes in Electrical Engineering 585, https://doi.org/10.1007/978-981-13-9783-7_36

In recent years, many papers have provided solutions and application which can realization of virtual-real link mapping in smart substation. Paper [10] provides a method of mapping virtual and real link, but the real link contains only real link between Intelligent Electronic Device. Though capacitance is realized easily, the real link information is only one part of the whole, lacking region, cubicle, Optical Distribution Frame (ODF) and other physical nodes, when these physical nodes have errors, it will also lead to virtual link's error warning. The physical link in paper [11] contains region, cubicle, ODF, etc, but in order to realizing virtual-real link mapping, this solution searches a variety of devices including device, ODF, switch, its link contains fiber connection in the cubicle and fiber connection out the cubicle. the connections are seriously complex, and includes too many devices, so it is high computational-complexity, and is not working well in terms of convergence. Papers [12, 13] uses SPCD to construct mapping relations between virtual and teal link, and based on this it establishes the topological relations between switch port. It can generate automatically static multicast table or VLAN configuration table in switch. But in real project, normal procedures are first letting SCD contain relation between devices, and based on SCD to extracting switch configuration information so as to achieve switch auto configuration. Papers [12, 13] provides a solution which is only based on SPCD to determine relation between devices, it does not provide supplementary information about relations between devices in SCD. When reformatting and extending, if integrator's configuration tool only supports regular practices, it will have to reconfigure SCD [14], so adding the amount of work heavily when reformatting and extending.

Our paper provides a scheme for mapping between virtual and real link in smart substation based on SPCD, which will first extract the physical link information from SPCD files, and establish mapping relational table between Cable element in SCD and physical link. It enables SCD contains the whole physical circuit information, and later using "Cable Automatic Search Algorithms" in our paper to shield new physical nodes and types of link in SPCD and establish mapping between virtual and real link in smart substation. Our solution not only ensures the integrity in physical link, containing region, cubicle, skip fiber, ODF, etc; but also when deducing real link based on virtual link, it can shield part of the physical node information, ignore type of connection, reduce the complexity of algorithm.

2 Basic Principles and General Ideas

The secondary circuit of the intelligent substation is composed of a real circuit and a virtual circuit [15–18]. The real loop is the physical medium that implements the virtual circuit transmission, and the virtual circuit is transmitted on the real circuit. "Technical Specification for Modeling and Coding Fiber Circuit in Smart Substation" proposes a fiber optic physical loop model file (SPCD file). The SPCD

file describes the two parts of the physical link information. The first part describes the relationship of the physical object and the hierarchical, including the small room, the screen cabinet, the device, the switch and the optical fiber distribution frame; the other part describes the relationship of the fiber connection, including the optical cable, the pigtail, the skip fiber and so on. Through the information of SPCD file, a complete physical loop (real loop) can be constructed.

The SCD model actually contains the information about the physical loop. The SCD model describes the physical port information about the device through the PhysConn. The PhysConn description is as follows:

```
<PhysConn type="Connection/RedConn">
      <P type="Plug">ST</P>
      <P type="Port">1-A</P>
      <P type="Type">FOC</P>
      <P type="Cable">LINE1</P>
</PhysConn>
```

The child element whose type attribute is “Cable” (hereinafter referred to as the Cable element) indicates the virtual cable number to which the physical port is connected. IEC61850-6 states that two PhysConns with the same Cable element have a physical connection [19]. The Cable element indicates the port-to-port connection relationship, but the connection relationship is a virtual connection relationship. because the actual physical link between the port and the port may pass through physical nodes such as a region, cubicle, and ODF, and they have directionality. Therefore, the scheme extracts the complete real loop information from the SPCD file and establishes a mapping table between the Cable element and the real loop model, so that the Cable element can not only represent the port-to-port connection relationship between the devices, but also includes the real-loop information between the ports and the ports.

The bay level network and the process level network of the intelligent substation usually adopt a star network structure, which determines the uniqueness of the physical path corresponding to the virtual circuit between the secondary devices. The SCD file mainly describes the logic loop (virtual loop) between the secondary devices. By using the Cable automatic search algorithm proposed in this scheme, the mapping relationship between the Cable element and the virtual link can be constructed. The virtual and real link mapping relationship can be finally realized by the established mapping table of Cable element and the real loop. The implementation process of this solution is shown in Fig. 1.

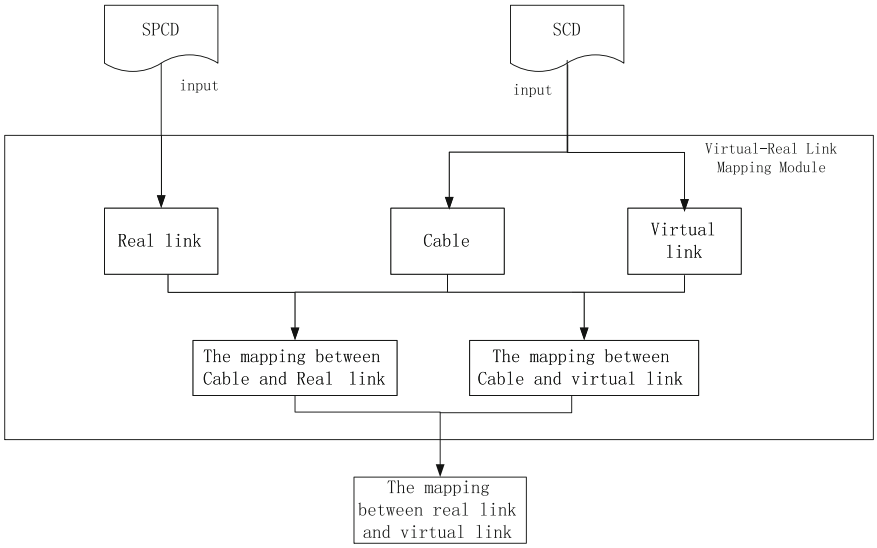

Fig. 1 The scheme of mapping between virtual and physical link

3 SCD Physical Link Modeling

3.1 Physical Node Information Encoding

A physical link refers to all physical node information that a signal passes through a port of one device (IED) to a port of another device (IED or switch). In a substation, a complete physical link must have many physical nodes, such as: fiber jumper, optical port, optical cable, device receiving port, and device sending port. The SPCD file is an XML format file. to conveniently query the location and connection relationship of the physical node,the physical nodes are encoded by using the elements in the SPCD. The elements and their attribute in the SPCD file are shown in Table 1.

The specific encoding methods of each physical node are as follows:

(1) Fiber: IntCore number.
(2) Optical Distribution Frame port: Optical Distribution Frame name. layer number. port number-direction. Among them, the number of X layers of ports per layer should be used in the name of optical matching, so that the total number of ports of optical matching can be queried easily.
(3) CABLE fiber optic: serial number of fiber core@ IN total number of fiber core@ optical cable number. It is easy to find out which fiber core is in the cable and how many fibers are in the cable.
(4) Tx port of device/switch: region number. cubicle number, IED name, board number, port number-Tx.

Table 1 Definite of element and attribute in SPCD

Element	Description	Attribute	Attribute explanation
Substation	Substation	name	Name
		desc	Description
		gridName	Grid
		areaName	Region name
		voltage	Voltage level
Region	Region	name	Name
		desc	Description
		area	Switch field identification
Cubicle	Cubicle	name	Name
		desc	Description
Unit	Device	name	Name
		desc	Description
		iedName	Device name
		manufacturer	Manufacturer
		type	Equipment model
		class	Including IED\ODF\ switches etc.
Board	Board	slot	Board identifier
		desc	Board description
		type	Board type
Port	Port	no	Port group number
		desc	Port description
		direction	Port direction (Tx/Rx)
		plug	Interface Type
		usage	Port function description
IntCore	Fiber connection in the cubicle	name	Skip fiber/twisted pair identifier
		portA	Path of the A port to which the skip fiber/twisted pair is connected
		portB	Path of the B port connected to the skip fiber/twisted pair
		type	Skip fiber type
Cable	Fiber connection out the cubicle	name	Physical cable identifier
		desc	Describe physical cable information
		length	Physical cable length
		coreNum	Number of physical cable cores
		cubicleA	Path of the A cubiclet connected to the physical cable
		cubicleB	Path of the B cubicle connected to the physical cable
		type	Physical cable type
Core	Core of optical cable out the cubicle	no	Cable core serial number
		reserve	Spare core identification
		portA	Path of the A port connected to the cable core
		portB	Path of the A port connected to the cable core

(5) Rx port of device/switch: region number. cubicle number, IED name, board number, port number-Rx.

3.2 Two-Way Physical Link Information Modeling

The physical link information described in the SCD is not directional, and the substation physical link is actually composed of two unidirectional links with opposite directions. When the same port of the same device transmits and receives signals, the transmitted signals pass through two different unidirectional links. A port of the device is composed of a transmitting port and a receiving port, and is respectively used as a transmitting port of one unidirectional link and a receiving port of another unidirectional link. Therefore, in order to describe the physical link more accurately, this paper uses a two-way modeling approach to describe the physical link.

The physical link information is modeled by the physical object information in the SPCD file, and the physical link information modeling rules includes two cases:

(1) Case of ODF: device/switch Tx port number@ skip fiber number@ ODF port number: cable number: ODF optical port number@ skip fiber number@ device/switch Rx port number.
(2) Case of no ODF: device/switch Tx port number@ skip fiber number@ device/switch Rx port number.

3.3 Establishing a Physical Link Model and Cable Mapping Table

In many old substations, the value of the Cable element in the SCD model may be empty, which makes it impossible to obtain the connection relationship between device ports through the SCD. Therefore, we need to first check if the SCD's Cable element is empty. If it is empty, we need to assign a value to the Cable element. A child element whose type attribute is "Port" (Port element) indicates the physical port name, which is usually composed of a board number and a port number. The port name in the SCD is the same as that in the SPCD. Therefore, the mapping between the Cable element and the physical link information can be established by using the port name. The specific implementation methods of the physical link model and the cable mapping table are described as follows.

First, the two-way physical link model is sequentially added with sequence number according to the extraction order, and the serial number is encoded as: "cable" + No (No = "1, 2, 3, 4 …"). Then, according to the device port name in the physical link information, the PhysConn element is retrieved in the SCD model.

When the Port element of the PhysConn node is consistent with the port information in the physical link information, the Cable element of the PhysConn node is extracted, if the Cable element is Empty, assign the physical link sequence number to the Cable element. If it is not empty, replace the Cable element value by the sequence number in the physical link model.

After the above method, a mapping table between the Cable element and the bidirectional physical link information is established, and expanded into the SCD model. The physical link model and the cable mapping table are in XML format, and the specific description is as follows:

```
<ExtSPCD:PhysLinks>
  <PhysLink No="cable1">
    < LinkDesc >  R01.C10.PL1101.801S-2.B-Tx@TX015@1-50n(4X8).F.B-
RT:1@IN12@CABLEGL-1B-11:1-50n(12X4).A.A-
RT@Tx019@R01.C17.ML1101.B01.C-Rx
    </LinkDesc >
    <LinkDesc >
  R01.C17.ML1101.B01.C-Tx@Tx018@2-50n(12X4).A.A-RT:2@IN12@CABLE
GL-1B-11:  2-50n(4X8).F.B-RT@TX016@R01.C10.PL1101.801S-2.B-Rx
    </LinkDesc >
  </PhysLink>
  <PhysLink No="cable2">
  <LinkDesc>.....</LineDesc>
  <LinkDesc>.....</LineDesc>
  </PhysLink>
 </ExtSPCD:PhysLinks >
```

The “PhysLink” element in the mapping table represents a two-way physical link information, and the two sub-elements “LinkDesc”respectively describes the physical link with one direction, and the No attribute of the PhysLink element is consistent with the Cable element of the SCD model. By extending this table in the SCD file, the mapping relationship between the Cable element and the physical link information is established.

4 Cable Automatic Search Algorithm

Through ExtRef elements, SCD file describes the virtual ends connection relationship between units. In 《Q/GDW 1396-2012 Data Model of Protection Relay in Project Based on IEC61850》 ruled to increase the description of physical port in receiving end at “intAddr” attribute of “ExtRef” elements. As follows:

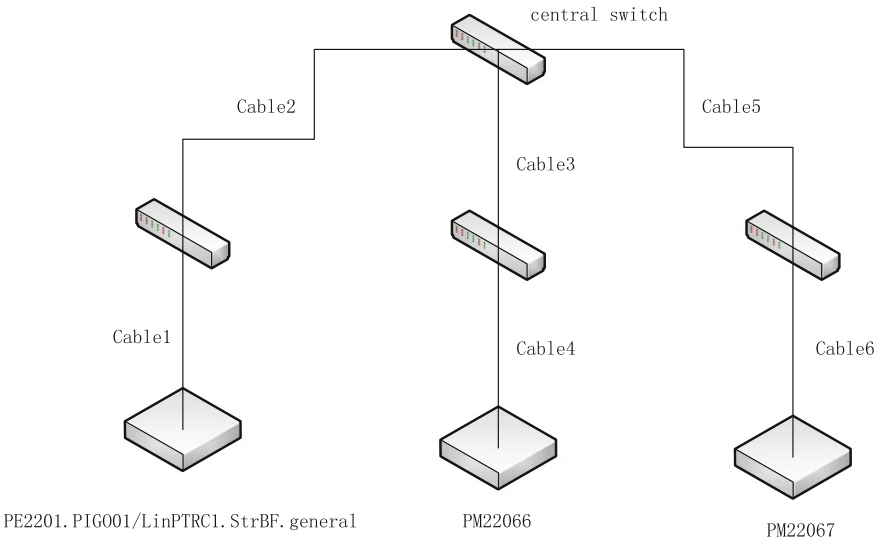

Fig. 2 The mapping between cable and virtual link

<ExtRef iedName="CB5012A" lnInst="1" ldInst="CTRL" lnClass="GGIO" doName="Ind" daName="stVal" prefix=" " intAddr="1-A:CTRL/gseGGIO0.SPCSO.stVal"/>

"1-A" means receiving end number, increasing physical port in virtual end defination, use this physical port as the link to connect virtual link and physical link build the scheme of mapping between virtual and physical link.

There are two ways to connect devices in a substation. First one is a point to point. It's an easier method to use. It means between each device use the straight communication way to connect each other. The second way is network mode. This method means the communication between devices were transmit through switch. Under this method, virtual circuit paired multiple Cable elements (As shown in Fig. 2). Cable1-Cable2-Cable3-Cable4 is the only physical way from virtual end PE2201.PIGO01/LinPTRC1.StrBF.general to PM22066.

The Cable auto search arithmetic that was presented in this paper use receiving end as the start point through the backtracking method to search all Cable elements virtual end passed from virtual end to sending end. Figure 3 shows how this method realized.

(1) Build a blank Cable element station.
(2) According to receiving end number and its' paired Cable element in virtual end definition to obtain the type of offside equipment and port number. Record this Cable element in Cable element station. Follow step 3.
(3) Judge the type of offside equipment. If it is IED unit follow step 4. If it is switch, follow step 5.

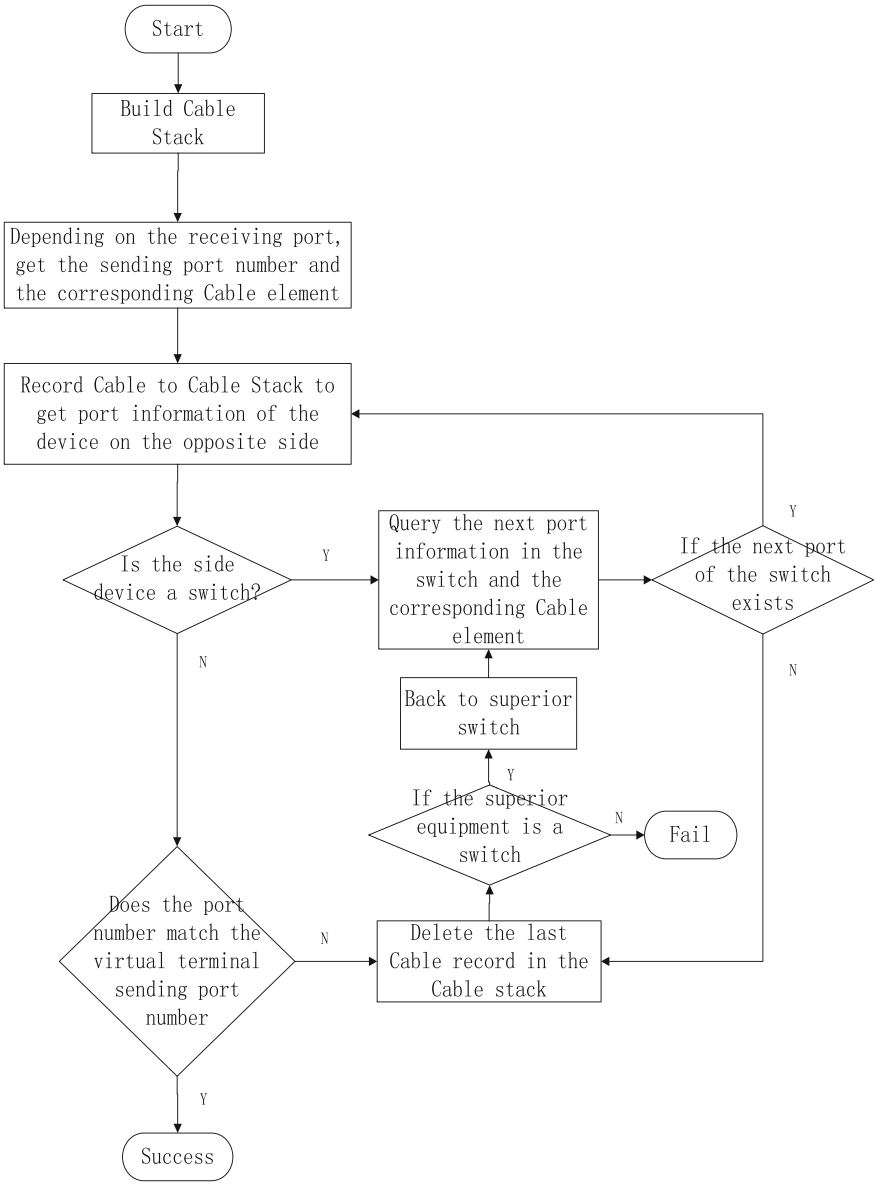

Fig. 3 Flow chart of cable automatic search

(4) Judge offside unit name and port number are the same as sending unit and port number in a virtual link or not. If the information is consistent then searching finished. If the information is not consistent, delete the last record information

in Cable element station then back to superior equipment. If the type of superior equipment is switch then follow step 5. If the type of superior equipment is IED equipment then mapping was failed and finish searching.

(5) Judge is there still have the not found port.

If not, delete the last record information in Cable element station then back to superior equipment. If the type of superior equipment is switch then follow step 5. If the type of superior equipment is IED equipment then mapping was failed and finish searching.

If yes, obtain other not found port and Cable element of switch. According Cable element, obtain offside equipment and port again and record Cable element in Cable element station then follow step 3.

5 Troubleshooting and Positioning

When a communication failure occurs, the receiving device cannot receive the GOOSE/SV signal normally, and sends link alarm. The link alarm indicates that there is a fault point on the process level network. Through the third chapter of this paper, all the physical nodes that the virtual link passes through have been obtained, including the above-mentioned nodes that may be faulty. Based on this set, it is easy to exclude non-fault points and confirm the specific location of the fault point.

First, according to the virtual link interruption alarm signal, query a set of physical nodes for the virtual link, for example, an alarm link between the protection device and the intelligent terminal, it's corresponding physical link set is {Cable1-Cable2}. And then, find the physical nodes by physical link set.

By comparing the physical nodes passed the normal virtual link with the physical nodes passed the alarm virtual link, if there is a cross path (the same physical node), the physical path of the intersection is normal. According to this way, the non-fault point can be effectively eliminated, the set of fault points can be minimized.

6 Implementation and Application

In practical application, when communication abnormality occurs in intelligent substation, if the protection device reports a virtual link interruption, substation operation and maintenance personnel use the virtual-real link visualization interface and search function of the system configuration tool to quickly find out all the real links through which the virtual link passes. Among them, if part of the virtual link corresponding to a real link has not reported interruption, it means that the real link has no problem, if all virtual links in a real link are interrupted, it means that the real

link is the fault point. Through this method, operation and maintenance personnel can quickly locate the fault point.

At the same time, based on the mapping relationship between virtual and real links, the developed substation system configuration tool can directly export switch CSD files without manual configuration, which improves the field work efficiency and reduces the probability of error. When rebuilding and expanding, engineers only need to care about the connection relationship of new equipment, which greatly reduces the workload of rebuilding and expanding.

7 Conclusion

This paper presents a virtual-real link mapping scheme for Smart Substation Based on SPCD. The complete physical circuit model is extended to SCD, and the mapping relationship between virtual and real links in intelligent substation is constructed. In order to study the condition monitoring and fault diagnosis of secondary equipment in intelligent substation, a feasible scheme is provided. This scheme models design information, it reduces the dependency on secondary drawings for intelligent station operators. It helps to improve the efficiency of operation and maintenance, reduces the cost of operation and maintenance, it provides data support for advanced applications such as secondary devices operations and debugging.

References

1. Wang Z, Dou Q, Wang X et al (2014) A construction-drawing design expression method of secondary system for smart substation. Autom Electr Power Syst 38(6):112–116
2. Liu W, Du L, Yang Q (2014) Research and application of smart substation virtual circuit visualization. Adv Power Syst Hydroelectr Eng 30(10):32–37
3. Zou X, Wang H, Wu X (2006) Discussion on practical issues of substation configuration language in IEC 61850 standards. Autom Electr Power Syst 30(15):77–80
4. Wang Z, Chen J, Ren Y et al (2010) Application of network communication recorder and analyzer in digital substations. Autom Electr Power Syst 34(14):92–95
5. Xu W, Zhang L (2010) Digital substation network communication line diagnosis system. Electr Power Autom Equip 30(6):121–124
6. Gao L, Yang Y, Liu Y et al (2015) Proof table based fault location method for process level channel in smart substations. Autom Electr Power Syst 33(4):147–151
7. Gao X, Yang Y, Jiang J et al (2014) Analysis of secondary circuit monitoring methods based on SCD. Power Syst Prot Control 42(15):149–154
8. Zhou C, Wu H, Hu G et al (2017) Non-intruding development of automatic test system based on IEC 61850 edition 2.0. Power Syst Prot Control 45(14):143–147
9. Luo L, Peng Q, Wang D et al (2018) Monitoring method of process level network in smart substation. Autom Electr Power Syst 42(11):151–156
10. Xu P, Dai B, Zhang C et al (2015) Research of mapping between secondary virtual and physical link and intelligent diagnosis method. Distrib Util 32(12):39–45

11. Gao L, Yang Y, Su L et al (2016) A modeling approach and design implementation of secondary system physical circuit for smart substation. Power Syst Prot Control 44(24): 130–139
12. Li P, Shan Q, Yang S et al (2018) Research and application of static multicast table automatic generation technology of process layer switch in smart substation. Zhejiang Electr Power 37 (7):43–48
13. Li P, Fan W, Wang G et al (2018) Research and application of VLAN configuration tables automatic generation technology in smart substation. Electr Power Eng Technol 37(1):122–129
14. Li J, Hu R, Wang L et al (2018) Engineering configuration scheme based on IEC 61850 ed 2.0 in smart substation. Autom Electr Power Syst 42(2):154–159
15. Q/GDW 383-2009 (2009) Technical guide for smart substation. State Grid Corporation of China, Beijing
16. Zhang Q, Jia H, Ye H et al (2015) Design and application of virtual secondary circuit monitoring in smart substation. Power Syst Prot Control 43(10):123–128
17. Yang Y, Gao X, Zhu H et al (2015) Case study on SCD application based on demo smart substation. Power Syst Prot Control 43(22):107–113
18. Hao S, Li Y, Zhang T et al (2017) Scheme of communication network and network management system for new generation smart substation. Autom Electr Power Syst 41 (17):148–154
19. IEC 61850-6 (2008) Communication networks and systems for power utility automation: part 6 configuration description language for communication in electrical substations related to IEDs

A Chromatographic Recognition Algorithm Based on Adaptive Threshold in Substation

Gaoming Wang, Gangqiang Xia and Qingwei Zhang

Abstract According to the requirement of gas chromatography identification in transformer oil of substation, an adaptive threshold chromatographic identification algorithm is designed. Traditional first derivative method only uses slope threshold to recognize chromatographic peaks, so the degree of automation is low and it is easy to be distorted. In view of these shortcomings, this paper improves the first derivative method. Based on the data pre-processing and peak identification algorithm, the appropriate threshold is determined, and the peaks are identified by combining the peak curves and the characteristics of the standard gas. Since the threshold parameter of the algorithm can be fixed, the overlapping peak detection is less affected by human influence, and further improves the accuracy of chromatographic identification.

Keywords Chromatographic peak identification · Threshold parameter · Overlapping peak detection

1 Introduction

At present, most of the peak recognition algorithms used in oil chromatography include time window method [1, 2], curve fitting method [3], pattern matching method [4], derivative method and so on. Conventional algorithms have the following shortcomings in the peak identification process. The peak shape of the chromatographic peak changes with time, and it is easy to introduce false peaks. Based on the text [5–7], combined with the characteristics of dissolved gas chromatography in power transformer oil, the maximum half-width is used as the reference for the sliding window width setting, and the appropriate threshold is added in the peak identification process, which can better remove the spurious peaks and greatly improve the detection accuracy of overlapping peaks.

G. Wang · G. Xia · Q. Zhang (✉)
Nari Technology Development Limited Company, Nanjing 211106, Jiangsu, China
e-mail: wanggaoming@sgepri.sgcc.com.cn

Y. Xue et al. (eds.), *Proceedings of PURPLE MOUNTAIN FORUM 2019-International Forum on Smart Grid Protection and Control*, Lecture Notes in Electrical Engineering 585, https://doi.org/10.1007/978-981-13-9783-7_37

2 Spectral Peak Identification Algorithm Based on Adaptive Threshold

2.1 Smoothing

The analog signal output from the chromatograph detector is converted to a digital signal by an analog-to-digital converter, and the digital signal is input to a computer through an interface circuit. These signals are often accompanied by high frequency noise, so the input signal needs to be filtered before the peak detection. In this paper, the extracted chromatographic data is filtered by depolarization averaging filtering and point-by-point slope.

First, the original data is filtered by the average value of the moving window, and then the filtered data is sloped point by point, and then the above steps are repeated. After two filtering and two slopes, a relatively smooth signal curve is obtained.

The specific implementation step is that the extremum averaging filtering divides the consecutive M number of sampling points into N equal parts, and then performs depolarization averaging filtering on each aliquot, and takes the filtering window size K*2 each time. Then the data is bubbled and sorted to remove the J number of extreme values, and finally the average is used to obtain new data.

The method of finding the slope point by point is to divide the continuous number of M sampling points into a number of N equal parts, and then perform point-by-point subtraction in each aliquot, that is, subtract the previous point from the previous point. Finally, the subtracted data is rearranged to obtain new data.

2.2 Find the Peak

The peak is divided into two parts. The first step is to find all the peaks, and the second step is to remove the peaks that do not meet the conditions specified by the fixed values.

First, the smoothed data is operated, and the minimum peak slope value (MinPeakSlope) is set, and divide the smoothed data into a number of m windows, each window containing the number of n data. When the data in the window satisfies the condition ($0 < \text{MinPeakSlope} < h_1 < h_2 \cdots < h_n$), it is judged that h_1 is the starting point of the peak at this time. Continue to move the window, when the data in the window meets the condition ($h_1 < \cdots < h_{m-1} < h_m > h_{m+1} > \cdots > h_k$, and $h_k < h_{k-1} \cdots < h_{m+1} < (-0.1)$), it is judged that h_m is the apex of the peak. Continue to move the window, when the data in the window satisfies the condition ($h_1 < h_2 \cdots < h_n < (0 - \text{MinPeakSlope}) < h_{n+1}$), it is judged that h_{n+1} is the end point of the peak at this time.

After all the peaks are found, the operation of eliminating clutter peaks is carried out, and the minimum peak height (MinHeight), minimum peak area (MinArea) and

minimum half-peak width (fMinHalf Width) are set. Then, the peak identification parameters of all peaks are calculated and compared with the set values. Only when these conditions are met at the same time is the required peak.

2.3 Adjust the Start and End Points of the Peak

After finding the desired peak, adjust the starting point and the ending point. The specific implementation is to compare the starting point and the ending point with the data in the window, and adjust the position of the starting point and the ending point appropriately by setting the condition.

2.4 Processing the Peak

For the case where the peak contains a peak, first set the minimum baseline slope (MinBaseSlop) and the maximum peak interval (MaxPeakInterval), and then calculate the slope of the identified peak and the peak width. When the slope is smaller than MinBaseSlop or the peak interval is greater than MaxPeakInterval, then Judging as a continuous peak. At this time, the starting point of the second peak is corrected to the end point of the previous peak. And then the peak height, retention time, and peak area of the continuous peak are calculated.

2.5 Qualitative and Quantitative

The calibration gas concentration is used as a reference object for quantitative and qualitative analysis of the identified peaks. First, all the peaks are arranged from small to large. Then, the maximum retention time error percentage (MaxTimeDiff) is set. The retention time of the identified peak is compared with the peak time of the calibration gas concentration. If the error in the comparison result is less than the maximum retention time error percentage (MaxTimeDiff), the peak belongs to this concentration value, so that the seven gases are sequentially identified.

The quantification process is that the identification peak is compared with the standard gas peak and multiplied by the calibration gas concentration value, and then the concentration value of each identified peak is obtained.

3 Implementation of Program

3.1 Determination of Threshold

According to the results of several tests, the required threshold settings are shown in Table 1.

3.2 Spectral Display and Algorithm Effects

According to the above algorithm and the set threshold, the seven gases dissolved in the transformer oil can be accurately identified. The spectrum is shown in Fig. 1. It can be seen that the baseline is very stable in the spectrum, and the curve noise of the peak is small. The peak height and peak area can be well calculated. In addition, the overlap peak of CO can be well detected, and the reference value of the starting point is redefined for overlapping peaks, which ensures the accuracy of recognition.

Table 1 Thresholds required based on multiple test results

MinHeight	MinArea	MinHalfWidth	MinPeakSlope	MaxTopWidth
10	100	25	0.01	100
MaxTimeDiff	MinBaseSlope	MaxPeakInterval	FltWinWidth	FltWinDead
8	3	25	16	4

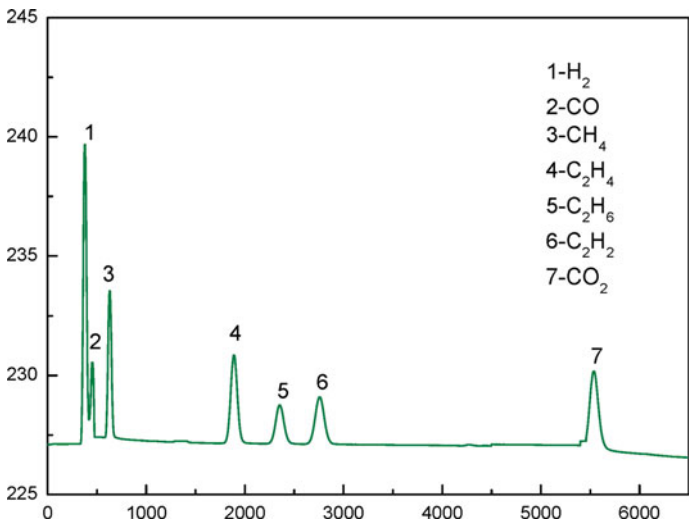

Fig. 1 The displayed spectrum according to the algorithm and the set threshold

4 Conclusion

In this paper, a threshold-based transformer chromatogram recognition algorithm is proposed. Based on the traditional slope threshold method, the algorithm adds a reasonable threshold value in the peak identification process, combined with the absolute retention time of the chromatographic peak and the peak of the peak to identify the suspected chromatographic peak. The probability of introducing false peaks is reduced, and the detection accuracy of overlapping peaks is improved. The experimental results show that the algorithm has good recognition accuracy and certain adaptive performance, which can meet the requirements of on-site online monitoring devices.

References

1. Zou S, Tong X, Qi L (2003) Development of transformer online monitoring technology. Autom Power Syst 27(25):61
2. Li H, Zhou F, Tan K (2005) Fourier infrared quantitative analysis for online monitoring of transformers. Autom Power Syst 29(18):62
3. Wei H, Lin L, Zhang Y (2013) Application of grey system theory in pattern recognition of chromatographic fingerprints of traditional Chinese medicine. Chin J Chromatogr 31(2):127
4. Liu M, Xia B, Yang J (2009) Automated chromatogram analysis—automatic identification and rapid resolution of spectral peaks. Chin J Chromatogr 27(3):351
5. Luo W, Tang L, Zhang Y (2010) Design of embedded peak recognition algorithm in portable gas chromatograph. Chin J Chromatogr 29(12):1216
6. Zhao W, Wang H, Qiu J et al (2014) Analysis of dynamic reliability of transformer based on monitoring data of oil chromatography. Autom Electr Power Syst 38(22):38–42. https://doi.org/10.7500/aeps20130802007
7. Zhang Z, Xiao D (2007) A small vacuum on-line extraction technology for the automatic chromatographic analysis of gas dissolved in insulating oil. Autom Electr Power Syst 31 (11):92–96

The State Detection Scheme of the Hard Plate in Substation Based on Hall Sensing Effect

Hao Xu, Xinjue Xia, Wenwu Liang, Fan Ouyang, Weijun Zhu, Haifeng Liu and Hui Li

Abstract The hardware platen on relay protective panels is the functional demarcation point and the blind spot of condition monitoring between protection device and the control circuit of primary equipments. Realizing the condition monitoring of the hardware platen is the basic need to promote the application of the ubiquitous internet of things in the relay protection specialty. In this paper, a method based on the Hall sensing effect is proposed to detect the state of the hardware platen in the substation, which can realize the automatic detection of the state of the hardware platen without disturbing the outlet control circuit. This paper first proposed the hall element selection scheme for hardware platen state detection, and then developed the configuration scheme of hardware platen state detection device for two kinds of the hardware platen, separated type and line spring type, designed hardware platen state detection integrated circuit, based on that an experimental platform was constructed and the validity and reliability of the proposed scheme was verified.

Keywords Hardware platen · Condition monitoring · Hall component · Layout scheme · Integrated circuit

1 Introduction

Since this year, the State Grid Co. Ltd. has begun to vigorously study and deploy the construction of the ubiquitous power Internet of things (UPIT) in order to make the operation safer, the management more lean, investment more precise and service better of the power grid. The spring breeze of UPIT has injected new vitality

H. Xu (✉) · W. Liang · F. Ouyang · W. Zhu · H. Liu · H. Li
State Grid Hunan Electric Power Co. Ltd. Research Institute, Changsha 410007, China
e-mail: 702110505@qq.com

X. Xia
Powerchina Hebei Electric Power Design & Research Institute Co., Ltd., Shijiazhuang 050031, China

Y. Xue et al. (eds.), *Proceedings of PURPLE MOUNTAIN FORUM 2019-International Forum on Smart Grid Protection and Control*, Lecture Notes in Electrical Engineering 585, https://doi.org/10.1007/978-981-13-9783-7_38

into the field of power and energy. Academia, business circles and even capital market are all eager to try. Substation relay protection tripping hardware platen is the functional dividing point between protection device and primary equipment control circuit and the blind spot of condition monitoring. The application of the UPIT in relay protection specialty is inevitable to promote the realization of real-time automatic monitoring of relay protection tripping hardware platen state. For newly built substations, intelligent platen or double contact platen can be used. However, for the alarming number of operation protective panels and their hardware platen in the whole country, the method of realizing condition monitoring by replacing hardware platen needs the cooperation of protection device and monitoring system to upgrade and reform, which has a huge workload, and it is difficult to obtain the necessary power cut time. Therefore, it is necessary to study the automatic monitoring technology of the tripping hardware platen condition on the basis of maintaining the existing structure and circuit of the protective panel and hardware platen, so as to improve the intelligent level of relay protection specialty [1–5].

Relay protection tripping hardware platen is located in the circuit breaker tripping circuit. Its operation reliability is very important to prevent the wrong operation of the circuit breaker and ensure the safe and stable operation of the system [6–10]. The condition monitoring of relay protection tripping hardware platen must be completely electrically isolated from the circuit breaker tripping circuit. Therefore, the non-contact and non-electric technology of hardware platen condition monitoring scheme is a natural and ideal choice. At present, there are two main types of the hardware platen condition detection schemes in literature and practice. One is to collect the image of the protective panel by installing cameras and detect the state of the hardware platen by gray recognition technology. The other is to install reflective coating and light source on the hardware platen and the protective panel respectively, and realize the state detection of the hardware platen by photoelectric detection principle. These two schemes are designed to realize intelligent monitoring of the hardware platen condition by equipping auxiliary components and non-electric contact technology under the existing the hardware platen structure, without introducing any interference into the exit tripping circuit, which has high safety. However, the reliability of the hardware platen condition monitoring component used in the scheme has some defects, which will be affected by the external light source, and in the meanwhile the first scheme will have some difficulties in image acquisition due to the low layout of the hardware platen.

In this paper, a method of the hardware platen state detection based on Hall sensor effect is proposed. Through the ingenious application of Hall element, the displacement change signals which occur in the process of the hardware platen operation are converted into electric signal output, and the hardware platen state detection is realized without disturbing the control circuit of the hardware platen. Firstly, Hall element selection scheme for the hardware platen state detection is proposed. Secondly, the configuration scheme of the hardware platen state detection device is designed for two types of the hardware platen: discrete type and linear spring type, and integrated circuits for the two types of hardware platen state

detection are designed. Based on this, an experimental platform is built, which verifies the effectiveness and reliability of the scheme.

2 Hall Element Selection and Its Adaptability Analysis

Hall element is a semiconductor sensor based on Hall effect. When the current passes through the conductor perpendicular to the direction of the external magnetic field, the potential difference between the two sides of the conductor body will occur in the direction perpendicular to the current and the magnetic field. This phenomenon is called the Hall effect. By measuring the Hall potential difference, and the magnetic field passing through the Hall element can also be detected.

Hall components are divided into two categories: switch-type and linear form. The output voltage of switch-type Hall element varies step by step with the input magnetic field density, and the output voltage of linear Hall element varies linearly with the input magnetic field density. Considering that the platen state itself is a Boolean logic variable, it is obviously more appropriate to select switch-type Hall element to detect the pressing state. According to the different induction modes, switch-type Hall elements can be further divided into four types: monopolar, bipolar, bipolar latch and omnipolar. This paper chooses a monopole Hall switch to trigger the Hall element when the magnet is close to it, and restore the Hall element when the magnet is far away, so as to realize the detection of the state of the hardware platen. Hall potential difference can be calculated by the following formula:

$$U_H = R_H \cdot I \cdot B/d \tag{1}$$

In the formula, R_H is the Hall coefficient, which is related to the material of the conductor; d is the thickness of the Hall element; I and B are the current and magnetic induction intensity passing through the Hall element, respectively. It can be seen from (1) when other conditions are fixed, different magnetic induction intensity can make Hall switch output different states. When Hall effect is used to detect the state of the hardware platen, magnets and Hall elements are respectively arranged on the back of the platen connector and the corresponding parts of the protective panel. Among them, the magnet generates magnetic field, and Hall element acts as a magnetic field detection device to induce the magnetic field intensity produced by the magnet. The protective hardware platen includes two types: discrete type and line spring type. They are quite different in structure and operation mode, and need to be treated differently.

2.1 State Detection Scheme of the Separate Hardware Platen

Figure 1 shows the installation diagram of the separate hardware platen state detection device. In the figure, the magnet is installed on the back of the platen connector, which is magnetophilic metallic texture. The magnet can be directly pasted on the back of the platen connector, or can be reinforced by glue. The Hall element is installed in the middle position of upper and lower pillars of the hardware platen on the protective panel. The distance between the magnet and the Hall element when the magnet moves vertically from the distance to the Hall element changing the Hall switch from off state to on state is defined as the trigger distance of the Hall element, and the distance between the magnet and the Hall element when the magnet moves vertically away from the Hall element from the near place changing the Hall switch changes from on state to off state is defined as the release distance of the Hall element. In order to avoid the state jump of Hall switch caused by small disturbance, the release distance of Hall switch is generally required to be greater than the trigger distance. There are many hardware platens on each protective panel, and magnets and Hall switches are required for each hardware platen. In order to ensure reliable operation and return of Hall element and avoid mistriggering of Hall element caused by adjacent magnets, the triggering distance and release distance of Hall element can be determined by the following formula:

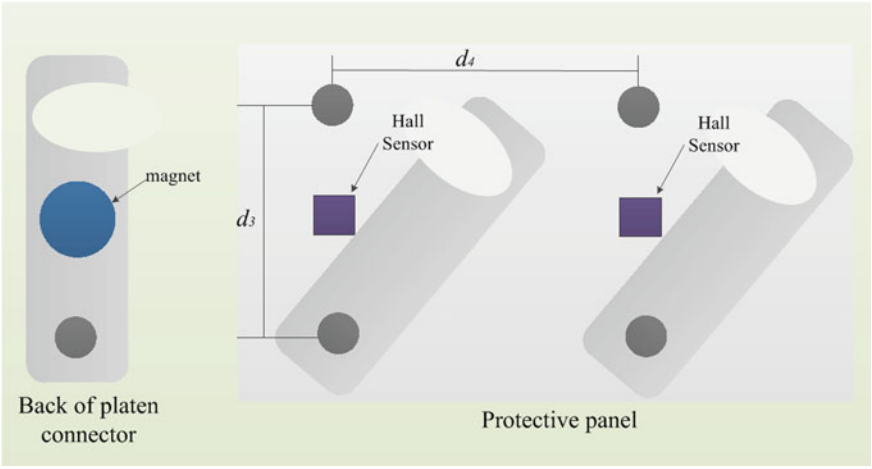

Fig. 1 Discrete strap state detect device installation diagram

$$\begin{cases} \min\left(k_2 \cdot D_{f1}, D_{f2}\right) > D_{sf} > D_{cf} > k_1 \cdot D_h \\ s.t.\ \ D_h = D_0 - D_1 - D_2, \\ k_1 = \sqrt{(D_0 + \Delta d)^2 + (d_3/2)^2} \Big/ D_0, \\ \sqrt{(D_0 + \Delta d)^2 + (d_3/2)^2} \Big/ D_{f1} < k_2 < 1, \\ D_{f1} = \sqrt{(D_0 - D_1 - D_2)^2 + \left(d_3 \sin\left(\theta_f/2\right)\right)^2}, \\ D_{f2} = \sqrt{(D_0 - D_1 - D_2)^2 + \left(d_4 - d_3 \sin\theta_f/2\right)^2 + \left(d_3/2 - d_3/2 \cdot \cos\theta_f\right)^2} \end{cases} \tag{2}$$

where D_{cf} is the trigger distance of the Hall element; D_{sf} is the release distance of the Hall element; D_h is the distance between the Hall element and the corresponding magnet when the hardware platen is of on state; D_{f1} is the distance between the Hall element and the corresponding magnet when the hardware platen is of off state; $k_1 > 1$, is the trigger coefficient of the Hall element, mainly considering the distance error caused by incomplete confinement of the lower-end nut of the hardware platen and the incomplete closure of the hardware platen with the upper-end support; Δd is the width of the hardware platen; D_{f2} is the distance between magnet and adjacent the hardware platen Hall element when the hardware platen is of off state; k_2 is less than 1, which is the release coefficient of Hall element, mainly considering the reliable release of Hall element when the hardware platen exits; D_0 is the vertical distance between the connecting plate and the protective panel when the connecting nut is fastened; D_1 is the thickness of Hall element; D_2 is the thickness of magnet; θ_f is the angle at which the joint rotates from on state to full farthest end.

Because of the narrow platen connector, the cross-section area and size of the magnet should not be too large, and the diameter should be less than the width and thickness of the platen, and the smaller the better. But even with the strongest magnetic material, the magnetic field can not be strong enough to trigger Hall switch when the hardware platen is in place in such a small size; moreover, from the point of view of large-scale application, magnets should be more common products in the market, which is cheap. Table 1 shows the magnetic characteristics of common Hall switches at two voltage levels. After measurement, the vertical distance between the platen connector and the protective panel is about 1 cm, that is, the Hall elements shown in Table 1 can not trigger the Hall switch when the hardware platen is put into on state. Therefore, in order to ensure the reliable triggering of Hall element, it is necessary to pad the Hall element to reduce the vertical distance between magnet and Hall element. The triggering distance and release distance of Hall element can still be determined by formula (1) with the increase of the thickness of magnetic field detection device.

Table 1 Magnetic properties of common hall elements

Hall component model	Test voltage (V)	Trigger distance (cm)	Release distance (cm)
SR13A	12	0.1	0.2
	24	0.4	0.6
SR13C	12	0.3	0.3
	24	0.7	0.8
SR13D	12	0.4	0.45
	24	0.7	0.9
SR13F	12	0	0
	24	0.3	0.35

2.2 *State Detection Scheme of Line Spring Hardware Platen*

Figure 2 shows the installation diagram of the state detection device of the wire spring hardware platen. The platen connector of the wire spring hardware platen is connected with the protective panel in the central part. Therefore, the magnet is considered to be installed at the top of the platen connector. The top of the spring-type the hardware platen is made of plastic material, which is not magnetophilic. The magnet can be embedded in the plastic shell of the platen connector, and the Hall element is still positioned directly below the magnet when the hardware platen is closed, and its action mechanism is the same as that of the separate hardware platen. The trigger distance and release distance of Hall element can be formulated as:

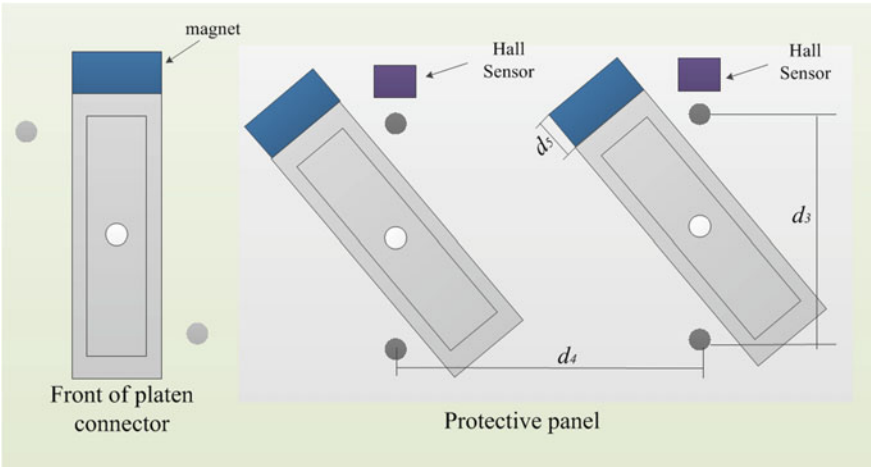

Fig. 2 Wire spring Structure strap state detect device installation diagram

$$\begin{cases} \min\left(k_4 \cdot D_{f3}, D_{f4}\right) > D_{sf} > D_{cf} > k_3 \cdot D_h \\ s.t.\ \ D_h = D_0 - D_1 - D_2, \\ D_{f3} = \sqrt{(D_0 - D_1 - D_2)^2 + \left((d_3 + d_5)\sin\left(\theta_f/2\right)\right)^2}, \\ D_{f4} = \sqrt{D_h^2 + \left(d_4 - (d_3 + d_5)\sin\theta_f/2\right)^2 + \left((d_3 + d_5)\left(1 - \cos\theta_f\right)/2\right)^2} \end{cases} \tag{3}$$

In the formula, D_{f3} is the distance between the Hall element and the corresponding magnet when the hardware platen is of off state; D_{f4} is the distance between the magnet and the Hall element adjacent to the hardware platen when the hardware platen is of off state; k_3 and k_4 are the reliability factors, because the position of the wire spring hardware platen is fixed, and $k_3 > 1 \cap k_4 < 1$ can meet the actual requirements. In order to ensure the reliable triggering of Hall element, the thickness of magnetic field detection device should be increased when detecting the state of wire spring hardware platen, just like the separate hardware platens.

3 Integrated Circuit Design for Hall Switch

Hall switch integrated circuit integrates Hall elements, amplification circuit and trigger circuit, and Hall effect is used to convert the variable magnetic flux density into electrical signal. After amplification, the trigger circuit is transformed into digital signal output. The Hall switches shown in Table 1 are all of three leads. Based on the conventional Hall integrated circuit structure, this paper designs the Hall switch integrated circuit diagram shown in Fig. 3. The output voltage of DC accumulator group in substation secondary system provides 24 V voltage power supply for magnetic field detection device. The positive pole of power supply is connected to the input end of Hall element through resistance R1 to provide current I for Hall element. This current exists all the time. Formula (1) shows that once a magnetic field with a certain magnetic field intensity crosses Hall element in space, Hall element will output Hall potential E_h. The illustration shows that the Hall element has only three leads. The power supply voltage and the Hall potential share a ground potential. The output of the Hall element is connected to the base of the transistor. Triode can play a dual role of switching and amplifying. When the Hall element has no Hall potential output, it is equivalent to the Hall element output terminal open circuit. The power supply voltage is directly added to the base of the transistor through R1 and R2, so that the transistor works in a saturated state. The collector and emitter of the transistor are turned on, and the OC gate circuit outputs a low level of about 0.2 V. When the Hall element has Hall potential output, the base potential is clamped because of the small Hall potential. The transistor operates in the cut-off state. The collector and emitter of the transistor are disconnected. The OC gate circuit outputs a high level, i.e. 24 V power supply voltage. The upper computer indirectly monitors the switching/withdrawing state of the hardware platen by detecting the output level of the OC gate circuit.

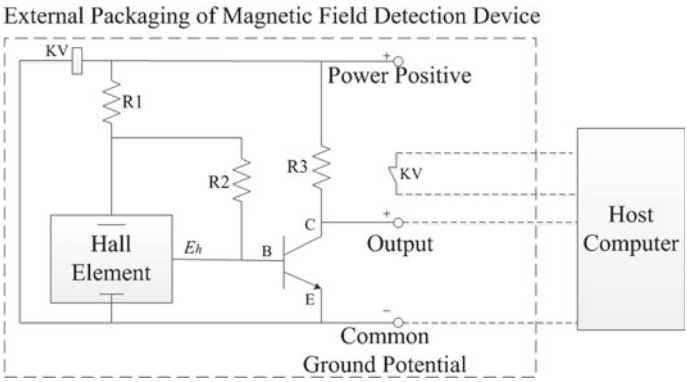

Fig. 3 Circuit design of magnetic field detection device

Each hardware platen detection device outputs two signals to the upper computer, uploads the output level of OC gate and the KV contact state along the way. KV is a power supply voltage monitoring relay. Its auxiliary contact is usually open. Voltage disturbance traversing ability of the hardware platen detection device is strong, which is mainly manifested in two aspects: firstly, the conduction voltage of triode (VBE) is low, about 0.75 V, far less than the power supply voltage, and when the power supply voltage fluctuates, it can also ensure that the triode is in the conduction state when Hall component does not output Hall potential; secondly, the output voltage is close to zero when the hardware platen is of on state, and the output characteristics of the switching withdrawing state are obviously different. Therefore, in order to ensure that the voltage disturbance does not affect the normal operation of the hardware platen detection device, the sensitivity of the power supply voltage monitoring circuit should not be too high, and the accurate response can be made when the power supply voltage disappears. The upper computer receives the feedback signal of the power supply monitoring loop and the output level signal of the OC gate circuit at the same time. When the power supply voltage disappears, it alarms in time. The detection results of the hardware platen detection device are not available, and vice versa.

As can be seen from Fig. 3, a set of magnetic field detection devices uses fewer components, including only one Hall element, one triode and three resistors, and the hardware cost is low. On the one hand, the protective panel is equipped with multiple hardware platens. Correspondingly, a number of hardware platen status detection devices should be equipped. The output of the electric signals of the hardware platen status detection devices is uploaded to the upper computer in the form of serial ports. Through the application and development of the upper computer, the functions of online monitoring, recording and remote directional transmission of the hardware platen status can be realized. It should be pointed out that the infiltration of external magnetic field may cause the output error of the hardware platen detection device, so in engineering practice, it is necessary to prohibit large

magnets from entering the vicinity of the report protective panel; if necessary, a metal mesh cover is installed at the bottom of the protective panel, and all the hardware platen detection devices are covered, so as to effectively shield the influence of external magnetic field on the hardware platen detection device under the premise of ensuring the visibility of the hardware platen.

4 Experimental Analysis

In order to verify the accuracy and reliability of the hardware platen condition monitoring device designed in this paper, based on Figs. 1 and 2, experimental platforms are built on RCS15GA-414 bus protective panel and GXH103B-123 line protective panel respectively for verification and analysis. The hardware platens of RCS15GA-414 bus protective panel and GXH103B-123 line protective panel are separate type and line spring type respectively, the vertical distance between the hardware platen and protective panel is 0.9 cm and 2 cm respectively. After pad thickness treatment, the vertical distance between magnet and Hall element is 0.3 cm when the hardware platen closes. In the experiment, the Hall element model is SR13C, the triode model is 22,222 N, the magnet is 0.6 * 0.6 * 0.2 cm NdFeB REE solid super-strong magnet, the power supply is 0–24 V adjustable DC power supply, and the output level of OC gate circuit is captured by digital oscilloscope. During the experiment, the power supply voltage is 0, 12 and 24 V respectively. The experimental results are shown in Table 2. Figures 4 and 5 show the capture results of the digital oscilloscope.

Repeated experimental results show that the hardware platen state detection device can accurately reflect the on/off status of the hardware platen at the normal working voltage level, and has high reliability. At the same time, the hardware platen detection device can accurately reflect the status of the hardware platen at the power supply voltage of 12 V, which shows that the hardware platen detection device has strong voltage disturbance crossing ability.

Table 2 Experimental simulation results table

Supply voltage (V)	0		12		24	
Output level	Plate on	Plate off	Plate on	Plate off	Plate on	Plate off
	Low level	Low level	Low level	High level	Low level	High level

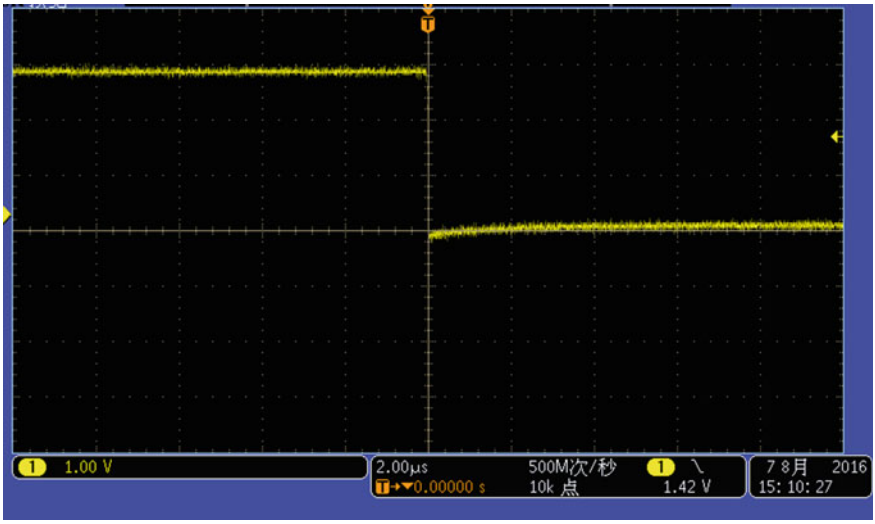

Fig. 4 Oscillograph when the state of strap change from in to out

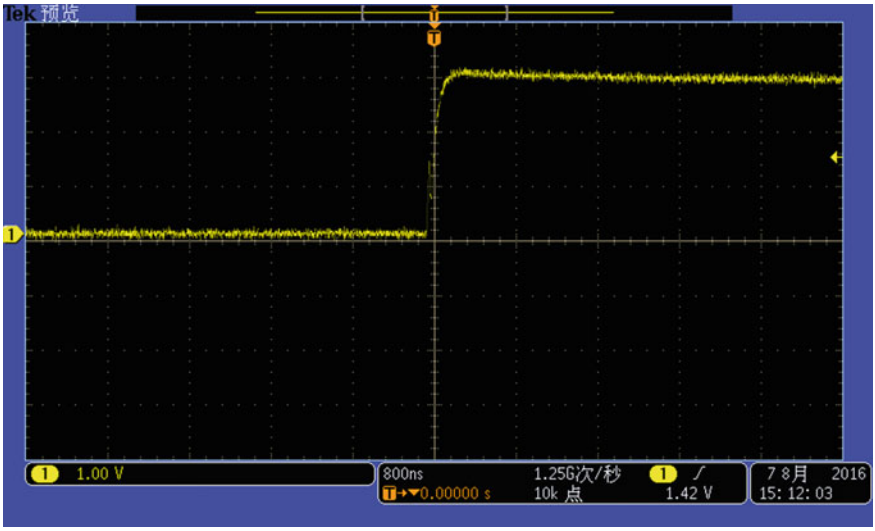

Fig. 5 Oscillograph when the state of strap change from out to in

5 Conclusion

The condition checking of substation hardware platen is carried out by field personnel, which restricts the intelligent development process of substation. In this paper, a kind of the hardware platen state detection scheme based on Hall sensing effect is proposed, and the corresponding Hall element selection scheme and layout scheme are proposed, and the hardware platen state detection integrated circuit is designed. The experimental results show that the scheme has strong sensitivity and anti-jamming ability, strong operability and wide application prospects.

References

1. Hu S, Li L, Zhu X et al (2019) Auxiliary safety measures of protection realy in smart substation based on switching of maintenance states. Autom Electr Power Syst 43(1):242–247
2. Wu X, Liu C, Li J et al (2008) Remote control technology and its application on relay protection and automatic device strap circuit. Autom Electr Power Syst 32(15):100–103
3. Yuan H, Qu G, Zhuang W et al (2014) Discussion on condition monitoring contents of secondary equipment in power grid. Autom Electr Power Syst 38(12):100–106
4. Chen G, Wang D, Qiu Y et al (2017) Challenges and development prospects of relay protection technology. Autom Electr Power Syst 41(16):1–11, 26
5. Wang J, Liu Z, Zhang C et al (2016) Exploration of new technology for relay protection testing. Autom Electr Power Syst 40(22):1–6
6. Yao J, Yang S, Gao Z et al (2007) Development trend prospects of power dispatching automation system. Autom Electr Power Syst 31(13):7–11
7. Zhao Z, Huang H, Zhao C et al (1999) Automatic management system for protective relaying. Autom Electr Power Syst 23(19):55–57
8. Li J, Tang Y (2014) Condition monitoring and mistake precaution system for power strap based on photoelectric detection. J Chongqing Univ 37(5):29–36
9. Xia Z, Luo Y, Tu G, Gong C (2005) Image auto-recognition of relay pressed board in on/off states based on visual information. Relay 33(4):40–44
10. Li Y, Li R, Lu Y et al (2017) Intelligent monitoring system design for circuit breaker operating circuit. Autom Electr Power Syst 37(10):211–217

Research on New Protection and Control System Scheme in Smart Substation Using On-site Module

Xiao Gong, Hang Lv, Dongchao Liu and Gui Yang

Abstract This paper studies a new sampling and control on-site module based on mature SOC chip technology, which is installed near primary equipment; and proposes a new protection and control system scheme in smart substation using on-site module and HSR ring network technology. It analyzes the delay characteristics of the application of HSR technology to implement the data transmission scheme of the on-site module, which shows that the scheme can meet the fast tripping requirements of the protection; proposes network flow control solution to improve network reliability, and proposes data transmission delay measurement technology to improve the synchronization reliability of network sampling, which effectively ensures the reliable application of the multi-bay protection that using the sampling and tripping method by network. The new protection and control system scheme simplifies the secondary system architecture, meets the technical development direction of intelligent primary equipment, and is beneficial to ensure the reliability and fast tripping of the protection device.

Keywords On-site module · Protection and control system scheme · HSR ring network

1 Introduction

Since 2009, the construction of smart substation of State Grid Corporation has experienced two development stages of the first generation and the new generation, forming a secondary system architecture based on the IEC61850 standardized network communication platform with features such as measurement and monitoring, control and protection, information sharing; and realizing the digitization, networking and intelligence of substation secondary system [1–3].

X. Gong (✉) · H. Lv · D. Liu · G. Yang
NR Electric Co., Ltd., Nanjing 211100, China
e-mail: gongx@nrec.com

Y. Xue et al. (eds.), *Proceedings of PURPLE MOUNTAIN FORUM 2019-International Forum on Smart Grid Protection and Control*, Lecture Notes in Electrical Engineering 585, https://doi.org/10.1007/978-981-13-9783-7_39

However, the current smart substation has also exposed some problems in its operation. For example, the secondary system of the smart station adopts a "three-layer two-net" structure, which increases the process layer network and the process layer equipment such as the merging unit and the smart terminal compared with the conventional station, and has a large number of devices with complicated maintenance; and increased the sampling and tripping intermediate links of the protection, leads to an increase in the overall tripping delay up to 7–10 ms. The quickness and reliability of the relay protection is reduced, which affects the safety of the power grid and the reliability of the power supply.

In order to solve the above problems, firstly, based on the mature SOC chip technology and FPGA technology, a new sampling and control on-site module which is installed near primary equipment is studied to replace the merge unit and the smart terminal. A new protection and control system scheme of smart substation based on on-site module and HSR ring network technology is proposed, which simplifies the secondary system architecture, reduces the intermediate links of the sampling and tripping of the protection, and is beneficial to ensure the quick-acting and reliability of the protection. The network flow control technology and the data transmission delay measurable technology are proposed to improve the reliability of data transmission and the synchronization of network sampling, and ensure the reliability of the multi-bay protection based on the network.

2 On-site Module

At present, the merging unit and the smart terminal device are adopted in the secondary system of the smart station for realizing the digitization of the analog value and the binary value. The merging unit integrates data collection, merging, and forwarding functions, but it is bulky and complex in structure. Once the merging unit fails to operate, it may affect the normal operation of several protection devices. The number of fiber interfaces in the merging unit is large, and the power consumption and heat generation are large, which affects the long-term reliability of the device.

Based on the principle of distributed processing, the on-site module with digital conversion, compact structure and distributed layout can replace the original smart terminal and merge unit, which can effectively solve the problem of the serious impact of single equipment failure. The on-site module and the primary device are installed in the same body, which is in line with the technical development direction of the intelligent primary device, and the current high-performance integrated chip technology, communication technology and equipment structure design level can meet the requirements of miniaturization, high protection level and configuration-free of the on-site module [4], the application of the on-site module can effectively simplify the network structure, significantly reducing the number of cables and fiber used.

2.1 On-site Module Classification

The main function of the on-site module is to realize the local digitization of the analog value such as voltage, current, oil temperature, oil level and the binary value of circuit breaker status, tap position, non-electricity signal, etc., which can replace the existing merging unit and smart terminal.

For the different primary equipment, following the principle of simplifying the types of equipment, the on-site modules are divided into four types: analog on-site module, binary on-site module, transformer on-site module and operating module according to functions, which can realize the collection, transmission and control of primary equipment information in the station. Based on these four types of on-site modules, the module is divided into 14 sub-categories for the versatility and coverage of the primary equipment, as shown in Table 1.

2.2 Typical Application Scenarios

(1) AIS bay

Circuit breaker: The phase-separated circuit breaker is equipped with three binary on-site modules, and the three-phase circuit breaker is equipped with one binary on-site module, which is installed in the local circuit breaker control cabinet.

Isolation switch or grounding switch: Configure one binary on-site module to be installed in the switch mechanism box.

Table 1 Sub-categories of the on-site module

No.	Type	Classification
1	Analog on-site module	Electromagnetic transformer bus voltage on-site module
2		Electromagnetic transformer voltage and current on-site module
3		Electromagnetic transformer voltage on-site module
4		Electromagnetic transformer current on-site module
5		Electronic transformer bus voltage on-site module
6		Electronic transformer voltage and current on-site module
7		Electronic transformer voltage on-site module
8		Electronic transformer current on-site module
9	Binary on-site module	Universal binary on-site module
10	Transformer on-site module	Transformer analog on-site module
11		Transformer binary on-site module
12		Transformer non-electrical on-site module
13	Operating on-site module	Three-phase operating module
14		Phase-separated operating module

(2) GIS bay

It includes the analog on-site module, binary on-site module and operating on-site module for the entire bay. Considering the convenience of maintenance and operation, these on-site modules are centralized installation in the GIS control cabinet.

(3) Transformer bay

The transformer is configured with a binary on-site module, an analog on-site module and a non-electrical on-site module.

These on-site modules are installed in the local control cabinet of the transformer.

Multiple on-site modules in each bay are installed in the switch field. The sampling data of on-site modules needs to be transmitted to the bay layer device, and the on-site modules need to receive the control signals of the bay layer device. The switch device is not suitable for local installation. Therefore, the HSR technology is the most suitable data transmission scheme currently used in this application scenario.

3 Scheme of Protection and Control System

3.1 Scheme Introduction

High-reliability Seamless Redundant Ring Network (HSR) is a high-availability seamless redundancy protocol [5, 6]. With a ring topology, the source node replicates all information and transmits it through two different paths. Once a network fails, it ensures that the data is transmitted through another path without any delay [7]. The network connection device RedBox (redundancy box) is used for HSR networking.

HSR technical features:

(1) Implement ring network redundancy by sending packet in both directions simultaneously.
(2) The application layer is simple to process, and only needs to send and receive packets according to a single network, without concern for the underlying dual-network backup and fault tolerance mechanism.
(3) Hot backup because of single-loop bidirectional packet, no need to switch data link when the network is faulty, the recovery time is 0, and the data transmission reliability is high.

Based on the on-site module, HSR ring network technology, the protection and control system of the existing smart substation is optimized, and the distributed on-site module is used to realize the digital conversion of analog and binary signals. And the on-site module ring network is constructed through the HSR ring network

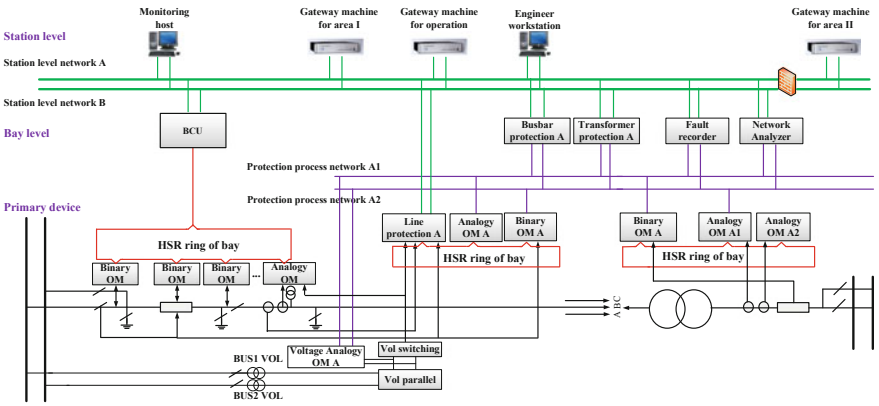

Fig. 1 Protection and control system scheme

to realize information exchange with the bay layer device. The protection and control system scheme is illustrated by the following 220 kV typical smart substation. In Fig. 1 OM means on-site module.

The protection and control system scheme features:

(1) A star redundant dual network is adopted for the station level.
(2) Multiple on-site modules in each bay are connected in hand-in-hand mode to form an HSR ring network.
(3) A star redundant dual network is adopted for the multi-bay protection, and the HSR ring network of each bay is connected to the star network.
(4) The protection and BCU respectively form a network, which is convenient for the maintenance and management according to professional requirements.

3.2 Networking and Configuration of BCU

Each bay is separately configured with an HSR ring network for BCU. The analog on-site module and binary on-site module are configured in HSR ring network, which data are sent to the BCU of each bay through the interface module.

The BCU is arranged indoors, installed in the control room panel, and communicates with the bay HSR ring network through the interface module.

3.3 Networking and Configuration of Protection

Each bay is separately configured with an HSR ring network. The bay of line is equipped with line protection of the cable sampling cable tripping, the binary

on-site module and the analog on-site module, and the on-site module provides sampling data for the busbar protection and other multi-bay devices. For the bay of transformer, in the HSR ring, the binary on-site module, the analog on-site module A1 (sampling data for the transformer protection) and the analog on-site module A2 (sampling data for the busbar protection and other multi-bay device) are provided. Two independent analog on-site modules A1 and A2 are configured to prevent all multi-bay protection being affected when a single analog module is malfunctioning or operating abnormally.

The line protection adopts the local arrangement, and the sampling and the tripping of protection are based on cable, thereby reducing the intermediate link of the protection realization, which is beneficial to improving the protection reliability and the tripping speed [8]. The line protection realizes initializing failure protection, receiving blocking reclosing and other functions through the protection process network.

The protection process network is set for the multi-bay protection, the star connection, and the various voltage levels use the same network to realize data exchange across voltage levels. For the dual protection, the independent network is configured. Considering that the protection device of the single configuration may have data exchange requirements with the protection devices of the dual configuration, the isolation device with the message filtering and flow control functions is configured between the dual networks. Only the subscription data is allowed to traverse the isolation device.

4 Time Delay Analysis and Reliability Technology of Network

4.1 HSR Delay Analysis

One bay may be configured with multiple on-site modules. These on-site modules are connected in a hand-in-hand mode. The data transmission delay of this scheme must be evaluated to estimate if it can satisfy the high real-time requirement of equipment such as protection and so on. The following is a data transmission delay analysis using the Gigabit HSR interface. As can be seen from Fig. 2, the HSR networking delay variation is mainly due to introducing a data queue in each RedBox, resulting in an increase in transmission delay. The GOOSE message sent by the BCU (Bay Control Unit) may introduce a delay link passing each RedBox, and the time delay may be increased because of the increase of the number of RedBox.

(1) Theoretical analysis of communication delay

Network scale: one BCU, the packet size is about 300 Byte; one circuit breaker on-site module, the packet size is about 1000 Byte; six isolation switch on-site

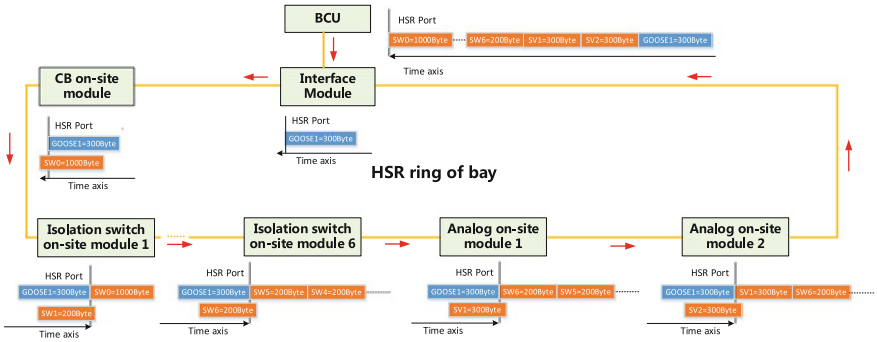

Fig. 2 Delay analysis of HSR ring network

modules, the packet size is about 200 Byte of one on-site module; two analog on-site modules, the packet size is about 300 Byte of one on-site module.

According to the network size analysis, the maximum delay of the data transmission theory of the BCU includes: considering the extreme situation, when the BCU message passes through each Redbox, the node just starts to send the data of this node.

Total amount of packets is:

$$(1000 + 200 \times 6 + 300 \times 2)\text{Byte} \times 8 = 22.4\,\text{KB} \tag{1}$$

Therefore, the congestion delay is :

$$\text{t1} = 22.4\,\text{KB} \times \frac{1\,\text{s}}{1000\,\text{MB}} = 22.4\,\text{us} \tag{2}$$

The data forwarding delay of each Redbox is 2 us, and the data accumulation forwarding delay of 9 Redbox is:

$$\text{t2} = 2 \times 9 = 18\,\text{us} \tag{3}$$

Therefore, the total delay is:

$$\text{t} = \text{t1} + \text{t2} = 22.4\,\text{us} + 18\,\text{us} = 40.4\,\text{us} \tag{4}$$

(2) Communication delay test

The delay performance of the HSR communication delay is different between the complete ring network and the single point broken chain. Therefore, the test needs to consider two cases.

The test plan is as follows:

RedBox1–RedBox8 forms the HSR ring network. The P1–P8 ports of the network tester are respectively connected to the corresponding numbered RedBox, P1–P2

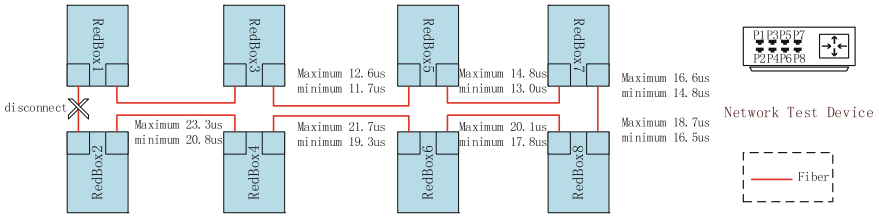

Fig. 3 Delay test of HSR ring network

simulate interface module, P3 simulate circuit breaker on-site module, P4–P5 simulate analog on-site module, P6–P8 simulate isolation switch on-site module.

a. Test the communication delay when the HSR ring connection and the two-way communication are under normal conditions. The test delay of the farthest node is between 16.6 and 17.2 us. The more the number of cascades, the greater the delay.
b. Test the communication delay when RedBox1 and 2 are disconnected from physical connection. The test delay of the farthest node is between 20.8 and 23.3 us. The more the number of cascades, the greater the delay (Fig. 3).

Conclusion: When the HSR ring network is smaller than the 15-level cascading scenario, the network load is less than 10%, and the HSR ring network delay is less than 100 us. The network delay meets the real-time requirements of the protection.

4.2 Reliability Technology of Network

The on-site modules in the bay can use HSR technology to realize data transmission without switch, and the multi-bay protection needs to receive the data of multiple bays. If the HSR ring network is used for multi-bay protection's data transmission, the large scale of the HSR ring network leads to increasing the transmission delay and reducing the reliability significantly, and greatly increased the possibility of ring network redundancy destruction caused by any device quitting from the ring network. Therefore, it is recommended to configure a homogenous redundant star network for data transmission requirements of multi-bay devices such as busbar protection, transformer protection, fault recorder.

The reliability of network transmission and the reliability of sampling synchronization are key indicators for the quality of data transmission of smart substation [9]. We propose using network flow control strategy to ensure the reliability of network transmission and delay measurable technology to ensure the reliability of network sampling synchronization.

(1) Flow control strategy

The conventional VLAN and multicast management technology can only realize transmitting packets in the specified area, and cannot effectively isolate the faulty packets. When there are a large number of storms in some MMS, GOOSE, or SMV packets, it could affect the IED device to receive the MMS, GOOSE, or SMV packets of other control blocks at the same time, which ultimately results in performance degradation or packet loss.

The method of accurate flow suppression sets the maximum flow setting for each GOOSE/SV data stream, and limits the flow when it exceeds the set value. The method ensures that the network has sufficient bandwidth to transmit normal GOOSE/SV data streams. The flow control technology completely solves the problem of mutual interference between various multicast packets on the process layer network, and minimizes the impact of faulty packets on normal network packets. The reliability of the process layer network is greatly improved (Fig. 4).

(2) Delay measurable technology

The principle of the network sampling synchronization mode based on the delay measurable technology is to accurately calculate the forwarding delay of the SV packet in the switch and write the delay into the SV packet. Packet transmission delay can be accumulated when multiple switches are cascaded [10, 11], as shown in Fig. 5.

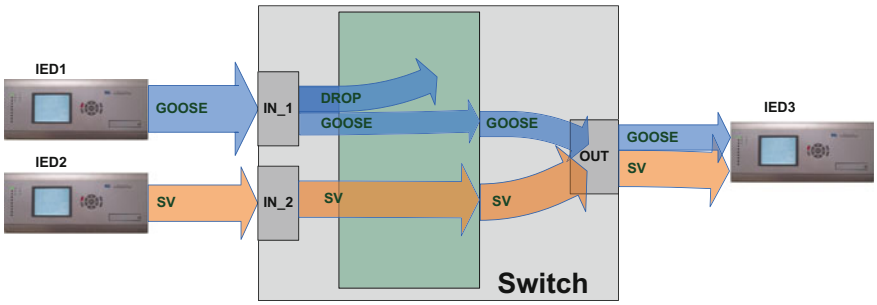

Fig. 4 Flow control diagram

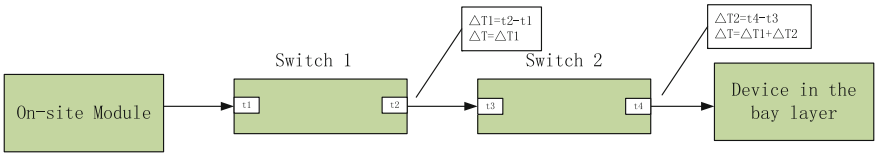

Fig. 5 Delay measurable technology diagram

The device in the bay layer can calculate the sampling time of the analog value by receiving the SV message:

$$T = T1 - T2 - T3 \tag{5}$$

T: Sampling time on the time base of the device in the bay layer;
T1: Time mark when sampling data arrival;
T2: Rated sampling delay of analog on-site module;
T3: Total delay of data transmission.

In Fig. 6, the value of T3 is:

$$T3 = \Delta T1 + \Delta T2 = (t2 - t1) + (t4 - t3) \tag{6}$$

Based on the delay measurable technology, the multi-bay protection can calculate the sampling times of the sampling data of different bays on the same time reference, thereby ensuring the synchronization reliability of the multi-bay protection in the network sampling mode. The delay measurable technology fundamentally solves the problem of network sampling dependence on external common clock signals, and significantly improves the reliability of the protection operation under the network sampling mode.

5 Conclusion

The new secondary system architecture proposed in this paper has the following advantages and features:

(1) The merging unit and the smart terminal are replaced with the on-site module, and the on-site module is installed in the same place with the primary device, which is in line with the technical development direction of the intelligent primary device.
(2) The HSR technology is adopted for the on-site module networking in each bay, link redundancy, and data transmission is not affected if "N − 1" fault, so the data transmission reliability is improved.
(3) The "two-layer-one-net" architecture is adopted for the BCU, which eliminates the process layer network and reduces the number of switches; The advantage of the architecture is that it can reduce the cost of networking.
(4) The sampling and the tripping of line protection are based on cable, reducing the intermediate link of the protection realization. The reliability and tripping speed performance are better than the line protection of the existing smart substation.

(5) The network sampling network tripping mode is adopted for the multi-bay protection, and the flow control strategy is adopted to ensure the reliability of the network transmission, and the delay measurable technology is adopted to ensure the synchronous reliability of the sampling. Compared with the mode of sampling and tripping directly connected through optical fibers or cables, the mode of sampling and tripping by network greatly reduces the use of optical fibers and cables, and is conducive to data sharing, in line with the development direction of smart substation networking.

From the aspects of network reliability, economic fast-tripping of protection and data sharing, the secondary system architecture scheme proposed in this paper has certain advantages over the existing smart substation, and it will have a good application prospect in the future smart substation construction.

Funded Project Science and Technology Project of State Grid Corporation of China. <Research on Secondary System Architecture and Key Equipment of the Third Generation Smart Substation>.

References

1. Ni Y, Yang Y, Fan C et al (2014) Discussion on integration of second device in smart substations. Autom Electr Power Syst 23(3):194–198
2. Fan C, Ni Y, Dou R et al (2011) Analysis of network scheme for process layer in smart substation. Autom Electr Power Syst 35(18):67–71
3. Zhou H, Zheng Y, Yang Z et al (2018) Implementation scheme of three-in-one network based on PRP/HSR in smart substation. Autom Electr Power Syst 38(10):216–223
4. Qiu Y, Wang D, Hu C, Dong X (2016) Application and practice of unprotected outdoor installation protection. Power Syst Prot Control 44(20):1–5
5. Hou W, Zhang P, Hu Y et al (2010) Reliability analysis for protection system based on high availability automation network. Power Syst Prot Control 38(18):44–48
6. Chen F, Yu C, Zhang Y et al (2017) Research on integrated solution of on-site substation relay protection. Electr Power Autom Equip 37(10):204–209
7. Wang D, Zheng Y, Zhou H et al (2017) Platform and key technology for distributed bus protection based on multi-HSR network. Autom Electr Power Syst 41(16):27–34
8. Wang D, Qiu Y, Ling G et al (2017) Application scheme and economical comparison of plug & play and outdoor installation protection in substation. Autom Electr Power Syst 41(16):12–19
9. Zhou H, Zheng Y, Jiang L et al (2014) An equal-interval sampling control and synchronization method for merging unit. Autom Electr Power Syst 38(23):96–100
10. Liu J, Li Y, Yang G (2015) Design of delay measurement switch in intelligent substation process level. Power Syst Prot Control 43(10):111–115
11. Zhang Y, Cai Z, Zhu Z et al (2015) Network sampling synchronization of relay protection based on transmission delay compensation. Autom Electr Power Syst 39(18):81–85

Insensitivity of Fiber-Optic Current Transducer to Vibration

Songjie Shi, Zhanyuan Liu, Jibiao Hou, Wuyang Zang, Xiaochen Niu, Yupeng Cai, Tianfeng Chu and Shuo Chen

Abstract The traditional fiber optical current transformer uses Y-branch waveguide modulator. However, Y-branch waveguide modulator produces abnormal noise current when it is subjected to vibration stress caused by the double-arm optical structure between the modulator and the coupler. In this paper, a new optical structure using reflective waveguide modulator is proposed because it has ability to eliminate the additional phase difference caused by vibration stress. Both results of laboratory and substation prove that reflective waveguide modulator can not only effectively reduce the impact of environmental stress on fiber optical current transformer, but also can eliminate the abnormal current caused by circuit breaker switching vibration. This study provides a new way of thinking and direction for the design and manufacture of high performance current transformer applying to high voltage and large current measurement field.

Keywords Optical measurement · Electro-optic modulators · Fiber optic current transducer · Power equipment · Protection

1 Introduction

With the rapid development of power industry, the voltage level and transmission capacity are continuously improved, and meanwhile a great deal of DC projects are constructed. The traditional electromagnetic current transformer has a series of shortcomings, e.g. magnetic saturation, small dynamic range, non-measurement direct current, flammable and explosive, serious electromagnetic interference and

S. Shi · W. Zang · Y. Cai · T. Chu
Electric Power Research Institute, State Grid Liaoning Electric Power Supply Co. Ltd., Shenyang, China

Z. Liu (✉) · J. Hou · X. Niu · S. Chen
State Key Laboratory, Advanced Power Transmission Technology Global Energy Interconnection Research Institute Co., Ltd., Beijing, China
e-mail: zhanyuanliu@foxmail.com

Y. Xue et al. (eds.), *Proceedings of PURPLE MOUNTAIN FORUM 2019-International Forum on Smart Grid Protection and Control*, Lecture Notes in Electrical Engineering 585, https://doi.org/10.1007/978-981-13-9783-7_40

heavy weight. Therefore, it is difficult to satisfy the requirements of the current measurement in the new generation of power system. In recent years, fiber optical current transformer (FOCT), based on the principle of Faraday magneto-optical effect, has been widely concerned in the field of special voltage and direct current transmission because of its advantages of no magnetic saturation, large measuring range and measurable DC. It also has a broad market prospect [1–3].

However, the FOCT has not been widely used in engineering at present. One of the important reasons is its sensitivity to the environment vibration. When the vibration form switch or other factors in the substation are transmitted to the FOCT equipment, the measured values' fluctuation will be caused. It therefore will easily lead to the protection system's mis-operation. Aimed to solve this problem, many domestic and foreign researchers have proposed various improvements of FOCT, e.g. torsional sensing fiber [4–6], elliptical birefringent fiber [7], direct connected lithium niobate modulator a. However, the schemes above have disadvantages of complex structure, high half wave voltage, harsh material and process requirements.

In this paper, a new scheme of FOCT is proposed, thatmainly improves the structure of the signal demodulation part: the reflective lithium niobate modulator is used instead of the traditional Y branched lithium niobate modulator. This scheme not only effectively improves the anti-vibration performance of the FOCT, but also saves the optical devices such as the tapered type polarization coupler sensitive to the external environment, and simplifies the system structure. The experimental results show that under the condition of strong external vibration (0–20 g, g is gravitational acceleration), the noise current of the new fiber optic current transformer is less than 1.3 A. The new scheme can reduce the complexity of understanding the dimming path, and effectively reduce the manufacturing cost of the transformer. It will provide a new idea and direction for designing and manufacturing safe and reliable FOCT.

2 Structure of FOCT Using Reflective Lithium Niobate Modulator

2.1 The Structure and Principle of a Reflective Lithium Niobate Modulator

The reflective lithium niobate modulator is coated with a reflective film on the two ends of the device, forming a LN electro-optic modulator with two end reflectors. Figure 1 [8] is a LN electro-optic phase modulator with double end reflection structure. After input light coupling into the waveguide, one reflection occurs on each of the two ends, and the output is finally out from the outlet end. This reflective lithium niobate modulator increases the length of the electro-optic region without increasing the length of the device, and thus reduces the half wave voltage of the electro-optic modulator and then reduce the difficulty of the system design.

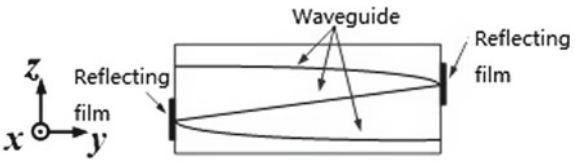

Fig. 1 Double reflection ends of LN electro-optic phase modulator

2.2 *Principle and Structure of FOCT System*

The schematic diagram is illustrated in Fig. 2. The primary bus passes through the sensitive part of the optical fiber, and the acquisition module is placed in the chassis. The light emitted by the light source passes through the beam splitter to reach the multifunction modulator, where the light is modulated by the square wave and converted to two beam polarized light. The light passes through the 1/4 wave plate spliced with 45°, and then become left-handed and right-handed light waves. When the two beams pass through the sensitive optical fiber, there is a phase difference produced between the waves due to the Faraday effect [9], which is

$$\Delta\varphi_{\mathrm{i}} = NVI \tag{1}$$

where N is the number of turns of sensitive optical fiber; V is the current Verdet constant; I is the primary current passing through a sensitive fiber coil. After the light return and passes through the 1/4 wave plate again, the two beams of light are

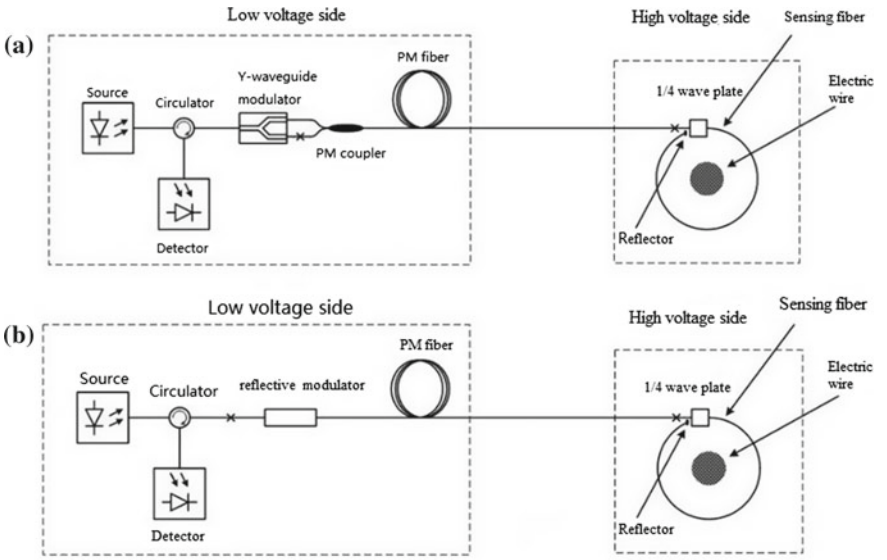

Fig. 2 **a** FOCT system structure with Y branched modulator, **b** FOCT system structure using reflective modulator

converted into linear polarized light and carry the information of $\Delta\varphi_i$, and then the light return to multifunction modulator through optical fiber delay line, two beams interference. The intensity expression after interference is expressed.

$$P = P_0[1 + \cos(\varphi_b + \Delta\varphi_i)] \tag{2}$$

where P is the intensity of output signal, P_0 is the peak intensity, and φ_b is the modulation amplitude.

After the light wave passes through the coupler, the detector on the CPU board converts the optical signal into the voltage signal. Using high-speed A/D converter, the analog signals are converted into digital signals received by the FPGA and DSP processing units; the digital sampling is completed in FPGA, and the noise reduction processing is carried out by digital comb filter technology. The measured results are transmitted through the optical fiber after the demodulation and digital integral control algorithms are completed within the DSP.

Figure 2a is the system structure diagram of the Y branch structure modulator. Y-waveguide modulator and Polarization-maintaining (PM) coupler are fused together by two optical fibers, as shown in Fig. 3. The interference intensity of light passing through two branches is:

$$P(t) = P_0\left[1 + \cos\left(\Delta\varphi_i + \varphi_{x1}(t-\tau) + \varphi_{x2}(t) - \varphi_{y2}(t-\tau) - \varphi_{y1}(t)\right)\right] \tag{3}$$

where φ_{x1} is additional phase of x polarized Light passing through L_1 branch; φ_{x2} is additional phase of x polarized Light passing through L_2 branch; φ_{y1} is additional phase of y polarized Light passing through L_1 branch. φ_{y2} is additional phase of y polarized Light passing through L2 branch. τ is the overall transit time of FOCT.

If there is no additional stress due to vibration, then

$$\begin{aligned} \varphi_{x1}(t-\tau) &= \varphi_{y1}(t) \\ \varphi_{y2}(t-\tau) &= \varphi_{x2}(t) \end{aligned} \tag{4}$$

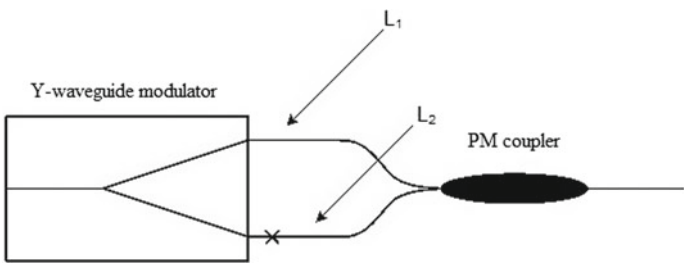

Fig. 3 Double-branch optical structure composed of Y-waveguide and PM coupler

Formula (3) is changed to

$$P(t) = P_0[1 + \cos\ \Delta\varphi_i] \tag{5}$$

In the same form as Formula (2), the interference intensity is only related to the phase difference caused by Faraday effect. In the case of vibration, due to the existence of elasto-optic effect, Formula (4) no longer holds, Formula (3) becomes:

$$P(t) = P_0[1 + \cos(\Delta\varphi_i + \Delta\varphi_v)] \tag{6}$$

In this Formula (6), $\Delta\varphi_v$ is the additional phase difference caused by vibration, which is indistinguishable from the phase difference $\Delta\varphi_i$ caused by current. It shows additional abnormal noise current in the sampling value of FOCT.

Compared to the traditional FOCT structure, the optical device of the polarization coupler is removed by using the reflective lithium niobate modulator instead of the traditional Y branch modulator. The structure of system is simplified, the cost of the product is reduced, and the anti-vibration performance of the system is improved. Figure 2b is the system structure diagram of the reflective lithium niobate modulator. In the case of vibration, the following relationship exists approximately when using this optical path structure.

$$\begin{aligned} \varphi_{x1}(t-\tau) &= \varphi_{y2}(t-\tau) \\ \varphi_{y1}(t) &= \varphi_{x2}(t) \end{aligned} \tag{7}$$

Therefore, the Formula (3) can still be changed into Formula (5). The additional phase difference caused by vibration can cancel each other, and it will not cause abnormal noise current.

3 Experimental Results and Discussion

3.1 Laboratory Vibration Measurement Results

On the low frequency vibration test platform, the fiber current transformer of the Y branch modulator is compared with the FOCT of the reflective modulator. The frequency of the shaking table is 100 Hz, the acceleration is 0–20 g (g is the acceleration of gravity), and the direction of vibration is perpendicular to the collector. The experimental results are shown in Fig. 4.

The experimental results show that the FOCT using the reflective modulator can eliminate the sensitivity to the environmental vibration, compared with that using the Y branch modulator. When the vibration acceleration is increased from 0 to 20 g, the noise current of the transformer using the Y branch modulator is obviously increased, and the maximum noise current of the transformer using the reflective modulator is 1.3 A.

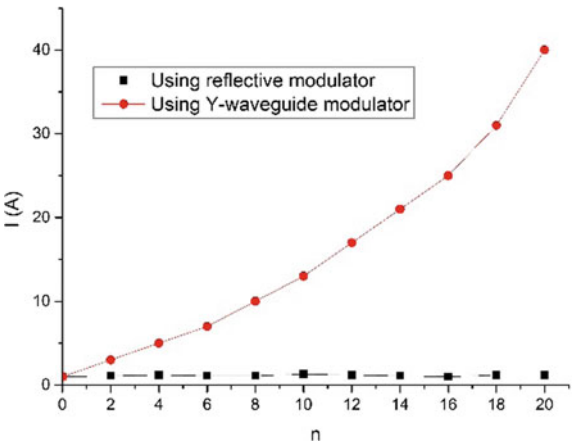

Fig. 4 Results of vibration test. The vertical coordinate I denotes the noise current; the horizonal coordinate n = a/g, where a is vibration acceleration

3.2 Test Result of Switch Dynamic Test in Substation

At the substation site, the C phase of a transmission lines is equipped with FOCT device. Figure 5 is the device structure diagram and the scene installation diagram.

First, the fiber optic current transformer with Y branch structure modulator is put into the collection box to carry out the experiment. In the process of substation's debugging, when relay protection personnel in the closing the circuit breaker is unloaded, the line protection action trip will start with outburst variables, and then accelerate after hand operation. The typical failure recorded by field persons is shown in Fig. 6a. During the operation of the circuit breaker, a significant noise current appeared in the C phase, with a maximum value of 6.8 A. After harmonic analysis, it was mainly concentrated in the 7 and 15 harmonics, and the fundamental wave approached to 0 (see Fig. 6b).

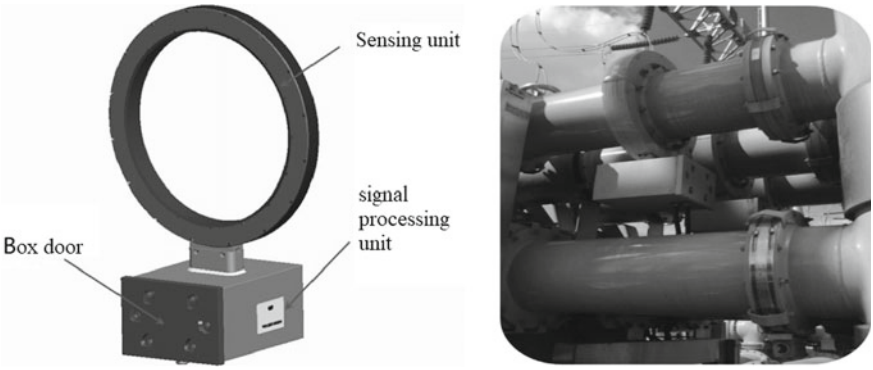

Fig. 5 Structure picture of GIS type FOCT

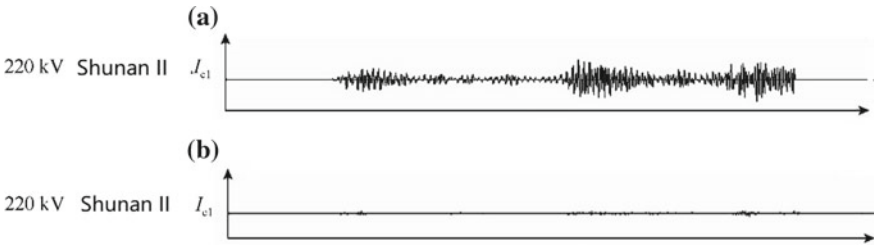

Fig. 6 **a** The application of Y branch structure modulator transformer on relay protection fault oscillograph; **b** the application of reflection type modulator on transformer relay protection fault oscillograph

The noise current should be influenced by the vibration which is produced by the circuit breaker mechanism, and thus affects the transmission characteristics of the FOCT.

Then, a fiber optic current transformer with a reflective modulator is put into the collecting box, and then the operation of the split circuit breaker is carried out. The maximum value of noise current is 1.01 A, and the recorded wave shape is shown in Fig. 6b.

Under the same conditions, the above experiments are repeated, and the maximum noise current results of the two kinds of structural current transformers are recorded as shown in Fig. 7, which the I_{max} is the maximum noise current and the n is the frequency of the operation.

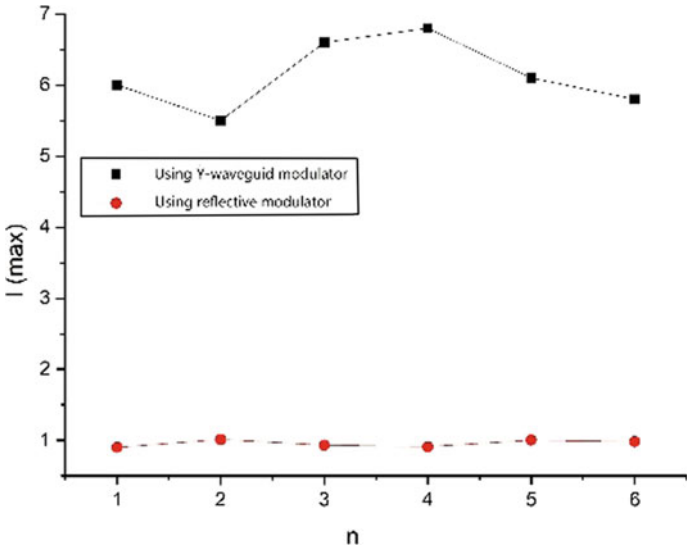

Fig. 7 The maximum noise current using different FOCTs under circuit breaker operation

The experimental results show that the sensitivity to environmental vibration can be basically eliminated by a fiber optic current transformer using a reflective modulator.

4 Conclusion

A design of the FOCT with integrated reflective modulator is proposed and verified. The output signal noise of the original and improved FOCT is compared, and then tested by using the low frequency vibration test bench. and the substation on-the-spot open circuit breaker. The experimental results show that (1) the improved FOCT reduces vibration sensitivity to environmental to achieve a stable measurement of current; (2) the new FOCT system simplifies the structure of the transformer, reduces the difficulty of the process, reduces the manufacturing cost of the transformer. This study provides a new way of thinking and direction for the design and manufacture of high performance current transformer applying to high voltage and large current measurement field.

Acknowledgements This work was supported by State Grid Corporation Science and Technology Project (2018YF-53)

References

1. Blake J, Tantaswadi P, de Carvaliho RT (1996) In-line Sagnac interferometer current sensor. IEEE Trans Power Delivery 11(1):116–121
2. Cheng S, Zhang G, Guo Z et al (2015) Influence mechanism of conductor eccentricity on all-fiber optic current transformers. Autom Electr Power Syst 39(13):137–143. https://doi.org/10.7500/aeps20140924007
3. Chen S, Liu ZY, Niu XC et al (2017) Study on lithium niobate low half-wave voltage electro-optic modulator. Semicond Optoelectron 3(38):342–344 (in Chinese)
4. Guo J, Si L, Yuan Z et al (2018) Self-diagnosing alarm algorithm for optical path fault of fiber optical current transformer. Autom Electr Power Syst 42(21):172–177. https://doi.org/10.7500/aeps20171117005
5. Laming RI, Payne DN (1989) Electric current sensors employing spun highly birefringent optical fibers. J Light-wave Technol 7(12):2084–2094
6. Liu Q, Wang ZP, Xu Y et al (2005) Research on the influence of optical current transformer on relay protection system. Power Grid Technol 29(1):11–14 (in Chinese)
7. Li C, Zhang C, Wang X et al (2013) Key techniques of reflective sagnac interferometer-type fiber optic current transformers. Autom Electr Power Syst 37(12):104–108. https://doi.org/10.7500/aeps201301075
8. Xu Y, Lu Y, Bu Q et al (2013) Analysis for effect of fiber-optic current transformer on protection accuracy and reliability. Autom Electr Power Syst 37(16):119–124. https://doi.org/10.7500/aeps201212032
9. Ulrich R, Simon A (1979) Polarization optics of twisted single-mode fibers. Appl Opt 18 (13):2241–2251

Research on SSD Based Automatic Virtual Terminal Connection of Smart Substation

Jia Li, Zhiyong Qiu, Dan Rao, Geng Li, Rui Fan, Qiang Gui and Yaoyao Zhang

Abstract In current design and configuration stages of smart substation, manual configuration of virtual terminal connection relation is needed, while the result would be generated repeatedly and user needs to select template for automatic connection based on template, that is likely to make mistake and difficult for check and management. Hence proceeding from the primary and secondary devices association in the SSD file, research on the virtual terminal connection relation template for typical bays of various voltage levels and connection types is made. A method of smart substation virtual circuit automatic connection is proposed. By realizing automatic process of bay mapping, device mapping and virtual terminal mapping from the model in the SCD to the template in system configuration tool of smart substation, this method could improve automation level and accuracy of system configuration and be used to check the correctness of the virtual terminal connection relation in the SCD file.

Keywords Smart substation · Virtual terminal connection · Automatic connection · Primary and secondary devices association · Typical bay

1 Introduction

Smart substation replaces the secondary circuit with optical cable and software logic, and describes the secondary system configuration of the whole station with the Substation Configuration Description (SCD) file, including the complete virtual terminal connection relationship between the secondary devices, i.e. virtual circuits.

J. Li (✉) · D. Rao · G. Li · R. Fan
NARI Technology Co. Ltd, Nanjing 211106, China
e-mail: lijia3@sgepri.sgcc.com.cn

J. Li · D. Rao · G. Li · R. Fan
State Key Laboratory of Smart Grid Protection and Control, Nanjing 211106, China

Z. Qiu · Q. Gui · Y. Zhang
East China Grid Corporation, Shanghai 200120, China

Y. Xue et al. (eds.), *Proceedings of PURPLE MOUNTAIN FORUM 2019-International Forum on Smart Grid Protection and Control*, Lecture Notes in Electrical Engineering 585, https://doi.org/10.1007/978-981-13-9783-7_41

So the configuration of the virtual circuits becomes the focus of the smart substation design and configuration phases [1–5]. In the current process of project implementation, it is generally the design institute to carry out system design, provide primary diagram and virtual terminal connection tables to the system integrator for system integration. System integrator engineers manually configure virtual circuits in the configuration tool according to the virtual terminal connection tables, and after that make manual verification.

In order to overcome the time-consuming and error-prone problems brought by the manual configuration of virtual terminal connection, in the design and configuration phases, the automatic connection of virtual terminals has been studied to a certain extent, and some definition methods and construction methods of virtual circuit template library or knowledge base are proposed [6–8], as well as virtual terminal description keywords based on virtual circuit template, to complete fuzzy matching of the virtual terminal, similarity calculation and other processing, and realize virtual terminal automatic connection [9, 10]. However, due to lots of smart substation voltage levels, primary connection types, device types, so there is need to choose the template of usage for secondary devices during automatically connection. Meanwhile manual selection of templates may also lead to a large number of virtual circuit connection errors, and this method is not conducive to virtual circuit verification and project management, because of template selection in this application mode has also become a new kind of configuration data. Although some virtual circuit automatic test methods are also proposed, it is usually not a correctness check of the virtual circuit from the source of the configuration, but a validity check of the configured virtual circuit [11–13].

Therefore, it is necessary to study the method of virtual circuit automatic connection based on the files provided by design institute, such as SSD files and ICD files. This paper presents a method of automatic virtual terminal connection for the SCD file of smart substation, making automatic map from bay and secondary devices to virtual circuit template by extracting the association relationships between primary and secondary devices in SSD file [14].

2 Analysis on the Relationship Between Virtual Circuit and SSD

At present, some SSD specifications [15, 16] point out that “based on the primary and secondary devices correlation in system description, combined with the standardized design specifications of relay protection and the specifications of relay protection model information, the virtual terminal connection configuration can be automatically generated by certain rules”. The following Table 1 gives an example of the primary and secondary devices associations in a typical 220 kV line bay with double bus connection.

Table 1 Configuration for association of primary devices and secondary logic nodes

Device type	Meaning	Topological connection device	Associated logic node
CBR	Circuit breaker	Intelligent terminal	Or Split-phase XCBR
		Protection	PTRC, RREC
		Measurement and control	CSWI, MMXU
DIS	Isolating switch	Intelligent terminal	XSWI
		Measurement and control	CSWI, CILO
CTR	Current transformer	Merging unit	Split-phase PTCTR, Split-phase MTCTR
VTR	Voltage transformer	Merging unit	Split-phase PTVTR, Split-phase MTVTR

Virtual terminal connection can be automatically configured according to the following rules:

(1) The current and the voltage of the line protection devices are taken from the TCTR and virtual TVTR associated with this bay respectively;
(2) All protection devices trip over the PTRC associated with the circuit breaker CBR, and the tripping object is the XCBR associated with the CBR;
(3) The reclosing is through the RREC associated with the circuit breaker CBR, and the closing object is the XCBR associated with the CBR;
(4) All control command are through the CSWI associated with the circuit breaker CBR or the isolation switch DIS, and the controlled object is the XCBR associated with the circuit breaker CBR or the XSWI associated with the isolation switch DIS;
(5) The voltage of bus bar protection device is taken from the TVTR associated with the bay, and the branch current is taken from the TCTR in the same bay associated with the PTRC of the bus bar protection device.

The above example shows that for typical bay, there is an intrinsic relationship between virtual terminal connection and SSD file. On the one hand, SSD describes which voltage levels are included in the substation and which bays are included in each voltage level, while the virtual terminal connection relation of typical bays is relatively definite. On the other hand, the sender IED or receiver IED of virtual circuit is associated with primary device. Therefore, virtual terminal connection relation templates can be predefined for typical bays of different voltage levels and different types of connections, and then map the bays configured in SSD to the typical bays defined in the templates, then the virtual terminal connection relation of IEDs which are associated with primary devices within bays can be established automatically according to the virtual terminal connection relation templates.

3 Automatic Virtual Terminal Connection Based on SSD

By analyzing the relationship between virtual terminal connection relation and on the SSD file, and the content of the SSD file, this paper presents a method of automatic virtual terminal connection of smart substation. The process of realizing virtual terminal automatic connection is as follows.

Step 1: Smart substation configuration tool software imports virtual terminal connection template file (hereinafter referred to as template).
Step 2: The tool imports the device model ICD file corresponding to the secondary device, names and creates IED.
Step 3: If there is an SSD file, import it. Otherwise, draw the main electrical wiring diagram in the tool according to the blueprint provided by design institute, including drawing voltage levels, bays, and primary devices. Finally, configure the primary and secondary devices association for the whole substation.
Step 4: The tool maps each bay in the main electrical wiring diagram to a typical bay in the template.
Step 5: The tool maps the IED associated with the primary device in the bay to the sender or receiver IED role in the typical bay.
Step 6: The tool maps the sender or the receiver virtual terminal in the IED to the sender or the receiver virtual terminal of the virtual circuit in the template, and then establishes the virtual terminal connection relation.

In the following, the template definition method, bay mapping method, IED mapping method and virtual terminal mapping method (see Fig. 1) are discussed in detail.

3.1 Template Definition

Typical bay virtual terminal connection relation template file does not vary from the project. It includes virtual terminal connection relation of typical bays in a variety

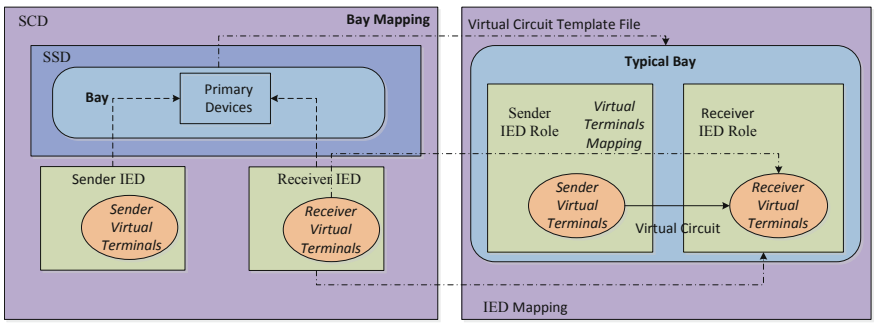

Fig. 1 Principle diagram of model mapping in automatic connection

```
<VirtualCircuitTemplate>
  <Bay mainDeviceType="CBR" desc="line bay" voltageLevel="220kV" connectionDesc="double bus connection"
multiSetProtection="true">
    <SecondaryDeviceSet>
      <SecondaryDeviceRole typeKey="I_L" desc="line intelligent terminal">
        <PrimaryDevice lnClass="XCBR" typeClass="CBR" desc="circuit breaker"/>
        <PrimaryDevice lnClass="XSWI" typeClass="DIS" desc="isolation switch"/>
      </SecondaryDeviceRole>
      <SecondaryDeviceRole typeKey="M_L" desc="line merging unit">
        <PrimaryDevice lnClass="TCTR" typeClass="CTR" desc="current transofrmer"/>
        <PrimaryDevice lnClass="TVTR" typeClass="VTR" desc="virtual voltage transformer" virtual="true" sourceDeviceKey="M_M
$AND$SameVoltage"/>
      </SecondaryDeviceRole>
    </SecondaryDeviceSet>
    <VirtualCircuitSet>
      <VirtualCircuitGroup txIEDTypeKey="I_L" rxIEDTypeKey="P_L" msgType="GOOSE">
        <VirtualCircuit txLnClass="XCBR" txVPortKey="circuit breaker phase A position" rxVPortKey="circuit breaker phase A position"/>
        <VirtualCircuit txLnClass="GGIO" txVPortKey="block reclosing by low pressure" rxVPortKey=" block reclosing by low pressure"/
      </VirtualCircuitGroup>
    </VirtualCircuitSet>
  </Bay>
```

Fig. 2 Segment of typical bay virtual terminal connection relation template file

of voltage levels and connection types. For versatility and ease of processing by smart substation system configuration tool software, XML file could be used to store template data, an example of segment of the template file (see Fig. 2) is as follows:

The nodes and their contents of the template file are shown in Table 2.

The Bay node in Table 2 contains a SecondaryDeviceSet node and a VirtualCircuitSet node, and the properties of the node are shown in Table 3.

The SecondaryDeviceRole node in Table 2 describes the role of the secondary device associated with the primary device in a typical bay, and the attributes of the node are shown in Table 4.

The PrimaryDevice node in Table 2 represents the primary device associated with the LN of the secondary device, and the properties of the node are shown in Table 5.

Table 2 Name and content of nodes in the template file

Node name	Node content
VirtualCircuitTemplate	Template file root node
Bay	Typical bay node, including primary devices within bay, associated secondary devices, and virtual terminal connection relation
SecondaryDeviceSet	Secondary device set node, including secondary device roles
SecondaryDeviceRole	Secondary device role node, describing the type of secondary device
PrimaryDevice	Primary device node, describing primary and secondary device correlation information
VirtualCircuitSet	Virtual circuit set node, containing virtual circuit groups contained in typical bays
VirtualCircuitGroup	Virtual circuit group node, which contains all virtual circuits in one direction between two secondary device roles
VirtualCircuit	Virtual circuit node, describing virtual terminal connection relation between two virtual terminals

Table 3 Name and content of attributes of the Bay node

Attribute name	Attribute content
MainDeviceType	Main device type of primary device within bay
Desc	Description of the typical bay
VoltageLevel	Voltage level of bay
ConnectionDesc	Connection type of the voltage level
MultiSetProtection	Flag of multiple sets of protection device

Table 4 Name and content of attributes of the SecondaryDeviceRole node

Attribute name	Attribute content
TypeKey	Secondary device role type keyword, which is composed of IED type and device type
Desc	Role description of secondary device

Table 5 Name and content of attributes of the PrimaryDevice node

Attribute name	Attribute content
lnClass	lnClass of LN associated with primary device
TypeClass	Device type of the primary device
Desc	Description of the primary device
Virtual	Flag of virtual primary device
sourceDeviceKey	Secondary device role keyword as actual data source when secondary device's LN is associated with virtual primary device

The VirtualCircuitGroup node in Table 2 contains all one-way virtual terminal connections between two secondary device roles, and the properties of the node are shown in Table 6.

The VirtualCircuit node in Table 2 represents the virtual circuit of two virtual terminals in a typical bay. The properties of the node are shown in Table 7.

Table 6 Name and content of attributes of the VirtualCircuitGroup node

Attribute name	Attribute content
txIEDTypeKey	Keywords of the sender IED secondary device role type
rxIEDTypeKey	Keywords of the receiver IED secondary device role type
msgType	virtual circuit message type: GOOSE or SV

Table 7 Name and content of attributes of the VirtualCircuit node

Attribute name	Attribute content
txLnClass	lnClass of the LN where the virtual terminal is sent
txVPortKey	Send virtual terminal description keywords
rxVPortKey	Receiving description keywords of virtual terminals

3.2 Bay Mapping

An example of the segment of the bay definition in the SSD file (see Fig. 3) is shown as follows.

Because the typical bays in the template file are typical bays with various voltage levels and connection types, mapping the bays in the SSD file to the typical bays in the template file needs to get following information.

(1) Connection type: Relevant specification requires that in the primary device bay model, the bay object contains a Private element to describe the bay type, and the type of the element is "CIME-btype". The element contains two properties: dType and desc, describing the connection type of the voltage level to which the bay belongs.
(2) Voltage level: According to the SSD file structure, the VoltageLevel node is the parent of the Bay node, so the voltage level could be obtained by getting the Voltage node that defines the voltage level in the VoltageLevel node, to which the Bay node belongs.
(3) Bay type: Because usually only one main primary device is included in a bay, the type property of the main primary device can be used as the bay type. The main bay devices include circuit breaker, transformer, bus, line, reactor, capacitor and so on.

The above connection type, voltage level and bay type can be matched with the value of attribute connectionDesc, voltageLevel and mainDeviceType of Bay nodes listed in Table 3 to determine the mapped typical bay.

```
<VoltageLevel name="110kV" desc="110kV">
  <Voltage multiplier="k" unit="V">110</Voltage>
    <Bay name="CBR15B"desc="15B switch bay">
      <Private type="CIME-btype" ecim:dType="6" ecim:desc="single bus connec-tion" />
      <ConductingEquipment name="CBR15B" desc="15B circuit breaker" virtu-al="false" type="CBR">
```

Fig. 3 Segment of bay definition in the SSD file

3.3 IED Mapping

The SSD file needs to contain complete primary and secondary devices association information [17]. For example, the LNode nodes representing logical nodes associated with a circuit breaker are defined in the SSD file as follows (see Fig. 4).

The above LNode nodes describe the information about the LNode nodes associated with the circuit breaker, including the IED name (iedName), logical device name (ldInst), logical node type (lnType) and logical node name combined by prefix, lnClass and lnInst, so the IED name associated with the primary device can be obtained through the LNode node. Relevant specifications stipulate that the name of IED should be named with five layers structure as shown in Table 8.

Therefore, IEDs can be mapped to specific secondary device roles in typical bays according to IED names in the following steps.

(1) IED grouping: According to the eighth character of IED name, i.e. IED set number, set the grouping number for IED: A, B, C, D or X (representing single set) to ensure that the virtual terminals of IEDs in different sets are not connected.
(2) Role mapping: To determine which secondary device role the IED can be mapped to in a typical bay, match the first 3 characters of the IED name, that is, the IED type and the device type with the typeKey attribute of the SecondaryDeviceRole node in Table 4. And at the same time, the type of the associated primary device and the lnClass of the associated logical node are matched respectively with the attributes typeClass and lnClass of the PrimaryDevice node in Table 5.
(3) Redirection of receiving data related to virtual primary device: In addition to the existing primary device, there are also virtual primary devices in the SSD file. Therefore, although these virtual primary devices are also associated with the relevant logical nodes, in fact, the data input of these logical nodes comes

```
<ConductingEquipment name=" CBR15B" desc="15B circuit break-er"virtual="false" type="CBR">
  <LNode lnInst="2"lnClass="PTRC" iedName="P_T2201A" ldInst="PIGO" lnType="" prefix=""/>
  <LNode lnInst="2"lnClass="PTRC" iedName="P_T2201B" ldInst="PIGO" lnType="" prefix=""/>
  <LNode lnInst="1"lnClass="MMXU" iedName="C_T1101" ldInst="MEAS" lnType="" prefix=""/>
  <LNode lnInst="1"lnClass="XCBR" iedName="I_T1101A" ldInst="RPIT" lnType="" prefix=""/>
  <LNode lnInst="1"lnClass="XCBR" iedName="I_T1101B" ldInst="RPIT" lnType="" prefix=""/>
```

Fig. 4 Segment of LNode nodes associated with a circuit breaker in the SSD file

Table 8 Structure of IED name

1st character	2nd character	3rd character	4th character	5th character	6th character	7th character	8th character
IED type		Device type	Voltage level		Device sequence number		IED set number

from the IED associated with other real primary devices. To determine the real data source IEDs, the virtual attribute in Table 5 of virtual primary device node should be "true" in the template, and the sourceDeviceKey attribute should be the device type keyword of the real receiving data source.

3.4 Virtual Terminal Mapping

The task of virtual terminal mapping is to find the sending virtual terminals in the sending IED and receiving virtual terminals in the receiving IED, according to the keywords of the VirtualCircuit node in the template to establish the virtual circuit. Although the virtual terminals' description or reference [18–21] associated with the protection device has been standardized in the relevant specification, the virtual terminals of secondary devices with GOOSE or SV communications with the protection devices are not covered, such as intelligent terminal, merging unit and so on.

Therefore, in order to increase the flexibility of matching, use $OR in virtual terminal keywords to connect multiple keywords that may need to be matched, and use $AND to connect multiple keywords that need to be matched at the same time. As the virtual terminal connection between bus protection device and other protection devices in different branches are related to the branch number, $BranchNumber is used in the template to represent the branch number, and the virtual terminal keywords to be matched are automatically converted based on the device sequence number in IED name and the branch numbers defined for bus protection device.

4 Application Analysis

The above virtual terminal automatic connection method based on SSD can be applied to the new station or the configuration of the station reconstruction and expansion.

The application steps in the integrated configuration of the new station are as follows:

(1) Importing ICD, SSD and virtual terminal connection template files.
(2) Automatically establishing virtual terminal connection relationship.
(3) Automatically generating virtual terminal connection reports R1 during the establishment process for users to check the automatic configuration results.

The application steps for substation reconstruction and expansion are as follows:

(1) Importing ICD, SSD and virtual terminal connection template files.
(2) Calculating the difference D1 between existing connection relations and templates in the station based on automatic connection results.
(3) Automatically establishing virtual terminal connection relations in the reconstruction and extension parts.
(4) Automatically generating virtual terminal connection report R2.
(5) Recording manual modification in report R3 during debugging.
(6) Calculating the difference D2 between existing connection relations and templates in the station based on automatic connection results.
(7) Check whether D2 = D1 + R2 + R3, and if not equal, it indicates that the virtual terminal connection relationship has been modified incorrectly and not recorded in the manual modification in report R3, which needs manual correction.

The above examples show that the application of virtual terminal automatic connection method can improve the efficiency of virtual terminal connection on the one hand, and is conducive to the configuration time needed for the virtual terminal connection of new station, on the other hand, it can improve the security of configuration modification during reconstruction and expansion, discover the changes of the undesirable virtual terminal connection relationship in advance, and shorten the debugging time.

5 Conclusion

In this paper, a method of automatic virtual terminal connection for smart substation is proposed. By using the primary devices topology and primary and secondary devices association contained in the SSD file, the bay mapping, IED mapping and virtual terminal mapping from SCD model to virtual terminal connection relation template file are automatically realized, and the automatic virtual terminal connection is completed. In order to apply this method better, it is necessary to improve configuration of the association for primary and secondary devices in the SSD file more efficiently and accurately. The deepening research and practical application of this method will play a positive role in improving the automation level and accuracy of system integration.

References

1. DL/T 860 (2006) Communication networks and systems in substations
2. Q/GDW 383—2009 (2009) Technical guide for smart substation. State Grid Corporation of China, Beijing
3. Zhang Q, Jia H, Ye H (2015) Design and application of virtual secondary circuit monitoring in smart substation. Power Syst Prot Control 43(10):123–128
4. Hao S, Li Y, Zhang T (2017) Scheme of communication network and network management system for new generation smart substation. Autom Electric Power Syst 41(17):148–154
5. Li J, Hu R, Wang L (2018) Engineering configuration scheme based on IEC 61850 Ed 2.0 in smart substation. Autom Electric Power Syst 42(2):154–159
6. Hu S, Li L, Zhu X (2017) Scheme and practice for improving engineering implementation efficiency of smart substation automation system. Autom Electric Power Syst 41(11):173–180
7. Yang H, Wen D, Gao L (2017) Automatic generation of secondary circuit virtual connection in smart substation. Power Syst Prot Control 45(23):116–121
8. Huang Z, Li Y, Li T (2017) Design and implementation of automatic generation technology of SCD file virtual circuit in smart substation. Power Syst Prot Control 45(17):106–111
9. Chen P, Lin C, Tang H (2013) A method for virtual terminals automatic connection based on key-character matching. Relay 41(18):132–137
10. Gao L, Yan P, Ruan S (2017) Application of similarity-calculation-based learning template library in design and check of virtual circuit. Electr Power Autom Equip 37(7):205–212
11. Hou L, Feng L, Yang Q (2015) Research of smart substation virtual circuit automatic checking. Power Syst Clean Energy 31(6):44–48
12. Gao X, Yang Y (2014) Jiang Jianning: analysis of secondary circuit monitoring methods based on SCD. Power Syst Prot Control 42(15):149–154
13. Zhou C, Wu H, Hu G (2017) Non-intruding development of automatic test system based on IEC 61850 edition 2.0. Power Syst Prot Control 45(14):43–147
14. Cheng Y, Yang X, Su X (2016) Study of secondary circuit simulation algorithm based on topology. Shaanxi Electr Power 44(11):57–61
15. Q/GDW 11662—2017 (2017) Technical specification of system configuration description files for smart substation. State Grid Corporation of China, Beijing
16. IEC 61850-6 (2008) Communication networks and systems for power utility automation: part 6 configuration description language for communication in electrical substations related to IEDs
17. Q/GDW 1396—2013 (2013) Data model of protection relay in project based on IEC61850. State Grid Corporation of China, Beijing
18. Q/GDW 1175—2013 (2013) Standardization design specification for power transformer, high voltage shunt reactor, bus bar protection and auxiliary equipments. State Grid Corporation of China, Beijing
19. Q/GDW 1161—2014 (2014) Standardization design specification for transmission line protection and auxiliary equipments. State Grid Corporation of China, Beijing
20. Q/GDW 1766—2015 (2015) Standardization design specification for 10–110 kV transmission line protection and auxiliary equipments. State Grid Corporation of China, Beijing
21. Q/GDW 1767—2015 (2015) Standardization design specification for 10–110 kV component protection and auxiliary equipments. State Grid Corporation of China, Beijing

Communication Technology Between Substations of Security and Stability Control System Based on IEC61850

Dongxu Chang, Qi Guo, Yihua Zhu, Zuyi Ren and Yang Bai

Abstract The traditional communication technology between substations of security and stability control system (SSC) has some inherent shortcomings. It does not conform to the trend of current technological development, and restricts the expansion and application of SSC. According to the IEC 61850-90-1 standard, using intelligent substation process layer GOOSE communication technology, a new communication technology between substations based on IEC61850 in SSC is proposed in this paper. The key technology of communication network architecture, communication capacity control, data flow control and visualization of decoupling configuration are deeply researched, and the typical project of Brazil Belo Monte SSC project is introduced. This technology has several advantages, such as stable and reliable communication, data transmission capacity, reusability and interoperability. It can meet the demand of information exchange between substations, and it represents the development direction of the communication technology of SSC.

Keywords Security and stability control system · Communication between substations · IEC 61850 · GOOSE

1 Introduction

The power system security and stability control system (SSC) is a system consisting of two or more substation security and stability control devices connected through communication equipment. It is an important facility of defense to ensure the security and stability operation of the power grid [1, 2]. In SSC, the power system

D. Chang (✉) · Q. Guo · Y. Zhu
Key Laboratory of Power System Simulation, Electric Power Research Institute, Southern Power Grid China, Guangzhou 510663, China
e-mail: changdx@csg.cn

Z. Ren · Y. Bai
NR Electric Co., Ltd, Nanjing 211102, China

Y. Xue et al. (eds.), *Proceedings of PURPLE MOUNTAIN FORUM 2019-International Forum on Smart Grid Protection and Control*, Lecture Notes in Electrical Engineering 585, https://doi.org/10.1007/978-981-13-9783-7_42

communication network is used to realize the transmission of the information of the power flow, the running state and the component fault between the substation devices. When serious failure occurred, the rapid centralized or decentralized generations cutting and load shedding measures of SSC are taken to keep the stability of power grid [3, 4]. The SSC is heavily dependent on the communication between substations. The real-time and reliability of the communication technology will directly affect the correctness of the SSC, and then affect the security and stability operation of the power grid.

The traditional communication scheme of SSC is the point to point mode, and the application layer data is fully and clearly self-defined. As the self-checking mechanism of the application layer data frame, the reliability of the data transmission is guaranteed and the basic requirement of the communication between the substations is satisfied, so it is widely used [5–7]. However, the communication scheme based on engineering custom and closed communication is very coupled with the SSC projects, the utilization rate of communication bandwidth is not high and the real-time performance is poor; the communication of the stability control devices of each manufacturer is not interoperable, and the reliability check of the communication is simple, and it does not conform to the trend of the current technology development.

With the gradual popularization and improvement of the smart substation based on the IEC61850 protocol, the acquisition, sharing and interoperation of the process layer messages in the substation become possible [8, 9]. It also provides rich experience and useful reference for the wide area information exchange between the substations. The technical report of the communication application between the substations IEC61850-90-1 [10] has been included in the IEC61850 Ed2.0. According to the existing application experience and specific requirements, this paper introduces a new communication technology between substations of SSC to realize the observability and configurability of communication network. This communication scheme will improve the effective utilization of the communication bandwidth, the standardization of the communication protocol and the reliability verification of the data. The independent text configuration makes the communication content and the device policy software part decoupled, and can meet the actual needs of the field, thus further improving and optimizing the performance of the SSC.

2 Introduction Traditional Communication Technology Between Substations Overview

With the development of the power system communication network, the power communication network has formed a special power communication network architecture based on the main features of optical fiber communication, hierarchical classification and self-healing ring network, mainly with synchronous digital

hierarchy/multi-service transport platform (SDH/MSTP) the equipment builds backbone transmission network [3].

Most of the SSCs adopt a hierarchical and distributed structure [3], which can be divided into master stations, control stations, and executive stations. The communication between substations is dominated by 2 Mbps dedicated fiber channels or 2 Mbps fiber multiplexed channels, and it uses a point to point advanced data link control (HDLC) protocol to translucent transparently. The stability control master station configuring a multiplex communication interface device, and the data sent to the control stations and the execution stations can be connected to the SDH device through the communication interface devices (MUX) conforming to the E1 standard. The typical communication architecture of SSC is shown in Fig. 1.

With the expansion of the SSC and the deepening of its application, the traditional communication scheme which is customized with the SSC project gradually shows its drawbacks in the aspects of communication capacity, universality and interactivity.

First, the communication between two stations is realized through the point to point communication. The network topology is customized according to the function of the system. When the system needs to be expanded, it not only needs to adjust and increase the original communication network, but also needs to upgrade the stability control device software of the related substation and power plants.

Second, as using the 1B4B coding mode, the amount of information that can be effectively transmitted under the condition of real-time data is less than 32 bytes. Also, the method of communication check is simple and the communication is easily interfered.

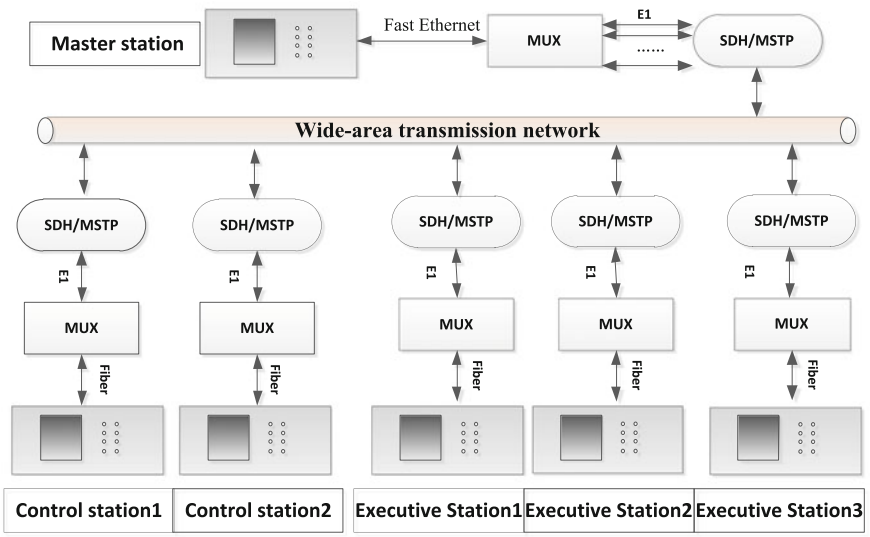

Fig. 1 Traditional communication architecture of SSC

Third, the communication protocol between the substations of the SSC is a custom protocol by the equipment manufacturer to customize the information needed for the transmission according to the function of the system. The communication mode is relatively closed and the communication interoperability between the various manufacturers is not strong.

At last, as the scale of its supporting SSC scale is becoming more and more large, the number of the main station access stations in some stable control areas is up to 50–60. The traditional communication networking mode can achieve [3, 4] by extending more communication single elements, and increasing the development and operation of the device. The complexity and reliability of communication are reduced.

Now the digital process layer communication has been generally used in the smart substations [12–15]. It has accumulated rich experience in the area of SV synchronous sampling and GOOSE transmission mechanism. With the rapid development of power system communication technology, these problems are urgently needed to extend the existing intelligent technology from the station domain to the wide area, realize the information sharing between the station and the whole regional power grid, and use the multi-dimensional information of the power grid to further improve and optimize the performance of the existing SSC and improve the power supply of the power grid.

3 Communication Architecture Between Substations Based on IEC61850

According to the IEC61850-90-1 technology report [10, 11], the communication between stations in the SSC can adopt the L2 layer tunneling protocol (L2TP) recommended by IEC61850-90-1, that is, allows the use of "direct access" to remote station functions to connect to variable power station networks, and two substations use high-speed channels to exchange information directly. Tunnels are configured for specific types of protocols, such as VLAN ID or static multicast. Considering bandwidth utilization, communication reliability and data flow control, GOOSE message is used as multicast message of SSC Layer 2. Also, the Manufacturing Information System (MMS) is used in the SSC station devices and dispatching center monitoring system to send the real-time operation and trip messages. The ideal communication architecture between substations of SSC based on IEC61850-90-1 is shown in Fig. 2.

The station control devices are directly connected to the SDH via optical fiber Ethernet. The SDH devices implement the process layer GOOSE message and the MMS point to multipoint multicast transmission on the wide area network, and prevent the unrestricted transmission of multicast packets through the time slot

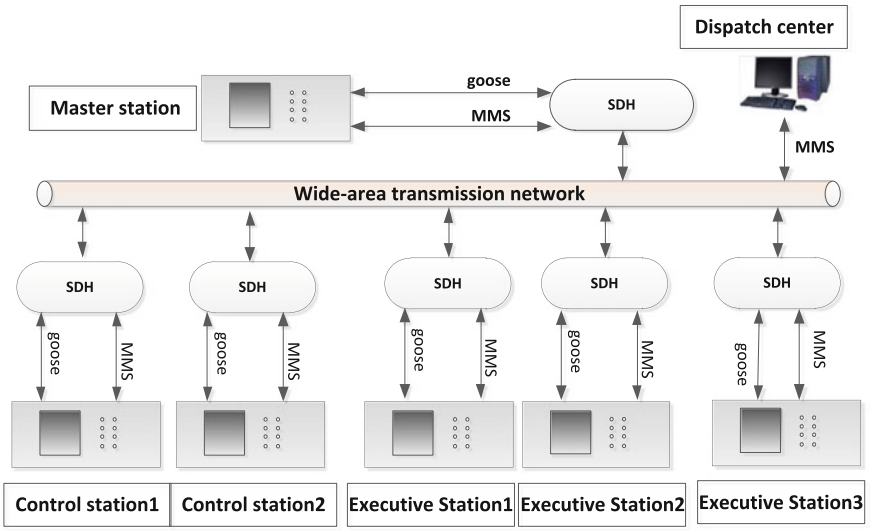

Fig. 2 Ideal communication architecture between substations of SSC based on IEC 61850

allocation and VLAN division, so as to avoid the bandwidth waste and network storm. It needs to upgrade the existing SDH equipment and have the shortcomings of the system communication configuration and the close coupling of the communication network topology. It is not suitable for the communication link design and management of the large area interconnected SSC.

In this paper, the communication scheme of Fig. 2 is partially corrected. For example, Fig. 3, by adding a new process layer switch to realize multicast traffic control, the GOOSE message between substations is implemented multicast communication in LAN and point to point communication in WAN, and then through Fast Ethernet (FE)-E1 protocol converter, the GOOSE message is converted to E1 signal and then access to SDH. The MMS message of the SSC is also connected to the SDH through the E1 interface.

The communication network topology of the scheme is consistent with the traditional SSC, and the existing communication network configuration does not need to make any changes. However, the implementation of multicast communication technology on the process layer switch based IEC61850 can solve the common, interactivity and extensibility of the traditional communication of SSC. In addition, because the process layer switch and FE-E1 protocol converter are both standard communication products, it can also avoid the common problem of the communication interface conversion device, thus making the communication interoperation of the stability control devices of different equipment manufacturers available.

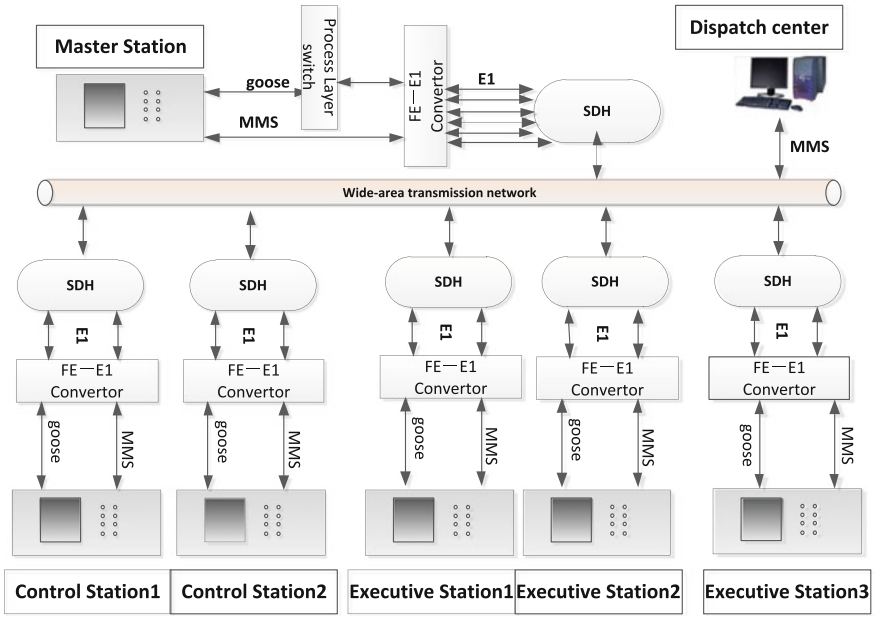

Fig. 3 Typical communication architecture between substations of SSC based on IEC 61850

4 Key Technology

4.1 Traffic Flow Control

In order to realize the security isolation of the data of the stable control system in the wide area network, it is necessary to divide the VLAN into the process layer switch and set up the VLAN ID for the corresponding communication ports of each substation device. The setup of VLANID is similar to the IED device of the smart substation and is included in the GOOSE message to control the transmission direction and traffic of the communication data. With the VLAN settings, the master station can send data to all other stations, but other stations can only send data to the master station. In this way, a multicast communication between the master station and the other stations is realized, and the network broadcast storm is effectively suppressed by the flow control of the process layer switch, and it is converted to the point to point communication on the wide area network.

At present, each control device of the mainstream manufacturer supports at least 60 or more GOOSE control blocks, meets the ability to communicate at the same time in 60 stations, and the process layer switches can also be extended through cascading. Therefore, this communication scheme can fully meet the needs of the development of the current control system and have good observability and controllability.

4.2 Communication Capacity Control

The regular GOOSE message [12, 13] sends 1 frame heartbeat messages at interval T_0 when no event triggers, when any GOOSE PDU data changes, triggers a GOOSE event, the device immediately sends out the new data, then the interval T_1 sends second frames, third frames, interval T_2 sends fourth frames ($T_2 = 2T_1$), interval T_3 sends fifth frames ($T_3 = 2T_2$). After the 5 frame, the GOOSE message is sent to the heartbeat message T_0. If the heartbeat signal is not received after 2 times T_0 (typical value is 10 s), the GOOSE break chain is reported, as shown in Fig. 4a.

However, the GOOSE PDU data transmitted by the stability control device contains real-time analog data, which will trigger an event in the minimum sampling interval. The current communication network cannot meet such a large scale of fast data transmissions and easily cause network congestion. In order to control data traffic, synchronization of GOOSE messages must be transmitted.

This paper proposes a simple method to solve this problem. A serial number F_n is added in GOOSE PDU, with a range of 0–255. F_n adds 1 to the interval T_s (T_s less than T_1), and when F_n is greater than 255, it starts again from 0 and adds 1. At the time of each interval of T_s, the amount of analog or switch in the valid data is refreshed to the latest value. At the same time, the information number $F_n + 1$, based on the transmission mechanism of the GOOSE message, will immediately trigger the sending of an event. Because T_s is less than T_1, GOOSE will again be

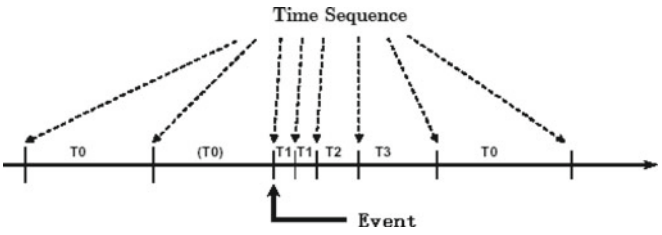

(a) Normal GOOSE transmission

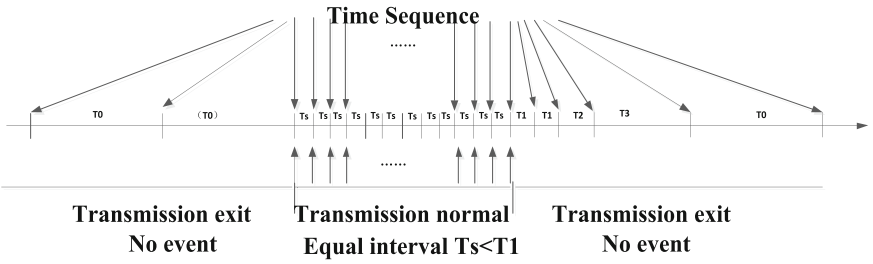

(b) GOOSE transmission between substations of SSC

Fig. 4 Process of GOOSE sending

triggered by events that are separated from T_s before retransmitting the message, sending a new GOOSE message. Therefore, the data received on the receiving side is the data refreshed according to the equal interval T_s, and the data of each frame are different. The transmission time sequence is shown in Fig. 4b. When the transmission side device is repair or other reasons need to exit, the device will not update the information serial number F_n, the GOOSE message enters the standard transmission mode. So the bandwidth occupied by GOOSE is much smaller than the bandwidth occupied by normal transmission when communication is out of service.

When the communication between stations is normal, F_n adds 1 at equal intervals of T_s; and when the communication channel between the two stations is abnormal or one of the transmission side exit, the reception side device has not been able to receive the new valid frame, which can distinguish the communication channel from the interrupt or exit state through the F_n no change over 1 s, without waiting for the 2 times of the T0 extension (generally 10 s). The receiving side can detect the state of the channel quickly and effectively, enabling or locking the relevant logic functions of the stability control device.

4.3 Communication Configuration Method

The communication models of all substations in the SSC should be established in accordance with the IEC 61850-90-1 specification, and should be included in the system exchange description (SED) file of the device. The debugger can automatically complete the communication configuration of the virtual terminal of the device through the Smart Substation Configuration Description Language tool (SCL) according to the SED files of the substations [14, 15].

This paper proposes a virtual terminal design method to improve the efficiency of communication configuration and maintenance. The virtual terminals are the sending ends or receiving terminals of data exchanged between substations. Virtual terminal technology of the communication between substations completely inherits the virtual terminal scheme of smart substation, and also inherits its graphical and visual advantages, which simplifies field debugging and maintenance.

The communication configuration is independent of the function of the SSC. When the function of SSC needs to be upgraded, the new SCD file is constructed only according to the new SED file of the substation, and the corresponding configuration files are generated to update the communication configuration of the stable control devices of each station. It is completely decoupled from the control strategy function of the device, thus reducing the complexity of system upgrade and maintenance.

Table 1 Comparison of the communication technologies between substations of SSC

Index	Traditional technology	Technology based IEC61850
Capacity	No more than 32 bytes per frame, only communicate with 16 factory stations at most	Each frame can reach 512 bytes, and it can communicate with 60 factory stations at most
Bandwidth utilization	No more than 25% of the actual bandwidth	Full use of the actual bandwidth rate with margin
Real-time	Frame multiplexing and multi frame check are needed, and the real-time performance is poor	The real-time data can reach the traditional technology level when the data transmission volume is the largest
Reliability	Simple custom and calibration methods	Universal data check and frame check union mechanism
Configuration	Not support	Decoupling configuration with SCL tools
Interoperability	Interoperability cannot be achieved based on specific communication protocols	Based on IEC 61850 specification, all manufacturers can interoperate

4.4 Technology Comparison

According to the above analysis and research, the comparison of the communication technology of SSC between the IEC 61850 and the traditional is shown in Table 1. As the result, the communication technology based on IEC61850 is much more stable and reliable, has large data transmission, reusability and interoperability. It can realize the decoupling configuration of the control strategy and the function of the communication.

5 Project Application Overview

The communication technology between substations proposed in this paper has been applied in the SSC project of Brazil Belo Monte HVDC, which consists of 5 substations. Xingu converter station, as the master station, judges the HVDC operation status and receives the transmission line fault information sent by three control stations of Manaus, TUCU and Parauapeba. According to the system control strategy and the fault information, the Xingu master station will send out the generations cutting command to the Belo Monte hydropower executive station. The SSC is divided into A, B system, and the communication A and B systems are also independent of each other, as shown in Fig. 5. Xingu master station A, B system each configuration 1 process layer switch, using VLAN technology to realize communication data distribution and traffic control; and configure 1 common Ethernet switches to assemble the MMS messages of A and B systems and

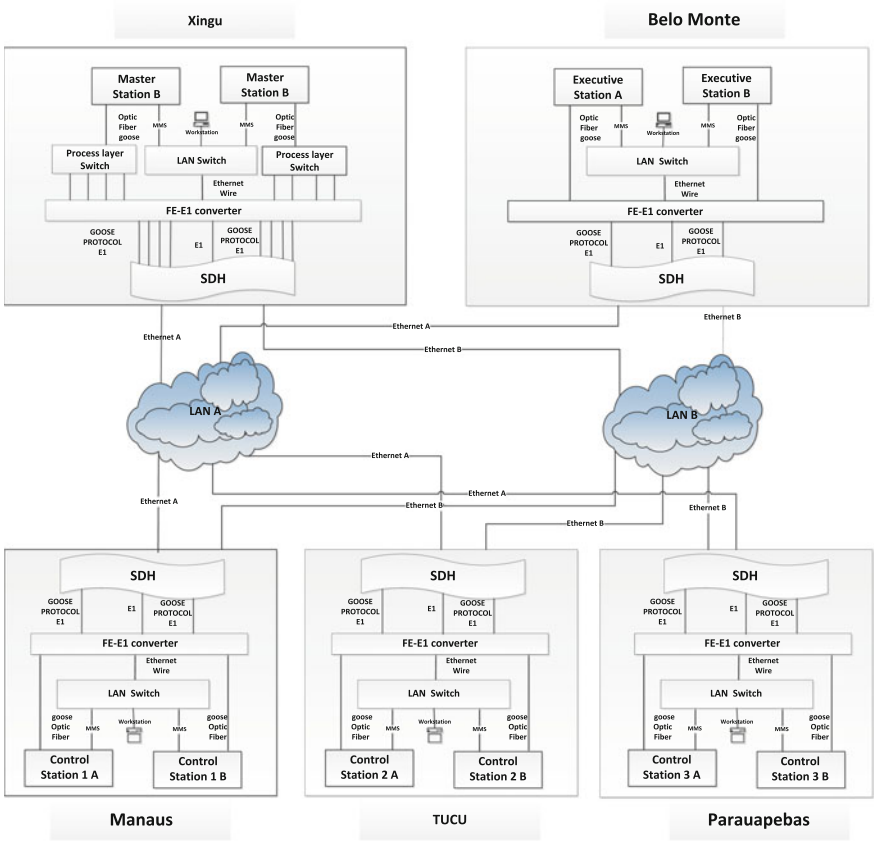

Fig. 5 Communication topological diagram of Brazil Belo Monte project

access to the FE-E1 protocol converter together with the communication GOOSE message between the substations. Other control stations and Belo Monte execution stations only need to configure 1 Ethernet switches and 1 FE-E1 converters because they only communicate with the Xingu master station.

The communication between substations is designed according to the communication technology proposed in this paper. According to the calculation, the GOOSE message frame of Xingu control master station communication is 208 bytes, and the communication bandwidth between each station is designed as 2 Mbps. In order to facilitate the subsequent upgrade and expansion of the system, the GOOSE message interval T_s is set to 5 ms and T_1 is set to 6 ms. The SED model of each station's communication forms the virtual terminal table of the whole system through the SCD tool, thus completing the communication configuration. The MMS message from each station is connected to the SDH device through the E1 interface and sent to the local or remote monitoring backstage by 2 M special tunnel.

The GOOSE information transmission between substations in the SSC project of Brazil Belo Monte HVDC has been put into operation successfully. At the same time, the communication scheme has also been applied in the more large-scale stabilization projects such as Ecuador national grid, and has successfully interoperable verification with the manufacturers of ABB, SIEMENS and other equipment manufacturers.

6 Conclusion

This paper designs communication scheme between substations of SSC based on the IEC 61850 standard, which includes the key technologies such as communication capacity control, traffic flow control, communication visualization decoupling configuration and so on. It realizes the advantages of the traditional inter station communication protocol and through the sending end. Time sequence control and wide area network VLAN ID allocation control data flow and data distribution to adapt to different types of communication network bandwidth and communication topology, and simplify the workload of communication configuration.

The communication technology based on IEC61850 has been mature and reliable, and it can be applied in some new SSC projects which are qualified. Due to the limitation on the bandwidth allocation of communication between stations of SSC, usually for 2 Mbps, only the L2TP direct transmission mode can be used at current situation, which limits the deep application of GOOSE wide-area multicast communication in SSC project. At the same time, as the wide-area multicast communication technology is introduced into power system communication network, it is necessary to further study whether it meets the requirements of current power system communication security. Based on the research results, the communication technology between substations of SSC is further improved and optimized to lay the foundation for popularization and application.

References

1. Guo Q, Han W, Zeng Y et al (2012) Security and stability control technology test and research platform based on real-time simulation part one framework and characteristics. Autom Electr Power Syst 36(20):1–5
2. Shao J, Li X, Fang Y (2007) Universal tester of security and stability control devices. Autom Electr Power Syst 31(17):90–93
3. Chen G, Li M, Xu T (2018) System protection and its key technologies of UHV AC and DC power grid. Autom Electr Power Syst 42(22):2–10
4. Luo Y, Chen D, Li Y et al (2018) Design of system protection scheme for North China Multi-UHV AC and DC strong coupling large receiving-end power grid. Autom Electr Power Syst 42(22):11–18

5. Xu T, Li G, Yu Zhao et al (2017) Design and application of emergency coordination control system for multi-infeed HVDC receiving-end system coping with frequency stability problem. Autom Electr Power Syst 41(8):98–104
6. Yin W, Yan Y, Pan Q et al (2018) Design of fast communication interface for precision load control system. Autom Electr Power Syst 42(10):143–149
7. Li D, Luo J (2016) Typical design of security and stability control system for UHVDC transmission. Autom Electr Power Syst 40(14):151–157
8. IEC61850-7-2 (2003) Communication networks and systems in substations-Part 7-2: basic communication structure for substations and feeder equipment–abstract communication service interface(ACSI)
9. Hu D, Wo J (2010) Virtual circuit system of smart substations based on IEC 61850. Autom Electr Power Syst 34(17):78–82
10. IEC/TR 561850-90-1 communication networks and system for power utility automation—Part 90-1: use of IEC61850 for the communication between substations. 2010–03
11. Ren Y, Cao F (2013) New development and new application of IEC61850. Autom Electr Power Syst 37(2):1–6
12. Wang Z, Wang G, Tong J et al (2017) Efficient integrity authentication method for GOOSE packet. Autom Electr Power Syst 41(2):173–177
13. Xu C, Sun Y (2007) A communication solution of process layer GOOSE in digitized substation. Autom Electr Power Syst 31(19):91–94
14. Li J, Hu R, Wang L et al (2018) Engineering configuration scheme based on IEC 61850 Ed 2.0 in smart substation. Autom Electr Power Syst 42(2):154–159
15. Li J, Wu F, Zhang X (2018) Communication method of protection information between substations and control centers based on IEC 61850 Ed 2.0. Autom Electr Power Syst 42 (3):130–135

Research on the Visualization Technology of the Secondary Circuit of Intelligent Substation Based on CIM/G

Xie Zhang, Haifeng Wang, Jian Zhang and Yulong Pei

Abstract With the wide application of IEC 61850, the actual electrical connection of the cable in the intelligent substation has been replaced by the other media such as the optical fiber, which directly causes the invisibility of the secondary circuit and brings inconvenience to the operation and maintenance. To solve these problems, the visualization technology of the secondary circuit of intelligent substation based on CIM/G is proposed in this paper. The automatic parsing technology of the secondary circuit connection relationship in the SCD file is introduced, together with the automatic generation technology of the visual interface. The visualization technology adopted here not only realizes the static layout of the physical circuit and the logic circuit in the monitoring interface, but also achieves the dynamic refresh of the graphical objects which reflects the real-time status of the circuit. Finally, the effectiveness of the proposed methods is successfully demonstrated by the practical application, and the comprehensive performance of this automatic visualization technology is evaluated to be superior to the traditional manual mode.

Keywords CIM/G · Secondary circuit · Visualization technology

1 Introduction

With the full application of the IEC 61850 standard in intelligent substations [1, 2], a large number of cables have been replaced by a small number of optical fibers, due to the characteristics of multi-channel information multiplexing in digital network communication. Corresponding to the actual terminal in the traditional panel, the virtual terminal is used to reflect the opening and closing state of the protection device. As a description file of the virtual terminal connection

X. Zhang (✉) · H. Wang · J. Zhang · Y. Pei
NARI Group Co. (State Grid Electric Power Research Institute), Nanjing, China
e-mail: zhangxie@sgepri.sgcc.com.cn

X. Zhang · H. Wang · J. Zhang · Y. Pei
NARI Technology Co. Ltd, Nanjing, China

Y. Xue et al. (eds.), *Proceedings of PURPLE MOUNTAIN FORUM 2019-International Forum on Smart Grid Protection and Control*, Lecture Notes in Electrical Engineering 585, https://doi.org/10.1007/978-981-13-9783-7_43

relationship in the entire intelligent substation, the substation system configuration description (SCD) file contains the logical connection relationship between the devices, which plays a very important role in substations [3–5].

With the rapid development of the power grid, the corresponding protection devices in the intelligent substation are gradually increasing. The number of nodes and the amount of data that need to be monitored and maintained are greatly increased, which has led to a larger size of the SCD file. Therefore, it is difficult to meet the actual needs of engineering configuration, operation and maintenance by manually viewing the SCD. The manual method is time-consuming and error-prone. Based on this situation, an intuitive, efficient, and accurate method is required to obtain the data flow relationships between devices in the intelligent substations during the configuration, operation and maintenance periods.

At present, there have been several literatures on the visualization technology of the secondary circuit. The monitoring scheme of the secondary circuit has been presented to introduce the static layout of the interface, which rarely mentions the dynamic refresh of the circuit state [6–8]. Different methods were also proposed to introduce the data mapping algorithm and the dynamic refresh technology, but the display of the physical circuit was not involved [9, 10]. Instead of the visualization technology, the fault diagnosis technology based on the logical connection relationship of the secondary circuit was introduced in [11, 12].

This paper proposes a visualization technology of the secondary circuit in the intelligent substation based on CIM/G specification [13–16]. The automatic parsing module of the secondary circuit connection relationship in the SCD file is studied. And the automatic generation module of the visual interface is designed, together with the automatic association technology between the SCD model data and the graphical objects. The visualization technology proposed in this paper not only realizes the static layout of the physical circuit and the logic circuit in the monitoring interface, but also achieves the dynamic refresh of the graphical objects which reflects the real-time status of the circuit.

The rest of this paper is organized as follows. Section 2 proposes the general architecture of this visualization technology, including the automatic parsing module, the automatic generation module and the automatic association module. Section 3 describes the detailed automatic parsing methods of the secondary circuit connection relationship based on SCD. And Sect. 4 designs the layout of the physical circuit and the logic circuit in the monitoring interface based on CIM/G specifications. The final result of the visualization is illustrated in Sect. 5 via practical applications. Finally, concluding remarks are presented in Sect. 6.

2 General Architecture

Based on the CIM/G specification, the visual interface of the secondary circuit in the intelligent substation is realized automatically, as shown in Fig. 1. Firstly, the SCD file is automatically parsed to obtain data information of each voltage level,

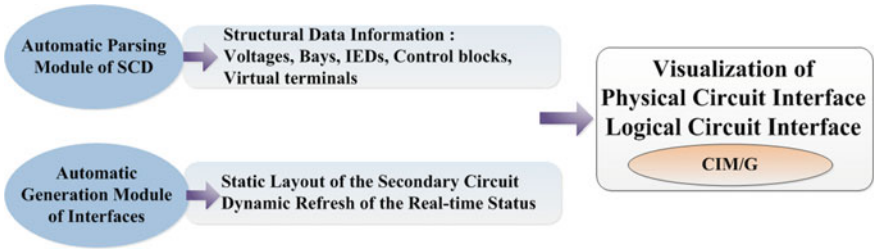

Fig. 1 Diagram of the general architecture

bay, device, control block, and virtual terminal. Secondly, through the topological analysis of the data information of each level, the coordinates of the graphical objects are calculated accordingly. Combined with the setting of other attributes of the graphical objects such as color, font, etc., the static layout of the physical circuit and the logic circuit is basically determined. Finally, according to the data mapping relationship between the data reference parsed from the SCD file and the remote signal value read in the database, such as the control block link state and the transmission data of the secondary circuit, the graphical objects with the corresponding references can be dynamically refreshed. Because the graphic file is generated based on the CIM/G specification which is consistent with the control center, the control center can browse the visualization interface of the secondary circuit directly, which provides a good technical support for the comprehensive monitoring of the intelligent substation.

3 Structure Analysis of the Secondary Circuit

There are mainly four parts defined in the SCD file [17, 18], the communication class (Communication), the primary device class (Substation), the intelligent electronic device class (IED) and the data type template class (DataTypeTemplate). The substation model is a hierarchical object based on the functional structure of the primary equipment of the substation. The main data level of Substation is substation-voltage-bay-equipment-subdevice. The IED class is the hardware device that forms the substation automation system. The main data level of IED is IED-server-logical device-logical node-data.

Based on the substation class, the data structure as voltage-bay-IED is obtained by the SCD auto-parsing module. The IED data structure includes the IED index number, the IED name, and the IED description. The switch is also considered as an IED and is included in the IED structure. Based on this structure, a static layout of the physical circuit monitoring interface can be obtained. Physical circuit interfaces of different voltage levels can be switched by thermal points automatically. As for the layout of the IEDs at the same voltage level, they are laid out in bays.

The protection device, the measurement and control device, the merging unit, the intelligent terminal, and the switch in the same bay are arranged according to the typical template.

Based on the IED class, the data structure of IED is also obtained by the SCD auto-parsing module, which contains the logical control block, the physical control block and the connection relationship of the terminals. The logical control block consists of the output block and the input block. In particular, the structure of the switch device includes only the physical control block, which describes the connection between its physical port and the physical port of other devices. The structure of the IED is shown in Fig. 2.

The typical structure of the virtual terminal is shown in Fig. 3a. The attributes of reference and description indicate the information of the corresponding virtual circuit, while value_reference represents the reference of the GOOSE/SV channel data transmitted on the virtual circuit. According to the principle of reference uniqueness, these two references are respectively mapped to a record in the monitoring system database. The structures of v_link_point and p_link_point respectively indicate the virtual terminal and the physical terminal connected to it, and the structure uniquely identifies the terminal by the IED index number, the control block index number, and the virtual terminal index number. Based on v_link_point and p_link_point in the structure, the virtual circuit connection relationship can be determined easily.

The typical structure of the physical terminal is shown in Fig. 3b. The attribute of portIdx is a unique identifier of the physical terminal, indicating the port number, and the attribute of portType represents the port type. Similarly, p_link_point represents another physical terminal structure that is directly connected to it. Combined with the p_link_point in the structure of the virtual terminal, the physical

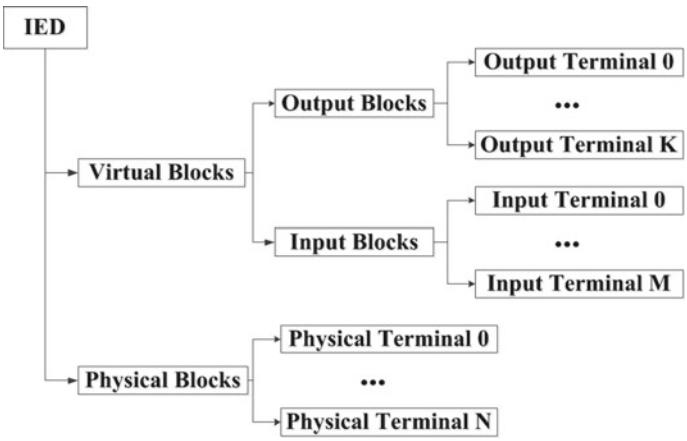

Fig. 2 Date structure of IED

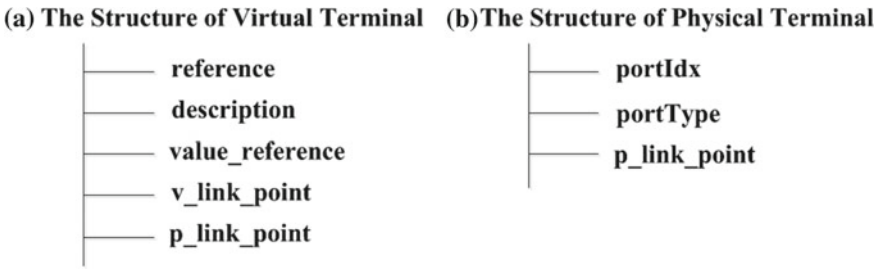

Fig. 3 Date structure of the virtual terminal and the physical terminal

connection relationship between the devices can be determined, and the correspondence between the physical circuit and the virtual circuit can also be determined.

4 Display of the Secondary Circuit

Based on the data structure parsed from the SCD file which is described above, the display of the physical circuit and the logical circuit can be achieved by combining with the automatic generation technology of the visual interface, the automatic association technology between the SCD model data and the graphical objects and the automatic linking technology between different pictures.

4.1 Display of the Physical Circuit

According to the hierarchical structure of voltage-bay-device-control block-secondary circuit obtained by SCD, the monitoring interface of the complete physical circuit in the substation can be realized, which includes the structural relationships of voltage, bay, devices and the physical connections between the devices. The physical circuit interfaces of different voltage levels are switched by thermal points, while the devices in each bay under the same voltage level are distributed in the same picture. The physical connection between the devices is described as the connection line and the information of the connection port can also be identified in the interface.

Based on the static layout of the physical circuit, the dynamic refresh of the graphical objects in the physical circuit monitoring interface can be realized, combing with the data mapping relationship with the signals in the database. Usually, the state of the device is associated with the accident signal in the monitoring system database [19], so the abnormality of the device can be displayed in real time through different colors. Meanwhile, the state of the physical circuit is

related to the state of the logical circuit it contains. Once the state of a logical circuit that it contains is abnormal, the physical circuit displays an abnormal state.

In the monitoring interface of the physical circuit, the virtual circuit connection inside the device and the physical circuit can be obtained through the automatic linking of the pictures. The virtual circuit related to the device can be viewed by clicking the graphical object of the device, while the virtual circuit in the physical circuit can be viewed by clicking the connection line which represents the physical connection.

4.2 Display of the Logical Circuit

Virtual Circuit Related to the Physical Circuit. This interface displays the connections of the logical control blocks involved in the physical circuit, including the transmitting device, the receiving device, the transceiver port information and the arrows between the transceiver. The connection line identifies the on-off state in different colors with the state value of the logical control block in the database.

Furthermore, the detailed virtual circuit can also be viewed by clicking the connection line between the control blocks, including the terminal names of the transceiver and the real-time state of the virtual circuit. Similarly, the on/off state of the virtual circuit is represented by connection lines of different colors.

Virtual Circuit Related to the Device. This interface displays the logical circuit connection between the device and other devices associated with it. The state of the virtual circuit, the value and the quality transmitted by GOOSE/SV channels can be viewed in this interface. Usually, the on-off state of the virtual circuit is identified by the connection lines of different colors. The transmission value is described by the dynamic data, and the different qualities are reflected by the different colors of the transmission value. Combined with the configuration of the plate information in the monitoring system database, the interface can also display the state of the plates such as the inspection plate, the outlet plate and the receiving plate.

Based on the correspondence between the graphical objects and the associated data stored in the CIM/G files, all of the monitoring interfaces described above can be refreshed dynamically. The graphic browser periodically queries the data values of the graphical objects in the database, and then displays different states of the graphical objects such as the connection line of the circuit. The dynamic refresh of the transmission value is also done in the same way.

As for the dynamic refresh of the physical circuit, it involves the states of multiple internal logical circuits. An expression is created to obtain the logical operation result of the multiple logical circuit states. And the relationship between the graphical object of the physical circuit and the corresponding expression result is also stored in the CIM/G files. Once one of the logical circuit states has changed, the result of the expression is updated in time, and the graphical object associated with the result of the expression is also dynamically refreshed.

5 Practical Application

Compared with the method of manual drawing, the scheme proposed in this paper can complete the display of the secondary circuit in a few minutes, which greatly shortens the engineering configuration cycle and improves the efficiency of the project implementation. In addition, the visual interface at multi-level can greatly facilitate the daily monitoring and maintenance, which is of great significance for ensuring the safe operation of the power grid. The secondary circuit visualization software developed based on this scheme has been developed and tested. The following figures show the typical secondary circuit monitoring interfaces implemented by the software. Figure 4 shows the typical physical circuit of the entire substation. Figure 5a shows the virtual circuit related to the physical circuit, and Fig. 5b shows the more detailed information. Figure 6 shows the virtual circuit related to a given device.

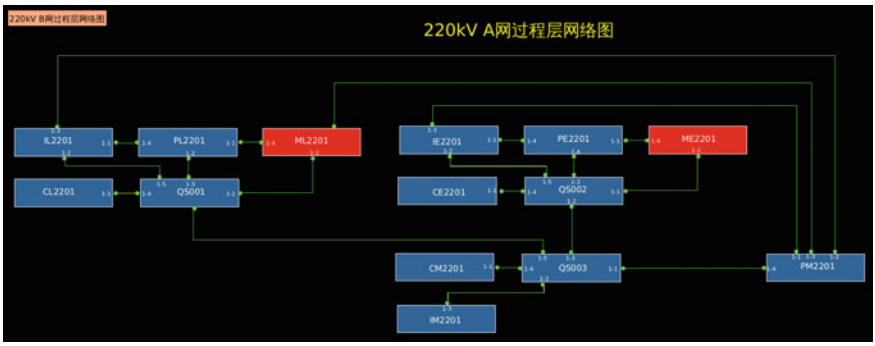

Fig. 4 Diagram of the physical circuit

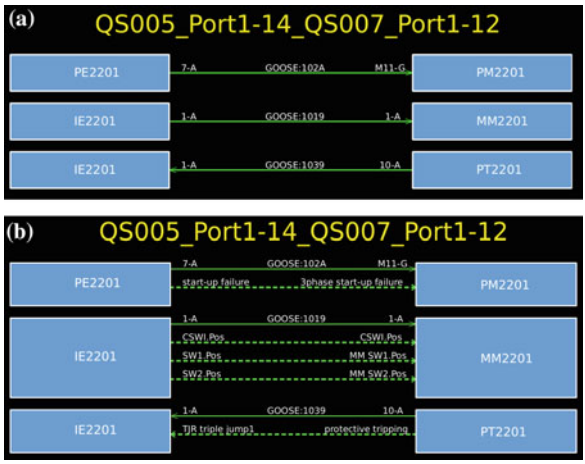

Fig. 5 Diagram of the virtual circuit related to the physical circuit

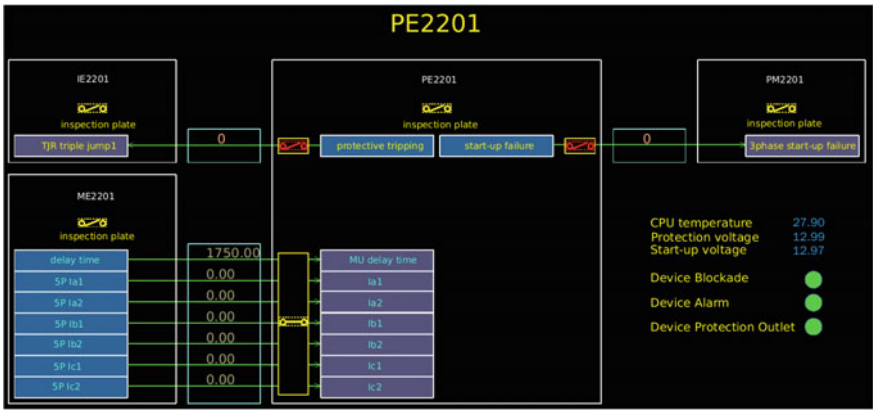

Fig. 6 Diagram of the virtual circuit related to the device

6 Conclusion

The visualization technology of the secondary circuit based on CIM/G is proposed for the intelligent substation in this paper. The automatic parsing technology of SCD is introduced, which is used to obtain the basic data structure. Moreover, the design of the interface of the physical circuit and the logical circuit is put forward. And the practical application of the secondary circuit monitoring interface is demonstrated. The comprehensive performance of this automatic visualization technology is evaluated to be superior to the traditional manual mode in the aspects of visualization and engineering, which greatly improves the efficiency and standardization of the project implementation. In the future, more abundant graphical elements will be included for the display needs of interfaces, such as the physical port status, the port light intensity information and so on.

Acknowledgements This article is supported by State Grid Science and Technology Project of China, under the program "Research and application of the wide area operation and maintenance technology for substation automation equipment".

References

1. Yang Y, Xu H, Gao L (2017) Multidimensional intrusion detection system for IEC 61850-Based SCADA networks. IEEE Trans Power Delivery (32):1068–1078
2. Maziku H, Shetty S (2017) Software defined networking enabled resilience for IEC 61850-based substation communication systems. Int Conf Comput 690–694
3. Yang Y, Gao X, Zhu H, Cui Y (2015) Case study on SCD application based on demo smart substation. Power Syst Prot Control (43)
4. Ye Y (2017) Study on SCD of full model and its application in the secondary system for smart substations. Autom Appl (12):97–98

5. Li J, Hu R, Wang L et al (2018) Engineering configuration scheme based on IEC 61850 Ed 2.0 in smart substation. Autom Electr Power Syst 42(2):154–159. https://doi.org/10.7500/aeps20170815010
6. Liu W, Du L, Yang Q (2014) Research and application of smart substation virtual circuit visualization. Adv Power Syst Hydroelectric Eng (30):32–37
7. Hou W, Xu D, Qiu Y, Wu Y, Wu J (2016) Research on visualization of substation configuration description file in intelligent substation. Zhejiang Electr Power (1):10–14
8. Liu X, Xi H, Qian B (2015) Virtual terminal graphical display method based on intelligent substation SCD file. Electr Appl (2):97–100
9. Zhang Q, Jia H, Ye H (2015) Design and application of virtual secondary circuit monitoring in smart substation. Power Syst Prot Control (43):123–128
10. Yan H, Yao Q, Xu X (2015) Research and application of smart substation secondary circuit visualization. Zhejiang Electr Power (9)
11. Ye Y, Sun Y, Huang T, Guo M, Huang Y (2016) Online state detection and fault diagnosis technology of relay protection secondary circuits in smart substation. Power Syst Prot Control (44):148–153
12. Ge L, Zhao G, Yang F, Wen J, Liu Q (2014) Research on the secondary circuit fault diagnosis methods. Smart Grid (6):28–31
13. Li W, Xin Y, Yaozhong X, Shen G, Huang K, Meng X, Wan S (2015) Scheme of power grid graphics maintenance and sharing based on CIM/G. Autom Electr Power Syst
14. Xu H, Ning J, Huang K, Zhang Y, Jiang C, Zhang Z (2017) CIM/G based multi-version management and display of graphics. Autom Electr Power Syst (41):164–169
15. Zhao J, Zhang L, Qian K, Zhao L, Li C, (2015) Key technologies of automatic power flow chart generation based on CIM/G and its application. Electr Power Autom Equip (35)
16. Wang M, Han X, Wu L et al (2018) CIM/G based web graphical display technology for power grid dispatching and control systems. Autom Electr Power Syst 42(6):81–85. https://doi.org/10.7500/aeps20170731004
17. Guo J, Wu W, Wang Y (2011) Parse for SCD file of smart substations based on TinyXML. Electr Power (31)
18. Wang L, Ma J, Wang C et al (2006) Application research of substation configuration description language SCL. Power Grid Technol (S1):99–102
19. Chen A, Ye FENG, Geng M et al (2013) A design method of database information model using IEC 61850 common data classes. Autom Electr Power Syst 37(13):88–92. https://doi.org/10.7500/aeps201206211

Wide-Frequency Synchrophasor Transfer Method Based on Channel TDM

Qi Peng, Ming-guo Hou, Jian Shen and Rong Xiang

Abstract Wide-frequency synchrophasor is the general term for synchrophasors of harmonics and interharmonics from low frequency to high frequency. Limited by existing transfer standard and transmission channel bandwidth, the current Wide Area Measurement System (WAMS) cannot transfer wide-frequency synchrophasors and can only transfer fundamental synchrophasors. This paper provides a wide-frequency synchrophasor transfer method from substation to master station, and focuses on the channel time division multiplexing (TDM) technology. The compatibility of the transfer method based on this technology with the existing protocol and the network characteristics are analyzed. At last, the feasibility of the method is verified by simulation experiments. Within the channel TDM method, the wide-frequency synchrophasor can be transferred from substation to master station under the existing WAMS architecture and transfer standard, and the transfer method satisfies the requirements of the existing physical channel bandwidth.

Keywords Wide area measurement system (WAMS) · Phasor measurement unit (PMU) · Wide-frequency synchrophasor · Channel time division multiplexing (TDM) · Compatible sequence

Q. Peng (✉) · M. Hou · J. Shen · R. Xiang
NARI Group Corporation (State Grid Electric Power Research Institute), Nanjing 211106, China
e-mail: pengqi@sgepri.sgcc.com.cn

Q. Peng · M. Hou · J. Shen · R. Xiang
NARI Technology Co. Ltd, Nanjing 211106, China

Q. Peng · M. Hou · J. Shen · R. Xiang
State Key Laboratory of Smart Grid Protection and Control, Nanjing 211106, China

Y. Xue et al. (eds.), *Proceedings of PURPLE MOUNTAIN FORUM 2019-International Forum on Smart Grid Protection and Control*, Lecture Notes in Electrical Engineering 585, https://doi.org/10.1007/978-981-13-9783-7_44

1 Introduction

High-voltage direct current transmission (HVDC), flexible AC transmission (FACTS), and the grid-connection of wind turbine generators (WTGs) induce wide-frequency oscillations such as low-frequency, sub/super-synchronous oscillations [1–5] which seriously threaten the safe and stable operation of the grid [6]. Therefor the State Grid Corporation of China proposed the real-time monitoring and warning requirements for wide-frequency oscillation based on the wide-frequency synchrophasor of PMU substation.

WAMS has been widely used in power grids within the world. Up to October 2017, the PMU has been installed in more than 3900 power plants and substations in China [7]. It plays an important role in grid operation monitoring, characteristic analysis, fault analysis, etc. [8–12]. However, it cannot cope with the demand of wide-frequency oscillation monitoring. First, the transfer standard can only support fundamental synchrophasor transfer between PMU substation and master substation [13]. There is no transfer specification for wide-frequency synchrophasors. Second, due to the limitation of physical channel bandwidth, a large number of wide-frequency synchrophasors calculated by the PMU substation cannot be transferred to the master station.

The research work of wide-frequency synchrophasor measurement and wide-frequency oscillations monitoring based on PMU has been carried out in-depth in China [14–18]. Literature [19] details a wide area sub-synchronous oscillation monitoring system based on improved PMU. Wide-frequency PMU has been developed. The work of wide-frequency synchrophasor calculation can be done in PMU substation, which can greatly reduce the cost of master station. So it is necessary to develop a real-time transfer method for wide-frequency synchrophasor which is compatible with the current WAMS architecture.

This paper proposes a wide-frequency synchrophasor transfer method. At first the architecture and transfer standard of the existing WAMS/PMU system are analyzed. Then according to the transfer indicators, introduces the transfer plan selection and details the channel TDM technology and procedure of the transfer method. Finally, the correctness and feasibility of the method are verified by simulation experiments. The method is fully compatible with the existing WAMS architecture.

2 Overview of Synchrophasor Transfer

2.1 WAMS Architecture and Transfer Standard

The WAMS consists of PMU substation, master station and data communication network [7]. The architecture is shown in Fig. 1. The PMU is responsible for data acquisition, and transfer the synchrophasors to master station in real time.

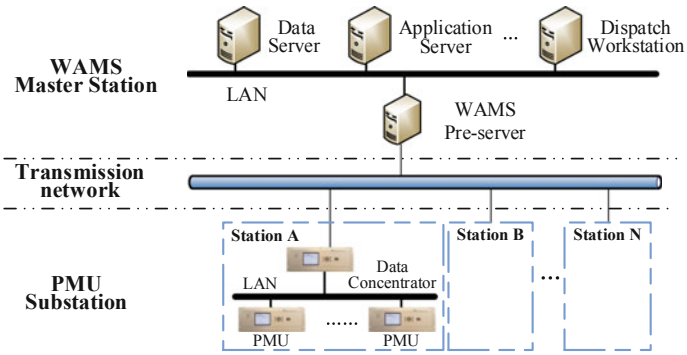

Fig. 1 Architecture of WAMS/PMU system

The current international synchrophasor transfer standard is IEEE std C37.118.2-2011. In China, GB/T 26865.2-2011 is used as the synchrophasor transfer standard. The two standards only support fundamental synchrophasor transfer. For the two standards are similar, all the discussion of transfer standard in the paper is based on the GB/T 26865.2-2011.

2.2 *Analysis of Existing System Network Data Flow*

At present, depending on the application of master station, there are mainly three transfer frequencies of synchrophasor data packets, which are 25, 50 and 100 Hz respectively. And the transfer frequency is set by the master station via the CFG2 packet.

Table 1 shows the PMU's synchrophasor data length of each type of bay in the data frame, where U1 and I1 mean positive sequence voltage and current, ROCOF means rate of change of frequency. In a synchrophasor data frame, an analog occupies 2 bytes, and a phasor data occupies 4 bytes.

Table 1 Synchrophasor data length of each type of bay in data frame

Measuring object	Measuring phasor	Measuring analog	Data length (Byte)
Busbar	Ua, Ub, Uc, U1	f, ROCOF	20
Line	Ia, Ib, Ic, I1, Ua, Ub, Uc, U1	P, Q, f, ROCOF	40
GSU transformer	Equivalent to 3 lines		120
Generator	1 line, add 2 internal potentials and 2 power angles	2 generator speeds, excitation voltage, excitation current, and steam valve opening	66

Consider the typical 500 kV substation with a reasonable margin. The substation consists of 2 GSU transformers, and high voltage side (500 kV part) is in the form of 3/2 wiring, which includes 3 complete series for total of 6 lines. The wiring form of medium voltage side (220 kV part) is dual-busbar & dual-busbar subsection for total of 12 lines. According to Table 1, the total data frame length is approximately 1040 B. And the data flow rate will be 25.5, 51, and 102 KB/s under 25, 50, and 100 Hz respectively. For a master station with an access capacity of 200 PMU substations, the real-time data access flow rate will be from 5 to 20 MB/s.

3 Wide-Frequency Synchrophasor Transfer Method

3.1 Design of Channel TDM Transfer

The design of the transfer plan needs to consider wide-frequency synchrophasor transfer period, data flow rate, protocol and application compatibility. And the range of the harmonics that can be transferred must also be considered.

The wide-frequency synchrophasor transfer period is inversely proportional to the data flow rate. At present, a dedicated channel with a bandwidth of 2 Mbps is used between the PMU substation and the dispatch data network. Therefore transfer period and data flow rate need to be balanced. According to literature [12], the length of the time window can be set to second level for FFT analysis. Therefore, it's able to be accepted to transfer the wide-frequency synchrophasor once per second.

For HVDC, according to literature [20, 21], the harmonic detected by the DC converter station and the new energy generation aggregation station should be increased to at least 25th harmonic. At present, the sampling rate of bay control unit and PMU in smart substation is 4 kHz. According to the sampling theorem, the 40th harmonic is the highest harmonic that can be calculated. Therefore, the range of harmonics which can be transferred is designed from 1st to 100th in the method.

The channel TDM technique multiplexes the data channels in the current data frame and transfers different phasors at different time. As shown in Fig. 2, at time T0, a phasor P0 is transferred in a certain fixed channel, but at other times, T1 or T2, the others phasors P1 and P2 are transferred in that channel. The advantage of channel TDM is that it can transfer more phasors without increasing data flow, and it is no need to modify the format of frame.

3.2 Realization of Channel TDM Transfer

It can flexibly configure the harmonics or interharmonics to transfer according to the actual needs of the site. When the actual need pays more attention on the

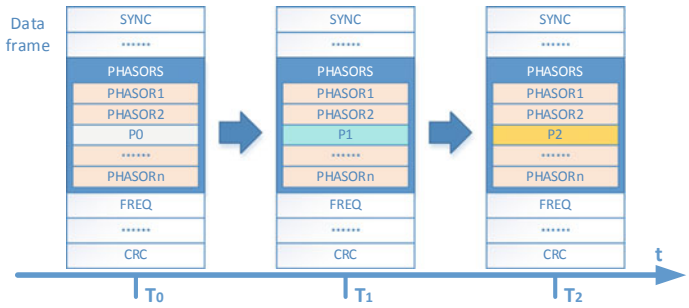

Fig. 2 Time division multiplexing of phasor channel

sub-synchronous oscillation, only the interharmonic channel can be configured. The specific implementation includes communication message extension and data synchronization.

Interharmonic Transfer

At first, add the interharmonic channels in the CFG1, which including 3 voltage interharmonic phasor channels, 3 current interharmonic phasor channels, and 6 frequency analog channels. The additional channels are shown in Table 2. All these additional channels can be configured flexibly according to the actual needs. Then in addition to the original fundamental phasor channel, data message also contains interharmonic channels.

For the timestamp of interharmonic data, each PMU data frame has an absolute timestamp to indicate the time of fundamental phasor data. When interharmonic channels are added in the data message, the timestamp will be shared both by fundamental data and interharmonic data. Because PMU calculates the interharmonics data once per second, so all timestamps of interharmonics transferred in a second are the same. We take the number of SecondSinceEpoch of the timestamp minus the time of calculation time window as the seconds of interharmonic data, and the part of FractionOfSecond always equals 0.

According to the transfer frequency of the PMU data frame, we can transfer 25, 50, and 100 interharmonics data in 1 s at 25, 50, and 100 Hz respectively. The interharmonics are transferred in the order of amplitude from highest to lowest. Figure 3 shows the interharmonic transfer under 25 Hz.

Table 2 Interharmonic channel addition

Channel type	Additional channel	Channel name
Phasor	Voltage interharmonic	UAI, UBI, UCI
	Current interharmonic	IAI, IBI, ICI
Analog	Frequency of voltage interharmonic	UAF, UBF, UCF
	Frequency of current interharmonic	IAF, IBF, ICF

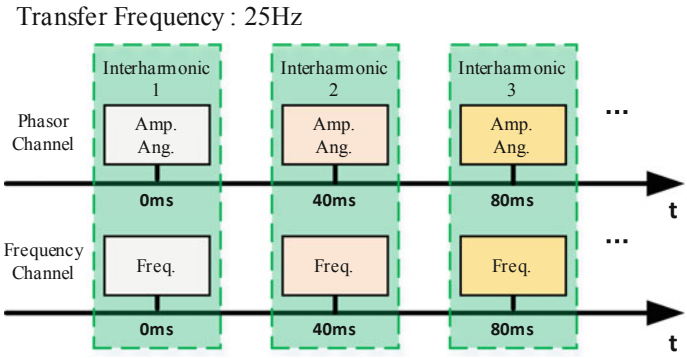

Fig. 3 Interharmonic channel transmission

The frequency in the frequency channel corresponds to the phasor in the phasor channel, and the interharmonics of one frequency point are uniquely determined.

Harmonic Transfer

Harmonic transfer is similar to interharmonic transfer. At first, the harmonic phasor channel needs to be added, as shown in Table 3. The timestamp is obtained in the same way as the interharmonic.

Different from the interharmonic transfer, harmonic transfer does not need to add frequency channel to indicate the frequency. It can rely on the compatible sequence to identify the order of harmonic under the multiplexing condition.

Stipulating that the fundamental phasor and 2nd–25th harmonic phasors are transferred at 25 Hz, the fundamental phasor and 2nd–50th harmonic phasors are transferred at 50 Hz, and the fundamental phasor and 2nd–100th harmonic phasors are transferred at 100 Hz.

If the data are transferred in normal order(from low order to high order), the phasors transferred at the same time are different order harmonics under three frequencies. As shown in Fig. 4.

To meet the compatibility of harmonic transfer at different frequencies, it is necessary to adjust the transfer order of harmonics. 100 Hz is the highest transfer frequency, including data frames of 50 and 25 Hz frequencies, while 50 Hz includes data frames of 25 Hz. Therefore, the harmonics at 25 Hz can be preferentially arranged, that is, the fundamental wave and the 2nd–25th harmonics are arranged in order of time under 25 Hz. Then arrange the next 25 harmonics data

Table 3 Harmonic channel addition

Channel type	Additional channel	Channel name
Phasor	Voltage harmonic	UAH, UBH, UCH
	Current harmonic	IAH, IBH, ICH

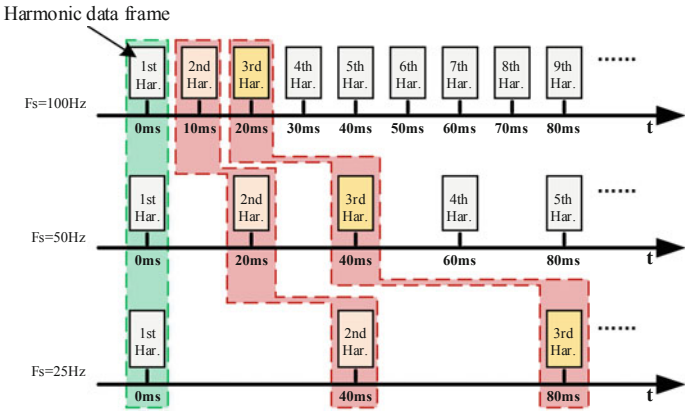

Fig. 4 Comparison of sequential transmission harmonic timings at different frequencies

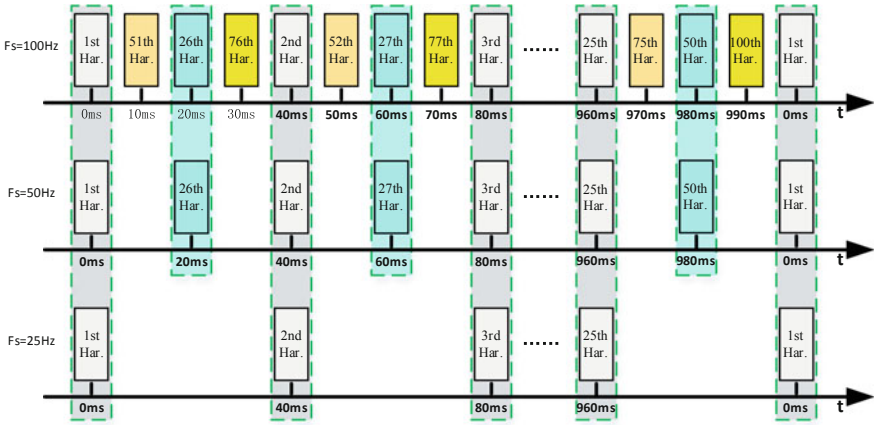

Fig. 5 Harmonic compatible sequence

(26th–50th harmonics) under 50 Hz, and finally arrange the last 50 harmonics data (51th–100th harmonics) under 100 Hz, as shown in Fig. 5. Then this sequence is fully compatible with three frequencies modes.

The time (milliseconds) of the data frame in which the nth harmonic is located can be uniquely determined by the following formula:

$$T_{hn} = 10 \times \left\{ 4Q + 2 \times (P\%2) + \left[\frac{P}{2} \right] \right\} \tag{1}$$

where

$$\begin{cases} P = \left[\dfrac{n-1}{25}\right] \\ Q = (n-1)\%25 \end{cases} ; (1 \le n \le 100)$$

When n = 1, it is the fundamental phasor data, and [*X*] represents the integer part of *X*.

3.3 Comparison of Data Flow

The timing diagrams of the fundamental, harmonic and interharmonic channels in the complete message are shown in Fig. 6.

Now consider the data flow under the case with maximum configuration which configures all additional channels of Tables 2 and 3. The comparison of the data volume of different measurement objects between wide-frequency data and fundamental data is shown in Table 4.

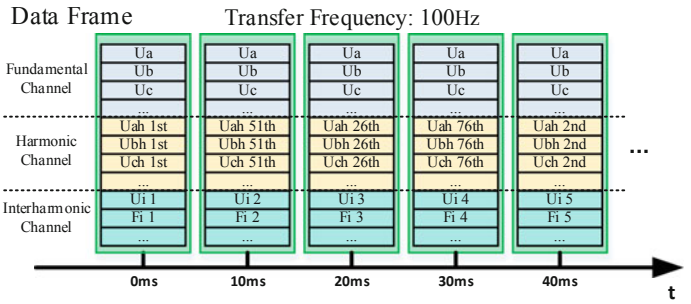

Fig. 6 Timing diagram of fundamental, harmonic and interharmonic channel

Table 4 Frame length comparison of wide-frequency data and original data

Object	Data length (Byte)		Remarks of additional channels
	Fundamental	After adding Harmonic and Interharmonic	
Busbar	20	50	Add 6 phasor channels and 3 analog channels
Line	40	100	Add 12 phasor channels and 6 analog channels
GSU	120	300	Equivalent to 3 lines
Generator	66	126	Equivalent to 1 line

As can be seen from the above table analysis, the length of wide-frequency data frame using channel TDM method is increased by about 1.5 times compared with current fundamental phasors message. Equally adopt the substation scale assumed in Sect. 2.2, the total data of a PMU substation data frame are about 2600 B, and the data flow of a PMU substation is about 63.6–253.9 KB/s. This indicator satisfies the bandwidth requirements of the dedicated bandwidth channel of the existing PMU substation.

4 Verification

The actual PMU system simulation are designed to verify the feasibility of the method. Test system is shown in Fig. 7. The signal source is simulated by RTDS (real-time digital simulation device), and the simulated master station communicates with the PMU. Finally, the spectrum diagram displayed by the simulation software is compared with the simulation result of Matlab. Since the PMU used in the test cannot calculate 100th harmonic, the highest order harmonic which can be calculated is 40th harmonic, so the highest order harmonic applied by the test signal is 40th harmonic.

The test PMU uses a 48 channels sampling configuration, adding 48 corresponding harmonics and interharmonic channels to the CFG2 file, and inputing the following test signals to the first channel, voltage Ua:

$$\begin{aligned} x = & U_n \sin(2\pi f_s t - \pi/3) + 0.2U_n \sin(2\pi \times 115t + \pi/3) \\ & + 0.2U_n \sin(2\pi \times 540t - \pi/3) + 0.3U_n \sin(2\pi \times 25 f_s t - \pi/18) \\ & + 0.15U_n \sin(2\pi \times 40 f_s t - \pi/10) \end{aligned} \quad (2)$$

where Un = 57.74 V, Fs = 50 Hz. The signal contains 25th and 40th harmonic data, as well as interharmonic of 115 and 540 Hz.

The Matlab simulation spectrum of the test signal is shown in Fig. 8.

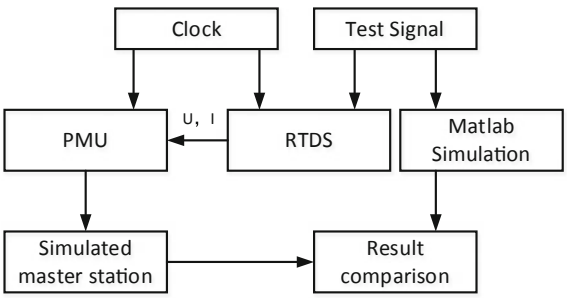

Fig. 7 Test system of PMU

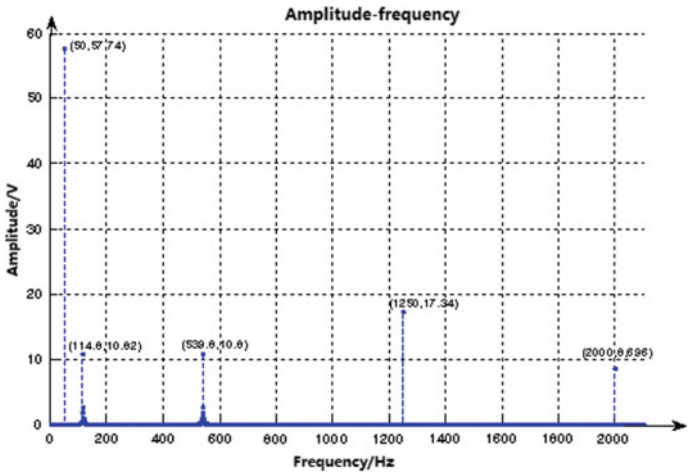

Fig. 8 Matlab simulation spectrogram of test signal

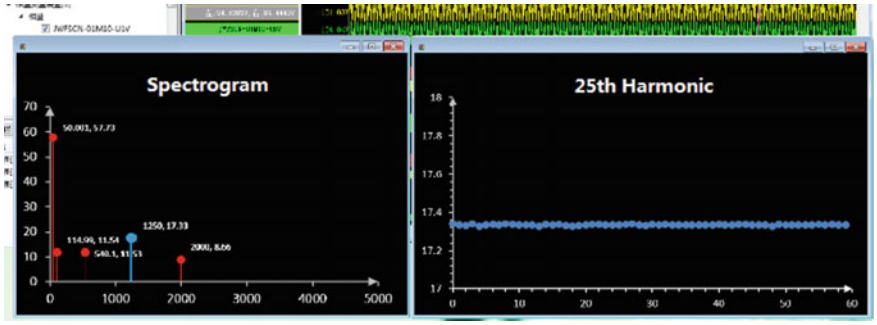

Fig. 9 Spectrogram and data variation with time

The simulation software simulates the master station pre-server, which can receive and display the data sent by PMU in real time, including the phasor spectrum and the channel value change with time.

The system verifies the data transfer at 25, 50, and 100 Hz respectively. Figure 9 shows the spectrum of the Ua channel under 100 Hz transfer frequency and the amplitude variation with time of 25th harmonic. The spectrogram of a certain moment contains the fundamental, 25th and 40th harmonics, and the interharmonics of 115 and 540 Hz, which is same as the result of Matlab simulation.

The test PMU uses 48 channels, with maximum configuration. The output channels include 160 phasor channels (64 fundamental phasor channels, 48 harmonic phasor channels, and 48 interharmonic phasor channels), and 80 analog channels. The actual message flow rate under 100, 50, and 25 Hz are 80.78, 40.39,

and 20.2 KB/s respectively. Considering the upper limit bandwidth of single PMU substation, it can support 5 PMUs (40 lines in total) to transfer wide-frequency data at 50 Hz transfer frequency.

5 Conclusion

With the promotion and application of wide-frequency measurement technology in substation, the master station will be able to effectively utilize the powerful computing capacity of the substation for more in-depth applications based on wide-frequency data. The wide-frequency synchrophasor transfer method proposed in this paper fully considers WAMS architecture and actual physical bandwidth, and use the channel TDM technology to reduce network bandwidth consumption caused by a large number of wide-frequency data. The method is fully compatible with the existing transfer standard, which inherits the procedure of establishment, connection, transmission, interruption and exception handling. That ensures the reliability of communication. The advantage in engineering application is also reflected in the asynchronous step-by-step upgrade mode between master substation and PMU substation. It can still guarantee the connection and realize the current WAMS function between two ends, in which one end with the wide-frequency data transfer and the other end without this capability. However, the current method has certain limitations in terms of wide-frequency data transfer frequency. The next step will be further researched in conjunction with the requirements of the master station.

Acknowledgments This research was supported by the fund project (Research on Key Technologies of Unified Measurement of Wide-frequency Electric Quantity for Grid Power Electronics, SGSXLF00FCJS1700047) from SGCC Science and technology program in China. The author is grateful for the support of the project panel and project team.

References

1. Lu J, Xiao X, Zhang J et al (2015) Mechanism and experiment of subsynchronous oscillation-dynamic stabilizer for suppressing subsynchronous oscillation with weak damping. Autom Electr Power Syst 39(4):135–140. https://doi.org/10.7500/AEPS20140702002
2. Chen B, Lin T, Chen R et al (2018) Analysis on characteristics of sub/super-synchronous oscillation caused by grid-connected direct-drive wind farm via VSC-HVDC system. Autom Electr Power Syst 42(22):44–51. https://doi.org/10.7500/aeps20170913007
3. Xie X, Wang Y, Liu H et al (2016) Detection method for sub-synchronous and super-synchronous harmonic phasors in power system. Autom Electr Power Syst 40 (21):189–194. https://doi.org/10.7500/AEPS20160104002
4. Mei Y, Zhang J, Zhou J et al (2018) Analysis and improvement measures on power oscillations in silin hydropower plant on July 6, 2017. Autom Electr Power Syst 42(16):187–191. https://doi.org/10.7500/aeps20170813002

5. Nian H, Pang B, Xu G et al (2018) Reshaping strategy of wide frequency impedance for DFIG system to suppress high frequency resonance under parallel compensation grid. Autom Electr Power Syst 42(18):48–56. https://doi.org/10.7500/aeps20170922010
6. Li M (2016) Characteristic analysis and operational control of large-scale hybrid UHV AC/DC power grids. Power Syst Technol 40(4):985–991. https://doi.org/10.13335/j.1000-3673.pst.2016.04.001
7. Zhang D, Yu Y et al (2017) Power system synchrophasor measurement technology and application, 1st edn. China Electric Power Press, Beijing pp 67–68,102–105
8. Yu M, Xie H, Song W, et al (2017) Impact of SVC control mode on voltage abnormal oscillation in wind power influx area. Autom Electr Power Syst 41(1):73–78. https://doi.org/10.7500/aeps20160525003
9. Bian X, Ding Y, Mai K et al (2018) Subsynchronous oscillation caused by grid-connection of offshore wind farm through VSC-HVDC and its mitigation. Autom Electr Power Syst 42(17):25–33. https://doi.org/10.7500/aeps20170703003
10. Liu M, Guo Y, Chen J (2013) Stability analysis of wind-hydro-electric combined system with doubly-fed wind generator unit. Jiangsu Electri Apparatus 11:20–24
11. Liu H, Li Y, Li Y et al (2016) Case study and mechanism analysis of sub-synchronous resonance in wind power plants. Electr Power 49(3):134–140. https://doi.org/10.11930/j.issn.1004-9649.2016.03.134.07
12. Liu H, Li J, Bi T et al (2017) Subsynchronous and supersynchronous inter-harmonic identification method based on phasor measurements. Power Syst Technol 41(10):3237–3243. https://doi.org/10.13335/j.1000-3673.pst.2017.1619
13. GBT 26865.2-2011 (2011) Real-time dynamic monitoring systems of power system—Part2: protocols for data transfer-ring
14. Hou M, Shen J, Tan Y el al (2015) Three-segment variable rate transmission of PMU real-time data. Autom Electr Power Syst (21):93–98. https://doi.org/10.7500/aeps20150312007
15. Zhang M, Shen J, Hou M et al (2016) Discussion on the on-line identification and warning of sub synchronous oscillation for PMU. Autom Electr Power Syst 40(16):143–146. https://doi.org/10.7500/aeps20151013003
16. Shen J, Zhou B, Wang Y et al (2015) Methods for im-provement of dynamic performance of PMU. Power Syst Prot Control 43(19):89–94
17. Bi T, Kong Ye, Xiao S et al (2012) Review of sub-synchronous oscillation with large-scale wind power transmission. J Electr Power Sci Technol 27(1):10–15
18. Wang M, Gao X, Wang B et al (2011) Online early-warning of sub-synchronous oscillations based on wide area measurement system. Autom Electr Power Syst 35(6):98–102
19. Qiu Y, Zhang X, Zhang C et al (2019) Research and construction of wide-area subsynchronous oscillation monitoring system in new energy influx area. Power Syst Prot Control 47(1):88–94. https://doi.org/10.7667/pspc180002
20. Li Z, Li J, Xia D (2006) Analysis of characteristic harmonics in ± 800 kV ultra high voltage direct current power transmission system. Power Syst Technol 30(24):6–9
21. GBT 26862-2011 (2011) Test specification for synchrophasor measurement unit for power systems

Strategy of Avoiding Reclosing in GIS Permanent Fault Under 3/2 Connection Mode

Shiyang Ding

Abstract At present, the equipment of substation is becoming more and more complex and GIS is the main equipment in substation. In this paper, According to the basic concept of IEC61850 technology system. The interoperability of relay protection devices for different kinds of different manufacturers is summarized. Combined with 3/2 wiring mode and protection configuration of a UHV substation. Analyze UHV substation's trip accident and expected failure modes. A method of optimizing the protection of 3/2 wiring is proposed to better deal with the uncertain events in substations.

Keywords IEC61850 · GIS · Interoperability · Fault diagnosis · Optimal configuration of relay protection

1 Introduction

Substation is not only the hub of voltage and current conversion in power system, but also the hub of power system information collection. Through the primary and secondary equipment of the substation, we can collect and calculate a large number of information such as current, voltage, phase, frequency, switching position, on-line monitoring data, device alarm and so on. How to make good use of this information is very important. In order to construct the seamless communication system of electric power system [1], China has quoted IEC 61850 ED 61850 as the domestic electric power industry standard DL/T 860. in order to construct the seamless communication system of electric power system, China has quoted V1.0 61850 as the domestic electric power industry standard. And has carried on the large-scale application in the substation automation construction [2]. IEC 61850 is not only a standard for substation communication, but also its basic ideas such as "adopting object modeling technology, device modeling and self-description to

S. Ding (✉)
State Grid Anhui Electric Power Co., Ltd. Maintenance Branch, Hefei 230000, China
e-mail: shiyang.ding@qq.com

Y. Xue et al. (eds.), *Proceedings of PURPLE MOUNTAIN FORUM 2019-International Forum on Smart Grid Protection and Control*, Lecture Notes in Electrical Engineering 585, https://doi.org/10.1007/978-981-13-9783-7_45

meet the requirements and development of application functions, and meeting the requirements of open interoperability of applications" [3]. It lays a theoretical and path foundation for the intelligence of substation.

Unpredictable equipment failures often exist in power systems. When the system is weakened, insufficient information, automatic system failure and human decision errors may cause new interference [4]. In recent years, many large area power outages abroad show that the misoperation, rejection and improper action of relay protection and safety control devices are often the direct cause of the accident or an important factor leading to the expansion of the accident [5]. The coupling effect of AC and DC is increasing day by day, which makes the risk of high power loss increasing, and gradually presents the characteristics of "integration" [6]. The DC commutation failure induced by AC fault at the end of UHV DC transmission network will cause a large amount of short-term power shortage of the system, which poses a great threat to the security and stability of the system [7]. In order to better deal with the impact of faults on the system, this paper proposes to use IEC61850 protocol and other technical means to locate and diagnose substation level faults according to the equipment status and wiring mode. Through these diagnostic information can better help people to reduce the impact of fault on the stability of the system. I hope to arouse your discussion by writing this article and throwing bricks to attract jade.

2 Complexity of Relay Protection Object and Its Related Influence

In the IEC61850 standard system, the task of relay protection is defined as monitoring various physical quantities (voltage, current, temperature, etc.) from the power network or switchgear. If a value of the monitored amount exceeds the preset first threshold, the relay protection function enters an alert state; if the monitored amount exceeds the second threshold (fault threshold), the relay protection device issues a trip command, To remove the protected object from the system. The behavior of relay protection, that is, protection algorithm, is controlled by a set of parameters, which can be changed by protection engineers through man-machine interface or some automatic equipment [8].

Traditional protected objects, including main transformer, switch, bus, line, reactor and other equipment. These devices are equipped with special protective devices and ensure that no dead zone is left. With the development of power grid, the object of relay protection is becoming more and more complex, and the primary equipment presents the characteristics of electronic power [9]. These new situations are worth paying attention to. GIS equipment is the main equipment in UHV AC substation. GIS has the characteristics of strong systematicness, high integration, small area, good reliability and so on. It is an important embodiment of the technical progress of power equipment manufacturing [10–12]. Especially in UHV

engineering, because of the reliability of external insulation design and the small area, gas insulated combiner has become the only choice [13–15]. The GIS equipment is composed of circuit breaker, isolating switch, grounding switch, bus, current transformer, voltage transformer, lightning arrester, casing and other electrical equipment, and its failure rate is much lower than that of each independent electrical equipment. However, once the fault location of GIS equipment is a difficult point, and the replacement period of components is longer, the reliability of the power grid is also facing a test. GIS equipment fault can be roughly divided into mechanical fault, insulation fault, secondary circuit fault, body leakage fault and so on, and the internal insulation fault is the main cause of tripping accident. GIS equipment failure may be in the installation process, due to the installation environment is not up to standard, dustproof measures are not in place and other reasons, resulting in GIS internal discharge caused by insulation flashover caused by insulation fault and then cause tripping.

Relay protection also needs to adapt to the change of primary equipment. GIS equipment is involved in the reach of switch protection, bus protection and line protection. UHV switch, the bus itself is GIS equipment, line protection contains switches that is GIS equipment. The practical experience shows that the short-circuit fault nature of the line and GIS equipment is not the same. The transient fault accounts for the majority of the line short-circuit fault, while the GIS short-circuit fault is mostly permanent fault. How to adapt the relay protection to the change of the object, first of all, from the interoperability of the protection device to do a brief analysis.

3 Interoperability Between Protective Devices

IEC61850 technology system shows that the function of substation automation system is control and monitoring. That is, the monitoring of the relay protection of the primary equipment and the power grid, and the monitoring of the system related to the system itself, such as the monitoring of communication. The function is divided into three layers: station, bay and process. The system requires that the functions can be freely assigned to intelligent electronic devices, and that the functions provided by different suppliers should be maneuverable. the interface model of the equipment is shown in Fig. 1.

It can be seen that the IEC61850 standard scientifically classifies the data, and through the definition of interfaces so that all kinds of intelligent devices can freely exchange information, and has a certain degree of interoperability. Interoperability refers to the ability of two or more IED provided by one or more manufacturing plants to exchange information and use that information to perform specific functions correctly.

The connotation of interoperability is rich. In the engineering practice of UHV substation, there is some kind of data exchange in the protection equipment in the interval layer and realizes the characteristics that can be operated with each

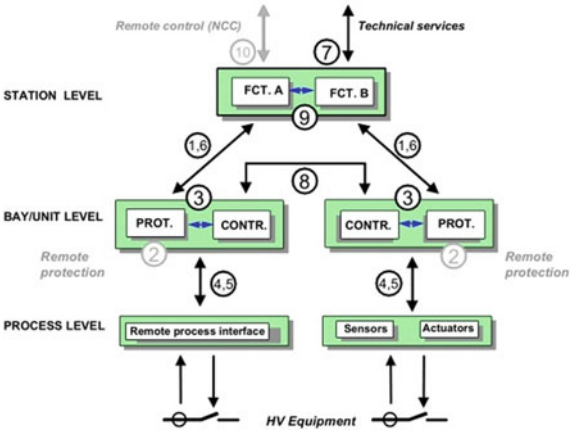

Fig. 1 Levels and logical interfaces in substation automation systems [3, 8]

other. In the typical protection configuration of UHV station, the failure function of switch protection device can start the bus protection device and make the bus differential protection operate. The line protection device can start the reclosing and failure function of the switch protection device. The protection devices between different manufacturers can interact with each other to improve the function of protection. Switch protection is the intermediary connecting each protection device. Generally speaking, the over-current protection function of switch protection is usually withdrawn, mainly to realize the function of failure and reclosing (Table 1).

The description of circuit breaker failure protection task in IEC61850 standard is that if the circuit breaker receives a trip signal of some kind of protection, such as line protection, the circuit breaker cannot be tripped because of the internal failure of the circuit breaker, then it must be tripped by the adjacent circuit breaker. Remove the fault, and the adjacent circuit breaker may include an outgoing

Table 1 Interoperability between partial relay protection

Interactions	Circuit breaker protection	Busbar differential protection	Line protection
Circuit breaker protection action	If it fails, the adjacent switch tripping	If it fails, start busbar differential protection	If it fails, use the remote tripping function
Busbar differential protection action	If there is a switch failure in the protection action range, the failure protects the logic action, the bus action latch reclosing	None	Indirect contact via circuit breaker protection
Line protection action	Failure protection and reclosing function, locking reclosing function	Indirect contact via circuit breaker protection	None

circuit breaker (line-to-end) of the opposite-side substation. For this reason, the circuit breaker failure protection is started by the protection trip command to monitor whether the fault current disappears. If there is a fault current, the trip signal is sent to all adjacent circuit breakers after a predetermined delay [8]. And reclosing is line protection. One of the functions of the power system operation experience shows that the vast majority of overhead line faults are temporary, permanent faults are generally less than 10%. Therefore, after the relay protection action removes the short-circuit fault, the arc will automatically extinguish, and in most cases the insulation at the short-circuit can be automatically restored. Therefore, the automatic reclosing of circuit breakers not only improves the reliability of power supply and reduces the loss of power outage, but also improves the transient stability level of power system and increases the transmission capacity of high-voltage lines. However, if reclosing occurs in a permanent failure, there are two main adverse effects. First, the power system will be affected by another fault, and second, the working conditions of the circuit breaker will become more serious [15]. Therefore, reclosing is mainly used for lines, while transformers, buses and other equipment do not use reclosing. Next, through fault cases and fault prediction [16], the protection action behavior is analyzed, a fault identification method in 3/2 wiring mode is proposed, and the protection configuration is optimized.

4 Optimal Configuration of Protection Under 3/2 Wiring Mode

The reach of protection is determined by the secondary wiring of the current transformer. According to the requirements of the substation acceptance standard: for 3/2 and other multi-circuit breaker wiring types, both sides of the circuit breaker should be equipped with current transformers, And its secondary winding should be arranged reasonably, To eliminate the dead zone between the circuit breaker and the current transformer. In order to remove the internal fault in time and keep the system stable [17].

A current transformer is installed on both sides of the circuit breaker of the UHV substation. The protective device ensures that the secondary windings of the current transformer are crossed to ensure that there is no dead zone. Bus differential protection wiring diagram, as shown in Fig. 2, the switch is represented by WXA61 and WXA6. The line is represented by WLA60. WLA60 line protection adopts WXA61 current transformer T11 side winding current and WXA62 current transformer T12 side winding current. It can be seen from the wiring mode that the protection scope of WLA60 line protection includes WXA61 and WXA62. The range of II bus differential protection includes WXA62. In the event of a WXA62 failure, action should be taken against both sets of protection. On the contrary, if the WLA60 line protection and the II bus differential protection operate at the same time, the fault should exist in the cross range of the two sets of protection, that is,

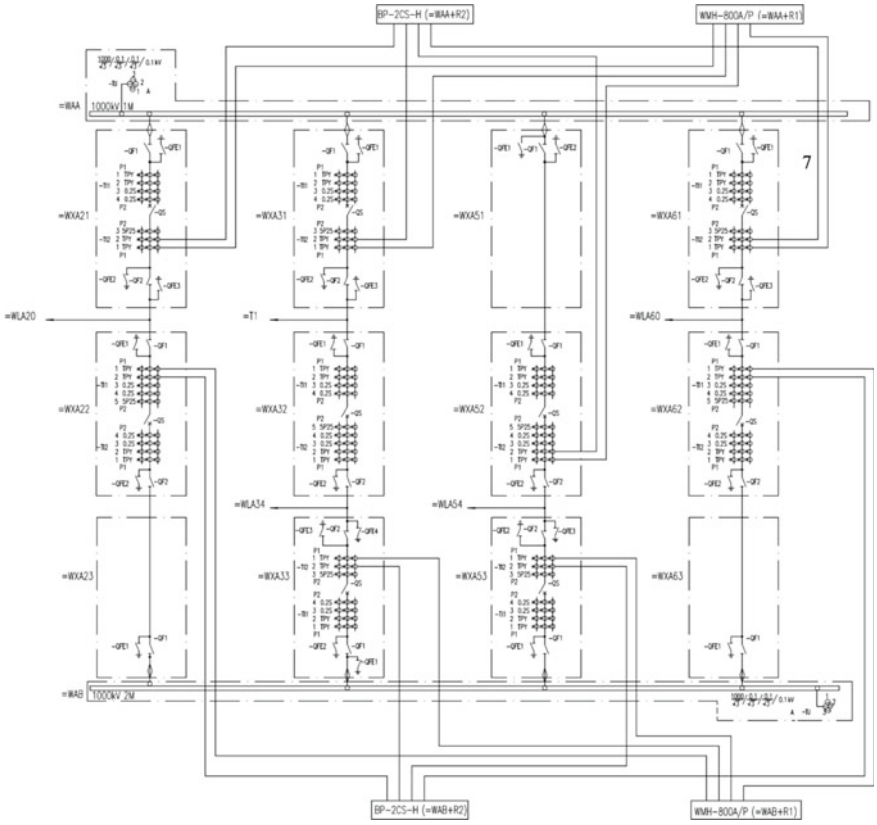

Fig. 2 Wiring diagram of busbar differential protection in a UHV substation

Table 2 A Substation Fault Briefing

Fault Name	1000 kV II busbar differential and WLA60 line tripping
Tripping process	17:18:38 WLA60 line first and second sets of phase separation current differential protection operation, jump A phase circuit breaker WXA61 circuit breaker A phase reclosing operation, reclosing successfully The first and second sets of bus differential protection of 1000 kV II bus jump on WXA22, WXA33 and WXA53 circuit breakers (WXA62 circuit breaker is in the open position and has no reclosing function) The first set of 3088 ms WLA60 line phase separation current differential protection jumps ABC three-phase

WXA62. Because of the characteristics of the secondary wiring, the fault range can be judged according to the protection action behavior.

Table 2 describes a fault example, and a brief analysis of the relay protection action shows that: when the fault occurs, the protection action has several

characteristics. First, the bus protection and the line protection operate at the same time, and the bus and the line are removed; Second, Bus protection directly tripped the bus, WXA62 protection reclosing did not put into operation; Third, the line protection reclosing operation, but the reclosing is not successful. From the point of view of protection operation logic, the fault short circuit point is at WXA62: after the fault, the SF_6 gas composition analysis of the field GIS equipment is carried out. After detection, the WXA62 switch A phase closing resistance component is abnormal, the SO_2 content 163.2 ppm, H_2S content 8.7 ppm, CO content 8.2 ppm, the other gas chamber SF_6 component is not abnormal, the WXA62 closing resistance fault is determined.

By analyzing this fault, the action behavior of relay protection can be optimized. The reclosing action of line protection reclosing is reclosing to the internal fault of GIS and tripping again, which has a secondary impact on the system and affects the stability of the system. AC/DC hybrid UHV large power grid requires high waveform, and the failure of reclosing is easy to lead to commutation failure. If this kind of fault is encountered again, the optimal action behavior of the protection is that the bus differential protection and the line protection action remove the fault, and lock the reclosing, so as to prevent the reclosing from affecting the stability of the power grid.

According to the insulation breakdown fault of the switch, the protection action behavior of other switches in the event of similar failure can be expected. For example, WAX31 circuit breaker fault: I bus differential protection action to remove the bus, main transformer protection action to trip the main transformer three sides, the fault point is isolated, the switch connected to the main transformer reclosing is not used, reclosing does not operate, the protection behavior is correct and reliable. WAX32 circuit breaker fault: main transformer protection action, because the main transformer protection only tripping function has no reclosing related functions, trip WAX32 circuit breaker, line protection action, because the reclosing function is configured according to the switch WAX33 reclosing in use, WAX33 reclosing, The line is electrified, and at this time the internal insulation of WAX32 is destroyed, there is a grounding point in the system, reclosing fails, and then jumps again and again. This results in the secondary impact of the system, and the protection action behavior is not optimal. WAX33 circuit breaker fault: line protection and II bus differential protection action, bus differential protection locking WAX33 switch reclosing, bus and line removal, fault point power supply removal, reclosing does not operate, protection behavior is reliable. On the contrary, if two different protection actions can locate the fault point according to the protection range, and optimize the action behavior of reclosing, avoid the internal fault of GIS switch.

At present, the protection action is in the order of milliseconds, and the reclosing action time is above 700 ms, so it is feasible to quickly optimize the reclosing action behavior. If different types of protection are started at the same time, intelligent substation and control center can use protection action information to

automatically locate the fault and send fault location information, which is more conducive to further shorten the maintenance working time. Improving the reliability of power grid and ensuring the safe and stable operation of power grid.

5 Conclusion

According to the object-oriented basic idea of IEC61850 standard system, combined with the characteristics of 3/2 connection mode and reach of primary equipment protection in hub substation, this paper puts forward a method to optimize the protection configuration. Making good use of all kinds of protection information to form the optimal action strategy of relay protection to avoid coincidence with permanent faults is conducive to the safe and stable operation of power system.

Through the study and judgment of the protection action behavior, the fault range can also be located quickly, and the background alarm information can be comprehensively analyzed to form a preliminary discrimination, which is beneficial to the dispatching and operation and maintenance personnel to correctly grasp the equipment situation and improve the efficiency of power grid fault disposal.

References

1. Tan W (2011) Seamless communication architecture in power systems. Electr Power Autom Equipment 21(11): 2–4
2. Gao Z, Huan H, Xu H, et al (2018) Discussion on applications of IEC 61850 and its development. Power Syst Prot Control 46(1):162–169
3. Communication networks and systems in substations Part 1: introduction and overview. 2005
4. Xue Y (2006) Space-time cooperative frame work for defending blackouts: partI from isolated defense lines to coordinated defending. Autom Electr Power Syst 30(1):8–16
5. Yi J, Bu G, Guo Q et al (2019) Analysis on black out in Brazilian power grid on March 21 2018 and its enlightenment to power grid in China. Autom Electr Power Syst 43(2):1–5
6. Shan X, Wang Y et al (2018) Scheme and application of integrated monitoring and fault co-disposal technology of UHV inter-connected power grid. Autom Electr Power Syst 42(2):84–91. https://doi.org/10.7500/aeps20170320005
7. Wang Q, Li T, Tang X et al (2019) Method of site selection for synchronous condenser responding to commutation failures of multi-infeed DC system. Autom Electr Power Syst 43 (1):222–226
8. Communication networks and systems in substations Part 5: communication requirements for functions and device models. 2006
9. Liu Z (2011) Quality management and control of gas insulated switch gear. China Electric Power Press, Beijing
10. Guo X (2006) Practical technology of the production run of the high-voltage switch gear. China Electric power Press, Beijing
11. Cui Y, Ma H, Wang T (2015) Fault analysis of GIS based on fault tree theory. High Voltage Apparatus 51(7):125–129

12. State Grid Corporation. Q/GDW168—2008 State of the transmission and distribution equipment maintenance testing procedures. 2008
13. Zuo Y (2013) Operation maintenance and trouble shooting of GIS. China Electric Power Press, Beijing
14. Luo X (1999) SF6 gas insulated enclosed switchgear. China Electric Power Press, Beijing
15. National Electric Power Dispatching and Communication Centre (2000) Practical technical question and answer of relay protection. China Electric Power Press, Beijing
16. Shan X, Dai Z, Cao L, Wang D (2018) An on-line identification of equipment risk for 3/2 circuit breaker connection. Autom Electr Power Syst 46(1):162–169
17. State Grid Corporation (2016) Q/GDW114 86—2015. Specification for acceptance of relay protection and security automatic equipment in intelligent substation

Research and Application of a Visual Component Aggregation Method

Linfeng Li, Dan Rao, Ling Luo and Heng Zhang

Abstract This paper introduces a visual component aggregation method. This method aggregates multiple function blocks to generate new function block or component, and supports aggregation between multiple components. Based on this method, a unified visual development system is implemented. The visual development system supports a device research and development process combining visual programming and configuration technology, provides the visual reuse function for the research and development of relay protection device and improves the efficiency of visual programming and configuration.

Keywords Visual programming · Visual configuration · Relay protection · Aggregation

1 Introduction

Since the 1990s, visualization technology has been applied to power systems [1], and visualization technologies based on SVG [2] standards have been used in a wide range of EMS and SCADA systems.

With the development of microcomputer protection, in order to solve the problems caused by the increasing complexity of protection logic and the diversification of hardware platform, visual programming technology has been introduced into microcomputer protection. Visualization programming technology draws on the PLC standard of IEC61131-3 [3], using function block to draw logic diagram and realize program function. This technology makes the programming process simpler and more intuitive, improves the degree of transparency of the program, and blocks the difference of the hardware. Symbol-based code reuse method improve the programming efficiency. In the relay protection industry, there are relatively mature products at home and abroad, such as ABB's "HiDraw", NR

L. Li (✉) · D. Rao · L. Luo · H. Zhang
NARI Technology Development Co. Ltd., Nanjing 211106, China
e-mail: lilinfeng@sgepri.sgcc.com.cn

Y. Xue et al. (eds.), *Proceedings of PURPLE MOUNTAIN FORUM 2019-International Forum on Smart Grid Protection and Control*, Lecture Notes in Electrical Engineering 585, https://doi.org/10.1007/978-981-13-9783-7_46

Electric's "ACCEL", NARI's "VisualIDE" all have visual programming and debugging functions, the device program is completely generated by graphics programming software.

In order to meet the requirement of free configuration of users, visual configuration technology is developing rapidly in the field of relay protection. Visual configuration technology in the microcomputer protection of power system, the configuration relationship between the protection components is described graphically, and the functions of parameter modification, LCD configuration, device diagram generation and so on are provided. Visual configuration software such as ABB's PCM600, NR Electric's "Pcs-explore", and NARI's "VICT" have been applied in the implementation of the project.

Because the visual configuration technology provides the function of self-configuration to protection products, it conforms to the actual situation of the modular module design of the protection device [4], and meets the flexible protection configuration needs of overseas users. At present, the visual programming tools and visual configuration tools of each manufacturer are basically used independently. Visual programming tools are mostly used in DC systems, generating code after compilation and downloading to the device. The communication Protection program based on the visual configuration is written manually by the coder and solidified in the protection device, and the component graphic containing the input and output parameter information needs to be made according to the program for configuration use. The component production process takes a long time and is error-prone. An aggregation method is promoted, which seamlessly combines visual programming and visual configuration technology to aggregate the functional blocks of visual programming software, extract and automatically generate the components needed for visual configuration software, and support the stacking function of function blocks and components.

This paper mainly expounds the principle of this method and the realization of visual development system based on this method.

2 Visual Development Technique

2.1 "VisualIDE" Visual Programming Tool

"VisualIDE" visual programming software combines modular, visual design concepts, drawing on the concept of FBD in IEC61131-3 (Function Block Diagram) [5], simplifying programming. Developers are able to build integrated program logic to protect products, improve development efficiency.

The software integrates engineering writing [6], code generation [7], one-click download, IEC61850 model generation [8], online debugging and other functions, supporting the protection of the product's entire development process work.

The function block is the smallest functional unit of the "VisualIDE", range from one logical operation to a protection algorithm [9], can be encapsulated into a separate function block for users to use. The function block has a transparent external interface, including input, output, parameters and function. Input and output and parameters are visible to the users [10].

Function blocks can be functionally described in the following formula:

$$o = f(p, i) \tag{1}$$

i and o represent the input and output collections of functions respectively; f represents the function of the protection logic algorithm; p corresponds to the parameters required for the operation of the function.

The visual programming environment will generate the running function of the configuration page by graph theory [11], get the scheduling order of the configuration from page the scheduling page of the application, generate the running function of the protection function.

2.2 *"VICT" Visual Configuration Tool*

Overseas users have the need to configure their own protection logic, so the relay protection products need to provide visual protection configuration capabilities to users based on existing visualization technology.

"VICT" provides users with protection function selection, parameter setting, scheduling order adjustment, in addition to the PLC configuration [12], LCD configuration, LED configuration, G language [13] diagram configuration and other functions, to help users achieve the protection device secondary configuration.

The protection component is the smallest unit of the visual configuration tool. Components are basically divided into the following types of components:

- Basic components: typically used to represent logical operations. In order to meet the configuration requirements, the whole set of PLC logic component [14] is implemented in accordance with the requirements of IEC61131-3 protocol.
- Special components: components that usually represent specific functions in the program, such as the dispatching component [15], which is usually used to set the priority of the protection component; The feedback component [16], which is used to crack the ring in the logical diagram and so on.
- Protection components: used to represent a component of a protection function. Such as overcurrent protection can be represented by a component.

As shown in Fig. 1, the left side of the protection component graphic is the input collection, and on the right is the output collection. The middle data corresponds to the parameter collection for the component.

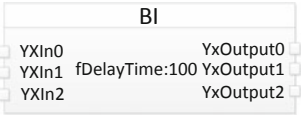

Fig. 1 Component graphics

According to the platform specification, the protection component needs to implement a uniform format of the running function and the structure.

2.3 The Docking Relation of Visual Development System

Visual programming is mostly used in the development of device programs. After the development of the device program is completed, the protection device has a complete protection function. Developers make protection component graphics symbols based on the basis of the protection program.

The algorithm engineers can focus on the function algorithm of the function block, and the visual configuration users can complete the construction of the device protection function without understanding the realization of the algorithm.

2.4 Current Problems in Visualization Technology

In the process of visual programming, there is the need for encapsulation multiplexing function blocks to generate new functional blocks, to avoid time-consuming and laborious duplication of effort of create new function block.

In addition, in the actual power system usage scenario, some of the protection logic is composed of other logic combinations, such as differential protection [17], which consists of Steady-State I section protection, steady-State II section protection and zero-sequence differential protection. In order to change the configuration granularity [18] and hide the key protection logic, it is necessary to embody this kind of stacking combination relationship between the protection logic in the visual configuration [19].

The production of protection components need to manually set the components of input, output, parameters and other properties. The process was cumbersome.

To sum up, it is important to design and implement an efficient method to generate new function blocks and protection components for connecting visual programming and visual configuration.

3 Method Principle

In the UML (Unified Modeling Language) [20] specification, *A* class can exist separately and can also form part of *N* class. This "whole-part" relationship between *A* and *N* can be achieved with aggregation.

In order to meet the needs of users and improve the efficiency of programming, this paper is divided into the following three ways to achieve component aggregation according to the specific application scenario.

3.1 Generate New Function Blocks with Function Blocks

This method can generate new function blocks from the original function block by aggregation technology, which is realized by the following steps:

Step One: Select the function block and drag it to the visual programming pages.
Step Two: As shown in Fig. 2, use lines to connect multiple base function blocks on pages.
Step Three: Generate code and symbol for new function block using the aggregate function integrated by the tool.

The tool uses a traversal algorithm to connect multiple function blocks on a page to generate a new function block.

Input with no line connected and input connected with external function block generate input for the new function block. If the Multiple inputs originate from the same external line, it is considered to be the same variable. The output of the new function block is equal to the no line connected output set of all child blocks. The parameters of the new function block are equal to the sum of the parameters of all child blocks.

The software generates a new function segment and run segment code according to the traversal algorithm, and replaces the input variable with the output variable according to the pull line relationship, and optimizes the generation script.

After the user adjusts the appearance of the graphic, it is automatically saved to the symbol library for programming reuse.

The method generates the "Exclusive or" function block by aggregating several basic logic function blocks in Fig. 2.

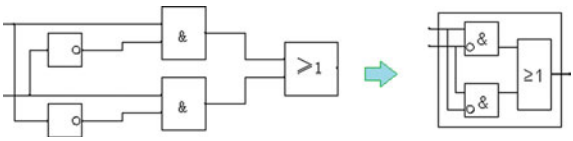

Fig. 2 Draw several function blocks

3.2 Generate Protection Component with Function Blocks

This method can use the function block to generate the code and graphics of the protection component through the aggregation technology, through the following steps to achieve:

Step One: Draw the base function block and connection to compose the application.

As shown in Fig. 3, dawn the function blocks of the application, the function blocks of the same page are connected to each other, and the jump symbols across the page pull-through are associated with each other.

Step Two: Mark the input and output of the function block with special tags.
Step Three: Generate code and graphics of the new component by the automatically generate component function which is integrated into the tool.

The tool uses a specific traversal algorithm to generate a protection component with the function block of all pages under Application. The function blocks in Fig. 3 will be aggregated to generate a protection component as shown in Fig. 4.

The structure of the new component contains all the variables of the function block, including input and output and parameters. Input that is connected by an internal cable will generate normal variable for the new component. The input of the new component consists of input selected by the user with a special symbol tag.

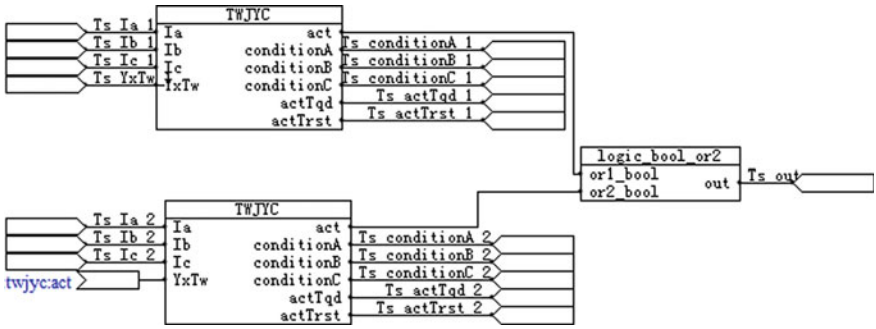

Fig. 3 Draw page to generate new component

Fig. 4 New component graphics

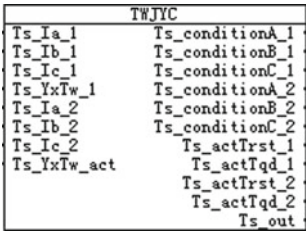

The output of the new component consists of output selected by the user with a special symbol tag. The parameter of the new component is generated by the parameters of the original component, and the input that is not marked or connected. Variables of functional blocks are automatically modified according to the serial number of functional blocks.

The function of the protection component is a set of function block functions.

If the same function block is used multiple times in the process, only one of the functions is retained in the component, saving code snippet space of device.

The program generates a run function based on the topology sort relationship of the graph. The run function of the function block is called in run segment code of the protection component in turn.

Step Four: Fill in the component name and save the information of the component.

The new component needs to fill in the component name and save to file. The tool will automatically generate the code and the graphics symbol of the protection component. Symbol in the library file does not contain code information, only input and output parameters information for visual configuration. In this way, the user can use the aggregation technology to reuse visual programming function block and directly realize all kinds of protection components. By compiling the code of the required protection components into the appliance program, users can enable the visual configuration function of the protection device.

In a visual programming project, multiple pages make up an app, and each app generates code for the protection component in the appliance program. Therefore, a visual programming engineering app can be aggregated to produce a protection component.

With this method, the device developer can not only generate protection components based on visual programming tools, but also use aggregation function to generate protection components independently. The method supports the visual configuration function, realizes the decoupling and seamless connection between visual configuration and visual programming technology, improves the flexibility and efficiency of the system, and meets the requirements of functional reuse.

3.3 Generate New Protection Component with Protection Components

In this method, a new protection component symbol is generated by aggregating the existing protection component symbols.

This method can be implemented in the following steps:

Step One: Create multiple pages, select the base component, and set the component instance name.

Step Two: Use the line to link the components, cross the page using the jump symbol to connect input and output.

Step Three: Generate the new component symbol by the automatically generate component function which is integrated into the visual configuration tool.

The symbol of the new component contains all the information of child components. Its input contains all the input of the child components, its output contains all the output of the child component, and its parameters contain all the parameters of the child components.

Step Four: Name the new component and save it.

The new component needs to fill in the component name and store it in the component library for making the project of visual configuration.

The new component exists as the parent of the child component. The input and output and parameter names of the child components remain the same, except for the component instance name that increases the parent component's instance name.

This method does not generate code for new components, but only logically adds a middle tier. In overseas projects, using this method, without re-modifying the program, the interface and parameters of the protection component can be opened to the user for configuration. This method controls the range of configuration and avoids the exposure of key logic during the visual configuration process.

4 Realize and Engineering Application

This method has been implemented in the way of software. The system is divided into two parts of the desktop software and the embedded module.

4.1 Desktop Software Design

The software architecture of the host computer of the visual development system is divided into three layers from top to bottom, as shown in Fig. 5.

The data support layer is responsible for managing the component library data, engineering data and communication links with the appliance, providing unified data to the logical layer.

The logical layer is responsible for processing graph logic, implementing optimization logic, generating code, compiling programs, generating configuration files, generating model files, communicating with appliances, downloading programs, online debugging and other specific functions.

The user interaction layer provides the user with component aggregation, visual programming and protection configuration services.

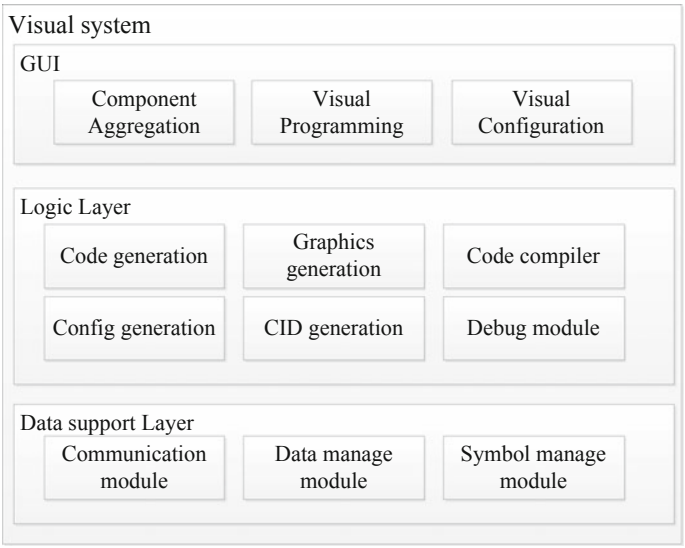

Fig. 5 Visual development system Software Structure on Master Computer

4.2 Embedded Module Design

In order to realize the visual configuration function, the visual configuration parsing module is added to the protection device. When the user completes the visual configuration, the generated configuration file is downloaded to the appliance. In the process of device initialization, the configuration parsing module reads the file information, initializes and instantiates each protection component according to the instance name and component name, and according to the link relationship in the configuration file, points the pointer entered by each component to the address of the output of the link, and finally reads the scheduling order and interrupt timeshare of each component to mount the running function of the component to each interrupt level.

After initialization, the main program invokes the component's running function one by one according to the interrupt time, scheduling order, and time slice order.

4.3 Engineering Application

Overseas project has variable customization needs. Project customers have the need for independent configuration. Aggregation technology can support the development of overseas protection devices.

Take the development process of busbar protection equipment as an example to illustrate how the aggregation can be used in project. Developers draw visual

programming logic [21], and use the aggregation method of the function block to generate the sampling function block from the function blocks of multiple single-point analog sampling. The sampling function block, Fourier transform function block and protection algorithm function block are aggregated to generate the program of busbar differential protection [22], mutation differential protection and so on. Then developers download the program to the device. Since the busbar protection logic is basically the same in multiple bays, in order to improve configuration efficiency, multiple protection components are aggregated into a universal busbar protection component. Finally the protection components graphics and the device are jointly delivered to user. Users can make secondary configuration to meet the protection requirements of different bays.

The developer uses the function block to generate a new function block, uses the function block to build the protection component logic, generates the protection component, encapsulates the multiple components into the high-level component to hide the internal realization, selectively opens the part signal and generates the component graphics library, then submits to the field engineer and the user to use. The field engineers used component graphics and PLC logic symbols to build Anti-misoperation [23] logic. Overseas user uses component symbols to achieve independent configuration.

The visual development system has been used in a number of overseas projects, such as TP project in Brazil, to help projects put into operation on time.

5 Conclusion

Based on the actual demand of protection programming and protection configuration, this paper puts forward a method to quickly generate new function blocks and components, and provides a more flexible and faster development way for protection device by aggregating the function block and existing components. By means of providing graphics symbols of protection components, the flexible configuration requirements of users are satisfied, and the development efficiency of protection products is improved. It has been proved by practice that this method is efficient and operable. Previous version management tools are no longer available in visual projects. How to implement version control in visualization project will become the future research direction of visualization technology.

References

1. Overbye TJ (2005) Power system visualization. Autom Electr Power Syst 29(16):60–65
2. Lai X, Chen Q, Xia Q (2012) Development of power system visualization platform and methods library based on SVG technology. Autom Electr Power Syst 26(16):76–82

3. Gong X, Yijun GE (2007) Current situation and trend of IEC 61131-3 programming language. Control Eng 14(1):99–101
4. Zhang Z, Zhou J, Cai Y (2017) Distribution automation terminal based on modular configuration design. Autom Electr Power Syst 41(13):106–110
5. Wang S, Xing J, Wang P (2007) The controller configuration software based on IEC 61131-3. Microcomput Inf 5(1):56–58
6. Liu K, Chen H, Feng Y (2014) New generation visual programming software for control and protection system. Ind Control Comput 27(10):82–87
7. Chen H, Liu K, Feng Y (2013) Design and application of supporting tool software for new generation protection and measuring-control devices. Autom Electr Power Syst 37(20):92–96
8. Li J, Hu R, Wang L (2018) Engineering configuration scheme based on IEC 61850 Ed 2.0 in smart substation. Autom Electr Power Syst 42(2):154–159
9. Zhong W, Wu C, Ding N (2011) Software architecture and design of the schematic programmable development platform of protective relay. Power Syst Prot Control 39(3):100–104
10. Lu J, Li Z, Chen G (2005) Design and implementation of a universal visual platform in protection and M&C fields. Autom Electr Power Syst 29(4):58–62
11. State Grid Corp.Q/GDW 624-2011 (2011) Specification for graphical description of power system
12. IEC 61131-3 programmable controllers (2003) Part 3: Programming languages
13. Li B, Ni C, Li B (2014) Analysis scheme for relay protection fault visualization in new generation smart substation. Autom Electr Power Syst 38(5):73–77
14. Jiang Z, Li Y, Wang L (2014) Research on visualization measurement and control system based on plug-in technology. Meas Control Technol 33(7):110–113
15. Zhao Z (2004) Discussion of graphical programming and protective relay development. Electr Power Autom Equip 24(2):70–73
16. Li J, Sun B, Zhang J (2013) Research on the feedback loop diagram of graphic-oriented programming in relay protection. Power Syst Prot Control 41(21):15–19
17. Deng Q, Du Q, Lu J (2008) Implement of visual programming in microcomputer-based protection. Relay 36(3):1–4
18. Li J, Lai Y, Li Y (2010) Protection design based on modular-programming graphic platform. Electrotech Electr 7:23–25
19. Huang H, Miao X, Quan X (2006) Relay protection platform based on elemental and programmable logic. Relay 34(14):11–14
20. Fowler M (2013) UML distilled (a brief guide to the standard object modeling language), 2nd edn. Addison Wesley, New Jersey, USA
21. Wang L (2018) Implementation of the visual programmable in protection technology of power system. Electr Eng 8(16):83–85
22. Chen A (2018) Coordination control and mode switching strategy for hybrid AC/DC microgrid with multi-bus structure. Autom Electr Power Syst 42(17):175–183
23. Hu H, Zheng J, Zhao D (2012) Anti-misoperation rules of substation visualization based on extensible markup language. Autom Electr Power Syst 36(24):54–57

Computing, IoT, Mobile Internet and AI in Smart Grid

Power Grid Modeling and Topology Analysis Based on Graph Database Conforming with CIM/E

Hua Huang, Zonghe Gao, Jiangpeng Dai, Yi Wang, Xin Shan, Mingyu Zhai, Guangyi Liu and Wei Wang

Abstract The power system is becoming larger and larger, and the operation is more frequent, which puts higher requirements on the real-time performance of analysis and calculation. The graph database is a new type of database that originated from the parallel processing of massive data in the Internet. The data model can visually express the topology of the grid and easily realize parallel traversal query. Firstly, the characteristics of graph database are introduced from the aspects of data model and data query, and the potential advantages of applying it to large-scale power system analysis and calculation are analyzed. Secondly, the design method of power system modeling is presented for satisfying the guidelines of integrity, consistency and efficiency conforming with CIM/E standard. Finally, a parallel power network topology analysis algorithm is implemented based on the graph database model for a provincial grid. The calculation results of the actual large-scale provincial power grid show that the proposed method can significantly improve the topology search efficiency.

Keywords Graph database · Graph computing · Power grid modeling · Network topology · CIM/E

H. Huang (✉) · Z. Gao · Y. Wang · X. Shan · M. Zhai · W. WangNARI Group Corporation, Nanjing 211106, China
e-mail: huanghua2@sgepri.sgcc.com.cn

NARI Technology Co. Ltd., Nanjing 211106, China

State Key Laboratory of Smart Grid Protection and Control, Nanjing 211106, China

J. Dai · G. Liu
Global Energy Interconnection Research Institute North America, San Jose, CA 95134, USA

Y. Xue et al. (eds.), *Proceedings of PURPLE MOUNTAIN FORUM 2019-International Forum on Smart Grid Protection and Control*, Lecture Notes in Electrical Engineering 585, https://doi.org/10.1007/978-981-13-9783-7_47

1 Introduction

Electric power system is revolutionizing into a highly interconnected, large and complex network with the development of technology and the growth of economy. The power system realizes the high degree of interconnection within thou-sands of kilometers through the high-voltage, large-capacity and long-distance transmission networks, and the scope of the interconnected large power grid is continuously expanded [1, 2]. On the other hand, intermittent renewable energy resources, adjustable loads and electric vehicles are connected to the grid [3–10], which makes the quantity of adjustable equipment increase massively and increase the uncertainty of operation mode. Therefore, the scale of the power system is becoming larger and larger, and the operation adjustment is more frequent. It is needed to improve the accuracy and real-time performance of the analysis and control for the grid.

The Energy Management System (EMS) is an important pivot for the operation of large power grids. The development of physical power grid requires that the EMS has the characteristics of "full, fast, accurate" [11], which can carry out the online simulation, calculation and analysis quickly and accurately for the global grid model of multi dispatching centers [12]. At present, the calculation cycle of EMS is usually 5 min, but the intermittent characteristic of wind or photovoltaic power may make the output fluctuate drastically within 1 min. Therefore, it is very important to improve the real-time performance of power system online analysis software.

The development of EMS is closely related to the advances in computer technologies [13–15]. The Database Management System (DBMS) is the core component of the EMS, which is generally includes the real-time and non-real-time database. The non-real-time database is used to non-frequently accessed data, typically using mature relational databases. The real-time database can adopt a relational, hierarchical or object-oriented data model, which is generally implemented in an in-memory database [16]. Although a lot of achievements have been made in computer hardware and software technologies such as massive memory, multi-core CPU, GPU and parallel computing, the state of art of power system analysis application dose not effectively harness the parallel capability for the reason that the traditional database and computation methods applied in EMS were not designed for parallel computing.

Graph Database (GDB) is a technology developed in recent years for the parallel analysis and processing of massive data in the Internet. Its original concept is derived from graph theory [17, 18]. Since the power system network topology can be described straightforwardly by graphs, it is promising to improve the computational efficiency of massive data processing by applying the graph database to large-scale power system analysis [19]. The CIM/E model is an efficient electric grid model exchange standard format presented by State Grid Corporation of China (SGCC), which simplifies CIM/XML model by optimizing the information to process network topology. The power system modeling and network topology are

the fundamental functions of EMS, and provides the infrastructure information for online calculation, simulation and analysis. This paper presents a power system modeling method conforming with CIM/E based on graph database, and a network topology algorithm to validates the advantages of graph database and graph computing.

2 Graph Database Rationale

The graph database consists of a graph-based dataset and a graph traversal-based computation engine. The following will firstly describe its features of the data model and data query method, and then analyzes its potential advantages for applying to power systems.

2.1 Data Model

The data model of graph database is described by using nodes (vertices) and edges based on graph theory, which is different from the traditional database. Data attributes are stored in nodes and edges, and relationships between data are described by edges between nodes.

The graph database and the traditional database have common attributes for the description of the entity. For example, the same set of attributes such as rated voltage, rated capacity and reactive power can be adopted to describe the shunt compensator by the relational, hierarchical or object-oriented database. Nevertheless, the description of the associations are very different from each other (shown in Table 1).

RDB is the most widely used database in power system applications, with the advantages of simplicity, easy maintenance, and user-friendly interface. However, it is difficult to describe the topology of power systems by relational database. HDB is in accordance with the hierarchical relationship of the actual power system,

Table 1 Description of associations in different databases

Database type	The description of relations
Relational database (RDB)	Foreign key, One-to-many, many-to-many associations can be described
Hierarchical database (HDB)	Hierarchical pointer, One-to-many association can be described easily but not many-to-many association
Object-oriented database (ODB)	Reference, One-to-many, many-to-many associations can be described
Graph database (GDB)	One-to-many, many-to-many associations can be described and attributes can be assigned to edges

by which it is easily to described the topological structure of the power system. At present, many power system analysis applications are implemented based on HDB. ODB can be integrated easily with object-oriented software engineering, but the implementation is more complicated than other databases, and there are no mature products [16]. The data model of GDB has a natural similarity with the power system network structure, and can describe the powers system topology straightforwardly.

2.2 Data Query Access

The data query includes a set of program interfaces for accessing data and related support services, which is the compute engine of the DBMS. The data model of GDB consist of vertices and edges, which can have computing functions and are both data storage units and dynamic computing units. Querying the dataset of a graph structure is called graph traversal or graph computing. Communication between vertices in a graph structure is realized by exchanging information through edges. "Local computation" and "coordinated collaboration" are used in a graph computing so that large-scale parallel computing can be easily achieved. At present, the parallel graph computing framework such as Pregel [20] mainly adopts the BSP [21, 22] (Bulk Synchronous Parallel Computing) model proposed by Valiant et al., which is a computation proceeds in a series of global supersteps for the data synchronization and calculation iteration of multi-computing nodes in complex network (shown in Fig. 1).

The data query method provided by a database is closely related to its data model. The data query method of the traditional database and the graph database is shown in Table 2.

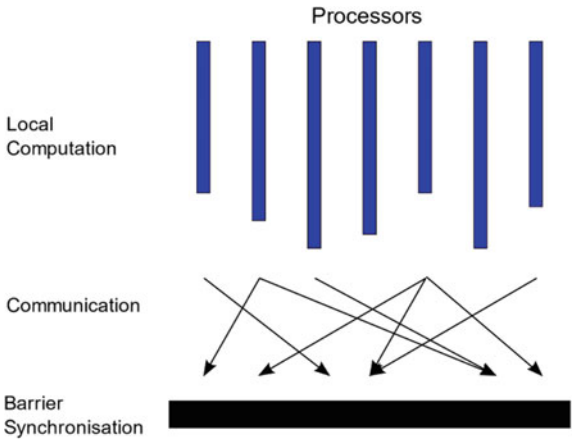

Fig. 1 Bulk synchronous parallel computing model

Table 2 Query methods of different database

Database type	Data query method
Relational database (RDB)	Cross-table queries need to join multiple tables to increase query complexity and reduce query performance
Hierarchical database (HDB)	Formatted model, high query efficiency, but multi-to-multi Association queries need to use virtual nodes or redundant data
Object-oriented database (ODB)	No mature products
Graph database (GDB)	Graph traversal, easy to parallelize, high query efficiency for large graphs

Traditional databases such as relational databases are increasingly unable to adapt to high concurrency and high speed I/O requirements in data query access for the massive data of the Internet. The data query of large graph is extremely efficient due to the feature of easy parallelization of graph database, and it is promising to achieve good results in massive data analysis and processing for large-scale power systems.

3 Power Grid Modeling Based on Graph Database

Power grid modeling based on graph database is the fundamental for applying graph computing technology to power system analysis and calculation. The basic principle of modeling is ensuring the integrity and consistency of the grid model confirming with the CIM/E standard, as well as improving the model access efficiency by adapting the characteristics of graph database.

3.1 Data Description Specification of CIM/E Model

CIM/E is a new and efficient power system model data description specification based on the common data model of IEC 61970-301, which is developed to solve the efficiency problem of CIM/XML. It is simple, efficient and suitable for describing and exchanging of large-scale gird models. CIM/E combines the traditional relationship-oriented data description of power systems with object-oriented CIM, which not only preserves the high efficiency of relation-oriented methods, but also absorbs the characteristics of object-oriented methods [23, 24].

The 26 types of objects such as power system base voltage and plant station are described by CIM/E in the form similar to relational tables. For instance, the shunt compensator (including shunt capacitors and reactors) object is described by the corresponding CIM/E file, which is shown in Fig. 2.

```
<ShuntCompensator::A Province>
@Num mRID          name      pathName              nomQ     V_rate     I_node BaseVoltage
VoltageLevel       Substation      Q      region_id
#170  117938015996739703   35kV.1-1#DKQ    AS.CNB/35kV.1-1#DKQ   -60.0000   35.0000
44999748349852 112871465677750275   113152941392658656   113997366322790551   0.0000 0
#171  117938015996739704   35kV.1-2#DKQ    AS.CNB/35kV.1-2#DKQ   -60.0000   35.0000
44999748349853 112871465677750275   113152941392658656   113997366322790551   0.0000 0
#172  117938015996739705   35kV.1-1#DRQ    AS.CNB/35kV.1-1#DRQ   50.0000    36.0000
44999748349884 112871465677750275   113152941392658656   113997366322790551   0.0000 0
.....
</ShuntCompensator::A Province>
```

Fig. 2 Shunt compensator object in CIM/E file

For instance, the shunt compensator (including shunt capacitors and reactors) object is described by the corresponding CIM/E file, which is shown in Fig. 2. The attributes of shunt compensator include 11 fields as shown in Fig. 2, which include the fundamental attributes such as mRID and name, as well as the attribute I_node describing topology and the attributes such as Voltage Level, Substation describing relationship.

3.2 Data Schema Design

The main task of the graph database schema design is to define the vertices, edges and related attributes according to the application scenario. The guidelines for power grid model design should include: (1) Integrity and consistency, which can fully describe the characteristics of the power system object and be as consistent as possible with the existing definitions; (2) Efficiency, which can maximize data access efficiency adapting to the graph database characteristics.

How to satisfy the guideline 1. The CIM/E model is developed on the basis of the Common Information Model (CIM), in which the data description of the grid equipment is universal; Therefore, the CIM/E can be utilized as the basic model for power grid modeling based on the graph databases. On this basis, the method is presented to satisfy integrity and consistency guideline, by which the power system objects are modeled as vertices, and the associations between objects are modeled as edges.

The power system network topology can be described straightforwardly by graph database model. The design guideline will be further discussed with the topology of the model system below, which includes 3 substations as shown in Fig. 3. The substations consist of busbars, breakers, disconnectors, generators and loads, etc., and are connected by AC lines between each other.

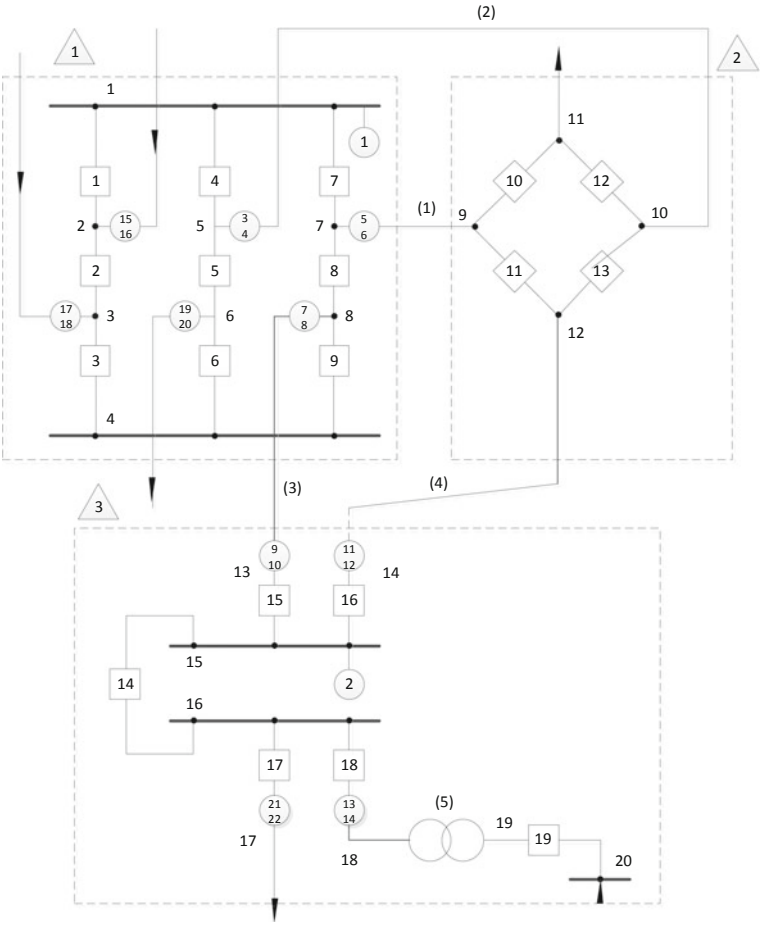

Fig. 3 Model power system

The power system devices such as busbars, breakers, disconnectors, genera-tors, loads and AC/DC lines are defined as vertices in the graph database, and the connected circuits between the devices are defined as edges. In addition, for establishing a topological association between devices, the attributes of physical nodes describing a device topology relationship in the CIM/E model are defined as vertices. The graph database model that satisfies guideline 1 is shown in Appendix Fig. 8.

How to satisfy the guideline 2. The guideline 2 is related to the design concept of the graph databases with vertex-centric, graph-based traversal access query. Following the design concept, the characteristics of the data access and query of the graph database include: (1) Direct access to the vertices but not direct access to the edges, which means that access to the edges needs to traverse the query from

the vertices; (2) The time required for the graph traversal is proportional to the number of hops passed, which means that the more vertices and edges of the graph, the longer it takes for access and query. Therefore, it is needed to optimize the data schema of vertices and edges in the graph database to improve the access efficiency on the basis of satisfying the guideline 1.

As can be seen from Fig. 3, the number of breakers and disconnectors is several times the number of devices such as transformers, busbars, generators, loads, and AC/DC lines. If the model of the breakers and disconnectors in the graph database shown in Appendix Fig. 8 can be modified from vertices to edges, then the number of vertices and corresponding edges will be significantly reduced, which can also reduce the hops of the graph traversal and improve the efficiency of graph databases access and query. The optimized graph database model is shown in Appendix Fig. 9, which can satisfy both the guideline 1 and the guideline 2.

In addition to the topological association, other associations between the devices such as the base voltage identification, voltage level identification, and plant station identification contained in the synchronous generator are also described in the CIM/E. The description method of the above associations is similar to the topological association. Firstly, the vertices such as the base voltage, voltage level, substation are modeled in the graph database, and then the above associations are described by the edges between the generator objects and the base voltage, etc.

In this paper, the data schema that satisfies both guideline 1 and guideline 2 will be used. The corresponding graph database model is shown in Appendix Fig. 9.

3.3 Data Model Loading

The data model loading parses the CIM/E file into graph-oriented vertex and edge datasets and stores them in the graph database.

Following the data schema, the 19 types of vertices such as control area, base voltage, substation, voltage level, busbars, synchronous generator, AC line, AC line segment, AC line dot, DC line, DC line dot, rectifier inverter, load, transformer, transformer winding, tap changer type, shunt compensator, series compensator and bay can be extracted from the CIM/E file to form datasets. Each dataset is independent and form data file corresponding to the type of vertex. Because there is no corresponding object to the vertex of physical node in the CIM/E exchange file, all objects in the CIM/E file containing the physical node attributes are scanned, and the attributes are accessed to form a union of the physical node data.

The edge is formed between the source object and the target object by parsing the reference attributes of them after forming the dataset of each vertex. For instance, the edges between the shunt compensators and the physical nodes are described by the pairs of nodes (mRID, I_node). As shown in Fig. 2, the edges are respectively (1179380159967703, 449997489852), (117938015996739704, 49997489853) and (117938015996739705, 44999748489884). All pairs of nodes describing various types of edges can be formed by scanning all objects of the

CIM/E exchange file in turn according to the reference attribute category, which can be stored as edge datasets. Both source objects and target objects of the edges of breakers and disconnectors are physical nodes, so the edge datasets of breakers and disconnectors are slightly different from the above-mentioned edges.

The load task of the graph database is executed after forming the dataset files of the vertices and edges. The vertices datasets can be loaded concurrently to improve the data loading efficiency.

4 The Network Topology Based on Graph Database

The network topology is a process of transforming the grid physical node (NODE) model into a computed bus (BUS) model based on the switching state [13]. Based on the constructed grid map database model, a parallel power grid topology analysis method is implemented by combining graph partitioning and graph computing in this paper.

4.1 Graph Partitioning and Network Topology

As shown in Fig. 3, the power grid consists of generator, loads, busbars, transformers, AC lines, breakers, disconnectors and physical nodes. The graph database model of the power system shown in Appendix Fig. 9 can be represented by a graph $G = (V, E)$. Where V is the set of vertices of the graph, E is the set of edges of the graph, and the vertices and edges are assigned attributes.

The objective of the graph partitioning is to divide the graph G into smaller components. Given an undirected graph $G = (V, E)$ and a positive integer p, find p subsets $V_1, V_2, \ldots, V_p$ of V, such that:

$$\bigcup_{i=1}^{p} V_i = V \text{ and } \bigcup_{i=1}^{p} V_i = V \text{ for } \bigcup_{i=1}^{p} V_i = V.$$

Any set $\cup_{i=1}^{p} V_i = V$ is called a p-way partition, as shown in Fig. 4. Each V_i is a part of the partitions and called a subgraph of the original graph G.

Fig. 4 Graph partition

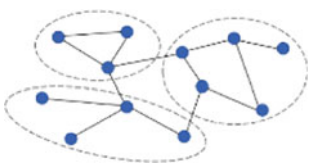

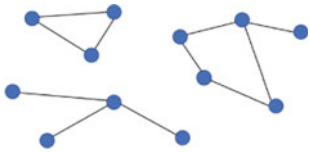

Fig. 5 Connected components

If any two vertices in a subgraph can be connected to each other by one or more edges, and any vertices are not connected to other vertices outside the subgraph, then the subgraph is called a connected component of the original graph *G*. For the graph partitions shown in Fig. 4, if the connected edges between the subgraphs are deleted, then the connected components of the graph G can be formed shown in Fig. 5.

The process of power system network topology is generally divided into two phases. The buses are formed in the first phase, and the electrical islands are formed in the second phase. Furthermore, a bus is a set of physical nodes connected through closed breakers and disconnectors, and an electrical island is a set of buses connected by branches components such as transformers and AC/DC lines. The buses and the electrical islands can be considered as subgraphs formed by different stages of graph partitions. Therefore, the network topology can be described by the graph portioning which is divided into two phases and satisfies certain constraints.

4.2 Parallel Network Topology Algorithm

The depth-first [13] or breadth-first search algorithms are used by traditional network topology method [25], which is implemented in serial program or parallel program of substation or partition level [26, 27]. The basic strategy for applying graph partitioning techniques to solve network topologies is to automatically form subgraphs by searching for connected components. The depth-first or breadth-first algorithms can be used for searching connected components, but which runs with low efficiency when dealing with large scale connected components. Based on graph partitioning technology and BSP graph computing parallel framework, this paper implements a fine-grained parallelized network topology method, which will be introduced in two stages.

Buses search. The buses are subgraphs of graph G, and the vertices in one subgraph can be connected through the edges represented breakers and disconnectors which are closed, and cannot cross the branch components such as transformers and AC/DC lines. The bus is formed with connected components search of graph G based on BSP model. The detailed steps are as follows:

(1) Initialization: Assign a unique BID to each vertex represented physical node for the whole graph.
(2) Sending initial message: Each vertex represented physical node checks its outgoing edges type and state. If the outgoing edge type is a breaker or disconnector which is closed, a message containing the BID value is sent along the outgoing edge, and each vertex transfers to halt.
(3) Receiving and processing message: Each vertex represented physical node receive messages from other vertices and parse to get the BIDs. If the BID received is smaller than the current BID of itself, the current BID is updated by the BID received, and the vertex transfers to an active state. Subsequently, a new message containing the current BID is sent along the outgoing edge.
(4) Checking the state of vertices: If all the vertices are transferred to halt, then go to step (5); otherwise, return to step (3).
(5) Add vertices represented bus to the graph database.
(6) exit.

The above steps are shown in Fig. 6. And each vertex has a compute function of comparing the BID between itself and the adjacent vertices to update the BID with a small value. Each vertex is assigned an independent worker process or thread attached to some processor, and each vertex executes local computation independently and sends messages to its adjacent vertices. Synchronization of all vertices is performed by the master process or thread to check the states of all vertices and control the iteration, and each iteration is called a superstep.

As shown in Appendix Fig. 9, the breakers CB10, CB11, CB12, CB13 in the substation 2 are all closed, and the initial BIDs of the vertices CN9, CN10, CN11,

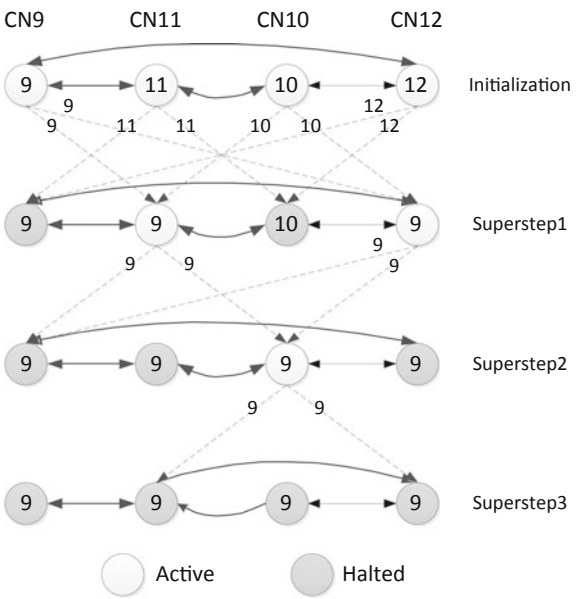

Fig. 6 Bus search based on BSP model

and CN12 are 9, 10, 11, and 12, respectively. The BIDs of all vertices are all updated to the minimum value of 9 using 3 iterations, revealing that these vertices are connected into the same subgraphs through the closed breakers and disconnectors, and meaning that the vertices are classified to the same bus.

The bus search process can be started simultaneously from all vertices in the graph, which is a node parallel mode of more fine grain. After all buses search processes are completed, a bus model is formed in the graph database.

Electrical islands search. The buses are connected through branch components such as transformers and lines after the formation. The detailed steps are as follows:

(1) Start from the vertices represented transformers and lines to search the adjacent vertices represented physical nodes along the outgoing edge, and then searching for the buses corresponding to the vertices represented physical nodes.
(2) Add the edge represented branch, the both vertices of which are the bus obtained in step (1).

As shown in Fig. 7, the computation graph model represented by G_{bus} is formed which consists of bus and branch through the above steps. The electrical island is a set of buses connected by branches and a subgraph of the computation graph.

Based on the bus-branch model graph and the BSP model, a node-level parallel algorithm similar to buses search is used for connectivity search and formation of electrical islands.

5 Case Study

A provincial power grid is presented in this paper for actual verification and case analysis. The provincial power grid consists of 2834 substations, 2851 busbars, 4540 generators, 2204 loads, 1343 lines, 4,456 transformers, 818 shunt

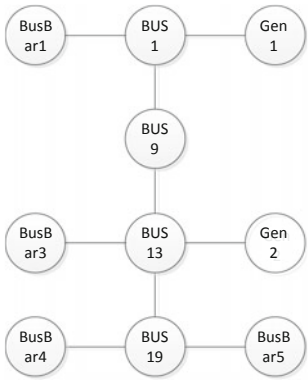

Fig. 7 Bus model graph

capacitors/reactors, 3 series compensators, 11,036 breakers, 21,828 disconnectors and 47,689 physical nodes.

Firstly, the data schema is defined with beakers and disconnectors described by edges, and then the CIM/E file is converted into the datasets of vertices and edges which are loaded into the graph database subsequently to build a physical node graph model of the power system. The graph model consists of 68,528 vertices and 58,499 edges. If the data schema is defined with all objects described by vertices as shown in Appendix Fig. 8, the number of vertices of the graph model will increase to 101,392, and the number of edges will increase to 91,363. Therefore, the number of vertices and edges in the graph can be significantly reduced by optimizing the data schema of breakers and disconnectors in graph databases, and the number can be reduced is the sum of the number of breakers and the number of disconnectors.

A real-time network topology analysis application based on the graph database for the above-mentioned power system is implemented. The application is run in the test environment with multi-core and multi-processor computer based on LINUX operating system. The hardware and software configuration are shown in Table 3.

The multithread technology is used to optimize running of the application, by which each vertex performs local computing concurrently, and the coordination and synchronization of local computing are implemented through message passing. The initial network topology analysis is performed for the whole power system, and then a bus-branch graph model consisting of 3293 buses and 3168 branches is built. Thereafter, the local topology is triggered by the subgraph connectivity analysis according to the signals of breakers and disconnectors received from the SCADA system, which is performed for the voltage level and the substation where the signals generate. The execution time results are shown in the following table compared with the traditional serial topology analysis method.

As shown in Table 4, the network topology process can be significantly speed up by the parallel network topology algorithm based on the graph database, and a millisecond-level fundamental model can be provided for online network analysis applications such as system topology coloring, state estimation and dispatcher power flow.

6 Conclusion

The power system network topology can be described straightforwardly and the parallel data query access can be easily achieved by graph database model, which has potential advantages for applying it to large-scale power system analysis and computing. A power grid data model design method based on graph database and

Table 3 Software and hardware test environment

Hardware and software	Configuration
CPU	Intel Xeon E5-26202 (2.1 GHz, 6 cores, 2 threads/core)
Memory	64 GB
Operation system	CentOS 6.8 (Linux)
Graph database platform	TigerGraph

Table 4 Software and hardware test environment

Analysis method	Execution time (s)
Traditional serial method	3.48
Parallel global network topology	0.0625
Parallel local network topology	0.0165
Traditional serial method	3.48

conforming with CIM/E is presented, and a data model loading application is developed in this paper. The power grid graph model built by this method has the advantages of consistency, integrity and high access efficiency. The parallel topology analysis method for power grid based on the graph database is implemented by combining graph partitioning and graph computing in this paper. The presented algorithm is a fine-grained node-level parallel algorithm compared with the traditional network topology algorithm. The actual test and verification of a provincial large-scale power grid show that the model and algorithm can speed up the data query access and the network topology analysis to provide a millisecond-level computation model for pow system online analysis and improve the overall efficiency of real-time computing for large-scale power grid.

Appendix

See Figs. 8 and 9.

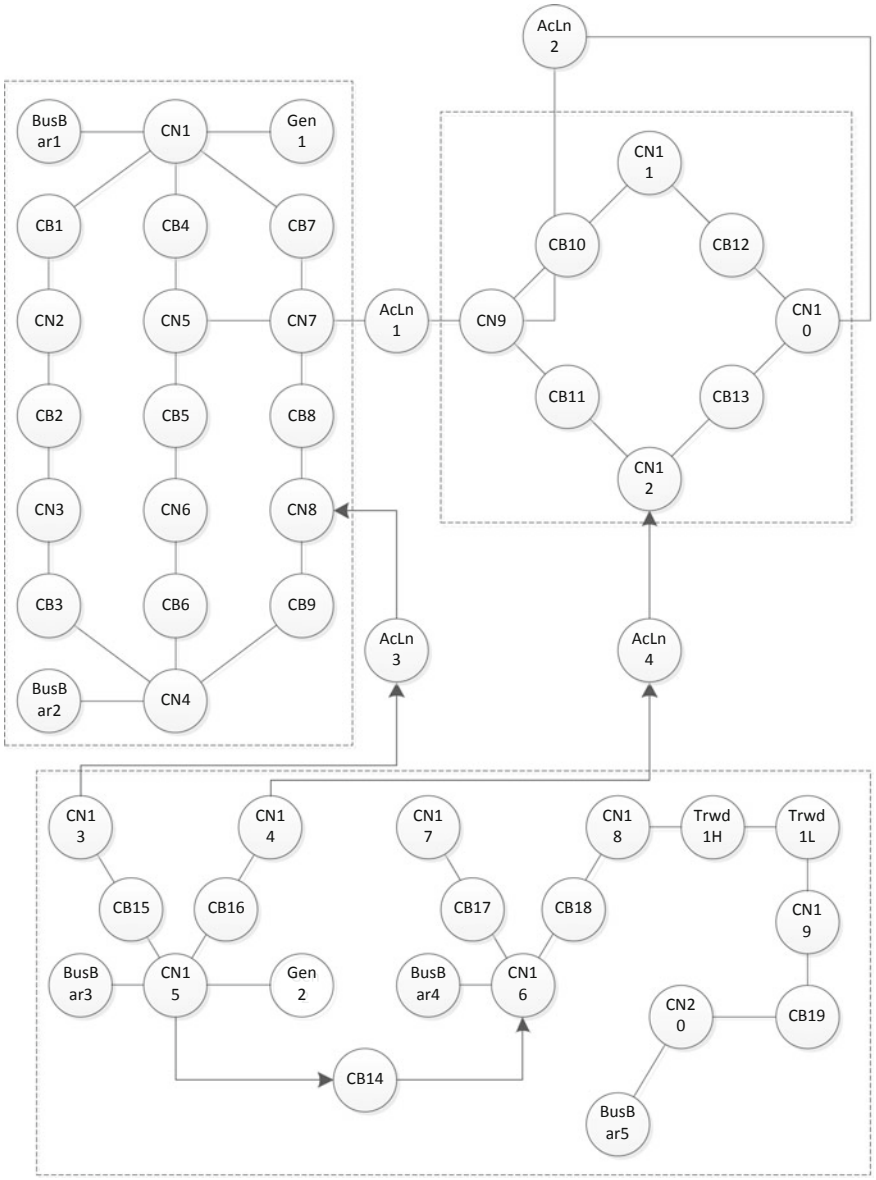

Fig. 8 Node model graph with all objects described by vertices

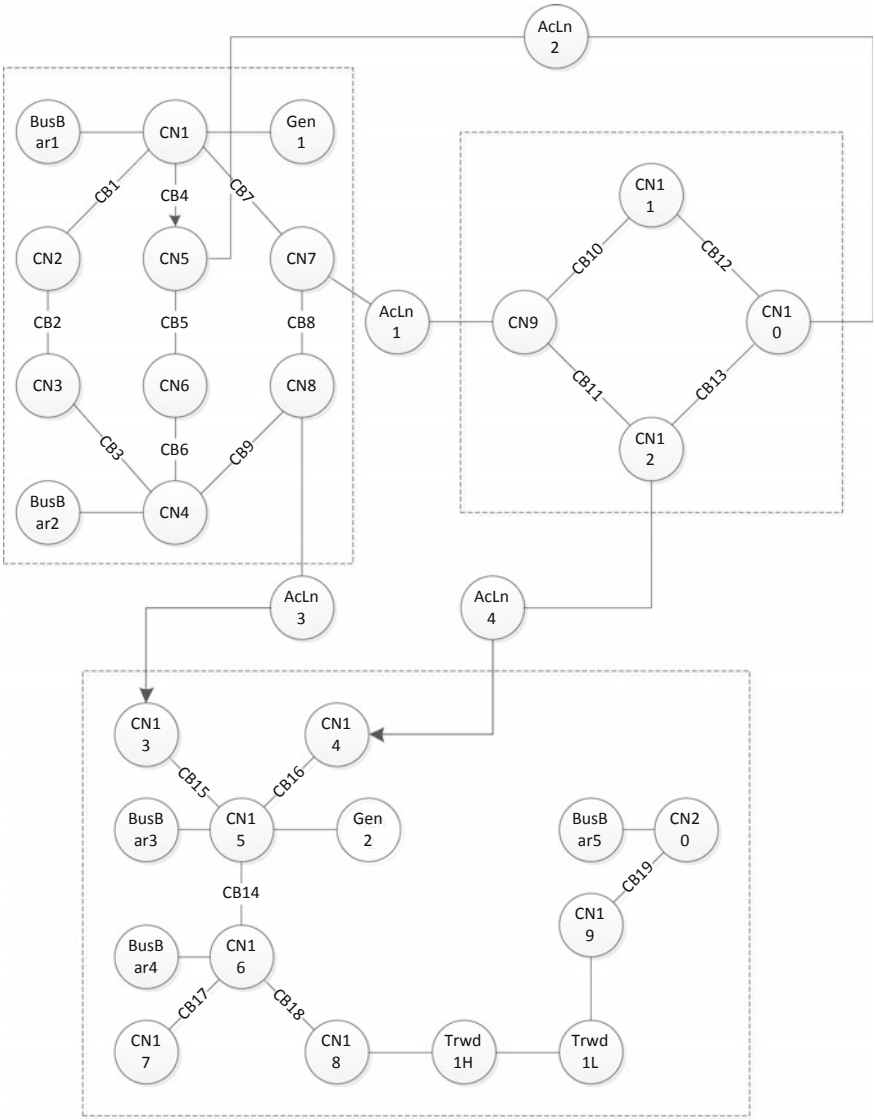

Fig. 9 Node model graph with beakers and disconnectors described by edges

References

1. Liu Z (2014) Ultra-high voltage AC/DC grids. Academic Press, Waltham, MA
2. Liu Z (2015) Global energy interconnection. Academic Press, Waltham, MA
3. Sun H, Guo Q, Pan Z et al (2015) Energy internet: driving force, review and outlook. Power Syst Technol 39(11):3005–3013

4. Sun H, Guo Q, Pan Z (2015) Energy internet: concept, architecture and frontier outlook. Autom Electr Power Syst 2015(19):1–8
5. Zhao J, Wen F, Yang A et al (2011) Impacts of electric vehicles on power systems as well as the associated dispatching and control problem. Autom Electr Power Syst 35(14):2–10
6. Ma L, Yang J, Fu C et al (2013) Review on impact of electric car charging and discharging on power grid. Power Syst Prot Control 3:140–148
7. Li H, Bai X (2011) Impacts of electric vehicles charging on distribution grid. Autom Electr Power Syst 35(17):38–43
8. Gao Z, Teng X, Zhang X (2010) Solution of active power dispatch and control scheme for interconnected power grids with large-scale wind power integration. Autom Electr Power Syst 34(17)
9. Xiao H, Pei W, Kong L (2016) Multi-time scale coordinated optimal dispatch of microgrid based on model predictive control. Autom Electr Power Syst 40(18):7–14
10. Ding M, Wang W, Wang X et al (2014) A review on the effect of large-scale PV generation on power systems. Proc CSEE 34(1):2–14
11. Xu H, Yao J, Nan G et al (2018) New features of application function for future dispatching and control systems. Autom Electr Power Syst 42(1):1–7
12. Xu H, Yao J, Yu Y et al (2018) Architecture and key technologies of dispatch and control system supporting integrated bulk power grids 42(6):1–8
13. Yu E, Liu G, Zhou J et al (1998) Energy management system (EMS). Science Press, Beijing
14. Yao J, Yang S, Gao Z (2007) Development trend prospects of power dispatching automation system. Autom Electr Power Syst 31(13):7–11
15. Yao J, Yang S, Shan M (2013) Reflections on operation supporting system architecture for future interconnected power grid. Autom Electr Power Syst 37(21):52–59
16. Shenming Z, Fanqiang B, Jianguo Y et al (2002) Real-time database management system (DBMS) that conforms to IEC61970 standard. Autom Electr Power Syst 26(24):26–30
17. http://tinkerpop.apache.org/docs/current/reference/#intro
18. https://en.wikipedia.org/wiki/Bulk_synchronous_parallel
19. Liu G, Liu K, Shi D et al (2017) Graph computation and its applications in smart grid. In: 2017 IEEE international congress on big data (BigData Congress). IEEE, pp 507–510
20. Malewicz G, Austern MH, Bik AJC et al (2010) Pregel: a system for large-scale graph processing. In: Proceedings of the 2010 ACM SIGMOD international conference on management of data. ACM, pp 135–146
21. Valiant LG (1990) A bridging model for parallel computation. Commun ACM 33(8):103–111
22. Valiant LG (2011) A bridging model for multi-core computing. J Comput Syst Sci 77(1): 154–166
23. Xin Y, Tao H, Li Y et al (2006) E language for electric power system model description. Autom Electr Power Syst 30(10):48–51
24. Mi W, Xin Y, Jiang G et al (2013) Comparative analysis of grid model exchange standard CIM/E and CIM/XML. Power Syst Technol 37(4):936–941
25. Chen X, Sun S, Qian F (2004) A fast power system network topology based on tracking technology. Power Syst Technol 28(5):22–24
26. Lang Y, Li J, Luo Y et al (2017) Large power grid topology analysis based on graph partitioning. Power Syst Prot Control 23:114–121
27. Xu D, Zhao M, Jiang H et al (2016) Power system parallel network topology algorithm applied to electromechanical transient real-time simulation of large-scale power system. High Voltage Eng 42(1):296–302

Comprehensive Evaluation of Power Quality via Sequential Floating Search Method

Dongyin Pan, Weidong Xu, Chi Zhang, Yujun Yin and Yunjun Sun

Abstract Comprehensive assessment of power quality is the basis for measuring power quality. SFSM (Sequential Floating Search Method) with Bhattacharyya distance is used to select the most effective power quality evaluation indices, then use three classical classifiers to verify the validity of the selected indices. Through analyzing the data collected by the monitoring points, each evaluation indicator is evaluated and screened. The reserved evaluation indices are searched by SFSM algorithm with the Bhattacharyya distance. SVM (support vector machine), KNN (K-nearest neighbor) and RBF (radial basis function) neural network are used to test the classification accuracies of the selected evaluation indices. The experimental results show that this method can find the best combination of power quality indices, which can reasonably evaluate the comprehensive evaluation level of power quality for a monitoring point.

Keywords Comprehensive assessment of power quality · Power quality assessment indicator selection · Bhattacharyya distance · Sequential floating search method

1 Introduction

Recently, electric energy is one of the widely used energy sources and has become one of the main indicators of a country's development level [1]. Therefore, the power quality problem has attracted the attention of the power grid sector, the power quality monitoring equipment manufacturer and the majority of power users [2–5]. For the problem with increasing serious power quality, scientists have successively formulated a series of national standards for power quality. However, it is a tedious and problematical task to assess the power quality level by one index, as there are many parameters in the problem of power quality evaluation [6].

D. Pan (✉) · W. Xu · C. Zhang · Y. Yin · Y. Sun
NARI Technology Co., Ltd., Nanjing, China
e-mail: 13814516956@139.com

Y. Xue et al. (eds.), *Proceedings of PURPLE MOUNTAIN FORUM 2019-International Forum on Smart Grid Protection and Control*, Lecture Notes in Electrical Engineering 585, https://doi.org/10.1007/978-981-13-9783-7_48

Therefore, it is necessary to establish a combined power quality criterion which can thoroughly describe the condition of the power system.

In recent years, domestic and foreign scientists have done a lot of researches on the comprehensive evaluation of power quality. The references [7–9] use the analytic hierarchy process, fuzzy mathematics, probability and statistics to evaluate the power quality. However, the above methods strongly depend on the subjective analysis of people which affects the objectivity of the evaluation results. This paper proposes to select the most effective evaluation indices from many candidate power quality factors based on Sequential Floating Search Method (SFSM) with Bhattacharyya Distance as its evaluation function. K-nearest neighbor classifier is used to determine the power quality level. The process of evaluation does not need to determine the weight manually to avoid the error caused by the subjective reasons in traditional evaluation methods. This method can provide an effective way for selecting power quality comprehensive evaluation indices.

2 Sequential Floating Search Method and Its Evaluation Function

2.1 Sequential Floating Search Method

The task of feature selection is to select a set of optimal features among many candidate features. Two problems need to be solved in feature selection. One is the evaluation function; the other is to find the optimal set of features with an algorithm within the limited time. Selecting d features among $D(D > d)$ features, all possible combinations are denoted as follows:

$$q = C_D^d = \frac{D!}{(D-d)!d!} \tag{1}$$

If all possible feature combinations are calculated and compared, the amount of calculation is too large to be accepted. The Sequential Floating Search algorithm can find the optimal feature subset efficiently.

The algorithm is also called the addition l and subtraction r algorithm, which is proposed by Padil et al. [10].

The process of Sequential Floating Search algorithm is summarized as follows.

Input: According to the evaluation function, calculate the evaluation value of each indicator, denoted as $J_k(g)$, here $k = 1, 2, \ldots, \mathrm{m}$, m is the number of indices.
Output: A subset which has the largest evaluation value, denoted as $J(d_k^{\max})$, here k is the total number of selected indices.
Step 1: The two evaluation indices g_i, g_j with the largest values $J_k(g_i), J_k(g_j)$ are retained, and can be grouped as one set, which is denoted as $d_2^{\max}\{g_i, g_j\}$, here $i < m, j < m$, $i \neq j$;

Step 2: If $k = m$, then quit;
Otherwise, the remaining evaluation index set, denoted as $D = D - d_k^{\max}$, are calculated separately according to $J(d_k^{\max} + g)$ to get the largest value, denoted as $J_C(d_{k+1}^{\max})$, here $g \in D$.
Step 3: Searching for a subset which has the largest evaluation value and the number of the subset is k from the subset in Step 2, denoted as $J'(d_k^{\max})$. If $J(d_k^{\max}) \geq J'(d_k^{\max})$, then $k = k + 1$, turn Step 2.

2.2 Evaluation Function

The Bhattacharyya Distance is an evaluation criterion based on probability distance [11]. In a two-class problem, the minimum classification error of the Bayesian classifier in the n-dimensional original space can be represented as follows:

$$\varepsilon_{ij} = P(\omega_i)^{1-s} P(\omega_j)^s \exp[-J_{ij}(s)] \tag{2}$$

Here, the prior probability of class i is denoted as $P(\omega_i)$, and the prior probability of class j is denoted as $P(\omega_j)$.

The definition of Chernoff Distance can be represented as follows:

$$J_{ij} = \frac{s(1-s)}{2}(\mu_i - \mu_j)^T [s\sigma_i + (1-s)\sigma_j]^{-1}(\mu_i - \mu_j) + \frac{1}{2}\ln\frac{|s\sigma_i + (1-s)\sigma_j|}{|\sigma_i|^s |\sigma_j|^{(1-s)}} \tag{3}$$

here s is a parameter between the inter-zone [0, 1]. If $s = 0.5$, Chernoff Distance is called Bhattacharyya Distance, which can be expressed as follows:

$$J_{ij} = \frac{1}{4}\frac{(\mu_i - \mu_j)^2}{(\sigma_i^2 + \sigma_j^2)} + \frac{1}{2}\ln[\frac{\sigma_i + \sigma_j}{2\sqrt{\sigma_i \sigma_j}}] \tag{4}$$

here μ_{i}, μ_{j} are the mean values of class i and class j respectively; σ_i, σ_j are the variances of class i and class j respectively.

3 Power Quality Evaluation Indicators and Division

3.1 Pre-selection of Power Quality Evaluation Indices

Since there is not a unified international standard for comprehensive evaluation of power quality, in this paper, the latest issued Power quality international standards are considered: Voltage Sag, Voltage Deviation, Voltage Fluctuation, Voltage

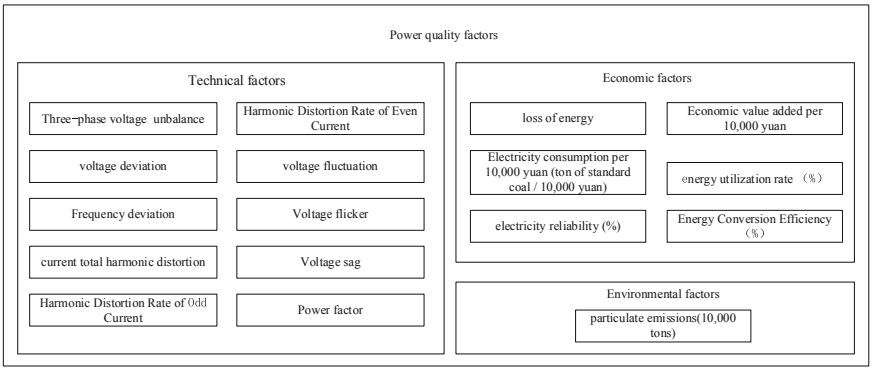

Fig. 1 The preliminary selected indices

Flicker, Harmonics in public supply network, Admissible Three-phase Voltage Unbalance Factor, Permissible deviation of frequency of power system, Power factor, and other seven national standards [12–16]. In addition, the national standards of economy and environmental protection emissions are also considered. A total of 17 candidate factors are initially formulated [17]. Figure 1 shows the candidate power quality evaluation factors.

3.2 Classification of Power Quality Assessment

The comprehensive evaluation level of power quality can be divided into five grades: high quality, good, medium, qualified, and unqualified, which are represented by Q1, Q2, Q3, Q4 and Q5 respectively. Among them, the qualified means that the power quality system is operating normally, and the energy consumption reaches the national standard; and the good means the power quality system not only has low energy consumption but also high productivity. The level limits of each power quality factor are shown in Table 1, and each index is represented by g_i.

4 Application of Sequential Floating Search Method in Power Quality Assessment Index Selection

4.1 Data Generation and Standardization

According to the principle of random distribution, *matlab2018* is used to stimulate 250 samples, and 50 samples in each category, which are represented by $x^*(i,j)$. In this paper, minimization method is used to dimension the power quality factors, as

Table 1 Rating of power quality assessment indicators

Evaluation indicator	Three-phase voltage unbalance (%): g_1	Voltage deviation (%): g_2	Frequency deviation (%): g_3	Current total harmonic distortion (%): g_4	Harmonic distortion rate of odd current (%): g_5
Q_1	≤ 0.5	≤ 1	≤ 0.01	≤ 1	≤ 0.8
Q_2	1	3	0.1	2	1.6
Q_3	2	5	0.2	3	2.4
Q_4	3	7	0.3	4	3.2
Q_5	>3	>7	>0.3	>4	>3.2

Evaluation indicator	Harmonic distortion rate of even current (%): g_6	Voltage fluctuation (%): g_7	Voltage flicker: g_8	Loss of energy (%): g_9	Particulate emissions (10,000 tons): g_{10}
Q_1	≤ 0.4	≤ 0.5	<0.2	≤ 0.1	≤ 10
Q_2	0.8	1	0.5	0.2	15
Q_3	1.2	1.5	0.8	0.3	25
Q_4	1.6	2	1	0.4	50
Q_5	>1.6	>2	>1	>0.4	>50

Evaluation indicator	Electricity consumption per 10,000 yuan (ton of standard coal/10,000 yuan): g_{11}	Voltage sag: g_{12}	Power factor: g_{13}	Electricity reliability (%): g_{14}	Economic value added per 10,000 yuan: g_{15}	Energy utilization rate (%): g_{16}	Energy conversion efficiency (%): g_{17}
Q_1	≤ 1600	≥ 0.9	≥ 0.9	≥ 99.99	≥ 15	≥ 95	≥ 90
Q_2	1850	0.8	0.85	99.96	12	90	80
Q_3	2000	0.5	0.8	99.7	9	85	70
Q_4	2150	0.1	0.75	99.5	6	80	60
Q_5	>2150	<0.1	<0.75	<99.5	<6	<80	<60

each factor may have different dimensions, resulting in a lack of comparability between the factors [18]. For these factors which are the smaller the better, the following formula is used for normalization.

$$x(i,j) = \frac{x_{\max}(j) - x^*(i,j)}{x_{\max}(j) - x_{\min}(j)} \tag{5}$$

For those factors which are the bigger the better, the following formula is used for normalization

$$x(i,j) = \frac{x^*(i,j) - x_{\min}(j)}{x_{\max}(j) - x_{\min}(j)} \tag{6}$$

here, $x(i,j)$ represents new samples, $x_{\max}(j)$ is the maximum value of the j indicator, $x_{\min}(j)$ is the minimum value of j indicator, $x(i,j)$ is the standardization value. For example, the first indicator is divided into the following intervals: $x_1 \leq 0.5$, $0.5 < x_1 \leq 1$, $1 < x_1 \leq 2$, $2 < x_1 \leq 3$, $3 < x_1 \leq 4$, $4 < x_1 \leq 5$, $x_1 > 5$.

4.2 Selection of Feature Subsets of Power Quality Assessment Indices

Sequential Floating Search Method (SFSM) is used to search the feature subset of the power quality factors. Here, the Bhattacharyya Distance is used as its evaluation function. Figure 2 shows the flow chart.

Figure 3 shows that the classification accuracy rate reaches 100% when five power quality indices are selected. The retained power quality assessment indices are: Frequency deviation, Current total harmonic distortion, Voltage flicker, Voltage sag and Electricity reliability.

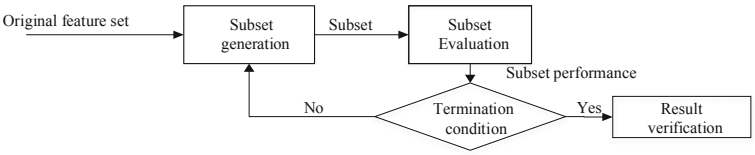

Fig. 2 The flow chart of feature selection

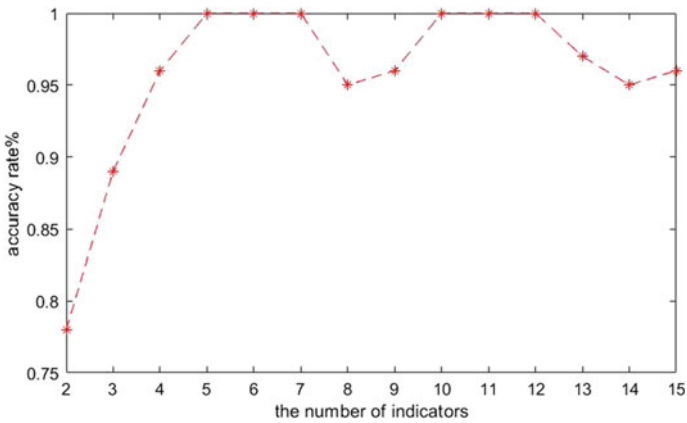

Fig. 3 The number of selected evaluation indicators and the corresponding classification accuracy rate

5 Classifier Verification

5.1 Verification of k-Nearest Neighbors Algorithm

Leave one cross validation (LOOCV) and independent test (IT) are used to assessment validation of the selected factors. In the process of leave one cross evaluation, samples are divided into 250 groups and each group is left as a test sample in experiment. This allows all the 250 samples to be used as training samples and test samples to make full use of the limited information. In the process of independent test, half of the samples is randomly selected as the training set, and the remaining half is used as the test set which can ensure the independence of the training set and the test set, avoiding the "over-fitting" phenomenon.

After K-nearest neighbor classifier verification, five power quality indices are selected, which are Frequency deviation, Current total harmonic distortion, Voltage flicker, Voltage sag, Electricity reliability are selected. These indices have the main effect on power quality level.

Figure 4 shows that the classification accuracy can reach up to 100% when the five evaluation indices are selected. It can conclude that: when the number of selected evaluation indices is small, the classification accuracy is low due to the lack of sufficient classification information; and when the number of evaluation indices is too large, the classification results can be affected by the unrelated evaluation indicators. In practical applications, the number of evaluation indices should be controlled.

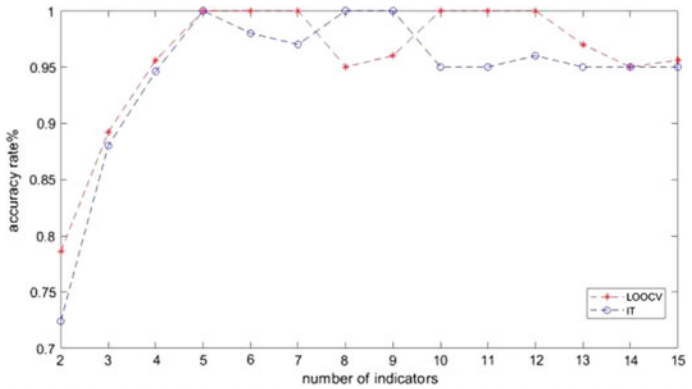

Fig. 4 Classification results of leaving one method and independent set test

Table 2 Validation of five features

SVM		RBFNN		KNN	
LOOCV	IT	LOOCV	IT	LOOCV	IT
95.6%	91.25%	89.3%	85.2%	100%	100%

Table 3 Electric power quality monitoring data of one enterprise in Jiangsu province

Evaluation indicator	g_1	g_2	g_3	g_4	g_5	g_6	g_7	g_8	g_9
Test data	1.8	1.9	0.1	2.6	1.4	0.88	1.33	0.47	0.23
Evaluation indicator	g_{10}	g_{11}	g_{12}	g_{13}	g_{14}	g_{15}	g_{16}	g_{17}	
Test data	14	1850	79.7	0.88	99.9	13	75	78	

5.2 *Verification and Comparison of Other Classifiers*

Support vector machine SVM and radial basis neural network RBFNN are used to validate the selected five power quality factors. The results are listed in Table 2.

5.3 *Application of Sequential Floating Search Method in Comprehensive Evaluation of Enterprise Power Quality Data*

We select the measured data of an industrial enterprise in Jiangsu, and evaluate the power quality of the enterprise. The data of each indicator are listed in Table 3.

Using the method proposed in this paper, the power quality level of the enterprise is good. The result shows that the company still has a certain energy-saving transformation space.

6 Conclusions

This paper focuses on selecting the power quality assessment indicators by using Sequential Floating Search algorithm to find the most effective set of power quality assessment indices. Bhattacharyya Distance is used as the evaluation function in Sequential Floating Search algorithm. This method is suitable for evaluation problem which has a large scale of factors. The sample identification experiment of the five power quality factors selected by the method in this paper has achieved a

high classification accuracy rate, indicating that this group of factors contains complete classification information. The method proposed in this paper provides reference and guidance for the study of selecting power factors in power quality assessment.

References

1. Tao S, Xu Y, Qi L (2015) Modern power quality measurement technology. China Electric Power Press
2. Wu X, Xing Q, Qu H et al (2017) Application of CEEMD in power quality disturbance detection. Power Syst Prot Control 45(3):48–55
3. Gong G, Chen Z, Lu J et al (2018) Clustering optimization strategy for electricity consumption behavior analysis in smart grid. Autom Electr Power Syst 42(2):58–63. https://doi.org/10.7500/aeps20170726009
4. Dai Y, Gao H, Gao Y et al (2018) Real-time pricing mechanism in smart grid with forecasting update of power demand. Autom Electr Power Syst 42(12):58–63. https://doi.org/10.7500/aeps20170614008
5. Wang Y, Tang W, Liu L et al (2015) Construction and application of power grid operation risk assessment and rating system. Autom Electr Power Syst 39(8):141–148. https://doi.org/10.7500/aeps20140702007
6. Wang J, Pang W (2017) Application of fisher discriminant classification in steady-state power quality assessment of photovoltaic grid-connected system. Electr Power Autom Equip 37 (3):50–54
7. Zhao X, Zhao C, Jia X et al (2005) Fuzzy synthetic evaluation of power quality based on changeable weight. Power Syst Technol 29(6):11–16
8. Tang H, Peng J (2003) Research on synthetic and quantificated appraisal index of power quality based on fuzzy theory. Power Syst Technol 27(12):85–88
9. Hui J, Jianchun P, Yaping O et al (2003) Power quality unitary quantification and evaluation based on probability and vector algebra. J Hunan Univ Nat Sci 30(1):66–70
10. Padil P, Novovicova J, Kittler J (1994) Floating search method in feature selection. Pattern Recogn Lett 15(11):1119–1125
11. Duda OR, Hart PE, Stork GD (2001) Pattern classification, 2nd edn. Wiley, New York, pp 46–48
12. Pan Y, Zhu W, Liu X et al (2008) Power quality power system frequency deviation GB/T 15945 - 2008. China National Standardization Administration Committee, Beijing
13. Qu T, Ren Y, Lin H et al (1993) Power quality utility grid harmonics GB/T14549 - 93. State Bureau of Technical Supervision, Beijing
14. Zhao G, Mei G, Liu X et al (2008) Power quality voltage fluctuations and flicker GB/T12326 - 2008. China National Standardization Administration, Beijing
15. Zhou S, Yu K, Tan Z et al (2008) Power quality supply voltage deviation GB/T 12325 - 2008. China National Standardization Administration Committee, Beijing
16. Jing D, Gu W, Zeng Y et al (2008) Power quality three-phase voltage imbalance GB/T 15543 - 2008. China National Standardization Administration Committee, Beijing
17. Ma L, Zhu R, Zhou X et al (2016) Energy efficiency evaluation and grading new method for high power consumption system. Control Eng 23(9):1375–1379
18. Zeng Z, Yang H, Zhao R (2011) Comprehensive evaluation of power quality in distributed generation system based on catastrophic decision making. Autom Electr Power Syst 35 (21):52–57

Key Constraint Variable Identification, Transient Stability Assessment and Feasible Region Generation of Power Grid Operation Based on Machine Learning Method

Binjiang Hu, Qi Guo and Yihua Zhu

Abstract The existing machine learning methods for the decision-making of power grid operation lack sufficient interpretability and focus on transient stability assessment. In response to this deficiency, this paper analyzed the process of humankind learning and decision-making in the field of power grid operation. To further speed up the decision making process, a model which combines correlation analysis, deep learning and decision tree used for key constraint variable identification, transient stability assessment and feasible region generation is proposed. This model is able to take advantage of feature extraction and fitting effect of deep learning, good interpretability of correlation analysis and decision tree. Experiment results on a subsystem in China Southern Power Grid demonstrate the feasibility and effectiveness of the model.

Keywords Power grid operation · Deep learning · Transient stability assessment

1 Introduction

With the rapid development of China's economy, the demand for electricity is increasing rapidly. At the same time, with the deep reform of the power market [1], the fast and accurate change of power grid operation mode becomes more and more important. For a long time, a lot of time domain simulation is carried out by experts to find out weak points of the power grid and formulate preventive measures [2]. When the system is small, the above-mentioned processing method that relies on the analysis and calculation of experts can satisfy the demand to the power system security and

B. Hu (✉) · Q. Guo · Y. Zhu
State Key Laboratory of HVDC, Electric Power Research Institute, CSG, Guangzhou 510663, China
e-mail: hubj@csg.cn

CSG Key Laboratory of Power System Simulation, Guangzhou 510663, China

Y. Xue et al. (eds.), *Proceedings of PURPLE MOUNTAIN FORUM 2019-International Forum on Smart Grid Protection and Control*, Lecture Notes in Electrical Engineering 585, https://doi.org/10.1007/978-981-13-9783-7_49

stability. However, when the power system is large, the above manual method is difficult to quickly predict whether the power system is stable and make decisions.

Experienced personnel can predict whether a power system is stable, which stem from their learning and accumulation from past experience. This learning and decision-making process of humankind can be done in artificial intelligence. In the past two decades, machine learning method have been used in power system transient stability assessment, but the algorithms are limited to artificial neural networks (ANN) [3], bayesian classifier [4], decision tree (DT) [5], support vector machine (SVM) [6] and other shallow learning methods. Due to the ability of shallow learning methods for input features, the generalization ability is limited when solving complex classification problems [7].

In recent years, the leap-forward development of deep learning has provided a new idea for power system transient stability assessment [8, 9], which builds multiple hidden layer neural network models for feature extraction and classification. Deep learning has achieved very good results in frontier fields such as image recognition and natural language processing [10]. Some researchers have introduced deep learning into the power system transient stability assessment [11, 12]. Deep learning has high evaluation accuracy and good generalization ability. However, the results given by deep learning are poorly interpretable and deep learning cannot reveal the weak points of the power system. This paper presents a model that combines correlation analysis, deep learning and decision tree used for power grid operation decision-making process which contains key constraint variables identification, transient stability assessment and feasible region.

2 Power Grid Operation Learning and Decision Model

2.1 Traditional Power Grid Operation Decision-Making

In traditional power grid operation decision-making process, see Fig. 1. The first step is to identify the key constraint variables in a specific power grid operation mode according to the experience of the expert experience, such as the transmission power limit, and then to adjust the key constraint variables. The second step, time domain simulation software, such as PSD-BPA, PSSE, etc. is used to perform the transient stability assessment. Then go back to step 1 until the feasible region of the power system is formed according to the simulation result, such as the generator power limit, the transmission power limit, etc.

When there are enough simulation samples to cover various possible modes of power grid operation, deep neural networks can be used to map the relationship between input features and transient stability. Many researchers have done a lot of work on the transient stability assessment using deep or shadow learning method. This paper presents a combined model for the entire power grid operation decision-making process.

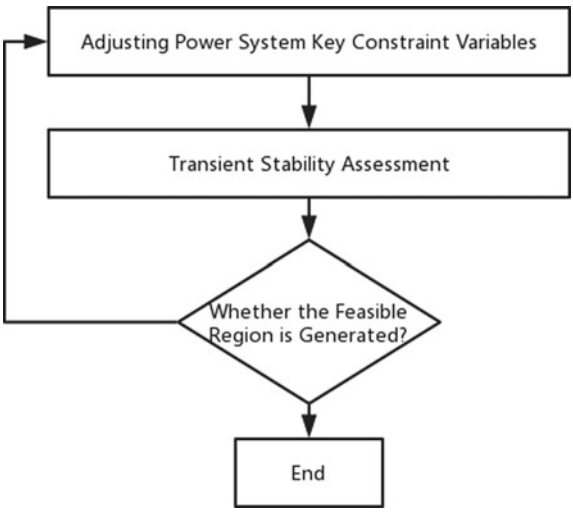

Fig. 1 Traditional power grid operation decision-making process

2.2 Key Constraint Variable Identification Model

In the transient stability assessment of the power system, there are many factors affecting the stability of the system. For a long time, combination of expert experience and a large number of stability calculations is used to find out the weak points of the power system. When the power system scale is small, this expert method is very effective, when the power system is large and needs to make quick decisions, this expert method is difficult to quickly analyze the power system. This paper will combine the correlation analysis algorithm in big data mining technology to quickly mine the key constraint variables that affect the stability of the power system.

Among the input features, the transmission line power, bus voltage and generator power are continuous variables. In the classification algorithm, the feature of the sample need to be discretized [13], which can effectively reduce the complexity of the learning algorithm and accelerate learning speed, and also simplify and generalize the acquired knowledge and improve the comprehensibility of the classification results. In this paper, the entropy-based continuous attribute discretization algorithm introduced in paper [14] is used. The chi-square test is a widely used hypothesis test method [15], which can be used for the correlation analysis of two categorical variables. The chi-square test is used to mine the key constraint variables that affect the stability of the power system.

2.3 Transient Stability Assessment Deep Neural Networks Model (DNN)

Feature selection and extraction. In the design of general artificial intelligence transient stability model, there are generally three ideas for the selection of input features [16, 17]: (1) Dynamic variables after disturbance, such as the rotor angle of the generator; (2) Steady-state variables before disturbance, such as generator power, branch current, load; (3) Steady-state and dynamic information. This model aims to predict whether the test system is stable without time domain simulation, the second idea is chosen in this paper.

Sample generation. (1) In order to construct a relatively complete sample space, different power system operation modes are formed by dynamically adjusting the load and generator power. (2) For different power system operating mode data, simulations were done by using the PSD-BPA software considering N-1 fault. if the relative rotor angles of the generators go out of step after a fault, this test system is considered unstable. (3) For the time domain simulation of PSD-BPA software, transmission line power, bus voltage and generator power are used as input features.

Model training. Since the power system is a nonlinear system and the deep neural network has a good fitting ability to nonlinear systems, this paper uses a deep neural network to classify samples of different input features. In order to determine the hyperparameters, this paper trains the DNN model using different number of neural network layers and different number of neurons in each layer.

Model evaluation. This paper takes 80% of the sample set as the training set, and the remaining 20% as the test set, and evaluates the generalization performance of deep learning through the accuracy of the training set and test set (Fig. 2).

2.4 Power System Feasible Region Generation Based on Decision Tree

Feasible region generation. Decision tree is constructed from a training set of samples in which each sample in the training set consists of an input vector and its correct classification. The diagram of a decision tree is an upside-down tree like a flow chart (Fig. 3). The decision-making process of a decision tree is a series of tests. The test is whether a particular element of the input vector exceeds a threshold. After training, the relationship between the input vector of all the stable samples and their threshold will determine the power system feasible region.

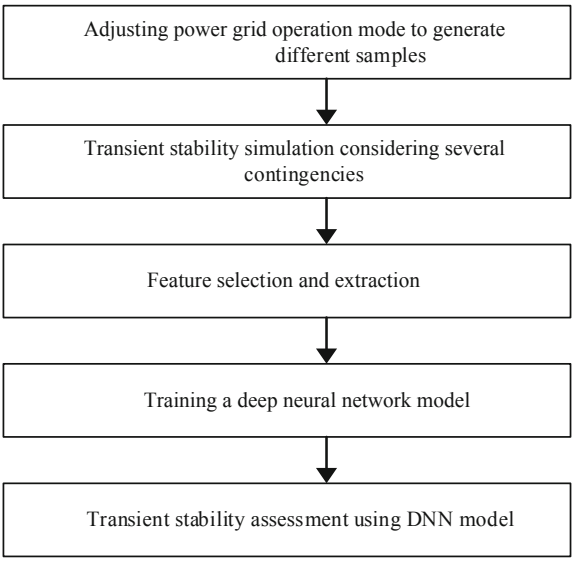

Fig. 2 Design implementation of DNN for TSA

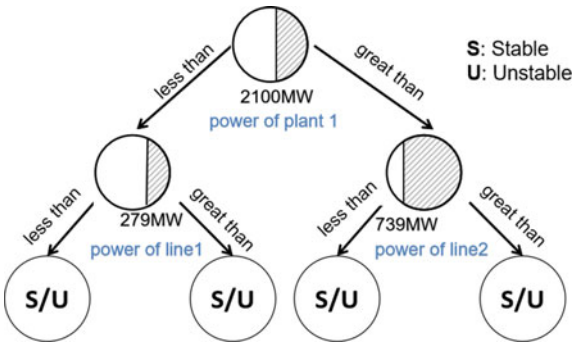

Fig. 3 Feasible region generation process of decision tree

3 Case Study

3.1 Design of Software and Hardware Framework

In order to improve the speed of sample generation and deep learning model training speed, this paper designs and builds a big data artificial intelligence software and hardware platform. The platform consists of five Dawning high-performance computing workstations, each with two Intel E5 2643 v4 processors, 128 GB RAM and 2T Intel SSD, one of which contains five NVIDIA Tesla P100 GPUs for model training. Hadoop HDFS and Apache Spark were installed to connect five workstations as a distributed file system and compute cluster. The PSD-BPA program is deployed on each workstation. The deep learning model is built using Keras whose back end is TensofFlow.

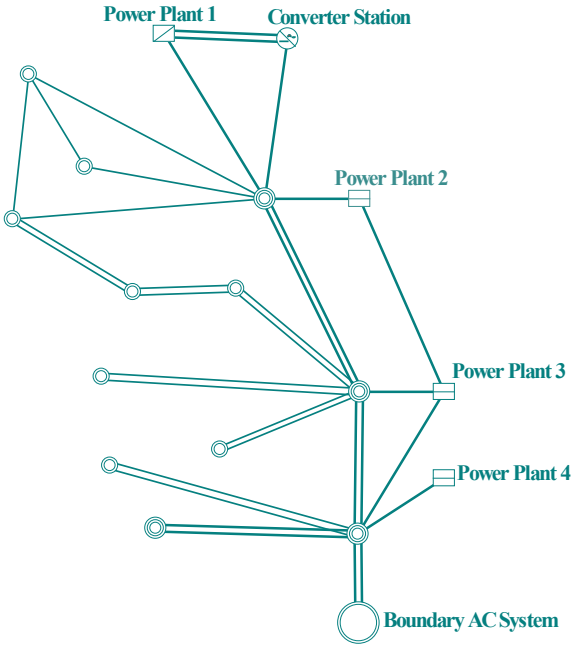

Fig. 4 One-line diagram of the partial test system

3.2 Test System

Figure 4 show the subsystem of the whole test system used for this paper. The whole system consists of 3,076,220 kV buses. The partial system consists of 9500 kV substations, 15,500 kV AC lines, and 8220 kV substations, 17,220 kV AC lines. The power plant 2, the power plant 3 and the power plant 4 unit are out of service. The generator power and the load are changed to generate 16,000 power grid operation samples. Three-phase grounding short circuit (N-1 or N-2) is said to occur at the busbar, the simulation time is 20 s. If the relative rotor angles of any two generators exceeds 360°, the system is considered unstable.

3.3 Result Analysis

Key constraint variables identification. After discretization of plant power, transmission line active power and bus voltage, the chi-square test is used for correlation analysis. The analysis results show that the stability of the test system is highly correlated with the red power plant and red transmission line which are shown in Fig. 5. Since the power plant 2, the power plant 3 and the power plant 4 are out of service, the transient stability of the test system is mainly affected by the power transmission channel of the power plant 1. The key constraint variables found by the correlation analysis are reasonable.

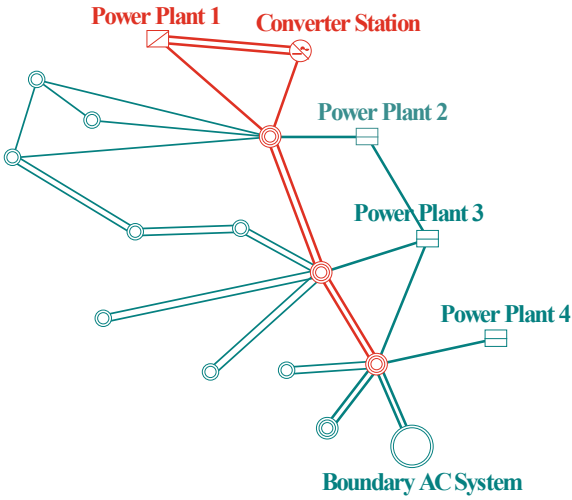

Fig. 5 Key constrained variables of the test system

The influence of the number of neurons per layer on the DNN. By setting the same number of neural network layers and training the same model with CPU and GPU, the simulation results show that: (1) When the number of neurons in each layer increases, the accuracy of the training set and the test set does not decrease significantly; (2) Training the same DNN with CPU or GPU does not affect the training and test accuracy; (3) When the number of single-layer neurons is small, the GPU acceleration performance is not obvious, and the time for GPU training is longer than the CPU training time (Table 1).

Table 1 DNN evaluation performance of different neuron numbers per layer

CPU/GPU	DNN configuration	Training time	Training set accuracy (%)	Test set accuracy (%)
CPU	10 layers × 10 neurons	4 s	94.8	98.7
GPU	10 layers × 10 neurons	28 s	96.1	96.9
CPU	10 layers × 100 neurons	7 s	98.4	97.2
GPU	10 layers × 100 neurons	28 s	98.3	98.9
CPU	10 layers × 1000 neurons	3 min 43 s	98.6	96.8
GPU	10 layers × 1000 neurons	28 s	98.5	96.2
CPU	10 layers × 10,000 neurons	4 h 20 min	98.3	98.2
GPU	10 layers × 10,000 neurons	8 min 26 s	98.2	98.8

Table 2 DNN error analysis

Sample No.	Stable/Unstable	Power of plant 1 (MW)	DNN prediction results
177	Stable	678	Correct
178	Stable	679	Correct
179	Unstable	680	Incorrect
180	Stable	681	Correct
181	Stable	682	Correct
182	Unstable	684	Incorrect
183	Unstable	685	Correct
184	Stable	686	Incorrect
185	Unstable	690	Correct
186	Unstable	691	Correct
187	Unstable	692	Correct

DNN error analysis. By analyzing the error of the DNN model, the incorrect predictions, such as the misclassification samples with sample number 179, 182, and 184, of the DNN model are mainly distributed in the stable and unstable transition interval of the test system. As the power of the plant 1 increases, the test system become unstable, but there is no boundary that divides the test into stability and instability (Table 2).

Power system feasible region generation analysis. Figure 6 shows the decision-making process in which X is the input feature vector. X[0], …, X [12] is the active power of 13,500 kV transmission lines. X[13] is the total power of plant 1. Number 1 and number 2 in formula value = [number 1, number 2] represent the number of unstable samples and the number of stable samples. The threshold in each decision node is the per unit value where the base value is 100 MW. When all stable samples are counted, we can get the power system feasible region. For example, $X[3] \leq 7.249$, $X[1] \leq 3.003$, $X[9] > 7.398$, $X[6] > 5.332$, $X[8] \leq 7.47$, this set of constraints is part feasible region.

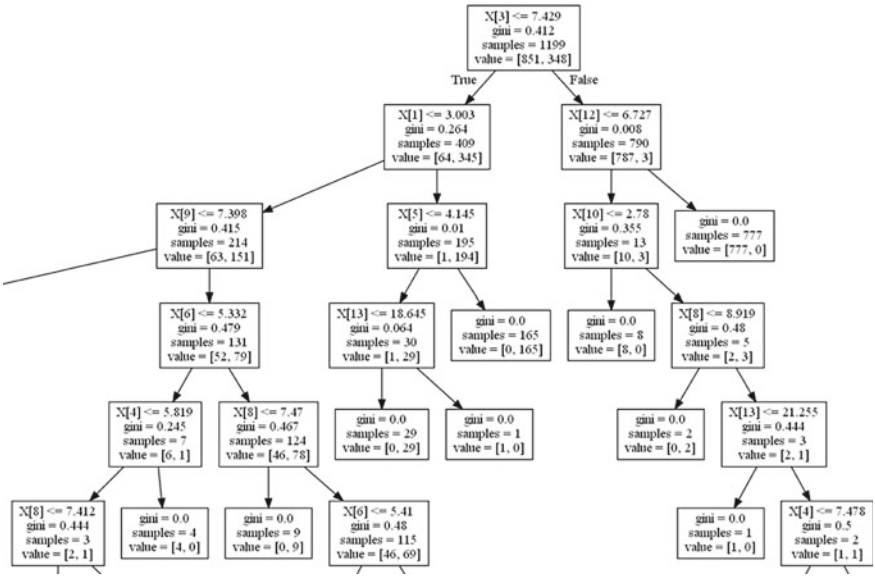

Fig. 6 Power system feasible region generation process by decision tree

4 Conclusion

Considering the decision-making process of power grid operation, a model that combines correlation analysis, deep learning and decision tree is presented in this paper. The proposed model is examined on a subsystem in China Southern Power Grid. The key constraint variables found by the correlation analysis are reasonable. The accuracy of the deep neural network is very high in the stable/unstable classification problem. Power system feasible region generation by decision tree is practical.

The sample generation algorithm used in this paper is a kind of simple but time consuming method. This method is not suit for large systems with more variables. Reinforcement learning algorithm used in Alpha Zero is a promising algorithm which can be used to solve the curse of dimensionality in large systems. The next step is to introduce reinforcement learning into the proposed model.

References

1. Pang Y (2018) The effect evaluation of competitive reform in China's electric power industry. Shandong University
2. Yu Z, Huang Y, Lu G (2015) A time series associative classification method for the operation rule extracting of transient stability. Proc CSEE 35(03):519–526

3. Gu X, Cao S, Zhang W (2000) A new framework for transient stability assessment based on neural networks. Proc CSEE 20(4):77–82
4. Lu J, Zhu Y, Zhao H, Liu Y (2009) Power system transient stability assessment based on boosting bayesian classifier. Trans China Electrotech Soc 24(05):177–182
5. Sun K, Likhate S, Vittal V et al (2007) An online dynamic security assessment scheme using phasor measurements and decision trees. IEEE Trans Power Syst 22(4):1935–1943
6. Ye S, Wang X, Liu Z, Qian Q (2011) Power system transient stability assessment based on support vector machine incremental learning. Autom Electr Power Syst 35(11):15–19
7. Bengio Y (2009) Learning deep architectures for AI. Found Trends® Mach Learn 2(1):1–127
8. LeCun Y, Bengio Y, Hinton G (2015) Deep learning. Nature 521(7553):436–444
9. Krizhevsky A, Sutskever I, Hinton GE (2012) Imagenet classification with deep convolutional neural networks. In: Advances in neural information processing systems. Curran Associates, Inc. Lake Tahoe, pp 1097–1105
10. Tan B, Yang J, Lai Q et al (2019) Data augment method for power system transient stability assessment based on improved conditional generative adversarial network. Autom Electr Power Syst 43(1):149–157
11. Zhu Q, Dang J, Chen J, Xu Y, Li Y, Duan X (2018) A method for power system transient stability assessment based on deep belief networks. Proc CSEE 38(03):735–743
12. Hu W, Zheng L, Min Y, Dong Y, Yu R, Wang L (2017) Research on power system transient stability assessment based on deep learning of big data technique. Power Syst Technol 41 (10):3140–3146
13. Dougherty J, Kohavi R, Sahami M (1995) Supervised and unsupervised discretization of continuous features. In: Machine learning proceedings. Morgan Kaufmann, Tahoe City, pp 194–202
14. He Y, Zheng J, Zhu L (2005) An entropy-based algorithm for discretization of continuous variables. Comput Appl 25(03):637–638
15. McHugh ML (2013) The chi-square test of independence. Biochem Med Biochem Med 23 (2):143–149
16. Wang T, Guan L, Zhang Y (2009) A survey on application of artificial intelligence technology in power system stability assessment. Power Syst Technol 33(12):60–65 + 71
17. Xue Y, Huang T, Chen G et al (2019) Review on case filtering in transient stability analysis. Autom Electr Power Syst 43(6):1–14

Spatial-Temporal Distribution and Impact Factors Analysis of Cloud-to-Ground Lightning Activity in Hubei China

Tian Hao, Fan Pen, Feng Wanxing, Wang Haitao and Li Jian

Abstract The cloud-to-ground lightning is a serious weather disaster, which has great harm to human security and fundamental construction. This paper explores the spatial-temporal distribution of cloud-to-ground lightning at Hubei Province in 2015. We firstly compute the Moran's index and the local Moran's index of the cloud-to-ground lightning density in each month. The distribution of the occurrence count, density and Moran's indexes is a parabola, and the peak locates in April and May of 2015. Then, we test the Moran's index results by *p*-value. The analysis shows that about 10% cloud-to-ground lightning region is clustered. Finally, we observed the probability of the lightning density is Quasi-Poisson distribution and fit the lightning density by General Additive Model (GAM). The experiment indicates precipitation, terrain roughness, altitude can be used for effectively predicting the ground lightning density level.

Keywords Cloud-to-ground lightning · Spatial-temporal analysis · Local Moran's index · GAM

1 Introduction

Lightning is a severe atmospheric phenomenon. Typically, more than 2000 thunderstorms are active throughout the world at given moment, producing one the order of 100 flashes per second [1]. Deaths and injuries to livestock and other animals, thousands of forest and brush fires, and millions of dollars in damage to buildings, communications systems, power lines, and electrical systems are also the result of lightning [2–4]. Therefore, the knowledge with the distribution

T. Hao (✉) · F. Pen · F. Wanxing · W. Haitao · L. Jian
NARI Group Corporation (State Grid Electric Power Research Institute), Nanjing, China
e-mail: tianhao@sgepri.sgcc.com.cn

Wuhan NARI Co., Ltd., State Grid Electric Power Research Institute, Wuhan, China

Hubei Key Laboratory of Power Grid Lightning Risk Prevention, Wuhan, China

Y. Xue et al. (eds.), *Proceedings of PURPLE MOUNTAIN FORUM 2019-International Forum on Smart Grid Protection and Control*, Lecture Notes in Electrical Engineering 585, https://doi.org/10.1007/978-981-13-9783-7_50

characteristics and impact factors of cloud-to-ground lightning is the important information to power lines selection, power lines safety and thunderstorm warning [5–7] etc.

Thunderstorms as atmospheric phenomena, characterized by both convective rainfall and lightning activity, result from physically related processes [8]. There are other researchers have studied the relationships between meteorological factors with lightning frequency and intensity [9–12]. Furthermore, Sokol et al. [13] indicated the lightning density with soil type, the positive relationship in all land classes except unsolidate shore. Royé et al. [1] observed that the probability of lightning density is Quasi-Poisson, and fitting the lightning density by GAM.

Spatial analysis refers to a series of theories and techniques for analyzing, simulating, predicting, and regulating spatial processes [14]. The purpose of this paper is to analyze the spatial and temporal distribution characteristics of the cloud-to-ground lightning in Hubei Province in 2015 and its relationship with topographic elements. The research process is as follows: Firstly, we analyzed characteristics and the spatio-temporal distribution of the cloud-to-ground lightning data in Hubei Province in 2015. The Moran's Index and local Moran's Index is used to indicated the spatial autocorrelation of the cloud-to-ground lightning data. Secondly, the corresponding factor indicators were calculated based on the existing topographic data, such as terrain slope, aspect, altitude, land cover etc. Finally, the selected factors and the cloud-to-ground lightning density were analyzed by GAM model, and the correlation between the factor and the cloud-to-ground lightning density was determined quantitatively.

2 Dataset and Methodology

In this study, the research data has three categories: cloud-to-ground lightning data, terrain data. The cloud-to-ground lightning data is the annual lightning of Hubei Province in 2015. The main parameters of the cloud-to-ground lightning data are position, time, polarity, current intensity and number of hits, etc. The terrain data is the elevation data of STRM-90m. Derived a series of topographic correlation factors based on elevation data, including slope, aspect, elevation coefficient of variation, slope coefficient of variation, section curvature, plane curvature and full cumulative curvature.

2.1 Datasets

The description of cloud-to-ground lightning data, terrain data is following:

Table 1 The description of the topographic factors

Factor name	Descriptions
Slope	Characterize the extent to which surface units are steep
Aspect	The angle between the projection of the slope normal at the horizontal plane and the true north direction
Elevation coefficient of variation	Ratio of elevation standard deviation to mean within a certain range
Slope coefficient of variation	Ratio of slope standard deviation to mean within a certain range
Section curvature	The second derivative of the surface elevation value
Plane curvature	The curvature perpendicular to the direction of the maximum slope
Full cumulative curvature	Product of plane curvature and slope curvature

(1) **Cloud-to-ground Lightning Data**
The study used the 2015 year-round cloud-to-ground lightning data of Hubei Province as the experimental object. The properties of the lightning data mainly include: lightning occurrence position (longitude and latitude), time, polarity (positive and negative), current intensity and number of hits, etc. This paper quantitatively analyzes the relevant parameters of the frequency, positive and negative proportions intensity, cloud-to-ground lightning density and grade distribution of flashes. The lightning density refers to the number of lightning per unit area, which can better reflect the strength of lightning activity and characterize the frequency of flash discharge, as a dependent variable indicator.

(2) **Geographic factors**
Terrain analysis is an important technique of understanding the terrain environment. Its main task is to extract factors represented the topography and find out the spatial distribution characteristics of the topography. The topographic factors usually include: slope, aspect, elevation coefficient of variation, slope coefficient of variation, section curvature, plane curvature and full cumulative curvature, etc. The description of the various topographic factors is shown in Table 1.

2.2 Exploratory Spatial Data Analysis Method

Spatial autocorrelation analysis is a spatial analysis method to reveal the spatial distribution characteristics of variables with their neighborhood effects. Generally, the closer the distance is the greater the correlation between the attributes. The spatial autocorrelation is categorized into two classes with global and local spatial autocorrelation [14].

The range of the global Moran's index is from −1 to 1. A positive value indicates a positive spatial correlation; otherwise a negative correlation. The zero value indicates that the spatial value of the attribute has no spatial correlation and is the spatial random distribution. In this study, the global Moran's index of the cloud-to-ground lightning density is calculated to estimate whether the spatial distribution of the ground flash density is randomly distributed or not.

Compared with the global spatial autocorrelation analysis, the local spatial autocorrelation analysis can detect the local spatial distribution and the correlation level of the neighborhood more finely. Local spatial autocorrelation analysis methods usually use local Moran's index statistics (LISA), G statistics, and Moran scatter plots to represent it. The formulation of local Moran's index [14] as following is:

$$I_i = (y_i - \bar{y}) \sum_{j=1}^{n} w_{ij}(y_j - \bar{y})/S^2 \tag{1}$$

where S^2 is the discrete variance of a property and $\bar{y}$ is the mean of y_i; w_{ij} is the weight matrix. Assuming that the properties of the spatial phenomenon are spatial random distribution, the expected and variance of the local Moran's index are:

$$E(I_i) = -\sum_{j=1}^{n} w_{ij}/(n-1) \tag{2}$$

$$\begin{aligned} V(I_i) = {} & (n - b_2) \sum_{j=1, j\neq i}^{n} w_{ij}/(n-1) \\ & + (2b_2 - n) \sum_{k=1, k\neq i}^{n} w_{ik} \sum_{h=1, h\neq i}^{n} w_{ih}/((n-1)(n-2)) - [E(I_0)]^2 \end{aligned} \tag{3}$$

$$b_2 = \sum_{j=1}^{n} (y_j - \bar{y})^4 / \left(\sum_{j=1}^{n} (y_j - \bar{y})^2 \right)^2 \tag{4}$$

From the *Local Moran's Index* and *z-score* can be concluded that the value of the attribute of the spatial phenomenon plays a role in the aggregated or dispersed distribution state of the global spatial attribute. That is, whether there is the spatial distribution of high-high, high-low, low-high and low-low.

2.3 Generalized Additive Model

The Generalized Additive Model (GAM) is a combination of a generalized linear model and an additive model. GAM is commonly used to analyze the relationship between response and explanatory variable on the nonlinear and non-monotonic condition. Therefore, it has been widely used to deal with complex nonlinear air pollution problems. GAM is a non-parametric expansion of a generalized linear model. The smooth spline function is used to analyze the nonlinear relationship between the explanatory variable and the response variable. When the degree of freedom of the spline function is one, the nonlinear relationship becomes a linear relationship. The GAM function is constructed in the mgcv package of the R language. The GAM equation is:

$$g(\mu_i)\, X_i\theta + f_1(x_{1i}) + f_2(x_{2i}) + \cdots + f_j(x_{ji}) + \varepsilon_i, \quad i = 1 \ldots n \tag{5}$$

where i is the ith day, n is the number of days observed, j is the number of influence factors; μ_i is the expected value of the corresponding variable, $g(\mu_i)$ is the connection function; f_j is the smooth function of the influence factor, x_{ji} representing the complex relationship between the cloud-to-ground lightning density and the influence factor; $X_i\theta$ represents the full parameter model component; ε_i represents the residual.

3 Experiments and Results

3.1 Study Area

Hubei Province lies in the middle reach of the Yangtze River with an area of 186,000 km^2. Situated 108′ 21″–116′ 07″ east longitude and 29′ 05″–33′ 20″ north latitude, it got its name from being in the north of the Dongting Lake. The terrain of Hubei Province is high in the west and low in the east and wide open to the south, the Jianghan Plain. Hubei has a sub-tropical monsoonal climate, with a mean annual temperature of 15–17 °C—the hottest month, July, averaging 27–30 °C and the coldest month, January, 1–5 °C—and a mean annual precipitation of 800–1600 mm [15].

The terrain of Hubei Province is roughly surrounded by mountains on the east, west and north, with a low level in the middle and a slightly incomplete basin open to the south. Among the total area of the province, the mountainous area accounts for 56%, the hills account for 24%, and the plain lake area accounts for 20%, belonging to the Yangtze River system. Figure 1 is the topographic map of Hubei Province.

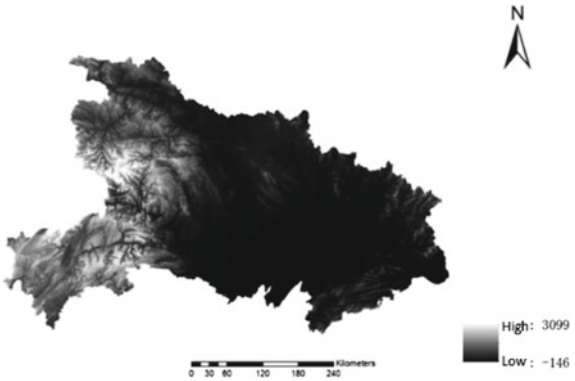

Fig. 1 The topographic map of Hubei Province, China

3.2 Spatial-Temporal Distribution of CG Lightning Activity

In 2015 year, the Moran's index of cloud-to-ground lightning density is 0.671355. That indicates that the lightning density is medium autocorrelation, moreover the most of region is high-high correlation. This shows that the height of the cloud-to-ground lightning has a certain spatial distribution. Figure 2b is a scatter plot and importance map of the spatial autocorrelation of the cloud-to-ground lightning density.

3.3 GAM Results

The histogram of cloud-to-ground lightning density in 2015 year shows Poisson distribution. And the GAM fitting result shows lightning density is positively correlated with terrain roughness, altitude. The aspect and slope of terrain is almost no correlation. The result is in Figs. 3 and 4.

4 Conclusions

We analyzed the spatial-temporal distribution and the relationship between the cloud-to-ground lightning density and terrain factors in 2015 year, and get the following conclusions. (1) The occurrence of cloud-to-ground lightning in Hubei Province showed significant clustering in time. In 2015, about 93% of the

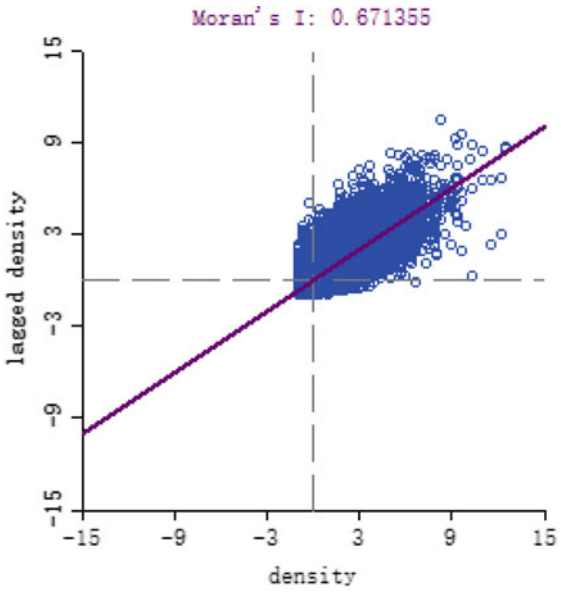

(a) Moran's index scatter plot

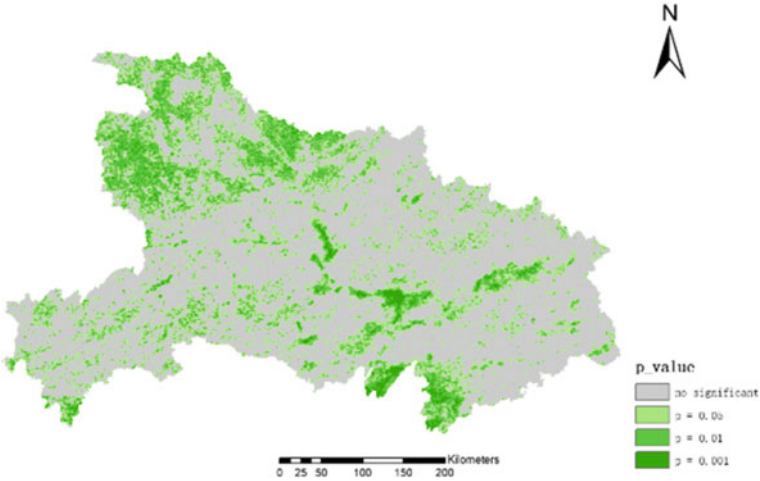

(b) The distribution of ground lightning density

Fig. 2 Moran's index scatter plot and distribution of ground lightning density at Hubei Province in 2015

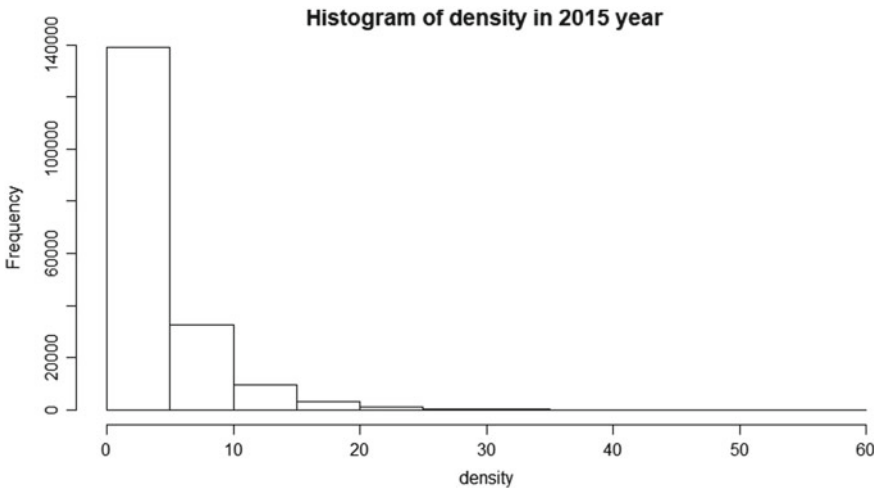

Fig. 3 The probability distribution of lightning density

cloud-to-ground density in Hubei Province occurred in spring and summer, which was significantly related to the climate characteristics of Hubei Province. Hubei shows the climatic characteristics of the transition from subtropical to warm temperate zone. When spring and summer alternate, it is the active season of plum rain. The rain is abundant, the air humidity is high, and it is easy to have rainy weather, which provides natural soil for the occurrence of ground flash. (2) The number of monthly occurrences of the cloud-to-ground lightning data and the monthly line density maps are parabolic in shape and peak in April–May, showing a decreasing trend in the previous and subsequent months. (3) The Moran's index of the annual flash density of Hubei Province in 2015 was 0.671355. The overall performance showed a certain clustering of the occurrence of ground flash, and the area of $P < 0.05$ accounted for 10% of the whole area of Hubei. This shows that in Hubei as a whole. In the region, about 10% of the regions are more likely to concentrate on the cloud-to-ground lightning. (4) The histogram of the lightning density shows a Poisson distribution. (5) Using GAM to fit the relationship between topographic factor and cloud-to-ground lightning density, indicating that the terrain roughness, attitude and water body distance have a certain degree of correlation. Joint analysis of the relationship between meteorological, topographic factors and the occurrence of cloud-to-ground lightning will be the focus of future research.

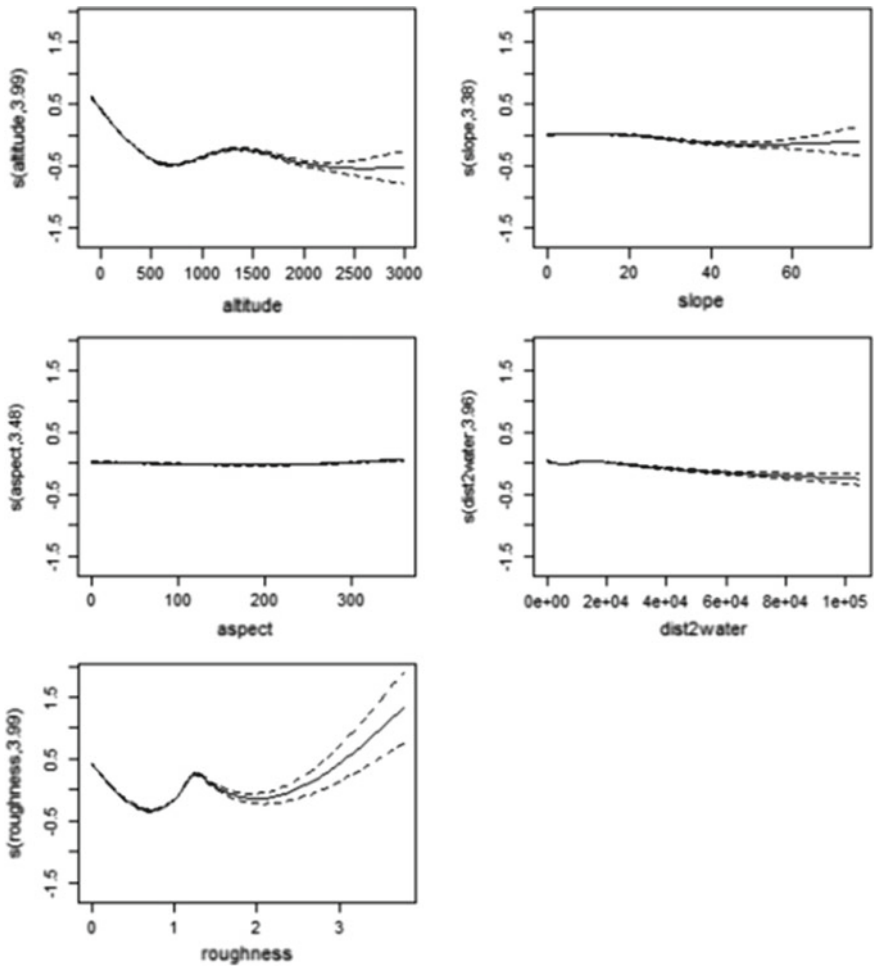

Fig. 4 The GAM fitting result between lightning density and attitude, slope, aspect, distance to water and roughness

Acknowledgements This work was supported by National Natural Science Foundation (51777037) and Science and Technology Guide Project of SGCC (524625170011). The authors are also thankful to the anonymous reviewers and editor for the critical and valuable comments.

References

1. Royé D, Lorenzo N, Martin-Vide J (2016) Spatial–temporal patterns of cloud-to-ground lightning over the northwest Iberian Peninsula during the period 2010–2015. Nat Hazards 92 (2):857–884
2. Kornei K (2018) Australian state forecasts deadly thunderstorm asthma. Science 359 (6374):380
3. Poelman DRA (2014) 10-year study on the characteristics of thunderstorms in Belgium based on cloud-to-ground lightning data. Mon Weather Rev 142:4839–4849
4. Ashley WS, Gilson CW (2009) A reassessment of US lightning mortality. BAMS 90: 1502–1518
5. Ge R, Chen LX, Wang YY (2017) Optimization and design of construction route for electricity market in China. Autom Electr Power Syst 41(24):10–15
6. Zhou TJ, Lu JZ, Wu CP (2018) Distribution characteristics of wildfire warning risk and fault interval for human power grid. Autom Electr Power Syst 42(10):135–142
7. Huang Y, Wei RZ, Zhou EZ (2018) Early warning method of transmission line damage under typhoon disaster. Autom Electr Power Syst 42(23):142–150
8. Soula S (2009) Lightning: principles, instruments and applications review of modern lightning research. Chap lightning and precipitation. Springer, Berlin, pp 447–463
9. Altaratz O, Kucienska B, Kostinski A (2017) Global association of aerosol with flash density of intense lightning. Environ Res Lett 12(11):114037
10. Guo J, Deng M, Lee SS (2016) Delaying precipitation and lightning by air pollution over the Pearl River Delta. Part I: Observational analyses. J Geophys Res Atmos 121(11):6472–6488
11. Li X, Pan Y, Mo Z (2018) Joint effects of several factors on cloud-to-ground lightning and rainfall in Nanning (China). Atmos Res 212:23–32
12. Galanaki E, Lagouvardos K, Kotroni V (2018) Thunderstorm climatology in the Mediterranean using cloud-to-ground lightning observations. Atmos Res 207:136–144
13. Sokol NJ, Rohli RV (2018) Land cover, lightning frequency, and turbulent fluxes over Southern Louisiana. Appl Geogr 90:1–8
14. Wang JF, Li XH, Christakos G (2010) Geographical detectors-based health risk assessment and its application in the neural tube defects study of the Heshun region, China. Int J Geogr Inf Sci 24(1):107–127
15. CHINADAILY Homepage. http://www.chinadaily.com.cn/m/hubei. Last accessed 2019/04/01

A CNN-Based Fault Section Location Method in Distribution Network Using Distribution-Level PMU Data

Weiqiang Yao, Xiaoqing Gao, Shu Liu, Yongjie Zhang and Xiaojun Wang

Abstract To improve the reliability of power supply, medium and low voltage distribution network always uses small current neural grounding in China. When the single phase to ground fault occurs, the fault feature is weak and fault section is hard to locate by traditional method. The development of distribution level phasor measurement units (D-PMUs) makes the visual and precise synchronous data available. In this paper, a new fault section location method based on Convolutional Neural Network (CNN) is proposed. The data cross-section is the input characteristic matrix of CNN model corresponding to the snapshot of the synchronous measurements of multi D-PMUs at a specific time, including current and voltage phasor. And the fault section and confidence of results would be given by the trained three-layer CNN model. This method only requires the snapshot data of single moment in the steady fault stage, so it is not affected by the fault initial phase angle and is robust to the noise and data loss or corruption. The accuracy, anti-interference capacity, and effectiveness of proposed method had been tested on a 20-node distribution network with distributed generation in PSCAD.

Keywords Fault section location · D-PMUs · CNN · Data cross-section

1 Introduction

In the medium and low voltage distribution networks, the grounding method in China mainly adopts small current neural grounding way to improve the reliability of power supply. But when the single phase to ground fault occurs, the fault current

W. Yao · S. Liu
State Grid Shanghai Electric Power Research Institute, Shanghai 200437, China

X. Gao
State Grid Shanghai Municipal Electric Power Company, Shanghai 200120, China

Y. Zhang (✉) · X. Wang
Beijing Jiaotong University, No. 3, Shangyuancun Haidian District, Beijing 100044, China
e-mail: 18117032@bjtu.edu.cn

Y. Xue et al. (eds.), *Proceedings of PURPLE MOUNTAIN FORUM 2019-International Forum on Smart Grid Protection and Control*, Lecture Notes in Electrical Engineering 585, https://doi.org/10.1007/978-981-13-9783-7_51

only has few amperes and the fault feature is weak and hard to detect and locate. And with more and more distributed generations (DGs) are introduced to distribution networks, it is more complicated to describe the fault characteristics. So the common protective devices, like conventional overcurrent relays, fails to act when the small current fault occurs. Till now, the problem of small current fault section location has not been well settled.

Nowadays, the research of fault section location methods has a great development. The signal injection method [1] is an effective way in particular application, but is limited by the high investment cost and unclear effect on electric equality. The methods based on transient traveling wave have successfully application in transmission lines [2, 3]. However, the complex structure and many branches reduce its applicability. In [4], a fault section location method based on Hilbert-Huang Transform (HHT) is proposed, but the effect of the distributed generation is not considered. Machine learning algorithms based methods have a great development in these years [5–7]. References [8, 9] made use of artificial neural networks (ANNs). And in [10], a method based on wavelet analysis and ANN was proposed. But because of the difference between transmission and distribution networks, the feasible and workable detection and location methods are still in the searching stage.

The development of distribution level phasor measurement units (D-PMUs) brings the high-precision synchronous phasor information [11, 12]. During these two years, some researchers has made contribution on the application of D-PMUs in fault detection and location. At Berkeley, an event detection method, namely hidden structure semi supervised machine (HS^3M), was established based on D-PMUs [13]. In [14], a two-layer architecture high impedance fault detection method based on SVM was proposed. This method only adopted the single-ended information of D-PMU to reduce the costs so that the accurate rate was not well enough.

In this paper, we proposed a new fault section location method in distribution network based on Convolutional Neural Network (CNN). The input characteristic matrix of CNN model is data cross-section, which means the snapshot of the synchronous measurements of multi D-PMUs at a specific time, including current and voltage phasor. Then, some data of designed scenarios were used to train the CNN model by Python. Meanwhile, a 20-node 10 kV distribution network was established in PSCAD/EMTDC for test. The results show that the method has good performance in veracity and reliability.

2 Fault Section Detection Structure Based on D-PMUs

A D-PMU is a high-precision power disturbance recorder adapted for making voltage phase angle or synchrophasor measurements, capable of storing and communicating data live. D-PMUs can provide high sampling data of three-phase voltage and current phasor with less error. All the measurements are GPS

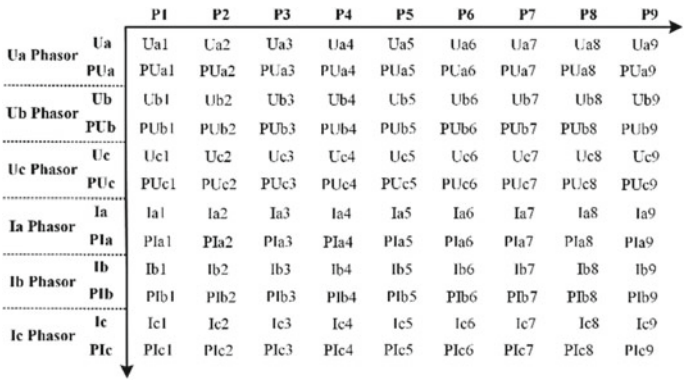

Fig. 1 The sketch map of data cross-section

time-stamped to provide time-synchronized observability [11]. The type of D-PMU employed in this paper is developed by the supported project, which can provide three-phase voltage and current phasor data. The sampling frequency of the phasor data reaches 100 samples/s. The amplitude error is less than ±0.2% and the error of phase angle is less than ±0.05°. Besides, this D-PMU can store a period of measurement data at local side.

In reality, uploading all measurements by D-PMUs in real time may be unrealistic. In the distribution network, assume that D-PMUs set on the line-end and load side. And data cross-sections are formed at the master station which represent the snapshot of the synchronous measurements of multi D-PMUs at a specific time. The data cross-section can be written as a $n \times m$ matrix as shown in Fig. 1. The rows of the matrix correspond to the D-PMU1 to D-PMUn, and the columns correspond to the measurement phasor data of each D-PMU.

In this structure, the analysis in master station only needs the cross-section information. So, the task of all the D-PMUs is uploading the phasor data at a lower frequency, storing a period of data at local side, and waiting the recall. At master station, trained CNN model is adopted to detect the status and fault section of the moment. The method only requires the snapshot data of single moment in the steady fault stage. If the fault status was diagnosed, the fault section would be detected immediately. And the stored data of the local D-PMUs (generally the high sampling level information during the previous 1 s) will be recalled to the master station for verification and further analysis. All the normal states are tagged as 0. And the different fault sections are tagged as the corresponding section number.

3 CNN Model for Fault Section Location

3.1 Introduction of CNN

CNN is a class of deep neural network in deep learning, which uses a variation of multilayer perceptrons designed to require minimal preprocessing. Convolutional networks were inspired by biological processes [15, 16] in that the connectivity pattern between neurons resembles the organization of the animal visual cortex. Individual cortical neurons respond to stimuli only in a restricted region of the visual field known as the receptive field. The receptive fields of different neurons partially overlap such that they cover the entire visual field. So the architecture of a CNN can take advantage of the two dimension data, such as an image or a matrix.

There are four main steps in CNN: convolution, subsampling, activation and full connectedness [17, 18].

Convolution. The first layers that receive an input signal are called convolution filters. Convolution is a process where the network tries to label the input signal by referring to what it has learned in the past. The convolution can emulate the response of an individual neuron to visual stimuli. Convolution has the nice property of being translational invariant. Intuitively, this means that each convolution filter represents a specific feature, and the CNN algorithm learns which features comprise the resulting reference. The output signal strength is not dependent on where the features are located, but simply whether the features are present.

By using shared weights, the convolutional layer can reduce the number of the free variables effectively. And the convolutional operation resolves the vanishing or exploding gradients problem in training traditional multi-layer neural networks with many layers by using backpropagation. Convolutional layer can be given by the following equation,

$$\mathbf{x}_j^l = f\left(\sum_{i \in M_j} x_j^{l-1} \cdot \mathbf{k}_{ij}^l + b_j^l\right) \tag{1}$$

where M_j is the collection of input maps, $\boldsymbol{k}_{ij}^l$ is the convolution kernel used for the connection between the ith input feature map and the jth output feature map, b_j^l is the bias corresponding to jth feature map, and f is a activation function, which will be introduced later.

Pooling. Inputs from the convolution layer can be smoothened to reduce the sensitivity of the filters to noise and variations. The function of this layer is weakening the influence of data deformation and it is capable to reduce dimensions, improve the accuracy, and avoid overfitting. The pooling layer is defined as the following form,

$$\mathbf{x}_j^l = f\left(\text{pooling}\left(\mathbf{x}_j^{l-1}\right) + b_j^l\right) \tag{2}$$

where pooling(.) represents the pooling function and b is bias. Here, the max pooling operation is adopt. It simply takes some $k \times k$ region and output a single value, which is the maximum in that region.

Activation. The activation layer controls how the signal flows from one layer to the next, emulating how neurons are fired in our brain. CNN is compatible with a wide variety of complex activation functions to model signal propagation, the most common function being the Rectified Linear Unit (ReLU), which is a non-linear activation function to deal with the non-linear problems and favored for its faster training speed.

Full Connected. FCs connect every neuron in one layer to every neuron in another layer, which take charge of the high-level reasoning. It is in principle the same as the traditional multi-layer perceptron neural network (MLP), where all possible pathways from the input to output are considered. Finally, choose the Softmax loss to determine a single class of mutually exclusive classes. The loss function specifies how training penalizes the deviation between the predicted and true labels. Here, the output result is the tag of each cross-section corresponding to the distribution network state and fault section.

So far, a fundamental CNN is established. And the aim of training a CNN is to obtain the weight kernels and the biases between layers by two steps: a forward process and a backward propagation. The task of the forward process is to get the output of each hidden layer, such as the convolutional feature map, the sampling feature map, and the activation of the fully connected layer with the current parameters. And the backward stage is used to learn the gradients of each parameter based on the loss function.

3.2 The Structure and Parameters of Proposed CNN Model

A CNN is easier to train and has many fewer parameters than a fully connected network with the same number of hidden units. In this method, the CNN model includes three convolutional and pooling layers and two full connected layer (FC). First convolution and pooling layer is a 1×1 convolution, which is used to increase the nonlinear characteristics without loss of resolution. The structure of proposed CNN model is shown as Fig. 2 and the parameters are shown as Table 1.

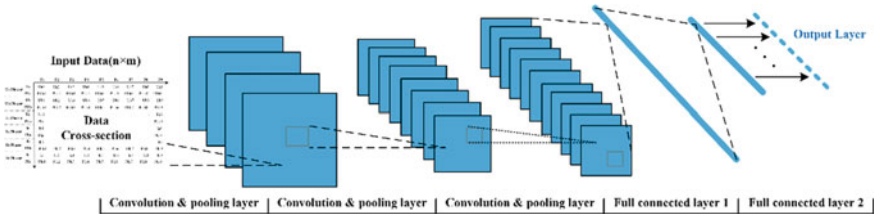

Fig. 2 The structure of CNN model

Table 1 Parameters of CNN model

Layer	Filter/ unit	Convolution kernel size	Pooling size	Pooling strides	Output feature (each filter)
Input layer	1	/	/	/	9 × 12
Convolution and pooling layer #1	32	1 × 1	/	/	9 × 12
Convolution and pooling layer #2	64	3 × 3	2 × 2	[1, 2]	8 × 6
Convolution and pooling layer #3	128	3 × 3	2 × 2	[2]	4 × 3
Full connected layer #1	/	/	/	/	1024
Full connected layer #2	/	/	/	/	21

4 Simulation and Results

4.1 Simulation

To validate the proposed method, a 20-node distribution network has been established in PSCAD/EMTDC. As shown in Fig. 3, a 10 kV/50 Hz resonant ground distribution network was simulated. The overcompensation rate is 8%. At node 3 and node 6, two 4 kW photovoltaic power generation devices are connected by inverter, and the control mode is constant power control. All the D-PMUs are set at the head and end of the whole network (M01, M02, M03, M3, M6, M11, M14, M17, M20). All the lines are overhead lines and the parameters is shown as Tables 2 and 3. Where, Z_{SA}, Z_{SB}, and Z_{SC} are the self impedances and $Z_{AB(BA)}$, $Z_{AC(CA)}$, and $Z_{BC(CB)}$ are the mutual impedances.

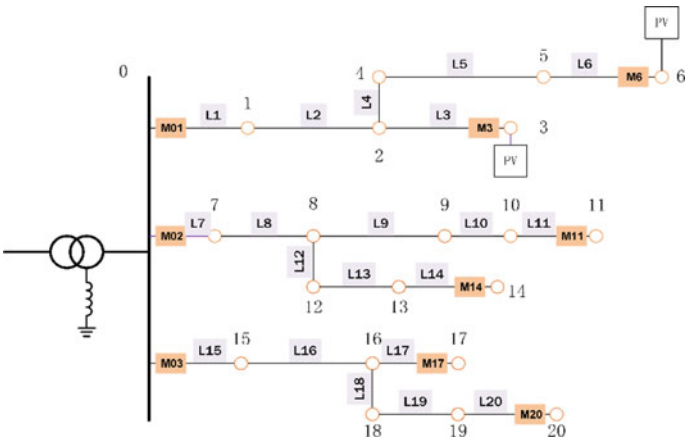

Fig. 3 20-node distribution network and the position of D-PMUs

Table 2 Line length parameters of distribution network

Length (km)	Line number
1.5	L3, L6
2	L1, L2, L4, L5, L7, L8, L9, L12, L13, L14, L16, L17, L18, L20
3	L10, L11, L15
4	L19

Table 3 Overhead line parameter

Parameter (Ω/km)	Value
Z_{SA}	0.1467 + 0.6462i
Z_{SB}	0.1503 + 0.6441i
Z_{SC}	0.1467 + 0.6462i
Z_{AB}, Z_{BA}	0.1143 + 0.3419i
Z_{AC}, Z_{CA}	0.1125 + 0.2995i
Z_{BC}, Z_{CB}	0.1143 + 0.3419i

4.2 Test Case

In the simulation, we assumed that all the fault type is A phase single-phase grounding fault. All the test cases are shown as Table 4. Where, the fault position "x%L-" means the fault occurred at x% of line L-. For example, "25%L1" means the fault occurred at 25% of line L1. "N-" means the fault occurred at the corresponding node. The fault occurred at the node is belong to the section which has the

Table 4 The set of test cases

Case	Fault position	Fault impedance	Fault initial phase angle	Case number
1	Normal state	\	\	50
2	5%L1 ~ 5%L20	R_{list}	0°	140
3	50%L1 ~ 50%L20	R_{list}	0°	140
4	85%L1 ~ 85%L20	R_{list}	0°	140
5	N1 ~ N20	R_{list}	0°	140
6	25%L1 ~ 25%L10	R_{list}	0°	70
7	25%L11 ~ 25% L20	R_{list}	25°	70
8	75%L1 ~ 75%L10	R_{list}	75°	70
9	75%L11 ~ 75% L20	R_{list}	90°	70
10	60%L1 ~ 60%L20	0.01, 5, 15, 30, 70, 90 Ω	30°	120

same name. That is, each section is combined by the line and the node after the line. The fault impedances are set as R_{list}: 0.01, 0.1, 1, 10, 20, 50, 100 Ω. Each case continued for 0.7 s, and the transient data of the first 0.1 s will be dropped. So, for each case, 60 groups data were saved.

In the list, case 1, case 2, case 3, case 4, and case 5 were used to train the CNN model. And the rest of the cases were tested.

4.3 Test Results

To quantify the performance of the proposed CNN model, the accuracy is defined in Eq. (3), with $|TP|$ being the amount of true positive classifications; $|TN|$, the amount of true negative classifications; $|FP|$, the amount of false positive classifications, e.g. a false alarm, and $|FN|$, the amount of false negative classifications, like missed faults.

$$\text{accuracy} = \frac{|TP| + |TN|}{|TP| + |FP| + |FN| + |TN|} \tag{3}$$

After training the CNN model by case 1–5, the accuracy score of the same data is 99.27%.

Different Fault Position. Test the trained CNN model by different fault position of case 6, the accuracy score is 97.83%. The accuracy of the algorithm is preliminarily verified. In different fault position of the whole distribution system, the CNN model can identify the fault section effectively.

Table 5 Test result for different fault initial phase angle

Case/fault position	Fault initial phase angle	Accuracy score (%)
Case1/25%L11 ~ 25%L20	25°	98.24
Case2/75%L1 ~ 75%L10	75°	98.41
Case3/75%L11 ~ 75%L20	90°	98.15

Different Fault Initial Phase Angle. Test the CNN model by case 7, 8, and 9. The accuracy score is shown as Table 5.

From the table, we can see that the proposed CNN model has no effect on fault initial phase angle. The main reason is this fault section location method adopts the steady-state after the fault occurred. The fault initial phase angle effects the transient process a lot but has little effect on steady-state.

The transient process of high fault impedance is longer than low impedance. So if the fault impedance is high enough, the steady-state of the fault needs to be collected several data later.

Different Fault Impedance. Test the CNN model by case 10, which includes the fault occurred at 60%L1 ~ 60%L20 with impedance 0.01, 5, 15, 30, 70, and 90 Ω. The accuracy score is shown as Table 6.

The result shows that the proposed method is not effected by the fault impedance within certain range. The fault impedance range depends on the training data setting. Due to time reasons, here the fault impedance range is below the 100 Ω. Note that the high impedance faults (HIF, the impedance is normally beyond 600 Ω) always manifest the process of arc, so the applicability for HIF of proposed method is not clear.

Noise. For evaluating the robustness to noise, Gaussian White Noise with different signal-to-noise ratios (SNRs) was added to the original data in case 10. The noise is set as 60, 50, 40, and 30 dB. The results are shown in Fig. 4.

As can be seen from the diagram, under the influence of 30 dB noise, the accuracy of the CNN model has significant reduction, was about 85%. So, the proposed method has requirements for the precision of data. In practice, considering the measurement error of D-PMUs and communication, the SNR of noise is commonly less than 50 dB. The robustness to this level of noise can be guaranteed.

Table 6 Test result for different fault impedance

Case/fault position/fault initial phase angle	Fault impedance (Ω)	Accuracy score (%)
Case10/60%L1 ~ 60%L20/30°	0.01	97.54
	5	98.31
	15	98.19
	30	97.68
	70	98.52
	90	98.07

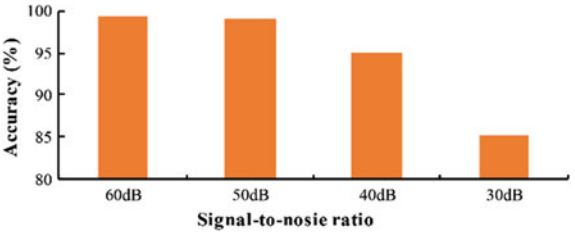

Fig. 4 Test result for different noise in case 10

Above all, the proposed method has more than 98% accuracy for all the test cases. And the results show that the fault position, fault initial phase angle, fault impedance (within certain range), and normal noise has little effect on the proposed method. Till here, all the accuracy result is for each single moment. By the further test, if continued 20 groups of data (0.2 s) were provided and choose the section with highest probability as the result, the accuracy of proposed method can reach 100%.

5 Conclusion

In this paper, a CNN-based fault section location method in distribution network is proposed. Cause the D-PMUs can provide the synchronous voltage and current phasor data, the CNN model can take the advantage of D-PMU data by data cross-section. The proposed method just need the snapshot data at a specific time to detect the fault and determine the fault section. Simulation results have verified that the proposed method has 98% accuracy and has little effect the fault position, fault initial phase angle, fault impedance (within certain range), and normal noise.

Acknowledgements This work is supported by National Key R&D Program of China (2017YFB0902800), Science and Technology Project of State Grid Corporation of China (52094017003D) and the Fundamental Research Funds for the Central Universities (2019YJS179).

References

1. Du G, Liu L et al (2010) Research on technology of grounding fault location combining FTU and “S” signal injecting method in distribution grid. Power Syst Prot Contr 12
2. Cai X, Song G et al (2011) A novel fault-location method for VSC-HVDC transmission lines based on natural frequency of current. Chin Soc Electr Eng 31(28):112–119
3. Duan JD, Liu J, Lu HL (2016) Fault location method based on traveling-wave instantaneous frequency for HVDC transmission lines. Proc CSEE 36(7):1842–1848
4. Zhao J, Ma N, Hou H et al (2018) A fault section location method for small current grounding system based on HHT. In: China international conference on electricity distribution (CICED). IEEE, China, pp 1769–1773

5. Zhao H, Liu H, Liu H et al (2018) Condition monitoring and fault diagnosis of wind turbine generator based on stacked autoencoder network. Autom Electr Power Syst 42(11):102–108
6. Zhao H, Yan X, Wang G et al (2019) Fault diagnosis of wind turbine generator based on deep autoncoder network and XGBoost. Autom Electr Power Syst 43(11):81–90
7. Wang S, Zhao D (2017) Research review and prospects for power grid fault diagnosis. Autom Electr Power Syst 41(19):164–175
8. Chen Z, Maun JC (2000) Artificial neural network approach to single-ended fault locator for transmission lines. IEEE Trans Power Syst 15:370–375
9. Aygen ZE, Seker S et al (1999) Fault section estimation in electrical power systems using artificial neural network approach. In: IEEE Transmission and Distribution Conference 2. IEEE, pp 466–469
10. Bhowmik PS, Purkait P, Bhattacharya K (2009) A novel wavelet transform aided neural network based transmission line fault analysis method. Electr Power Energy Syst 31:213–219
11. Wang X, Xie X et al (2017) Micro-PMU for distribution power lines. CIRED Open Access Proc J 1:333–337
12. von Meier A, Stewart E et al (2017) Precision micro-synchrophasors for distribution systems: a summary of applications. IEEE Trans Smart Grid 8(6):2926–2936
13. Farajollahi M, Shahsavari A et al (2018) Locating the source of events in power distribution systems using micro-PMU data. IEEE Trans Power Syst 33(6):6343–6354
14. Wang X, Zhang Y et al (2018) Two-layer coordination architecture HIF detection with μPMU data. J Eng 2018(15):1033–1037
15. Fukushima K (1980) Neocognitron: a self-organizing neural network model for a mechanism of pattern recognition unaffected by shift in position. Biol Cybern 36(4):193–202
16. Matsugu M, Mori K, Mitari Y et al (2003) Subject independent facial expression recognition with robust face detection using a convolutional neural network. Neural Netw 16(5–6): 555–559
17. Guo X, Chen L, Shen C (2016) Hierarchical adaptive deep convolution neural network and its application to bearing fault diagnosis. Measurement 93:490–502
18. Lawrence S, Giles CL, Tsoi AC et al (1997) Face recognition: a convolutional neural-network approach. IEEE Trans Neural Netw 8(1):98–113

Research on Grid State Portrait Technology and Its System Realization

Bo Wang, Sheng Huang, Feifei Li, Yiming Zheng, Tingxiang Lu and Xin Shan

Abstract Based on the traditional user portrait technology and concept, this paper extracts various indicators that reflect the characteristics of grid operation state from the main aspects of grid operation to construct the grid state portrait label system and label generation method, establishes the grid state portrait analysis model, and evaluates the grid state trend. On this basis, the grid state portrait application system is designed and implemented, and the in-depth analysis of the grid state portrait and operation data is realized by means of an intuitive comprehensive display method. The practical application results show that the system can intuitively reflect the grid operation situation from multiple dimensions, discover and display data rule related to equipment or grid, which can provide technical support for power grid operators to conduct monitoring, take preventive measures and make decision for power grid operation.

Keywords Portrait technology · Operation state of power grid · Trend analysis · Big data analysis · Comprehensive display

This work was supported by the science and technology project "Research and Application of Intelligent Technology for Real-time Dispatching of Power Grid Based on Artificial Intelligence" (52460817A029) of NARI Technology Co., Ltd.

B. Wang (✉) · S. Huang · F. Li · Y. Zheng · T. Lu · X. Shan
NARI Group Corporation (State Grid Electric Power Research Institute), Nanjing, China
e-mail: wwwbo1981@163.com

S. Huang · F. Li · Y. Zheng · T. Lu · X. Shan
NARI Technology Co., Ltd., Nanjing, China

State Key Laboratory of Smart Gird Protection and Control, Nanjing, China

Y. Xue et al. (eds.), *Proceedings of PURPLE MOUNTAIN FORUM 2019-International Forum on Smart Grid Protection and Control*, Lecture Notes in Electrical Engineering 585, https://doi.org/10.1007/978-981-13-9783-7_52

1 Introduction

With the increasingly complex operation characteristics of the power grid and the increasingly large operational information, higher requirements are placed on the operational decision of the power grid: the grid operators need to grasp the power grid operation trend more accurately and comprehensively, evaluate the operational risks of the whole power system and its internal equipment, and improve the reliability of grid operation [1, 2]. A large amount of operation and analysis data is accumulated in the power dispatching system, which provides a big data foundation for the in-depth analysis of the characteristics of the power grid operation trend. However, in the face of such a large amount of historical operation record information, it is worthy of further study on how to better mine its value and clearly describe the operating situation of the grid in a simple and intuitive way. The appearance of user portrait technology and concept provides a new way to intuitively depict and characterize the operation situation of power grid.

The traditional user portrait refers to the labeled user model abstracted from the user's attributes, preferences, habits, behaviors and other information. By labeling, users can be described by some highly generalized and easy-to-understand features, which makes it easier for people to understand users and is convenient for computer processing. User portrait technology has a good application in user behavior prediction, personalized recommendation, and precision marketing [3, 4]. In the field of power, some related researches and applications of portrait technology have been carried out in recent years. For example, study the application of portrait technology in pattern recognition of electricity consumption behavior and user classification to support customer load prediction and assist the formulation of electricity consumption suggestions and pricing policies [5, 6]; Study the application of power user portraits in the identification of risk electricity fees and risk customer to achieve the purpose of controlling the risk of electricity fees recovery and formulating targeted risk prevention measures [7]; Study equipment portrait technology based on power equipment operation data to enable equipment data to be presented in a more vivid and tangible form, which is convenient for operators to understand and use, and improve their work efficiency [8]; Study the application of power customer portraits in customer grouping, differentiated services, targeted marketing, etc., to achieve precise marketing and enhance customer satisfaction [9, 10]; Through the construction of the life cycle portrait of power assets, the overall portrait of power asset characteristics can be realized, and the refined and differentiated management of the asset life cycle can be improved [11]. However, in general, the current research and applications of portraits technology in power field are mostly around power users and power equipment. The portrait construction and application of the grid operation state has not been seen, and the research and exploration of the grid state portrait technology is lacking.

In this paper, by referring to the traditional user portrait technology and concept, a method of constructing a grid state portrait is proposed. It extracts various indicators that reflect the characteristics of grid operation state from the main aspects of

grid operation to form the portrait label system of power grid state and to establish a grid state portrait analysis model by extracting, sampling, mining and analyzing the snapshot data of power grid operation. Then, in the big data analysis point of view, a grid state portrait application system is designed and implemented for displaying data rule associated with equipment or power grids from time, space, object and other dimensions, and providing a service support for the better monitoring, prevention and decision-making of power grid for operators and realizing the in-depth analysis of the grid state portrait and the grid operation data of the whole network.

2 Grid State Portrait Label System

Portrait labels usually refine and describe the characteristics of the subject in the form of semantic and short text. However, power grid operation state data are mostly numerical, which cannot directly reflect the semantic characteristics. Therefore, it is necessary to construct appropriate rules to discretize the numerical data, transform the quantitative data into qualitative labels, and form semantic labels that are easy to understand.

The grid state portrait mainly extracts the characteristics that characterize the grid operation situation from the aspects of grid steady-state operation, grid balance capability and grid transient security, and constructs grid state label which is used to describe and evaluate the grid state and health situation. The framework of grid state portrait label system is shown in Fig. 1.

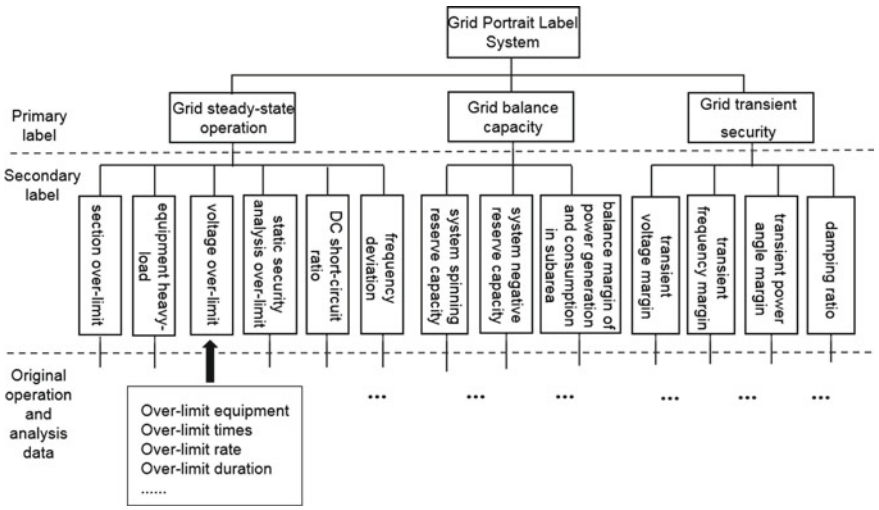

Fig. 1 The framework of grid state portrait label system

The grid state portrait label system is mainly composed of two levels: the primary label reflects the classification of the main operating state indexes of the grid, and the secondary label reflects the sub-label items that constitute and support the primary label. Among them, the secondary label is obtained by the feature statistics, calculation and labeling of the corresponding original operation and analysis data, while the primary label is obtained by the further aggregation and calculation of the secondary label. The label system of grid state portrait mainly includes:

Grid steady-state operation label. It mainly describes the important monitoring indicators of power grid daily operation under the condition of stable operation, including: section over-limit label, equipment heavy-load label, voltage over-limit label, static security analysis over-limit label, DC short-circuit ratio label, frequency deviation label.

Grid balance capability label. It mainly describes the important power balance of the power generation and consumption in whole grid or local areas, including: system spinning reserve capacity label, system negative reserve capacity label and the balance margin of power generation and consumption in subarea.

Grid transient security label. It mainly describes the transient stability margin of the power grid under the expected fault conditions, including: transient voltage margin label, transient frequency margin label, transient power angle margin label and damping ratio label.

3 Generation Method of Grid State Portrait Label

In order to reflect the operation situation of power grid and evaluate the trend of grid health state, the historical year-on-year value of the original data corresponding to each label is selected as the label eigenvalue for subsequent label generation, and conduct statistical calculation on the label eigenvalue in monthly time range. Through the value comparison of the same historical period, the change trend of power grid health state can be better reflected. The main steps of label generation include:

Step 1: Define the original data value that reflect the secondary label.

For voltage over-limit label, section over-limit label, equipment heavy-load label and static security analysis over-limit label, since they usually have multi-dimensional features, such as over-limit/heavy-load percentage, over-limit/heavy-load duration, over-limit/heavy-load times, taking a single feature as the original data for the label will result in lacking comprehensiveness of the label description. Therefore, this kind of label should be defined based on the consideration of multiple dimensions. The original data definition of this kind of secondary labels is shown in formula (1):

$$C = \frac{\sum_{s=1}^{N} B_s}{\sum_{s=1}^{N} n_s} \tag{1}$$

$$B_s = \sum_{i=1}^{n_s} (y_i \times t_i) \tag{2}$$

where: C is the original data value of the secondary labels of over-limit type, B_s is the comprehensive over-limit index of the equipment s, n_s is the over-limit number of the equipment s, N is the amount of the over-limit equipment, y_i is the i-th over-limit rate of the equipment s, t_i is the i-th over-limit duration of the equipment s;

In addition to the above-mentioned secondary labels of over-limit type, the original data of the remaining secondary labels in the label system are defined as the statistical mean value of the corresponding indicator data.

Step 2: Calculate the secondary label eigenvalue. The calculation formula is shown in formula (3):

$$A_{i2} = \frac{A_{it} - A_{il}}{A_{il}} \times 100\% \tag{3}$$

where: A_{i2} is the i-th secondary label eigenvalue, A_{it} is original data value for one month of this year of the i-th secondary label, A_{il} is original data value for the same month of last year of the i-th secondary label, $i = 1, 2, \ldots M$, M is the number of secondary labels.

Step 3: Calculate the primary label eigenvalue by aggregating the secondary label eigenvalues.

According to the definition of the grid state portrait label, different secondary labels have different polarities. For some secondary labels, the larger the original data value, the better, and for some, the smaller the better. The original data value of each secondary label can be divided into two categories: extremely large type and extremely small type. Where, the labels with extremely large features include: system spinning reserve capacity, system negative reserve capacity, the balance margin of power generation and consumption in subarea, DC short-circuit ratio, transient voltage margin, transient frequency margin, transient power angle margin, damping ratio; The labels with extremely small features include: voltage over-limit, section over-limit, equipment heavy-load, static security analysis over-limit, frequency deviation.

Therefore, in the calculation of the primary label eigenvalue, the consistency of the secondary label eigenvalues should be considered. The definition of the primary label eigenvalue is shown in formula (4):

$$A_k = \sum_{i=1}^{m_k} (\alpha \times w_i \times A_{i2}) \tag{4}$$

$$\alpha = \begin{cases} 1 & A_{i2} \text{ is the extremely large type} \\ -1 & A_{i2} \text{ is the extremely small type} \end{cases} \tag{5}$$

where, A_k is the k-th primary label eigenvalue, $k = 1, 2, \ldots J$, J is the number of the primary label, m_k is the number of the secondary label contained in the k-th primary label, A_{i2} is the eigenvalue of the i-th secondary labels contained in the k-th primary label, w_i is the weight coefficient and $\sum_{i=1}^{m_k} w_i = 1$. The weight coefficient can be defined according to the importance degree of the secondary label, and the default value of w_i is $1/m_k$.

Step 4: Labelling representation of eigenvalues.

After calculating the label eigenvalues of each level, they are labeled according to the setting threshold, and finally the portrait labels that reflect the state of power grid are obtained.

In this paper, six types of state labels are designed to reflect the changes in the health trend of the power grid, which are severely worse, obviously worse, slightly worse, slight improvement, obvious improvement and significant improvement. They respectively represent the different health trend states of the grid state portrait labels.

When a label eigenvalue A_n falls within a given state label threshold range (the threshold range can be adjusted according to actual conditions, and the default setting value is given here), the corresponding state label $Label_n$ is given to the portrait label, as shown in the formula (6).

$$Label_n = \begin{cases} \textit{seriously worse} & A_n \le -20\% \\ \textit{obviously worse} & -20\% < A_n \le -10\% \\ \textit{slightly worse} & -10\% < A_n < 0\% \\ \textit{slight improvement} & 0\% \le A_n < 10\% \\ \textit{obvious improvement} & 10\% \le A_n < 20\% \\ \textit{significant improvement} & A_n \ge 20\% \end{cases} \tag{6}$$

4 System Implementation Architecture

Based on the above definition of the grid state portrait label system and considering the comprehensive and intuitive display of the portrait, the grid state portrait application system is designed and implemented with B/S architecture in non-production control area based on the basic data extraction of production control area. The system implementation architecture is shown in Fig. 2.

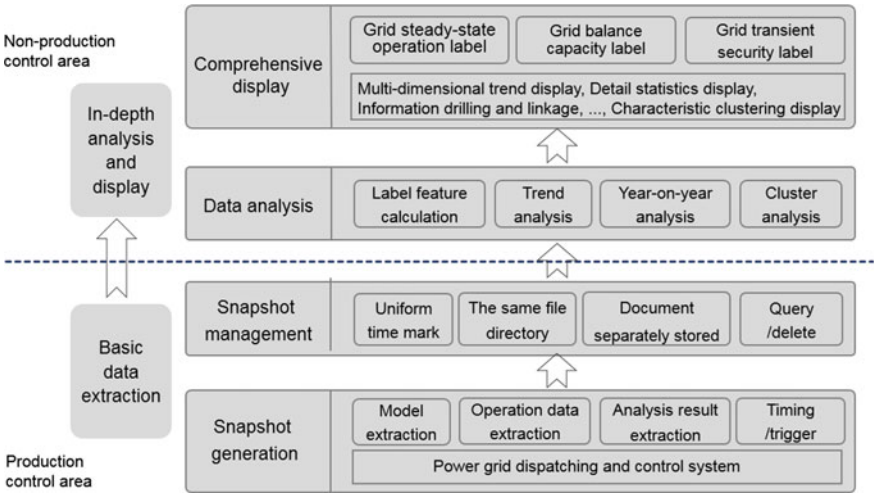

Fig. 2 Grid state portrait application implementation architecture

4.1 Snapshot Generation

Snapshot generation realizes the extraction of the basic data of the grid state portrait, mainly including the model, operation data and application analysis results of the same time section. Where, the model snapshot generation is made by reading model and parameters from the relational database; The snapshot generation of the operation data is made by using the big data SQL engine to read the historical operation data at the specified time to generate the data files; The snapshot generation of analysis results is made by online periodic real-time sampling to generate data files. And the snapshot generation supports timing generation mode and trigger generation mode.

4.2 Snapshot Management

Snapshot management function adopts distributed file system for the storage of snapshots. According to the business, multiple files are generated from the holographic data of the power grid. The snapshots of different business data use unified time mark, and the business snapshot files with the same time mark are stored in the same directory as a complete snapshot of the whole network business. At the same time, since the amount of snapshot data is very large, the snapshot files are stored in compression mode.

Snapshot management also provides functions including snapshot deletion, snapshot query, etc. The snapshot deletion function automatically removes expired

snapshots at a self-defined interval, and manual snapshot deletion is also supported. The snapshot query function provides efficient and batch queries for specified historical snapshot files.

4.3 Data Analysis

Data analysis is mainly based on the generated snapshot data to complete the calculation of the grid state portrait characteristics, the statistical analysis of relevant data, the trend analysis and big data analysis, etc., mainly including:

Based on the grid state portrait label system and its presentation method, to realize statistical analysis for the various types of grid state characteristics in equipment, region, grid and other dimensions, and form multilevel analysis results.

Based on the characteristic statistics of power grid state, to realize the trend analysis on multiple time scales, including annual/monthly/day/hour/minute.

To realize the year-on-year/month-on-month analysis of the state characteristics of the power grid to find their important changes.

Based on big data analysis technologies, to adopt clustering algorithm to conduct clustering analysis from the multiple characteristics dimensions (such as over-limit time frame, over-limit duration and over-limit rate, etc.) of a single equipment to reveal the regularities of the over-limit events.

4.4 Comprehensive Display

Comprehensive display function is realized mainly based on the various, vivid and interactive data visualization diagram provided by ECharts plugin, which can achieve the display of grid state portrait trend and detailed information, information level drilling and linkage, the features sorting and multi-dimensional analysis display, the year-on-year/month-on-month trend display of state characteristics, multi-dimensional clustering analysis and display and so on. It provides an intuitive and convenient comprehensive display effect for intelligent query and retrieval, the mining and analysis of grid operation state and its trend change information.

5 Practical Application Effect

In the power dispatching and control cloud system of Jiangsu Province, according to the research and design ideas in this paper, the construction and implementation of the grid state portrait system are carried out. Through the snapshot generation of application data and stock historical data extraction, the relevant grid operation and analysis data from 2017 to 2018 are obtained, which are used for the calculation,

analysis and display of grid state portrait labels and characteristic data. Specific practical application effects are as follows.

Firstly, on the overall level of grid state portrait, the state and change trend of all portrait labels are displayed in different levels according to the grid state portrait label system from the three aspects of grid balance capacity, grid steady-state operation and grid transient security. Through the historical comparison of each secondary label, to find the trend changes and characteristic information of the grid state in various main aspects, so as to intuitively grasp the overall development and change of the grid state. As shown in Fig. 3a, it can be found from the state of voltage over-limit label that the current trend change of voltage over-limit is obviously improved compared with the same period of last year, and the over-limit duration, over-limit times and over-limit rate are reduced to varying degrees.

Secondly, on the secondary label level, through the further multi-dimensional trend analysis of each secondary label, deep mining can be made for the label features to form multi-level analysis in the dimensions of region, subarea, equipment, so as to help the operators find the regularity and features of label data from multiple perspectives and fast locate the key objects that influence the label trend. As shown in Fig. 3b, It can fast access to the voltage over-limit trend analysis interface by the voltage over-limit label, can conduct multi-perspectives and in-depth analysis about the voltage over-limit trend of the entire grid from the region, subarea, equipment dimensions, and can quickly locate the most serious over-limit object in each dimension. For example, the subareas with the maximum year-on-year changes in the total over-limit times and the total over-limit duration is

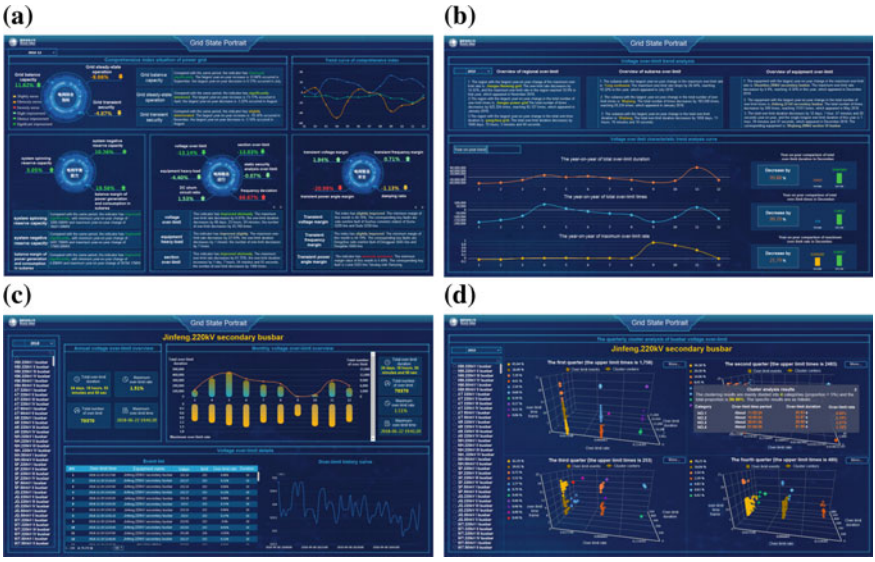

Fig. 3 The practical application effects of grid state portrait

Wujiang; The equipment with the maximum year-on-year change in the total over-limit times is: Jinfeng.220 kV secondary busbar.

Then, in the equipment level, through the further analysis on the attribute characteristics of key equipment, detailed analysis and information drilling display for attribute characteristics of key equipment can be carried out from the aspects of characteristic statistical trend change and event details of the equipment, so as to enable operators to comprehensively grasp the operation characteristics of key equipment from multiple attribute dimensions. As shown in Fig. 3c, For the equipment—Jinfeng.220 kV secondary busbar found in trend analysis of voltage over-limit label, It can quickly enter the detailed information interface for analysing the characteristics of voltage over-limit events of the equipment, and can conduct statistical analysis and demonstration of the equipment over-limit characteristics from multi-attribution dimensions such as the statistical trend change of the over-limit characteristics (the over-limit duration, the over-limit rate, the over-limit times), the over-limit event details and according curves.

Finally, based on big data analysis technology, a multi-dimensional clustering analysis is carried out from multiple feature dimensions of a single equipment using clustering algorithm. Through the distribution of the clustering centers, the main categories and representative characteristics of equipment over-limit events are found, which provides intuitive and visual display for revealing the event rule of the equipment. As shown in Fig. 3d, the interface shows the quarterly clustering analysis results of the voltage over-limit events of Jinfeng.220 kV secondary busbar. It can be found from the distribution of the over-limit event clustering centers: the voltage over-limit events of the equipment in the second quarter is mainly divided into four categories: it is mainly concentrated at about 01:54, 11:02, 16:59 and 20:51 of each day, the over-limit rate is basically 0.02% and the over-limit duration is about 20–30 s. These analysis results provide a visual demonstration for revealing the over-limit rule characteristics of the equipment.

6 Conclusion

Based on the technology and concept of traditional user portrait, this paper constructs a grid state portrait label system and label generation method by extracting various indicators reflecting the characteristics of the grid state from the main aspects of the grid operation, and designs and realizes the grid state portrait application system on this basis. This system can display the rule of multi-dimensional data relating to equipment or grid from time, space, object and other dimensions, realize deep analysis on the grid state portrait and the grid operation data, and provide a rich, intuitive comprehensive display effect for intelligent query and retrieval, the mining and analysis of the grid operation state and its trend change.

However, the grid state portrait label system constructed at present only preliminarily covers part of the labels of power grid operation state, and the portrait for

the power grid is incomplete. The extension of the label system can be further studied on this basis, and the label system and application system functions can be improved by considering such aspects as fault assessment, weak mode, equipment maintenance, energy supply and external meteorological risks to more comprehensively and deeply depict the operation state and development trend of the power grid, perceive the operation risk and optimization space of the power grid, improve the accurate judgment and control level of dispatching operators on the operation quality and efficiency of power grid, and provide effective guidance for the optimization and adjustment of operation strategy.

References

1. Wang T (2015) Research on operational trends and critical links identification of power systems. Bei Jing, North China Electric Power University
2. Gang L, Changhai Y, Yunpeng L et al (2017) Challenges and prospects of fault prognostic and health management for power transformer. Autom Electr Power Syst 41(23):156–167
3. Wang X (2014) The application of big data technology in precision marketing. Inform Commun Technol 6:21–26
4. Zhai X (2018) Study on the intelligent recommendation system of personalized resources based on personas. J Libr Inform Sci 3(12):17–21
5. Fu J, Xun X, Luo D et al (2018) Research on construction technology of electric power user behavior portrait. Electrotech Appl 37(13):18–23
6. Wang C, Zheng H (2018) A portrait of electricity consumption behavior mode of power users based on fuzzy clustering. Electr Measur Instrum 55(18):77–81
7. Xie J-K, Xu Q, Ding B-M (2016) Application of customer models in the risk control of electricity fees' recovery. Power Demand Side Manag 18(1):74–76
8. Wei Du, Peng Jiang, Wenhao Wang et al (2016) Research on technology and application of big data portrait based on transformer. Power System and Big Data 44(19):85–90
9. Xiang-qian Y, Lin-xin W, Yun-bing L et al (2017) Application research on the customer's portrait of electric power marketing information. Comput Technol Autom 36(4):122–126
10. Shijun Zhang, Feng Chen, Zhiying Wang et al (2018) The construction and the application of customer profile with multiple dimensions based on power big data. Electrotech Appl 37 (8):18–25
11. Zhao Y, Ma J, Zhang K (2018) Research on the label portrait technology based on life cycle of electricity assets. Power System and Clean Energy 34(1):51–58

A Line Loss Calculation Method for Power Grid Partition Based on Complex Network Community Discovery Algorithm

RunQing Bai, Kai Yi, Xin He, WeiZhou Wang, Geng Wang and Jiao Yu

Abstract With the interconnection and inter-supply of power systems in various regions, the emergence of multi-voltage class electromagnetic ring networks, the convergence of conventional load flow algorithms is facing severe challenges, and real-time calculation of theoretical line loss cannot be realized. In this paper, the community discovery idea of complex network theory is applied, and the parallel calculation method for line loss of power grid partition based on improved Fast-Newman algorithm is proposed. The method makes full use of the advantages of Fast-Newman algorithm to deal with the large-scale complex networks. On the basis of network Weighted, combined with the characteristics of power grid to improve the algorithm's agglomeration process, and the rapid partition of the power grid is realized. Further, by formulating the equivalence principle of the partition boundary, the partitions are completely separated. On the basis of partition independence, the SPMD parallel architecture in MATLAB is used to complete the parallel computing of each partition. Finally, the regional power grid is taken as an example to verify that the method has good accuracy, and its calculation speed and convergence are in line with the requirements of real-time calculation.

Keywords Theoretical line loss · Parallel computing · Network partition · Community structure · Fast-Newman algorithm

R. Bai · X. He
State Grid Gansu Electric Power Company,
Electric Power Research Institute, 730050 Lanzhou, China

K. Yi (✉)
College of Information and Electrical Engineering,
China Agricultural University, 100083 Beijing, China
e-mail: cauyikai@163.com

W. Wang · G. Wang · J. Yu
State Grid Gansu Electric Power Company, 730000 Lanzhou, China

Y. Xue et al. (eds.), *Proceedings of PURPLE MOUNTAIN FORUM 2019-International Forum on Smart Grid Protection and Control*, Lecture Notes in Electrical Engineering 585, https://doi.org/10.1007/978-981-13-9783-7_53

1 Introduction

Line loss rate is an important evaluation indicator for power supply companies [1]. At present, the line loss statistics of the domestic power grid mainly use the measurement value of the measurement automation system. In order to avoid the occurrence of statistical errors, it is necessary to use the theoretical line loss calculation value and the statistical value for comparison and evaluation [2]. However, with the interconnection and intercommunication of power systems in various regions, the emergence of multi-voltage class electromagnetic ring networks, the convergence of conventional load flow algorithms is facing a severe test [3]. In addition, the measurement data often appears abnormal, and it is very difficult to calculate the theoretical line loss of the whole network for the above reasons.

The refined line loss calculation mainly uses the load flow algorithm, the distribution network generally adopts the back/forward sweep method [4], and the transmission network adopts the Newton method. Most of the existing calculation methods realize the load flow calculation of the power grid by filling the measurement data [4, 5], and do not consider the real-time and convergence of the algorithm when applied to large-scale networks.

The community structure is an important component of complex network theory. It reveals that a complete network consists of many community. In recent years, community discovery algorithms have many applications in the power grid [6–8]. However, most of the existing researches are aimed at medium-scale networks and are computationally complex, which is difficult to meet the needs of large-scale grid fast computing. The improved Fast-Newman algorithm proposed in this paper has a great improvement in computing time and is suitable for rapid partitioning of large-scale networks.

After analyzing and comparing the characteristics of each community discovery algorithm, this paper makes full use of the speed and accuracy of the Fast-Newman algorithm to calculate large-scale networks, and applies it to the theoretical line loss calculation of the whole network of power system. On the basis of fast partitioning, the independence and parallelization of the load flow calculation of each partition is realized by the replication of the boundary nodes and the equivalent of the exchange power. The accuracy and convergence of the partition calculation are well, which satisfies the requirements of large-scale grid fast line loss calculation, and provides feasible ideas for real-time line loss analysis and refined line loss management.

2 Complex Network Community Structure Theory

2.1 Community Discovery Algorithm

The community structure is ubiquitous in complex networks, and its internal nodes have strong coupling, and the coupling between the communities is sparse. This

feature facilitates computational convergence within the partition. At present, the main community discovery algorithms include Kenighan-Lin algorithm [9], spectral bisection method [10], GN splitting algorithm [11], Clauset optimization algorithm [12], Fast-Newman aggregation algorithm [13], Louvain Algorithm [12], BGLL hierarchical aggregation algorithm [14] and so on. The above algorithm is originally applicable to a binary network with no weight. The relationship between each node is only connected or not, and cannot reflect the different connection tightness between nodes.

There are certain differences in the networks to which different community discovery algorithms are applied. For example, in the actual network analysis, the Kenighan-Lin algorithm needs to determine the number of community divisions in advance; the Louvain algorithm may lose important nodes when dealing with large networks [14], and randomly merge nodes that increase module degree during clustering process, which is not suitable for real-time systems; the GN algorithm based on modularity index optimization proposed by Girvan and Newman has higher accuracy, but because each split process needs to calculate the edge betweenness of the whole network, the computational complexity is high, can only be applied in medium-sized networks [12]. Based on the GN splitting algorithm, Newman proposed the Fast-Newman algorithm to reduce the complexity of the algorithm. Compared with the GN algorithm, the Fast-Newman algorithm has been greatly improved in time, and has been successfully applied to a cooperative network of 50,000 nodes, which has the advantage of dealing with large-scale networks. The time complexity of each algorithm is shown in Table 1.

2.2 *Network Modularity Index*

In order to measure the quality of network division, it is necessary to develop quantitative evaluation indicators for the community structure. The most widely used is the network modularity function Q [14] proposed by Newman et al. The closer the Q value is to 1, the greater the expectation value of the internal tightness of the community is than the random network, indicating that the quality of the network partition is higher.

Assume that the network is divided into n communities in some form. Use e_{ij} to indicate the ratio of the number of edges between community i and community j to the total number of edges of the network. The expression of the modularity function Q is:

Table 1 Time complexity comparison of each community discovery algorithm

Algorithm	Time complexity
GN	$O(n^3)$
Louvain	$O(n^2T)$
Fast-Newman	$O(n^2)$

$$Q = \sum_{i=1}^{n} \left(e_{ii} - a_i^2\right) \tag{1}$$

where e_{ii} is the ratio of the number of inner edges of the community i to the total number of edges; $a_i = \sum_{j=1}^{n} e_{ij}$, represents the ratio of the edge connected to the internal node of the community i to the total number of edges of the network.

2.3 Fast-Newman Algorithm

Fast-Newman algorithm is a fast and agglomerative algorithm based on greedy thought. It takes the highest module value as the target. Each time, the node with the largest module increment is agglomerated first, which greatly reduces the complexity of the algorithm and is suitable for large-scale networks [13]. The algorithm flow is as follows:

1. Consider each node in the complex network as an independent community, and the number of network nodes n is the number of communities, thereby constructing the initial connection matrix:

$$E = \begin{bmatrix} 0 & e_{12} & \cdots & e_{1n} \\ e_{21} & 0 & \cdots & e_{2n} \\ \vdots & \vdots & \ddots & \vdots \\ e_{n1} & e_{n2} & \cdots & 0 \end{bmatrix} \tag{2}$$

$$e_{ij} = \begin{cases} \frac{1}{2m}; & \text{if node } i \text{ and } j \text{ are connected} \\ 0; & \text{others} \end{cases}$$

   where m is the total number of edges of the complex network.
2. Combine the connected nodes in turn to calculate the increment of the module, and a pair of nodes with the largest increase or the least decrease in the module degree are selected for merging. The module degree increment is expressed as:

$$\Delta Q_{ij} = 2\left(e_{ij} - a_i a_j\right) \tag{3}$$

   Treat the merged node as a new community. Update the module degree Q of the network.
3. Repeat step 2 until all nodes are merged into one community. The partitioning scheme corresponding to the maximum module degree in the cohesion process is selected as the optimal solution.

3 Parallel Line Loss Calculation of Power Grid Partition

3.1 Weighted Reprocessing of the Network

The traditional Fast-Newman algorithm is applicable to binary networks with no weight. If the unweighted algorithm is used to analyze the weighted network with actual physical meaning, not only will a large amount of network information be lost, but also the quality of the network partition will be reduced, which will further affect the rationality of the result.

The power grid acts as a weighted network with practical physical meaning. Its edge weight needs to be able to reflect its own structural characteristics and has practical significance. According to the physical characteristics of the power line, the line admittance is selected as the edge weight of the power grid, and the sum of all line admittances is taken as the total weight of the network. The higher the admittance value of the communication line between the two nodes, the higher the connection tightness and the more likely they are condensed into a community. The initial connection matrix of the power network with admittance as the edge weight is:

$$W = \begin{bmatrix} 0 & w_{12} & \cdots & w_{1n} \\ w_{21} & 0 & \cdots & w_{2n} \\ \vdots & \vdots & \ddots & \vdots \\ w_{n1} & w_{n2} & \cdots & 0 \end{bmatrix} \tag{4}$$

where w_{ij} represents the sum of the power line admittances connecting node i and node j.

Define the total network weight as:

$$S = \sum_{i=1}^{n} \sum_{j=1}^{n} w_{ij} \tag{5}$$

Combined with the research ideas of the community detection theory and the structural characteristics of the power network, the modularity index applicable to the weighted power network are:

$$Q' = \frac{1}{2S} \sum_{i=1}^{n} \sum_{j=1}^{n} \left(w_{ij} - \frac{k_i k_j}{2S} \right) \delta(c_i, c_j) \tag{6}$$

If node i and node j belong to the same community, $\delta(c_i, c_j)$ is equal to 1, otherwise equal to 0; $k_i = \sum_{j=1}^{n} w_{ij}$, represents the weight of node i in the weighted network, that is, the sum of the admittances of the lines communicating with the remaining nodes.

The network modularity increment corresponding to the weighted modularity index can be expressed as:

$$\Delta Q'_{ij} = \frac{1}{2S}\left(2w_{ij} - \frac{k_i k_j}{S}\right) \tag{7}$$

where w_{ij} is the connection tightness between the communities i and j, and k_i is the weight of the community i in the network.

3.2 Power Grid Partition

3.2.1 Simplification of the Network Topology

Using the community discovery algorithm to process the power grid requires some network simplification. The specific simplification rules are as follows:

1. The grid selects the typical wiring method, and the switching of the power equipment is no longer considered in the partitioning process.
2. The station wiring of power plants and substations is not considered in the partition process, and the charging capacitance of the transmission line is not considered.
3. All power devices in the network are abstracted into indiscriminate computing nodes, ignoring the existence of grounding points.
4. Ignore the directionality of the network, all power lines and transformer branches are regarded as the network edge with weight, and the edge weight is line admittance.

3.2.2 Algorithm Improvement Based on the Characteristic of Power Grid

Targeted improvement and optimization of the Fast-Newman algorithm to further improve the accuracy and speed of the algorithm when applied to the power grid.

In the actual calculation process, the impedance of the transformer branch is much larger than that of the transmission line, which easily causes the transformer nodes to be divided into different partitions, resulting in a partition error. For distribution transformers, once the impedance branch is split, isolated transformer nodes appear, causing significant interference to subsequent calculations.

Before the network partition, the same transformed busbars are condensed into a community, which reduces the initial number of communities and increases the calculation speed.

3.2.3 The Flow of Partition Algorithm

The partition process of the grid is as follows.

1. Simplify the network, each node in the power grid is regarded as an independent community, calculate the total weight S of the network, and generate an initial connection matrix G;
2. The busbars on each side of the transformer are first agglomerated;
3. Calculate the modularity increment $\Delta Q'$ of the connected community in turn, and select the two communities corresponding to the maximum increment $\Delta Q'_{max}$ to merge;
4. The merged two communities are treated as a new community, and obtain the merged new network. Calculate the module degree Q'_t of the new network;
5. Repeat steps 3–4 until all nodes are merged into one community;
6. The scheme corresponding to the maximum module degree in the merge process is selected, and after being corrected by the boundary node, it is used as the final partition result.

3.3 Parallel Calculation of Line Loss

The boundary equivalence principle formulated in this paper achieves the decoupling of adjacent partitions by copying boundary nodes and establishing boundary equality constraints. On the basis of complete separation of the partitions, further select the appropriate reference nodes to complete the parallel line loss calculation in the area.

3.3.1 Partition Decoupling

Figure 1a shows the boundary node i at the same time in three partitions. The node is copied according to the number of partitions in which it is located, and a separate subnet is obtained, as shown in Fig. 1b. The voltages u of the respective replica nodes is equal. The inter-partition exchange powers is obtained by the measurement data collected by the metering device, and is recorded as P_b and Q_b.

Promote to n partitions of shared boundary nodes. A receiving grid that derives energy from a neighboring area is defined as a powered partition. Similarly, an area that transfers energy to other areas is defined as a transmission partition. Assuming that there are l powered partition and k transmission partitions, there are boundary equality constraints as follows:

$$\begin{cases} u_{i1} = u_{i2} = \cdots = u_{in} \\ P_{b,1} + P_{b,2} + \cdots P_{b,l} = P_{b,l+1} + P_{b,l+2} + \cdots P_{b,l+k} \\ Q_{b,1} + Q_{b,2} + \cdots Q_{b,l} = Q_{b,l+1} + Q_{b,l+2} + \cdots Q_{b,l+k} \end{cases} \tag{8}$$

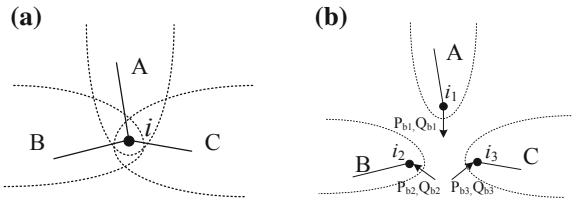

Fig. 1 The separation of subnets

The boundary node of the powered partition obtains energy from the neighboring area, which is equivalent to the power node, and its power generation power is P_G. Similarly, the boundary node of the transmission partition transmits energy to the adjacent area, which is equivalent to the load node, and the load power is P_L. The relationship between the equivalent power or equivalent load of each partition and the partition exchange power is:

$$\begin{cases} P_{G,i} = P_{b,i}^{l} \\ Q_{G,i} = Q_{b,i}^{l} \quad i = 1, 2, \ldots, l \\ P_{L,j} = P_{b,j}^{k} \quad j = 1, 2, \ldots, k \\ Q_{L,j} = Q_{b,j}^{k} \end{cases} \tag{9}$$

After the boundary equivalence, each partition becomes a completely independent network. The Central hub substation in the region is selected as the reference node, and the Newton-Raphson method is used to calculate the load flow to obtain the voltage U and the phase angle δ of each node. The power loss $\Delta\tilde{S}_{ij}$ of each line can be obtained from the basic theorem, see Eq. (10), and then the theoretical network loss value of each partition is obtained.

$$\begin{cases} \Delta\tilde{S}_{ij} = \tilde{S}_{ij} + \tilde{S}_{ji} \\ \tilde{S}_{ij} = \dfrac{\dot{U}_i}{2}\left[\dot{U}_i y_{ij0} + \left(\dot{U}_i - \dot{U}_j\right) y_{ij}\right]^* \\ \tilde{S}_{ji} = \dfrac{\dot{U}_j}{2}\left[\dot{U}_j y_{ji0} + \left(\dot{U}_j - \dot{U}_i\right) y_{ij}\right]^* \end{cases} \tag{10}$$

where $\dot{U}_i$ and $\dot{U}_j$ are the node voltages at both ends of the line, and y_{ij} and y_{ij0} are the series admittance and ground admittance of the line, respectively.

3.3.2 Partitioned Parallel Computing

For parallel computing, MATLAB introduces a parallel computing toolbox that is widely used in numerical analysis and engineering computing to solve numerical computation-intensive problems.

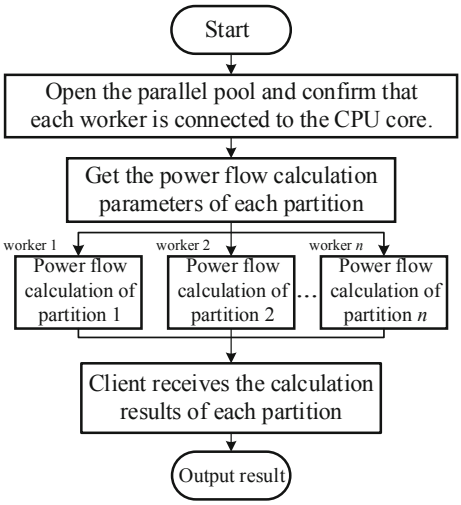

Fig. 2 The flow chart of parallel computing

The line loss calculation for each partition runs the same load flow program, but due to the difference of partition topology and measurement information, there are different input parameters for the corresponding program. This feature is in line with the SPMD application scenario, and can be parallelized using the SPMD parallel structure. The flow of parallel computing is shown in Fig. 2.

Using *client* and *worker* mode, *client* is the MATLAB side of writing and starting parallel code, responsible for assigning tasks and summarizing results. *Worker* is the multiple execution end of parallel code. In the figure, *n* represents the number of manageable *worker* in the parallel pool. One work unit *worker* is responsible for the load flow calculation of one partition, and the parameters of each partition are passed to the corresponding *worker*. After executing the load flow calculation program in parallel, each *worker* stores the calculation result in a cell array and returns it to the *client* in a unified manner.

4 Case Analysis

Taking a power grid in a certain area of Gansu as an example, the typical operation mode of full-wiring and full-boot in the summer of 2018 is selected. The method of this paper is used to calculate the partition line loss. The area contains 330, 110, 35 kV and other voltage levels, including 183 computing nodes, 274 transmission lines and 50 substations. Containing a wealth of measurement information, a total of 472,340 data were collected.

In the process of grid division, the curve of the network modularity index Q is shown in Fig. 3, and the abscissa indicates the number of times of node aggregation. The curve with "+" in the figure represents the modularity index change of the

improved algorithm; the unmarked curve represents the module degree change before the improvement. After 41 times of aggregation, the weighted modularity index Q of the improved algorithm reaches a maximum value of 0.713, while the modularity of the unmodified algorithm still does not reach the extreme value.

The power grid is divided by the GN splitting algorithm, the Louvain clustering algorithm, the unmodified Fast-Newman algorithm (F-N) and the improved algorithm (Improved F-N), and the partition result are shown in Table 2.

It can be seen from the data in the table that although the optimal module degree of the improved algorithm is slightly lower than the other algorithms, the existence of isolated nodes is successfully eliminated. Compared with the other community discovery algorithms, the improved Fast-Newman algorithm has faster calculation speed while satisfying the quality of network partitioning, and does not lose important nodes like the Louvain hierarchical clustering algorithm. It is more able to meet the actual computing needs of large-scale networks.

The power grid partition result of the improved algorithm is shown in Fig. 4. The original multi-voltage level ring network in the network is effectively decomposed.

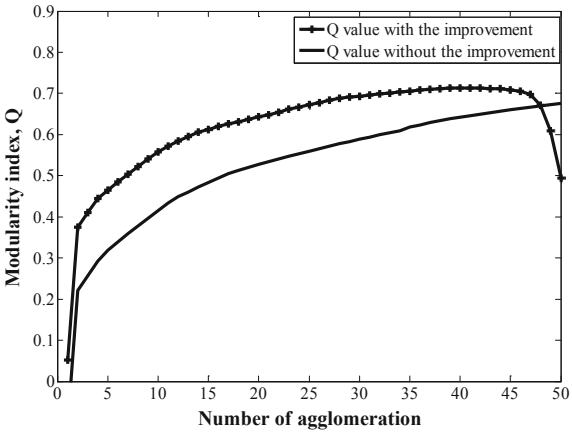

Fig. 3 The curve of modularity index Q

Table 2 Comparison of partition results of different algorithms

Algorithm	Number of partitions	Optimal modularity	Number of isolated nodes	Condensation time (s)
GN	8	0.738	0	20.2
Louvain	9	0.741	3	10.6
F-N	19	0.735	8	1.924
Improved F-N	10	0.713	0	0.201

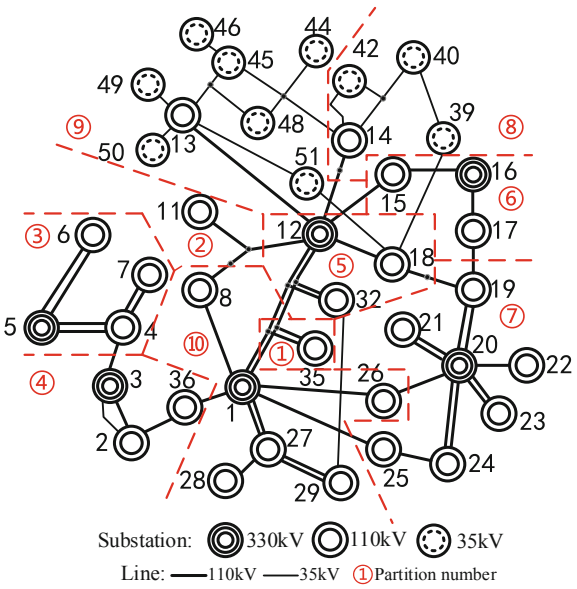

Fig. 4 The result of power grid partition

Table 3 The statistics of line loss calculation results

Partition number	Activ loss (MW)	Reactive loss (MVar)
1	0.275	3.14
2	0.475	1.53
3	0.152	4.75
4	1.613	5.55
5	0.253	2.69
6	0.442	6.32
7	0.387	7.28
8	0.084	0.51
9	0.263	1.72
10	0.921	9.88
Total partition	4.865	43.37
Whole network	4.849	43.06

The typical daily data is selected for load flow calculation. The calculation results of line loss for the whole network and each partition are shown in Table 3.

The calculation result of the all partitions has only a small difference compared with the total network loss. The active loss differs by 0.016 MW and the deviation rate is 0.33%. The reactive power loss is 0.31 MVar, and the deviation rate is 0.72%.

Compared with the time of convergence of load flow iteration, the parallel computing time is 0.017S, and the whole network calculation time is 0.126S. It is visible that parallel computing of partitions greatly saves computation time. On the other hand, as the scale of the power grid expands, this time savings will be more significant, meeting the needs of real-time line loss calculations for large-scale power networks.

The calculation results of the actual case show that:

1. The weighted Fast-Newman algorithm can effectively discover the community structure of the power grid and achieve efficient regional division.
2. The improved Fast-Newman algorithm effectively avoids the occurrence of isolated nodes in the partitioning process and greatly saves partition time.
3. Partition line loss calculation results are highly accurate, and can significantly reduce time cost in a distributed computing environment.

5 Conclusion

Fine line loss management is the basis for the development of scientific decision-making for loss reduction, and is also an inevitable requirement for the development of power grids. This paper proposes a partition line loss parallel calculation method based on complex network theory. The calculation results are highly accurate and can be calculated in real time, providing strong data support for line loss management.

After verification by actual examples, compared with other community discovery algorithms, the improved Fast-Newman algorithm can effectively discover the community structure of large-scale power grids, and has excellent calculation speed, which meets the requirements of real-time line loss calculation. The parallel computing of each partition is realized on the basis of network division, which overcomes the problem that the calculation of the theoretical line loss of large-scale network is difficult. How to further improve the accuracy of line loss calculation is the focus of the next research work.

Acknowledgements The research was financially supported by the State Grid Corporation Science and Technology Project (contract number: 522722180003).

References

1. Zhu Z, Ye F (2012) Improved method for theoretical line loss calculation of low-voltage distribution network. Electr Measur Instrum 49(11):6–10+70
2. Bin LI, Kang YAN, Fa LUO, Yidan LU (2018) Comprehensive application of optimal benchmarking in line loss lean management of city-level power grid enterprises. Autom Electr Power Syst 42(23):184–192

3. Jia CAO, Xiaoyuan XU, Zheng YAN et al (2017) Application of several Levenberg-Marquardt methods with higher-order convergence in power flow calculation. Power Syst Technol 41(04):1181–1187
4. Yajing GAO, Hongjia MIAO, Wenchuan WU et al (2015) An impedance compensation based forward/backward sweep power flow algorithm for three-phase four-wire distribution networks. Autom Electr Power Syst 39(07):47–51
5. Tiefeng Zhang, Xin Lv, Yueying Lv, Wanchun Yang (2015) Study of incomplete measured synchronous line loss calculation in distribution network. Electr Measur Instrum 52(01): 91–96
6. Dong YANG, Yutian LIU (2013) A new method for electromagnetic loop partitioning based on quantitative analysis of network community structure characteristics. Autom Electr Power Syst 37(21):66–71
7. Gaofeng PAN, Xinghua WANG, Xiangang PENG, Xiaomei WU (2013) Improved network partition and pilot node selection method for reactive power/voltage control based on community detection algorithm. Power Syst Prot Contr 41(22):32–37
8. Yu L, Sun Y, Xu R, Li K (2017) Improved particle swarm optimization algorithm and its application in reactive power partitioning of power grid. Autom Electr Power Syst 41(03): 89–95+128
9. Kerniighan BW, Lin S (1970) An efficient heuristic procedure for partitioning graphs. Bell Labs Tech J 49(2):291–307
10. Pothen A, Simon HD, Liou KP (1990) Partitioning sparse matrices with eigenvectors of graphs. SIAM J Matrix Anal Appl 11(3):430–452
11. Girvan M, Newman MEJ (2001) Community structure in social and biological networks. Proc Natl Acad Sci USA 99(12):7821–7826
12. Xie Z, Wang X (2005) An overview of algorithms for analyzing community structure in complex networks. Complex Syst Complex Sci 2(3):1–12
13. Newman MEJ (2004) Fast algorithm for detecting community structure in networks. Phys Rev E 69(6):066133
14. Wang X, Liu Y (2009) Overview of algorithms for detecting community structure in complex networks. J Univ Electr Sci Technol China 38(05):537–543

Daily Power Load Curves Analysis Based on Grey Wolf Optimization Clustering Algorithm

Chong Gao, Yaxiong Wu, Junxi Tang, Huazhen Cao and Lvpeng Chen

Abstract When the fuzzy C-means clustering algorithm (FCM) is applied to solve the problem of daily load curve clustering analysis, its performance is usually affected by selection of the initial clustering center and the sample similarity is often characterized directly by distance of each samples, which causes clustering easy to fall into local optimum. In this paper, the daily load characteristic value index is used to deal with the data dimension reduction of the daily load curve and a fuzzy C-means clustering algorithm optimized by grey wolf optimizer (GWO-FCM) is proposed. GWO-FCM uses GWO to optimize the initial clustering center for FCM, which combines the global search capability of GWO and the local search capability of FCM The results shows that the proposed method can perform daily load curve clustering analysis effectively and obtain good robustness.

Keywords Clustering analysis of daily load curves · Data dimension reduction · GWO-FCM

Foundation item: Supported by the Technical Projects of China Southern Power Grid (No. GDKJXM20172939).

C. Gao · Y. Wu · J. Tang · H. Cao
Grid Planning & Research Center, Guangdong Power Grid Co. Ltd., CSG, Guangzhou 510030, China

C. Gao · Y. Wu · J. Tang · H. Cao
Guangdong Power Grid Development Research Institute Co. Ltd., Guangzhou 510030, China

L. Chen (✉)
Suzhou Huatian Power Technology Co. Ltd., Suzhou 215000, China
e-mail: chenlvpeng123@163.com

Y. Xue et al. (eds.), *Proceedings of PURPLE MOUNTAIN FORUM 2019-International Forum on Smart Grid Protection and Control*, Lecture Notes in Electrical Engineering 585, https://doi.org/10.1007/978-981-13-9783-7_54

1 Introduction

With the acceleration of social and economic growth and the vigorous development of emerging industries, there will emerge more and more types of power users. At the same time, the differences of typical daily load curve characteristics of different power consumers in the same industry are also increasing. Taking traditionally simple and crude analysis methods based on user-reported categories as load classifications are no longer suitable for the development of next-generation power systems and energy Internet. The refined daily load curve characteristic analysis can help the grid to perform real-time optimization scheduling, formulate reasonable demand response management measures, the expansion planning and distribution network planning [1].

At present, many clustering analysis methods have been used to extract typical daily load characteristics of power users [2, 3], such as Fuzzy C-Means Algorithm (FCM) [4], K-MEANS algorithm [5], DBSCAN algorithm [6] and self-organizing map neural network(SOM) [7], etc. Among them, FCM algorithm performs excellent in operational efficiency, clustering effect and robustness of the algorithm. However, there are two disadvantages to performing daily load curve clustering directly using the traditional FCM algorithm:

(1) Clustering analysis was performed directly using the distance between the original daily load curve data as a similarity criterion. This will lead to a poorer clustering performance and ignore the intrinsic characteristics of the load curve.
(2) The clustering effect of FCM algorithm is susceptible to the initial point position.

To solve the above problems, this paper firstly selects the load characteristic index to reduce the dimension of the original daily load curve data, and proposes a fuzzy mean clustering algorithm based on GWO to perform the clustering analysis of daily load curve. The proposed algorithm combines the advantages of the GWO algorithm and the FCM algorithm. It can use GWO's global search capability to search the optimal initial clustering center for FCM algorithm quickly, reduce the sensitivity of FCM algorithm to the initial clustering point, obtain the approximate global optimal clustering and improve the clustering effect of daily load curve. In a word, the proposed method can solve two shortcomings of traditional cluster analysis mentioned above.

2 Dimensionality Reduction of Daily Load Curve Data

In a traditional clustering method, the similarity of data samples is usually judged by the distance between the original sample data. However, as a kind of time series data, the daily load curve data is greatly affected by factors, such as user type, weather and time-sharing price policy. As a result, the power consumption

Table 1 Daily load characteristic indexes

Time slot		Indicator name	Calculation method
Full day	00:00–24:00	Load ratio	$I_1 = P_{av}/P_{max}$
		Peak-to-valley rate of full-day	$I_2 = (P_{max} - P_{min})/P_{max}$
Peak period	14:00–17:00 19:00–22:00	Load ratio of peak period	$I_3 = P_{av.peak}/P_{max}$
Regular period	08:00–14:00 17:00–19:00 22:00–24:00	Load ratio of regular period	$I_4 = P_{av.sh}/P_{max}$
Valley period	00:00–8:00	Load ratio of valley period	$I_5 = P_{av.val}/P_{max}$

characteristics of user data cannot be directly reflected by the distance. Under high-dimensional raw samples, data may exhibit undesirable equidistance. The daily load clustering analysis not only needs to pay attention to the equidistance of the daily load curve data, but also analyzes the similarity of its shape and contour to understand the user's electricity habits and characteristics.

The load characteristic index can comprehensively reflect the user's power consumption characteristics [8]. Five characteristic indexes are selected according to the division plan of the peak and valley period of Guangdong Power Grid for data dimensionality reduction. The definitions and calculation methods of indexes are shown in Table 1.

In Table 1, P represents the power load; the subscripts av, max and min represent the mean, the maximum and the minimum respectively; the subscripts peak, val and sh represent the peak period, the valley period and the shoulder period, respectively.

The daily load characteristics of the load users can be described from the time scales of the whole day, the peak period, the shoulder period and the valley period using the indexes $I_1 - I_5$. The physical meanings of each indexes are different, which can describe the internal characteristics of the daily load curve more comprehensively.

3 Fuzzy C-Means Clustering Algorithm Based on GWO

3.1 Fuzzy C-Means Clustering Algorithm

FCM is a clustering classification algorithm that ultimately makes the similarity between the samples classified into the same class as high as possible, while making the difference between the samples classified into the different class as high as possible. FCM is improved on the basis of ordinary C-means clustering, and the concept of fuzzy set is introduced to realize flexible fuzzy clustering [9].

3.2 GWO

The GWO is a group search intelligent algorithm proposed by Mirjalili S et al. The algorithm treats each feasible solution as a wolf and treats the optimal solution as a prey. By referring to the wolf group level and hunting habit, each solution is graded and searched to find the optimal solution [10].

3.3 GWO-FCM Clustering Algorithm

As a gradient-based search algorithm, FCM clustering algorithm has the advantages of rapid convergence and excellent local search ability. The traditional FCM algorithm starts from the initial cluster center matrix or the fuzzy partition matrix. Since the initial matrix is randomly generated, if the initial values are different, the clustering results may be different. Therefore, if the initial value is not properly selected, the clustering result may fall into local optimum. This problem is particularly prominent when the number of samples is large. The GWO has excellent global search ability, rapid convergence speed, and is not easy to fall into local optimum. Therefore, considering the combination of GWO and FCM algorithm to fully utilize the advantages of global optimization of GWO and strong local convergence of FCM algorithm, reduce the dependence of FCM algorithm on initial value selection, and obtain better clustering effect.

Coding of Grey Wolf Particle. It can be seen from the above analysis that the FCM algorithm can select the fuzzy partition matrix $\boldsymbol{U}$ or the cluster center matrix $\boldsymbol{P}$ for initialization. For the clustering analysis problem in daily load curve of power users, it is usually necessary to process and analyze the load curve data of a large number of users, which will result in that the data number n of the data sample set is too large. If the elements in the fuzzy partition matrix $\boldsymbol{U}$ are used to form the code of the grey wolf, the coding dimension reaches the $c \times n$ dimension, and the high dimension will affect the efficiency of the GWO. After the data reduction operation on the original data, the feature quantity m of a single piece of data is often much smaller than the number of its data pieces n. Therefore, the element structure of the cluster center matrix $\boldsymbol{P}$ is selected as the encoding of the grey wolf particles, and the particle dimension can be reduced to $c \times m$ dimension. Then the particle code can be expressed as:

$$\boldsymbol{p}_i = (p_{11}, \ldots, p_{1m}, \ldots, p_{c1}, \ldots, p_{cm}) \tag{1}$$

Fitness Function. The FCM algorithm needs to construct a suitable fitness function to evaluate the quality of each grey wolf particle. The fitness function defined in this paper is as follows:

$$\min J(\boldsymbol{U},\boldsymbol{P}) = \sum_{j=1}^{n}\sum_{i=1}^{c} u_{ij}^{g} d_{ij}^{2} \tag{2}$$

$$f(\boldsymbol{p}_i) = \frac{1}{J(\boldsymbol{U},\boldsymbol{P})} \tag{3}$$

For an individual grey wolf, the smaller the corresponding target value $J(\boldsymbol{U},\boldsymbol{P})$, the higher the fitness value $f(\boldsymbol{p}_i)$, indicating that the clustering effect is better.

The position of each grey wolf in the wolves represents a feasible solution in the problem space, indicating a method for selecting the initial cluster center. Therefore, the position of wolves α, β and δ in each iteration of the GWO. The update of information only needs to correspond to each initial clustering center according to the fitness value.

Conversion conditions between GWO and FCM algorithm. The GWO-FCM algorithm is mainly divided into two parts: the first part uses the GWO to search for a better initial clustering center in the feasible domain, and the second stage uses the local search ability of the FCM algorithm. Based on the optimal initial clustering center, the iterative calculation performs local optimization and completes cluster analysis.

The variance of the wolf population fitness is defined as follows:

$$\sigma^2 = \frac{1}{z}\sum_{i=1}^{z}\left[f(p_i) - f_{avg}\right]^2 \tag{4}$$

where z is the wolf number; f_{avg} is the average of all grey wolf individuals. The magnitude of fitness variance σ^2 characterizes the degree of convergence of grey wolf individuals. When the value of σ^2 is small, the degree of dispersion of the wolf group's fitness value is not high, the GWO tends to converge, and its global search ability begins to decline. Therefore, when the value of σ^2 is less than the set threshold ξ, the GWO-FCM algorithm is switched from the first stage to the second stage, that is, the clustering analysis is performed by using the FCM, so that the later convergence is faster.

The algorithm flow of GWO-FCM. The flow chart of GWO-FCM algorithm are shown in Fig. 1.

The GWO-FCM algorithm is described as follows:

Step(1): Initialize the wolves. Set the required clustering number c, randomly generate c clustering centers to encode the grey wolf position, and then initialize the position of a grey wolf; repeat S times to obtain the initial wolf composed of S initial grey wolf group. Then calculate the fitness degree of each wolf in the wolves, and select the top three grey wolf individuals, which are recorded as wolf α, β and δ in order;

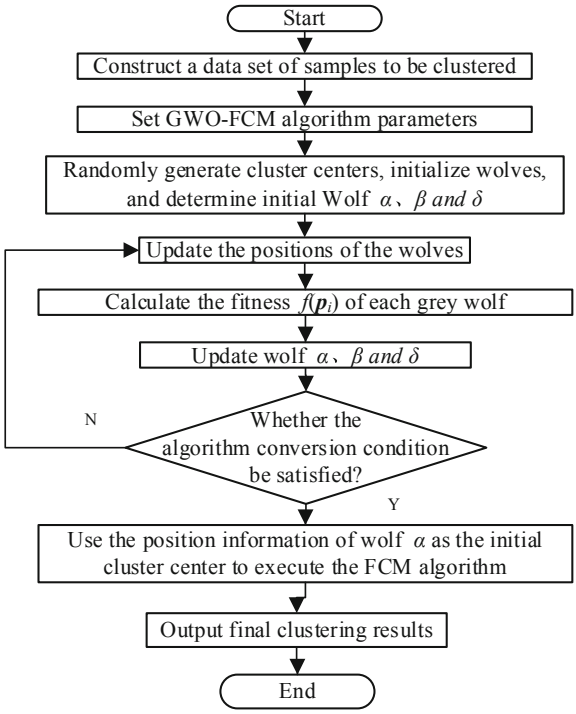

Fig. 1 Flow chart of GWO-FCM algorithm

Step(2): Update the wolf position. Updating the positions of the wolves in the wolves;

Step(3): Calculate the fitness value of each grey wolf $f(\boldsymbol{p}_i)$;

Step(4): Update the wolf rank. Select three grey wolves with the best fitness value, and update the positions of wolf α, β and δ in order;

Step(5): Determine the conversion conditions. If the wolf group fitness variance σ^2 is less than the threshold ξ or the number of algorithm loop iterations reaches the maximum number of iterations, the GWO iterative global search phase is stopped, and the wolf α position is set as the initial cluster center of the FCM algorithm; otherwise, go to Step(2);

Step(6): Use the result of step(5) as the initial clustering center and execute FCM algorithm. The final clustering center $\boldsymbol{P}$ and the fuzzy partition matrix $\boldsymbol{U}$ are output according to the principle of maximum membership.

4 Implementation Method

4.1 Dataset Preprocessing

Data Cleaning. First, remove the load curve data with abnormal or missing data. Then use the smoothing formula or other interpolation algorithm to change or fill the daily load curve data with a small amount of abnormal or missing data.

Input sample set construction. The daily load curve data of the completed data cleaning is subjected to data dimensionality reduction using the daily load characteristic indicators listed in Table 1. The load data in the existing metrology automation system is usually 96 sampling points per day, and the sampling interval is 15 min. After data cleaning has been completed, the number of remaining daily load data is N, the dimension of the original data sample set is reduced from the original $N \times 96$ dimension to $N \times 5$ dimension by data dimension reduction.

4.2 Evaluation Index of Clustering Effectiveness

The silhouette coefficient can be used to reflect the tightness and separability of the class. This index can determine the optimal cluster number and evaluate the clustering effect when the number of clusters is unknown. For the profile x, the profile coefficient characteristic index is defined as shown in Eqs. (5)–(7):

$$SIL(x) = \frac{D_a(x) - D_b(x)}{\max(D_a(x), D_b(x))} \tag{5}$$

$$D_a(x) = \frac{\sum_{s \in C_k, s \neq x} d(x, s)}{|C_k| - 1} \tag{6}$$

$$D_b(x) = \min_{C_j : 1 \leq j \leq c, j \neq k} \left\{ \frac{\sum_{s \in C_k,} d(x, s)}{|C_j|} \right\} \tag{7}$$

where $SIL(x)$ represents the silhouette coefficient of the sample x; x represents the sample belonging to the class C_k; $D_a(x)$ and $D_b(x)$ represent the average distance between the x and C_k internal residual objects, and the minimum average distance of x and non-C_k class objects, respectively.

The silhouette coefficient varies between [−1, 1]. When the silhouette coefficient is closer to 1, indicating that the tightness of C_k class and class separability to which x belongs are better, and so is the clustering effect. If the silhouette factor is less than 0, the clustering fails.

The average of the overall clustering was evaluated using the mean of the silhouette coefficients of all data samples. It is expressed as Eq. (8):

$$SLIMEAN = \frac{1}{N} \sum_{i=1}^{N} SIL(x_i) \tag{8}$$

The larger the *SLIMEAN*, the better the overall clustering effect. The maximum number of clusters c that make *SLIMEAN* is the optimal number of clusters.

5 Experimental Results and Analysis

5.1 Input Dataset Construction

The clustering study selected the actual daily load curve data of 1536 users in a normal working day in May 2017 in a city of Guangdong. The data collection upload interval is 15 min, and the amount of single-day load data per user is 96 points. The original daily load curve data is preprocessed using the construction method of the input data set described in Sect. 4. After processing, the final example contains 1498 data strips, and the matrix to be clustered falls from 1498 × 96 dimensions to 1498 × 5 dimensions. Compare the clustering analysis of the processed matrix to be clustered by the algorithm proposed in this paper with the clustering results of the FCM algorithm after normalizing the data with 96 sampling points as the input.

The specific parameters are set as follows: the maximum cluster number $c_{max} = 8$; the minimum clustering number $c_{min} = 2$; the fuzzy degree coefficient $g = 2$; the wolf group size is 25; the maximum iteration number takes $l_{max} = 300$. The parameters of the traditional FCM algorithm are as follows: the degree of fuzzification is $g = 2$; the maximum number of iterations is $t_{max} = 100$, and the threshold of the objective function is 10^{-7}.

5.2 Results of Clustering

Table 2 shows the clustering effectiveness index calculation results of the two methods in the case of setting different cluster numbers. Figure 2 shows the trend of the mean value of the contour coefficients of the two methods under different clustering numbers. Combined with Table 2 and Fig. 2, the SLIMEAN mean value of both algorithms is maximized when the number of clusters is 4. Therefore, the optimal number of clusters for both algorithms is 4. At the same time, the SLIMEAN mean value index using the clustering result of this method is larger than the SLIMEAN mean value obtained by the traditional FCM method when the clustering number takes any other value, and the clustering effect is better. This also shows that the proposed method combines the global search ability of GWO with the local search ability of FCM algorithm, and reduces the possibility that the clustering result converges to local optimum.

Figure 3 shows the clustering results of the daily load curve of the clustering algorithm, where the red curve is the average of the overall load of the class. Since the algorithm has the process of data dimensionality reduction, the clustering center of each dimensionality reduction index can be obtained, and various typical load curves cannot be directly obtained. This paper considers that the daily load curve averaged as the same type of load is the typical daily load curve for this type of load. In the clustering results obtained by the algorithm of this paper, the number of

Table 2 Calculation results of clustering effectiveness index

GWO-FCM		FCM	
Cluster number	SLIMEAN	Cluster number	SLIMEAN
2	0.6801	2	0.6801
3	0.6887	3	0.6638
4	**0.7018**	4	**0.6975**
5	0.6053	5	0.5931
6	0.4778	6	0.4722
7	0.4655	7	0.3563
8	0.4665	8	0.4613

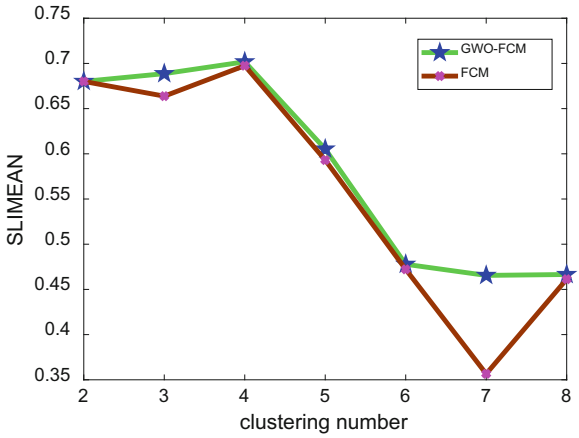

Fig. 2 Variation trend of clustering effectiveness index

curves belonging to each category are 384, 354, 362 and 398, respectively. The traditional clustering algorithm is used to obtain the clustering results, and the number of curves belonging to each category are 375, 365, 372 and 386, respectively the number of classifications and classification results are basically the same.

5.3 Robustness Test of Algorithm

Select the 6 types of daily load curves known in [11]. Based on the known correct clustering results, random noise with a ratio r is added to each data point of each typical curve to obtain The daily load curves of 6 categories and 200 strips of each class are used as cluster samples to verify the robustness of the clustering algorithm.

The robustness of the algorithm is analyzed by using the optimal clustering number, clustering validity index and accuracy. In this paper, the ratio of the total number of correctly classified load curve data to the number of all load curves is taken as the accuracy rate. The results of the comparison of the robustness test results are shown in Table 3.

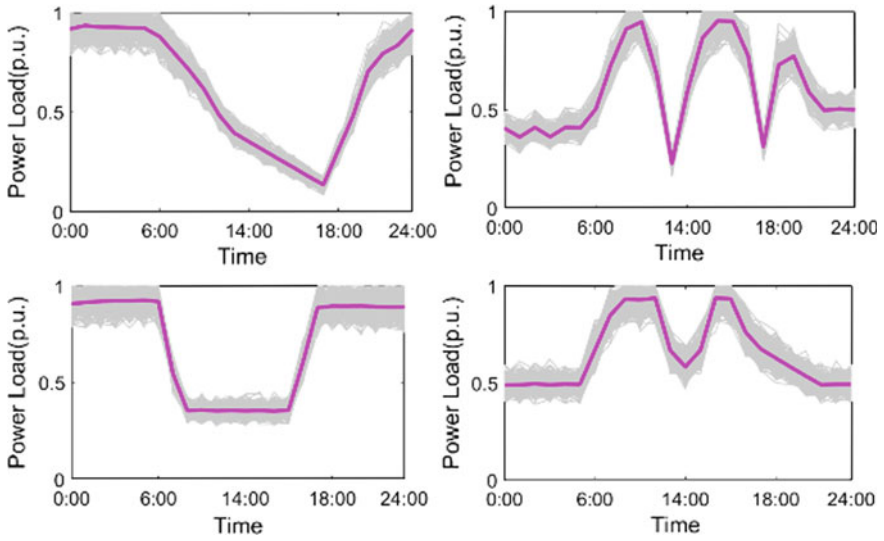

Fig. 3 Daily load curve clustering result based on the proposed algorithm

Table 3 Comparison of algorithm robustness

Noise ratio/%	GWO-FCM			FCM		
	Optimal cluster number	Cluster validity index	Accuracy (%)	Optimal cluster number	Cluster validity index	Accuracy (%)
5	6	0.8121	100.0	6	0.8121	100.0
10	6	0.6921	100.0	5	0.6616	83.3
15	6	0.6029	100.0	5	0.3962	83.4
20	6	0.5172	99.9	5	0.3376	83.4
25	6	0.4257	99.8	5	0.3337	82.9
30	5	0.3552	83.4	4	0.2766	66.7
35	3	0.2417	50.0	3	0.2152	49.8
40	3	0.1983	50.0	3	0.1819	49.8

It can be seen from Table 3 that when the noise ratio r is increased, the optimal clustering numbers of the two clustering algorithms are changed, and the clustering effectiveness index and the accuracy rate are both decreased. When the noise ratio r is less than 25%, the optimal clustering number is always 6 and the accuracy is close to 100%. For the traditional FCM algorithm, when the noise ratio r increases to 10%, the optimal clustering number changes, the classification accuracy begins to decrease, and the robustness is poor. Although the noise ratio r is greater than 25%, the optimal clustering number of the two algorithms is not 6, the clustering effectiveness index and accuracy of the proposed method are slightly higher than

the traditional FCM algorithm. Therefore, the robustness of the proposed method is better than the traditional FCM algorithm.

6 Conclusion

In this paper, a daily load curve reduction dimension clustering method based on grey wolf optimization and fuzzy mean clustering algorithm is proposed. Firstly, the load characteristic index is used to reduce the data of the original daily load curve data, and the proposed algorithm is used to perform the daily load curve reduction dimension clustering analysis. The example shows that this method can improve the global search ability of traditional FCM clustering algorithm and reduce the possibility that the clustering result falls into local optimum. It has engineering feasibility and good robustness.

With the continuous development of smart grids, the requirements for refined power grid planning and grid operation management are constantly improving. How to combine multi-source data fusion, select typical load characteristic index system, and establish a more refined clustering method is the future research direction.

References

1. Bofeng L, Yunfei M, Hongjie J et al (2018) Decision method of power supply access for large consumers based on load feature library. Autom Electr Power Syst 42(6):66–72
2. Al-Otaibi R, Jin N, Wilcox T et al (2017) Feature construction and calibration for clustering daily load curves from smart-meter data. IEEE Trans Industr Inform 12(2):645–654
3. Zigui J, Rongheng L, Fangchun Y et al (2018) A fused load curve clustering algorithm based on wavelet transform. IEEE Trans Industr Inf 14(5):1856–1865
4. Kong X, Hu Q, Dong X, Zeng Y et al (2017) Load data identification and repair method based on improved fuzzy C-means clustering. Autom Electr Power Syst 41(09):90–95
5. Tzortzis L (2009) The global Kernel K-Means algorithm for clustering in feature space. IEEE Trans Neur Netw 20(7):1181–1194
6. Guilan W, Guoliang Z, Hongshan Z et al (2016) Fast clustering and anomaly detection technique for large-scale power data stream. Autom Electr Power Syst 40(24):27–33
7. Kohonen T (1982) Self-organized formation of topologically correct feature maps. Biol Cybern
8. Xiaodi W, Junyong L, Youbo L et al (2019) Typical load curve shape clustering algorithm using adaptive piecewise aggregation approximation. Autom Electr Power Syst 43(01):110–121
9. Phu VN, Dat ND, Ngoc Tran VT et al (2017) Fuzzy C-means for english sentiment classification in a distributed system. Appl Intell 46(3):717–738
10. Mirjalili S, Mirjalili SM, Lewis A (2014) Grey wolf optimizer. Adv Eng Softw 69(3):46–61
11. Chicco G, Napoli R, Piglione F (2006) Comparisons among clustering techniques for electricity customer classification. IEEE Trans Power Syst 21(2):933–940

GPU-Accelerated Batch Electromechanical Transient Simulation of Power System

Yi Wang, Licheng Sun, Ziheng Wang and Yanjun Feng

Abstract State-of-the-art Graphics Processing Unit (GPU) has superior performances on float-pointing calculation and memory bandwidth, and therefore has great potential in many computationally intensive power system applications, one of which is batch-Electromechanical transient time simulation (ETTS) of power system. The computation speeds of the traditional method is slow. When dealing with batch simulation in multiple scenarios, the power consumption of multi-machine cluster system is large and the acceleration effect is limited by the number of processors. This paper proposes a superior GPU-Accelerated algorithm for batch-ETTS based on the implicit integration alternating solution method (IIASM), which extracts data-level fine-grained parallelism and increases the efficiency of memory access by combed design in solving batch dynamic element injection current and batch sparse linear systems (SLS). By offloading the tremendous computational burden to GPU, the algorithm of this paper can limit the time in one alternate iteration of single ETTS within 0.5 ms for one system with over 10,000 nodes.

Keywords GPU · Batch-ETTS · Implicit integration alternating solution method · SLS

Y. Wang (✉)
NARI Group Corporation (State Grid Electric Power Research Institute), Nanjing 210003, China
e-mail: wang-yi2@sgepri.sgcc.com.cn

NARI Technology Co. Ltd., Nanjing 211106, China

State Key Laboratory of Smart Grid Protection and Control, Nanjing 211106, China

L. Sun
Anhui Electric Power Research Institute, Hefei 230061, China

Z. Wang · Y. Feng
Southeast University, Nanjing 210096, China

Y. Xue et al. (eds.), *Proceedings of PURPLE MOUNTAIN FORUM 2019-International Forum on Smart Grid Protection and Control*, Lecture Notes in Electrical Engineering 585, https://doi.org/10.1007/978-981-13-9783-7_55

1 Introduction

Electromechanical transient simulation of power system, an effective approach to analyze the stability of power system, is one of the significant simulation tools to the power system planning, dispatching and scientific research [1, 2]. Nowadays, there are two main methods towards electromechanical transient simulation, namely time simulation [3] and direct method [4]. Time simulation is the most common approach to the execution of electromechanical transient simulation of power system, but serial electromechanical transient simulation algorithm often consumes a lot of time and fails real-time requirements. The analysis of the transient process of power grid depends on detailed modeling and simulation. Fine-grained parallel computing devices such as Graphics Processing Unit (GPU) can significantly improve the transient simulation efficiency of power grid [5–7].

State-of-the-art GPU, with Single Instruction Multiple Threads (SIMT) architecture, has superior performances on float-pointing calculation and memory bandwidth. Therefore, GPU offers an alternative and potentially superior solution for batch-ETTS problem.

When referring to existing researches to accelerate ETTS, two different technical frameworks can be proposed: Space Paralleled Algorithm and Time Paralleled Algorithm [8]. The principle of space paralleled algorithm is to divide large power systems into several subsystems and calculate [9, 10]. Bordered block diagonal form (BBDF) [11, 12], which is implemented on the cluster processing LU factorization. Time paralleled algorithm was first introduced into power system transient simulation by Alvarado [13]. Its principle is to solve the difference equations of differential equations on multiple integral time steps simultaneously with the network equations. Two kinds of iterative methods, namely Gauss-Jacobi-Newtown (G-J) [14] and Gauss-Seidel-Newtown (G-S) [15, 16], are commonly used today. But they are both hard to be implemented as program. In this regard, we proposed a novel parallel algorithm for batch-ETTS on GPUs.

The paper is organized as follows. Section 2 presents the principles and process of implicit integration alternating solution method [17]. In Sect. 3, the proposed GPU-accelerated batch up-looking LU factorization and batch dynamic element injection current solver are presented. Section 4 proposes a novel GPU-accelerated batch-ETTS algorithm. Three cases are tested and compared in Sect. 5. Finally, Sect. 6 makes the conclusion of this paper.

2 Algorithm Principles

2.1 The Principles of IIASM

Implicit integration alternative solution has both the good numerical stability of implicit integral and the flexibility of explicit integral. Figure 1 shows the workflow of this algorithm.

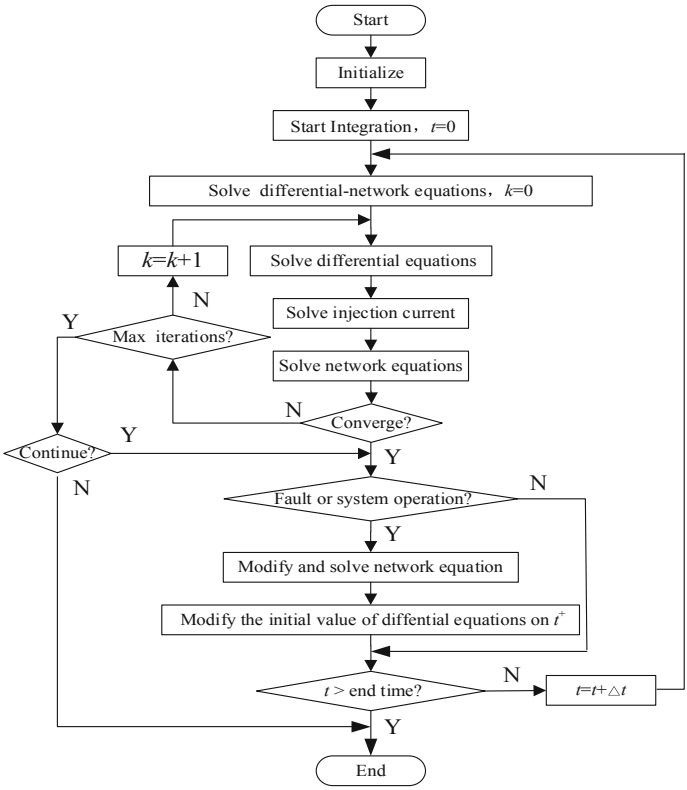

Fig. 1 The basic workflow of implicit alternative solution

The mathematical model of dynamic elements are expressed as

$$\dot{X}_d = f_d(X_d, V_d) \tag{1}$$

$$I_d = g_d(X_d, V_d) \tag{2}$$

where $\boldsymbol{X}_d$ is the state vector of dynamic elements, $\boldsymbol{I}_d$ is the injection current of dynamic element, $\boldsymbol{V}_d$ is the node voltage of dynamic component.

Differential-algebraic equation are expressed as

$$\dot{X} = f(X, V) \tag{3}$$

$$I(X, V) = Y_N V \tag{4}$$

where $\boldsymbol{X}$ is system state vector, $\boldsymbol{V}$ is the node voltage vector, $\boldsymbol{I}$ is the node injection current vector, $\boldsymbol{Y}_N$ is the node admittance matrix.

Using the state vector $\boldsymbol{X}_n$ and the node voltage $\boldsymbol{V}_n$ of time t_n, the detailed principle of solving $\boldsymbol{X}_{n+1}$ and $\boldsymbol{V}_{n+1}$ of time $t_{n+1} = t_n + \Delta t$ is

From (3) and (4) we can get the following non-linear equations.

$$X_{n+1} = X_n + \frac{\Delta t}{2}[f(X_n, V_n) + f(X_{n+1}, V_n)] \tag{5}$$

$$I(X_{n+1}, V_{n+1}) = Y_N V_{n+1} \tag{6}$$

Then the iterative solution is used to solve non-linear equations. LU factorization is executed on the coefficient matrix before iteration begins. We can simply use factorized table to do backward or forward substitution.

2.2 The Principles of Dynamic Elements Solver

The dynamic component on the power system network only affects the injection current of the node where it is located. Moreover, this current is only related to the state variables of the dynamic element and the node voltage, which does not depend on other dynamic elements. This is the key to decoupling implicit integration alternative solution and it is the main reason why we can use GPU to parallelize and boost this problem.

The classical second-order model of the synchronous generator is expressed as

$$\begin{cases} T_J \dfrac{d\omega}{dt} = T_m - \mathrm{Re}(\dot{E}' \overset{*}{I}) - D(\omega - 1) \\ \dfrac{d\delta'}{dt} = \omega - 1 \end{cases} \tag{7}$$

$$\dot{U} = \dot{E}' - (r_a + \mathrm{j}X'_d)\dot{I} \tag{8}$$

where Re is real part calculation, and * means conjugation, $\dot{E}' = E'\angle\delta'$.

In the above classical second-order model, there are two state variables, namely ω and δ'. For the sake of simplicity, the first formula in Eq. 7 is abbreviated as $\omega = f_d(\omega, \dot{I})$. Knowing the kth iteration result of the $n + 1$ time step: state vector ω^k_{n+1}, δ'^k_{n+1} and voltage $\dot{U}^k_{n+1}$, the detailed process of solving the k+1th iteration of current is shown below:

Step 1, solving the current $\dot{I}^k_{n+1}$: $\dot{I}^k_{n+1} = (E'\angle\delta'^k_{n+1} - \dot{U}^k_{n+1}) \Big/ (r_a + jX'_d)$

Step 2, solving the state vector:

$$\omega_{n+1}^{k+1} = \omega_n + \frac{\Delta t}{2}\left[f_d(\omega_n, \dot{I}_n) + f_d(\omega_{n+1}^k, \dot{I}_{n+1}^k)\right] \tag{9}$$

$$\delta'^{k+1}_{n+1} = \delta'_n + \frac{\Delta t}{2}\left[(\omega_n - 1) + (\omega_{n+1}^{k+1} - 1)\right] \tag{10}$$

Step 3, solving the current $\dot{I}_{n+1}^{k+1}$: $\dot{I}_{n+1}^{k+1} = (E' \angle \delta'^{k+1}_{n+1} - \dot{U}_{n+1}^k) \Big/ (r_a + jX'_d)$

Step 4, replacing $\dot{I}_{n+1}^k$ and ω_{n+1}^k with $\dot{I}_{n+1}^{k+1}$ and ω_{n+1}^{k+1}, continue step 2 and step 3

Step 5, comparing whether the $\dot{I}_{n+1}^{k+1}$ error obtained by the previous two calculations is less than the converged allowance. And if it is less than, the end will occur; otherwise, continue the iteration of *Step 4*.

3 GPU-Based Parallel Algorithms of IIASM

In compliance with SIMT architecture, four general design criteria for GPU-based algorithms should be followed. Criterion 1: exploring parallelism fully to saturate the numerous computing cores on GPU. Criterion 2: fulfilling coalesced memory access to improve memory efficiency. Criterion 3: avoiding thread divergence of thread warp. Criterion 4: reducing data communication between CPU and GPU. In the workflow of IIASM, solving SLS and dynamic element injection current are the two most time-consuming parts, so the GPU-accelerated algorithms are elaborated according to the four design criteria below.

3.1 GPU-Accelerated Single SLS LU Factorization

As shown in Table 1, in order to accelerate the up-looking LU factorization, multiple GPU threads are used to solve the executable rows concurrently. This kind of parallelism is determined by the sparse structure of L. As is shown in Fig. 2, the number of rows which can be parallelized in each layer declines dramatically as the number of layers increases. This phenomenon will be more notable in matrices with higher order (Tables 1, 2 and Fig. 2).

In view of this phenomenon, Domino Algorithm in Table 2 is proposed. With Domino Algorithm, we can do part of the factorization operation ahead of time, other than waiting for all the dependencies to finish, thus increased the efficiency.

Table 1 Hierarchical paralleled sparse up-looking LU factorization

Algorithm 1 Hierarchical paralleled sparse up-looking LU factorization

```
// l represents the number of layers
  for i = 1: l do
    while there are still undo rows in the current level do in parallel
      allocate M blocks for M (i) rows in the i^st level
      // M (i) represents the i^th layer have M (i) rows in total
      // in one block
      32 threads in one block factorize one row in parallel
    end while
  end for
```

Table 2 Domino optimization based paralleled up-looking LU factorization

Algorithm 2 Domino optimization based Paralleled up-looking LU factorization

```
for i = 1: n do //n means the order of the matrix
  for j = 1 : K (i)-1 where L( K (i), j) ≠ 0 do
  //K (i) represents the i^th row to be eliminated
    while mark (j) == 1 do //mark (j) is the flag bit of row j
      multi-threads in one block factorize K (i) row in parallel
    end while
  end for
  Mark (K (i)) = 1; //put its flag bit as 1 when K (i) row is done
end for
```

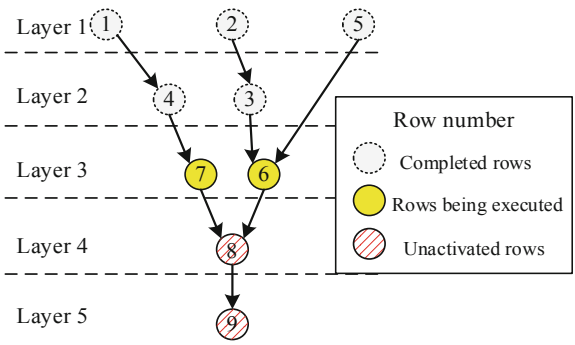

Fig. 2 The dependence graph of a 9-order matrix

3.2 GPU-Accelerated Batch SLS LU Factorization

Considering that batch electromechanical transient simulation contains a large number of sparse structures, a batch up-looking LU factorization algorithm is designed to realize a bunch of sparse matrices LU factorization. To be concrete, the principle is shown in Fig. 3. The principle of batch sparse matrices up-looking LU factorization mainly consists of the following points: (1) Unified sparse structure; (2) Task-level parallelism; (3) Memory merge access principle. And Batch LU factorization algorithm is given in Table 3.

The principle of GPU-accelerated batch triangular equations solution is similar to the batch up-looking LU factorization Algorithm. A thread block is used to update the right vector of the same row of all trigonometric equations. The right vector is also stored in memory continuously.

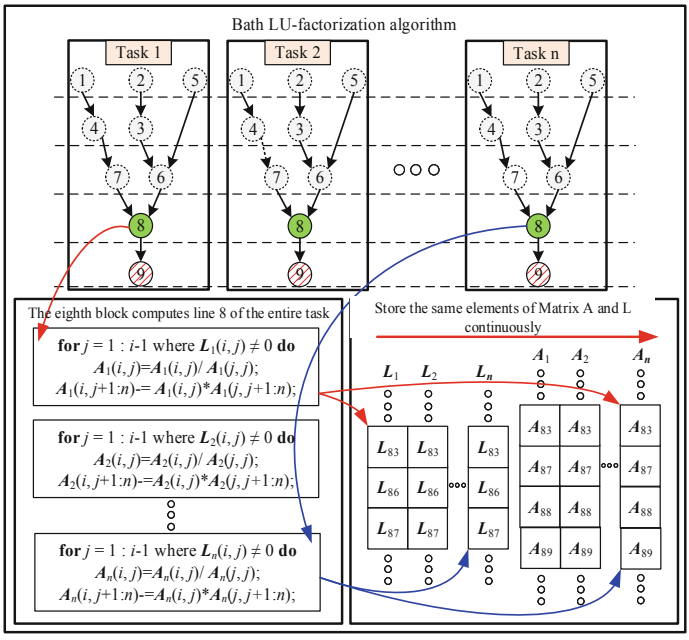

Fig. 3 Batch LU factorization algorithm schematic diagram

Table 3 GPU-based batch LU factorization algorithm

Algorithm 3 GPU-based Batch LU factorization algorithm

while there are unfinished rows do in parallel
//Thread block i for row i of the batch LU task.
$i \leftarrow$ block ID and $t \leftarrow$ thread ID in this block;
for j = 1 : i-1 where $\boldsymbol{L}_t(i,j) \neq 0$ **do**
$\boldsymbol{A}_t(i,j) = \boldsymbol{A}_t(i,j) / \boldsymbol{A}_t(j,j)$;
$\boldsymbol{A}_t(i, j{+}1{:}n) = \boldsymbol{A}_t(i,j) * \boldsymbol{A}_t(j, j{+}1{:}n)$;
end for
Set $\boldsymbol{K}_t(i)$ to true;
end while

3.3 GPU-Accelerated Batch Dynamic Element Solver

The injection current calculation process of each motor is the same, but the number of iterations is different. According to the principle above, tasks of solving injection current for dynamic elements in electromechanical transient simulation is packaged and solved in batch. The details are shown in Fig. 4.

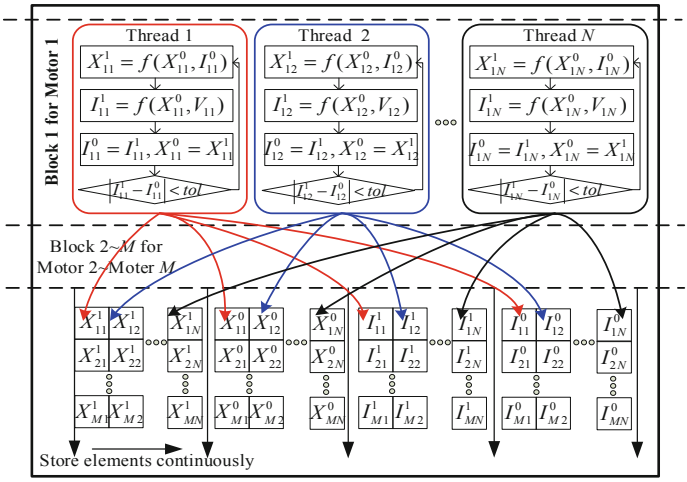

Fig. 4 Optimization design of batch dynamic element injection current solver

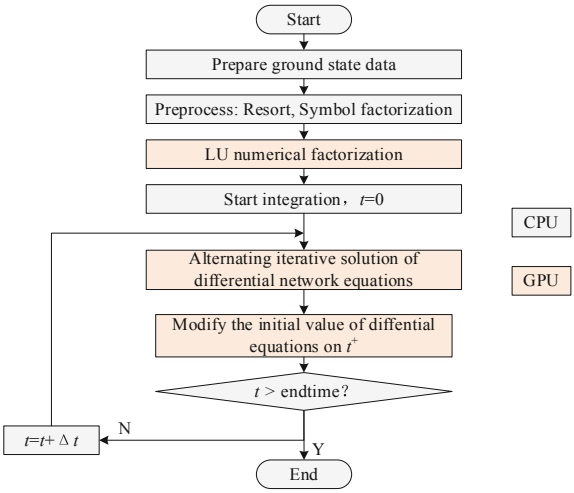

Fig. 5 GPU-accelerated batch-ETTS algorithm for multiple scenarios

4 Batch-ETTS Algorithm Based on IIASM

Based on the batch LU factorization and dynamic element injection current solver algorithm, a novel GPU-accelerated batch-ETTS algorithm for multiple scenarios is proposed in this section.

The framework of the proposed GPU-accelerated batch-ETTS algorithm is given in Fig. 5.

5 Case Study and Performance Comparison

5.1 Case Study

The test platform is the server equipped with a NVIDIA Tesla K40 GPU and two 6-core Intel Xeon E5-2620 CPU. The operating system is CentOS 6.7 and the CUDA version is 8.0. The three cases are IEEE-118 bus test case, European 1354-bus system case and 9241-bus system case extracted from MATPOWER [18].

(1) Batch dynamic element injection current solver

The detail test information of case 3 with 1445 generators is presented in below. Table 4 illustrates that the time of single simulation quickly tends to saturation with the increase of batch number, and finally gradually tends to 0.014 ms.

(2) Batch SLS solver

According to Table 5, when the batch number is under 256, time increases rather slowly with that becoming larger. When the batch scale is under 256, the band

Table 4 Injection current of dynamic elements calculation in case 3

Kernel	Kernel time of different batch number (ms)						
	1	32	128	512	1024	2048	3072
Initialization	0.0140	0.0579	0.2177	0.8373	1.6568	3.1136	4.8421
Iteration	0.0979	0.4054	1.5238	5.8611	11.5975	22.7950	34.9925
Current solution	0.0043	0.0156	0.0446	0.1618	0.3183	0.6265	0.9248
State vector refreshment	0.0045	0.0307	0.1202	0.4635	0.9241	2.4523	2.7023
Total time	0.1206	0.5095	1.9063	7.3236	14.4966	28.9873	43.4616
Single simulation	0.1206	0.0159	0.0149	0.0143	0.0142	0.0142	0.0141

Table 5 Band width of LU factorization and for/backward substitution in case 3 (GB/s)

Batch	1	32	64	128	256	512	1024	2048	3072
LU	1.75	17.05	32.03	56.59	113.54	136.15	162.63	189.76	192.89
Backward	3.45	31.85	57.87	83.33	105.90	131.72	153.07	188.49	191.02
Forward	0.54	5.83	9.92	17.12	22.93	43.14	87.51	134.23	161.73

Table 6 Performance of GPU-accelerated batch LU factorization (ms)

Matrix order	KLU	GPU (batch size = 2048)	Speed up
236	0.14	0.0006	233.3
2708	3.41	0.0125	272.8
18482	46.83	0.2924	160.2

width only reach 39% of the theoretical peak. When that increases to over 512, the actual band width can keep stable at 190 GB/s, which reached a peak of 66% theory.

The overall performance of GPU accelerated batch sparse triangular equations with forward and backward substitution is similar to LU factorization in that with the increase of batch number.

5.2 Performance Comparison

Compared with KLU solution, batch LU factorization achieved very high speedup effect. As is shown in Table 6, average single solution of LU factorization is 200 times faster than the KLU serial solution. When the order of matrix is smaller, the GPU speedup is relatively better.

6 Conclusion

In this paper, a batch SLS algorithm with task-level coarse-grained parallel mode and data-level fine-grained parallel mode is designed for simulation in multiple scenarios. Then, according to the parallelism of two layers, the algorithm of dynamic elements injection current is proposed. Finally, a batch transient simulation algorithm based on GPU acceleration is designed according to the principle of implicit integration alternative solution.

Case studies on Case 3 shows that, when the batch size is equal to 3072, the proposed batch LU factorization on NVIDIA Tesla K40 reaches its performance saturation point 0.29 ms per SLS and achieves 160 times speedup compared with KLU. By means of offloading the massive SLS and batch dynamic element injection current subtasks to GPU, the proposed batch-ETTS algorithm can limit the time in one alternate iteration of single ETTS within 0.5 ms for one system with over 10,000 nodes.

References

1. Shu Y, Zhang W, Zhou X et al (2017) Analysis and recommendations for the adaptability of China's power system security and stability relevant standards. CSEE J Power Energy Syst 3:334–339
2. Zhao L, Guo Q, Qin Q et al (2008) Analysis of stability characteristics of UHV synchronous power grid. Proc CSEE 34:47–51
3. Yu Y, Chen L (1988) Power system safety and stability, 1st edn. Science Press, Beijing (1988)
4. Shao H (1991) Direct method analysis of power system stability analysis, 1st edn. Water Resources and Electric Power Press, Beijing
5. Chen Y, Song Y, Huang S et al (2017) GPU-based techniques of parallel electromagnetic transient simulation for large-scale distribution network. Autom Electr Power Syst 19:82–88
6. Wang M, Chen Y, Huang S et al (2018) Power flow computation method for large-scale ill-conditioned systems applied to CPU and GPU coordination architecture. Autom Electr Power Syst 10:82–86
7. Zhao J, Liu J, Li P et al (2018) GPU based parallel algorithm oriented to exponential integration method for electromagnetic transient simulation. Autom Electr Power Syst 6: 113–119
8. Xue W, Wu S, Wang X et al (2002) Research progress on parallel algorithm for power system transient stability simulation. J Syst Simul 2:177–182
9. Xue W, Wu S, Wang X et al (2003) Parallel simulation of large scale power system transient process based on cluster machine. Proc CSEE 8:39–44
10. Wu JQ, Bose A, Huang JA et al (1995) Parallel implementation of power system transient stability analysis. IEEE Trans Power Syst (3):1226–1233
11. Chan KW (2001) Parallel algorithms for direct solution of large sparse power system matrix equations. IEE Proc C: Gener Transm Distrib 6:615–622
12. Su X, Mao C, Lu J (2002) Parallel power flow calculation for diagonal block plus edge model. Power Syst Technol (1):22–25
13. Alvarado FL (1979) Parallel solution of transient problems by trapezoidal integration. IEEE Trans Power Appar Syst 3:1080–1090

14. Granelli GP, Montagna M, La Scala M et al (1994) Relaxation-Newton methods for transient stability analysis on a vector/parallel computer. IEEE Trans Power Syst 2:637–643
15. La Scala M, Brucoli M, Torelli F et al (1990) A Gauss-Jacobi-Block-Newton method for Parallel transient stability analysis (of power systems). IEEE Trans Power Syst 4:1168–1177
16. La Scala M, Sbrissai R, Torelli F (1991) A pipelined-in-time parallel algorithm for transient stability analysis. IEEE Trans Power Syst 2:715–722
17. Tang Y (1997) Power system stability calculation implicit integration. Power Syst Technol 2:1–3
18. Zimmerman RD, Murillo-Sánchez CE, Thomas RJ (2011) MATPOWER: steady-state operations, planning, and analysis tools for power systems research and education. IEEE Trans Power Syst 1:12–19

Modular Operational Reliability Evaluation of Power Distribution Room Based on Data Learning

Xiaobo Dou, Haoyi Zhang, Yuchao Luo, Ruoxuan Sun and Jianlong Sun

Abstract Modular design is a planning mode which improves the rationality and exactness of power network design. When analyzing operational reliability of distribution network, current methods are not in real-time and lack accuracy which means operational reliability analysis based on real-time operation data can better meet the needs of future modular planning. This article presents a method of modular power distribution room operational reliability evaluation of based on data learning. Firstly, take advantage of the ELM neural network to deal with distribution network data and establish the learning model of organ outage factor. Secondly, compute the outage rate of organs and organ sets according to the result of the learning model. Build power availability calculation model of load node in module and form operational reliability evaluation index of modular power distribution room. In the end, use examples to test and verify the effectiveness of the method proposed. The result shows that the operational reliability evaluation method based on ELM neural network presented in this article is effective.

Keywords Power distribution room design · Operational reliability · ELM neural network

X. Dou · H. Zhang (✉) · R. Sun
Southeast University, Nanjing, China
e-mail: 458426569@qq.com

Y. Luo · J. Sun
Research Institute of Economics and Technology of State Grid
Jiangsu Power Company, Nanjing, China

Y. Xue et al. (eds.), *Proceedings of PURPLE MOUNTAIN FORUM 2019-International Forum on Smart Grid Protection and Control*, Lecture Notes in Electrical Engineering 585, https://doi.org/10.1007/978-981-13-9783-7_56

1 Introduction

As the terminal of the whole power grid, distribution network's design quality and reliability have a vital impact on people's production and life.[1] In order to improve the quality of distribution network construction and reduce the cost of construction, researchers introduced modular distribution room which is usually composed of transformer modules, bus modules and inbound and outbound modules [1]. Although modular distribution room design is of high design reliability, the reliability evaluation after its completion is also a problem that must be studied and considered.

Commonly used methods of distribution network reliability evaluation include simulation methods and analytical methods [2]. The traditional simulation method includes three analysis steps: state selection, state estimation and index calculation. The system size has little influence on the calculation complexity of Monte Carlo method, but it has the disadvantage of long calculation time when dealing with high reliability requirement system [3, 4]. Analytical method can be divided into three types when evaluating system reliability: state space methods, network methods and system state enumeration methods. The state space method [5] obtains the protection reliability by establishing the state space diagram and solving the Markov state equation. The network method builds reliability evaluation model based on distribution network topology [6, 7]. The system state enumeration method [8–10] directly enumerates the system state and neglect the transition between states.

When traditional simulation methods and analytical methods are used to evaluate the reliability of distribution net-work, the operation mode is fixed and organ reliability model as well as parameters are invariable [11–13]. The influence of real-time operation conditions such as unit operation mode, load real-time change and network structure change on the consequences of network failure are ignored, it becomes difficult to characterize the reliability of sys-tem operation accurately. Especially, the outage probability of organs varies with the operation time, geographical environment and network structures [14–16]. For organs in a specific area, the probability of failure also has its particularity. Reference [16] determines the probability of fault occurrence in one area based on the operation dispatch data and historical reliability statistics, it randomly generates faults based on Monte Carlo probabilistic simulation algorithm to evaluate the operational reliability. This provides a train of thought for introducing data learning method to solve the problem of operational reliability evaluation.

In recent years, the theory of data learning has been developed and applied rapidly. The technology of data learning can use self-learning ability, generalization ability and non-liner processing ability to mine the implicit rules of data, so as to find the relationship between real-time data and fault output in database [17]. Modular distribution room is consisted of lines, switches and transformers.

[1]*State Grid corporation Science and Technology Project "Modular Design and Empirical Research on Distribution Network of High Reliability Power Supply Area" (5210K017000B).*

Accordingly, the operational reliability is mainly affected by the reliability of line, distribution equipment and switches. As one feedforward neural network with strong learning ability [18], ELM neural network has the advantages of fast speed and high precision in analyzing this kind of distribution network reliability data. Therefore, this paper introduces ELM neural network to study the regional relationship between outage probability of different types of equipment and outage factors.

On the basic of distribution network operational reliability research, this paper proposed one algorithm based on data learning to evaluate operational modular distribution room reliability. This method reflects the difference of outage probability in different regions. Firstly, construct learning model of outage equipment based on ELM neural network according to local distribution network data. Secondly, substitute the revised outage probability of the equipment into the module to calculate the outage rate of a single organ, then calculate the outage rate and power supply efficiency of each sub-module. In the end, compare the operational reliability of different modular distribution room design schemes and get the optimal design scheme. This method use data prediction and the outage probability is revised according to massive local history data, the physical concept is clear and easy to understand and analysis accuracy is high.

2 Operational Reliability of Modular Distribution Room Based on Data Learning

Modular distribution room design is a new design method which simplifies complex distribution network topology and improves the quality and reliability of distribution network. The distribution room is usually composed of transformer modules, bus modules and inbound and outbound modules. In order to obtain the optimal module design scheme and give specific measures to improve the reliability index of modular operation of distribution network, this paper proposed a method of operational reliability analysis of modular distribution room based on data learning.

The outage probability of organs varies regionally with the change of operation time and geographical environment. The influence of different factors on the operational reliability of organs is analyzed by data learning method, and the outage probability of organs in the region is obtained. The organs are connected in series and parallel to form a distribution room, the set outage rate can be calculated by calculating the outage rate of single organ. Finally, the power supply efficiency of load nodes can be obtained and the optimal module design scheme is evaluated. The schematic diagram is shown in Fig. 1.

The scheme consists of two parts: the learning model of organ outage factors based on ELM neural network and the operational reliability evaluation module of modular distribution room based on data learning results.

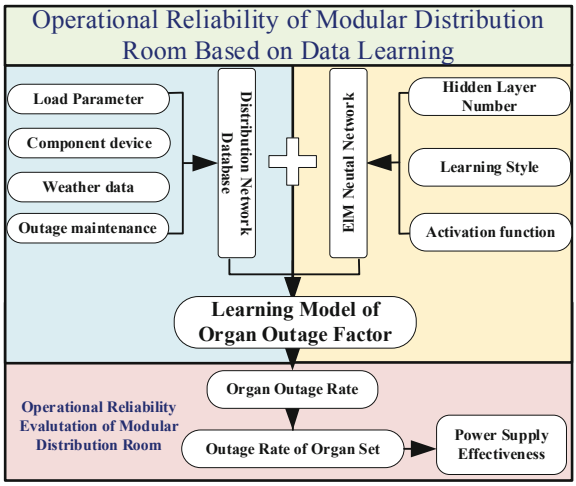

Fig. 1 Reliability assessment method for modular design based on data learning

Learning Model of Organ Outage Factors Based on ELM Neural Network. This module mainly takes load active power, load reactive power, load current, weather conditions, equipment operating age and maintenance status as input, and three types of power outage equipment as output. When the activation function, learning mode and hidden layer number of ELM neural network is decided, the learning model of power outage equipment could be established and the relationship between different fault factors and different power outage equipment will be found.

Operational Reliability Evaluation Module of Modular Distribution Room Based on Data Learning. This part updates the original failure probability to regional organ outage probability based on the failure probability of different equipment under different factors obtained from the learning model. Then, calculate the outage rate of organ sets composed of different organs in series and parallel and accordingly calculate the power supply efficiency of the load node. Finally, evaluate the operational reliability of modular design scheme and give suggestions for improving operational reliability.

3 Learning Model of Power Outage Equipment Based on ELM Neural Network

3.1 ELM Neural Network Design

Extreme Learning Machine (ELM) is a new hidden layer feedforward neural network [19]. The structure includes the input layer, the hidden layer and the output layer. The extreme learning machine randomly initializes input weights and biases,

then obtains corresponding output weights and biases. With the objective of minimizing training errors, the output weights of hidden layer nodes are determined by the algorithm.

Input Layer and Output Layer. The function of the input layer is to receive external signals and data, and the output layer realizes the output of the system processing results.

Hidden Layer. The hidden layer is between the input layer and the output layer. It consists of a large number of parallel nodes with computational functions. Through these nodes, the non-linear relationship between the input layer and the output layer is established. One mathematical model of Extreme Learning Machine with L hidden nodes and activation function g(x) can be expressed as:

$$\sum_{i=1}^{L} \beta_i g\left(\boldsymbol{W}_i \cdot \boldsymbol{X}_j + b_i\right) = o_j, \quad j = 1, 2, \ldots, N \tag{1}$$

In the equation, $\boldsymbol{W}_i = [w_{i1}, w_{i2}, \ldots, w_{im}]^T$ is the weight vector between hidden layer node i and the input layer node. $\boldsymbol{\beta}_i = [\beta_{i1}, \beta_{i2}, \ldots, \beta_{im}]^T$ is the weight vector between hidden layer node i and the output layer node, m represents the dimensions. b_i is the offset for hidden layer node i. o_j is the result of the Extreme Learning Machine.

Activation Function. Activation functions are classified into three categories: sigmoid function, hard limit function and sinusoidal function. In the learning model of power outage equipment based on ELM neural network, hard limit function with speed ad-vantage is adopted because of the low frequency of special data and the few data types. The mathematic expression of hard limit function is:

$$\eta_N(\omega, \lambda) = \begin{cases} \omega, & |\omega| \geq \lambda \\ 0, & |\omega| < \lambda \end{cases} \tag{2}$$

3.2 Learning Objectives of ELM Neural Network

The learning objective of ELM neural network is to approach the samples with minimum error, which means β_i, W_i and b_i should exist and Eq. (1) can be represented by matrix:

$$\boldsymbol{H\beta} = \boldsymbol{U} \tag{3}$$

In the equation, $\boldsymbol{H}$ is the output of hidden layer nodes, $\boldsymbol{\beta}$ is weight vector of output and $\boldsymbol{U}$ is desired output.

$$\boldsymbol{H}(w_1,\ldots,w_L,b_1,\ldots,b_L,x_1,\ldots,x_N) = \begin{bmatrix} g(w_1\cdot x_1+b_1) & \cdots & g(w_L\cdot x_1+b_L) \\ \vdots & \cdots & \vdots \\ g(w_1\cdot x_N+b_1) & \cdots & g(w_L\cdot x_N+b_L) \end{bmatrix}_{N\times L} \tag{4}$$

$$\boldsymbol{\beta} = \begin{bmatrix} \beta_1 \\ \vdots \\ \beta_L \end{bmatrix}_{L\times 1} \quad \boldsymbol{U} = \begin{bmatrix} u_1 \\ \vdots \\ u_N \end{bmatrix}^T \tag{5}$$

In the extreme learning machine algorithm, once the input weight and the offset of the hidden layer are randomly determined, the output matrix is uniquely determined. The output weight can be obtained by the least square method and it come out to be:

$$\boldsymbol{\beta} = \boldsymbol{H}^+\boldsymbol{U} \tag{6}$$

$\boldsymbol{H}^+$ is Moore-Penrose generalized inverse of hidden layer output matrix $\boldsymbol{H}$. In addition, the number of hidden layers should be taken into account when building the network model of extreme learning machine, and the parameters should be optimized. The number of the hidden layer should be considered carefully and be no more than $\boldsymbol{N}$.

Cluster learning is applied to the outage equipment. According to the probability that the test samples conform to the real situation under different hidden layers, the number of hidden layers with the highest probability is selected. After the learning, a number of checking data will be introduced and examine the model, if the result is not misleading, it turns out that the model has certain accuracy.

4 Operational Reliability Evaluation Module of Based on Data Learning Results

4.1 Organ Outage Rate Calculation

In the ELM neural network based on extreme learning mechanism, six kinds of new data including load reactive power, load current, weather condition, equipment operating age and maintenance status are input to predict the fault state under this condition.

The outage equipment is divided into three categories: line, distribution and switch. By analyzing the learning results, respectively obtain correlation factors s_{iw}, s_{ie} and s_{ia} between each type of blackout equipment and weather disasters, equipment maintenance and equipment aging.

The annual average outage times and outage duration of three types of components are respectively $\lambda_1, \lambda_2, \lambda_3$ and t_1, t_2, t_3. Thus, the outage rate of components under weather disasters, equipment maintenance and equipment aging can be obtained.

$$p_{iw} = \frac{\lambda_i s_{iw} t_i}{8760}, \tag{7}$$

$$p_{ie} = \frac{\lambda_i s_{ie} t_i}{8760}, \tag{8}$$

$$p_{ia} = \frac{\lambda_i s_{ia} t_i}{8760} \tag{9}$$

Equations (7), (8) and (9) respectively show the probability of organ outage caused by weather factors, the probability of organ outage caused by equipment overhaul and the probability of organ outage caused by equipment aging. These outage probability is related to correlation factors, annual average outage times and outage duration. Accordingly, the total outage rate of organ i is:

$$p_i = \frac{\lambda_i t_i}{8760}(s_{iw} + s_{ie} + s_{ia}) \tag{10}$$

4.2 Theoretical Calculation of Power Supply Efficiency of Load Bus

If a group of series organs fail and there is no spare, this will lead to overall outage and the reliability is based on the sum of all the organs' outage rate. These kind of organs are classified as A organs, and the series is named Φ_A. The equivalent outage probability of Φ_A is:

$$P_{\Phi_A} = \sum_{i \in \Phi_A} p_i \tag{11}$$

If the organs are in parallel with each other, this means once part of one line is blackout, the other lines can still supply power to load bus. These kind of organs are defined as Φ_B. They only blackout when the organs fail together. Therefore the total rate is the quadrature of all the organs' outage rate. The equivalent outage probability of Φ_B is:

$$P_{\Phi_B} = \prod_{i \in \Phi_B} p_i \tag{12}$$

The components in the power supply path are divided into three parts: the input organ set, the feed organ set and the intermediate organ set. The set is composed of lines, switches and distribution elements in series and parallel.

In order to provide reliable power supply at load point, it is necessary that the collection of feeder organs, input organs and intermediate organs on the main power supply path be in normal operation at the same time. Accordingly, the power supply efficiency η_M of load bus can be expressed as:

$$\eta_M=[(1-P_I)(1-P_L)(1-P_O)]^{8760} \tag{13}$$

In the equation, P_I is equivalent outage probability of input organ set, P_L is equivalent outage probability of feed organ set and P_O is equivalent outage probability of intermediate organ set. The result of the equation provide an expectation of one system's outage during one year.

4.3 Operational Reliability Evaluation Model of Modular Distribution Room

The technological process of modular distribution room operational reliability evaluation consists four steps. The specific process is shown below:

Step 1. Use ELM neural network to learn the normal operation and outage data. Then find relevance factors between different outage equipment and different outage factors by correlation analyzing.
Step 2. According to the annual average outage status of components in the region, calculate outage probability caused by different factors. Meanwhile, consider whether measures to reduce the impact of such factors should be taken in modular design. In the end obtain the total outage probability of one organ.
Step 3. According to the calculation rules of sub-module outage rate, respectively calculate the outage probability of input line, output line and intermediate organ set (P_I, P_L, P_O) for a specific load bus.
Step 4. According to the outage rate of each sub-module, calculate final annual power efficiency η_M of load bus.

5 Example Analysis

5.1 Outage Equipment Learning of Example

In order to cooperate with the work of the fund project, city X inquired data according to the distribution automation system and offered two documents: Medium Voltage Blackout in City X, 2014-2018 and Statistical Analysis of

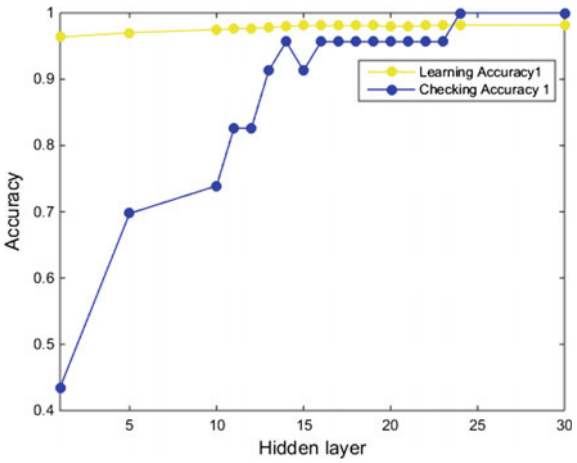

Fig. 2 Learning results of ELM neural network

Equipment History Data in City X. In the table of medium voltage blackout, fault type, outage time, outage equipment name and number can be collected. In the statistical analysis table of equipment history data, the operation status including load active power, load reactive power and load current are obtained according to the outage time.

In the example, 1000 groups of normal operation and 50 groups of failure data were selected. The input is load active power, load reactive power, load current, weather condition, maintenance status and equipment operating age. After random disruption, 1000 groups were used for learning and 50 groups were used for verification. The learning accuracy and calibration accuracy are obtained as shown in Fig. 2.

In the graph, the learning accuracy represents the learning accuracy of 1000 sets of data, and the checking accuracy represents the accuracy of 50 checking data. According to the figure, the higher the number of hidden layers is, the higher the accuracy of the result is. The learning accuracy is high since the very beginning and the accuracy of checking data grows quickly with the hidden layer number. The curve nearly saturated at about 24 layers, reaching 100%.

After completing the ELM neural network learning, 300 groups of inputs are randomly generated to compare the out-put of three types of outage equipment: line, distribution transformers and switches. The learning results are analyzed and the correlation factors between each type of outage equipment and weather disasters, equipment maintenance and equipment aging are obtained. The results are shown in Appendix 1.

High equipment operating age, equipment overhaul and bad weather are the main causes leading to various types of equipment failure for different reasons. To Line failure, the most important factor that leads to line outage is the equipment overhaul, with a correlation probability of 58.3%. Followed by bad weather, 20.8%.

To switch, the problem of equipment operating age contributes to over 80% of the switch failure. To transformer equipment, operating age is the biggest problem, 42.8% of the outage case is related to it.

In addition, other reasons, including user impact, traffic vehicle damage, animal factors, are uncontrollable factors, which are not considered in the study of the optional reliability of distribution room.

5.2 Outage Rate Calculation of Organs and Submodules

According to Sect. 3.1, the outage rate of organs in a particular area is affected by the correlation factor s_{ij}. The correlation factor represents the correlation between outage probability of various organs and weather problem, equipment maintenance and equipment aging in the region. Substitute the correlation factors to Eq. (10), obtain line outage rate of $9.02 \times 10^{-5}\lambda_1 t_1$, transformer outage rate of $6.57 \times 10^{-5}\lambda_2 t_2$ and switch outage rate of $1.14 \times 10^{-4}\lambda_3 t_3$ in this region.

PB-1 scheme shown in Fig. 3 is one kind of indoor distribution module in this region. It includes transformer module, bus module and in-out module. The main connection is a single bus, which adopts 2-in and 2-feedback design.

Distribution room module is divided into three parts: input organ set, intermediate organ set and feeder organ set. The outage rate of each sub-module is calculated as follows:

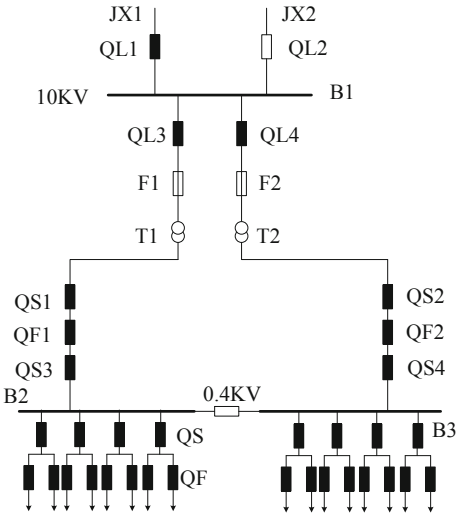

Fig. 3 Modular design scheme PB-1 of distribution room

The two inlet line are spare to each other and belong to class B organ set. The single inlet line belongs to the class A organ set. Therefore, the PB-1 scheme.

$$P_{I1} = (P_{JX} + P_{QL} + P_X)^2 \tag{14}$$

In the equation, P_{JX} is the outage rate of incoming transformer, referring to transformer equipment. P_{QL} is the outage rate of breakers, referring to switch equipment. P_X is the outage rate of line, P_{I1} is incoming organ set outage rate.

The middle organ set can be divided into two sets of class A organs. Therefore, the PB-1 scheme.

$$P_{O1} = (P_T + 5P_{QF} + P_X)^2 + P_{QS} \tag{15}$$

Among them, QL, QF and F are switch gear, T is distribution equipment and X is line equipment, P_{O1} is the outage rate of middle organ set.

Feedback organs are assembled as a single load point, so in PB-1 scheme.

$$P_{L1} = P_{QS} + P_{QF} + P_X \tag{16}$$

Among them, QS and QF are switch gear, X is line equipment, P_{L1} is the outage rate of feedback organ set.

5.3 *Effectiveness Calculation of Power Supply at Load Points of Different Design Schemes*

According to statistical data, the annually average outage time of line λ_1 is 0.05, and the average outage time is 8.8 h. When it comes to transformer equipment, λ_2 becomes 0.02 and the average outage time is 10.5 h. To switch equipment, λ_3 is 0.07 and the average outage time is 5.7 h.

Then substitute Eqs. (14), (15), (16) to Eq. (13), it can be calculated that in the modular design of PB-1 distribution room, the power supply efficiency of each load point is 0.137.

Appendix 2 shows other four modular design schemes of distribution room in one pacific city's distribution network and the computation process of power supply effectiveness at load points.

Meanwhile, in view of the problems of line equipment caused by bad weather, modular packaging and replacing overhead lines with cables are adopted to cut down. After applying this improvement measure to five kinds of modular design schemes, the efficiency of power supply is optimized as shown in Table 1.

According to the table, using the method proposed in this paper, the power supply efficiency of the modular design schemes PB-2 and PB-4 in distribution room are higher than that of the other three schemes. Literature [13] proposes a method to calculate the probability of failure based on historical data. Five kinds of

Table 1 Annual power availability of five scheme

Scheme	Main electrical wiring	Annual power supply effectiveness	Annual power supply effectiveness (modular packaging)
PB-1	Single Bus	0.137	0.142
PB-2		0.218	0.233
PB-3	Two Divided Bus Single Bus	0.135	0.141
PB-4		0.216	0.232
PB-5	Single Bus Section Connection mode	0.143	0.156

modular design annual average outage times (SAIFI) are calculated by this method. The SAIFI indexes of PB-1 and PB-3 equal and the SAIFI indexes of PB-2, PB-4 and PB-5 equal and are lower than those of the former two, which indicates that they are more reliable in operation.

At the same time, the distribution rooms with drawer-type low-voltage cabinets (PB-2, PB-4) have higher reliability of power supply than those with fixed low-voltage cabinets (PB-1, PB-3). PB-4 uses two independent single buses and more series organs, so its reliability is lower than PB-2.

In summary, the theory of this paper and traditional method formed a unified conclusion. The modular design scheme PB-2 of distribution room has the highest operational reliability.

6 Conclusion

In this paper, a theoretical calculation and evaluation method of operational reliability based on big data learning is proposed for modular distribution room design. The ELM neural network is innovatively used to learn the correlation between outage equipment and fault factors, and the correlation factors are given to calculate the power supply efficiency of different design schemes of distribution rooms and to evaluate their operational reliability. At the same time, the learning results of extreme learning machine have certain guiding significance for improving the operational reliability of distribution networks. The final conclusions are as follows:

In ELM neural network, when the Hard Limit activation function is used with 24 hidden layers, the learning speed and accuracy of outage equipment is the fastest, and the requirement of data quantity is small, which is suitable for the present situation that faults are few and available data size in distribution network is insufficient.

According to the correlation factors between power outage equipment and fault factors obtained from the regional historical data, combined with the average number and time of power outages per year, the outage rate of components more in line with the characteristics of the region can be calculated, thus the outage rate of components set can be calculated, the power supply efficiency of the design scheme

of distribution room can be obtained, and the operational reliability of modular distribution room can be evaluated.

The calculation and comparison of five modular distribution room design schemes show that the PB-2 scheme has the best reliability in operation. According to the learning results of extreme learning machine, the modular encapsulation and cable substitution for overhead line should be adopted in the design and construction process, which can further improve the reliability of the module distribution network.

Appendix 1

See Fig. 4.

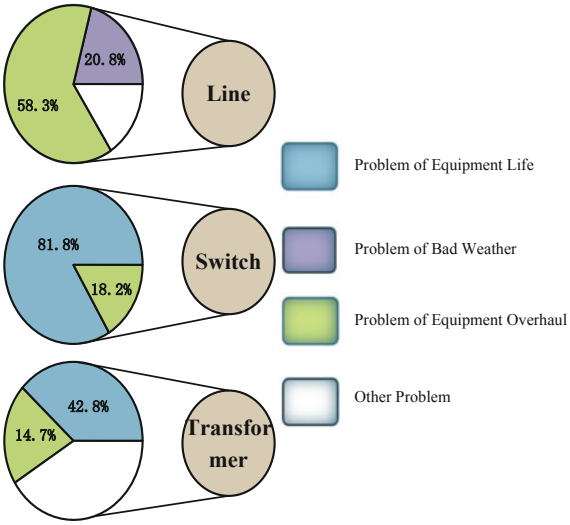

Fig. 4 Correlation analysis of power failure equipment and breakdown factors of the example

Appendix 2

Figure 5 shows the other four modular design schemes of distribution room in one pacific city's distribution network.

Figure 5a is PB-2 modularization scheme for distribution room of the city. Its main connection is single bus, using 2-in and 2-feedback line. The outage rate of the input organ set, the intermediate organ set and the feeder organ set are calculated as follows:

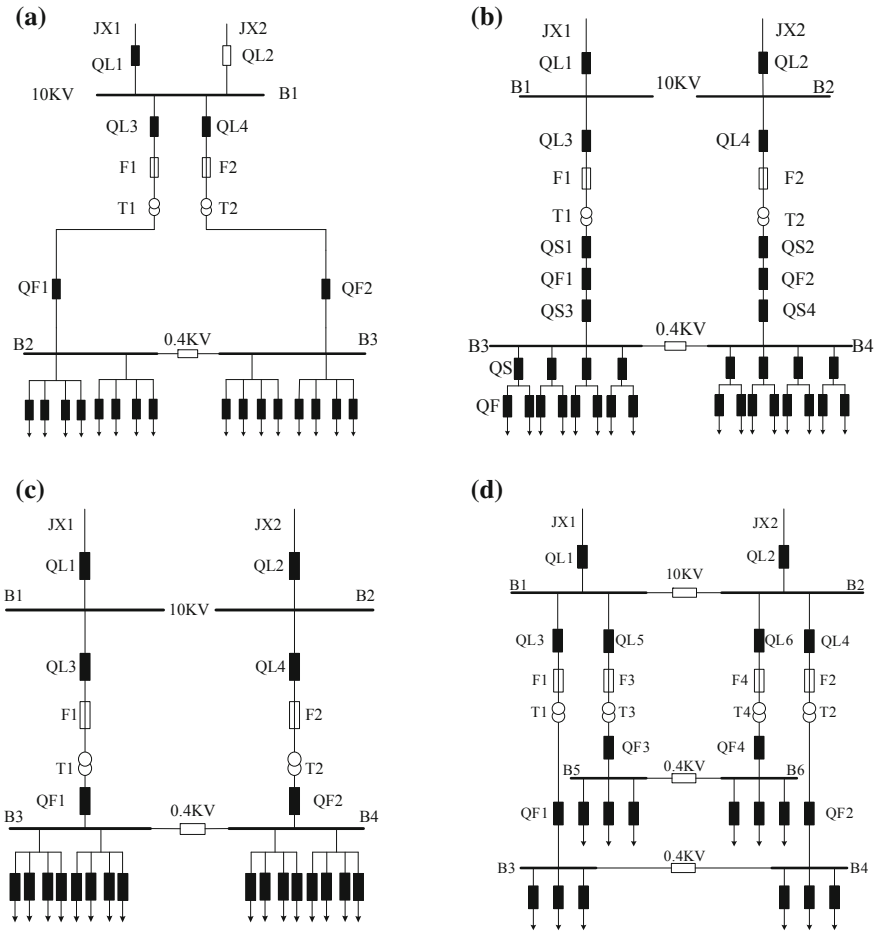

Fig. 5 Modular design scheme PB-2-5 of distribution room

$$\begin{cases} P_{I2} = (P_{JX} + P_{QL} + P_X)^2 \\ P_{O2} = (P_T + 4P_{QF} + P_X)^2 + P_{QS} \\ P_{L2} = P_{QS} + P_X \end{cases} \tag{17}$$

By substituting the annual average outage times and the annual average outage time, the power supply efficiency of each load point in the modular design of PB-2 distribution room η_{M2} turned out to be 0.218.

Figure 5b is PB-3 modularization scheme for distribution room of the city. It adopts two independent single buses, using 2-in and 2-feedback line. The outage rate of the input organ set and the feeder organ set are calculated as follows:

$$\begin{cases} P_{I3} = (2P_T + 6P_{QF} + 2P_X)^2 + P_{QS} \\ P_{L3} = P_{QS} + P_{QF} + P_X \end{cases} \tag{18}$$

By substituting the annual average outage times and the annual average outage time, the power supply efficiency of each load point in the modular design of PB-3 distribution room η_{M3} turned out to be 0.135.

Figure 5c is PB-4 modularization scheme for distribution room of the city. It adopts two independent single buses, using 2-in and 2-feedback line. The outage rate of the input organ set and the feeder organ set are calculated as follows:

$$\begin{cases} P_{I4} = (2P_T + 4P_{QF} + 2P_X)^2 + P_{QS} \\ P_{L4} = P_{QS} + P_X \end{cases} \tag{19}$$

By substituting the annual average outage times and the annual average outage time, the power supply efficiency of each load point in the modular design of PB-4 distribution room η_{M4} turned out to be 0.216.

Figure 5d is PB-5 modularization scheme for distribution room of the city. Its main connection is single bus segment, using 2-in and 2-feedback line. The outage rate of the input organ set, the intermediate organ set and the feeder organ set are calculated as follows:

$$\begin{cases} P_{I5} = (P_{JX} + P_{QL} + P_X)^2 + P_{QS} \\ P_{O5} = (P_T + 2P_{QF} + P_X)^2 + P_{QS} \\ P_{L5} = P_{QS} + P_X \end{cases} \tag{20}$$

By substituting the annual average outage times and the annual average outage time, the power supply efficiency of each load point in the modular design of PB-5 distribution room η_{M5} turned out to be 0.143.

References

1. Wang D (2014) Thinking of standardization and modularization in distribution network. Telecom World (08)
2. Zhao H, Wang Z, Xie K, Li W (2013) Comparative study on reliability assessment methods for medium voltage distribution network. Power Syst Technol 37(11):3295–3302
3. Bie C, Wang X (1997) The application of Monte Carlo Method to reliability evaluation of power systems. Autom Electr Power Syst 06:68–75
4. Liang H, Cheng L, Liu S (2011) Monte Carlo simulation based reliability evaluation of distribution system containing microgrids. Power Syst Technol 35(10):76–81
5. Zhang X, Wang C, Cheng X (2008) Reliability analysis model for protective relaying system of UHV power network based on Markov state-space method. Power Syst Technol 32 (13):94–99 (in Chinese)
6. Liu H, Li J, Zhang J et al (2017) Power supply capability evaluation of medium voltage distribution system considering reliability. Autom Electr Power Syst 41(12):154–160

7. Li K, Ma X, Xing H et al (2010) Modification model of reliability network equivalent of distribution system reliability evaluation. J Electr Power 25(2):103–106 (in Chinese)
8. Dai W, Wu J (2002) Fast evaluation for distribution network reliability based on minimal path. Electr Power Autom Equip 22(7):29–31 (in Chinese)
9. Xie K, Zhou J, Billinton R (2003) Reliability evaluation algorithm for complex medium voltage electrical distribution networks based on the shortest path. IEE Proc Gener Trans Distrib 150(6):686–690
10. Zhang P, Guo Y (2002) Large scale distribution system reliability evaluation based on failure mode and effect analysis. Tsinghua Univ (Sci&Tech) 42(3)
11. Ge S, Sun H, Liu H, Zhang Q, Li J (2019) Power supply capability evaluation of active distribution network consideration reliability and post fault load response. Autom Electr Power Syst 43(6):77–84 + 91 + 85–90 + 126 + 92–94
12. Sun Y, Cheng L, Liu H (2005) Power system operational reliability evaluation based on real-time operating state. Power Syst Technol 29(15):6–12 (in Chinese)
13. Shi C, Ning X, Sun Z, Kang C, Du Y, Ma G (2018) Quantitative risk assessment of distribution network based on real-time health index of equipment. High Volt Eng 44 (02):534–540
14. Cheng L, He J, Sun Y (2006) Impact of transmission line's real-time reliability model parameter upon power system operational reliability evaluation. Power Syst Technol (13):8–13
15. Yin C, Tang W, Wen L, Lan J, Lin J, Li S, Li N (2018) A new method for reliability evaluation of distribution network considering the influence of typhoon. Power Syst Prot Control 46(04):138–143
16. Liu Y, Xie D (2007) Power grid reliability evaluation system based on real-time measurement data. RELAY (15):28–31 + 38
17. Hu L, Diao Y, Liu K, Luan W, Sheng W (2017) Operational reliability analysis of distribution network based on big data technology. Power Syst Technol 41(01):265–271
18. Yu J, Liu J, Xu L, Zhang Z, Jiang J, Gu J (2014) Distribution grids of high reliability for core areas of large cities. Autom Electr Power Syst 38(20):74–80 + 114
19. Huang GB, Zhu QY, Siew CK (2006) Extreme learning machine: theory and applications. Neurocomputing 70(1):489–501

Target Recognition and Evaluation of Typical Transmission Line Equipment Based on Deep Learning

Ziqiang Zhou, Guangyu Yuan, Wanxing Feng, Shanqiang Gu and Peng Fan

Abstract The traditional method of conducting regular inspections for high-voltage transmission towers is mainly based on manual inspection. Workers need to board the tower for visual inspection during operation, which is not only unsafe, but also inefficient. With the gradual popularization of drones in the use of power industry, automated inspections based on artificial intelligence and image processing technology have become possible. In the complex background of aerial images, doing defect detection for key equipment components of high-voltage transmission lines is a challenging problem, and achieving the goal of target recognition of transmission line equipment is the basis of defect detection. Based on the deep learning technology, this paper researches the target recognition of transmission line equipment by using aerial image, focusing on insulator and anti-vibration hammer. The process is as follows: Firstly, the image data should be preprocessed. Secondly, the data should be marked and the data set should be divided. Then the two networks of Faster R-CNN and YOLOv3 are used for training. Finally, the trained model is evaluated.

Keywords Deep learning · Transmission line equipment · Target recognition · Drone inspection

Z. Zhou (✉) · G. Yuan · W. Feng · ShanqiangGu · P. Fan
NARI Group Corporation (State Grid Electric Power Research Institute), Nanjing 211106, China
e-mail: zhouziqiang@sgepri.sgcc.com.cn

Z. Zhou · W. Feng · ShanqiangGu · P. Fan
Wuhan NARI Co., Ltd., State Grid Electric Power Research Institute, Wuhan 430074, China

Y. Xue et al. (eds.), *Proceedings of PURPLE MOUNTAIN FORUM 2019-International Forum on Smart Grid Protection and Control*, Lecture Notes in Electrical Engineering 585, https://doi.org/10.1007/978-981-13-9783-7_57

1 Introduction

The power system plays an important role in people's livelihood and the economy. The power grid is a major component of the power system. Due to the wide geo-graphical area, large scale of power grids and long transmission lines in China, it is very difficult to carry out comprehensive operation and maintenance on the power grid. The traditional method of conducting regular inspections on high-voltage transmission towers is mainly based on manual inspection. Workers need to go to the tower for visual inspection during operation, which is not only difficult to ensure, but also inefficient.

In order to improve the efficiency of operation and maintenance of transmission lines, State Grid Corporation has now adopted the UAV inspection method [1]. UAV inspection significantly reduced the labor cost and the risk of field operations, but the image data collected by the drone inspection was massive, and the manual analysis of the data was huge. Therefore, it is necessary to automatically analyze the graphic data collected by the drone through automated means [2]. To achieve automatic analysis of the target state of the transmission line, it is firstly necessary to identify the position of the target in the image [3]. This paper intends to identify the insulators and anti-vibration hammers as the typical components in transmission line.

The image background of the drone inspection is complicated, the contrast between the parts and the background is relatively low, and there is a lot of interference. The original image target recognition algorithm is mainly based on the shape (edge, contour) and texture features of the target, such as using Hough transform [4–10]. These methods are limited to a specific category, and in practical applications, affected by imaging conditions, external environment and changes in illumination, gray-scale distortion and image noise are generated, and the effectiveness and reliability are not ideal and there is no extension. The use of machine learning methods for target recognition has become a hot topic, such as the use of Haar-like features and cascaded AdaBoost algorithm for target recognition [11–15]. Compared with the original target recognition algorithm, the machine learn-ing method improves the reliability, but the accuracy and efficiency of the target recognition are still insufficient, and the accuracy cannot be improved as the number of samples increases. In recent years, deep learning has achieved sensational results in the field of image recognition and target recognition. The typical R-CNN target recognition scheme was proposed by Girshick et al. [16], but its accuracy and recognition efficiency are not ideal. The Fast R-CNN [17] scheme and the Faster R-CNN [18] scheme were subsequently proposed. In 2018, Redmon et al. presented a model YOLOv3 with a complex backbone network and using feature pyramids for target recognition [19].

In this paper, two typical components of insulators and anti-vibration hammers in transmission line components are trained using Faster R-CNN and YOLOv3 target recognition networks, and finally the mAP of the two components in the two networks are compared.

2 Target Recognition Preparation

2.1 Data Preprocessing

The inspector controls the drone and collects images of the equipment related to the transmission line. Image pixels are in the order of a million. Because the environment of the high-voltage transmission line is different, the illumination, the distance of the viewpoint, the posture and the background texture are complex and changeable. Not only the size and posture of the target are different, but the background may be woods, farmland, houses, etc. Therefore, the data needs to be preprocessed.

The data used in this paper exist problems of too high image resolution, etc. In order to unify the standard and standardize the verification effect of the image recognition method, the long side of the image is unified to 1000 pixels.

2.2 Data Annotation

After data pre-processing, 45,369 pictures are sorted out. insulators, anti-vibration hammers need to be marked in these pictures. The marked procedure is implemented by PyQt, as shown in Fig. 1. Each box in the figure is labeled with one part, and the boxes of different colors represent different parts. Image annotation is an important foundational work. “insulator” stands for insulator and “hammer” stands for anti-vibration hammer.

Fig. 1 Picture annotation interface

2.3 Data Set Partition

In this paper, there are 45,369 images as sample data sets, which are relatively abundant. There is no need to use data set expansion technology to expand the data set, but the sample data set is divided into training data set, verification data set and test data set. By writing the corresponding Python program, the sample data set is divided, and the proportion of the division is 6:2:2, corresponding to 27,221:9,074:9,074 pictures. The validation data set is used to aid training and the test data set is used to evaluate the performance of the corresponding model.

2.4 Evaluation Criteria

In this paper, the VOC2007 target recognition task evaluation standard mAP value [20] is used to evaluate the same data set using Faster R-CNN and YOLOv3 target recognition networks. mAP is the abbreviation of "mean Average Precision", "Precision" is the precision, "Average Precision" is the precision of 11 aliquot candidates, and "mean Average Precision" is the average of all categories of APs.

"Precision" represents the proportion of true positive samples in a sample that is predicted to be positive. The positive class prediction is expressed as "TP" for positive classes, "FP" for positive classes, and "Precision" (abbreviated as "P") for the following formula:

$$P = \frac{TP}{\mathrm{TP} + \mathrm{FP}}$$

When calculating mAP, the recall rate ("Recall") parameter should be used, and "Recall" indicates the proportion of positive examples in the sample that are correctly predicted. The positive class prediction is expressed as "TP" for positive classes, "FN" for negative class predictions, and "Recall" (abbreviated as "R") for the following formula:

$$\mathrm{R} = \frac{TP}{\mathrm{TP} + \mathrm{FN}}$$

By using different confidence thresholds in the target recognition network, "Recall" can be got at "0, 0.1, 0.2, 0.3, 0.4, 0.5, 0.6, 0.7, 0.8, 0.9, 1.0" The corresponding "Precision" value at 11 points, and the values are averaged to obtain the value of AP.

3 Model Training and Evaluation

3.1 Model Training

The hardware configuration and main parameters of the experimental platform used for model training and evaluation are shown in Table 1. The experimental platform software configuration and main parameters are shown in Table 2.

The training data set and the verification data set are trained by two target recognition networks, Faster R-CNN and YOLOv3 respectively. The used networks use the source code given in the corresponding paper, and the classification network used in Faster R-CNN uses. ResNet-50 network, YOLOv3 classification network uses the Darknet network. Each network was trained for nearly 48 h, and finally the corresponding trained model was obtained, and then the test data set was evaluated using the model. Figure 2 is an effect diagram identified by the trained YOLOv3 network model.

3.2 Evaluation Results

The mAPs of the two target recognition network models are calculated separately (the IOU threshold is taken as 0.5), and the results are shown in Table 3.

Table 1 Hardware configuration and main parameters of the experimental platform

Name	Version	Parameters
CPU	Intel Core i7-8750H	2.20 GHz 6 core
Graphics card	Nvidia GeForce GTX1080 with Max-Q Design	8G
RAM	Hynix DDR4	24 GB 2667 MHz
Hard disk	Samsung NVMe MZVLW1T0	SSD 1T

Table 2 Software configuration and main parameters of experimental platform

Name	Version
OS	Ubuntu 16.04.5
GCC	5.4.0
GPU development kit	CUDA 10.0.0.130
GPU deep learning library	libcuDNN 7.4.2.24
Python	Python2.7
OpenCV	3.4.4.19
Pytorch	1.0
Caffe	2.0

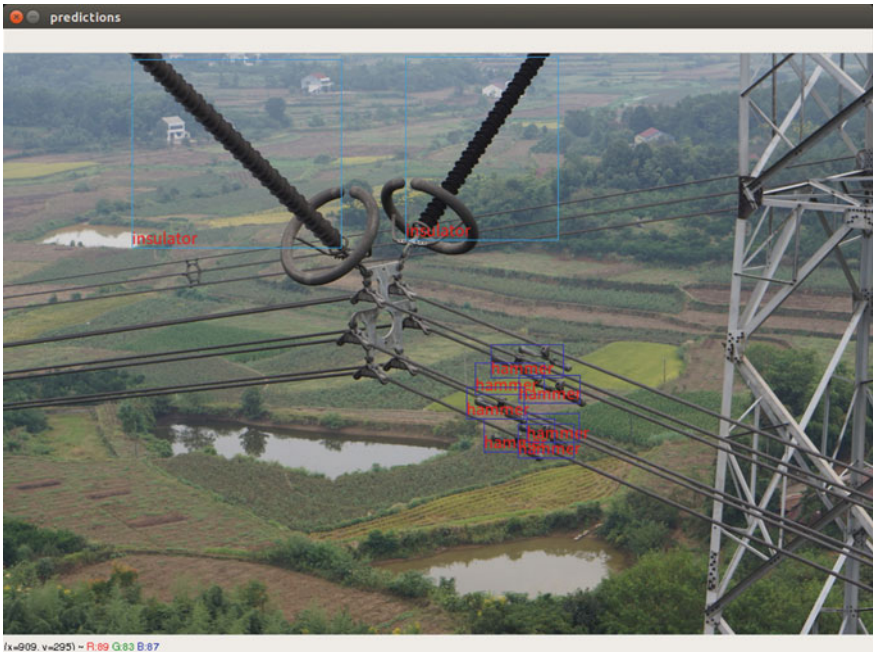

Fig. 2 Recognition effect diagram of YOLOv3 network model after training

Table 3 mAP value of two target recognition network models

	Insulator	Anti-vibration hammer	Average
Faster R-CNN(ResNet-50) [18]	0.8793	0.7547	0.8170
YOLOv3-608 [19]	0.7969	0.5090	0.6530

As can be seen from the table, for the same network, the mAP for the insulator identification is higher than the mAP for the anti-vibration hammer identification. When the identified target is an insulator, the mAP value obtained with Faster R-CNN is 10% higher than the mAP value obtained with YOLOv3; when the identified target is an anti-vibration hammer, the mAP value obtained with Faster R-CNN Compared with the mAP value obtained with YOLOv3, it is 48% higher.

Table 4 shows the average time for the recognition of a single picture by the two target recognition network models. It can be seen from the table that the processing speed of the YOLOv3 on the transmission line equipment is much higher than that of the Faster R-CNN, which achieves real-time video processing speed.

Table 4 Average recognition time of tow target recognition network models for single picture

	Average recognition time (s)
Faster R-CNN(ResNet-50) [18]	0.2391
YOLOv3-608 [19]	0.0251

3.3 Analysis of Results

In the 45,369 sample samples, there are 89,093 insulator targets and 36,909 anti-vibration hammer targets (see Fig. 3). The number of insulator samples is relatively more, so the training effect is better. Secondly, the image size of the insulator target is generally larger than the image size of the anti-vibration hammer target, and has higher resolution; finally, the geometric characteristics of the insulator are more significant than the anti-vibration hammer. Therefore, the mAP of the insulator target recognition is greater than the mAP of the anti-vibration target recognition. At the same time, these three points have little impact on Faster R-CNN and have a greater impact on YOLOv3, so Faster R-CNN is more robust than YOLOv3.

For the target recognition of other equipment on the transmission line, the number of target samples, the image size and resolution of the target, and the geometric characteristics of the target are significant, which will have an important impact on the recognition results.

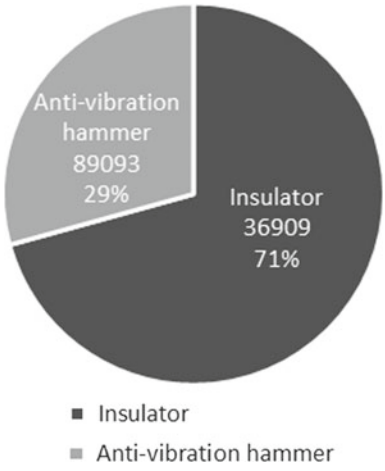

Fig. 3 Contrast chart of number of various targets

4 Conclusion

In this paper, 45,369 pictures are obtained through data preprocessing, and the pictures are marked with two kinds of typical components such as insulator and anti-vibration hammer. Then the data set is divided, and the training is performed by Faster R-CNN and YOLOv3 network respectively, and then the corresponding trained models are obtained. Finally, the mAP values of each model are calculated and analyzed. Through the data results, the following selection of the target transmission network selection for the transmission line equipment has the following guiding functions: If you pursue higher mAP, you can use the Faster R-CNN network or its related transformation network; if you mainly pursue recognition speed, you can use the YOLOv3 network or its related transformation network.

The target recognition of transmission line equipment is the basis of equipment defect analysis. Through the target identification, the corresponding parts are found, and the defects of the transmission line equipment can be effectively found through the target identification of the secondary defect parts or the defect and defect-free classification. Thereby realizing the automatic analysis of pictures and improving the efficiency of maintenance and repair of transmission lines.

Image recognition based on deep learning requires sufficient sample images and accurate annotation. This is difficult to achieve in cases where the sample is difficult to collect effectively, but the sample can be expanded using a variety of sample expansion techniques in a limited sample case.

References

1. Tang M, Dai L, Lin Z et al (2013) Application of unmanned aerial vehicle in power line inspection. Electr Power 46(3):35–38
2. Zhou N, Liao J, Wang Q, Li C, Li J (2019) Analysis and prospect of application status of deep learning in smart grid. Autom Electr Power Syst 43(04):180–197
3. Li G, Zhang B, Zhao W, Liu Y, Gao S (2018) Data science problems in power equipment condition assessment: challenges and prospects. Autom Electr Power Syst 42(21): 10–20 + 177
4. Chen X, Wu Y, Zhao L (2010) Identification of OPGW vibration damper based on random Hough transformation. Heilongjiang Electr Power 32(1):1–2, 5
5. Hu C, Wu G, Cao H et al (2008) Research of obstacle recognition based on vision for high voltage transmission line inspection robot. Chin J Sens Actuators 21(12):2092–2096
6. Fu J, Shao G, Wu L et al (2017) Defect detection of line facility using hierarchical model with learning algorithm. High Voltage Eng 43(1):266–275
7. Wang W, Liu G (2008) Image edge detection of the insulator. Microcomput Inf (27): 308–309, 154
8. Jin L, Hu J, Yan S (2013) Image-based fault diagnosis method for high-voltage transmission line spacers. High Voltage Eng 39(5):1040–1045
9. Wang W, Zhang J, Han J et al (2015) Transmission line breakage and foreign object defect detection method based on drone image. J Comput Appl 35(8):2404–2408

10. Zhao J, Wang Z, Liu S (2015) Transmission line identification based on texture features of gray level co-occurrence matrix. Yunnan Electr Power 43(2):126–129
11. Zhai Y, Wang D, Zhao Z (2016) Insulator identification method based on target suggestion and structure search. J North China Electr Power Univ (Nat Sci Ed) 43(4):66–71, 78
12. Jin L, Yan S, Liu Y (2012) Anti-vibration hammer recognition based on Haar-like features and cascaded AdaBoost algorithm. J Syst Simul 24(9):1806–1809
13. Cao W, Wang Y, Yin F et al (2011) Research on obstacle recognition method for deicing robot of high voltage transmission line. Chin J Sci Instrum 32(9):2049–2056
14. Jiang H, Cui H, Liu F et al (2005) High-voltage transmission line fault classifier based on fuzzy logic and support vector machine. Electr Power (3):13–17
15. Cheng L, Yu T, Zhang X, Yin L (2019) Application and prospect of machine learning in energy and power systems. Autom Electr Power Syst 43(01):15–43
16. Girshick R, Donahue J, Darrell T, Malik J (2015) Region-based convolutional networks for accurate object detection and segmentation. IEEE Trans Pattern Anal Mach Intell 38(1):142–158
17. Girshick R (2015) Fast R-CNN. In: IEEE international conference on computer vision, pp 1440–1448
18. Ren S, He K, Girshick R, Sun J (2015) Faster R-CNN: towards real-time object detection with region proposal networks. IEEE Trans Pattern Anal Mach Intell 39(6):1137–1149
19. Redmon J, Farhadi A (2018) YOLOv3: an incremental improvement. arXiv preprint arXiv: 1804. 02767
20. Everingham M, Van Gool L, Williams CK, Winn J, Zisserman A (2010) The Pascal visual object classes (VOC) challenge. IJCV 303–338

Short-Term Bus Load Forecasting Method Based on CNN-GRU Neural Network

Maoya Shen, Qifeng Xu, Kaijie Wang, Mengfu Tu and Bingxiang Wu

Abstract In recent years, with the rapid development of the power market and smart grid, higher and higher requirements are put forward for load forecasting technology, and deep learning is also widely used in the filed. Aiming at the small load base of bus load, strong time series and large influence by relevant factors, this paper proposes a short-term bus load forecasting method based on CNN-GRU neural network. The method processes the input historical load, date type, weather data, renewable energy generation, time-of-use electricity price and other related factors through the CNN network, intelligently extracts the dominant factors and compresses the generated timing feature vectors, and then performs bus load forecasting through the multi-layer GRU network. Taking several bus load data from a certain city in the east from 2012 to 2018 as samples/tests, CNN-GRU and traditional BPNN forecasting methods were used for prediction. The experimental results show that CNN-GRU deep neural network has higher precision and better prediction effect when dealing with bus load forecasting.

Keywords Short-term bus load forecasting · CNN · GRU · Neural network

M. Shen (✉) · K. Wang · M. Tu · B. Wu
NARI Group Corporation (State Grid Electric Power Research Institute),
Nanjing 211106, Jiangsu Province, China
e-mail: shenmaoya@sgepri.sgcc.com.cn

M. Shen · M. Tu · B. Wu
State Key Laboratory of Smart Grid Protection and Control,
Nanjing 211106, Jiangsu Province, China

Q. Xu
State Grid Zhejiang Electric Power Co., Ltd., Hangzhou 310007,
Zhejiang Province, China

Y. Xue et al. (eds.), *Proceedings of PURPLE MOUNTAIN FORUM 2019-International Forum on Smart Grid Protection and Control*, Lecture Notes in Electrical Engineering 585, https://doi.org/10.1007/978-981-13-9783-7_58

1 Introduction

Power load forecasting is not only the basis for reliable and stable operation of modern power systems but also an important part of EMS energy management system. Simultaneously, it is also the premise of real-time trading in the power market, smart grid dispatching, and power system decision making. Power load forecasting is divided into system load forecasting and bus load forecasting [1]. The bus load not only has a smaller base, larger fluctuations, stronger timing, more burrs, but also affected by date type, weather and equipment maintenance etc. In addition, related factors such as equipment maintenance/load transfer, renewable energy generation, and time-of-use electricity price will also affect bus load forecasting results. The short-term bus load forecasting is more difficult than the system load forecasting [2].

Traditional load forecasting studies fall into two categories. One is a predictive model based on time series analysis, such as moving average, Kalman filtering, and multiple linear regression [3–5]. This type of model analyzes the historical change Rules and trends of composite sequences and based on these characteristics to forecast future load. However, the model cannot accurately reflect nonlinear relationships and complex features; The other type is based on machine learning methods and predictive models of feed-forward neural networks, such as Support Vector Machine (SVM), Random Forest (RF), Gradient Boosting Decision Tree (GBDT), etc. [6–10]. Since this type of model does not include memory cells, it is not possible to consider the timing characteristics in the load data.

In recent years, some deep neural networks have gradually been applied to load forecasting [11], Long Short Term Memory (LSTM) is a variant of the Recurrent Neural Network (RNN), it regulates the information flow through the internal department mechanism, selectively saves and forgets the information, and solves the short-term memory problem and the gradient disappearance problem of RNN, it can effectively deal with sequence problems that are far away and has been applied to some short-term power load forecasting [12, 13]. On the basis of LSTM, Gated Recurrent Units (GRU) simplify the gating unit. On the basis of retaining the original functions, the convergence speed is faster and the effect is better. However, there are many types of factors affecting the bus load. GRU and LSTM cannot effectively deal with the related factors such as equipment maintenance, load transfer, time-of-use electricity price, weather data and date type.

In order to comprehensively consider the influence of various features and the time series characteristics of bus load changes, this paper proposes a short-term bus load forecasting method based on CNN-GRU deep neural network, which is recorded as CNN-GRU forecasting model. The method inputs historical bus load data, weather data, date type information, equipment maintenance, load transfer, and time-of-use electricity price into the CNN as multi-dimensional features, using CNN to learn the intrinsic connection of data and generate time series feature vectors, and then realize short-term bus load forecasting through GRU. The method uses CNN to intelligently extract the dominant correlation factors of bus load

forecasting time series data, and effectively improves the nonlinear analysis ability of various influencing factors while considering the time-serials property of the bus load.

2 Principles of CNN and GRU Deep Neural Networks

2.1 Principles of CNN

Convolutional neural network (CNN) simulates biological vision and extracts data features through local perception and weight sharing. It has been widely used in image recognition and text categorization [14]. In this paper, CNN is used to identify the underlying data feature map, and the effective data is extracted from the original feature map by repeated CONV-POOL operation. Through the full connection flattening operation, a complete feature vector sequence is established as an effective input of the GRU. The process of eigenvalue extraction and pooling dimension reduction of four-layer convolution neural network is shown in Fig. 1.

2.2 Principles of GRU

LSTM is a master of recurrent neural networks with many variations, such as GRU. They all deal with long-term and short-term information through the gating mechanism to achieve the purpose of maintaining long-term information, and by controlling the propagation of gradient information, thus alleviating the phenomenon of gradient disappearance.

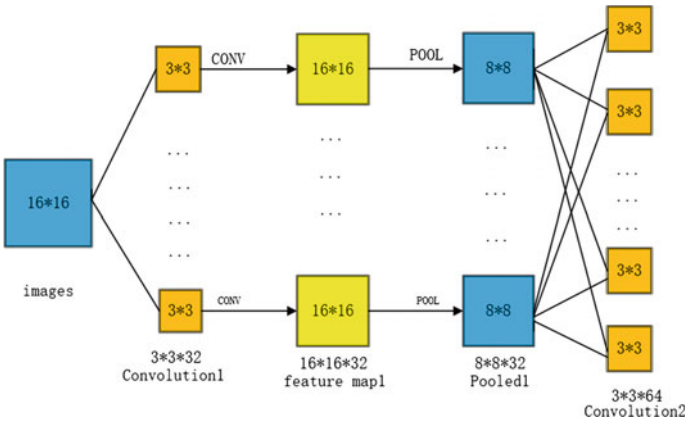

Fig. 1 Schematic diagram of eigenvalue extraction and pooling dimension reduction of four-layer CNN

GRU is a new generation of recurrent neural network, as shown in the GRU unit model. Compared with LSTM, GRU removes the cell state unit, and uses the hidden state for information transfer, and integrates LSTM architecture, containing two gating units, an update door and a reset door [15]. The update gate is a combination of the forgetting gate and the input gate in the LSTM, which determines which information to forget and which information needs to be remembered, and the reset gate is used to control the degree of forgetting of the past information. This simplified structure reduces the training parameters and speeds up the convergence while ensuring the memory ability of the neurons, thereby improving the prediction accuracy. The unit model of GRU is shown in Fig. 2.

The internal information flow can be expressed by the following formula:

$$z_t = \sigma(W_z \cdot [h_{t-1}, x_t]) \tag{1}$$

$$r_t = \sigma(W_r \cdot [h_{t-1}, x_t]) \tag{2}$$

$$\tilde{h}_t = \tan h(W \cdot [r_t * h_{t-1}, x_t]) \tag{3}$$

$$h_t = (1 - z_t) * h_{t-1} + z_t * h_t \tag{4}$$

The input of the GRU is the hidden layer h_{t-1} at the previous moment and the current input x_t, and the output is the hidden layer information h_t at the current moment. z_t and r_t are the update and reset gates of the GRU, respectively, and the candidate hidden layer $\tilde{h}_t$ is calculated by r_t, thereby measuring how much hidden layer information is retained at the previous moment. The z_t is used to calculate how much candidate hidden layer $\tilde{h}_t$ needs to be added and finally obtain the output h_t at the current moment.

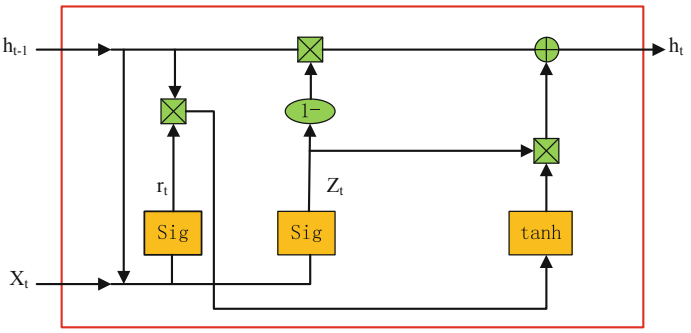

Fig. 2 Unit model of GRU

3 Bus Load Forecasting Method Based on CNN-GRU

3.1 Influencing Factors of Bus Load

The bus load is similar to the system load, with strong periodicity and similar load fluctuations between weeks. The workload on the working day changed steadily. On weekends and rest days, due to the decline in the proportion of industrial load, the proportion of commercial and civilian use increased, and the overall load level was lower than the working day, and showed regular fluctuations; the decline in industrial load on statutory holidays is more pronounced, and the difference in load characteristics from normal days is greater. Overall, the bus load is more affected by the type of date. When establishing the forecasting model, the influence of the day type factor should be fully considered [16].

Meteorological factors indirectly affect the changes in bus load by influencing people's travel and electricity usage. Among them, temperature, humidity and rainfall have a greater impact, especially in the winter and summer, meteorological factors will cause short-term fluctuations in load [2].

When equipment such as unit, line or main transformer is inspected in the busbar area, or when the system operation mode changes in the busbar area, the load distribution of the relevant busbar area will change greatly, which seriously interferes with the prediction accuracy. This is also the main reason why the bus load forecast is different from the system load forecast.

When the lower grid side of the bus load is connected to a small power source (such as small hydropower, distributed photovoltaic or wind power), the power generation of the small power supply will offset some of its power consumption and reduce the power supply requirement of the bus load to the main network. This is the reason for another major difference between bus load and system load.

From the research on the implementation of peak and valley electricity prices at home and abroad, it is known that this measure has a significant effect on reducing the daily load fluctuations and shifting peaks and valleys by increasing price leverage. In this paper, the influencing factors of the three-step electricity price of peace time, valley time, and peak time in the day are added to the prediction model.

The pros and cons of the predictive model play a crucial role in the prediction process, especially in neural networks lacking prior knowledge. Based on the analysis of the above-mentioned influencing factors, this paper takes the date type, meteorological factors, load transfer and time-of-use electricity price as the main relevant factors, and uses the historical bus load data together as the data input of the prediction model, as shown in Table 1.

Table 1 Summary of influencing factors

Influencing factor	Feature	Description
Historical data	Short-term load Long-term load	Bus load value at time t in the last two weeks Bus load value at time t in the last three years
Regional load change	Equipment overhaul Load transfer Small power output	Overhaul plan load Transfer load Small power output load
Meteorological factors	Temperature, humidity Wind speed, cloud Wind direction, precipitation	Forecast temperature(humidity, wind speed, wind direction and precipitation) at time t
Date type	Holidays (New Year Day, Spring Festival, …) Working day Weekend	Detailed date type, including working day, weekend, or various holidays
Time-of-use electricity price	Peak time Valley time	Corresponding time price

3.2 CNN-GRU Network Model

The CNN-GRU prediction model proposed in this paper consists of two parts. The CNN module is mainly responsible for receiving input data, extracting dominant features, and compressing feature dimensions for output. The GRU module receives the CNN compressed feature sequence and completes the load prediction.

There are many different factors affecting the accuracy of bus load prediction, and they are independent timing sequences. In order to meet the data format requirements of the predictive model input CNN, historical bus load data, day type, meteorological factors, load transfer and time-of-use electricity price are connected in series to form a feature vector, and enter the vector map into the CNN in a time series manner. There are 16 influencing factors at a single moment. In order to make full use of various influencing factors, the feature map size after CNN processing is set to 16 * 16, and the convolution step size is set to 1. The convolution process is performed according to the same mode, so the corresponding padding size is 1, and the size of the convolution kernel is calculated as 3 * 3 by the following formula. The smaller core size can extract the underlying features as much as possible. Where S is the convolution step size, P is the fill size, and F is the convolution kernel size.

$$H_{output} = W_{output} = \frac{H_{input} - F + 2p}{S} + 1 \tag{5}$$

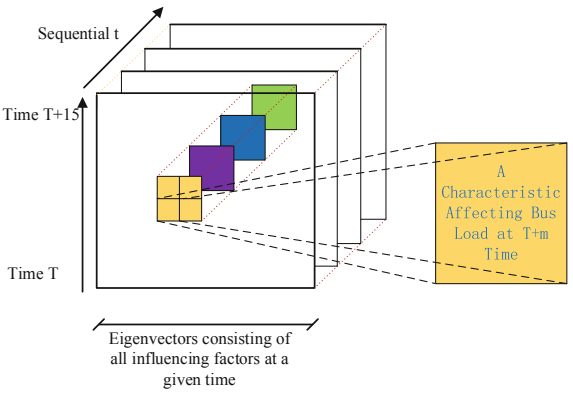

Fig. 3 Input layer data format of CNN-GRU network

According to the technical specifications of the daily load forecast, the load value of 96 points on the next day is predicted one day in advance, and the time interval at each time is 15 min. The time-ordered input data chain is shown in Fig. 3.

The CNN-GRU network model proposed in this paper is shown in Fig. 4. The model is divided into two parts: feature extraction and load prediction. The feature extraction part is divided into four layers of CNN, and the convolution and pooling operations are repeated. The number of filters in each layer is 32, 64, 128, 256, the pooling receptive field is 2 * 2, and the step size is 2. Set the convolution kernel step size to 1, and the pooling step size to 2, and the pooling mode to the maximum pooling. In this way, the down-sampling of the spatial dimension is entirely responsible for the pooling layer, and the convolutional layer is only responsible for transforming the depth of the input data.

GRU units can also be superimposed like LSTM, and the layered GRU units will achieve higher capacity network depth and better processing of complex sequences.

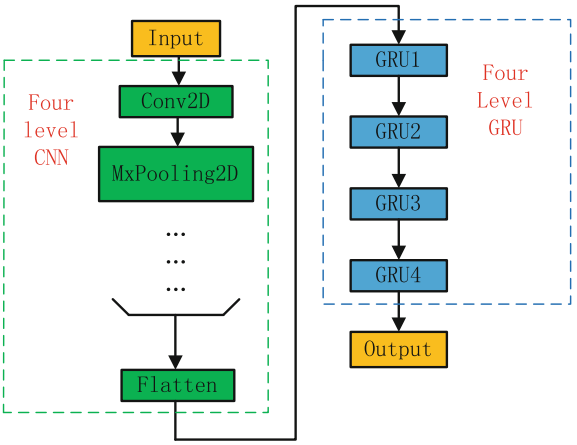

Fig. 4 CNN-GRU network model

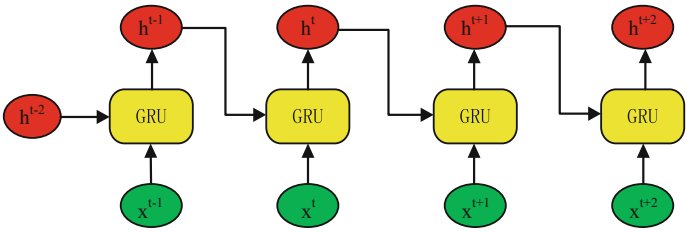

Fig. 5 GRU unit superimposed in chronological order

Through repeated experimental analysis, it is found that the four-layer GRU unit performs relatively better in bus load forecasting, and the training efficiency and accuracy are higher. Figure 5 shows the GRU unit being superimposed in time series. The GRU output of each layer together with the state of the hidden layer at the previous moment constitutes the input of the next moment, set the first three layers of return sequences to true, and get the complete sequence as the input to the next layer, and the last layer's return sequences is set to false to get the final output, that is, each timestep has a time prediction value.

4 Experiment and Result Analysis

This paper selects several bus load data from a certain city in the east from 2012 to 2018, as well as related date types, meteorological data, renewable energy generation plans, and time-of-use electricity price data as experimental data. The data from 2012 to 2017 is used as sample data, and the data of 2018 is used as test data. In order to verify the effectiveness of the proposed algorithm, the traditional BP neural network (BPNN) model is implemented at the same time, and the experimental comparison analysis is carried out. In order to verify the effectiveness of the proposed algorithm, the bus load selection covers these transformers with various characteristics, such as renewable energy generation, industrial load, and civil/commercial load. In addition, in order to highlight the research focus, the experiment excluded equipment maintenance and load transfer.

4.1 Data Preparation and Feature Processing

Bus load data and renewable energy generation are collected at 96 sections (15 min) per-day, and weather data is collected 24 h per day. In the experimental analysis, the weather data is interpolated to 96 points, that is, the same as the bus load. Considering that the actual system failure or abnormal due to channel or other

reasons, this paper uses the method of Ref. [17] to correct the bus load data, renewable energy generation and weather data.

Since each feature of the bus load has different unit and order of magnitude, the data set is standardized by the min-max method. All feature data is mapped to the [0, 1] interval, and the unit limit of the data is removed, and converted into a dimensionless pure number for comparison and weighting.

$$x_{norm} = \frac{x - x_{min}}{x_{max} - x_{min}} \tag{6}$$

where x_{norm} is the value after normalization.

Since the date type (such as working days, weekends, and holidays) and time-of-use electricity price are discrete values. In order to calculate the distance between features more reasonable, the paper uses the One-Hot method to extend the value of discrete features to the Euclidean space, effectively avoiding the shortcomings of tag coding.

4.2 Forecast Evaluation Criteria

According to the relevant assessment indicators used by power supply companies, the relative error indicators can reflect the correctness and accuracy of the prediction results. It is very sensitive to extreme and minimal error responses, and the smaller the value, the more accurate the prediction result. For a certain section i, the calculation formula of the relative error is:

$$E_i = \frac{|y_i - \hat{y}_i|}{y_b} \times 100\% \tag{7}$$

y_i is the measured bus load at section i, $\hat{y}_i$ is the predicted bus load at section i; y_b is the power reference value for the bus load, and its value is generally 305 MW. The daily average error and accuracy of the bus load is calculated as follows:

$$E_{Day} = \sum_{i=1}^{N} E_i / N \tag{8}$$

$$A_{Day} = \left(1 - \frac{\sum_{i=1}^{N} E_i^2}{N}\right) * 100\% \tag{9}$$

N is 96, and E_i is the relative error of the i-th (i = 1, 2, …, 96) section of the day.

4.3 Analysis of Results

In this paper, several bus loads in the test data set are predicted and compared in different time intervals of 2018 (covering the Spring Festival holiday, temperature stability period, high temperature period in summer, transition period from autumn to winter). Table 2 shows the comparison results of daily average error and daily accuracy. The CNN-GRU method proposed in this paper has higher accuracy in the test period, and its average relative error is 4.12%, and the average prediction accuracy is 96.46%. In four periods, the average prediction error of the CNN-GRU method was reduced by 0.79, 1.71, 1.75, and 0.33%, respectively, and the prediction accuracy was improved by 1.11, 2.22, 1.65, 1.34, and 0.41%.

Since the time interval of the experiment contains different seasons and typical holidays, the tested bus load contains multiple types of main transformers, indicating that the forecasting method proposed in this paper has a great improvement in prediction accuracy.

Figure 6 is a comparison of the predicted results of two methods for the measured load and experiment of a bus load for three consecutive days from April 17 to April 23, 2018.

Table 2 Comparison of bus load indicators in different time periods

Period	BPNN		CNN-GRU	
	E_{Day}	A_{Day}	E_{Day}	A_{Day}
Jan 16th to Mar 2nd	6.18	93.86	5.39	94.97
Apr 15th to May 17th	4.78	95.67	3.07	97.89
July 27th to Aug 18th	4.89	95.96	3.14	97.61
Oct 26th to Nov 21st	5.20	94.97	4.87	95.38
Average	5.26	95.12	4.12	96.46

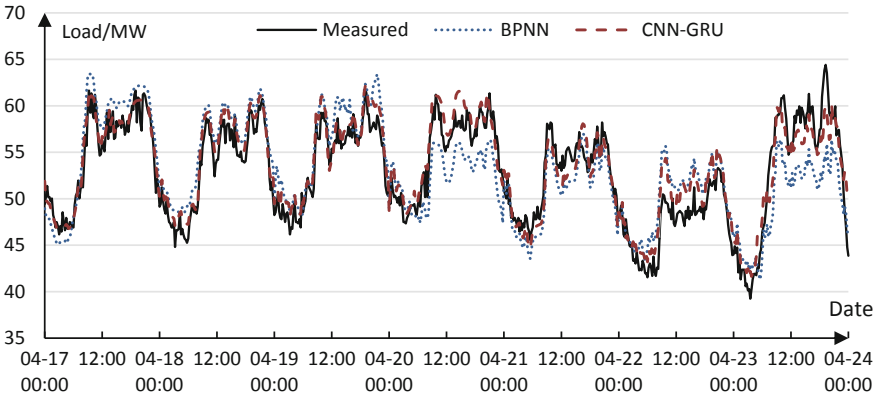

Fig. 6 Comparison chart of April 2018 predicted results

It can be seen from Fig. 6 that both methods can predict the change trend of bus load more accurately, but the proposed method has better fitting effect and less prediction error. When the bus load shape changes greatly, the proposed method can better predict the changing trend of bus load and improve the prediction accuracy.

5 Conclusion

This paper proposes a CNN-GRU network prediction model and introduces deep learning into bus load forecasting. This model fully considers the impact of various factors such as historical data, date type, weather data, load transfer, time of use electricity price on bus load forecasting. It relies on the powerful feature mining ability of CNN to extract and reconstruct the input sequence. Then a GRU deep neural network with four layers is constructed. Two simplified gating units of the GRU are used to efficiently process the reconstructed time series data of the CNN output to be responsible for bus load prediction. Compared with the traditional prediction method, the CNN-GRU deep neural network proposed in this paper has higher prediction accuracy and more flexible portability.

Acknowledgements This work is supported by the State Grid Corporation of China Science Project (52110418002A).

References

1. Kang C, Xia Q, Liu M (2017) Power system load forecasting. China Electric Power Press, Beijing
2. Li B, Men D, Yan Y et al (2015) Bus load forecasting based on numerical weather prediction. Autom Electr Power Syst 39(1):137–140
3. Caprio UD, Genesio R, Pozzi S et al (2010) Short term load forecasting in electric power systems: a comparison of ARMA models and extended wiener filtering. J Forecast 2(1):59–76
4. Osteragova E, Ostertag O (2012) Forecasting using simple exponential smoothing method. Acta Electrotech Inf 12:62–66
5. Nury AH, Hasan K, Alam MJB (2017) Comparative study of wavelet-ARIMA and wavelet-ANN models for temperature time series data in Northeastern Bangladesh. J King Saud Univ Sci 29(1):47–61
6. Wu Q, Gao J, Hou G et al (2016) Short-term load forecasting support vector machine algorithm based on multi-source heterogeneous fusion of load factors. Autom Electr Power Syst 40(15):67–72
7. Lin WM, Tu CS, Yang RF et al (2016) Particle swarm optimization aided least-square support vector machine for load forecast with spikes. IET Gener Trans Distrib 10(5):1145–1153
8. Wu X, He J, Zhang P et al (2015) Power system short-term load forecasting based on improved random forest with grey relation projection. Autom Electr Power Syst 39(12):50–55
9. Zheng K, Yang C (2017) Research of short-term load forecasting on Gradient Boosting Decision Tree (GBDT). GuiZhou Electr Power Technol 20(2):82–84, 90

10. Wu Y, Lei J, Bao L et al (2018) Short-term load forecasting based on improved grey relational analysis and neural network optimized by bat algorithm. Autom Electr Power Syst 42(20): 67–72
11. Zhou N, Liao J, Wang Q et al (2019) Analysis and prospect of deep learning application in smart grid. Autom Electr Power Syst 43(21):180–191
12. Narayan A, Hipel KW (2017) Long short term memory networks for short-term electric load forecasting. In: IEEE international conference on systems, man, and cybernetics (SMC), October 5–8, Banff, Canada, pp 2573–2578
13. Lu J, Zhang Q, Yang Z et al (2019) Short-term load forecasting method based on CNN-LSTM hybrid neural network model. Autom Electr Power Syst 43(8):131–137
14. Zhang X (2015) Research on algorithm and application of deep learning based on convolution neural network. XiDian University
15. Wang Z, Zhao B, Ji W et al (2019) Short-term load forecasting method based on GRU-NN model. Autom Electr Power Syst 43(5):50–58
16. Gou X (2004) Research on power system bus load forecasting. Sichuan University
17. Chen Y, Mu G, Duan F (2002) Identification and management to anomalous data in short term load forecasting. J Northeast China Inst Electr Power Eng 22(2):1–5

Design and Implementation of Intelligent Voice Service for New Generation of Power Grid Dispatch and Control System

Zhihua Wang, Jixiang Sun, Feng Gao, Kun Zhao, Hui Peng and Kun Huang

Abstract Aiming at the new requirement of natural language human-computer interaction in the new generation of power grid dispatch and control system, this paper designs and implements intelligent voice interaction service based on the voice engine of companies such as iFLYTEK and SinoVoice, combining the technology of Microservice, Redis database, Word2Vec, etc. By shielding the interface differences of commercial voice engines and providing a simple and consistent service-based interface, it is conducive to the convenient development of voice-related applications in the power grid dispatch and control system. The platform can flexibly change and expand the underlying commercial voice engine according to the actual needs, manage the context in the multi-round dialogue process. It can also store a large amount of voice information to provide support for later data mining and user behavior analysis.

Keywords Intelligent voice interaction · Power grid dispatch and control system · Microservice · Redis · Word vectors

J. Sun (✉) · K. Zhao · H. Peng · K. Huang
NARI Group Corporation (State Grid Electric Power Research Institute), Nanjing 211106, Jiangsu, China
e-mail: sunjixiang@sgepri.sgcc.com.cn

J. Sun · K. Zhao · H. Peng · K. Huang
NARI Technology Co., Ltd., Nanjing 211106, Jiangsu, China

H. Peng · K. Huang
State Key Laboratory of Smart Grid Protection and Control, Nanjing 211106, Jiangsu, China

Z. Wang · F. Gao
State Grid Shanghai Municipal Electric Power Company, Shanghai 2000120, China

Y. Xue et al. (eds.), *Proceedings of PURPLE MOUNTAIN FORUM 2019-International Forum on Smart Grid Protection and Control*, Lecture Notes in Electrical Engineering 585, https://doi.org/10.1007/978-981-13-9783-7_59

1 Introduction

With the development of artificial intelligence technology, the voice interaction technology has gradually gained the attention of the IT community. More and more technology companies have joined in the research of voice interaction. In addition to Apple, Google, Microsoft, and Amazon [1], there are also many companies in China that have emerged in the field of voice interaction, such as iFLYTEK, SinoVoice, Baidu and Sogou [2]. They all have launched their own voice capability engines, and each engine has its own advantages and disadvantages.

With the gradual application of artificial intelligence technology in the field of power grid [3], the new generation of power grid dispatch and control system takes voice interactive service as an important part of the common component module. But there is no uniform access interface standard between the above engines, which is not conducive to the development of voice software ecosystem within the power grid dispatch and control system [4]. In order to solve the above problem, the voice interactive service intends to provide uniform interface by shielding the differences of engine interfaces, and provides convenient ASR (automatic speech recognition), TTS (text to speech), NLU (natural language understanding), multi-round DM (dialogue management) and knowledge QA (question and answer) services for other modules in the system, which are Service-based and easy to expand.

This paper mainly introduces the basic architecture of the intelligent voice service and the key technologies involved, verifies the effectiveness and timeliness of the voice interaction service through experimental data, and makes a prospect for its application in the new generation power grid dispatch and control system.

2 The Overall Architecture of Intelligent Voice Service

See Fig. 1.

2.1 Access Layer

The voice-related functions in the new generation power grid dispatch and control system will be applied to multiple types of terminals such as PC workstations, mobile phones and tablets, involving various operating systems such as Linux, Windows and Android.

Therefore, the access layer provides multiple access methods (TCP/IP, HTTPS, JSON) for the foreground application. After receiving various types of external requests, the access layer converts these requests to a unified form and then passes them to the agent layer.

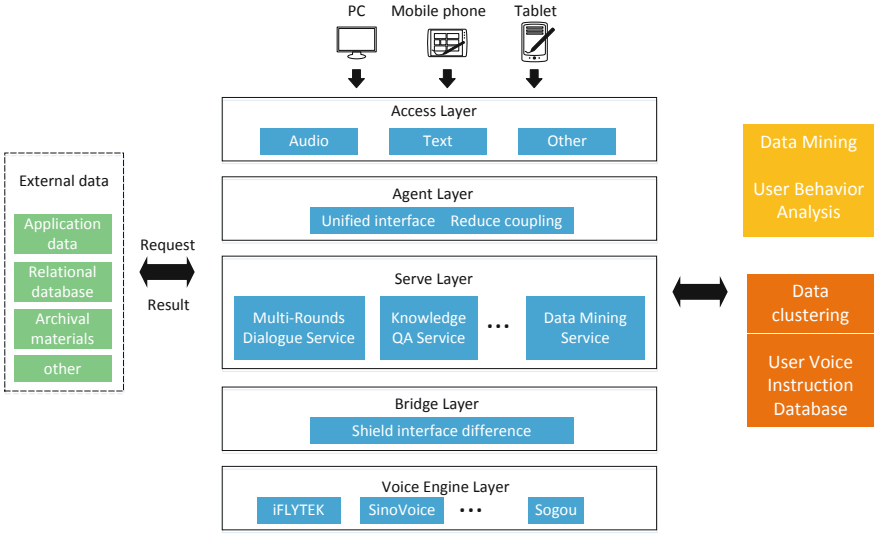

Fig. 1 The overall architecture of intelligent voice service

2.2 *Agent Layer*

The main function of the agent layer is to unify the micro-services entrance of the service layer, aggregate the back-end services, shield the internal structure of the service layer for the access layer, and make the changes in the service layer (service offline/online/upgrade) transparent to the access layer, so that the access layer can focus on the work about network communication.

2.3 *Service Layer*

Service layer is the core part of voice interaction service, which is divided into ASR (automatic speech recognition), TTS (text to speech), NLU (natural language understanding), multi-round DM (dialogue management) and knowledge QA (question and answer) services according to specific business. It can query business data and issue operation instructions by interacting with external data. At the same time, the user's interactive instructions are stored in the voice instruction database to facilitate subsequent data mining and user behavior analysis.

2.4 Bridge Layer

The function of bridge layer is to shield the interface differences of various voice engines, so that the upper voice application is not affected by the changes of the lower commercial voice engine. The bottom voice capability engine can be selected flexibly according to the actual conditions and the technical characteristics of each manufacturer when implementing voice interaction service.

2.5 Voice Engine Layer

The voice capability engines of companies such as iFLYTEK, SinoVoice, Sogou and Baidu all have high technical level, and each has mature product applications in ASR, TTS and NLU.

3 Key Technologies in Building Intelligent Voice Service

3.1 Unified Access Interface for Micro-services Based on API Gateway

Microservice [5] is an emerging software architecture, which is widely used in the field of electric power [6]. This architecture reduces complexity and can be easily upgraded and extended by breaking down applications and services into smaller, loosely coupled components.

The voice interaction service described in this paper refers to the idea of Microservice Architecture, which is subdivided into a set of interrelated micro-services such as ASR (automatic speech recognition), TTS (text to speech), NLU (natural language understanding), multi-round DM (dialogue management) and knowledge QA (question and answer) according to the actual business module (Fig. 2). Each service can be deployed independently and expanded on demand and the communication between micro-services in this system uses REST (representational state transfer) protocol [7].

Since the micro-services are stateless within the system, an agent (API Gateway) [8] is designed between each service and the external interface through which the service can be registered and managed. All clients and consumers access the micro-services through the agent and handle all non-business functions at the agent level. From the perspective of object-oriented design, it is similar to the appearance mode [9]. This API Gateway has the following effects in the voice interaction service described in this article:

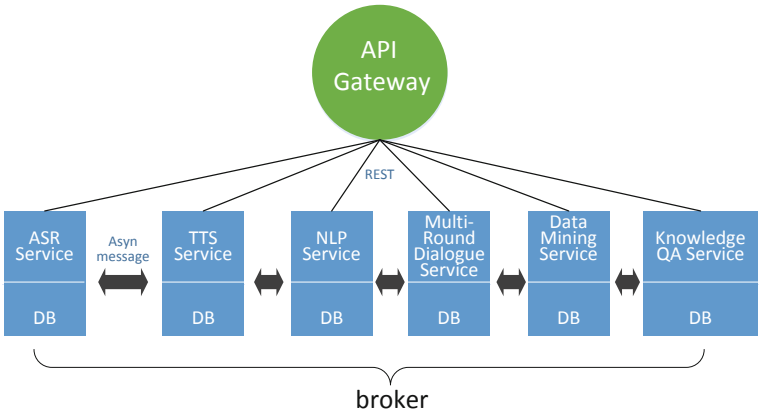

Fig. 2 Unified access interface for micro-services based on API Gateway

1. Providing uniform service access to make micro-services transparent to the access layer;
2. Decoupling access layer and service layer while aggregating back-end services, saving traffic and improving performance;
3. Unified maintenance and management of user login information and privileges;
4. Provide context management mechanisms for multi-round dialogue.

3.2 Dialogue Management Service Based on Limited-Case Mechanical Method

The DM is the "brain" in the dialog system, and the dialog manager will update the dialog state and select one or more selected system actions. Common dialog management methods include: limited-case mechanical method, framework-based method, statistical method, and end-to-end neural network learning method [10]. In this paper, limited-case mechanical method is used for session management. As shown in Fig. 3, each state is associated with a specific operation performed in that state. The conditions entered by the user have boundaries, which are paired to the next state by <status, user input>. This method is easy to achieve high accuracy, but it is difficult to expand to more complex areas.

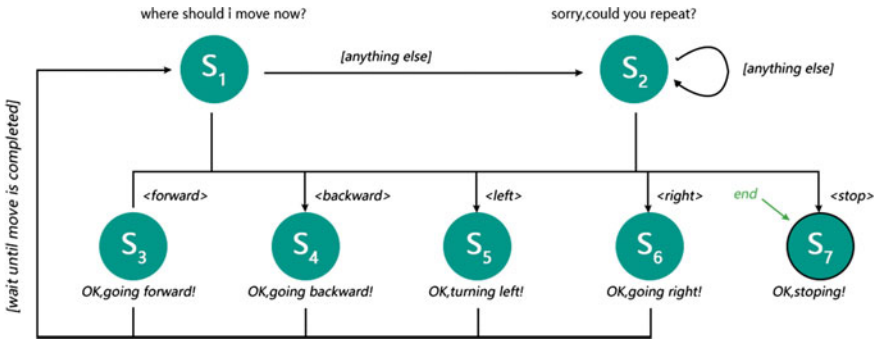

Fig. 3 Dialogue management service based on limited-case mechanical method

3.3 *Redis-Based Multi-round Dialogue Context Management*

In the process of man-machine dialogue, multiple rounds of conversation are often required to fully express the user's instruction intent, while general micro-services are stateless within the system, so the context information of the dialogue requires a unified management mechanism.

This paper adopts the context management technology based on Redis [11]. When the user initiates a new multi-round dialogue, the multi-round dialogue service will generate a global unique ID, update and store the context information during the session together with the ID. The context information can be quickly queried from Redis database by ID and the ID can also be used to clear the context to end this multi-round dialogue (Fig. 4).

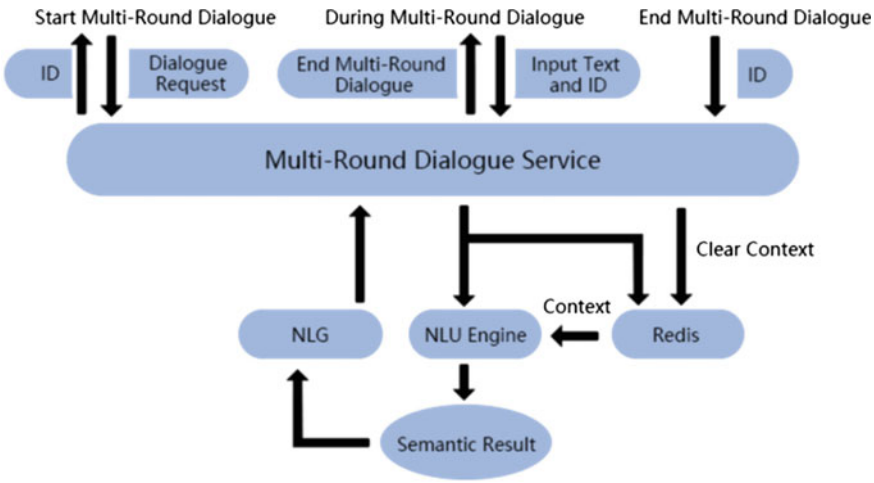

Fig. 4 Redis-based multi-round dialogue context management

3.4 Knowledge QA Based on Word Vector

The knowledge QA (question and answer) service in this paper is mainly used to query the operation rules in the field of power grid dispatching and control. The difficulty lies in how to match the user's spoken query language to a standard question in the pre-set question base.

In order to solve this problem, the equipment name, bus name, operation ticket text and telephone recording record of dispatching station are collected as professional corpus, and the corpus resources shared by Information Retrieval Laboratory of Harbin University of Technology are used as general corpus. According to the different weights of the application of professional corpus and general corpus, the word segmentation method of 'lexicon + word frequency statistics' [12] is adopted. The word vector [13] is learnt from these text data unsupervised, and a set of word library suitable for the power grid dispatch and control system is established by using word vector processing framework (such as Word2Vec) [14]. The vector processing diagram is shown in Fig. 5, and the process is described as follows:

1. word segmentation and vector processing
   a. Use the maximum matching method (forward and reverse) to compare with the thesaurus. When encountering a word that cannot be matched, cut the whole into a word and update to the basic vocabulary;
   b. After entering the next text, continue to use the updated basic vocabulary to continue the word segmentation;
   c. After the word segmentation, the word vector is generated and iteratively calculated, and the corresponding model is used to optimize the word vector.
2. update the thesaurus [15]
   a. After the training is over, update the basic vocabulary and word vector;
   b. Finally, remove the word vector and word less than a predetermined threshold in the thesaurus.

On the basis of the above, the standard question matching process is shown in Fig. 6:

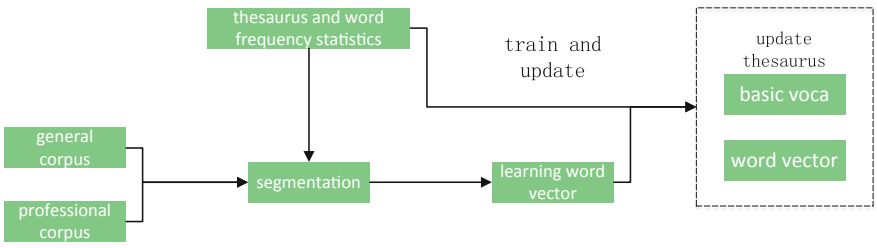

Fig. 5 Word vector processing diagram

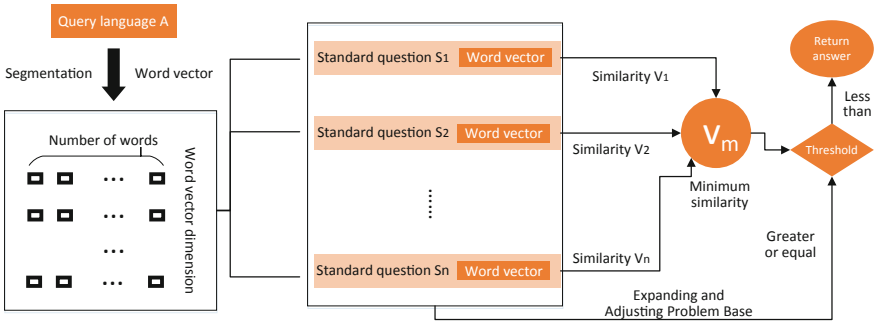

Fig. 6 Knowledge QA based on word vector

3.5 *User Behavior Analysis Based on Clustering*

The data mining service can cluster and analyze the transcribed results of voice data, and combine user login information to mine user's behavior habits, so as to gradually improve intelligent level of the voice interaction service.

In this paper, the original K-Means [16] algorithm is optimized, and the Bisecting K-means algorithm [17] is used to process the voice instructions to achieve accurate division of the user's voice interaction behavior. The Bisecting K-means algorithm is a distance-based non-hierarchical clustering algorithm. On the basis of the minimum error function, the data is divided into a predetermined number K, and the distance is used as a similarity evaluation criterion. That is, the closer the distance between the two objects is, the greater the similarity is. The similarity between samples is measured by Euclidean distance (Eq. 1), d(i,j) is the Euclidean distance between the sample vectors, and x_i and x_j are the elements in the vectors.

$$\mathrm{d}(\mathrm{i},\mathrm{j}) = \sqrt{\left(x_{i1} - x_{j1}\right)^2 + \left(x_{i2} - x_{j2}\right)^2 + \cdots + \left(x_{ip} - x_{jp}\right)^2} \tag{1}$$

Sum of the Squared Error (SSE) is used as the objective function of the cluster (Eq. 2), Ci is the center of the cluster i, and dist(Ci, x) represents the Euclidean distance between the samples x and Ci. The K-means are run twice to generate two different clusters, and the smallest one of SSE is selected.

$$\mathrm{SSE} = \sum_{i=1}^{k} \sum_{x \in Ci} dist(Ci, x)^2 \tag{2}$$

The specific steps of the Bisecting K-means algorithm are as follows:

1. Treat all data as a cluster and classify the sample data into K classes;
2. When the number of clusters is less than K, calculate the total error for each cluster;

3. Perform K-Means clustering on a given cluster with a K value of 2;
4. Calculate the total error after dividing the cluster into two clusters and the total error of clusters not participating in the partition, and select a cluster with the smallest total error to divide;
5. When the number of centroids is less than K, go to step 2, otherwise, get the clustering result.

4 Application Cases

In order to realize the voice interactive service of the new generation power grid dispatch and control system and verify its effectiveness and real-time performance, the following development and verification environment was built:

1. Four servers, 32-core CPU, 64G memory, 1T hard disk, and Rocky6.0.80;
2. Extracted data from model libraries of State Grid Shanghai Electric Power Corporation and State Grid Jiangsu Electric Power Corporation to optimize models and build verification sets;
3. Purchased AI + Speech Capability Engine of iFLYTEK to provide basic ASR, TTS and NLU capabilities.

There are many proper nouns in the field of power grid dispatching and control, so common language models are difficult to achieve satisfactory results in speech recognition. In order to solve the problem, various types of proper nouns were extracted from the grid model data, and the training of proprietary language models was carried out. In order to test the training effect of the model, 100 station names, 500 circuit breaker names and 500 bus names were randomly selected from the model to form the test set at each time. Five staff members read the contents of the test set and calculated the average recognition rate. After half a year of language model optimization, the recognition rate of the station name, circuit breaker name and bus name has been significantly improved (Fig. 7).

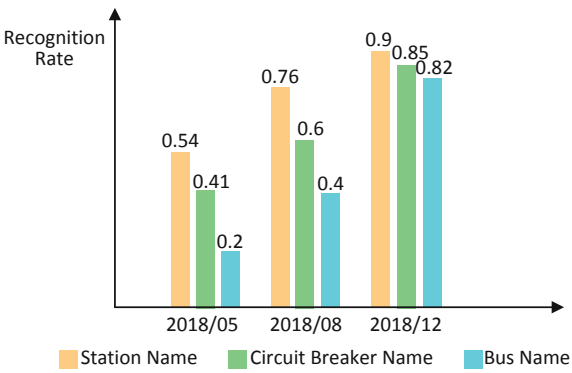

Fig. 7 Recognition rate of ASR in voice interactive service

Table 1 Real-time performance of the voice interaction service

Service	Concurrent quantity (1 server)	Concurrent quantity (3 server)	Response delay
ASR	70	210	Clause response time <800 ms
NLU	30	90	<410 ms
TTS	90	270	First response time <500 ms
Multi-round dialogues	30	90	<800 ms
Knowledge QA	30	90	<800 ms

In addition to ensuring functional correctness, the voice interactive service should also ensure real-time performance. The response time of the machine to the user should be guaranteed within 1 s. It was verified that the voice interactive service described in this paper has good real-time performance in ASR, NLU, TTS, Multi-Round Dialogues and Knowledge QA, and the concurrent amount increased linearly with the expansion of hardware (Table 1).

Based on the above research, the pilot work of voice interactive service was carried out in State Grid Shanghai Electric Power Corporation and State Grid Jiangsu Electric Power Corporation, and achieved good pilot results in Linux, Windows, Android and web environment.

5 Conclusion

In this paper, the voice interactive service which was suitable for the new generation of power grid dispatch and control system was designed by combining many technologies, such as Microservice, Redis, Word Vectors, and K-Means Clustering. Firstly, the overall framework of the voice interactive service was given and its microservice-based architecture model was described. Secondly, the Redis-based multi-round dialogue context management method was proposed. Finally, the standard problem matching method based on word-vector was proposed. In addition, it also provides preliminary processing for data mining and user behavior analysis through clustering voice commands. All those above provided a feasible basis for the application and promotion of voice interactive services.

With the systematic collection of professional corpus, large-scale training of language model and targeted optimization of knowledge base, voice interaction service will inevitably be more and more closely integrated into the daily production work, thus becoming an important mean of human-computer interaction in the new generation of power grid dispatch and control system.

Acknowledgements This work was supported by the Science and Technology Project of the State Grid Corporation of China: Research and Application of Key Technologies of Common Components of New Generation Grid Dispatch and Control System Platform (新一代电网调度控制系统平台公共组件关键技术研究与应用).

References

1. López G, Quesada L, Guerrero LA (2017) Alexa versus Siri versus Cortana versus Google assistant: a comparison of speech-based natural user interfaces
2. Jiang N Service recommendation method and apparatus with intelligent assistant: U.S. Patent Application 14/981,247[P]. 2016-5-12
3. Shan X, Lu X, Zhai M et al (2019) Analysis of key technologies for artificial intelligence applied to power grid dispatch and control. Autom Electr Power Syst 43(1):49–57. https://doi.org/10.7500/aeps20180629002
4. Bin Y, Bo X, Yuhua H et al (2014) State-of-art and trend of speech interaction for mobile intelligent terminal. Inf Commun Technol
5. Hongjian L (2018) Analysis on the application of microservice architecture and container technology. Wirel Internet Technol
6. Shi L, Shao P, Zhang X et al (2017) Discussion on architecture of new-generation electricity trading platform. Autom Electr Power Syst 41(24):67–76. https://doi.org/10.7500/aeps20170614003
7. Fielding, RT (2000) Architectural styles and the design of network-based software architectures. University of California, Irvine
8. Chu H, Li M, Xu F et al (2014) ConHA: an SOA-based API Gateway for consolidating heterogeneous HA clusters. In: IEEE international conference on cluster computing. IEEE
9. Gessert F, Bucklers F, Ritter N (2014) Orestes: a scalable database-as-a-service architecture for low latency. In: IEEE international conference on data engineering workshops. IEEE
10. Roy N, Pineau J, Thrun S (2000) Spoken dialogue management using probabilistic reasoning. ACL
11. Gao-Jun L, Di-Ao W (2013) Research of Redis-based distributed storage method for massive small files. Comput Eng Sci 35(10):58–64
12. Wang Z, Ren H, Lu X (2018) Key technologies of AI in customer service system. Telecommun Sci (12)
13. Tao L, Cichen W, Huakang L (2017) Development and construction of knowledge graph. J Nanjing Univ Sci Technol
14. Antonellis I, Bouras C, Poulopoulos V (2006) Personalized news categorization through scalable text classification. In: Asia-pacific web conference. Springer, Berlin, Heidelberg
15. Hu M, Liu B (2004) Mining and summarizing customer reviews. In: Proceedings of the tenth ACM SIGKDD international conference on knowledge discovery and data mining, Seattle, Washington, USA, 22–25 Aug 2004. ACM
16. Zhao M, Xu S, Gao H et al (2016) Strategy of electric vehicle emergency power supply based on fuzzy K-means algorithm. Autom Electr Power Syst 40(5):91–95. https://doi.org/10.7500/aeps20150304001
17. Yu H-T, Li Z, Yao N-M (2012) Research on optimization method for K-means clustering algorithm. J Chin Comput Syst 33(10):2273–2277

Semantic Knowledge Matching Based on BERT for Dispatching Fault Disposal Information

Jixiang Lu, Tao Zhang, Jinjun Lu, Yun Li, Hongsheng Xu and Ziqi Li

Abstract Power grid dispatching fault disposal documents are essential for dispatching operators while it is a challenge for them to use these documents efficiently and promptly due to unstructured text data. Recently a new language representation model, BERT (Bidirectional Encoder Representations from Transformers) has created state-of-the-art models for a wide variety of natural language processing tasks with fine-tuning. In this work, we propose a semantic knowledge matching approach based on redesigned fine-tuned BERT model for dispatching fault disposal documents. The experimental results demonstrate that our proposed approach achieves significant sentence-level semantic accuracy for the offline knowledge such as previous fault handling records and fault disposal documentations, The semantic knowledge matching result can also be referred for online fault handling automatically and promptly to improve grid disposal handling efficiency. This approach can be deployed as common one for natural language proceeding tasks of power grid.

J. Lu (✉) · T. Zhang · J. Lu · Y. Li · H. Xu · Z. Li
Technology Research Center of NARI Group Corporation, Nanjing, China
e-mail: lujixiang@sgepri.sgcc.com.cn

T. Zhang
e-mail: zhangtao11@sgepri.sgcc.com.cn

J. Lu
e-mail: lujinjun@sgepri.sgcc.com.cn

Y. Li
e-mail: liyun@sgepri.sgcc.com.cn

H. Xu
e-mail: xuhongsheng@sgepri.sgcc.com.cn

Z. Li
e-mail: liziqi@sgepri.sgcc.com.cn

J. Lu · J. Lu
State Key Laboratory of Intelligent Power Grid Protection and Operation Control, Nanjing, China

Y. Xue et al. (eds.), *Proceedings of PURPLE MOUNTAIN FORUM 2019-International Forum on Smart Grid Protection and Control*, Lecture Notes in Electrical Engineering 585, https://doi.org/10.1007/978-981-13-9783-7_60

Keywords Dispatching fault disposal · NLP · BERT · Semantic knowledge matching · Sentence representation

1 Introduction

At present, the dispatching and control operators in China make online analysis and dispose the power grid dispatching fault based on empirical knowledge and the pre-compiled dispatching fault disposal plan documentations. The documents accumulate basic predicted dispatching faults which are usually used by the dispatching operators as fault handling reference and operation guidelines. Due to the increasing load and expanding large scale of the power grid, it is impossible to predict all real time faults in the fault disposal documentations. How to use these documentations efficiently and promptly will be a challenge for dispatching operators. The Natural Language Processing (NLP) technique has been increasingly boosting as a branch of artificial intelligence deep learning technique in recent years. It is frequently involved in machine translation, speech recognition, natural language understanding and natural language generation [1, 2]. The request is raised for applying NLP to facilitate grid dispatching operators to understand unstructured text data semantically and detect the corresponding knowledge in fault disposal documents promptly, which could make power grid dispatching and control operation more accurate and intelligent. Similar to other deep learning tasks, the biggest common challenge in NLP is the shortage of massive training data. The dispatching fault disposal documents nowadays contain only a few thousands plain text sentence. To mitigate the training data shortage, data augmentation method is usually used to generate more training samples in deep learning. Some researchers suggest to make text data augmentation by replacing some words with synonyms. But it is hard to augment text data with this method in that power dispatching operations contents are professional domain specific. NLP transfer learning is another technique to address the data sparsity [3]. It approaches benefit from training on enormous amount of unannotated text corpora and getting pre-trained general-purposed language model, then fine tune the pre-trained model with domain specific sparse text data. BERT [4] model, released by Google in Oct. 2018, has implemented this NLP transfer learning with multiple pre-trained models provided in public. Inspired by BERT, we successfully make use of pre-trained general-purposed language encoders from BERT and revise the model, then fine-tune it in dispatching fault disposal documentations processing. We deploy this method to get semantic knowledge matching from dispatching fault disposal documents. The results prove that this method is helpful for dispatching operators, significantly improving their fault handling performance and efficiency.

Our contributions can be summarized as follows:

1. To the best of our knowledge, this paper is the first work to exploit dispatching fault disposal documentation contextualized embedding with BERT pre-trained model, and improve the semantic knowledge matching performance with fine-tuning.
2. We redesign fine-tuned BERT model and make the new model by employing a weighted sum of BERT internal layer hidden states. It creates state-of-the-art accuracy for grid dispatching fault disposal learning tasks.
3. We propose a general method of Chinese domain language text representations for domain specific task with sparse training text data, which can be used in common NLP task processes.

The rest of paper is organized as follows: First, we present related work in Sect. 2. Then, describe contextual embedding generation for dispatching fault disposal documents with BERT pre-trained model and the new designed fine-tuned BERT model in Sect. 3. We show experiment results and provide an in-depth analysis in Sect. 4. Finally some conclusions are given in Sect. 5.

2 Related Work

Understanding human language is a challenging task for computers, as they were originally designed for crunching numbers. In order to make computers comprehend text as humans do, it needs to encode the complexities and nuances of natural language into numbers, presented as word embedding (word encoding). Word2Vec is introduced and popularized by Mikolov et al. [5] on word embedding process. Word embedding allows the semantic meaning of a word to be represented as a real-valued vector, semantically similar words are represented by geometrically close vectors. But the word vector remains stable and cannot dynamically alter the word representation based on the contextual information. For example, the word "bank" in "open a bank account" and "on the river bank" has different meaning. ELMo [6] and BERT are such deep contextualized word representations. ELMo considers the word embedding as the input feature of downstream task and work with Bi-LSTM while BERT can be used by downstream task directly with fine-tuning. BERT model has being boosted recently, Guo et al. [7] worked on reading answer from Database without SQL form, they propose method to learn from question and search result directly in tables with BERT based model; Si et al. [8] enhanced clinical concept extraction with BERT model for contextualize representations; Zhang et al. [9] used BERT model on text summarization task successfully; Huang et al. [10] used BERT model on neural Chinese word segmentation which is faster and more accurate than the previous state-of-the-art BiLSTM-CRF model. For grid dispatching fault text analysis and handling, Wei et al. [11] made some research on unstructured text data mining and fault

classification based on RNN-LSTM; Cao et al. [12] made text classification based on TextCNN for power grid user fault repairing information. Shan et al. [13] described fault disposal robot technology, based on knowledge graph technique and slot filling for disposal guidelines. All research above cannot reach high accuracy in contextual representations due to the language model limitation, but they shed light on our work.

3 BERT Model with Fine-Tuning

BERT, which stands for Bidirectional Encoder Representations from Transformers, is published by Google and it is trained based on the corpus of 3.3 billion texts. BERT's key technical innovation is applying mask language model for unsupervised bidirectional training of transformer [14] and next sentence prediction. This characteristic allows the model to learn the context of a word based on all of its surroundings. BERT is undoubtedly a breakthrough in the use of Machine Learning for NLP and it has substantially advanced the state-of-the-art results in a number of NLP tasks, such as GLUE [15] benchmark for natural language processing, SQuAD v2.0 [16] for question and answering and SWAG [17] for multiple choice questions about a rich spectrum of grounded situations.

BERT's attention model between encoder and decoder is crucial and it is a function that maps the input (a query q, a set of key-value pairs) to an output. Output is weighted sum of values where weight of each value is computed by an inner product of query and corresponding key. Scaled dot-product attention is listed as (1):

$$\text{Attention}(q, K, V) = \sum_i \frac{e^{q.k_i}}{\sum_j e^{q.k_j}} v_i \tag{1}$$

The BERT input representation is a concatenation of word token embeddings, position embeddings, and the segment embeddings. A special classification embedding ([CLS]) is inserted as the first token and a special separation token ([SEP]) is added as the final token as well. Compared with Bi-LSTM which process the sequence step by step, BERT learns features in parallel for all steps so that the decoding speed can be accelerated.

Google has just released 7 different out-of-box pre-trained models publicly and Chinese support model is included as well. It uses character-based tokenization for Chinese training from massive Wikipedia Chinese corpus and 110 K Chinese language WordPiece vocabulary. The BERT Chinese pre-training model is made up with 12 straightforward layers (i.e., transformer blocks), with 768 hidden size and 3072 feed-forward/filter size accordingly for each layer. We modified the BERT

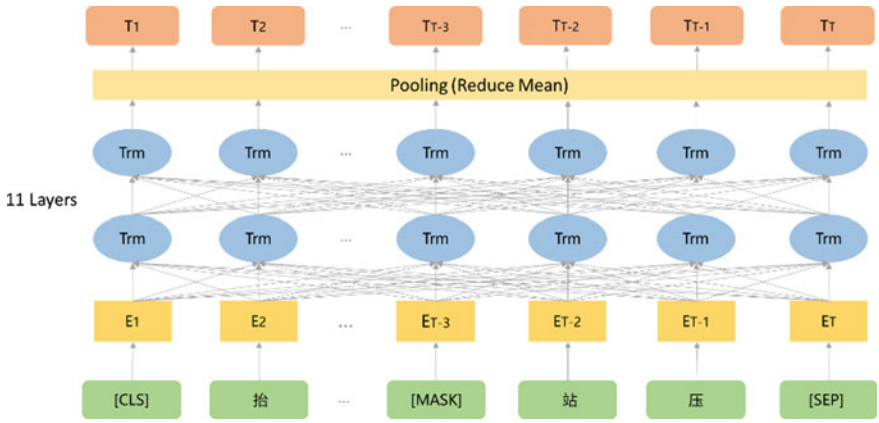

Fig. 1 The architecture of contextual representations model based on Chinese BERT

fine-tuning model architecture by simply taking the second-to-last layer of BERT model and do the pooling with reduce mean strategy, 11 layers totally in our model. Figure 1 gives the architecture of contextual representations model based on Chinese BERT model.

Generally, BERT Chinese pre-trained model contains 3 items in the package: a TensorFlow checkpoint file containing the pre-trained weights, a vocabulary file to map WordPiece to word id and a configuration file which specifies the hyper-parameters of the model. These 3 files need to be defined clearly when to use the pre-trained model. The pre-trained model can be migrated to construct new model by adding final layer to the pre-training model and keeping all other layer parameters frozen, then use few specific task data as input to retrain the model. Since it only need generate few parameters for last layer and no need to train the whole millions of parameters from the scratch. The advantage of fine-tuning is to greatly accelerate the convergence speed of task training and achieve good effect while model training cost is inexpensive.

BERT pre-trained model is based on massive Wikipedia data (2500 M words) and BookCorpus data (800 M words), which encoded enough prior knowledge of the language into the model. But this prior knowledge is not specific to any particular domain, such as power grid dispatching. So we will use power grid dispatching text data to fine-tune the pre-trained model. Figure 2 provides the workflow of semantic knowledge matching.

In summary, pre-training model learns from plain text data that is available on the web in public, with the goal of capturing the general grammar and contextual information of a language. Fine-tuning model learns from a specific task such as reading comprehension or data from a particular domain such as power grid.

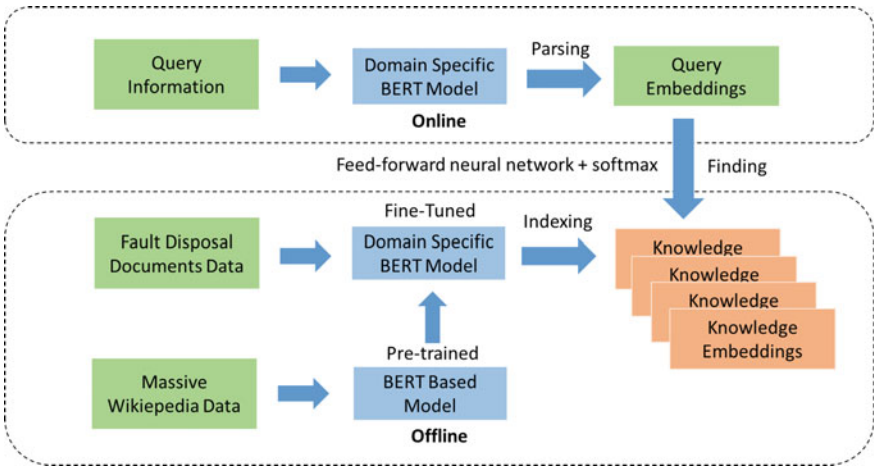

Fig. 2 The work-flow of semantic knowledge matching

4 Experiment

4.1 Data Set

We use fault planning and disposal procedures text data of East China area power grid dispatching as input dataset, just follow the BERT training data format and add the [CLS] and [SEP] tokens in the right place in each sentence accordingly, totally 8757 sentences. Training samples and test samples were randomly selected to ensure the versatility of the model test. We convert the fault disposal documents to plain text format as input text file with some necessary cleanup, in the file each paraphrase is arranged as predicted fault name, grid stability requirement, post-fault mode and fault procedure guidelines in sequence. Each paraphrase is delimited by empty line. To get the contextual word representations, we simply take the second-to-last layer of fine-tuned BERT model and do pooling operation as Fig. 1 shown, then get the semantic embedding for each sentence with fixed length.

4.2 Fine-Tune

During fine-tuning, maximum sequence length for each sentence is set to 128 and maximum prediction per sequence as 20, the masked language model probability is set 15% which is BERT recommended. So 3 random words will be masked per sequence. Adam [18] is used for optimization with an initial learning rate of 5e-5. The dropout probability is 0.1. Proportion of training to perform linear learning rate "warm_up" is 0.1. The output is a set of TFRecord data file in a simple

record-oriented binary format. Training steps are set as 10,000 steps. Firstly we extract a variable length sentence into a fixed length 768-dimensional vector, then we perform offline semantic compilation for all fault disposal texts in documents and generate corresponding 768-dimensional vector list. When a new online query is coming, we encode it as a 768-dimensional embedding vector and compute its dot product with the pre-compiled embedding vectors, so query and document will be mapped in same space, finally the top-k similar knowledge will be returned promptly in descending order, which is very useful for dispatching operator.

Table 1 list the benchmark results from the BERT pre-trained model with fine-tuning and from the model without fine-tuning. Based on the results, we can figure out the average of accuracy is 96.130% for the model with fine-tuning compared with 75.125% for the model without fine-tuning. It indicates the fine-tuning method is necessary for domain specific task no matter the pre-trained model is general-purposed and pre-trained on so massive corpora such as BERT model.

Table 1 The accuracy and loss benchmark model with fine-tuning and without fine-tuning

Data set	Round	With fine-tuning			Without fine-tuning
		eval_accy	eval_loss	eval_accy	eval_loss
opt__train_800_1.tsv & opt_dev_200_1.tsv	1	0.965	0.14962012	0.82	0.50313574
	2	0.97	0.12835178	0.675	0.96522987
	3	0.965	0.14664508	0.5	0.92602134
	4	0.955	0.1346364	0.885	0.29733983
	5	0.95	0.16376495	0.775	0.69384164
opt__train_800_2.tsv & opt_dev_200_2.tsv	1	0.955	0.15455307	0.82	0.50765723
	2	0.97	0.12640835	0.67	0.68823576
	3	0.945	0.18697582	0.525	0.86452204
	4	0.96	0.16557154	0.785	0.54136354
	5	0.97	0.12200645	0.84	0.47623637
opt__train_800_3.tsv & opt_dev_200_3.tsv	1	0.965	0.12098686	0.84	0.5015608
	2	0.97	0.09104013	0.695	0.72487104
	3	0.97	0.13240388	0.89	0.3574343
	4	0.97	0.09955174	0.835	0.37291923
	5	0.955	0.12914191	0.53	0.86407274
opt__train_800_4.tsv & opt_dev_200_4.tsv	1	0.97	0.16031155	0.85	0.4470843
	2	0.96	0.13002577	0.87	0.3904172
	3	0.965	0.16088077	0.575	0.84775263
	4	0.945	0.17905125	0.755	0.6356970
	5	0.955	0.18540974	0.89	0.32880098

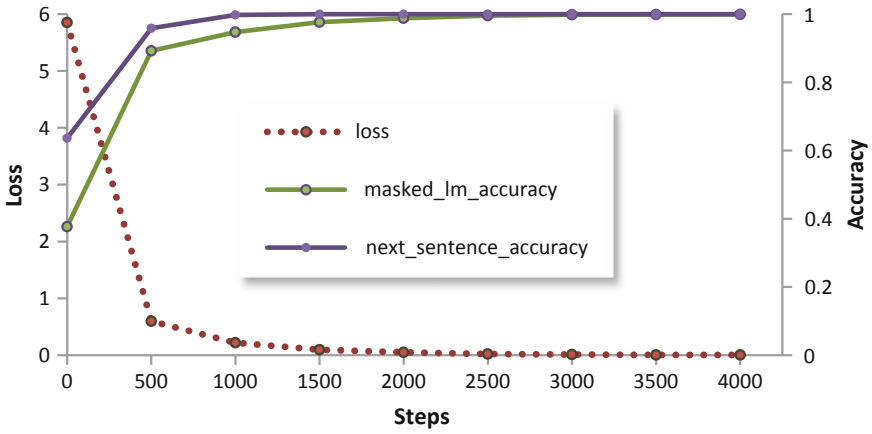

Fig. 3 Accuracy and loss of the fine-tuned BERT model for different training steps

4.3 Result

Our fine-tuned BERT model enjoys higher masked accuracy as Fig. 3, better next sentence prediction performance and lower loss as the number of training steps grows before reaching the extreme values. The curve of loss shows a rapid drop of the loss between 0 and 500 training steps. When the number of training step reaches 2000, the loss is almost 0. The curve of masked_lm_accuracy indicates that the masked_lm_accuracy greatly grows before 500 training steps and is almost 1 with the number of training step reaching 2000; Similar to the masked_lm_accuracy, the next_sentence_accuracy almost reaches 1 as the model is trained for 1000 steps and it also rapidly grows between 0 and 500 steps.

Compared with the original BERT model, our fine-tuned one performs better in terms of doing fuzzy semantic matching on the sentences of the fault planning and disposal procedures text data of East China area power grid dispatching.

5 Conclusion and Future Work

In this paper, we present semantic knowledge matching approach which fine-tunes the pre-trained Chinese BERT base model with domain specific unstructured sparse text data. We redesign fine-tuned BERT model and make the new model general for contextual representations with low bias. This approach is experimentally successful on East China area dispatching fault disposal documents and reaches state-of-the-art accuracy of particular domain NLP task. The Chinese BERT pre-training model we use is character-based. Unlike English text, Chinese has no spaces and cannot be separated from sentence directly. So Chinese word

segmentation will be carried out and incorporate with BERT based model more accurately in Chinese text in further study. Also, BERT based model is computationally inefficient due to a large number of parameters, for example, 110 million parameters in BERT base model and 340 million parameters in BERT large model. Performance improving, pruning, quantization and optimization on the fine-tuned model will be another focus in future work as well.

Acknowledgements This work is supported by National Key Development Plan Program (No.2017YFB0902605) and State Grids Science and Technology Program (Research on Key Technologies of Knowledge Mapping in Power Grid Fault Processing), and partially supported by Collaborative Innovation Center of Novel Software Technology and Industrialization.

References

1. Zhou N et al (2019) Developing Status and Prospect Analysis of Deep Learning in Smart Grid. Autom Electr Power Syst 43(04):180–197
2. Xin Shan et al (2019) Analysis of key technologies for artificial intelligence applied to power grid dispatch and control. Autom Electr Power Syst 43(01):49–57
3. Lefeng Cheng et al (2019) Machine learning for energy and electric power systems state of the art and prospects. Autom Electr Power Syst 43(01):15–43
4. Devlin J, Chang MW et al (2018) Bert: pre-training of deep bidirectional transformers for language understanding. arXiv preprint. arXiv:1810.04805
5. Mikolov T, Sutskever I, Chen K, et al (2013) Distributed representations of words and phrases and their compositionality. Adv Neural Inf Proc Syst 3111–3119
6. Peters ME, Neumann M, Iyyer M, et al (2018) Deep contextualized word representations. arXiv preprint. arXiv:1802.05365
7. Guo T, Gao H (2019) Table2answer: read the database and answer without SQL. arXiv preprint. arXiv:1902.04260
8. Si Y, Wang J, Xu H et al (2019) Enhancing clinical concept extraction with contextual embedding. arXiv preprint. arXiv:1902.08691
9. Zhang H, Gong Y, Yan Y et al (2019) Pretraining-based natural language generation for text summarization. arXiv preprint. arXiv:1902.09243
10. Huang W, Cheng X, Chen K et al (2019) Toward fast and accurate neural chinese word segmentation with multi-criteria learning. arXiv preprint. arXiv:1903.04190
11. Wei D, Wang B, Lin G et al (2017) Research on unstructured text data mining and fault classification based on RNN-LSTM with malfunction inspection report. Energies 10(3):406
12. Cao YK, Zhao T (2018) Text classification based on text CNN for power grid user fault repairing information. In: 2018 5th international conference on systems and informatics (ICSAI). IEEE, pp 1182–1187
13. Shan X, Zhu B, Wang B et al (2018) Research on deep learning based dispatching fault disposal robot technology. In: 2018 2nd IEEE conference on energy internet and energy system integration (EI2). IEEE, pp 1–6
14. Vaswani A, Shazeer N, Parmar N, Uszkoreit J, Jones L, Gomez AN, Kaiser Ł, Polosukhin I (2017) Attention is all you need. Adv Neural Inf Process Syst 6000–6010
15. Wang A, Singh A, Michael J et al (2018) Glue: a multi-task benchmark and analysis platform for natural language understanding. arXiv preprint. arXiv:1804.07461
16. Rajpurkar P, Zhang J, Lopyrev K et al (2016) Squad: 100,000+ questions for machine comprehension of text. arXiv preprint. arXiv:1606.05250

17. Zellers R, Bisk Y, Schwartz R, Choi Y (2018) SWAG: a large-scale adversarial dataset for grounded commonsense inference. In: Empirical Methods in Natural Language Processing, pp 93–104
18. Kingma DP, Ba J (2014) Adam: a method for stochastic optimization. arXiv preprint. arXiv:1412.6980

Constant Voltage Output Wireless Power and Information Transmission System Based on ZCS Resonance Point Switching Method

Xiaohua Huang, Bin Wei, Chong Xu, Zhen Wu and Chenyang Xia

Abstract Using the stroboscopic mapping model, the ZCS resonance working point of the ICPT system is obtained, and the single-channel 2FSK signal modulation and demodulation are realized based on the resonance point switching. In order to eliminate the influence of transmission signals of different resonance points on the load voltage, a buck converter is added and the controller is designed. The simulation and experimental results show that the technology can effectively reduce the volume and cost of the ICPT system while realizing wireless power and information transmission and constant voltage output.

Keywords ICPT · Constant voltage output · Wireless power and information transmission · ZCS resonance

1 Introduction

With the improvement of automation and intelligent requirements, the Inductively Coupled Power Transfer (ICPT) system is required to have the ability to realize non-contact transmission of signals and power at the same time [1–5]. At present, the simultaneous transmission of power and signals in ICPT system is divided into RF technology [6], double channel transmission [7, 8] and single-channel transmission [9]. Though RF technology is widely used, the cost increases. The cross-coupling interference between the two sets of the dual-channel magnetic circuit mechanisms is exist. Compared with the above technology, the single-channel technology has received more attention and research.

X. Huang (✉) · B. Wei · C. Xu
China Electric Power Research Institute, Beijing 100192, China
e-mail: bluesky198210@163.com

Z. Wu · C. Xia
School of Electrical and Power Engineering, China University of Mining and Technology, Xuzhou, Jiangsu 221116, China

Y. Xue et al. (eds.), *Proceedings of PURPLE MOUNTAIN FORUM 2019-International Forum on Smart Grid Protection and Control*, Lecture Notes in Electrical Engineering 585, https://doi.org/10.1007/978-981-13-9783-7_61

For the single-channel wireless power and information transmission technology, mainly adopts amplitude modulation, frequency modulation, and phase modulation. A technique is proposed by using harmonic transmission signals [10]. In this paper, the stroboscopic mapping method is used to obtain the ZCS resonance working point of the ICPT system. 2FSK signal modulation and demodulation based on resonant point switching. In order to eliminate the influence of signal transmission a DC–DC converter is added and the controller is designed to realize the synchronous transmission of 2FSK energy and signal under the condition of a constant output voltage.

2 Wireless Power and Information Transmission ICPT System in Constant Voltage Output

Figure 1 is the schematic diagram of wireless power and information transmission ICPT system. It is mainly composed of a DC power supply E, a buck circuit, and a primary inverter, a primary side transmitting mechanism, a secondary side pickup mechanism, and a rectifier circuit. The primary side transmitting mechanism includes a resonant capacitor C_p, a transmitting coil L_p, The power transmission channel comprises a compensation capacitor C_s, a pickup coil L_s and an internal resistance R_s.

The principle of synchronous transmission of power and signal is: The frequency of the device is based on 2FSK to achieve signal modulation, at the pickup terminal, demodulation is performed by 2FSK, changing the operating frequency of the inverter to realize the signal modulation. In the pickup side, a sampling resistor

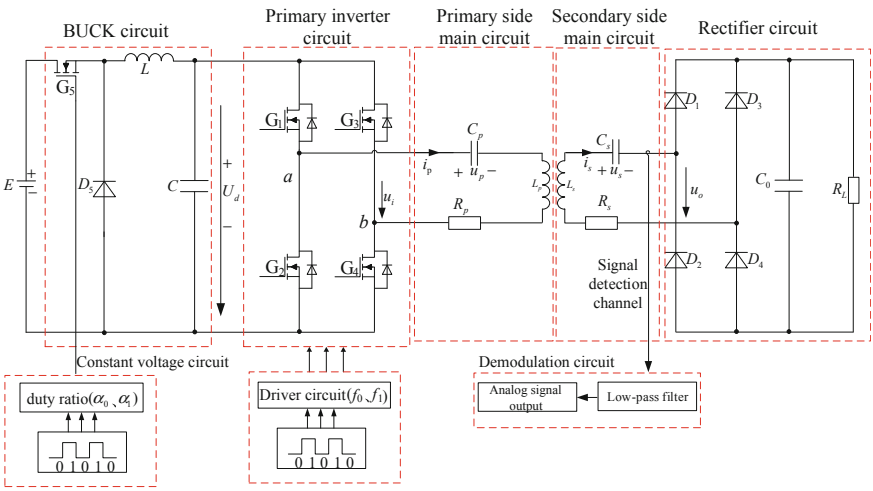

Fig. 1 The principle of synchronous transmission of power and signal in ICPT system

R_{SENSE} with a small resistance is added to sample the current on the resistor, and a second-order active low-pass circuit is used to realize signal demodulation.

The principle of constant output control is: When the system frequency is changed, the output voltage is also affected. Therefore, in order to ensure accurate modulation and demodulation of the signal and constant voltage output, a buck circuit is added, which can keep constant voltage output by changing the its duty ratio.

3 Calculation and Analysis of Multiple Resonance Points

The power and signal synchronous transmission system of Fig. 1 is simplified to Fig. 2, the load R_L in the rectifier circuit is equivalent.

$$R_{eq} = \frac{8}{\pi^2} R_L \tag{1}$$

3.1 Stroboscopic Mapping Modeling and Soft Switching Operating Point

Based on the [11], the soft-switch operating point is obtained by using stroboscopic mapping. The differential equation of the system can be expressed as

$$\begin{cases} \frac{di_p}{dt} = \frac{-L_S u_i + L_s R_p i_p + L_s u_P + M(R_{eq} + R_s) i_s + M u_s}{M^2 - L_P L_S} \\ \frac{du_p}{dt} = \frac{1}{C_p} i_p \\ \frac{di_s}{dt} = \frac{-M u_i + M R_p i_p + M u_P + L_p (R_{eq} + R_s) i_s + L_p u_s}{M^2 - L_P L_S} \\ \frac{du_s}{dt} = \frac{1}{C_s} i_s \end{cases} \tag{2}$$

$x = [i_p u_p i_s u_s]$ is the system state variable, and $u = [u_i]$ is the system input. Then the system state space model is obtained by the differential Eq. (2).

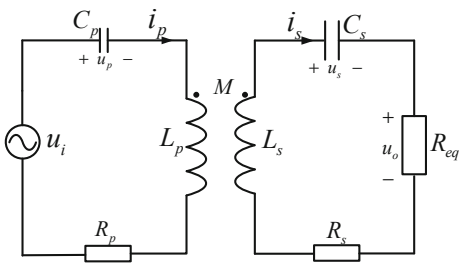

Fig. 2 Powe transfer topology

$$\dot{x} = Ax + Bu \tag{3}$$

In Eq. (3)

$$A = \begin{bmatrix} \frac{L_s R_p}{\Delta} & \frac{L_s}{\Delta} & \frac{M(R_s + R_{eq})}{\Delta} & \frac{M}{\Delta} \\ \frac{1}{C_p} & 0 & 0 & 0 \\ \frac{MR_p}{\Delta} & \frac{M}{\Delta} & \frac{L_p(R_{eq} + R_s)}{\Delta} & \frac{L_p}{\Delta} \\ 0 & 0 & \frac{1}{C_s} & 0 \end{bmatrix} \tag{4}$$

$$B = \begin{bmatrix} -\frac{L_s}{\Delta} & 0 & -\frac{M}{\Delta} & 0 \end{bmatrix}^T \tag{5}$$

In Eq. (5), $\Delta = M^2 - L_P L_S$.

The system stable soft switch fixed point can be expressed as

$$f_{i_p}(t) = Y(I + \Phi(\frac{t}{2}))^{-1}(I - \Phi(\frac{t}{2}))A^{-1}BE_{dc} \tag{6}$$

Table 1 System parameters

Parameter	Value	Parameter (μH)	Value
C_p (μF)	0.05	L_p	12.67
R_p (Ω)	0.05	L_s	12.67
C_s (μF)	0.05	M	5.067
R_L(Ω)	5		

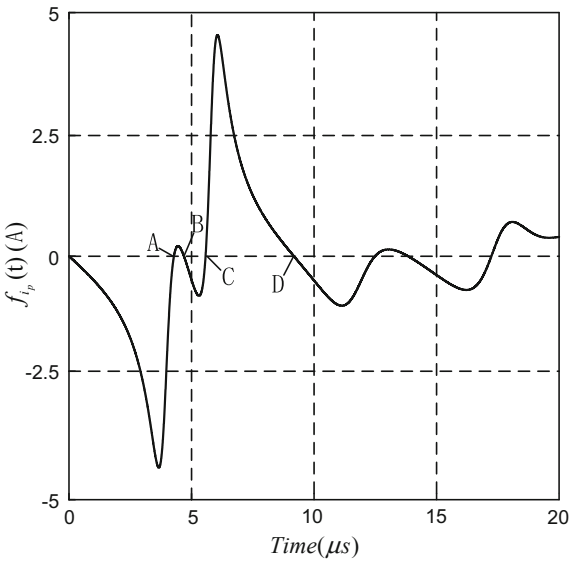

Fig. 3 Soft switch fixed point function curve

In order to analyze the switching resonance point of the SS topology ICPT system, the values of the system parameters are set as shown in Table 1.

Based on Matlab simulation software, through the stroboscopic mapping fixed point function formula (6), the time curve of drawing current is shown in Fig. 3.

Where, A, B, C, and D are the four points of the curve zero crossing, respectively, and their operating frequencies are (A) 234 kHz, (B) 213 kHz, (C) 179 kHz, (D) 109 kHz.

3.2 *Steady-State Waveform Analysis of Soft Switching Operating Point*

The relationship between the output waveform of the inverter and the output voltage of the inverter under steady state is shown in Fig. 4.

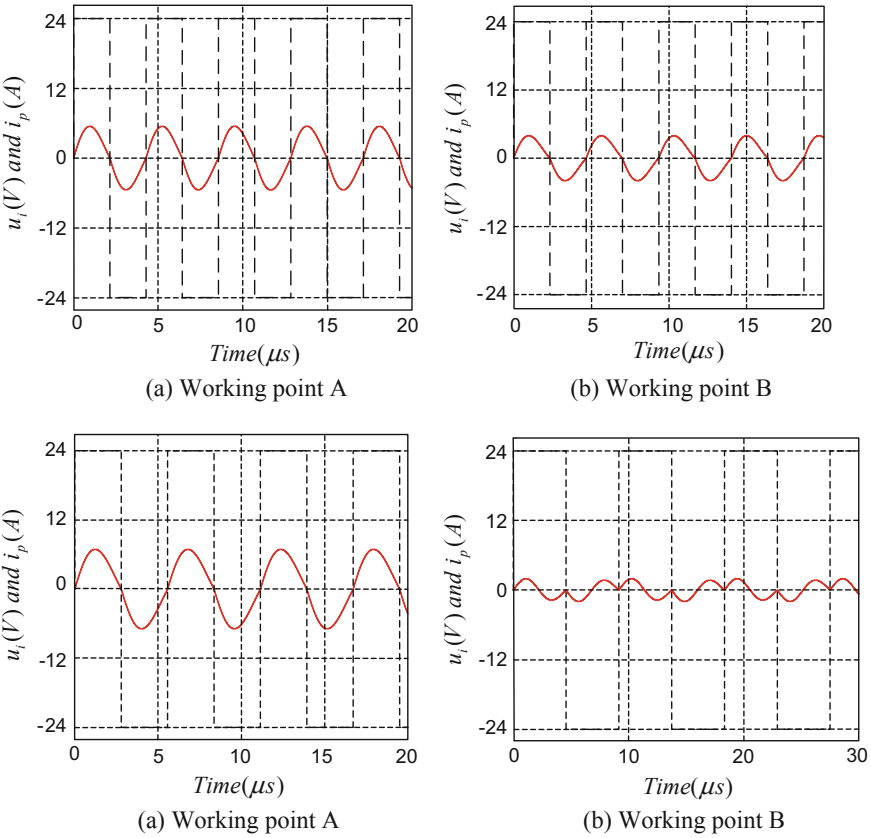

Fig. 4 Inverter output current and voltage waveform (i_i-solid line, u_i-dashed line)

At points, A, B, and C, the inverter output current and voltage switching frequency are the same, and there is a large transmission power at the operating points. Therefore, the system uses this frequency as the operating frequency to reduce the loss of the device. At operating point D, the inverter output current is zero-crossed twice in a half cycle. The oscillating frequency is twice as the switching frequency. There is a large distortion at which most of the power is fed back into the power supply. Generally, the operating point of the inverter output current and voltage with the same phase is adopted, so the circuit A, B, and C can be used as the operating frequency of the system.

4 Modeling of Power and Signal Synchronous Transmission

In Sect. 3, the switching of the resonance point will inevitably bring about the change of the characteristics of the system. In order to analyze the influence of the frequency of different resonance points, the wireless power and information transmission system of the ICPT system is required to be modeled and its characteristics are analyzed.

According to Fig. 2, the secondary side impedance $Z_S(\mathrm{j}\omega)$ can be obtained as

$$Z_{\mathrm{s}}(j\omega) = j\omega L_{\mathrm{s}} + \frac{1}{j\omega C_s} + R_{\mathrm{s}} + R_{eq} \tag{7}$$

The system input impedance $Z(\mathrm{j}\omega)$ is

$$Z(j\omega) = \frac{(\omega M)^2}{Z_{\mathrm{s}}(j\omega)} + j\omega L_{\mathrm{p}} + \frac{1}{j\omega C_p} + R_{\mathrm{p}} \tag{8}$$

In the resonant circuit, the voltage output by the DC voltage under the high-frequency inverter circuit is usually a square wave with a duty ratio of 50% is

$$u_i(t) = \begin{cases} U_d & t\,mod \in [0, \frac{T}{2}) \\ -U_d & t\,mod \in [\frac{T}{2}, T) \end{cases} \tag{9}$$

Its Fourier series expansion is

$$u_i(t) = \frac{4U_d}{\pi}(sin(\omega t) + \frac{1}{3}\sin(3\omega t) + \frac{1}{5}\sin(5\omega t) + \cdots) \tag{10}$$

In Eqs. (9) and (10), it is possible to ignore the harmonics and only consider the fundamental wave content, so the voltage source can be written as

$$\dot{U}_i(t) = \frac{4U_d}{\pi} sin(\omega t) \tag{11}$$

The primary current and the secondary current are

$$\dot{I}_{\mathrm{p}}(j\omega) = \frac{\dot{U}_i}{Z(j\omega)} \tag{12}$$

$$\dot{I}_s(j\omega) = \frac{1}{Z_s(j\omega)} \cdot \dot{I}_{\mathrm{p}}(j\omega) \cdot j\omega M \tag{13}$$

The system efficiency can be obtained from Eqs. (7–13).

$$\eta = \frac{|\dot{I}_s(j\omega)|^2 \cdot R_{eq}}{|\dot{I}_s(j\omega)|^2 \cdot R_{eq} + |\dot{I}_p(j\omega)|^2 \cdot R_p + |\dot{I}_s(j\omega)|^2 \cdot R_s} \tag{14}$$

The voltage across the equivalent load is

$$\dot{U}_{\mathrm{o}}(j\omega) = \dot{I}_s(j\omega) \cdot R_{eq} \tag{15}$$

So, the voltage on the equivalent load can be shown in Table 2.

In Table 2, f_1 and f_2 correspond to the working point A and C respectively. The load voltage values under these two operating points are large, and the load voltage changes are small, and the buck circuit performs better the voltage stabilization control.

Based on 2FSK modulation, at different operating frequencies, the voltage of the equivalent load also changes. When the baseband transmission signal is '1', the operating frequency is f_1, and when the baseband transmission signal is '0', the operating frequency is f_2. The voltage output of the system is different, like Fig. 5.

In order to eliminate the influence of 2FSK signal transmission on power, use the buck circuit to realize constant voltage output, as shown in Fig. 6.

Table 2 Equivalent load voltage at different operating points

Working frequency f	Equivalent load voltage U_{O}
Working point A	$0.84U_{\mathrm{d}}$
Working point B	$0.70U_{\mathrm{d}}$
Working point C	$0.94U_{\mathrm{d}}$
Working point D	$0.04U_{\mathrm{d}}$

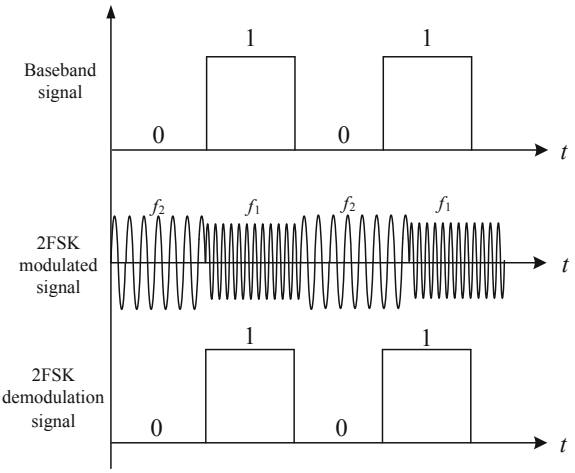

Fig. 5 Modulation and demodulation in ZCS resonant point switching mode

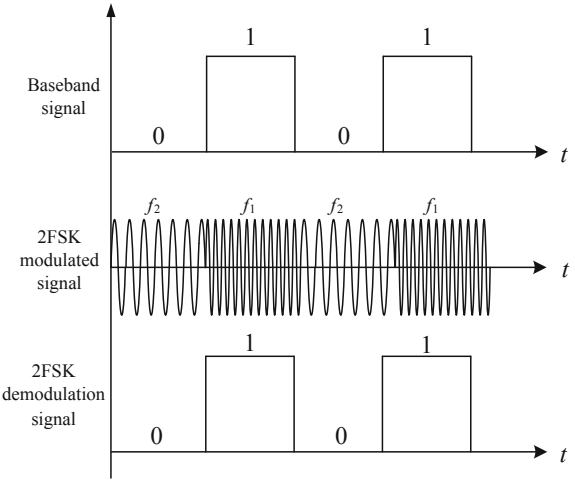

Fig. 6 Constant voltage output modulation and demodulation mode in ZCS resonant point

5 Voltage Regulation Control in ZCS Resonant Point Mode

In this part, the buck converter design method is given as Fig. 7.

According to Table 2, when the inverter operates at frequency f_1 = 234 kHz, f_2 = 179 kHz, the voltage on the equivalent load is as shown in Eq. (16).

$$\begin{cases} U_{o1} = 0.84U_{d1} \\ U_{02} = 0.94U_{d2} \end{cases} \tag{16}$$

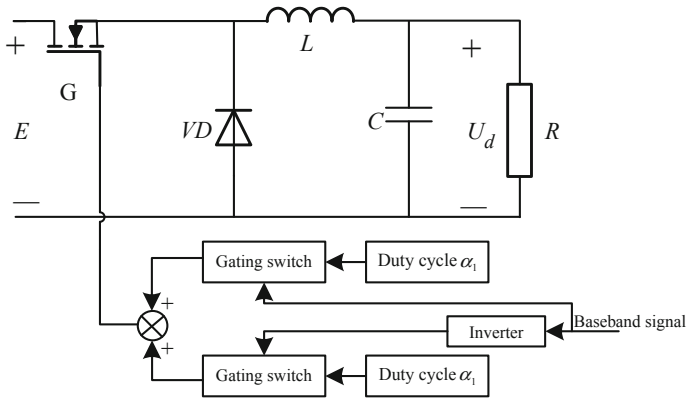

Fig. 7 BUCK main circuit

When the f_1 = 234 kHz, the equivalent load voltage is U_{o1}, the input voltage before the inverter is U_{d1}. When f_2 = 179 kHz, the voltage of the equivalent load is U_{o2}, and the input voltage before the inverter is U_{d2}. So

$$\begin{cases} U_{d1} = \alpha_1 E \\ U_{d2} = \alpha_2 E \end{cases} \tag{17}$$

It can be seen from Eqs. (16) and (17) that under the condition of constant voltage, the duty ratio of the buck circuit can be obtained.

6 Signal Demodulation Circuit

The second-stage active low-pass circuit is used to demodulate the current on the secondary circuit is shown in Fig. 8.

The design principle is as follows: First, the secondary resistor circuit R_{SENSE} voltage is used as the input of the second-order active low-pass circuit, and the UA741 is a general-purpose operational amplifier chip with a bandwidth gain of 1 MHz. A second-order active low-pass filter circuit with a gain of 1.58 in the passband (A_{VF} = 1.58) is selected. The capacity of the designed capacitor is $C = 0.1$ nF, the resistance of the resistor is R = 8 kΩ, and the bandpass cutoff frequency is

$$f_H = \frac{1}{2\pi RC} \tag{18}$$

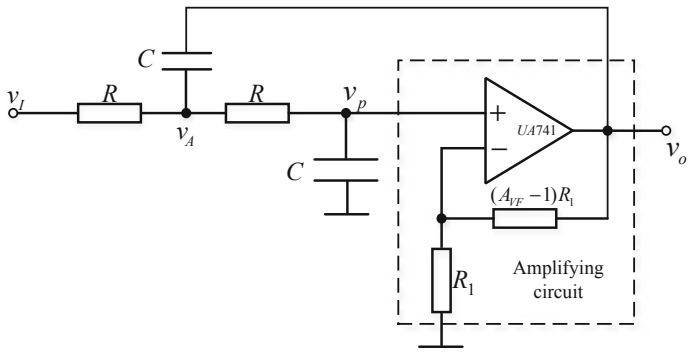

Fig. 8 Second-order active low-pass filter circuit

7 Experimental Analysis and Verification

The experimental platform is built according to the parameters in Table 1, as shown in Fig. 9. The system's output voltage is 24 V and the output power is 115 W.

The inverter frequency is switched between 179 and 234 kHz, and the transmission data string is '10011100', which is demodulated according to the current on

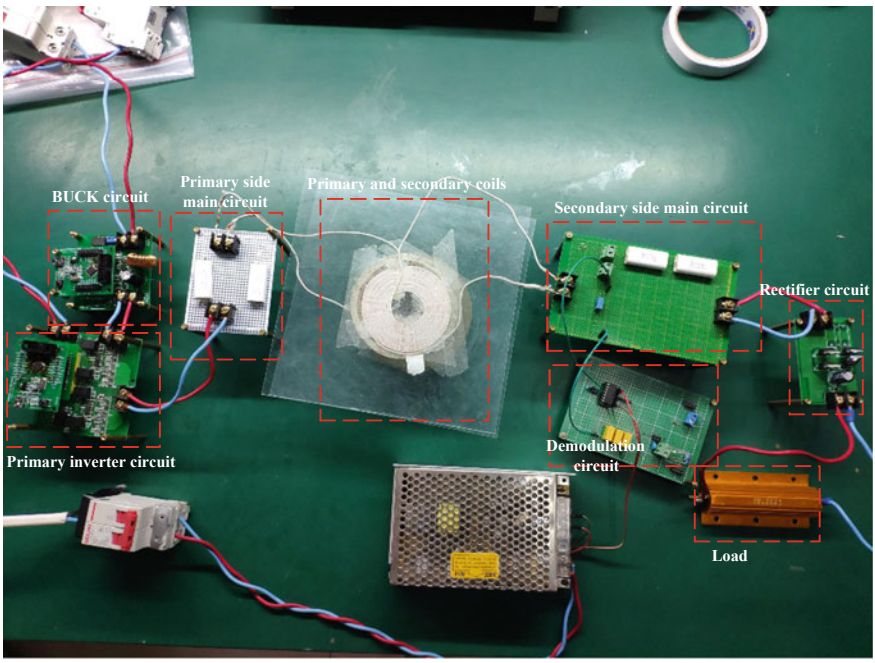

Fig. 9 Experiment platform

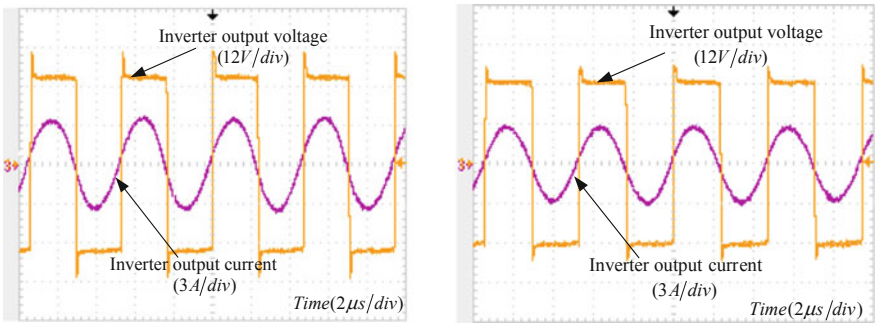

(a) f_1=234kHz (b) f_2=179kHz

Fig. 10 Inverter output current and voltage waveforms at different operating frequencies

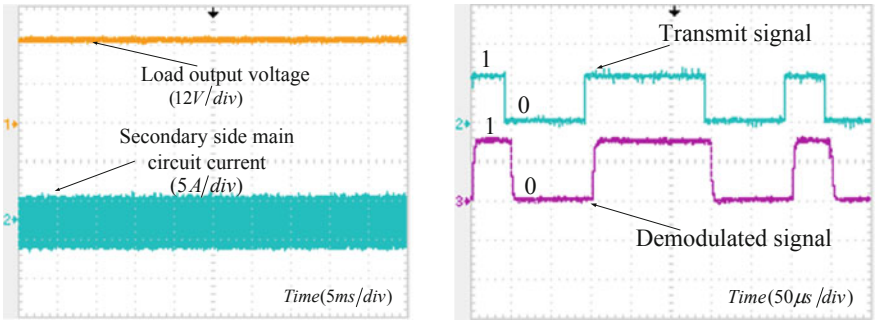

(a) Output voltage (b) Signal transmission and demodulation wave

Fig. 11 Output voltage and Signal transmission and demodulation wave

the sampling resistor. The inverter frequency is f_1 = 234 kHz, and the signal '1' is transmitted. When f_2 = 179 kHz, the signal '0' is transmitted.

Figure 10 are waveform diagrams of the inverter output current and voltage for the inverter operating at 179 and 234 kHz operating frequency, respectively.

It can be seen that the inverter works in the ZCS state at both operating frequencies, realizing the soft-switching operation of the inverter.

Figure 11a shows the load output voltage and the secondary main circuit current waveform of the buck circuit voltage regulation under two operating frequencies. Figure 11b is a waveform diagram of a baseband signal and a signal demodulation signal, and the system transmits a signal of '10011100'.

It can be seen that the output voltage of the load is constant 24 V, which realizes regulated output of the system under the synchronous transmission of power and signal, And the signal transmission rate is 20 kbps, and the signal delay is about

5 μs. The feasibility and correctness of the parameter design of the second-order active low-pass filtering designed in this paper are verified.

8 Conclusion

An isochronous transmission ICPT system based on ZCS resonant point switching regulator output energy signal is proposed, the 2FSK modulation method was adopted. Selecting the resonant frequency of the two soft switching operating points reduces the loss of the inverter and improves the efficiency of the system. At the same time, a buck circuit is added to achieve a regulated output, which improves the quality of the electrical energy.

Acknowledgements This work is supported by State Grid Corporation of China Headquarter Science and Technology Project (Research on Communication and Interoperability of Magnetic Coupling structure in Wireless charging system of Electric vehicle).

References

1. Xia CY, Zhu WT (2018) A load identification method for ICPT system utilizing harmonics. JEET 13(6):2178–2186
2. Covic GA, Boys JT (2013) Inductive power transfer. IEEE 101(6):1276–1289
3. Xia CY, Wang W (2018) Robust control for inductively coupled power transfer systems with coil misalignment. IEEE 33(9):8110–8122
4. Xia CY, Sun Y (2012) Parameter optimization of magnetic circuit mechanism for coupled magnetic resonance power transmission system. J Electrotech 27(11):139–145
5. Ren SY, Xia CY (2018) Cross-shaped magnetic coupling structure for electric vehicle IPT charging systems. JPE 18(4):1278–1292
6. Zhao ZM, Liu F (2016) Overview of wireless charging for electric vehicles. J Electrotech 31 (20):30–40
7. Xia CY, Ren SY (2017) Inductively coupled power transfer system with fundamental wave and harmonic wave two-path parallel transmission. Autom Electr Power Syst 41(7):93–100
8. Xia CY, Ren SY (2018) Inductive power and signal synchronous transmission based on parallel paths of fundamental wave and harmonic wave. Autom Electr Power Syst 42(5):169–175
9. Sun Y, Yan PX (2016) Research on real-time synchronous transmission method of power signal sharing channel in ICPT system. Proc CSEE 36(19):5172–5178
10. Yan Z, Xiang Z, Wu L, Baoyun W (2018) Study of wireless power and information transmission technology based on the triangular current waveform. IEEE 33(2):1368–1377
11. Tang CS, Sun Y, Su YG et al (2009) Determining multiple steady-state ZCS operating points of a switch-mode contactless power transfer system. IEEE 24(2):416–425

Short-Term Power Load Forecasting Based on Empirical Mode Decomposition and Deep Neural Network

Limin Cheng and Yuqing Bao

Abstract Short-term load forecasting predicts the hourly load of the future in few minutes to one-hour steps in a moving window manner based on historical and real-time data collected. Effective forecasting is the key basis for in-day scheduling and generator unit commitment in modern power system. It is however difficult in view of the noisy data collection process and complex load characteristics. In this paper, a short-term load forecasting method based on empirical mode decomposition and deep neural network is proposed. The empirical modal number determination method based on the extreme point span is used to select the appropriate modal number, so as to successfully decompose the load into different timescales, based on which the deep-neural-network-based forecasting model is established. The accuracy of the proposed method is verified by the testing results in this paper.

Keywords Short-term load forecasting · Empirical mode decomposition · Neural network

1 Introduction

Load forecasting provides a key basis for the modern power system operators to determine scheduling, generator unit commitment, electricity prices, transaction evaluation, etc. The accuracy of forecasting directly affects the performance of power scheduling. Load forecasting can be generally divided into long-term load forecasting (LTLF), medium-term load forecasting (MTLF), short-term load forecasting (STLF) and very-short-term load forecasting (VSTLF), respectively [1–4]. Among them, the STLF covers forecasting ranging from a few minutes up to one hour [5], and is mainly used for real-time power scheduling and short-term main-

L. Cheng · Y. Bao (✉)
Nanjing Normal University (NARI School of Electrical Engineering and Automation), Nanjing 210023, Jiangsu Province, China
e-mail: baoyuqing@njnu.edu.cn

Y. Xue et al. (eds.), *Proceedings of PURPLE MOUNTAIN FORUM 2019-International Forum on Smart Grid Protection and Control*, Lecture Notes in Electrical Engineering 585, https://doi.org/10.1007/978-981-13-9783-7_62

tenance [6]. However, the load components have different characteristics and randomness in the short-term scale, making accurate STLF difficult. Therefore, it is necessary to further design new methods of STLF.

Nowadays, a lot of research works on STLF are reported. On one hand, the methods of forecasting input data selection mainly involve the similar-day [7] or the analysis of economic, social, human comfort and climatic factors [8]. On the other hand, the forecasting algorithm is mainly divided into classical approaches (CA) and computational intelligence approaches (CIA). CA mainly include time-series method, liner extrapolation method and Kalman filtering method [5, 9, 10]. These methods are fast in calculation, but have high requirements on the stability of data sequences. CIA mainly include BP neural network (NN), extreme learning machine neural network, etc. [11–13]. With CIA, complex nonlinear input-output relationships can be established automatically through supervised learning using a database of solved examples, and the general applicability of predictive models can be improved. However, the CIA with a single NN, may not be able to accurately capture complicated load features, the combined computational intelligence approaches (CCIA) is a general trend [14, 15]. The CCIA mainly guarantees the accuracy and reliability of forecasting from two aspects: one is to improve the input quantity according to the load characteristics and the influencing factors, and the other is to optimize the forecasting model according to the advanced nature of the intelligent algorithm. Combining the wavelet decomposition method with data filtering and NN to improve forecasting accuracy [11]. Combining the influencing factors of load and principal component analysis (PCA) to improve the input of NN can improve the accuracy of forecasting and avoid the phenomenon of "over-fitting" [16].

Notwithstanding the above methods play important roles in improving the models of STLF, in terms of feature extraction and forecasting algorithms, there still need work to further improve the forecasting performance:

For feature extraction, most load forecasting methods consider the key influencing factors of historical load, meteorology, etc., but most of the methods used in the decomposition of timescale are conventional methods such as wavelet decomposition [11, 13, 17]. In [15], the author proposes the use of empirical mode decomposition (EMD) to solve the problem of wavelet decomposition for short-term wind power forecasting. It has mature adaptive decomposition capabilities, does not require prior knowledge of transform basis functions, and has significant advantages in dealing with non-stationary and nonlinear data. However, the literature [15] does not discuss the choice of the modal number. The modal number in the EMD determines the extraction effect of the load periodic components, which in turn affects the results of load forecasting.

For forecasting algorithms, STLF is mostly based on traditional NN, which greatly limits the further improvement of forecasting accuracy. The deep belief network (DBN) can realize the training of multi-layer network. It is a kind of deep neural network (DNN). It consists of a multi-layer constrained Boltzmann machine stack, which can be used to solve the complex and nonlinear problems of STLF. For the load forecasting problem based on DNN, the literature [18] proposed a method

based on DNN with Pretraining Using Stacked Autoencoders (DNN-SA), which had achieved good results in the day-to-day load forecasting. Literature [19] uses the Deep Residual Network (DRN) to realize monthly electricity consumption forecasting, and applies DNN to medium and long-term load forecasting. Despite the fact there are DNN methods developed for load forecasting, the relevant research works on SLTF are very limited, and it is worthy of further research.

Focusing on the above two problems, this paper proposes an STLF method based on EMD and DBN. For the problem of uncertain modal number of EMD, the EMD based on extreme point span (EPSEMD) is proposed. A model of STLF based on DBN is established for each mode. Finally, the accuracy of the proposed method is verified by the testing results with the actual data of a city in Henan Province in the summer of 2017.

2 Feature Extraction Method Based on EMD

2.1 Basic Working Principle of EMD

EMD is a time-frequency analysis method suitable for non-stationary and nonlinear signal processing proposed by Dr. Huang Wei in 1998. It is an adaptive decomposition method [20]. The purpose of EMD is to decompose complex non-stationary and nonlinear signals into a series of intrinsic mode functions (IMFs) of different frequencies according to the time characteristic scale of the signal [21, 22].

2.2 Modal Number Determination Method of EMD Based on Extreme Point Span

In this paper, the EPSEMD is proposed to extract the key features within the daily period component of the load. Based on the existing EMD model, the EPSEMD based on the extreme point span is used to set the termination condition of the EMD process, so as to obtain the optimal empirical modal number. The EPSEMD follows the basic principle of the periodic characteristic stability of $r(t)$ and the low similarity of IMFs, which ensures the role of EMD in the forecasting model. The algorithm of EPSEMD is shown in Fig. 1.

The EPSEMD implementation steps are as follows:

Step 1: Randomly generate the initial maximum modal number $N_{\max\_mode}$, input the EMD model, complete an EMD decomposition, and obtain the remainder, denoted as $r(t)$.

Step 2: Using the local extremum solving function (*extrema*), calculate all the maximum points of $r(t)$, and record the number of maxima points, denoted as N_{total}.

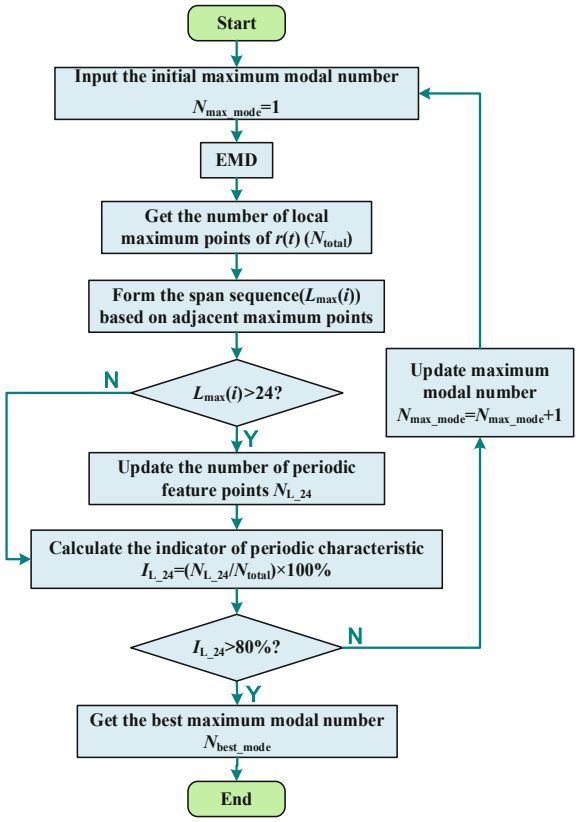

Fig. 1 Flow chart of EPSEMD algorithm

Step 3: Calculate the span of adjacent maximum points to form a discrete span sequence, denoted as $L_{\max}(i)$.

Step 4: Determine whether each discrete span satisfies the preset span period condition. If the span meets the preset span period condition ($L_{\max}(i) > 24$), each IMF is considered to be a key feature within the daily period of the load, and the number of extreme points of the periodic feature is updated, which is recorded as $N_{\mathrm{L\_24}}$, otherwise it is not updated.

Step 5: Calculate the periodic characteristic index $I_{\mathrm{L\_24}}$ according to the $N_{\mathrm{L\_24}}$ and the N_{total}.

$$I_{\mathrm{L\_24}} = \frac{N_{\mathrm{L\_24}}}{N_{\mathrm{total}}} \times 100\% \tag{1}$$

Step 6: Determine whether the periodic characteristic index I_{L_24} is greater than 80%. If it is satisfied, the empirical modal number is considered to be the optimal value. Otherwise, the maximum empirical modal number N_{best_mode} is updated, and steps 1–5 are repeatedly executed until the best empirical modal number is obtained.

3 Cases Analysis

In the following cases, the forecasting models are verified by the short-term forecasting of the actual load data from July to August in a city in Henan Province in 2017.

3.1 Load Forecasting Based on EPSEMD

Load data decomposition based on EPSEMD is tested based on actual load data. Figure 2 is the original load data sequence, Fig. 3a is the five-layer EMD mode, and Fig. 3b is the three-layer EMD mode. The original load data sequence is compared with the IMFs sequence and the $r(t)$ sequence in both EMD modes. It can be seen from Figs. 2 and 3a that the periodic fluctuation of the $r(t)$ in the five-layer EMD mode is not obvious, and cannot reflect the variation trend of the periodic characteristics of the original load data. From Figs. 2 and 3b, it can be seen that the $r(t)$ sequence has fluctuating cyclically in the three-layer EMD mode, which can reflect the variation trend of the periodic characteristics of the original load data. In the three-layer EMD mode, the IMF_1 to IMF_3 component sequences reflect real-time load randomness, intraday load fluctuations, and load trend changes of load characteristics, respectively. It can be seen that the three-layer EMD mode has a explicit physical meaning, and the similarity between the modes is small, which is beneficial to improve the forecasting accuracy of STLF. The above conclusions are further explained in the actual scenario when the extreme point span-modality index is set to 80%, and the EPSEMD selection result is reasonable.

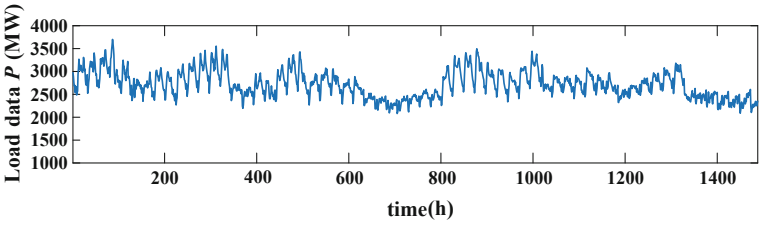

Fig. 2 Data sequence of original load

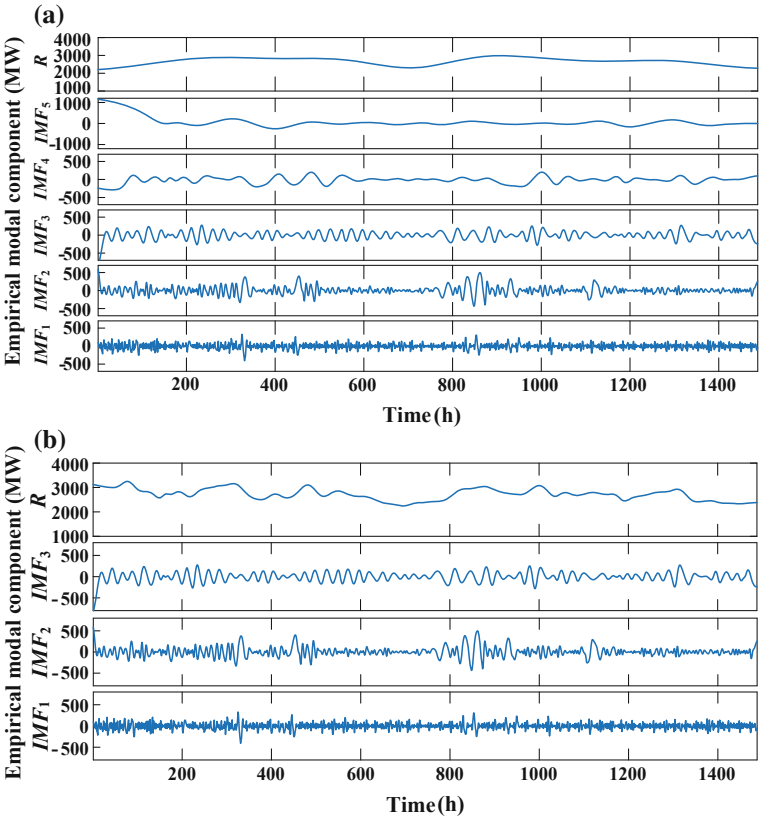

Fig. 3 Five-layer and three-layer EMD, **a** five-layer EMD mode, **b** three-layer EMD mode

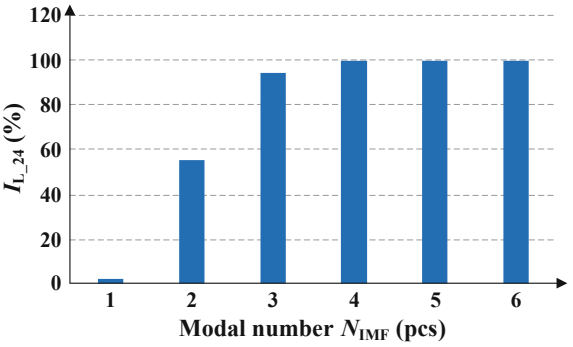

Fig. 4 Modal index distribution map based on EPSEMD

Based on EPSEMD, the modal index distribution map is obtained as shown in Fig. 4. It can be seen from Fig. 4 that when the modal number N_{IMF} increases from 1 to 4, the index (I_{L_24}) gradually increases. However, if the modal number NIMF

continues to increase, I_{L_24} assumes saturation, that is, I_{L_24} is maintained at 100% no longer increases or decreases. In this paper, I_{L_24} = 80% is set as the best index, that is, the modal number of three layers is selected as EMD.

3.2 *Input Variable Selection Based on Load-Temperature Based Correlation and PCA*

The relationship between $r(t)$ and $T(t)$ ($r(t) - T(t)$) is shown in Fig. 5. The relationship between $r(t)$ and $T(t)$ maximum points ($r(t) - T(t)_{max}$) is shown in Fig. 6. From Figs. 5 and 6, the following $T(t)$ of $P(t)$ changes periodically, and the change of $P(t)$ lags behind the change of $T(t)$ about 3 h.

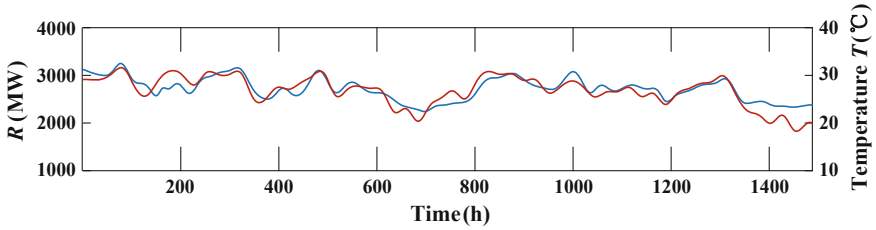

Fig. 5 Relationship between EMD $r(t)$ and temperature $T(t)$

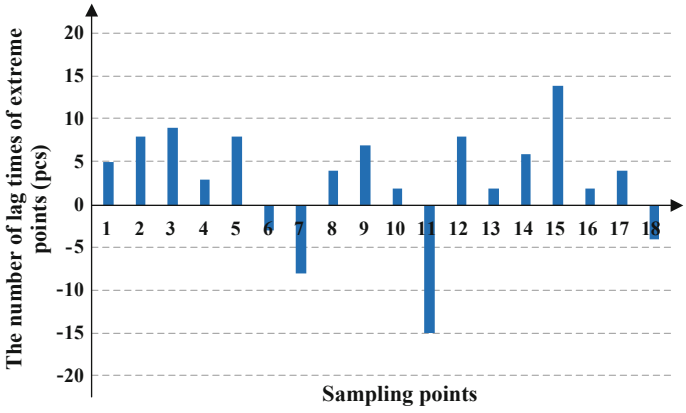

Fig. 6 Relationship between EMD $r(t)$ maximum and temperature $T(t)$ maximum

3.3 Comparison of Forecasting Results

In order to illustrate the effectiveness of the proposed method, the following five forecasting models are established in the following cases.

Comparison of the different feature extraction methods.

Case 1 (Ori_DBN): No feature extraction is performed on the original load data $P(t)$, and $P(t)$ is directly predicted by DBN. The structure of the Case 1 is as shown in Fig. 7a, and it is necessary to establish a DBN deep neural network.

Case 2 (Wav_DBN [13, 17] and EMD_DBN): The time-scale decomposition of the original load data $P(i)$ is performed, and the DBN-based STLF model is established for the components of different time scales. In the first method, the original load data $P(t)$ is wavelet-decomposed to obtain five components D_1, D_2, D_3, D_4 and A_4, and then D_1, D_2, D_3, D_4 and A_4 are respectively predicted by DBN, and finally five forecasting are made. The result is reconstructed to obtain a predicted value. In the second method, EMD decomposition is performed on the original load data $P(t)$ to obtain four modal components IMF_1, IMF_2, IMF_3, IMF_4 and a $r(t)$, and then IMF_1, IMF_2, IMF_3, IMF_4 and $r(t)$ are respectively predicted by DBN, and finally five forecasting are made. The result is reconstructed to obtain a predicted value. The Case 2 structure is shown in Fig. 7b, c, and five DBN deep neural networks need to be established, respectively.

Case 3 (EMD_EPS_DBN): Based on EPSEMD to obtain the best empirical decomposition modal number $\mathrm{NUM}_{\mathrm{best}}$, $IMF_1 \sim IMF_{\mathrm{best}}$ and $r(t)$ are predicted by a forecasting method with better results in Case 2, and the forecasting results are obtained. The Case 3 structure is shown in Fig. 7d.

Case 4 (EMD_EPS_PCA_DBN): Add PCA analysis method based on Case 3 and select the valid input variable set of DBN. The Case 4 structure is shown in Fig. 7e.

Next, this paper uses the actual load data and meteorological data from July to August in a city in Henan Province in 2017 to test the validity of each Case (1–4). The data of the first 864 h (36 days) is used as the input data of the forecasting model, and the last 168 h (7 days) is used as the output data of the forecasting model to complete the test of each case. The comparison of the forecasting results of each case is shown in Fig. 8a–c.

The test results shown in Fig. 8a–c that the EMD_EPS_PCA_DBN model can be closer to the actual value, and the forecasting effect is the best and the highest precision. At the same time, comparing the MAPE indicators in Table 1 can lead to the following results:

(1) *Compared with the single DBN model and Wav_DBN model, the forecasting accuracy of the combined model using EMD is improved.*

Compared with the Ori_DBN and Wav_DBN models, the MAPE is respectively increased by 9.62 and 5.68%, which shows the effectiveness of EMD is better than wavelet decomposition in STLF.

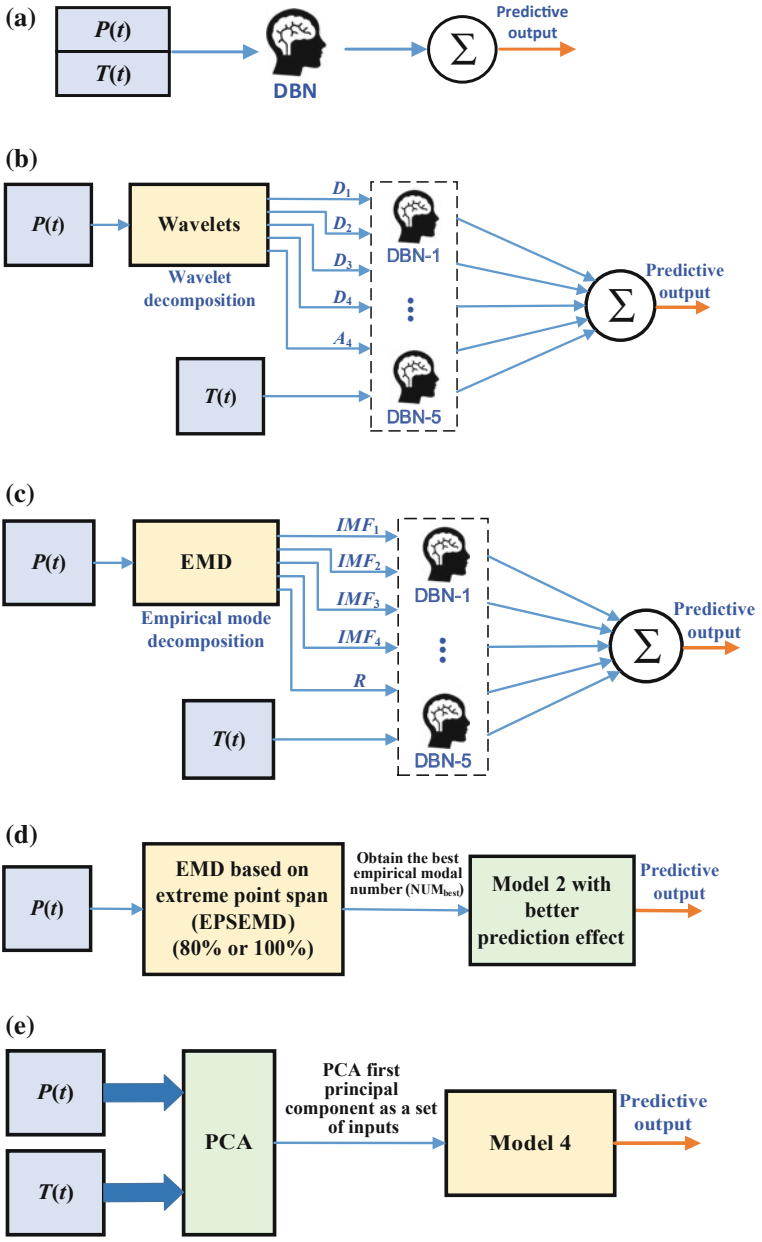

Fig. 7 Structure of five predictive cases, **a** directly forecasting model based on original data (Ori_DBN), **b** forecasting model based on wavelet decomposition (Wav_DBN), **c** forecasting model based on traditional EMD (EMD_DBN), **d** forecasting model based on EPSEMD (EMD_EPS_DBN), **e** forecasting model based on EPSEMD and PCA (EMD_EPS_PCA_DBN)

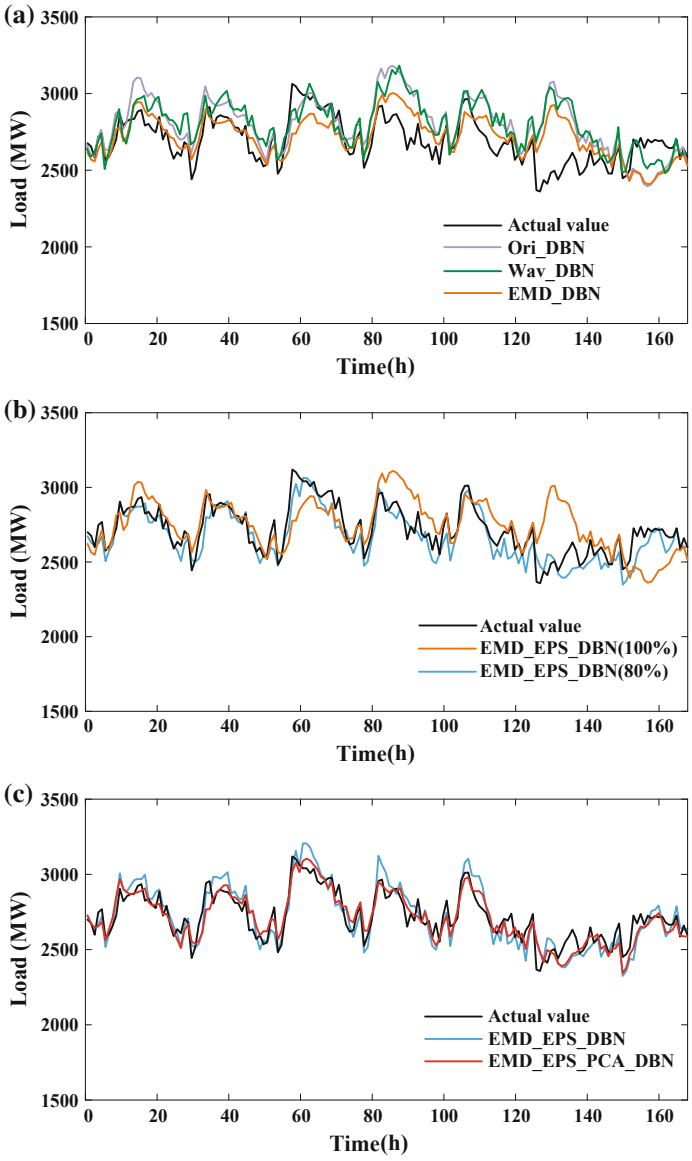

Fig. 8 Comparison of forecasting results of each Case (1–4), **a** comparison of forecasting results based on different time scale decomposition methods, **b** comparison of forecasting results based on, **c** comparison of forecasting results based on PCA optimized EMD_EPS_DBN model

Table 1 Forecasting results based on feature quantity extraction methods optimization

Forecasting model	EPS index (%)	MAPE (%)
Ori_DBN	/	2.39
Wav_DBN	/	2.29
EMD_DBN	/	2.16
EMD_EPS_DBN	100	2.16
EMD_EPS_DBN	80	2.03
EMD_EPS_PCA_DBN	80	1.89

(2) *Based on the traditional EMD, EPSEMD is used to optimize EMD, and improves forecasting accuracy.*

When the EPSEMD characteristic index I_{L_24} is 80%, the EMD_EPS_DBN model is increased by 6.02% compared with the MAPE of the EMD_DBN model; When the characteristic index I_{L_24} is 100%, the optimization effect of the EMD_EPS_DBN model relative to the EMD_DBN model is not obvious, indicating that the I_{L_24} is set to 80%, which is beneficial to the *IMF*s and $r(t)$ approximating the characteristics of the power load in the short-term, that is, the real-time load randomness, intraday load fluctuations, and load trend changes, and weekly cycle load characteristics, which in turn contribute to improved forecasting accuracy.

(3) *PCA weakens the influence of input variable similarity on forecasting accuracy to some extent.*

The MAPE of the EMD_EPS_PCA_DBN model is 6.9% higher than the MAPE of the EMD_EPS_DBN model.

4 Conclusion

In order to improve the accuracy of STLF, this paper proposes a STLF method based on EPSEMD and DBN, and validates the proposed method. The contributions of this paper can be summarized as following:

EPSEMD is used to extract the characteristics of the load on the timescale of the very-short-term. This design can help to improve the effectiveness of feature extraction. The STLF model is established based on EPSEMD and deep neural networks (DBN), so that the accuracy is improved.

Furthermore, the future work may be designing the DNN-based STLF method with other deep-neural-network methods.

References

1. Kang CQ, Xia Q, Zhang BM (2004) Review of power system load forecasting and its development. Autom Electr Power Syst 28(17):1–11
2. Abu-Shikhah NF (2011) Medium-term electric load forecasting using singular value decomposition. Energy 36(7):4259–4271
3. Černe GF (2018) Short-term load forecasting by separating daily profiles and using a single fuzzy model across the entire domain. IEEE Trans Ind Electron 65(9):7406–7415
4. Charytoniuk WF (2002) Very short-term load forecasting using artificial neural networks. IEEE Trans Power Syst 15(1):263–268
5. Liu KF (1996) Comparison of very short-term load forecasting techniques. IEEE Trans Power Syst 11(2):877–882
6. Lu Z, Wang MK (2006) Ultra-short term load forecasting based on short term load forecasting. Autom Electr Power Syst 30(16):102–104
7. Wu YF (2018) Short-term load forecasting based on improved grey relational analysis and neural network optimized. Autom Electr Power Syst 42(20):67–74
8. Douglas APF (1998) The impacts of temperature forecast uncertainty on Bayesian load forecasting. IEEE Trans Power Syst 13(4):1507–1513
9. Debs ASF (1988) Modern power systems control and operation, 2nd edn. Springer, Boston
10. Lu JXF (2019) Short-term load forecasting method based on CNN-LSTM hybrid neural network model. Autom Electr Power Syst 2019(08):131–137
11. Guan CF (2013) Very short-term load forecasting: wavelet neural networks with data pre-filtering. IEEE Trans Power Syst 28(1):30–41
12. Fan SF (2006) Short-term load forecasting based on an adaptive hybrid method. IEEE Trans Power Syst 21(1):392–401
13. Li SF (2015) A novel wavelet-based ensemble method for short-term load forecasting with hybrid neural networks and feature selection. IEEE Trans Power Syst 31(3):1–11
14. Han LF (2007) A hybrid approach of ultra-short-term multinode load forecasting. In: 2007 IEEE international power engineering conference. IEEE, Singapore, pp 1321–1326
15. Yang MF (2018) Ultra-short-term multistep wind power prediction based on improved EMD and reconstruction method using run-length analysis. IEEE Access 6:31908–31917
16. He DF (2012) Ultra-short-term wind power prediction using ANN ensemble based on PCA. In: 7th international power electronics and motion control conference. IEEE, Harbin, pp 2108–2112
17. Bessec MF (2017) Short-run electricity load forecasting with combinations of stationary wavelet transforms. Eur J Oper Res 264(1):149–164
18. Hosein SF (2017) Load forecasting using deep neural networks. In: 2017 IEEE power & energy society innovative smart grid technologies conference. IEEE, Washington, DC, pp 1–5
19. Kunjin CF (2018) Short-term load forecasting with deep residual networks. IEEE Trans Smart Grid 1
20. Looney DF (2009) Multiscale image fusion using complex extensions of EMD. IEEE Trans Signal Process 57(4):1626–1630
21. Camarenamartinez DF (2016) Novel down-sampling empirical mode decomposition approach for power quality analysis. IEEE Trans Ind Electron 63(4):2369–2378
22. Chen PYF (2016) Hardware design and implementation for empirical mode decomposition. IEEE Trans Ind Electron 63(6):3686–3694

Designing and Application of High Voltage Overhead Transmission Line Typhoon Disaster Prediction Method

Xiangxian Zhou, Te Li, Wendong Jiang, Binxiao Mei, Yang Zou and Lin Li

Abstract Typhoon is among the worst nightmares for the high voltage power transmission network operators in coastal areas. It's long been a challenge to predict the typhoon caused faults. This paper first analyzed mechanism of typhoon caused high voltage overhead transmission lines faults. Then proposed a numerical weather forecast based typhoon disaster prediction method. The relation between gust and 10-min average wind speed is analyzed and the criteria for determine jumper wire swing and tower structure damage risk level are proposed. Lastly, the experience of the application of proposed prediction method in Zhejiang province is introduced. The proposed method has been proved to be effective in prediction of typhoon disaster, though the numerical weather forecast model should be improved to represent the terrain effect more accurately.

Keywords Transmission lines · Typhoon · Jumper wire swing

This work was supported by State Grid Science and Technology program No. 5211WZ16002S.

X. Zhou (✉) · T. Li · B. Mei
State Grid Zhejiang Electric Power Research Institute (State Grid Typhoon Monitoring & Warning Center), Hangzhou 310014, China
e-mail: Zhouxiangxian04@126.com

W. Jiang
State Grid Zhejiang Electric Power Company, Hangzhou 310012, China

Y. Zou
CEEC Zhejiang Electric Power Design Institute, Hangzhou 310012, China

L. Li
State Grid Materials Company, Beijing 100021, China

Y. Xue et al. (eds.), *Proceedings of PURPLE MOUNTAIN FORUM 2019-International Forum on Smart Grid Protection and Control*, Lecture Notes in Electrical Engineering 585, https://doi.org/10.1007/978-981-13-9783-7_63

1 Introduction

According to the experience from the operation of power grid in China, typhoon disaster is one of the severest natural disasters that threatening the operation of power grid [1]. Wu et al. analyzed how 98 transmission towers were collapsed during typhoon "Saomoi" in Wenzhou in 2006 [2]. The Hainan power grid blackout during typhoon "Damrey" in 2006 [3]. Over 550 thousands of customers lose electric power supply during typhoon "Meranti" in 2016 in Fujian province [4]. The State Grid Typhoon Monitoring&Warning Center was set up in late 2017, which aims at prediction of typhoon disaster in 7 provinces and 1 city in east coast of China. This paper presents the high voltage overhead transmission lines typhoon disaster prediction method used in State Grid Typhoon Monitoring&Warning Center.

Early warning of typhoon disaster is of great value for the operators of power gird. Prediction of power grid typhoon disaster has long been a challenging problem for both the researchers and practitioners. Tao et al. measured the windage yaw characteristics of jumper insulators during typhoon, which conclude that the tilt angle of jumper insulators during typhoon is not strongly correlated with the wind speed but of sporadic nature [5]. Sun et al. analyzed the experience from operation of power grid in face of typhoon "Rammasun" in Guangdong province, which successfully used the typhoon route and the power grid geographic information system (GIS) to predict the impact of typhoon [6]. Wu et al. analyzed how the string wind and heavy rainfall can lead to large scale power grid outage and used the natural disaster evaluation results as input parameter for the power system stability analysis [7]. Wang et al. reviewed how the power grid companies in China handling typhoon disasters, which conclude that the typhoon disaster warning technology used in China is very primitive [8]. Fang et al. proposed a typhoon disaster warning method that was based on the analysis of distance between the transmission lines and the route of typhoon [9]. Xu et al. investigated how the jumper wire swing caused by strong wind and conclude that the hilly terrain can significantly enhance the chance of wind caused transmission line fault [10].

Although there are abundant of existing documents about the overhead transmission line typhoon disaster, there is no well-established method that can be used to predict the typhoon disaster of large scale high voltage power transmission network. This work designed a numerical weather forecast based typhoon disaster prediction method and presents the experience from the application of this method.

2 Mechanism of Damage from Typhoon

Three kinds of damage can be caused by typhoon. The first one and the most common one is the strong wind can push the jumper wire close to the tower and cause breakdown of the air gap between the jumper wire and the tower. The second

one is that the wind load on the conductor and the tower can break conductor and sometimes even damage the tower structure. The third one is that the wind can bring conductive materials like aluminum films up to the transmission line structure, which can cause single phase or multiple phase fault.

The swing of jumper wire will cause temporary fault which usually can be eliminate by single phase auto-reclose. Since the jumper wire structure is relatively small, the gust that sustain only several seconds [11] can cause fault. One prominent feature of typhoon is it is much more turbulent than other kinds of strong wind [12], which makes the gust (3-s average wind, V_3) much higher than 10-min average wind speed (V_{600}) and thus frequently cause transmission line jumper wire swing faults. The level of gust that can lead to jumper wire swing faults is different from tower to tower, and the accurate evaluation of the hazardous gust level is both unrealistic and unnecessary for the prediction of typhoon impact of large scale power transmission networks. In this work, the transmission line designing wind speed is used as hazardous gust level to predict jumper wire swing.

The damage of tower structure usually can cause permanent faults and usually takes weeks or even months to restore the power supply. The mechanism behind the damage of transmission line tower structure is quite complicate. In this work, the hazardous levels of ultra-high voltage (UHV) transmission line towers are analyzed by the wind load stress analysis, while hazardous levels of other transmission line towers are assumed to be equal to design wind speed (V_{design}). The fault caused by drifting materials brought by strong wind is quite random and unpredictable, so it is not include in the typhoon disaster prediction of this work.

3 Disaster Prediction Method

3.1 Determination of Vulnerable Tower Subset

The disaster prediction method proposed in this paper is shown in Fig. 1. The first step is to compare the location of transmission towers and the typhoon route, and then the vulnerable tower subset is determined. The numerical weather forecast results of the gust of the towers are compared to the V_{design} to determine if there is jumper wire swing risk. For the UHV transmission lines, the load stress analysis results under the predicted wind speed are used to determine if there is tower damage risk. The tower damage risk of other transmission lines are determined by compare V_{600} and V_{design}. Finally, the predicted jumper wire swing risk and the tower damage risk are output to the warning system.

To save the computation cost and thus improve the efficiency of the typhoon disaster prediction method, the vulnerable tower subset should be determined first and then detailed analysis can be apply to the towers in this subset. The vulnerable

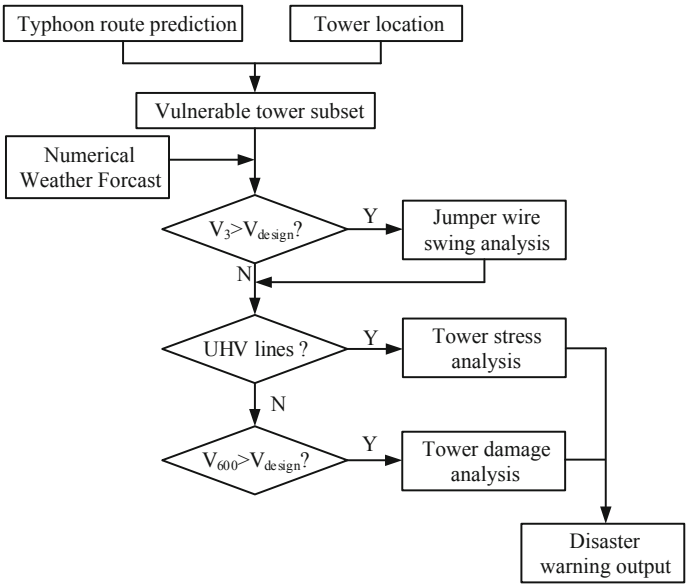

Fig. 1 Flow chart of overhead transmission lines typhoon disaster prediction method

towers are defined as the towers locate inside the predicted level 7 (Beaufort scale) wind circle which is available in typhoon route forecast published by National Meteorological Center.

3.2 Numerical Weather Forecast

The Weather Research and Forecasting (WRF) model [13] is a widely used numerical weather forecasting model, which compute the meteorological elements, like wind, temperature, air pressure and precipitation, based on the assimilation of global meteorological monitoring data. The predicted wind speed is the most important input parameter for the typhoon disaster warning method in shown in Fig. 1. The predicted wind speed used in this paper is based on a version of WRF which covers the east part of China. The spatial resolution of this WRF model output is 9 km × 9 km which is not accurate enough for typhoon disaster warning. A downscaling algorithm is used to refine the weather forecast results to 1 km × 1 km spatial resolution. The downscaling algorithm incorporates the local terrain characteristics and used the computational fluid dynamic (CFD) technique to refine the weather forecast result. The weather forecast program running 2 times a day and predict the future 72 h wind and precipitation. The typical predicted 72 h maximum wind speed and predicted future 72 h accumulative precipitation is shown in Fig. 2.

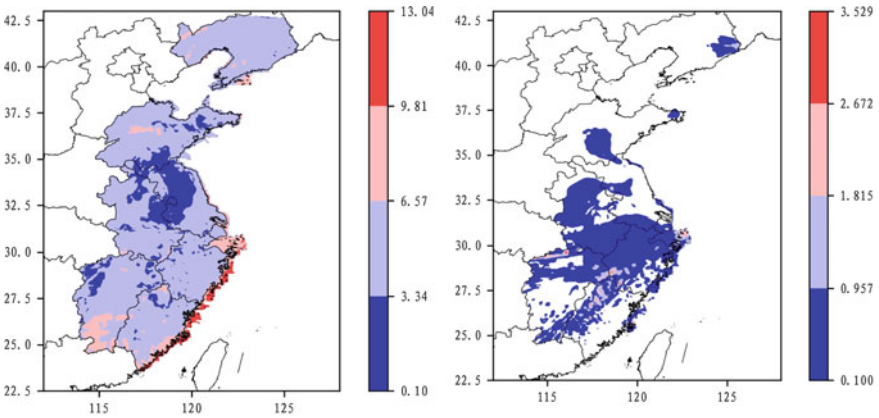

(a) 72h maximum wind speed (m/s) (b) 72h accumulative rainfall (mm)

Fig. 2 The numerical weather forecast results

The predicted wind speed from the numerical weather forecast is close to V_{600} rather than the V_3. To predict the jumper wire swing during typhoon, V_3 need to be derived from V_{600}. The relation between V_3 and V_{600} is derived from the monitored data in Zhejiang province. There are 1920 sets of weather monitoring stations on the high voltage transmission towers in Zhejiang province. Figure 3a shows the histogram of the monitor maximum V_{600} and V_3 from the weather monitoring stations on the high voltage transmission towers in Zhejiang province during typhoon Maria, Ampil, Jongdari, Capricorn and Rumbia in 2018, where the V_3 is averagely 3.6 m/s higher than V_{600}. The histogram of the difference between V_3 and predicted wind speed is shown in Fig. 3b. The relation between V_3 and V_{600} from long time monitoring history in Zhejiang province was used to predict V_3, which is:

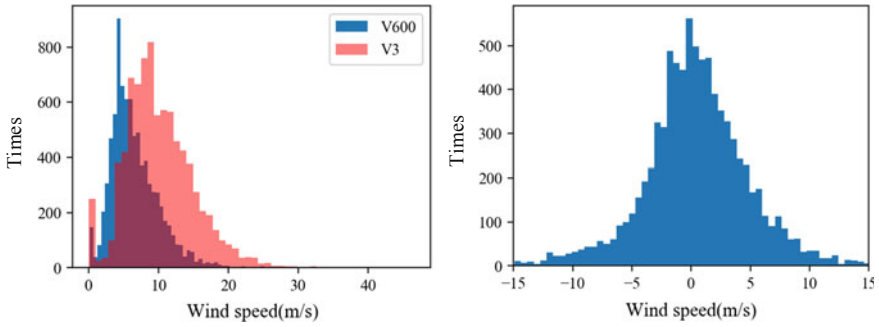

(a) Distribution of V_{600} and V_3 (m/s) (b) Distribution of V_3-$V_{prediction}$ (m/s)

Fig. 3 The monitored V_{600} and V_3 during typhoons in 2018 in Zhejiang province

$$V_3 = N(V_{\text{prediction}} + 0.42, 5.8) \quad (1)$$

where N is the normal distribution, $V_{\text{prediction}}$ is the predicted wind speed from numerical weather forecast.

3.3 UHV Tower Stress Analysis

UHV transmission lines are of the strategic importance for the safety operation of the power grid in eastern China. During developing the typhoon disaster prediction method, a simplified 3-dimensional tower stress analysis program was developed to evaluate the performance of the UHV transmission lines under deferent wind load. Typical analysis results of a ±800 kV transmission line tower are shown in Fig. 4, where the proportion of tower material stress to its design limit increase rapidly when the wind speed increase from 24 to 44 m/s. The UHV tower wind load stress analysis results are carried out under the wind speed from 20 to 60 m/s with step 2 m/s. Since the stress analysis takes long time to complete, the stress analysis

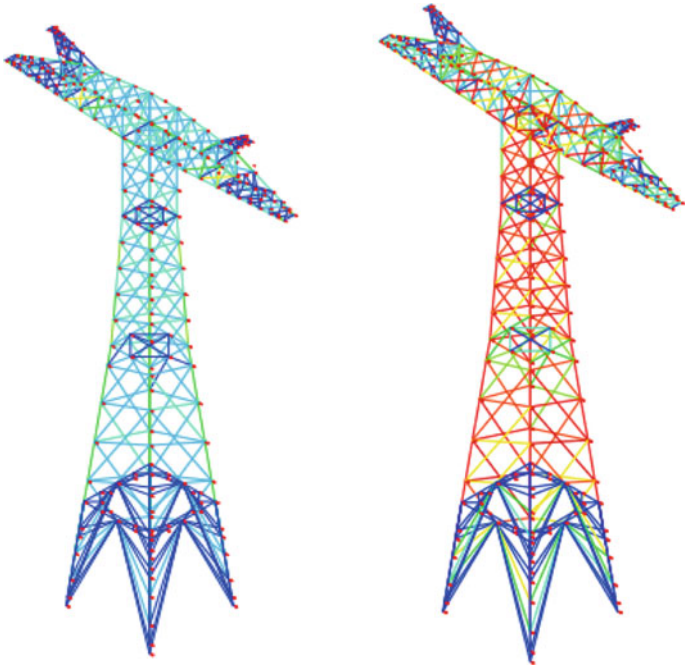

(a) Wind speed 24 m/s (b) wind speed 44 m/s

Fig. 4 The stress analysis results of a ±800 kV transmission line tower (the redder the high of material stress to its design limit)

Table 1 Criteria for typhoon disaster warning

Jumper wire swing risk		Tower structure damage risk	
Probability of V_3 exceed V_{design} (%)	Risk level	Probability of V_{600} exceed V_{design} (%)	Risk level
5–10	Level 4	10–25	Level 4
10–15	Level 3	25–40	Level 3
15–20	Level 2	40–55	Level 2
20<	Level 1	55<	Level 1

results are computed and stored in the database, and when the typhoon is approaching, the analysis results will be extracted based on the predicted wind speed of the tower. The damage of UHV towers then can be evaluated by analyzes how many tower materials stress exceed its design limit.

As shown in Fig. 1, when the typhoon is approaching, the vulnerable tower subset is selected first, and then the predicted wind speed is computed for the towers in the vulnerable subset. The jumper wire swing risk is evaluated by comparing V_3 and tower design wind speed V_{design}, the jumper wire swing risk level is determined based on the probability of V_3 exceed V_{design} which are listed in Table 1. The tower structure damage risk of 110, 220 and 500 kV transmission lines are determined based on the probability of V_{600} exceed V_{design} which are also listed in Table 1. The tower structure damage risk of UHV transmission lines are determined by evaluation of wind load stress analysis results.

4 Application of Prediction Method

From June 2018, the prediction method designed in this paper was applied in the typhoon disaster warning in Zhejiang province. The strongest typhoon that influenced Zhejiang province in 2018 is “Maria” that the center speed is as high as 42 m/s when it landed. According to the prediction method, no tower structure damage waring was made and there are no tower structure damage happened during typhoon “Maria” in Zhejiang province. There are 6 jumper wire swing faults happened during “Maria” in Zhejiang province, which are listed in Table 2. The prediction method gave 4 jumper wire swing fault tower level 4 to level 2 risk, while the prediction method failed to give other 2 transmission line jumper wire swing risk warning.

The first reason for the missing of warning for 2 transmission lines is that the wind speed can significantly distorted by certain terrain while the numerical weather forecast models used in this prediction method cannot represent this distortion with high level of resolution. The second reason is that the jumper wire swing fault is with sporadic characteristics, which can happen when the wind speed has not exceed the V_{design} of transmission lines.

Table 2 Jumper wire swing faults during 2018 typhoon "Maria"

No.	Line code number	$V_{predict}$	V_{design}	Probability of V_3 exceed V_{design} (%)	Predicted risk level
1	1136	22.1	35	2.6	No risk
2	1253	29.8	35	19.5	Level 2 risk
3	1102	14.9	29	1.0	No risk
4	1174	21.1	29	9.9	Level 4 risk
5	1533	21.6	27	19.6	Level 2 risk
6	1031	24.1	33	7.2	Level 4 risk

5 Conclusion

This paper designed a typhoon disaster prediction method for large scale high voltage power transmission network, the conclusions are:

(1) The jumper wire swing is correlated with gust while tower structure damage is usually related to 10-min average wind speed.
(2) The predicted wind speed from numerical weather forecast should be treated as 10-min average wind speed and the gust can be estimate from the relation proposed in this paper.
(3) Although the prediction method proposed in this paper successfully predicted jumper wire swing faults during typhoon "Maria", the jumper wire swing are with sporadic nature and the numerical weather forecast model need further improvement.

References

1. Zhang Y (2006) Status quo of wind hazard prevention for transmission lines and countermeasures. East China Electric Power 34(3):28–31
2. Wu M, Bao J, Ye Y et al (2007) Transmission line accident analysis of Wenzhou grid caused by super typhoon "SAOMAI". Electr Power Constr 28(9):39–41
3. Tang S, Zhang M, Li J et al (2006) Review of blackout in Hainan on September 26th-cause and recommendation. Autom Electr Power Syst 30(1):1–7
4. Chen W (2017) Analysis of damage of Fujian power grid caused by typhoon Meranti. Energy Environ 1:106–109
5. Tao L, Li T, Gan H et al (2017) Analysis of windage yaw characteristics of the jumper insulators in typhoon. Insul Surge Arresters 2(5):157–159
6. Sun J, Xin T, Wang Y (2014) Experience of Guangdong power grid resisting super typhoon "Rammasun" and introspection. Insul Surge Arresters 27(12):80–83
7. Wu Y, Xue Y, Xie Y et al (2016) Space-time impact of typhoon and rainstorm on power grid fault probability. Autom Power Syst 40(2):20–29
8. Wang H, Luo J, Xu T et al (2017) Questionnaire survey and analysis of natural defense techniques of power grids in China. Autom Electr Power Syst 34(23):5–10

9. Fang S, Fang L, Xiong X et al (2014) A typhoon disaster early warning method for power grid based on effective decision boundary. Power Syst Prot Control 42(18):83–88
10. Xu H, Lou W, Li T et al (2017) Wind-induced swing investigation on transmission line jumper wire under hilly terrain. J Zhejiang Univ (Eng Sci) 51(2):264–272
11. Harper BA, Kepert JD, Ginger JD (2010) Guidelines for converting between various wind averaging periods in tropical cyclone conditions. WMO, Geneva
12. Song L, Mao H, Huang H et al (2005) Analysis on boundary layer turbulent features of landfalling typhoon. Acta Meteorol Sin 63:915–921
13. Done J, Davis CA, Weisman M (2004) The next generation of NWP: explicit forecasts of convection using the Weather Research and Forecasting (WRF) model. Atmospheric Science Letters 5(6):110–117

Intelligent Monitoring, Measurement and Maintenance Technology

1200 kV High Power Testing Laboratory Configuration and Design Method of Equipment Layout in Oscillating Circuit

Wenjie Zhou, Shen Hong and Yong Chen

Abstract A new high-power laboratory is constructed by SGCC, there are some new equipment adopted in the laboratory. In the paper, we talk about the configuration of the laboratory and illustrate the equipment layout method of such testing system. First, we choose different circuits to meet the aim of the high power tests with some compromises. Second, we calculate most test parameters of synthetic test circuit, the key calculating procedure is transforming the variables of equations to dimensionless form. It will make the number of independent variables reduce from 8 to 5. Third, overvoltage is simulated between different devices by ATP-EMTP program, it is important to take parasitic parameters of the circuit into account. At last, we get a reasonable insulation distance between different devices by some non-standard equipment test and insulation coordination method, it is the theoretical basis for equipment layout design.

Keywords Synthetic test · Design method · Overvoltage · High power test

1 Introduction

State Grid (Changzhou) electric equipment testing laboratory focus on high power tests. It is consisted of a synthetic test lab, medium voltage direct test lab, high voltage direct test lab, high power transformer test lab, an insulation test lab, a mechanical test hall. We can apply synthetic test on circuit breaker up to 1200 kV, and the current output of short circuit generator is 80 kA R.M.S. The insulation test hall can satisfy the ultra-voltage insulation test for circuit breaker, transformer, post insulators and other equipment.

The article focus on two topics, basic configuration of the laboratory, the design method of equipment layout in oscillating circuit hall.

W. Zhou · S. Hong · Y. Chen (✉)
NARI Group Corporation, No. 218 Donghai Road, Changzhou 213033, Jiangsu, China
e-mail: chen-yong@sgepri.sgcc.com.cn

W. Zhou
e-mail: zhouwenjie@sgepri.sgcc.com.cn

Y. Xue et al. (eds.), *Proceedings of PURPLE MOUNTAIN FORUM 2019-International Forum on Smart Grid Protection and Control*, Lecture Notes in Electrical Engineering 585, https://doi.org/10.1007/978-981-13-9783-7_64

2 Laboratory Configuration

We can get the basic configuration of the High Power Test Laboratory in Fig. 1. There are divided into different part as follows [1]:

First, Medium voltage and High voltage power supply and power distributing system, it is the power provider to different test areas, second, synthetic laboratory, it will imply synthetic experiment from 72.5 to 1200 kV mainly, direct tests lower than 252 kV, then medium voltage laboratory, the main aim is to imply direct tests of circuit breaker blow 40.5 kV, sudden short circuit test for transformer under 45 kV, and there is a high power transformers laboratory (HPTR) in order to test transformers up to 500 kV, finally, a short time current (STC) laboratory, it is used for short time current (STC) tests.

The allocation of high-power test laboratory can be seen in Fig. 2. We can get detailed laboratory configuration in the following.

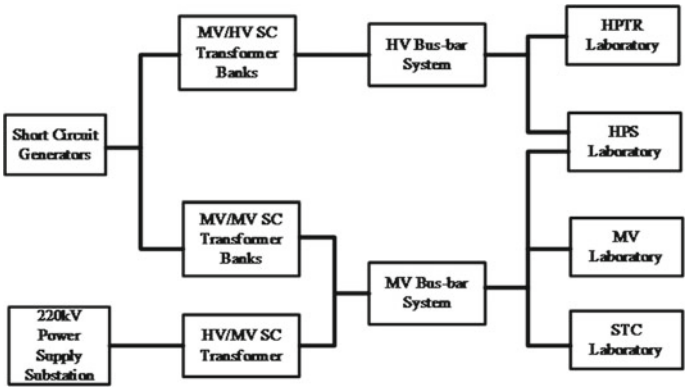

Fig. 1 HPTL configuration (basic)

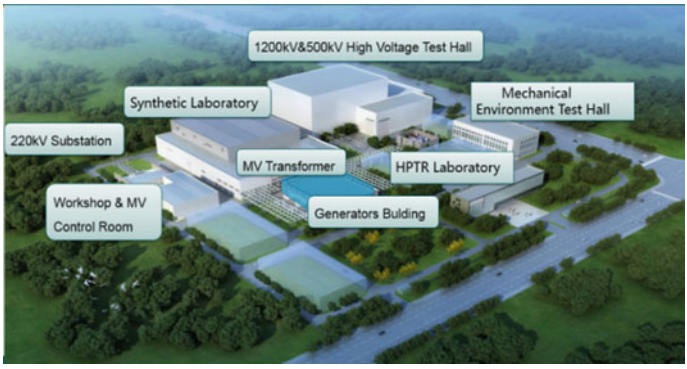

Fig. 2 Allocation of the lab areas

2.1 Test Facilities

There are four types of test facilities in the laboratory. It is composed of two HPS test chambers, four MV test chambers, a HPTR laboratory and a STC laboratory.

2.2 Power Supply and Distribution System

The whole system are consist of a 220 kV substation and two short circuit generators, and in accordance with the bus-bar and disconnects distributing power to different areas.

There are two power supply buildings, a 220 kV Power Supply Substation and a generator building, and the distributing system can be divided in two types. One is medium voltage short-circuit transformers and a 45 kV Transformer Ratio Changers Bays, another one is high voltage short-circuit test transformers and the voltage is up to 252 kV, these transformer ratio changers will make the coils of the transformer be in series or in parallel. The changer systems are installed near the power supply buildings, then the bus-bar length will be much shorter. As a result, the parasitic impedance of the bus-bar will be lower. We also adopted enclosed bus-bar between the generators and short circuit transformer to increase the power of the short circuit generators.

2.3 Complimentary and Ancillary Areas

The areas can be functionally divided into two parts. Control buildings and warehouses.

There are two control buildings for power supply. One is for short circuit generator, another one is for 220 kV substation. Each control room is as close as possible to the power supply, they only execute power starting operation.

The generators can be controlled by MV control room, in the MV control room, we can do the parallel operation of two generators, control of 220 kV substation. There are warehouses and workshops nearby, it will support the testing activities in all test rooms. Other space is dedicated to offices for technical staff etc.

HPS control building can all power supplies, short circuit generators and substation, and it will control all tests. The control building located adjacent to synthetic test hall and short time current laboratory. The warehouse of HV1 and HV2 are located near HPS laboratory, there is an Assembly and Disassembly Hall nearby (short for ADH). Equipment to be tested in HV2 will be prepared there. ADH of high power transformer laboratory is in the high voltage insulation laboratory.

3 Process of Design Method

3.1 Select a Reasonable Method of the Tests

It is designed to imply tests up to 1200 kV by different synthetic test circuits. There are numerous test duties like terminal fault, short line fault, out phase fault test, and the range of test current is designed from 30 to 80 kA. A rational parameter of the equipment will reduce the cost of equipment and area for the laboratory construction, and it is critical for the layout of the oscillating circuit. First, we should get the theoretical value of different test circuits for all the test designed in the laboratory. Obviously, adopting the most equivalent test method will make the construction of the laboratory expensive, and it is difficult to realize technically. So, considering comprehensively above-mentioned factors, the calculation is based on Table 1.

And the definition of test duty can be found in STL 101 [2] and IEC 62271-100.

3.2 4p Weil Circuit Calculation Method

The basic principle of synthetic circuit is Weil circuit [3], schematic of Weil circuit [4] is in Fig. 3, U^*_{cs0} is the initial charging voltage of C_h, other definition of variables can be found in Fig. 3. We need to produce a standard TRV wave [5]. It is named Ur* in Fig. 3.

As for i^*_{c0} and C_{td}, From the test circuit breaker, at the time of zero-crossing point of current, all reactors in the circuit can be considered disconnecting, so only C_{td} and R_1 are connected in the circuit. It can be considered that R_1 and C_{td} influence

Table 1 Circuits for different test duties

Rated voltage (kV)	Duty	Test circuit	Number of breaking poles
≤ 550	Terminal fault	W circuit	Full pole
	Short-line-fault	W circuit	Full pole
	Out-Phase-fault	COP [2]	Full pole
800	T100 T60	Weil	Full pole
	T30 T10	Weil or CTF[a]	Full pole
	Short-line-fault	W circuit	Full pole
1200	Out-phase	COP[b]	Full pole
	T100	CTF	Full pole
	T30	W circuit	Half pole

[a]CTF: The first injection circuit is current, the TRV is implied from high voltage side, another side is earthed

[b]COP: the first injection circuit is voltage, the TRV is implied from different sides. OP test and TF test can be considered, OP is preferred

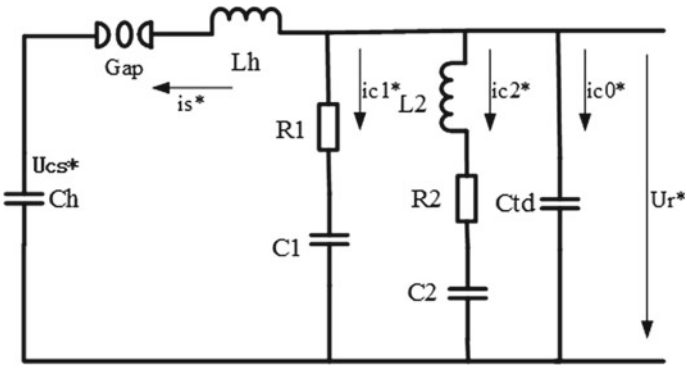

Fig. 3 Principle of four parameter oscillating circuit (Weil circuit)

the first part of transient recovery voltage. Capacitance of C_{td} is very small, it only influence the very beginning of the wave, as a result, we can calculate the t_d by (1), t_d: delay time, the detail definition of t_d can be found in IEC 62271-100. The equations of the circuit shows in (2)–(6).

$$C_{td} = \frac{t_d}{R_1} \tag{1}$$

$$i_s^* = -i_{c_1}^* - i_{c_2}^* - i_{c_0}^* \tag{2}$$

$$U_{cs}^* = \frac{1}{C_h}\int i_s^* dt + U_{cs0}^* \tag{3}$$

$$U_r^* = L_h \frac{di_s^*}{dt} + U_{cs}^* \tag{4}$$

$$U_r^* = \frac{1}{C_1}\int i_{c_1}^* dt + R_1 i_{c_1}^* \tag{5}$$

$$U_r^* = \frac{1}{C_2}\int i_{c_2}^* dt + R_2 i_{c_2}^* + L_2 \frac{di_{c_2}^*}{dt} \tag{6}$$

There are 8 independent variables according to upper equations. The variables include C_h, L_h, R_1, C_1, R_2, C_2, L_2, U_{cs}^*, but there are only 6 independent equations, so the roots of the equations are not unique, and it is an atypical circuit synthesis problem.

The circuit equations variables can be transformed to dimensionless form [1, 6–9] by (7)–(17), u_1 is defined in IEC 62271-100.

$$\mathrm{A1} = \frac{C_h}{C_h + C_1} \tag{7}$$

$$\mathrm{r1} = \frac{R_1}{2Z_s} \tag{8}$$

$$\mathrm{r2} = \frac{R_2}{2Z_2} \tag{9}$$

$$A = \frac{C_h}{C_h + C_1 + C_2} \tag{10}$$

$$K1 = \frac{L_2}{L_h} \tag{11}$$

$$Z_2 = \sqrt{\frac{L_2}{C_2}} \tag{12}$$

$$Z_s = \sqrt{\frac{L_h}{A1 \times C_1}} \tag{13}$$

$$\mathrm{K2} = \frac{C_2}{C_1} \tag{14}$$

$$\beta = \frac{1}{A} = \frac{U^*_{cs0}}{u_1} \tag{15}$$

$$\omega = \frac{1}{L_h \times a_1 \times C_1} \tag{16}$$

$$\theta = \omega \times t \tag{17}$$

Then (2)–(6) can be transformed to dimensionless forms as (18)–(22). There is six independent variables: β, r1, r2, K1, K2 and a1. The new current i_s, i_{c1}, i_{c2} are transformed by i^*_s, i^*_{c1}, i^*_{c2} divided by rated short circuit current.

$$i_s = -i_{c_1} - i_{c_2} - i_{c_0} \tag{18}$$

$$\mathrm{U}_{cs} = (1 - A1) \int i_s d\theta + \beta \tag{19}$$

$$\mathrm{U}_r = \frac{di_s}{dt} + U_{cs} \tag{20}$$

$$U_r = A1 \int i_{c_1} d\theta + 2r1 \times i_{c_1} \tag{21}$$

$$U_r = \frac{A1}{K2}\int i_{c_2} d\theta + 2r2 \times \sqrt{\frac{K1 \times R_1}{K2}} i_{c_2} + K1\frac{di_{c_2}}{d\theta} \tag{22}$$

According to the equivalence requirement of synthetic test, the value of R_1 need to be the same as power system wave impedance [1, 9, 10], it depends on the rated voltage and short circuit current of the power system. So R_1 can be regarded as a known number.

Now the number of dimensionless independent variables is only five. It will reduce the calculating workload.

First, we calculate dimensionless parameter repeatedly, and we get the relationship between dimensionless parameters and dimensionless voltage wave. Then we get a series of curves between TRV and dimensionless parameters, at last, we get some empirical formula for calculation for Weil circuit which can fulfil the IEC standard [4]. On the basis of Weil circuit formula, we have also get empirical formula for other test circuit.

The CTF circuit is designed for the highest voltage 1200 kV test [11–13], and it is the most equivalent circuit for 1200 kV test in the world [14]. The principle can be seen in Fig. 4. It is combined of two oscillating circuits. The gap of the second oscillating circuit should be trigged exactly on the highest voltage of the first oscillating loop within 10 μs [15]. As a result, the dispersion time of the gap should be less than 10 μs. The voltage range of the gap is from 100 to 1200 kV, when it is under the highest working voltage, it is impossible to fulfill the requirement trigging by electric spark. Therefore, we adopted a plasma trigged sphere gap, the plasma will spray from two sides of the gap and the sphere diameter is 1.2 m. The gap is still under test to adjust its performance.

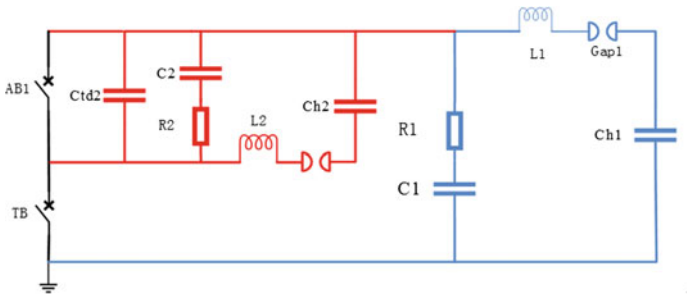

Fig. 4 CTF circuit, blue line: first oscillating loop; red line: the second oscillating loop

3.3 Simulation and Test Verification of Key Non-standard Equipment

We calculated the fault currents and overvoltage between different equipment under critical test duties. The critical condition is the maximum power test duty, 800 kV 80 kA SLF test, and the maximum voltage test duty 1200 kV 80 kA T100. And it is critical calculating for the equipment layout of oscillating circuit.

It is very important to take parasitic parameters into account, because the parasitic impedance and capacitance of the bus-bar and reactors [16], once the test breaker is reignited, the very high oscillating voltage wave will reflect and refract in the whole circuit [17]. It may damage the reactors and cause breakdown of the earth bus-bar. Therefore, the earth bus-bar of the first oscillating circuit should be insulated. Some calculation result for 800 kV SLF test can be seen in Table 2. Of course, the calculation is not very accurate, but it can be a reference for the insulation design. According to the result, bus-bar of the first oscillating circuit should be insulated up to 145 kV.

In order to apply the 1200 kV test, we select the most equivalent test circuit, the principle can be seen in Fig. 4. It is combining current injection circuit and voltage injection circuit. It is consisted of two oscillating circuit, the second voltage loop is superimposed on first voltage loop at a proper time. As a result, withstand voltage level of the equipment of second voltage loop is very high. As for Ch2, the withstand voltage of the base of capacitor stack is 1050 kV SI, when we choose a normal post insulator under test, it cannot withstand the 1050 kV SI, because it is fixed on the ground, but in a substation, the insulators are fixed on a high steel bracket. You can see the test of the base in Fig. 5. The main withstand voltage of the capacitor stack is lower than the rated voltage of the post insulator [18]. We had done insulation test of key non-standard equipment like grading ring as shown in Fig. 6. It shows a ring of the capacitor stack, the U_{50} of such structure is 1938 kV SI, the distance is 7 m and the dispersion value is 3.18% [19].

The parameter of the insulators in the base can withstand over than 1050 kV SI, but the real U_{50} of such base is only 1007 kV.

Table 2 Overvoltage between different devices in 800 kV SLF test (Part Data)

Device	Ch1 bottom	Ch1 top	Lh1 head	Lh1 tail	Lpf1 head	Lpf1 tail
Ch1 bottom (kV)	377	820	1899	1166(re)	1964	1160(re)
Ch1 top (kV)		1104	1133	1336	1256	1388(re)
Lh1 head (kV)			1684	1773	683(re)	1507(re)
Lh1 tail (kV)				898	1964	1404
Lpf1 head (kV)					1869	1849
Lpf1 tail (kV)						1186(re)

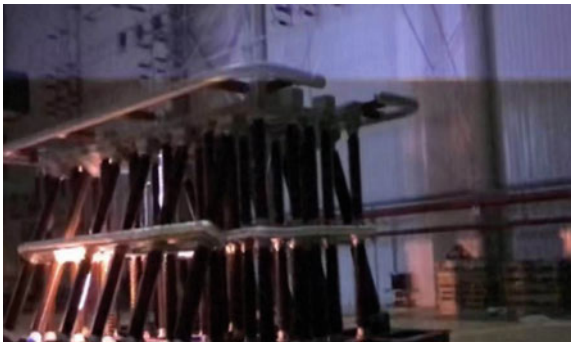

Fig. 5 Insulation test of base of Ch2 stack

Fig. 6 Insulation test for non-standard equipment, grading ring of a capacitor stack, Copper nets were laid on the ground

3.4 Fix the Actual Technical Parameter of Equipment

After we get most parameters of different test duties, we should get the accurate number and scale of the equipment in oscillating hall in order to make a reasonable layout.

Taking main capacitors as an example, first, we fix the highest charging voltage of the stack is 1200 kV because the highest charging voltage of main capacitor is 820 kV in 800 kV SLF test and the charging voltage of each capacitor should be less than 70% rated voltage for safety. Each capacitor is 100 kV and 3 μF according to the manufactory for convenience, as a result, the value of capacitor each stage should be set as 3, 6, 12 μF etc., and each stage of the capacitor stack is 100 kV. The next step is that we should fix the maximum value of capacitor of each stage. The basic principle is that the value can make as many capacitance combinations as possible that are close to the theoretical values for all test duties. That means sum of variances between actual value and theoretical capacitor value should be the lowest.

As a result, we add a new capacitor 1.5 μF in each stage in order to reduce errors.

3.5 Main Optimized Equipment of Synthetic Circuit

Main Capacitor Stacks. As mentioned in Sect. 3.4, the highest charging voltage of the two capacitor stacks is 1200 kV, and the maximum capacitance is 45 μF of each stage. The post insulator should be higher than normal as seen in Fig. 5.

Frequency Modulation Capacitor Stacks. There are 14 stages of the capacitor stacks, each stage is 130 kV DC. the minimum capacitance is adjusted to 0.025 μF and the maximum is 12 μF.

HV Reactor Banks. There are two types of reactors, one type is to adjust the current and modulate the transient recovery voltage, others are modulating power frequency recovery voltage, according to the calculated overvoltage as shown in Table 2, parameter of most reactors should withstand 1950 kV switch impulse voltage and the maximum parameter of power recovery reactor is 5000 mH for T10 test.

3.6 The Design Method of Equipment Layout

By the results of simulation calculation, we obtain most parameters of the test duties, based on such data, we can made the optimized parameter of different device like item 3.4, we can get the detailed technical parameters of the equipments, then the manufacturer can determine the specific number and size of the equipments. The simulation results of overvoltage between different devices like shown in Table 2, then the safe distance between different equipments can be roughly determined by insulation coordination. But some non-standard equipment should be fixed by insulation test like shown in Fig. 5. Taking frequency modulate capacitor as an example, the withstand voltage of the capacitor ring is $1938\ \text{kV} - 3 \times 3.18\% = 1753\ \text{kV}$ according to the test result [20], so the distance between modulate capacitor stack and other equipment including earth should be over than 7 m. and we put the capacitor stack 10 m away from other equipment.

4 Conclusion

We will imply the highest voltage test by the most equivalent synthetic test circuit soon in the new built laboratory, in order to make the layout of the synthetic circuit reasonable, we did a lot of calculation for most test duties by transforming the circuit equation dimensionless form, then we can get the test parameters, based on the result, we did the simulation of key test duties in order to get the critical operation of all the equipment, especially the overvoltage between different equipment. At last, according to the result of some insulation test for non-standard

equipment, combining with insulation coordination method and experience of the manufacturers, the reasonable layout of the equipment is obtained.

References

1. Zhou W, Hong S, Chen Y, Zhang L (2018) 1200 kV high power testing laboratory configuration and optimized design method of oscillating circuit. In: 2018 IEEE international conference on high voltage engineering and application (ICHVE), ATHENS, Greece, pp 1–4
2. Short-Circuit Testing Liaison (2006) STL guide 101 high-voltage switchgear and controlgear part 101: synthetic testing, 2006 edn.
3. Li G, Gao X, Liu HJ, Huang S, Zhang JB, Dong W (2018) High power short circuit breaking and closing test technology of high voltage AC circuit breaker. High Volt Appar 54(02):68–75+83
4. Kurozawa Y, Takahashi T, Saito K et al (1989) Four-parameter transient recovery voltage circuits appropriate for test extra high voltage circuit breakers. CIGRE Paper, Sarajevoi Yugoslavia, pp 13–32
5. High-voltage switchgear and controlgear—Part 100: High voltage alternating-current circuit breakers. IEC 62271-100 2012 (2012)
6. Wang R (1987) Calculation and adjustment limitation of four-parameter TRV in high power testing circuits and their comparison. Power Deliv IEEE Trans Power Deliv 3:758–764
7. St-Jean G, Wang RF (1983) Equivalence between direct and synthetic short-circuit interruption tests on HV circuit breakers. IEEE Trans Power Appar Syst 102(7):2216–2223
8. Wang R-F (1992) Optimization of breaking-capacity testing circuits. Proc CSEE 12(2):1–9
9. Wang R-F (1982) Some question about equivalence of direct test and synthetic test. High Volt Appar 1982(06):3–14
10. Sheng BL, van der Sluis L (1996) Comparison of synthetic test circuits for ultra-high-voltage circuit breakers. IEEE Trans Power Delivery 11(4):1810–1815
11. Smeets RPP, Kuivenhoven S, Knol P, Hofstee A (2009) High-power testing of 1100 kV/1200 kV circuit breakers. South Power Syst Technol 3(6):1–8
12. Pei Z, Yao S, He J, Ye H (2007) A new synthetic test circuit for UHV circuit breakers. Proc CSEE 27(33):65–69
13. van der Sluis L, Damstra GC, Kemper HW (1992) Synthetic test methods experience and future developments. Cigre Paper 13-203, Paris, France
14. Sun M, Yao S, Du W, Li G, Liu P, Wen P (2013) High power test of UHV switchgears. High Volt Appar 49(9):108–112
15. Zhang J, Zhao J, Wu S, Li Y (2015) Design and discharge characteristic discussion of 1000 kV controllable high-voltage ignition ball. High Volt Appar 151(12):0184–0189
16. Zhang Y, Gui D, Xu W (2018) Protection scheme of control winding for 500 kV magnetically controlled shunt reactor. Autom Electr Power Syst 42(19):148–153
17. Yang H, Cai Y, Qu Z, Deng Y, Lu Y, Zhao R (2018) Key techniques and development trend of soft open point for distribution network. Autom Electr Power Syst 42(7):153–165
18. Yan Z, Zhu D (2015) High voltage insulation technology, 3rd edn. China Power Press, China
19. Chen C, Wang C, Gao Y (2017) High-voltage testing technology, 4th edn. Tsinghua University Press, China
20. Zhao X, Xu J, Lu T, Zhao C, Yuan J (2018) Overvoltage analysis on overhead line based MMC-HVDC system under single-pole-to-ground. Autom Electr Power Syst 42(7):44–49

Current Unbalance Cluster Analysis Based on Self-organizing Competitive Neural Network

Peng Wu, Ruiqi Liang, Haocheng Zhou, Kai Wang, Youchun Liu and Hongming Zhu

Abstract In power system, current unbalance is a kind of common fault that seriously affects the safety and efficiency of power system. There are many reasons that may cause three-phase unbalance, and now rely on manpower to judge according to specific conditions. This paper proposes a new algorithm for clustering analysis of unbalanced three-phase current data. We define a serials of feature parameters, and then use self-organizing competitive neural network for clustering analysis to subdivide current unbalance into five categories. In the experiment, a large amount of historical current data is analyzed by the proposed algorithm. We get five categories with obvious features and differences. The clustering results are reasonable and interpretable. The algorithm makes full use of the large amount of unmarked historical data produced by power system, and is helpful for the early warning of current unbalance and pre-judgment of causes.

Keywords Current unbalance · Self-organizing competitive neural network · Clustering algorithm · Feature extraction

1 Introduction

Any deviation in current waveform from perfect sinusoidal, in terms of magnitude or phase shift is termed as unbalance. On distribution level, the load imperfections cause current unbalance which travel to transformer and cause unbalance in the three-phase voltage [1].

P. Wu · H. Zhou · Y. Liu · H. Zhu
Jiangsu Electric Power Information Technology Co. Ltd., Nanjing 210000, China

R. Liang (✉) · K. Wang
School of Information Science and Engineering, Southeast University, Nanjing 210000, China
e-mail: query11235@gmail.com

Y. Xue et al. (eds.), *Proceedings of PURPLE MOUNTAIN FORUM 2019-International Forum on Smart Grid Protection and Control*, Lecture Notes in Electrical Engineering 585, https://doi.org/10.1007/978-981-13-9783-7_65

Current unbalance may be caused by the following reasons [2, 3]:

- Large and/or unequal distribution of single-phase load—This can occur when low voltage single-phase services are connected to the phase closest to the neutral. The same problem can occur at medium voltage levels when single-phase distribution transformers are connected to the conductors that are easiest to reach.
- Phase to phase loads—This occurs with some equipment that simply requires single phase, but at line-to-line voltage.
- Unbalanced three phase loads—Some three phase loads are comprised of both single and three-phase equipment. It is important that these loads are balanced to meet the power company's requirements.

At present, the specific causes for current unbalance are mainly determined by on-site analysis manually. In fact, different types of current unbalances will appear differently in historical power grid data. Therefore, we can use historical data of power grid to pre-judge the causes or types of current unbalance.

How to scientifically utilize the huge amount of data generated by power system [4] has attracted attention of scholars. A new algorithm for fault tracing in power grid based on big data platform has been put forward in [5]. Paper [6] clusters electricity consumption behavior patterns based on the big data of power system. Density-based spatial clustering of applications with noise (DBSCAN) has been used to analyze abnormal electricity consumption [7].

Current unbalance is a kind of common fault with a large number of data samples. Most of these samples did not have any label of the cause. A small number of samples were manually processed and labeled with their causes. But many of the labels are very vague, and there is no uniform standard. So we can only classify current unbalance data with a clustering algorithm that does not require data labels.

This paper proposes a series of new feature parameters as input to the self-organizing competitive neural network. Section 2 describes in detail the definition and significance of these feature parameters. Section 3 presents the self-organizing competitive neural network used in this paper. Section 4 shows the experiment using power grid data of Jiangsu province and the analysis of its results. At last, we give out the conclusion and propose future work ideas.

2 Feature Parameters

Current unbalance is usually calculated by two methods:

(1) Current unbalance rate is equal to the ratio of the difference between the maximum current and the minimum current to the maximum current.
(2) The current unbalance rate is equal to the ratio of the difference between the maximum current and the minimum current to the average value of three-phase currents.

In this article, we adopt the first method. So current unbalance rate I_{un} is defined as:

$$I_{un} = \frac{I_{\max} - I_{\min}}{I_{\max}} \times 100\% \tag{1}$$

where $I_{\max} = \max\{I_A, I_B, I_C\}$, $I_{\min} = \min\{I_A, I_B, I_C\}$.

According to Eq. (1), the value of I_{un} may be large in the following four cases:

(1) $I_{\max}$ is too small;
(2) The value of $I_{\min}$ is too small or even close to zero. When $I_{\min}$ is close to 0, I_{un} will be close to 1;
(3) $I_{\max} - I_{\min}$ is very large;
(4) The above three cases are mixed.

So four parameters are used to represent the number of time points of different cases:

(1) N_0 is the number of time points when I_{un} is smaller than $U_{\max}$, which is the maximum value of normal I_{un}.
(2) N_1 is the number of time points when $I_{\max}$ is smaller than $B_{\max}$, which is the lower bound of $I_{\max}$.
(3) N_2 is the number of time points when $I_{\min}$ is smaller than $B_{\min}$, which is the lower bound of $I_{\min}$.
(4) N_3 is the number of time points when $I_{\max} - I_{\min}$ is bigger than $C_{\max}$, which is the upper bound of $I_{\max} - I_{\min}$.

Let N be the total number of sample points in a whole day. Time points whose three-phase currents satisfy the fourth case will be will be counted repeatedly into N_1, N_2, N_3. Sum of N_0, N_1, N_2, N_3 may be more than N.

We also need some parameters to indicate the correlation between the three phase currents. R_{AB}, R_{AC}, R_{BC} are the Euclidean distances between each pair of the normalized three-phase currents $\tilde{i}_A$, $\tilde{i}_B$, $\tilde{i}_C$:

$$\begin{aligned} R_{AB} &= \sqrt{\sum_{0}^{N-1} (\tilde{i}_A - \tilde{i}_B)^2} \\ R_{AC} &= \sqrt{\sum_{0}^{N-1} (\tilde{i}_A - \tilde{i}_C)^2} \\ R_{BC} &= \sqrt{\sum_{0}^{N-1} (\tilde{i}_B - \tilde{i}_C)^2} \end{aligned} \tag{2}$$

Define X as the input vector of self-organizing competitive neural network. X is a seven-dimension vector:

$$X = (N_0, N_1, N_2, N_3, R_{AB}, R_{AC}, R_{BC}) \tag{3}$$

3 Self-organizing Competitive Neural Network

Self-organizing neural networks can analyze and compare objective events through repeated observations [8]. It searches for its inherent laws and correctly classifies things with common features. This kind of network is similar to the learning mode of biological neural network in human brain. It can automatically change the network parameters and structure by automatically searching for the inherent regulations and essential attributes of samples [9]. This is also the origin of the self-organizing name. Self-organizing neural networks mostly adopt competitive learning rules.

The basic idea of a competitive neural network is that each neuron in the network competition layer gains a chance to respond to the input pattern through competition [10, 11]. Finally, only one neuron becomes the winner of the competition. The connection weights associated with the winning neurons move toward to the direction which is beneficial to its competition. Self-organizing Competition neural network detects some regularity of clustering objects, so that the resulting cluster can be regarded as a mapping of the underlying features to the high-level characteristics. Partitioning clustering algorithms, such as K-means, cannot be used for non-convex sets of data and are susceptible to noise data. Hierarchical clustering algorithm is difficult to determine the number of clustering results. We hope that the results of clustering have realistic physical significance, and the self-organizing competitive neural networks meet the requirements in various clustering algorithms (Fig. 1).

Competitive networks can be divided into a input layer and a competition layer. Assume that the input layer consists of D neurons and the competition layer has M neurons. The weight of the network connection is: $\omega_{ij}(i = 1, 2, \ldots, D; j = 1, 2, \ldots, M)$.

In the competition layer. The neurons compete with each other and eventually only one neuron wins to fit the current input sample. The neurons that win the competition represent the classification pattern of the current input sample. The state of the competitive layer neuron j is calculated as follows [12]:

$$S_j = \sum_{i=1}^{D} \omega_{ij} x_i \tag{4}$$

where x_i is the i-th element of input vector X. According to the competition mechanism, the neuron with the largest weight in the competition layer wins the

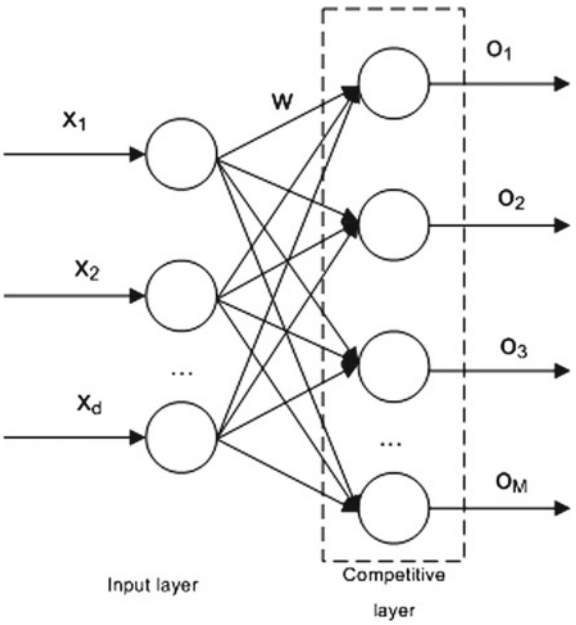

Fig. 1 Structure of self-organizing competitive neural network

competition. After competition, the weights are modified as follows for all input layer neurons i [12]:

$$\Delta\omega_{ij} = \eta(\frac{x_i}{m} - \omega_{ij}) \tag{5}$$

where η is learning rate, $0 < \eta \ll 1$, and $m = \sum_{i=1}^{D} x_i$. Equation (5) guarantees that the weight adjustment can satisfy the sum of all weight adjustments to be 0.

4 Experiment

All training data and test data in the experiment were from the power grid of some cities in Jiangsu Province in 2018. Power grid data is sampled every 15 min. So there are 96 sample points each day, $N = 96$. All the data in the data set are current imbalance data that has been screened out by the State Grid of Jiangsu Province. There is no data for normal conditions of the grid or other types of faults. We used 1000 pieces of data to train the network and tested it with 200 pieces of data, each piece of data was collected by a distribution transformer during a day.

The data at each time point contains the current values i_A, i_B, i_C of three phases A, B, and C, and current unbalance I_{un} calculated according to Eq. (1). For each day, we calculated point numbers of different condition N_0, N_1, N_2, N_3 and Euclidean distances between each pair of the normalized three-phase currents R_{AB}, R_{AC}, R_{BC} to get input vector X.

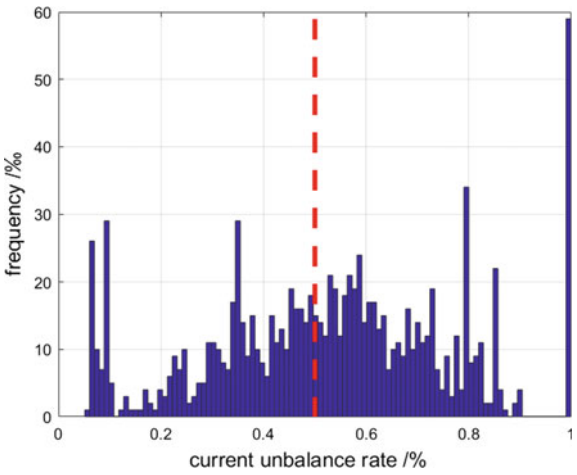

Fig. 2 The probability distribution of current unbalance rates of training data

In order to make the neural network reach the steady state better, too large values or sharply changing values will cause instability of the entire network training [13, 14]. So we have further processed the input vector X. The final input vector is:

$$X' = (N_0/N, N_1/N, N_2/N, N_3/N, R_{AB}/10, R_{AC}/10, R_{BC}/10) \tag{6}$$

Range of each element of X' is $[0, 1]$. The parameters when training the network are set to: $D = 7$ (7 input neurons), $M = 5$ (5 competitive layer neurons, datas were divided into 5 categories), $\eta = 0.05$, $U_{\max} = 0.5$, $B_{\max} = 50$, $B_{\min} = 20$, $C_{\max} = 100$. The selection of above threshold values is based on actual experience and statistical distribution of data. Figure 2 shows the probability distribution of current unbalance rates of training data, and it can be seen from Fig. 2 that $U_{\max} = 0.5$ can divide the current unbalance rates into two parts of roughly equal numbers (Fig. 3 and Table 1).

Each category has the following features:

Type 1: Current unbalance rates are not high at most of the time points, current unbalance is mainly because the maximum and minimum currents differ greatly.

Type 2: Current unbalance rate is low and Euclidean distances of the three phase currents are also small.

Type 3: Current unbalance is very serious, and Euclidean distances of the three phase currents are large. All of the three abnormal situation defined in Sect. 2 exist in a mixture.

Type 4: Current unbalance is mainly caused by the low minimum current, which even close to 0.

Type 5: Current unbalance is mainly because the maximum and minimum currents differ greatly like type 1, but much more serious.

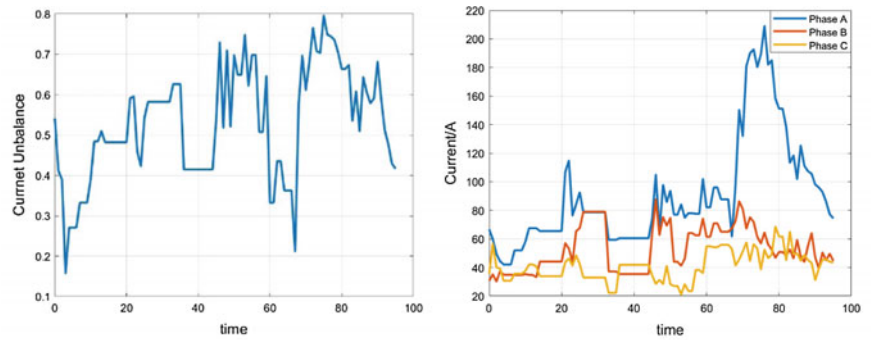

Type 1

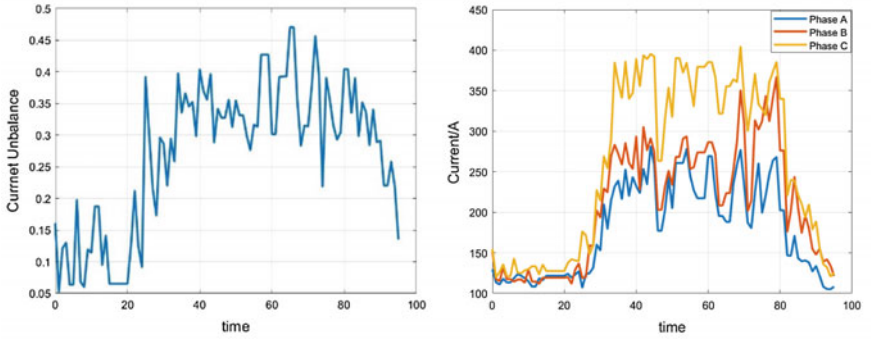

Type 2

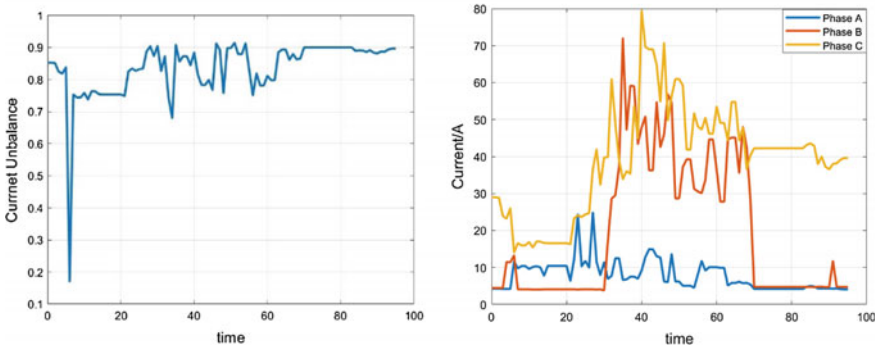

Type 3

Fig. 3 Current unbalance and currents examples of each type

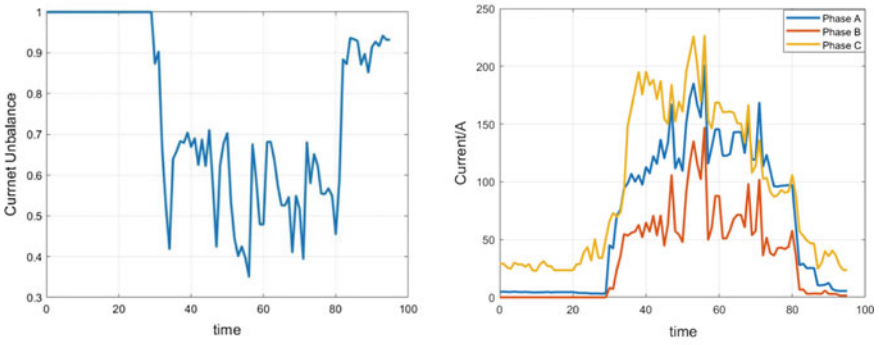

Type 4

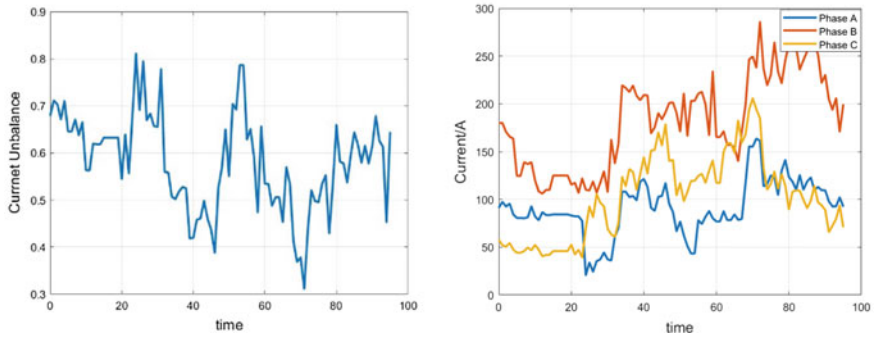

Type 5

Fig. 3 (continued)

Table 1 Proportion of each type

	Type 1	Type 2	Type 3	Type 4	Type 5
Proportion	27.0%	23.0%	17.5%	18.0%	14.0%

5 Conclusion and Future Work

This paper proposes new feature parameters for cluster analysis of current unbalance using a self-organizing competitive neural network. The results obtained can help determine the seriousness and underlying causes of current unbalance. It can be used as fault monitoring and warning for power grid systems. In this paper, the classification of current unbalance is not elaborate enough, and only the values of three-phase currents have been taken into consideration. In future work, we will consider more types of data for more detailed classification.

References

1. Mousazadeh Mousavi SY et al (2017) Flexible compensation of voltage and current unbalance and harmonics in microgrids. Energies 10(10):1568
2. Lagier T, Ladoux P (2016) Analysis of voltage and current unbalance in a multi-converter topology for a DC-based offshore wind farm. In: PCIM Europe 2016; International exhibition and conference for power electronics, intelligent motion, renewable energy and energy management. VDE
3. Kalyuzhny A, Kushnir G (2007) Analysis of current unbalance in transmission systems with short lines. IEEE Trans Power Delivery 22(2):1040–1048
4. Zhao J et al (2017) Data science for energy systems: theory, techniques and prospect. Autom Electr Power Syst
5. Wang L et al (2018) Framework of fault trace for smart substation based on big data mining technology. Autom Electr Power Syst 42(3):84–91
6. Gong G et al (2018) Clustering optimization strategy for electricity consumption behavior analysis in smart grid. Autom Electr Power Syst 42(2):58–63
7. Tian L et al (2017) Abnormal power consumption analysis based on density-based spatial clustering of applications with noise in power systems. Autom Electr Power Syst 41(5):64–70
8. Su MC, Chang HT (2001) A new model of self-organizing neural networks and its application in data projection. IEEE Trans Neural Netw 12(1):153–158
9. Alam P et al (2000) The use of fuzzy clustering algorithm and self-organizing neural networks for identifying potentially failing banks: an experimental study. Expert Syst Appl 18(3): 185–199
10. Hiew BY, Tan SC, Lim WS (2017) A double-elimination-tournament-based competitive co-evolutionary artificial neural network classifier. Neurocomputing 249:S0925231217305672
11. Serban IV et al (2016) Building end-to-end dialogue systems using generative hierarchical neural network models. In: Thirtieth AAAI conference on artificial intelligence
12. Cohen MA, Grossberg S (1983) Absolute stability of global pattern formation and parallel memory storage by competitive neural networks. IEEE Trans Syst Man Cybern 5:815–826
13. Xu P, Xu S, Yin H (2007) Application of self-organizing competitive neural network in fault diagnosis of suck rod pumping system. J Petrol Sci Eng 58(1-2):43–48
14. Park D-C (2000) Centroid neural network for unsupervised competitive learning. IEEE Trans Neural Networks 11(2):520–528

The Fault Diagnosis of Infrared Bushing Images Based on Infrared Thermography

Chao Wei, Yang Liu, Yifan Bie, Shengquan Wang, Yiming Wu, Tonglei Wang and Kangyong Yin

Abstract The aim of this paper is to diagnose the bushing faults by making use of the infrared images. Before diagnosing the bushing faults, the preprocessing and segmentation should be processed. The preprocessing, which includes adaptive median filtering, K-means, opening operation, is applied to filter the noise and remove the background. To segment the bushing from the image, simple linear iterative clustering (SLIC) is applied which allows the bushing segmented according to the shape of it and makes it works better. After analyzing the thermal characteristics of the fault image of bushings from the *DL/T-664-2016 Application rules of infrared diagnosis for live electrical equipment*, it can be concluded that diagnose the fault area's relative position can be a great way to diagnose the bushing, so it's regarded as a principle to classify the faults. In this paper, we selected some typical infrared bushing images with faults. After the processing, the results have been verified that the method is able to segment the bushing and diagnose the fault preliminarily.

Keywords Adaptive median filtering · K-means · Opening operation · SLIC · Fault diagnosis

1 Introduction

In recent years, based on data from various studies and power facilities, transformer faults caused by bushings have accounted for 5–50% of the total number of transformer faults. Bushings, leading the cable out from the transformer and make it connected to the grid, serve as an important component of the transformer [1]. It's

C. Wei · Y. Liu · S. Wang · Y. Wu · T. Wang · K. Yin
State Grid Jiangsu Electric Power Co., Ltd. Research Institute, Nanjing 211103, China

Y. Bie (✉)
Jiangsu Key Laboratory of New Energy Generation and Power Conversion, Nanjing University of Aeronautics and Astronautics, Nanjing 211106, China
e-mail: byf960326@163.com

Y. Xue et al. (eds.), *Proceedings of PURPLE MOUNTAIN FORUM 2019-International Forum on Smart Grid Protection and Control*, Lecture Notes in Electrical Engineering 585, https://doi.org/10.1007/978-981-13-9783-7_66

critical to ensure the bushing maintains good insulation properties so that the current can be well conducted and the power system can run safely [2]. The relevant statistics also show that more than half of the electrical equipment failures in the power system are caused by the thermal faults which contain connection failure, current leakage and magnetic leakage. The thermal failures can be well observed by the infrared image [3].

Under the existing working mode, the infrared image fault recognition is mainly based on manual recognition, which has high requirements on the professional quality of personnel. The computer-assisted analysis methods can automatically extract, identify and analyze the collected infrared images, which can reduce the labor intensity and the dependence on technicians [4]. It is more conducive to the processing of infrared image data and the statistical analysis.

In recent years, some computer-assisted analysis methods for automatically diagnosing by infrared images have been proposed. There are infrared thermography based methods using OTSU [5], K-means [6, 7], simple linear iterative clustering (SLIC) [8] and etc., all of which need to segment the target through finding the appropriate threshold, but they ignore the shape of the target itself, which may lead to failure in the image which has more complex background. So there is threshold combined with edge detection method to solve the problem, but it's too dependent on the choice of edge detection operator [9]. All of the former methods just proposed how to extract the targets, while there are artificial intelligence methods to not only segment but also diagnose the bushings. They extract different feature vectors from the preprocessed image and then use artificial intelligence such as supporting vector machine (SVM) [10, 11], back propagation (BP) Neural Networks [12, 13], Multi-Layer Perceptron (MLP) Neural Networks [14] to classify the fault. But the artificial intelligence methods require adequate fault images which is hard to satisfy [15, 16].

In this paper, a new method is proposed to remove the background interference based on K-means and opening operation then segment the target bushing through SLIC. With target bushing segmented, the fault area can be located so that the fault can be diagnosed through the relative position of the bushing. This method can segment the bushing with the shape of bushing taken into consideration, and classify the fault preliminarily.

2 Infrared Thermography-Based Target Extraction

The infrared image diagnosis of the transformer bushings can be influenced by the background temperature and the heating of various electrical components in the power system. Therefore, filtering the noise and removing the background interference should be applied as the preprocessing. And then, we need to segment the bushing are from the picture, which requires us segment it taking the thermal shape of bushings into consideration, so we decided to segment the image with SLIC.

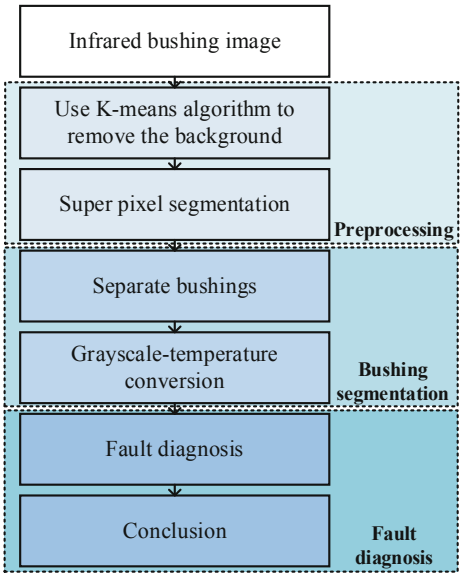

Fig. 1 The program flow of the infrared bushing image diagnosis

Due to the standard and the quality of every bushing picture is different, so there might be a few bushings in one image. If they are not segmented one by one, it will be of great difficulty to diagnose them properly. Then we need to figure out how many bushings there are and separating bushings one by one.

In order to identify and diagnose the faults better, the infrared image should be preprocessing first, then get the bushing segmented, and the program flow is shown as Fig. 1.

2.1 Infrared Image Preprocessing

Adaptive median filtering. The traditional filtering method requires the input of the expected signal to the system which makes the filtering system perform better. But when there are different pictures processing, the expected signal value is often different and also unknown. Therefore, a new filtering method is needed, which can automatically calculate the value of the required input signal to filter the picture, so that different pictures can be optimized for noise reduction processing. Based on this situation, adaptive median filtering is introduced to filter the system.

K-means algorithm. Then the K-means algorithm is used to separate the foreground and the background of the image. The principle is the difference between the grayscale of them, while the background grayscale is much lower than the bushing area.

The K-means algorithm is an unsupervised learning algorithm that does not rely on predefined classes and class labels. After arbitrarily selecting K data objects,

which are selected as the initial cluster center, and then assign other points to the cluster closest to itself by calculating the Euclidean distance and the grayscale of other points to the cluster center. Then continuously calculate the cluster center of the new class, and select the remaining objects again for classification, and repeat this process until the standard measure function begins to converge. The standard measure function generally uses the error squared function. Since the infrared image is generally a single band, the data dimension of the K-means algorithm is 1, then the time complexity of the algorithm is O(nk). The steps of the K-means algorithm are as follows:

(a) Take some K attribute value vectors as the center of the initial cluster, and set K values to be $Y_1(n)$, $Y_2(n)$, …, the number of loop processing is set to n, and the initial value is set as 1.
(b) All attribute value vectors X are classified by the following equation such that the vectors in the vector set $\{X\}$ belong to the center of the cluster, $Y_1(n)$, $Y_2(n)$, …, the corresponding subset $S_1(n)$, $S_2(n)$, …, $S_l(n)$, $S_k(n)$.

$$dl = \min\{dj\} \rightarrow X \in Sl(n), N \triangleq \{1, 2, K\} \tag{1}$$

(c) Here is the distance between d_j and $Y_j(n)$, which is defined by:

$$dj \triangleq \|X - Yj(n)\| \tag{2}$$

(d) Calculate the new cluster center $Y_l(n + 1)$ of each subset by:

$$Y(n+1) = \sum_{X \in Sl(n)} X/Nl \tag{3}$$

(e) For all clusters, the processing ends when the following formula is established, otherwise it returns to step (b) to continue processing.

$$Yl(n+1) = Yl(n), l \in NK \tag{4}$$

To meet the needs, the cluster center is classified as three categories, and then the category with the lowest average grayscale is eliminated, which means the background is removed, and the effect of the algorithm is shown as Fig. 2.

Morphological calculation. Then the infrared image is preprocessed according to the morphological opening operation, which can not only remove the noise in the infrared image, but also enhance the contrast between the bushing and the background in the infrared image.

The basis of mathematical morphology is the corrosion and expansion operator, which consist of the morphological transformation. The opening operation of the structural element b on the image f is denoted as $f \circ b$, which is defined as follows:

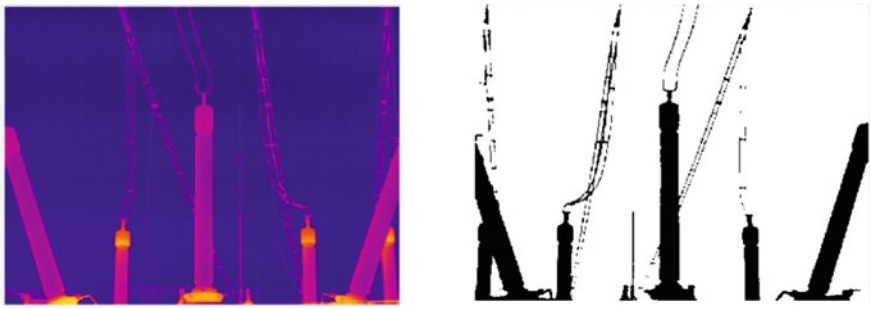

(a) the infrared bushing image

(b) the bushing image after using K-means

Fig. 2 The process of removing the background by K-means

$$f \circ b = (\Theta b) \oplus b \tag{5}$$

where, the Θ represents the corrosion operation and the $\oplus$ represents the expansion operation. The equation is equivalent to f being corroded by b. The result of the subsequent etching will be expanded by b. In general, the opening operation is used to remove small objects and to separate the small objects while keeping grayscale levels and the scale of areas unchanged. The purpose of the opening operation in the infrared image is to separate the tiny parts such as wires in the background of the image. As Fig. 3 shows, most of the wires has been removed and the bushings are kept.

Fig. 3 The noise of bushing infrared image is removed after the opening operation

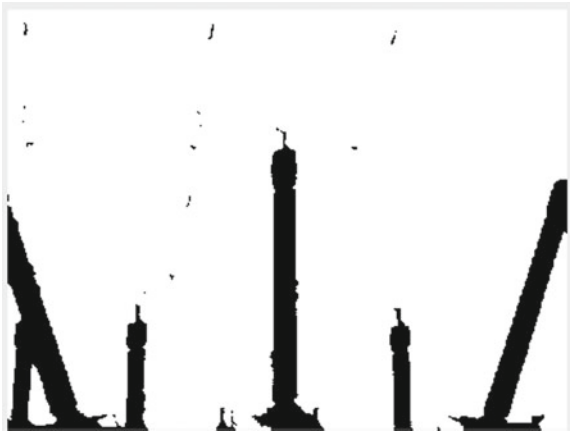

2.2 SLIC Super Pixel Segmentation Algorithm

According to the thermal characteristics of the infrared image, it can be seen that the normal segmentation method which segment targets by the threshold cannot take the shape of bushings into consideration, which have an impact on the target segmentation. Using the SLIC (Super Pixel HSV Spatial Transformation) algorithm to segment the bushing area reduces the interference of other device in the background and extracts the target with the contour of the image itself.

The main idea of the SLIC algorithm is to firstly convert the image from the RGB color space to the CIE-lab color space $[l, a, b, x, y]^{\mathrm{T}}$ which is made up with the (l, a, b) color value and the (x, y) coordinate of each pixel. Secondly, for an image with N pixels, splitting it into K super-pixel sets, and initializing the cluster center $C_k = [l_k, a_k, b_k, x_k, y_k]^{\mathrm{T}}$. the distance between each cluster center is defined as $s = (N/K)$. By calculating the degree of similarity between each pixel and the closest cluster center, and the new cluster center will be updated to the position of the 5-dimensional vector average of the pixel points in the same category. And then the process will be iterated until the centers is no longer changed, finally the pixel will be assigned a reasonable label. The measure of similarity is shown as follows:

$$d_{lab} = \sqrt{(l_k - l_i)^2 + (a_k - a_i)^2 + (b_k - b_i)^2} \tag{6}$$

$$d_{xy} = \sqrt{(x_k - x_i)^2 + (y_k - y_i)^2} \tag{7}$$

$$D(i,k) = d_{lab} + \frac{m}{s} d_{xy} \tag{8}$$

where the d_{lab} is the color distance, d_{xy} is the spatial distance, s is the distance of the cluster center, $D(i, k)$ is the similarity between the i-th pixel and the k-th cluster center.

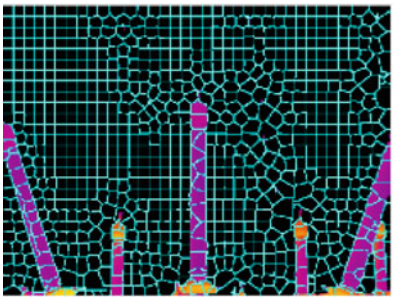

(a) The infrared image divided into k sets

(b) The segmented infrared image

Fig. 4 The process of segmenting the bushing by SLIC

We can learn from Fig. 4 that the SLIC algorithm can split the image into tiny parts according to the shape of the bushing and also the color. And then we can segment the bushing through.

2.3 Fault Diagnosis

The key of fault diagnosis is to reasonably separate the bushings and accurately extract the image areas of the them. A tool is provided in the image processing toolbox for labeling connected-domain area on a binary image. The command returns a calibration matrix of the same size as the input image, and different objects in the input image will be divided into different integer values. The connected area with a larger area in the figure can be extracted and regarded as the bushings.

The different colors of the image in the infrared image correspond to different temperatures, and the grayscales of the different colors are proportional to the temperature. This correspondence is represented in the color chart of the infrared image. In order to identify the fault points characterized in the infrared image of the bushing, we need to convert the image into a temperature matrix by using the corresponding relationship between color and temperature on the color chart, we must first compare the gray temperature change matrix on the color card. Find and then identify and diagnose the fault.

According to the *DL/T-664-2016 Application rules of infrared diagnosis for live electrical equipment*, the system accesses the working state of the bushing by two conditions:

(a) whether there is an area exceeding 55 °C;
(b) whether the average temperature difference between the phases differs by more than 10 °C;

If there is any condition satisfied, it is determined that the bushing is working abnormally. If the average temperature and the maximum temperature are far greater than the standard value, it is determined that the casing is a dielectric loss fault; if the above situation does not occur Straight line detection of the image, if there is a significant temperature boundary line in the image and the average temperature under the boundary line is higher than the average temperature on the boundary line, it is determined that the casing is the transformer casing oil level; if there is no obvious boundary line, The ordinate of the highest temperature point in the image is extracted, and it is determined which part of the casing the point is located, and the part is faulty.

3 Result Analysis

In order to verify the effectiveness of the algorithm for infrared target detection, this paper selects an infrared bushing image as the target for verification. The result is shown in Fig. 5. This method can remove most of the noise to segment the bushing and diagnosis the fault of it.

(a) The infrared bushing image

(b) The segmented bushing image

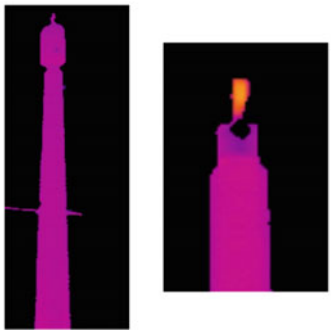

(c) the separated bushings

Fig. 5 The process of separating bushings apart

According to the calculation result of the algorithm, the central coordinate of the fault area is located at 88.73% of the bushing, and the fault type is diagnosed as a joint fault, which is consistent with the type of its label. Based on the Intel i7-7700HQ, 16 G byte storage, Nvidia 1060 6G graphic card, and the MATLAB programming platform, each image can be dealt within 2–3 s. The algorithm would work faster when it's applied to other programming platform.

4 Conclusions

In this paper, the method has been verified to remove the background of the image, extract the bushing and diagnose it. The datasets come from the 2016–2018 infrared image detection database of Jiangsu Electric Power Research Institute. After the verification, preliminary conclusions can be drawn as follows:

(1) The algorithm is able to diagnose faults based on the infrared image of the bushing, and has good effects on diagnosing some specific infrared bushing images;
(2) It's of great difficulty to ensure the quality of infrared images detected in actual work. In most cases, the background is noisy and the bushing image is annihilated in noise which makes it hard to extract the bushings. So the further work will be carried out to improve the accuracy of bushing extraction and improve the accuracy of fault diagnosis.

Acknowledgements The authors acknowledge the financial support of State Grid Jiangsu Electric Power CO., LTD. (Research on Live Detection and Online Monitoring for Bushings of High Voltage Converter Transformer).

References

1. Murugan R, Ramasamy R (2015) Failure analysis of power transformer for effective maintenance planning in electric utilities. Eng Fail Anal 55:182–192
2. Hashemnia N, Abu-Siada A, Islam S (2016) Detection of power transformer bushing faults and oil degradation using frequency response analysis. IEEE Trans Dielectr Electr Insul 23 (1):222–229
3. Transformer bushing reliability, https://e-cigre.org/publication/755-transformer-bushing-reliability. Last accessed 2019/03
4. Qiwei D, Wang W, Chen Z (2016) Infrared target detection and false alarm elimination based on multi-feature fusion decision. In: Proceedings of the 2016 progress in electromagnetic research symposium (PIERS)
5. Wang Y (2018) Improved OTSU and adaptive genetic algorithm for infrared image segmentation. In: Proceedings of the 2018 Chinese control and decision conference (CCDC)
6. Jiang B, Shi F, Cui D et al (2012) Improved K-means clustering infrared target detection method. J Appl Opt 33(4):766–769
7. Zhang J-Y, Xu W, Zhang W et al (2014) A novel compression algorithm for infrared thermal image sequence based on K-means method. Infrared Phys Technol 64:18–25
8. Wang J, Wang P (2015) Research on stochastic DPM region localization algorithm based on adaptive super-pixel segmentation. Mech Electr 41(5):991–1003
9. Zhao Y, Wang E (2010) Research on edge detection of infrared image based on matlab transformer fault. Comput Technol Autom 29(2):89–91
10. Rahmani A, Haddadnia J, Seryasat O (2010) Intelligent fault detection of electrical equipment in ground substations using thermo vision technique. In: Proceedings of the 2010 2nd international conference on mechanical and electronics engineering
11. Fan S, Yang S (2011) Infrared electric image segmentation using fuzzy renyi entropy and chaos differential evolution algorithm. In: Proceedings of the 2011 international conference on future computer sciences and application
12. Cui H, Xu Y, Tang Z et al (2013) The methods in infrared thermal imaging diagnosis technology of power equipment. In: Proceedings of the 2013 IEEE 4th international conference on electronics information and emergency communication
13. Jadin MS, Ghazali KH, Taib S (2013) Thermal condition monitoring of electrical installations based on infrared image analysis. In: Proceedings of the 2013 Saudi international electronics, communications and photonics conference

14. Jadin MS, Ghazali KH, Taib S (2014) Detecting ROIs in the thermal image of electrical installations. In: Proceedings of the 2014 IEEE international conference on control system, computing and engineering (ICCSCE 2014)
15. Janssens O, Rik VDW, Loccufier M et al (2017) Deep learning for infrared thermal image based machine health monitoring. IEEE/ASME Trans Mech 151–159
16. Chen N, Chen G, Li H et al (2019) Temperature difference threshold of infrared detection of low value porcelain insulators. Electr Power Eng Technol 38(01):102–106

Optimization of Post-disaster Rush Repair Strategy for Distribution Network Considering Network Reconfiguration

Chen Yu, Shangxuan Li, Han Wu, Kang Chang and Bingqian Liu

Abstract Natural disasters (such as snowstorms, typhoons, etc.) can result in a large number of physical failures in distribution network. Optimizing the rush repair strategy of physical failures in post-disaster restoration can reduce economic loss and accelerate the restoration process. In current research, the optimization of repair path and strategy for a single repair team is studied, while the complexity of rush repair and the travel cost are not fully considered, and the effect of tie lines in restoration cannot be ignored. Therefore, an optimization of rush repair strategy method is established in this paper considering the combined action of repair teams, tie lines and the dynamic change of the repair strategy caused by network reconfiguration. With the objective of minimizing the total loss during the restoration, the status of repair teams, failures and tie lines are employed as decision variables. Next, the rush repair model is solved through a two-layer solution strategy. Simulated Annealing Algorithm and Genetic Algorithm are adopted respectively to solve the two layers. So that, the best rush repair strategy can be obtained. Finally, the efficiency of the proposed approach is demonstrated by testing on PG&E 69 node system.

Keywords Service restoration · Rush repair · Distribution systems · Genetic algorithm · Simulated annealing algorithm · Network reconfiguration

C. Yu (✉) · S. Li · K. Chang
NARI Group Corporation (State Grid Electric Power Research Institute), Nanjing 211106, China
e-mail: yuchen@sgepri.sgcc.com.cn

S. Li
Nanjing University of Science and Technology, Nanjing 210094, China

H. Wu · B. Liu
State Grid Fujian Electric Power Research Institute, Fuzhou 350007, China

Y. Xue et al. (eds.), *Proceedings of PURPLE MOUNTAIN FORUM 2019-International Forum on Smart Grid Protection and Control*, Lecture Notes in Electrical Engineering 585, https://doi.org/10.1007/978-981-13-9783-7_67

1 Introduction

Due to the low design standards of distribution network, a large number of physical failures of distribution network will occur during natural disasters (such as snowstorms, typhoons, etc.) [1]. In the extreme snow and ice disaster in 2008, the power grids of 16 provinces (autonomous regions and municipalities directly under the Central Government) suffered severe damages such as tower collapse, substation trips, large-scale power outages, etc., which result in nearly one billion CNY economic loss directly and indirectly [2]. After the disaster happened, repair teams need to arrange the repair strategy according to the physical failures. Efficient repair strategy can reduce outage time and improve the reliability of distribution network.

The problem of rush repair strategy is a combinatorial optimization problem [3, 4]. In current research, some studies focus on the principles for rush repair [2, 5, 6]. Some papers proposed some path optimization algorithms for rush repair [7]. However, the methods utilize a single repair team to repair a single failure. A multi-target repair model is discussed and established in [8], and a genetic topology hybrid algorithm is proposed to solve this model. However, tie lines are not considered and only one repair team is considered to perform the repair strategy in sequence. In [9], Genetic algorithm (GA) and search algorithm are combined to deal with the optimization of rush repair strategy which is applied to a single repair team and does not fully consider the impact of travel time. Not only the problem of multi-repair team corresponding to the multi-failure is optimized, but also the tie lines is considered in the repair process [10]. Due to the different capabilities, the differences between repair times that the different repair team costs on the different type of failures are ignored.

In existing research, the shortest repair time [11] and the minimum load loss [12] are objective functions. In [13], a two-stage adaptive algorithm is presented to adjust the rush repair strategy through the flexible switching operations. However, the optimization ignores the influence of tie lines in restoration process. In [14], a new graph chain representation for the huge radial network is proposed to generate the rush repair strategy, which is solved through GA. In [15], a model for evaluating the typhoon resistance of the distribution network considering the network reconfiguration and the restoration process in the disaster area is proposed. Reference [16] established an optimization model for allocating emergency power sources with uncertain load demands and dispatching time periods. All of the three researches ignore the strategy of repair teams.

There are a lot of researches on models and algorithms focusing on rush repair problems, including vehicle routing problems (VRP) [17–19] and network reconfiguration [20–24]. In [17], the repair time is taken as optimization target and the emergency rescue vehicle path model is established. Besides, the corresponding Simulated Annealing Algorithm (SA) is designed to solve this model. However, the approach lacks the connection with the electrical part of distribution network.

Due to the VRP and network reconfiguration are combinatorial optimization problems, model decision variables contain discrete variables so that the optimization process is complicated. In lots of researches, the heuristic algorithms are

chosen to solve the nonlinear models. Heuristic knowledge and empirical judgment which is used to solve nonlinear and discontinuous objective function problems, also play an important role in rush repair problems. Similar to VRP problems, it is also applied to make rush repair strategies. Starting with the initial feasible solution, the optimal path solution is achieved by reselecting and changing a series of failures between different routes [18].

Therefore, this paper proposes an optimization model based on the intelligent algorithm for post-disaster rush repair strategy, which fully considers the VRP problem and network reconfiguration. The maximum load restoration after tie line actions is regarded as the objective function of the GA while the minimum load loss in rush repair process is the objective function of SA. This paper mainly focuses on the scenarios in which the failure information is completely and accurately acquired. Assume that all failure locations are known. Firstly, the failures are isolated from the network due to the remote control switch operations and the strategy is formulated considering the normal operate constraints such as radial network constraint for distribution network. Then the tie lines and the repair teams are optimally coordinated. The whole algorithm is decided into two stages. Firstly, the tie line actions are optimized through GA. Then the initial repair strategy is formulated by SA. In the initial strategy, considering the network reconfiguration caused by repairing failures, the tie line states are generated after each failure repaired corresponding to the sequence of failure repair time. Finally, the optimal post-disaster repair strategy is generated through the disturbance of the initial strategy. The approach mentioned above is all written by MATLAB, and the effectiveness of the method is proved on PG&E 69 node system.

2 Optimization Model of Post-disaster Repair Strategy

The optimization model is divided into two layers. The status of tie lines is generated by GA, while the strategy of repair teams is generated by SA, which is the main part.

2.1 Objective Function

The global objective function is minimizing the total load loss during the repair process, which can be expressed as:

$$\min\left[A_0^T P^L t_1 + \sum_{r=1}^{G-1} A_r^T P^L (t_{r+1} - t_r)\right] \tag{1}$$

where A is node state matrix whose dimension is N; N is the number of nodes; t is the repair moment of failures; G is the number of failures; P^L is the load matrix of unit time whose dimension is N.

The tie line actions should be adjusted to improve the restoration capacity of distribution network. The objective function should be changed to maximize the load restoration after the tie line actions adjusted, which can be expressed below:

$$\max \sum_{r \in G} A_{rc}^T P^L \tag{2}$$

where A_{rc} is the state matrix of nodes. 1 means the nodes is connected while 0 otherwise. *loads* is the node load matrix. In order to reduce the tie line action costs, the objective function is minimizing the tie line action number:

$$\min \sum_{act=1}^{D} r_{act} \tag{3}$$

where D is the number of the tie lines; r_{act} represents the state changes of the tie lines, 1 means that tie line state turns interruption to closure or closure to interruption and 0 otherwise.

2.2 Constraints

In order to simplify the problem, this paper do not consider the possible increasing of node voltage and branch power flow exceeding the limit caused by the use of other emergency equipment in this stage. That is to say, it supposes that both branch current constraint and node voltage constraint meet the requirements during the scheduling optimization process of distribution network. Specially, the power P_k flowing past the branch k meets $|P_k| \leq P_{k\max}$, and $P_{k\max}$ represents the allowed maximum power (kW) of branch k; node voltage U meets $U_{\min} \leq U \leq U_{\max}$, and $U_{\min}$ represents the minimum value of node voltage (kV), $U_{\max}$ means the maximum value of node voltage (kV).

Repair Team. In order to make the most of resources, each failure should be corresponding to only one repair team, and any repair team could be corresponding to multiple failures, which can be expressed as:

$$\sum_{v=1}^{V} \sum_{i=0}^{N} x_{ijv} = 1 \quad j \in \{1, 2, \ldots, N\} \tag{4}$$

$$\sum_{v=1}^{V} \sum_{j=0}^{N} x_{ijv} = 1 \quad i \in \{1, 2, \ldots, N\} \tag{5}$$

where x_{ijv} indicates that the repair team v moves from failure i to failure j, which 1 is true and 0 otherwise.

Parameter Initialization.

$$t_0 = f_0 = 0 \tag{6}$$

where t_i is the time when the repair team arrived at failure i, f_i is the repair time that failure i needs.

Radial Network Structure.

$$b_{ij} + b_{ji} = \alpha_l \tag{7}$$

$$\sum_{j \in N(i)} b_{ji} = 1 \tag{8}$$

$$b_{0j} = 1 \tag{9}$$

where b_{ij} represents the state variable of the parent-child node i and j; 1 means that i is the parent node of j and 0 otherwise. α_l is the state variable of the feeders that if they are connected; $N(i)$ represents child node set to node i. The first set of constraint (7) indicates that if node i and j are connected, there must be 1 parent node and 1 child node; The second set of constraint (8) indicates that any connected node has only one parent node; The network established in this paper is a single-source network, thus constraint (9) indicates that the head node which supply power must be the parent node.

This paper draws on the ideas in literature [8, 12, 14, 19, 20, 22]. When the number of repair team is far less than the number of failures, the strategy of rush repair is further optimized by network reconfiguration in restoration and then the post-disaster loss of distribution network is reduced greatly. Since the model is a nonlinear model, an intelligent algorithm is used in the subsequent chapters.

3 Solution of Proposed Model

Since the optimization of post-disaster rush repair strategy is a combinatorial optimization problem whose process is very complicated. However, Greedy Algorithms can only get the local optimal solutions. Therefore, this method uses bionic intelligent algorithm to get out of the local optimal solution. The algorithm in this paper is divided into two layers. The first layer generates the repair strategy, and the second layer generates the plan of tie lines. First, the initial solution is generated by SA. After each failure is repaired, the final tie line action plan is determined. In other words, GA is nested within the objective function of the main program. Thus, the total power loss of the whole strategy is obtained, and on this basis, the optimal solution is generated after continuous disturbance of the solution.

To simplify the problem, this paper assumes that all repair teams have the same capability characteristics. The same type of failures has the same repair time for different repair teams. Each action takes a certain amount of time to perform. The research presented in this paper mainly concerns on the scenario that the tie line has no delay for immediate action, and there is no other time between movement and repairment.

Two-layer solution flow chart is shown in Fig. 1.

3.1 Genetic Algorithm

Genetic Algorithm is more suitable for formulating the state of tie lines in the coding properties of its solution. It is divided into the following steps:

(1) Enter initial parameters (including variation and crossover probability) and then randomly generate initial populations;
(2) Calculate the fitness value of each chromosome in the population;
(3) Generate new solutions. In this process, the chromosomes of the original population are selected, mutated and crossed. The size of the new population is consistent with the original population, and the chromosomes of the new population are selected and reproduced by roulette according to the probability of accumulation.

Accumulation probability formula, which can be expressed as:

$$q_i = \sum_{j=1}^{i} P(x_j) \tag{10}$$

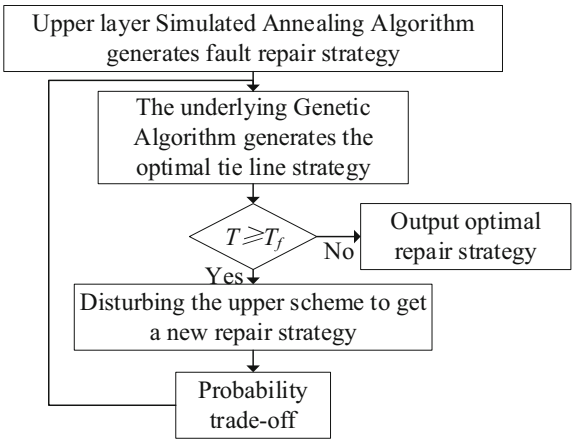

Fig. 1 Two-layer solution flow chart

where $P(x_j)$ is the ratio of the objective function value of chromosome j to the sum of all chromosome target functions of the population.

The fitness function is expressed as:

$$C_i = \frac{1}{1 + f_{obj.i}} \tag{11}$$

where $f_{obj.i}$ is the objective function value of chromosome i.

The population size is usually taken as 100. The mutation probability is 0.2 and the crossover probability is 0.7. The chromosome is consists of 0 and 1, where 0 represents the disconnection of the tie line and 1 represents the closure.

3.2 Simulated Annealing Algorithm

Each chromosome in the algorithm is consist of repair team number and failure number. The first number is repair team number. This algorithm combines the local search and global search methods and can get the global optimal solution which is faster than the global search methods. It has the following two advantages:

(1) Local search can reliably obtain an optimal solution within a certain range in a short time;
(2) The global search avoids to fall into the local optimal solution and further it generates the global optimal solution;

Simulated Annealing Algorithm accepts the solution that is inferior to the current solution with a certain probability through the Metropolis criterion, thus jumping out of the local optimal solution.

The Metropolis criterion is usually expressed as:

$$p = \begin{cases} 1 & E(x_{new}) < E(x_{old}) \\ \exp\left(-\frac{E(x_{new}) - E(x_{old})}{T}\right) & E(x_{new}) \geq E(x_{old}) \end{cases} \tag{12}$$

4 Case Analysis

4.1 Case Simulation Scenario

The efficiency of the proposed approach is demonstrated on PG&E 69 node system. Whose topology is shown in Fig. 2. Red × indicates a line with failures, F1(30–31), F2(33–34), F3(65–66), F4(88–89), F5(15–16), F6(20–21), F7(24–25), F8(35–36), F9(55–56) and F10(49–50) respectively. Blue dotted line represents the tie line which is Y1(10–70), Y2(12–20), Y3(14–90), Y4(26–54) and Y5(38–48). There are four repair teams, A, B, C and D, which are not marked in Fig. 2.

Assuming that all the failures occur simultaneously, the Isolating switches act immediately to isolate the failures. At the same time, repair teams set out to perform their repair tasks.

4.2 Simulation Results

The simulation results are shown in the following tables.

The plan of repair teams is shown in Table 1.

Table 2 shows the timing of the repair strategy. Trans(A,24–25) indicates that repair team A starts to drive to the failure 24–25 at time 0. Repaired(A,24–25) indicates that the failure 24–25 is repaired by the repair team A at time 90.

Table 3 shows the action of the tie line.

At 575, all repairment is completed. During this period, all repair teams are not idle and fully utilized. At each moment, the tie line scheme has reached the maximum load that can be recovered, and the curve of load restoration shows a clear upward trend.

Figure 3 shows the load restoration curve.

The load restoration curve shows that the proposed method can significantly improve the load recovery efficiency. The trend of the curve shows that the final strategy is reasonable and the closest to the optimal solution. The total load loss is 51,634 MW.

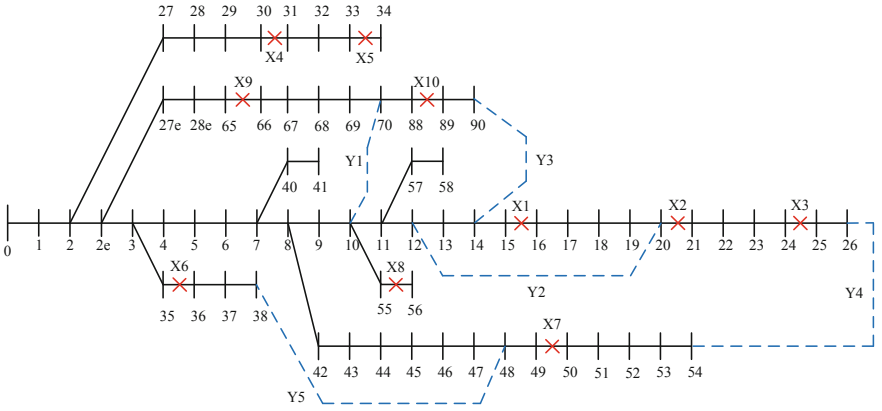

Fig. 2 PG&E 69 node system

Table 1 Plan of repair teams

A	24–25, 55–56, 88–89, 65–66, 20–21
B	30–31
C	33–34
D	49–50, 15–16, 35–36

Table 2 Timing of the repair strategy

Time (min)	Operation
0	Trans(A,24–25), Trans(B,30–31), Trans(C,33–34), Trans(D,49–50)
90	Repaired(A,24–25), Trans(A,55–56)
91	Repaired(D,49–50), Trans(D,15–16)
96	Repaired(B,30–31)
109	Repaired(C,33–34)
192	Repaired(D,15–16), Trans(D,35–36)
218	Repaired(A,55–56), Trans(A,88–89)
308	Repaired(D,35–36)
336	Repaired(A,88–89), Trans(A,65–66)
438	Repaired(A,65–66), Trans(A,20–21)
575	Repaired(A,20–21)

Table 3 Timing of tie lines

Time	Turn off	Turn on
0	Y4	Y1, Y2, Y3, Y5
90	Y3, Y4, Y5	Y1, Y2
91	Y2	Y1, Y3, Y4, Y5
96	Y3	Y1, Y2, Y4, Y5
109	Null	Y1, Y2, Y3, Y4, Y5
192	Y2, Y3	Y1, Y4, Y5
218	Y2, Y3	Y1, Y4, Y5
308	Y2, Y3, Y5	Y1, Y4
336	Y1, Y2, Y5	Y3, Y4
438	Y1, Y2, Y3, Y5	Y4
575	Y1, Y2, Y3, Y4, Y5	Null

5 Conclusion

The post-disaster rush repair strategy of distribution network is a combinatorial optimization problem. In the case of a large-scale outage caused by major natural disasters, this paper uses SA and GA to provide power companies with a detailed repair strategy to ensure rapid restoration of power and economic loss.

The model gives each step time of post-disaster rush repair strategy, including the action of tie lines. It provides a detailed and effective reference for the actual repair process. The strategy proposed in this paper is more practical than the similar references.

In addition, there are other factors that affect the final strategy, such as node voltage limit, current limit, material limit, etc. Distributed generators can also accelerate the repair process and the repair time is not fixed. Since this article is in the early stages of research, these factors will be further considered in subsequent studies.

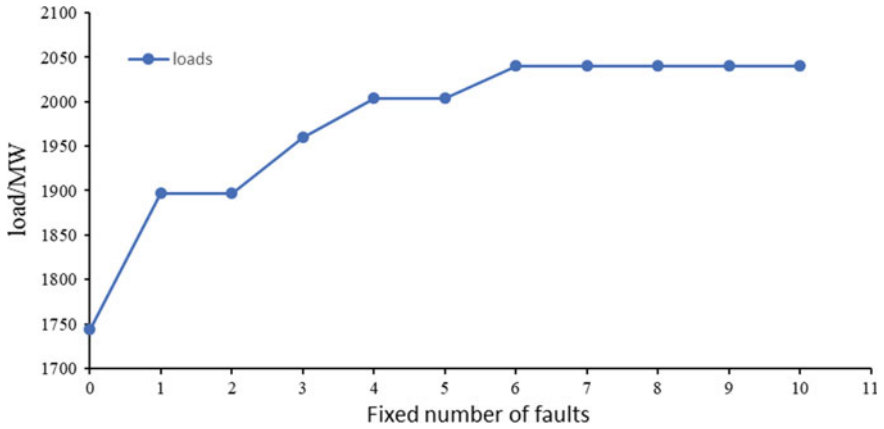

Fig. 3 Load restoration curve

Acknowledgements Research supported by Science and Technology Project of SGCC (Key Technology of resilient distribution network for Enhancing Dynamic restoration and commanding under extreme disaster, 52130418000L) and State Key Laboratory of Smart Grid Protection and Control.

References

1. Zhang J (2014) Utility theory-based rush repair strategy of post-disaster distribution networks with the re-al-time adjustment. Yanshan University
2. Wen-Liang Z, Xiao-Xin Z, Xiao-Min B et al (2008) Countermeasures against sudden events to ensure the security of urban power supply systems. Proc CSEE 28(22):1–7
3. Hu Z, Guo R, Lan H et al (2015) Islanding model of distribution systems with distributed generators based on directed graph. Dianli Xitong Zidonghua/Autom Electr Power Syst 39 (14):97–104
4. Li F, Xu T, Lin J et al (2015) Island partition of distribution network considering uncertainty of distributed generators and loads. Autom Electr Power Syst 39(14):105–113, 132
5. Bin JI, Bo W, Cuiping XU (2013) Development and application of the command platform for the production and repair of distribution network. Smart Grid
6. Zhang WB, Chen XH, Zhou J et al (2013) Study on rush-repair scheme for distribution network failure. Adv Mater Res 860–863:2554–2559
7. Mazzeo S, Loiseau I (2004) An ant colony algorithm for the capacitated vehicle routing. Electron Notes Discret Math 18:181–186
8. Zhang J, Zhang L, Huang X (2008) A multi-failure rush repair strategy for distribution network based on genetic-topology algorithm. Autom Electr Power Syst
9. Lei D, Yongli Z, Lei Z (2011) Research on optimal path lines based on improved ant colony algorithm. Electr Power Sci Eng
10. Lu Z, Sun B, Liu Z et al (2011) A rush repair strategy for distribution networks based on improved discrete multi-objective BCC algorithm after discretization. Dianli Xitong Zidonghua/Autom Electr Power Syst 35(11):55–59
11. Huang X, Zhang L, Shu J et al (2007) Maintenance schedule optimization model in distribution systems. Autom Electr Power Syst 31(1):33–37

12. Yongbo Y, Bo J, Huayun Y et al (2012) Service restoration with consideration of rush repair. In: Power engineering & automation conference. IEEE
13. Li J, Song X, Wang Y et al (2016) Service restoration for distribution network considering the uncertainty of restoration time. In: 2016 3rd international conference on systems and informatics (ICSAI). IEEE
14. Delbem ACB, Carvalho AD, Bretas NG (2003) Optimal energy restoration in radial distribution systems using a genetic approach and graph chain representation. Electr Power Syst Res 67(3):197–205
15. Biyun C, Cuizhen LI, Hong Q et al (2018) Evaluation of typhoon resilience of distribution network considering grid reconstruction and disaster recovery. Autom Electr Power Syst
16. Zhikui W, Lei S, Zhenzhi L et al (2018) Optimal allocation of emergency power sources considering uncertainties of loads and dispatching time periods. Autom Electr Power Syst 42 (2):34–41
17. Lei H, Laporte G, Guo B (2011) The capacitated vehicle routing problem with stochastic demands and time windows. Comput Oper Res 38(12):1775–1783
18. Lin SW, Ying KC, Lee ZJ et al (2006) Vehicle routing problems with time windows using simulated annealing. In: IEEE international conference on systems. IEEE
19. Breedam AV (1995) Improvement heuristics for the vehicle routing problem based on simulated annealing. Eur J Oper Res 86(3):480–490
20. Esmaeilian HR, Jashfar S, Fadaeinedjad R et al (2012) Bardsir network reconfiguration using graph theory-based binary genetic algorithm to reduce loss and improve voltage profile. In: 2012 proceedings of 17th conference on electrical power distribution networks (EPDC). IEEE
21. Santos AC, Delbem ACB, London JBAJ et al (2010) Node-depth encoding and multiobjective evolutionary algorithm applied to large-scale distribution system reconfiguration. IEEE Trans Power Syst 25(3):1254–1265
22. Shamsudin NHSM, Basir MSSM, Abdullah AR et al (2015) Losses minimization in network reconfiguration for failure restoration via a uniform crossover of genetic algorithm. In: International symposium on technology management & emerging technologies. IEEE
23. Ravibabu P, Ramya MVS, Sandeep R et al (2010) Implementation of improved genetic algorithm in distribution system with feeder reconfiguration to minimize real power losses. In: International conference on computer engineering & technology. IEEE
24. Yasin ZM, Rahman TKA (2007) Influence of distributed generation on distribution network performance during network reconfiguration for service restoration. In: IEEE international power & energy conference. IEEE

Protocol Conformance Test Sequence Generation for Q/GDW11709.2 Based on FSM

Huijie Ge, Jianxin Liu and Lin Sang

Abstract In order to realize healthy communication and accurate information exchange between the charging tariff and control unit (referred to as TCU) and electric vehicles during charging service, the enterprise standard Q/GDW11709.2 of State Grid Corporation of China stipulates the communication protocol between TCU and charging pile. The protocol standard is the basis of the interconnection between the TCU and the charging controller (referred to as CTR), and the protocol conformance test is the precondition of ensuring the protocol implementation and healthy communication, one of the major components of protocol testing is generating test sequences. Based on the study of the communication protocol and mechanism between the TCU and the CTR, the finite state machine (referred to as FSM) model of Q/GDW11709.2 communication protocol is established, and the UIO sequence of each state in the state machine is calculated.

Keywords Protocol conformance testing · FSM · UIO sequence · Test sequence

1 Introduction

With the country's strong support for the electric vehicle industry, the number of electric vehicles has increased significantly in recent years. And higher requirements have been put forward for charging facilities and charging technology of electric vehicles at the same time. According to the development trend of the market and technology, State Grid Corporation of China push for filling in the construction of the power station actively and initiate the design and development of the

H. Ge (✉)
State Grid Electric Power Research Institute, Nanjing, China
e-mail: 13591994251@163.com

J. Liu · L. Sang
Nari Group Co. Ltd., Nanjing, China

J. Liu
Nari Technology Nanjing Control System Co. Ltd., Nanjing, China

Y. Xue et al. (eds.), *Proceedings of PURPLE MOUNTAIN FORUM 2019-International Forum on Smart Grid Protection and Control*, Lecture Notes in Electrical Engineering 585, https://doi.org/10.1007/978-981-13-9783-7_68

charging tariff and control (referred to as TCU). The corporation officially released the enterprise standard "Q/GDW 11709-2017 charging tariff and control unit of electric vehicles" in 2018 [1]. The standard is divided into four parts:

Part 1: technical conditions;
Part 2: communication protocol with charging pile;
Part 3: communication protocol with Internet of vehicles platform;
Part 4: inspection specifications.

Part 2 of the standard specifies the mode and content of communication between the TCU and the charging controller (CTR) in the charging pile. Protocol is the foundation of interconnection, and protocol testing is the premise of ensuring the implementation and normal operation of the protocol. Only by communicating in accordance with the agreed rules of the protocol, can the two sides transmit information correctly and effectively. However, the communicators are often designed and developed by different manufacturers, and everyone has different understanding of the protocol standard. As a result, the implementation of the protocol may not always meet the requirements of the protocol standard, and even wrong protocol implementation may occur. Therefore, protocol conformance testing is very necessary. Protocol conformance testing is the basis of other protocol testing and can reduce the risk of errors during operation. Conformance testing is to test the implementation of the protocol under test in a certain network environment with a set of test sequences. By comparing the similarities and differences between the actual output and the expected output, the consistency between the implementation under test and the protocol standard can be determined. The main content of this paper is to study the communication protocol between TCU and CTR, analyze the communication process and content, use the Finite-state Machine (FSM) theory to formally describe the communication protocol, and use UIO sequence to generate conformance test sequence, which lays the foundation for the implementation of conformance test of communication protocol.

2 Establish the FSM Model of Communication Protocol

2.1 Finite State Machine Theory

Finite-state machine is a formal model that represents a finite number of states and the behavior of transitions between them. A finite state machine M can be represented as a directed graph, it can also be represented by a six-tuple: $M = \{S, S0, \delta, \lambda, I, O\}$ [2]. Where S is a finite set of states; $S0 \in S$ is the initial state; δ is a state transition function; λ is the output value; I is the limited input character set; O is the finite output character set ($\lambda \in O$). Figure 1 is a simple FSM model, in which vertices correspond to each state of FSM and edges represent migration paths. $(S_i, I_k/O_m, S_j)$ used to represent an edge marked with I/O from S_i to S_j, that is, when FSM is in state Si, it accepts input I_k, outputs O_m, and replaces it with state S_j [3].

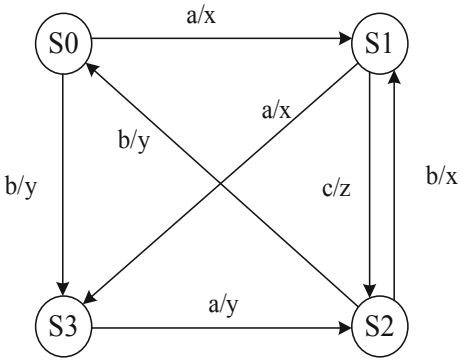

Fig. 1 A simple FSM model

2.2 *FSM Model of Communication Protocol Between TCU and CTR*

TCU is the key to connecting charging facilities, car networking platforms and users.

During the charging process, TCU receives the scheduling from the superior internet of vehicles platform and the charging demand from users, then judges the current operation to be performed, and passes relevant instructions to the CTR inside the charging pile, which triggers the relevant circuit module to perform the corresponding action.

"Q/GDW 11709.2 charging control unit for electric vehicles—part 2: communication protocol with charging pile" stipulates the definition of the communication physical layer, data link layer, interaction process, message classification, message format and content between the TCU and CTR based on the Control Area Network (referred to as CAN) under the management of State Grid Corporation of China. Meanwhile, the interaction process between the TCU and the CTR is also given in the standard, and the main flow chart of the interaction is shown in Fig. 2.

According to the protocol standard specified in Q/GDW 11709.2 and combined with the actual charging service flow, the states and transitions of the charging stage are sorted out, and the communication protocol is formally described by the FSM model. The FSM directed graph model of the communication protocol between the TCU and CTR is shown in Fig. 3.

Each state will be described in Table 1.

Each edge of the directed graph represents the migration condition and migration path.

L1: Close switches K1 and K2, conduct the low pressure subsidiary loop, power on initialization; L2: The connection between the vehicle and the charger is detected, and the heartbeat frame message receiving/sending is normal; L3: The heartbeat frame receiving/sending is abnormal; L4: Heartbeat frame message receiving 3 s timeout; L5: Stop receiving/sending all other messages except heartbeat frames, and continue this state for 30 s; L6: No version check reply frame

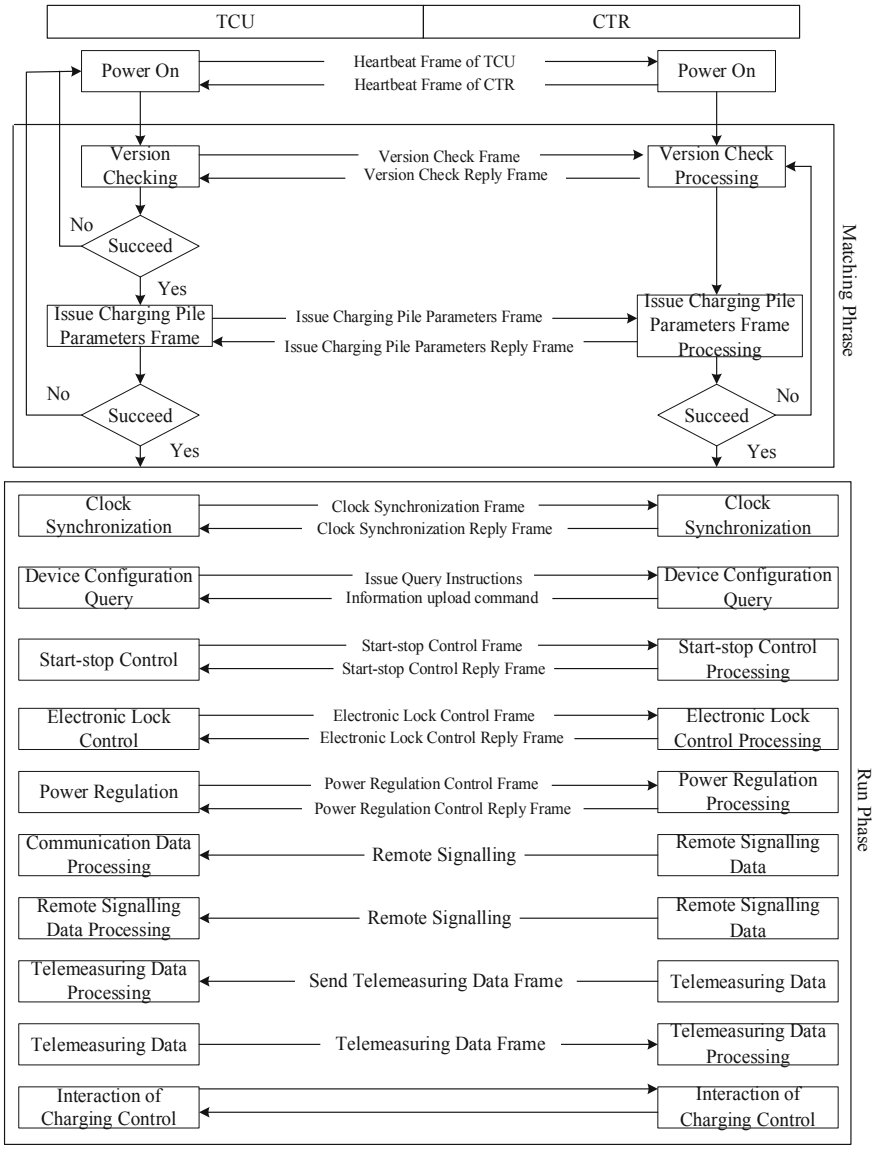

Fig. 2 Main interaction flow chart between TCU and CTR

received or received a different version; L7: Pass the version check; L8: Receiving the issue charging parameter response frame for 5 s timeout; L9: Parameter matching successful, need to control the electronic lock; L10: Lock failure or 5 s timeout; L11: Locking success; L12: No response frame message from CTR; L13: Receiving the clock synchronization reply frame for 5 s timeout; L14: The time of

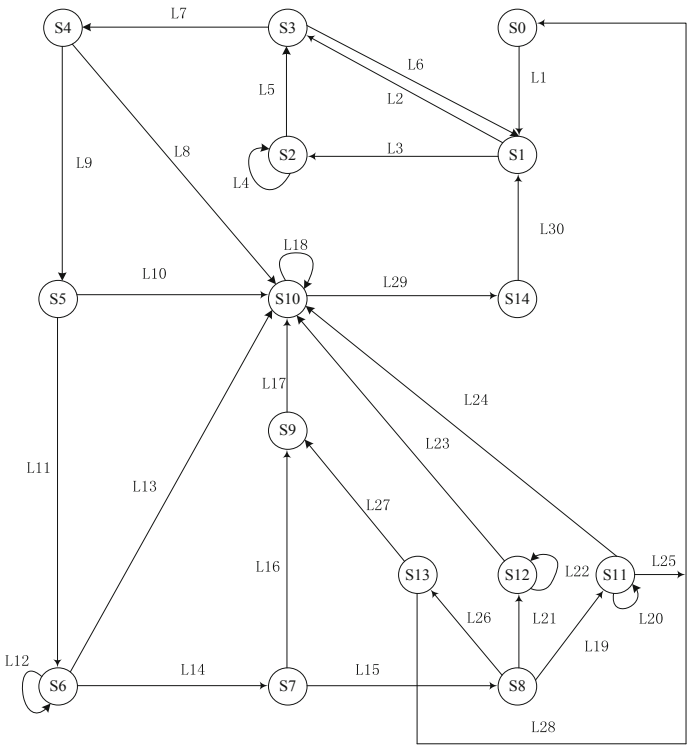

Fig. 3 FSM directed graph of communication protocol between TCU and CTR

Table 1 State instruction

State	Instruction	State	Instruction
S0	Power off	S8	Charging operation
S1	Data interaction	S9	Fault detection
S2	Heart detection	S10	Error
S3	Version checking	S11	Remote signaling
S4	Parameters matching	S12	Telemetry
S5	Electronic lock control	S13	Termination of charging
S6	Clock synchronization	S14	Reset
S7	Start-up		

TCU and CTR is synchronous/If the time is asynchronized, synchronize the time to the time of the CTR; L15: Pass the insulation detection, be all set, close switches K1 and K2, conduct the current power supply circuit, start-up; L16: Boot failure; L17: Detect the cause of failure; L18: Receive the error frame message normally; L19: Sent the remote signaling message periodically during the charging operation;

L20: Receive/sent the remote signaling message normally; L21: Sent the telemetry message periodically during the charging operation; L22: Receive/sent the telemetry message normally; L23: Sent the telemetry message for 5 s timeout; L24: Sent the remote signaling message for 5 s timeout; L25: CTR fault (Set the fault bit of the remote signaling message to 1); L26: Complete the charging requirement/ Receive the charging service stop instruction from the Internet of Vehicles Platform; L27: Receive the charging service stop instruction from the Internet of Vehicles Platform, disconnect switches K3 and K4; L28: Stop charging under general condition; L29: Set the corresponding bit to correct number, receive the error message for 5 s timeout; L30: Reset.

3 Common Method of Generating Test Sequences

There are mainly the following test sequence generation methods based on FSM model in conformance testing of communication protocols: transition tour method (referred to as T method); distinguishing sequences method (referred to as D method); charactering sequences method (referred to as W method); unique input/ output sequences method (referred to as U method) [4, 5].

T method generates the corresponding test sequence by traversing each state transition in the FSM. T method is relatively simple, and the generated test sequence length is shorter. But the method does not check the state after migration in the test process, and the detection ability of this method is lower.

D method is to use the distinguishing sequences to generate the test sequence. A distinguishing sequence is a sequence of input events that are the same for all states, but the outputs for different initial state are different. The test sequence generated by D method has strong error detection ability, but the length of test sequence is long. In fact, not all FSM have DS sequences, so the D method is not universal.

W method is an extension of the D method, which uses the signature sequence set W to replace the DS sequence. The signature sequence set is a set containing n input event sequences. The same W set produces different outputs for different states, similar to the DS sequence. When there is only one input sequence in the W set, the W method is equivalent to the D method. W method has strong universality, because W set always exists for FSM of communication protocol. But the test sequence generated by the W method is also longer.

U method is to uses UIO sequences to generate test sequences. UIO sequence is a subset of DS sequences and W sets, which can uniquely identify a state. When the FSM is in this state, once it accepts the input in the corresponding UIO, the output is different from the others when it receives the same input in any other state. The test sequence generated by U method is relatively short and has strong error detection ability. It is worth noting that the U method is used for almost all FSM.

4 Generate Conformance Test Sequence of Q/GDW 11709.2 Communication Protocol

4.1 Generate Test Sequence by T Method

Almost any FSM can generate a set of test sequences by traversing all the states using the T method. China Postman Problem Algorithm is a method proposed by Professor Guan Meigu, a famous cartographer in China, to help postmen choose a shortest path that traverses all the targets. It is a specific algorithm of T method.

The thought of China Postman Problem Algorithm is to construct a strongly connected directed graph, and the euler loop of the strongly connected directed graph is the shortest path. This method is used to solve the test sequence, that is, the directed graph of FSM is constructed into a strongly connected graph, and the obtained euler loop is the protocol consistency test sequence. The specific steps of China Postman Problem Algorithm for asymmetric directed graph are as follows:

(1) Calculate the in-degrees and out-degrees of each node, $d'(i) = d^-(v_i) - d^+(v_i)$.
(2) Add a super start point v_s, as to meet the $d'(i) > 0$ of the nodes, add $d'(i)$ directed edges (v_s, v_i), their rights all are 0; add a super sink point v_t, as to meet the $d'(j) < 0$ of the nodes, add $|d'(j)|$ directed edges (v_j, v_t), their rights all are 0, then get Fig G′.
(3) In Fig G′, find the road P_{st} whose two endpoints are v_s and v_i, such as (v_s, v_i) and (v_j, v_t), whose sum of each side is once and only once, and note the number of repetitions of these paths in Fig G.
(4) Count the number of repetitions of each side, and the directed euler loop in G is the test sequence.

Among, $d^+(i)$ means out-degree, that is to say, v_i is the start point; $d^-(i)$ means in-degree, that is to say, v_i is the terminal point.

According to the directed graph model of the FSM of the protocol shown in Fig. 3, transition paths from Fig. G are added to construct a strongly connected directed graph G′. Fig G′ is shown in Fig. 4. The number beside the dotted line in Fig G′ indicates the number of path supplements. Find the euler loop traversing graph G′, and the test sequence with a length of 84 is as follows:

L1,L4,L2,L6,L3,L5,L7,L8,L29,L30,L2,L7,L9,L10,L18,L29,L30,L2,L7,L9,L11,
L12,

L13,L29,L30,L2,L7,L9,L11,L14,L16,L17,L29,L30,L2,L7,L9,L11,L14,L15,
L26,L27,L17,L29,L30,L2,L7,L9,L11,L14,L15,L26,L28,L1,L2,L7,L9,L11,L14,
L15,L21,L22,

L23,L29,L30,L2,L7,L9,L11,L14,L15,L19,L20,L24,L29,L30,L2,L7,L9,L11,
L14,L15,L19,L25.

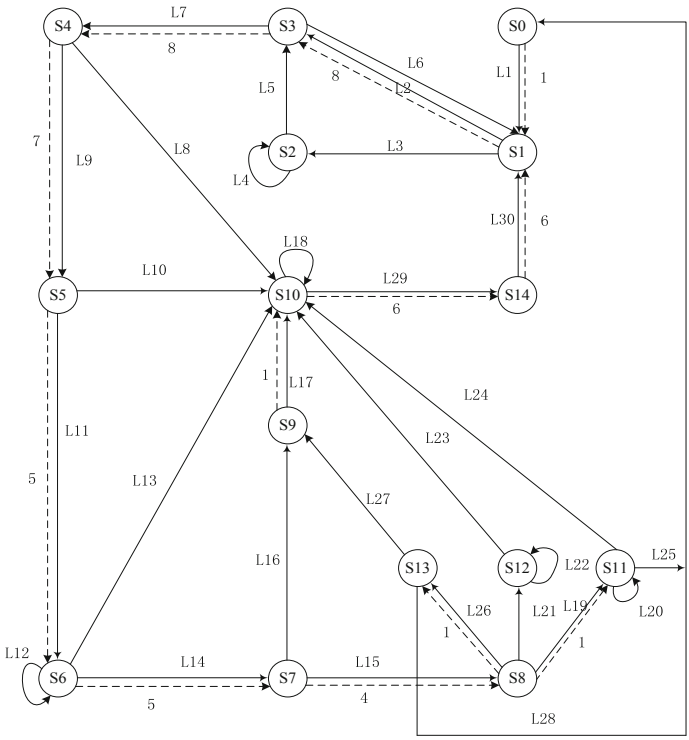

Fig. 4 Strongly connected directed graph G′

4.2 Generate Test Sequence by U Method

4.2.1 Generate UIO Sequences

The general method to generate UIO sequences is as follows [6]

- Establish relationships between all edges and input/output sets.
- Find the input and output sequences whose length is 1 of each state in FSM.
- Check if the sequence is unique. If so, this sequence is the UIO sequence of that state. If not, the resulting sequence is not the UIO sequence for that state. Then go to (4) to continue looking for the UIO sequence [7].
- For the state that whose UIO sequence have not been found yet, continue to find the input/output sequence of length K + 1 from the input/output sequence of length K, then check whether it is unique. Repeat this step until the UIO sequence for each state is found or the sequence length exceeds $2n^2$ (n is the number of states of FSM) [8].

According to the FSM of the communication protocol of Q/GDW 11709.2 in Fig. 3, solve the UIO sequence of each state. A two-dimensional array can be used

Table 2 UIO sequence of each state in FSM

State	UIO sequence	State	UIO sequence
S0	L1	S8	L26
S1	L3	S9	L17
S2	L5, L7	S10	L29
S3	L7	S11	L25
S4	L9	S12	L22
S5	L11	S13	L27
S6	L14	S14	L30
S7	L15		

to represent the relationship between each edge in the directed graph of FSM and the input and output sets. Then the UIO sequence of each state can be calculated. When solving UIO sequences of Si, find out all I/O (input and output) sequences starting from state Si and check their uniqueness firstly. If no sequence satisfies the uniqueness, repeat the sequence length K + 1 until all states find UIO sequences or the sequence length exceeds $2n^2$.

The UIO sequence of each state in the FSM of TCU and CTR communication protocol is shown in Table 2.

4.2.2 Generate Conformance Test Sequences

The general steps for generating conformance test sequences based on UIO sequences are as follows [9]:

(1) Firstly, solve the UIO sequence of each state in FSM.
(2) The FSM of the communication protocol between TCU and CTR is represented by the directed graph G = (V,E) in Fig. 3. Among the graph, $V = \{v_1, v_2, \ldots, v_n\}$ is the state set of FSM; $E = \{(v_i, v_j; i_m/o_n)|v_i, v_j \in V, i_m \in I, o_n \in O\}$ is the migration set for FSM. There is a migration $e(v_i, v_j; i_m/o_n) = \{i_m/o_n, UIO(v_j)\}$ for every migration. This migration is called "pseudo-migration". Thereinto, v_i represents the initial state of the test; v_j represents the state after executing the migration path i_m/o_n; UIO (v_j) represents the UIO sequence of state v_j. The graph containing only pseudo-migrations is called "pseudo-graph", represented by $G'' = (V, E'')$. Thereinto, $E'' = \{(v_i, v_j; i_m/o_n)|v_i, v_j \in V, i_m \in I, o_n \in O\}$ is a pseudo-migrated set of FSM. The pseudo-graph G′ is generated according to the directed graph G of FSM, and G′ is shown in Fig. 4.
(3) Then the pseudo-graph G″ is symmetrically extended to generate a directed symmetric graph G* = (V, E*). Thereinto, $E^* = E \cup E''$, that is, edges taken from E are added in the pseudo-graph G′ to obtain the directed symmetric graph G*. The directed symmetric graph G* obtained from the pseudo-graph in Fig. 5 is shown in Fig. 6.

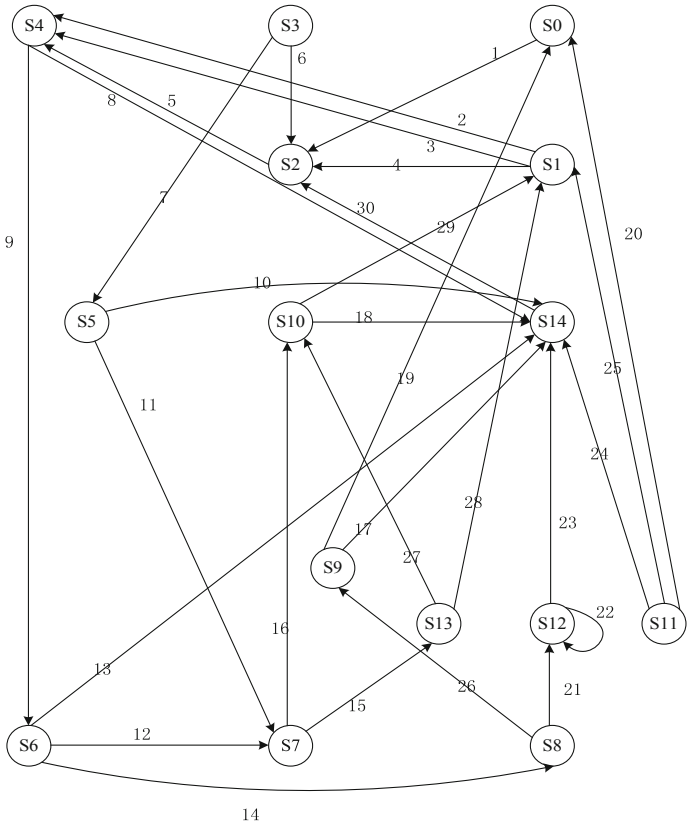

Fig. 5 Pseudo-graph G″

The dotted lines in Fig. 5 represent the extended edges, all taken from Fig G.

(4) Starting from the initial state, euler traversal is constructed, and the obtained sequence is the test sequence of protocol conformance test.

The conformance test sequence of the communication protocol between TCU and charging pile obtained by this method is 1,L5,7,11,15,27,29,2,9,14,26,17,30, 5,9,14,21,23,L30,3,L9,11,L15,L19,20. All the paths in the pseudo-graph are represented by migration, and the test sequence whose length is 46 can be obtained as follows:

L1,L3,

L5,L7,L9,L11,L24,L5,L26,L27,L17,L29,L30,L2,L7,L9,L11,L14,L15,L26,L27, L17,L29,L30,L3,L5,L7,

L9,L11,L14,L15,L21,L22,L23,L29,L30,L3,L5,L7,L9,L11,L24,L15,L19,L20, L25.

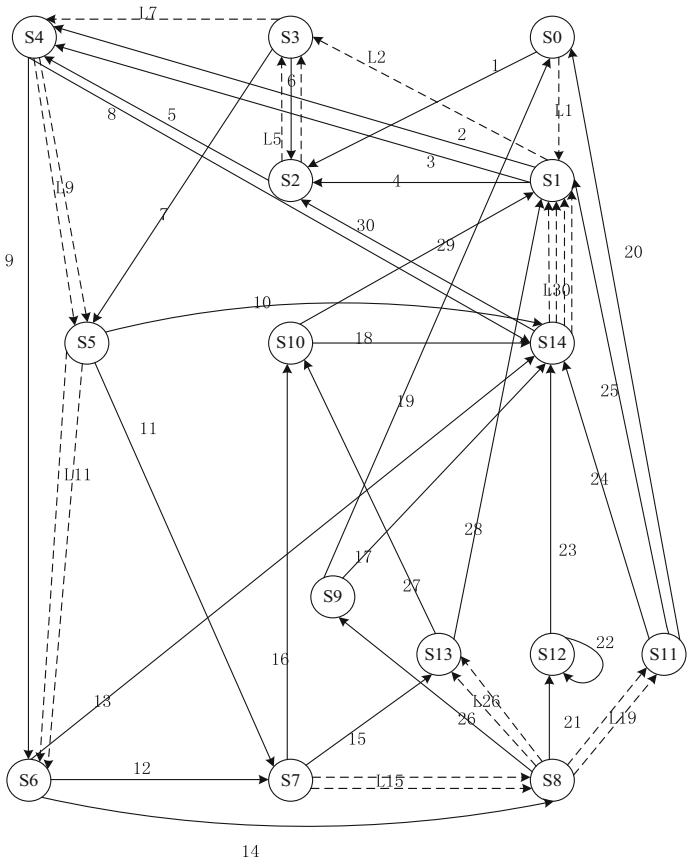

Fig. 6 Directed symmetric graph G*

5 Conclusion and Expectation

As the unified development and design of the TCU of electric vehicle charging facilities have just been completed, and relevant regulations and standards have just been issued, implemented or tried out, a lot of current testing work is still not comprehensive and perfect. On the basis of understanding the communication principle and content between TCU and CTR, paper studied the specific content and requirements of "Q/GDW 11709.2 charging control unit for electric vehicles—part 2: communication protocol with charging pile", sorted out all the states and transition conditions in the protocol, established the FSM model, and calculated the conformance test sequences by using the China Postman Problem Algorithm in T method and the UIO algorithm in U method, based on the directed graph of FSM of the protocol and the Graph Theory. By comparison, it is obvious that the test sequence length obtained by the UIO method is nearly 50% shorter than that

obtained by the China Postman Problem method. The length of test sequence is one of the important factors affecting test efficiency. The shorter the test sequence length is, the higher the test efficiency is.

The work of this paper solves one of the major difficulties in TCU and CTR communication test and communication protocol conformance test: generating test sequences with low redundancy and high coverage, which lays a theoretical foundation for test implementation. However, this paper only adopted some general methods to generate test sequences, which were applied to the communication protocol between the CTR and the TCU to generate the protocol conformance test sequences. The obtained test sequences can be optimized later to obtain the optimal test sequences.

Acknowledgements This work is supported by the science and technology project "Research and Demonstration Application of Key Technologies for Charging Interoperability, Security and Remote Detection of EV Charging Facilities" of State Grid Corporation of China.

References

1. Q/GDW 11709-2017 charging tariff and control unit of electric vehicles, 2017
2. Jiang Z (2007) Teaching reference book of formal language and automata theory. Tsinghua University Press, pp 54–83
3. Brand D, Zafiropulo P (1583) On Communicating finite-state-machines. JACM 30(2):323–342
4. Liu P (2010) FSM-based test cases generation and test optimization. Shanghai University
5. Zhu X, Xu J, Zou B, Zhang Z, Sun L (2010) Network protocol conformance testing: an overview. Comput Sci, 36(12):5–7, 36
6. Xu J, Baohua Z, Qu Y (2004) A new UIO test sequence generation algorithm. J Univ Sci Technol China 34(6):710–715
7. Wang P (2008) Research on test case automatic generation technology of digital audio-visual content management system. Inner Mongolia University
8. Tang J, Huang X, Qian J et al (2013) A FSM-based test sequence generation method for RPL conformance testing. In: Green computing and communications, pp 591–597
9. Ma X, Gao X, Mei S (2005) Two kinds of generating algorithms of test sequences based on UIO and their comparison. Comput Eng Appl 22:76–79, 102

Identifying Critical Patterns of Cascading Failure in Power Systems Based on Sequential Pattern Mining with Gap Constraints

Lu Liu, Linzhi Li and Hao Wu

Abstract The propagation features of cascading failure in power system are basis for identifying critical branches and understanding the mechanisms of cascading failure. This paper defines propagation features as minimum sequential patterns with gap, and propose a method to identify critical patterns and branches. The proposed method is tested on IEEE 39-, 118-bus test systems. The case studies show the method can effectively identify critical patterns and branches from massive cascading failure simulation data. We also illustrate that the identification results help understand the features of power flow transmission and topology structure, and propagation correlations between branches.

Keywords Critical pattern identification · Cascading failure · Sequential pattern mining · Gap constraint · Minimum pattern

1 Introduction

Although cascade failures in power system are rare events, each occurrence of them will bring about enormous economic losses and serious social-safety threat [1]. In particular, under the background of renewable energy integration and hybrid AC/DC system, the causes and evolutions of cascade failures in power system turn to be even more complicated. Therefore, it is necessary to study the propagation features and mechanisms in cascading failure.

Cascading failures are a series of branches trip consecutively [2]. The fault chains formed from the process of cascading failure record the branch propagation association relationship. With the spread of cascading failures, the faults will gradually weaken the system and eventually cause blackouts.

L. Liu · L. Li · H. Wu (✉)
College of Electrical Engineering, Zhejiang University, Hangzhou 310027, Zhejiang, China
e-mail: vuhao@zju.edu.cn

L. Liu
e-mail: liuluzjuee@zju.edu.cn

Y. Xue et al. (eds.), *Proceedings of PURPLE MOUNTAIN FORUM 2019-International Forum on Smart Grid Protection and Control*, Lecture Notes in Electrical Engineering 585, https://doi.org/10.1007/978-981-13-9783-7_69

At present, cascading failure analyses are mainly carried out from two perspectives: simulations of the cascading failure process and statistical analyses of cascading failure data. For the simulation analyses, one kind of types are abstract models, which analyze the propagation mechanism of cascading failure from the point of network topology [3, 4]. The abstract models have advantages in quick calculation, but will cause great information losses in representing the characteristics of real power system. The other kind of types are cascading failure simulation models, for instance, OPA models [5, 6], Manchester model [7], hidden failure model [8].

These models are established with the detailed physical characteristics of power system, whereas the calculation of these models is time-consuming and it is difficult to consider both vulnerable spots in the initial cascading stages and faults interaction in the subsequent stages. As a matter of fact, the simulation results contain the branch propagation association relationship, and can be used as an important data source for identifying key factors of cascading failure propagation [9].

The statistical analyses based on cascading failure data have been used for risk assessment [10], critical branch identification [11–13] and other issues. Furthermore, data analysis and mining method can effectively mine valuable information from big data, which is now popular in power system analysis with the continuous development of power system [14–16]. There are some researches on cascading failure using data mining techniques [17–19]. Reference [17] proposed a PageRank-based fast screening method to identify the vulnerable branches, and the interaction between branches are taken into account. Reference [18] based on DNNE data mining method, efficiently predicts overall cascading risk of an N-k contingency. Reference [19] use PrefixSpan algorithm to mine the cascading failure propagation pattern, which reflects important transmission sections. Generally, the cascading failure sequence that causing sever blackout appears in transmission-outage group, which means there exists patterns consisting of outage transmissions in the sequences. Therefore, it is significant to mine the patterns that lead to serious cascading failure from cascading failure data.

In this paper, we propose the cascading failure minimum pattern mining with gap (CFMPG mining) method based on the sequential pattern mining with gap constrains algorithm. The minimum patterns in the method are the concise groups of branches, which are the minimum units that cause load losses and could appear in the initial or subsequent stages of cascading failures. The method is used to mining the cascading failure minimum pattern with gap (CFMPG) from fault chains, and the branches in CFMPG could sequentially trip continuously or discontinuously. The critical CFMPGs we found using the method could effectively predict and block the critical fault propagation process. Furthermore, upgrading the branches in the critical CFMPGs could reduce the risk of the cascading failure in different stages and hence improve the total system stability.

The remainder of this paper is organized as follows. Section 2 proposes the relevant concepts and defines propagation features as sequential patterns with gap constraints. The CFMPG mining method and the correlation analyses index of

branches are introduced in Sect. 3. Section 4 studies the IEEE 39-, 118-bus test systems to validate the proposed method. Section 5 concludes the paper.

2 Define Propagation Features as Sequential Patterns with Gap Constraints

2.1 Concept of Sequential Pattern Mining with Gap Constraints

Pattern matching can be seen as one of the essential tasks in pattern mining, whose essential task is calculating the support of a pattern [20, 21]. In recent years, many research works have focused on pattern matching with gap constraints (or flexible gaps) [22–24], which could be employed in many fields, such as computational biology to find special protein sites [25], in time series analysis [26], and feature selection for sequence classification [27].

A gap constraint can be written as "$p_1[a, b]p_2$", where 'p_1' and 'p_2' are two characteristic elements, a and b are two integer numbers that represent the minimal and maximal numbers of elements between 'p_1' and 'p_2' [22]. Then pattern P with gap constraints can be written as $p_1[\min_1, \max_1] \cdots p_j[\min_j, \max_j] \cdots [\min_{m-1}, \max_{m-1}]p_m$. For instance, subsequences "ACT" and "AGGCBT" are two occurrences of pattern "A[0,2]C[0,1]T", since both sequences share the same characteristic elements "A", "C" and "T", and there are zero or two elements between "A" and "C", zero or one element between "C" and "T" in subsequences respectively.

Though pattern matching with gap constraints meets more flexible demands, the complexity and challenges of the algorithm increase meanwhile.

2.2 Data Structure Representation of Cascading Failure

The process of cascading failure in power system has time-ordered and fault events correlation characteristics. In the initial stage of cascading failure, the components in system quit operation due to the random disturbance, and cause power flow transformation, which might consequently trigger branch overloading or hidden failure in the subsequent stages. With the coordination of dispatch scheme, operators redispatch the system to interrupt the development of cascading, otherwise might lead to a large-scale blackout. Over each stage of cascading failure, the components run out of operation might cause system load loss consecutively, and eventually output the total system load loss.

The fault chain (FC) and fault load loss chain (FLLC) can be obtained from cascading failure simulation or real power system data. Among the cascading failure simulation models, the steady models, such as OPA model, are the most

popular because of the high computing efficiency and reliable analytical results, which can be divided into AC and DC power flow based steady models. The DC based model is simplified from AC [28], which overlooks the transmission resistance and the direct relationships between reactive power and voltage. Though the accuracy of power flow calculation result of DC is lower than AC, DC model reduces the model complexity and accelerates computing, which is promising in fast cascading failure simulation. In this paper, given the computational efficiency and tolerable power flow calculation error, we obtain FCs and FLLCs using DC power flow based steady model.

FCs reflect the failure propagation mechanism and the role of branches in path propagation. FLLCs represents the system load loss at different stages, which could reflect the load loss level of different cascading failure states. In the passage, FCs and corresponding FLLCs are represented by discrete sequences as follows:

$$FC_i = \left\{ L^i_{m_1}, \cdots, L^i_{m_j}, \cdots, L^i_{m_k} \right\}, \tag{1}$$

$$FLLC_i = \left\{ l^i_{m_1}, \cdots, l^i_{m_j}, \cdots, l^i_{m_k} \right\}, \tag{2}$$

where $L^i_{m_j}$ is the jth branch tripped in the ith FC, $l^i_{m_j}$ is the load loss of fault state $\left\{ L^i_{m_1}, \cdots, L^i_{m_j} \right\}$, m_j is the position index, k is the length of FC_i or $FLLC_i$.

Load loss is the most direct consequence of cascading failure in power system. Different branches (sets) or fault stages correspond to different load losses. In order to explore the correlation between the development process of cascading failure and the corresponding load loss, this paper takes the load losses as characteristics and splits FCs into different fault states, and records the corresponding state loss, as shown in Table 1. After splitting all FCs and statistically analyzing the fault states, the number of each state is obtained. And the database *DB* is established, which has three sub-database: fault state database *STATE,* load loss of state database *LOSS,* number of state database *NUM.*

Table 1 Split FCs into fault states

FC Num		Fault state of different stages			
		1	2	3	…
⋮	⋮	⋮			
i	*STATE*	$\left\{ L^i_m \right\}$	$\left\{ L^i_{m_1}, L^i_{m_2} \right\}$	$\left\{ L^i_{m_1}, L^i_{m_2}, L^i_{m_3} \right\}$	…
	LOSS	$l^i_{m_1}$	$l^i_{m_2}$	$l^i_{m_3}$	
⋮	⋮	⋮			

2.3 Cascading Failure Pattern with Gap

The development of cascading failure is the result of flow transfer, system structure, and operation state. Given the upgrading and state transformation of power grid is a long-term slow process, this paper analyzes the cascading failure paths and critical pattern with gap ("pattern" hereinafter) under the determined power network structure and operation state. At this point, although the evolution of cascading failure paths is various, it contains the common characteristics and rules of the cascading propagation. Identifying the leading branches (sets) and extracting high-risk fault patterns have a significant effect on analyzing cascading propagation mechanism, preventing and interrupting fault propagation, and mitigating system cascading risk.

Among the FCs, branches (sets) causing severe system load losses not always appear continuously. Generally, part of the critical branch (set) outage would not likely cause load loss, but once all of the branches in set outage would produce severe load loss. Moreover, the set appear discontinuous, other branches could insert into the gap of any two branches of the set.

Consequently, this paper defines the cascading failure pattern with gap as follows:

$$P = p_1[\min_1, \max_1] \cdots p_j[\min_j, \max_j] \cdots [\min_{m-1}, \max_{m-1}]p_m, \tag{3}$$

where $p_j, j \in [1, m]$ is the jth branch in pattern P; $[\min_j, \max_j]$ is the gap constraint interval, which represents the number of insert branches allowed between P_j and p_{j+1}; m is the length of the pattern P. When the gap constraint interval is same for all gaps, the cascading failure pattern with gap can be written as:

$$P[\min, \max] = p_1 p_2 \cdots p_m \tag{4}$$

For instance, for the original FCs in Table 2, we can extract pattern P [−4, +4] = [4, 9, 13, 30]. FC_1 and FC_2 share the same elements as P, and the fault sequence can be adjusted through gap constraint. FC_3 and FC_4 include P elements, meanwhile insert branch (set) {10}, {19,16} before P. FC_3 inserts {18,8} between branch 9 and 13.

The above example shows that different FCs are not completely consistent in branch outage sequence and FCs' length, nevertheless they share the same

Table 2 Fault chain sequence

Num	Branch sequence
1	{13,4,9,30}
2	{4,13,9,30}
3	{10,13,9,30,4}
4	{19,16,13,9,30,4}
5	{30,4,9,18,8,13}

cascading failure pattern with gap constraints, which appears frequently. Moreover, a FC might possess not only one pattern, which will be stated in detail in Sect. 3.

3 Method of Cascading Failure Minimum Pattern Mining with Gap (CFMPG Mining)

3.1 Extract Cascading Failure Minimum Pattern Mining with Gap (CFMPG)

The database *DB* is obtained by decomposing the FCs into different length of fault states, which exist no gap. In order to extract cascading failure pattern with gap, we need to truncate the state whose state cost is zero firstly, where the state cost is defined following:

$$Sc_j^i = DB(NUM)_j^i \times DB(LOSS)_j^i \tag{5}$$

So long as the zero-cost states are deleted from *DB*, the states could not be searched afterwards. The reason truncating the zero-cost states is that these states are not the minimum units produce load loss, and the information of these states is included in the subsequent states of the same FC. Therefore, this step causes no information loss. Let the truncated *DB* be *DBcut*.

The minimum cost set proposed in this paper refers to the minimum branch group causes load loss, and gap is existed. The method to extract the minimum cost set is based on ***Eclat algorithm*** [29], adopts bottom-up extraction method. For instance, for FC sequence $S = \{D, T, A, W, C\}$, the extraction process is show in Fig. 1.

The main inversion process is as follows:

- Step1: Select one FC as sequence S, and take it as the original parent generation.

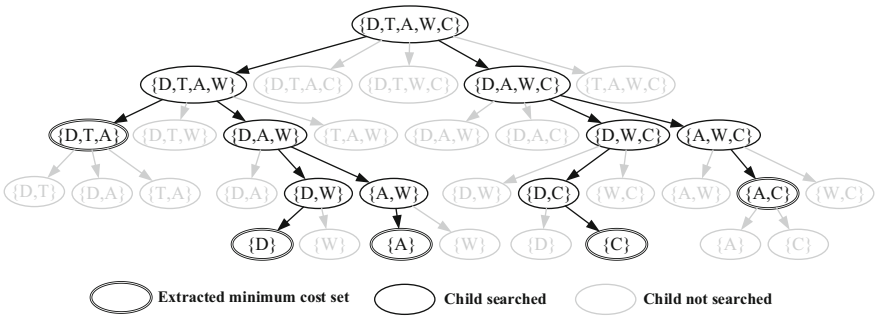

Fig. 1 Minimum cost set extraction of the inversion tree

- Step2: Remove one element in the parent in sequence to obtain the children generation, whose number is the length of parent generation. Search each child in *DBcut*, if exists, takes the child as new parent and delete the new parent in *DBcut*; otherwise the inversion of the child is terminated, record the child as the extracted minimum cost set.
- Step3: Execute the inversion procedure for new parent generation, repeat **Step2**, until no parent exists children, the inversion of original parent S is end.

After the above extraction process, redundant branches between minimum cost set can be removed, as shown in the double coil in Fig. 1.

In order to improve the search efficiency and avoid repeated searches for the same child, we implement two rounds of extraction. In the first round, remove the child searched in *DBcut*, make sure the other parents' inversion no longer search for this child. Therefore, the searched minimum cost set is not the minimum fault unit causing load loss, and we need to conduct the second-round extraction based on the result of the first round, in which the search database is the original DBcut without removement and the child searched will not be removed. The minimum cost sets obtained after the two rounds of extraction is called cascading failure minimum pattern with gap (CFMPG).

The original *DBcut* database contains many states, and longer the states, there might conclude more CFMPGs. Therefore, start with the longest state in *DBcut* and apply the extraction process above. Since the inversion tree can effectively cover multiple states from a certain *STATE*, it only takes several inversion trees to cover all states in *DBcut(STATE)*.

3.2 Statistical Analysis of CFMPGs

The pattern load loss of CFMPG can be found in *DBcut(LOSS)* with no gaps, which can be seen as the pure CFMPG without disturbance of other branches or patterns. However, the corresponding support count is unavailable in *DBcut*, for which we apply pattern matching based on the original FCs. The pattern matching method in this paper is based on ***the pattern matching algorithm based on gap constraints*** [22]. Take the FCs in Table 2 as an example.

Firstly, Convert the FCs into a vertical data format and add sequences' position value, consequently forms the vertical search database *VSDB* shown in Table 3. In the *VSDB*, $VSDB(i,:)$ represents the situation of branch i outages in each FC, $VSDB(:,j)$ represents the number and sequence of branches outage in FC_j, element *0* in VSDB indicates branch i is absent in FC_j.

Then, produce the pattern matching approach based on *VSDB* and CFMPGs. Define $P(i-)$ as the first i items of pattern P, which is the subset of P, and $P(i)$ as the ith item of P. The main process of pattern matching approach is as follows:

Table 3 *VSDB*: vertical search database of FCs

Branch Num	FCs Num					
	1	2	3	4	5	…
4	2	1	5	6	2	…
8	0	0	0	0	5	
9	3	3	3	4	3	
10	0	0	1	0	0	
13	1	2	2	3	6	
16	0	0	0	2	0	
18	0	0	0	0	4	
19	0	0	0	1	0	
30	4	4	4	5	1	
31	0	0	0	0	0	

- Step1: Make the $P(i-)$ as prefix, and search in the *VSDB* for the sequence numbers of FCs which appear the prefix, as *Prefix chain.*
- Step2: Make the $P(i+1)$ as suffix, the $P(i)$ as the last state of prefix. Search in *VSDB* for the sequence numbers of FCs, in which the position value of $P(i+1)$ is greater than $P(i)$, as *Suffix chain.*
- Step3: Take the intersection of *Prefix chain* and *Suffix chain,* which is the new *Prefix chain* for the new prefix $P(i+1-)$.
- Step4: Repeat above Steps until prefix $P(i-)$ is equal to pattern P, the pattern matching process is terminated. Then length of *Prefix chain* is the support count of pattern P, which is written as $\sup_P$.

Up to now, the pattern database *PDB* is established, which contains three sub-database: minimum pattern database *PDB(PATTERN)*, load loss of pattern database *PDB(LOSS)*, support count of pattern database *PDB(SUP).*

3.3 Identification of Critical CFMPGs

There are patterns like $P_1 = [1, 42, 4]$, $P_1 = [42, 7, 4]$, $P_3 = [42, 30, 3, 4]$ in *PDB (PATTERN)*, which share the same load loss. The aim of this part is to mining the frequent pattern of the set of these patterns. For the pattern set $\{P_1, P_2, P_3\}$ above, the result of pattern mining is $P[0, 2] = [42, 4]$, which we call frequent synthetic pattern. The support count of synthetic pattern is $\sup_P = \sup_{P_1} + \sup_{P_2} + \sup_{P_3}$, the synthetic pattern's load loss l_p is the same as patterns above.

The method of synthetic pattern mining for pattern set is frequent sequence pattern mining, which is based on ***Apriori algorithm*** [30]. Based on the apriori principle, we can know that if a set of items is frequent, then all subsets must also be frequent. Hence, set the minimum support count as *minsup*, if the support count of subset is less than *minsup,* the subset is considered to be infrequent items and

terminate the subsequent derivation of this subset as a prefix. The main process of frequent sequence pattern mining is as follows:

- Step1: Search for the patterns sharing the same load loss in *PDB*, record the patterns as a pattern set.
- Step2: Scan the pattern set and record the 1-frequent item that meets the minimum support *minsup*.
- Step3: Let k-frequent item L_k as prefix, the elements in L_k as suffix. Then the k + 1-candidate item C_{k+1} is formed with prefix and suffix, and the corresponding support count can be calculated.
- Step4: According to the *minsup* and support count of C_{k+1}, prune item in C_{k+1} and get k + 1-frequent items L_{k+1}.
- Step5: Repeat **Step3** and **Step4** until frequent item L_{k+1} is unavailable, the mining process is terminated.

Frequent patterns of different lengths can be obtained by the mining process above. We select the longest frequent pattern as the synthetic pattern of the pattern set.

After the synthetic pattern mining for several pattern sets, the pattern database *PDBcut* is finally formed. Furthermore, in order to identify the critical CFMPGs, we define the risk of cascading failure load loss evaluating indicator *RI*, which is the product of pattern support and pattern load loss, seen in Eq. (7).

$$RI_P = \frac{\sup_P}{N} loss_P, \tag{6}$$

where $\sup_P$ is the support count of pattern P, $\sup_p = PDBcut(SUP_P)$; N is the number of original FCs; $loss_P$ is the load loss of pattern P, $loss_p = PDBcut(LOSS_P)$.

3.4 Correlation Analyses Index of Branches in Power System

In order to analyze the correlation of branches, intuitively represent the association relationships of branches in the critical CFMPGs, we propose the correlation analyses index of branches as follows. The frequency of branch i can be represented as Bf_i:

$$Bf_i = \frac{\sum_{k \in N_{FC}} T_i^{FC_k}}{N_{FC}}, \tag{7}$$

where N_{FC} is the number of FCs; $T_i^{FC_k}$ is the indicator of branch i in FC_k, 1 for existent and 0 for inexistent.

Using the data from *PDB(PATTERN)* and *PDB(SUP)*, we can obtain the degree of branch propagation association Re_{ij}, which represents frequency of branch propagation $i \rightarrow j$ in all patterns:

$$\mathrm{Re}_{ij} = \frac{\sum_{k \in N_P} T_{ij}^{P_k} \bullet \mathrm{sup}_{P_k}}{\mathrm{sum}_{N_P}}, \tag{8}$$

where N_P is the number of pattern type, $T_{ij}^{P_k}$ is the indicator of propagation $i \rightarrow j$ in P_k, 1 for existent and 0 for inexistent, sup_{P_k} is the support count of P_k, sum_{N_P} is the total support of all patterns.

3.5 Complete Procedures of CFMPG Mining Method

The CFMPG mining method and the whole solution diagram of identifying critical patterns is illustrated in Fig. 2.

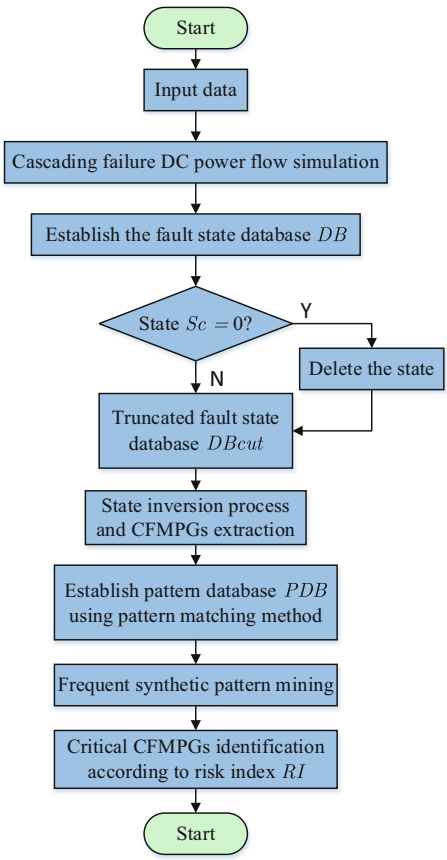

Fig. 2 Solution diagram of the proposed method to identify critical CFMPGs

4 Simulation and Analysis

The proposed method is tested on the IEEE 39-bus [31] and the modified IEEE 118-bus system [32], to validate the proposed CFMPG mining method of identifying the critical CFMPGs ("pattern" hereinafter refers to "CFMPG").

4.1 IEEE 39-Bus Test System

The IEEE 39-bus test system includes 46 branches and 6254.23 MW system load. The passage uses the DC power flow model [12] to simulate system cascading failure, and output the FCs and FLLCs. In order to verify the validity of CFMPG mining method identifying the critical CFMPGs, we firstly count the change of the number of pattern types generated with the input FCs' numbers, as shown in Fig. 3.

It can be seen that as the number of FCs is increasing, the number of CFMPGs' types is tending to convergence, which means with the increase of FCs to a certain extent, CFMPG mining method could cover the vast majority of fault patterns. On the other hand, the patterns appearing in large sample sizes indicate the low occurrence frequency, which means these patterns is hard to totally trigger and does a small effect on critical CFMPGs identifying, and can be avoided by strength the other branches or patterns.

We input 65,000 FCs and FLLCs into the CFMPG mining method. According to the result, the number of CFMPGs' types is 612, and the number of CFMPGs is

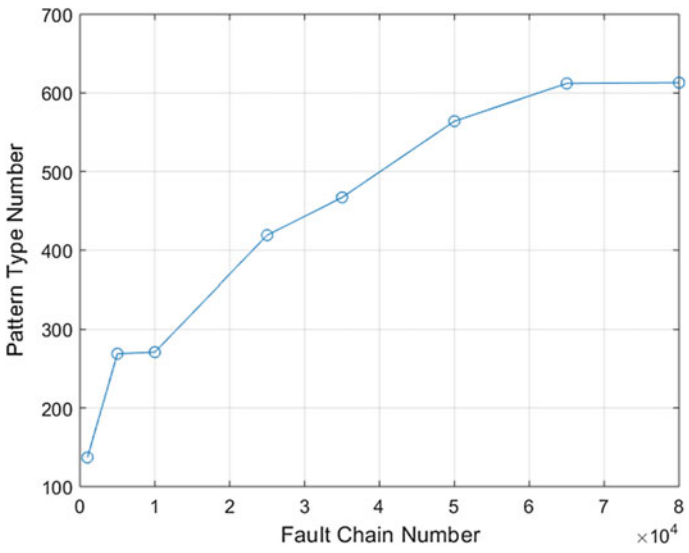

Fig. 3 Trend of pattern type number change with FCs number

335,755. Since each pattern appears in one FC is no more than one time, an average of 5.17 CFMPGs appear in one FC. It indicates that there might exist not only one CFMPG in one FC.

After the frequent synthetic pattern mining, the number of CFMPGs' types is 161 in the end, and the risk indicator of pattern ranked in descending order is shown in Fig. 4. We find that there is a significant difference in *RI* between the high-risk patterns and low-risk patterns, which indicates that there are a few critical CFMPGs in power system. The top 10 high-risk patterns in IEEE 39-bus system is shown as Table 4.

The patterns in Table 4. do not constrain the upper and lower limits of the gap, hence multiple branches can insert into the patterns and the support can be fully searched in the original FCs. In addition, CFMPGs may not only appear in the initial stage of cascading fault, but also be triggered by other branches or patterns. Therefore, strengthening the high-risk CFMPGs can interrupt the propagation of both vulnerable spots in the initial cascading stages and subsequent failure stages.

The connection diagram of IEEE 39-bus system is shown in Fig. 5. We find that though the high-risk patterns are not connected geographically, they are located in the key position of the system, which facilitate isolating the system into different sub-networks and block the active power transmission of generators. For example, when branches in pattern [38,28] outage, ZONE1 is isolated from the system. Generator 35 and 36 no longer offer active power for other load buses outside ZONE1. The same as [3,42,1] isolate the ZONE2, and [13,23] isolate the ZONE3. Through analysis above, it is found that the branches in high-risk CFMPGs are always important channels for power flow transmission.

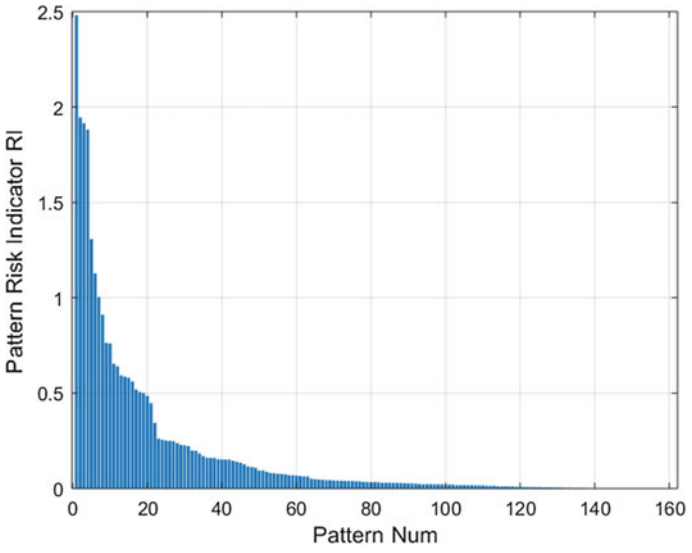

Fig. 4 Descending *RI* ranking of CFMPGs

Table 4 Top 10 high-risk CFMPGs in IEEE 39-bus system

Num	Pattern	*RI*	Support
1	[35,38]	3.7965	0.3012
2	[38,28]	3.3922	0.2692
3	[3,42,1]	1.9443	0.2414
4	[13,23]	1.5916	0.4043
5	[38,29]	1.3075	0.2650
6	[4,42]	1.1280	0.7219
7	[35,28]	0.7641	0.1744
8	[35,29]	0.6537	0.1761
9	[18,19]	0.6404	0.1627
10	[9,13,26]	0.5926	0.0733

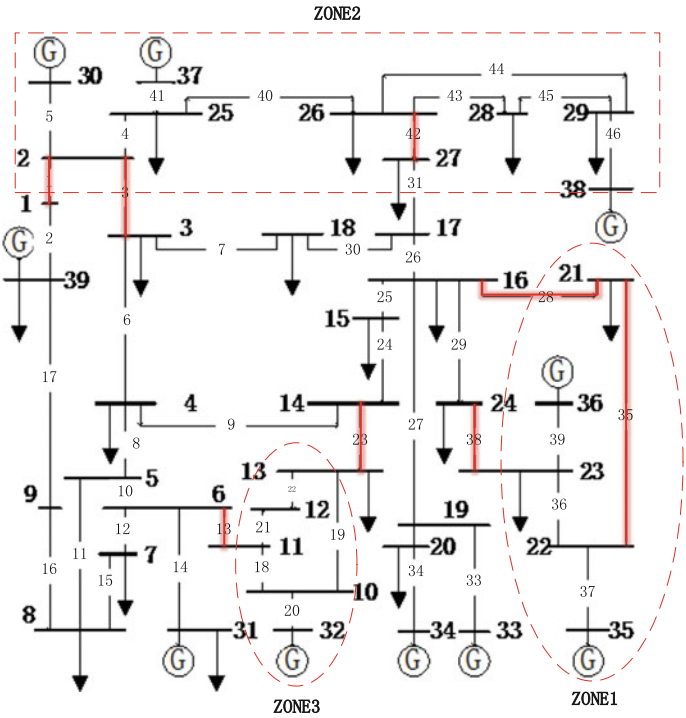

Fig. 5 Connection diagram of IEEE 39-bus system

In order to verify whether the high-risk CFMPGs have a major impact on the cascading failure of system risk, we expand the branches in high-risk CFMPG [33, 34]. The branch expansion is as follows [12]:

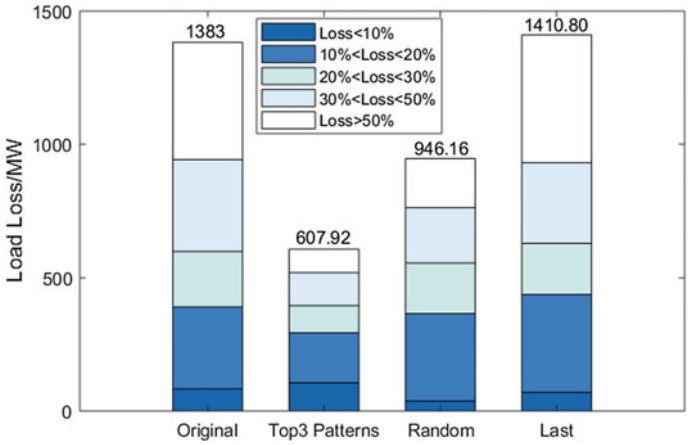

Fig. 6 The blackout risks with different branches upgraded of IEEE 39-bus system

$$\begin{cases} F'_{i,c} = F_{i,c} + \Delta F \\ F'_{i,\max} = F_{i,\max} + \Delta F \end{cases}, \tag{9}$$

where ΔF is the expansion capacity, $F_{i,c}$ and $F_{i,\max}$ is the low and up capacity limit of the ith branch. The branches expand the capacity reduce the outage probability in cascading propagation to some extent. Therefore, upgrading the high-risk CFMPGs can effectively reduce the risk of system blackout. Here, we take $\Delta F = 500\,\text{MW}$. Select the top 3 CFMPGs to perform branch expansion, the result is shown in Fig. 6. As a comparison, we compare the cascading failure results with the original system, random-selected branches with the same branch numbers, and the last CFMPGs with the same branch numbers.

By comparison, it can be found that upgrading the top 3 patterns, which totally consist of 6 branches, can greatly reduce the risk of medium and large-scale blackout, and have no obvious effect on the small-scale blackout, or even slightly aggravate the small-scale blackout. The effect of randomly selecting 6 branches has much to do with the selected expansion branches. Selecting 6 branches from the last of the CFMPGs to expand capacity, it can be found that it has a certain effect on small-scale blackout, but basically has no effect on mitigating medium and large-scale power failure accidents.

4.2 IEEE 118-Bus Test System

To further validate the proposed approach, case studies are also performed on the improved IEEE 118-bus system, which has 186 branches and 3733 MW load. In the same way, 50,000 FCs and FLLCs obtained by DC power flow cascading

Table 5 Top 10 high-risk CFMPGs in IEEE 118-bus system

Num	Pattern	RI	Support
1	[7]	0.1836	0.1676
2	[8,37]	0.1373	0.0744
3	[127,126]	0.1212	0.1818
4	[60,62,68,110,96,109]	0.0584	0.0136
5	[8, 16, 19, 22]	0.0289	0.0052
6	[61,66,67,96,109,110]	0.0239	0.0177
7	[8, 18, 19, 22]	0.0236	0.0041
8	[8, 18–20]	0.0195	0.0036
9	[183]	0.0157	0.0055
10	[57,58,61,96,109,110]	0.0109	0.0084

failure simulation of IEEE 118-bus system are input into the CFMPG mining method, and consequently get the CFMPGs ranked in descend sort according to *RI*, which is shown in Table 5.

In order to verify the effect of mining high-risk CFMPGs, in the same way, select the critical patterns to perform expansion plan. Due to the large size of the IEEE 118-bus system, the top 4 patterns, which totally consist of 11 branches, are expanded for the purpose of intuitively showing the expansion effect. As a comparison, we verify the result of reference [13], in which shows the ***weighted hypertext-induced topic search (HITS) algorithm*** to identify the key branches. Table 6 shows the critical branch identification results of algorithm in [13]. We select the top 11 branches to perform expansion plan.

Figure 7 shows the expansion effect of the two methods. The CFMPG mining method do better in identifying the patterns which lead to medium and large-scale blackout, whereas it has less advantage than the HITS method in identifying small-scale blackouts. Given the fact that the realistic power system is robust to small disturbances, performing the dispatch scheme to interrupt cascading outage is

Table 6 Critical branch identification results of HITS algorithm

Num	Branch
1	37(8–30)
2	116(69–75)
3	41(23–32)
4	119(69–77)
5	108(69–70)
6	22(16–17)
7	121(77–78)
8	125(79–80)
9	39(17–31)
10	54(30–38)
11	107(68–69)

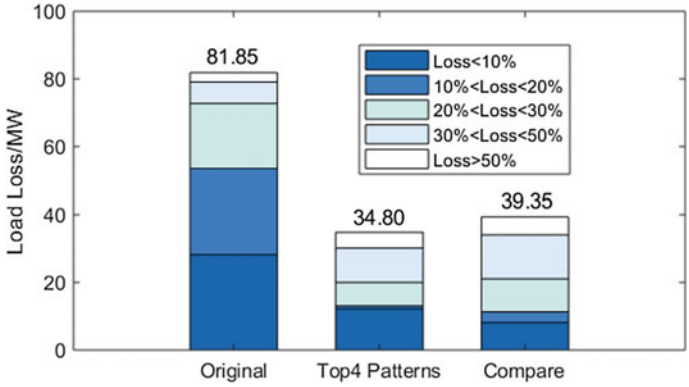

Fig. 7 The expansion effects with different methods for IEEE 118-bus system

more effective for small-scale cascading failure. Therefore, identifying the patterns triggering medium and large-scale blackout and upgrading the branches of the patterns, could effectively reduce system load loss and mitigate cascading failure risk of system.

Furthermore, in order to find the associated relationships between branches in CFMPGs, we draw the Branches-correlation network of CFMPGs, as shown in Fig. 8. The nodes in Fig. 8 are branch names of IEEE 118-bus system. The size and color of the node represent the frequency at which a branch appears in a FC. The larger the node size and the darker the color, the higher the frequency of the branch in FCs. The links that connect nodes in Fig. 8 represents the branches-correlation of CFMPGs. The thicker the link and darker the color, the stronger the branch propagation association, which means it is more frequently that this branch propagation appears in the patterns. Considering visibility requirements, links whose

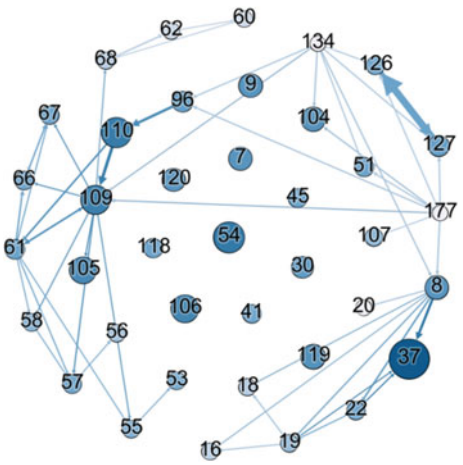

Fig. 8 Branches-correlation network of CFMPGs in IEEE 118-bus system

degree of propagation association less than 2% of the maximum one are removed from the figure. The same as the frequency of node, we only show the first 20 nodes according to the *Bf* value.

It can be found that branch with strong association relationship often exists in the high-risk CFMPGs, such as 96 → 110, 110 → 109, 8 → 37. A branch with higher node frequency may correspond to strong degree of branch propagation association at the same time, indicating that the branch plays a key role in the development of fault propagation in cascading failure, such as node 109 and node 110. In addition, some branches have a high frequency, but the corresponding propagation association is low. One case is that the node is a single-branch pattern, such as node 7, which is a pattern with *RI* value in top 1. In the other case, the probability of such branch be the element of a pattern is low, and it belongs to the line that is easy to trigger by pattern outages, such as 54 and line 106.

5 Conclusions

The paper proposes the cascading failure minimum pattern mining with gap (CFMPG mining) method, which considers both the frequency of pattern occurrence and the load loss of pattern, and the critical CFMPGs mined from the massive simulation data using the proposed method are the minimum groups of branches that causes load losses and could appear in both initial and subsequence stages of cascading continuously and discontinuously. Cases of IEEE 39-, 118-bus test systems prove the effectiveness of the proposed method in identifying the critical patterns and branches, analyzing the propagation features of cascading failure, which is promising for online application.

Based on the proposed method, the authors also plan to use the CFMPGs to predict the development of cascading failure, and analyze the mobility of pattern mining under different operating conditions in the future studies.

Acknowledgements This work is partly supported by State Grid Corporation of China (Project: The research and development of multi-sandpile theory based blackout early warning technologies and systems in interconnected power grids).

References

1. Guo H, Zheng C et al (2017) A critical review of cascading failure analysis and modeling of power system. Renew Sustain Energy Rev 80:9–22
2. Wang A, Luo Y, Tu G, Liu P (2011) Vulnerability assessment scheme for power system transmission networks based on the fault chain theory. IEEE Trans Power Syst 26:442–450
3. Ding M, Han P (2007) Study of failure spreading mechanism in the small-world power grid. Autom Electr Power Syst 31:6–10

4. Watts DJ, Strogatz SH (1998) Collective dynamics of 'small-world' networks. Nature 393:440–442
5. Dobson I, Carreras BA, Lynch VE, Newman DE (2001) An initial model for complex dynamics in electric power system blackouts. In: Proceedings of the 34th annual Hawaii international conference on system sciences. IEEE, Maui, pp 710–718
6. Mei S, He F, Zhang X et al (2009) An improved OPA model and blackout risk assessment. IEEE Trans Power Syst 24:814–823
7. Nedie DP, Dobson I, Kirschen DS et al (2006) Criticality in a cascading failure blackout model. Int J Electr Power Energy Syst 28:627–633
8. Phadeke AG, Thorp JS (1996) Expose hidden failures to prevent cascading outages. IEEE Comput Appl Power 9:20–23
9. Hines P, Dobson I, CotillaSanchez E, Eppstein M (2013) "Dual graph" and "random chemistry" methods for cascading failure analysis. In: 46th Hawaii international conference on system sciences. IEEE, Wailea, pp 2141–2150
10. Rezaei P, Hines P, Eppstein MJ (2015) Estimating cascading failure risk with random chemistry. IEEE Trans Power Syst 30:2726–2735
11. Wei X, Zhao J, Huang T, Bompard E (2017) A novel cascading faults graph based transmission network vulnerability assessment method. IEEE Trans Power Syst 33: 2995–3000
12. Li L, Wu H, Song Y (2018) Temporal difference learning based critical component identifying method with cascading failure data in power systems In: 2018 IEEE power & energy society general meeting (PESGM). IEEE, Portland, pp 1–5
13. Luo C, Yang J, Sun Y Identify critical branches with cascading failure chain statistics and hypertext-induced topic search algorithm. In: 2017 IEEE power and energy society general meeting (PESGM). IEEE, Location, pp 1–5 (2017)
14. Zhao J, Dong Z, Wen F et al (2017) Data science for energy systems: theory, techniques and prospect. Autom Electr Power Syst 41:1–11
15. Zhang Y, Hu C, Huang S et al (2017) Apriori algorithm based data mining and analysis method for secondary device defects. Autom Electr Power Syst 41:147–151
16. Chen G, Zhang Y, Hao S et al (2017) Association mining based intelligent identification method of key parameters for reactive power optimization. Autom Electr Power Syst 41: 109–116
17. Ma Z, Shen C, Liu F et al (2019) Fast screening of vulnerable transmission lines in power grids a PageRank-based approach [J]. IEEE Trans Smart Grid 10:1982–1991
18. Jia Y, Xu Z, Lai L, Wong K (2016) Risk-based power system security analysis considering cascading outages. IEEE Trans Industr Inf 12:872–882
19. Liu Y, Huang S, Mei S, Zhang X (2019) Analysis on pattern of power system cascading failure based on sequential pattern mining. Autom Electr Power Syst (43), 34–40
20. Navarro G (2014) Spaces, trees, and colors: the algorithmic landscape of document retrieval on sequences. ACM Comput Surv 46:1–47
21. Wu Y, Wang L, Ren J et al (2014) Mining sequential patterns with periodic wildcard gaps. Appl Intell 41:99–116
22. Wu Y, Li S, Liu J et al (2018) NETASPNO: approximate strict pattern matching under nonoverlapping condition. IEEE Aceess 6:24350–24361
23. Nip K, Wang Z, Xing W (2016) A study on several combination problems of classic shop scheduling and shortest path. Theor Comput Sci 22:175–187
24. Fredriksson K, Grabowski S (2008) Efficient algorithms for pattern matching with general gaps, character classes, and transposition invariance. Inf Retr 11:335–357
25. Navarro G, Raffinot M (2003) Fast and simple character classes and bounded gaps pattern matching, with applications to protein searching. J Comput Biol 10:903–923
26. Tan C, Min F, Wang M et al (2016) Discovering patterns with weak-wildcard gaps. IEEE Access 4:4922–4932
27. Li C, Yang Q, Wang J, Li M (2012) Efficient mining of gap-constrained subsequences and its various applications. ACM Trans Knowl Discov Data 6:1–39

28. Dobson I, Carreras B, Lynch V, Newman D (2001) An initial model of complex dynamics in electric power system blackouts. In: Proceedings of the 34th annual Hawaii international conference on system sciences. IEEE, Maui, pp 710–718
29. Mohammed JZ (2000) Scalable algorithms for association mining. Knowl Data Eng 12: 372–390
30. Agrawal R, Imielinski T, Swami A (1993) Mining association rules between sets of items in large databases. In: Proceedings of the 1993 ACM SIGMOD international conference on management of data. ACM, Washington, pp. 207–216
31. Matpower User Manual (2018) http://www.pserc.cornell.edu/matpower/#docs
32. JEAS IEEE118. http://motor.ece.iit.edu/Data/JEAS_IEEE118.doc
33. Hines P, Dobson I, Rezaei P (2017) Cascading power outages propagate locally in an influence graph that is not the actual grid topology [J]. IEEE Trans Power Syst 32:958–967
34. Wenli F, Zhigang L, Ping H, Shengwei M (2016) Cascading failure model in power grids using the complex network theory. IET Gener Transm Distrib 10:3940–3949

Study on Distribution Voltage of Deteriorated Insulator Based on Finite Element Method

Jian Li, Jian Li, Hao Luo, Lei Zheng, Qiang Fan, Yuhui Peng, Zhen Dong and Kai Qu

Abstract Under the long-term influence of electrical load and natural environmental factors, the insulation performance of the insulator will gradually decrease, and deteriorated insulators with different degrees of deterioration will appear in the insulator string. The presence of degraded insulators can pose a significant risk to the safe operation of the power system. In order to study the influence of insulators with different degradation degrees on the voltage distribution of insulator strings in 500 kV transmission lines, this paper studies the distribution voltages of different positions, different numbers and different degraded insulators in 500 kV transmission line insulator strings based on finite element method. The simulation results show that the voltage drop of the insulator with a lighter degree of degradation is very low, and it is more difficult to identify by the distributed voltage. The deteriorated insulator has a certain lifting effect on the voltage of its adjacent insulator. Finally, the effects of different degrees of deteriorated insulators on the voltage distribution are studied by experiments. The conclusions are consistent with the simulation results.

Keywords Finite element · Degraded insulator · Distributed voltage · Degradation degree

J. Li · Q. Fan · Y. Peng
Southwest Branch of State Grid Corporation of China, Chengdu 610000, China

J. Li · H. Luo · L. Zheng
Wuhan NARI Limited Liability Company, State Grid Electric Power Research Institute, Wuhan 430074, China

J. Li · H. Luo · L. Zheng
Hubei Key Laboratory of Power Grid Lightning Risk Prevention, Wuhan 430074, China

Z. Dong (✉) · K. Qu
School of Electrical Engineering, Wuhan University, Wuhan 430072, China
e-mail: 252520064@qq.com

Y. Xue et al. (eds.), *Proceedings of PURPLE MOUNTAIN FORUM 2019-International Forum on Smart Grid Protection and Control*, Lecture Notes in Electrical Engineering 585, https://doi.org/10.1007/978-981-13-9783-7_70

1 Introduction

Insulators are an important part of overhead lines. Due to the influence of various external factors, the insulator in operation may deteriorate, and its insulation resistance will be greatly reduced. Then it is usually called zero-value insulator or low-value insulator [1–3]. When the lightning overvoltage acts on the zero-value insulator, the zero-value insulator completely brakes down, and the powerful lightning current flows from the porcelain gap in the head of the zero-value insulator, which will cause overheating of the zero-value insulator. Therefore, it poses a great threat to transmission system [4, 5]. Checking the status of running insulators is one of the main measures to ensure stable operation of power systems. For the detection of deteriorated insulators, there are generally the following method: ultrasonic method, ultraviolet imaging method, ultraviolet pulse method, pulse current method, infrared imaging method, voltage distribution method. Ultrasonic method belongs to non-contact detection, which is convenient to operate [6]. However, due to the strong high-voltage magnetic field in the field, the sensitivity to distinguish the deteriorated insulator is low. Ultraviolet imaging is difficult to generalize in practice due to its high cost. The pulse current method has the advantages of low detection cost and convenient operation, but the sensitivity is low due to the ambient temperature and the humidity [7–9]. The infrared imaging method is based on the characteristic of the temperature rise of the deteriorated insulator [10]. However, this method is greatly affected by environmental factors such as the sun and meteorological conditions, so it is limited in practical applications. The voltage distribution method is based on the principle that the voltage of the degraded insulator is reduced [11–13]. Because the method is mature and the sensitivity is relatively high, it is a common method for checking out the deteriorated insulator in engineering [14]. Based on the finite element software ANSYS Electronics Desktop, we calculated the voltage distribution characteristics of insulators string with deteriorated insulator at different position in the 500 kV line. It provides a theoretical basis for the discrimination of the deteriorated insulator [15].

2 Electric Field Model of Insulator String a Subsection Sample

2.1 Model of the Insulator

Take a 500-km single-returned glass tower suspension I string with 30 pieces of FC-300/195 insulators with a diameter of 320 mm, a structural height of 195 mm and a creepage distance of 485 mm as an example. The insulator model built in ANSYS is shown in Fig. 1.

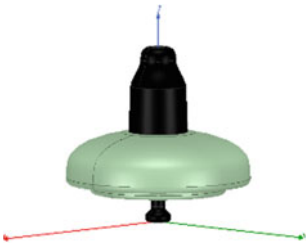

Fig. 1 Simulation model of the insulator

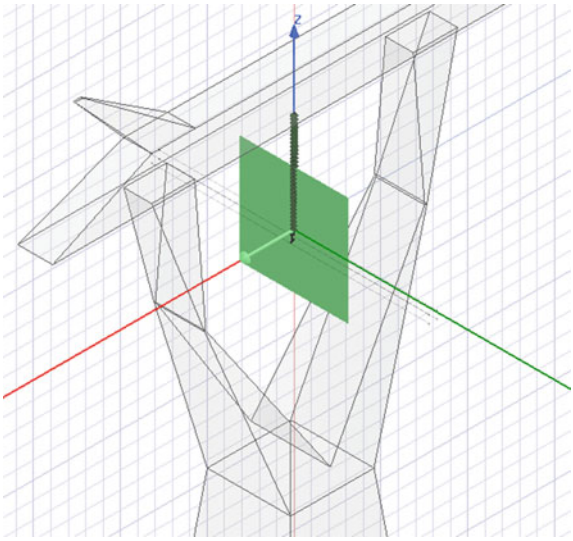

Fig. 2 Overall electric field simulation model

The three-dimensional model of the electric field including the whole of the tower and the insulator string is shown in Fig. 2.

2.2 Setting of Each Medium Simulation Parameter

The electric field of the insulator string at any instant can be considered to be stable, so it is treated as the electrostatic field in the simulation. The main materials of the model are: tower, steel foot, steel cap, iron, umbrella for porcelain, cement and aluminum for wire. The main material properties of the electrostatic field are relative dielectric constants, and they are shown in Table 1.

Table 1 Relative dielectric constant of each material

Material	Steel	Porcelain	Cement	Aluminum	Air
Relative permittivity	1	5.6	14	81	1.0006

2.3 Verification of Simulation Model

In ANSYS, the electrostatic field calculation is performed on the three-dimensional model of the insulator string, and the electric field cloud diagram of the cross section of the insulator string is shown in Fig. 3.

It can be seen from the simulation results that the electric field strength at both ends of the insulator string is higher. It is consistent with the actual electric field distribution.

A control line is drawn at the beginning and the end of the center of the insulator string, and the voltage difference between the steel leg and the steel cap of each insulators the distribution voltage of the insulator. The distribution voltage of the good insulator string is calculated as shown in Fig. 4. The measurement result of distribution voltage of the insulator string of a 500 kV line in Guizhou Province is shown in the red curve of Fig. 4. It can be seen that the result of simulation experiment is close to the actual voltage distribution, which shows the correctness of the simulation model, so that we can study the influence of the deteriorated insulator on the distribution voltage of the insulator string.

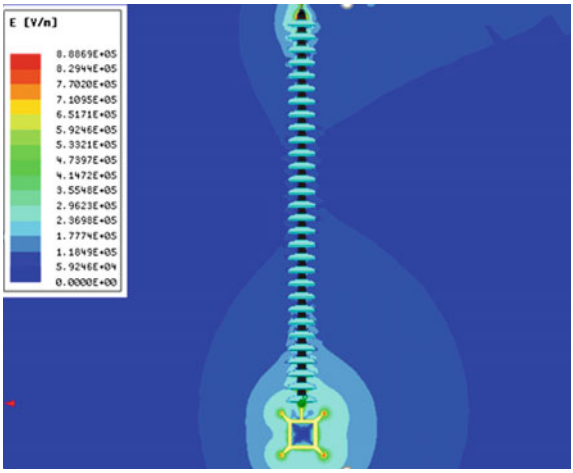

Fig. 3 Insulator string electric field distribution

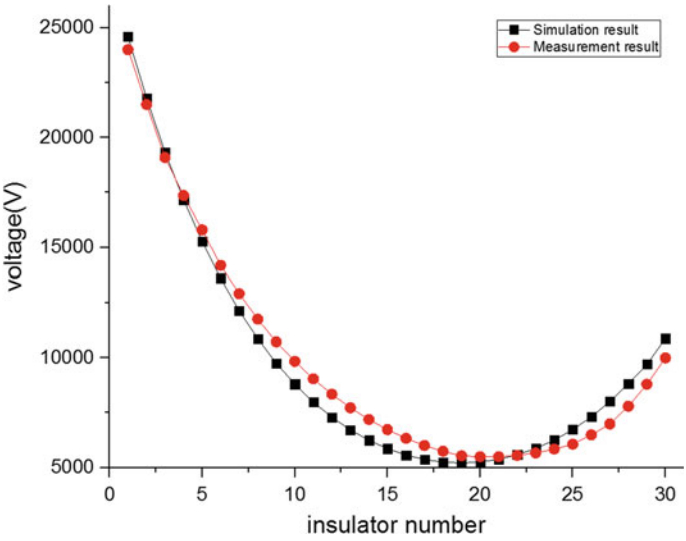

Fig. 4 Voltage distribution of the insulators

3 Effect of Degraded Insulator on Distribution Voltage Model of the Insulator and Tower

3.1 Simulation Model Parameter Setting for Deteriorated Insulator

The cross-section of the insulator in the simulation model is shown in Fig. 5.

Fig. 5 Cross-section of the insulator

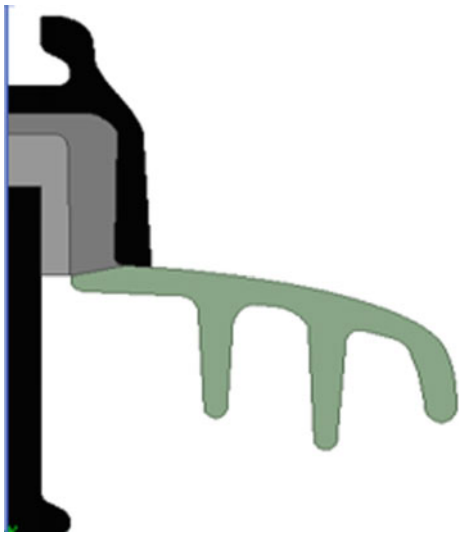

When the insulator with severe deterioration is in operation, the penetrating air gap existing in the porcelain and cement between the steel cap and the steel foot may be broken down and short-circuited, but the deteriorated mild insulator will not be completely short-circuited. Therefore, for the heavily deteriorated insulator, we have both the gray and dark gray portions set to the metal material. However, for the slightly deteriorated insulator, only the gray portion is set as the metal material.

3.2 *Effect of Different Degraded Insulators at Different Positions on Distribution Voltage*

In order to study the effect of deteriorated insulators with different degrees of deterioration on the distribution voltage of the insulator string, we first set the insulator at the head end position of the insulator string as a severely degraded insulator and a lighter deteriorated insulator. The simulation result distribution is shown in Fig. 6.

From Fig. 6, it can be seen that the distributed voltage on the deteriorated insulator is greatly reduced, which makes it easy to be identified from the voltage distribution of the insulator string. For insulators with a less deteriorated degree, the distribution voltage on the insulator will also decrease, but the magnitude is much smaller than that of the insulator with severe deterioration, and it is even difficult to see from the voltage distribution curve by the naked eye. Therefore, for a slightly

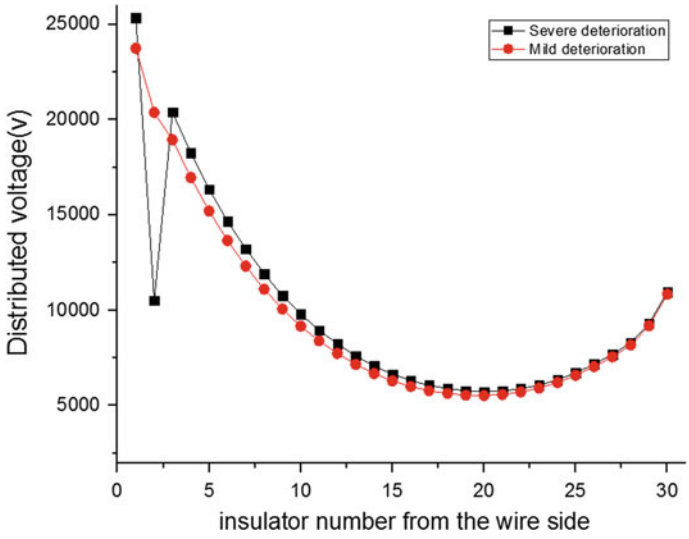

Fig. 6 Effect of different degraded insulators at the head

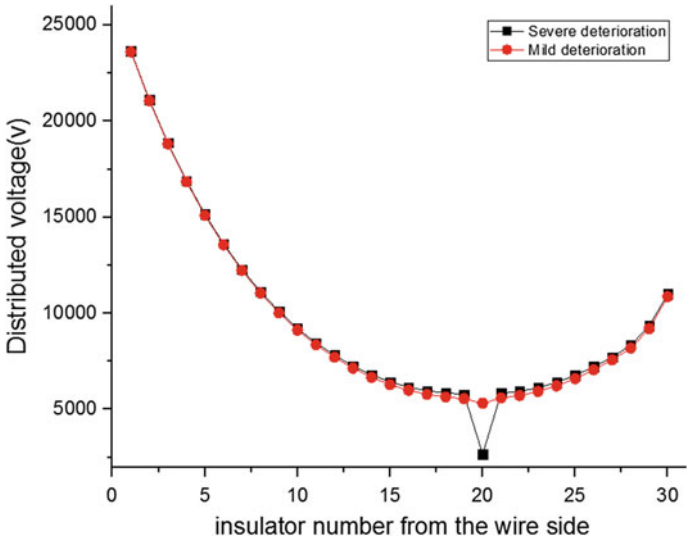

Fig. 7 Effect of different degraded insulators in the middle

deteriorated insulator, it is necessary to identify it by a distributed voltage curve of the insulator string by a certain mathematical method.

Similarly, in order to distinguish the influence of different positions, we also set the insulators at the middle and the end of the insulator string to be seriously deteriorated insulators and lighter deteriorated insulators. The simulation results are shown in Figs. 7 and 8.

From Figs. 6, 7, and 8, it can be seen that regardless of whether the deteriorated insulator is located at the head, middle or end of the insulator string, the degree of degradation has a uniform effect on the distributed voltage. However, when the degree of deterioration is the same, it can be seen that the voltage drop of the deteriorated insulator of the first part is more obvious, the end is second, and the middle part is the least obvious. Therefore, the lightly deteriorated insulator in the middle portion is more difficult to recognize, and the deteriorated insulator of the first portion is easily recognized.

3.3 Influence Between Adjacent Deteriorated Insulators

T A comparison of the distribution voltage of a good insulator string and an insulator string with a deteriorated insulator taking the 20nd piece as an example is shown in Fig. 9.

It can be seen from Fig. 9 that the voltage drop of the deteriorated insulator itself has an effect of increasing the distribution voltage of other insulators. In particular,

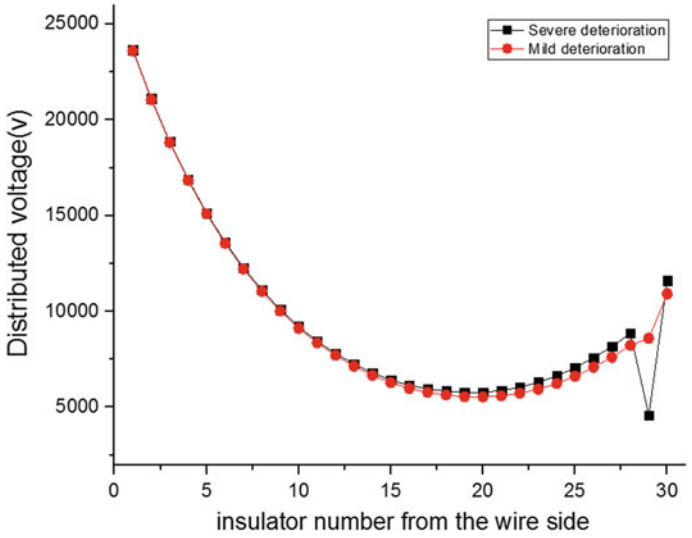

Fig. 8 Effect of different degraded insulators at the end

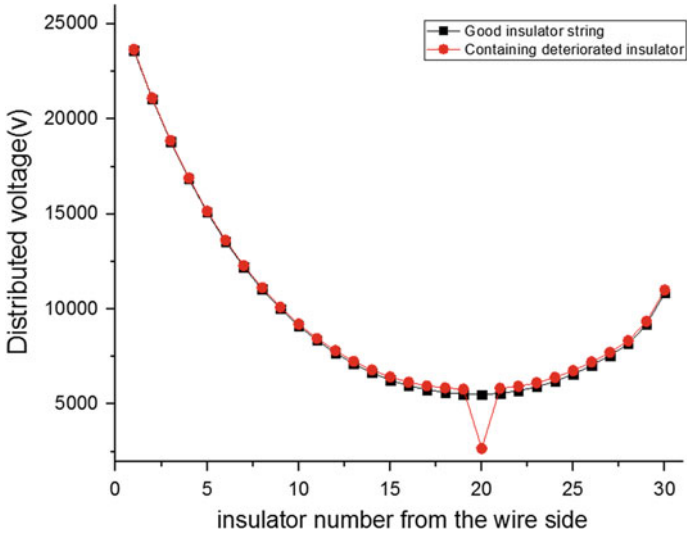

Fig. 9 Comparison of voltage distribution with or without deteriorated insulator

the adjacent insulators are greatly lifted, but as the distance is further, the effect is smaller. It can be seen from the figure that the adjacent four insulators on the left and right sides of the deteriorated insulator are greatly affected, and the influence becomes small when separated by four or more. Considering that the distance

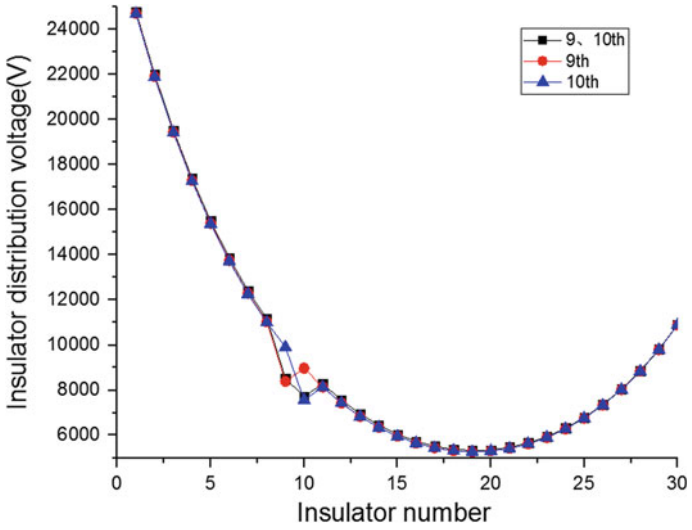

Fig. 10 Comparison of voltage distribution with or without deteriorated insulator

Table 2 Comparison of distribution voltage drop of adjacent deteriorated insulators

Degraded insulator number	Percentage of distribution voltage change (%)
9th, 10th	12.6, 12.4
9th	15.5
10th	15.4

between the two deteriorated insulators is relatively close, the voltage rises to the left and the voltage drop becomes smaller, so it is more difficult to identify. Therefore, we separately set the distribution of two pieces of deteriorated insulators adjacent to each other and separated by four insulators. The voltage is compared to study the effect of this effect.

When considering the influence of the adjacent time, the ninth and tenth pieces are taken as an example. The 9th and 10th sheets are respectively set to deteriorate simultaneously and deteriorate individually, and the comparison chart is as shown in Fig. 10. The calculation results of the distribution voltage drop percentage are shown in Table 2.

The two pieces of deteriorated insulator are arranged to be separated by four insulators, and the voltage drop calculation results are shown in Fig. 11 and Table 3.

It can be seen from the calculation results of Tables 2 and 3 that when the two pieces of deteriorated insulators are close to each other, the mutual voltage distribution is greatly affected, reaching 3%. As the distance increases, the impact becomes smaller. When separated by four pieces, the influence between each other

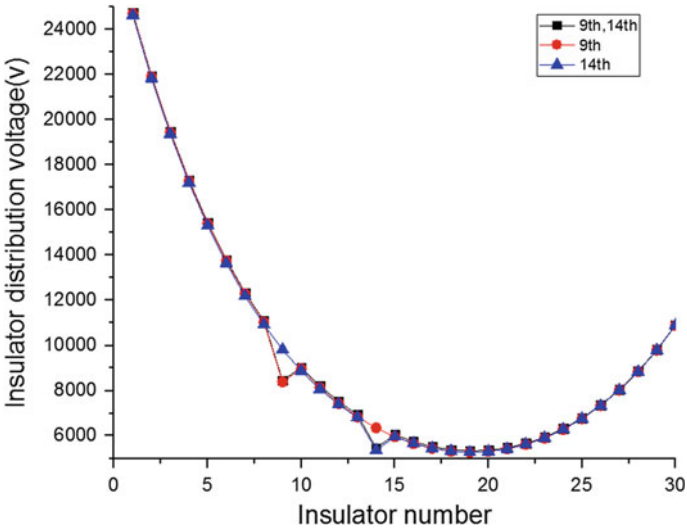

Fig. 11 Comparison of voltage distribution with or without deteriorated insulator

Table 3 Comparison of distribution voltage drop of adjacent deteriorated insulators

Degraded insulator number	Percentage of distribution voltage change (%)
9th, 14th	14.9,14.8
9th	15.5
14th	15.3

has been reduced by less than 1%. Therefore, when two pieces of the insulator are very close to each other, it is more difficult to detect by the distributed voltage method.

It can be seen from the calculation results of Tables 2 and 3 that when the two pieces of deteriorated insulators are close to each other, the mutual voltage distribution is greatly affected, reaching 3%. But as the distance increases, the impact is small. When separated by four pieces, the influence between each other has been reduced by less than 1%. Therefore, when two pieces of the insulator with a relatively low degree of deterioration are close to each other, it is more difficult to detect by the distributed voltage method.

4 Test

According to the installation environment of the insulator string, the experimental equipment is sequentially connected in the order of the crossarm, the insulator string and the wire, and the test platform shown in Fig. 12 is formed. A power-frequency voltage with a voltage effective value of 289 kV is applied to the insulator. The measurement of the distribution voltage of the insulator string is performed by the voltage measuring robot. The measurement of the distribution voltage of the insulator string is performed by the voltage measuring robot. The measurement result of distribution voltage of normal insulator string is shown in Fig. 13.

It can be seen that the voltage distribution of the test results is not as smooth as the simulation results. This is due to measurement errors in the measuring device.

In order to investigate the effect of insulators on voltage distribution at different degrees of deterioration, the eighth insulator was replaced with a deteriorated insulator with insulation resistance of about 100, 200, and 300 MΩ, that is, heavily deteriorated, moderately deteriorated, and slightly deteriorated insulator. The measurement results of the voltage distribution are shown in Fig. 14.

It can be seen from Fig. 14 that the voltage drop of the heavily deteriorated insulator is large and easy to discriminate, but the voltage drop of the moderately and slightly deteriorated insulator is relatively small, and it is prone to leakage through the voltage distribution. Especially for the slightly deteriorated insulator, its voltage drop is small, and it is easy to be misjudged directly by voltage distribution discrimination.

Fig. 12 Test platform of the insulators string

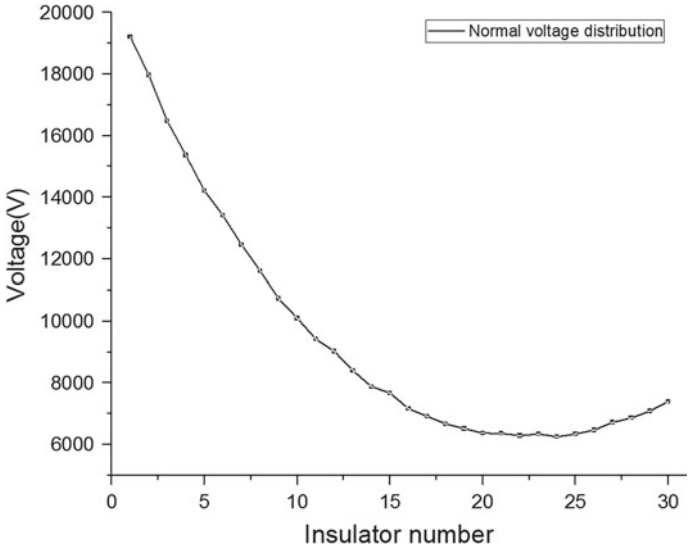

Fig. 13 Voltage distribution of normal insulator strings

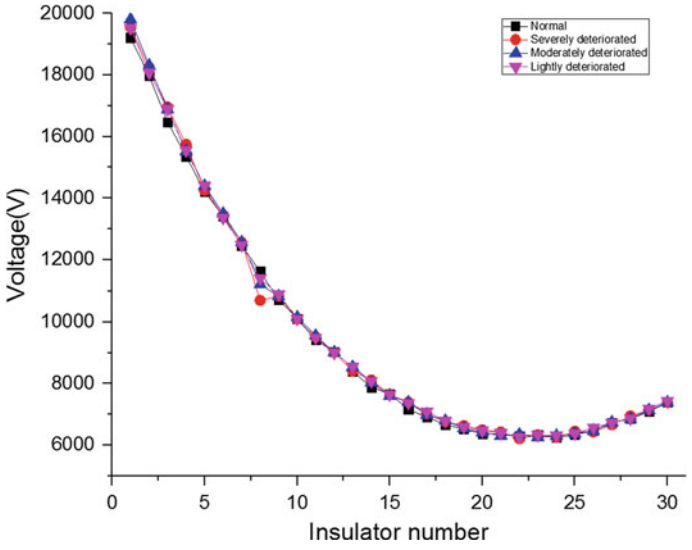

Fig. 14 Voltage distribution with a insulator of different degrees of deterioration

5 Conclusion

By simulating and testing the insulators with different degrees of deterioration at different locations, we can draw the following conclusions.

(1) The voltage drop of the heavily deteriorated insulator with insulation resistance below 100 MΩ is large, and it is easy to judge by voltage distribution.
(2) Insulators with a lighter degree of degradation have a lower voltage drop and may not be directly visible from the voltage distribution curve. Mathematical methods are needed for identification.
(3) When the degree of deterioration of the insulator is the same, it is easier to identify at the head, followed by the end, and finally the middle.

Fund Support State Grid Corporation of Science and Technology Guide Project (Key Technology Research and Equipment Development for Ultra High-Voltage EHV Long-Chassis Grid Power Transmission and Transformation).

Project Number: 524625170046.

About the author: Jian Li, male, (1967–), Ph.D. graduate student, Professor-level senior engineer, engaged in power grid construction and operation management.

References

1. Zhao Z (2013) High voltage engineering. China Electric Power Press
2. Huang X, Yang Y, Zhang W et al (2018) Method of gray density of porcelain insulators based on image enhancement. Autom Electr Power Syst 42(14):151–157
3. Li P, Fan J, Li G (2007) Electric field distribution calculation and grading ring design of insulators string for 1000 kV UHVAC lines. Electr Power 39(10):33–36
4. Liu Y, Tian J, Liu X (2010) Numerical analysis of potential distribution of porcelain insulator strings for 750 kV double-circuit transmission lines on the same tower. High Volt Eng 36 (7):1644–1650
5. Wu G, Wang T (1997) Effect of deteriorated insulators on the voltage distribution of long-chain insulators. High Vol Eng 23(4):59–60
6. Wei Z, Ling F, Jingyu M et al (2016) Recognition algorithm for ice thickness of transmission line insulators. Autom Electr Power Syst 40(21):195–202
7. Zhou Z, He J, Chen J (2006) Voltage equalizer ring to improve the insulator voltage distribution. High Volt Technol 32(11):45–48
8. Peng X, Nie Y, Liu Y (2006) Application of fuzzy pattern recognition in insulation detection of insulator strings. Autom Electr Power Syst 14:71–75
9. Ye L, Zhou W, Yang S et al (2015) Effects of contaminations on voltage distribution along insulator string. High Volt Electr Appl 51(09):103–108
10. Jiang X, Huang B (2008) Calculation of voltage distribution along insulator strings of UHVAC transmission line by electric-network method. High Volt Eng 34(1):7–70
11. Huo F, Gu L, Chen Y(2010) Simulation and test of potential distribution for 750 kV insulator string. High Volt Appar 46(3):49–52
12. Zhang D (2018) Heating and discharge mechanism of wet contaminated insulators. High Volt Technol (03):1–9

13. Zuo G, Ma L, Xu C et al (2019) Detection method based on cross-connected convolutional neural network. Autom Electr Power Syst 43(04):101–108
14. Zhang Y, Peng Z, Fu Q et al (2018) Influence of environmental humidity on voltage distribution and infrared thermal image detection of porcelain insulator strings. Power Syst Technol 42(04):1342–1349
15. Q/GDW 516-2010 (2010) Inspection code of deteriorating suspension insulators for 500–1000 kV transmission line

Research and Implementation of Conductive AC Charging Interoperability Test for Electric Vehicles

Xuan Zhang, Wei Zhang, Yuan Sun, Xuling Li and Lin Sang

Abstract With the rapid development of the electric vehicle industry, the charging interoperability problems are becoming more and more serious, and the requirements for charging reliability and safety are also getting higher and higher. AC charging is widely used because of easy to install and operate. Based on the existing AC charging system, this paper analyzed each charging state including the connection confirmation phase, charge ready phase, startup and charging phase, shutdown phase during the AC charging process. The interoperability test use cases of the vehicle and AC charging equipment were proposed. Through the construction of the interoperability test system, PWM signal parameters, the voltage of detection points, the transition between each state and the simulation of the abnormal faults for the vehicle and AC charging equipment were completed. Test results shown that the charging matching degree between the vehicle and the AC charging equipment using these protection strategies was improved. These effective measures minimized the safety risk and strengthen prevention capability of the charging process.

Keywords Interoperability · AC charging · Electric vehicle

1 Introduction

Due to prominent oil and environmental issues, the new energy industry is developing rapidly [1–3]. It is imperative to develop new energy vehicles. The number of new energy vehicles in China is increasing at a rate of more than 100% per year. The United States and European countries are launching a plan to ban fuel vehicles, and global new energy vehicles are welcoming a rapid development stage.

X. Zhang (✉) · W. Zhang · Y. Sun · X. Li · L. Sang
NARI Group Corporation/State Grid Electric Power Research Institute, Nanjing 211106, China
e-mail: zhangxuan2@sgepri.sgcc.com.cn

Y. Xue et al. (eds.), *Proceedings of PURPLE MOUNTAIN FORUM 2019-International Forum on Smart Grid Protection and Control*, Lecture Notes in Electrical Engineering 585, https://doi.org/10.1007/978-981-13-9783-7_71

According to the statistics of China Electric Vehicle Charging Infrastructure Promotion Alliance (EVCIPA), the number of charging infrastructure in the year of 2018 was 808,000, including 330,000 public piles and 480,000 private piles. The number of possessions had increased by 350,000 compared with 2017. There were 190,000 public AC charging equipment. Large-scale vehicles and charging facilities were put on the market, which brought higher demands on charging interoperability and safety.

However, from the effect of the implementation of GB/T 18487.1-2015 [4] and the market feedback, the safety and reliability were still important issues for the charging interoperability. Domestic testing laboratories and research institutes had carried out research on electric vehicle AC charging. Mr.Sun analyzed the main cause of unqualified parameters of PWM signal [5]. Mr.Zhu designed the interoperability testing for AC charging equipment [6]. Mr.Yin proposed the measures to improve the BMS(Battery Management System) fault response rate of the charging facility by using the analytic hierarchy process [7]. An algorithm to calculate the short-term reserve capability of EV (given by Mr.Wu) [8] and a variable threshold optimization algorithm (given by Mr.Zhou) [9] were both aimed at Vehicle-to-Grid technology to improve the imbalance between power supply and demand. These studies had not focused on the interoperability requirements for electric vehicles and the AC charging equipment. This paper presented the interoperability test use cases based on the AC charging process, proposed corresponding security solutions, and verified these test methods in the laboratory.

2 AC Charging System

2.1 Charging Mode

Charging mode is the method for connection of an electric vehicle to the supply network to supply energy to the vehicle [10]. AC charging mainly uses mode 2 and mode 3.

Mode 2 is a method for the connection of an electric vehicle to a standard socket-outlet (based on GB 2099.1 and GB 1002 in China or corresponding to the relevant IEC standards) of an AC supply network utilizing an AC supply equipment with a cable and plug, with a control pilot function and system for personal protection against electric shock placed between the standard plug and the electric vehicle. AC charging equipment using Mode 2 charging shall provide a protective earthing conductor from the standard plug to the vehicle connector.

The rated values for current and voltage shall not exceed:

- 8 A and 220 V AC single-phase for standard socket-outlet with 10A;
- 13 A and 220 V AC single-phase for standard socket-outlet with 16A.

Mode 3 is a method for the connection of an electric vehicle to an AC supply equipment permanently connected to an AC supply network, with a control pilot function that extends from the AC supply equipment to the electric vehicle. Electric vehicle charging equipment using Mode 3 charging shall provide a protective earthing conductor to the socket-outlet and/or to the vehicle connector.

2.2 Charging Connection

AC charging mainly uses case B connection and case C connection. For supply current greater than 32A AC, it should be used case C connection.

Case B connection is connection of an electric vehicle to a supply network with a cable assembly detachable at both ends, as shown in Fig. 1.

Case C connection is connection of an electric vehicle to a supply network utilizing a cable and vehicle connector permanently attached to the electric vehicle charging station, as shown in Fig. 2.

2.3 Typical Control Pilot Circuit

The typical control pilot circuit is shown in Fig. 3. The detail definition of parameters is in GB/T 18487.1-2015 Annex A. The circuit in the AC charging equipment side is composed of the supply control device, contactors K1 and K2, resistor R1 and switch S1, and in the vehicle side includes resistors R2, R3, diode

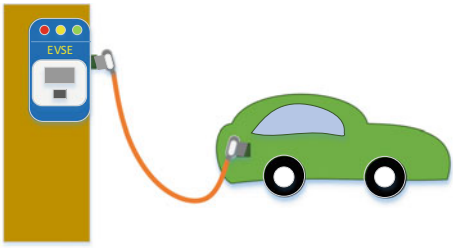

Fig. 1 Case B connection

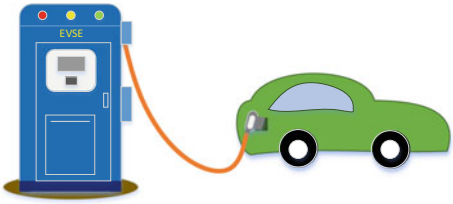

Fig. 2 Case C connection

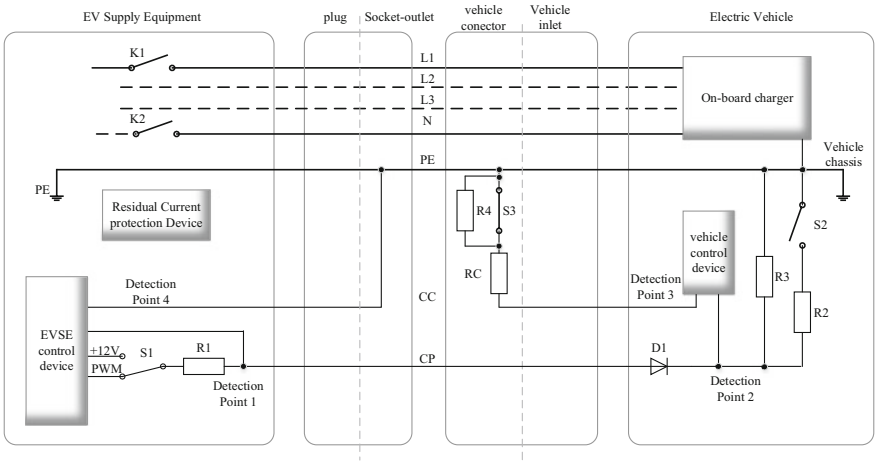

Fig. 3 Typical control pilot circuit for Case B connection under charging mode 3

D1, switches S2 and S3, on-board charger and vehicle control device. Resistor R4 and RC are mounted in the vehicle connector. Switch S1 and S2 are internal switches. After the vehicle coupler and the plug and socket-outlet are fully connected, the electronic lock shall be completed locked. When the vehicle finishes self-checking and detectes PWM signals, switch S2 shall close. Then the AC charging equipment will start charging. Other control pilot circuits also have Charging Mode 2 and Case C Connection under Charging Mode 3.

Before charging, the AC charging equipment measures the voltage value of detection point 1 or 4 to judge whether the plug and the socket-outlet are fully connected. The vehicle control device measures the voltage value of detection point 3 to judge whether the vehicle connector and the vehicle inlet are fully connected. If the AC charging equipment has no failure and the connector and inlet have been fully connected (for case B connections under charging mode 3), switch S1 shall change from the +12 V status to the PWM status, and the PWM signal shall be output to the vehicle. If the on-board charger finishes self-detection and finds no failure, PWM signal shall be detected on the detection point 2 of the control pilot circuit, switch S2 shall be closed. Then, the AC charging equipment conducts AC power supply circuit and outputs the voltage. During the charging, the maximum supply capacity is controlled by the vehicle control device through the duty cycle of the PWM signal at detection point 2, the rated capacity of the cable by judging the resistance value between detection point 3 and PE. When the expected the shutdown requirement is reached, swiping the card and other triggering shutdown signal can stop charging process normally.

3 Interoperability Test for AC Charging

3.1 Interoperability Test Use Cases

According to the working principle of the AC charging system, interoperability test use cases for AC charging were given in Table 1.

Table 1 Interoperability test use cases for AC charging

Use case name	Use case item	Test object
Charging coupler test	Structural size test	EV/AC charging equipment
	Plug space size test	EV/AC charging equipment
	Inlet space size test	EV/AC charging equipment
Charging state test	Connection confirm phase test	EV/AC charging equipment
	Charge ready phase test	EV/AC charging equipment
	Startup and charging phase test	EV/AC charging equipment
	Normal shutdown phase test	EV/AC charging equipment
Connection control timing test		EV/AC charging equipment
Charging control output test	PWM duty cycle change test	EV
	PWM duty cycle overrun test	EV
	PWM frequency overrun test	EV
Charging error state test	Switch S3 open test	EV
	CC pin/line broke test	EV/AC charging equipment
	CP pin/line broke test	EV/AC charging equipment
	CP earthing test	AC charging equipment
	PE continuity loss test	AC charging equipment
	Over-current test	AC charging equipment
	Switch S2 re-close test	AC charging equipment
	AC supply power loss test	EV/AC charging equipment
	PWM signal loss test	EV
Charging control pilot circuit test	CP circuit voltage test	EV/AC charging equipment
	CC circuit resistance test	EV

In addition to normal charging state and process, charging interoperability test use cases were specifically designed for typical faults, such as abnormal charging coupler connection fault, abnormal control pilot signals, etc. occurred during actual charging in the field. These were more likely to cause charging safety hazards on charging equipment, vehicle and users.

3.2 Interoperability Test System

Interoperability test system for AC charging equipment was shown in Fig. 4, mainly including AC power supply, AC load, electric vehicle control simulation box/AC charging equipment control simulation box, measuring instruments (such as oscilloscope, signal generator, etc.), main control unit, etc. AC charging equipment was set to work under rated load condition, and test condition contained failure test of rated operating condition and parameter which were out of normal range. The vehicle under test needed to be discharged before the test to facilitate subsequent testing.

3.3 Coupler Interoperability Test Requirement

AC supply coupler and vehicle coupler shall meet the requirements of GB/T 20234.1-2015 [11] and GB/T 20234.2-2015 [12]. The dedicated gauge and the scale division of 0.02 mm or similar metrological apparatus were provided to check the critical dimensions of AC charging coupler (vehicle connector, vehicle inlet, plug, and socket-outlet). Insertion of connector into vehicle inlet and plug into socket-outlet is intuitively obvious and free of multiple orientations.

Fig. 4 AC charging interoperability test system

Latch mechanism is present and prevents inadvertent or accidental decoupling. The socket-outlet and vehicle inlet under more than 16A shall have the electronic locking device to prevent accidental disconnection during charging. When electronic lock is not reliably locked, the AC charging equipment or the vehicle shall stop charging or not start charging.

4 Test Procedure and Results

4.1 Test Condition

Connecting to the test system, the interoperability test on AC charging equipment and electric vehicles were done separately. Key parameters, such as the voltage of detection point 1, the voltage of detection point 3 voltage (if possible), PWM signal parameters, charging voltage, charging current, abnormal trigger signals were collected by the measuring instruments.

4.2 Control Pilot Parameters Test

The AC charging equipment sample was a single-phase output with a maximum current of 16A AC. Result of control pilot parameters were given in Table 2. During the charging (state 3), the voltage of detection point 1 was within the standard range, and the AC charging equipment allowed normal charging.

4.3 Charging State Test

AC charging only relied on PWM signal parameter changes for communication, so the vehicle and the AC charging equipment had higher requirements on the PWM

Table 2 The result of control pilot parameters

Charging state	Detecting point 1 (V)	Detection point 4	PWM duty cycle	PWM frequency	Rise/fall time
State 1	12.2	≠0	–	–	–
State 2	8.97	0	–	–	–
State 2′	9.00 −12.2	0	27.01%	1000 Hz	4.244 μs 5.605 μs
State 3	5.89	0	–	–	–
State 3′	5.80 −12.2	0	26.99%	1000 Hz	3.428 μs 7.833 μs

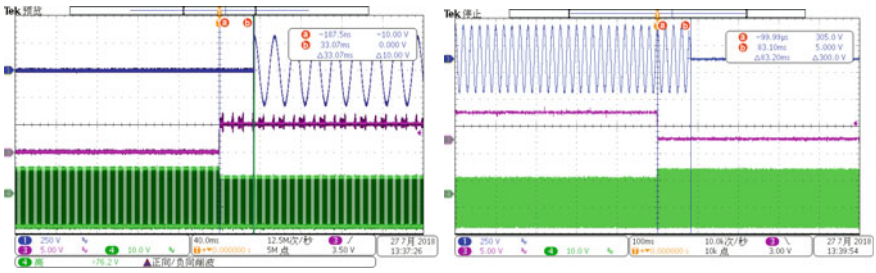

(a) charging state 2'-> state 3' (b) charging state 3'-> state 2'

Fig. 5 The result of AC charging transition process test

output timing and signal parameter quality. See Fig. 5, the charge state transition process for the charge start phase and the normal shutdown phase was shown respectively. When the vehicle was ready for charging (closed switch S2), the AC charging equipment would conduct the AC power supply circuit within 3 s. When the vehicle stopped charging (open switch S2), the AC power supply circuit would disconnect within 100 ms.

4.4 Charging Error Test

During the charging process, abnormal fault might occur, such as the vehicle connector unplugged, the protection earth continuity loss, etc. By corresponding protective measures, the vehicle and the AC charging equipment should detect the fault in time and stop charging (see Fig. 6). These means ensured the user's personal safety and equipment reliability.

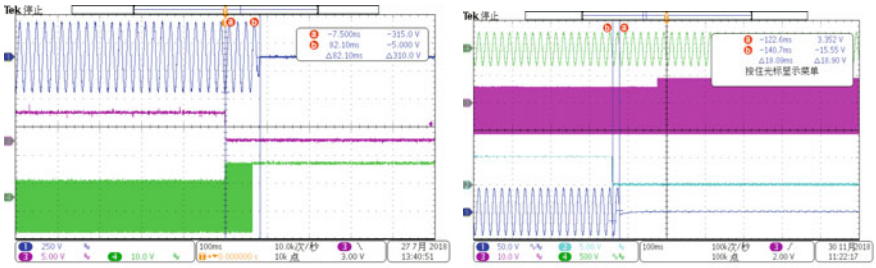

(a) unplug during charging (b) open switch S3during charging

Fig. 6 The result of AC charging abnormal shutdown test

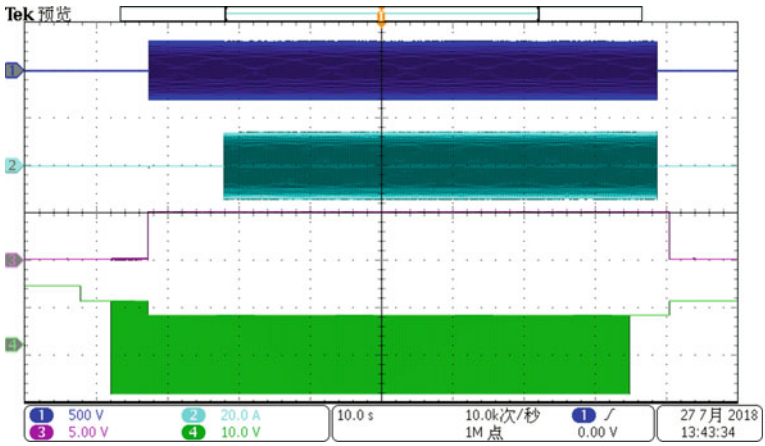

Fig. 7 The result of AC charging process

4.5 Charging Timing Test

After testing the vehicle and the AC charging equipment separately, we had to verify the charging ability. The charging process was shown in Fig. 7. During the test period, the charging process was stable and reliable without any abnormal shutdown.

To further verify the rationality of these test methods, our laboratory organized electric vehicle charging interoperability test activity. 12 domestic mainstream AC charging equipment, 4 pure AC charging vehicles and 9 AC and DC charging vehicles had accomplished on-site matching test. The qualification rate of one charge matching was 94.5%. Most of the problems were mainly the response timeout for abnormal faults. Later, the manufacturers would modify and improve the design according to the standard requirements.

5 Conclusion

This paper deeply analyzed the AC charging system of electric vehicles, and proposed the interoperability test use cases of the vehicle and AC charging equipment. By constructing an interoperability test system, the evaluation of safety and interoperability between the charger and the vehicle during the charging process was realized in the laboratory. The test results shown that after the relevant tests in the laboratory, the degree of charging matching in the field was greatly improved.

The part of recommended test methods had been written into national standards (GB/T 34657.1-2017 [13] and GB/T 34657.2-2017 [14]). Follow-up research will focus on the safety issues in the field operation and use, continue to improve relevant test methods, implement more scientific test methods, analyze and solve more problems in the actual charging process, to ensure safely and reliably charging.

Acknowledgements This work was supported by Science and Technology Project of State Grid Corporation of China (Study on Key Technologies for Warning Intelligent Diagnosis and Safety Early and Operation and Maintenance Service System of Electric Vehicle bi-directional charging).

References

1. Li LL (2017) Interpretation and prospect of China's electric vehicle charging infrastructure policy. Distrib Util 34(1):2–7 (in Chinese)
2. Yue WZ, Zhang J, Liu YQ (2019) A study on the relationship between industrial policy and market performance: a case study of China's electric vehicle charging infrastructure. Res Econ Manag 40(2):82–94 (in Chinese)
3. Luo WY, Zhou H, Li JB (2017) Summary of the development status of electric vehicle charging facilities at home and abroad. Mech Electr Inf (24):156–157 (in Chinese)
4. GB/T 18487.1–2015 (2015) Electric vehicle conductive charging system–part 1: general requirements. Standards Press of China, Beijing (in Chinese)
5. Sun Y, Dan FZ, Sang L, Zhang X (2017) Statistic and analysis on typical problem of PWM signal of AC charging spot. Electr Meas Instrum 54(23):118–122 (in Chinese)
6. Zhu B, Hou XZ, Sun HL et al (2017) Study of interoperability test method on electric vehicle charging equipment. Electr Meas Instrum 54(22):71–76 (in Chinese)
7. Yin ZD, Wang S, Zhang YX et al (2017) Assessment of response of charging facilities to protection demands of battery management systems. Autom Electr Power Syst 41(22):133–137 (in Chinese)
8. Wu JA, Xue YS, Xie DL et al (2018) Evaluation and simulation analysis of reserve capability for electric vehicles. Autom Electr Power Syst 42(13):101–107 + 168 (in Chinese)
9. Zhou TP, Sun W (2018) Electric vehicle-to grid technology based on microgrid. Autom Electr Power Syst 42(03):98–104 + 117 (in Chinese)
10. IEC 61851–1:2017 (2017) Electric vehicle conductive charging system–part 1: general requirements. https://webstore.iec.ch/publication/33644
11. GB/T 20234.1–2015 (2015) Connection set for conductive charging of electric vehicle–part 1: general requirement. Standards Press of China, Beijing (in Chinese)
12. GB/T 20234.2–2015 (2015) Connection set for conductive charging of electric vehicle–part 2: AC charging coupler. Standards Press of China, Beijing (in Chinese)
13. GB/T 34657.1–2017 (2017) Interoperability test specifications of electric vehicle conductive charging–part 1: supply equipment. Standards Press of China, Beijing (in Chinese)
14. GB/T 34657.2–2017 (2017) Interoperability test specifications of electric vehicle conductive charging–part 2: vehicle. Standards Press of China, Beijing (in Chinese)

Electric Vehicle DC Charger Charging Protocol Conformance Testing System

Xuling Li, Xuefeng He, Chen Dong, Xuan Zhang and Lin Sang

Abstract With the development of electric vehicle industry, the charging compatibility between charging facilities and electric vehicles has become the focus of attention of charging operators, charging facilities manufacturers, electric vehicle manufacturers and users. For electric vehicle DC charging, the communication protocol between the DC charger and electric vehicle plays an important role in the interoperability of chargers and vehicles, which is the basis for realizing charging information exchange and charging control, and is the guarantee for safe charging of DC electric vehicles. This paper firstly introduces the charging time-sequence and communication protocol between DC chargers and electric vehicles, then designs the DC charger protocol conformance testing system, which can verify the communication message of dc charging communication protocol, the timeout processing of BMS message, the consistence of charging output, and the abnormal processing of vehicle charging. Currently, the system has been widely used in the field test and laboratory test for DC chargers with significant effect.

Keywords Electric vehicle · DC charger · Conformance test

1 Introduction

With the large-scale development and market operation of electric vehicles and charging facilities, the charging compatibility between charging facilities and electric vehicles has become the focus of attention of charging operators, charging facilities manufacturers, electric vehicle manufacturer and users [1]. In October 2017, the Standardization Administration of the P.R.C. released three Chinese national standards for electric vehicle conductive charging interoperability testing and protocol conformance testing [2–5], this series of standards specifies the

X. Li (✉) · X. He · C. Dong · X. Zhang · L. Sang
NARI Group Corporation/State Grid Electric Power Research Institute,
Nanjing 211106, China
e-mail: lixuling@sgepri.sgcc.com.cn

Y. Xue et al. (eds.), *Proceedings of PURPLE MOUNTAIN FORUM 2019-International Forum on Smart Grid Protection and Control*, Lecture Notes in Electrical Engineering 585, https://doi.org/10.1007/978-981-13-9783-7_72

Inspection specifications and test conditions for conductive charging system in physical interface, control pilot circuit, dc charging communication protocol, etc. The standard GB/T34658-2017 "conformance test for communication protocols between off-board conductive charger and battery management system for electric vehicle" specifies the testing for communication transmission rate between DC charger and vehicle, message frame format, charging message, charging logic, exception handling in different charging stages, moreover, this protocol conformance test is used as the basis of other interoperability testing items.

This paper introduces the charging process and charging protocol between the electric vehicles and DC chargers, designs a charging protocol conformance test system, and classifies test cases based on the test standard of GB/T34658-2017, introduces relevant testing methods.

2 EV DC Charging Protocol

The communication network between the dc charger of electric vehicles and vehicles is based on CAN2.0. The physical layer and the data link layer follow SAE J1939-11 [6] and SAE J1939-21 [7], respectively, and the application layer adopts the method of periodic transmission and event-driven to complete the charging information interaction [8].

The whole charging process is divided into four stages: low-voltage auxiliary power-on and charging handshake phase, charging configuration phase, charging phase, and charging end phase. DC charging control pilot circuit sequence [9] cooperates with communication logic, communication message exchange to complete charging and abnormal processing.

After the charging coupler is mated, the charger and the vehicle confirm the connection according to the respective detection point voltages, and start the communication process after the charger completes self-inspection, which includes low-voltage auxiliary power-on, identity identification and pre-charge insulation detection. In the charging parameter configuration stage, charging parameters from each side are matched, and the charger completes the pre-charging process. In the charging stage, the vehicle BMS sends the charging request according to the output capacity of the charger and its own demand, and the charger adjusts the output voltage and current. At the same time, the two sides interact with real-time information such as voltage, current, temperature and traction battery state, and take this as the basis for the abnormal evaluation. At the end of charging, it is used to settle the electric quantity, charging time, SOC value and other related information. Figure 1 shows the DC charging process and the interactive information at each stage, where K1 and K2 are output contactors on the charger side, and K5 and K6 are charging contactors on the vehicle side.

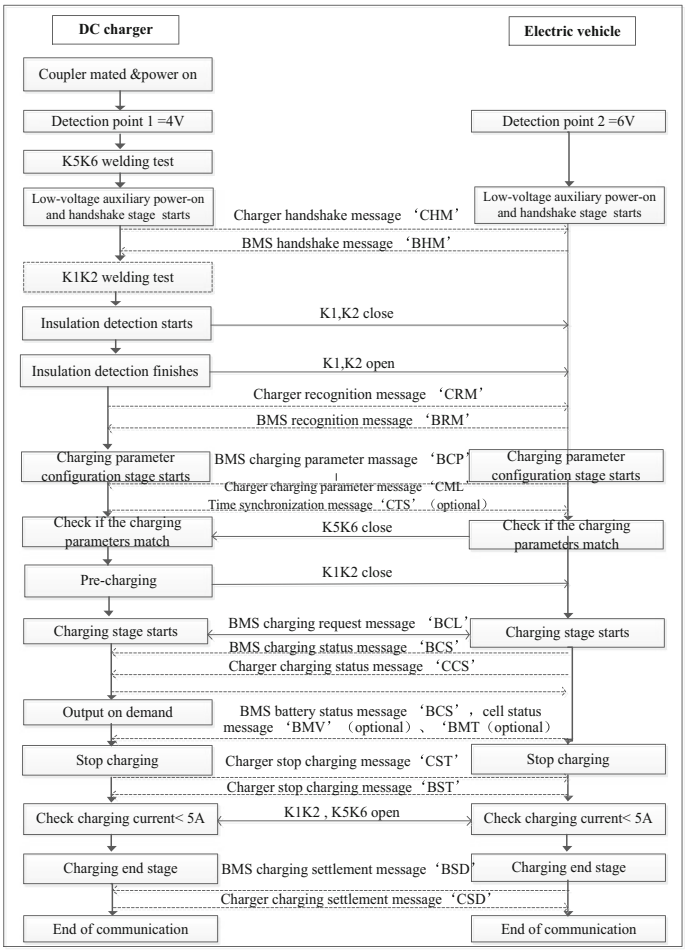

Fig. 1 Flow chart of DC charging

3 DC Charger Protocol Consistency Test System

As shown in Fig. 2, the DC charger protocol conformance test system consists of three parts: vehicle control pilot circuit simulation device, vehicle battery simulation device, and protocol conformance test software. In order to measure the voltage of each detection point of the pilot circuit and collect the actual output of the sample, measuring instruments such as power analyzers, oscilloscopes are also be used in this system.

The vehicle control pilot circuit simulation device is shown in Fig. 3, including vehicle inlet and vehicle charging contactors K5, K6. Among them, DC+, DC−, PE, CC1, CC2, A+, A−, S+, S− are designed in the form of jack, which is

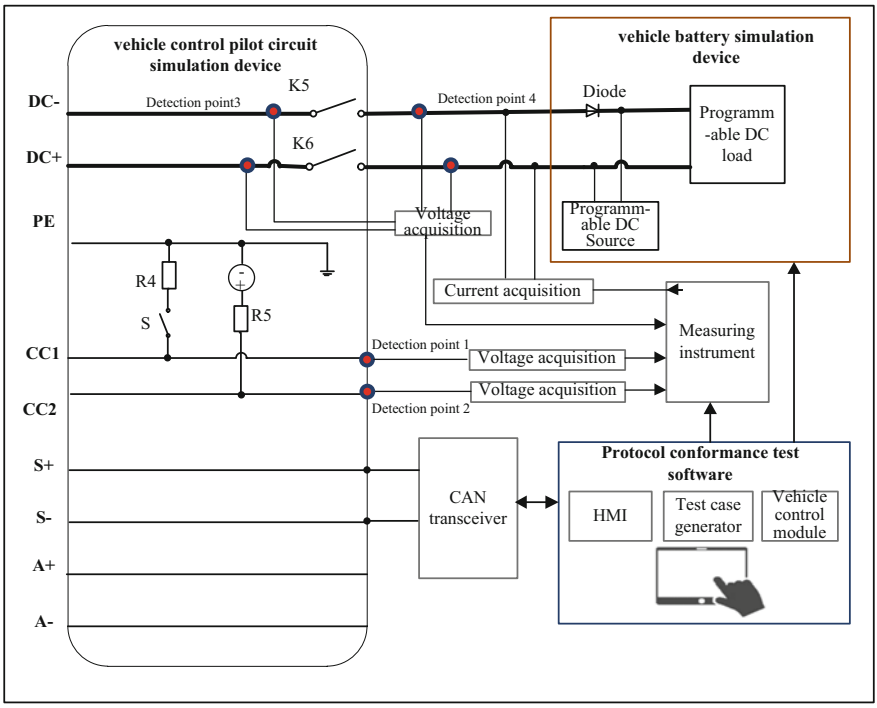

Fig. 2 Structure chart of DC charger conformance test system

Fig. 3 Electric vehicle control pilot simulation device

convenient to connect oscilloscope, multimeter probe and other external portable measuring instruments; the CC1 line is equipped with a resistor R4 of 1 KΩ, in order to reduce the repeated insertion and removal of the charging coupler during the test, a S dial switch is equipped to analog cable connection and disconnection. Contactors K5 and K6 are controlled by the vehicle controller. In the charging

Table 1 Description of the check points

Detection point	Description
Detection point 1	The voltage value between CC1 and PE, the voltage range of the detection point 1 is [3.2 V, 4.8 V] when the charger is completely connected, and the indicator light is green
Detection point 2	The voltage value between CC2 and PE, the voltage range of the detection point 2 is [5.2 V, 6.8 V] when the charger is completely connected, and the indicator light is green
Detection point 3	The voltage value between DC+, DC−, the voltage inside the charger output contactor K1, K2, when K1 and K2 close, it is consistent with the voltage of the detection point 4, when K1 and K2 open, it is the output voltage of the charging module
Detection point 4	The voltage value between DC+, DC−, the voltage outside the charger output contactor K1, K2, when K1 and K2 close, it is consistent with the voltage of the detection point 3, when K1 and K2 open, it is the battery voltage

parameter configuration stage, when the vehicle is ready, K5, K6 close and conduct the charging circuit, electric vehicle and charger will enter the normal charging process by interacting communication message. CC2 line is equipped with a resistor R5 of 1 KΩ and a power supply of 12 V. When the charging cable is inserted into the vehicle control pilot circuit simulation device, the tested charger determines whether the charger is completely connected by detecting the voltage value change of detection point 1: when the voltage value at the detection point 1 change from 6 to 4 V, it indicates that the charger connection is completed and communication can start. Similarly, the vehicle controller determines the connection status of the coupler according to the voltage at detection point 2. Table 1 is a detailed description of each detection point in Fig. 2.

The vehicle battery simulation device includes a programmable DC power supply and a DC load, which are controlled by a vehicle control module of the protocol conformance test software. The DC power supply is used to simulate the battery voltage output. During the charging parameter configuration phase, after the vehicle controller closes contactors K5 and K6, the charger needs to check the consistency between the actual battery voltage and the interaction voltage value in the communication message. Therefore, the analog value of the battery voltage should be consistent with the parameter in the communication message. During the charging process, the output voltage and current of the charger changes within the specified range through load adjustment.

The protocol conformance test software includes the test cases related to the standard GB/T34658. Moreover, the software is a closed-loop system [10, 11] and supports secondary development, users can customize new test cases. It can automatically execute the test cases, which improves the test efficiency.

Figure 4 shows the protocol conformance test software, which includes data acquisition and processing, human-machine interface, test case generation, vehicle control and other function. The test software receives the message through the

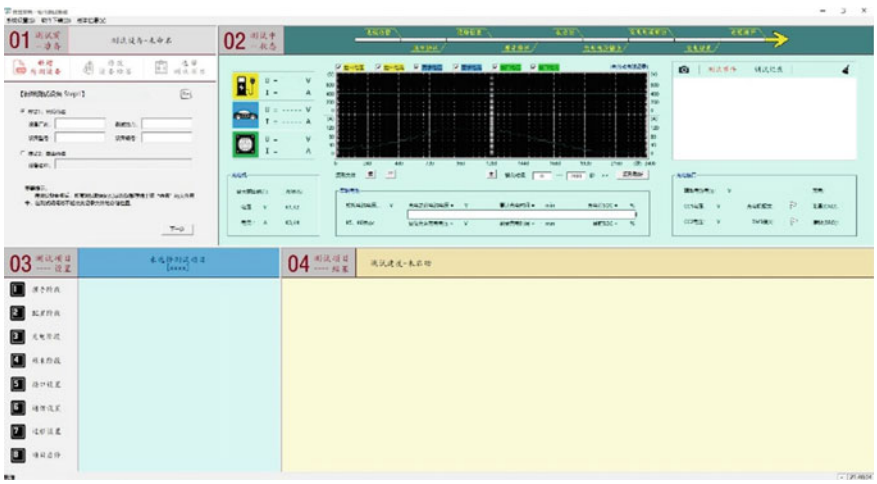

Fig. 4 HMI of DC charger conformance test software

Vector CAN controller, and the relevant information is transmitted to the vehicle control module after analysis, so as to complete the control of the vehicle battery simulation device and charging contactors. The human-machine interface is used to display interface-related connection status, vehicle contactors K5, K6 continuity, communication message parameter information, test case details and test status information, etc.

Before the test begins, the interface state of the test device shall be set firstly. CC1, CC2, PE, S+, S−, A+ and A− (the system does not need the auxiliary power supply provided by the charger under test; A+ and A− are normally connected) shall be set as connected state, and DC+ and DC− as disconnected state.

After the charging cable of the charger under test is connected to the vehicle control pilot circuit simulation device, the test system judges that the connection is completed according to the voltage of the detecting point 2, the indicator light at detection point 2 turns green, and the protocol conformance test software can be used to pick test cases and set message parameters at each stage.

4 Testing Method

4.1 Test Cases and Classification

The charging conformance test between electric vehicle DC charger and vehicle includes physical layer test, data link layer test and application layer test [12]. This paper focuses on the application layer charging consistency testing. In order to facilitate the test, according to different test methods of test cases, the test cases (see

first column of Table 2) can be divided into four categories: (1), Verification of communication message of charger; (2), Verification of BMS message timeout processing; (3), Verification of Output consistency; (4), vehicle charging abnormal processing verification, as shown in Table 2. In fact, in other application scenarios, such as high-power charging, plug and charge etc., test cases of protocol consistency also can be classified and tested in this way. The test case classifications sorted according to GB/T34658-2017 are shown in Table 2.

Table 2 DC charger protocol conformance test cases

Test case ID	Test case item	Category
DP1001, DP1002	CHM message communication logic, period, message format	1
DP1003	CRM message communication logic, period, message format	1
DN1001, DN1002, DN1003	Timeout processing of receiving BRM message	2
DN1004	Timeout processing of receiving BCP message	2
DP2001, DP2002	CML, CTS (optional) message communication logic, period, message format	1
DP2003	CRO message communication logic, period, message format	1
DP1002	K5K6 welding test	4
DP1002	Insulation detection output voltage test	3
DN2001, DN2002	Timeout processing of receiving BCP message	2
DN2003–DN2008	Timeout processing of receiving BCP message	2
DN2009	Welding test of vehicle charging contactors	4
DN2010	Timeout processing of receiving BCL message	2
DP2003	Pre-charging test	3
DP3001	CCS message communication logic, period, message format	1
DP3002	Receiving BMV, BMT message test	2
DP3003–DP3005	Vehicle abnormal state fault handling	4
DP3006, DP3007	CST message communication logic, period, message format	1
DN3001, DN3003, DN3005, DN3007	Timeout processing of receiving BCS message	2
DN3002, DN3004, DN3006, DN3008	Timeout processing of receiving BCL message	2
DN3009, DN3010	Timeout processing of receiving BST message	2
DP4001, DP4002	CSD message communication logic, period, message format	1
DN4001–DN4004	Timeout processing of receiving CSD message	2

In the table, the first number of the test cases ID represents the charging stage, 1 is for low-voltage auxiliary power-on and handshake stage, 2 is for charging parameter configuration, 3 is the charging stage, and 4 is the charging end stage.

4.2 Test Method

Verification of Communication Message of Charger
This type of test item is to verify the validity of the message sent by the tested charger at each stage, the communication logic of the message (start/end transmission condition), the message period, the message format, and the parameter value definition. The test system simulates the control pilot sequence and communication flow of the BMS under normal charging conditions according to Fig. 1. The oscilloscope records the actual output voltage and current of the corresponding detection points in each stage, and the synchronous CAN controller receives messages to make qualification judgment.

Verification of BMS Message Timeout Processing
The purpose of this type of test items is to verify whether the charger under test fails to receive BMS message due to communication fault, or if the communication status is good but the received BMS message is not meet requirements. If the correct message is not received within the timeout period, the tested charger should send the current message according to the period and maintain the current control pilot state. Otherwise, the corresponding timeout information should be written in error message that will be sent to the other side. During the communication process, the test system simulates communication failures by disconnecting or shorting the S + and S− lines, and simulating the wrong BMS communication messages through the protocol conformance test software.

Table 3 shows the time tolerance requirements of communication messages.

Verification of Output Consistency
Insulation detection output voltage test. This test item is to verify whether the output voltage value of insulation detection of the charger meets the smaller values of "maximum allowable charging voltage of BMS" and "maximum output voltage of the charger" at the stage of low-voltage auxiliary power-on and handshake. The test system simulates the vehicle communication handshake message (message

Table 3 Tolerance requirement of message time

Parameter	Nominal(t)	Tolerance
Time-out time	1 s	+0.2 s
	5 s	+0.5 s
	$\geq$ 10 s	+3 s
Cycle time	10 ms	±3 ms
	$\geq$ 50 ms	±(t × 10%) ms

code 'BHM') "total maximum allowable charging voltage" within the scope of the output voltage of the charger, higher than the maximum output voltage of the charger limit, lower than the minimum output voltage of the charger. Whether the insulation detection output voltage meets the requirement is judged by the voltage value of the detection point 3.

Pre-charging testing. The test item is to verify whether the pre-charge process of the tested charger during the charging parameter configuration phase is consistent with the standard. The test system simulates the normal vehicle battery voltage (i.e., the tolerance of voltage at the detection point 4 and the battery voltage in the communication message(message code 'BCP') is less than 5%, the voltage at the detection point 4 is within the normal output voltage range of the charger), the abnormal vehicle battery voltage (the tolerance of voltage at the detection point 4 and the battery voltage in the communication message(message code 'BCP') is more than 5%). When the pre-charging condition satisfies the contactors K1, K2 close and the charger module output voltage is adjusted to smaller 1–10 V than actual battery voltage. Otherwise the charger sends a timeout error message and the pre-charge is unsuccessful.

Verification of Abnormal Handling of Vehicle Charging

Welding test of vehicle charging contactors. The purpose of this test project is to verify whether the tested charger judges the opening and closing states of vehicle charging contactors K5 and K6 before communication getting started, so as to prevent the battery damage caused by unsafe charging in the case of vehicle fault from affecting personal safety. The vehicle control pilot circuit simulator of testing system connects the tested charger, when the indicator light at the testing point 2 is green, closes DC+, DC− to simulate the normal voltage of the battery (lateral voltage of K1, K2 is less than 10 V), abnormal voltage of the battery (lateral voltage of K1, K2 is equal or higher than 10 V). The tested charger should be able to judge contactors K5, K6 abnormal welding when the voltage on the outside of K1, K2 is higher than 10 V, and the corresponding error messages written in error message will be sent to the BMS.

Vehicle abnormal state fault handling. The test item is to verify the response of the tested charger when vehicle suspends charging with abnormal battery information. The test system simulates that the battery status information of the traction battery in the charging stage changes from "normal" to "too high/too low/untrusted state", and determines whether it meets the requirements by receiving the message of the charger and the voltage value at the detection point 3.

5 Conclusion

The incompatibility of electric vehicles and chargers has brought a significant impact on the development of electric vehicles and the construction and operation of charging infrastructure. The consistency of charging communication protocol is

the basis and guarantee of DC charging. Based on the deep analysis of the DC charging process and information interaction process of electric vehicles, the DC charger protocol conformance test system is constructed, the test cases are classified, and the corresponding test methods are introduced.

At present, the system has been widely used in field and laboratory DC charger communication protocol conformance test. The system effectively tested and has found the issues like timeout processing, output consistency, vehicle charging exception handling in multiple batches of DC chargers. The test results and practical application show that the system runs stably and reliable with significant effect. In the future, we will continue to study the secondary development function of the test system and make it to be used in high power charging, plug and charge, wireless charging and other application scenarios.

Acknowledgements This work was supported by Science and Technology Project of State Grid Corporation of China (Study on Key Technologies for Warning Intelligent Diagnosis and Safety Early and Operation and Maintenance Service System of Electric Vehicle bi-direction charging).

References

1. THE STATE COUNCIL Homepage. http://www.gov.cn/zhengce/content. Last accessed 2019/3/29 (in Chinese)
2. NJITT Homepage. http://www.gb688.cn/bzgk/gb/nd?no=323. Last accessed 2019/3/29 (in Chinese)
3. GB/T 34657.1-2017 (2017) Interoperability test specifications of electric vehicle conductive charging—part 1: supply equipment. Standards Press of China, Beijing (in Chinese)
4. GB/T 34657.2-2017 (2017) Interoperability test specifications of electric vehicle conductive charging—part 2: vehicle. Standards Press of China, Beijing (in Chinese)
5. GB/T 34658-2017 (2017) Conformance test for communication protocols between off-board conductive charger and battery management system for electric vehicle. Standards Press of China, Beijing (in Chinese)
6. SAE J1939-11 (2006) Physical layer, 250 k bits/s, twisted shielded pair. SAE International
7. SAE J1939-21 (2006) Data link layer. SAE International
8. GB/T 27930-2015 (2015) Communication protocols between off-board conductive charger and battery management system for electric vehicle. Standards Press of China, Beijing (in Chinese)
9. GB/T18487.1-2015 (2015) Electric vehicle conductive charging system—part 1: general requirements. Standards Press of China, Beijing (in Chinese)
10. Zheng YK, Wei BY, Shu P et al (2016) Design and implementation of closed-loop conformance testing system for IEC 61850 server part one testing platform and Ed 1.0 test cases. Autom Electr Power Syst 40(23):157–162 (in Chinese)
11. Wu DQ, Wan F, Li P et al (2016) Design and implementation of closed-loop conformance testing system for IEC 61850 server part two Ed 2.0 and extended application in China. Autom Electr Power Syst 40(24):157–163 (in Chinese)
12. Zhang X, Ma YH, Li ZM (2015) Research on compatibility testing of communication between off-board charger and electric vehicle. Electr Meas Instrum 52(16):101–106 (in Chinese)

A Design Method of In-band Communication Link in Power-Over-Fiber Application System

Haiquan Wang, Gengtao Guo, Lei Jiang, Jiwen Yao and Yulong Ma

Abstract Power-over-fiber (POF) technique is a commonly way to transmit power externally into the low-power remote modules in specific distributed measurement systems. This paper briefly analyzes the technical characteristics and application limitations of different implementations of In-band communication used in the POF system. Based on the analysis of the characteristics of key components such as laser diode (LD) and photoelectric converter (PPC), this paper proposes a closed-loop digital modulation method that takes the characteristics of photovoltaic voltage signals as feedback to control the drive current of LDs, and then the In-band communication link over the power supply fiber can be established. After that, this paper explains the architecture design, control circuit, feed-back demodulation design and closed-loop control software design of the POF system with In-band downlink capability. The specific test verifies that the proto-type realizes the downlink communication in POF system at 1 Mbps rate between the host and remote module which runs in industrial temperature environment. The method can meet the communication requirements of parameter configuration, sampling calibration and other functions in the industrial distributed measurement system.

Keywords Power-over-fiber · In-band communication · Closed-loop digital modulation · Laser diode

1 Introduction

The new digital measurement technology on smart grid sensing layer such as electronic current transformers (ECT) has been widely used in intelligent substations and DC converter stations. In the specific measurement systems working in high or ultra-high voltage (UHV) transmission system with harsh electromagnetic environment, the data processing host and the distributed remote module must be

H. Wang (✉) · G. Guo · L. Jiang · J. Yao · Y. Ma
NARI Technology Co. Ltd., Nanjing 211000, China
e-mail: wanghaiquan@sgepri.sgcc.com.cn

Y. Xue et al. (eds.), *Proceedings of PURPLE MOUNTAIN FORUM 2019-International Forum on Smart Grid Protection and Control*, Lecture Notes in Electrical Engineering 585, https://doi.org/10.1007/978-981-13-9783-7_73

electrically isolated. Power can't be directly transmitted through the wire or cable. POF system takes optical fiber medium as the power supply channel, which can realize safe, low-cost and all-weather isolation. It is one of the important energy supply methods for such applications [1–7]. For example, most of the high-voltage ECTs take the POF system as power supply for the remote module of on the primary side.

A typical schematic diagram of POF system is shown as Fig. 1. The system can be easily divided into local power supply side and remote power receive side: The local power supply side includes a laser diode (LD) current controller, a drive circuit, and a LD; the remote power receive side includes a photoelectric converter (PPC) and a regulated power supply [8]. In the system, the LD converts electrical energy into light energy on the local side, and then transmits the light energy to the remote side through the optical fiber. The PPC on the remote side converts the light energy into electrical energy. Finally, the voltage regulation circuit convert the energy to be the power of remote module.

The distributed measure system supplied by power-over-fiber system, contains downlink communication (from the host to the remote module) and uplink communication (from the remote module to the host) [8]. The uplink communication generally adopts an independent fiber and there are mainly two ways for the downlink communication.

1. Time-division multiplexing of power supplied fibers, which realizes composite transmission of signals and energy [9]. The transmission is generally achieved on switch the transmitting optical power of laser diode [5].
2. Independent fiber.

The switch method can transmit signal in a high extinction ratio which has good environmental adaptability [10]. However, the method has some shortcomings.

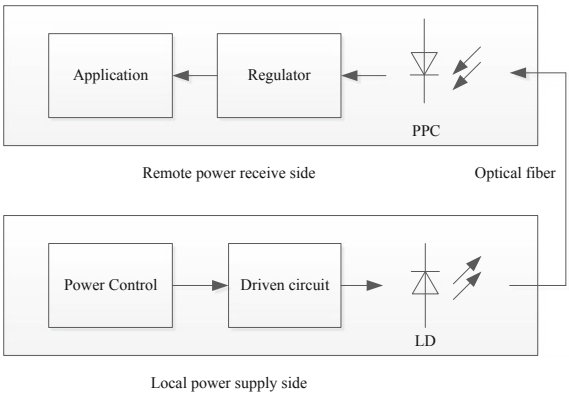

Fig. 1 Typical schematic diagram of POF system

1. When the signal is transmitting, the power supply would be completely shut down. Consequently, in the communication state, the supply power of POF system is reduced significantly per unit time.
2. The LD is switched at high speed according to the baud rate of the signal communication, which is not a normal design working mode for LD. The switching process would inevitably generate electrical stress which has a negative impact on the device life time and affects the reliability of the whole system.

Independent fiber doesn't affect the reliability of power supply, but it also has some defects. On the one hand, Extra power consumption is required because of the dedicated receiver and circuit, which make a challenge to the system design, on the other hand, the increase number of optical fibers makes the fiber laying more complicated and add the risk points of the system.

In order to meet the application requirements of online parameter configuration, sampling calibration and other functions which can improve the maintenance convenience in the distributed measurement system supplied by POF system, it is urgent to study the downlink communication technology that can be applied in engineer field. This paper proposes a design of In-band communication link over the power supply fiber through closed-loop digital modulation method based on the characteristics study of key components in the engineering environment. The implementation architecture and method of the system are described in detail and specific tests of prototype are carried out to verify the communication performance in industrial temperature.

2 Research on Implementation Method of In-band Communication Link in POF System

In order to avoid the shortcomings of the switch method, an amplitude-shift keying (ASK) digital modulation for modulating the transmitted optical power is considered. The principle is to modulate the laser current, control the transmitting optical power, which leads the change of PPC output voltage to realize signal transmission. Binary 0 is transferring when the optical power is low, otherwise, binary 1 is transferring. The judgments can be executed on the PPC output voltage relative to the transferring optical power [9]. Compared to the switch method, the method does not shut down the LD in the modulation process, which reduce the switch electrical stress on components and the impact on power supply. In addition, the bandwidth increases when the signal setup time is less than switch method. It is especially suited to In-band communication link in POF system while the linear control module of the POF system need to be established.

2.1 Key Component Characteristics

The typical relationship between the output optical power of LD, the input current and temperature are shown in Fig. 2a. There is a threshold current when the LD works. When the input current exceeds the threshold current, the output optical power is approximately linear with the current. As the temperature rises, the threshold current becomes higher and the output efficiency decreases brought by the laser gain attenuation.

When the input optical power is constant, the curve of PPC output voltage changing with temperature without load is Fig. 2b. The PPC output voltage has a negative temperature coefficient as which is shown in the figure. As the temperature rises, the PPC output voltage falls.

When the ambient temperature is constant, the relationship between PPC output voltage, input light power and load characteristics is shown in Fig. 3. The PPC output voltage increases along with the input light power, when the open circuit voltage and short circuit current rises. Besides, from the load characteristic respect, PPC has the best working point.

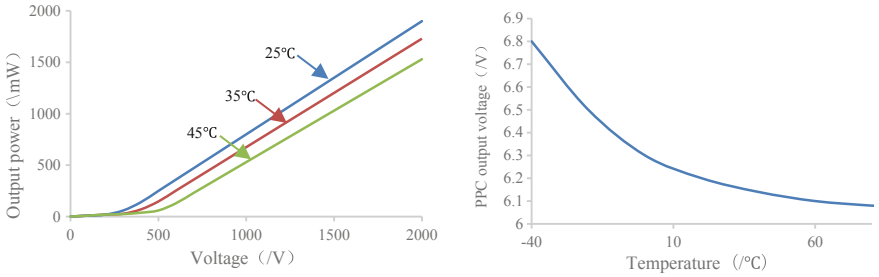

(a) LD (b) PPC

Fig. 2 Typical temperature characteristics of LD and PPC

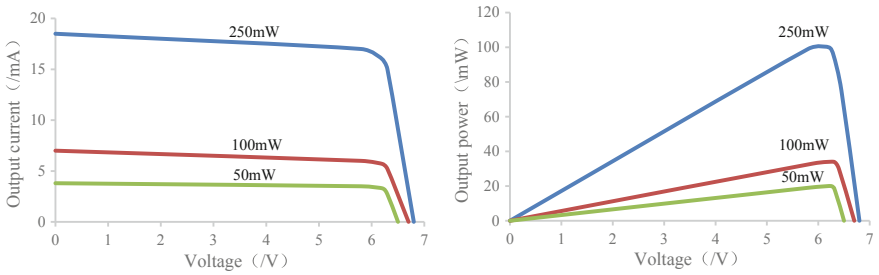

Fig. 3 Typical volt-ampere and volt-power characteristics of PPC

2.2 Digital Modulation Method Research

However, as the characteristics of key components are all nonlinear, the ASK linear control model can't be adopted for POF system [11]. For instance, if disturbance factors affect the characteristics of the POF system which changes the PPC voltage, the digital signal on the demodulation side will exhibit pulse broadening and signal transmission may fail when the LD modulation current keep stable. To solve this problem, a closed-loop digital modulation principle is proposed in this paper, and the principle diagram is shown in Fig. 4. When the signal on the decoder side exhibit pulse broadening caused by disturbance, there will be difference between the given signal pulse width on the modulation side and the feedback signal pulse width on the decoder side. The error value is amplified and transformed to control the LD modulation current. By changing the transmitted optical power amplitude through LD current control, the PPC modulation voltage on the decoder side changes, so that the signal pulse width of the decoder side signal gets close to the given one. Since the distributed measurement system that supplied by POF system has a downlink communication channel already, there is no need to establish a new feedback channel, and the design implementation of the method can be simplified.

As an example, when the system characteristic is disturbed by ambient temperature, the closed-loop modulation process of the method is shown in Fig. 5. The increasement of ambient temperature changes the PPC output voltage, which leads

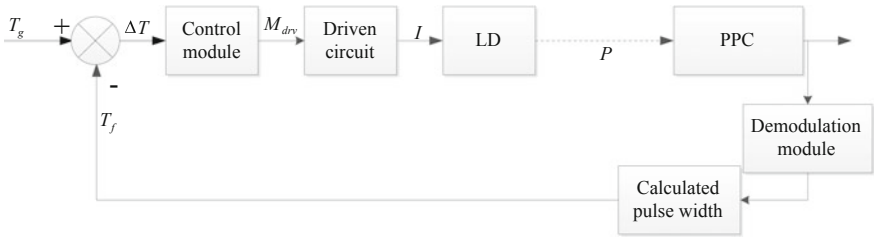

Fig. 4 The schematic diagram of closed-loop digital modulation method

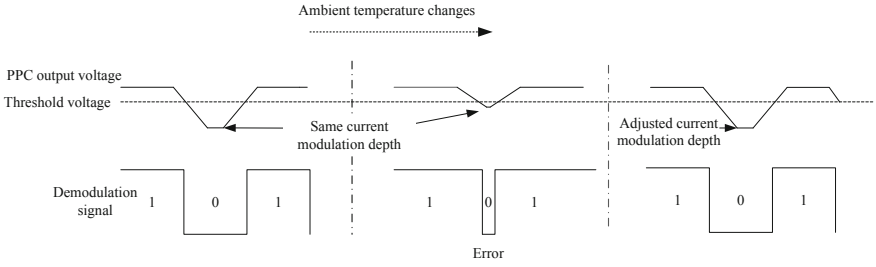

Fig. 5 The adjustment process of closed-loop digital modulation when temperature changes

to the failure of demodulation. At the time, the LD modulation current goes lower, the PPC modulation voltage falls, then the signal pulse width follows the given value which recovery the signal transmission.

3 System Design

3.1 System Architecture Design

The system architecture of In-band communication link in POF system designed in this paper is shown in Fig. 6.

The local power supply side includes a LD power control module, a drive circuit, and a LD. The remote power receive side includes a PPC, a demodulation module, an information feedback module and a regulated power supply. There are downlink and uplink connect optical fibers between the two sides.

The LD power control module implements dual closed-loop control of power supply and digital modulation, which produce the control value of LD drive current. The power supply closed loop is an outer loop, and the digital modulation loop is an inner loop. The power supply control sub-module performs the closed-loop power supply current control, which maintains the state of POF system near the optimum operating point. The digital modulation sub-module performs the closed-loop digital modulation control, which ensure the reliability of In-band communication link. The information feedback module completes the collection of feedback information (PPC output voltage and demodulated digital signal characteristics) and uplink message transmission.

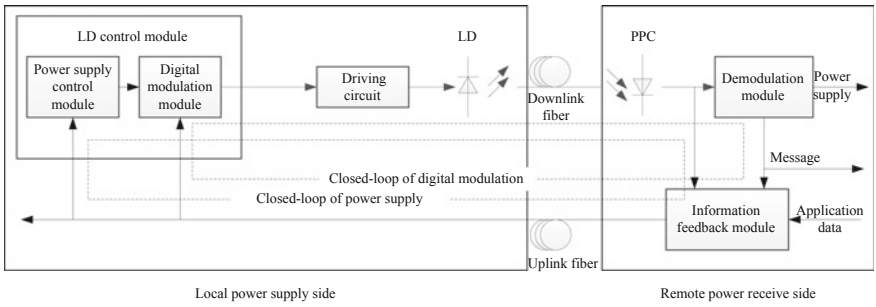

Fig. 6 The schematic diagram of POF system with In-band communication link

3.2 LD Drive Circuit Design

The schematic of LD current drive circuit designed is shown in Fig. 7. This circuit automatically realizes the digital control of LD current based on the automatic analog feedback control principle.

In the circuit, the digital value of LD drive current is converted into an analog control voltage by the high speed DAC chip, and the voltage is compared with the feedback voltage of the LD current sensing resistor R5 to generate a control voltage. As the base voltage of the MOSFET, it controls the MOSFET on-resistance to change the circuit loop resistance in the constant voltage source circuit, so that the current follows the given value automatically. R3 and C2 form a low-pass filter for feedback voltage signal. In practical application, MOSFET needs necessary gate voltage overshoot limiting circuit according to gate characteristics for protection. As current feedback resistance, R5 is calculated from the maximum output voltage of DAC chips and the maximum run current of LD while the power of resistance may be very large. It can be reduced by addition amplification circuit in the feedback circuit to simplify the design. Anti-parallel diodes D1 with the LD limits the possible reverse voltage and the RC circuit acts as an absorption loop for the peak interference voltage.

3.3 Demodulation Module Circuit Design

In the in-band communication link in the POF system based on digital closed-loop modulation method, the PPC output voltage changes from control factors which

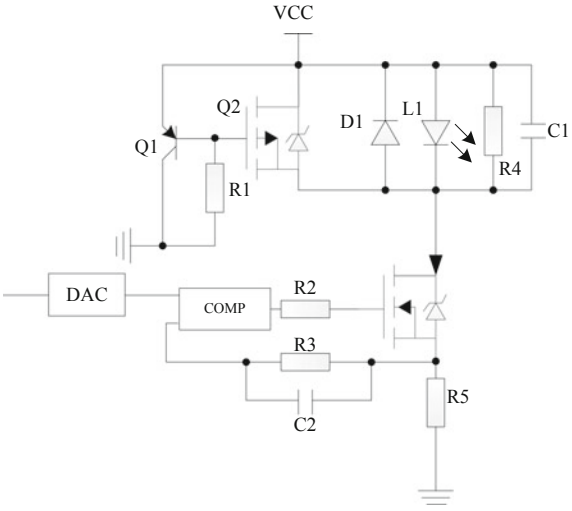

Fig. 7 The schematic of LD drive circuit

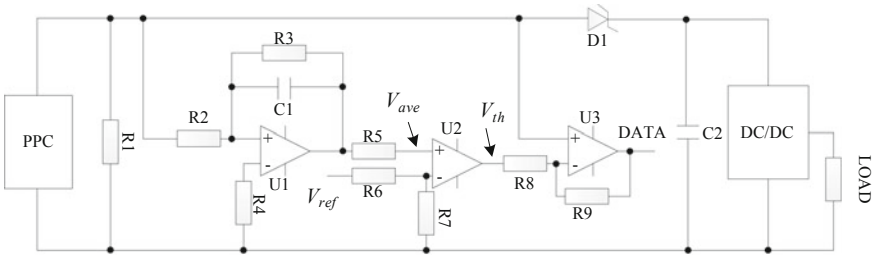

Fig. 8 The schematic diagram of demodulation circuit

include supply regulation, signal modulation and system characteristics alternation which are caused by interferences. The average value of the photoelectric output voltage within one period can be approximated as a judge reference for signal demodulation. Besides, the threshold voltage needs to be properly selected to reduce the decoder error rate. The demodulation circuit is respectively shown in Fig. 8.

In the demodulation circuit, the PPC output voltage connects to the low-pass filter to produce an approximate average voltage. The signal decision threshold voltage V_{th} is obtained by subtracting V_{ave} from the preset noise filter voltage V_{ref} through subtraction circuit. V_{th} is compared with the real-time photoelectric output voltage by the hysteresis comparator U3 to realize signal demodulation.

When choosing the noise filtering voltage, all the relative factors such as measure noise, demodulation signal slew rate and expected communication bandwidth should be considered. After practical verification, the value is 0.05 V in this design. C2 is a storage capacitor, which can reduce the voltage fluctuation brought by modulation or power supply adjustment to ensure the reliability of power supply. Schottky diode D1 acts as an isolation device, which isolates the C2 voltage from the PPC output voltage [12]. Otherwise, when receiving the modulated signal, the PPC output voltage will remain unchanged due to C2 which would lead to demodulation error [13]. When the D1 is cut off, and the R1 is the discharge resistance for energy of parasitic capacitance in the PPC. However, when the resistance serves as the load of the remote module, the resistance should not be too small.

3.4 LD Power Control Module Design

In digital ASK modulation, once the communication baud rate set, the signal pulse width is fixed. In the signal modulation, the control value is determined by different preset value according to the current transmission signal. However, when implementing the closed-loop digital modulation method in In-band communication link in the POF system, the system can't be seen as an ideal system when the signal

pulse width is uncertain. When the signal changes from "1" to "0", the falling edge of demodulation signal is determined by the fall time T_{fall} that the PPC output voltage drops to the threshold voltage. Similarly, when the signal changes from "0" to "1", the rising edge of demodulation signal is determined by the rise time T_{rise} that the PPC output voltage rises to the supply voltage from the threshold point. As the modulation voltage of PPC falls, the T_{fall} and T_{rise} reduces when supply voltage and load characteristics are stable according to the characteristics of demodulation circuit. It is difficult to calculate T_{fall} and T_{rise} in real time which are related to the supply optical power, modulation voltage and load characteristics of the PPC output circuit. Therefore, the control objectives of the closed-loop digital modulation method proposed in this paper is not making the signal pulse width on the decoder side equal to the preset signal pulse width decided by the baud rate, but guarantee signal decoding correctly through suitable signal pulse width. Obviously, when the signal pulse width on the decoder side is approaching to the given T_{set}, the control margin decreases, the LD modulation current should go lower and the impact of In-band communication link on supply power increases.

To reduce the signal pulse width T_g of the control objective and simplify the design of the control system, Manchester code is adopted for message coding. On the one hand, there is always a transition at the middle of each bit period in Manchester code. The abundant bit-change information makes it easy for the controller to get enough characteristics information of signal pulse width, and improves the anti-interference ability of the system. On the other hand, Manchester codes are self-clocking signal. Bit transitions include both clock and data information. As long as the correct clock data recovery (CDR) is guaranteed, the correct decoding can be achieved. The digital code decoder module designed in this paper allows more than 20% signal jitter when it performs CDR for Manchester code. In order to minimize the loss of supply power and retain the control margin, this paper considers the control objective as follows.

$$T_g = 90\% T_{set} \tag{1}$$

The signal pulse width on the decoder side is obtained by timing the output signal of the decoding circuit through a high-speed clock in the processor of the remote module, and the statistical minimum of all "0" and "1" bit-width in a frame message is taken as T_f. There are more complex codes which have better bandwidth utilization.

The specific implementation flow chart of the module is shown in Fig. 9.

According to the communication bandwidth and baud rate, the modulation period and the control objective T_g are calculated in advance in the design stage. In modulation process, the feedback message is parsed to get T_f and the difference between T_f and T_g can be calculated, then the LD modulation current is produced according to the control algorithm and different current control values for modulation in the period can be calculated, after that the output value of modulation module is determined through the following principle that when the transmission

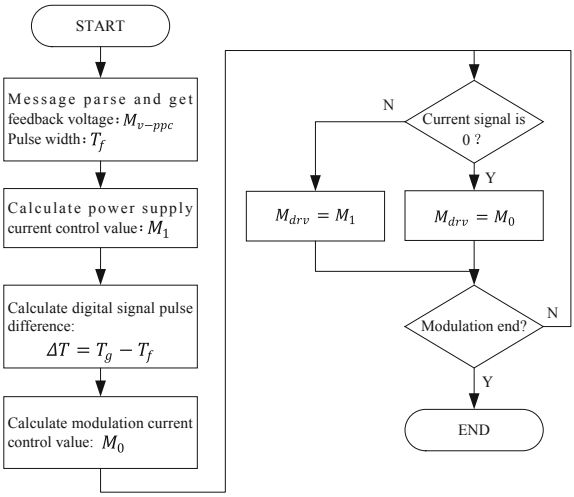

Fig. 9 The flow chart of the LD power control module

symbol is "1", the control value of output LD drive current is the power supply current, otherwise, the control value of output LD drive current is the modulation current. In order to reduce the calculation to meet the embedded processor capability, the paper adopt gradient descent algorithm in the power supply current control and incremental PI algorithm in the modulation current control while there are more excellent algorithms to obtain better control effect. The digital control values M_0 and M_1 can be calculated as following. $U(N)$ is the PPC output voltage, $\nabla T(N)$ is the signal pulse difference between given and feedback. The Ks are coefficient set in the application tests.

$$M_0(N) = M_0(N-1) + K_l \cdot (U(N) - U(N-1)) \tag{2}$$

$$M_1(N) = M_1(N-1) + K_p \cdot (\nabla T(N) - \nabla T(N-1)) + K_i \cdot \nabla T(N) \tag{3}$$

To ensure reliability of power supply, the LD drive current will be set to the maximum admissible value when the POF system is powered on. Analogously, to ensure the reliability of communication, the LD modulation current is set to zero at the initial, when the closed-loop digital modulation is similar to the switch method.

4 Performance Test

The prototype is designed to test the system performance. The parameters of this prototype are shown in Table 1.

Table 1 Parameters of the prototype [14]

Component	Parameters	Value
LD	Maximum output power	2.0 W
	Maximum threshold current	0.35 A
	Maximum forward voltage	2.0 V
	Maximum operating current	2.0 A
PPC	Typical output voltage	6.0 V
	Maximum output power	500 mW
	Load	120 mW

The communication baud rate of the In-band link is 1 Mbps, the message transmission frequency is 1 kHz, length is 64 bytes and the CRC check codes are added at the end of the frame to facilitate packet verification in the prototype. Environmental test is conducted to verify the performance of the prototype over the industrial temperature range. The remote module is placed in the environmental test chamber, the temperature range is set from −40 to 85 °C, the rate of temperature change is 10 K/h, the time duration is 36 h.

The oscilloscope waveforms of sensing resistors voltage which represents the laser diode current are shown in Fig. 10. The supply current is 1.1 A and the modulation current is 0.8 A. According to the characteristics of the LD, the supply optical power is about 0.85 W and the modulation optical power is about 0.5 W. The maximum power loss is about 10% in closed-loop modulation method while the loss is up to 26% in switch mode in the above communication specification.

Typical decoding waveform and PPC output voltage is shown in Fig. 11. The decoder signal quality is relatively good. CRC check is executed on the decoder message. In 36 h, 66 Gbits has been transmitted and the bit error is zero. The decoder signal quality is relatively good.

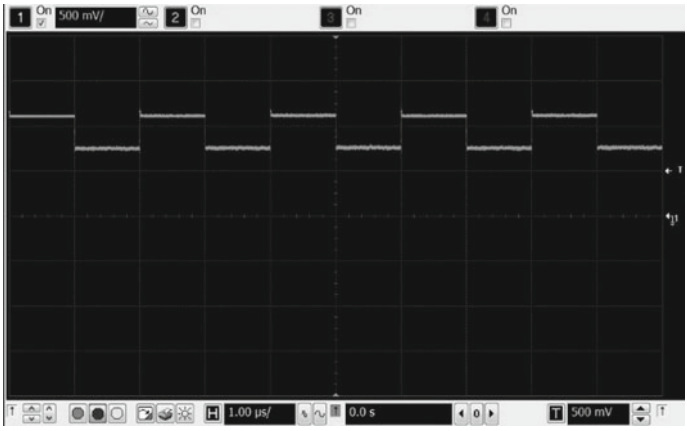

Fig. 10 Waveforms of LD current

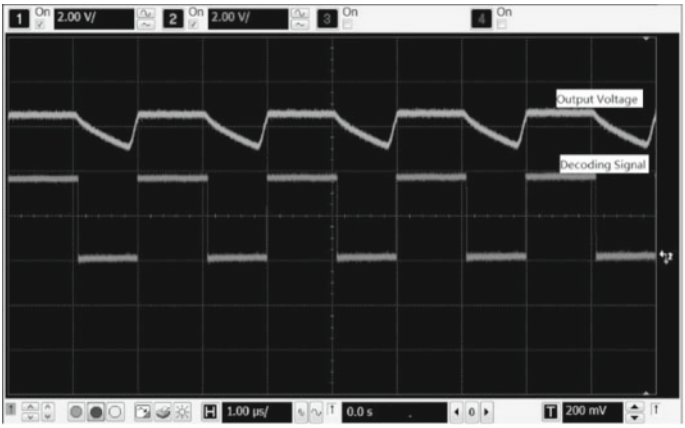

1.output voltage, 2.decoding signal

Fig. 11 Waveforms of decoder circuit

5 Conclusion

Aiming at the difficulty of downlink communication in distributed measurement system supplied by POF technology, this paper presents a closed-loop digital ASK modulation method to control the modulation current of LD based on demodulation signal pulse width, which solves the modulation problem caused by the non-linear characteristics of key components in the system. It realizes the downlink in the band of power supply optical fiber with higher bandwidth in industrial temperature environment, which makes it possible to configure parameter and correct the accuracy of remote module parameters online in distributed measurement system supplied by POF technology. Besides, the method lays a technical foundation for improving the maintenance convenience of the system in the future.

References

1. Nazare FVBD, Werneck MM (2010) Temperature and current monitoring system for transmission lines using power-over-fiber technology. In: Instrumentation and measurement technology conference (I2MTC), 2010 IEEE, pp 779–784
2. Werthen J, Cohen M (2006) Photonic power: delivering power over fiber for optical networks. In: 2006 international conference on photonics in switching, Heraklion, Crete, pp 1–3
3. Li Z, Li C, Li Z et al (2015) A high accuracy on-line calibration method for electronic voltage transformers with digital output. Autom Electr Power Syst 39(13):163–167
4. Shao X, Peng H, Wang N (2017) Electronic voltage transformer based on double integrator for power quality detection in smart grid. Autom Electr Power Syst 41(13):156–161
5. Zhu M, Luo Q, Cao M et al (2018) Test and analysis of transfer characteristics of electronic current transformer. Autom Electr Power Syst 42(24):143–149

6. Werneck MM, Abrantes ACS (2004) Fiber-optic-based current and Voltage measuring system for high-voltage distribution lines. IEEE Trans Power Deliv 19(3):947–951
7. Perhirin S, Audo F, Guegan M et al (2013) A power-over-fiber system and its low consumption remote equipment for submarine applications. In: 2013 MTS/IEEE OCEANS-Bergen, Bergen, pp 1–6
8. Qiu H, Li K, Duan X, Fan X, Lu B (2006) Opt-electic transmission system of low power consumptions for optically powered electronic current trasnformers. Autom Electr Power Syst 30(20):72–76
9. Kamiyama D, Yoneyama A, Matsuura M (2018) Multichannel data signals and power transmission by power-over-fiber using a double-clad fiber. IEEE Photon Technol Lett PP (99):1–1
10. Agrawal GP (2011) Fiber-optic communication systems, 4th edn
11. Johannisson P, Agrell E (2014) Modeling of nonlinear signal distortion in fiber-optic networks. J Lightw Technol 32(23):4544–4552
12. Lee YD, Nae KK, Lee E et al (2007) ASK modulator for RFID system using a novel variable DGS resonator. In: 2007 European microwave conference, Munich, pp 1660–1663
13. Personick SD (2013) Receiver design for digital fiber optic communication systems. Bell Syst Techn J 52(6):843–874
14. https://www.lumentum.com/en/products/diode-laser-830-nm-fiber-coupled-2w-2486-l4-series. Last accessed 2018/11/21

Research on EMI Noise Suppression Method Based on Electromagnetic Shield of Cabinet

Yangyang Chen, Quan Liu, Wei Yan, Chongming Zhu, Yang Zhao and Bo Yu

Abstract For the radiated EMI (Electromagnetic Interference) noise generated by the inverter power supply, this paper studies the EMI noise suppression based on the electromagnetic shielding of the cabinet. By modeling the inverter power cabinet in the CST simulation environment, the electromagnetic shielding effect of the cabinet under different cabinet models is analyzed, and the simulation results are analyzed to optimize the shielding effectiveness of the cabinet. Finally, it is applied to the specific case and adopted rectification. After the suppression measures, the tested equipment can successfully pass the test and verify the effectiveness of the method. This paper provides a reference and basis for the research of radiated electromagnetic interference noise of inverter power supply and the later rectification of technicians.

Keywords Radiated electromagnetic interference noise · Shielding effectiveness · Cabinet modeling

1 Introduction

Modern science is developing towards high frequency, high speed, stronger sensitivity, high installation density and better reliability. With the development and progress of society, various electronic equipments have penetrated into various fields such as industry, agriculture, military and family. Consequently, the electromagnetic environment becomes increasingly complex, thus research of electromagnetic compatibility problem becomes more and more important [1, 2].

Y. Chen (✉) · C. Zhu · B. Yu
State Key Laboratory of Smart Grid Protection and Control, NARI Group Corporation, Nanjing 211000, Jiangsu, China
e-mail: chenyangyang@sgepri.sgcc.com.cn

Q. Liu · W. Yan · Y. Zhao
Nanjing Normal University, Nanjing 210042, Jiangsu, China

Y. Xue et al. (eds.), *Proceedings of PURPLE MOUNTAIN FORUM 2019-International Forum on Smart Grid Protection and Control*, Lecture Notes in Electrical Engineering 585, https://doi.org/10.1007/978-981-13-9783-7_74

At present, scholars at home and abroad have also done a series of studies on cavity shielding efficiency. Wu Xin and Qian Zhaoming of Zhejiang University directly obtained the distribution of electric field interference on the surface of the transmission control cabinet by using an EMC scanner, so that the sensitive lines can avoid the areas with strong electromagnetic field when wiring, and put them in the areas with weak interference, so as to reduce interference. Then, according to the interference and coupling coefficient, they developed an auxiliary design software, which preliminarily solved part of the design problem of electromagnetic compatibility of the transmission control cabinet [3]. Meng Peiwen, Guo Hao et al. established the coupling model of the cavity with holes under the condition of plane wave radiation by using the time-domain finite integral method, and specifically studied the influence of the length, width and depth of rectangular holes on the shielding efficiency of the cabinet [4]. M. P. Robinson, R. Azaro et al. analyzed the scattering matrix equation and transmission matrix equation of the complex multi-cavity, and proposed a fast algorithm for the shielding efficiency of the multi-cavity based on the electromagnetic topology theory, which greatly improved the simulation efficiency and the simulation accuracy [5, 6]. X. Y. Mao, Tao Liu et al. estimated the shielding efficiency of metal shielding cavities with holes by using pattern matching method and matrix method, and obtained that the shielding efficiency of square holes was better than that of rectangular holes with the same pore area through cavity modeling [7–10].

Although the above method has analyzed and optimized the algorithm and shielding efficiency of the metal cabinet with holes, it still has some shortcomings. For example, the selection of the number of heat dissipation holes and cable bundle holes in the cavity will affect the electromagnetic field generated by the power electronic system in its meter transformer, instead of only discussing one or a small number of holes in the cabinet. Although the above study analyzed the drive circuit inside the transmission control cabinet and the harmonic generated by the inverter system, it did not analyze the whole system including the high-power. In view of this, based on the existing references and the preliminary research in the laboratory [11–13], this paper will analyze the shielding effectiveness principle and the cabinet simulation model, and put forward the optimization scheme, which is an accurate and feasible optimization method for radiated noise. This method has the theoretical basis and the simulation experiment basis, which has provided the reliable basis for the staff's later rectification work.

This paper is divided into three parts. The first part discusses the shielding efficiency principle, the second part introduces the modeling and verification of the inverter power cabinet under the CST simulation environment, the third part is the application case, the optimization method is applied to the inverter power cabinet to verify the effectiveness of the method.

2 Shielding Effectiveness Principle

The electromagnetic characteristics of inverter power cabinet are mainly analyzed from its own electromagnetic shielding effectiveness. Normally, the shielding cabinet is made of metal, and the shielding body can be divided into three categories according to the sealing situation: complete shielding, non-complete shielding and woven shielding. The complete shielding body has no holes or joints, which is rarely seen in practical applications. Non-complete shielding means that the shielding body is connected with the external space by structures such as holes and slots. Braided shielding refers to the shielding layer formed by braided metal with good shielding effect, such as copper braided shielding cable.

The electromagnetic field radiated by the inverter through the space is divided into the magnetic field part and the electric field part. When shielding and restraining them through the cabinet, the shielding efficiency of electric field component and magnetic field component should be considered respectively.

$$SE_E = 20\lg\frac{E}{E_1} \tag{1}$$

$$SE_H = 20\lg\frac{H}{H_1} \tag{2}$$

In the formula, E and H refer to the electric field intensity and magnetic field intensity at a specific position without adding the shielding cabinet (when the space is open), E_1 and H_1 refer to the electric field intensity and magnetic field intensity at the same position after adding the shielding cabinet. SE_E and SE_H are respectively defined as the electric field shielding efficiency and magnetic field shielding efficiency of the shielding efficiency of the shielding cabinet, and the unit is dB.

Define the electromagnetic wave propagation parameters, Γ_1 is the reflection coefficient of electromagnetic wave when it enters the shielding cabinet from space, and Γ_2 is the reflection coefficient of electromagnetic wave when it enters the external free space from inside the shielding cabinet. E_0 is defined as the magnitude of the field when the plane wave reaches the shielding cabinet. From the transmission line theory, we can get (3) and (4).

$$\Gamma_1 = \frac{Z_M - Z_W}{Z_M + Z_W} \tag{3}$$

$$\Gamma_2 = \frac{Z_W - Z_M}{Z_M + Z_W} \tag{4}$$

According to (5), Z_W refers to the free space wave impedance.

$$Z_W = \sqrt{\mu/\varepsilon} \tag{5}$$

In formula (5), μ is the permeability of the medium, and the size is $4\pi \times 10^{-7}\mathrm{H/m}$. ε is the dielectric constant of the medium, and the size is $(1/36\pi) \times 10^{-9}\mathrm{F/m}$, so we can calculate that $Z_W \approx 377\pi$.

Z_M refers to the wave impedance of the shielding cabinet, which is determined by the conductivity and permeability of the shielding cabinet.

$$Z_M = \sqrt{\frac{j\omega\mu}{\sigma + j\omega\varepsilon}} \approx \frac{1+j}{\sigma\delta} \tag{6}$$

Part of the electromagnetic wave passes through the interface of the shielding body and enters the shielding body. This part can be defined as the transmission coefficient T_1, and the second interface of the shielding body is defined as the transmission coefficient T_2.

$$T_1 = 1 + \Gamma_1 \tag{7}$$

$$T_2 = 1 + \Gamma_2 \tag{8}$$

As shown in Fig. 1, the single-layer metal shielding body model, scattering is caused by electromagnetic waves radiating from the radiation source to the surrounding space in the cavity. The electromagnetic waves are reflected and superimposed for many times inside the closed cavity, and finally leak to the outside of the cavity through the hole slots and holes, forming radiated EMI noise and causing interference to the peripheral sensitive equipment. Let the thickness of the metal shield be t. The electromagnetic wave enters the shielding body from the free space

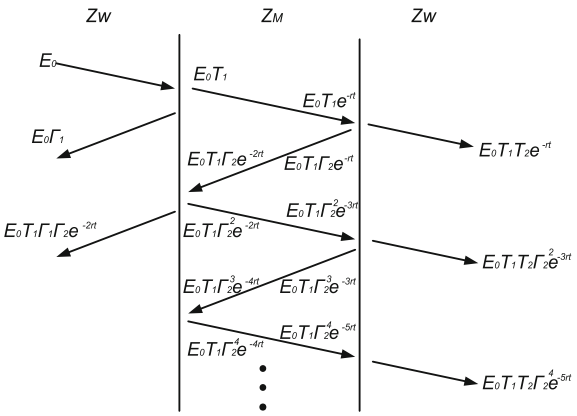

Fig. 1 Electromagnetic scattering principle

with the field intensity as E_0, passes through two interfaces of the shielding body successively, and finally scatters out of the shielding body. At this time, the field intensity is E_1.

The electromagnetic wave with a field intensity of E_0 passes through the interface of the shielding body from free space. After passing through the shielding body medium, the field intensity attenuates to E_0T_1. After passing through the shielding body medium, the field intensity attenuates to $E_0T_1e^{-rt}$. Part of the delimited reflection is still propagating in the shielding medium, and the field intensity is $E_0T_1\Gamma_2e^{-rt}$. The magnitude of the electromagnetic field emitted from the shielding body after passing through the interface for two times is $E_0T_1T_2\Gamma_2^{2n}e^{-(2n+1)rt}$. Finally, the superposition is the field strength after passing through the shielding cabinet.

$$\begin{aligned} E_1 &= \sum_{n=0}^{k} E_0T_1T_2\Gamma_2^{2n}e^{-(2n+1)rt} = E_0T_1T_2e^{-n}\frac{1-\Gamma_2^{2n}e^{-2nrt}}{1-\Gamma_2^2e^{-2rt}} \\ &\approx E_0T_1T_2e^{-n}\frac{1}{1-\Gamma_2^2e^{-2rt}} \end{aligned} \tag{9}$$

Consequently, We can obtain the shielding efficiency of the cabinet.

$$\begin{aligned} SE_E &= 20\lg\frac{E}{E_1} = 20\lg\frac{1-\Gamma_2^2e^{-2rt}}{T_1T_2e^{-rt}} \\ &= 20\left\{\lg e^{rt}\frac{(Z_M+Z_W)^2}{4Z_MZ_W}\left[1-\left(\frac{Z_M-Z_W}{Z_M+Z_W}\right)^2e^{-2rt}\right]\right\} \end{aligned} \tag{10}$$

According to the above analysis, the size of SE_E is mainly determined by the following factors:

1. Design of shielding cabinet structure and selection of shielding layer material and thickness;
2. The frequency of the shielding signal required;
3. Type of electromagnetic field shielded;
4. Discontinuity of electromagnetic field caused by the existence of holes and slots in the shielding cabinet.

Therefore, in order to obtain the best shielding efficiency under the working condition of the inverter circuit, it is necessary to optimize the design of the high-power inverter power cabinet to achieve the optimal electromagnetic shielding effect.

3 Cabinet Modeling

In the following, the shielding effectiveness of the cabinet will be analyzed from the four aspects of the structural parameters, including the position of the opening, the shape of the opening, the slit of the opening and the shielding material, so as to provide a theoretical basis for the design of the actual transmission control cabinet.

According to the actual inverter power cabinet, the cabinet model as shown in Fig. 2 is established. The external size of the cabinet is 800 mm × 500 mm 1500 mm (width × depth × height), the weight is 780 kg, and the internal is the transmission control circuit. Since the simulation operation time is long and the efficiency is very low under this model, and the influence of the shock absorber and other devices on the upper and lower sides of the cabinet on the shielding efficiency of the transmission control cabinet can be ignored.

Preserve the actual cabinet features such as cable bundle holes and gaps in the cabinet, and modify the material parameters of the simulation model according to the actual cabinet material.: the temperature of 7850 kg/m^3 density, resistivity of 1.3e−8 Ω/m, relative permeability is set to 0.98, the electrical conductivity is set to 0 (Both sides of the cabinet are coated with insulating varnish), thickness of 8 mm. Based on the model, CST simulation is used to analyze the electromagnetic characteristics and shielding efficiency of inverter power cabinet.

3.1 Effect of Hole Position on Shielding Efficiency of Cabinet

The sweep frequency range is set as 25 Hz–1 GHz, and the sweep frequency step is 10 kHz. Exciting source is set as plane wave, radiation 1 V/m and located at the center of cabinet. In the model, a probe is set in each of three positions outside the cabinet.

The number of holes and area of each hole remain unchanged and modify the simulation model of the cabinet. Holes location are shifted from the top surface of

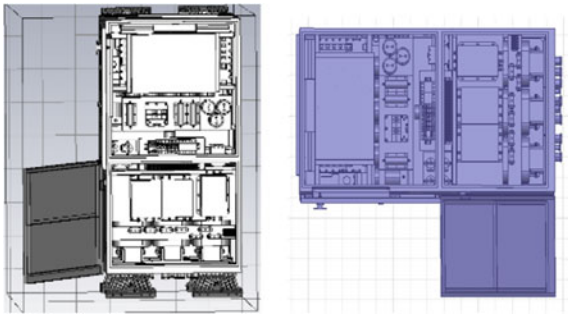

Fig. 2 CST modeling for transmission control cabinet

the cabinet to the bottom of the back side. The center of the holes is 50 mm away from the bottom, so as to facilitate the passage of the cable bundle.

The shielding effectiveness simulation was performed on the set of three field probes. The simulated electric field curves under the two open-hole modes were fitted, and the results were shown in Figs. 3, 4 and 5.

After analysis and it was found that the cabinet shielding efficiency for the low frequency band 25 Hz–150 MHz is good, but when frequency is higher than 150 MHz, the shielding efficiency has been significantly decreased and finally tends to be stable. By comparison, it is found that the shielding efficiency of electric field in the frequency range of 25 Hz–500 MHz at the two kinds of holes models is roughly the same. According to the resonance simulation analysis of the cabinet, in the low frequency band, the resonance points are few and the resonance energy is low, so it has little influence on the shielding efficiency of the cabinet. However, in the relatively high frequency band, the resonance frequency points become more and more intensive and the energy becomes higher, so that at these resonance points, the radiation signal is enhanced and the shielding efficiency is weakened. However, between 500 MHz and 1 GHz, the electric field intensity value on the coupling curve of the model cabinet with holes on the back at the position of field probe 1 and field probe 2 is lower than that of the model cabinet with holes on the top, but the simulation data of the model cabinet with holes on the top at the position of field probe 3 is better than that of the model cabinet with holes on the back.

According to the initial formula analysis, the distance has a great influence on the electric field intensity. The farther the distance is, the greater the attenuation of electric field intensity is. Although the center of the incident plane waves in the two models is 500 mm away from field probe 3, and the plane wave scattering through the cabinet gap and reached to the probe 3 position and the electric field energy is roughly same, but in the top model, hole position is far away from the detection point, electromagnetic wave scattering through the hole to detect electric field energy is low, while in the back hole model, hole position is close to the detection

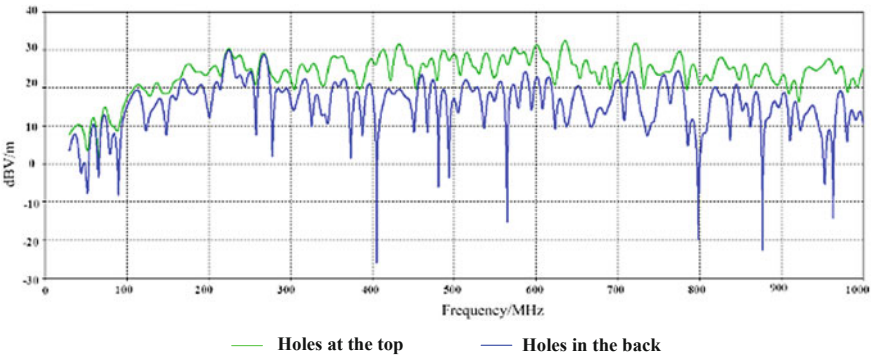

Fig. 3 Shielding efficiency comparison in probe 1

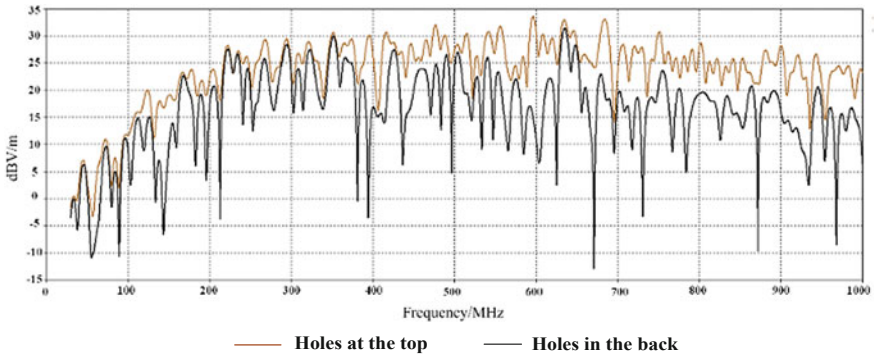

Fig. 4 Shielding efficiency comparison in probe 2

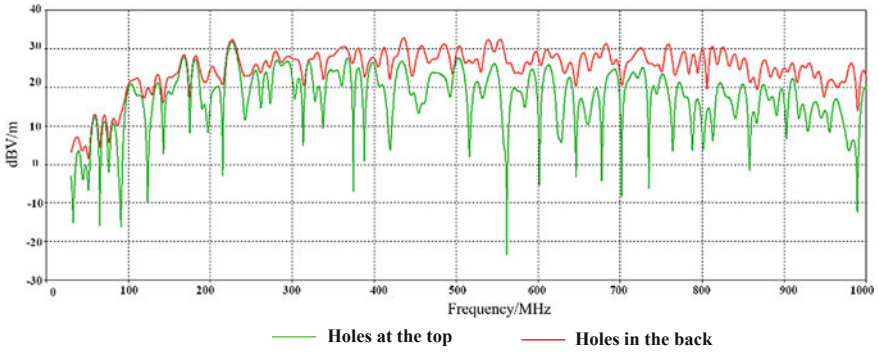

Fig. 5 Shielding efficiency comparison in probe 3

point, thus the electric energy received is higher. This explains why the shielding effectiveness of at probe point 3 of back hole model is lower than that of the top hole model. However, by observing the shielding effectiveness comparison diagram, it can be found that the shielding effectiveness of the back hole model at the position of field probe 1 and field probe 2 is 5.63 and 4.15 dB respectively better than that of the top hole model, while the shielding effectiveness of the top hole model at the position of field probe 3 is 1.98 dB better than that of the back hole model. In addition, because the back side of the inverter power cabinet is usually placed on the side of the ship, the back side is facing the ship silo, and is not facing the sensitive receiving equipment. In conclusion, under the premise of the same number of holes, shape and area, the shielding efficiency of the back hole model is better than that of the top hole model.

3.2 *Effect of Hole Shape on Shielding Efficiency of Cabinet*

Through the above simulation analysis, it can be seen that the shielding efficiency of the cabinet body under the back hole model is better than the top hole model, so the hole position is fixed 50 mm away from the bottom. In order to better study the effect of inverter power cabinet structure on shielding efficiency, the shielding efficiency is analyzed by changing the hole shape from round to square and regular hexagon.

Due to strict requirements on heat dissipation and cable bundle width, it is necessary to ensure the same area of the hole. The radius of circular hole is 30 mm. According to the equal area principle, when the hole shape is changed to square, the side length shall be 53.17 mm. When the shape is regular hexagon, the side length shall be 32.99 mm.

A planar incident wave with radiation of 1 V/m is set at the center of the cabinet, and a field probe is placed at position 1 for simulation. Since the hole position is on the back, the different shapes have little influence on the shielding effectiveness on probe 1 and probe 2 positions, so no more discussion is needed here. It is only to discuss the shielding effectiveness of probe 3 at the back hole model. The simulation comparison of shielding effectiveness is shown in Figs. 6 and 7. Among them, green, blue and red are regular hexagon, circle and square respectively.

It can be seen from the above analysis that the shielding effectiveness of regular hexagonal hole is better than that of square hole in almost all frequency bands, and the shielding effectiveness of the entire frequency band is 3.32 dB better than that of circular hole. Compared with the circular hole, it is found that the shielding efficiency of regular hexagonal hole is nearly equivalent to that of square hole in the low frequency band below 100 MHz and the middle frequency band within 600–840 MHz, and the regular hexagonal hole is slightly better than that of square hole. However, in the remaining frequency band, the regular hexagon hole is 2.14 dB better than the square hole on average. It can be seen that the shielding efficiency of

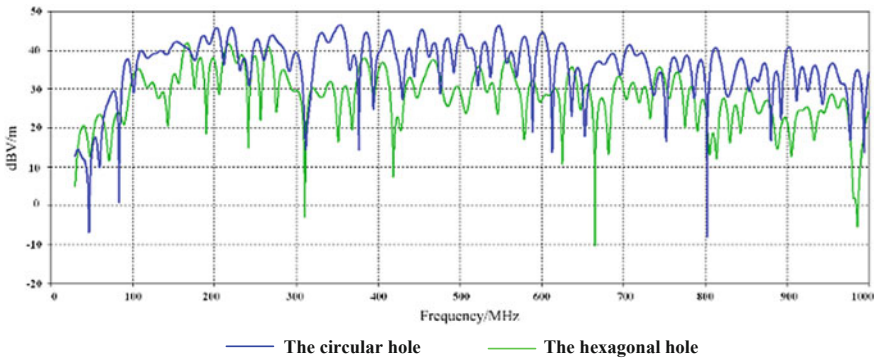

Fig. 6 Comparison of shielding effectiveness between regular hexagonal and circular hole

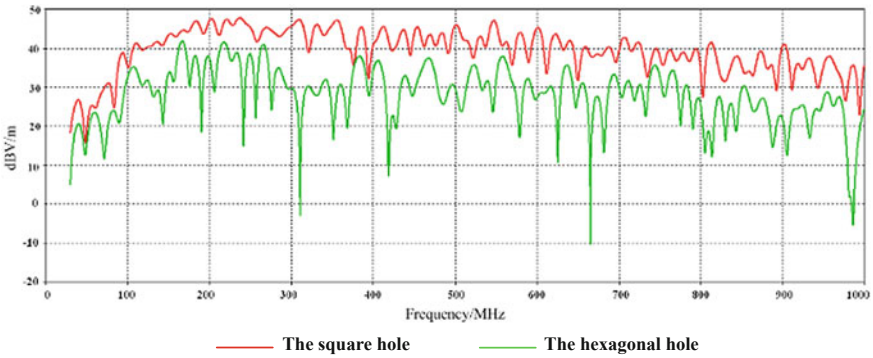

Fig. 7 Comparison of shielding effectiveness between regular hexagonal and square hole

regular hexagonal hole is better than that of circular hole and square hole. Therefore, it is determined that the hole shape is confirmed as regular hexagon, with the side length of 32.99 mm and the position at the back side 50 mm from the bottom.

3.3 *Effect of Shielding Layer on Shielding Efficiency of Cabinet*

When there is alternating current or alternating electromagnetic field in the cabinet, the induced electromagnetic field inside the cabinet is unevenly distributed, and the current is concentrated in the "skin" part of the cabinet, that is, the current is concentrated on the thin layer on the surface of the cabinet, and the closer to the cabinet on the surface of the body, the higher the density of the current, the higher the power loss of the cabinet. This phenomenon is called skin effect. After entering the inside of the good conductor of the cabinet, the field strength will decrease rapidly, so we only set the probe on the inside surface of the cabinet. We define skin depth δ as the distance when the current density of the good conductor in the cabinet decreases to $1/e$ of the current density on the inner surface of the cabinet, and the expression of current density $\overrightarrow{J}$ can be obtained.

$$\overrightarrow{J} = J_x\vec{e}_x = \sigma E_x\vec{e}_x \tag{11}$$

The corresponding expression of magnetic field density can be obtained.

$$\overrightarrow{H} = H_y\vec{e}_y \tag{12}$$

We get a system of differential equations combining maxwell's equations.

$$\nabla \times \overrightarrow{H} = -J\frac{d\overrightarrow{D}}{dt} \tag{13}$$

$$\nabla \times \overrightarrow{E} = -\mu\frac{d\overrightarrow{H}}{dt} \tag{14}$$

The rate of change of electric field and magnetic field with coordinates is deduced.

$$\frac{\partial H_y}{\partial z} = -\sigma E_x \tag{15}$$

$$\frac{\partial E_x}{\partial z} = -\mu\frac{H_y}{t} \tag{16}$$

$$\frac{\partial^2 H_y}{\partial z^2} - j\omega\mu\sigma H_y = 0 \tag{17}$$

By defining the propagation constant as γ and $\gamma^2{=}j\omega\mu\sigma$, the expression of electromagnetic field intensity in one-dimensional space and the relation between γ and δ can be derived.

$$H_y{=}H_{y0}e^{-\gamma z} \tag{18}$$

$$E_x{=}\frac{\gamma}{\sigma}H_y e^{-\gamma z} = E_0 e^{-\gamma z} \tag{19}$$

$$J_x{=}\gamma H_{y0}e^{-\gamma z} = J_0 e^{-\gamma z} \tag{20}$$

$$\gamma{=}\sqrt{j\omega\mu\sigma}{=}\partial + j\beta = (1+j)\frac{1}{\delta} \tag{21}$$

In the above equation, α is the attenuation coefficient of the electromagnetic wave, and β is defined as the phase shift coefficient of the electromagnetic wave, so the skin depth δ can be deduced (Table 1).

Table 1 Shielding copper foil parameters

Shielding characteristic	Parameter
Shielding material	Cu (99.98%)
Shield thickness	0.065 mm
Electrical conductivity	$\sigma = 5.82 \times 10^7/\Omega\,\mathrm{m}$
Magnetic permeability	$\mu = 4\pi \times 10^{-7}$ H/m
adhesion	$\sigma = 1.3 - 1.5\,\mathrm{kg}/25\,\mathrm{mm}$
Relative conductivity	$\sigma_r{=}1$
Relative permeability	$\mu_r = 1$

$$\delta = \frac{1}{\sqrt{\pi f \mu \sigma}} \tag{22}$$

So we can simplify (22).

$$\delta = \frac{1}{\sqrt{\pi f \mu \sigma}} = \frac{1}{15.185\sqrt{f}}(\mathrm{m}) \tag{23}$$

According to the establishment of the theoretical shielding model, the absorption loss of the shielding body can be expressed as $20\lg e^{rt}$. After the electromagnetic wave passes through the metal shielding body, the presence of induced current will lead to power loss. In addition, the heating of the material will also absorb certain electromagnetic wave energy, resulting in an exponential trend of decrease in the size of the field intensity. We can simplify the expression for the absorption loss.

$$20\lg e^{rt} = 8.686 \cdot rt = 8.686\frac{t}{\delta} \tag{24}$$

It can be seen from the expression of absorption loss that:

1. With the same shielding cabinet materials, the absorption loss is related to the thickness of the shielding cabinet. The thicker the shielding cabinet is, the greater the absorption loss will be;
2. With the same shielding cabinet material and thickness, the absorption loss is related to the electromagnetic wave frequency through the shielding cabinet. The higher the frequency is, the greater the absorption loss is;
3. The absorption loss of the shielding body is also related to the skin depth, that is, the conductivity and magnetic permeability of the shielding cabinet material. At the same frequency, the higher the conductivity and magnetic permeability of the shielding material is, the greater the absorption loss is.

According to the skin effect, using the previously optimized transmission control cabinet, under the model of the regular hexagonal hole on the back side, optimize the setting again, and set a layer of copper foil on the inside of the cabinet, the thickness is set to 0.065 mm, and the copper foil is laid. After that, the field probe is set and simulated in the same position, and the comparison between the shielding performance and the unshielded layer is as shown in Fig. 8. Blue and brown are the shielding effectiveness before and after the shielding layer is laid.

It can be seen from the above analysis that the shielding effectiveness of regular hexagonal aperture is better than that of square aperture in almost all frequency bands, and the shielding effectiveness of the entire frequency band is better than that of circular aperture 3.32 dB on average through calculation. Compared with the circular hole opening, it is found that the shielding efficiency of regular hexagonal hole opening is equivalent to that of square hole opening in the low frequency band below 100 MHz and the middle frequency band within 600–840 MHz, and the regular hexagonal hole opening is slightly better than that of square hole opening.

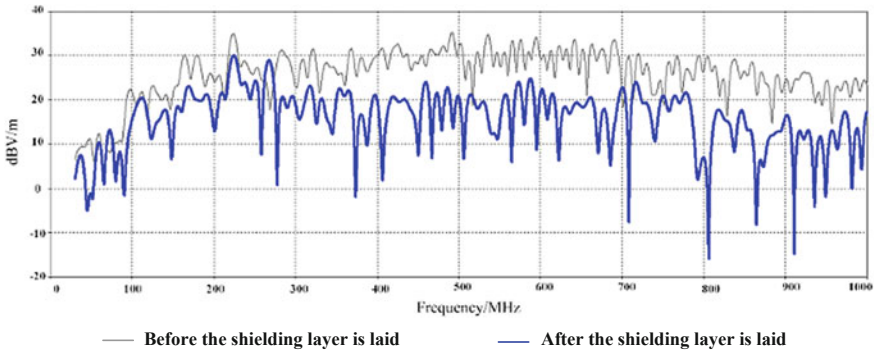

Fig. 8 Comparison of shielding effectiveness between hexagon and square holes

However, in the remaining frequency band, the regular hexagon hole opening is better than the square hole opening 2.14 dB on average. It can be seen that the shielding efficiency of regular hexagonal opening is better than that of circular opening and square opening. Therefore, it is determined that the opening is a regular hexagon opening, with the side length of 32.99 mm and the position at the back side 50 mm from the bottom side.

4 Electromagnetic Shielding Test of Inverter Power Cabinet

Combined with high-power inverter power cabinet and test environment, according to test criteria, the measurement result of the cabinet radiation noise is shown in Fig. 9. The upper side line in the figure is the test limit result, and the lower side line is the measured result.

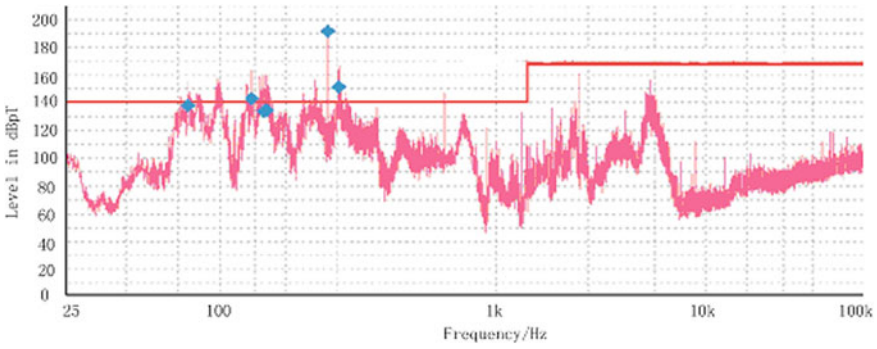

Fig. 9 Measured results

The field probe is used to extract the cabinet radiation noise. Figure 10 is the test result, which shows that the main radiation is concentrated on the top and the front and rear panels of the top.

In view of the above test results analysis, and according to the simulation analysis in Chap. 4, combined with the actual, take the following corrective measures:

1. As shown in Fig. 11, a layer of isolation plate is added horizontally in the red line area on the DC bus to shield the radiation to the top of the cabinet;

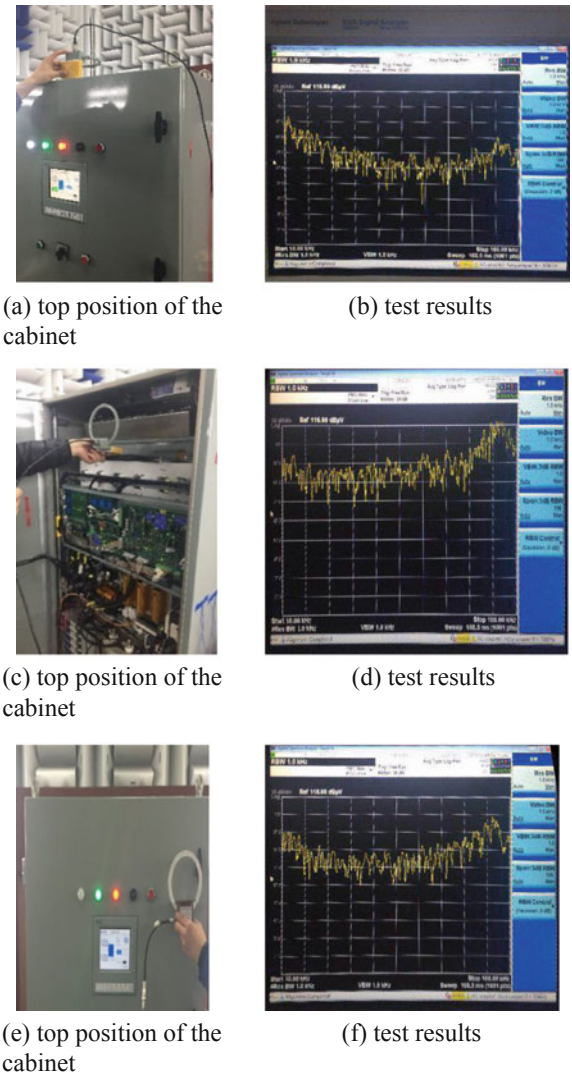

(a) top position of the cabinet (b) test results

(c) top position of the cabinet (d) test results

(e) top position of the cabinet (f) test results

Fig. 10 Position of the field probe and electromagnetic characteristics

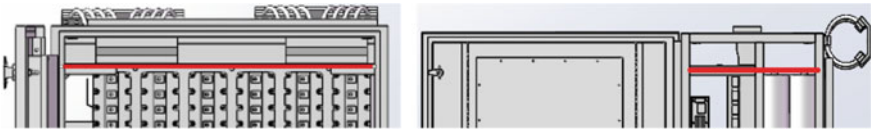

Fig. 11 Corrective measures for the top of the cabinet

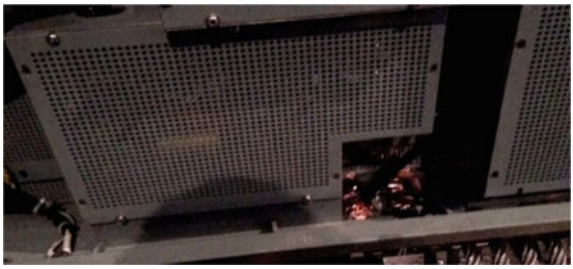

Fig. 12 Laying of internal shielding layer of cabinet

2. A layer of copper foil shielding layer is laid inside the cabinet, as shown in Fig. 12, to isolate radiation noise;
3. Magnetic leakage treatment of gaps and holes in the cabinet board: since the front of the cabinet can be opened, and there is gap space between the door and the cabinet, in addition, the inverter circuit inside the cabinet is wrapped in steel shell by module, and magnetic leakage at the gap of cable holes should also be controlled. Insulation paint is applied between the panels and insulation rings are placed between the cable holes of the steel shell of the internal circuit to prevent magnetic leakage, as shown in Fig. 13.

After taking the above rectification measures, We carry out the test again. Compared with the results before the rectification, the original excess frequency band was optimized with 8.3 dB, and the test was successfully passed in Fig. 14, which verified the effectiveness of the rectification plan.

Fig. 13 Magnetic leakage control measures of cabinet

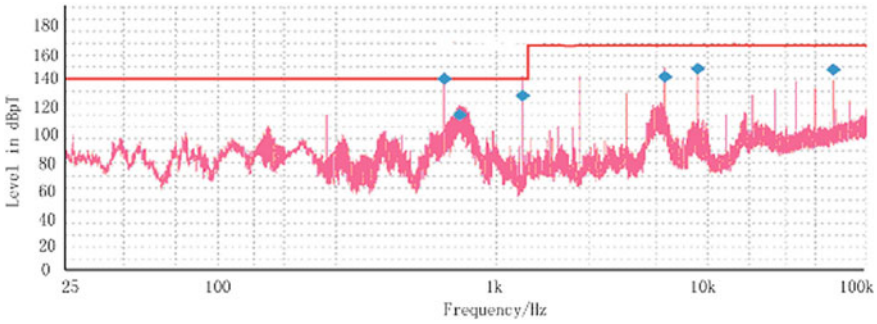

Fig. 14 Measured results

5 Conclusion

This paper mainly analyzes the influence of cabinet characteristics on shielding efficiency of transmission control cabinet. The influence of opening position, opening shape and shielding layer design on shielding efficiency of transmission control cabinet is studied. In the CST simulation environment, a simplified model of the actual transmission control cabinet was established, and an equivalent excitation source was set to simulate its shielding effect. It was concluded that under the premise of the same number of holes, shape and area, the shielding effect of the back opening was better than that of the bottom opening. The shielding efficiency of regular hexagonal opening is better than that of circular opening and square opening. The copper foil laying of the shielding layer can improve the shielding efficiency of the cabinet about 7.63 dB. It provides a theoretical reference for the optimization of the actual transmission control cabinet.

Acknowledgements This paper is supported by Project Supported by National Natural Science Foundation of China (51475246); National Natural Science Foundation of Jiangsu Province (BK20161019); Aviation Science Foundation (20172552017).

References

1. Paul CR (2006) Introduction to electromagnetic compatibility, 2nd edn. Wiley, New York
2. Aouine O, Labarre C, Costa F (2008) Measurement and modeling of the magnetic near field radiated by a buck chopper. IEEE Trans Electromag Compat 50(2):445–449
3. Robinson MP, Benson TM, Christopoulos C et al (1998) Analytical formulation for the shielding effectiveness of enclosures with apertures. IEEE Trans Electromag Capability 40(3):240–248
4. Azaro R, Caorsi S, Donelli M et al (2002) A circuital approach to evaluating the electromagnetic field on rectangular apertures backed by rectangular cavities. IEEE Trans Microw Theory Techn 50(10):2259–2266

5. Konefal T, Dawson JF, Marvin AC et al (2006) A Fast multiple mode intermediate level circuit model for the prediction of shielding effectiveness of a rectangular vox containing a rectangular aperture. IEEE Trans Electromag Compat 47(4):678–691
6. Mao XY, Ping AD (2010) An improved model of robinson equivalent circuit analytical model. Sci China Technol Sci 53(7):1993–1999
7. Wu TL, Lin YH, Wang TK et al (2005) Electromagnetic bandgap power/groud planes for wideband suppression of ground bounce noise and radiated emission in high-speed circuits. IEEE Trans Microw Theory Techn 53(9):2935–2942
8. Zhao Y, Yan W, Zhao B (2010) EMI radiated noise diagnosis and estimation for HF circuits. Trans China Electrotech Soc 25(10):6–13
9. Zhao Y, Luo Y (2010) Rapid analysis and prediction method of radiation interference of high frequency circuit. Chin J Radio Sci 25(3):6–13
10. Zhao Y, Dong Y (2011) EMI noise analysis and process for large-power switched reluctance motor. Proc CSEE 31(21):135–141
11. Zhang F, Yang G (2018) Design specification and processing in big-data analysis system for monitoring and operation of smart grid. Autom Electr Power Syst 42(19):177–183
12. Gao J, Wu X (2018) Non-linear programming method of solving parameters of unity power factor resonant converter. Autom Electr Power Syst 42(6):128–134
13. Liang Y, Liu J (2018) Analysis and suppression strategy of dead-time effect for voltage source converter. Autom Electr Power Syst 42(24):135–142

Computation of the Three-Dimensional Electric Field Using Particle Swarm Optimization Charge Simulation Method

Yongjin Yu, Kecheng Zhao and Yubin Wang

Abstract In this paper, particle swarm optimization (PSO) and charge simulation method (CSM) are combined to calculate the three-dimensional electric field of sphere-plane electrode, rod-plane electrode and simplified high-voltage insulator string. The optimization variable of PSO is the coordinate or charge quantity of the simulation charge, and the fitness function is the potential error of the matching point. In the calculation of the sphere-plane electrode, the calculation results verify the effectiveness of PSOCSM; the comparison with GACSM highlights the advantages of short calculation time and high precision of PSOCSM. In the calculation of the rod-plane electrode, a method to reduce the optimization variables of PSO is proposed to further improve the computational accuracy and optimization efficiency of PSOCSM. In the calculation of the rod-plane electrode and the high voltage insulator string, the comparison results of GACSM and PSOCSM reflect the excellent optimization performance of PSO. The research results provide a new calculation method for electric field calculation of high voltage electrical appliances.

Keywords Particle swarm optimization charge simulation method · Three-dimensional electric field · Numerical calculation · Optimization variable

1 Introduction

Electric field numerical calculation is an indispensable part of insulation analysis and insulation design of high voltage electrical equipment [1]. Commonly used electric field numerical calculation methods include finite element method, boundary element method and CSM. Among these commonly used methods, the

Y. Yu · K. Zhao (✉)
Shandong University of Science and Technology, Qingdao 266590, China
e-mail: 17860751233@163.com

Y. Wang
State Grid Technology College, Jinan 250002, China

Y. Xue et al. (eds.), *Proceedings of PURPLE MOUNTAIN FORUM 2019-International Forum on Smart Grid Protection and Control*, Lecture Notes in Electrical Engineering 585, https://doi.org/10.1007/978-981-13-9783-7_75

CSM is widely used because of its high precision, the easiest to understand, the relatively simple programming, and the obvious advantages in solving the open field problem [2–5].

In view of the cumbersome problem of simulation charge and matching point adjustment in the traditional CSM (TCSM), Chinese and foreign scholars have used some intelligent algorithms to optimize the CSM in recent years [6–9]. In [7], GACSM is used to calculate the electric field. However, due to problems such as poor local search ability, easy premature convergence, and slow convergence rate, the accuracy of electric field calculation is not high. In [8], the improved GA (IGA) is proposed to optimize the CSM, but the problem of poor local search ability of GA is still not solved. Moreover, the matching points are set less in the calculation, which does not reflect the performance of the algorithm well.

In this paper, PSO and CSM are combined to calculate the three-dimensional electric field of the sphere-plane electrode, the rod-plane electrode and the high voltage insulator string. The validity and practicability of the method are verified by calculation results. The superior performance of PSOCSM is demonstrated by comparison with GACSM.

2 Particle Swarm Optimization Charge Simulation Method

2.1 Traditional Charge Simulation Method

The basic principle of CSM is to replace the continuously distributed free or bound charge of a conductor or electrode surface with some dummy discrete charge called simulation charge. Once the electric fields generated by these dummy simulation charges satisfy the potential boundary conditions, these dummy simulation charges can be used to calculate the electric field at any point in the region of interest according to the superposition principle of the electric field [10]. Depending on the geometry of the electrodes, different simulation charges such as point charge, line charge, and ring charge can be used.

The basic formula for CSM is:

$$PQ = \varphi \tag{1}$$

In the formula:

P is determined by the relative position of the simulation charge and the matching point, which is a $m * n$ matrix of potential coefficients, m is the number of matching points, and n is the number of simulation charges.
Q is an simulation charge quantity matrix.
φ is a known matching point potential matrix.

The number and position of the simulation charges is the key to determining the accuracy of the electric field calculation. In the TCSM, the determination of these parameters is mostly based on personal experience and has greater randomness.

2.2 Particle Swarm Optimization

The idea of PSO is to find the optimal solution of the particle swarm through iteration. Suppose the position and velocity of the ith particle in the D-dimensional search space are

$$\begin{aligned} \boldsymbol{X_i} &= (x_{i1}, x_{i2}, \ldots, x_{iD}) \\ \boldsymbol{V_i} &= (v_{i1}, v_{i2}, \ldots, v_{iD}), \quad i = 1, 2, \ldots, N \end{aligned}$$

In each iteration, the particle updates itself by tracking two optimal particles; the first is the particle's individual optimal particle p_{i}; the other is the global optimal particle p_{g}. The iteration formula is [11–13]:

$$\begin{aligned} v_{id} &= w * v_{id} + c_1 r_1 (p_{id} - x_{id}) + c_2 r_2 (p_{gd} - x_{id}) \\ x_{id} &= x_{id} + v_{id} \quad (1 \le d \le D) \end{aligned} \tag{2}$$

where c_1, c_2 are acceleration constants, r_1, r_2 are random numbers in the range (0, 1), and w is the inertia weight.

2.3 PSOCSM

The determination of the quantity, magnitude and position of the simulation charge is actually an optimization problem [7], so using intelligent algorithms to optimize these parameters can improve the calculation accuracy and efficiency of the CSM and reduce manual work. In this paper, PSO and CSM are combined to calculate the electric field. The optimization variable of PSO is the coordinate or charge quantity of the simulation charge, and the fitness function is the potential error of the matching point. Figure 1 is a flow chart of the PSOCSM.

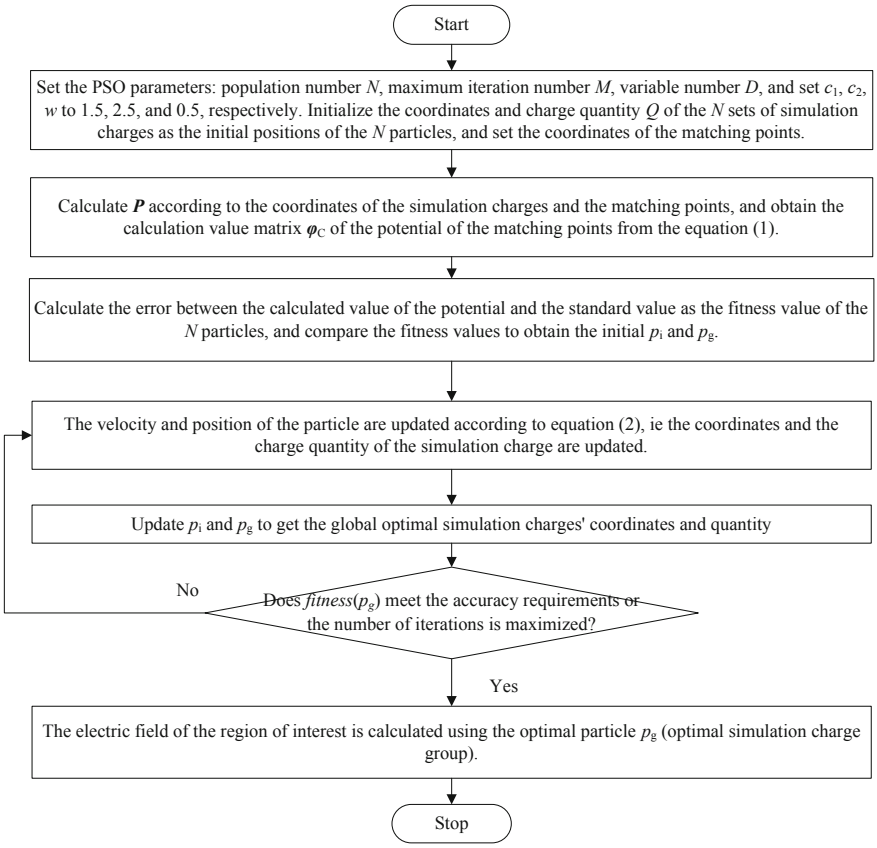

Fig. 1 The flow chart of PSOCSM

3 Calculation Example of Electric Field

3.1 Sphere-Plane Electrode

Figure 2 shows the sphere-plane electrode model. Two point simulation charges are placed in the sphere electrode, and " × " is the position of the point simulation charge. In the figure, H = 4 cm and R = 1 cm. The charge quantities q_1, q_2 and the vertical coordinates z_1 and z_2 of the simulation charge are taken as optimization variables. 100 matching points are uniformly set on the sphere electrode. The number of matching points here is much larger than the number of simulation charges in order to better satisfy the electrode boundary conditions.

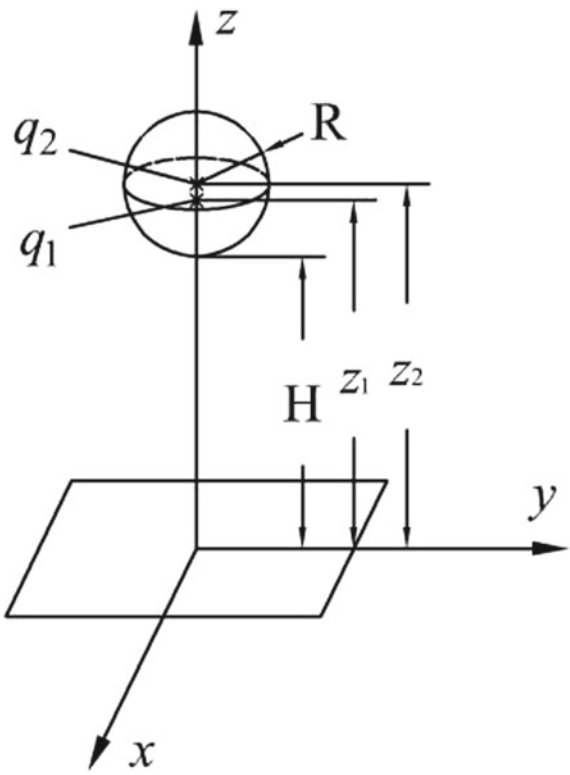

Fig. 2 Sphere-plane electrode model

z_1 and z_2 are not equal and the restrictions are as follows:

$$\begin{cases} 4\text{cm} < z_1 < 6\text{cm} \\ 4\text{cm} < z_2 < 6\text{cm} \end{cases}$$

Set the fitness value function of the PSO to:

$$fitness = \sum_{i=1}^{n} \frac{|\varphi_{iC} - \varphi_S|}{n * \varphi_S} \tag{3}$$

In the formula:

φ_S The standard potential value of the sphere electrode matching point, taken as 1 V here.

n the number of matching points.

φ_{iC} The potential value of two simulation charges acting on the ith matching point.

The smaller the fitness function value is, the smaller the potential error of the matching points is. Optimization goal is

$$\text{minimize}\,\{fitness\}$$

The parameters of the PSO are sequentially set to the population number $N = 50$, the number of optimization variables $D = 4$, and the maximum number of iterations $M = 100$. In the actual calculation, after 100 iterations, 0.4479 s, calculated *fitness* = 1.7565e−6. The coordinates and charge quantities of the optimized simulation charge are shown in Table 1.

Figure 3a is a comparison of the calculated value of potential and the standard value of potential of the matching point, which is calculated from the data of Table 1. It can be seen from Fig. 3a that the potential value of the matching point calculated by the optimized simulation charge is very close to the standard value, which proves the validity and high precision of the PSOCSM.

Table 2 compares the calculation accuracy and efficiency of PSOCSM with GACSM and TCSM (the accuracy of GACSM is the calculation accuracy of [8], and the calculation time is the running time of the program written according to the content of [8]. The calculation accuracy of TCSM is taken from the literature [7]). It can be seen from Table 2 that the calculation accuracy and computational efficiency of PSOCSM are higher than those of GACSM. Figure 3b is an equipotential line diagram of the sphere-plane electrode, calculated from the data of the simulation charge of Table 1.

Table 1 Optimization calculation result

x/cm	*y*/cm	*z*/cm	*Q*/C
0	0	5.000280	1.104787e−10
0	0	4.902379	1.299195e−11

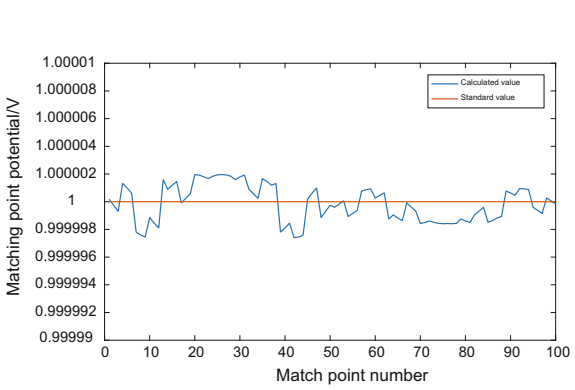

(a) Comparison of potentials at matching points

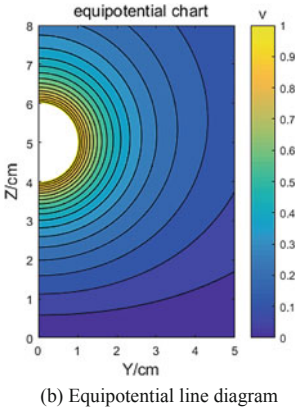

(b) Equipotential line diagram

Fig. 3 Electric field calculation result of the sphere-plane electrode

3.2 Rod-Plane Electrode

Figure 4a is a rod-plane electrode model diagram in which H = 1 cm, R = 1 cm, and L = 5 cm. The dashed line is the ring simulation charge centered on the z-axis. 3 ring simulation charges are placed in the hemisphere portion, and 7 ring simulation charges are placed in the rod portion. Since the model is an axisymmetric structure, only 23 matching points are set in the right half. Take the *xy* plane as the 0 potential plane, and the standard potential of the matching point is taken as 1 V.

Since the radius r and the vertical coordinate z of the ring simulation charge need to be determined, if the r, z, and Q of the 10 ring simulation charges are simultaneously optimized, the number of optimization variables is large. In order to reduce the number of optimization variables and further improve the optimization calculation efficiency, only r and z of the ring simulation charge are optimized, and the simulation charge quantity matrix $\boldsymbol{Q}$ is obtained by inverse matrix calculation

Table 2 Comparison of calculation error and time

Method	Calculation error	Calculation time/s
PSOCSM	1.7565e−6	0.4479
GACSM	4.2708e−5	3.6311
TCSM	5.76e−4	–

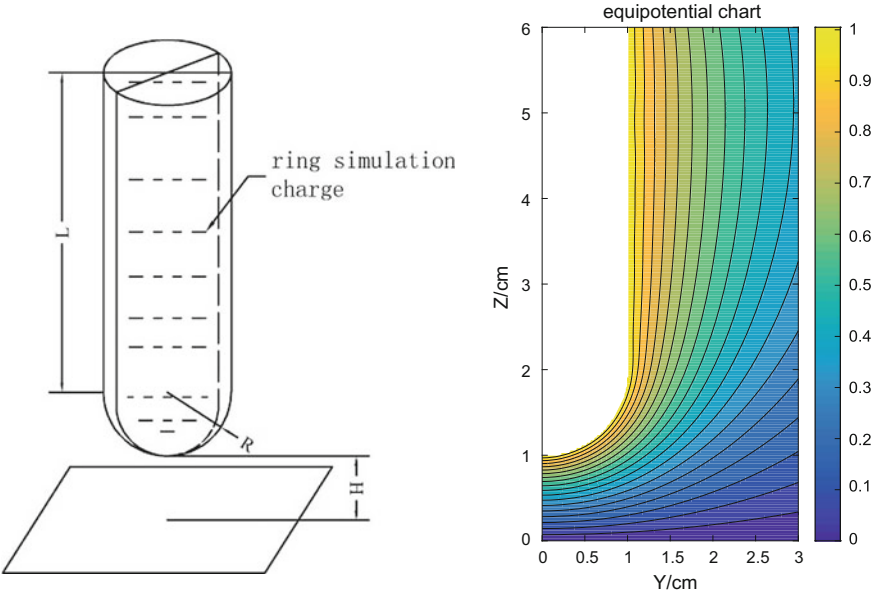

(a) Rod-plane electrode model (b) equipotential line diagram

Fig. 4 Rod-plane electrode model and equipotential line diagram

$\boldsymbol{Q} = \boldsymbol{P}^{-1}\boldsymbol{\phi}$ of Eq. (1) in the optimization process. Then calculate the potential of the matching point by Eq. (1) (Note: the calculated value of the matching point potential is not equal to the standard value, because the $\boldsymbol{P}$ matrix is not a square matrix, so $\boldsymbol{Q}$ is only the least squares solution). It is assumed that the radius r of the ring simulation charge in the rod portion is the same, so it can be set to one variable at the same time. The other variables are the radius r and z coordinates of the ring simulation charge in the hemisphere portion and the z coordinate of the ring simulation charge of the rod portion. The total number of optimization variables is $D = 14$. Reducing the number of optimization variables can improve the optimization efficiency of the algorithm.

If the initial values r and z of the ring simulation charge are not well set, the optimization calculation sometimes still has an unsatisfactory accuracy. In this case, first find the area of the matching point with a large potential error, properly adjust the r and z of the adjacent simulation charge, or directly delete the simulation charge, or add a new simulation charge. The adjusted simulation charge group is then set to the new initial value and optimized for calculation until the accuracy requirement is met.

The PSO related parameters are set to the number of populations $N = 10$, the maximum number of iterations $M = 50$, the number of optimization variables $D = 14$, and still take the formula (3) as *fitness*. In the actual calculation, *fitness* = 1.8301e−3 is obtained after 50 iterations. Table 3 shows the accuracy comparison before and after the reduction of the number of optimization variables. As can be seen from Table 3, reducing the optimization variables can significantly improve the calculation accuracy. Table 4 shows the comparison results between PSOCSM and GACSM of the same model in [7]. It can be seen from Table 4 that the number of simulation charges used by PSOCSM is only 1/ 6 of that of GACSM, but the calculation accuracy of the two methods is almost the same, which reflects the excellent optimization performance of PSOCSM. The r, z, and Q of the ring simulation charge obtained by the optimization calculation are shown in Table 5. Figure 4b is a plot of the equipotential line of the rod-plane electrode calculated from the simulation charge data of Table 3.

Table 3 Accuracy comparison before and after the reduction of the number of optimization variables

Number of optimization variables of PSOCSM(D)	Calculation accuracy
30	2.9541e−2
14	1.8301e−3

Table 4 Comparison between PSOCSM and GACSM

	Number of simulation charges	Calculation accuracy
PSOCSM	10	1.8301e−3
GACSM	58	7.4420e−4

Table 5 Optimization calculation result

No.	*r*/cm	*z*/cm	*Q*/C	No.	*r*/cm	*z*/cm	*Q*/C
1	0.10	1.37	1.0584e−11	6	0.59	3.81	2.0237e−11
2	0.44	1.55	4.3370e−11	7	0.59	4.48	2.4144e−11
3	0.61	1.91	−4.1066e−11	8	0.59	5.32	2.4724e−12
4	0.59	2.68	1.7758e−11	9	0.59	6.00	1.8602e−11
5	0.59	3.16	1.9527e−11	10	0.59	6.59	5.8504e−11

3.3 High Voltage Insulator String

Figure 5a is a simplified model diagram of a 64 kV high voltage insulator string, insulator piece is represented by an ellipse. There are 7 insulator sheets, and the standard voltage distribution from the high voltage terminal to the low voltage terminal is 18.5, 10, 8.5, 7, 5, 6, 9 kV. Each insulator has a major axis radius of 12.7 cm and a height h = 14.6 cm [14–16].

According to the shape of the insulator piece, 4 ring simulation charges are placed in each insulator, and a total of 28 ring simulation charges are set. Since it is an axisymmetric structure, 10 matching points are set in the right half of each insulator, and a total of 70 matching points are set. Here, the voltage of the insulator string is considered to be linearly distributed, and the potential value of each matching point is obtained by linear interpolation [14–16]. Still take the formula (3) as the fitness value function. In the variable setting, the 8 variables to be optimized are the radius *r* and *z* coordinates of the 4 ring simulation charges in each insulator. Considering that the matching points on the top and bottom insulators are less

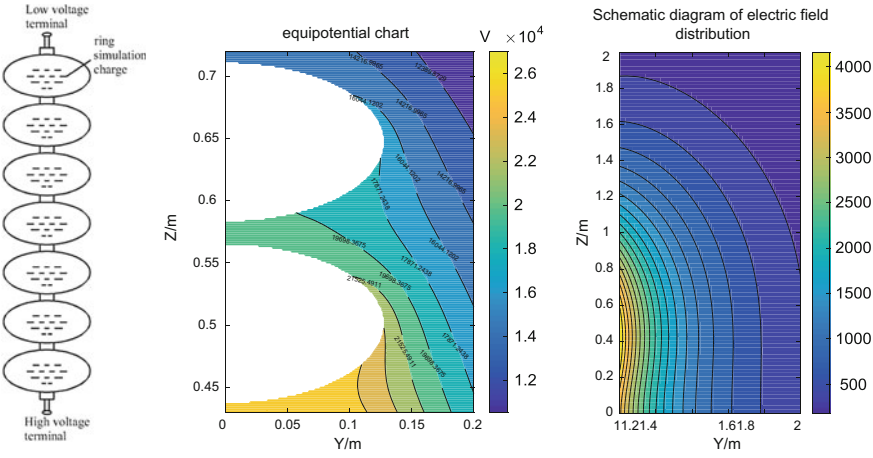

(a) Model (b) Equipotential line diagram (c) Electric field distribution

Fig. 5 Model of high voltage insulator string and distribution of potential and electric field

affected by the simulation charge in the other parts of the insulator, the simulation charges in the top and bottom insulators are separately optimized.

The electric field calculation is performed using the optimization calculation method of Sect. 3.2. The relevant parameters of PSO are set to the maximum number of iterations $M = 50$, the number of populations is $N = 10$, and the number of optimization variables is $D = 8$. In the actual calculation, after 50 iterations, the *fitness* = 7.0337e−3 is obtained, and the precision is high.

A comparison with the IGACSM of the same model in [8] is shown in Table 6. It can be seen from Table 6 that the number of matching points of PSOCSM is about 12 times that of IGACSM (the more matching points, the better the whole insulator string can be simulated, the electrode boundary conditions can be better satisfied), but the potential error of the matching point is almost the same. This embodies the excellent optimization ability of PSOCSM, that is, it can search for a set of optimal simulation charge groups to make more matching points meet the calculation accuracy requirements.

The calculation results of the r, z, and Q of the ring simulation charge are shown in Table 7. The equipotential line diagram of the 4th and 5th insulators of the high-voltage insulator string from the high-voltage terminal to the low-voltage terminal is shown in Fig. 5b, and the electric field distribution diagram at 1–3 m on the right side of the insulator string is shown in Fig. 5c.

Table 6 Comparison between PSOCSM and IGACSM

	Number of matching points	Calculation accuracy
PSOCSM	70	7.0337e−3
IGACSM	6	4.6255e−4

Table 7 Optimization calculation result

No.	r/cm	z/cm	Q/C	No.	r/cm	z/cm	Q/C
1	3.30	1.36	2.0991e−09	15	6.20	49.84	−5.9095e−11
2	7.65	3.99	1.1782e−09	16	10.21	50.12	7.6387e−11
3	5.51	5.84	−9.3787e−10	17	3.74	60.51	6.1074e−12
4	10.88	5.70	3.1570e−10	18	7.90	62.64	1.7136e−11
5	3.74	16.71	1.3904e−11	19	6.20	64.44	−3.4714e−11
6	7.90	18.84	6.0931e−11	20	10.21	64.72	5.3059e−11
7	6.20	20.64	−1.1215e−10	21	3.74	75.11	6.5444e−12
8	10.21	20.92	1.9849e−10	22	7.90	77.24	2.4264e−11
9	3.74	31.31	1.2469e−11	23	6.20	79.04	−3.4550e−11
10	7.90	33.44	4.3011e−11	24	10.21	79.32	3.3246e−11
11	6.20	35.24	−7.9113e−11	25	3.80	90.55	3.1573e−11
12	10.21	35.52	1.2076e−10	26	8.88	92.66	8.1198e−11
13	3.74	45.91	9.6509e−12	27	4.93	93.60	−7.5769e−11
14	7.90	48.04	3.3047e−11	28	9.54	94.45	−6.2183e−11

4 Conclusion

In this paper, PSO and CSM are combined to calculate the electric field of the sphere-plane electrode, the rod-plane electrode and the high voltage insulator string, and the following conclusions are drawn:

1) The calculation accuracy and efficiency of PSOCSM are higher than those of GACSM.
2) Reducing the number of optimization variables of PSOCSM can improve its calculation accuracy and optimization efficiency.
3) PSOCSM has better optimization performance than GACSM, that is, when setting less simulation charge or setting more matching points, high precision results can still be obtained.

References

1. Huang D (2007) Electric field of electrical apparatus based on the improved charge simulation method. Shenyang University of Technology, pp 25–29
2. Han C (2006) Research on optimum CSM for electric field of electric apparatus. Shenyang University of Technology, p 5
3. Guo T, Luo R, Yang Y et al (2019) Research on electromagnetic environment of the 750 kV/330 kV mixed voltage quadruple circuit transmission line on the same tower. High Volt Apparat 55(1):157–164
4. Wu Q, Liu X, Yang T et al (2018) Transient insulation numerical analysis method of GIS under lightning impulse voltage. High Volt Eng 44(12):4098–4104
5. Wu Q, Liu X, Zou J et al (2018) Numerical solution and accuracy validation of electric field using response surface methodology and geometric feature charge simulation method. High Volt Eng 44(6):2060–2066
6. Elrahman MKA (2011) Adapting particle swarm optimisation for charge simulation method. IET Sci Meas Technol (04):96–101
7. Liu X, Wang E, Cao Y, Hong F (2000) Computation of three dimensional electric field using the optimized charge simulation method. Trans China Electr Soc (06):14–17 + 55
8. Fan Y, Wei H, Wendong D et al (2009) A genetic algorithm-based improved charge simulation method and its application. Compel 28(6):1701–1709
9. Elrahman MKA (2014) Fully optimised charge simulation method by using particle swarm optimisation. IET Sci Meas Technol 9(4):435–442
10. Ma X, Gu W (2005) Charge simulation method analysis of static field based on MATLAB language. Insul Surge Arresters (03):41–46
11. Tang J, Wang D, Jia H et al (2018) Optimal economic operation of active distribution networks based on hybrid algorithm of surrogate model and particle swarm optimization. Autom Electr Power Syst 42(04):95–103
12. Huang S (2009) Survey of particle swarm optimization algorithm. Comput Eng Des 30 (08):1977–1980
13. Wen Z, Sun H (2017) Matlab intelligent algorithm. Tsinghua University Press, Beijing

14. Yang F (2008) Study on forward and inverse problem of power frequency electric field of transmission and distribution apparatuses and power frequency electromagnetic environment. Chongqing University, pp 33–35
15. Yang F, Li J, Yao D, He W (2004) Charge simulation method based insulator non-touching electric field mapping method. Autom Electr Power Syst 28(15):95–99
16. Yang F, He W, Yao D, Li J (2003) The research on the application of CSM in on-line detection of defective insulators. High Volt Eng 29(12):24–25 + 42

Automatic Detection of Environmental Change in Transmission Channel Based on Satellite Remote Sensing and Deep Learning

Zhi Yang, Chuang Li, Wenhao Ou, Xiangze Fei, Binbin Zhao, Xiao Ma, Deshuai Yuan and Qiongqiong Lan

Abstract The detection of environmental change in transmission channel based on high-resolution satellite remote sensing is the emerging trend in the operation and maintenance of power grid. To improve the precision, a change detection method based on the deep learning was put forward in this paper. Firstly, by the improved change vector analysis algorithm and grey level co-occurrence matrix considering the neighborhood information, the spectral and texture changes of images at different times were calculated. Moreover, the most probably changed and unchanged zone samples were extracted through setting the adaptive sampling interval. Additionally, the modified deep convolutional neural network model Inception-v3 was constructed and trained. The in-depth features in changed and unchanged zone were extracted, and the changed zone was distinguished effectively. The results showed that the proposed method could effectively extract the environmental change in transmission channel, and the accuracy reached over 92.5%, which was obviously superior to the contrast methods.

Keywords Transmission line · Automatic change detection · Satellite remote sensing · Deep learning

1 Introduction

Recently, a large number of (ultra) high voltage lines were constructed in our country. Since the safety and stability of transmission line is directly correlated with the transmission channel environment, the inspection and change detection of

Z. Yang (✉) · C. Li · W. Ou · X. Fei · B. Zhao · X. Ma
China Electric Power Institute, Haidian District, Beijing, China
e-mail: yangzhi0713@foxmail.com

D. Yuan
China University of Mining and Technology, Beijing, China

Q. Lan
China Centre for Resources Satellite Data and Application, Beijing, China

Y. Xue et al. (eds.), *Proceedings of PURPLE MOUNTAIN FORUM 2019-International Forum on Smart Grid Protection and Control*, Lecture Notes in Electrical Engineering 585, https://doi.org/10.1007/978-981-13-9783-7_76

transmission channel environment is extremely important to guarantee the safe operation of power grid. So far, the inspection of transmission channel is mainly based on the labor on the ground, on-line monitor device [1, 2], unmanned aerial vehicle (UAV) [3, 4] and helicopter [5]. However, for the traditional means, there exist the problems such as high activity cost, large constraint in environmental conditions, high risk and complicated examination and approval for flight, and thus it is difficult to guarantee the comprehensive monitoring on the normalized and multi-temporal channel. Furthermore, the monitoring requirements on the environmental change in transmission channel at regular intervals cannot be satisfied [5].

In recent years, the satellite remote sensing technology develops rapidly. The decimeter-level (0.3−0.8 m) image resolution is obtained. The update frequency is rose to about 1 day. Compared with the traditional observation means including the labor, helicopter and UAV, the satellite remote sensing possesses the following obvious advantages [6]: (1) wide coverage, (2) short renewal period, (3) less limitation in the environmental conditions and (4) large information capacity. It is suitable for the large power grid with wide-range configuration, long distance power transmission and complicated environment change. Thus, the environmental change detection of transmission channel based on the satellite remote sensing has attracted more and more attention [7, 8].

The change detection of satellite remote sensing has been one of the hotspots in remote sensing research area currently. With the remote sensing images in the same region at different times, the changed zone is analyzed and confirmed, so as to extract the environmental change information of ground object [9]. Among the existing change detection methods of high-resolution image, due to the differences in high-resolution satellite sensors and imaging conditions of multi-temporal remote sensing image, it is difficult to eliminate the image registration error even if after the fine registration. This directly leads to inconsistency in contrastive image areas and low detection accuracy. Although there exist some multi-source high-resolution change detection methods, there has still been no universal and effective method at present [10]. The main reason is that the same ground object has different manifestations at different times in images with different resolutions when comparing high-resolution images. It is difficult to extract the proper characteristics and compare directly. Therefore, for the registration error and feature extraction, the improved change vector analysis considering the neighborhood information was put forward in this paper. Moreover, by the deep learning, the automatic environment change detection of transmission channel in high-resolution remote sensing images was realized.

2 Methodology

Firstly, the high-resolution satellite remote sensing images in the same section of transmission channel at different times were obtained. Secondly, the fine registration between two high-resolution satellite remote sensing images was realized, and

the image with lower resolution was resampled. By the histogram matching method, the relative radiometric correction was carried out. On that basis, the modified change vector analysis considering the neighborhood information was put forward. In combination of the grey co-occurrence matrix method, the spectral and texture changes in images with different time phases were extracted, respectively. Then the change intensity map was generated, and the error due to inconsistency between local contrast areas during the change detection was reduced. The distributions of spectral and texture change were summarized, respectively. By setting the adaptive sampling interval, the most probably changed and unchanged pixel were selected as the training samples. Finally, the deep convolutional neural network model inception-v3 incorporating the intrusive monitoring was constructed to train the sample, and extract the abstract features in changed and unchanged zone. On this basis, all pixels in two images were divided into changed and unchanged group. And the final environmental change detection chart of transmission channel was formed (see Fig. 1).

2.1 *Spectral Change Considering Neighborhood Information*

The literature [11] proposed the robust change vector analysis (RCVA) algorithm to improve the preliminary detection precision of environmental change, so as to choose better training samples for deep learning. As for RCVA algorithm, the details are as follows: if there is the minimum difference in spectral information between the

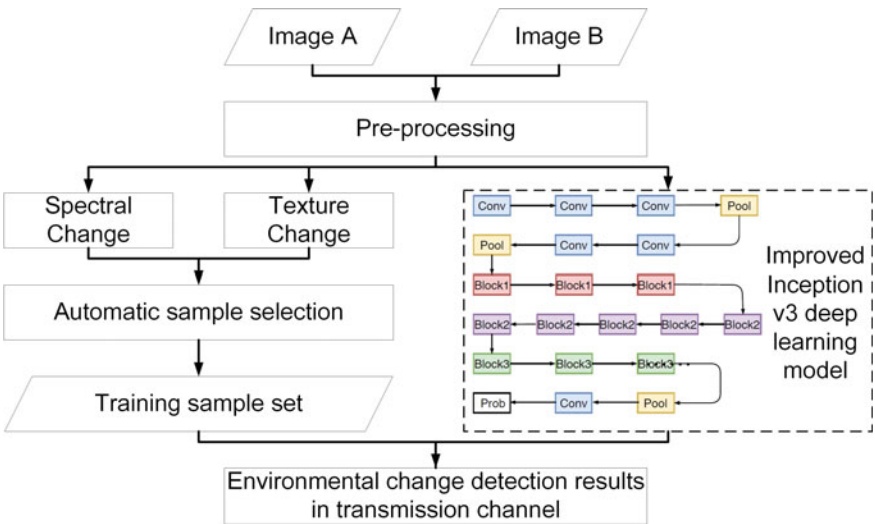

Fig. 1 Flow chart of change detection

pixel within the range of x_2 ($j \pm w, k \pm w$) and the pixel x_1 (j, k), the pixel includes the most corresponding ground information of pixel x_1 (j, k). In other words, during the contrast detection of high-resolution remote sensing image, if there are geometric registration errors in two images, and the spectral difference between one pixel in image 1 and another pixel within neighborhood range of pixel in image 2 is minimum, the two pixels are the corresponding pixels of ground object with the same name, and then the effects of registration error are reduced effectively. However, RCVA algorithm proposed in [11] only considered the spectral difference from the view of single wave band of pixel and then merged all wave bands, instead of the overall spectral difference of corresponding pixel. As a result, the corresponding image points of the ground object with the same name in each wave band are different, and it is hard to carry out the subsequent comparison. For this purpose, the modified RCVA method was put forward to decrease the effect of registration error in this paper. In the modified RCVA, a moving window with the size of $2w + 1$ was used for spectral change detection considering the adjacent pixel. The computational procedure is divided into two steps. Firstly, through each point in image t_2 and the point with the smallest spectral difference in the adjacent pixel of the point in image t_1, the difference image x_{diff_a} was acquired. Then, x_{diff_b} was obtained by the same method in image t_1, specific as shown in formulas (1) and (2).

$$x_{diff_a}(j,k) = \min_{(p\in[j-w,j+w],q\in[k-w,k+w])} \left\{ \sqrt{\sum_{i=1}^{n} \left(x_2^i(j,k) - x_1^i(p,q)\right)^2} \right\} \tag{1}$$

$$x_{diff_b}(j,k) = \min_{(p\in[j-w,j+w],q\in[k-w,k+w])} \left\{ \sqrt{\sum_{i=1}^{n} \left(x_1^i(j,k) - x_2^i(p,q)\right)^2} \right\} \tag{2}$$

Secondly, by the Eq. (3), the variation diagrams of spectral information M_s taking the neighborhood information into account was obtained.

$$M_s = \begin{cases} x_{diff_b}(j,k), & x_{diff_a}(j,k) \geq x_{diff_b}(j,k) \\ x_{diff_a}(j,k), & x_{diff_a}(j,k) < x_{diff_b}(j,k) \end{cases} \tag{3}$$

2.2 Texture Change Considering Neighborhood Information

The grey level co-occurrence matrix (GLCM) is a universal method to describe the texture through the spatial correlation features of image grey [12]. Therefore, in this paper, GLCM variance was selected to extract the texture features. The calculation is shown as formula (4).

$$GLCM^{i}_{\text{var}} = \sum_{i=1}^{N}\sum_{j=1}^{N} p(l,g,d,\theta,i)\,(l-u_i)^2 \tag{4}$$

where $p\ (l, g, d, \theta, i)$ is the frequentness from the pixel with the grey level of l in the ith wave band to the pixel with the grey level of g at a distance of d in the image. θ is the generation direction of GLCM. μ_i is the mean value of $p\ (l, g, d, \theta, i)$, and N is the grey level. In this paper, 7×7 window was selected to extract $GLCM^{i}_{var}$.

In order to consider the neighborhood information, for the difference chart of textural features in the ith wave band of point (j, k), it is calculated according to $GLCM^{i}_{var_{x1}}$ of point x_1 with the time phase t_1 and $GLCM^{i}_{var_{x2}}$ of point x_2 with the time phase t_2 in Sect. 1.1, among which the points x_1 and x_2 are the homologous image points of point (j, k). And then the texture variation diagram taking the neighborhood information into account was obtained. The texture change intensity M_t is calculated by the formulas (5) and (6).

$$GLCM^{i}_{diff} = GLCM^{i}_{\text{var}_{x2}} - GLCM^{i}_{\text{var}_{x1}} \tag{5}$$

$$M_t = \sqrt{\sum_{i=1}^{n} \left(GLCM^{i}_{diff}\right)^2} \tag{6}$$

where n is the number of spectral bands in the satellite remote sensing image.

2.3 Adaptive Selection of Training Sample

After acquiring the spectral change map M_s and texture change map M_t, to improve the change detection precision by deep learning, it is necessary to effectively choose the most probably changed and unchanged zone. In this paper, by setting the adaptive parameter of sample extraction T, the most probably changed and unchanged training samples were extracted. In the unchanged zone, the texture and spectral change are both smaller. Thus, the pixels of $T\%$ with the smallest spectral and texture change are considered as the unchanged zone. In the changed zone, the texture and spectral change are relatively large, so the pixels of $T\%$ with the largest spectral and texture change are selected as the changed zone (see Fig. 2).

2.4 Construction and Training of Improved Inception-V3 Model

In this paper, the network model structure is based on Inception-v3 [13]. The parameter size of Inception-v3 is relatively small, and less than half of 60 million of

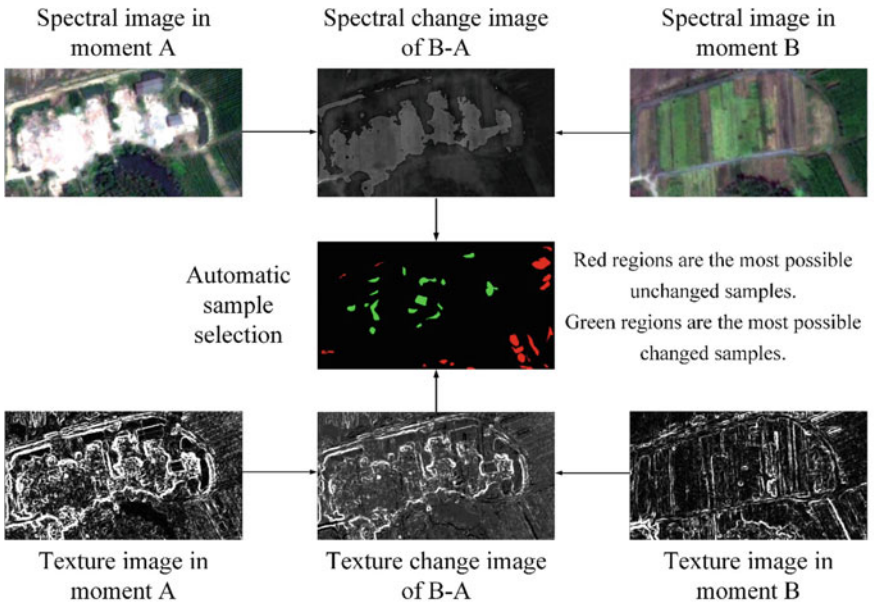

Fig. 2 Automatic sample selection in combination of spectral and texture change

parameters for AlexNet, and much smaller than 0.14 billion of parameters for VGGNet. In the whole network, the floating-point calculation is 5 billion times, which is higher than 1.5 billion times of Inception-v1, but lower than that of VGGNet.

As for the concern of computational complexity of deep models, FLOPS is used in this study. FLOPS stands for the floating point operations, which is a universal index for estimating the computational complexity of any given deep learning model. Due to the fact that computation in deep neural network is dominated by multiply-adds in fully connected and convolutional layers, the cost of non-linearities, dropout, and normalization are ignored when calculating the FLOPS. Table 1 shows that when compared with VGG (15.8 billion FLOPS), Inception based models have a much lower FLOPS, which is 1.5 billion of Inception-v1 and 5 billion for Inception-v3, respectively. The reason why Inception-based models show a lower computation complexity mainly lies in the global average pooling (GAP) layer used instead of fully connected layer in VGG. Besides, the move from fully connected layers to average pooling has also improved the top-1 accuracy by about 0.6% in the ImageNet classification [13]. Therefore, Inception-v3 is slightly more accurate and much more efficient than

Table 1 FLOPS of VGG, Inception-v1 and Inception-v3

Model	VGG	Inception-v1	Inception-v3
FLOPS/billion	15.8	1.5	5

VGG. It can be transplanted to the normal server easily, and then offer fast response.

To solve the vanishing gradient problem due to the increase in the depth of network Inception-v3, through the deep supervision, by adding many classifiers softmax in the middle of network, the vanishing gradient problem is avoided effectively. Meanwhile, the decrease in calculated performance due to the application of random sparse interlinkage for enhancing the learning ability by the traditional neural network model is solved.

Meanwhile, by the transfer learning method, the parameters of previous convolution and pooling layer in the network structure Inception-v3 remain unchanged, and only the final classification layer in the model is trained in this paper. In the ultimate classifier softmax of original network Inception-v3, there are 1000 output nodes (because of 1000 categories in ImageNet). Thus, it is needed to convert to the required number of output nodes by deleting the last network layer. As this research focuses on the recognition of changed and unchanged zone, the ultimate classifier softmax in the network Inception-v3 only needs to be divided into two node types, that is, the changed and unchanged zone.

During the network training, Adam is chosen as the optimizer, and the initial learning rate is set as 1e−3. The cross-entropy is selected as the loss function. At the same time, to optimize the training process, the learning rate is adjusted to 1/10 of original at intervals of 100 epochs. Through the early-stop method, the over fitting is further avoided. Firstly, the model with the current highest verification precision is recorded, and the step size is set as N. If the precisions of N models are all not improved after the model with the highest precision, the training will be ended, and returned to the model with the highest precision. Then it will be taken as the final change detection model.

3 Experiment and Result Analysis

3.1 Experimental Area

In this paper, two typical sections of in Zhejiang-Jiahu intensive channel were selected as experimental area (see Fig. 3). In the Zhejiang-Jiahu intensive channel, there are 1000 kV Hu-An and An-Tang I/II transmission lines, ±800 kV Fu-Feng and Jin-Su transmission lines, and ±500 kV Lin-Feng and Ge-South transmission lines. In the construction and operation process of Zhejiang-Jiahu intensive channel, the construction work and illegal building in the line protection zone are increasing, and the channel environment changes greatly. The environment change detection surrounding the channel has important significance to the safety and stability of transmission line.

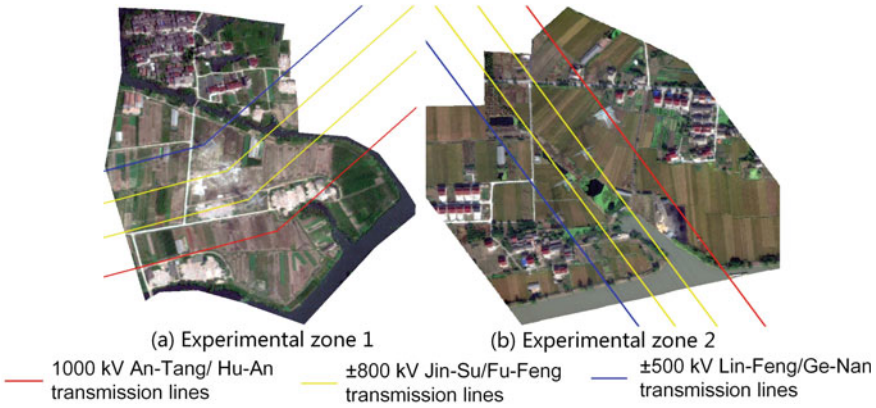

Fig. 3 Geographical distribution of experimental area

3.2 Data Acquisition

For the above experimental area, the 0.3 m worldview-2 satellite images were acquired on May 1, 2010 and May 16, 2012 (see Fig. 4). The pixel numbers of Zone 1 and 2 are 2218 × 2737 and 3222 × 2549, respectively. From Fig. 4, it can be seen that ±500 kV Lin-Feng/Ge-South lines and ±800 kV Fu-Feng line had been completed, while ±800 kV Jin-Su line was under construction, and 1000 kV An-Tang/Hu-An lines had not yet started in May 2010. Thus, during this period, there were a lot of illegal buildings and construction operations due to house removal around the transmission channel. In May 2012, the satellite remote sensing image showed that the other lines all had been put into operation except for 1000 kV An-Tang/Hu-An lines. Additionally, the illegal buildings around channel reduced, and the house removal areas all had been translated into farmland and vegetation, which were the major changes in channel environment of experimental area. Figure 4c, f show the visual interpretation of channel environment change in two experimental areas, respectively. The black and white represent the changed and unchanged zone, respectively. This will be acted as the reference value to verify the accuracy of automatic detection algorithm in this paper.

3.3 Experimental Result Analysis

Figure 5 shows the environmental change detection of transmission channel trained by the improved model Inception-v3 in two experimental areas, as the window size $w = 3$, and the sample extract parameter $T = 15$. Combined Figs. 4 and 5a, b, the proposed method better detects the changed zone including the areas translated

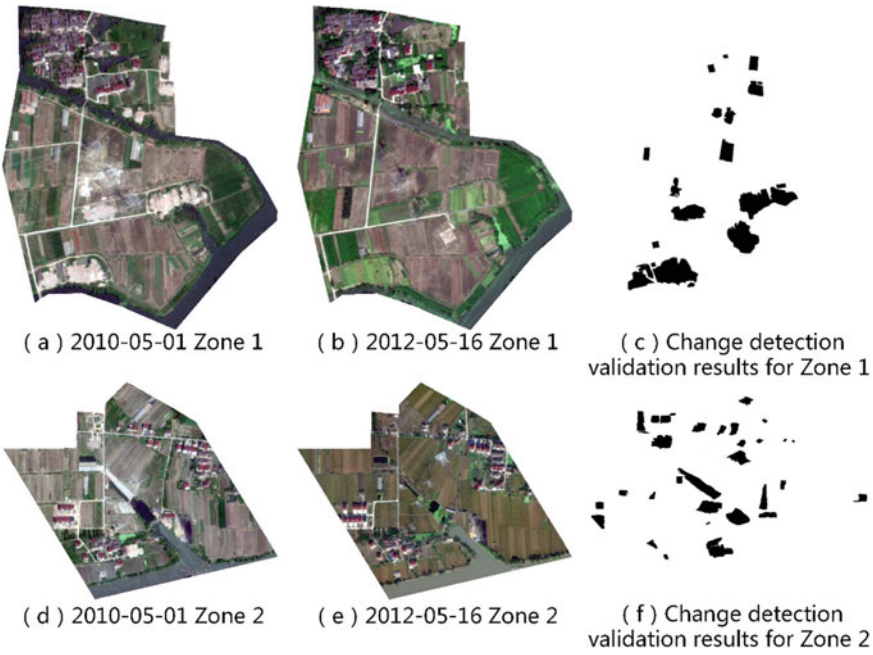

Fig. 4 Data collection and change detection of validation data in experimental area

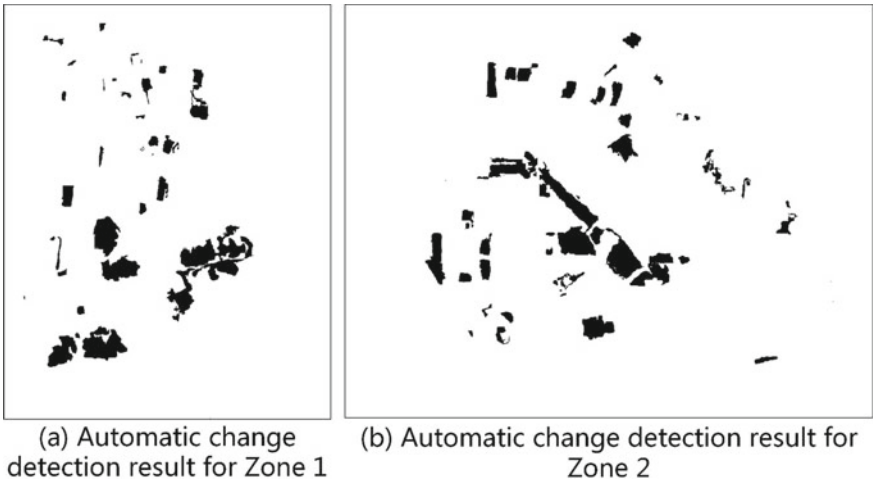

Fig. 5 Environmental change detection of transmission channel in experimental area

from house removal to farmland and vegetation, decreased and increased building area and newly increased forest area around the transmission channel from 2010−2012. This illustrates the validity of this research.

For the quantitative analysis, Figs. 5a, b and 4c, f are contrasted respectively. The precision of environmental change detection in transmission channel are evaluated by 3 indexes, including the accuracy, false alarm rate and missing detection rate, as shown in Table 1. By the proposed method, the accuracy of environmental change detection is over 92.5%, and the false alarm rate and missing detection rate are approximately 16.8 and 6.5% in experimental area, respectively. This indicates that the method proposed based on satellite remote sensing and deep learning method has a good effect in environmental change detection of transmission channel.

To further verify the feasibility and validity of the proposed method, the proposed method is compared with change vector analysis (CVA), robust change vector analysis (RCVA) [11], and purposive fast independent component analysis (PFICA) [14] in change detection results of experimental area 1 (see Table 2).

Table 2 shows that using traditional method CVA, the change detection accuracy of high-resolution remote sensing images is lower, while the corresponding change detection accuracy by improved RCVA and PFICA increases obviously. The change detection accuracy of the proposed method is the highest, and the false alarm rate and missing detection rate are both lower than that of other traditional algorithms. In terms of efficiency, the proposed method considers the spectral and texture neighborhood information, and trains learning by the deep convolutional neural network, so the time used is slightly longer than that of other algorithms, but at the same order with most of comparing algorithms. From the perspective of business requirement, the environmental change detection accuracy of transmission channel is extremely important. Therefore, by the comprehensive consideration of change detection accuracy and algorithm complexity, the proposed method is an effective method to detect environmental change of transmission channel and inspect the power grid (Table 3).

Table 2 Accuracy of channel environment change detection based on the proposed method

Pixel number		Change detected	Un-change detected	Accuracy (%)	False alarm rate (%)	Missing detection rate (%)
Area 1	Actual change	1,297,825	82,375	92.78	16.58	5.97
	Actual un-change	258,023	3,079,383			
Area 2	Actual change	4,143,285	295,348	92.64	17.01	6.65
	Actual un-change	849,184	10,259,790			

Table 3 Comparison of accuracy and time consumption by different methods

Method	Accuracy (%)	False alarm rate (%)	Missing detection rate (%)	Time (s)
CVA	51.42	39.93	28.33	195.85
RCVA	69.22	31.60	17.27	1054.11
PFICA	82.10	23.66	11.46	1877.81
Proposed method	92.78	16.58	5.97	2834.43

4 Conclusions

In this paper, an automatic detection method of environmental change in transmission channel was put forward based on high-resolution satellite remote sensing image and deep learning. Firstly, spectral and texture change were calculated by proposing an improved CVA and GLCM with considering neighborhood information. Then, an adaptive automatic algorithm was proposed for the training sample selection. The selected training samples were put into the modified deep convolutional neural network model Inception-v3, and the change can be detected effectively.

The experimental results showed that the proposed method could effectively detect the environmental change of the transmission channel. The accuracy of the proposed method was over 92.5%, obviously superior to the traditional methods.

Although the proposed method has acquired better change detection results, the shadow of ground object reduces the precision of the computerized automatic identification to some extent. To improve the change detection precision, a universal, effective and high-efficiency change detection method considering multi-sensors, multi-temporal and multi-feature information will be established in future.

References

1. Li Y, Teng Y, Leng O et al (2018) Reliability evaluation of on-line monitoring device over transmission line based on data drive concept. Proc CSEE 38(15):4410–4419 + 4641
2. Wu Y, Zheng N, Su H et al (2017) Smart hydropower station oriented real-time automatic inspection approach for on-line monitoring states and its application. Autom Electr Power Syst 41(9):123–129
3. Shi M, Qin K, Li K et al (2017) Design and testing on autonomous multi-UAV cooperation for high-voltage transmission line inspection. Autom Electr Power Syst 41(10):117–122
4. Liu Z, Du Y, Chen Y et al (2019) Simulation and experiment on the safety distance of typical ±500 kV DC transmission lines and towers for UAV inspection. High Volt Eng 45(2):426–432
5. Meng L, Zhang L (2012) A helicopter-borne stable pod for high voltage electricity-line-cruising. Autom Electr Power Syst 36(21):113–117

6. Qing W, Xiaodong Z, Guanzhou C et al (2018) Change detection based on faster R-CNN for high-resolution remote sensing images. Remote Sens Lett 9(10):923–932
7. Li L, Fan C (2017) Land-cover classification of electric transmission lines of hierarchical classification based on object-oriented. Geomat Spat Inf Technol 5(1):143–146
8. Wu X, Li Y, Liu X et al (2012) SAR image power line corridor changing detection based on multi-scale joint segmentation. J Electr Power Sci Technol 27(4):51–56
9. Leichtlet T, Gei C et al (2017) Unsupervised change detection in VHR remote sensing imagery.Int J Appl Earth Obs Geoinf 54:15–27
10. Zhang X, Chen X, Li F et al (2017) Change detection method for high resolution remote sensing images using deep learning. Acta Geod Cartogr Sinica 46(8):999–1008
11. Thonfeld F et al (2016) Robust change vector analysis (RCVA) for multi-sensor very high resolution optical satellite data. Int J Appl Earth Obs Geoinf 50:131–140
12. Xiao P, Zhang X et al (2016) Change detection of built-up land: a framework of combining pixel-based detection and object-based recognition. ISPRS J Photogramm Remote Sens 119:402–414
13. Szegedy C, Liu W, Jia Y et al (2015) Going deeper with convolutions. In: 2015 IEEE conference on computer vision and pattern recognition (CVPR)
14. Ghaffarian S, Ghaffarian S (2014) Automatic building detection based on purposive fast ICA (PFICA) algorithm using monocular high resolution google earth images. ISPRS J Photogramm Remote Sens 97:152–159

A Spectrum Correction Approach for Power System Sub-harmonic Analysis

Zhongmin Sun, Yulin Chen, Qiaogen Gu, Yu Cui and Dongchao Liu

Abstract Parameters identification of power system inter-harmonic is research emphasis recently, because it can be seriously interfered by nearby harmonic leakage. The sub-harmonic lower than power frequency is not only disturbed by power frequency component, but also interfered by negative frequency component itself. A variety of analytical methods are used for acquiring the parameters of the signal but difficult to eliminate various confounding factors adequately. Therefore, as sub-harmonic component can be interfered by both negative frequency component and power frequency component, an improved low frequency spectrum correction model was established, and different frequencies of sub-harmonics were analyzed with scanning way. Simulation results show that the proposed method for identification of sub-harmonic parameters has higher accuracy, small computation and is easy for project implementation.

Keywords Sub-harmonic · Negative frequency · Fundamental frequency · Fast fourier transform (FFT)

1 Introduction

With the wide application of fluctuating load and frequency converter in power system, the detection and measurement of inter-harmonics has drawn more attention from researchers. Among them, the inter-harmonics whose frequency are lower than the fundamental frequency are also known as sub-harmonics. Research shows that sub-harmonics can produce zero-crossing deviation, voltage fluctuation, flicker, sub-synchronous oscillation and other hazards in power system [1]. The accurate measurement of sub-harmonics is of great significance to the division of harmonic

Z. Sun (✉) · Y. Chen · Q. Gu · D. Liu
NR Electric Co. Ltd., Nanjing 211102, China
e-mail: sunzm@nrec.com

Y. Cui
State Grid Jiangsu Electric Power Co. Ltd., Nanjing 210024, China

Y. Xue et al. (eds.), *Proceedings of PURPLE MOUNTAIN FORUM 2019-International Forum on Smart Grid Protection and Control*, Lecture Notes in Electrical Engineering 585, https://doi.org/10.1007/978-981-13-9783-7_77

responsibility, the control of harmonic pollution and the improvement of power quality. In the field of harmonic analysis of power system, the most commonly used method is the discrete Fourier transform (DFT) and its fast algorithm, the fast Fourier transform (FFT) [2].

As it is difficult to achieve synchronous sampling, the DFT-based harmonic analysis method will produce spectrum leakage in the case of non-synchronous sampling condition [3, 4]. In order to reduce errors, a variety of spectral correction methods have been developed, such as interpolation method [5, 6], all-phase spectrum method [7], Kalman filter based method [8] and energy barycenter correction method [9]. However, the negative frequency component in signal was not taken into account among the mentioned methods, which may have good performance in solving the case of complex exponential signal with single frequency or signal with no dense spectral components. However, for real low-frequency sinusoidal signals, these correction methods need to be further improved.

The measured voltage and current signal is a real sinusoidal signal in power system, which is a stable fundamental frequency component. When the waveform of standard signal is distorted and sub-harmonic is produced, it is difficult to accurately measure the parameters of the sub-harmonic. On one hand, the sub-harmonic is easily affected by its negative frequency because of its low frequency. On the other hand, the low-frequency component is relatively small compared with the fundamental frequency, and the leakage interference caused by the fundamental frequency component is also serious.

The influence of negative frequency on spectrum analysis was studied in [10], which depicted that the negative frequency component not only has practical physical significance, but also must be considered if the signal frequency is relatively low in order to reduce the analysis error. Some spectrum analysis methods based on DFT, such as FFT phase difference method [11] and all-phase FFT phase difference method [12], can effectively improve the accuracy of spectrum analysis by considering the influence of negative frequency component. Furthermore, to improve the low-frequency correction performance, a complex ratio correction method was proposed, in which the influence of negative frequency on spectral line selection was taken into account [13]. Besides, a spectrum correction method by considering the influence of negative frequency was proposed [14]. By solving the equations, the corrected low-frequency parameters were obtained, which can suppress the interference of negative frequency to some extent.

Normally, the influence of harmonics and inter-harmonics has small effect on the fundamental frequency components. Therefore, the measurement accuracy of fundamental frequency is very high in off-line condition. To make it possible, odd frequency point correction and multi-layer DFT interpolation correction algorithm are proposed [15], which can reduce spectral interference to fundamental frequency component through phase rotation and spectral line superposition. In addition, [16] suppressed spectral leakage by weighting power harmonic signals through the convolution window, and eliminated the fence effect by interpolation, thus obtaining accurate fundamental frequency measurement values. Therefore, under the condition of stable power signal, the measurement error of fundamental

frequency parameters can meet the precision requirements of the method proposed in this paper if the appropriate time window is selected for off-line measurement.

Based on the above analysis, in this paper, on the basis of [14] and considering the influence of fundamental frequency components, an improved spectrum correction model suitable for the measurement of sub-harmonic parameters in power systems was proposed. By modifying the results of discrete Fourier transform and solving the three-spectral line equations, spectral interference among signals can be effectively suppressed.

In this paper, the sub-harmonics with different frequencies were analyzed by scanning at an interval of 0.2 Hz. The simulation results show that the improved method has higher measurement accuracy when measuring the sub-harmonics with fundamental frequency, which verifies the effectiveness of the proposed method.

2 Spectrum Interference of Sub-interharmonics

In the estimation of harmonic parameters, the voltage and current signal is cosine/sine signal as $A\cos(\omega t+\theta)$. According to the Euler's identity, the signal function $A\cos(\omega t+\theta)$ can be transformed into $0.5Ae^{\mathrm{j}(\omega t+\theta)}+0.5Ae^{-\mathrm{j}(\omega t+\theta)}$. The truncation of the signal is equivalent to adding a rectangular window to the signal and the amplitude spectrum can be obtained through discrete time Fourier transform (DTFT), as shown in Fig. 1. When in asynchronous sampling condition, the DFT result of the signal will generate the phenomenon of spectrum leakage. As can be seen from Fig. 1, the lower the measured sub-harmonic frequency is, the more serious the spectrum interference will be, and the influence of negative frequency cannot be ignored.

Meanwhile, the voltage and current signal of the power system has a stable fundamental frequency component with a relatively large amplitude. When take the sub-harmonic as the concerned component, its negative component combined with the fundamental wave would become the main interferences.

Figure 2 shows the phasors of time-domain discrete signals after DFT when sub-harmonic f_p is 0.1, 5, 25 and 49 Hz, respectively. The positive frequency component is the concerned part, and the negative frequency and power frequency part are the interference components, which together constitute the phasors through DFT.

As can be seen from Fig. 2, when sub-harmonic f_p is close to 0 Hz, its negative frequency component is the main interference. When sub-harmonic f_p is close to 50 Hz, the leakage part of fundamental frequency turns out to become the main interference.

Therefore, for the specific object, sub-harmonic in power system, it is necessary to consider the negative frequency and fundamental frequency interferences to improve the measurement accuracy of sub-harmonic parameters, especially when the frequency is close to 0 Hz or fundamental frequency.

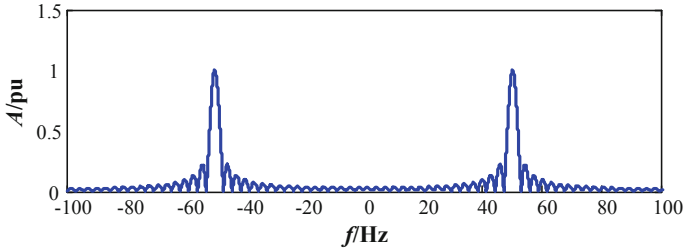

(a) Amplitude response in which positive and negative frequency components are far

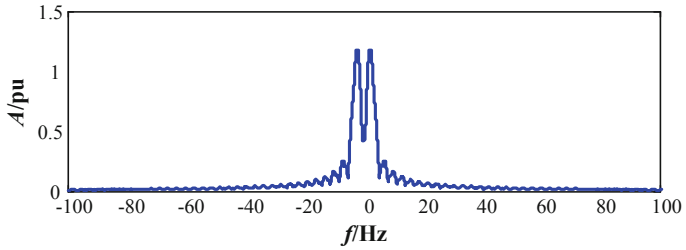

(b) Amplitude response in which positive and negative frequency components are adjacent

Fig. 1 Spectral interference between positive and negative frequency components

3 Spectrum Correction with Multiple Interferences

Assume the time domain signal of the power system containing sub-harmonics as [14]

$$x(t) = A_p \cos(\omega_p t + \varphi_p) + A_0 \cos(\omega_0 t + \varphi_0) + B \tag{1}$$

where, ω_p, A_p, φ_p and ω_0, A_0, φ_0 are the analog angular frequency, amplitude and initial phase angle of low-frequency signal and fundamental frequency signal respectively, and B are DC offset.

The signal obtained from (1) is truncated by a rectangular window, and the Fourier transform of it is as

$$\begin{aligned} X(\omega) = \int_0^T x(t) e^{-\mathrm{j}\omega t} dt = \frac{A_p e^{\mathrm{j}\varphi_p} D(\omega - \omega_p)}{(\omega - \omega_p)} + \frac{A_p e^{-\mathrm{j}\varphi_p} D(\omega + \omega_p)}{(\omega + \omega_p)} \\ + \frac{A_0 e^{\mathrm{j}\varphi_0} D(\omega - \omega_0)}{(\omega - \omega_0)} + \frac{A_0 e^{-\mathrm{j}\varphi_0} D(\omega + \omega_0)}{(\omega + \omega_0)} + 2B \frac{D(\omega)}{\omega} \end{aligned} \tag{2}$$

where, $D(\omega) = \mathrm{e}^{-\mathrm{j}\frac{\omega T}{2}} \sin \frac{\omega T}{2}$.

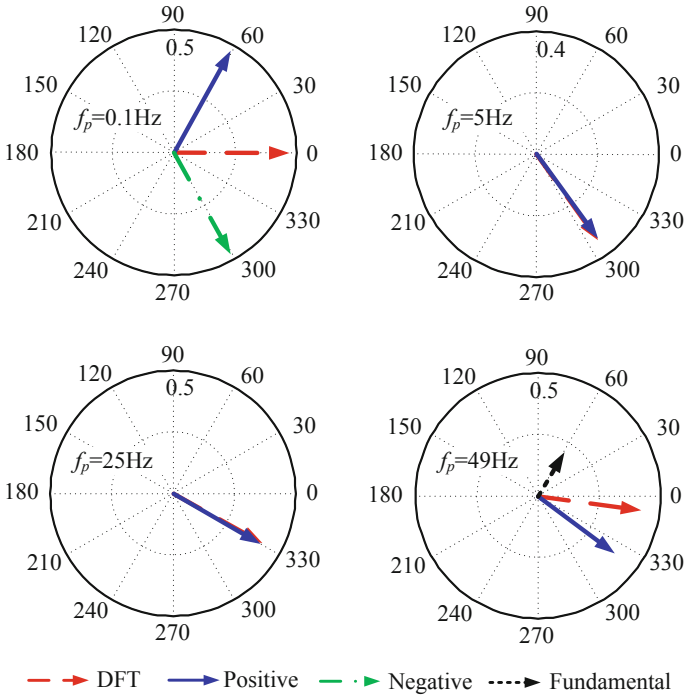

Fig. 2 Spectral interference of sub-harmonic

Let us define

$$\begin{aligned} X'(\omega) &= X(\omega) - \frac{A_0 e^{j\varphi_0} D(\omega-\omega_0)}{(\omega-\omega_0)} - \frac{A_0 e^{-j\varphi_0} D(\omega+\omega_0)}{(\omega+\omega_0)} \\ &= \frac{A_p e^{j\varphi_p} D(\omega-\omega_p)}{(\omega-\omega_p)} + \frac{A_p e^{-j\varphi_p} D(\omega+\omega_p)}{(\omega+\omega_p)} + 2B\frac{D(\omega)}{\omega} \end{aligned} \tag{3}$$

In Eq. (3), the influence of power frequency component has been eliminated in $X'(\omega)$. $\omega = k\Delta\omega$ was used to discretize Eq. (3), where $\Delta\omega = \frac{2\pi}{T} = \frac{2\pi f_s}{N}$ is the spectral resolution, and k is the position of spectral line.

The highest spectral line of the concerned sub-harmonic component is k_2, the prior line and the later line are k_1 and k_3 respectively. Thus, $\omega_1 = k_1\Delta\omega$, $\omega_2 = k_2\Delta\omega$, $\omega_3 = k_3\Delta\omega$. Equation (4) can be derived as

$$D(\omega_1 \pm \omega_p) = D(\omega_2 \pm \omega_p) = D(\omega_3 \pm \omega_p) \tag{4}$$

Also

$$2B\frac{D(\omega)}{\omega} = 2B\frac{e^{-\mathrm{j}(\omega T/2)}\sin \omega T/2}{\omega} = 0 \tag{5}$$

Then, the equation set (6) that can be established by using three spectral lines.

$$\begin{cases} \left(\omega_1 - \omega_p\right)^{-1} D^+ + \left(\omega_1 + \omega_p\right)^{-1} D^- - X'(\omega_1) = 0 \\ \left(\omega_2 - \omega_p\right)^{-1} D^+ + \left(\omega_2 + \omega_p\right)^{-1} D^- - X'(\omega_2) = 0 \\ \left(\omega_3 - \omega_p\right)^{-1} D^+ + \left(\omega_3 + \omega_p\right)^{-1} D^- - X'(\omega_3) = 0 \end{cases} \tag{6}$$

where, $D^{\pm} = A_p e^{\pm \mathrm{j}\varphi_p} D\left(\omega \mp \omega_p\right)$ is a constant.

Therefore, Eq. (6) is a linear equation set, which can be regarded as a homogeneous system of equations, and the corresponding non-zero solution vector is $\{D^+, D^-, -1\}$, and the existence of such non-zero solution condition is that the determinant of coefficient matrix is zero, which is shown in (7).

$$\begin{vmatrix} \left(\omega_1 - \omega_p\right)^{-1} & \left(\omega_1 + \omega_p\right)^{-1} & X'(\omega_1) \\ \left(\omega_2 - \omega_p\right)^{-1} & \left(\omega_2 + \omega_p\right)^{-1} & X'(\omega_2) \\ \left(\omega_3 - \omega_p\right)^{-1} & \left(\omega_3 + \omega_p\right)^{-1} & X'(\omega_3) \end{vmatrix} = 0 \tag{7}$$

Thus, the explicit expression of ω_p can be solved as

$$\omega_p = \sqrt{\mathrm{M}_2/\mathrm{M}_1} \tag{8}$$

where

$$\mathrm{M}_1 = \begin{vmatrix} 1 & \omega_1 & X'(\omega_1) \\ 1 & \omega_2 & X'(\omega_2) \\ 1 & \omega_3 & X'(\omega_3) \end{vmatrix}, \mathrm{M}_2 = \begin{vmatrix} 1 & \omega_1 & \omega_1^2 X'(\omega_1) \\ 1 & \omega_2 & \omega_2^2 X'(\omega_2) \\ 1 & \omega_3 & \omega_3^2 X'(\omega_3) \end{vmatrix}$$

The amplitude and phase can be amended by specific spectral lines as

$$X'(\omega_2) = A_p \mathrm{e}^{\mathrm{j}\varphi_p} \Phi + A_p \mathrm{e}^{-\mathrm{j}\varphi_p} \Psi \tag{9}$$

where

$$\Phi = \frac{T}{2}\mathrm{sinc}\frac{\left(\omega_2 - \omega_p\right)T}{2}\mathrm{e}^{-\mathrm{j}\frac{(\omega_2-\omega_p)T}{2}}, \Psi = \frac{T}{2}\mathrm{sinc}\frac{\left(\omega_2 + \omega_p\right)T}{2}\mathrm{e}^{-\mathrm{j}\frac{(\omega_2+\omega_p)T}{2}}$$

Bond with the conjugate of Eq. (9), an equation set can be established as

$$\begin{cases} X'(\omega_2) = A_p e^{j\varphi_p}\Phi + A_p e^{-j\varphi_p}\Psi \\ X'^*(\omega_2) = A_p e^{-j\varphi_p}\Phi^* + A_p e^{j\varphi_p}\Psi^* \end{cases} \tag{10}$$

The amplitude and phase correction formula of the sub-harmonic component, which can be obtained from Eq. (10), is as shown in (11).

$$A_p e^{j\varphi_p} = \frac{\Phi^* X'(\omega_2) - \Psi X'^*(\omega_2)}{|\Phi|^2 - |\Psi|^2} \tag{11}$$

4 Simulation Analysis

To verify the effectiveness and accuracy of the algorithm, discrete signals are generated according to Eq. (12) for simulation calculation.

$$x(t) = A_p \cos(2\pi f_p t + \varphi_p) + A_0 \cos(2\pi f_0 t + \varphi_0) + B \tag{12}$$

Each parameter of the signal is shown in Table 1.

When the signal was truncated by a rectangular window, DC offset has no influence on other DFT discrete spectral lines according to formula (5). So it is rational to assume B = 0.

The synthetic signal was analyzed by direct DFT method (Method 1), DFT method with Hamming window (Method 2), low-frequency correction method (Method 3) proposed in [14] and the algorithm proposed in this paper (Method 4). Combined with practical project, in order to reflect the feasibility of the algorithm in the case of errors in power-frequency measurement, random error e, where $e \in [-10^{-2}, 10^{-2}]$, is superimposed on fundamental frequency parameters. The estimation results are shown in Fig. 3.

Table 1 Parameters of simulation experiment

Parameter	Setting value
Fundamental amplitude	$A_0 = 1$
Fundamental phase	$\varphi_0 = 10°$
Fundamental frequency	$f_0 = 50$ Hz
Sub-harmonic amplitude	$A_p = 0.5$
Sub-harmonic phase	$\varphi_p = 30°$
Sub-harmonic frequency	f_p = [1:0.2:48] Hz
Sampling frequency	$f_s = 300$ Hz
Samples	$N = 512$

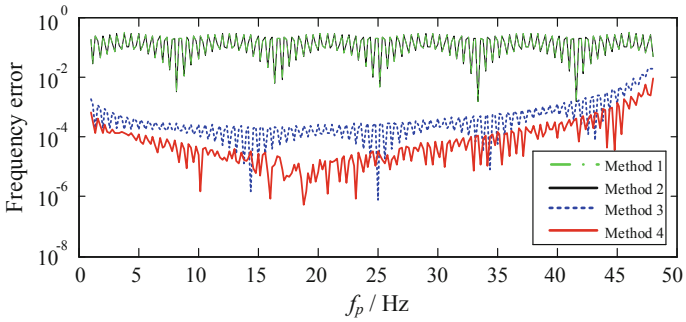

(a) Absolute error of frequency calculation

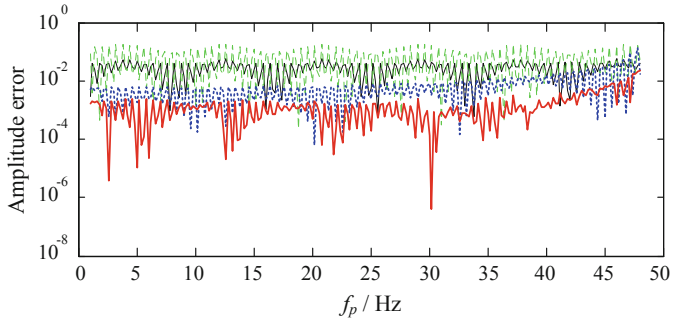

(b) Absolute error of amplitude calculation

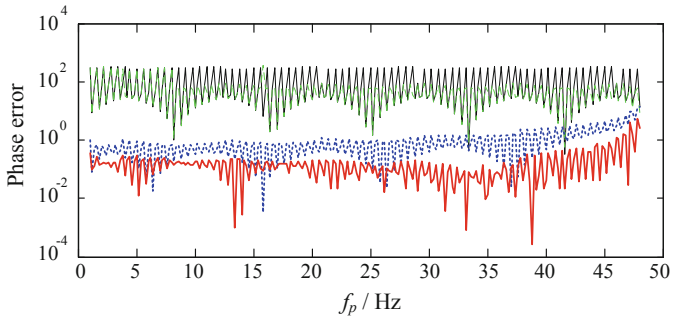

(c) Absolute error of phase calculation

Fig. 3 Comparison of absolute error in estimating sub-harmonic

From Fig. 3, despite the random error in fundamental frequency, the measurement accuracy of sub-harmonic spectrum correction method is better than other methods, showing good adaptability.

When the synthetic signal contains noise, which is always existing in real field, the sub-harmonic will not only be disturbed by other spectra, but also be affected by noise. In order to verify the adaptability of the algorithm under noise condition, Gaussian white noise was superimposed in the signal of Eq. (12). Figure 4 is the measurement error results of each method when the signal to noise ratio (SNR) is

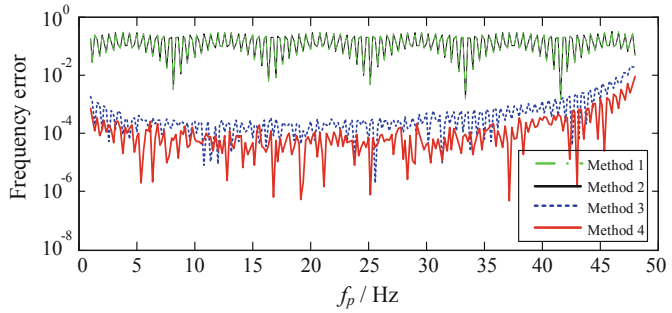

(a) Absolute error of frequency calculation

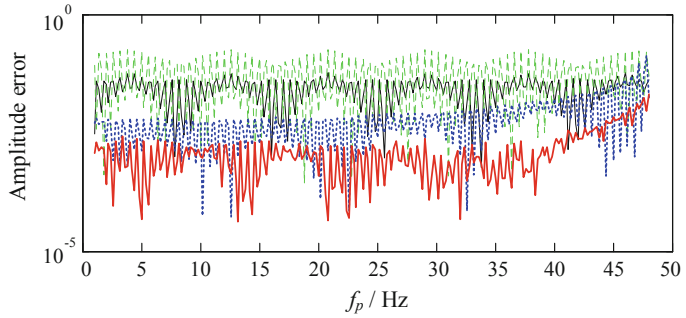

(b) Absolute error of amplitude calculation

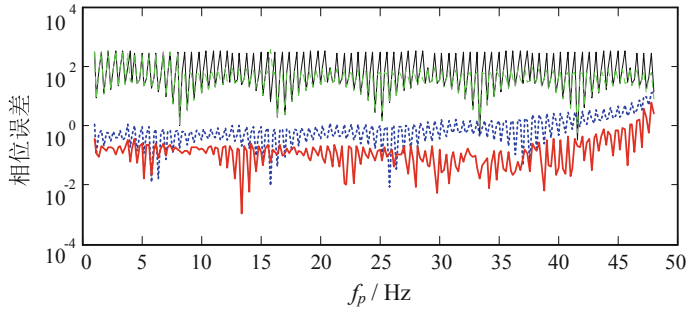

(c) Absolute error of phase calculation

Fig. 4 Comparison of absolute error in estimating sub-harmonic with noise

60 dB. It can be seen that the algorithm in this paper still has obvious better precision when the signal contains noise.

The simulation results show that the spectrum correction method, which considering the influence of negative frequency and fundamental frequency, can effectively reduce the spectrum interference. Since the time domain expression of the correction parameter is obtained, the influence of the fence effect can be eliminated without complex algorithm, and the high-precision low-frequency

sub-harmonic analysis is realized. Moreover, when the power frequency measurement error and signal noise are taken into account, the proposed algorithm still shows good adaptability.

5 Conclusion

This paper presents a discrete spectrum correction method for sub-harmonic signal of power system by eliminating influence from negative frequency component and fundamental component. An improved spectrum correction model is constructed based on three spectral lines near the specific spectrum peak. Afterward, the corrected sub-harmonic parameters are obtained. The simulation results show that this method has the ability to reduce the interference of the negative frequency and fundamental frequency components for the measured sub-harmonic components. Furthermore, the small computation burden is beneficial to practical realization.

The proposed method only targets the stable sub-harmonic signal, which may not suitable for the low-frequency damping oscillation. Moreover, under the dynamic condition, such as the start of large motor, the fundamental frequency parameters will change significantly, which also has an impact on the accuracy of sub-harmonic measurement.

Acknowledgements This work was supported by Science and Technology Project of State Grid Corporation of China(SGCC) with contract No. SGLNJZ00YJJS1800187.

References

1. Haixue L (2010) Origin of interharmonic and its effects on power system. Power Suppl Technol Appl 13(5):1–6
2. International Electrotechnical Commission (2002) IEC61000-4-7 general guide on harmonics and interharmonics measurements, for power supply systems and equipment connected thereto. Geneva, Switzerland
3. Ming D, Yuliang Y, Lin L et al (2018) Synchronized grid-connected parameter measurement based on all-phase discrete Fourier transform with adaptive sampling sequence length. Autom Electr Power Syst 42(13):175–181
4. Sun Z, Chen Y, Zhang J (2018) An improved measurement method for wideband multi-frequency signal. In: 2018 2nd IEEE conference on energy internet and energy system integration (EI2). IEEE, Beijing, pp 1–6
5. Yu W, Miao Y, Yonggang P et al (2017) New explanation of frequency domain methods for harmonic analysis and its generalization [J]. Autom Electr Power Syst 41(20):70–77
6. Jiangfei L, Longdao C (2019) Improved interpolation algorithm applied to power harmonic analysis. Autom Electr Power Syst 43(8):138–144
7. Xiaohong H, Zhaohua W (2008) High accuracy parameter estimation of sinusoidal signal based on all-phase spectrum analysis. Electr Power Autom Equip 28(7):54–57
8. Yu W, Huiyong H, Miao Y et al (2017) Measurement method of dual Kalman filtering for three-phase grid signals. Autom Electr Power Syst 41(16):171–178

9. Kang D, Chunsong Z, Zhijian Y (2010) Frequency estimation accuracy analysis and improvement of energy barycenter correction method for discrete spectrum. J Mech Eng 46 (5):43–48
10. Yuwen M, Yaqing T, Haitao Z et al (2011) Advances and trends in spectrum analysis methodology with negative frequency contribution. Electr Meas Instrum 48(5):27–32
11. Haitao Z, Yaqing T (2008) A new method for phase difference measurement based on FFT with negative frequency contribution. Acta Metrol Sinica 29(2):168–171
12. Siwei T, Zhiliang R, Changcun S (2013) Improvement of phase difference correcting spectrum method based on all-phase FFT. Syst Eng Electron 35(1):34–39
13. Kuifu C, Jianwen W, Senwen Z (2008) Spectrum correction based on the complex ratio of discrete spectrum around the main-lobe. J Vib Eng 21(3):314–318
14. Kuifu C, Jianwen W, Senwen Z (2008) Correction of frequency spectrum for low frequency components. J Vib Eng 21(1):38–42
15. Yamei L, Jin H, Honggeng Y (2012) Multilayer DFT interpolation correction approach for power system harmonic analysis. Proc CSEE 32(25):182–188
16. Zhongmin S, Zhengyou H, Tianlei Z (2016) A kind of hybrid convolution window and its application in harmonic analysis. Trans China Electrotechn Soc 31(16):207–214

Video Shake Detection

Peng Wu, Tong Li, He Yang and Qipeng Chen

Abstract Video surveillance systems play an irreplaceable role in power scene monitoring. However, in the process of image acquisition, video surveillance equipment will inevitably have various external interference factors. This paper proposes an effective method for video shake detection. This method incorporates the classical BOW (bag-of-words) model into the traditional projection method to get the acquired feature representation in a higher level and make it more robust. In addition, we focus on the local characteristics of the image and use a block operation. The experimental results show the effectiveness of our method.

Keywords Shake detection · Gray projection · BOW

1 Introduction

1.1 A Subsection Sample

The video surveillance system is small in size and stable in operation. It brings convenience to production. For example, it can replace human work for monitoring and control in some harsh environments, which can save a lot of human resources costs; and it will not produce physiological defects such as visual fatigue. It can ensure production safety and provide objective guidance. At present, in the power scene, the video surveillance system has been more and more widely used. For power industry applications, video surveillance provides full-time monitoring of all important power equipment, combined with intelligent algorithms to give accurate and intelligent decision making. However, in the process of image acquisition,

P. Wu · H. Yang (✉) · Q. Chen
Artificial Intelligence on Electric Power System State Grid Corporation Joint Laboratory (GEIRI), Global Energy Interconnection Research Institute, Beijing 102209, China
e-mail: yanghe@geiri.sgcc.com.cn

T. Li
State Grid Liaoning Electric Power Research Institute, Shenyang, Liaoning 110006, China

Y. Xue et al. (eds.), *Proceedings of PURPLE MOUNTAIN FORUM 2019-International Forum on Smart Grid Protection and Control*, Lecture Notes in Electrical Engineering 585, https://doi.org/10.1007/978-981-13-9783-7_78

video surveillance equipment will inevitably have various external interference factors. For example, camera shake caused by wind or other irresistible factors may cause anomalies of shake in video image, resulting in reduced performance of the monitoring system. The degradation of such images will present significant challenges to subsequent algorithmic modules, which may give erroneous decisions.

In recent years, researchers have proposed a series of effective practical algorithms for the shake detection [1]. The most obvious feature of video shake is the overall displacement between the frame and the frame. After the displacement is detected, further logical decision is made to determine whether the video is shake. Therefore, basically the video shake is detected around how to detect the displacement. Methods commonly used nowadays in displacement estimation include gray projection method [2], block matching method [3], feature point matching method [4, 5] and optical flow method [6].

The common optical flow method uses fast corner detection and LK sparse optical flow [7, 8]. In actual use, because the optical flow depends on the detection of the feature points, if the current environment has no way to find more corners, the estimated displacement will be very inaccurate. If you want to get better results, the calculation will be very large. And the optical flow method is very easy to produce erroneous estimation for moving objects in the actual environment, and the robustness is poor. As the same as the optical flow method, the feature point matching method depends on the finding of feature points, and to find a more accurate feature point this method usually has a very large amount of calculation, the actual running speed is actually slow. The gray projection method [1, 2] is a more common method, the calculation amount is relatively small, and the actual effect is also good. However, the gray histogram features extracted by the gray projection method are sensitive to external interference factors, which makes it less robust, especially in the environment with complex power-transforming scenarios. Therefore, this paper combines the advantages of gray projection method with the word bag model to extract higher-level features to improve the detection accuracy of gray projection method. This research may be a premise to future improve object identification applications in the electric power system scenarios, like in [9].

2 Method

2.1 Overview

The gray projection method is actually an operation for simplifying the extraction of image distribution features. The image features are converted into curves along the row and column coordinates in units of pixel rows and columns of the two-dimensional image, thereby making it easier to calculate the image distribution characteristics. This paper will propose a more effective method based on gray projection method. The whole algorithm framework includes the followings.

Pre-processing: The environment of the actual captured video in the power scene is usually more complicated. We first use image smoothing filtering. The advantage of filtering is that it can eliminate the influence of the edge of the image. When the image moves fast, the edge information is unique on each image, that is, the edge information of each image is different, thus causing the projected waveform to be very different at the edge. Histogram equalization is then performed to stretch the contrast of the image and further filter the effects of noise or other interference factors.

Grayscale projection feature extraction: The grayscale projection operation that is used in the conventional image processing is performed, that is, the pixel grayscale value is accumulated in the row and column directions. This way we will get a row vector and a column vector respectively. The resulting projection vector then go through a mean normalization operation, that is, we subtract the mean of all elements of the vector from each element in the vector.

High-level feature extraction: If only the gray projection vector is used, the displacement error we obtain may be large. Here we will introduce the classic BOW model [10, 11] and block operation, and the higher level feature extraction will be described in detail in the next section.

Similarity calculation: With eigenvectors, we can calculate the distance metric for any two features. There are many ways to measure distances. Since the object is a high-dimensional pocket vector, we use a simple chi-square distance here.

2.2 High-Level Feature Extraction

If the overall image displacement is calculated, when there are too many moving objects in the image, it is easy to cause misjudgment due to the movement of the object. Therefore, the image can go through non-overlapping block operations, and the blocks are overlapped and sampled. For example, for a certain frame image, 4×4 blocks are taken, and in each block, the method of overlapping sampling sub-blocks is performed, and it is noted that the sampled sub-blocks are kept the same in size. Thus, for each frame of image we can get a series of sub-block row and column projection vectors. For convenience, we splice this row and the column vector and name it x, indicating the underlying feature representation of the sub-block. For all frame images in a video, we can get the underlying feature set of all sub-blocks in the video frame $X = \left\{x_i^n\right\}_{n=1}^{N}$, where x_i^n is the nth projected feature of the sub-block image in the ith frame.

The Bag-of-words model is a commonly used document representation method in the field of information retrieval. In information retrieval, the BOW model assumes that for a document, its word order and grammar, syntax and other elements are ignored, and it is only regarded as a collection of several words. The appearance of each word in the document is independent and doesn't depend on whether other words appear. That is to say, any word that appears in any position in

the document is independently selected regardless of the semantic meaning of the document. Through observation, we will find that although there are differences between different instances of the same type of target, we can still find some commonalities between them. In this paper, we will incorporate the underlying projection vector into the BOW model, where the BOW model can be in the form as follows:

$$\min\|x - B\alpha\|_2^2 \, s.t. \|\alpha\|_1 = 1 \|\alpha\|_0 = 1 \tag{1}$$

where x is an arbitrary underlying feature representation, α is the high-level feature representation of the output, and B is the cluster center set constructed by the K-Means algorithm. The word table is constructed using the K-Means algorithm for all of the underlying feature sets in the video frame. K-Means algorithm is an indirect clustering method based on the measure of similarity between samples. This algorithm divides N objects into K clusters with K as the parameter. The data in the same cluster has high similarity and different clusters share low similarity. Depending on the distance between the underlying projection vectors, the K-Means algorithm can be used to combine words with similar meanings as the basic vocabulary in the word list. For a certain frame image, we can extract the projection vectors of many sub-blocks, which can be replaced by the word approximation in the word list; then pass each sub-block in the statistics block to the corresponding word in the vocabulary in the block. The number of occurrences can be expressed as a vector of K dimensions. For example, if one frame of image is divided into 16 blocks, then 16 K-dimensional vectors will be obtained.

2.3 Video Shake Displacement Metric

For any two frames in the video, we can get the corresponding high-level feature vector. Use the chi-square distance to measure their distance:

$$d\left(X^i, X^j\right) = \frac{1}{R}\sum_{r=1}^{R} \chi^2\left(P_r^i, Q_r^j\right) \tag{2}$$

where P_r^i, Q_r^j is the r-th block high-dimensional feature representation in the i-th frame image X^i and the j-th frame image X^j, respectively; χ^2 is the chi-square distance $\chi^2(x, y) = \sum_n \frac{(x_n - y_n)^2}{x_n + y_n}$.

In order to effectively measure the displacement between video frames, we calculate the distance by sampling two frames in a certain step size. The distance between all sampled frame pairs is then averaged as a measure of the displacement of the entire video.

Table 1 Comparison of experimental results

Method	Total	False negative	False positive	Detection rate (%)
Projection method [5]	10	2	1	70
Block projection method [1]		1	0	90
Our method		0	0	100

3 Experimental Results

In order to verify the effectiveness of the algorithm, we collected 5 segments of normal video and 5 segments of shake video in the substation scenario. The number of blocks taken in the block operation is set to 4×4, the sub-block size is uniformly set to 16×16, and the K-Means parameter K is 256. Note that for fairness of comparison, we use the same block operation for projection. We use a grid search method to find the optimal threshold for shake decisions of the following three methods. The specific experimental comparison results are shown in Table 1.

From the comparison of the above experimental results, We find the blocking method is effective and the high-level feature representation we extracted makes the detection more robust.

4 Conclusion

We propose an effective method for video shake detection in power monitoring scenarios. The method uses a block operation to focus on the local characteristics of the image; we combine the projection vector for the bottom layer with the classic BOW model to obtain a higher-level feature representation. The experimental results show the effectiveness of the proposed algorithm and achieve a 100% detection rate.

Acknowledgements The work was supported by State Grid Corporation of China Headquarters Project (5455HJ180015) which is 'Research regarding the Substation Robotic Intelligent Inspection Technique based on Actively Cooperated Intelligent Sensing Devices'.

References

1. Wu H, Deng HB (2013) A video stabilization method based on sub-block gray projection. Acta Armamentarii 34(4):406–411
2. OuYang W (2012) Research and implementation of surveillance video and image anomaly diagnosis system based on image analysis. Huazhong Normal University, WuHan
3. Xu L, Lin X (2007) Global motion estimation for video stabilization. J Tsinghua Univ (Sci Technol) 47(1):92–95

4. Hu R, Shi RJ, Shen F et al (2007) Video stabilization using scale-invariant feature. In: Proceedings of the 11th international conference information visualization. IEEE Computer Society, Washington, DC, pp 871–877
5. Beijing Wen'an Technology Development Co., Ltd. (2011) Video quality diagnosis system and its implementation: China, 201110053434. 4[P]. 2011-09-07
6. Peng Y, Ye Q, Huang J, Jiao J (2010) Video stabilization algorithm content complete. J Image Graph 15(9):1384–1390
7. Bouguet JY (2013) Pyramidal implementation of the Lucas Kanade feature tracker description of the algorithm. [2013-01-21]. http://robots.stanford.edu/cs223b04/algo_tracking.pdf
8. Shi JB, Tomasi C (1994) Good features to track. In: Proceedings of the 1994 IEEE computer society conference on computer vision and pattern recognition. IEEE Computer Society, Washington, DC, pp 593–600
9. Huang X, Yang L, Zhang Y, Cao W, Li L (2018) Image enhancement based detection method of non-soluble deposit density levels of porcelain insulators. Autom Electr Power Syst 42 (14):151–157
10. Wallach HM (2006) Topic modeling: beyond bag-of-words. In: International conference on machine learning
11. Fei-Fei L, Perona P (2005) A Bayesian hierarchical model for learning natural scene categories. In: Proceedings of CVPR

The Methods of Calculating Heights of Lightning Rods and the Design of the Calculating Software

W. L. Liu

Abstract It is essential to calculate the height of lightning rods in order to make them function efficiently. But sometimes the calculation can be complex. In order to calculate the heights of lightning rods, we follow the principle of "Centering on the axis line and firstly focus on the upper level". With the help of tools like Borland C++ Builder, a computing software for calculating the height of lightning rods was designed, and it can cover the calculations of the height(s) of one single lightning rod; two lightning rods of the same height; and two lightning rods with different heights, using polygon method. It can also deal with the calculation of the height of one single lightning rod using rolling ball method. The main points of the calculation, the main program code of the software and several examples are shown in the paper. After comparison and verification, the results given by the software are reliable. The use of the software can greatly reduce the burden of calculation during the design of lightning rods.

Keywords Lightning rods · Calculation of heights · Polygon method · Design of software

1 Introduction

The lightning rods has the disadvantage of counterattack. It is very important for the lightning rods to play its protective effect and save metal materials by setting the installation position of the lightning rods correctly and calculating the rods height accordingly [1–5].

In the national standard [6, 7], the calculation method of the protection range of lightning rods under various arrangement forms is obtained. The protection range of lightning rods is studied and a new calculation method is acquired in the references [8–11]. But the protection range is obtained under the condition of known rods

W. L. Liu (✉)
Changchun Institute of Technology, Changchun 130012, China
e-mail: 645125163@qq.com

Y. Xue et al. (eds.), *Proceedings of PURPLE MOUNTAIN FORUM 2019-International Forum on Smart Grid Protection and Control*, Lecture Notes in Electrical Engineering 585, https://doi.org/10.1007/978-981-13-9783-7_79

height. In engineering practice, on the contrary, the lightning rods is set after the protected object. How to calculate the rods height is a problem that must be solved.

Reference [12] has studied the calculation of rods height of the multiple lightning rods, but it does not involve the case of an individual rods and two rods. Reference [13] has studied the calculation method of rods height of lightning rods in various arrangement modes and compiled software to realize automatic calculation, but it is relatively simple when the height and radius of protected objects are given.

Considering the protection efficiency and economy of the lightning rods comprehensively, this paper puts forward the calculation principle of "axis symmetry, top priority" according to Reference 6, supplemented by the correction of various factors, gives the calculation method of the height of the lightning rods in different layout forms, and designs the software for calculating the height of the lightning rods by using the Borland C++ Builder development tool. The software can input the characteristic size of the protected object. With the data of influencing factors, the computational task of complex engineering can be completed instantaneously, and the computational efficiency can be improved.

2 Analysis of Computing Principles

The lightning rods can reliably protect the protected objects to save metal materials under the premise that the lower the height, the better. When designing a lightning rod, the first thing is to determine the location of the lightning rods. Only when the location of the lightning rods is determined can the protection relationship between the lightning rods and the protected object be discussed. Because any shape of the protected object can be converted into an enlarged rectangle, as shown in Fig. 1, the position 1 is the lightning rods, and the position 2 is the farthest point to be protected. When the lightning rods is set on the axis of the equivalent rectangle of the protected object, the principle of axis symmetry is put forward because of the minimum protection radius and corresponding pin height of the lightning rods. If the lightning rods cannot be set on the axis due to the limitation of field conditions, the axis offset can be corrected when calculating; if the cylindrical object is protected, the rectangular width can be taken as 0 m.

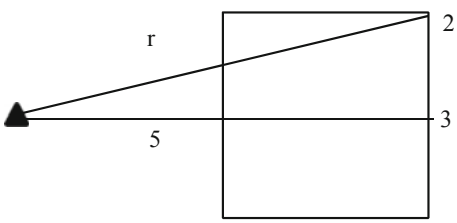

Fig. 1 The setting of a lightning rod and its protecting radius

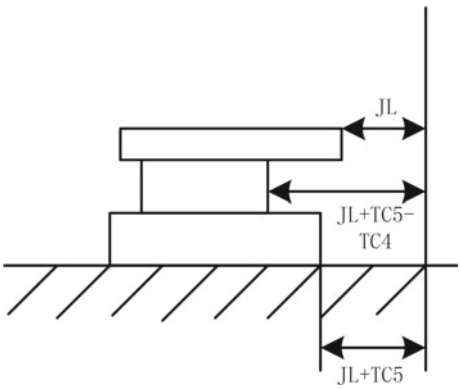

Fig. 2 The amendment of the exterior of the protected object

In the engineering practice, the shape of the protected object may be complex, as shown in Fig. 2. In order to facilitate calculation, the data of length, width and height of the three characteristic planes of the lowest level, middle level and the highest level of the protected object are given. In determining the installation position of the lightning rods, priority should be given to setting the lightning rods on the side of the lowest protection radius of the highest level. This is the principle of top priority. The purpose is to make the height calculation of the lightning rods of the protected object with the complex shape clear and simple. But in the calculation, it is necessary to take the maximum height of the lightning rods calculated according to the three characteristic horizontal planes as the rods height to be adopted to ensure that the lightning rods protect all the positions of the protected object.

3 Modified Calculation of Influencing Factors of Rods Height

When calculating the height of the lightning rods, it is necessary to correct the factors such as grounding resistance R, altitude HB, axis deviation PC of the lightning rods location, protrusion or indentation dimension TC of the highest level plane relative to the lowest level and the height of the lightning rods.

A: Correction of grounding resistance. When the grounding resistance changes, it will affect the safe distance between the lightning rods and the protected object JL, which needs to be corrected. The formula is as follows:

$$JL \geq 0.2 \times R + 0.1 \times h_x \tag{1}$$

whereas h_x is the height of the protected object. As shown in Fig. 1, in order to prevent counterattack, JL is not less than 5 m [6].

B: Altitude correction. When the altitude changes, the safe distance between the lightning rods and the protected object is corrected. The formula is as follows:

$$\begin{cases} K_a = 1 & HB \leq 1000 \\ K_a = \frac{1}{1.1 - H \times 10^{-4}} & 1000 < HB \leq 4000 \end{cases} \tag{2}$$

C: Axis deviation correction. Achieve two roles: If limited by the site, the lightning rods cannot be set on the axis of the protected object, it can input the deviation value of the axis to change the position and correct the rods height. If the position of the lightning rods is fixed and the shape of the protected object is irregular, the axis deviation of the horizontal plane can be set at different heights to correct the height of the lightning rods.

D: Correction of the effect of the irregular shape of protected object on the rods height. As shown in Fig. 2, taking the minimum horizontal plane axial length as the benchmark, the data of the middle and the highest level plane projection or indentation are given, and the protection radius is revised to solve the protection problem of the protected object of the complex shape.

E: Rods height effect correction. The protection range of the lightning rods increases with the increase of the height, but the range of increase may be smaller and smaller, so the height effect correction is needed. The formula for calculating the height influencing factor P is as follows:

$$\begin{cases} P = 1 & h \leq 30 \\ p = \frac{\sqrt{5.5}}{h} & 30 < h \leq 120 \\ p = 0.5 & h > 120 \end{cases} \tag{3}$$

4 Rods Height Calculation

There are two methods for calculating the protection range of lightning rods: broken line method and rolling ball method. Based on these two methods, the software for calculating the height of lightning rods is designed respectively. Due to the limitation of layout, this paper only introduces the calculation principle and software design of needle height based on broken line method.

4.1 Individual Lightning Rods

The essence that the protected object is protected by an individual lightning rods is that the distance from the farthest point of the protected object to the lightning rods is less than the protection radius of the lightning rods on this level at different altitudes.

Therefore, the essence of the problem of calculating the height of the lightning rods is to determine the protection radius according to the distance between the farthest point and the lightning rods on the horizontal plane of the different height of the protected object, and then calculate the height of the lightning rods.

Formula for calculating the height of an individual lightning rods [6]:

$$\begin{cases} h = r_x/p + h_x & h_x \geq \frac{1}{2}h \\ h = (r_x/p + 2h_x)/1.5 & h_x < \frac{1}{2}h \end{cases} \tag{4}$$

whereas r_x is the protection radius. Key points of rods height solution:

A: The installation position of the lightning rod is determined and the protection radius b_x is calculated. The protection radius is determined by the distance of the farthest point between the protected object and the lightning rods on the horizontal plane of different heights. The calculation method is shown in Fig. 1. In the right triangle Δ123, one right-angled side is 1/2 width plus axis deviation, the other right-angled side is safe distance plus length, and the oblique side is the protection radius. When the axis deviation is 0 and JL = 5 m, on the horizontal level 5 m high, the protection radius is as $r_x = \sqrt{(5+5)^2 + 2.5^2} \approx 10.3\,\text{m}$ follows:
When the axis deviation is 2 m, the protection radius is as follows:

$$r_x = \sqrt{(5+5)^2 + (2.5+2)^2} \approx 11\,\text{m}$$

B: Calculate the rods height. According to formula 4, we need to try to calculate it, first assume that the protected object is higher than 1/2 of the rods height, calculate the rods height, if the conditions are met, the rods height calculation is correct; if the conditions are not met, use the formula when the protected object is lower than 1/2 of the rods height to recalculate, and get the rods height to be used. If it is a protected object with irregular shape, the rods height should be calculated according to the protection radius of several high horizontal planes, and the maximum value should be obtained. When the rods height is higher than 30 m, the height influencing factor should be considered.

4.2 Two Lightning Rods

With the increase of the height, the protection range of an individual lightning rods becomes smaller and smaller. If the individual lightning rods is too high, it is better to change it into two or multiple short lightning rods.

Key points for solving the height of two equal-height lightning rods:

A: The installation position of the lightning rod is determined. According to the principle of axis symmetry, two lightning rods are set on the axis of the protected

object. According to the calculation results of the safe distance, the safe distance between the lightning rods and the protected object is determined. Considering the protrusion or indentation of the protected object on the middle and the highest levels, the distance D between two equal-height lightning rods is determined. For example, in Fig. 2, the safe distance between the protected object and the lightning rods is JL, the length of the protective object on the lowest level is C1, and the distance between the two rods is 2JL + C1 + TC5 if the highest level is more prominent than the lowest level.

B: b_x, 1/2 of the minimum width of the protection range between the two rods is determined. It is determined according to half of the maximum width of the protected object on the different horizontal levels. When there is any axis deviation, add the absolute value of the deviation value for correction calculation.

C: The minimum height of the protection range between the two rods is calculated. According to the heights of b_x and the protected object, the formula 5 is used to take the maximum value of h_0 calculated on the three horizontal planes.

$$h_0 = b_x/1.5 + h_x \tag{5}$$

It should be noted that b_x must be first figured out and then h_0.

D: Calculate the rods height. According to formula 6, the height of the lightning rods is calculated according to h_0, and the height effect correction calculation is carried out.

$$h = h_0 + \frac{D}{7p} \tag{6}$$

If two unequal-height lightning rods are used, find the rods height of the high rods according to the protected object that the high rods needs to protect. This is very important. If the high rods is not calculated first, the distance between the low rods and the virtual short rods cannot be determined.

4.3 Three Equal-Height Lightning Rods

Key points of rods height solution:

A: Determination of the positions of three rods. The three lightning rods are arranged in an isosceles triangle, as shown in Fig. 3. Protected objects of any shape between the three rods can be transformed into rectangular enlarged dimensions on a horizontal plane. According to the principle of axis symmetry, the lightning rods 1 and 2 are arranged on both sides of the lateral axis of the protected object, and the position is adjusted by the axis deviation. It should be noted that when 1 or 2 rods are arranged on the axis, the rods height is not the lowest, but this arrangement can

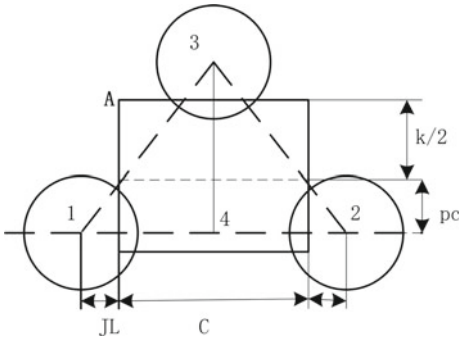

Fig. 3 The settlement of three lightning rods with the same height

be easily programmed; theoretically, the height of two rods may be the lowest on both sides of the bottom of the rectangular axis. The lightning rods 3 is arranged on the longitudinal axis.

B: Determination of the distance between lightning rods. The distance between 1 and 2 rods is determined by calculating the distance between two equal height lightning rods. The distance between 1 and 3 rods is the oblique edge of the right triangle 134 in the figure. The two right edges are (JL + C/2) and (JL + K/2 + PC), respectively.

C: Determination of b_x. The determination of b_x between 1 and 2 rods is based on the 1/2 width and deviation of the protected object. In Fig. 3, a positive deviation is defined when a 1–2-pin line is offset to the bottom of the rectangle; a negative deviation is defined when a 1–2 rods line is offset to the top of the rectangle. When the deviation value is greater than 0 and less than 1/2 width, that is, when the 1–2 rods connection is close to the bottom edge of the protected equivalent rectangle, take it; when the deviation value is greater than 1/2 width, that is, when the 1–2 needle connection is outside the bottom edge of the protected equivalent rectangle, take it; when the deviation value is less than 0, when the 1–2 rods connection is close to the top edge of the protected equivalent rectangle, take it, when the distance between 1–2 rods and 3 needle is too close, obviously, this is true. It is unreasonable to assign a value to b_x.

The determination of b_x between the rods 1 and 3 is calculated according to the vertex A of the protected object in the protective Fig. 3. The formula is as follows:

$$b_x \approx (0.5K + PC) - JL \times (JL + 0.5K + PC)/(JL + 0.5C)$$

In this way, the calculation of b_x may make the data larger, but it increases the safety margin and meets the requirements of the engineering design. When b_x is less than 0, let $b_x = 0$.

D: According to the method of calculating h_0 and rods height of two equal height lightning rods, the maximum height of one rods and three rods is taken as the needle height to be applied.

E: Limited by the site conditions, 3 rods may not be set on the longitudinal axis, and can be corrected by adjusting the protrusion or indentation size of the protected object.
F: When four or more rods are needed, the rods height is calculated according to the different combinations of each three needles, and then the maximum value is obtained.

5 Software Design

The software is designed by using Borland C++ Builder 6.0 development tool. The flow chart of the lightning rods height calculation software is shown in Fig. 4.

The following points should be paid attention to when the software is designed:

A: The complex shape of the protected object is the main factor affecting the design of the lightning rods, which results in a large amount of work in the programming of this part of the program code. However, only considering the various changes of prominence and indentation, can the reliability of the lightning rods protection be ensured.
B: When calculating the height of an individual lightning rods, it is necessary to calculate the height of the lightning rods according to the height of the protected

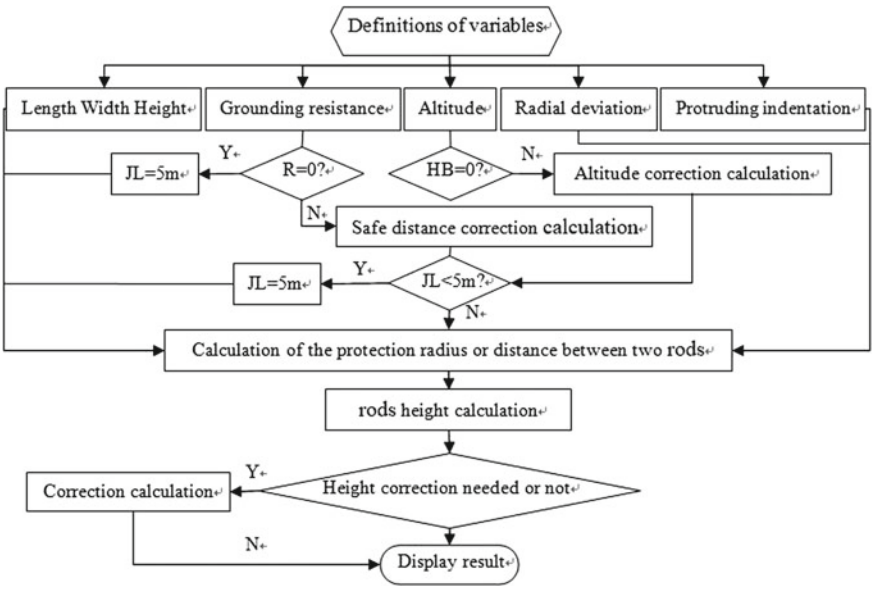

Fig. 4 Software flow chart

object less than half of the height of the rods, so as to solve the problem that the height influencing coefficient P is more than 1 when the critical height of the rods is 30 m.

C: When calculating the height of two equal-height lightning rods, the lowest height of the protection range between the two rods is calculated according to the height of b_x and the protected object, and the highest value of the h_0 calculated on the three levels is used to calculate the rods height to avoid the defect of incomplete protection which may be caused by the principle of "top priority".

The software interface is shown in Fig. 5.

Input data: The lowest level of the protected object is 20 m long, 10 m wide and 5 m high. The middle level is 15 m long, 12 m wide and 10 m high. The highest level is 10 m long, 10 m wide and 15 m high. The grounding resistance is 0 and the altitude is 1. No axis deviation and no prominent data are given to indicate that the protected objects are aligned at one end of the three horizontal planes. The lightning rods is located on the axis of the side of the alignment end, and the calculation results are as follows: the safe distance is 5 m; the height of an individual lightning rods is 30.59 m; the height of two equal- height lightning rods is 22.62 m and the distance is 30 m; when two unequal-height lightning rods are used, the height of the high rods is 30.59 m and the height of the low rods is 16.70 m, which means that the individual rods is enough and the short needle cannot be added. When three

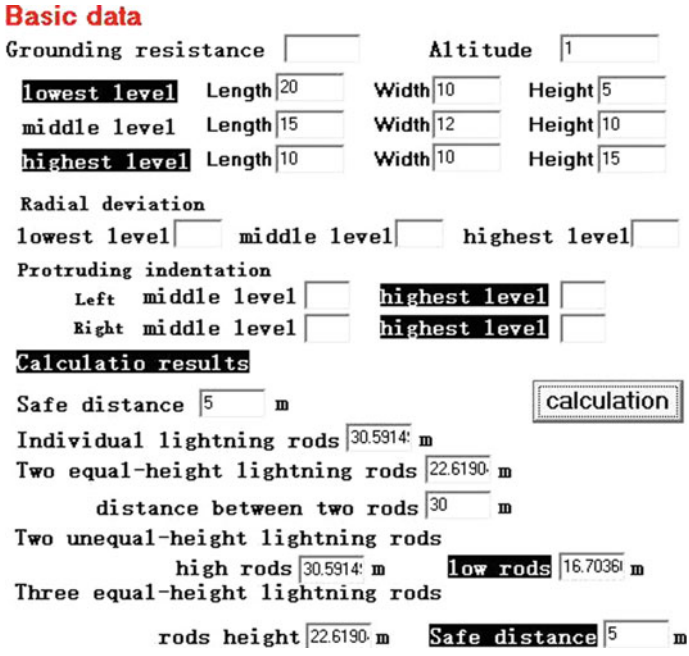

Fig. 5 Results of the calculation (before correction)

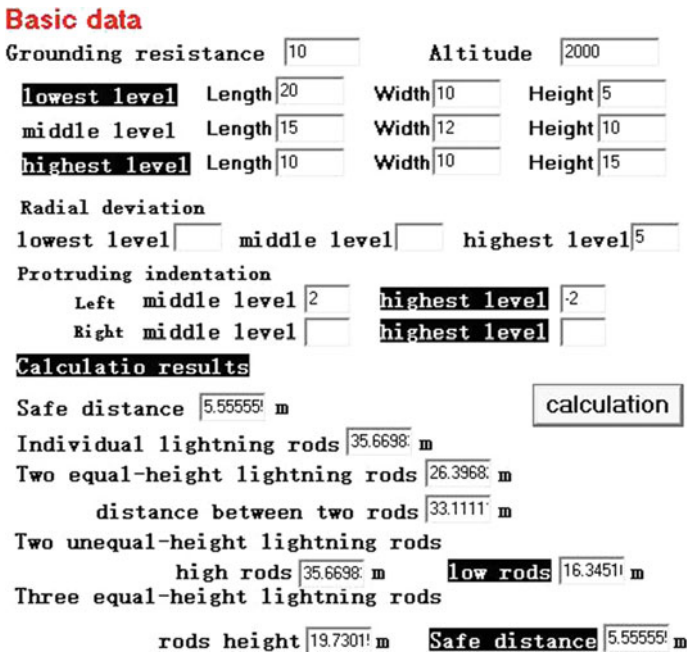

Fig. 6 Results of the calculation (corrected)

equal-height lightning rods are used, the rods height is 22.62 m, which is equal to the rods height of two equal-height lightning rods, indicating that two rods are enough.

The size of the protected object remains unchanged. When the grounding resistance is 10 Ω, the altitude is 2000 m, the axis deviation of the highest horizontal plane is 5 m, the left side of the middle horizontal plane protrudes 2 m, and the left side of the highest horizontal plane retracts 2 m, the software calculation results are shown in Fig. 6. The lightning rods should be set on the left side with a safe distance of 5.56 m and a height of 35.67 m for an individual lightning rods; the height of two equal-height lightning rods is 26.40 m and the distance is 33.11 m; the height of two unequal-height lightning rods is 35.67 m for a high rods and 16.35 m for a short rods, which is obviously unreasonable; and the height of three equal-height lightning rods is 19.73 m.

6 Conclusion

Aiming at the complex engineering problem of lightning rods height calculation, this paper innovatively puts forward the calculation principle of “axis symmetry, top priority” to make the height calculation of lightning rods clear; take into account

the effect of various factors, revise the height calculation of lightning rods, so that the calculation results are more in line with the engineering practice; give the key points of solving the rods height of various lightning rods layout modes and design software, which only needs to be transported. Only when the basic data of the protected objects are input can the calculation work be completed and the working efficiency be improved. After a lot of comparison and checking, it is proved that the calculation results of the software are accurate.

References

1. Ma HD (1998) The modelling experimental theory and contention about the protection zone of lightning rod. Eng Phys S1:16–25
2. Zeng R, Zhou X, Wang Z et al (2013) Review of research advances and fronts on international lightning and protection. High Volt Eng 41(1):1–13
3. Wan HJ, Wei GH, Chen Q et al (2013) Three-dimensional numerical simulation of lightning discharge and its application. High Volt Eng 39(2):430–436
4. Xie SJ, He JJ, Chen WJ et al (2012) Simulation study on the development process of the upward leader incepted from lightning rod. Proc Chin Soc Electr Eng 32(10):32–40
5. Xie SJ (2013) Simulation tests and models of the selection process in negative cloud-to-ground lightning flash. Huazhong University of Science & Technology, Wuhan, China
6. GB, T50064-2014 (2014) Code for design of overvoltage protection and insulation coordination for AC electrical installations. China Planning Press, Beijing, China
7. GB, TGB50057-2010 (2011) Design code for protection of structures against lightning. China Construction Press, Beijing, China
8. Zhao XG, Zhou Y, Li H et al (2014) Research on visualization of protection scope for lightning rod based on matlab. J Logist Eng Univ 4:44–48
9. Zeng Y, Wang HB, Zhou M (2014) Lightning protection design for some lightning rods in hub substation based rolling sphere method. Electr Eng 15(9):24–26
10. Huang XP, Xiao X, Wang XZ et al (2005) 3D visualization of protecting area of lightning rod. J Comput-Aided Des Comput Gr 17(9):2129–2132
11. Sun YX, Wang JJ (2002) Computer and analysis to the area against thunder strike of the lightning rob based on matlab. Proc CSU-EPSA 14(6):63–66
12. Fan C, Chang MS, Bai LS et al (2015) Research on the quick design for height of multi lightning rods. Insul Surge Arresters 138(5):86–90
13. Zhang X (2002) Development and application of design and calculation software for lightning rods used in power plants and substations. Electr Power Constr (2):58–60

Super-Resolution Reconstruction of Fine-Grained Fittings Image of Transmission Line Based on Compressed Sensing

Peng Wu, Chengqi Li, Guoqiang Lin, Jia Luo and He Yang

Abstract The abstract should summarize the contents of the paper in short terms, i.e. 150–250 words. Aiming at the low resolution problem of fine-grained fittings image of trans-mission line, an image super-resolution reconstruction algorithm based on compressed sensing is proposed. The K-SVD (K-Singular Value Decomposition) algorithm is used to implement sparse representation according to the theory of compressed sensing. The reconstruction is performed by OMP (Orthogonal Matching Pursuit) algorithm. The proposed algorithm has good de-noising effect and shortened processing time. The fine-grained fit-tings image that has correlation with the reconstructed image is trained to enhance the reconstruction effect and is used for high-quality recovery of the fine-grained fittings image of the transmission line. The simulation results verify the effectiveness of the proposed algorithm, and the reconstructed image has a better improvement in subjective visual effects and objective evaluation indicators.

Keywords Compression sensing · Inspection image · Super-resolution reconstruction

1 Introduction

With the improvement of the automation of the power grid and the increasing number of UAVs, the line inspection of drones is widely used. UAVs are equipped with cameras to inspect the transmission lines and obtain video images of electric

P. Wu · G. Lin (✉) · H. Yang
Artificial Intelligence on Electric Power System State Grid Corporation Joint Laboratory (GEIRI), Global Energy Interconnection Research Institute, Beijing 102209, China
e-mail: linguoqiang@geiri.sgcc.com.cn

C. Li
State Grid Shandong Electric Power Research Institute, Shandong 250021, China

J. Luo
North China Electric Power University, Beijing 102209, China

Y. Xue et al. (eds.), *Proceedings of PURPLE MOUNTAIN FORUM 2019-International Forum on Smart Grid Protection and Control*, Lecture Notes in Electrical Engineering 585, https://doi.org/10.1007/978-981-13-9783-7_80

fittings and environments of transmission lines in real time. By using the backstage analysis algorithm, the abnormal phenomena, such as defects of the fittings, can be detected in time. Then it's possible to trigger the fault alert automatically or perform the pre-set fault processing to provide necessary protection for the safe operation of the power line [1, 2].

During the work of acquiring images by UAVs, the quality of images may be degraded due to reasons like small size of the fittings. One of the most notable condition is that the captured video images have low resolution and the details of the original images cannot be distinguished. To increase the resolution only by improving hardware will increase the cost. Therefore, the super-resolution reconstruction of images through software algorithms has become a research hotspot in recent years.

Super-resolution image reconstruction is a very active area of current re-search, which overcomes the inherent resolution limitations of low-cost imaging sensors.

Super-resolution reconstruction of images is mainly divided into three methods, the first is based on interpolation; the second is based on reconstruction and the third is based on machine learning. As a new method to represent images, the sparse representation, based on compressed sensing, provides a new research idea for image super-resolution reconstruction through dictionary learning. These research results have gained extensive attention and application in the fields of medicine and remote sensing [3, 4]. The traditional method of generating super-resolution images usually re-quires inputting multiple low-resolution images of the same scene, so these methods also need to align sub-pixel precision, which brings new problems such as registration errors. Single-image super-resolution reconstruction algorithm based on sparse representation can strengthen the compatibility between local and global adjacent image blocks, and has good effects. The reference [5–9] used deep learning network to improve reconstruction quality, but need GPU environment. The K-SVD method in [10] can learn the dictionary according to the adaptive learning and obtain a good reconstruction effect, and also shortened processing time, so it is used usually.

In this paper, aiming at the low resolution problem of fine-grained fittings image of transmission line captured by UAV, an image super-resolution reconstruction algorithm based on sparse coding is proposed. According to the theory of com-pressed sensing, the K-SVD algorithm is used to implement sparse representation, and the OMP algorithm is used to complete the reconstruction process. Besides, it is possible to complete enhance reconstruction by correlated UAV image training, aiming at high quality recovery for UAV images for transmission line inspections. The simulation results verify the effectiveness of the proposed algorithm, which shows that the reconstructed image has a better improvement in subjective visual effects and objective evaluation indicators. This research may be a premise to future improve object identification applications in the electric power system scenarios, like in [11].

2 Basic Knowledge of Compressed Sensing

2.1 Theoretical Framework of Compressed Sensing

The theoretical framework of compressed sensing (CS) is shown in Fig. 1. It includes three key parts: sparse representation, coding measurement and signal reconstruction.

The primary problem with CS theory requires that the signal be sparse or sparsely represented on a sparse representation. When given a one-dimensional signal $x = [x_1, x_2, \ldots, x_N]$ with an original signal length of N, if x can be represented linearly by a set of standard orthogonal transform bases Ψ, this process can be called a sparse representation. After sparse representation, in the original signal x, only a few of the transform coefficients are non-zero, and the transform coefficients of other terms are 0 or tend to 0. This set of standard orthogonal transform bases are called a sparse representation bases. The original signal x is sparsely transformed on the orthogonal transform bases ψ to obtain a sparse representation signal S, as shown in Fig. 2.

In practical applications, most signals are non-sparse, but they can be represented as sparse signals with some sparse transform bases. This kind of signals are called approximate sparse signals. When the traditional sparse transform base cannot sparsely represent the original signal, an over completed dictionary appears. The K-SVD construction method is one of the common constructive methods for adaptive learning over completed dictionary. It can learn the dictionary according to the adaptive learning of the signal itself and obtain a good reconstruction effect.

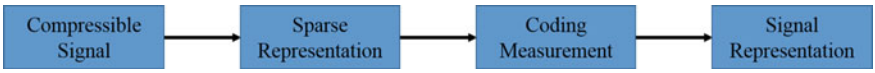

Fig. 1 Compressed sensing theory framework

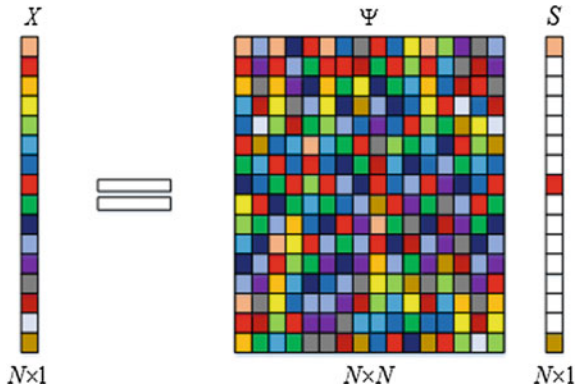

Fig. 2 Sparse representation of the signal

Another key part of compressed sensing is the design of the reconstruction algorithm. It follows the basic principle that the algorithm should reconstruct the original signal quickly, stably, accurately or approximately accurately with as few compressed measurements as possible.

2.2 *Sparse Representation and K-SVD Dictionary Construction*

At present, sparse representation mostly uses an over-complete dictionary. The number of atoms in an over-complete dictionary is much larger than the number of atoms in the signal itself. Using an over-complete dictionary to sparsely represent the original signal can represent multiple types of signals and maximize the match of the structural characteristics of the original signal itself. The methods to construct an over-complete dictionary are mainly divided into two types. One is a method based on mathematical models, and the other is based on learning.

K-SVD is a dictionary learning algorithm for sparse representation. This algorithm, based on singular value decomposition, is widely used in the field of image processing [10, 11]. In the K-SVD algorithm, the update iteration of the dictionary is performed atom by atom in a simple and efficient manner, and the current dictionary atom and correlation coefficient are updated simultaneously in the update process to speed up the dictionary training. It can construct an over-complete dictionary D so that the given training signal can be sparsely decomposed based on D. The target equation is shown as Formula (1):

$$\min_{D,X}\left\{\|Y - DX\|_F^2\right\} \quad s.t \quad \forall i, \|x_i\|_0 \leq K \tag{1}$$

In the Formula (1), $D = [d_1, d_2, \ldots, d_N] \in R$ is an initialized over-complete dictionary, Y is a given training signal, X is a matrix composed of sparse coefficients, and x_i is the number i column of X. K represents the upper limit of the number of non-zero elements contained in the sparse coefficient. In the process of training, K-SVD algorithm can be divided into two parts, which are sparse coding and dictionary update:

(1) Sparse coding: The initial over-complete dictionary D is fixed, and the sparse coefficient matrix X is solved by using the OMP algorithm for the target equation. The hard threshold is used as the stop condition for in the iterative process.
(2) Dictionary update: In this process, the sparse coefficient matrix X remains unchanged, and each column of the over-complete dictionary D is updated one by one. When the number k column of D is to be updated, the objective function of Formula (1) can be converted into the Formula (2):

$$\|Y - DX\|_F^2 = \left\|Y - \sum_{j=1}^{N} d_j x^j\right\|_F^2 = \left\|\left(Y - \sum_{j\neq k} d_j x^j\right) - d_k x^k\right\|_F^2 = \left\|E_k - d_k x^k\right\|_F^2 \tag{2}$$

To remove the 0 elements in the samples, define the set $\omega_k = \{i | 1 \le i \le L, x^k(i) \ / = 0\}$ and a matrix Ω_k of size $L \times |\omega_k|$. which has a value of 1 at $(\omega_k(i), i)$ and a value of 0 at the rest elements. Let $x_R^k = x^k \Omega_k$ and $Y_R^k = Y\Omega_k$, then the Formula (2) could be written as:

$$\left\|E_k \Omega_k - d_k x^k \Omega_k\right\|_F^2 = \left\|E_R^k - d_k x_R^k\right\|_F^2 \tag{3}$$

After the singular value decomposition of E_R^k, which is $E_R^k = U\Delta V^T$, the atom d_k in D is replaced by the first column of the matrix U. The x_R^k is updated by the multiplied value of first column of the matrix V with $\Delta(1, 1)$, and the loop iterates until the convergence condition is met.

2.3 Reconstruction Algorithm

In CS theory, signal reconstruction is the most critical step in its three core steps. The reconstruction algorithm are directly related to the effect and running time of the final signal reconstruction. At present, the reconstruction algorithms of compressed sensing are mainly divided into two categories:

(1) Convex optimization algorithm, which is to broaden the 0 norm to 1 norm and solve the reconstruction by linear programming. Such algorithms mainly include gradient projection method, base tracking method, minimum angle regression method and so on.
(2) The greedy algorithm, which approximates the signal vector by selecting the appropriate atom and undergoing a series of incremental methods. The algorithms mainly include Matching Pursuit (MP) and Orthogonal Matching Pursuit (OMP), Regularized Orthogonal Matching Pursuit (ROMP), etc. [12].

The convex optimization algorithm is characterized by the exact solution, but requires higher computational complexity. The greedy iterative class reconstruction algorithm achieves a good balance in both time complexity and reconstruction effects, and thus has become a research hotspot.

The OMP algorithm is an improvement on the MP algorithm. After iteration, the atoms selected in the sparse dictionary are combined into a matrix, and the matrix is orthogonalized. Since this matrix consists of all selected dictionary atoms, the matrix changes after iteration. Therefore, the orthogonal projection operator matrix

generated by it will be different each time, which means that one atom in the sparse representation dictionary will not be repeatedly selected twice, and the calculated residual will always be guaranteed to be orthogonal to the selected atom. Through the above process, the optimality of sparse dictionary atom selection is guaranteed, and the reconstructed effect is better than the one through the matching tracking algorithm.

3 Super-Resolution Reconstruction Based on Compressed Sensing

In this paper, the image super-resolution reconstruction based on compressed sensing is implemented through the system structure shown in Fig. 3. The working principle of the system is as follows: firstly, the high-resolution image is used for training and learning, and the dictionary is obtained. Then the low-resolution image to be reconstructed is sparsely encoded, and then the reconstructed dictionary is used to reconstruct the high-resolution signal. The low resolution images used in this paper are obtained by down-sampling the degraded the high resolution image.

4 Experiment and Result Analysis

In order to verify the super-resolution reconstruction effect of the proposed algorithm, the UAV images are selected for experimental simulation in this paper, and the bicubic interpolation algorithm and the compression sensing algorithm are

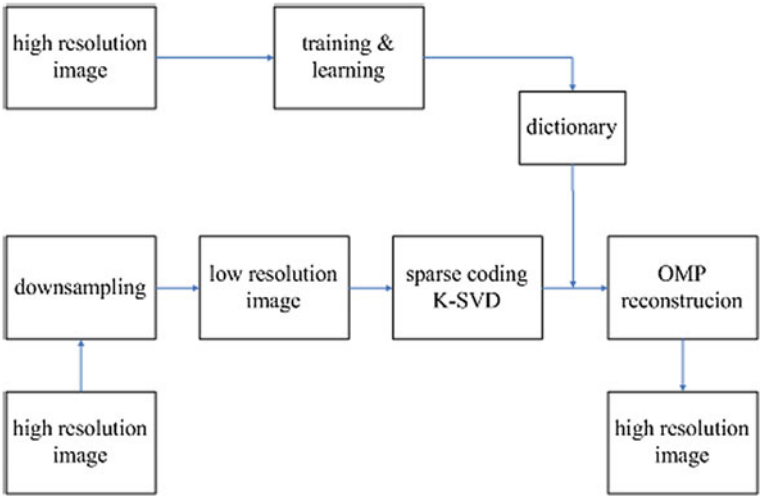

Fig. 3 Structure of image super-resolution reconstruction system based on compressed sensing

chosen for experiments. The experimental environment includes an Inter Core i5-6200U CPU @2.30 GHz with 8.00 GB memory and MATLAB R2019a for programming. Finally a comparison of effect after reconstruction using two algorithm are given, as well as a performance comparison based on two objective evaluation, which are peak signal-to-noise ratio (PSNR) and structural self-similarity (SSIM).

The definition of PSNR is as follows:

$$PNSR = 10 \times \ln \frac{Q^2 \times M \times N}{\sum_{j=1}^{M} \sum_{i=1}^{N} \left(\hat{f}(i,j) - f(i,j)\right)^2} dB$$

Q in the above equation represents the number of gray levels of image quantization, $\hat{f}(i,j)$ and $f(i,j)$ represent the gray values of the pixels at row i, column j of the processed image and the original images respectively. M and N respectively represent the length and width of the image.

The definition of SSIM is as follows:

$$\text{SSIM} = [l(x,y)^{\alpha}]\left[c(x,y)^{\beta}\right][s(x,y)^{\gamma}] = \frac{4\mu_x\mu_y\sigma_{xy}}{\left(\mu_x^2 + \mu_y^2\right)\left(\sigma_x^2 + \sigma_y^2\right)}$$

In the above equation, μ_x and μ_y represent the mean values of the image blocks x and y respectively, and σ_x^2 and σ_y^2 represent the variance of the image blocks x and y. σ_{xy} represents the covariance between x and y.

According to the process shown in Fig. 3, 100 selected UAV high-resolution images are first used for training, and a K-SVD dictionary is generated. Then, four low-resolution images are sparsely encoded, and the dictionary is also utilized to reconstruct high- resolution images. The results in Fig. 4 and Table 1 show the comparison of super-resolution reconstruction effects of four UAV images reconstructed by the bicubic interpolation algorithm and the compressed sensing algorithm proposed in this paper.

Figure 4a on the left shows the reconstruction result obtained by using the bicubic interpolation algorithm, and Fig. 4 is the result obtained by the compression sensing algorithm. It is obvious that the reconstruction effect of CS algorithm is better than bicubic interpolation algorithm, and the compressed sensing algorithm performs much better in the detail of the images, especially in the detail along edges. Table 1 shows the PSNR and SSIM data comparison after reconstructed by the two methods, the values of PSNR and SSIM obtained by the compressed sensing algorithm are significantly higher than values obtained by the bicubic interpolation algorithm.

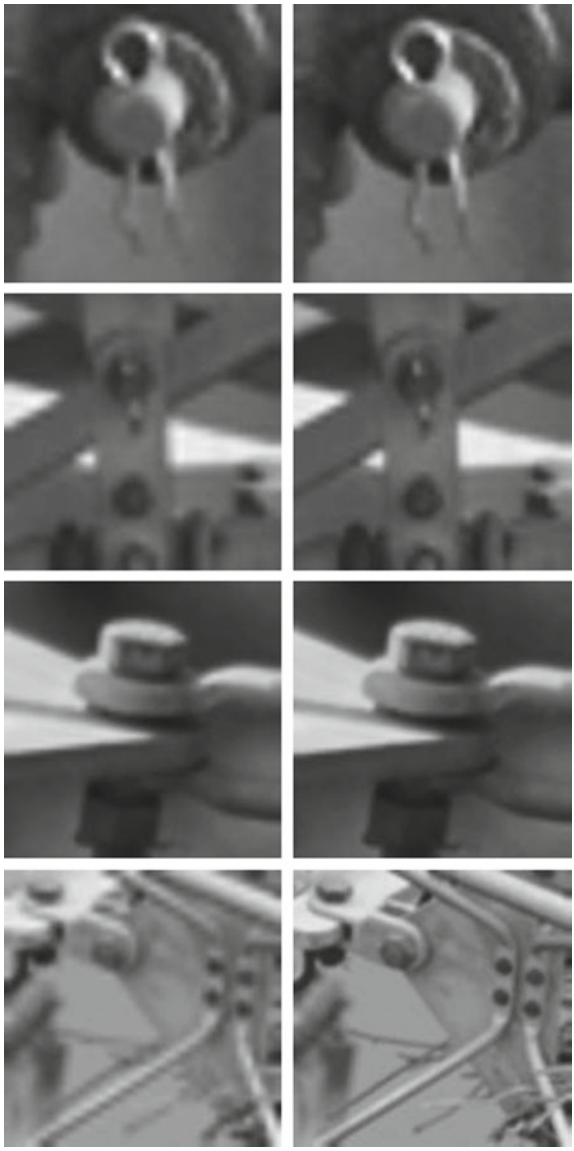

Fig. 4 Comparison of image super-resolution reconstruction effects by different algorithms. Compared with results in reference [8], PSNR (dB) and SSIM data are slightly low, but deep learning-based method have difficulties in training the network and need high performance GPU, our proposed method has little requirement to the running environment. Left column: **a** bicubic difference algorithm. Right column: **b** compressed sensing algorithm

Table 1 Comparison of PSNR (dB) and SSIM data after reconstruction of different algorithms

Images of experiment	Evaluation index	Bicubic interpolation algorithm	Compressed sensing algorithm
Image 1	PSNR	24.79	26.17
	SSIM	0.8432	0.8671
Image 2	PSNR	25.45	26.88
	SSIM	0.8141	0.8528
Image 3	PSNR	29.60	31.40
	SSIM	0.9410	0.9562
Image 4	PSNR	28.57	30.94
	SSIM	0.8547	0.9322

5 Conclusions

Recently, the UAV inspection of transmission lines has been widely used. By analyzing images acquired by UAVs, it is possible of finding abnormalities and failures in time. Aiming at the low resolution problem of fine-grained fittings images of transmission line captured by UAVs, an image super-resolution reconstruction algorithm based on compressed sensing is proposed. Firstly, K-SVD algorithm is used to implement sparse representation, and OMP algorithm is used for reconstruction. Then UAV images correlated with the reconstructed images are trained to enhance the reconstruction effect. Simulation results show that the reconstructed images are improved in both subjective visual effects and objective evaluation indicators.

Acknowledgements The work was supported by State Grid Corporation of China Headquarters Project (5455HJ180017) named 'Applicability Research regarding the Use of AI-based Image Recognition in Power Transmission and Transforming Inspection'.

References

1. Lu SY, Zhang Y, Li JX et al (2017) Application of mobile robot in high voltage substation. High Volt Eng 43(01):276–284
2. Xia YF, Song XM et al (2018) Technology research status and prospect of transmission line condition based maintenance by robot. High Volt Appar 54(7):53–63
3. Sun QS (2017) Remote sensing image super-resolution reconstruction in multi-scale compressed sensing framework. J Nanjing Normal Univ (Nat Sci Ed), 40(01):39–47
4. Hua XY, Xu ZJ (2015) Algorithm on super-resolution reconstruction of sonar image based on compressive sensing. Inf Technol Netw Secur 34(13):49–52
5. Dong C, Chen CL, He K, Tang X (2016) Image super-resolution using deep convolutional networks. IEEE Trans Pattern Anal Mach Intell 38(2):295–307

6. Kim J, Lee JK, Lee KM (2015) Accurate image super-resolution using very deep convolutional networks. In: Proceedings of the computer vision and pattern recognition. IEEE, pp 1646–1654
7. Tai Y, Yang J, Liu X (2017) Image super-resolution via deep recursive residual network. In: Proceedings of the IEEE conferences on computer vision and pattern recognition. IEEE Computer Society, pp 2790–2798
8. Duan LJ, Wu C et al (2019) Deep residual network in wavelet domain for image super-resolution. J Softw 30(4):941–953
9. Wang Z, Liu D, Yang J, Han W, Huang T (2016) Deep networks for image super-resolution with sparse prior. In: Proceedings of the IEEE international conference on computer vision. IEEE, pp 370–378
10. Rubinstein R, Faktor T, Elad M (2012) K-SVD dictionary-learning for the analysis sparse model. In: Acoustics, speech and signal processing (ICASSP), 2012 IEEE international conference on IEEE, pp 5405–5408
11. Huang X, Yang L, Zhang Y, Cao W, Li L (2018) Image enhancement based detection method of non-soluble deposit density levels of porcelain insulators. Autom Electr Power Syst
12. Shi MM, Li L (2016) An image compressed sensing algorithm based on novel stagewise regulation OMP algorithm. Comput Technol Dev 26(11):14–18

Design and Implementation of Centralized Operation and Hierarchical Management System for Substations

Rongrong Cao, Yunfeng Sun, Mingyu Zhai, Zhihong Yang and Yun Li

Abstract The existing work of operation and maintenance for substations is mainly realized by manual on-site inspection. It is repeated and cumbersome, and costs lots of time. With the rapid growth of the number of substations, the increase in the number of operation and maintenance personnel cannot keep up with the development speed of the power grid equipment, which brings great work pressure to the operation and maintenance of substations. In order to solve the problem, this paper proposes a design and implementation method of centralized operation and hierarchical management system for substations. The system collects the information in the substations and sends it to the center, and combines the information collected by the center and then sends it to the upper center to achieve the goal of centralized operation and hierarchical management for substations. The system has been used in practical applications and it greatly reduces the load and time of operation and maintenance work. It improves the management level of substation operation and maintenance and makes it more scientific, standardized and reasonable.

Keywords Substation · Center · Operation · Maintenance · Centralized · Hierarchical

1 Introduction

In recent years, in order to realize the leap of the traditional power grid to the efficient, economical, clean and interactive modern power grid, improve the safe and stable operation level of the power grid and optimize the allocation of resources, the smart substation has entered the stage of comprehensive construction

R. Cao (✉) · Y. Sun · M. Zhai · Z. Yang · Y. Li
NARI Technology Development Co., Ltd, Nanjing, China
e-mail: caorongrong@sgepri.sgcc.com.cn

R. Cao · Y. Sun · M. Zhai · Z. Yang
State Key Laboratory of Smart Grid Protection and Control, Nanjing 211106, China

Y. Xue et al. (eds.), *Proceedings of PURPLE MOUNTAIN FORUM 2019-International Forum on Smart Grid Protection and Control*, Lecture Notes in Electrical Engineering 585, https://doi.org/10.1007/978-981-13-9783-7_81

[1]. At present the substation operation and maintenance personnel mainly still use the manual on-site inspection method to realize the maintenance of the substation equipment. It is repeated and cumbersome, and costs lots of time. With the construction and development of the grid, the number of substations is increasing, and the operation and maintenance personnel cannot increase simultaneously, which brings great pressure to the operation and maintenance of substations [2]. If this contradiction is not solved well, it will affect the reliability of the equipment and further threaten the reliability of the power supply.

Operation and maintenance management plays an important role in power grid production and command business. By improving the level of operation and maintenance management, it can raise the quality of power grid construction and grid operation efficiency. And the life cycle management level of the grid equipment [3] is also enhanced. There are significant economic and social benefits in ensuring energy transmission and optimizing resource allocation. At present, most of the research on substation operation and maintenance work is focused on the formulation of work rules and regulations [4]. There is few research on system design and implementation.

By comparing existing monitoring techniques, the article [5] proposes to establish a centralized control system for substation operation and maintenance in order to meet the requirements of centralized operation and maintenance for substations. With the development of substation auxiliary system, some manufacturers have carried out the research of remote management system for substation operation and maintenance. Some of these mainly focus on substation auxiliary information [6]. They lack equipment-related operational information. And some others get the equipment-related operational information all from the substation automation system [5, 7]. The construction and maintenance work of the system is large, and it takes up more network bandwidth between the center and the substations.

Therefore, in order to resolve the problems above, it is necessary to study better design and implementation method of centralized operation and hierarchical management system for substations.

2 System Structure

2.1 Overall Architecture

There are two parts in the system, substation and center. The workstation of substation collects the information in the substation and sends it to the center. The center combines the information collected by itself and then sends it to the upper center. The system realizes the comprehensive functions of data collection, display, alarm, analysis, storage, report, query, excavation and management required for operation and maintenance by constructing a unified and centralized platform. The overall architecture is shown in Fig. 1.

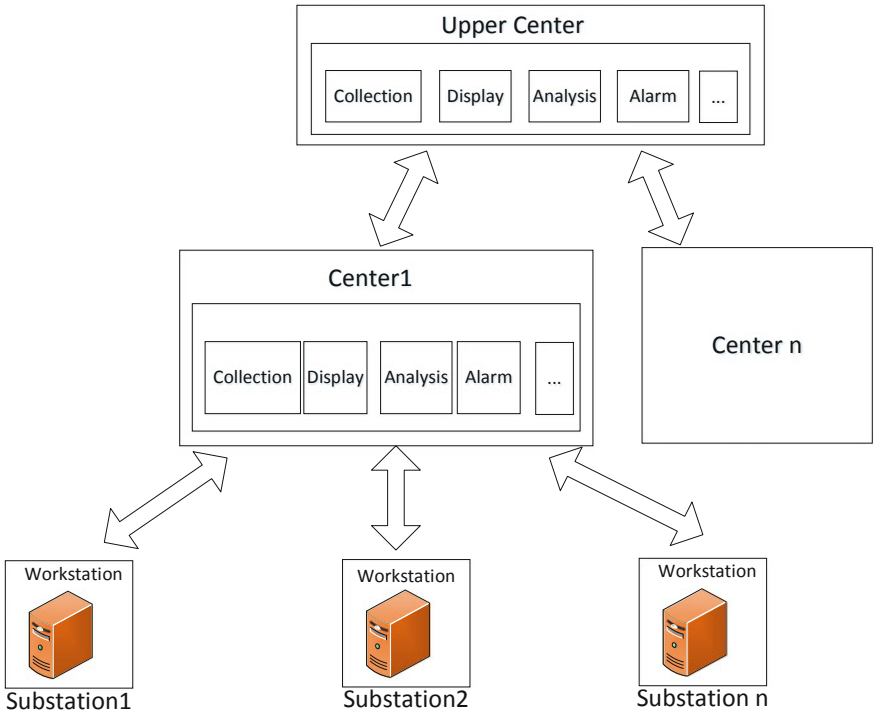

Fig. 1 Overall architecture

2.2 Substation Information Collection

By adding a workstation in the substation, the information of the substation can be collected. Substation information mainly includes data of automation system and auxiliary systems. The substation information collection is shown in Fig. 2.

In our system most of the equipment operation information is collected through the smart grid dispatching and control system in the center. This can greatly reduce the construction and maintenance work of the system and the network bandwidth occupation between the substation and the center. Little information cared about by the operation and maintenance personnel but not collected in the smart grid dispatching and control system can be transferred to the workstation from the substation automation system through isolation device.

The information of various auxiliary systems is sent to the workstation through the IEC61850 protocol. The monitoring model information is sent to the workstation through the SCD file. The workstation can obtain these data of the substation auxiliary systems, such as the temperature, humidity, wind speed, three-phase value of switch, SF6, oil temperature and level of the transformer and winding temperature, alarm information from robot inspection, the action numbers and leakage

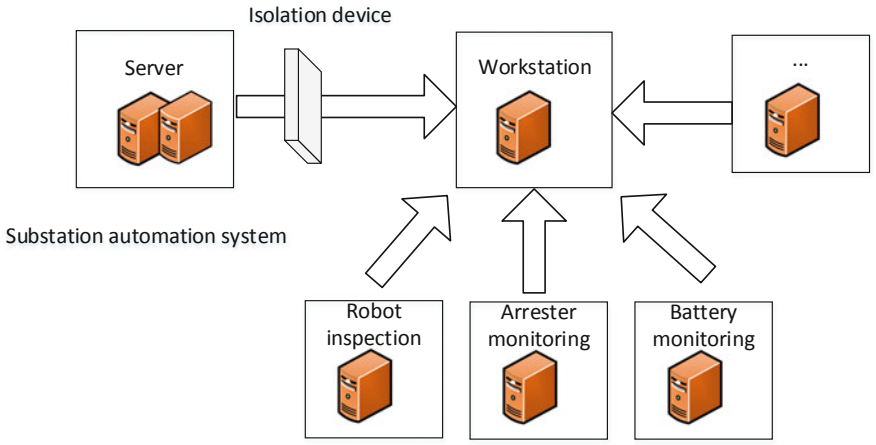

Fig. 2 Substation information collection

current from the arrester monitoring, the voltage, current, internal resistance, alarm information from the battery monitoring and so on.

At the same time, the workstation can be used as an extension of the system in the substation. Operation and maintenance personnel can use this workstation to perform operation and maintenance such as report composing and query, equipment defect management and shift management.

2.3 Substation Information Sending

The workstation in substation uniformly sends the collected information of the substation to the center of the system through the information network. It can communicate with the central server through the IEC101 protocol, the 104 protocol or others. When the substation information is modified, the grid model, data and alarms will be automatically synchronized to the center without manual intervention. The substation information sending is shown in Fig. 3.

2.4 Center Information Collection

In addition to collecting information from substations, the center obtains relevant information from the smart grid dispatching and control system, the PMS, the equipment monitoring system, the mobile inspection and so on. The center information collection is shown in Fig. 4.

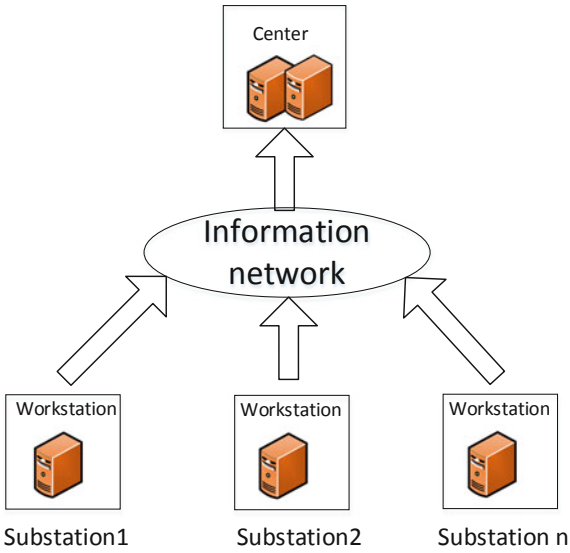

Fig. 3 Substation information sending

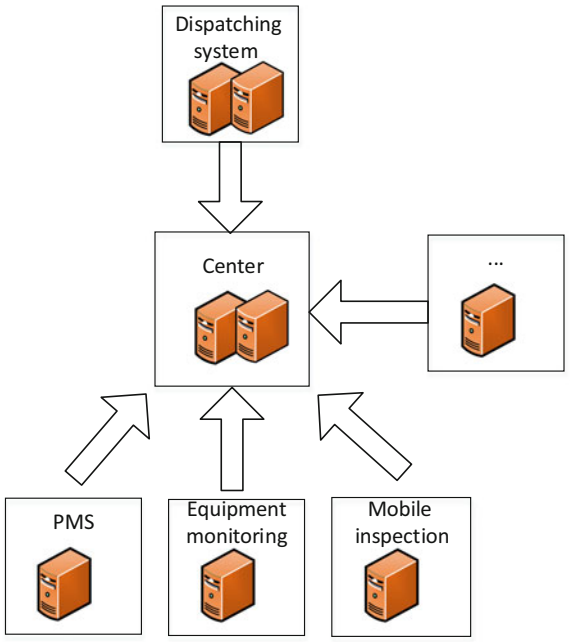

Fig. 4 Center information collection

From the previous chapters we know that the main information of the system is obtained from the smart grid dispatching and control system. And this can reduce a lot of repeated work in system construction and maintenance. The center acquires

the existing models, graphs, real-time data, alarms and protection information from the dispatching system, such as current, voltage, power, switch status, substation diagram, bay diagram and so on. These information is automatically synchronized to the center via the wide-area information exchange bus without manual intervention.

The relevant management information of the operation and maintenance equipment is sent to the center by the PMS. And the information of micro-meteorology, core current, insulation, gas chamber density and so on can be transmitted from the equipment monitoring system. The on-site inspection information can be get from the mobile inspection system.

The center collects relevant information needed for the substation operation and maintenance from the existing related systems, and then realizes unified monitoring, statistics, analysis and demonstration of substations. It achieves the goal of centralized management for substations and whole process control of the substation equipment. The system reduces the workload of the operation and maintenance personnel and at the same time it does not increase the workload of construction and maintenance.

2.5 Center Information Sending

In the center, the relevant information is also sent to the upper center. And the center accepts the control of the upper center. It achieves the goal of hierarchical management of the substation operation and maintenance work. The number of stages of the center can be adjusted according to actual needs. The center information sending is shown in Fig. 5.

3 Applications

The system developed in this paper has been put into operation in Ningxia Province and all its cities. The application of the system greatly reduces the operation and maintenance time of the team, improves the efficiency of the operation and maintenance personnel, and decreases the labor cost (see Fig. 6).

From Fig. 6 we can see that the overall inspection time of a 330 kV substation is reduced from an average of 4–2 h, and the battery monitor time is reduced from an average of 1 h to 10 min, the whole station temperature measurement time is reduced from an average of 3.5 h to 20 min, and the shift time is reduced from an average of 1 h to about 20 min.

The system realizes the promotion of full coverage in the substation operation and maintenance business process, including multi-platform data docking, daily work simplification, equipment operation status control, and real-time monitoring of maintenance work.

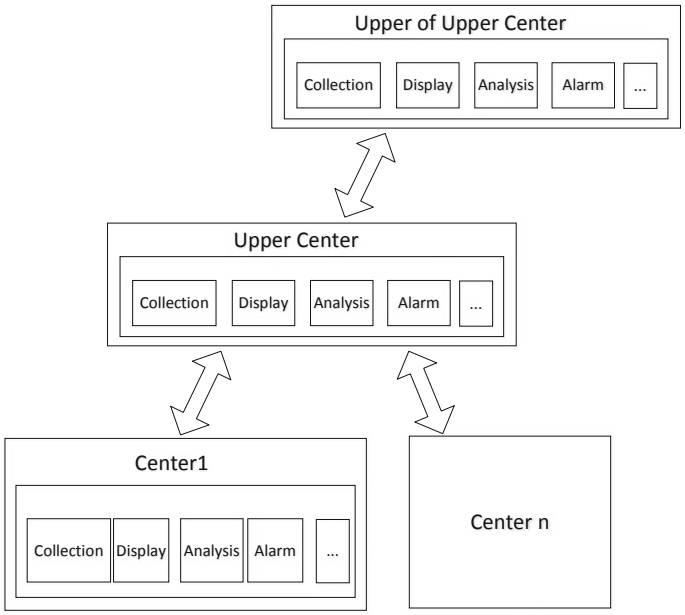

Fig. 5 Center information sending

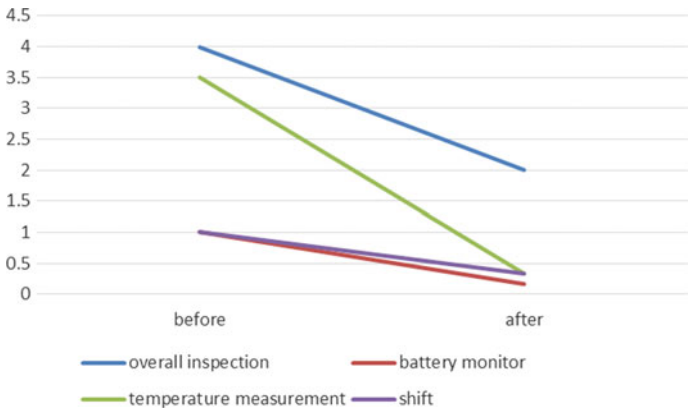

Fig. 6 Comparison of working hours before and after system application

4 Conclusion

This paper designs and implements a centralized operation and hierarchical management system for substations. The system realizes the comprehensive functions of data collection, display, alarm, analysis, storage, report, query, excavation and

management required for operation and maintenance by constructing a unified and centralized platform.

The system reduces the burden on the operation and maintenance personnel through the transformation of multi-system decentralized management into integrated panoramic management. It solves the contradiction between the increasing number of substation equipment and the insufficient number of operation and maintenance personnel.

The system strengthens the basic management and centralized control of unattended substations and improves the lean management level of substations. It enhances the quality and effectiveness of operation and maintenance work, making the management of substation operation and maintenance more scientific, standardized and reasonable.

With the construction of the ubiquitous power Internet of Things, the system can access more accurate operation and maintenance data, which can better support the advanced applications of operation and maintenance.

References

1. Liu M, Hu S, Zhu X (2019) Analysis and display method of network monitoring business chain in smart substation. Autom Electr Power Syst (04):160–166
2. Xu Y (2012) Discussion on the integration plan of substation operation and maintenance. China Electr Power Educ (33):144–145
3. Gao T, Gao T (2013) Discussion on the integrated mode of operation and maintenance in overhaul. China Electr Power Educ (8):216–217
4. Wang H (2018) Analysis and practice of integrated operation and maintenance scheme for substation. Sci Technol Innov Herald (35):150–152
5. Zhou Y, Shen Y, Li Y (2018) Contrast of construction mode of centralized monitoring technology for substation operation and maintenance. Electron Technol Softw Eng (10): 131–133
6. Su Q (2016) Application of intelligent remote management system for substation operation and maintenance. Electron Technol Softw Eng (14):81
7. Song T, Feng C (2018) Application of substation intelligent assist system. Electron Technol Softw Eng (19):239–240

Publishing Technology Based on Multi-server for Distributed Fault Diagnosis Information

Dan Rao, Hualiang Zhou, Youjun Li and Yingrui Wang

Abstract Distributed line fault diagnosis system and information release technology are of great significance to grid security operation and maintenance. Combined with the development and application of the actual system, a multi-server based distributed fault diagnosis information security releases technology is proposed. From the source of device data to the end of publishing terminal, take various technical means such as security output, secure access, and network isolation to achieve information security. Real-time and consistency of data is achieved through multi-server deployment, physical isolation of servers, and real-time synchronization of heterogeneous databases. The principles of network security access and network isolation are described in detail. The security interaction between the monitoring center server and the mobile App server, information synchronization, module design and implementation methods are successfully certified by the China Electric Power Research Institute and implemented in Shanxi Province. High-voltage AC 1000 kV transmission line running on the network.

Keywords Extra high voltage (EHV) transmission line · Fault location · Transmission line measurements · Online monitoring system · Information safety

1 Introduction

Transmission lines of distribution network have such features: many points, long length, wide surface, complex network structure, distributed in the harsh environment of the wild, coupled with the tower, porcelain bottles, gold, distribution equipment are dispersed, all those make great difficulties when Inspecting of the equipment. In addition, in the actual running, the equipment often suffer from natural disasters (lightning strikes, torrential rain, heavy snow, heavy winds, other extreme weather, birds and other factors) and external force damage (various of

D. Rao (✉) · H. Zhou · Y. Li · Y. Wang
NARI Group Corporation, Nanjing 211106, China
e-mail: roadan@sgepri.sgcc.com.cn

Y. Xue et al. (eds.), *Proceedings of PURPLE MOUNTAIN FORUM 2019-International Forum on Smart Grid Protection and Control*, Lecture Notes in Electrical Engineering 585, https://doi.org/10.1007/978-981-13-9783-7_82

construction, traffic accidents, human theft and other reasons), the damage cause the line grounding short-circuit tripping, and even the line broken, the line paralysis, resulting in a large area of power outage, which not only impact China's power grid stability, safety, but also affect the normal power supply, all those will bring some harm to the people's property and life.

Therefore, it is an important work to find out the fault point and repair the circuit in time, Domestic colleges (universities) and research institutions in transmission, fault location and location algorithm have been more in-depth research [1–5], Traveling wave location algorithm [6, 7] is relatively mature, however, with the development and research of network communication technology [8, 9] and security protection technology [10–13], the advantages of GRPS communication and 4G technology in communication capacity and efficiency are more and more widely used in the power industry. Especially the wide application of mobile phone App [14, 15], makes the operations more intelligent and information more convenient, improves quality of the fault diagnosis of the overall system.

Information publishing have two key technologies: One is information safety, how to publish information from intranet to extranet and meet the requirements of power safety. The other is the way to publish information to user and the contents in information. Now, the common way is short message. the information safety is mature in network domain, but in the power distribution domain, the technology is not be applied yet. In the short message notification method, the fault information is insufficient, and users must go to the monitoring center to obtain more information needed to locate the location of the terminal or line point where the fault occurs, the cause of the fault, fault waveform and other important data content. The process result in a long time to deal with the fault, the terminal has no liquid crystal display, event At the spot of the fault location, you can not read the data of device working condition, coordinate position and other information, the inconvenience information cause the operation and maintenance wasting long time and more people, affect the timely restoration of power grid.

2 Fault Diagnosis System Information Flow

2.1 Data Flow Framework

In the fault diagnosis system, data source comes from the line fault monitoring terminal, and the data is stored in the central station server, synchronized to the App server, and pushed to the mobile phone client.

Figure 1 depicts the data flow and data processing flow of a distributed fault diagnosis system. The terminal periodically sends the working condition information through GRPS/4G, and the pre-module periodically writes the working condition information into the database, and the one-way 104 protocol periodically sends the data from the database to the App server to provide the mobile client

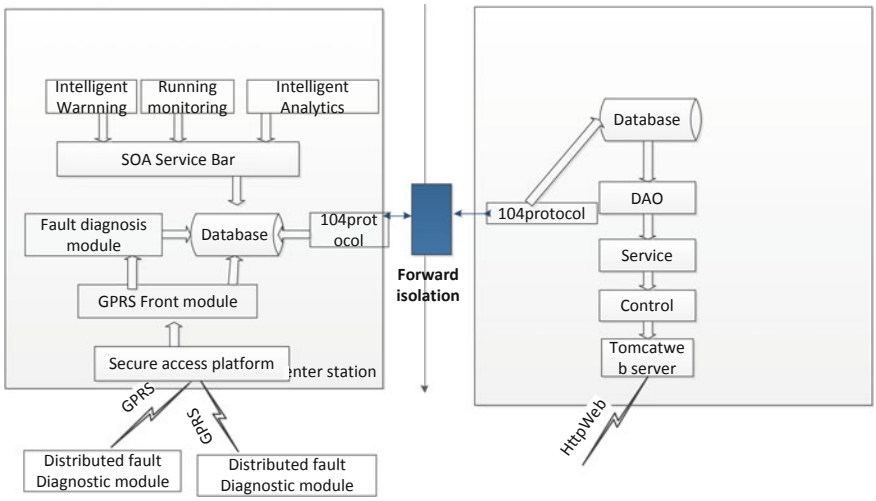

Fig. 1 Dataflow of diagnosis system

query. The monitoring terminal sends the fault waveform and the fault data through GPRS, and the GPRS pre-processing module notifies the fault diagnosis module to perform fault location and fault diagnosis through the message mechanism, the fault diagnosis module diagnoses the fault location according to the waveform data. Write the fault details to the database. And through the message bus service, the fault module send message to notify the alarm pop-up window, light on the GIS terminal corridor, 104 module real-time push fault report to the App server.

2.2 Data Security Access and Release

The line monitoring terminal is distributed according to the transmission line conductor, the power line data of the transmission line is collected, and the traveling wave current at the time of the fault is transmitted to the central station. The central station server is deployed on the internal network to prevent illegal links of the external network. The internal network is accessed by the monitoring terminal and the central station are physically isolated by accessing the security platform. The security platform is a non-transparent network gate. The dual-machine design is adopted to isolate the internal network connection part and the external network connection part through a physical isolation card. Both sides of the system use TCP port monitoring to proxy the internal and external network connections, and the external network part integrates the authentication and encryption functions of the monitoring terminal to judge the legality of the terminal connection and the message, thereby ensuring data confidentiality and integrity during data transmission.

The internal and external networks use virtual IP and NAT technologies to implement IP access to different network segments. The so-called virtual IP is to virtualize an IP address of the intranet in the isolation device. For the external network IP, virtualize the IP address of the external network to the intranet IP, so that the intranet host can access the virtual IP of the external host. The purpose of accessing the external network host, and the external network host can also access the virtual IP of the internal network host to access the intranet. As shown in Fig. 2, when the client of the intranet host initiates a TCP connection to the external host server, the source IP address of the packet is 192.168.0.39, and the destination IP address is the virtual IP address of the external host 192.168.0.1. After NAT is translated, the source IP address of the packet arriving at the external network is the virtual IP address 202.102.93.1 of the intranet host, and the destination IP address is the IP address of the external host 202.102.93.54. The source IP address of the TCP response packet from the external host to the internal host is 202.102.93.54, the IP address of the external host. And the destination IP address is the virtual IP address 202.102.93.1, the IP address of the internal host. After the NAT of the isolation device, the source IP address of the response packet arriving at the internal network is the virtual IP address 192.168.0.1, the IP of the external network host, and the destination address is the IP address of the internal network host 192.168.0.39.

The App server is a server connected to the mobile client through the wireless public network, and the concurrent external network connection of the multi-client is oriented. The central station internal server and the external network server pass the one-way data transmission through the forward security isolation device, and isolate the TCP connection of the external network server. Prevent untrusted link from passing and attacking on the intranet central station data server. The App server is connected to the internal network and the external network through dual network cards, and the internal network and the central station server are isolated by a one-way isolation device. The unidirectional isolation device also physically separates the two networks through the dual-board, and the physical connection between the dual-boards through the high-speed physical transmission chip.

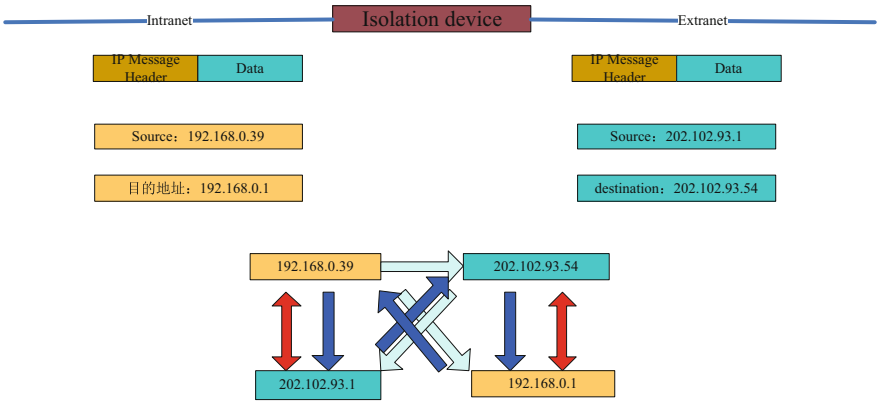

Fig. 2 IP NAT exchange example

The security isolation device implements the one-way transmission control of TCP: the reverse TCP response prohibits carrying application data, and the application layer has a response byte of at most 1 byte. The isolated data transmission application prohibits the use of SQL commands to access the database and is based on Bidirectional data transmission in B/S mode. The start of the transmission is initiated by the intranet central station, and the reverse response message is not allowed to carry data. The response message is in the state of all 0s or all 1s of 1 byte. The data center station uses a one-way 104 protocol to transmit packets to the App server. App server messages cannot penetrate the isolation device to the central station server.

2.3 *Reliable Data Synchronization and Backup*

After the monitoring center server and the App server pass through the isolation device, data transmission and synchronization are periodically scheduled through the one-way 104 TCP protocol. The central station server database includes a line information table, a device information table, a tower table, a line fault record table, terminal fault information, and a fault waveform.

The line information, the tower information, and the distributed fault terminal information are unidirectionally synchronized to the mysql database of the App application server by means of a one-way 104 protocol using a timed (daily) update.

As shown in Fig. 3, when a line fault or a terminal fault occurs, the application sends a message to notify the central station service program, and the central station service program transmits the line fault message (and the recorded wave file) to the

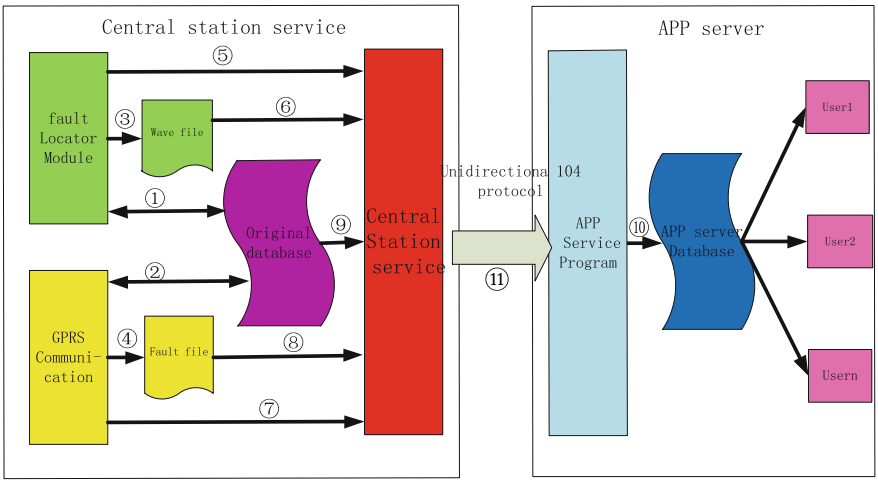

Fig. 3 Synchronous workflow of information

App service program through the one-way 104 protocol. After the App service obtains the information, it is stored in it's own mysql database and local disk, and the line fault information is pushed to the mobile phone user.

The monitoring center adopts active and standby dual-system redundant backup, and uses the file management service to provide cross-machine reading and writing by encapsulation of network access. Real-time monitoring of the data synchronization function of the redundant dual-machine. The file service process provides complete disaster recovery and fault handling capabilities to ensure system data reliability and security.

3 Monitoring System Data Processing Key Technology

3.1 Basic Functions of the Monitoring Center

The monitoring operation and maintenance center is mainly responsible for collecting and storing, analyzing and displaying various operational information of the diagnostic terminal of the transmission line, including pre-processing, fault diagnosis module, GIS module and advanced core modules.

Pre-module: Data exchange with the line terminal through a dedicated protocol, parsing and sending messages.

Fault diagnosis module: The Pre-module transmits the speed-sampling waveform to the fault diagnosis module through the message queue, and the fault diagnosis module accurately locates the fault by the effective extraction of the traveling wave signal and the accurate judgment of the starting time of the traveling wave head.

GIS module: draw the terminal trace diagram of the whole line by the coordinate position of the tower, the coordinate position of the terminal, the tower and terminal serial number. And when the fault happen, the exact fault location will be marked on the line.

Database and advanced applications: The monitoring center station is based on the SOA integrated monitoring architecture development. The database is divided into real-time database and historical database, providing rich data access interfaces and strategies, and advanced applications such as working condition curve drawing, fault statistics and analysis based on historical database.

3.2 Fault Process Module

The processing flow of the data processing module includes: reading the tower information table of the database; receiving the fault recording path, parsing the corresponding commodity file and synthesizing the total fault recording file; performing polarity determination on the registered device, determining the fault

interval, and selecting Performing a two-terminal device for ranging; extracting features of the waveform, analyzing whether the fault satisfies the characteristics of non-lightning strike, direct lightning strike, and lightning strike to determine the fault type; and performing wavelet transform on the fault waveform to extract the accurate time of the wave head; According to the corresponding formula, calculating the distance measurement result; according to the ranging result, getting the distance between the tower near the fault point and the distance from the fault point; writing the final test result into the system history database, and pushing the alarm information. The flowchart is as shown in Fig. 4.

3.3 One-Way 104 Protocol

The standard IEC 104 protocol is a two-way transmission power industry protocol based on TCP/IP. It is mainly used to transmit remote signaling and telemetry data. The reverse transmission is blocked by isolation, and only TCP push packets sent by the monitoring center server are allowed. The protocol transmits remote and telemetry data based on the point-number table mode. It does not support fixed value, fault information with fault transmission and waveform file transmission.

The system needs to transmit fault information, as well as waveforms of line faults and device faults. ASDU is applied to the standard IEC104 protocol, extend "ASDU2A" type for transmission line failure, extend of "ASDU2B" type for transmission line fault waveform, extend "ASDU2C" transmission device fault waveform. As shown in Fig. 5.

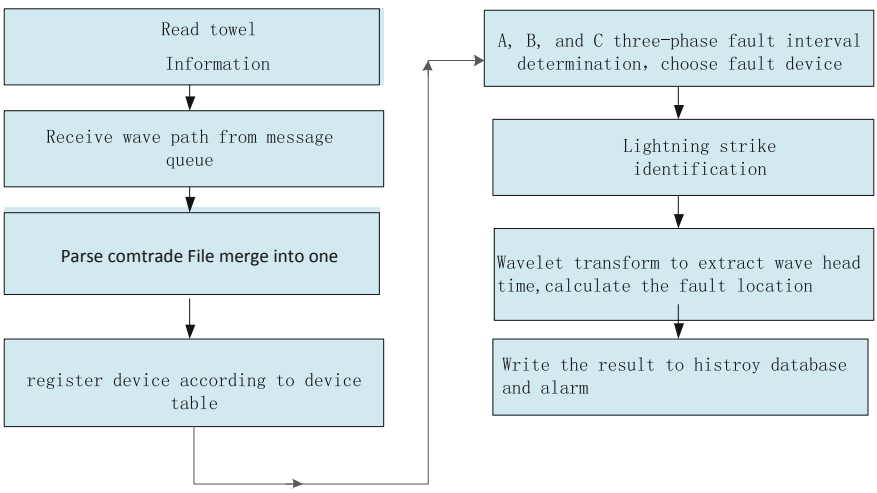

Fig. 4 Workflow of fault process

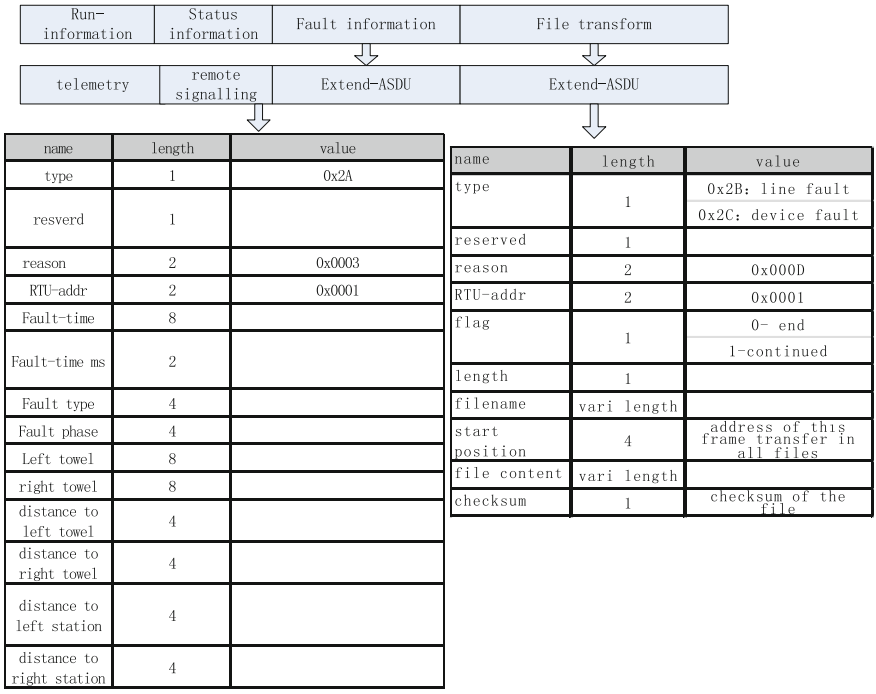

name	length	value
type	1	0x2A
resverd	1	
reason	2	0x0003
RTU-addr	2	0x0001
Fault-time	8	
Fault-time ms	2	
Fault type	4	
Fault phase	4	
Left towel	8	
right towel	8	
distance to left towel	4	
distance to right towel	4	
distance to left station	4	
distance to right station	4	

name	length	value
type	1	0x2B: line fault 0x2C: device fault
reserved	1	
reason	2	0x000D
RTU-addr	2	0x0001
flag	1	0- end 1-continued
length	1	
filename	vari length	
start position	4	address of this frame transfer in all files
file content	vari length	
checksum	1	checksum of the file

Fig. 5 Extension of IEC104

4 App Mobile Operation and Maintenance Key Technology

4.1 App Operation and Maintenance System Basic Module

The main functions of the App operation and maintenance server are: receiving the working condition information, fault information and message information pushed by the central station, storing the information to the database; responding to the request of the mobile client and actively pushing the fault data; maintaining the user information who have the authority to access the server. The App operation and maintenance system is divided into a front module and a back module. The front module mainly includes mobile phone applications and server system maintenance programs. The back module mainly includes a one-way 104 protocol module and a web server background processing module.

One-way 104 protocol processing module: The protocol processing module of the one-way 104 includes point table mapping, protocol receiving and processing. The point table file is offline synchronized, and the point table file includes a dot number, a table name, a description and the mapping relationship between the data items and the protocol information, the databases filled by the point table mapping.

The protocol processing is to update the value of the data item after receiving the 104 protocol message by mapping the database location after the information body.

Web server back-end processing module: The back-end processing module adopts SSM (Spring+SpringMVC+MyBatis) three-tier system. The whole system is divided into a presentation layer, a control layer, a service layer, and a DAO layer. SpringMVC is responsible for request and view management, spring implements business object management, and myhabits is a wrapper for jdbc, which makes the underlying operations of the database transparent and responsible for the object persistence engine.

4.2 Dual Mechanism Notification

The notification mechanism of the failure notification includes SMS notification and web service push, the SMS notification is notified through the telecommunications operator network, and the web message is pushed through the protocol and net between the background service and the mobile client. The web information interaction is the client's active request, and the server responds passively because the server does not know the client's IP address and status. Due to the fault information data is very emergent and important, it must be sent to the client. The small-cycle polling method of the client Pull add consumption of mobile phone power and mobile Internet data. The mobile terminal must establish a long-term data flow link with the server. Send the data just when it have data. If there is no data, no mobile Internet traffic is consumed. Due to the limited IP of IPv4, the mobile phone connects to the Internet, and the address is translated by the carrier gateway NAT (Network Address Transaction). If there is no data communication for a period of time, the NAT corresponding item will be eliminated according to the policy, resulting in the link terminal, and the server cannot obtain the client IP. In order to prevent NAT from failing, in the mobile client, through the RTC management module, when the scheduled time arrives, the CPU is woken up, the heartbeat task is executed, and the external network IP is maintained. When the server has fault information need to be send, it is sent to the authorized client group through the custom message body organization for the json object. When the server checks that the push fails, the SMS short message push is started to ensure that the user receives the fault information in a timely and effective manner.

4.3 App Upgrade Release and Deployment

Distributed fault diagnosis for the deployment status of multiple provinces, the system is deployed to different provinces at the same time, and the login IP of the province can be flexibly added and modified without affecting the user's use. The App servers includes one center server and many provincial-distributed servers.

centre server Deployed in the factory, the provincial servers are deployed in the provincial companies. The centre server is responsible for the release and relocation of the mobile app. The new version of the App is released in the centre server. When the version function is updated, the App is prompted to update from the center server. According to the province selected by the user, the centre server returns the provincial company server IP address, and the App client establishes a secondary connection according to the returned IP address. User authentication and permission information are deployed in each province and each province server is physically isolated. Only authenticated users can make a valid connection. The user who outside the authority cannot connect to the server, it ensure the security and reliability of the server connection.

5 Engineering Application

The 1000 kV Henghong I/II line is a cross-regional line, which is jointly maintained by Shanxi provinces. It is difficult to find the fault point after the line fault. The existing traveling wave and protection ranging products have low reliability and accuracy. To meet the requirements of finding the point of fault location, new technologies are needed. The distributed fault diagnosis system adopts distributed traveling wave measurement technology to greatly improve the positioning accuracy and reliability. Through the secure information release technology, the engineering operation and maintenance personnel can conveniently grasp the on-site information in real time by mobile phone.

The multi-server-based distributed fault diagnosis information release technology achieves the requirements of information security release by adding multiple hardware devices and link lengths, and also provides a media basis for coexistence of internal and external network data, based on this secure medium. It can mine more diagnostic applications and provide users with valuable predictions and warnings, which is the direction of subsequent in-depth research.

References

1. Jiang Z, Miao S, Liu P (2016) Fault observability model based fault location technique for transmission grids. Power Syst Prot Control 44(15):1–9
2. Gao Y, Zhu Y, Yan H, Chen X (2016) A new fault location method of transmission lines based on double-terminal traveling wave. Power Syst Prot Control 44(8):8–13
3. Shen H (2014) Research and application of distributed fault location and diagnosis system for transmission lines. Mech Electr Inf 1(8):134–136
4. Yao L, Yu L, Shi X et al (2015) Application of distributed intelligent fault dispute system in overhead transmission lines. Electrotechnical Appl S2:452–456
5. Huang Z (2013) Research and application of transmission line fault diagnosis technology based on distributed traveling wave location. Guangxi Electr Power 36(06):1–4

6. Li Z, Wu L, Tian B et al (2017) Traveling wave fault location using multi-point measurement information of regional power grid. Autom Electr Power Syst 41(8):146–152
7. Ye R, Wu H, Dong X (2019) Fault identification of double lines on same tower based on phase difference of initial traveling wave. Power Syst Prot Control 47(3):118–128
8. Zhao Z, Shi G, Han S et al (2009) A heterogeneous wireless sensor network based remote district high-voltage transmission line on-line monitoring system. Autom Electr Power Syst 33(19):80–84
9. Wang D, Chen C, Yan J et al (2016) Pondering a new-generation security architecture model for power information network. Autom Electr Power Syst 40(2):6–11
10. Gao L, Li S (2014) Improved identity-based authenticated key exchange protocols. Comput Eng 11(140):113–117
11. Ni M, Yan J, Bo R, Tang Y (2016) Power system cyber attack and its defense. Autom Electr Power Syst 5:148–151
12. Gao K, Xin Y, Li Z et al (2015) Development and process of cybersecurity protection architecture for smart grid dispatching and control systems. Autom Electr Power Syst 39 (1):48–52
13. Ding M, Li X, Zhang J (2018) Effect of SCADA-oriented cyber attack on power system reliability. Power Syst Prot Control 46(11):37–45
14. Cui Y, Wu Y, Zhang Z et al (2018) Intelligent mobile operation and maintenance technology and its application of relay protection based on power wireless virtual private network. Power Syst Prot Control 46(23):175–181
15. Gu K, Hu W, Zhao K et al (2018) Design and implementation of a hand-held device for power data acquisition and analysis based on mobile network. Power Syst Prot Control 46(8):110–116

Lean Management Method for Distribution Network Assets Operation and Maintenance Based on RFID

Qiong Liu, Peng Cheng, Jian Cao, Zhao Nan Zhou and Tao Zheng

Abstract Aiming at the problems of large workload, low efficiency of distribution network assets management and the inability of traditional technical which means to meet the requirement of lean asset management brought by the rapid expansion of distribution network scale, a lean management method for distribution network assets operation and maintenance based on RFID is proposed by studying the RFID tags direct scanning technology, internet of things technology, big-data processing technology. The proposed method has been applied to the lean management system for distribution network assets operation and maintenance. The pilot application in some cities indicates that with the traditional methods of power network assets management, the proposed method can achieve the functions of real-time access, maintenance and data verification of distribution network assets, ensure the consistency, real-time and synchronization of distribution network assets information, reduce the workload of distribution network assets information management, and can significantly improve the accuracy of asset information and the ease of control in the process of operation and maintenance.

Keywords RFID · Internet of things · Distribution network assets management · Ubiquitous power internet of things

Q. Liu (✉) · P. Cheng · J. Cao · Z. N. Zhou · T. Zheng
NARI Group Corporation/State Grid Electric Power Research Institute, Nanjing 21000, Jiangsu, China
e-mail: liuqiong@sgepri.sgcc.com.cn

Q. Liu · P. Cheng · Z. N. Zhou · T. Zheng
NARI Technology Co., Ltd., Nanjing 21000, Jiangsu, China

J. Cao
China Real-Time Database Company Limited, Nanjing 21000, Jiangsu, China

Y. Xue et al. (eds.), *Proceedings of PURPLE MOUNTAIN FORUM 2019-International Forum on Smart Grid Protection and Control*, Lecture Notes in Electrical Engineering 585, https://doi.org/10.1007/978-981-13-9783-7_83

1 Introduction

With the in-depth development of the Chinese national electric power reform, the strategic goal of "Three Types, Two Networks" and the development of "Strong Smart Grid, Ubiquitous Power Internet of things" [1], the Chinese national grid vigorously implements the construction and transformation of the distribution network, which has faced many problems. (1) There are too many kinds and quantities of distribution network equipment. Traditional inventory work is too heavy and inefficient. The equipment records and real property information can't be updated accurately in time [2]. (2) The lack of tracking and management technology means for the whole process of equipment installation, maintenance and scrap, resulting in low utilization rate of assets and high risk of loss [3]. (3) The operation and maintenance of the distribution network is mainly based on offline inspections, planned maintenance, and other offline modes. Lack of real-time access to equipment assets and operational information means that it is unable to obtain status of equipment and environment in real time, and cannot effectively support on-site work such as inspection and repair of daily equipment of the distribution network [4]. (4) Traditional technology can no longer meet the requirement of lean asset management brought by the rapid expansion of distribution network scale. It is urgent to apply new technology means to solve these problems faced by distribution network assets management. Reference [5] introduces Radio Frequency Identification (RFID) technology, describes the important role of RFID in the construction of the Internet of Things, and presents the application of RFID technology in monitoring, asset management and other aspects. Reference [6] uses advanced and reliable Internet of Things RFID technology and wireless communication technology, to realize the functions of distribution equipment management and equipment condition assessment management to ensure the safe and stable operation of equipment. According to the policy for developing smart charging and swapping service network. Reference [7] is proposed a method which through integration of RFID, sensor network and a variety of communication technologies, combined with context information of time and position for vehicles, resource status information, service settlement information and etc. As the result, the whole process of automatic management of vehicle service is formed.

In view of the above problems, a lean management method for distribution network assets operation and maintenance based on RFID is proposed, combined with RFID tags direct scanning technology, internet of things technology, big-data processing technology etc. The proposed method can achieve the functions of real-time access, maintenance and data verification of distribution network assets, ensure the consistency, real-time and synchronization of distribution network assets information, reduce the workload of distribution network assets information management, and can significantly improve the accuracy of asset information and the ease of control in the process of operation and maintenance. The proposed method can solve the lack of whole process tracking management for equipment installation, maintenance, scrap and the other, as well as the lack of technical means to

grasp equipment assets and operation information in time. At the same time, it can also solve the problems of timely update of assets information, low utilization rate of assets and high risk of loss.

2 Key Technology

2.1 Radio Frequency Identification (RFID)

Radio Frequency Identification (RFID) is a non-contact automatic identification technology. The reader realizes the exchange of device information by reading and writing electronic tags. With the development of RFID tag technology, tag fusion intelligent sensor has become a new trend. The application of sensor labels can effectively solve the problems which is difficult to collect environmental information such as temperature, humidity, water level and access control of distribution facilities such as ring main unit, cable branch boxes, switching stations and standardized stations, and provide data basis for intelligent operation and fine management of distribution network.

RFID tag encryption is an important measure to prevent information leakage, data tampering and forgery of distribution network assets. It is also an inevitable requirement to avoid misoperation of field operation and maintenance personnel, and ensure accurate decision-making of production management system. Dealing with the security of RFID is more challenging than dealing with the network security of computer systems. That is for the following two reasons: (1) The data transmission of RFID system is wireless, which is easier to be eavesdropped; (2) Because of the low cost, the computing power of the tags cannot be very high, so the data security is not guaranteed. The existing security solutions of RFID system can be divided into two categories: The first is to prevent the communication between tags and readers through physical methods; The second is to increase the security mechanism of tags through logical methods.

2.2 Internet of Things Technology

The Internet of Things (IOT) enables objects to communicate with the outside world and become “intelligent objects”. Technology includes perception layer, network layer and application layer. The perception layer consists of data acquisition sub-layer, short distance communication technology and collaborative information processing sub-layer. Data acquisition in IOT involves sensors, RFID, multimedia information acquisition, two-dimensional code and real-time positioning technology. The network layer transmits all kinds of information from the perception layer to the application layer through the basic bearer network.

The application layer provides general basic services such as information processing, intelligent computing, data analysis and so on to realize the application of IOT in many fields [8].

3 Design of Lean Management Method for Power Network Assets Operation and Maintenance Based on RFID

Based on the technology of RFID, IOT and the big-data processing, the proposed method reads the content of RFID tags through handheld mobile terminals, and enters the data into the lean management master station of distribution network assets operation and maintenance through 4G network. Through the lean management master station of power network assets operation and maintenance, the verification task and corresponding information of power network assets are sent to the handheld mobile terminal. The handheld mobile terminal feeds back the verification information to the management master station by scanning the content of the on-site RFID tag, so as to verify the accuracy of the data of the on-site equipment in real time.

3.1 System Architecture

Lean management system of distribution network assets operation and maintenance based on RFID includes management master station and assets operation and maintenance equipment. Asset operation and maintenance equipment includes RFID tags on distribution network assets and handheld mobile terminals for reading the contents of RFID tags. The handheld mobile terminal is connected to the management master station through secure access platform and 4G wireless network. Handheld mobile terminals acquire distribution network assets information through RFID tags and send it back to the management master station synchronously, so as to achieve the consistency between the field distribution network assets information and the management master station assets information. Management master station sends operation and maintenance task information to distribution network assets through handheld mobile terminal (see Fig. 1).

Management master station. The management master station includes asset management module, task information management module, operation and maintenance task delivery module, and operation and maintenance information analysis module. The asset management module is used to manage the physical information and operational information of distribution network assets. The task information management module is used to manage task information. The operation and maintenance task delivery module is configured to send operation and maintenance

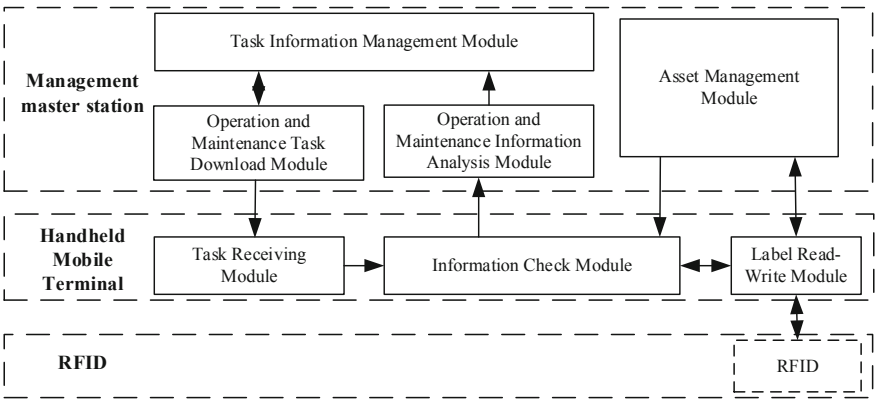

Fig. 1 System architecture

task information to the handheld mobile terminal. The operation and maintenance information analysis module is used to analyze the operation and maintenance information returned by the handheld mobile terminal, including the statistics of the field asset information errors and the statistics of the device loss.

Handheld mobile terminal. The handheld mobile terminal includes task receiving module, information checking module and tag reading-writing module. Task Receiving Module is used to receive the task information from the management master station. The information verification module is used to verify whether the information of field distribution network assets is consistent with the information of distribution network assets in the asset management module. The tag reading-writing module is used to read and write the contents of RFID tags. Among them, "write" means to write the distribution network assets information in the asset management module into the RFID tags, and "read" means to display the content of the RFID tags and send it back to the asset management module. The handheld mobile terminal is connected with the management master station through secure access platform and 4G network. The system supports mobile terminals to return the field operation data to the master station in two ways: (1) to return the field operation information to the master station in quasi-real time, prompt the operation steps and save or transmit the results in time according to the different types of field operation; (2) to support off-line mode for field operation, and to upload information with the master station in the case of 3/4G network or WIFI.

RFID tags. RFID tags can be passive or active. Among them, passive RFID tags are non-contact automatic identification, anti-metal, high reliability, encryption, high security, and expandable storage capacity. Active RFID tags can read farther and can fuse sensor devices. With the development of RFID tag technology, tag fusion intelligent sensor has become an application trend. The application of sensor labels can effectively solve the problems which is difficult to collect environmental information such as temperature, humidity, water level and access control of

distribution facilities such as ring main unit, cable branch boxes, switching stations and standardized stations, and provide data basis for intelligent maintenance of distribution network and fine management.

By reading the content of RFID tags, handheld mobile terminals can acquire distribution network assets information and realize real-time access to equipment records. The management master station receives the information of distribution network assets returned by the handheld mobile terminal, and realizes the real-time input of power network assets account. Manage the master station to send the verification task information and the corresponding grid assets information to the handheld mobile terminal. The handheld mobile terminal scans the content of the RFID tags, feeds back the verification information to the management master station, and achieves the verification of distribution network assets information.

3.2 Business Process of Real-Time Entry Function of Power Network Assets Record

Step 1. The tag reading-writing module of the handheld mobile terminal is used to identify the content of RFID tags on distribution network assets and obtain the physical information of distribution network assets.
Step 2. Through the handheld mobile terminal, real-time detection of distribution network assets on-site data and synchronous return of management master station are carried out.
Step 3. The management master station manages the physical information of distribution network assets and maintains the operation information through the asset management module.
Step 4. By interacting with the management master station in real time, the handheld mobile terminal acquires the information of grid assets in the management master station, including physical information and operation information.
Step 5. The handheld mobile terminal of distribution network assets maintenance writes the information of distribution network assets acquired from the management master station into the RFID tags through the tag reading-writing module.

3.3 Business Process of Real-Time Access Function for Power Network Assets Record

Step 1. The tag reading-writing module of the handheld mobile terminal is used to identify the content of RFID tags on distribution network assets and obtain the physical information of distribution network assets.

Step 2. The tag reading-writing module of the handheld mobile terminal reads the specific asset information of the related equipment in the management master station through the device information.

3.4 Business Process of Information Verification Function for Power Network Asset

Step 1. The management master station sends the verification task information and the corresponding grid asset information to the handheld mobile terminal of grid assets maintenance through the maintenance task sending module. Among them, the verification task information includes task time, executor, execution team, plan completion time, task package name, and distribution network asset information include asset ID, asset name, operation information and physical information.
Step 2. The task receiving module of handheld mobile terminal receives the verification task information from the management master station through wireless network.
Step 3. According to the task content, the information verification module of the handheld mobile terminal scans the RFID tags content through the tag reading-writing module and manually checks the field data. Then, the module compares the field data with the data in the asset management module from the management master station, and synchronously transmits the comparison results back to the master station to complete the field verification task. Among them, the verification results include normal, inconsistent information, absence of field equipment, and specific description.
Step 4. The management master station conducts real-time fault diagnosis through online calculation of big data backstage. The information analysis module of operations and maintenance statistical analysis of field feedback verification information and check processing. At the end of the processing, modify the processing status to "processed" and fill in the processing operation information.
Step 5. Through the task information management module, the management master station manages the task information including task executor, completion time and so on.

4 Practical Application

According to "Smart Grid Promoted by the New Information and Communication Technologies" and "One Strong Three Excellences"—the modern company innovation and development strategy of the Chinese State Grid Corporation, Ningbo Power Supply Company was selected to indicate pilot application.

Table 1 Application results

Time consuming	Traditional method	This paper
Maintenance of distribution station room/station	1.5 h	3 min
Maintenance of line/kilometers	5–10 h/km	<2 h/km
Maintenance of all equipment	3 months	20 days

On the basis of stock assets management, the management and application of incremental assets are carried out. Through checking the assets information of 50 power lines and affiliated distribution equipment, and installing the RFID tags in 20 power lines, the basic information collection of 27 kinds of power distribution network equipment such as medium voltage cables, distribution stations and ring main unit under these power lines in the demonstration area is carried out with single-hop lines as the unit. Through clearing up and checking the basic data of more than 3000 distribution network equipment and subsequent timely maintenance work, the distribution network assets and equipment have been successfully sorted out and mastered. The average maintenance time of distribution station record is reduced from 1.5 h to 3 min. The operation and maintenance of line can save 0.3 man-h/km, and the efficiency of field operation is greatly improved (Table 1).

5 Summary

Through the RFID tags direct scanning technology based on IOT, the proposed lean management method for distribution network assets operation and maintenance based on RFID could input, access and verify grid assets information by handheld mobile terminals directly, could get high efficiency in the distribution network assets information management, and could effectively ensure the consistency, timeliness and synchronization in the information between on-site distribution network assets and the management master station assets.

Through the handheld mobile terminal, the proposed method could detect the field data of the equipment in real time, synchronously return the data to the management master station, and view the real-time operation data of the distribution network online.

Through the online calculation of big data backstage, real-time fault diagnosis can be made, and the results can be fed back to the mobile terminal on site in real time to help the operation and maintenance personnel deal with faults on site.

With the function of distribution network assets information analysis, the proposed method is easy to carry out error data statistics and loss statistics of distribution network assets information, reduce the workload of distribution network assets account management, significantly improve the accuracy of account and easy to control in the process of operation and maintenance.

Acknowledgements This work was supported by the project of "Study and application of multi-energy micro-grid source-network-load-storage coordinated control system" of NARI Group Corporation (State Grid Electric Power Research Institute).

References

1. Liu YH (2019) Construction of intelligent training ecosphere with high standard ubiquitous in power internet of things. State Grid News, 2019/03/28
2. Wang XZ, Zhou B, Chen X (2015) Discussion on optimization of maintenance plan for distribution network. Low Carbon World 71–72
3. Lu Y, Zheng L (2012) Application of RFID technology in fixed assets management of Guangdong power grid. Friends Account (12):53–55
4. Song YL, Song YF (2019) Intelligent patrol technology of distribution network based on RFID. Electron Technol Softw Eng (4):82
5. Yang YB, Ding XH, Zhu JD, Bai YZ (2010) Assumption of internet of things applied in electric vehicle charging facilities. Autom Electr Power Syst 34(21):95–98
6. Li L (2015) Research on intelligent distribution patrol system based on RFID technology. Changchun University of Technology, China
7. Xue F, Lei XZ, Zhang XS, Liu HC (2013) A managing system based on RFID and context awareness for electric vehicle charging and swapping stations. Autom Electr Power Syst 37 (8):41–45
8. Hu YL, Sun YF, Yin BC (2012) Information perception and interaction technology in internet of things. Chin J Comput (6):1147–1163

Research on Construction of Infrared Image Classification Model of Substation Equipment Based on CNN

Kehui Zhou, Zhiwei Liao and Xiaochun Zang

Abstract Infrared Intelligent detection is the key research direction of infrared fault detection of power equipment. However, different types of equipment and different processing purposes lead to a variety of fault detection methods. If the manual method is used to classify the equipment, the efficiency of fault detection will be greatly reduced. In this paper, based on convolutional neural networks, based on RGB and HSV color space conversion, a classification model suitable for infrared images of power equipment is constructed. Firstly, the structure characteristics and training process of CNN are introduced. After that, based on RGB and HSV color space conversion, the infrared image of substation equipment is processed, and the target area of suitable size is extracted to establish network training and test set. Finally, a CNN-based infrared image classification model is established, and its good applicability is verified by case analysis.

Keywords Substation equipment · Infrared detection · CNN · Image processing · Image classification

1 Introduction

As an essential element of power system operation, electrical equipment analysis is a powerful guarantee for the stable operation of power systems [1]. Infrared detection technology based on the principle of infrared radiation has become the necessary means for daily maintenance of electrical equipment with the advantages of non-contact, high efficiency and intuitive image. It plays an important role in the state detection of devices such as arresters, circuit breakers and insulator strings [2–4]. However, the current technology also has the disadvantages of excessive human factors and low intelligence. With the rise of inspection robots and intelligent substations [5], infrared detection technology based on image processing and

K. Zhou (✉) · Z. Liao · X. Zang
School of Electric Power, South China University of Technology, Guangzhou, China
e-mail: 2903807982@qq.com

Y. Xue et al. (eds.), *Proceedings of PURPLE MOUNTAIN FORUM 2019-International Forum on Smart Grid Protection and Control*, Lecture Notes in Electrical Engineering 585, https://doi.org/10.1007/978-981-13-9783-7_84

machine learning has become a development trend. The literature [6, 7] propose to use the partial feature aggregation description vector as the fully connected layer of the deep learning network to mark the insulator string in the infrared image. In [8], the temperature histogram of the infrared image of the arrester is proposed to extract the characteristic quantities such as the highest temperature, average temperature and temperature standard deviation, which are used as part of the neural network input to determine the state of the leakage current of the arrester.

From the above literature analysis and summary, different types of equipment and different processing purposes lead to diversity in method selection, both in image processing method selection and in machine learning method selection. If selecting the processing method flow according to the traditional manual classification result is still adopted, the infrared detection process will be further complicated. Therefore, it is imperative to introduce image classification into the infrared detection, which is helpful to greatly improve the intelligence degree. The image classification method based on Convolutional Neural Network (CNN) has gained extensive attention, research and application due to its excellent performance in multiple image classification competitions [9, 10]. In [11], based on the characteristics of each layer of convolution-al neural network, an insulator detection method based on cross-connected convolutional neural network is proposed. In [12] proposed a method for image recognition of power equipment combined with deep learning and random forests to solve the problem of intelligent analysis and identification of massive unstructured image data. Based on the convolutional neural network, this paper explores and constructs a classification model suitable for infrared images of power equipment. Firstly, it introduces the structural characteristics and training process of CNN. Then, an infrared image preprocessing method for equipment classification is proposed. Based on this, a network of the training and test is established. Finally, the good applicability of the CNN-based infrared image classification model is verified from the classification accuracy and classification efficiency by examples.

2 The Structure and Principle of CNN

At the end of the last century, foreign scholars proposed a character recognition model based on CNN and achieved good results in handwritten digit recognition [13]. Then, with proposal of deep learning concept, the expansion of database scale and hardware development, CNN models with better recognition and deeper levels emerge in an endless stream. Overall, the basic structures of the network are still composed by input layers, convolution layers, excitation layer, pooling layer, fully connected layer and the output layer.

The CNN realizes image feature extraction through the alternating of the convolution layer and the pooling layer, wherein the convolution layer convolves the input image or the output of the upper layer through a learnable convolution kernel

to obtain a feature map. Each convolution kernel can convolve a combination of multiple feature maps, which is calculated as follows:

$$c_j^l = \sum_{i \in M_j} x_i^{l-1} \otimes k_{ij}^l + b_j^l \tag{1}$$

Wherein, c_j^l is the value of the l convolutional layer j channel, which is obtained by convolving the $l-1$ layer feature map; M_j is a c_j^l calculated feature atlas, which can be a combination of l layer feature maps; k_{ij}^l is a convolution kernel whose number determines the output characteristics of the layer; b_j^l is the offset. For each l layer output feature map, the convolution kernel corresponding to the calculated l layer feature map may be different, and $\otimes$ represents the convolution calculation. The formula is as follows:

$$S_{ij} \otimes K_{ij} = \sum_{i=1}^{m} \sum_{j=1}^{m} S_{ij} K_{ij} \tag{2}$$

Wherein, m is the convolution kernel size; K is the convolution kernel value, S is the input image or the feature map value. The convolution kernel traverses the entire image in a certain step size s to obtain a convolution result for the image.

Each feature map in the CNN greatly reduces the network parameters through the weight sharing and partial perception of the convolution kernel. It extracts the advanced features of the image through the combination of features from the bottom layer to the upper layer. The output of the convolutional layer is nonlinearly mapped by the excitation layer, and ReLU is the commonly excitation function in CNN. The pooling layer, also known as the lower layer, is usually located in the middle of a continuous convolution layer, which can reduce features and ensure partial invariance of features [14]. Common pooling methods are maximum pooling and average pooling. The maximum pooling usage is higher in reality. As shown in Fig. 1, the same color area is a pooled area (taking 2 × 2 cores as an example), and the maximum value in the area is taken as the output result and reconstitute the feature map.

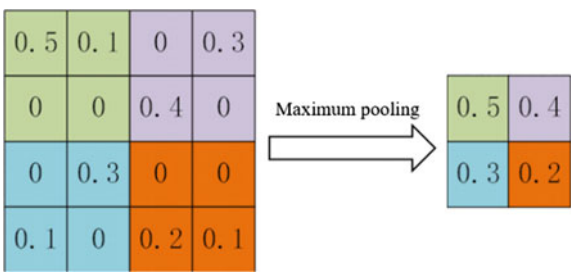

Fig. 1 The maximum pooling method

The fully connected layer is usually located in the upper layer of the CNN and is connected to each neuron in the previous layer. The weighted summation of the input feature map is spliced into a one-dimensional feature, which is equivalent to convolution with the same convolution kernel as the size and size of the previous layer, which is used to extract the advanced features of the image as input to the classifier. For classification tasks, the output layer is usually a classifier, with softmax being the most common [15].

CNN training is similar to traditional neural networks, used Gradient descent algorithm and backpropagation algorithm. The training process consists of forward propagation of signals and reverse propagation of errors. For forward propagation, the weights W and offsets b are first randomly initialized, and then the output values H of each layer are calculated based on the initialization data:

$$H = F(WX + b) \tag{3}$$

Wherein, H is the calculated output value for each layer; W is the weight matrix; b is the offset; F is the excitation function. The input data is calculated and transformed by each layer to obtain the final output layer data Y.

In the case of backpropagation, the difference E between the actual output and the expected output is calculated by constructing the error function. The form of E is related to the selected error function type and the gradient descent method. The commonly used error function is the sum of squared error functions. In the case of using small batch gradients:

$$E = \frac{1}{k}\sum_{i=1}^{k}\frac{1}{2}\sum_{j=1}^{m}(y_{ij} - t_{ij})^2 \tag{4}$$

Wherein, k is the number of samples in each mini-batch; m is the number of output neurons; t is the expected output. Among them, the small batch gradient descent method refers to dividing all samples equally into multiple Mini-batch, and each parameter updating process uses one of them to calculate, which has the advantages of both speed and accuracy. Update the weight and offset by gradient descent so that the output of the network reaches or approaches the desired output. The update formula is:

$$\begin{aligned} W^{(i+1)} &= W^{(i)} - \eta\frac{\partial E}{\partial W} \\ b^{(i+1)} &= b^{(i)} - \eta\frac{\partial E}{\partial b} \end{aligned} \tag{5}$$

Wherein, η is the learning rate [16].

3 Infrared Image Background Separation and Component Area Extraction

The number of devices in the substation is large and the distribution is dense. As a result of infrared image acquisition, the window not only contains the target equipment at the center position, but also includes many other surrounding equipment and supporting steel frame and other background interference, as shown in Fig. 2. The infrared image of the target device contains interferences such as current transformers, isolation switches and steel frames, which seriously affect the state judgment of the target equipment. If the original infrared image is directly applied for classification and judgment, it not only has high requirements on hardware such as computing resources, but also the accuracy of classification cannot be guaranteed. Therefore, with reference to the current infrared detection process, this paper first preprocesses the infrared image to improve the accuracy of classification and lay the foundation for the intelligent judgment of the subsequent device state.

3.1 Background Separation Based on RGB and HSV Color Space Conversion

In order to better extract the target area from the original image, the conversion of the RGB color space and the HSV color space is realized. The RGB color space is based on three basic colors of red, green and blue, and forms a rich color expression

Fig. 2 Original infrared image

by superimposing different components; The HSV color space is based on hue, saturation and value. The saturation refers to the degree of close to the spectral color, and the value ranges from 0 to 1. The larger the value, the higher the saturation, the darker the color, and the closer to the spectral color. The conversion relationship between the RGB color space and the saturation S in the HSV color space is:

$$S = \begin{cases} 0 & \max = 0 \\ 1 - \min/\max & \max \neq 0 \end{cases} \tag{6}$$

Wherein, $\max = \max(R, G, B)$, $\min = \min(R, G, B)$.

In the RGB color space, the R component is [255, 0, 0]. According to (6), it converts to the red saturation dimension value S = 1 in the HSV space. According to this feature, a number of vertices are selected in the original image, respectively marked and connected in red. The boundary is extracted and the enclosed area is filled and the unrelated interference is eliminated to obtain the target area, as shown in Fig. 3.

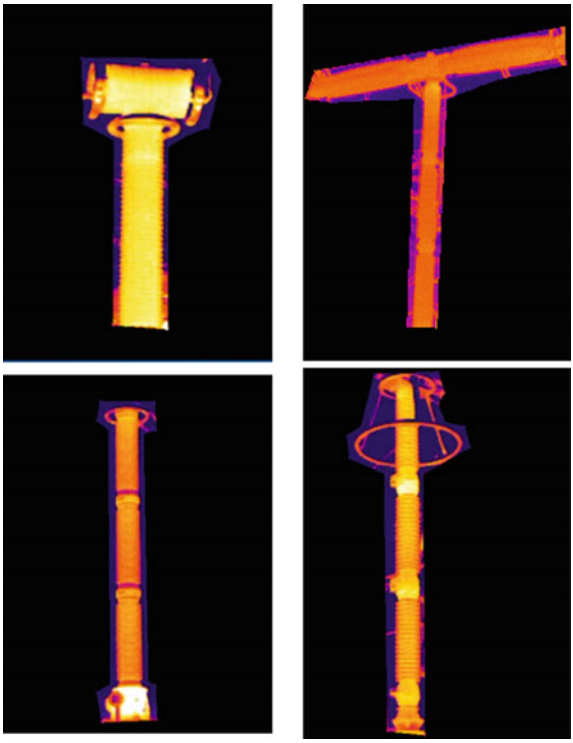

Fig. 3 Target area extraction

Fig. 4 Target area scaling

3.2 A Subsection Sample Target Area Scaling

Generally speaking, due to the different models of the infrared camera, the size of the infrared image captured is not the same. To unify the input image size and save computing resources, it is necessary to scale the target and retain the target information to the greatest extent. In this paper, we first detect the start and end rows, columns ($r_{\min}$, $r_{\max}$, $c_{\min}$ and $c_{\max}$) of the target area in Fig. 3, and extract the minimum rectangular outline of the target device, and then extend the image dimension to the adjacent square area with the center of the rectangular outline as the origin. Taking the image size of the MNIST dataset and the CIFAR10 dataset as a reference, this paper scales the extracted image of the target area of 300*300 to the size of 32*32 dimension, as shown in Fig. 4.

4 The Structure and Principle of CNN-Based Infrared Graphics Classification

4.1 Construction of a Training Set

Based on the image preprocessing method of Sect. 2, the original infrared images acquired in the substation are extracted and adjusted to appropriate sizes, which lay foundation to expand the scale of the training set, improve the applicability of the model, perform enhanced processing such as rotation and translation on the processed image and form a training set. This paper considers the classification of 7 types of 500 kV key equipment in substation, including arrester, circuit breaker, current transformer, voltage transformer, insulator string, isolation switch and high voltage casing. There are 1500 sheets of each training picture, a total of 10,500 pictures for training. Parts of the sample image is shown in Fig. 5.

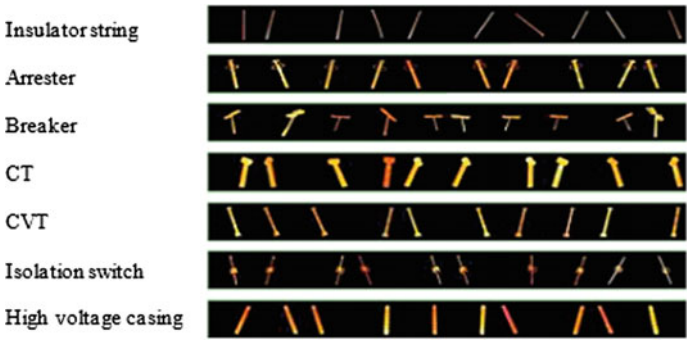

Fig. 5 Parts of the sample image

4.2 Network Construction

The infrared image classification CNN structure designed is as follows:

(1) Input layer-Input: input 32*32*3 the infrared image of the devices;
(2) Convolution layer-Conv1: the layer has 32 convolution kernels of 5*5, expanding the boundary of the input image in each direction by 2 pixels (Padding = 2) and moving step length is 1;
(3) The pooling layer-Pooing1: the layer adopts the maximum pooling; the pooling area size is 3 × 3 and the moving step size is 2;
(4) Convolution layer-Conv2: the layer has 32 convolution kernels of 5*5; Padding = 2 and the convolution kernel moves by 1 step;
(5) The pooling layer-Pooing2: the layer adopts the maximum pooling, the pooling area size is 3 × 3, and the moving step size is 2;
(6) Convolution layer-Conv3: the layer has 64 convolution kernels of 5*5; Padding = 2 and the moving step is 1;
(7) The pooling layer-Pooing3: the layer adopts the maximum pooling, the pooling area size is 3 × 3, and the moving step size is 2;
(8) Fully connected layer-FC1: output 64 one-dimensional features;
(9) Fully connected layer-FC2: output 7 one-dimensional features, which is the number of classifications;
(10) Output layer-Output.

There is a ReLU excitation layer between each convolution layer and the pooling layer. The network structure is shown in Fig. 6.

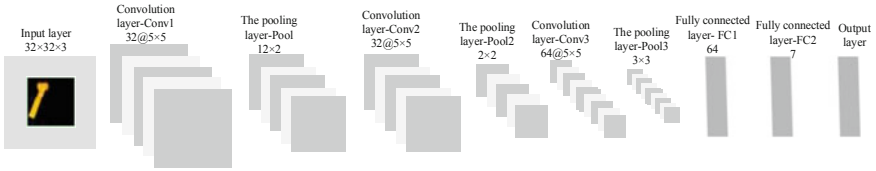

Fig. 6 The network construction

4.3 Network Training

This paper completes the construction, training and testing of CNN models on the MATLAB platform. MATLAB fully updated the neural network toolbox in 2017b version, which is more convenient for deep learning research and application from model construction, parameter setting and hardware support. As described above, after completing the CNN network structure construction, this paper uses the small batch gradient descent algorithm to train on the GPU, where the Min-batch size is set to 128, each Epoch contains 82 iterations, and the maximum iteration Epoch is set to 40. The training platform parameters are shown in Table 1.

After repeated adjustments to select appropriate training parameters, the iterative process of each step of the training process is shown in Fig. 7. As can be seen from the Fig. 7, the network training process is faster. After 20 steps of iteration, the recognition rate of each Mini-batch reaches 100%.

4.4 Case Analysis

After completing the network training, the selected part of the infrared image taken from the 500 kV substation is preprocessed to form a test set. Testing the network training result and the result is shown in Table 2.

From Table 2, the infrared image classification CNN of the substation key equipment designed and trained in this paper has a high recognition accuracy rate.

Table 1 The training platform parameters

Item	Parameter
System version	Windows 7 Ultimate SP1
CPU model	Intel(R) Core (TM) i5-4590
Memory	8G
GPU model	NVIDIA GTX750
Display memory	1G

Fig. 7 Training progress

Table 2 The network training result

Equipment type	Insulator string	Arrester	Circuit break	CT
Number	693	810	732	810
Error recognition	0	1	2	0
Total time (s)	6.99	10.67	11.16	12.64
Average time (s)	0.010	0.013	0.015	0.015
Recognition rate (%)	100	99.9	99.7	100
Equipment type	CVT	Isolation switch	High voltage casing	
Number	735	243	96	
Error recognition	0	0	0	
Total time (s)	10.54	3.44	1.30	
Average time (s)	0.014	0.014	0.014	
Recognition rate (%)	100	100	100	

On the test set of 4000 images, there are only three misidentification samples, which has achieved a recognition rate of 99.9%. It has a high operational efficiency comparable to that of the manual and is fully applicable to the level of practical work. It lays a solid foundation for the subsequent intelligent diagnosis of key equipment infrared images.

5 Conclusion

In this paper, the convolutional neural network is applied to the substation infrared detection work to assist and promote the development of intelligent state judgment based on infrared equipment. Aiming at the infrared image of the complex background in the substation, an image preprocessing method for target device extraction is proposed. And based on this method, the image database of 7 type of infrared devices including insulator string, arrester and circuit breaker are constructed. What's more, CNN structure for image classification is proposed. The test results show that the network structure has high recognition accuracy and operational efficiency.

With the gradual deepening of the standardization of infrared detection work, the way of high-quality infrared image acquisition is more diversified. The introduction of intelligent methods in the process of mass data processing is a research hotspot and development trend. With strong learning and generalization capabilities, CNN is widely favored in the field of computer vision. With the increasing and perfect computing resources and large-scale databases, its application in infrared detection and even power systems will be more extensive and in-depth.

References

1. Li G, Zhang B, Zhao WQ et al (2018) Data Science issues in state evaluation of power equipment: challenges and prospects. Autom Electr Power Syst 42(21):10–20
2. Jin LJ, Tian ZR, Gao K et al (2016) Discrimination of insulator contamination grades using information fusion of infrared and visible images. Proc CSEE 36(13):3682–3691
3. Lu ZM, Liang JC, Wang TZ et al (2015) Application of SF6 infrared imaging leakage detection technology in live detection for UHV. Insulating Mater 48(09):29–33
4. Zhang JG (2015) Application of infrared temperature measurement technology to live detection of zinc oxide arrester. High Voltage Apparatus 51(6):200–204
5. Chen AW, Yue QM, Zhang ZY et al (2012) An image recognition method of substation breakers state based on robot. Autom Electr Power Syst 36(06):101–105
6. Zhao Z, Xu G, Qi Y (2016) Representation of binary feature pooling for detection of insulator strings in infrared images. IEEE Trans Dielectr Electr Insul 23(5):2858–2866
7. Zhao ZB, Fan XQ, Xu GZ et al (2017) Aggregating deep convolutional feature maps for insulator detection in infrared images. IEEE Access 5:21831–21839
8. Abdul-Malek Z (2017) Electrical and temperature correlation to monitor fault condition of Zno surge arrester. In: International conference on information technology, computer, and electrical engineering, IEEE, pp 182–186
9. Krizhevsky A, Sutskever I, Hinton GE (2012) Imagenet classification with deep convolutional neural networks. In: International conference on neural information processing systems. Curran Associations Inc., New York, pp 1097–1105
10. Simonyan K, Zisserman A (2014) Very deep convolutional networks for large-scale imaged recognition [2014-4-20]. https://arxiv.org/abs/1409.1556
11. Zuo GY, Ma L, Xu CF et al (2019) Insulator detection method based on cross-connected convolutional neural network. Autom Electr Power Syst 43(04):101–108

12. Li JF, Wang QR, Li M (2017) Electric equipment image recognition based on deep learning and random forest. High Voltage Eng 43(11):3705–3711
13. LeCun Y, Bottou L, Bengio Y et al (1998) Gradient-based learning applied to document recognitio. Proc IEEE 86(11):2278–2324
14. Chang L, Deng XM, Zhou MQ et al (2016) Convolutional neural networks in image understanding. ACTA Automatica Sinica 42(9):1300–1312
15. Wei D, Gong QW, Lai WQ et al (2016) Research on internal and external fault diagnosis and fault-selection of transmission line based on convolutional neural network. Proc CSEE 36:21–28
16. Zhang GX, Hu Z (2011) Improved BP neural network model and its stability analysis. J Central South Univ (Sci Technol) 42(01):115–124